GEOTECHNICAL SPECIAL PUBLICATION NO. 178

GEOCONGRESS 2008

Geosustainability and Geohazard Mitigation

PROCEEDINGS OF SELECTED SESSIONS OF GEOCONGRESS 2008

EDITED BY
Krishna R. Reddy
Milind V. Khire
Akram N. Alshawabkeh

ASCE

GEO INSTITUTE

GEOTECHNICAL SPECIAL PUBLICATION NO. 178

GEOCONGRESS 2008

GEOSUSTAINABILITY AND GEOHAZARD MITIGATION

PROCEEDINGS OF SESSIONS OF GEOCONGRESS 2008

March 9–12, 2008
New Orleans, Louisiana

SPONSORED BY
The Geo-Institute of the American Society of Civil Engineers

EDITED BY
Krishna R. Reddy
Milind V. Khire
Akram N. Alshawabkeh

Published by the American Society of Civil Engineers

Library of Congress Cataloging-in-Publication Data

Geocongress-2008 (2008 : New Orleans, Louisiana)
Geosustainability and geohazard mitigation : proceedings of sessions of Geocongress 2008, sponsored by the Geo-Institute of the American Society of Civil Engineers March 9-12, 2008, New Orleans, Louisiana / edited by Krishna R. Reddy, Milind V. Khire, Akram N. Alshawabkeh.
p. cm. -- (Geotechnical special publication ; No. 178)
Includes bibliographical references and index.
ISBN 978-0-7844-0971-8
1. Environmental geotechnology--Congresses. I. Reddy, Krishna R. II. Khire, Milind V. III. Alshawabkeh, Akram N. IV. Title.

TD171.9.G44 2008
628.4--dc22 2008001082

American Society of Civil Engineers
1801 Alexander Bell Drive
Reston, Virginia, 20191-4400

www.pubs.asce.org

ISBN 978-0-7844-0971-8
Manufactured in the United States of America.

Geotechnical Special Publications

1 *Terzaghi Lectures*
2 *Geotechnical Aspects of Stiff and Hard Clays*
3 *Landslide Dams: Processes, Risk, and Mitigation*
7 *Timber Bulkheads*
9 *Foundations & Excavations in Decomposed Rock of the Piedmont Province*
11 *Dynamic Response of Pile Foundations–Experiment, Analysis and Observation*
14 *Geotechnical Aspects of Karst Terrains*
15 *Measured Performance Shallow Foundations*
16 *Special Topics in Foundations*
17 *Soil Properties Evaluation from Centrifugal Models*
18 *Geosynthetics for Soil Improvement*
19 *Mine Induced Subsidence: Effects on Engineered Structures*
21 *Hydraulic Fill Structures*
22 *Foundation Engineering*
23 *Predicted and Observed Axial Behavior of Piles*
24 *Resilient Moduli of Soils: Laboratory Conditions*
25 *Design and Performance of Earth Retaining Structures*
27 *Geotechnical Engineering Congress*
28 *Detection of and Construction at the Soil/Rock Interface*
29 *Recent Advances in Instrumentation, Data Acquisition and Testing in Soil Dynamics*
32 *Embankment of Dams–James L. Sherard Contributions*
33 *Excavation and Support for the Urban Infrastructure*
34 *Piles Under Dynamic Loads*
35 *Geotechnical Practice in Dam Rehabilitation*
37 *Advances in Site Characterization: Data Acquisition, Data Management and Data Interpretation*
39 *Unsaturated Soils*
40 *Vertical and Horizontal Deformations of Foundations and Embankments*
41 *Predicted and Measured Behavior of Five Spread Footings on Sand*
42 *Serviceability of Earth Retaining Structures*
43 *Fracture Mechanics Applied to Geotechnical Engineering*
44 *Ground Failures Under Seismic Conditions*
45 *In Situ Deep Soil Improvement*
46 *Geoenvironment 2000*
47 *Geo-Environmental Issues Facing the Americas*
48 *Soil Suction Applications in Geotechnical Engineering*
49 *Soil Improvement for Earthquake Hazard Mitigation*
50 *Foundation Upgrading and Repair for Infrastructure Improvement*
51 *Performance of Deep Foundations Under Seismic Loading*
52 *Landslides Under Static and Dynamic Conditions–Analysis, Monitoring, and Mitigation*
53 *Landfill Closures–Environmental Protection and Land Recovery*
54 *Earthquake Design and Performance of Solid Waste Landfills*
55 *Earthquake-Induced Movements and Seismic Remediation of Existing Foundations and Abutments*
56 *Static and Dynamic Properties of Gravelly Soils*
57 *Verification of Geotechnical Grouting*
58 *Uncertainty in the Geologic Environment*
59 *Engineered Contaminated Soils and Interaction of Soil Geomembranes*
60 *Analysis and Design of Retaining Structures Against Earthquakes*
61 *Measuring and Modeling Time Dependent Soil Behavior*
62 *Case Histories of Geophysics Applied to Civil Engineering and Public Policy*
63 *Design with Residual Materials: Geotechnical and Construction Considerations*
64 *Observation and Modeling in Numerical Analysis and Model Tests in Dynamic Soil-Structure Interaction Problems*
65 *Dredging and Management of Dredged Material*
66 *Grouting: Compaction, Remediation and Testing*
67 *Spatial Analysis in Soil Dynamics and Earthquake Engineering*
68 *Unsaturated Soil Engineering Practice*
69 *Ground Improvement, Ground Reinforcement, Ground Treatment: Developments 1987-1997*
70 *Seismic Analysis and Design for Soil-Pile-Structure Interactions*
71 *In Situ Remediation of the Geoenvironment*
72 *Degradation of Natural Building Stone*
73 *Innovative Design and Construction for Foundations and Substructures Subject to Freezing and Frost*

137 *Legal and Liability Issues in Geotechnical Engineering*
138 *Site Characterization and Modeling*
139 *Calibration of Constitutive Models*
140 *Slopes and Retaining Structures under Seismic and Static Conditions*
141 *International Perspectives on Soil Reinforcement Applications*
142 *Waste Containment and Remediation*
143 *Geomechanics: Testing, Modeling, and Simulation*
144 *Sinkholes and the Engineering and Environmental Impacts of Karst*
145 *Seismic Performance and Simulation of Pile Foundations in Liquefied and Laterally Spreading Ground*
146 *Asphalt Concrete: Simulation, Modeling and Experimental Characterization*
147 *Unsaturated Soils 2006*
148 *Advances in Unsaturated Soil, Seepage, and Environmental Geotechnics*
149 *Site and Geomaterial Characterization*
150 *Soil and Rock Behavior and Modeling*
151 *Advances in Earth Structures: Research to Practice*
152 *Ground Modification and Seismic Mitigation*
153 *Foundation Analysis and Design: Innovative Methods*
154 *Pavement Mechanics and Performance*
155 *Underground Construction and Ground Movement*
156 *Geomechanics II: Testing, Modeling, and Simulation*
157 *Computer Applications in Geotechnical Engineering*
158 *Contemporary Issues in Deep Foundations*
159 *Case Studies in Earth Retaining Structures*
160 *Dynamic Response and Soil Properties*
161 *Embankments, Dams, and Slopes: Lessons from the New Orleans Levee Failures and Other Issues*
162 *Problematic Soils and Rocks and In Situ Characterization*
163 *Geoenvironmental Engineering*
164 *Innovative Applications of Geophysics in Civil Engineering*
165 *Geosynthetics in Reinforcement and Hydraulic Applications*
166 *Educational Activities in Geotechnical Engineering*
167 *Geotechnics of Soil Erosion*
168 *Grouting for Ground Improvement: Innovative Concepts and Applications*
169 *Soil and Material Inputs for Mechanistic-Empirical Pavement Design*
170 *Probabilistic Applications in Geotechnical Engineering*
171 *Advances in Shallow Foundations*
172 *Soil Improvement*
173 *Advances in Measurement and Modeling of Soil Behavior*
174 *Designing Our Underground Space*
175 *Field Measurements in Geomechanics 2007*
176 *Analysis of Asphalt Pavement Materials and Systems: Emerging Methods*
177 *GeoCongress 2008: Geotechnics of Waste Management and Remediation*

This page intentionally left blank

Preface

Geo-engineers and geo-scientists are increasingly confronted by new challenges in protecting and preserving our environment and infrastructure. Innovative and emerging scientific concepts and technologies are always needed to address a wide range of complex geoenvironmental issues such as groundwater protection and remediation, management of waste disposal, sustainable development and mitigation against natural and man-made geohazards.

In 1995, ASCE organized a conference on "Geoenvironment 2000: Characterization, Containment, Remediation and Performance of Environmental Geotechnics" in New Orleans, Louisiana. This conference highlighted the role of geo-professionals and the wide range of geoenvironmental engineering challenges, such as the design, construction, and monitoring of containment facilities as well as engineering mitigation of environmental geo-hazards. In 1997, ASCE organized another specialty conference on "In Situ Remediation of the Geoenvironment," in Minneapolis, Minnesota.

Due to rapid industrialization, increased environmental awareness, and the complexity of tackling past unsafe waste disposal practices; geoenvironmental engineering has continued to evolve as a discipline that bridges between engineering and basic sciences to address geo-specific environmental problems. It was imperative to organize GeoCongress 2008, March 9-12, 2008, in New Orleans, Louisiana to highlight recent advances, new directions and opportunities for sustainable engineering to protect the environment and infrastructure.

The Congress attracted a significant number of papers and more than 400 were accepted. The papers were divided into three Geotechnical Special Publications (GSPs) that capture the multidisciplinary aspects and the challenges of the sustainability of the geoenvironment.

The first GSP, *Geotechnics of Waste Management and Remediation*, tackles the challenges of sustainability in remediation and waste management, and covers topics on new and conventional remediation technologies, design and operational aspects of bioreactor landfills, innovations in design and assessment of covers and liners, management of mining wastes, and recycle and reuse of waste materials.

The second GSP, *Geosustainability and Geohazard Mitigation*, tackles the challenges of sustainability in geotechnics, and covers topics on education, sustainable materials and infrastructure, risk-based analysis and design, and impacts and mitigation of geohazards.

The third GSP, *Characterization, Monitoring and Modeling of GeoSystems*, covers mechanical and chemical soil behavior, testing, and modeling. The GSP presents innovations on subsurface characterization and monitoring, characterization of rocks, problematic Soils and waste materials; and sensor technologies. Recent developments in numerical and computational geotechnics, emerging technologies, fate and transport modeling, uncertainty modeling, and micro- and environmental geo-mechanics are also covered in this GSP.

The paper review process was managed by the editors and Paper Review Board. The review board had a very active and essential role in reviewing papers, organizing the conference sessions, and making the GSPs possible. The editors sincerely appreciate the help and patience of the Review Board. The editors also appreciate the help of Ms. Sheana Singletary of ASCE for her help in managing paper submissions and dealing with the glitches of the database.

We hope that these GSPs will serve as valuable references to all working in geoengineering.

Editors
Krishna R. Reddy
Milind V. Khire
Akram N. Alshawabkeh

Review Board

Stephan Jefferis, Environmental Geotechnics, Ltd.
Hsein Juang, Clemson University
Edward Kavazanjian, Arizona State University
Amid Khodadoust, University of Illinois Chicago
Debra Laefer, University College Dublin
Mengjia Li, Gundle/SLT Environmental, Inc. (GSE)
Shu-Guang Li, Michigan State University
William Likos, University of Missouri
Ning Lu, Colorado School of Mines
Ronaldo Luna, University of Missouri-Rolla
Laloui Lyesse, Swiss Federal Institute of Technology Lausanne
Krishnanand Maillacheruvu, Bradley University
Jay Meegoda, New Jersey Institute of Technology
Mysore Nataraj, University of New Orleans
Vincent Ogunro, University of North Carolina at Charlotte
Jun Otani, Kumamoto University
Sibel Pamukcu, Lehigh University
Junboum Park, Seoul National University
Kok-Kwang Phoon, National University of Singapore
Ali Porbaha, California State University, Sacramento
Anand Puppala, University of Texas-Arlington
Ellen Rathje, University of Texas-Austin
Chris Ryan, Geo Solutions, Inc.
Shadi Saadeh, California State University, Long Beach
Rodrigo Salgado, Purdue University
Charles Shackelford, Colorado State University
Joseph Sinfield, Purdue University
Chung Song, The University of Mississippi
Burak Tanyu, GeoSyntec Consultants, Inc.
Hani Titi, University of Wisconsin Milwaukee
Binod Tiwari, California State University, Fullerton
David Toll, Durham University
Erol Tutumluer, University of Illinois Urbana-Champaign
Cumaraswamy Vipulanandan, University of Houston
Andrea Welker, Villanova University
Nazli Yesiller, Consultant, San Luis Obispo
Zhanping You, Michigan Technological University
Lei Yuan, GeoSyntec Consultants, Inc.
Mourad Zeghal, Rensselaer Polytechnic Institute
Dimitrios Zekkos, Geosyntec Consultants, Inc.
Limin Zhang, The Hong Kong University of Science and Technology
Xiong Zhang, University of Alaska Fairbanks
Thomas Zimmie, Rensselaer Polytechnic Institute

Contents

Geohazard Mitigation

Keynote Paper

Impacts of Geohazards

Mitigation of Geohazards

Geosustainability

Sustainability in Geotechnics

Sustainable Materials and Infrastructure

Indexes

Our Role as Engineers in Mitigating Natural Hazards

Robert B. Gilbert[1], M. ASCE, P.E.

[1]Professor, Department of Civil, Architectural and Environmental Engineering, The University of Texas at Austin, ECJ 9.227, Austin, Texas 78712, bob_gilbert@mail.utexas.edu

ABSTRACT: As civil engineers, we have a central role and responsibility in mitigating the impact of natural hazards. Our role is extremely challenging and it requires that we be leaders in our own profession, among other professions, and in the public. I present the following framework to guide engineers in fulfilling our role and responsibility:

1. Decision making is the key to hazard mitigation.
2. Risk analyses should be designed specifically to produce information relevant to decision making.
3. Mitigating consequences can be the most effective means to mitigate natural hazards.
4. Performance depends on systems; the enormous scale and complexity of systems for hazard mitigation, both in space and in time, makes it difficult to achieve a high level of reliability.
5. Dealing with uncertainty is a real challenge; physical factors and the role of uncertainty in decision making are important considerations in how best to account for and represent uncertainty in hazard mitigation.
6. Effective communication is essential in mitigating natural hazards; it is important that we reach out to and work with specialists who are experts in communication.

I use hurricane protection in New Orleans as a case history to illustrate and demonstrate this framework.

INTRODUCTION

> American Society of Civil Engineers Code of Ethics, Fundamental Canon #1:
> "Engineers shall hold paramount the safety, health and welfare of the public…"

Natural hazards, such as hurricanes, earthquakes and floods, can be catastrophic. More than 200,000 people died due to the 2004 tsunami in the Indian Ocean. Hurricane Katrina in 2005 caused thousands of fatalities, hundreds of billions of dollars of property damage and the irreparable devastation of a major city. While natural hazards cannot be prevented, the impact that these hazards have on the safety, health and welfare of the public can be mitigated.

As civil engineers, we have a central role in mitigating the impact of natural hazards. We are responsible for identifying the means available to mitigate their impact. These means can range from preventing impacts with natural and man-made barriers to avoiding impacts with land-use and evacuation policies. We are responsible for assessing how much the possible means for mitigation will cost and how well they will work. Finally, we are responsible for working with the owners, operators and users to decide which mitigation means to use, how to implement them and how to maintain and sustain them. These decisions are the key to hazard mitigation.

Our role is extremely challenging. It requires that we collaborate with numerous and varied disciplines beyond engineering: scientists to understand a hazard and how natural and man-made systems will respond in the face of a hazard, sociologists to understand how people will respond to a hazard and to various means for mitigation, economists to understand costs and impacts, policy makers to understand how to implement mitigation means, and communication specialists to understand how to engage the public in making and implementing decisions for hazard mitigation. It requires that we interact with the owners and operators, which will generally be public agencies and governmental bodies, and that we interact with the users, the public we are trying to protect. It requires that we participate in difficult decisions that directly affect the safety, health and welfare of the public and that are constrained by limited resources.

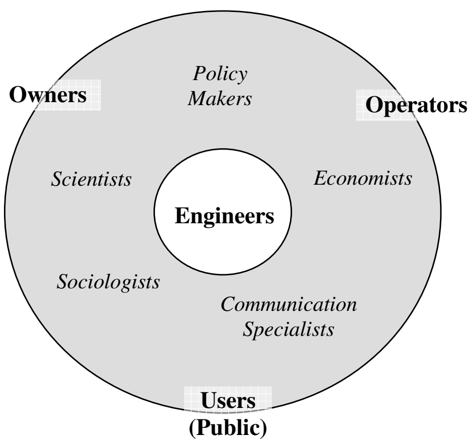

FIG. 1. Central Role of Engineers as Leaders in Mitigating Impacts from Natural Hazards (adapted from the Center for Creative Leadership)

Our role in hazard mitigation requires that we be leaders, as represented conceptually in Figure 1. We need to be leaders in our own profession (the inner circle in Fig. 1). We need to be leaders among the disciplines that provide input and guidance to the decision makers and implementers (the middle circle in Fig. 1). And, we need to be leaders within the groups who will make, implement and be affected by hazard mitigation decisions (the outer circle in Fig. 1). Being a leader means that we transcend boundaries and put ourselves at the center of these groups. Stepping up to this role is our ethical responsibility and provides the true value of our profession to society.

I present here a framework to guide engineers in fulfilling our central role and responsibility in hazard mitigation. I will use the New Orleans Hurricane Protection System as a case history to illustrate and demonstrate the main ideas. Background information for this case history can be found at ASCE (2005), ASCE (2007), ILIT (2006) and IPET (2007). I feel that this case history is relevant because it underscores the significant challenges in effectively mitigating natural hazards and because it coincides with the venue for this conference. However, the framework is general and the ideas are applicable to a variety of different natural hazards, locales, and means of mitigation.

DECISION MAKING IS KEY

The decisions about which mitigation means to use, how to implement them and how to maintain and sustain them are the key to hazard mitigation. Therefore, our role in hazard mitigation should consistently be cast in the light of how decisions are going to be made and implemented.

Decision trees are useful tools for organizing, deliberating about and making decisions (Benjamin and Cornell 1970; Ang and Tang 1984). Decision trees structure the basic components of a decision: alternatives, outcomes and consequences, as illustrated in Figure 2. The sequence of the limbs from left right indicates the order of events in the decision-making process. Decision trees incorporate uncertainty in that the outcomes are not known with certainty. In the example in Figure 2, the decision about mitigation will be made before knowing whether or not a major hurricane will impact the area in the next 50 years.

Decision trees provide a common platform from which all of the stakeholders (Fig. 1) can collaborate. They prompt questions such as the following:

- What are all of the possible alternatives to mitigate natural hazards? How do the possible alternatives interact with one another? For example, does the presence of engineered barriers inadvertently lead to complacency so that evacuation is less effective? Do engineered barriers damage natural barriers such as wetlands?
- What is known about the occurrence and magnitude of the hazard? What is known about how well an alternative will work? Will the performance of an alternative change with time?
- What are the consequences associated with implementing an alternative and with its performance? Which consequences are relevant to the various stakeholders? Over what time horizon should consequences be considered – 1 year, 50 years, 100 years?

Decision trees can be expressed in any accessible language and they are commonly used in a variety of different scientific, economic and public policy applications.

Therefore, decision trees facilitate communication and collaboration with and among the decision makers, implementers and users.

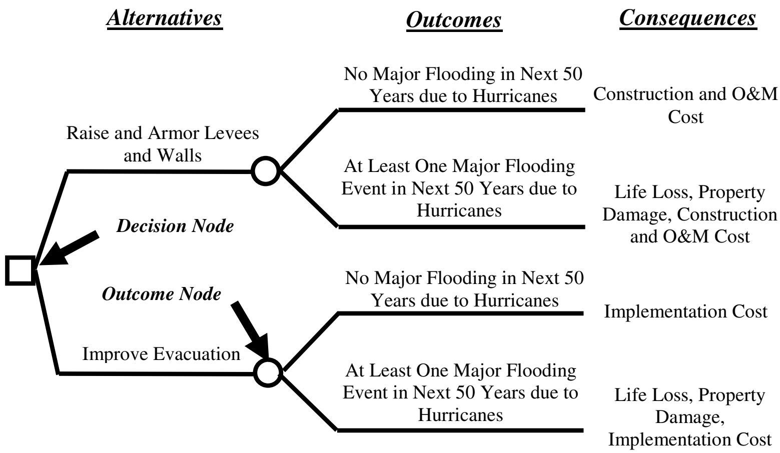

FIG. 2. Example Decision Tree for New Orleans Hurricane Protection System

Decision trees provide a framework for making decisions. For comparative purposes, the value of a decision alternative is expressed in terms of the expected consequences associated with that alternative. The expected consequences represent a weighted average of all the possible consequences listed on the right-hand side of the decision tree (Fig. 2), where each possible consequence is weighted by its probability of occurrence:

$$\begin{matrix}\text{Expected} \\ \text{Consequence}\end{matrix} = \sum_{\text{all i outcomes}} \begin{pmatrix}\text{Consequence} \\ \text{for Outcome i}\end{pmatrix} \times \begin{pmatrix}\text{Probability} \\ \text{for Outcome i}\end{pmatrix} \tag{1}$$

To illustrate, Table 1 shows an example set of calculations for the decision tree in Fig. 2 using monetary cost as a measure of value. While illustrative, the quantitative values in Table 1 for consequences and probabilities are reasonable for the New Orleans Hurricane Protection System. Improving the engineered barriers reduces the probability of major flooding, but does not protect life and property in the event that a major flood occurs (Table 1). Conversely, improving evacuation reduces the consequence of a flood if it occurs, but does not reduce the probability of a major flood occurring. A comparison of expected consequences provides a practical and convenient means for comparing the decision alternatives in the face of uncertainty about whether or not another major hurricane flooding event will occur in the next 50 years. It also provides a theoretically sound and defensible means of comparison (e.g., Benjamin and Cornell 1970, Kenney and Raiffa 1976, and Ang and Tang 1984).

Table 1. Example Calculation of Expected Values for Decision Tree in Fig. 2

Alternative	Outcome	Consequence (2007 Dollars)	Probability
Raise and Armor Levees and Walls	No Major Flooding Event in Next 50 Years due to Hurricanes	$10 billion	0.9
	At Least One Major Flooding Event in Next 50 Years Due to Hurricanes	$100 billion + $10 billion	0.1
	Expected Consequence = 10x0.9 + 110x0.1 = $20 billion **Risk = 100x0.1 = $10 billion**		
Improve Evacuation	No Major Flooding Event in Next 50 Years due to Hurricanes	$5 billion	0.5
	At Least One Major Flooding Event in Next 50 Years Due to Hurricanes	$25 billion + $5 billion	0.5
	Expected Consequence = 5x0.5 + 30x0.5 = $17.5 billion **Risk = 25x0.5 = $12.5 billion**		

A challenging but crucial consideration in decision making is how consequences are valued. For example, the analysis in Table 1 is cast entirely on the basis of cost, and a monetary value has been explicitly associated with the loss of life in the event of a major flooding event. We place monetary value on human life collectively as a society with government regulations; we do it personally as individuals with life insurance policies. For example, The Economist (2004) estimates the monetary value placed on a human life by society in the United States at about $7 million. While civil engineers tend to be uncomfortable with the idea of putting a quantitative value on human life, it is imperative that we deal with it explicitly, whether in monetary terms or some other measure such as utility (e.g., Kenney and Raiffa 1976). It is our responsibility to participate in and provide guidance to the difficult decisions that affect human safety and are constrained by limited resources. Structuring decisions and decision criteria as in Fig. 2 and Table 1 provides a framework for us to fulfill this responsibility.

RISK ANALYSIS IS INPUT TO DECISION MAKING

Risk analysis provides input to the process of making decisions. Risk is defined as an expected value:

$$\begin{matrix}\text{Expected}\\ \text{Risk} = \text{Consequence} = \\ \text{due to Hazard}\end{matrix} \sum_{\text{all i outcomes}} \begin{pmatrix}\text{Consequence}\\ \text{for Outcome i}\\ \text{due to Hazard}\end{pmatrix} \times \begin{pmatrix}\text{Probability}\\ \text{for Outcome i}\\ \text{due to Hazard}\end{pmatrix} \quad (2)$$

Note the similarity to Equation (1); risk is one piece of the expected consequence for a decision alternative. In a simplistic sense, Equation (1) for the expected consequence can be re-expressed in terms of risk as follows:

$$\begin{matrix}\text{Expected}\\ \text{Consequence}\end{matrix} = \text{Risk} + \text{Implementation} \quad (3)$$

In the example in Table 1, the hazard is flooding due to a hurricane; the corresponding risk is \$10 billion for the "Raise and Armor Levees and Walls" alternative and \$12.5 billion for the "Improve Evacuation" alternative (Table 1). While the risk associated with improving evacuation is greater, the total expected cost for this alternative is actually smaller than that for strengthening the barriers. This example underscores that risk is an input to and not the end in making decisions.

The perspective that risk provides input to decision making is helpful in guiding the risk analysis. The emphasis in risk analysis should be placed on the outcomes, consequences and probabilities that differentiate the decision alternatives. For example, New Orleans can flood due to events not associated with hurricanes, such as rainfall and riverine flooding. However, the risks associated with these types of flooding may not be relevant nor need to be quantified for making decisions about the Hurricane Protection System.

A risk evaluation chart is a useful tool to guide decision making. These charts plot boundaries or thresholds for the tolerable frequency of failure events with associated consequences, as illustrated on Figure 3. They are commonly referred to as F-N charts, where F stands for the frequency of failure and N stands for the number of consequences. The intent of these charts is to establish a benchmark level of risk that is considered tolerable by stakeholders in exchange for benefits, such as economical energy. A risk is considered tolerable if the combination of frequency and consequence falls below the threshold. Excellent discussions concerning the basis for, applications of, and limitations associated with these types of charts are provided in Fischhoff et al. (1981), Whitman (1984), Whipple (1985), ANCOLD (1998) and Bowles (2001), and USBR (2003) and Christian (2004).

The F-N curve in Figure 3 shows three evaluation thresholds for comparison. The bottom two thresholds, which apply to public dam projects in the United States, were developed by the Bureau of Reclamation (USBR 2003). The lower USBR threshold provides a boundary above which the risk is not considered tolerable, while the upper USBR threshold provides a boundary above which the risk is not acceptable and urgent action is required. The top threshold on Figure 3 applies to the offshore oil industry (Bea 1991, Stahl et al. 1998, and Goodwin et al. 2000). The differences in risk thresholds for public dams and offshore facilities reflect differences in perspectives of the stakeholders. The failure of a major dam can endanger the general public, while the failure of an offshore platform endangers the platform workers, who voluntarily and knowingly choose to work there.

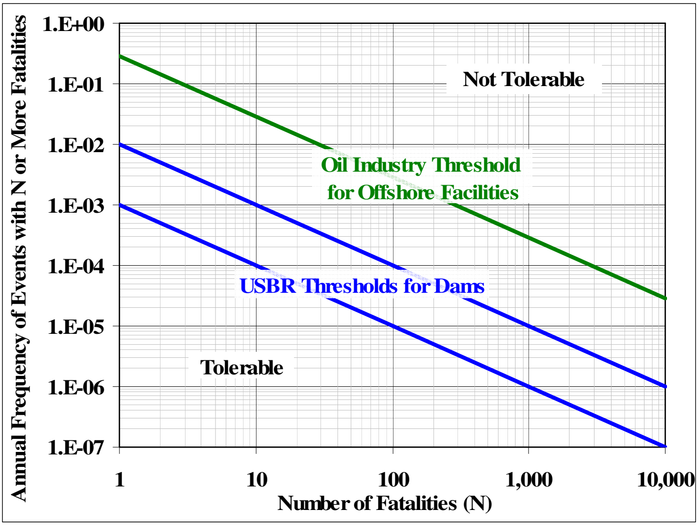

FIG. 3. Published Risk Evaluation Guidelines for Human Fatalities (adapted from Gilbert et al. 2007)

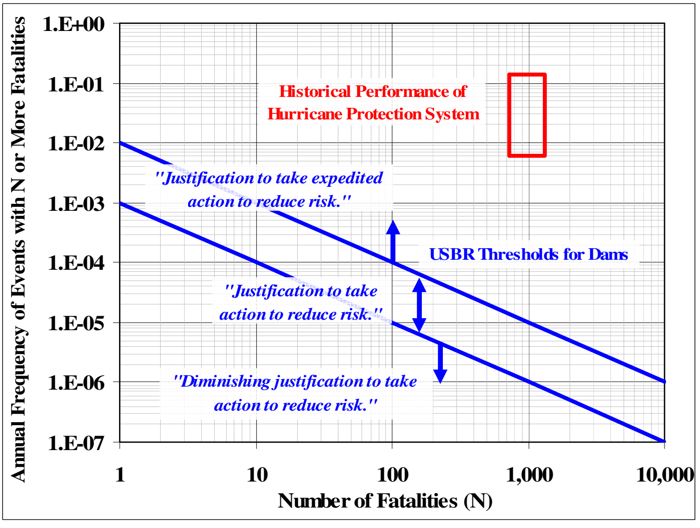

FIG. 4. Evaluation of Risk for Hurricane Protection System in New Orleans (adapted from ASCE 2007)

The New Orleans Hurricane Protection System is related to a major dam in Figure 4. The box labeled "Historical performance of Hurricane Protection System" is established based on the number of fatalities due to the failure during Hurricane Katrina and the occurrence of one major failure in approximately 40 years of service (ASCE 2007). Both the consequence and frequency associated with failure of the Hurricane Protection System are represented as ranges to account for uncertainty in these estimates.

The risk to human life associated with the Hurricane Protection System is well above what would be considered to be tolerable or acceptable for a major dam in the United States. This information is significant and needs to be communicated to and deliberated with the decision makers and the public. What is an acceptable risk for the Hurricane Protection System? It is our responsibility as civil engineers to help society, the government and the people of New Orleans answer this question.

MITIGATING CONSEQUENCES CAN BE EFFECTIVE

The alternatives or means for reducing the risks from natural hazards can broadly be classified into the components that make up risk in Equation (2) and Figure 3, consequences and probabilities of outcomes. If we want to move the box associated with the New Orleans Hurricane Protection System closer to the thresholds established for major dams, then the box needs to either move to the left by reducing the consequences associated with major flooding or move down by reducing the probability that major flooding will occur. We as engineers tend to focus on reducing risk by making failures less probable, e.g., increasing the reliability of the levees and walls by making them higher or stronger. However, mitigating consequences can often be more effective in reducing risk.

In the case of New Orleans, mitigating consequences could be achieved with more effective evacuation in advance of a hurricane. The offshore oil industry in the Gulf of Mexico provides a great lesson in mitigating consequences. In 2005, offshore facilities were subjected to two of the largest hurricanes recorded, Hurricanes Katrina and Rita. The impacts to offshore facilities were much greater than anything ever experienced previously: more than 150 platforms and numerous pipelines were severely damaged or destroyed and direct costs of tens of billions of dollars were incurred (MMS 2006). In comparison, the direct costs due to property damage onshore in New Orleans from Hurricane Katrina were very similar to those offshore. However, in contrast to New Orleans where thousands of people died, the evacuation of tens of thousands of offshore workers in advance of both storms was 100 percent effective and there were no lives lost.

Effective evacuation requires a concerted investment in planning, preparation, transportation and communication. It also requires patience by the public because for every evacuation that is truly needed, there will be many evacuations where the storm track will turn away from New Orleans after the city has been evacuated. Therefore, the costs and benefits, in terms of risk reduction, for any means of hazard mitigation need to be balanced within a decision framework, as exemplified in Figure 2 and Table 1.

PERFORMANCE DEPENDS ON SYSTEMS

The available means for mitigating natural hazards generally rely on large, complicated systems that need to perform over long periods of time. The scale of these systems, both in space and in time, makes it difficult to control their performance and achieve a high level of reliability.

To illustrate this system effect, the New Orleans Hurricane Protection System consists of more than 600 km of earthen levees and walls, hundreds of gates that need to be closed in advance of each hurricane, and tens of federal and local authorities who are responsible for its operation and maintenance. The levees, floodwalls and gates surrounding the city form a series of components that all must perform successfully in order for the system to perform successfully; failure of any component will lead to a failure of the system. In contrast, a major dam will typically have a length that is less than 1 km, or nearly 1,000 times shorter than the Hurricane Protection System.

Consider treating the Hurricane Protection System as 600 1-km long dams in design, construction, operation and maintenance. Based on Figure 4, we would want to achieve a probability of failure of approximately 1 in 100,000 per year for a dam. Say we accomplish this level of reliability by designing each dam to have a 0.001 probability of failure when it is subjected to the 100-year hurricane storm surge, giving an annual probability of failure of 0.001 times 1/100 per year or 1 in 100,000 per year. If each individual dam performs independently in response to the hurricane surge, then the probability of failure increases with the length of the system (Figure 5). In the event of a major hurricane, the probability of failure for the 600-km long system is nearly 1 even though each 1-km segment has a probability of failure that is only 0.001. Therefore, the failure probability for the system will be nearly 1,000 times greater than that for an individual segment, explaining why the Hurricane Protection System plots in Figure 4 so far above what would be considered tolerable for a dam.

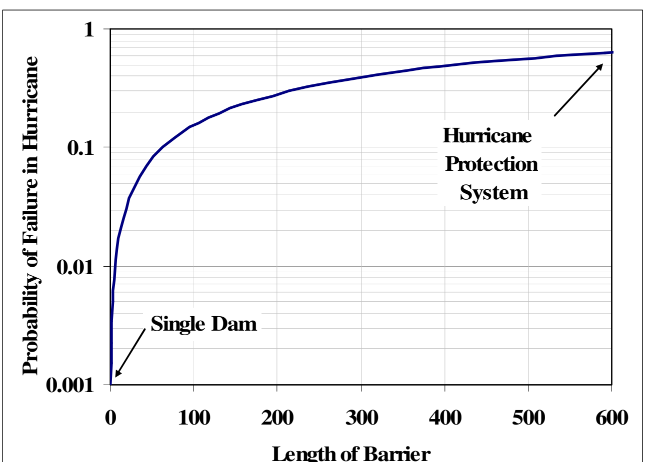

FIG. 5. Probability of Failure versus Length of System

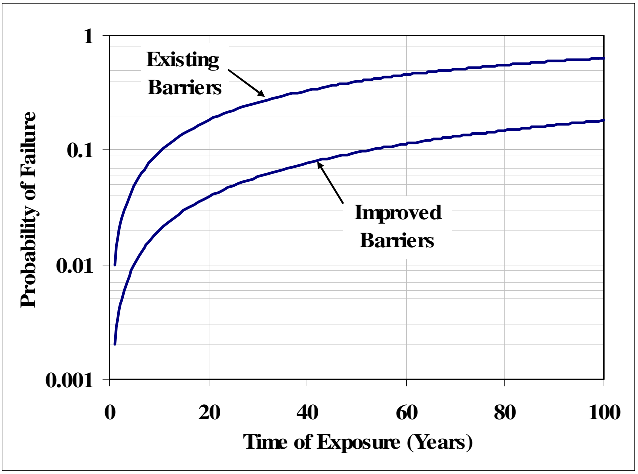

FIG. 6. Probability of Failure versus Time of Exposure

Furthermore, the Hurricane Protection System has essentially an unlimited design life. The failure probabilities of 0.1 and 0.5 listed in Table 1, where failure is defined as the occurrence of at least one major flooding event due to a hurricane in the next 50 years, may seem rather large compared what is typically expected for an engineered system. They are seemingly large because they reflect the effect of exposure to hurricanes over a 50-year period. For the alternative that the walls and levees are raised and armored, an annual failure probability of about 1 in 500 years could be achieved. Conversely, the existing barriers have an annual failure probability of about 1 in 100 years without improvement. The failure probability increases dramatically as the time of exposure increases (Figure 6). With the existing barriers, there is greater than a 50-percent probability that they will fail again in the next 100 years.

Consideration of system effects here underscores that mitigation of consequences (e.g., evacuation of people in advance of a hurricane) may be the most effective means of reducing the risk versus increasing the reliability of the system itself.

UNCERTAINTY REQUIRES HANDLING WITH CARE

Quantifying and accounting for uncertainty is a challenge. We do not know when, where and what hurricanes will occur. We do not know whether the record of hurricanes over the past 50 years is representative for what might happen over the next 50 years. We do not know how possible subsidence, sea level rise and global warming will affect the occurrence and intensity of storm surges. We do not know how well the Hurricane Protection System will perform when subjected to a particular hurricane. We do not know what the life loss, property damage and other consequences will be if there is flooding from a hurricane. We do not know how much a particular means for hazard mitigation will cost to implement. Furthermore, the performance of systems for hazard mitigation is generally governed by extreme circumstances, such as the Hurricane Katrina with a peak storm surge that is 30 percent greater than anything ever observed before along the entire coast of the Gulf of Mexico.

The following guidelines are provided to overcome the challenges associated with representing uncertainty:

- Physical factors are important in developing realistic representations of uncertainty, even when these factors are not necessarily mathematically convenient to model. Important physical factors can include upper or lower bounds on variables; correlations and non-linear relationships between variables, particularly between extreme values; probability distributions that do not follow a convenient form such as normal or lognormal distributions; and uncertainty in the statistical models themselves (i.e., epistemic uncertainty). An example is incorporating information about components that were loaded by Hurricane Katrina and did not fail into a model predicting the future performance of the Hurricane Protection System.
- Acquiring information to reduce uncertainty is not always beneficial. If a decision will be the same whether or not the additional information is obtained, then there is essentially no value in obtaining the information. An example is drilling closely-spaced borings along the alignment of a levee. If the geology is relatively uniform or if a very conservative design will be adopted regardless of the site-specific conditions, then having closely-spaced borings is not necessarily justified by the cost.
- Sensitivity analyses within the decision framework are very helpful in identifying which uncertainties are and are not important for making decisions. For example, if we would choose to improve evacuation versus strengthening walls and levees whether the probability of flooding is 1 in 100 or 1 in 500 years, then there is no need to further refine this probability assessment. Sensitivity analyses in the context of decision making are particularly helpful in dealing with the possibility of extreme events. While the set of future possibilities for natural hazards is essentially unbounded, the set of potential means for mitigating these hazards is bounded by limitations in resources. Therefore, considering uncertainty from the top-down of what decisions need to be and can be made is important.

EFFECTIVE COMMUNICATION IS ESSENTIAL

Effective communication is essential in mitigating natural hazards and it is an essential component for engineers in taking on a leadership role. Since communication is not our expertise, we need to work with specialists who are experts in communication. Mileti (2007) provides an excellent state-of-the-art summary, from the perspective of a sociologist, about hazard communication with the public. He emphasizes that there is a known social psychology of hazard education and communication and that a body of knowledge, tools and experts exists to do it effectively.

In addition to getting outside help, we also need to consider communication in how we develop and present results from our technical analyses. One area where we struggle is in communicating uncertainty or risk. We typically summarize the information in mathematical terms, such as probabilities or expected values. However, these mathematical measures are not very descriptive or physically meaningful.

Mileti (2007) stresses that people don't think in terms of probabilities; instead, we think in binary terms of whether something will or will not happen. For example, a homeowner in New Orleans would be interested in what the possible flood levels are in their lifetime. A simulation of future flood levels at their house over the next 50 years is shown on Figure 7. In this simulation, one flood occurs in the year 2019 and the water level rises to 9 feet above the ground surface (which is about 6 feet above the floor elevation in the house). In mathematical terms, this simulation was produced from a model where there was a 1 in 100 annual probability of occurrence for a flood event (that is, it is a "100-year event") and an expected flood level of 11 feet if one occurs. Integrating this mathematical information gives an expected annual flood level of 0.1 feet. An annual probability of 0.01 and an annual flood level of 0.1 feet are meaningless to the homeowner; either their house will or will not get damaged by flooding in the next 50 years.

An idea for improving communication is to use a graphical technique called multiples (Tufte 1990). Multiples are small-scale images positioned within the eye span on a single page showing the range of possibilities. Uncertainty multiples (Gilbert et al. 2006) apply this concept to convey uncertainty. Figure 8 shows how uncertainty in the future, and therefore risk, can be conveyed with uncertainty multiples. Each image depicts a possible future in terms of flooding. It shows that while there may be no floods in our lifetime, flooding is not a rare event. It shows that it is possible, but not likely, to have more than one flood in our lifetime. It shows that if a flood does occur, the water will probably be at least 5 feet above the ground surface and could be well over 10 feet high. Uncertainty multiples potentially provide a very effective means for conveying and visualizing uncertainty and risk in all of their richness.

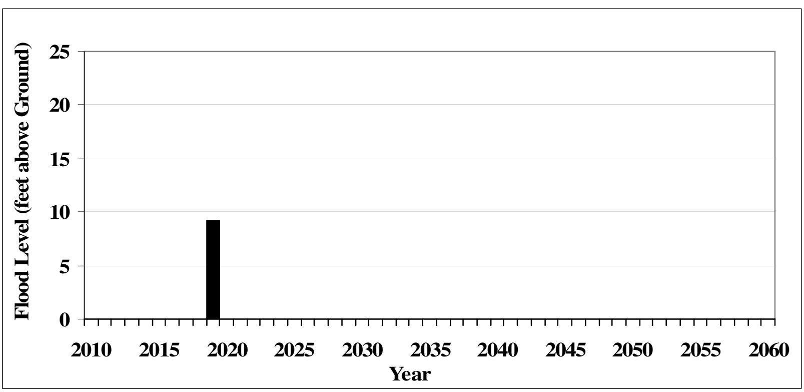

FIG. 7. Simulated Values of Flood Levels in Future

FIG. 8. Uncertainty Multiples for Future Flood Levels (each image reflects Fig. 7)

CONCLUSION

As civil engineers, we have a central role in mitigating the impact of natural hazards. We are responsible for identifying the means available to mitigate their impact, for assessing how much the possible means for mitigation will cost and how well they will work, and for working with owners, operators and users to decide which mitigation means to use and how to implement, maintain and sustain them. These decisions are the key to hazard mitigation and the key to our role in hazard mitigation.

I have presented a framework to guide our role in hazard mitigation. It has the following components:

1. Decision making is the key to hazard mitigation.
2. Risk analyses should be designed specifically to produce information relevant to decision making.
3. Mitigating consequences can be the most effective means to mitigate natural hazards.
4. Performance depends on systems; the enormous scale and complexity of systems for hazard mitigation, both in space and in time, makes it difficult to achieve a high level of reliability.
5. Dealing with uncertainty is a real challenge; physical factors and the role of uncertainty in decision making are important considerations in how best to account for and represent uncertainty.
6. Effective communication is essential in mitigating natural hazards; it is important that we reach out to and work with specialists who are experts in communication.

I am hopeful that this framework provides a perspective that guides our collaboration, participation and leadership in all aspects of hazard mitigation. I am also hopeful that this framework inspires individual engineers to get actively involved and become leaders. Stepping up our role in hazard mitigation is our ethical responsibility.

ACKNOWLEDGMENT

I wish to acknowledge the following organizations for supporting the research and consulting upon which this paper is based: American Petroleum Institute, American Society of Civil Engineers, BP, CALFED, ExxonMobil, National Science Foundation, Offshore Technology Research Center, Shell, State of Texas Advanced Research and Technology Programs, Unocal, United States Army Corps of Engineers, and United States Minerals Management Service. I would also like to acknowledge the support of my colleagues and students at The University of Texas at Austin, as well as the Hudson Matlock Professorship Fund. The views and opinions expressed herein are my own and do not reflect any of the organizations, parties or individuals with whom I have worked.

REFERENCES

ANCOLD (1998). Guidelines on Risk Assessment. Working Group on Risk

Assessment, Australian National Committee on Large Dams, Sydney, New South Wales, Australia.

Ang, A. A-S. and Tang, W. H. (1984). Probability Concepts in Engineering Planning and Design, Volume II - Decision, Risk and Reliability. John Wiley & Sons, New York.

ASCE (2005). "Preliminary Report on the Performance of the New Orleans Levee Systems in Hurricane Katrina on August 29, 2005." A Report by the Reconnaissance Teams from American Society of Civil Engineers and University of California at Berkeley, Report No. UCB/CITRIS – 05/01, http://www.asce.org.

ASCE (2007). "The New Orleans Hurricane Protection System – What Went Wrong and Why." A Report by the External Review Panel of ASCE, American Society of Civil Engineers, Reston, Virginia.

Bea, R. G. (1991). "Offshore Platform Reliability Acceptance Criteria." *Drilling Engineering*, Society of Petroleum Engineers, June, 131-136.

Benjamin, J. R. and Cornell, C. A. (1970). Probability, Statistics, and Decision for Civil Engineers. McGraw-Hill, Inc., New York.

Bowles, D. S. (2001). "Evaluation and Use of Risk Estimates in Dam Safety Decisionmaking." *Proceedings*, Risk-Based Decision-Making in Water Resources, ASCE, Santa Barbara, California, 17 pp.

Christian, J. T. (2004). "Geotechnical Engineering Reliability: How Well Do We Know What We Are Doing?" *Journal of Geotechnical and Geoenvironmental Engineering,* ASCE, 130 (10), 985-1003.

Fischhoff, B., Lichtenstein, S., Slovic, P., Derby, S. L. and Keeney, R. L. (1981). Acceptable Risk. Cambridge University Press.

Gilbert, R. B., Najjar, S. S., Choi, Y. J. and Gambino, S. J. (2007). "Practical Application of Reliability-Based Design in Decision Making." Book Chapter in Reliability-Based Design in Geotechnical Engineering: Computations and Applications, Phoon Ed., Taylor & Francis Books Ltd, in press.

Gilbert, R. B., Tonon, F., Freire, J., Silva, C. T. and Maidment, D. R. (2006). "Visualizing Uncertainty with Uncertainty Multiples." *Proceedings,* GeoCongress 2006, Atlanta, Georgia.

Goodwin, P., Ahilan, R. V., Kavanagh, K. and Connaire, A. (2000). "Integrated Mooring and Riser Design: Target Reliabilities and Safety Factors." *Proceedings, Conference on Offshore Mechanics and Arctic Engineering,* 185-792.

ILIT (2006). "Investigation of the Performance of the New Orleans Flood Protection Systems in Hurricane Katrina on August 29, 2005." Independent Levee Investigation Team Final Report, University of California at Berkeley, http://www.ce.berkeley.edu/~new_orleans.

IPET (2007). "Performance Evaluation of the New Orleans and Southeast Louisiana Hurricane Protection System," Draft Final Report of the Interagency Performance Evaluation Task Force, U.S. Army Corps of Engineers, *https://IPET.wes.army.mil.*

Kenney, R. L. and Raiffa, H. (1976). Decision with Multiple Objectives: Preferences and Value Tradeoffs. J. Wiley and Sons, New York.

Mileti, D. S. (2007), "Public Hazards Communication and Education: The State of the Art." www.incident.com/access/images/6/68/PUB_HAZ_COMM_PAPER.doc.

MMS (2006). Presentation at Offshore Operators Committee Meeting, Houston,

Texas, June.
Stahl, B., Aune, S., Gebara, J. M. and Cornell, C. A. (1998). "Acceptance Criteria for Offshore Platforms." *Proceedings*, Conference on Offshore Mechanics and Arctic Engineering, OMAE98-1463.
The Economist (2004). "The Price of Prudence – Governments Must Protect Their Citizens, But Not at Any Cost." *A Survey of Risk*, January 24, 6-8.
USBR (2003). Guidelines for Achieving Public Protection in Dam Safety Decision Making. Dam Safety Office, United States Bureau of Reclamation, Denver, Colorado.
Whitman, R. V. (1984). "Evaluating Calculated Risk in Geotechnical Engineering." *Journal of Geotechnical Engineering,* ASCE, 110 (2), 145-188.
Whipple, C. (1985). "Approaches to Acceptable Risk." *Proceedings*, Risk-Based Decision Making in Water Resources, ASCE, Santa Barbara, California, 31-45.
Tufte, E. R. (1990). Envisioning Information. Graphics Press, Cheshire, Connecticut.

A Simplified Model for the Linear Elastic Analysis of Laterally Loaded Caissons

Varun, S.M.ASCE[1], Dominic Assimaki, M.ASCE[2] and George Gazetas, M.ASCE[3]

[1]Graduate Research Assistant, Georgia Institute of Technology, 790 Atlantic Drive, NW, Atlanta, GA30332-0355; varun.varun@gatech.edu
[2]Assistant Professor, Georgia Institute of Technology, 790 Atlantic Drive, NW, Atlanta, GA30332-0355; dominic.assimaki@ce.gatech.edu
[3]Professor, National Technical University of Athens, Department of Civil Engineering, Geo-technical Division; gazetas@ath.forthnet.gr

ABSTRACT: The transient response of large embedded foundation elements of length-to-diameter aspect ratio D/B=2-6, is characterized by a complex stress distribution at the pier-soil interface that cannot be adequately represented by means of existing models for shallow foundations or flexible piles. While 3D numerical solutions are feasible, they are infrequently employed in practice due to their associated cost and effort. Prompted by the scarcity of simplified models for design in current practice, we here propose a Winkler model that accounts for the multitude of soil resistance mechanisms mobilized at their base and circumference, while retaining the advantages of simplified methodologies for the design of non-critical facilities. The frequency dependent spring functions are developed on the basis of finite element simulations. Numerical simulations for transfer functions and transient system response to vertically propagating shear waves are also successfully compared with the analytically predicted response.

INTRODUCTION

Pier foundations are large blocks of intermediate length-to-diameter aspect ratio (D/B) = 2-6, with diameter ranging from 3 to 10 meters. Large diameter caisson foundations are typically used as bridge foundation elements, deep-water wharves, and overpasses whereas small diameter caissons are extensively encountered either as single foundation components of transmission towers and heliostats or in groups in foundation systems of high rise buildings, multi-storey parking decks and scour vulnerable structures (O'Neil and Reese, 1999).

Categorized according to their geometry characteristics as intermediate embedded foundations when compared to shallow and deep elements, caisson foundations are currently designed by means of: (i) existing shallow embedded foundation methods (e.g., Novak & Beredugo, 1972; Kausel, 1974; Elsabee & Morray, 1977; Mita & Luco, 1989; Gazetas, 1983) or (ii) flexible pile approaches (also referred to as p-y curves) developed semi-empirically as a function of the soil type (e.g. Lam and

Chaudhury, 1997). Alternatively, while three-dimensional numerical solutions are feasible, their application for the design of non-critical facilities is typically prohibited by the associated site investigation cost, computational time, and user expertise required.

The comparable dimensions of depth to diameter of caisson foundations imply that within the context of assessing the global foundation stiffness, neither the circumference nor the base resistance mechanisms may be neglected (shallow foundation theory). On the other hand, pier foundations typically extend through layered soil formations, and the associated vertical soil stiffness variability needs to be accounted for (p-y curve approach). Results presented in this paper show that caisson foundations are indeed expected to behave as rigid elements upto (D/B) ratios of 6 for typical soil-caisson impedance contrasts. Nonetheless, the embedded foundation solutions are applicable only for low embedment ratios (D/B < 2).

SIMPLIFIED MODEL DESCRIPTION

A Dynamic Winkler model that properly accounts for the multitude of soil resistance mechanisms mobilized at the base and the circumference of laterally loaded piers is proposed in this section. Figure 1a schematically depicts the stress distribution at the foundation-soil interface, when a typical caisson is subjected to a combination of a lateral concentrated load (V) and a moment (M) on the top.

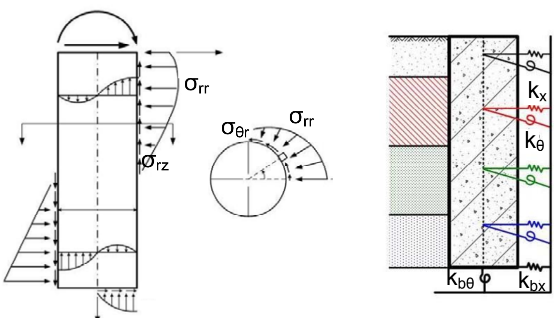

(a) (b)

Figure 1: (a) Primary resistance mechanisms contributing to the global foundation stiffness. (b) Four spring model implemented in this study.

Following Assimaki et al. (2001) and Gerolymos & Gazetas (2006), following four mechanisms significantly contributing to the pier response are identified and captured macroscopically using the Winkler model: (a) lateral resistance per unit length due to normal stresses along the shaft (k_x); (b) resisting moment per unit length due to vertical shear stress along the shaft (k_θ); (c) lateral base resistance due to horizontal shear stress (k_{bx}); and (d) base resisting moment due to normal stresses ($k_{b\theta}$).

The model is based on the approximation of plane strain conditions proposed by Novak et al. (1978) assuming that the response of each soil layer is decoupled from the overlying and underlying ones. As a result, the total response can be obtained through integration of the total resistance offered by the individual springs for each layer.

EULER-BEAM APPROXIMATION

Approximating the response of a laterally loaded caisson using Euler beam theory, the general solution for deformed configuration can be written as:

$$u(z) = A_1 e^{-cz}\cos(dz) + A_2 e^{-cz}\sin(dz) + A_3 e^{-c(D-z)}\cos(d(D-z)) + A_4 e^{-c(D-z)}\sin(d(D-z)) \quad (1)$$

where c, d are functions of normalized k_x and k_θ. For typical pile-soil impedance ratios and low D/B ratio, the maximum value attained by the terms (c*z and dz*) is << 1 and by neglecting higher order terms, the response may be approximated as rigid body motion, $u(z) = u_t - \theta z$, where u_t is the translation at the top and θ is the rotation. Using plane strain solution (Novak et al., 1978) for distributed springs and circular foundation stiffness on elastic halfspace (Veletsos & Verbic, 1974) for base concentrated springs, Varun et al. (2007) observed that: (i) For D/B<8 the base has a significant effect on the response and hence cannot be neglected; (ii) the range of D/B ratio for rigid body approximation is also a function of the impedance contrast E_p/E_s; (iii) For stiffness ratios on the order of 10^4-10^5 (typical reinforced concrete or steel casing) the variation in rotation along the length is less than 5% for aspect ratios D/B<6, rendering the rigid body approximation valid.

STIFFNESS MATRIX FORMULATION FOR RIGID BODY MOTION

The dynamic springs are formulated in a complex form to describe the dynamic effect on static stiffness (K_{stat}) using frequency dependent stiffness coefficient $k(a_o)$, and the radiation damping of energy away from the foundation during cyclic vibrations $C(a_o)$:

$$K^* = K_{stat}k'(a_o) + ia_oC(a_o) \quad (2)$$

where $a_o = \omega B / V_s$ is the dimensionless frequency and ω, B, and V_s namely the loading frequency, pier diameter and soil shear wave velocity correspondingly. The dynamic response at any point along the caisson is here approximated by:

$$u^*(z) = u_t^* - \theta^* z, \quad (3)$$

where the asterisk superscript (*) indicates the complex response (both amplitude and phase). Successively, using dynamic equilibrium of forces in the horizontal direction and the overturning moment and expressing the resulting equations in matrix form after normalizing with respect to the Young's modulus of soil (E_s) and the diameter of pier (B), i.e., the stiffness and geometry characteristics of the surrounding soil and foundation element, we get:

$$\begin{bmatrix} V^*/EB^2 \\ M^*/EB^3 \end{bmatrix} = \begin{bmatrix} K_{xx}^*/EB & K_{xr}^*/EB^2 \\ K_{rx}^*/EB^2 & K_{rr}^*/EB^3 \end{bmatrix} \begin{bmatrix} u_t^*/B \\ \theta^* \end{bmatrix} \quad (4)$$

$$\frac{K_{xx}^*}{EB} = \left[\frac{k_x^*}{E}\left(\frac{D}{B}\right) + \frac{k_{bx}^*}{EB}\right] - \left(\frac{\pi}{8(1+\nu)}\frac{\rho_p}{\rho_s}a_o^2\right)\left(\frac{D}{B}\right) \quad (5)$$

$$\frac{K_{xr}^*}{EB^2} = -\left[\frac{1}{2}\frac{k_x^*}{E}\left(\frac{D}{B}\right)^2 + \frac{k_{bx}^*}{EB}\left(\frac{D}{B}\right)\right] + \left(\frac{\pi}{16(1+\nu)}\frac{\rho_p}{\rho_s}a_o^2\right)\left(\frac{D}{B}\right)^2 \tag{6}$$

$$\frac{K_{rr}^*}{EB^3} = \left[\frac{1}{3}\frac{k_x^*}{E}\left(\frac{D}{B}\right)^3 + \frac{k_{bx}^*}{EB}\left(\frac{D}{B}\right)^2 + \frac{k_\theta^*}{EB^2}\left(\frac{D}{B}\right) + \frac{k_{b\theta}^*}{EB^3}\right] - \left(\frac{\pi}{24(1+\nu)}\frac{\rho_p}{\rho_s}a_o^2\right)\left(\frac{D}{B}\right)^3 \tag{7}$$

The stiffness matrix described by Eq.4 is next evaluated numerically using *flexibility approach* by computing the displacements at the top and rotations of the pier resulting from the application of a unit lateral force and a unit overturning moment, and inverting the response matrix.

The simulations for this study are performed using the finite element software package DYNAFLOW (Prévost, 1983). Both the soil formation and pier are simulated using 8 node brick elements. Linear elastic material models were implemented and perfect bonding was assumed at the interface. Mesh sensitivity studies were conducted for the element size, far-field shape and far-field distance. Comparison of back calculated global stiffness showed that none of existing formulations simultaneously captures all three stiffness terms for the foundation system and therefore, there exists a clear need to calibrate the springs of the proposed model. For details of comparison, the reader is referred to Varun et al. (2007).

Calibration of static springs

The translational springs along the length and base of the pier (k_x and k_{bx}) are evaluated by equating the overall lateral and coupled stiffness (Eq. 5-6) to the corresponding numerical results, while the rotational distributed and concentrated springs are interpreted by matching the global rotational stiffness of the foundation (Eq. 7). The variation of the springs as a function of the foundation aspect ratio is shown in Figure 2.

By examining Eq. 7, it is observed that as the aspect ratio D/B increases, the contribution of k_θ and $k_{b\theta}$ to the global rotational stiffness K_{rr} compared to k_x and k_{bx} decreases. In turn, K_{rr} becomes increasingly insensitive to changes in values of these two springs rendering their evaluation by means of back calculation cumbersome for large values of the aspect ratio (D/B>0.75 for $k_{b\theta}$, and D/B>5-6 for k_θ). Therefore, for the aspect ratio region beyond which the rocking stiffness becomes insensitive to changes of the aforementioned springs, the corresponding mechanism may be neglected altogether further simplifying the model. Overall, the response of pier can be broadly classified into three main zones depicted in Figure 2. For a complete description of the behavior of individual springs as a function of the aspect ratio, the reader is referred to Varun (2006).

Simplified expressions for springs are derived by means of least-square curve fitting for the aspect ratio range under investigation (namely D/B=2 to 6) as follows:

$$\frac{k_x}{E} = 1.828\left(\frac{D}{B}\right)^{-0.15} \qquad \frac{k_{bx}}{EB} = 0.669 + 0.129\left(\frac{D}{B}\right) \qquad \frac{k_\theta}{EB^2} = 1.106 + 0.227\left(\frac{D}{B}\right) \tag{8}$$

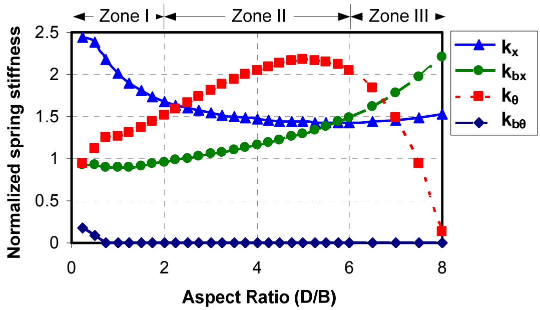

Figure 2: Variation of stiffness coefficients for 4 springs with aspect ratio D/B.

Sensitivity analyses indicated that the overall stiffness terms are for the most part insensitive to changes in Poisson ratio. Therefore, the spring functions described above are evaluated independent of the value of Poisson ratio without loss of accuracy for the range of interest.

Calibration of dynamic springs

For the calibration of the dynamic spring functions, instead of a monotonic load, sinusoidal forcing functions were applied at the top of the foundation and both the amplitude and phase difference of displacements and rotations were numerically computed. Next, the response was expressed in complex functions, and equation of the analytical formulations to the numerical results lead to the evaluation of the spring stiffness functions. The variation of spring coefficients with dimensionless frequency was approximated by the following expressions:

$$k_x' = 1 - 0.1a_o\,; \quad k_{bx}' = 1\,; \quad k_\theta' = 1 - 0.225a_o \tag{9}$$

$$\frac{C_x}{E} = \begin{cases} 1.85a_o & a_o < 1 \\ 1.85 & a_o > 1 \end{cases};\quad \frac{C_{bx}}{EB} = \begin{cases} 0.6a_o & a_o < 0.6 \\ 0.36 & a_o > 0.6 \end{cases};\quad \frac{C_\theta}{EB^2} = \begin{cases} -0.21\left(\frac{D}{B}\right)a_o & a_o < 1 \\ -0.21\left(\frac{D}{B}\right)(2-a_o) & 1 < a_o < 2 \\ 0 & a_o > 2 \end{cases}$$

Note that the attenuation coefficients for the distributed rotational springs C_θ attain negative values in the frequency range of interest, an effect that indicates that waves produced by the side shear resistance are out of phase and destructively interfere with the wavefield produced by the translational mechanisms thus obstructing the energy radiation away from the system. The validity of the approximate expressions derived above is evaluated in the ensuing by comparison of the analytically predicted response computed by means of the fitted expressions to the numerically predicted response of the foundation-soil system.

KINEMATIC SOIL-STRUCTURE INTERACTION

The inability of a stiff foundation to comply with the deformation field imposed by the soil in the free-field subjected to seismic incident waves is translated into effective forces and moments being applied on the foundation. The rigidly responding foundation causes filtering of the far-field motion, a phenomenon that materializes for wavelengths comparable or shorter than the dimensions of the foundation. This effect referred to as kinematic interaction and schematically depicted in Figure 3.

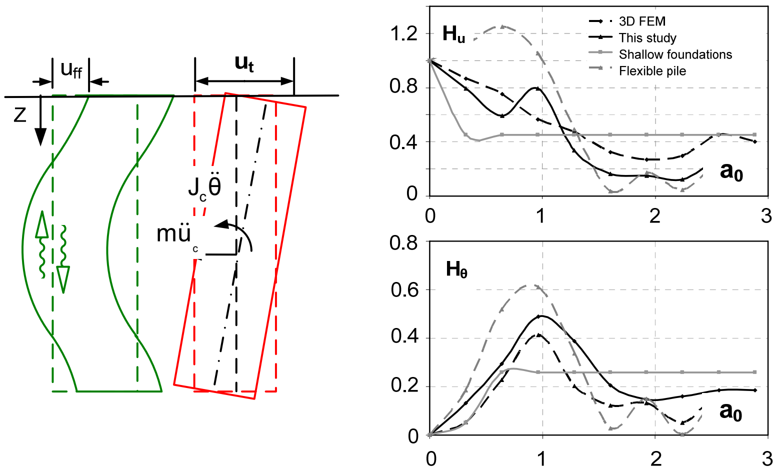

Figure 3: Schematic illustration of kinematic soil-structure interaction due to motion incompatibility between the far-field and the rigid foundation (left) and resulting transfer functions for translation and rotation for D/B = 4 (right)

Assume a vertically propagating anti-plane (SH) shear wave $u_{ff}(z) = u_{ff}\cos(a_o z/B)$. Defining as relative displacement and rotation the functions $u_{rel}(z) = u(z) - u_{ff}(z)$ and $\theta_{rel}(z) = \theta(z) - \theta_{ff}(z)$, the effective forcing functions are derived as:

$$\frac{V_{eff}^*}{EB^2} = \frac{u_{ff}^*}{B}\left(\frac{k_x^*}{E}\frac{1}{a_o}\sin(a_o\frac{D}{B}) + \frac{k_{bx}^*}{EB}\cos(a_o\frac{D}{B})\right) \tag{10}$$

$$\frac{M_{eff}^*}{EB^3} = \frac{u_{ff}^*}{B}\left(\begin{array}{l}\frac{k_x^*}{E}\frac{1}{a_o^2}\left(1-\cos(a_o\frac{D}{B}) - a_o\frac{D}{B}\sin(a_o\frac{D}{B})\right) - \frac{k_{bx}^*}{EB}\frac{D}{B}\cos(a_o\frac{D}{B}) - \\ \ldots - \frac{k_\theta^*}{EB^2}\left(1-\cos(a_o\frac{D}{B})\right)\end{array}\right) \tag{11}$$

Comparison between the analytically derived and numerically evaluated transfer functions illustrated that the analytical solution obtained by using the 3-spring model allows the kinematic interaction effects of pier foundation elements to be captured within an acceptable degree of accuracy while substantially reducing the associated computational time. Though it does not capture quantitatively the amplitude of the rocking response, the model does predict the resonant and destructive interference frequencies (i.e. the maxima and minima) of the corresponding transfer function quite well. Also, the analytically predicted values are for the most part conservative, i.e., the predictions represent less pronounced reduction in the translational motion and higher induced rocking motions. Finally, the analytical transfer functions are bounded between the shallow foundation theory formulations Elsabee & Morray (1977) and the pile kinematic response Gazetas et al (1993), a result that verifies that the proposed formulation is indeed a better approximation to the target soil-foundation system response approximation than the currently employed models.

The analytical expressions for transfer functions can be easily implemented in a very simple code and used to calculate the foundation response corresponding to any transient loading by means of Fourier decomposition and reconstruction of the signal. Figure 4 illustrates an example with seismic displacement time history prescribed at the base of the numerical model. For numerical simulation, the far-field (1D) response is initially computed and imposed at the corresponding far-field location of the numerical domain in form of effective forces.

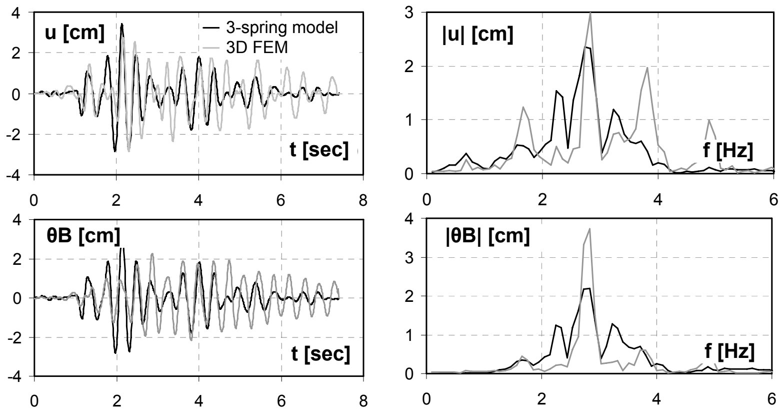

Figure 4: Comparison of analytical and numerical results for translation and rotation of caisson foundation subjected to transient motion

Comparison between the analytically-predicted and numerically-evaluated response illustrates that the model is able to capture the response of the pier within an acceptable degree of accuracy at a substantially reduced computational time without any need for the user expertise required to conduct the numerical simulations. The dominant frequency in both translational and rocking motion response evaluated by means of the analytical model is found to be in excellent agreement with the numerical results, while the peak translation and rotation amplitude are overestimated ($u_{Winkler}$ = 3.7cm vs. u_{3DFE} = 2.3cm, and $\theta_{Winkler}B$ = 3.4cm vs. $\theta_{3DFE}B$ = 2.2cm), since only the three major resistance mechanisms are accounted for.

CONCLUSIONS

We have described the development of an analytical model for the prediction of the response of cylindrical caisson foundations characterized by aspect ratios D/B = 2-6 and embedded in linear elastic soil media, using a three spring Winkler–type model.. It is shown that caisson response can be approximated as rigid body for low aspect ratios (< 6 for typical pile-soil stiffness ratios). Shear tractions along the shaft (k_θ) are shown to have a significant contribution to global response and thus cannot be neglected. Analytical expressions are developed for the global foundation stiffness matrix and for the kinematic interaction transfer functions that are used to predict the seismic response of the caisson. The response predicted by means of these translation and rotation transfer functions is compared to 3D finite element simulations, and results show that the proposed model is able to capture the transient response of the system with acceptable degree of accuracy.

REFERENCES

Assimaki, D., Chatzigiannelis, I., Gerolymos, N., and Gazetas, G. (2001)."Lateral response of caisson foundations." *Proc. 4th National Conference on Geotechnical and Geoenvironmental Engineering*, Athens, Greece.

Elsabee, F., and Morray, J. P. (1977). "Dynamic behavior of embedded foundations." Research Rep. R77-33, MIT.

Gazetas, G. (1983). "Analysis of Machine Foundation Vibrations: state of the art." *Soil Dynamics and Earthquake Engineering*, Vol. 2, 2-42.

Gazetas, G., Fan, K., and Kynia, A. (1993). "Dynamic response of pile groups with different configurations." *Soil Dynamics and Earthquake Engg*, Vol. 12, 239-257.

Gerolymos, N., and Gazetas, G. (2006). "Development of Winkler Model for Static and Dynamic Response of Caisson Foundations with Soil and Interface Nonlinearities." *Soil Dynamics and Earthquake Engineering*, Vol. 26(5), 363-376.

Kausel, E. (1974). "Forced vibrations of circular foundations on layered media.", Res. Rep R79-6, MIT.

Lam, I. P., and Chaudhury, D. (1997). "Modeling of drilled shafts for seismic design." NCEER Rep. II2D-2.5, NCEER, SUNY, Buffalo.

Mita, A., and Luco, J.E. (1989). "Dynamic response of a square foundation embedded in an elastic halfspace." *Soil Dynamics and Earthquake Engg*, Vol. 8(2), 54-67.

Novak, M., and Beredugo, Y.O. (1972). "Vertical Vibration of Embedded Footings." *Journal of Soil Mech. and Foundations Div. ASCE*, Vol. 98(SM12), 1291-1310.

Novak, M., Nogami, T., and Aboul-Ella, F. (1978). "Dynamic soil reactions for plane strain case." *Journal of Engineering Mechanics Div. ASCE*, Vol. 104(4), 953-9.

O'Neil, M. W., and Reese, L. C. (1999). "Drilled shaft: Construction procedures and design methods.", FHWA-IF-99-025, FHWA., Washington D.C.

Prevost, J.H. (1983). *Dynaflow*, Princeton University, Princeton, NJ.

Varun (2006) A simplified model for lateral response of Caisson Foundations, MS Thesis, Georgia Institute of Technology, Atlanta, GA

Varun, Assimaki, D. and Gazetas, G. (2007) *Linear Elastic Transient response of deep rigid foundations*, The 2nd Japan-Greece Workshop on Seismic Design, Observation and Retrofit of Foundations, April 3-4, Tokyo, Japan

Veletsos, A.S., and Verbic, B. (1974). "Basic response functions for elastic foundations." *Journal of Engineering Mechanics Division ASCE*, Vol. 100(EM2), 189.

Behavior of Strip Footings on Reinforced and Unreinforced Sand Slope

Fathi Abdrabbo[1], M.ASCE, Khaled Gaaver[2] and Enas A. Omer[3]

[1] Professor, Faculty of Engineering, Alexandria University, Egypt; f.m.abdrabbo@excite.com
[2] Assistant Prof., Faculty of Engineering, Alexandria University, Egypt; khaledgaaver@yahoo.com
[3] M. Sc. Student, Faculty of Engineering, Alexandria University, Egypt; Enasmr@yahoo.com

ABSTRACT*:* The problem of the bearing capacity of strip footings on sand slope attracts the attention of many researchers. Some of the research work is devoted to improve the methods of the bearing capacity calculations, and the other for the improvement of the stability of the slope supporting the footing. To shed some lights on this problem, plate loading tests were conducted on a strip footing model of side dimension equal to 50 mm. The effects of the relative density of sand, the embedment of reinforcement, and the edge distance of the footing were studied. The study indicated that the improvement of the bearing capacity of a strip footing resting on reinforced sand slope depends upon the depth of the reinforcing layer, relative density of sand, and the edge distance of the footing. Comparisons between the achieved laboratory test results on unreinforced sand slope and the calculated values from published closed-form solutions were carried out. Also, the bearing capacity factors ($N_{\gamma q}$) of strip footings on reinforced sand slope were calculated.

INTRODUCTION

The applications of geotextile reinforcement in geotechnical engineering are widely spread nowadays. Among of these applications is the use of reinforcement to improve the bearing capacity of foundations. This application has attracted the attention of many researchers such as Binquet and lee (1975), Akinmusuru and Akinbolade (1981), Das *et al*. (1994), Consoli *et al*. (2002), Bathurst *et al*. (2003), and Abdrabbo *et al*. (2004). When a footing is constructed on or near a slope, the bearing capacity of the footing may be significantly reduced compared with the same footing resting on horizontal ground surface. The reduction depends on the location of the footing with respect to the slope, the slope angle, and the properties of the supporting soil. One of the possible methods to improve the bearing capacity of the footing near a slope is to reinforce the supporting soil with geosynthetics. Lee and Manjunath (2000) conducted series of numerical and model tests to evaluate the bearing capacity of a strip footing resting on reinforced sand slopes. The study emphasized on the effects of geogrid reinforcements and its location on the ultimate bearing capacity and settlement characteristics of strip footings.

LABORATORY MODEL

The soil bin which contains the sand and the footing model has a parallelogram shape of inside dimensions 2.0 m by 0.6 m in plan and 0.62 m in height. One long side wall of the soil bin was made from transparent glass to enable observing side view of the footing models during testing. The other walls of the soil bin were made from steel plates. To minimize side friction along the walls, plain Mylar sheets were used as liner for these walls. A strip model footing was made from a steel plate and provided with notch at the center of the top surface, to accommodate a bearing ball. The footing has a length of 580 mm, width (B) of 50 mm, and 15 mm in thickness.

A non-woven geotextile reinforcing material was used in this study. The geotextile is 3.5 mm thickness under 2 kN/m^2 (ASTM D-5199), the fabric weight 350g/m^2 (ASTM D-5261), the permeability 0.25 cm/s (ASTM D-4491), and the transmissivity 200 L/M/H under pressure of 2 kN/m^2 (ASTM D-4716). The sand was medium/ coarse particles. The effective diameter of sand is 0.14 mm whereas the uniformity coefficient 4.55. The specific gravity of sand particles is 2.64, the minimum dry unit weight 16.70 kN/m^3 (ASTM D-4254), and the maximum dry unit weight 18.74 kN/m^3 (ASTM D-4253). The optimum moisture content is 10% (ASTM D-698). The sand was formed inside the bin at different relative densities by pouring designed weight of sand into a certain volume of the bin. The footing was placed on the top surface of the formed soil in a way that the length of the footing is running the full width of the tank. Load was applied incrementally using the loading machine via calibrated proving ring. Each load increment was kept constant up to the rate of footing settlement becomes less than or equal to 0.002 mm/minute for three consecutive readings. The footing settlements were measured using two dial gauges of accuracy 0.01 mm. After completion of each test, the soil was carefully removed from the bin and the geotextile was visually inspected for any tear. It is important to note that, the width and depth of soil bin are greater than six times of the footing width so the bin boundary effects on the test results were considered insignificant. For the details of sand formation and loading process, refer to Omer (2006).

RESUTS AND DISCUSSION

Tests were performed on footing model with various reinforcement embedment depth to footing width ratios (d/B). For each (d/B) ratio, the edge distance of the footing (X/B) was 0, 1, and 2. The sand slope was kept constant at (2H to 1V) during all tests. Typical load-settlement relationships are presented in figure (1). Reference test was carried out at the same conditions of the footing and sand slope but without reinforcement. The ultimate bearing capacity of the footing is defined as the stress while the settlement of the footing proceeds unlimitedly. In case where load-settlement relationship exhibits a peak value of stress, the ultimate bearing capacity becomes well defined and equal to the peak value. Bearing capacity ratio (BCR) was calculated as the ratio between the ultimate bearing capacity of the strip footing on reinforced soil and the ultimate bearing capacity of the same footing on unreinforced soil. The footing displacement at the ultimate/peak load (S_F) is used through the presentation of the test results.

The variations of (BCR) and (S_F/B) against (d/B) are shown in figures (2-a) and (2-b) respectively. The figures indicated that the inclusion of geotextile reinforcement improves the performance of the strip footing in a way that the bearing capacity of the footing is increased and the settlement is reduced. There is an embedment depth of the reinforcing layer at which the (BCR) gets its peak value. This depth is called optimum embedment depth, which depends upon the edge distance of footing (X/B). The optimum depth ratio is equal to 0.5 in case of (X/B) is less than or equal to 1 and equal to 1.0 in case of (X/B) = 2, figure (2-a). Figure (2-b) indicates that (S_F/B) reached the minimum value at the optimum depth of reinforcement. These findings are highly consistent qualitatively with the model test results obtained by Selvadurai and Gnanendran (1989). The behavior of reinforced slope can be explained by the "deep footing effect" as suggested by Huang *et al.* (1994). The soil mass enclosed by reinforcing layer and footing-soil interface behaves as a fictitious rigid footing and transfers a major part of the footing load into deep zone, provided that there is no lateral bulging. The friction stresses developed at the footing-soil interface and along the reinforcing layer produce lateral confinement of the reinforced zone. The effect of this confinement on the stability of the sand slope decreased as the reinforcing layer goes deeper and consequently the bearing capacity of the footing decreased due to anticipated bulging of soil towards the side slope. At the same time, the load causing instability of the sand slope increased as the superimposed load at ground surface transferred deeper into the soil. These two factors are in contradictory, so there is an optimum depth of reinforcement at which the fictitious footing was formed without lateral bulging. The optimum depth of reinforcement is about 0.5 in case of (X/B) = 1, and about 1.0 in case of (X/B) = 2. At larger depths of embedment than the optimum depth, the contribution to the load-transfer mechanism caused by the presence of the reinforcement is reduced significantly.

In order to investigate the effect of the embedment ratio (d/B) on the (BCR) at different relative density of sand, figure (3) was developed. The figure illustrates that the optimum depth ratio varies from 0.25 to 0.50 in case of (X/B) = 0.0 and for all relative densities (Dr = 60%, 70%, and 85%). The optimum depth ratio varies from 0.50 to 0.80 in case of (X/B) =1.0, and varies from 0.50 to 1.00 in case of X/B =2.0. It can be concluded that the optimum depth ratio is not appreciable affected by (Dr) within the accuracy of test results. These results are in agreement qualitatively with Yoo (2001). Figures (2) and (3) demonstrated that the optimum depth ratio of the reinforcing layer depends upon the edge distance (X/B). At (X/B) = 0, the failure of footing soil system is dominated by the slope instability, but when (X/B) becomes

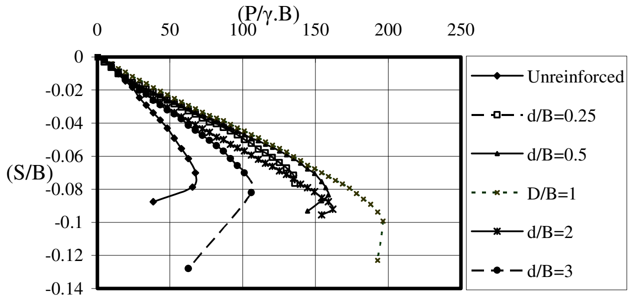

FIG. 1. Normalized stress (P/γ.B) versus (S/B) at X/B = 1.00 and Dr = 85%

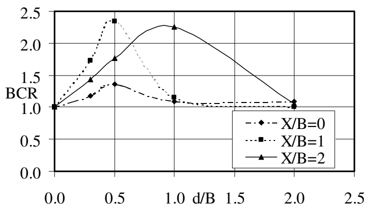

FIG. 2-a. BCR versus d/B, Dr=70%

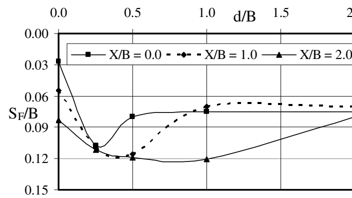

FIG. 2-b. S_F/B versus d/B, Dr=70%

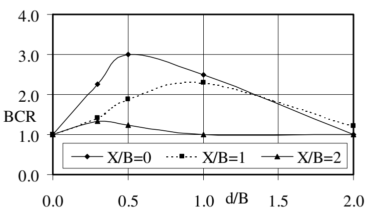

FIG. 3-a. BCR versus d/B, Dr = 60%

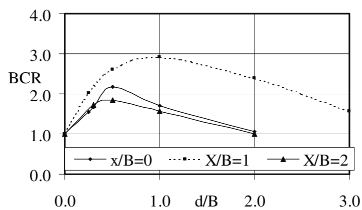

FIG. 3-b. BCR versus d/B, Dr=85%

larger than 1.0, the failure is dominated by the shear stresses developed on shear planes performed in soil beneath the footing. At (X/B) = 0, the optimum depth ratio of reinforcement is 0.5, while at (X/B) >0, the optimum depth ratio of reinforcement becomes greater than 0.5 and approaches to unity.

Series of tests were performed at different (X/B) ratios. During each series of tests, the (d/B) ratio was kept constant at a specified value. Figures (4-a), and (4-b) showed that for unreinforced sand slope, the bearing capacity of strip footing increases as (X/B) increased. In case of reinforced sand slope, the bearing capacity of strip footing depends upon two main factors; the depth of the fictitious rigid footing and the stability of side slope. The first factor depends on the depth of reinforcing layer while the other factor depends on the relative density of sand. So it can be concluded that two inter-related factors, depth ratio (d/B) and relative density of sand (Dr), are affecting the response of strip footing on reinforced sand slope. Furthermore figures (4-a) and (4-b) showed that at any given edge distance, the ultimate bearing capacity of a strip footing near a reinforced slope is considerably higher than that of the same footing near unreinforced slope, this behavior reflects the beneficial effect of reinforcement in improving the bearing capacity of strip footing near a slope. The effect is obvious in case of soil with low relative density. This can be attributed to the modulus of deformation of soil relative to the modulus of deformation of the reinforcing layer. For higher values of (Dr), the modulus of deformation of soil is approaching that of reinforcing material so the existence of reinforcement may not be effective.

Figure (5) illustrates the ultimate bearing capacity (qu) of a strip footing near unreinforced sand slope versus (X/B) values at different relative densities of soil. It can be concluded that the bearing capacity increased as the edge distance of the footing increased, in case of (Dr) > 70%. For soil having small relative density, there is unappreciable effect of the edge distance of the footing on the bearing capacity, for (X/B) > 1. This can be attributed to the failure patterns underneath the footing. In case of soil with (Dr) ≤ 70%, local shear failure underneath the footing with a limited wedge extent is anticipated. In case of soil with (Dr) > 70%, general shear failure of footing-soil system is expected, and the soil wedges may extend to intersect with side slope

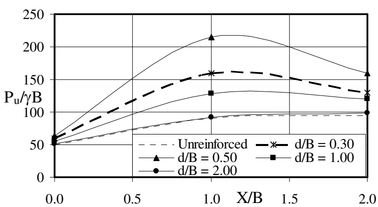

FIG. 4-a. (Pu/B.γ) versus(X/B), Dr = 60%

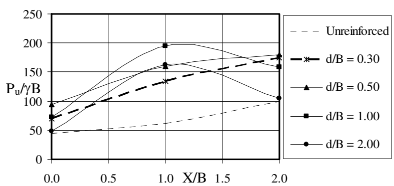

FIG. 4-b. (Pu/B.γ) versus(X/B), Dr = 85%

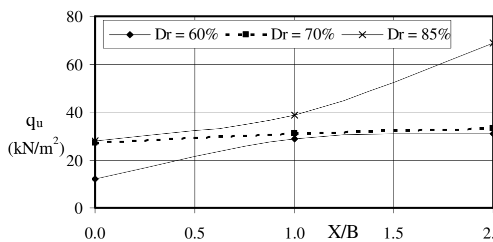

FIG. 5. Ultimate bearing capacity (qu) versus (X/B) for unreinforced soil

COMPARISON BETWEEN EXPERIMENTAL AND THEORETICAL BEARING CAPACITY VALUES

Four methods were implemented to asses the experimental ultimate bearing capacity of footing-soil system from the achieved load-settlement relationships. These methods are; (a) two tangent lines were drawn from the initial and end points of the load-settlement relationship and the point of intersection of these two tangents was projected to the X-axis to obtain the ultimate bearing capacity, (b) the ultimate load for each test was determined at (S/B) = 5%, (c) The ultimate load is defined as the maximum load, while the settlement of the footing proceeds unlimitedly, in case where a peak value of load is obvious, the ultimate load becomes well defined and equal to the peak value, and (d) the ultimate load for each test was considered as the load corresponding to (S/B) = 2.5%. The theoretical bearing capacity was calculated using Meyerhof (1957), Gemperline (1988), and Graham *et al* (1988). Figures (6) to (8) indicated that Meyerhof equation underestimates the bearing capacity of a strip footing resting near a sand slope. The underestimation depends upon the method implemented for interpreting the ultimate bearing capacity, Omer (2006). The underestimation factor varies between 0.32 and 0.60. Gemperline equation agrees with the measured bearing capacity obtained, by method (a), while, underestimated the value obtained by methods (b) and (c), and overestimate the value obtained by method (d) by a factor 1.142. Graham *et al* equation agrees well with the predicted values by methods (a) and (d), and underestimated the value obtained by methods (b) and (c). If we considered the average of the obtained values of the ultimate bearing capacity, it can be concluded that Meyerhof equation underestimate the bearing capacity value by a factor 0.4, while Gemperline by a factor 0.87 and Graham *et al* by a factor 0.81. Gemperline and Graham *et al* equations give, nearly, the same results (Omer 2006). In order to calculate the bearing capacity of a strip footing on reinforced sand slope, Meyerhof (1957) equation was suggested, but with different bearing capacity factor ($N\gamma q$), figure (9). These factor are valid only for strip footings resting on top surface of sand with (Dr) = 60%, and slope of 2:1.The factor ($N\gamma q$) depends upon (X/B) ratio, (d/B), and Dr (Omer 2006). These values should be used with caution due to scale effects.

SCALE EFFECTS

The scale effect phenomenon of the footing was explored by many authors; De Beer 1963, Tatsuoka *et al.* 1994, Kusakabe 1995, and Cerato & Lutenegger 2007. Cerato and Lutenegger (2007) showed that the interpretation of the bearing capacity factor ($N\gamma$) from model footings is dependent on the footing width (B). Tatsuoka *et al.* (1994) reported that the scale effects are resulted from two factors; the mean stress level beneath the footing and the particle size. Kusakabe (1995) stated that the particle size effect ($B/d_{50\%}$) becomes insignificant on the obtained results, when ($B/d_{50\%}$) becomes greater than 50 – 100. In our study, the value of ($B/d_{50\%}$) is about 100. Consequently the effect of the second factor on the test results is avoided. The effect of the first factor is difficult to be avoided unless a modification of the bearing capacity factor is carried out, Shiraishi (1990).

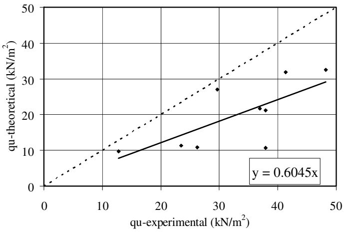

FIG. 6. Experimental and theoretical results (Meyerhof, 1957), method (d)

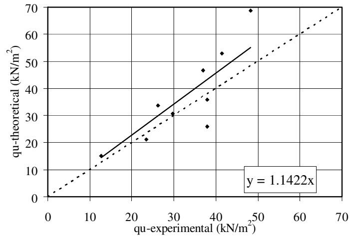

FIG. 7. Experimental and theoretical results (Gemperline, 1988), method (d)

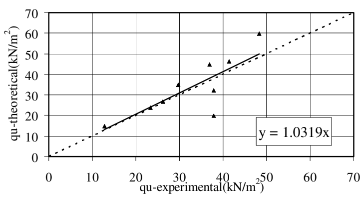

FIG. 8. Experimental and theoretical results (Graham *et al*, 1988), method (d)

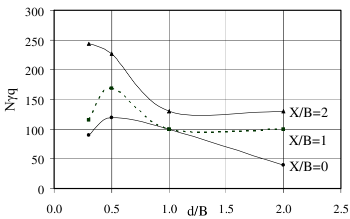

FIG. 9. Values of $N_{\gamma q}$ versus d/B, single reinforcement, and Dr=60%

CONCLUSIONS

1. Geotextile reinforcement is effective in the improvement of bearing capacity of a strip footing resting near a sand slope. The effect of reinforcement depends on the geotextile depth, relative density of sand, and location of the footing with respect to the slope face.
2. The optimum depth ratio of geotextile reinforcement varies from 0.25 to 0.50 in case of (X/B) =0.0, from 0.50 to 0.80 in case of (X/B) =1.0, and from 0.50 to 1.00 in case of (X/B) =2.0. The effect of reinforcement on the bearing capacity of sand slope is more pronounced in soil with low relative density.
3. For unreinforced sand, there is no effect of sand slope having Dr ≤ 70% on the footing performance in case of X/B ≥ 1.0 while the sand slope with Dr = 80% affects the footing behavior.
4. Meyerhof equation underestimated the bearing capacity of a strip footing on sand slope by a factor of 0.4, while Gemperline and Graham et al by a factor of 0.87 and 0.81 respectively.

REFERENCES

Abdrabbo, F. M., Gaaver, K. E., And Elwakil, A. Z., (2004) "Behavior of square footings on double reinforced soil" *5th Int. Conf. on Ground improvement* *techniques*, Malaysia: 280-287.

Akinmusuru, J. O., and Akinbolade, J. A. (1981) "Stability of loaded footings on reinforced soil" *J. Geotechnical Engrg.*, 107: 819-827.

Bathurst, R. J., Blatz, J. A., and Burger, M. H. (2003) "Performance of instrumented large-scale unreinforced and reinforced embankments loaded by a strip footing to failure" *Cand. Geotechnical J.*, 40: 1067-1083.

Binquet, J., and Lee, K.L. (1975) "Bearing capacity analysis of reinforced earth slabs" *J. Geotechnical Engrg.*, 101: 1257-1276.

Cerato, A. B., and Lutenegger, A. J. (2007) "Scale effects of shallow foundation bearing capacity on granular material" *J. Geotechnical & Geoenv. Engrg.*, 133 (10): 1192-1202.

Consoli, N. C., Montardo, J. P., Prietto, P. D., and Pasa, G. S. (2002) "Engineering behavior of a sand reinforced with plastic waste" *J. Geotechnical & Geoenv. Engrg.*, 128 (6): 462-472.

Das, B. M., Khing, K. H, Shin E. C., Puri, V. K., and Yen, S. C. (1994) "Comparison of bearing capacity of strip foundation on geogrid reinforced sand and clay" *8th Int. Conf. on Comp. Meth.and Adv. in Geomech.*, USA: 1331-1336.

De Beer, E. E. (1963) "The scale effect in the transposition of the results of deep-sounding tests on the ultimate bearing capacity of piles and casson foundations" *Geotechnique*, 13 (1):39-75.

Gemperline, M. C. (1988) "Centrifuge modeling of shallow foundations" *Proc., ASCE spring convention.*

Graham, J., Andrews, M., and Shields, D. H. (1988) "Stress characteristics for shallow footings in cohesionless slopes" *Cand. Geotechnical J.*, 25 (2): 238-249.

Huang, C., Tatsuoka, F., and Sato, Y. (1994) "Failure mechanisms of reinforced sand slopes loaded with a footing" *Soils and Foundations* 24 (2): 27-40.

Kusakabe, O. (1995) "Chapter 6: Foundations" *Geotech. Centrifuge Technology,* R. N. Taylor, ed., Blackie Academic & Professional, London: 118-167.

Lee, K. M., and Manjunath, V. R. (2000) "Experimental and numerical studies of geosynthetic reinforced sand slopes loaded with a footing" *Cand. Geotechnical J.*, 37: 828-842.

Meyerhof, G. G. (1957) "The ultimate bearing capacity of foundations on slopes" *4 Int. Conf. on Soil Mech. and Found. Eng*. London, (1): 384-387.

Omer, E. A. (2006) "Behavior of strip footing on reinforced earth slope" *M. Sc. Thesis*, Alexandria University, Egypt.

Selvadurai, A. P. S., Gnanendran, C. T. (1989) "An experimental study of a footing located on a sloped fill, influence of a soil reinforcement layer" *Cand. Geotechnical J.*, 26(3): 467-473.

Shiraishi, S. (1990) "Variation in bearing capacity factors of dense sand assessed by model loading tests" *Soils and Foundations* 30 (1): 17-26.

Tatsuoka, F., Siddiquee, M. S. A., and Tanaka, T. (1994) "Link among design, model tests, theories and sand properties in the bearing capacity of footing on sand" *13 th Int. Conf. on Soil Mech. and Found. Eng*. New Delhi, India, (1): 87-88.

Yoo, C. (2001) "Laboratory investigation of bearing capacity behavior of strip footing on geogrid reinforced sand slope" *Geotext. and Geomembr.* 19: 279-298.

Design and Testing of Prestressed Square Concrete Piles: A Case History

Raymond Mankbadi[1], P.E., M. ASCE, Kuang-yu Yang[2], P.E., M. ASCE and Aravinda Ramakrishna[3], P.E., A. M. ASCE.

[1] Director of Geotechnical Engineering, Hardesty & Hanover, LLP., 850 Bear Tavern Road, suite 206, West Trenton, NJ 08628.
[2] Supervisor Engineer, Geotechnical Unit, New Jersey Department of Transportation, 1035 Parkway Avenue, Trenton, NJ 08625.
[3] Geotechnical Engineer, Hardesty & Hanover, LLP., 850 Bear Tavern Road, suite 206, West Trenton, NJ 08628.

ABSTRACT: The Route 52 Causeway reconstruction project in Ocean City, New Jersey involves the replacement of existing bridges supported on combination of timber and pre-cast reinforced concrete piles. A case history involving the geotechnical design and construction of the pier foundations for the low-level portions of the proposed replacement structure for proposed Route 52 causeway project is presented.

Pier foundations for the low-level portions of the proposed replacement structure are supported on 762-mm (30-in) square prestressed concrete piles. The design concepts of the piles are outlined. Static load test results performed on two square concrete piles, one at the land pier and the other at the water pier are presented. The adequacy of the design method adopted for the estimation of the axial capacity during the design phase is evaluated based on the results of the static load test, as well as the Pile Driving Analyzer (PDA) and Case Pile Wave Analysis Program (CAPWAP) data. The paper also discusses the installation procedures and load-testing programs for the square concrete piles. Finally, recommendations regarding design, construction and dynamic testing of relatively large-diameter piles are presented based on the results of the static load test, as well as the PDA and CAPWAP data.

INTRODUCTION

The project involves design and construction of the Route 52 Causeway. The existing Route 52 Causeway is an approximately two-mile long crossing of Great Egg Harbor between Somers Point on the New Jersey mainland and Ocean City on the barrier island. See Figure 1: Project Location Map.

The complete reconstruction of this facility involves staged construction of an approximately two-mile continuous bridge to replace the existing four structurally deficient and geometrically obsolete bridges, including the two movable bridges, as well as the embankment roadways on the tidal marsh islands. The construction of the project is separated into two contracts. Construction Contract A1 comprises the construction of the low-level portions of the proposed replacement structure on the Rainbow Islands and across Elbow Thorofare and Rainbow Channel, as well as the construction of appurtenant ramps, bulkheads and miscellaneous structures. The remaining two bridges will be constructed in Contract B.

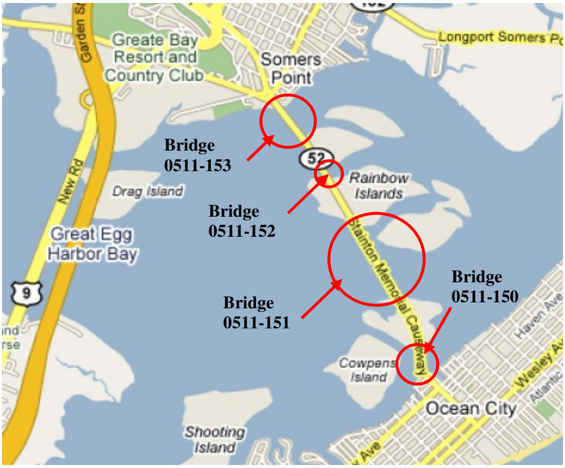

FIG. 1. Project Location Map

Construction of Contract A1 started in July 2006 and is ongoing. The new bridge piers and abutments are supported on 762-mm (30-in) and 610-mm (24-in) square prestressed concrete piles respectively.

This paper addresses the adequacy of the design method chosen during the design phase based on the results of the pile-testing program. In addition, a comparison study between the results of static and pile dynamic test results are also addressed to assess the reliability of dynamic test results. Finally, recommendations regarding design, construction and dynamic testing of square piles are presented based on the results of the static load test, as well as the PDA and CAPWAP data.

SUBSURFACE CONDITION AND PILE INSTALLATION PROCEDURE

The typical soil profile encountered along the land and water test site is given in Figure 2. In general, the stratigraphy illustrated in Figure 2 may be divided into two units ranging from overlaying loose to medium dense sand & silt and clay material on top of deeper medium dense to very dense Cohansey sand with interbedded clay lenses. The water test pile was jetted to approximately 2.1 m (7.0 ft) above the minimum tip elevation in order to achieve the required penetration without overstressing the pile in both compression and tension during driving. The land test pile was installed to the required penetration without jetting.

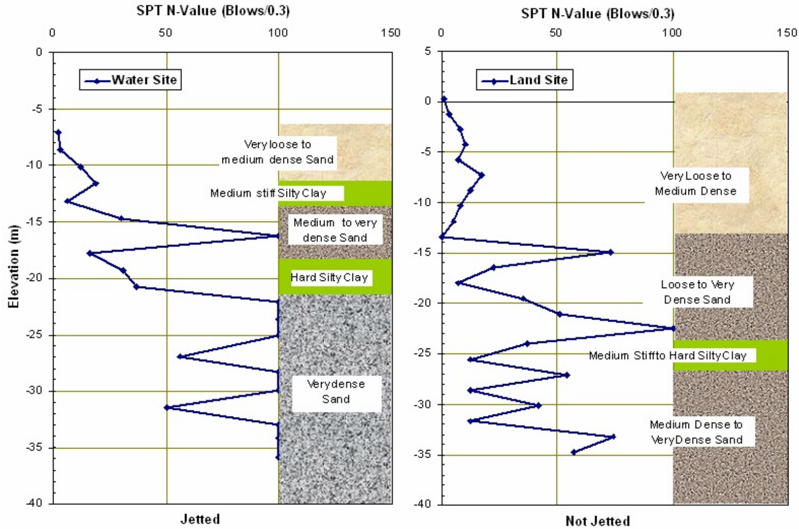

FIG2. Typical Soil Profile at Water and Land Test Sites

DESIGN CONSIDERATIONS

The evaluation of the ultimate capacity of piles in cohesionless soils is complicated since the driven capacity is related to many factors that are project specific, such as the site location, soil profile layering, soil layer properties, pile types, pile size, pile shape and construction method. Analysis has been performed using the effective stress (ύ) method in accordance with FHWA-HI-97-013 with the ύ and the N_t coefficients estimated from Figures 9.20 & 9.21 given by Fellenius (1991) for prestressed concrete piles. In addition, while estimating the geotechnical axial capacity of prestressed concrete piles, we assumed the following:

1. The 762-mm (30-in) piles are manufactured with a concrete compressive strength of 44.8 MPa (6500 psi), with 36, 12.7-mm diameter Grade 270 high-tensile-strength wire strands and Grade 60 reinforcing steel and elastic modulus of 35852 MPa (5200 ksi)
2. Streambed material in the 100-year scour prism above the total scour line has been removed and is not available for bearing.
3. Jetting reduces the skin friction by about 50% of the original calculated capacity in the jetted zone (Poulos and Davis 1980).
4. All piles are spaced at least three (3) diameters center to center.

The ultimate capacity required during driving was estimated to be 9198 kN (2068 kips) and 9964 kN (2240 kips) at the land and water test site locations respectively. It was estimated that the desired capacity would be reached at a pile-tip elevation of -20.4 m (-67.0 ft) and -32.0 m (-105.0 ft) at the land and water test site respectively.

PILE TESTING PROGRAM

The pile-testing program was developed to determine the ultimate failure load of the foundation pile and/or to determine the pile capacity required to support the applied load without excessive or continuous displacement. The load-testing program of Contract A1 called for two static (compression) load tests on dynamically monitored and instrumented 762-mm (30-in) square prestressed concrete test piles at land and water pier locations. The land test pile was a sacrificial pile but the water test pile was a production pile. The contract installation criteria and the maximum testing loads are summarized in Table 1.

Table 1. Pile Installation and Static Load Test Criteria

Location	Prestressed Concrete Pile Size	Minimum Tip Elev.	Required Ultimate Driving Resistance	Maximum Tip Elev.	Maximum Required Static Test Load
Land Site	762 mm	-18.9 m	9198 kN	–20.4 m	12677 kN
Water Site	762 mm	-30.3 m	9964 kN	-32.0 m	12677 kN

Pile Instrumentation Program

A pile instrumentation program was implemented to measure the response of the pile under axial compression along the shaft. Ten and fourteen strain gages were embedded in the land and water test piles respectively during casting the concrete. The strain gages data were used to evaluate the stresses, and thereby the loads at points along the pile length, in addition to evaluate the pile-to-soil load transfer pattern. In addition, Tell Tales and dial gages were also utilized.

PILE DYNAMIC TEST

Measurement of force and acceleration near the pile top during driving has become a routine practice (Likins et al., 1988). These measurements are recorded by PDA tests during driving, and are then processed by CAPWAP, which evaluates pile capacity, pile driving stresses, pile integrity and driving systems performance. PDA was required for the development of the production pile installation criteria, to provide more reliable capacity and performance data.

A Pileco D160-32 Diesel Impact Hammer was chosen by the contractor to drive the 762-mm (30-in) concrete test piles used in the project. Pileco D160-32 hammer had a ram weight of 144.0 kN (32.28 kips) and an operating energy in the range of 119 to 291 kN-m (161,375.0 to 395,080 lb-ft). The hammer was operated with a 457-mm-thick (18-in-thick) wooden pile cushion. During the installation of the test pile, the hammer-operating stroke was adjusted based on the observation of the driving stresses. During pile driving, the hammer energy was controlled to satisfy the following conditions:

1. The maximum compressive and tensile driving stress should be less than 26.6 MPa (3.86 ksi) and 8.5 MPa (1.24 ksi) respectively as recommended by AASHTO.
2. A fresh pile cushion should be maintained all the time.

The results of the dynamic testing during initial driving and restrike are summarized in Table 2. As per the special provision of the contract, two restrikes were performed: the first restrike after a 24-hour waiting period from the initial driving and the second restrike after an additional 7-day waiting period from the first restrike. In general, lesser capacity was achieved at the end of the initial driving and higher capacity was achieved during restrike. This can be attributed to the soil set-up effect.

Table 2. Pile Dynamic Test Results

Actual Pile Tip Elevation	Hammer Size	Test Condition	Reported Blow Count (Blows/25.4 mm)	Capacity from CAPWAP Analysis		
				Total Capacity	Shaft Resistance	Toe Bearing
Water Site Test: 54 NB Pile No. 9 (Jetted)						
-32.2 m	D160-32	EOD	6	8491 kN	1908 kN	6583 kN
-32.2 m	D160-32	BOR1	4	9697 kN	3461kN	6236 kN
-32.2 m	D160-32	BOR2	5	9786 kN	4448 kN	5338 kN
Land Test Site (Not Jetted)						
-19.8 m	D160-32	EOD	3	7397 kN	3443 kN	3954 kN
-19.8 m	D160-32	BOR1	4	8456 kN	4408 kN	4048 kN
-20.5 m	D160-32	BOR2	6	8807 kN	4724 kN	4079 kN

EOD: End of Drive, BOR1: Beginning of Restrike after 24 Hr, BOR2: Beginning of Restrike after 7days.

STATIC LOAD TEST

The static load test was performed to determine pile axial capacity as well as to verify the results of the pile dynamic test. A static load test allows a more rational design. The static load test results are generally more reliable than the dynamic test results. As per contract specification, the static load tests were performed by procedures outlined in ASTM D1143 using the quick load compression test method, except that the tests were taken until plunging failure occurred or the capacity of the loading systems reached 12677 kN.

As per AASHTO recommendations for piles greater than 610 mm (24 in), but less than 914 mm (36 in) in diameter, the axial resistance is determined by linear interpolation between diameters of 610 mm (24 in) and 914 mm (36 in). AASHTO also suggests that the Davisson Method under-predicts the ultimate pile axial capacity for pile diameters greater than 610 mm (24.0 in). Therefore, the compression test results were evaluated as per FHWA SA-91-042, Kyfor et al. (1992) for pile diameters greater than 610 mm (24 in). Based on FHWA recommendations, the ultimate capacity of the test piles is 9119 kN (2050 kips) and 12677 kN (2850 kips) for land and water sites, respectively. Refer to Figure 3 for the load versus deflection curve for the static load test at the land and water test sites.

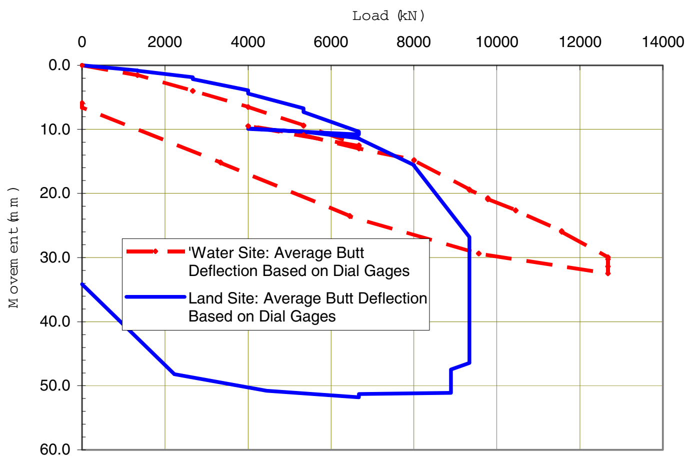

FIG. 3. Static Load Test Results (Load-Settlement Curve)

The static load test result of the land site yields a slightly lesser capacity than the anticipated 9199 kN (2068 kips) during design. It should be noted that the original foundation was designed with a safety factor of 2.25, but with the implementation of the static load test, the safety factor can be revised to 2.0. Therefore, it was concluded that the performance of 762-mm (30-in) prestressed concrete piles on the land site is acceptable.

COMPARISON BETWEEN DYNAMIC AND STATIC LOAD TEST

The results of the PDA and the results of the static load tests at both the land and water site were compared to check the reliability of the pile dynamic test.

As shown in Figure 4, the dynamic test results underestimated the pile ultimate capacity by only 311.4 kN (70 kip) at the land site and 2891.3 kN (650.0 kip) at the water site. The similarity between PDA results and static load test results for the ultimate capacity at the land site and the disparity between the two tests at the water site may be attributed to the following factors:

Time Ratio

The soil is greatly disturbed when a pile is driven into the soil, particularly if jetting is utilized. As the soil surrounding the pile recovers from the installation disturbance, a time-dependent change in pile capacity occurs due to soil setup or relaxation. Therefore, an important factor when comparing capacities obtained from dynamic and static testing is to consider the time of testing for both the static load test and the dynamic restrike test (Goble et al., 1980; Skov and Denver, 1988). The term "Time Ratio" is defined as the ratio between the number of days difference between the end of driving to restrike and the end of driving to the static load test. Likins et al. (1988) showed that setup increases linearly with log time and that the time effect may be considered negligible if the time ratio is between 0.33 and 1.25. Piles with lower time ratios usually yield a significant difference between static and dynamic test results. The time ratios for the land and water test sites were 0.16 and 0.23 respectively. This, in addition to the fact that Cohansey sand has relatively high silt content, may indicate that the time ratio may have been an important factor in this project. Therefore, it was concluded that time ratio and soil setup played a major role in the difference in capacity observed between the results of the static and dynamic test results at the water test site.

Soil Mobilization

Fellenius et al. (1989) showed that capacities determined in a dynamic analysis will agree fairly well with the results of a static test, provided that the CAPWAP analysis is performed on a material where the hammer has been able to mobilize the full soil resistance and where the effect of time and soil setup are considered. For this project, during pile driving the land test pile experienced good penetration in soil strata, indicating full mobilization of the soil resistance, whereas the water test pile experienced little penetration due to jetting, indicating partial mobilization of soil resistance. Therefore, it was concluded that pile penetration played a major role in mobilization of soil resistance and the observed results for the static and dynamic tests at the land and water test sites.

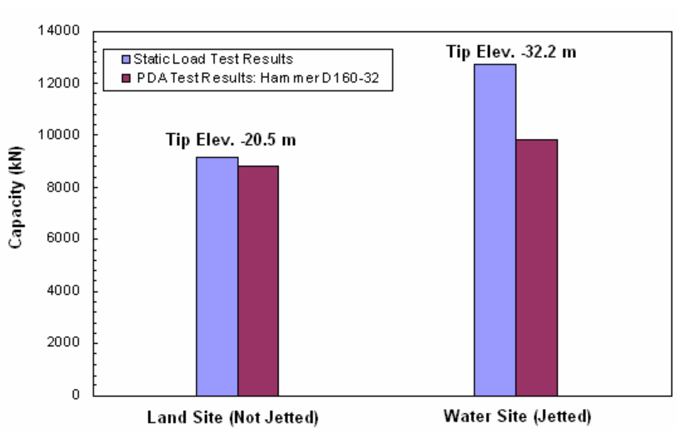

FIG. 4. Comparison of Static and Dynamic Test Results

ADEQUACY OF THE DESIGN METHOD

Based on the results of the pile-testing program, it was concluded that the design "effective stress (ύ)" method chosen to estimate the pile axial capacity during the design yielded reliable results at both land and water test sites. However, the land pile test program yielded a slightly lesser capacity than originally anticipated during the design, most likely attributed to local geology. Therefore, it was concluded that the local geology should be considered during design.

CONCLUSION

The static load test is recommended so that the degree of conservatism involved in the PDA and CAPWAP data is addressed. Relying only on dynamic testing can lead to the implementation of costly and timely measures during construction such as lowering the estimated tip elevation beyond what was anticipated during design.

The pile dynamic test yields good results when CAPWAP analysis is performed on a material where the hammer has been able to mobilize the full soil resistance and has been able to consider the effects of time and soil setup.

Pile instrumentation program was successful in determining the distribution of the applied test loads along the shaft and the pile toe.

Dynamic testing practice for piles is limited when mobilizing the maximum available soil resistance is of concern.

Most widely accepted design methods need to be modified to take method installation and regional geology into account for analyzing the pile behavior.

Documentation of dynamic and static test results for square concrete piles in other projects is greatly needed in order to advance the state of practice for the design and construction of square piles.

ACKNOWLEDGEMENT

This paper is based on the design and construction work of Michael Baker Jr., Inc. (the prime designer), Hardesty & Hanover, LLP. New Jersey Department of Transportation, and George Harms Construction Co, Inc. We are grateful to Jack Mansfield and Dave Lambert of NJDOT for their support and dedication. We are also grateful to Glen Schetelich and Andy Coates from Hardesty & Hanover, Inc. and John Pizzi from STV Incorporated for their valuable comments and suggestions.

REFERENCES

ASTM D-1143-81 (1997). " *Standard Test Method for Piles Under Static Axial Compressive Load*" Annual Book of ASTM standards, American Society for Testing and Material (ASTM), Section4, Volume 04.08 Soil and Rock (I)

American Association of State Highway and Transportation Officials (AASHTO) "*AASHTO LRFD Bridge Design Specification*", 2006 Interim Revisions.

American Association of State Highway and Transportation Officials (AASHTO, 2001) "*AASHTO Bridge Design Specification*", 17th edition.

Fellenius B.H., Riker R.E., O'Brien A.J., and Tracy G.R (1989) "*Dynamic and Static Testing in Soil Exhibiting Set-Up*" Journal of Geotechnical Engineering, Vol. 115, No. 7, pp. 984-1001

Fellenius, B.H. (1991). "*Chapter 13-Pile Foundation Engineering Handbook*" Second Edition, H.S. Fang, Editor, Van Nostrand Reinhold Publisher, New York.

FHWA Publication No. FHWA HI 97-013, "*Design and Construction of Driven Pile Foundations*". Revised November 1998.

GRLWEAP, "*Wave Equation Analysis of Pile Driving, Version 1998-2*", Pile Dynamics Inc., 1999.

Hardesty & Hanover, LLP. "*Geotechnical Engineering & Foundation Report: Route 52 Causeway Construction Contract A*", March 2006.

Goble, G., Rausche, F., and Likins, G., (1980) " *The Analysis of Pile Driving-A State-of-the-Art*, Proc. of the International Seminar on the Applications of Stress-Wave Theory on Piles, Stockholm, Sweden.

Kyfor, Z.G., Schnore, A.R., Carlo, T. A. and Bailey, P.F. (1992). "*Static Testing of Deep Foundations*". Report No. FHWA-SA-91-042, U.S. Department of Transportation, Federal Highway Administration, Office of Technology Applications Washington, D.C

Likins, G.E., Hussein, M., and Rausche, F. (1988). "*Design and Testing of Pile Foundation*. " Third International Conference on the Application of Stress-Wave Theory of Piles, Canada.

Skov, R., and Denver, H. (1988). " *Time-Dependence of Bearing Capacity of Piles*." Third international Conference on the Applications of Stress-Wave Theory to Pile, Canada.

York, D., Brusey, W., Clement, F., and Law, S. (1994). "*Setup and Relaxation in Glacial Sand." Journal of Geotechnical Engineering, Vol 120 ASCE.*

Effect of Compressive Load on Uplift Capacity of Single Piles: An Investigation

Eswar.P[1], Naga S.T[2], N.R.Patra[3], M.ASCE

1, 2.M.tech students, Geotechnical Engineering division, Department of Civil Engineering, IIT KANPUR, U.P-208016, INDIA.
3: Corresponding Author, Assistant Professor, Geotechnical Engineering division, Department of Civil Engineering, IIT KANPUR, UP-208016, INDIA .
Phone:+91-5122597623, FAX:+91-5122597395, E-MAIL: nrpatra@iitk.ac.in

ABSTRACT: In this paper, an analytical model has been proposed to predict the net ultimate uplift capacity of single piles embedded in sand subjected to stage compressive loading of 0%, 25%, 50%, 75% and 100% of their ultimate capacity in compression. The following parameters have been considered as variables: density of foundation medium, embedded length to diameter ratio (L/d) of piles, stages of compressive loads. The presence of compressive load on the pile decreases the net ultimate uplift capacity of pile and the decrease depends on the magnitude of presence of the compressive load. It may be due to change in the particle size distribution, soil pile friction angle, or soil compressibility. The change in soil-pile friction angle has been considered in the present model. To validate the model, a comparison has been made with the available laboratory model test results (Dash and Pise2003) and the results obtained from the present model.

INTRODUCTION

Structures like transmission towers, mooring systems for ocean surface, submerged platforms, bridge abutments are constructed on pile foundations where in the piles are subjected to uplift loads. A good number of laboratory model and large scale field test results on ultimate uplift capacity of single piles in granular soil are available (Downs and Chieurzzi 1966; Meyerhof and Adams 1968; Das et al 1977, Poulos and Davis 1980; Chaudhuri and Symons 1983; Levacher and Sieffert 1984; and Chattopadhyay and Pise 1986).The design of a pile foundation under compressive loads/uplift loads are based on the allowable loads .Such allowable loads can be obtained by applying a suitable factor of safety on net ultimate uplift capacity of piles. As the super structure load is acted on the foundation, the compressive load by the super structure will act gradually. Again the construction of foundation and super structure are made in stages. For example, if fifty percent of construction of super structure is over, then it may impact 50% of compressive load on pile foundation. Because of wind load or earthquake load, the piles in the foundation may subject to uplift. This is a typical case of post construction where the compressive load comes first to foundation by staged construction of super structure prior to the uplift load. The full static compressive load comes on foundation when the super structure is completed in all respects. A few investigations are available on the study of uplift behavior of single piles subjected to stage compressive load (Dash and Pise 2003). Based on the model studies, Dash and Pise (2003) assumed the variation of soil-pile friction angles with percentage stage compressive loading. In this paper, a generalized model has been proposed to predict the net ultimate uplift capacity of single piles subjected to stage compressive loads. The model takes into consideration of soil density, embedment length to diameter ratio and stage compressive loads. The results obtained from the proposed model have been compared with the available laboratory model test results.

EXISTING PREDICTIVE MODELS

In the following section the commonly applied predictive models are presented in brief.

STANDARD MODEL

Assuming that failure takes place on a cylindrical surface along the shaft the net uplift capacity of a vertical pile can be estimated as follows,

$$P_{nu} = \frac{\pi}{2} K_s d\gamma L^2 \tan\delta \qquad (1)$$

Where, K_s is the lateral earth pressure coefficient, d is the diameter of the pile, γ unit weight of the soil, L is the length of the pile, δ , is the soil-pile friction angle. As suggested by Levacher and Sieffert (1984) and Das (2003) for bored piles K_s can be taken as equal to $K_s = (1\text{-}\sin\phi)$.

TRUNCATED MODEL

Field engineers generally estimate the uplift capacity of the pile by assuming a slip surface as a truncated cone with the enveloping sides rising at $\phi/2$ degrees from the vertical. Dead weight within the frustum is usually considered as the ultimate uplift capacity of the pile.

$$P_{nu} = \frac{\pi}{3} L^3 \tan^2 \frac{\phi}{2} \gamma \qquad (2)$$

MEYERHOF'S MODEL (1973)

Ignoring the weight of the pile he suggested an expression for the pull-out resistance assuming that under axial pull the failed soil mass has a roughly similar shape as for a shallow anchor.

Thus,

$$P_{nu} = \frac{\pi}{2} K_u d\gamma L^2 \tan\delta \tag{3}$$

Where K_u=uplift coefficient and can vary with in wide limits and depends on soil properties, type of pile and method of installation.

DAS MODEL (1983)

Based on the model tests, he reported that unit skin friction at the soil-pile interface increases linearly with depth up to a critical embedment ratio. The critical embedment ratio is dependent on the relative density (D_r) and expressed as,

$$\left(L/d\right)_{cr} = 0.156D_r + 3.58 \quad (\text{For } D_r \le 70\%) \tag{4}$$

and

$$\left(L/d\right)_{cr} = 14.5 \qquad (\text{For } D_r \ge 70\%) \tag{5}$$

The net ultimate uplift capacity of piles in sand can be estimated as,

$$P_{nu} = \frac{1}{2} p\gamma L^2 K_u \tan\delta \quad [\text{If } L/d \le (L/d)_{cr}] \tag{6}$$

$$P_{nu} = \frac{1}{2} p\gamma L_{cr}{}^2 K_u \tan\delta + p\gamma L_{cr} K_u \tan\delta (L - L_{cr}) \; [\text{If } L/d > (L/d)_{cr}] \tag{7}$$

CHATTOPADHYAY AND PISE'S MODEL (1986)

They proposed a generalized theory to evaluate uplift resistance of a circular vertical pile embedded in sand. Assuming the failure surface to be curved, they estimated the net uplift capacity of a pile embedded in sand as,

$$P_{nu} = A_1 \gamma\pi d L^2 \tag{8}$$

Where A_1 =Net uplift capacity factor and depends on ϕ ,δ, and L/d ratio.

The accuracy of the predictions made by using standard model would mainly depend on the correctness of the assumed value of the coefficient of lateral earth pressure. The cone model overestimates the uplift capacity values for long piles. Meyerhof's model needs the use of graphical charts for choosing the uplift coefficient. To apply Das's model, the use of Meyerhof's charts are needed to choose the value of the uplift coefficient. The model proposed by Chattopadhyay and Pise underestimates the net uplift capacity when L/d ratio is 30 or above. Comparing all the models, the proposed model is simpler and neither involves any complicated analysis nor needs any graph.

PROPOSED MODEL

The failure surface is assumed to be a truncated cone with the edges passing through the tip of the pile at an angle of β with respect to the vertical axis of the pile as shown in FIG.1. The angle depends on factors like friction angle and the angle of dilatancy (ψ), which is a function of relative density of the soil. From literature it is found that this angle has been assumed to be any of the following, namely dilatancy angle (ψ), $\phi/2$ or a function of ϕ (Dicken and Leung 1990). Different trial values of β, the angle that the slip surface makes with the vertical were taken to estimate the theoretical uplift capacity of piles and compared with the experimental observations as reported by others (Meyerhof and Adams 1968; Das et al 1977, Poulos and Davis 1980; and Chattopadhyay and Pise 1986). It is observed that an angle equal to $\phi/6$ and $\phi/4$ for loose sand and dense sand are in good agreement with the experimental results.

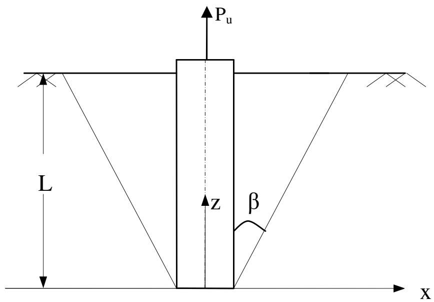

K = Coefficient of lateral earth pressure
β = Angle of failure surface with vertical
ΔR = Normal force
ΔQ = Resultant vertical force
ΔT = Mobilized shear resistance
ΔP = Net uplift force on the element considered

FIG. 1. Pile and Failure Surface

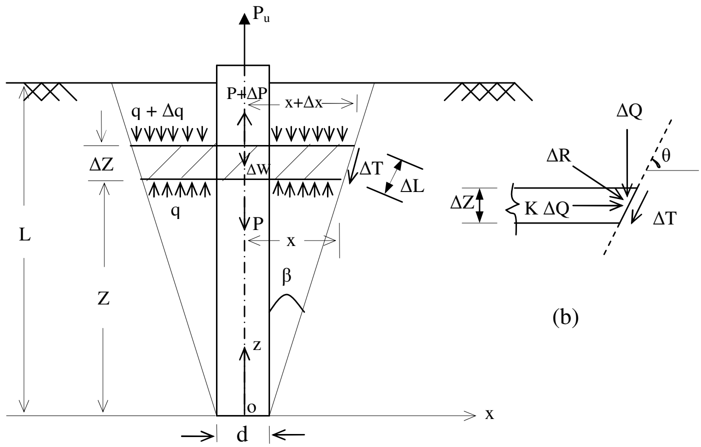

(a)

FIG. 2. Free body diagram of the wedge

During uplift of a pile, an axi-symmetric solid body of revolution of soil along with the pile assumed to move up along the resulting surface. The movement is resisted by the mobilized shear strength of the soil along the failure surface and self- weight of the soil and pile. In limiting equilibrium condition, ultimate capacity of the pile attained. A circular wedge of thickness ΔZ at a height Z above the tip of the pile is considered. Forces acting on the wedge are shown in FIG. 2. For evaluating the mobilized shear resistance ΔT along the failure surface of length, ΔL at limiting condition it is assumed that ΔT =ΔR tan ϕ, in which ΔR is normal force acting on the failure surface of the wedge. Further the coefficient of lateral earth pressure (K) within the wedge is taken as (1- sinϕ) tanδ/ tanϕ. This expression for K has to be chosen so that δ= ϕ, $K=K_0$ = (1- sinϕ), and for other values of δ<ϕ, K is a function of K_0,δ, and ϕ (Chattopadhyay and Pise 1986).

From FIG. 2.

$$\Delta R = \Delta Q \cos\theta + K \Delta Q \sin\theta \tag{9}$$

Where

$$\Delta Q = \gamma\left(L - Z - \frac{\Delta Z}{2}\right)\Delta L \tag{10}$$

$$\Delta R = \gamma\left(L - Z - \frac{\Delta Z}{2}\right)(\cos\theta + K\sin\theta)\frac{\Delta Z}{\sin\theta} \tag{11}$$

and

$$\Delta T = \gamma\left(L - Z - \frac{\Delta Z}{2}\right)(\cos\theta + K\sin\theta)\frac{\Delta Z \tan\phi}{\sin\theta} \tag{12}$$

Considering the vertical equilibrium of the circular wedge, and assuming that weight of the pile of length ΔZ is equal to the weight of the soil corresponding to the volume occupied by the pile for the length ΔZ;

$$\begin{aligned}&(P+\Delta P) - P + q\pi x^2 - (q+\Delta q)\pi(x+\Delta x)^2 \\ &-\Delta W - 2\pi\left(x + \frac{\Delta x}{2}\right)\Delta T \sin\theta = 0\end{aligned} \tag{13}$$

Substituting the value of ΔT from Eq. 12 in Eq. 13 and simplifying

$$\begin{aligned}&\frac{\Delta P}{\Delta Z} = \pi q \frac{\Delta x}{\Delta Z}(2x+\Delta x) + \pi\frac{\Delta q}{\Delta Z}(x+\Delta x)^2 + \pi\frac{\Delta q}{\Delta Z}(x+\Delta x)^2 \\ &+\pi(x+\Delta x)^2\gamma + 2\pi\left(x+\frac{\Delta x}{2}\right)\gamma\left(L-Z-\frac{\Delta Z}{2}\right)(\cos\theta + K\sin\theta)\tan\phi\end{aligned} \tag{14}$$

In the limit, Eq.14 can be written after substituting q= γ (L-Z).

$$\begin{aligned}&\frac{dp}{dZ} = 2\pi\left(\frac{Z}{\tan\theta} + \frac{d}{2}\right)\gamma(L-Z)\frac{1}{\tan\theta} \\ &+2\pi\left(\frac{Z}{\tan\theta} + \frac{d}{2}\right)\gamma(L-Z)(\cos\theta + K\sin\theta)\tan\phi\end{aligned} \tag{15}$$

$$\frac{dP}{dZ} = C_1(L-Z) + C_2(LZ - Z^2) \tag{16}$$

Where, $$C_1 = \pi d\gamma\left[\frac{1}{\tan\theta} + (\cos\theta + K\sin\theta)\tan\phi\right] \quad (17)$$

$$C_2 = \frac{2\pi\gamma}{\tan\theta}\left[\frac{1}{\tan\theta} + \left(\cos\theta + K\sin\theta\right)\tan\phi\right] \quad (18)$$

Hence gross uplift capacity of the pile P_u is given by

$$P_u = \int_0^L dPdZ = \int_0^L \left[C_1\left(L - Z\right) + C_2\left(LZ - Z^2\right)\right]\, dZ \quad (19)$$

$$P_u = \frac{C_1}{2}L^2 + \frac{C_2}{6}L^3 \quad (20)$$

$$\text{Net uplift capacity } P_{nu} = P_u - \frac{\pi d^2}{4}L\gamma \quad (21)$$

The net uplift capacity of single piles subjected to stage compressive load can be found using this model. Assuming the effects of the compressive load on the pile only alters the soil-pile friction angle δ (Dash and Pise 2003). The soil friction angle ϕ remains unchanged. An empirical relation has been proposed to get the available soil-pile friction angle. It depends on stage loading factor and L/d ratio factor. This relation has been developed by considering the experimental results as reported by Dash and Pise (2003). The available soil-pile-friction angle δ after stage loading can be obtained from the following equation

$$\delta_{available} = \delta_{initial} - \text{stage loading factor} \times L/d \text{ factor} \times \delta_{initial} \quad (22)$$

Where, $\delta_{available}$ = the available soil-pile friction angle after stage loading, stage loading factor = 0.25 or 0.5 or 0.75 or 1.0 depending upon the stage loading (25%, 50%, 75%, 100%), L/d factor = 1.8, $\delta_{initial}$ = the soil-pile friction angle before stage loading. By changing $\delta_{available}$ in K, the net uplift capacity factor can be found out by this model.

THEORITICAL RESULTS:

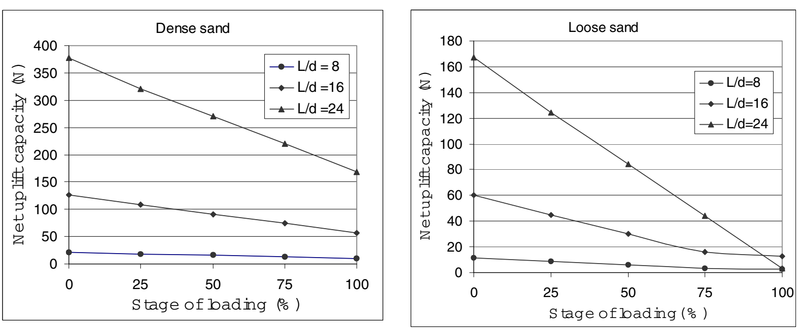

(a) (b)

FIG. 3. Net uplift capacity versus stage compressive loading ((a) Dense sand (b) Loose sand)

The values of net uplift capacity of single piles are evaluated from Eq.21 for different stage compressive loading 0%, 25%, 50%, 75%, 100%. It is shown in FIG. 3. In general, the net uplift capacity decreases with increase in stage compressive load for both loose and dense sand. For L/d = 8 and 16, the decrease is more up to 50% stage compressive loading and thereafter it remains constant. However for L/d = 24, the net uplift capacity decreases with increase in stage compressive loading.

COMPARISON:

Model test results of Das and Pise(2003) reported uplift tests results of rough pile of 19 mm diameter, for slenderness ratio varying from 8 to 24 .The relative density of sand used were35%, 80% and the corresponding values of ϕ were 30^o, 38^o and γ=1.5 gm/cc,1.64 gm/cc respectively. For predicting net ultimate uplift capacity of piles the soil-pile friction angles were taken as 21^o, 29^o respectively. Theoretical net uplift capacity of piles was predicted from eq 21. Measured values of net uplift capacities of piles for different L/d ratios are plotted against the predicted values in Fig. 4.The ideal line having an equation $P_{measured=}$ $P_{predicted}$ is also plotted. The measured values ($P_{measured}$) are the observed values taken from the experiment model studies. The predicted values ($P_{predicted}$) are the values obtained from the present model. It is found that for 67 % of data (10 out of 15) the error is within ± 35% for both loose and dense sand. However, for loose sand, the prediction made by Dash and Pise (2003) overestimates the values at a range of 50 to 130% for 0% compressive load.

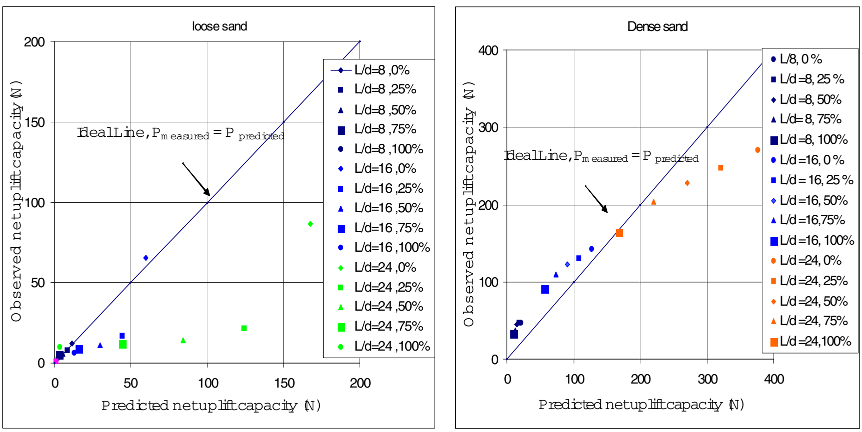

(a) (b)

FIG. 4 .Observed versus predicted values ((a) Loose sand (b) Dense sand)

CONCLUSION: From the foregoing study the following conclusions are drawn: An analytical method has been proposed to predict the net ultimate uplift capacity of single piles subjected to stage compressive loading. The effects of parameters like soil density, embedment length to diameter ratio and stage compressive loads are incorporated in the proposed analysis**.** The net ultimate uplift capacity decreases with increase in stage compressive loading for both loose and dense sand. Comparisons have been made with the available experimental model tests results and the values obtained from the proposed analytical model. The range of error in most of the cases is within ±35%. The proposed model is capable of predicting net ultimate uplift capacity of single piles subjected to stage loading.

REFERENCE:

Chattopadhyay, B.C. and Pise, P.J (1986) “Uplift capacity of piles in sand.” *J. Geotech Eng.,* 112(9):888-904.

Chaudhuri, K. P. R. and Symons, M. V. (1983). “Uplift resistance of model single piles.” Proc. of the Conf. on Geotech. Practice in Offshore Engineering, ASCE, 335-355

Das, B.M, (1983)” A procedure for estimation of uplift Capacity of rough piles”. *Soils Found* 23(3):122-126.

Das, B.M., Seeley, G.R. and Pfeile, T.W., (1977)” Pull out resistance of rough rigid piles in granular soils”. *Soils Found* 17(3):72-77.

Dash, B.K and Pise, P.J (2003)” Effect of compressive load on uplift capacity of model piles”. *J. Geotech and Geoenvironmental Eng*. ASCE 129(11):987-992.

Dicking, E.A. and Leung CF (1990)” Performance of piles with enlarged bases subjected to uplift forces”. *Canadian Geotech J.* 27(5):546-556.

Downs, D. I., and Chieurzzi, R. (1966). “Transmission tower foundation.” *J. Power Div. (Am. Soc. Civ. Eng.)*, 92(2), 91-114.

Levacher,. D.R. and Sieffert, J.G., (1984) “Test on model tension piles “*.J Geotech Eng.* ASCE 110(12):1735:1748.

Meyerhof, G.G., (1973) “Uplift resistance of inclined anchors and piles”, *Proceedings of the 8th International conference on soil Mechanics and Foundation Engrg.* Moscow, vol.2, pp 167-172.

Meyerhof, G.G. and Adams, J. I. (1968). “The ultimate uplift capacity of foundation.” Can. Geotech. J., 5(4), 225-244.

Poulos, H. G., and Davis, E. H. (1980). “ Pile foundation analysis and design.” Ist ed., John Wiley and Sons, New York, USA.

Laboratory Investigation of the Behavior of Square Footings on Reinforced Crushed Limestone

Murad Abu-Farsakh[1], Qiming Chen[2], and Radhey Sharma[3]

[1]Research Assistant Professor, Louisiana Transportation Research Center, Louisiana State University, Baton Rouge, LA 70808; and Adjunct Professor, Dept of Civil and Environmental Engineering, Louisiana State University, Baton Rouge, LA.
[2]Research Associate, Louisiana Transportation Research Center, Louisiana State University, Baton Rouge, LA 70808.
[3]Associate Professor, Dept of Civil and Environmental Engineering, Louisiana State University, Baton Rouge, LA 70803.

ABSTRACT: This research study aims at investigating the behavior of spread footings on reinforced crushed limestone using laboratory model tests. The model tests were conducted inside a steel box with dimensions of 1.5 m (length) × 0.91 m (width) × 0.91 m (height) using a steel plate with dimensions of 152 mm × 152 mm (6 in × 6 in). The parameters investigated in this study include the number of reinforcement layers and the tensile modulus and type of reinforcement. The investigation also evaluated the behavior of reinforced limestone foundations. Because of serviceability requirement in actual foundation application, the test results were evaluated in terms of the bearing capacity ratio (BCR) at limit settlement levels and the settlement reduction factor (SRF) at different surface pressures. The test results showed that the inclusion of reinforcement can appreciably improve the soil's bearing capacity up to a factor of 2.85 at a settlement ratio of 10% and reduce the footing settlement up to 75% at a surface pressure of 5500 kPa (798 psi). It was also observed that an increase in number of reinforcement layers increases the bearing capacity and reduces the settlement. The results also showed that reinforcements with higher tensile modulus performed better than reinforcements with lower tensile modulus, and that steel reinforcement performed better than geosynthetic reinforcement.

INTRODUCTION

In many cases of construction, shallow foundations are built on top of existing cohesive soil deposits or embankment soils of low to medium plasticity, resulting in low bearing capacity and/or excessive settlement problems. This can cause structural damage, reduction in the durability, and/or deterioration in the performance level. Conventional treatment methods were either to replace part of the weak cohesive soil by an adequately thick layer of stronger granular fill, increase the dimensions of the footing, or a combination of two. An alternative and more economical solution is the use of reinforced soil foundation (RSF). This can be done by either reinforcing cohesive soil directly or replacing the poor soils with stronger granular fill (e.g. crushed limestone) in combination with geosynthetics reinforcement. The resulting composite zone (reinforced soil mass) will improve the load carrying capacity of the footing and provide better pressure distribution on top of the underlying weak soils, hence reducing the associated settlements.

In the past thirty years, a significant amount of research efforts has been made to investigate the behavior of the RSF. Different researchers attempted to evaluate the benefits of using RSFs through bearing capacity ratio (BCR), which is defined as the ratio of the bearing capacity of the RSF to that of the unreinforced soil. An early study conducted by Binquet and Lee (1975a) evaluated the bearing capacity of metal strips on reinforced sand soil. Since then, numerous experimental studies have been conducted to study the bearing capacity of footings on reinforced sandy soil (e.g., Huang and Tatsuoka, 1990; Omar et al., 1993; Yetimoglu et al., 1994; Adams and Collin, 1997; Lee and Manjunath, 2000), reinforced clayey soil (e.g., Ramaswamy and Puroshothama, 1992; Shin et al., 1993; Das et al., 1994) and reinforced gravel (e.g., DeMerchant, et al., 2002; Uchimura, et al., 2004). All these works indicated that the use of reinforcements can significantly increase the soil's bearing capacity and reduce the settlement of footing. Binquet and Lee (1975b) identified three possible failure modes depending on the configuration and tensile strength of reinforcement. They also developed a design method for a strip footing on reinforced sand based on the concept of tension membrane effect. Huang and Tatsuoka (1990) presented two mechanisms that can describe the increase in bearing capacity of RSF: deep footing mechanism and wide-slab mechanism. They substantiated the strain restraining effect (confinement effect) by successfully using short reinforcement with a length (l) equal to the footing width (B) to reinforce sand.

The main objective of this paper is to investigate the behavior of footings on reinforced crushed limestone. For this purpose, extensive laboratory model tests were conducted on reinforced crushed limestone. The parameters investigated in the model tests include the number of reinforcement layers (N), and the tensile modulus and type of reinforcement.

MATERIAL PROPERTIES AND TEST PROGRAM

Material properties and model foundation

A series of laboratory model footing tests were conducted on reinforced crushed limestone at the Geotechnical Engineering Research Laboratory (GERL) at the Louisiana Transportation Research Center (LTRC). The foundation soil consisted of a crushed limestone with a uniformity coefficient of 20.26 and a coefficient of curvature of 1.37. The crushed limestone has 100% passing 37.5 mm (1.5 in) opening sieve, 81% passing 19 mm (0.75 in) opening sieve, 47% passing No.4 opening sieve and 4% passing No. 200 opening sieve with an effective particle size (D_{10}) of 0.465 mm (0.018 in) and a mean particle size (D_{50}) of 5.662 mm (0.223 in). The maximum dry density of the soil was 2,268 kg/m^3 (142 lb/ft^3) with an optimum moisture content of 7.5% as determined by Standard Proctor test (ASTM 698). This crushed limestone was classified as GW according to the Unified Soil Classification System (USCS), and A-1-a according to the AASTHO classification system. Large scale (304.8 mm × 304.8 mm × 130.9 mm) (12 in × 12 in × 5.15 in) direct shear tests on this crushed limestone at the maximum dry density indicated internal friction angle of 53°.

The model footing used in the tests was a steel plate with dimensions of 152 mm × 152 mm (6 in × 6 in) (B×L) and 25.4 mm (1 in) thickness. The model tests were conducted in a 1.5 m (60 in) long, 0.91 m (36 in) wide, and 0.91 m (36 in) deep steel test box. The testing procedure was performed according to the ASTM D 1196-93 (ASTM 1997), where the load increments were applied and maintained until the rate of settlement was less than 0.03mm/min over three consecutive minutes. The load and the corresponding footing settlement were measured by a ring load cell and two dial extension gauges, respectively.

Five types of geogrids: GG1, GG2, GG3, GG4 and GG5, one type of steel wire mesh, SWM, and one type of steel bar mesh, SBM, were used as reinforcement in the tests. The size of reinforcement was 1.47m × 0.86m (58 in × 34 in) in all tests. The physical and mechanical properties of these reinforcements as provided by the manufacturers are listed in Table 1.

Section Preparation and Compaction Control

The crushed limestone was placed and compacted in lifts inside the steel test box. The thickness of each lift was 51 mm (2 in). The test samples were prepared by hand mixing the crushed limestone and water. The amount of crushed limestone needed for each lift was calculated first. Then, the crushed limestone was poured into the box, raked level, and compacted using a 203 mm × 203 mm (8 in × 8 in) plate adapted to a vibratory jack hammer to the predetermined height. The jackhammer delivers compaction energy of 58.3 m·N (43 ft·lb) and blows at a rate of 1400 per minute.

The nuclear density gauge and the geogauge stiffness device were used to measure the density and stiffness/modulus for each lift for construction control. The dry densities varied from 2,243 to 2,333 kg/m^3 (140 lb/ft^3 to 146 lb/ft^3) with moisture contents ranging from 5.5 to 6%. The corresponding geogauge stiffness moduli were in the range of 70 to 90 MPa (10,153 to 13,053 psi) for the crushed limestone with and without reinforcement inclusion.

TABLE 1: Properties of reinforcements

Reinforcement	Polymer Type	Structure	T^a, kN/m		J^b, kN/m		Aperture Size, mm
			MD^c	CD^d	MD^c	CD^d	
GG1 geogrid	Polypropylene	Extruded	4.1	6.6	205	330	25×33
GG2 geogrid	Polypropylene	Extruded	6.0	9.0	300	450	25×33
GG3 geogrid	Polypropylene	Extruded	8.5	10.0	425	500	25×31
GG4 geogrid	Polyester	Woven	7.3	7.3	365	365	25×25
GG5 geogrid	Polypropylene	Extruded	6.1	9.0	305	450	21×25
SWM	Stainless Steel	-	236	447	11780	22360	25×51
SBM	Steel	-	970	970	48480	48480	76×76

[a]Tensile Strength (at 2% strain), [b] Tensile Modulus (at 2% strain), [c]Machine Direction, [d]Cross Machine Direction

Experimental Testing Program

Laboratory model tests were conducted on both unreinforced and reinforced crushed limestone under unconfined condition (i.e. surface footing). Two series of tests with a total of twenty two tests were conducted. One was performed to evaluate the effect of number of reinforcement layers, and the other was performed to study the effect of reinforcement type and tensile modulus. Table 2 summarizes the testing program and test variables.

TEST RESULTS AND ANALYSIS

The results of the laboratory model tests are summarized in Table 2. Because of serviceability requirement, foundations are always designed at a limited settlement level in engineering practice. Consequently, the test results were evaluated in terms of the bearing capacity ratio (BCR) at limited settlement levels. In this table the BCRs obtained at settlement ratios, (*s/B*) = 2%, 5% and 10%, are presented. The settlement ratio (*s/B*) is defined as the ratio of footing settlement (*s*) to footing width (*B*). *u* is the spacing between the footing and top layer of reinforcement and *h* is the vertical spacing of reinforcement layers. The results of the model footing tests are also graphically shown in Figure 1.

Effect of number of reinforcement layers

Several laboratory model footing tests were conducted on crushed limestone material reinforced with multiple layers of reinforcement. Seven different types of reinforcement were used; geogrids: GG1, GG2, GG3, GG4, and GG5, and steel: steel wire mesh, SWM, and steel bar mesh, SBM. The reinforcement layers were placed at a spacing of 51 mm (2 in) (*u/B*=*h/B*=1/3). Figure 1 shows that the performance of crushed limestone foundation was improved noticeably even with one layer of reinforcement (Figure 1a). Investigating the load-settlement curves, one can see that the shapes and slopes of curves of reinforced soil foundations are very similar to those of unreinforced soil foundations for the settlement ratio (*s/B*) less than 0.015, which corresponds to a footing pressure of about 2000 kPa; and that the reinforcing effect starts mobilizing when the *s/B* ratio exceeds the threshold of 0.015.

TABLE 2: Summary of model tests

Test No.	Reinforcement configuration	u mm	h mm	s/B = 2%		s/B = 5%		s/B = 10%.	
				q*, kPa	BCR	q*, kPa	BCR	q*, kPa	BCR
LNR-1	Unreinforced	...	...	2372	...	4032	...	5177	...
LGG11	N=1, GG1	51	...	2390	1.01	4174	1.04	5711	1.10
LGG12	N=2, GG1	51	51	2418	1.02	4267	1.06	6502	1.26
LGG13	N=3, GG1	51	51	2442	1.03	4727	1.17	7889	1.52
LGG21	N=1, GG2	51	...	2463	1.04	4701	1.17	6636	1.28
LGG22	N=2, GG2	51	51	2526	1.06	5123	1.27	7640	1.48
LGG23	N=3, GG2	51	51	2673	1.13	5270	1.31	8695	1.68
LGG31	N=1, GG3	51	...	2547	1.07	4791	1.19	6929	1.34
LGG32	N=2, GG3	51	51	2611	1.10	5177	1.28	8602	1.66
LGG33	N=3, GG3	51	51	2727	1.15	5514	1.37	9289	1.79
LGG41	N=1, GG4	51	...	2397	1.01	4513	1.12	6145	1.19
LGG42	N=2, GG4	51	51	2428	1.02	4607	1.14	6706	1.30
LGG43	N=3, GG4	51	51	2499	1.05	5063	1.26	8747	1.69
LGG51	N=1, GG5	51	...	2390	1.01	4421	1.10	6659	1.29
LGG52	N=2, GG5	51	51	2427	1.02	4480	1.11	7353	1.42
LGG53	N=3, GG5	51	51	2448	1.03	4891	1.21	8555	1.65
LSWM1	N=1, SWM	51	...	2705	1.14	4972	1.23	7235	1.40
LSWM2	N=2, SWM	51	51	2743	1.16	5548	1.38	10334	2.00
LSWM3	N=3, SWM	51	51	2886	1.22	6565	1.63	12331#	2.38
LSBM1	N=1, SBM	51	...	2802	1.18	5407	1.34	8271	1.60
LSBM2	N=2, SBM	51	51	3087	1.30	7445	1.85	13914#	2.69
LSBM3	N=3, SBM	51	51	3147	1.33	7455	1.85	14744#	2.85

* q = applied surface pressure, # extrapolated value

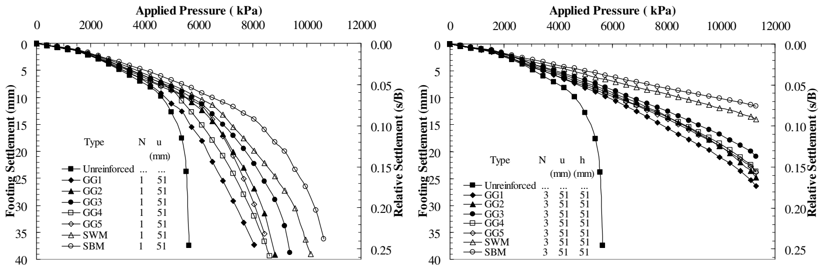

a. Single reinforcement layer b. Three reinforcement layers

FIG. 1: Pressure-settlement curves for plate load tests with different types of reinforcements

Figure 2 presents the effect of number of reinforcement layers on the BCR. As shown in the figure, the BCRs increase with increasing the number of reinforcement layers. It can be noticed from Figure 2 that the effect of number of layers is more appreciable at *s/B*=10% than at *s/B*= 2%. It is obvious that the reinforced benefit is directly related to the footing settlement, which can be explained by achieving better mobilizing of the reinforcements with settlement. Studies conducted by other researchers have also shown that increasing the number of reinforcement layers would increase the BCR of reinforced soils (e.g., Binquet and Lee, 1975a; Huang and Tatsuoka, 1990; Yetimoglu et al., 1994; Adams and Collin, 1997).

The effect of number of reinforcement layers on the settlement reduction factor (SRF) is shown in Figure 3. The SRF is defined here as the ratio of the settlement of the footing on a reinforced crushed limestone (s_r) to that on an unreinforced crushed limestone (s_{ur}) at a specified surface pressure, i.e. SRF = s_r/s_{ur}. It is obvious that the reinforcement would reduce the immediate footing settlement. The figure also shows that the SRFs decrease with increasing number of reinforcement layers. With three layers of reinforcement, the immediate footing settlement can be reduced by about 60% at a footing pressure of 5500 kPa (798 psi).

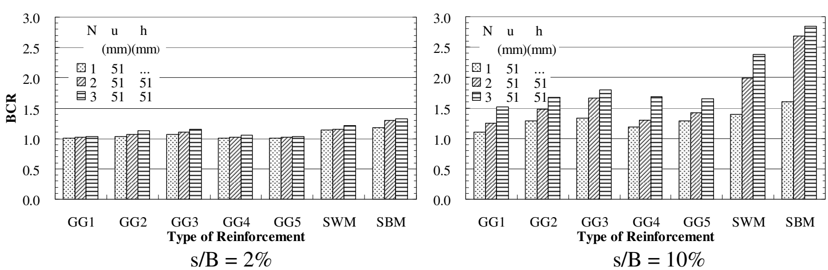

s/B = 2% s/B = 10%

FIG. 2: BCR versus type of reinforcement

Effect of tensile modulus and type of reinforcement

Seven different types of reinforcement were used to reinforce crushed limestone in the model footing tests. The properties of these reinforcements were presented earlier in Table 1. The GG1, GG2 and GG3 geogrids are made of the same material and have similar structure (single layer/extruded). GG2 geogrid has higher tensile modulus than GG1 geogrid. As seen in Figure 1, the crushed limestone reinforced by GG2 geogrid performs better than that

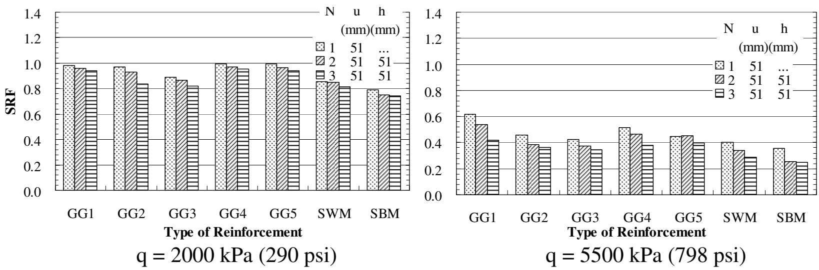

FIG. 3: SRF versus type of reinforcement

reinforced by GG1 geogrid. GG3 geogrid, which has the highest tensile modulus among these three geogrids, has the best performance. As compared to GG2 geogrid, GG4 geogrid (woven) and GG5 geogrid (multi-layer/extruded) have different structure and smaller aperture size, but with almost similar tensile modulus. In the meanwhile, the similar performance of crushed limestone reinforced with GG2, GG4, and GG5 geogrid was observed in the present study. This result suggests that the structure and aperture size of geogrid within the examined range have minimal influence on the performance of the reinforced crushed limestone, which indicated similar degree of geogrid-crushed limestone interlocking. To further study the effect of tensile modulus, two stiff metal grid reinforcements were used in the present study: steel wire mesh (SWM) and steel bar mesh (SBW). SWM has a tensile modulus of about 30 times higher than the geogrids used in the present study, while the tensile modulus of SBM is around 3 times higher than that of SWM. Figure 1 indicates that the crushed limestone reinforced with SWM and SBM performs much better than those reinforced with geogrids. For three layers of reinforcement at settlement ratio of *s/B*=10%, BCRs of SWM and SBM reinforced crushed limestone are nearly 1.3 and 1.6 times as large as that for GG3 geogrid reinforced crushed limestone, respectively. As shown in Figure 2, this study clearly demonstrates that the performance of reinforced crushed limestone improves with increasing the tensile modulus of reinforcement. However, the effect of reinforcement tensile modulus at low settlement level (*s/B*=2%) is not significant when compared to that at a settlement ratio of *s/B*=10%. For example, at *s/B*=2%, the BCR of reinforced crushed limestone for three layers of SBM (with the highest tensile modulus) is 28% higher than that for three layers of GG1 geogrid (with the lowest tensile modulus); while this difference increases to 88% as the settlement ratio increases to *s/B*=10%. So the effect of reinforcement tensile modulus seems to be a function of footing settlement. Again, this can be explained by achieving better mobilizing of the reinforcement with increasing footing settlement.

The BCRs at different settlement ratios (*s/B*) for the model footing tests on crushed limestone material reinforced with multiple layers of different types of reinforcement are presented in Figure 4. It can be seen that the BCRs increase with the increase of settlement ratio (*s/B*). At relatively low settlement ratio (*s/B*), the increase of the bearing capacity of SWM and SBM reinforced sections has marginal difference from geogrid reinforced sections. However, with the increase of settlement ratio (*s/B*), the BCRs of footings on crushed limestone sections reinforced with SWM and SBM increase at a faster rate compared to those on geogrid reinforced crushed limestone sections.

Figure 5 depicts the settlement reduction factors (*SRF*) as a function of applied surface pressure (*q*) for the model tests on crushed limestone sections reinforced with multiple layers of different types of reinforcement. As shown in Figure 5, higher modulus geogrids provide better reduction in settlement than lower modulus geogrids. It is clear that the settlements of

SWM and SBM reinforced sections are much smaller than those of geogrid reinforced sections. In all cases, the SRFs decrease with increasing the surface pressure. It is also noted that the SRF decreases suddenly at a footing pressure of about 300 kPa; and it becomes stabilized at a footing pressure of 700 kPa and higher. and that the rate of decrease in SRFs increases suddenly at surface pressure of about 4500 kPa (653 psi). This trend may be expected in the light of the fact that 4500 kPa (653 psi) is close to the ultimate bearing capacity of unreinforced crushed limestone.

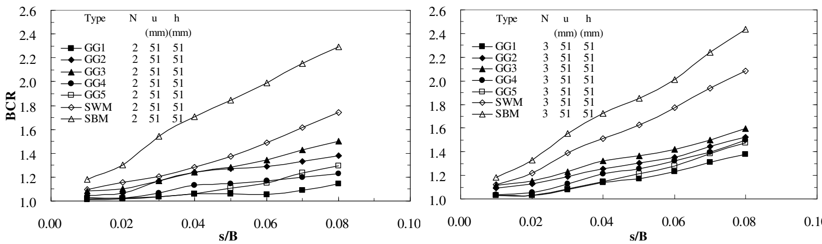

a. Two reinforcement layers b. Three reinforcement layers

FIG. 4: BCR versus settlement ratio (s/B)

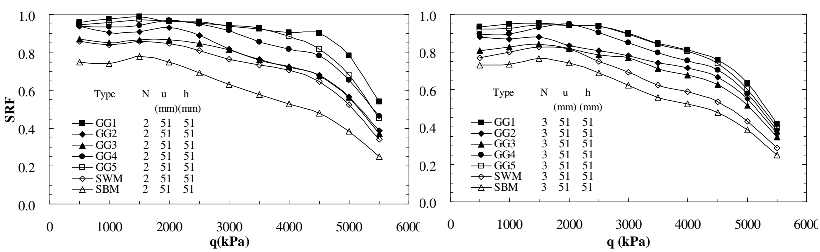

a. Two reinforcement layers b. Three reinforcement layers

FIG. 5: SRF versus applied surface pressure (q)

CONCLUSIONS

Based on the test results, the following conclusions can be drawn:

a. The inclusion of reinforcement can appreciably improve the soil's bearing capacity and reduce the footing settlement. The soil's bearing capacity can be increased up to a factor of 2.85 at a settlement ratio of 10% and the footing settlement can be reduced up to 75% at a surface pressure of 5500 kPa (798 psi). The reinforced benefit is directly related to the footing settlement.
b. The bearing capacity ratio (BCR) increases with increasing the number of reinforcement layers; while the settlement reduction factor (SRF) decreases with increasing number of reinforcement layers.
c. Geogrids with higher tensile modulus perform better than geogrids with lower tensile modulus. The structure and aperture size of geogrid have minimal influence on the performance of the reinforced crushed limestone in this study.
d. The performance of footings on crushed limestone reinforced with steel wire mesh (SWM) and steel bar mesh (SBM), which have much higher tensile modulus than geogrids used

in the present study, is much better than footings on geogrid reinforced crushed limestone. The effect of tensile modulus is not significant at small settlement; and this effect seems to be a function of settlement.

ACKNOWLEDGEMENT

This research is funded by the Louisiana Transportation Research Center (LTRC Project No. 04-2GT) and Louisiana Department of Transportation and Development (State Project No. 736-99-1242). The authors would like to express their thanks to Mark Morvant, Zhongjie Zhang, and Gavin Gautreau at LTRC for providing valuable help and support in this study

REFERENCES

Adams, M.T., and Collin, J.G., 1997. "Large model spread footing load tests on geosynthetic reinforced soil foundations." *Journal of Geotechnical and Geoenvironmental Engineering*, ASCE, Vol. 123, No.1, pp. 66-72.

ASTM, 1997. "Standard test Method for Nonrepetitive Static Plate Load Tests of Soils and Flexible Pavement Components, for Use in Evaluation and Design of Airport and Highway Pavements". pp.112-113.

Binquet, J., and Lee, K.L., 1975a. "Bearing capacity tests on reinforced earth slabs." *Journal of Geotechnical Engineering Division*, ASCE, Vol. 101, No.GT12, pp. 1241-1255.

Binquet, J., and Lee, K.L., 1975b. "Bearing capacity analysis on reinforced earth slabs." *Journal of Geotechnical Engineering Division*, ASCE, Vol. 101, No.GT12, pp. 1257-1276.

Das, B.M., Shin, E.C., and Omar, M.T., 1994. "The bearing capacity of surface strip foundations on geogrid reinforced sand and clay – a comparative study." *Geotechnical and Geological Engineering*, Vol. 12, No. 1, pp. 1-14.

DeMerchant, M.R., Valsangkar, A.J., and Schriver, A.B., 2002. "Plate load tests on geogrid-reinforced expanded shale lightweight aggregate." *Geotextiles and Geomembranes*, 20, pp. 173-190.

Huang, C.C., and Tatsuoka, F., 1990. "Bearing capacity reinforced horizontal sandy ground." *Geotextiles and Geomembranes*, Vol. 9, pp. 51-82.

Lee, K.M., and Manjunath, V.R., 2000. "Experimental and numerical studies of geosynthetics-reinforced sand slopes loaded with a footing." *Canadian Geotechnical Journal*, Vol. 37, pp. 828-842.

Omar, M.T., Das, B.M., Puri, V.K., and Yen, S.C., 1993. "Ultimate bearing capacity of shallow foundations on sand with geogrid reinforcement." *Canadian Geotechnical Journal*, Vol. 20, No. 3, pp. 435-440.

Ramaswamy, S.D., and Puroshothama, P., 1992. "Model footings of geogrid reinforced clay." *Proceedings of the Indian Geotechnical Conference on Geotechnique Today*, Vol. 1, pp. 183-186

Shin, E.C., Das, B.M., Puri, V.K., Yen, S.C., and Cook, E.E., 1993. "Bearing capacity of strip foundation on geogrid-reinforced clay." *Geotechnical Testing Journal*, ASTM, Vol. 16, No. 4, pp. 534-541.

Uchimura, T. and Tatsuoka, F., Hirakawa, D., and Shibata, Y., 2004. "Effects of reinforcement stiffness on deformation of reinforced soil structures under sustained and cyclic loading." Proceedings of Asian Regional Conference on Geosynthetics, Seoul, PP. 233-239.

Yetimoglu, T., Wu, J.T.H., and Saglamer, A., 1994. "Bearing capacity of rectangular footings on geogrid-reinforced sand." *Journal of Geotechnical Engineering*, ASCE, Vol. 120, No.12, pp. 2083-2099.

Louisiana Highway 1 Pile Load Test Program

Sanjoy Chakraborty[1], M. ASCE, P.E. and Michael W. Montgomery[2], M. ASCE, P.E.

[1]Senior Engineer, Wilbur Smith Associates, 1301 Gervais Street, Columbia, SC 29201; schakraborty@wilbursmith.com
[2]Vice President, Wilbur Smith Associates, 2835 Brandywine Road, Suite 400, Atlanta, GA 30341; mmontgomery@wilbursmith.com

ABSTRACT: The Louisiana DOTD is constructing an elevated highway between Golden Meadow and Fourchon in southern Louisiana to replace the existing Highway Louisiana 1 which is prone to flooding and closure under severe weather. The proposed design calls for the construction of approximately 27.4 km of access-controlled, elevated roadway consisting of low-level and medium-level bridges, two elevated interchanges, and one fixed high-level bridge over Bayou LaFourche with a 107-m main span. As part of the design, a pile load test program was conducted at selected locations along the proposed highway alignment. The load test program verified that pile capacity and length predictions can be made with confidence based on the borings and Cone Penetrometer soundings conducted during the geotechnical investigation of the site. It also confirmed that axial loads at least 50% greater than those tabulated in the LA-DOTD Bridge Design Manual can be achieved at this site for prestressed concrete piles in the size range of 0.41 to 0.76-m (16 to 30 inches). A third finding is that significant pile "set up" (increase in axial capacity over time after driving) occurs in the site's soils.

INTRODUCTION

Louisiana Highway 1 (LA-1) is the primary transportation route connecting Golden Meadow and Fourchon in Southern Louisiana. It is located in the rapidly subsiding and shrinking marshes of coastal Louisiana at elevations currently below 1.5-m above MSL. LA-1 is the only highway serving Port Fourchon, the primary support location for the offshore oil industry in the Gulf of Mexico. LA-1 also serves as a hurricane evacuation route for Grand Isle, Port Fourchon and Leeville. The existing roadway is prone to flooding and closure during severe weather and since it continues to subside the problem will continue to worsen.

In order to enable use of the highway during severe weather events, the Louisiana Department of Transportation and Development (LA-DOTD) has begun construction on an elevated highway between Golden Meadow and Fourchon to replace the existing roadway. The design prepared by Wilbur Smith Associates calls for the construction of approximately 27.4-km of access-controlled, elevated roadway consisting of low-level and medium-level bridges, two elevated interchanges, and one fixed high-level bridge over Bayou LaFourche with a 107-m main span.

Virtually all of the new alignment will be constructed over marshland or water. In order to minimize impact to sensitive coastal marshes the new alignment will be supported on driven piles, which constitute a significant portion of the cost of the project. A pile load test program was planned and executed during the summer of 2004 to provide information related to geotechnical design of the foundations. The primary objective of the load test program was to minimize foundation costs by enabling the use of lower safety factors in design, significantly improving pile length estimates and quantities, providing valuable information related to the time-dependent nature of pile setup which would govern the rate at which construction could proceed, and hopefully allow the prospective contractors to minimize their perceived risks by providing them with this information.

REGIONAL GEOLOGY

Southeastern Louisiana is geologically composed of Holocene Coastal Marshes. This environment is the product of several thousand years of river basin sediment deposition and re-routing. The soil in this area can be characterized as undifferentiated alluvial and deltaic sediments including Fat Clay (CH), Clay (CL), Organic Clay (OH), Peat (PT), Silt (ML), Silty Sand (SM), Clayey Sand (SC), Poorly Graded Sand (SP), and various combinations thereof. The uniformity of deposited layers is extremely variable and inter-bedding between sands, silts, and clays is common. This undifferentiated mixture of soils was encountered to depths of over 60-m below the mud line; however, sand becomes more prevalent and separated towards the bottom of these deeper borings. Underlying the Holocene marshes are Pleistocene soils of remnant valley trains, or river outwash deposits of sand, gravel, and silt. In the area of the test site the top of the Pleistocene age formation is located approximately 90 to 110-m below the existing ground line.

PILE LOAD TEST LOCATIONS

Pile load testing was conducted at four locations (T2 through T5) along the proposed alignment of Phase 1, extending from Fourchon in the south to just north of the high level crossing over Bayou Lafourche in Leeville (to the north). The selected locations were as follows:

T2	North Approach to Main Span
T3	Main Span
T4	Low-Level South Approach to Main Span
T5	Northern Portion of Phase 1A

A major constraint in planning the program was access. Approximately 5.5-km of canals was dredged in order to provide access to the test locations. At each test location, a 90 x 90 meter area was excavated to a depth of 2.5-m below mean water elevation in order to accommodate barges that would serve as the work platform. It is estimated that approximately 290,000 m^3 of material were excavated and deposited by the side of the canal to a height conducive to marsh creation.

TEST PILES AND PROCEDURES

Nine test piles were driven and load tested using the static or Statnamic testing method, as well as dynamic testing for setup evaluation. A summary of the load tests is provided in Table 1. At the time of the test pile program, pile types had not been selected for the heavily loaded main spans or approaches, and span lengths had not been set for the low level trestle structure. A variety of pile types was selected for testing in an attempt to maximize the information generated on load transfer and time-dependent effects.

The main span over Bayou Lafourche will be supported by large piers subject to scour and vessel impact loads. Because of the heavy anticipated pile loads, relatively large piles were selected for testing at T3 – 0.76-m square prestressed concrete (PSC), 0.76-m diameter steel pipe pile and 1.37-m spun cast cylinder pile. The piles at T3 were driven inside steel casings from which the soil had been removed to an approximate elevation of -21-m to approximate post scour conditions. The approaches to the main spans were assumed to be trestle bents up to some significant height, and pile supported footing bents where the height of the structure made trestle bents impractical. A 1.37-m spun-cast cylinder pile, considered appropriate for both trestle and footing bents was selected for T2. The other option for the footing bents was considered to be a larger number of smaller piles, so 0.41-m and 0.61-m prestressed concrete piles were selected.

Phase 1A is to be constructed using an end-on construction technique since a temporary earth-fill construction causeway could not be permitted for environmental reasons. Construction would begin at each end of Phase 1A with construction of the end bents and approaches, and progress by driving piles for successive bents and placement of bridge deck sections once the piles had achieved design capacity following time-dependent setup which would be determined by dynamic testing (Pile Driving Analyzer). Very large piles were excluded from consideration since crane and hammer size would be limited by construction requirements. Because three options (short, medium and long spans) are included in this contract and contractor flexibility to propose modifications was desired, 0.61-m prestressed concrete piles were selected for testing at T4 and T5. A range of allowable loads had to be considered. It was assumed that the data from the 0.61-m piles could be used to predict lengths for smaller or larger prestressed piles if a contractor so desired. Steel piles were not selected for testing at the causeway locations because of concerns over corrosion in a hostile environment and the probable high cost of steel relative to concrete piles.

Table 1. Pile Load Test Summary

Pile Type	Pile Length (m)	Test Method	Date Driven	Date Tested	Pile Tip Elevation (m)	Pile Capacity (kN)
T2 - 29º 15'00N, 90º 13'03W (North approach to main span)						
1.37-m Cylinder	48.8	Statnamic	7/9/04	7/16/04	-45.3	5756
0.41-m Square PSC	39.6	Static	7/7/04	7/14/04	-36.4	1898
T3 - 29º 14'51N, 90º 12'34W (Support for main span)						
1.37-m Cylinder	48.8	Statnamic	6/6/04	6/22/04	-45.1	6200
0.76-m Square PSC	57.9	Static	6/4/04	6/17/04	-54.4	7333
0.76-m Steel Pipe Pile	59.4	Static	6/1/04	6/16/04	-55.8	7098
T4 - 29º 13'50N, 90º 11'50W (Low level trestle)						
0.61-m Square PSC	64.0	Static	7/27/04	8/2/04	-61.7	7360
0.61-m Square PSC	48.8	Static	7/27/04	8/2/04	-46.5	3827
T5 - 29º 13'05N, 90º 11'34W (low level trestle - Phase 1A)						
0.61-m Square PSC	51.8	Static	8/9/04	8/17/04	-49.7	3418
0.61-m Square PSC	44.2	Static	8/9/04	8/17/04	-42.1	3284

The nine test piles were each instrumented with five to nine levels of strain gauges in order to evaluate load distribution in skin friction along the length of the piles and end bearing resistance. Strain gauges for concrete piles consisted of temperature compensating embedded sisterbar resistive gauges consisting of Micro-Measurements gauge type CEA-060-125UW-350, with an accuracy of at least 0.25 microstrain. Each sisterbar also incorporated a temperature gauge to allow measurement of temperature. Strain gauges for the pipe pile consisted of either weldable or bolt type resistive gauges manufactured by Geokon. Resistance type gauges were used on this project due to their quick response times to enable measurement of strains during pile driving.

Piles were driven to target tip elevations using three hammer systems, the Vulcan 020, 030 and 040, depending on the size of the pile and anticipated driving resistance. Tip elevations were estimated using subsurface exploration data as described in the Geotechnical Exploration Report prepared by Soil Testing Engineers, Inc. (Boutwell and Tsai, 2004). Pile driving was monitored using a Pile Driving Analyzer, and the PDA data were used for CAPWAP analyses to estimate resistance in skin friction and end bearing. Multiple restrikes were conducted on each pile at designated time intervals following end of initial driving to estimate change in pile capacity as a function of time. The piles were then tested using either a static load test procedure or the Statnamic method.

Static load tests were conducted on seven of the instrumented test piles in accordance with ASTM Standard D1143, "*Standard Test Method for Piles under Static Axial Compressive Load*". Compressive axial loads were applied to the pile using a 1200-ton-capacity hydraulic jack manufactured by Elgood-Mayo Corp. The applied load was measured with a ring type electronic resistance load cell manufactured by Geokon with a working capacity of 1000 tons. Vertical movement at the pile head was monitored electronically using LDC Captive Guided DC LVDT Displacement Transducers manufactured by RDP Group. Readings from a dial gauge were also monitored to serve as backup. All instrumentation other than the jack mounted pressure gauge and the dial gauge were monitored using a MEGADAC electronic data acquisition system, linked to a portable computer. The data were backed up to removable media at the end of the test for analysis and interpretation.

The two 1.37-m concrete piles were tested using the Statnamic device, as the larger axial capacity of these piles made conventional static load testing impractical. The Statnamic device consists of a cylinder that supports reaction weights and is placed on top of the pile head. The device and reaction weights are initially supported by a reaction frame constructed around the test pile. The rapid combustion of special pelletized fuel within the Statnamic device produces gasses under high pressure that propel the device and the reaction weights upwards and away from the top of the pile. The pile is thus subjected to a dynamic force that is equal to the product of the mass of the Statnamic device and its acceleration during the launch pulse. The loading pulse is spread over a relatively long duration, typically on the order of 50 to 100 milli-seconds.

DISCUSSION OF LOAD TEST RESULTS

Load test data were processed using the Matlab® software. These included the load cell, the hydraulic jack pressure transducer, displacement transducers (LVDT), and strain gauges. The axial force in the pile at a particular strain gauge level at any load step was computed as the product of the cross section area, the modulus of elasticity and the average strain recorded at that level at that load step. The loads derived from the top level of strain gauges which were located above the ground line were compared to the readings from the load cell and the pressure transducer and used to adjust the elastic modulus of the pile used in the analysis. The axial force in the pile as a function of elevation at various load steps was plotted for interpretation. Unit skin friction for individual pile segments were computed by dividing the difference in axial loads at consecutive levels by the surface area of the pile between those levels. Unit skin friction values computed at the peak load were plotted as a function of elevation. The load readings from the load cell were compared to the load readings derived from the pressure transducer used to electronically monitor hydraulic jack pressure. The averaged load reading (load cell and pressure transducer) was plotted against the average pile head displacement recorded by the LVDTs. The ultimate or failure load for the pile was defined using the criterion described in Section 19.7.5 of *FHWA-HI-97-013: Design and Construction of Driven Foundations, Vol. II, Rev. 1998.*

Our analyses of the load test data indicated that the distribution of skin friction along the length of the piles and end bearing resistance were generally consistent with the soils encountered within the soil borings and CPT soundings at the test sites. Measured pile ultimate capacity ranged from 1900-kN for the 0.41-m concrete pile at T2 to 7,366-kN for the 64-m long, 0.61-m prestressed pile at T4. Unit skin friction typically ranged from about 9.6-kPa at shallow depths to about 53-kPa or higher at greater depths. Shorter piles that were tipped in relatively soft to medium clays exhibited end bearing resistance ranging from 525 to 1050-kPa. Longer piles that were driven to bearing on dense sand exhibited end bearing resistance ranging from 3900 to 4200-kPa.

The LA-DOTD Bridge Design Manual specifies (tabulates) maximum design axial compressive pile loads based on pile type and pile size (cross section). A Factor of Safety of 2.0 for pile axial capacity design was selected since the design would be supported by load test data. One objective of the load test program was to demonstrate that the LA-DOTD specified design pile loads could be increased by up to 50 percent for all piles other than the cylinder and steel piles, i.e. the load test program would have to demonstrate ultimate pile capacities at least three times larger (1.5 x Factor of Safety of 2.0) than the LA-DOTD specified design loads. The lengths of the test piles at the test locations were determined based on this assumption except for the cylinder piles. Table 2 provides the DOTD specified design loads along with load test ultimate capacities at each test location. The results indicate that for each test pile other than the cylinder piles and the steel pipe pile at T3, the load tested ultimate capacity is indeed three times (or more) than the DOTD specified allowable pile loads.

One factor affecting the rate of construction for Phase 1A (low level trestle) is the time-dependent nature of pile setup. The test piles were monitored during driving and at predetermined restrike intervals using a Pile Driving Analyzer (PDA) in an effort to quantify this factor. CAPWAP analyses were conducted on selected blows near the end of drive and at each restrike to refine capacity estimates provided by the PDA. Unfortunately, the results of CAPWAP analyses could not be correlated well with the load test results. For a significant number of test piles, the CAPWAP predicted pile capacity was somewhat lower than the load test indicated capacity, typically by 10 to 20 percent, but by as much as 40 percent for the shorter piles which were not driven to bearing on sand. Also, the CAPWAP predicted end bearing resistance was typically higher than the load test indicated end bearing. No obvious explanations are available to explain these inconsistencies. In theory, the CAPWAP solution is not unique, and may be affected both by the quality of the measurements as well as the experience of the operator. Also, for piles driven to bearing within dense sands, the hammer used during the restrikes may not have sufficiently mobilized (zero set for restrikes) the pile to enable good PDA measurements and subsequent CAPWAP analyses.

Table 2. Axial Pile Capacity

Pile Type	Pile Length (m)	Load Test Ultimate Pile Capacity (kN)	LA-DOTD Maximum Design Load (kN) (*1*)	Effective Factor of Safety (*2*)
Test Site 2 - 29º 15'00N, 90º 13'03W (North approach to main span)				
1.37-m Cylinder	48.8	5760	2491	2.31
0.41-m Square PSC	39.6	1899	578	3.28
Test Site 3 - 29º 14'51N, 90º 12'34W (Support for main span)				
1.37-m Cylinder	48.8	6205	2491	2.49
0.76-m Square PSC	57.9	7339	1735	4.23
0.76-m Steel Pipe Pile	59.4	7103	3047	2.33
Test Site 4 - 29º 13'50N, 90º 11'50W (Low level trestle)				
0.61-m Square PSC	64.0	7366	1068	6.90
0.61-m Square PSC	48.8	3830	1068	3.59
Test Site 5 - 29º 13'05N, 90º 11'34W (low level trestle - Phase 1A)				
0.61-m Square PSC	51.8	3421	1068	3.20
0.61-m Square PSC	44.2	3287	1068	3.08
Notes: (1) Maximum Allowable Axial Compressive Load - Page 6(6) of LA-DOTD Bridge Design Manual (2) Effective Factor of Safety refers to ratio of Load Test Ultimate Pile Capacity to LA-DOTD Max. Allowable Axial Compressive Load				

Based on the restrike and load test data, it appears that the rate of setup is most rapid within the first four to eight hours following driving, and diminishes with time following this period. Table 3 shows the gain in capacity as indicated by CAPWAP analysis at the 24 and 48 hour restrikes at T4 and T5 relative to the CAPWAP indicated capacity at the end of drive. The data indicate that the axial capacity of the test piles at T4 and T5 increased approximately 47 and 66 percent on average at 24 and 48 hours following end of initial drive.

Table 3. Capacity Gain at 24 and 48 Hours, T4 and T5

	T4-48.8m	T4-64m	T5-44.2m	T5-51.8m	Mean
24 Hour Gain	1.61	1.26	1.64	1.36	1.47
48 Hour Gain	2.11	1.41	1.76	1.35	1.66

Publication guidelines prevent a more detailed discussion of the pile load test program within this paper. The reader is referred to the report prepared by WSA (Chakraborty and Montgomery, 2004) for a comprehensive description of the program, background information and test results. The report may be obtained by contacting the Louisiana DOTD at their Baton Rouge office.

CONCLUSIONS

The LA-1 relocation is one of the largest and most ambitious projects undertaken by the La-DOTD. Since the majority of the new alignment will consist of low level bridges built over environmentally sensitive wetlands, foundation cost has a huge impact on the cost of the project. The pile load test program conducted by WSA demonstrated that axial capacity predictions based on subsurface exploration data can be made reliably, thereby increasing confidence in design and enabling the use of smaller factors of safety which resulted in significant cost savings. It also confirmed that axial loads at least 50% greater than those tabulated in the LA-DOTD Bridge Design Manual can be achieved at this site for prestressed concrete piles in the size range of 16 inches to 30 inches. The load test program also provided valuable information related to time dependent pile setup, which has a significant impact on the timeline of construction.

ACKNOWLEDGMENTS

The authors appreciate the support of the La-DOTD. In particular, we would like to thank David Miller and Stephen Meunier of the DOTD who were involved in all aspects of project development and the day to day workings at the project site. We would also like to acknowledge the valuable support provided by various subcontractors on the project, including Applied Foundation Testing, Boh Brothers Construction Co., Soil Testing Engineers and others.

REFERENCES

ASTM D 1143. "Standard Test Methods for Deep Foundations Under Static Axial Compressive Load". ASTM International.

Boutwell, G.P. and Tsai, C.N. (2004). “Geotechnical Interpretation Report, Phase 1A, LA-1 Relocation”. Soil Testing Engineers, Inc., Baton Rouge, LA.

Chakraborty, S. and Montgomery, M.W. (2004). “Report on Pile Load Test Program: LA-1 Improvements”. Wilbur Smith Associates, Baton Rouge, LA.

National Highway Institute (1998). “Design and Construction of Driven Pile Foundations”. Publication No. FHWA HI 97-013, Federal Highway Administration, Vols. 1 and 2.

State of Louisiana Department of Transportation and Development (2005). “Bridge Design Manual”, Ver. 1.4, Baton Rouge, LA.

Bearing capacity of foundations resting on a spatially random soil

Abdul-Hamid Soubra[1], Dalia S. Youssef Abdel Massih[2] and Mikaël Kalfa[3]

[1] Professor, University of Nantes, GeM, UMR CNRS 6183, Bd. de l'université, BP 152, 44603 Saint-Nazaire cedex, France. E-mail: Abed.Soubra@univ-nantes.fr
[2] PhD Student, University of Nantes & Lebanese University, BP 11-5147, Beirut, Lebanon. E-mail: Dalia.Youssef@univ-nantes.fr
[3] Post Graduate Student, University of Nantes, GeM, UMR CNRS 6183, Bd. de l'université, BP 152, 44603 Saint-Nazaire cedex, France

ABSTRACT: The paper presents the effect of the spatial variability of the soil properties on the ultimate bearing capacity of a vertically loaded shallow strip footing. The deterministic model used is based on numerical simulations using the Lagrangian explicit finite difference code FLAC^{3D}. The cohesion and the angle of internal friction of the soil are modelled as non normal anisotropic random fields. The methodology used for the discretization of the random fields is based on the spectral representation method proposed by Yamazaki and Shinozuka (1988). The results have shown that the average bearing capacity of a spatially random soil is lower than the deterministic value obtained for a homogeneous soil. A critical case appears when the autocorrelation distances are equal to the footing breadth. The average value of the ultimate footing load is more sensitive to the horizontal autocorrelation distance than the vertical one. Finally, it has been shown that accounting for the spatial variability of the soil properties gives a higher reliability index of the foundation than the one obtained with the assumption of random variables.

INTRODUCTION

The spatial variability of the soil properties may largely affect the behaviour of geotechnical structures. This variability is widely dealt with as uncertainties in soil properties. Several authors have investigated the reliability-based analysis of foundations. Some authors have modelled the uncertainties of the different parameters as random variables (*e.g.* Low and Phoon 2002) without introducing the spatial variability of the soil parameters. Others (Cherubini 2000) have considered the effect of the soil spatial variability by using a simplified approach. Later on, several authors (Griffiths et al. 2002, Fenton and Griffiths 2003 and Popescu et al. 2005 among others) have modelled the uncertain soil parameters as random processes more rigorously. They have examined the effect of the spatial variability of these parameters on the ultimate bearing capacity using finite elements models combined with Monte Carlo simulations. However, most of these studies (except Fenton and Griffiths 2003) consider only a single random process in their analysis.

In this paper, the effect of the soil spatial variability on the reliability analysis and design of a vertically loaded strip foundation is presented. The punching mode of the ultimate limit state is analyzed. Only the cohesion and the angle of internal friction of the soil are modelled as non normal anisotropic random fields. The cohesion is considered to be Log-normally distributed while the angle of internal friction follows a Beta distribution. Several realisations of the random fields are performed using Monte Carlo simulations. The methodology used for the discretization of the non-gaussian random fields is based on the spectral representation method proposed by Yamazaki and Shinozuka (1988). This method is fast, easy to apply and allows one to take into account the soil anisotropy regarding the autocorrelation distances.

After a brief description of the methodology used in this paper, the deterministic model is first described and then, the stochastic numerical results are presented and discussed.

METHODOLOGY

Generation of non-Gaussian random fields

The approach described by Popescu et al. (1998) based on the spectral representation method was used to generate sample functions of a 2D non-Gaussian stochastic vector field according to a prescribed spectral density function and a prescribed (non-Gaussian) probability distribution function. It should be mentioned that the spectral density function $S(\omega)$ is related to the autocorrelation function $\rho(\tau)$ of the random process by the following relation:

$$S(\omega) = \frac{1}{2\pi} \int_{-\infty}^{+\infty} \rho(\tau) e^{-i\omega\tau} d\tau \qquad (1)$$

First a Gaussian vector field is generated according to the target spectral density function using the Fast Fourier Transformation (FFT) algorithm. Next, this Gaussian vector field is transformed into the desired non-Gaussian field using a memory less non-linear transformation coupled with an iterative process. For the description of the theoretical bases of the spectral representation method, one can refer to Shinozuka and Deodatis (1991) and Popescu et al. (1998).

Monte Carlo simulations

For each set of assumed statistical parameters of the soil properties random fields, several realizations of the random field are generated in Matlab 7.0 by the spectral representation method using Monte Carlo simulations. The bearing capacity and the slope of the foundation corresponding to each realisation are calculated based on numerical simulations using the Lagrangian explicit finite difference code FLAC^{3D}. The data transfer from the stochastic mesh used to generate the random fields to the finite difference mesh of FLAC^{3D} is performed using the mid point method. The unbiased mean and standard deviation of the footing load are obtained using the following equations:

$$\mu_{P_u} = \frac{1}{n_{sim}} \sum_{i=1}^{n_{sim}} P_u \qquad (2)$$

$$\sigma_{P_u} = \sqrt{\frac{1}{n_{sim}-1} \sum_{i=1}^{n_{sim}} \left(P_u - \mu_{P_u} \right)^2} \qquad (3)$$

where n_{sim} is the number of the sample size of the random field realizations.

An exchange of data between FLAC^{3D} and Matlab 7.0 in both directions was necessary to enable an automatic resolution of the Monte Carlo simulations for the generation of the soil properties random fields and the calculation of the geotechnical system responses (*i.e.* ultimate footing load, footing displacement, footing slope). The link between FLAC^{3D} and Matlab 7.0 was performed using text files and FISH commands. FISH is an internal programming option of FLAC^{3D} which enables the user to add his own subroutines.

DETERMINISTIC MODEL

The deterministic model used for the calculation of the ultimate footing load, the vertical footing displacement and the footing slope is based on numerical simulations using FLAC^{3D}. A soil domain of width 15B and depth 2.5B is considered (Figure 5). The bottom and right vertical boundaries are far enough from the footing and they do not disturb the soil mass in motion (*i.e.* velocity field) for all the soil configurations studied in this paper. A non uniform optimized mesh composed of 1620 zones is used (Figure 5). Since this is a 2D case, all displacements in the Y direction (see Figure 5) are fixed. For the displacement boundary conditions, the bottom boundary was assumed to be fixed and the vertical boundaries were constrained in motion in the horizontal direction. A conventional elastic-perfectly plastic model based on the Mohr-Coulomb failure criterion is used to represent the soil. A strip footing of width equal to 2m and depth 0.5m is simulated by a weightless elastic material. It is divided horizontally into eight zones. The footing elastic properties used are the Young's modulus E=25 GPa and the Poisson's ratio υ=0.4. Compared to the soil elastic properties (E=240MPa, ν=0.2), these values are well in excess of those of the soil and ensure a rigid behavior of the footing. The footing is connected to the soil *via* interface elements that follow Coulomb law. The interface is assumed to have a friction angle equal to the soil angle of internal friction, dilation equal to that of the soil and cohesion equal to the soil cohesion in order to simulate a perfectly rough soil-footing interface. Normal stiffness $K_n=10^9$ Pa/m and shear stiffness $K_s=10^9$ Pa/m are assigned to this interface. These parameters do not have a major influence on the failure load.

For the computation of the bearing capacity of a rigid rough strip footing subjected to a central vertical load using *FLAC^{3D}*, the following method is adopted: an optimal controlled downward vertical velocity of 5.10^{-6} m/timestep (*i.e.* displacement per timestep) is applied to the bottom central node of the footing in order to allow the rotation of the footing due to the soil spatial variability (*i.e.* soil variability). Damping of the system is introduced by running several cycles until a steady state of plastic flow is developed in the soil underneath the footing. At each cycle, the vertical footing load is obtained by using a *FISH* function that calculates the integral of the normal stress components for all elements in contact with the footing. The value of the vertical footing load at the plastic steady state is the ultimate footing load.

NUMERICAL RESULTS

The numerical results presented in this paper consider the case of a shallow strip foundation with breadth *B=2* m subjected to a central vertical load. The soil has a unit weight of 18 kN/m^3. The cohesion and the angle of internal friction are modeled as two independent random fields. The illustrative values used for the statistical moments of c and φ are as follows: $\mu_c = 20\,kPa$, $\mu_\varphi = 30^\circ$, $COV_c = 20\%$, $COV_\varphi = 10\%$. The dilation angle was taken equal to $2\varphi/3$. For the probability distributions of the random fields, c follows a log-normal distribution while φ is assumed to be bounded ($0^o < \varphi < 45^o$) and a Beta distribution is used.

An anisotropic autocorrelation function is used in this paper for both the cohesion and the angle of internal friction. It is given by an exponential first order function as follows (*e.g.* Vanmarcke, 1983):

$$\rho(\delta x, \delta y) = e^{-2\sqrt{\left(\frac{\delta x}{D_h}\right)^2 + \left(\frac{\delta y}{D_v}\right)^2}} \tag{4}$$

where D_h and D_v are the autocorrelation distances in the horizontal and vertical directions respectively and, δx and δy are the lag distances in the horizontal and vertical directions respectively.

Convergence of the Monte Carlo simulations

Figures (1) and (2) show the effect of the sample size on the predicted mean μ_{P_u} and coefficient of variation COV_{P_u} of the ultimate footing load. The case considered in these figures corresponds to an isotropic autocorrelation function with $\delta_x = \delta_y = 2\,\text{m}$. It can be seen that the predicted mean and coefficient of variation remain practically constant for sample size larger than 100. Consequently, only 100 realizations of the soil properties random fields are used in all subsequent calculations. For this number, estimated mean bearing capacities will have a standard error (± one standard deviation) equal to the sample standard deviation times $1/\sqrt{n_{sim}} = 0.1$, or 10% of the sample standard deviation. Similarly, the estimated variance will have a standard error equal to the sample variance times $\sqrt{(2/(n_{sim}-1))} = 0.142$, or about 14% of the sample variance. This means that estimated quantities will generally be within about 14% of the true quantities.

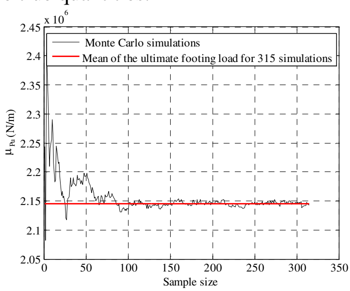

FIG. 1: Mean of the ultimate footing load versus the sample size

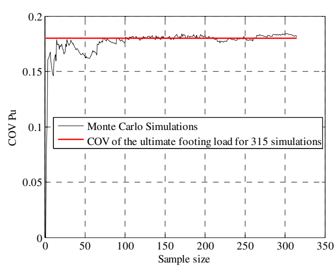

FIG. 2: Standard deviation of the ultimate footing load versus the sample size

Figure (3) and (4) present respectively the load-displacement curves and the load-slope curves of the footing obtained for all the soil realizations of the Monte Carlo simulations. These figures also present the mean curves of all simulations. It can be noticed that the mean value of the footing slope is very close to zero. However, the footing slope corresponding to each realization is different from zero. Figure (5) shows the deformed mesh obtained for a random soil realization. This figure shows that the inherent spatial variability of the soil shear strength parameters can modify drastically the basic form of the failure mechanism. Differential settlements appear in the spatially varying soil leading to the rotation of the footing. This is impossible in a deterministic homogeneous soil analysis of a symmetrical problem.

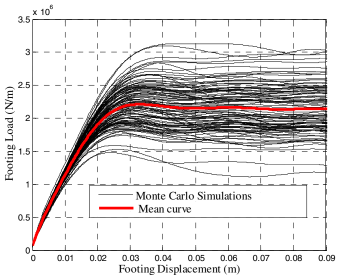

FIG. 3: Load-displacement curves from Monte Carlo simulations

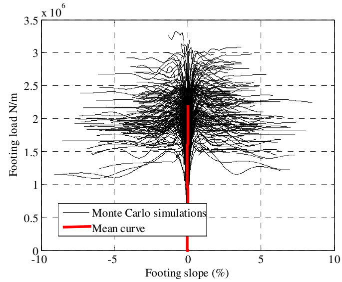

FIG. 4: Load-slope curves from Monte Carlo simulations

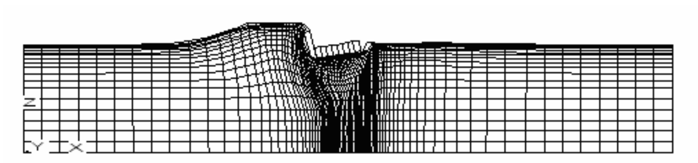

FIG. 5: Deformed Mesh corresponding to a realization of the random soil

Predicted mean and standard deviation of the ultimate footing load

Figures (6) and (7) show respectively, in a dimensionless form, the variation of the predicted mean and standard deviation of the ultimate footing load with the autocorrelation distance for an isotropic random soil (*i.e.* $\delta_x = \delta_y$) and for different values of the coefficient of variation of the random fields.

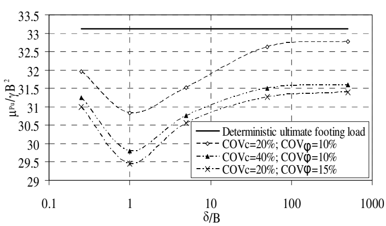

FIG. 6: Mean value of P_u versus the autocorrelation distance (isotropic random soil)

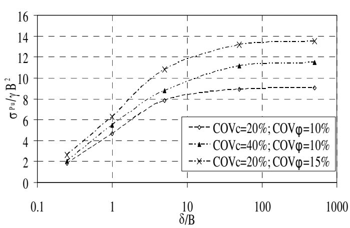

FIG. 7: Standard deviation of P_u versus the autocorrelation distance (isotropic random soil)

One can notice that the average bearing capacity of a spatially random soil is lower than the deterministic value obtained for a homogeneous soil for which the soil properties are set equal to their mean values. A critical case appears in figure (6) when the autocorrelation distances are close to the footing breadth. For this case, the curve of the mean value of the footing load reaches a minimum. This case was also obtained in Fenton and Griffiths (2003). Concerning the standard deviation of the ultimate footing load, it always increases with the increase of the autocorrelation distances. From the two figures, one can conclude that the statistical parameters of the bearing capacity are more sensitive to the variation of the angle of internal friction than the cohesion.

Effect of the vertical and horizontal autocorrelation distances on the mean value of the ultimate footing load

Figure (8) presents the variation of the mean ultimate footing load with the vertical and horizontal autocorrelation distances. For each curve in figure (8), one autocorrelation distance is set equal to 2 m and the second one varies from $\delta/B = 0.5\,\text{m}$ to $\delta/B = 50\,\text{m}$. It can be noticed that the mean ultimate footing load is more sensitive to the variation of the horizontal autocorrelation distance than the vertical one.

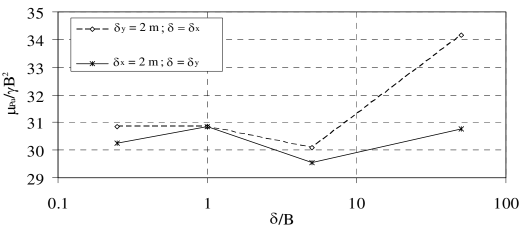

FIG. 8: Mean value of the ultimate footing load versus the autocorrelation distances for an anisotropic random soil

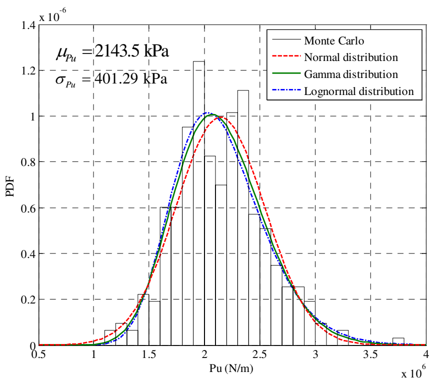

FIG. 9: Histogram and fitted probability density distributions of the ultimate footing load

Reliability index

By fitting the histogram of the ultimate footing load obtained from the Monte Carlo simulations to an empirical probability density function [Normal (N), Lognormal (LN), Gamma (G)] (*cf.* Figure 9), one can approximate the reliability of the footing, subjected to a prescribed service applied load P_s, against punching failure by calculating the Hasofer-Lind reliability index as follows:

$$\beta_{HL} = \min_{\frac{P_u}{P_s} \le 1} \left| \frac{x_{P_u} - \mu_{P_u}^N}{\sigma_{P_u}^N} \right| = \left| \frac{P_S - \mu_{P_u}^N}{\sigma_{P_u}^N} \right| \tag{6}$$

where $\mu_{P_u}^N$ et $\sigma_{P_u}^N$ are respectively the equivalent normal mean and standard deviation of the ultimate footing load.

Table 1 shows that the reliability index decreases with the increase of the autocorrelation distances. Consequently, accounting for the spatial variability of the soil properties gives a higher reliability index than the one obtained with the assumption of random variables. Table 2 presents a comparison between the reliability index values obtained for large autocorrelation distances $\left(\delta = \delta_x = \delta_y = 100\,\mathrm{m}\right)$ and the ones obtained by Youssef Abdel Massih and Soubra (2007). In the later reference, the soil shear strength properties were modeled by random variables and the response surface methodology was used to calculate the reliability index based on FLAC^{3D} simulations. A good agreement between the two results was noticed when assuming a Gamma distribution for the ultimate footing.

Table 1. Reliability index for different values of the autocorrelation distance $\left(\delta = \delta_x = \delta_y\right)$ and for different probability distribution of the ultimate load.

δ/B	β_{HL}								
	$COV_c = 20\%$ $COV_\varphi = 10\%$			$COV_c = 40\%$ $COV_\varphi = 10\%$			$COV_c = 20\%$ $COV_\varphi = 15\%$		
	N	LN	G	N	LN	G	N	LN	G
0.5	11.51	18.68	-	9.89	15.89	-	7.57	12.14	-
1	4.26	6.78	4.96	3.44	5.39	4.6	2.93	4.54	3.88
5	2.60	4.14	3.49	2.24	3.51	2.95	1.81	2.80	2.34
50	2.43	3.91	3.27	1.84	2.89	2.41	1.53	2.37	1.95

Table 2. Reliability index for large autocorrelation distances $\left(\delta_x = \delta_y = 100\,\mathrm{m}\right)$ and for different safety factors F when $COV_c = 20\%,\ COV_\varphi = 10\%$

F	β_{HL}			
	N	LN	G	Random variables (Youssef Abdel Massih and Soubra 2007)
3.19	2.5	4.14	3.44	3.49
2.08	1.88	2.55	2.26	2.12
1.54	1.25	1.43	1.34	1.21
1.35	0.91	0.93	0.91	0.81
1.23	0.64	0.59	0.59	0.55
1.00	0.05	0.19	0.14	0.00

CONCLUSIONS

The paper presents the effect of the spatial variability of the soil shear strength parameters on the ultimate bearing capacity of a vertically loaded shallow strip footing. The deterministic model used is based on numerical simulations using the Lagrangian explicit finite difference code FLAC^{3D}. The cohesion and the angle of internal friction of the soil are modelled as non normal anisotropic random fields. The cohesion is considered to be Log-normally distributed while the angle of internal friction follows a Beta distribution. An anisotropic exponential first order autocorrelation function is used in this paper for the two random processes. Several realisations of the random field are generated by the spectral representation method using Monte Carlo simulations. The ultimate footing load was calculated for all the realisations. The results have shown that the inherent spatial variability of the soil shear strength parameters can modify drastically the basic form of the failure mechanism. Differential settlements appear in the spatially random soil leading to the rotation of the footing. This is impossible in a deterministic homogeneous soil analysis of a symmetrical problem. The average bearing capacity of a spatially varying soil was found lower than the deterministic value obtained for a homogeneous soil. A critical case appears when the autocorrelation distances are equal to the footing breadth. It was found that the statistical parameters of the bearing capacity are more sensitive to the variation of the angle of internal friction than the cohesion. Also, the average value of the ultimate footing load was found more sensitive to the variation of the horizontal autocorrelation distance than the vertical one. The probability distribution of the bearing capacity was analysed. Several types of the probability distribution function were fitted to the histogram of the obtained bearing capacities. After assuming a probability distribution for the ultimate foundation load, a reliability analysis was performed. The Hasofer-Lind reliability index was calculated for the assessment of the footing reliability. It was found that accounting for the spatial variability of the soil properties gives a higher reliability index than the one obtained based on the assumption of random variables.

REFERENCES

Cherubini, C. (2000). "Reliability evaluation of shallow foundation bearing capacity on c', φ' soils." *Can. Geotech. J.*, 37, 264-269.

Fenton, G. A., and Griffiths D. V. (2003). "Bearing capacity prediction of spatially random c-φ soils." *Can. Geotech. J.*, 40, 54-65.

Griffiths, D. V., Fenton, G. A., and Manoharan, N. (2002). "Bearing capacity of rough rigid strip footing on cohesive soil: Probabilistic study." *J. of Geotech. & Geoenv. Engrg., ASCE*, 128(9), 743-755.

Low, B. K., and Phoon, K. K. (2002). "Practical first-order reliability computations using spreadsheet." *Probabilistics in Geotechnics*: *Technical and Economic Risk Estimation*, Austria, 39-46.

Popescu, R., Deodatis, G., and Prevost, J.H. (1998). "Simulation of homogeneous non-Gaussian stochastic vector fields" *Prob. Engrg. Mech.*, 13(1), 1-13.

Popescu, R., Deodatis, G., and Nobahar, A. (2005). "Effect of random heterogeneity of soil properties on bearing capacity." *Prob. Engrg. Mech.*, 20, 324-341.

Shinozuka, M., and Deodatis, G. (1988). "Response variability of stochastic finite element systems." Journal of Engineering Mechanics, 114(3), 499-519.

Shinozuka, M., and Deodatis, G. (1991). "Simulation of stochastic processes by spectral representation." *Applied Mechanics Reviews*, ASME, 44(4), 191-204.

Vanmarcke, E. (1983). "Random Fields: Analysis and Synthesis." Published by *MIT Press, Cambridge MA*, 382p.

Yamazaki, F., and Shinozuka, m. (1988). "Digital generation of non-Gaussian stochastic fields." *J. of Engrg. Mech.*, 114(7), 1183-1197.

Youssef Abdel Massih, D.S., and Soubra, A.-H. (2007). "Reliability-based analysis of strip footings using response surface methodology." *Int. J. of Geomech.*, *ASCE*, accepted, in press.

Multiple Resistance Factor Methodology for Service Limit State Design of Deep Foundations using a "t-z" Model Approach

Lance A. Roberts[1], M. ASCE., Bradley S. Gardner[2], and Anil Misra[3], M. ASCE.

[1] Assistant Professor, South Dakota School of Mines and Technology, 501 E. St. Joseph Street, Rapid City, SD 57701, Lance.Roberts@sdsmt.edu
[2] Geotechnical Engineer, Burns & McDonnell, 9400 Ward Parkway, Kansas City, MO 64114, bgardner@burnsmcd.com
[3] Professor of Civil Engineering, University of Missouri-Kansas City, 5100 Rockhill Road, 350H Flarsheim Hall, Kansas City, MO 64110. misraa@umkc.edu

ABSTRACT: For the AASHTO Load and Resistance Factor Design (LRFD) of deep foundations, resistance factors must be applied to the calculated nominal load capacity to determine the nominal resistance of the foundation. The deep foundation is adequate if the nominal resistance is greater than the calculated factored load. In most current methods, the side and tip resistance are calculated separately and are added to determine the nominal capacity of the foundation. When using the "t-z" model, however, the percentage of the design load carried by side resistance and tip resistance is known at any applied load. Therefore, it is beneficial to consider how the uncertainties in the side and tip resistance model parameters each affect the uncertainty in the total load capacity of the foundation. In this paper, resistance factors have been calculated for the design of deep foundation systems based on side and tip resistance. The model parameters are back-calculated using actual load test data and the variability in the side and tip parameters is examined separately in a series of *Monte Carlo* simulation analyses. Histograms of the deep foundation load capacity, corresponding to an allowable total displacement, are developed for the simulations and analyzed to calculate separate side and tip resistance factors.

INTRODUCTION

The implementation of the AASHTO Load and Resistance Factor Design (LRFD) specifications must be fully completed in all states within the next few years. The basis of the LRFD methodology is the application of load factors, with values greater than unity, to the loads and the application of resistance factors, with values less than unity, to the calculated ultimate capacity. The load and resistance factors are evaluated by accounting for possible sources of variability in the design parameters and thus permit the rational inclusion of uncertainty in the design. For the design of deep foundation systems at the ultimate or the service limit state, resistance factors must be applied to the calculated nominal load capacity to determine the nominal resistance of the foundation. The deep foundation is considered adequate if the nominal resistance is greater than the calculated factored load.

The nominal load capacity of the deep foundation system can be determined using any number of approaches. In most methods, the resistance along the length of the deep foundation and the resistance at the tip are calculated separately and are added together to determine the total nominal ultimate load capacity of the foundation. When using a "t-z" approach, however, the percentage of the nominal ultimate load carried along the length of the foundation and at the tip is considered directly based on the strength and stiffness characteristics of the soil-structure interface and tip components. Therefore, it is beneficial to consider how variability in the side and tip resistance model parameters independently affects the uncertainty in the total nominal load capacity of a deep foundation system.

In this paper, separate resistance factors have been calculated for the side and tip resistance of a deep foundation element. The model parameters are back-calculated using several sets of load test data and the variability in the side and tip parameters examined separately in a series of *Monte Carlo* simulation analyses. Because the bonded length of deep foundations is realized to be a predominant factor in the percentage contribution of the side and tip resistance to the ultimate load capacity, the foundation length was varied in the simulations to further understand the effects of uncertainty in the side and tip model parameters. Since serviceability calculations are often overly simplified in general deep foundation design, the foundation load capacity at an allowable total displacement has been considered. Load capacity histograms are developed and analyzed to determine the probability of load capacity failure of the deep foundation and develop resistance factors.

DEEP FOUNDATION LOAD-DISPLACEMENT MODEL

The use of a soil-structure interaction model, such as the "t-z" model, is a practical method to determine the load-displacement behavior of deep foundations. In the "t-z" model, the axial resistance of the soil along the foundation and at the tip is represented by a spring-slider system. Similar assumptions are commonly made for analytical and numerical models for load-displacement behavior of piles and drilled shafts (cf. Randolph and Wroth 1978, Misra and Chen 2004). The load-displacement behavior of the springs can be assumed to be either ideal elasto-plastic or hyperbolic, both in the drained or undrained conditions. In addition, the strength and stiffness parameters of the springs can be assumed constant along the

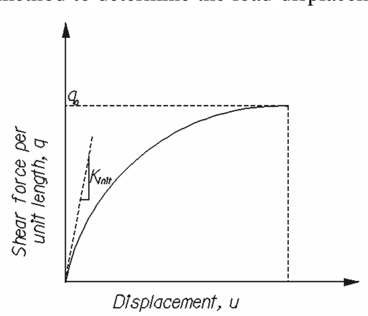

Figure 1. Soil-structure interface force-displacement relationship for a hyperbolic spring-slider system.

length of the foundation or assumed to increase linearly with depth (i.e. confining stress). In general, the soil-structure interface parameters are related to the deep foundation construction techniques and the properties of the soil strata. Figure 1 shows the force-displacement behavior for a hyperbolic spring-slider system, as depicted by the shear force per unit length q, versus displacement u, curve. In Figure 1, K_{init} is the initial tangent shear modulus of shaft-soil interface sub-grade reaction, and q_o is the ultimate (asymptotic) strength of the soil-structure interface, given by the product of the shaft perimeter and the ultimate shear strength of the soil-structure interface in drained or undrained conditions, denoted by τ_u. Similar curves can be developed for the tip soil as well.

For most deep foundations, the load transfer occurs via the soil-structure interface in the interaction zone, L_b. The upper 0.3m to 1.5m of the soil-structure interface, called the non-interacting zone, L_d, is considered to have negligible shear resistance due to ground disturbance from construction, fill placement, moisture content variation, and frost. The governing equation for the "t-z" model is given as:

$$K_m \frac{d^2 u}{d z^2} - K\, u(z) = 0 \tag{1}$$

where, $u(z)$ is the deep foundation deformation, K_m is the deep foundation axial stiffness, and K is the shear modulus of soil-structure interface sub-grade reaction. For non-linear behavior of the soil-structure interface and tip soil, a finite difference method to numerically solve Eq. 1 may be utilized (Misra et al. 2007). The boundary condition at the tip depends upon the type of loading. Under a compression load, the deep foundation will develop a tip force, P_t, proportional to the tip displacement, u_t, given by:

$$P_t = K_t\, u_t \tag{2}$$

where, K_t is the tip soil stiffness. Based on theories for rigid punch bearing upon elastic half-space, the initial tangent tip soil stiffness, K_{ti}, may be related to foundation diameter and the elastic properties of tip soil as follows (Johnson 1985):

$$K_{ti} = \frac{0.3\pi D E_s}{(1-\mu_s^2)} \tag{3}$$

where, E_s is the tip soil elastic modulus, μ_s is tip soil Poisson's ratio, and D is the diameter of the deep foundation element.

As the compressive load on the deep foundation element increases, the percentage of the load carried by the tip soil also increases. At some load, the soil-structure interface will yield completely and the soil at the tip of the deep foundation will carry all additionally applied loads. The ultimate capacity of the tip soil can be determined assuming a punching shear failure, such as:

$$P_{utip} = q_t\, A_m \tag{4}$$

where, q_t is the unit tip bearing resistance and A_m is the cross sectional area of the deep foundation element. Most foundation design textbooks contain formulas for the determination of the unit tip bearing resistance based upon the tip soil properties. When the load at the tip of the deep foundation, P_t, reaches the tip bearing capacity given by Eq. 4, the deep foundation element fails by plunging.

BACKCALCULATION AND VARIABILITY OF MODEL PARAMETERS

The soil-structure interface and tip soil parameters have a complex dependency upon the soil properties and construction techniques. These parameters may be empirically obtained by analyzing the measured load-displacement curve obtained from load tests at given installations. The following model parameters are needed in the "t-z" approach: the soil-structure interface parameters, τ_u and K, and the tip soil parameters, q_t and K_t. Therefore, utilizing actual field load-displacement data, the model parameters were back-calculated using the "t-z" model. The load-displacement curve fitting procedure is described in Misra and Roberts (2006). In the development of separate resistance factors for the side and tip resistance of deep foundation elements, it was determined to use field load-displacement data for a series of drilled shafts given in Phoon et al. (1995) and Rollins et al. (2005). In Phoon et al. (1995), the drilled shafts were installed in clay and were subjected to compression loading. In Rollins et al. (2005), the drilled shafts were installed in gravels and sands and were subjected to pullout loading. The authors were also able to obtain two additional sets of field load-displacement data. The first set of data was obtained from several auger cast test (APG) piles installed as part of a large expansion project for a coal-fired power plant north of Kansas City, Missouri. The auger cast piles were installed in silty-sands overlying dense sandstone and the data included auger cast piles subjected to both pullout and compression load tests, in addition to strain gauge instrumentation. The second set of data was obtained from load tests conducted on four pipe piles installed near the downtown area of Rapid City, South Dakota. The pipe test piles were installed in silty-clay alluvium overlying dense shale and were subjected to compression loading. In Table 1, the mean value of the soil-structure interface and tip soil parameters that were back-calculated from each set of load-displacement data are provided.

It is well-accepted that uncertainty exists in any geotechnical design. Currently, the design uncertainty is managed by assigning either a global factor of safety to the calculated ultimate design capacity or by assigning nominal safety factors to the individual components (i.e. soil properties) that comprise the total design. Irrespective of the method, safety factors are typically assigned based on an individual designer's comfort level and without quantification of actual design uncertainty. To address this problem, a reliability-based design process that rationally incorporates the magnitude of uncertainty needs to be implemented for a safe, efficient, and consistent design. A reliability-based design methodology based on the LRFD approach is becoming increasingly utilized in the design of geotechnical structures (AASHTO 2004). In the LRFD method, resistance factors, with values less than or equal to 1.0, are applied to the calculated nominal resistance of the foundation. The advantage of resistance factors over a global factor of safety is the fact that resistance factors are determined using the probabilistic approach ensuring that uncertainty is rationally incorporated in the design. In addition, resistance factors can be calibrated to produce designs that consistently achieve a desired level of reliability (Phoon et al. 1995). To determine the appropriate resistance factors for design, one must quantify the variability of the soil-structure interface and tip soil parameters. Using the load-displacement data at a given site, the standard deviation, and subsequently, the coefficient of variation

(COV), of the back-calculated parameters can be obtained. To illustrate the methodology for the development of separate resistance factors for the side and tip capacities, in this paper, a COV of 30% was assumed for all the parameters.

Table 1. Back-calculated model parameters for load test data.

Load test data	Soil-structure interface		Tip stratum	
	τ_u (kPa)	K_{init} (MPa)	E_s (MPa)	q_t (kPa)
APG piles	90	40	120	25000
Phoon	90	89	100	2500
Rollins	130	62	-	-
Pipe piles	100	82	110	7200

PROBABILISTIC ANALYSIS WITH *MONTE CARLO* SIMULATION

The *Monte Carlo* simulation technique was employed to perform the probabilistic computations in this paper (Misra et al. 2007). Altogether, 5,000 trials using pairs of randomly generated model parameters based upon a prescribed probability distribution function were performed for each simulation. The lognormal probability distribution function was utilized for both the interface and the tip soil model parameters. Two sets of simulations were performed. The first set of simulations were conducted using the back-calculated values of the interface parameters from each load test data while assuming very weak strength and stiffness parameters for the tip soil. The second set of simulations were conducted using the back-calculated values for the tip soil parameters while assuming very weak strength and stiffness parameters for the soil-structure interface. Both sets of simulations were conducted by varying the bonded length of the deep foundation element from 3m to 36m, utilizing 3m increments. The diameter of the deep foundation element was assumed as 406mm, 910mm, 910mm, and 195mm for the simulations conducted using the auger cast (APG) data, Phoon data, Rollins data, and pipe pile data, respectively. The deep foundation axial stiffness, K_m (product of A_m and E of pile material), was assumed as 4025MN for the simulations conducted using the APG data, 20374MN for the simulations conducted using the Phoon and Rollins data and 1570MN for the simulations conducted using the pipe pile data. For all simulations, the following constants were assumed: $\mu_s = 0.30$, $L_d = 1$m, and $R_f = 1.0$. It should be noted that vertical spatial correlations were ignored in this paper. This assumption was based on results developed in Fenton and Griffiths (2007) that suggest the use of single random variables to model the soil behavior for deep foundations.

The load-displacement curves generated from *Monte Carlo* simulations were analyzed to determine the probability distribution function, and consequently, the COV of load capacity corresponding to an allowable displacement of 25mm (see Misra and Roberts 2006). This value of allowable displacement is consistent with the maximum service limit state displacement utilized in the design of deep foundation elements. Using the load capacity COV, Ω_R, the resistance factor, ϕ_R, can be obtained from the following relationship (Baecher and Christian 2003):

$$\phi_R = \frac{\lambda_R \left(\frac{\gamma_D \, E(Q_D)}{E(Q_L)} + \gamma_L \right) \sqrt{\frac{1+\Omega_{QD}^{\;2} + \Omega_{QL}^{\;2}}{1+\Omega_R^{\;2}}}}{\left(\lambda_{QD} \frac{E(Q_D)}{E(Q_L)} + \lambda_{QL} \right) e^{\beta_T \sqrt{\ln\left[\left(1+\Omega_R^{\;2}\right)\left(1+\Omega_{QD}^{\;2}+\Omega_{QL}^{\;2}\right)\right]}}} \tag{5}$$

where, λ_R is the bias of the resistance, λ_{QD} and λ_{QL} are the bias of the dead load and live load, respectively, γ_D and γ_L are the load factors for the dead load and live load, respectively, Ω_{QD}, Ω_{QL}, Ω_R, are the COV for the dead load, live load, and resistance, respectively, $E(Q_D)$ and $E(Q_L)$ are the expected values of the dead load and live load, respectively, and β_T is the target reliability index.

In the resistance factor calculations for this paper, the values for the bias of the dead load and live load were taken as 1.03 and 1.15, respectively. The COV of the dead load and live load was taken as 0.08 and 0.18, respectively. These values are based on magnitudes given by Baecher and Christian (2003) for typical highway bridge structures. All load factors were assumed equal to unity due to the service limit state (SLS) condition. The ratio of the expected dead load to the expected live load does not significantly affect the value of the resistance factor (Baecher and Christian 2003, Paikowsky et al. 2004); thus, this ratio was set to 2.0, based on typical values for highway bridge structures. The bias of the resistance was assumed to be equal to unity given that the "t-z" method fit the load-displacement data reasonably closely. The target reliability index, β_T was assumed as 2.6, which corresponds to a probability of failure approximately equal to 0.5%. The results of the resistance factor calculations are presented in Figure 2 for the SLS. Figure 2a presents resistance factors for the side resistance while Figure 2b presents resistance factors for the tip resistance. The resistance factors are presented with respect to length of the deep foundation system.

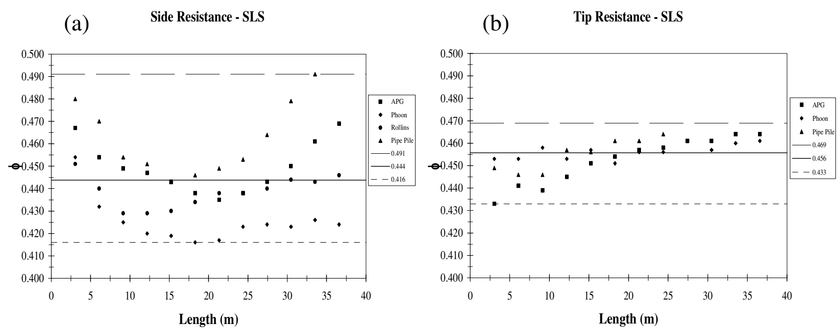

Figure 2. Resistance factors for the (a) side and (b) tip resistance at the SLS.

Figure 2 contains a series of lines to identify the maximum, minimum, and mean resistance factor. Note that the magnitude of the resistance factors have not been rounded to the nearest 0.05, as is typical in practice, to provide a true representation of the calculated values from the simulations. As observed, the maximum and minimum resistance factor values are within ±10% of the mean for the side resistance and within ±5% of the mean for the tip resistance. The resistance factor variation in Figure 2 is predominately due to the variation in load capacity COV at the prescribed allowable displacement. Needless to say, the load capacity COV is a complex function of the load-displacement curve shape, which in turn is a complex function of the interface strength and stiffness parameters, as well as the foundation stiffness, diameter and length. Thus, for some combination of foundation geometry, stiffness and interface parameters, it is possible that the resistance factor will be greater compared to another foundation system at the same allowable displacement. This has significant implication in the design of deep foundations at the service limit state, as additional efficiency in the design is possible by fully understanding the effect of load-displacement curve shape on the variability of the load capacity and, ultimately, the value of the resistance factor. This is especially true for foundation systems whose load capacity is predominately derived from side resistance. For the tip soil, the resistance factors show relatively smaller variations with length.

In the presented multiple resistance factor approach, the engineer must determine the percentage of the load capacity provided by the side resistance and the tip resistance. Using a “t-z” model, the percentage of the applied load carried by the side and the tip resistance is always known at the allowable displacement. The appropriate resistance factor for the side and tip resistance can then be applied to each component of the load capacity utilizing the “t-z” analysis in order to compute the total deep foundation load capacity at the given allowable displacement.

CONCLUSIONS

In this paper, separate resistance factors for the soil-structure interface and tip resistance of a deep foundation element have been calculated. With the use of a “t-z” model, the soil-structure interface and tip soil parameters were back-calculated from actual load test data at a number of sites and for different types of deep foundations. Utilizing the back-calculated model parameters, a series of *Monte Carlo* simulations were conducted. Simulations for side and tip resistance were conducted separately to examine the variability from each load capacity source. The bonded length of the deep foundation element was varied in the simulations. From the simulations, probability distribution functions were determined for load capacities corresponding to a given allowable displacement. The load capacity coefficient of variations (COV), were then utilized to calculate separate resistance factors for the soil-structure interface and tip. The results of the resistance factor calculations indicate that the variability in the resistance at the service limit state is a complex function of the load-displacement curve shape, which in turn, is a complex function of the interface and tip strength and stiffness, as well as the foundation stiffness, diameter and length. By utilizing a “t-z” model and considering separate side and tip resistance factors, efficient and consistent design may be achieved.

ACKNOWLEDGMENTS
The authors would like to acknowledge Kansas City Power and Light (KCP&L) and Burns and McDonnell, Kansas City, Missouri, for use of the load test data on the auger cast piles. The authors would also like to acknowledge FMG Engineering, Inc., Rapid City, South Dakota, for use of the load test data on the pipe piles.

REFERENCES

AASHTO (2004). *LRFD Bridge Design Specifications*. 3rd Edition. American Association of State Highway and Transportation Officials, Washington, D.C.

Baecher, G.B. and Christian, J.T. (2003). *Reliability and Statistics in Geotechnical Engineering.* Wiley, West Sussex, UK.

Duncan, J.M. and Chang, C.-Y. (1970). "Nonlinear analysis of stress and strain in soils", *Journal of the Soil Mechanics and Foundations Division*, ASCE, vol. 96, SM 5, pg. 1629-1653.

Duncan, J.M., Byrne, P., Wong, K.S., and Marby, P. (1980). *Strength, Stress-Strain, and Bulk Modulus Parameters for Finite Element Analyses of Stresses and Movements in Soil Masses.* Report No. UCB/GT/80-01, College of Engineering Office of Research Services, University of California – Berkeley, Berkeley, CA.

Fenton, G.A. and Griffiths, D.V. (2007). "Reliability-based deep foundation design", Proceedings, Geo-Denver 2007, Denver, CO.

Harr, M.E. (1996). *Reliability-Based Design in Civil Engineering.* Dover Publications, Inc., Mineola, New York.

Johnson, K.L. (1985). *Contact Mechanics*. Cambridge University Press, London, UK.

Kondner, R.L. (1963). "Hyperbolic stress-strain response: cohesive soils", *Journal of the Soil Mechanics and Foundation Division*, ASCE, vol. 89, SM 1, pg. 115-143.

Misra, A. and Chen, C.-H. (2004). "Analytical solutions for micropile design under tension and compression", *Geotechnical and Geological Engineering*, 22(2), 199-225.

Misra, A. and Roberts, L.A. (2005). "Probabilistic axial load-displacement relationships for drilled shafts", Proceedings, Geo-Frontiers 2005, Austin, TX.

Misra, A. and Roberts, L.A. (2006). "Probabilistic analysis of drilled shaft service limit state using the 't-z' method", *Canadian Geotechnical Journal*, 43(12), pg. 1324-1332.

Misra, A., Roberts, L.A., and Levorson, S.M. (2007) "Reliability analysis of drilled shaft behavior using finite difference method and Monte Carlo simulation", *Journal of Geotechnical and Geological Engineering,* 25(1), pg. 65-77.

Paikowsky, S.G., Birgisson, B., McVay, M., Nguyen, T., Kuo, C., Baecher, G., Ayyub, B., Stenersen, K., O'Malley, K., Chernauskas, L., O'Neill, M. (2004). *NCHRP Report 507: Load and Resistance Factor Design (LRFD) for Deep Foundations*, Transportation Research Board, National Research Council, Washington, D.C

Phoon, K-K., Kulhawy, F.H., and Grigoriu, M.D., (1995) *Reliability-Based Design of Foundations for Transmission Line Structures*, Report TR-105000, Electric Power Research Institute, Palo Alto, CA, July 1995.

Randolph, M.F. and Wroth, C.P. (1978). "Analysis of deformation of vertically loaded piles" *Journal of the Geotechnical Engineering Division*, ASCE, 104(12), pg. 1465-1488.

Rollins, K.M., Clayton, R.J., Mikesell, R.C., Blaise, B.C. (2005). "Drilled shaft side friction in gravelly soils". *Journal of Geotechnical and Geoenvironmental Engineering*, 131(8), pg. 987-1003.

Reliability-based analysis and design of foundations resting on a spatially random soil

Abdul-Hamid Soubra[1] and Dalia S. Youssef Abdel Massih[2]

[1] Professor, University of Nantes, GeM, UMR CNRS 6183, Bd. de l'université, BP 152, 44603 Saint-Nazaire cedex, France. E-mail: Abed.Soubra@univ-nantes.fr
[2] PhD Student, University of Nantes & Lebanese University, BP 11-5147, Beirut, Lebanon. E-mail: Dalia.Youssef@univ-nantes.fr

ABSTRACT: This paper presents the effect of the spatial variability of the soil shear strength parameters on the reliability analysis and design of a vertically loaded shallow strip footing against bearing failure. The deterministic model used is based on the upper-bound method of limit analysis. The Hasofer-Lind reliability index based on the most critical probabilistic failure surface is calculated for the assessment of the footing reliability. The random fields used in the analysis are the soil shear strength parameters. Normal and non-normal anisotropic random fields with or without cross correlation are considered. The two random fields are averaged along the potential slip lines of the failure mechanism. It was found that the assumption of negative cross correlation, soil heterogeneity and anisotropy regarding the autocorrelation distance gives a higher reliability index than the hypothesis of no cross correlation, homogeneous and isotropic soil. The failure probability was found more sensitive to the variability of the angle of internal friction than the cohesion. For design, an iterative procedure is performed to determine the breadth of the footing for a target failure probability.

INTRODUCTION

Several authors have investigated the reliability-based analysis of foundations against bearing failure. Some authors have modelled the uncertainties of the different parameters as random variables (*e.g.* Low and Phoon, 2002) without introducing the spatial variability of the soil parameters. Others (Cherubini 2000) have considered the effect of the soil spatial variability (*i.e.* soil heterogeneity) by using a simplified approach. Later on, several authors (Griffiths et al. 2002; Fenton and Griffiths 2003 and Popescu et al. 2005 among others) have modelled the uncertain soil parameters more rigorously as random processes and have examined the effect of the spatial variability of these parameters on the ultimate bearing capacity by using finite elements codes. However, most of these studies (except that of Fenton and Griffiths 2003) consider only a single random process in their analysis and require high computation time due to the use of Monte Carlo simulations.

In this paper, the effect of the soil spatial variability on the reliability analysis and design of a vertically loaded strip foundation is presented. Two random processes concerning the soil cohesion and angle of internal friction are used in the analysis. The two random fields are assumed to be anisotropic with different values of vertical and horizontal autocorrelation distances. The punching mode of the ultimate limit state is analysed. A limit analysis model based on the non-symmetrical multiblock failure mechanism presented by Soubra (1999) is used here. This model is rigorous and has the advantage of being more efficient than the commonly used finite element approach which requires much more computation time. In this model, the random fields are averaged along the different potential slip lines of the failure mechanism. After a brief description of the basic concepts of spatial averaging, reliability index and failure probability, the probabilistic model and the corresponding numerical results are presented and discussed.

BASIC RELIABILITY CONCEPTS

Spatial averaging of a random field

The average value of a random field $Z(x, y)$ over a domain *A* is given by :

$$Z_A = \frac{1}{A}.\int_A Z(X).dX \tag{1}$$

If the random field is averaged over a one-dimensional domain as for the slip lines of the failure mechanism used in this paper (*cf.* Figure 1), the domain *A* will correspond to the distance *L* of the segment along which a local average of the random field is defined. By averaging the random field over two arbitrary situated segments L_i and L_j, two variables representing two local averages are found accordingly to equation (1) and a correlation may exist between these variables. This correlation is calculated by averaging the correlation between the random variables at all points on both segments. It is given by (Knabe et al. 1998):

$$\rho(L_i, L_j) = \frac{1}{L_i L_j} \int_0^{L_i} \int_0^{L_j} \rho(u) ds dl \tag{2}$$

where u is the distance that separates any two points of the two segments L_i and L_j.

Reliability index and failure probability

The Hasofer-Lind reliability index is defined by:

$$\beta_{HL} = \min_{G(x)\leq 0} \sqrt{\left(\frac{x-\mu}{\sigma}\right)^T [R]^{-1} \left(\frac{x-\mu}{\sigma}\right)} \tag{3}$$

in which $(x-\mu)/\sigma$ is the vector of the *n* centred and reduced random variables, *R* is the correlation matrix and *F* is the failure region. The minimisation of (3) is performed subject to the constraint $G(x) \leq 0$ where the limit state surface $G(x) = 0$, separates the *n* dimensional domain of random variables into two regions: a failure region *F* represented by $G(x) \leq 0$ and a safe region given by $G(x) > 0$. An intuitive interpretation of the reliability index was suggested in Low and Tang (1997) where the concept of an expanding ellipse led to a simple method of computing the Hasofer-Lind reliability index in the original space of the random variables for both normal and non-normal variables with or without correlation. The method of computation of the reliability index using the concept of an expanding ellipse suggested by Low and Tang (1997) is used in this paper. From the Hasofer-Lind reliability index β_{HL}, one can approximate the failure probability by using the First Order Reliability Method *FORM* as follows:

$$P_f \approx \Phi(-\beta_{HL}) \tag{4}$$

where $\Phi(\cdot)$ is the cumulative distribution function of a standard normal variable.

RELIABILITY ANALYSIS OF A STRIP FOUNDATION ON A SPATIALLY RANDOM SOIL MEDIUM

In this paper, the effect of the spatial variability of the soil shear strength parameters on the reliability analysis and design of a strip foundation subjected to a central vertical load is presented. The cohesion c and the angle of internal friction φ are considered as random fields. A deterministic model based on the upper-bound method of limit analysis is used to study the punching failure mode of the ultimate limit state. Due to the soil heterogeneity, the non-symmetrical multiblock failure mechanism presented by Soubra (1999) is adopted (*cf.* Figure 1).

Failure mechanism

The present failure mechanism is composed of a sequence of *n* triangular rigid wedges. It is described by $2n$ angular parameters $[\alpha_i\,(i=1,...,n),\ \beta_i\,(i=1,....,n)]$. V_i and $V_{i,i+1}$ are respectively the velocity of block i and the inter-block velocity between blocks i and $i+1$. The first wedge ABC is translating as a rigid body with a downward velocity V_1 inclined at an angle φ_{o1} to the discontinuity line AC. Note that the foundation is assumed to move with the same velocity as that of the first block (*i.e.* V_1). The wedge i is assumed to move with a velocity V_i inclined at φ_{oi} to line d_i (*cf.* Figure 1) where φ_{oi} is the average value of the random field of the angle of internal friction along the line d_i. The inter-block velocity $V_{i,i+1}$ is inclined at φ_{ri} to line l_i where φ_{ri} is the average value of the random field of the angle of internal friction along the segment l_i. As for the angle of internal friction, the random field of the cohesion is averaged along each line of the mechanism; c_{oi} is the average value along the line d_i and c_{ri} is the average value along the line l_i. The calculation of ultimate bearing capacity of the footing is performed by equating the total rate at which work is done by the foundation load, the soil weight in motion and the ground surface surcharge to the total rate of energy dissipation along the lines of velocity discontinuities of the failure mechanism.

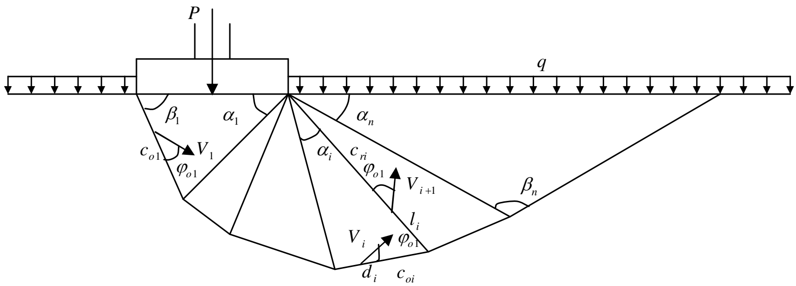

FIG. 1. Non-symmetrical multiblock failure mechanism

Performance function, autocorrelation function and reliability index

The performance function used in the reliability analysis is defined with respect to the punching failure mode of the soil. It is given as follows:

$$G = \frac{P_u}{P_S} - 1 \tag{4}$$

where P_u is the ultimate foundation load and P_S is the vertical applied load.

An anisotropic autocorrelation function is used in this paper for both the cohesion and the angle of internal friction. It is given by an exponential first order function as follows (*e.g.* Vanmarcke, 1983):

$$\rho(\delta x, \delta y) = e^{-2\sqrt{\left(\frac{\delta x}{D_h}\right)^2 + \left(\frac{\delta y}{D_v}\right)^2}} \tag{5}$$

where D_h and D_v are the autocorrelation distances in the horizontal and vertical directions respectively and, δx and δy are the lag distances in the horizontal and vertical directions respectively. Two different values of the cross-correlation $\rho_{c,\varphi}$ are considered in this paper.

The Hasofer-Lind reliability index given by equation (3) is used for the computation of the reliability of the foundation. The vector of random variables x in this equation is composed of the local average values of the soil shear strength random fields. Consequently, the reliability index depends on $4n-2$ random variables $\left(c_{rj}, \varphi_{rj}, c_{oi}, \varphi_{oi}\right)$ with $i = 1,...,n$ and $j = 1,...,n-1$. The correlation matrix [R] is a square matrix of dimensions $(4n-2)\times(4n-2)$ in which $(2n-1)^2$ components are determined by equation (2) using numerical integration. Each component represents the local average correlation between two average values of the random field along two different lines of the failure mechanism. Others $(2n-1)^2$ components correspond to the value of the cross-correlation of the two random fields. The numerical integration is performed using the Gauss-Legendre quadrature method.

NUMERICAL RESULTS

The numerical results presented in this paper consider the case of a shallow strip foundation with breadth *B=2* m subjected to a vertical load. The soil has a unit weight of 18 kN/m^3. No surcharge loading $(q=0)$ is considered in the analysis. The illustrative values used for the statistical moments of the shear strength random fields are as follows: $\mu_c = 20\,kPa$, $\mu_\varphi = 30^\circ$, $COV_c = 20\%$, $COV_\varphi = 10\%$. For the probability distributions of the random fields, two cases are studied. In the first case, referred to as *normal* random fields, c and φ are considered as normally distributed random fields. In the second case referred to as *non-normal* random fields, c follows a log-normal distribution while φ is assumed to be bounded and a beta distribution is used. For both cases, uncorrelated (*i.e.* $\rho_{c,\varphi}=0$) or negatively correlated ($\rho_{c,\varphi}=-0.5$) random fields are considered.

Probabilistic failure surface

A common approach to determine the reliability of a stressed soil mass is based on the calculation of the reliability index β_{HL} corresponding to the deterministic failure surface. In this paper, a more rigorous approach is used. It consists in the determination of the reliability index by minimizing the quadratic form of equation (3) not only with respect to the values of the local averages but also with respect to the geometrical parameters of the failure mechanism (α_i, β_i) (see Figure 1). Notice that the correlation matrix [R] should be calculated for each function evaluation during the minimization process. This is because of the change in the potential failure mechanism. Thus, $(2n-1)^2$ numerical integrations are required for each function evaluation. This approach leads to a much higher computation time than calculating the reliability index using the deterministic surface. A comparison of the reliability index and the corresponding critical mechanism as obtained by the two approaches is presented in figure (2) for $P_S = 1000$ kN/m, $D_h = 10\,m$, $D_v = 2\,m$, $\rho_{c,\varphi}=0$ and n=10. The minimization of the quadratic form of equation (3) is performed with respect to (*6n-2=58*) parameters $(\alpha_i, \beta_i, c_{rj}, \varphi_{rj}, c_{oi}, \varphi_{oi})$ ($i=1,...,n-1$ and $j=1,...,n$). The surface corresponding to the minimum reliability index is referred to here as the critical probabilistic surface. The reliability index calculated with respect to the critical probabilistic surface is smaller (*i.e.* more critical) than the one calculated using the critical deterministic surface (*cf.* Figure 2).

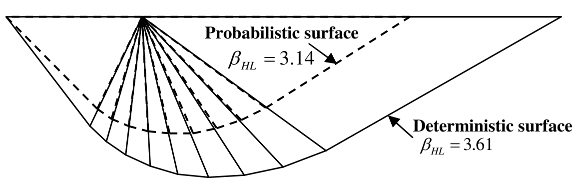

FIG. 2. Deterministic and probabilistic failure surfaces

It was found that the probabilistic failure surface is significantly sensitive to a variation of the applied load and nearly insensitive to the variation of the coefficient of variation, the autocorrelation distances and the cross-correlation of the soil properties. Thus, in the next sections, only one probabilistic failure surface will be determined for a given applied load (*i.e.* a given safety factor) and given values of μ_c and μ_φ. This significantly reduces the computation time of the minimization process.

Variation of the reliability index with the statistical parameters of the shear strength properties

Figure (3) shows the variation of the reliability index with the autocorrelation distance for *normal* and *non-normal* isotropic fields ($D = D_v = D_h$). Both uncorrelated and negatively correlated random fields are considered. A safety factor *F=3* is used. It can be shown that the reliability index corresponding to uncorrelated fields is smaller than the one of negatively correlated fields. One can conclude that assuming negatively correlated shear strength parameters gives economic design in comparison to assuming uncorrelated ones. For the case in hand, the results of *normal* and *non-normal* fields are nearly identical. One can also notice that for a high soil heterogeneity corresponding to small values of D/B, one obtains a high reliability index which means that the assumption of soil heterogeneity increases the reliability of the foundation and thus leads to economic designs.

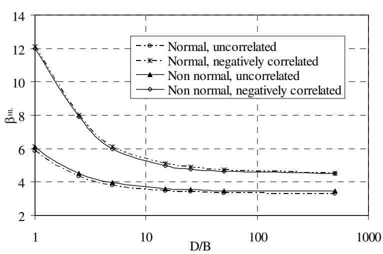

FIG. 3. Effect of the probability distribution and cross-correlation on β_{HL}

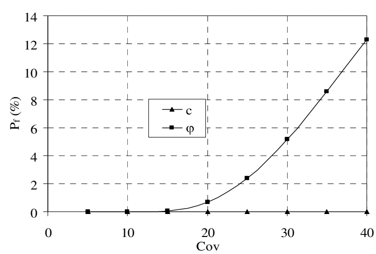

FIG. 4. P_f versus COV$_c$ and COV$_\varphi$

Sensitivity of the failure probability to the variability of the soil shear strength

Figure (4) shows the *FORM* failure probability versus the coefficient of variation of c or φ. For each curve, the coefficient of variation of a random field is hold to the same constant value given in the introduction of the section "Numerical results" and the coefficient of variation of the second field is varied over the range 5% - 40%. A safety factor $F = 3$ is used. Anisotropic *non-normal* random fields with no cross correlation ($D_h = 10m$, $D_v = 2m$, $\rho_{c,\varphi} = 0$) are considered. The results show that for the present case, the failure probability is highly influenced by the coefficient of variation of φ, the greater the scatter in φ the higher the failure probability of the foundation. This means that the accurate determination of the statistical properties of this parameter is very important in obtaining reliable probabilistic results. In contrast, the coefficient of variation of c does not significantly affect the failure probability.

Influence of the anisotropy of the soil shear strength random fields

In general, the variability of the soil in the horizontal direction is different from that in the vertical direction. Figure (5) shows the variation of the failure probability with the ratio D_v/D_h for D_h varying between 0.1 and 100 m. One can conclude from this figure that for the practical case $D_v/D_h < 1$ for which the variability in the vertical direction is higher than that in the horizontal direction, the reliability index is underestimated if the calculation is performed using the assumption of isotropic fields (*i.e.* $D_v/D_h = 1$) and leads to non-economic design. When both autocorrelation distances highly increase, the reliability index tends to the value corresponding to the case of random variables.

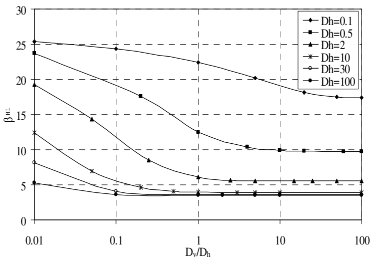

FIG. 5. Influence of anisotropy on the reliability index

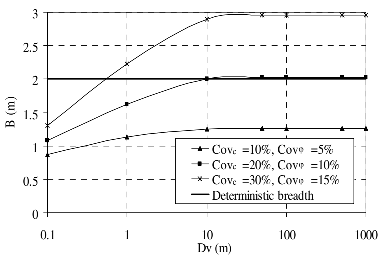

FIG. 6. Comparison between probabilistic and deterministic design

Probabilistic design

The conventional approach used in the design of a shallow foundation is to prescribe a target safety factor (generally $F = 3$) and to determine the corresponding breadth B of the footing. Recently, a reliability-based design (*RBD*) has been used by several authors (*e.g.* Low 2005) on the case of a homogeneous soil. In this paper, a *RBD* is used for spatially varying soil. The approach consists in the calculation of the footing breadth B for a target reliability index of 3.8 as suggested by Eurocode 7 for the ultimate limit states. This foundation breadth is called hereafter "probabilistic foundation breadth". Figure (6) presents the deterministic and the probabilistic foundation breadth for different values of the coefficients of variation of the shear strength random fields and their vertical autocorrelation distance. Anisotropic ($D_h = 10\,m$) *non-normal* random fields with no cross correlation are considered. This figure also presents the deterministic breadth corresponding to a safety factor of 3. It can be noticed that the probabilistic foundation breadth increases with the increase of D_v and the increase of the coefficients of variation of the shear strength random fields. The assumption of isotropic random fields (*i.e.* $D_v = D_h = 10\ m$) gives higher foundation breadth in comparison to the practical case of anisotropy corresponding to higher horizontal autocorrelation distance (*i.e.* $D_v < D_h$). As a conclusion, the deterministic footing breadth may be greater or smaller than the probabilistic foundation breadth, depending on the soil variability.

CONCLUSION

This paper presents the effect of the soil shear strength spatial variability on the reliability analysis and design of a shallow strip footing against bearing failure. The deterministic model used is based on the upper-bound method of limit analysis. The Hasofer-Lind reliability index and the *FORM* failure probability were calculated. The random fields used in the analysis are the soil shear strength parameters. Normal and non-normal anisotropic random fields with or without cross correlation are considered. It was found that the reliability index calculated with respect to the critical probabilistic surface is smaller (*i.e.* more critical) than the one determined using the critical deterministic surface. The probabilistic failure surface is significantly sensitive to a variation of the applied load (*i.e.* safety factor) and nearly insensitive to the variation of the coefficient of variation, the autocorrelation distances and the cross-correlation of the soil properties. The failure probability is more sensitive to the variability of the angle of internal friction than the cohesion. For the practical case for which the variability in the vertical direction is higher than that in the horizontal direction, the reliability index is underestimated if the calculation is performed using the assumption of isotropic fields and leads to non-economic design. Finally, the deterministic footing breadth may be greater or smaller than the probabilistic foundation breadth, depending on the soil variability.

REFERENCES

Cherubini, C. (2000). "Reliability evaluation of shallow foundation bearing capacity on c', φ' soils." *Can. Geotech. J.*, 37, 264-269.

Fenton, G. A., and Griffiths D. V. (2003). "Bearing capacity prediction of spatially random c-φ soils." *Can. Geotech. J.*, 40, 54-65.

Griffiths, D. V., Fenton, G. A., and Manoharan, N. (2002). "Bearing capacity of rough rigid strip footing on cohesive soil: Probabilistic study." *J. of Geotech. & Geoenv. Engrg., ASCE*, 128(9), 743-755.

Knabe, W., Przewlocki, J. and Rozynski, G. (1998). "Spatial averages for linear elements for two-parameters random field." *Prob. Engng. Mech.* 13(3), 147-167.

Low, B. K. (2005). "Reliability-based design applied to retaining walls." *Géotechnique*, 55(1), 63-75.

Low, B. K., and Phoon, K. K. (2002). "Practical first-order reliability computations using spreadsheet." *Probabilistics in Geotechnics*: *Technical and Economic Risk Estimation*, Austria, 39-46.

Low, B. K., and Tang, W. H. (1997). "Efficient reliability evaluation using spreadsheet." *J. of Engrg. Mech.*, *ASCE*, 123, 749-752.

Popescu, R., Deodatis, G., and Nobahar, A. (2005). "Effect of random heterogeneity of soil properties on bearing capacity." *Prob. Engrg. Mech.*, 20, 324-341.

Soubra, A.-H. (1999). "Upper-bound solutions for bearing capacity of foundations." *J. of Geotech. & Geoenv. Engrg., ASCE*, 125(1), 59-68.

Vanmarcke, E. (1983). "Random Fields: Analysis and Synthesis." Published by *MIT Press, Cambridge MA*, 382p.

Statistical Analysis of O-Cell Test Data for Nominal Load Capacities of Drilled Shafts

Xiaoming Yang[1], Jie Han[1], Robert Henthorne[2], and Robert L. Parsons[1]

[1] Department of Civil, Environmental, and Architectural Engineering, the University of Kansas, Lawrence, KS 66045, USA
[2] Kansas Department of Transportation, Topeka, KS 66603, USA

ABSTRACT: The Osterberg cell (O-cell) test has been increasingly used for evaluating load capacities of drilled shafts. In this test, the pre-installed O-cell jack simultaneously produces an upward force to the upper portion of the shaft and a downward force to the lower portion of the shaft at an equal magnitude, which can be used to estimate the side resistance and the tip resistance of the shaft separately. In this study, 25 O-cell test datasets were collected for the test shafts installed in rock or weak rock. Seven interpretation methods ("Davisson's, Chin's, Butler and Hoy's, FHWA 0.05D, Fuller and Hoy's, Brinch-Hansen's 80%, and creep limit method) were used to estimate the nominal bearing capacities of all drilled shafts based on the equivalent "top-down" curves. The mean value of the nominal load capacities based on these seven methods was considered as the representative capacity. A "bias" was calculated as the ratio of the nominal load capacity by a specific interpretation method to the representative load capacity. Statistical analysis was performed for all seven methods. It is concluded that the FHWA 0.05D and Butler and Hoy's methods resulted in the mean bias close to 1.00 and the small COV value. The FHWA 0.05D method is recommended for the reliability analysis for the resistance factor of drilled shafts based on O-cell test data.

INTRODUCTION

With the rapid development of reliability based design (RBD) methods in geotechnical engineering, Load and Resistance Factor Design (LRFD) has been increasingly used in the United States. The basic idea of LRFD is to use load and resistance factors, rather than a single factor of safety, to account for the uncertainties and target the designed structure to a certain reliability index. Although LRFD is a simplified RBD method, extensive work is needed to calibrate resistance factors for each design scenario and method. A good example is the design of drilled shafts in intermediate geomaterials (IGM, i.e., geomaterials with mechanical behavior between typical soils and rocks, e.g., heavily consolidated clays, shale, limestone, and decomposed rocks, etc.).

The capacity of a drilled shaft consists of two components, side resistance and base resistance. The design method for drilled shafts adopted by FHWA is based on the study of O'Neill and Reese (1999). Paikowsky (2004) collected 91 load test data in IGM and calibrated the resistance factors of side and total resistance for this design method at different target reliability indices. However, conventional shaft load tests cannot separate side and base resistance accurately. In the AASHTO LRFD bridge design specification (AASHTO, 2007), a side resistance factor for drilled shafts in IGM equal to 0.6 is recommended based on Paikowsky's study, and a base resistance factor of 0.55 is recommended to account for more uncertainties in base resistance prediction. In order to calibrate the side and base resistance factors separately, 25 O-cell load test data were collected from sites in the Midwest of the United States.

The Osterberg cell (O-cell) test was invented by Dr. Jorj O. Osterberg and first used in the 1980s (Osterberg 1984). Unlike the conventional top load test, the load in this test is applied by a cell, which is often pre-installed in the shaft somewhere near the tip. This cell simultaneously produces an upward force to the upper portion of the shaft and a downward force to the lower portion of the shaft at an equal magnitude, which can be used to estimate the side resistance and the tip resistance of the shaft separately. Figure 1 shows the comparisons between the conventional load test and the O-cell load test.

In practice, engineers often equalize the "up" and "down" load-displacement curves from an O-cell test to the "top-down" load-displacement curve from a conventional pile load test as shown in Fig.2. In this equalization, the shaft compression is calculated and included in the development of the equivalent "top-down" curve. Several methods have been proposed by researchers to estimate the differential compression of the shaft in an O-cell test versus that in a top load test, e.g., LOADTEST Inc. (2001), Ooi et al. (2004), and Kwon et al. (2005). The method proposed by LOADTEST Inc. (2001) was adopted in this study. It is common that either the side resistance or the tip resistance or both do not reach failure. Therefore, extrapolation of the test data is needed to determine the nominal resistance. A hyperbolic model was adopted in this study to extrapolate the test data.

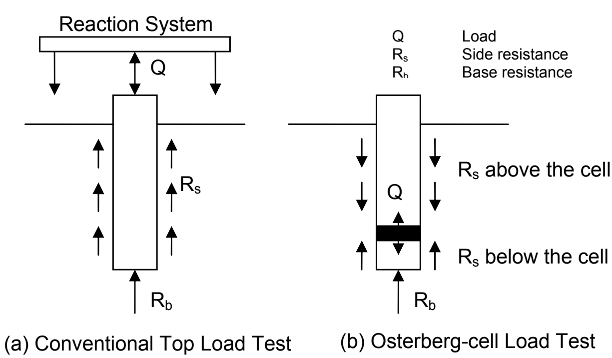

Fig. 1. Comparison of conventional top load test and O-cell load test

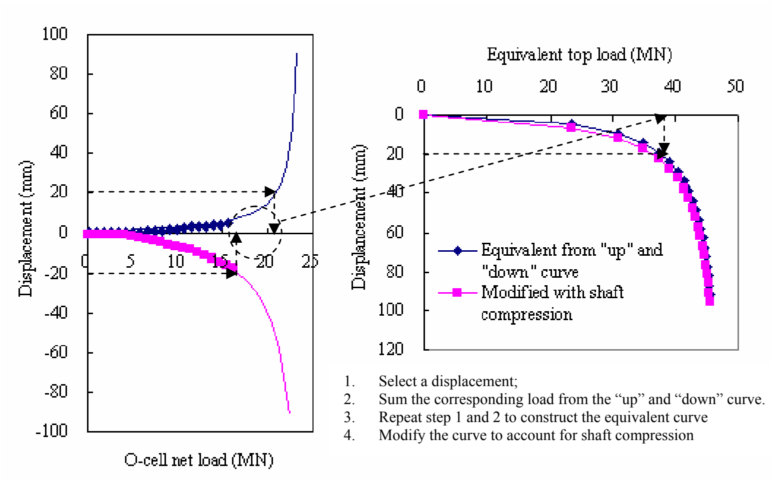

Fig. 2. Construction process of equivalent top load test curve

From an equivalent load-displacement curve, nominal capacities can be determined using different methods. The displacement at failure determined from the equivalent load-displacement curve can then be used to calculate side and base resistance capacities from the Osterberg data by reversing the procedure used to construct the equivalent top load test curve. Seven methods were selected in this study to determine the nominal load capacity from a load-displacement curve. LOADTEST Inc (2001) used a "creep limit" criteria. FHWA (O'Neill and Reese, 1999) suggested the use of the load corresponding to a displacement of 5% shaft diameter (FHWA 0.05D) if the plunging of the curve is not reached. Other methods include Brinch-Hansen's 80% (1963), Butler and Hoy's (1977), Chin's (1970), Fuller and Hoy's (1970), and Davisson's criterion (1972). Paikowsky (2004) examined five different methods and used the mean value as the representative capacity. By comparison, he adopted the FHWA 0.05D method as the criterion for the resistance factor calibration. Ooi (2004) also compared different extrapolation equations and capacity criteria and found that the most reliable methods were Chin's (1970) hyperbolic equation for extrapolation of the load-displacement curve and Davisson's criterion for determination of the nominal capacity.

In this study, Chin's equation (Eq. 1) was used for the curve extrapolation except for the Brinch-Hansen's 80% method (Eq. 2) because the Brinch-Hansen's 80% method has its own extrapolation approach as part of the solution.

$$\frac{s}{P} = C_1 s + C_2 \tag{1}$$

$$\frac{\sqrt{s}}{P} = C_1 s + C_2 \tag{2}$$

To be clear, the seven methods discussed above are listed below, which were used in this study:

a. Creep Limit
b. FHWA 0.05D
c. Davisson's
d. Brinch-Hansen's 80%
e. Butler and Hoy's
f. Fuller and Hoy's
g. Chin's (1970)

STATISTICAL ANALYSIS OF TEST DATA

Based on the available test data, each test was interpreted with the above seven methods except tests no. 9 - no. 14, which have no creep data. Figure 3 presents the calculated side resistance for all 25 shafts based on these seven methods. It is shown that these methods yielded results with certain differences. The "Creep Limit" method consistently predicted the lowest capacity value and the Chin's method always yielded the highest predicted value. The "Creep Limit" criterion is based on the measured data without any extrapolation and is over-conservative, especially when the test is terminated at the O-cell reaching its capacity before the full mobilization of either the side or base resistance. The Chin's method mathematically calculates the nominal load capacity when the hyperbolic curve reaches an infinite displacement. Therefore, these two methods were not included in the subsequent analysis. The mean value of the capacities from the other five methods was taken as the representative capacity, or "real" capacity of the shaft. Figure 3 presents the calculated side resistance for all 25 shafts, Figure 4 presents the calculated base resistance while Figure 5 presents the calculated total load capacity. As shown in Fig. 5, the calculated total load capacities range from 3.6 to 269.6 MN.

A concept "bias" was used in this study to examine the remaining five methods (i.e., FHWA 0.05D, Davisson's, Brinch-Hansen's 80%, Butler and Hoy's, and Fuller and Hoy's methods). "Bias" is defined as the ratio of the capacity by each interpretation method over the representative capacity (Paikowsky, 2004). This approach is similar to the Paikowsky (2004) one except that the side and base resistance were examined separately in this study.

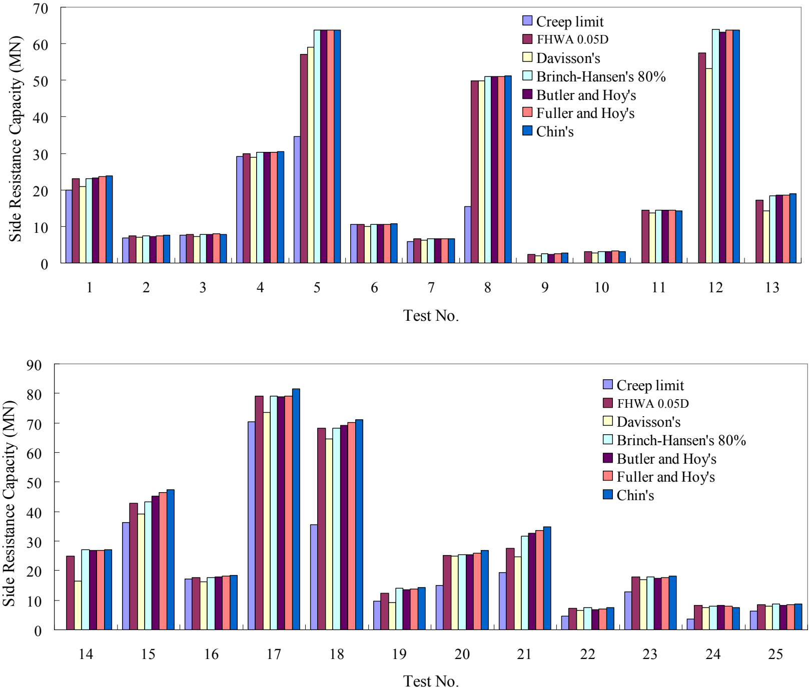

Fig. 3. Calculated side resistance

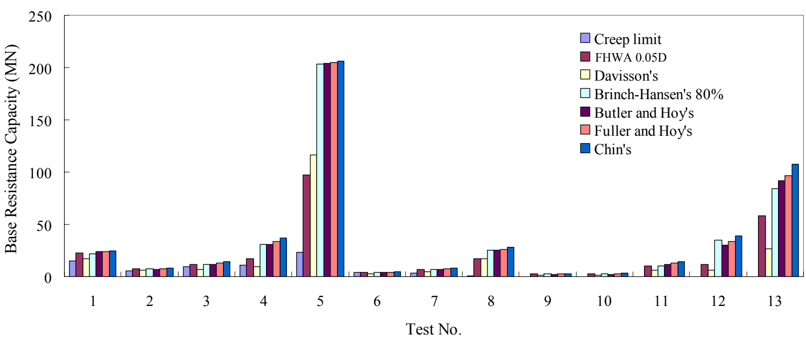

Fig. 4. Calculated base resistance

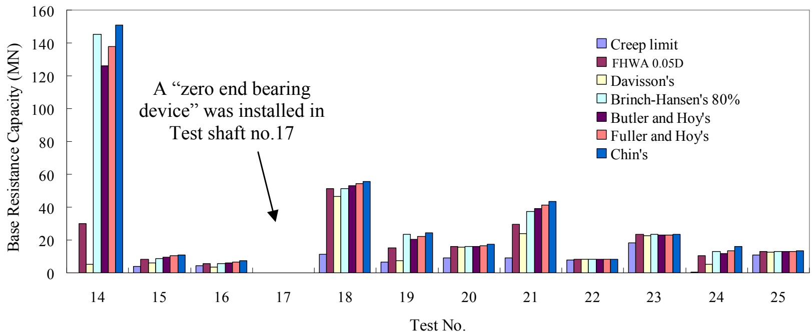

Fig. 4. Calculated base resistance (continued)

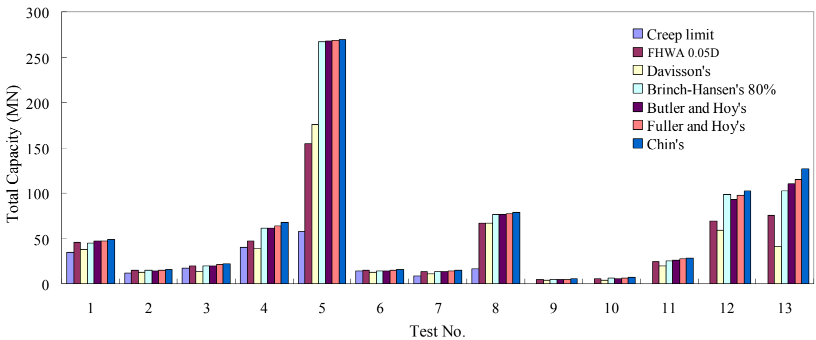

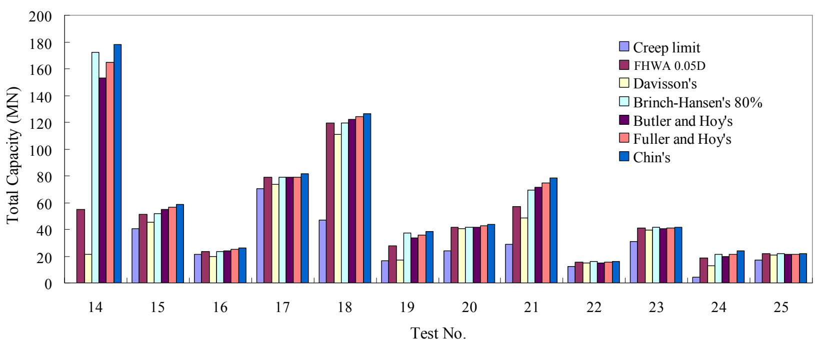

(c) Total capacity

Fig. 5. Calculated total load capacity

The calculated "bias" values for all five methods were statistically analyzed and their results are provided in Table 1. Table 1 shows that except Davisson's method, the other four methods are very reliable and comparable. The comparison shows that the FHWA 0.05D method yielded a side resistance prediction equal to the representative value with a low standard deviation of 0.03. Since Butler and Hoy's method had the lowest COV values for all three capacities, it is considered the most reliable method from the statistical point of view. However, Butler and Hoy's method overestimated the capacities as compared with the representative values. FHWA 0.05D method yielded the closest and conservative mean values of the side, base, and total load capacity to representative values. Therefore, the FHWA 0.05D method was selected in this study for future resistance factor calibration.

Table 1. Statistical Results of Five Different Criteria

	FHWA 0.05D			Davisson's			Brinch-Hansen's 80%			Butler and Hoy's			Fuller and Hoy's		
	Side	Base	Total	Side	Base	Total	Side	Base	Total	Side	Base	Total	Side	Base	Total
m	1.00	0.91	0.95	0.91	0.66	0.79	1.03	1.13	1.08	1.02	1.11	1.07	1.04	1.19	1.11
σ	0.03	0.20	0.13	0.08	0.24	0.18	0.03	0.16	0.11	0.03	0.12	0.09	0.03	0.14	0.10
COV	0.03	0.22	0.14	0.09	0.36	0.23	0.03	0.14	0.10	0.03	0.11	0.08	0.03	0.12	0.09

Note: m=mean value; σ=standard deviation; COV=coefficient of variation.

CONCLUSIONS

Twenty-five O-cell test data were collected in this study for drilled shafts in rocks. Seven methods available in the literature were selected to estimate the load capacities of all 25 drilled shafts. Calculated load capacities from five methods (FHWA 0.05D, Davisson's, Brinch-Hansen's 80%, Butler and Hoy's, and Fuller and Hoy's methods) were used for statistical analysis. The comparison showed that Butler and Hoy's criterion is the most reliable method. However, the FHWA 0.05D method provided the closest and conservative predictions of the load capacities to the representative values. Therefore, the FHWA 0.05D method is recommended for resistance factor calibration in the future studies.

ACKNOWLEDGEMENTS

This research is financially sponsored by the Kansas Department of Transportation (KDOT) through the KTRAN program. Mr. Mark Hunt and Mr. Robert Henthorne at KDOT are the project monitors for this project. Mr. William (Bill) Ryan at Loadtest, Mr. Don King at King Construction, Mr. Pete Nix at DLZ Ohio, Inc., and Mr. Lyle Simonton at Subsurface Contractors, Inc. provided part of O-cell test data. All the above support is greatly appreciated.

REFERENCES

AASHTO (2007). *LRFD Bridge Design Specifications*. American Association of State Highway and Transportation Officials, Third Edition, Washington, DC, USA.

Brinch-Hansen, J. (1963). "Discussion on hyperbolic stress-strain response: Cohesive soils." *Journal of Soil Mechanics and Foundation Engineering*, American Society of Civil Engineers, 89(4), 241-242.

Butler, H.D. and Hoy, H.E. (1977). *Users Manual for the Texas Quick-Load Method for Foundation Load Testing*. Federal Highway Administration, Office of Development, Washington, DC, USA.

Chin, F.K. (1970). "Estimation of the ultimate load of piles not carried to failure." *Proceedings of the 2nd Southeast Asian Conference on Soil Engineering*, 81-90.

Davisson, M.T. (1972). "High capacity piles." *Proceedings of Soil Mechanics Lecture Series on Innovations in Foundation Construction*, American Society of Civil Engineers, Illinois Section, Chicago, March 22nd, 81-112.

Fuller, R.M. and Hoy, H.E. (1970). *Pile Load Tests Including Quick Load Test Method, Conventional Methods and Interpretations*. Highway research Board, HRB 333, Washington, DC, USA, 78-86.

Kwon, O.S., Choi, Y., Kwon, O., and Kim, M.M. (2005). "Comparison of the bidirectional load test with the top-down load test." *Journal of the Transportation Research Board*, 1936, Transportation Research Board of the National Academies, Washington, DC, 108-116.

LOADTEST Inc. (2001). *Data Report on Drilled Shaft Load Testing (Osterberg Method), Ellsworth, KS-K-156 Over Union Pacific Railroad & Side Road (LT-8790)*. Prepared for Kansas Department of Transportation, Topeka, KS, USA.

O'Neill, M.W. and Reese, L.C. (1999). *Drilled Shafts: Construction Procedures and Design Methods*. Report No. FHWA-IF-99-025, Federal Highway Administration, Washington, DC, USA, 758p.

Ooi, P.S.K., Chang, B.K.F., and Seki, G.Y. (2004), "Examination of proof test extrapolation for drilled shafts." *Geotechnical Testing Journal*, 27(2), 1-11.

Osterberg, J. O. (1984). "A new simplified method for load testing drilled shafts." *Foundation Drilling*, 23(6), 9-11.

Paikowsky, S.G. (2004). *Load and Resistance Factor Design (LRFD) for Deep Foundations*. NCHRP (Final) Report 507, Transportation Research Board, Washington, DC, USA, 126p.

Reliability Analysis of Bearing Capacity Equations for Drilled Shafts Socketed in Weathered Rock

Sung Jun Jung[1], M.S., Jin Man So[2], BEngr
Sung Ryul Kim[3], Ph.D., Myoung Mo Kim[4], Ph.D., M.ASCE

[1] Graduated Student, Department of Civil Engineering, Seoul National University, San 56-1, Shinlim-Dong, Kwanak-Ku, Seoul, 151-742, Korea, brian76@snu.ac.kr
[2] Graduated Student, Department of Civil Engineering, Seoul National University, San 56-1, Shinlim-Dong, Kwanak-Ku, Seoul, 151-742, Korea, deuxsjm@hotmail.com
[3] Assistant Prof., Department of Civil Engineering, Dong-A University, Hadan-2Dong, Saha-Gu, Busan, 604-714, Korea, sungryul@dau.ac.kr
[4] Prof., Department of Civil Engineering, Seoul National University, San 56-1, Shinlim-Dong, Kwanak-Ku, Seoul, 151-742, Korea, geotech@snu.ac.kr (corresponding author)

ABSTRACT: As the use of drilled shafts for the foundation of a large size structure increases, the evaluation of the reliable bearing capacity of a pile has become important. The purpose of this study is to examine the reliability of bearing capacity equations for drilled shafts socketed in weathered rock by comparing the bearing capacity values obtained by the bearing capacity equations with the measured ones. To this aim, 17 static load test data obtained from four field sites were collected, and based on these test data, the ultimate bearing capacity of rock-socketed piles were acquired. Three bearing capacity equations widely used in practice were selected for the reliability analysis. They are the AASHTO method (1996), Carter & Kulhawy method (1988), and FHWA method (1999). The comparison of the bearing capacity values showed that FHWA method predicted the bearing capacities most closely to the measured ones on average, whereas the Carter & Kulhawy method (1988) and AASHTO method (1996) consistently predicted bearing capacities conservatively with acceptable discrepancy.

INTRODUCTION

With the increase in the construction of heavy and large structures, large-diameter drilled shafts are becoming more widely used in practice. They are socketed into rocks to ensure high bearing capacity. It has become more important to properly evaluate the bearing capacity of the rock-socketed pile because the rock-socketed pile has to support a much larger load than the soil-embedded piles.

The purpose of this study is to examine the reliability of some bearing capacity equations for drilled shafts socketed into weathered rock by comparing the bearing capacity values from static load tests with the values calculated from the bearing capacity equations.

Seventeen static load test data from four field sites were collected for comparisons. Three bearing capacity equations such as the AASHTO method (1996), Carter & Kulhawy method (1988), and FHWA method (1999) were selected to compare their estimations with measured bearing capacities.

MEASURED BEARING CAPACITY FROM STATIC LOAD TEST

In cooperation with universities, laboratories and corporations etc, a total of 80 static load test data were collected and reviewed. But only 17 data from four field sites were found reliable and useful for this study (Kwon, 2004). The diameters of the drilled shafts ranged from 0.4 to 1.5 m, and the socketed depths into rock ranged from 0.2 to 18.3 m. Slowly maintained load tests or cyclic load tests were applied as specified in the American Society for Testing and Materials (ASTM) Designation 1143. The rock properties at the tip and shaft of 17 drilled shafts are summarized in Table 1.

Table 1. Properties of Foundation Rock Masses

Site	Pile No.	Weathering Grade[1]	q_u (MPa)		Em[2] (MPa)		Eur[3] (MPa)		RQD (%)		RMR	
			tip	shaft	tip	shaft	tip	shaft	tip	shaft	tip	shaft
WR-1 (D=0.4m)	1	MW	56.7		548.4	-	2810	-	23	0	25	
	2	MW	84.7		-	887.2	-	2280	37		33	
	3	MW	55.5		-	169.5	-	650	45	55	38	
	4	MW	55.5		-	169.5	-	650				
	5	MW	57		-	-	-	860	31	49	33	
WR-2 (D=1.5m)	6	MW	78.7		150.7		336		20		25	
WR-3 (D=1.0m)	7	HW	47.8[4]		203.5	195.5	905		0		22	
	8	HW										
	9	HW			-	170.2	-	973.5				
	10	MW			834.5	583.5	2752	1931.6	42	40	42	
	11	MW			931.5		2748		50	52	45	
WR-4 (D=0.4m)	12	HW	12.3	20.2	-	-	-	-	0		7	
	13	CW	36.1	15.6	111	61.9	619	162.1				
	14	CW	17.3	15.7	57.8	56.7	191	162.5				
	15	CW	15.7				163					
	16	HW	30.4	12.0	-	-	-	-				
	17	HW	11.7	12.2	-	-	-	-				

1) MW = Moderately Weathered, HW=Highly Weathered, CW=Completely Weathered
2) initial loading modulus from a pressuremeter test
3) unloading and reloading modulus from a pressuremeter test
4) The only data available in the site

There are various procedures for determining the ultimate bearing capacity of a pile from a load-settlement curve of the static pile load test. Among them, five methods, such as the Davisson method(Davisson, 1972), the 25.4 mm method(Terzaghi & Peck, 1967), the 0.1D method(Terzaghi, 1942), the FHWA 5% criterion(O'Neill and Reese, 1999) and the ASCE method(ASCE, 1997) were investigated for their universal validity. Each method is briefly outlined in Table 2.

Table 2. Various Methods for Determining the Ultimate Bearing Capacity from a Load-Settlement Curve

Method	Description
Davisson (1972)	The offset line is generated by adding the elastic settlement to a constant (if the pile diameter, D<600 mm, then the constant=3.81+D/120 mm and if D≥600 mm, then the constant=D/30 mm).
Δ=25.4mm (1967)	The load corresponding to pile head settlement of 25.4mm is defined as the ultimate bearing capacity
Δ=0.1D (1942)	The load corresponding to pile head settlement of 0.1 D is defined as the ultimate bearing capacity
FHWA 5% (1999)	The load corresponding to pile head settlement of 0.05 D is defined as the ultimate bearing capacity
ASCE (1997)	The principle of the ASCE method is the same as that of the Davisson method except that the constant in the ASCE method is (0.15+1/100) inch

The ultimate bearing capacity determined by the various methods is listed in Table 3. When the ultimate bearing capacity could not be obtained from a load-settlement curve, the curve was extended by using a hyperbolic function.

Table 3. Measured Bearing Capacities

Site	Pile No	Diameter (m)	Depth of Rock Socket (m)	Ultimate Bearing Capacity (kN)				
				Davisson	FHWA 5%	25.4mm	0.1D	ASCE
WR-1	1	0.4	0.36	850	950※	1000※	1050※	850※
	2	0.4	0.2	900	1500	1700	2450	900
	3	0.4	0.48	1200	1500	1750	2000※	1250
	4	0.4	1.08	2440※	2600※	2700※	2800※	2550※
	5	0.4	0.76	2600	2900	3200	3500※	2650
WR-2	6	1.5	5	60700※	53700※	28050※	70100※	46750
WR-3	7	1.0	2.3	24640※	24900※	16700	33300※	17600※
	8	1.0	2	16520※	16650※	13000	20100※	12500
	9	1.0	2.15	18800	19200※	12000	26800※	10500
	10	1.0	1.9	25900※	27300※	18500	36200※	19950※
	11	1.0	1.7	37480※	30100※	20250※	40200※	22900※
WR-4	12	0.4	6	2100	2300	2550	3000※	2100
	13	0.4	3	1650	2000	2150	2450	1650
	14	0.4	3	600	950	1050	1450	600
	15	0.4	3	750	1000	1100	1250	750
	16	0.4	9	3030※	2900	3300※	4100※	3400※
	17	0.4	6	2200	2500	2950	3800	2250

※: Extrapolated values using hyperbolic function

To compare the various methods in determining the bearing capacity values, the ratio of the average of the ultimate bearing capacities obtained from the five methods to the bearing capacity obtained from each method(K_{sx}) was calculated and the average values of the K_{sx} are tabulated in Table 4.

Table 4. K_{sx} for Various Methods

Method	Number of Available Pile	Average of K_{sx}	Standard Deviation of K_{sx}
Davisson (1972)	17	1.13	0.23
Δ =25.4mm (1967)	17	1.12	0.29
Δ =0.1D (1942)	17	0.76	0.09
FHWA 5% (1999)	17	1.00	0.06
ASCE (1997)	17	1.26	0.20

As shown in Table 4, the average K_{sx} value of the FHWA 5% criterion is exactly equal to 1. And the values of K_{sx} from the Davisson method and the 25.4mm settlement criterion are larger than 1 but by relatively small amount, and this means that the methods give conservative values with acceptable discrepancy. In this study, the FHWA 5% criterion and the Davisson method were used to examine the reliability of the bearing capacity equations.

PREDICTED BEARING CAPACITY BY THE BEARING CAPACITY EQUATIONS

Table 5 presents a summary of the methods used to estimate the bearing capacity of drilled shafts, detailing the equations for shaft and tip resistances, and the required parameters.

Table 5. Brief Description of Bearing Capacity Equations

Design Method	Resistance Component	Equation	Parameter
Carter & Kulhawy (1988)	Tip Resistance	$q_{max} = [s^{0.5} + (m \cdot s^{0.5} + s)^{0.5}]q_u$	q_u : uniaxial compressive strength of intact rock m, s : mass properties
	Shaft Resistance	$f_{max} = 1.42 p_a \left(\frac{q_u}{p_a}\right)^{0.5}$	P_a : atmospheric pressure
AASHTO (1996)	Tip Resistance	$Q_{TR} = N_{ms} C_o A_t$	N_{ms} : coefficient factor to estimate q_{ult} for rock C_o : uniaxial compressive strength of intact rock A_t : area of shaft tip
	Shaft Resistance	$Q_{SR} = \pi B_r D_r (0.144 q_{SR})$	B_r : diameter of rock socket D_r : length of rock socket q_{SR} : ultimate unit shear resistance
FHWA (1999)	Tip Resistance	$q_{max} = 3K_{sp}\Theta q_u$	K_{sp} : empirical factor Θ : depth factor
	Shaft Resistance	$f_{max} = 0.65 p_a \left(\frac{q_u}{p_a}\right)^{0.5} \leq 0.65 p_a \left(\frac{f'_c}{p_a}\right)^{0.5}$	P_a : atmospheric pressure f'_c : compressive cylinder strength of the concrete

Table 6 presents a summary of the predicted bearing capacities calculated by the bearing capacity equations. Only the total bearing capacity was used for the analysis because no load transfer data was available. In the same table, bias factors of the result from each bearing equation with respect to the measured bearing capacity by the Davisson method and the FHWA 5% method are shown.

Table 6. Predicted Bearing Capacities

Site	Pile No.	Davisson (kN)	FHWA 5% (kN)	Carter & Kulhawy(1988)			AASHTO(1996)			FHWA(1999)		
				Total Resistance (kN)	Dav./ Total	FHWA/ Total	Total Resistance (kN)	Dav./ Total	FHWA/ Total	Total Resistance (kN)	Dav./ Total	FHWA/ Total
	1	850	950※	N.A[1]	N.A	N.A	640	1.33	1.48	N.A[1]	N.A	N.A
	2	900	1500	1040	0.87	1.44	920	0.98	1.63	5170	0.17	0.29
WR-1	3	1200	1500	910	1.32	1.65	640	1.88	2.34	3560	0.34	0.42
	4	2440※	2600※	1320	1.85	1.97	710	3.44	3.66	3870	0.63	0.67
	5	2600	2900	1450	1.79	2.00	690	3.77	4.20	4050	0.64	0.72
WR-2	6	60700※	53700※	25480	2.38	2.11	14090	4.31	3.81	65330	0.93	0.82
	7	24640※	24900※	7080	3.48	3.52	4050	6.08[2]	6.15 [2]	18300	1.35	1.36
	8	16520※	16650※	4380	3.77	3.80	3960	4.17	4.20	17900	0.92	0.93
WR-3	9	18800	19200※	4580	4.10	4.19	4000	4.70	4.80	18060	1.04	1.06
	10	25900※	27300※	6600	3.92	4.14	3930	6.59[2]	6.95[2]	17930	1.44	1.52
	11	37480※	30100※	6610	5.67	4.55	17850	2.10	1.69	17940	2.09	1.68
	12	2100	2300	N.A[1]	N.A	N.A	970	2.16	2.37	N.A[1]	N.A	N.A
	13	1650	2000	N.A[1]	N.A	N.A	750	2.20	2.67	N.A[1]	N.A	N.A
WR-4	14	600	950	N.A[1]	N.A	N.A	750	0.80	1.27	N.A[1]	N.A	N.A
	15	750	1000	N.A[1]	N.A	N.A	750	1.00	1.33	N.A[1]	N.A	N.A
	16	3030※	2900	N.A[1]	N.A	N.A	1070	2.83	2.71	N.A[1]	N.A	N.A
	17	2200	2500	N.A[1]	N.A	N.A	900	2.44	2.78	N.A[1]	N.A	N.A

1) Not Available because the rocks are completely weathered or RQD=0

2) discarded in the statistical analysis because the values exceed the value of the mean plus two times the standard deviation

RELIABILITY ANALYSIS OF BEARING CAPACITY EQUATIONS

Calculated bearing capacities of 17 test piles are plotted against the measured ones in Figs. 1 and 2. Regression lines are also shown in the Figures. It is noted from the Figures that the FHWA method predicted bearing capacities almost identical to the measured ones on average. On the other hand, the Carter & Kulhawy method and the AASHTO method consistently predicted the bearing capacity values, conservatively.

Tables 7 and 8 summarized the bias factors (measured/ calculated bearing values) of each method. As anticipated, the bias factor ranges from 2.5 to 3.0 for the Carter & Kulhawy method and the AASHTO method, whereas that of FHWA is slightly smaller than 1.

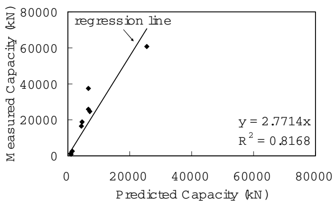

(a) Carter & Kulhawy method

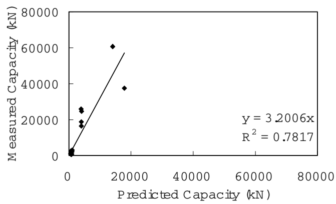

(b) AASHTO method

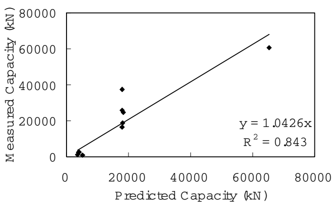

(c) FHWA method

Fig 1. Comparison of Predicted and Measured Capacity using Davisson Method

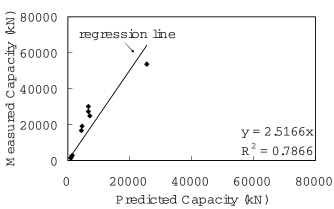

(a) Carter & Kulhawy method

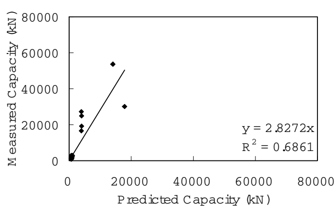

(b) AASHTO method

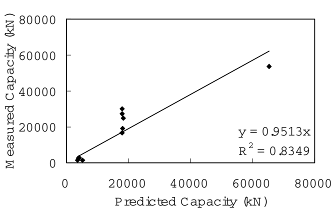

(c) FHWA method

Fig 2. Comparison of Predicted and Measured Capacity using FHWA 5% Method

Table 7. Statistical Data for Davisson Method

Design Method	Number of Available Piles	Average	Standard Deviation	COV (%)
AASHTO (1996)	15	2.54	1.28	0.51
Carter & Kulhawy (1988)	10	2.92	1.51	0.52
FHWA (1999)	10	0.96	0.57	0.59

Table 8. Statistical Data for FHWA 5% Method

Design Method	Number of Available Piles	Average	Standard Deviation	COV (%)
AASHTO (1996)	15	2.82	1.16	0.41
Carter & Kulhawy (1988)	10	2.94	1.21	0.41
FHWA (1999)	10	0.95	0.46	0.49

CONCLUSIONS

The purpose of this study was to examine the reliability of bearing capacity equations for drilled shafts socketed into weathered rock by comparing the predicted capacity with the measured capacity from static load tests. The following conclusions were obtained.

1. Five methods determining the ultimate bearing capacity from a load-settlement curve of a static pile load test were reviewed for their universal validity. The FHWA 5% method was found to give the average value of the ultimate bearing capacities determined by the five methods, and the Davisson method and the 25.4mm settlement criterion gave conservative values with relatively small discrepancy from the mean value of the five methods.
2. FHWA method (1999) estimated the bearing capacity of piles the most closely to the measured values, on average. The Carter & Kulhawy method (1988) and the AASHTO method (1996) consistently predicted bearing values conservatively by up to a factor of 3.

ACKNOWLEDGMENT

This study was conducted under a research contract between the Korea Institute of Construction Technology (KICT) and the Ministry of Construction and Transportation (MOCT), Republic of Korea. And this research was supported by SNU SIR Group of the BK21 Research Program funded by Ministry of Education & Human Resources Development.

REFERENCES

AASHTO (1996), *Standard Specifications for Highway Bridges : 16th Edition* (1996), AASHTO, Washington, DC.

Carter, J. P., and Kulhawy, F. H. (1988), *Analysis and design of drilled shaft foundations socketed into rock*, Report EL-5918, Electric Power Research Institute, Palo Alto, California.

Davisson, M. (1972), "High Capacity Piles", *In Proceedings, Soil Mechanics Lecture Series on Innovation in Foundation Construction*, ASCE, Illinois Section, Chicago, IL, pp.81-112

Kwon (2004), *Effect of Rock Mass Weathering on Resistant Behavior of Drilled Shaft Socketed into Weathered Rock*, phD thesis, Seoul National University, Seoul Korea.

O'Neill, M. M., and Reese, L. C. *Drilled Shafts: Construction Procedures and Design Methods.* Publication No. FHWA-IF-99-025, U.S. Department of Transportation, Federal Highway Administration, 1999

Standard Guidlines for the Design and Installation of Pile Foundations (1997), ASCE 20-96 (1997), American Society of Civil Engineers.

Terzaghi, K. (1942), Discussion of the Progress Report of the Committee on the Bearing Value of Pile Foundations, *Proceedings, ASCE*, Vol. 68, pp.311-323

Terzaghi, K., and Peck, R.B. (1967), *Soil Mechanics in Engineering Practice.* Wiley.

Load and Resistance Factor Design of Strip Footings

Gordon A. Fenton[1], Xianyue Zhang[2], and D. V. Griffiths[3]

[1] Professor, Department of Engineering Mathematics, Dalhousie University, Halifax, Nova Scotia, Canada B3J 2X4; Ph: (902) 494-6002; email: Gordon.Fenton@dal.ca
[2] Jacques Whitford, 805-8th Avenue SW, Suite 300, Calgary, Alberta Canada T2P 1H7; Ph: (403) 441-5062; email: Juliana.Zhang@JacquesWhitford.com
[3] Professor, Division of Engineering, Colorado School of Mines, Golden, Colorado 80401-1887, USA; Ph: (303) 273-3669; email: D.V.Griffiths@mines.edu

Abstract

This paper proposes a Load and Resistance Factor Design (LRFD) approach for the bearing capacity design of a strip footing. The load factors used are as specified by the National Building Code of Canada. The resistance factors required to achieve a certain acceptable failure probability are estimated as a function of the spatial variability of the soil as well as by the level of "understanding" of the soil properties in the vicinity of the foundation. The analytical results are validated by simulation. The results are primarily intended to aid the development of the next generation of reliability-based geotechnical design codes, but can also be used to guide current designs.

Introduction

Design of a shallow footing typically begins with a site investigation aimed at determining the strength of the founding soil or rock. Once this information has been gathered, the geotechnical engineer is in a position to determine the footing dimensions required to avoid entering various limit states. The limit states that are usually considered in the footing design are serviceability limit states (typically deformation) and ultimate limit states. The latter is concerned with safety and includes the load-carrying capacity, or *bearing capacity*, of the footing.

This paper develops a load and resistance factor design (LRFD) approach for strip footings designed against bearing capacity failure. The design goal is to determine the footing dimensions such that the *resistance* to the load, R_u, satisfies

$$\phi_g R_u \geq \sum_i \alpha_i L_{i_c} \tag{1}$$

where ϕ_g is the *geotechnical resistance factor*, R_u is the *ultimate geotechnical resistance*, I is the *importance factor*, α_i is the i'th *load factor*, and L_{i_c} is the i'th *characteristic load effect*. The goal of this paper is to determine the relationship between ϕ_g and the probability that the designed footing will experience a bearing capacity failure.

The ultimate geotechnical resistance, R_u, is determined using characteristic soil properties, in this case characteristic values of the soil's cohesion, c, and friction angle, ϕ. Only one load combination will be considered in this paper, $\alpha_L L_{L_c} + \alpha_D L_{D_c}$, where $L_{L_c} = k_L \mu_L$ is the characteristic live load defined as a bias factor, $k_L = 1.41$ (Allen, 1975), times the mean live load, μ_L, and $L_{D_c} = k_D \mu_D$ is the characteristic dead load, similarly defined as a bias factor $k_D = 1.18$ (Becker, 1996), times the mean dead load, μ_D. The live and dead load factors, $\alpha_L = 1.5$ and $\alpha_D = 1.25$, respectively are as specified by the National Building Code of Canada (NBCC, 2006).

To determine the resistance factor, ϕ_g, required to achieve a certain acceptable reliability of the constructed footing against bearing failure, the founding soil will be modeled as a 2-D random field and the design process involves first taking a series of m soil samples are over depth at a single location a distance r from the footing center (as in a CPT or SPT sounding). The characteristic cohesion, $\hat{c}$, and characteristic friction angle, $\hat{\phi}$, are computed from the observations (denoted by a superscript o) as follows,

$$\hat{c} = \exp\left\{\frac{1}{m}\sum_{i=1}^{m} \ln c_i^o\right\}, \qquad \hat{\phi} = \frac{1}{m}\sum_{i=1}^{m} \phi_i^o \tag{2}$$

The soil will be assumed weightless so that the characteristic ultimate bearing stress, $\hat{q}_u$, simplifies to

$$\hat{q}_u = \hat{c}\hat{N}_c \tag{3}$$

where $\hat{N}_c$ is the characteristic bearing capacity factor

$$\hat{N}_c = \frac{e^{\pi \tan\hat{\phi}} \tan^2\left(\frac{\pi}{4} + \frac{\hat{\phi}}{2}\right) - 1}{\tan\hat{\phi}} \tag{4}$$

Since $R_u = B\hat{q}_u$, where B is the footing width, Eq. 1 can be solved for the required footing width

$$B = \frac{I\left[\alpha_L L_{L_c} + \alpha_D L_{D_c}\right]}{\phi_g \hat{q}_u} = \frac{I\left[\alpha_L L_{L_c} + \alpha_D L_{D_c}\right]}{\phi_g \hat{c}\hat{N}_c} \tag{5}$$

The design philosophy is to find the required footing width B such that the probability that the actual load, L, exceeds the actual resistance, $q_u B$, is less than some small acceptable failure probability, p_m. If p_f is the actual failure probability, then

$$p_f = \mathrm{P}\left[L > q_u B\right] = \mathrm{P}\left[L > \bar{c}\bar{N}_c B\right] \tag{6}$$

where $q_u = \bar{c}\bar{N}_c$ and $\bar{c}$ and $\bar{N}_c$ are those effective *uniform* soil properties which give the same bearing capacity as the actual spatially variable soil. The value of $\bar{N}_c$ is obtained by using an effective friction angle $\bar{\phi}$ in Eq. 4. A sucessful design methodology will have $p_f \le p_m$. Substituting Eq. 5 into Eq. 6 and collecting random terms to the left of the inequality leads to

$$p_f = \mathrm{P}\left[L\frac{\hat{c}\hat{N}_c}{\bar{c}\bar{N}_c} > \frac{I\left[\alpha_L L_{L_c} + \alpha_D L_{D_c}\right]}{\phi_g}\right] \tag{7}$$

Letting $Y = L(\hat{c}\hat{N}_c)/(\bar{c}\bar{N}_c)$ means that

$$p_f = \mathrm{P}\left[Y > \frac{I\left[\alpha_L L_{L_c} + \alpha_D L_{D_c}\right]}{\phi_g}\right] \tag{8}$$

and the task is to find the distribution of Y. Assuming that Y is lognormally distributed (an assumption found to be reasonable by Fenton et al., 2007, and which is also supported to some extent by the central limit theorem), then

$$\ln Y = \ln L + \ln \hat{c} + \ln \hat{N}_c - \ln \bar{c} - \ln \bar{N}_c \tag{9}$$

is normally distributed and p_f can be found once the mean and variance of $\ln Y$ are determined. The mean of $\ln Y$ is

$$\mu_{\ln Y} = \mu_{\ln L} + \mu_{\ln \hat{c}} + \mu_{\ln \hat{N}_c} - \mu_{\ln \bar{c}} - \mu_{\ln \bar{N}_c} \tag{10}$$

and the variance of $\ln Y$ is

$$\sigma^2_{\ln Y} = \sigma^2_{\ln L} + \sigma^2_{\ln \hat{c}} + \sigma^2_{\ln \bar{c}} + \sigma^2_{\ln \hat{N}_c} + \sigma^2_{\ln \bar{N}_c} - 2\mathrm{Cov}\left[\ln \bar{c}, \ln \hat{c}\right] - 2\mathrm{Cov}\left[\ln \bar{N}_c, \ln \hat{N}_c\right] \tag{11}$$

where the load, L, and soil properties, c and ϕ have been assumed mutually independent.

Analytical approximation to the probability of failure

To find the terms in Eq's 10 and 11, it is assumed that the effective cohesion, $\bar{c}$, is a geometric average over a domain of size $D = W \times W$ immediately under the footing (see Figure 1). Similarly, the effective friction angle is assumed to be an arithmetic average over the same domain;

$$\bar{c} = \exp\left\{ \frac{1}{D} \int_D \ln c(\underset{\sim}{x})\, d\underset{\sim}{x} \right\}, \qquad \bar{\phi} = \frac{1}{D} \int_D \phi(\underset{\sim}{x})\, d\underset{\sim}{x} \tag{12}$$

The dimension W was found by trial and error to be best approximated as 40% of the average mean wedge zone depth,

$$W = \frac{0.4}{2} \hat{\mu}_B \tan\left(\frac{\pi}{4} + \frac{\mu_\phi}{2}\right) \tag{13}$$

where μ_ϕ is the mean friction angle (in radians), within the zone of influence of the footing, and $\hat{\mu}_B$ is an estimate of the mean footing width obtained by using mean soil properties (μ_c and μ_ϕ) in Eq. 5. To first order, the mean of N_c is,

$$\mu_{N_c} \simeq \frac{e^{\pi \tan \mu_\phi} \tan^2\left(\frac{\pi}{4} + \frac{\mu_\phi}{2}\right) - 1}{\tan \mu_\phi} \tag{14}$$

Armed with the above information and assumptions, the components of Eq's 10 and 11 can be computed as follows given the basic statistical parameters of the loads, c, and ϕ, the number and locations of the soil samples, and the averaging domain size D.

Assuming that the total load L is equal to the sum of live and dead loads, i.e. $L = L_{L_e} + L_D$, both of which are random, then

$$\mu_{\ln L} = \ln(\mu_L) - \tfrac{1}{2} \ln\left(1 + V_L^2\right), \qquad \sigma^2_{\ln L} = \ln\left(1 + V_L^2\right) \tag{15}$$

where $\mu_L = \mu_L + \mu_D$ is the sum of the mean live and (static) dead loads, and V_L is the coefficent of variation of the total load defined by

$$V_L^2 = \frac{\sigma^2_{L_e} + \sigma^2_D}{\mu_{L_e} + \mu_D} \tag{16}$$

With reference to Eq. 2,

$$\mu_{\ln \hat{c}} = \mu_{\ln c}, \qquad \sigma^2_{\ln \hat{c}} = \sigma^2_{\ln c}\gamma(\Delta x, H) \tag{17}$$

where γ is the variance function defined by

$$\gamma(D_1, D_2) = \frac{4}{(D_1 D_2)^2}\int_0^{D_1}\int_0^{D_2}(D_1 - \tau_1)(D_2 - \tau_2)\rho(\tau_1, \tau_2)\, d\tau_1\, d\tau_2 \tag{18}$$

Similarly, with reference to Eq. 12,

$$\mu_{\ln \bar{c}} = \mu_{\ln c} \qquad \sigma^2_{\ln \bar{c}} = \sigma^2_{\ln c}\gamma(W, W) \tag{19}$$

Since $\mu_{\hat{\phi}} = \mu_\phi$ (see Eq. 2), the mean and variance of $\hat{N}_c$ can be obtained using first order approximations to expectations of Eq. 4 (Fenton et al., 2003), as follows,

$$\mu_{\ln \hat{N}_c} = \mu_{\ln N_c} \simeq \ln \frac{e^{\pi \tan \mu_\phi}\tan^2\left(\frac{\pi}{4} + \frac{\mu_\phi}{2}\right) - 1}{\tan \mu_\phi} \tag{20}$$

$$\sigma^2_{\ln \hat{N}_c} \simeq \sigma^2_{\hat{\phi}}\left(\frac{d \ln \hat{N}_c}{d\hat{\phi}}\bigg|_{\mu_\phi}\right)^2 = \sigma^2_{\hat{\phi}}\left[\frac{bd}{bd^2 - 1}\left[\pi(1 + a^2)d + 1 + d^2\right] - \frac{1 + a^2}{a}\right]^2 \tag{21}$$

where $a = \tan(\mu_\phi)$, $b = e^{\pi a}$, $d = \tan\left(\frac{\pi}{4} + \frac{\mu_\phi}{2}\right)$. The variance of $\hat{\phi}$ is given by Fenton et al. (2007) as

$$\sigma^2_{\hat{\phi}} = \sigma^2_\phi\gamma(\Delta x, H), \qquad \sigma_\phi \simeq \frac{0.46(\phi_{max} - \phi_{min})s}{\sqrt{4\pi^2 + s^2}} \tag{22}$$

where all angles are measured in radians.

Since $\mu_{\bar{\phi}} = \mu_\phi$ (see Eq. 12), the mean and variance of $\bar{N}_c$ can be obtained in the same fashion as for $\hat{N}_c$ – in fact, they only differ due to differing local averaging in the variance calculation so that $\mu_{\ln \bar{N}_c} = \mu_{\ln N_c}$ and $\sigma^2_{\ln \bar{N}_c}$ is obtained using $\sigma^2_{\bar{\phi}} = \sigma^2_\phi\gamma(W, W)$ in Eq. 21 instead of $\sigma^2_{\hat{\phi}}$.

The covariance between the observed cohesion values and the effective cohesion beneath the footing is Cov $[\ln \bar{c}, \ln \hat{c}] \simeq \sigma^2_{\ln c}\gamma_{DQ}$, where the averaging domains are shown in Figure 1 and

$$\gamma_{DQ} = \frac{1}{(W^2\Delta x H)^2}\int_{-W/2}^{W/2}\int_{H-W}^{H}\int_{r-\Delta x/2}^{r+\Delta x/2}\int_0^H \rho(\xi_1 - x_1, \xi_2 - x_2)\, d\xi_2\, d\xi_1\, dx_2\, dx_1 \tag{23}$$

which can be evaluated by Gaussian quadrature (see Griffiths and Smith, 2006, for details).

The covariance between $\bar{N}_c$ and $\hat{N}_c$ is similarly approximated by Cov $\left[\ln \bar{N}_c, \ln \hat{N}_c\right] \simeq \sigma^2_{\ln N_c}\gamma_{DQ}$ where $\sigma^2_{\ln N_c}$ is obtained by using σ^2_ϕ (see Eq. 22) in Eq. 21 instead of $\sigma^2_{\hat{\phi}}$. Substituting these results into Eq's 10 and 11 gives

$$\mu_{\ln Y} = \mu_{\ln L} \tag{24}$$

$$\sigma^2_{\ln Y} = \sigma^2_{\ln L} + \left[\sigma^2_{\ln c} + \sigma^2_{\ln N_c}\right]\left[\gamma(\Delta x, H) + \gamma(W, W) - 2\gamma_{DQ}\right] \tag{25}$$

which can now be used in Eq. 8 to produce estimates of p_f. Letting $q = I\left[\alpha_L L_{L_c} + \alpha_D L_{D_c}\right]$ the probability of failure becomes

$$p_f = \mathrm{P}\left[Y > q/\phi_g\right] = \mathrm{P}\left[\ln Y > \ln(q/\phi_g)\right] = 1 - \Phi\left(\frac{\ln(q/\phi_g) - \mu_{\ln Y}}{\sigma_{\ln Y}}\right) \tag{26}$$

where Φ is the standard normal cumulative distribution function.

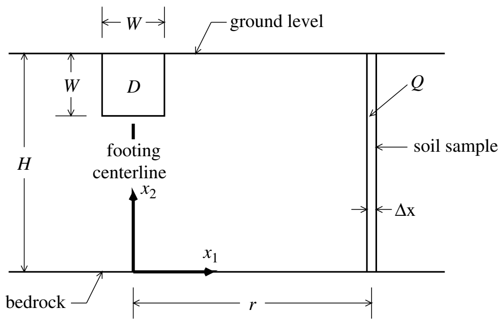

Figure 1. Averaging regions used to predict probability of bearing capacity failure.

Required resistance factor

Eq. 26 can be inverted to find a relationship between the acceptable probability of failure, $p_f = p_m$, and the resistance factor, ϕ_g, required to achieve that acceptable failure probability,

$$\phi_g = \frac{I\left[\alpha_L L_{L_c} + \alpha_D L_{D_c}\right]}{\exp\left\{\mu_{\ln Y} + \sigma_{\ln Y} z_{p_m}\right\}} \tag{27}$$

where z_{p_m} is the standard normal value which satisfies $\Phi\left(z_{p_m}\right) = 1 - p_m$. For example, if $p_m = 0.001$, then $z_{p_m} = 3.09$.

The following parameters will be varied to investigate their effects on the resistance factor required to achieve a target failure probability p_m;

1) Three values of p_m are considered, 0.01, 0.001, and 0.0001, corresponding to reliability indices of approximately 2.3, 3.1, and 3.7, respectively.
2) The correlation length, θ is varied from 0.0 to 50.0 m.
3) Four coefficients of variation for cohesion are considered, $V_c = 0.1, 0.2, 0.3$, and 0.5. The corresponding coefficients of variation for friction angle are $V_\phi = 0.07, 0.14, 0.20$, and 0.29.
4) Three sampling locations are considered: $r = 0, 4.5$, and 9.0 m from the footing centerline (see Figure 1 for the definition of r).

Figure 2 shows the resistance factors required for three cases; a) sampling directly under the footing ($r = 0$), b) sampling at a distance of 4.5 m, and c) at a distance of 9.0 m from the footing centerline. The worst case correlation length is clearly between about 1 to 5 m, as evidenced by the fact that in all plots the lowest resistance factor occurs when $1 < \theta < 5$ m. This worst case correlation length is of the same magnitude as the footing width ($\hat{\mu}_B = 1.26$ m).

As expected the smallest resistance factors correspond to poorest understanding of the soil properties under the footing (i.e. when the soil is sampled 9 m away from the footing centerline). When the cohesion coefficient of variation is relatively large, V_c = 0.5, with corresponding $V_\phi \simeq 0.29$, the worst case value of ϕ_g is 0.23 in order to achieve p_m = 0.001. In other words, there will be a significant construction cost penalty if a footing is designed using a low quality site investigation which is unable to reduce the residual variability to less than V_c = 0.5.

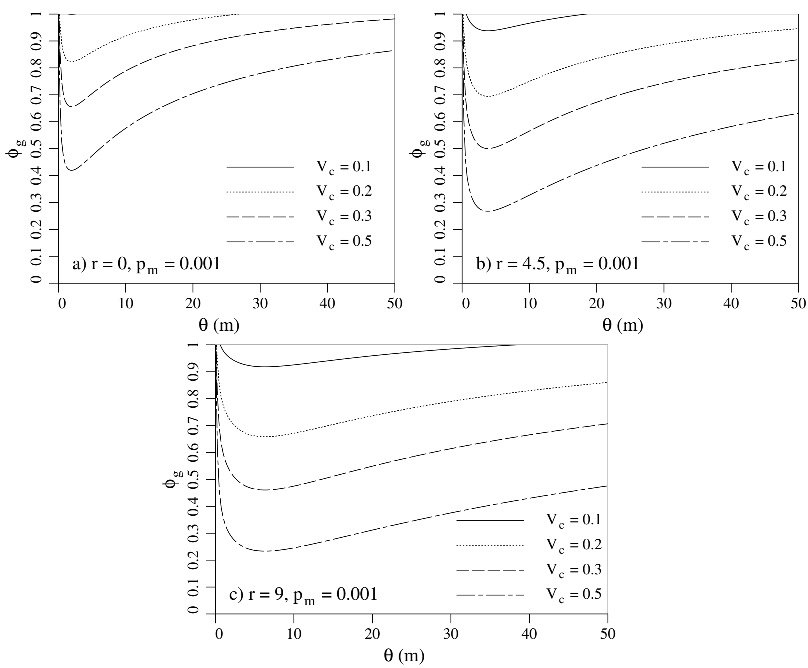

Figure 2. Resistance factors required to achieve acceptable failure probability, p_m = 0.001, when soil is sampled at three different distances, r in m, from the footing centerline.

The "worst case" resistance factors required to achieve the indicated maximum acceptable failure probabilities, as seen in Figure 2, are summarized in Table 1. The Table also includes two other acceptable failure probability values. In the absence of better knowledge about the actual correlation length at the site in question, these factors are the largest values that should be used in the LRFD bearing capacity design of a strip footing.

If the moderate case where V_c = 0.3 and p_m = 0.001, the worst case ϕ_g is 0.66, 0.50, and 0.46 for r = 0, 4.5, and 9.0 m, respectively. Foye et al. (2006) recommend a resistance factor of 0.7 for a similar problem, which agrees quite well with the r = 0 result. The Canadian Foundation Engineering Manual (CFEM, 2006) recommends ϕ_g = 0.5, which agrees with the r = 4.5 result, while the Australian Standard Bridge Design code (2004) recommends ϕ_g = 0.45, which is in very close agreement with the

r = 9.0 result. Possibly the Australian code assumes worse site investigations, or is aimed at a lower acceptable failure probability.

Apparently the resistance factor recommended by Foye et al. (2006) assumes very good site understanding – they specify that the design assumes a CPT investigation which is presumably directly under the footing. Foye's recommended resistance factor is based on a reliability index of β = 3, which corresponds to p_m = 0.0013, which is very close to that used in Table 3 (p_m = 0.001). The small difference between the "current study" r = 0 result and Foye's may be due to differences in load bias factors – these are not specified by Foye et al.

Table 1. Worst case resistance factors for various coefficients of variation, V_c, distance to sampling location, r, and acceptable failure probalities, p_m.

	r = 0.0 m			r = 4.5 m			r = 9.0 m		
V_c	p_m = 0.01	0.001	0.0001	p_m = 0.01	0.001	0.0001	p_m = 0.01	0.001	0.0001
0.1	1.00	1.00	0.90	1.00	0.94	0.83	1.00	0.92	0.81
0.2	0.98	0.82	0.71	0.86	0.69	0.58	0.83	0.66	0.55
0.3	0.82	0.66	0.54	0.67	0.50	0.39	0.63	0.46	0.36
0.5	0.59	0.42	0.32	0.42	0.27	0.18	0.38	0.23	0.16

The agreement between the r = 4.5 result and that by the Canadian Foundation Engineering Manual (CFEM, 2006) is to some extent fortuitous, since the CFEM resistance factor is derived by calibration with past design methodologies which is quite different than the analytical approach taken here. The CFEM resistance factor apparently presumes a reasonable, but not significant, understanding of the soil properties under the footing (e.g. r = 4.5 rather than r = 0). The corroboration of the rigorous theory proposed here by an experience-based code provision is, however, very encouraging. The authors also note that the CFEM is the only source for which the live and dead load bias factors used in this study can be reasonably assumed to also apply.

Summary

The resistance factors recommended in Table 1 are conservative in (at least) the following ways; 1) it is unlikely that the correlation length of the residual random process at a site will equal the "worst case" correlation length, 2) the soil is assumed weightless in this study (adding weight increases bearing capacity), and 3) often more than one CPT is taken at the site in the footing region.

On the other hand, the resistance factors recommended in Table 1 are unconservative in (at least) the following ways; 1) measurement and model errors are not considered in this study. The statistics of measurement errors are very difficult to determine, since the true values need to be known. Similarly, model errors, which relate both the errors associated with translating measured values (e.g. CPT measurements to friction angle values) and the errors associated with predicting bearing capacity by an equation such as Eq. 3 with the actual bearing capacity are extremely difficult to measure simply because the true bearing capacity along with the true soil properties are rarely, if ever, known. In the authors' opinions this is the major source of unconservativism in the presented theory. When confidence in the measured soil properties or in the model used is low, the results presented here can still be employed by assuming that the soil samples were taken further away from the footing location than they actually were (e.g. if low-quality soil samples are taken directly under the footing, r = 0, the resistance factor corresponding to a larger value of r, say r = 4.5 m should be used), 2) the failure probabilities given by the above theory are slightly underpredicted when soil samples are taken at some distance from the footing. The effect of this underestimation on the recommended resistance factor has been shown to be relatively minor but nevertheless unconservative, and 3) c and ϕ are assumed independent, rather than negatively correlated, which leads to a somewhat higher probability of failure and correspondingly lower resistance factor, and so somewhat unconservative results. The authors note that this statement is contrary to the conclusion made in Fenton et al. 2003 (which was intended to refer to a positive correlation) – in any case, the effect of positive or negative correlation of c and ϕ was found in Fenton et al. to be quite minor.

To some extent the conservative and unconservative factors listed above cancel one another out. The comparison of resistance factors to other sources demonstrates that the 'worst case' theoretical results presented in Table 1 agrees quite well with current literature and LRFD code recommendations, assuming moderate variability and site understanding, suggesting that the theory is reasonably accurate. The theory provides an analytical basis to extend code provisions beyond calibration with the past.

One of the major advantages to a table such as 1 is that it provides geotechnical engineers with evidence that increased site investigation will lead to reduced construction costs and/or increased reliability. In other words, Table 1 is further evidence that you pay for a site investigation whether you have one or not (Institution of Civil Engineers, 1991).

References

Allen, D.E. (1975). "Limit States Design – A probabilistic study," *Can. J. Civ. Eng.*, **36**(2), 36–49.

Australian Standard (2004). *Bridge Design, Part 3: Foundations and Soil-Supporting Structures*, AS 5100.3–2004, Sydney, Australia.

Becker, D.E. (1996). "Eighteenth Canadian Geotechnical Colloquium: Limit states design for foundations. Part II. Development for the National Building Code of Canada," *Can. Geotech. J.*, **33**, 984–1007.

Canadian Geotechnical Society (2006). *Canadian Foundation Engineering Manual*, 4th Ed., Montreal, Quebec.

Engineers, Institution of Civil (1991). *Inadequate Site Investigation*, Thomas Telford, London.

Fenton, G.A. and Griffiths, D.V. (2003). "Bearing capacity prediction of spatially random $c - \phi$ soils," *Can. Geotech. J.*, **40**(1), 54–65.

Fenton, G.A., Zhang, X., and Griffiths, D.V. 2007. Reliability of strip footings designed against bearing failure using LRFD, submitted to *Georisk*.

Foye, K.C., Salgado, R. and Scott, B. (2006). "Resistance factors for use in shallow foundation LRFD," *ASCE J. Geotech. Geoenv. Eng.*, **132**(9), 1208–1218.

Griffiths, D.V. and Smith, I.M. (2006). *Numerical Methods for Engineers*, ((2nd Ed.)), Chapman & Hall/CRC Press Inc., Boca Raton.

NRC, (2006). *User's Guide – NBC 2005 Structural Commentaries (Part 4 of Division B)*, (2nd Ed.), National Research Council of Canada, Ottawa.

Phoon, K-K. and Kulhawy, F.H. (1999). "Characterization of geotechnical variability," *Can. Geotech. J.*, **36**, 612–624.

A Practical Application of Simplified Probabalistic Embankment Stability Analysis

John W. France[1], M. ASCE, P.E.

[1]Vice President and National Dam Technology Leader, URS Corporation, 8181 East Tufts Avenue, Denver, CO 80112; john_france@urscorp.com

ABSTRACT: An industrial company desired to drain one of its process water supply lakes to excavate material from the bottom of the reservoir. The embankment is founded on claystone bedrock. Uncertainty existed concerning the strength of the foundation claystone. If a weak layer is postulated in the foundation, stability analyses indicated that the embankment would be unstable with an empty reservoir. Dam failure would disrupt the planned reservoir excavation project and have negative business impacts on the owner's operations but would not threaten lives or property owned by others. A simplified probabilistic stability analysis approach was used to augment traditional stability analyses and guide the decision to proceed with the project. The embankment was monitored for early signs of movement, and measured embankment movements were minimal when the lake was lowered.

INTRODUCTION

This paper describes analysis that was performed to support draining one of a series of lakes that are used to store process water for an industrial facility.

The owner of the facility desired to drain one of the lakes, designated Lake 3 for this paper, so that earth material could be excavated from the bottom of the lake. The excavation would serve two purposes. Firstly, it would provide borrow material to backfill a nearby area, so that the area could be reused. Secondly, the excavation would increase the storage volume of the lake.

The water level in Lake 3 was regularly varied as part of facility operations, but the lake was never completely drained in the more than 20-year history of its operation. It was recognized that the drawdown of the lake would apply a new loading to the embankment dam that impounds the lake, and that the stability of the dam under this loading needed to be evaluated.

To prevent significant impacts to facility operations, the lake drawdown needed to be limited to certain months of the year, and the lake could be unavailable for use for no more than a few months. Consequently the lake needed to be lowered quickly, and the excavation also needed to be completed quickly.

PROJECT DESCRIPTION

A general layout of Lake 3 is presented in Figure 1. The zoned earthfill dam in question separates Lake 3 from an adjacent lake, designated Lake 4 for this paper. The remaining perimeter of Lake 3 is comprised of excavated slopes and low earthfill dams between Lake 3 and two other lakes, designated Lakes 1 and 2 for this paper. A cross section of the embankment dam between Lakes 3 and 4 is shown in Figure 2. This section of the dam was the most critical section with respect to stability. The embankment consists of a central clay core flanked by sand and gravel shells, all founded on claystone bedrock. All embankment zones are compacted earthfill, placed using modern construction practices. The embankment was constructed in the mid-1980s.

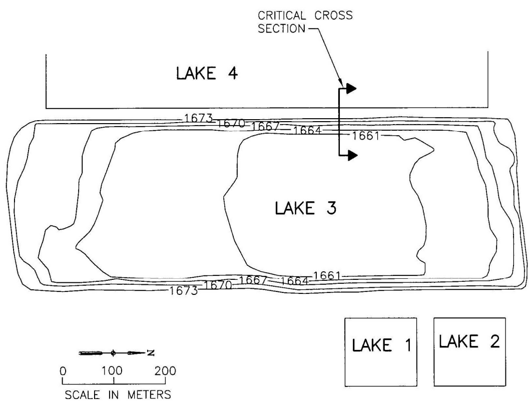

FIG. 1. Plan View of Lake 3

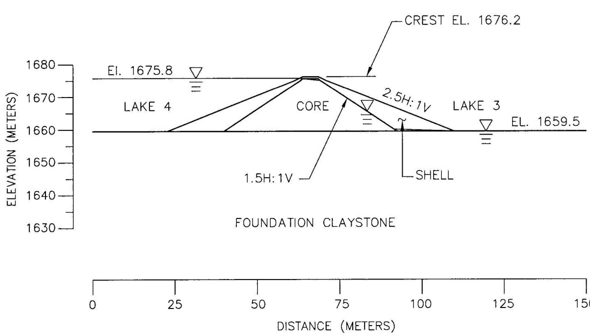

FIG. 2. Lakes 3/4 Embankment Cross Section

If the dam between the two lakes failed while Lake 3 was drained, water would flow from Lake 4 to Lake 3 until the water levels in the two lakes equalized. No water would be discharged off of industrial facility property, and the rate of rise in the water level in Lake 3 would be slow enough that construction workers in the lake area would be able to escape to high ground. Therefore, the consequences of slope failure during the lowering of Lake 3 are judged to not likely include potential loss of life or offsite impacts, but rather would be limited to damage to facility property and disruption to facility business operations.

EMBANKMENT AND FOUNDATION MATERIALS

The embankment core is composed of compacted low plasticity clay (USCS classification CL), derived from on-site residual soils and claystone bedrock, with estimated drained strength parameters from laboratory tests ranging from a friction angle (ϕ') of 31° with zero cohesion (c') to a friction angle of 34.1° with 12 kPa cohesion.

The embankment shells are composed of compacted sand and gravel (USCS classification SW-SP), derived from local deposits, with estimated drained strength parameters of a friction angle (ϕ') of 34° with zero cohesion (c').

The foundation rock at the site is part of a claystone formation. Logs of borings completed at the site indicate that the foundation rock formation at this site is primarily claystone, with occasional sandstone interbeds. Laboratory test results generally indicate that the claystone classifies as low plasticity (CL); liquid limits typically ranging from 33% to 48% with one sample having a liquid limit of 53%, plasticity indices ranged from 19% to 35%, percent fines (minus No. 200 sieve size) ranging from 84% to 100%, and the clay fraction ranged from 12% to 65%.

At some sites in the general area of the project, the foundation formation in question has been found to include clay seams with low residual strengths. Randonly oriented slickensides were observed in the cores samples obtained at the Lake 3 site, but no evidence was found of continuous, low strength slickenedsided zones. However, it could not be concluded with certainty that a weak layer does not exist within the bedrock at the site.

Repeated direct shear tests were performed on rock core samples obtained at the site. Peak and residual strength parameters were interpreted from the direct shear tests. Two sets of direct shear tests were performed. Prior to URS Corporation's involvement in the project, a series of ten direct shear tests were completed by others, using a strain rate of 0.0051 cm/minute. This strain rate is potentially too high to achieve representative drained strength parameters in a claystone material. The apparent peak and residual strength envelopes from that series of tests are shown on Figures 3 and 4.

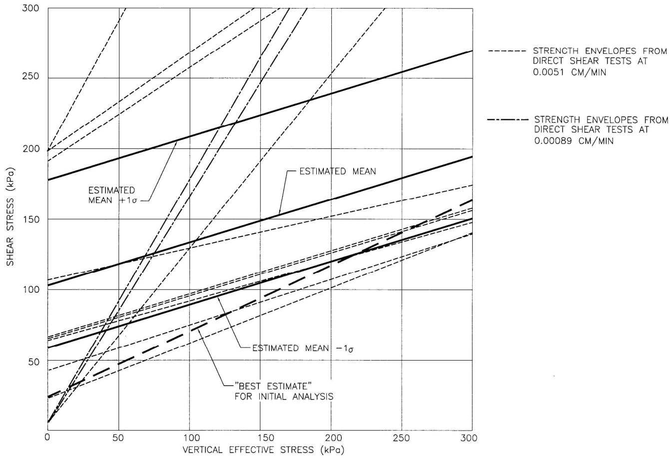

FIG. 3. Bedrock Peak Strength Results From Direct Shear Tests And Strength Parameters Used in Analyses

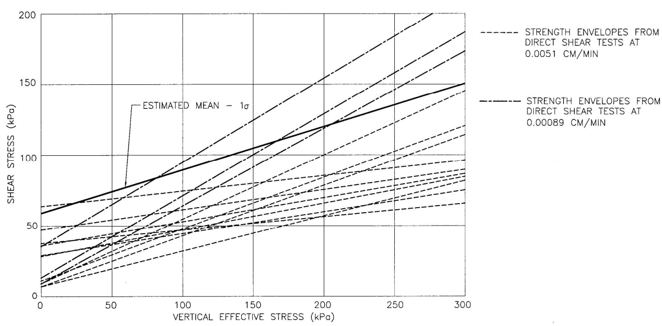

FIG. 4. Bedrock Residual Strength Results From Direct Shear Tests

From Figure 4, it is noted that the residual strength envelopes from several of the first series of tests have low friction angles and relatively large cohesion intercepts. Residual strength envelopes typically do not have large cohesion intercepts. It is possible that the residual strength envelopes reported from this first series of tests were based on partially drained conditions instead of fully drained conditions, because of the higher than desirable strain rate.

URS performed three supplemental direct shear tests with a much slower strain rate of 0.00089 cm/minute. The apparent peak and residual strength envelopes from this series of tests are also shown on Figures 3 and 4.

CONVENTIONAL STABILITY ANALYSES

Conventional stability analyses were completed for a range of strength estimates to evaluate the potential impacts of possible weak layers in the foundation rock. The analyses were completed using 1) conventional limit equilibrium slope stability analysis methods with the computer program UTEXAS4 (Wright, 2004) and 2) the numerical finite difference deformation analysis computer program FLAC version 5.0 (Itasca Consulting Group, 2004) using the strength reduction method (Dawson and Roth, 2005).

Both short-term undrained and long-term drained loading conditions were evaluated in the stability analyses. The short-term conditions reflect the stability of the slope immediately after complete drainage of Lake 3. This loading condition assumes that the fine-grained materials, including the embankment core and the foundation claystone, remain undrained. Results from stability analysis for this condition indicate a minimum factor of safety equal to 1.29, which compares favorably with the minimum factor of safety of 1.2 recommended in United States Department of Interior, Bureau of Reclamation guidelines (U.S. Department of the Interior, Bureau of Reclamation, 1987).

The planned time period for which Lake 3 was to be kept fully drained was between 5 and 6 months. This duration is long enough that it is reasonable to assume that the fine-grained soils would completely drain, leading to the development of drained shear strengths, which could be considerably lower than the undrained strengths.

Initially, stability analyses were completed for best estimate drained peak strengths. As noted above, the range of measured peak strengths was very wide for the claystone bedrock. For the initial "best estimate" analyses, a friction angle (ϕ') of 25° and a cohesion (c') of 24 kPa were used. These values were judged to be prudent design values for claystone bedrock with index properties that classify as a low plasticity clay (CL). As shown in Figure 3, the resulting strength envelope lies in the lower range of peak strength envelopes measured in the direct shear tests. For the best estimate analysis, the strength parameters for the embankment core were taken as a friction angle (ϕ') of 32° and a cohesion (c') of zero, and the strength parameters for the embankment shells were taken as a friction angle (ϕ') of 34° and a cohesion (c') of zero. The resulting minimum calculated factor of safety was 1.52.

Parametric analyses were completed to evaluate the effects on the calculated factor of safety of reducing the strength in a horizontal layer in the claystone foundation rock, which was judged to be the most likely configuration of a weak layer in the flat-lying bedrock geology at the site. To evaluate the potential effect of such a feature, analyses were completed considering a possible 0.6-meter thick, horizontal weak plane in the claystone foundation rock. The results of this evaluation are compiled in Table 1.

Table 1. Analysis Results: Weak Foundation Plane

Sliding Plane Characteristics			Calculated Minimum Factor of Safety
Cohesion, c′ (kPa)	**Friction Angle, ϕ′** (degrees)	**Depth** (meters)	
0	20	0.6	1.08
0	20	1.5	1.10
0	20	3.0	1.16
0	15	0.6	0.87
0	15	1.5	0.92
0	15	3.0	0.98

SIMPLIFIED PROBABILISTIC STABILITY ANALYSES

To further evaluate the effects of uncertainty in the key parameters in the stability analysis, particularly the strength of the foundation claystone, a simplified probabilistic method (Duncan, 2000) was employed. The method includes the following steps:

1. Estimate the most likely values of the parameters involved in the analysis and compute the factor of safety using those values, designated F_{MLV}.
2. Estimate the standard deviations of the parameters that involve uncertainty.
3. Compute the factors of safety with each parameter increased by one standard deviation and decreased by one standard deviation from the most likely value, with the values of the other parameters equal to their most likely values. The differences between the factors of safety thus calculated are designated ΔF_i.
4. Apply the Taylor series technique (Wolff, 1994; U.S. Army Corps of Engineers, 1997 and 1998) to calculate a standard deviation, σ_F, and a coefficient of variation, V_F, for the factor of safety, using the following equations:

$$\sigma_F = \left[\left(\frac{\Delta F_1}{2}\right)^2 + \left(\frac{\Delta F_2}{2}\right)^2 + \ldots \left(\frac{\Delta F_i}{2}\right)^2\right]^{1/2} \tag{1}$$

$$V_F = \frac{\sigma_F}{F_{MLV}} \tag{2}$$

5. Use F_{MLV} and V_F in available tables or equations to calculate the probability that the factor of safety is less than 1.0, designated P_f, assuming a log normal distribution of factor of safety.

For the probabilistic analysis in this case, uncertainties were considered for three parameters: the phreatic surface in the embankment, the embankment core strength, and the foundation bedrock strength. The variations in parameters considered in the probabilistic analysis are summarized in Table 2.

The variation of the foundation bedrock strength was characterized based on an evaluation of the available direct shear strength data (see Figures 3 and 4). Beginning with the peak strength envelopes, the three envelopes with friction angles higher than 60° were neglected as outliers. For most of the the remainder of the envelopes, the friction angle was found to vary over a relatively narrow range from 13° to 22°. It was decided to use a constant friction angle of 17°, and to portray the strength variation using cohesion. The distribution of cohesion values was found to approximate a log normal distribution, which was used to estimate the mean and standard deviation reflected in the values given in Table 2. On Figure 3, the mean, mean minus one standard deviation (mean - 1σ), and mean plus one standard deviation (mean + 1σ) values of foundation bedrock strength are compared with the peak strength envelopes. Finally, the mean minus one standard deviation envelope was compared with the residual strength envelopes (Figure 4) and found to be generally lower than the envelopes from direct shear tests performed at the lower strain rate and higher than the envelopes from tests performed at the higher strain rate. This was judged to be reasonable, because the envelope is located in the range of the 20^{th} to 30^{th} percentiles of all of the strength data (peak and residual).

Table 2. Variations In Parameters

Parameter	Mean - 1σ	Mean	Mean + 1σ
Phreatic surface elevation at dam centerline, meters[1]	1672	1673	1674
Embankment core strength[1]	c′ = 0 ϕ′ = 30°	c′ = 0 ϕ‘ = 32°	c′ = 0 ϕ‘ = 34°
Foundation bedrock strength[2]	c′ = 58.9 kPa ϕ′ = 17°	c′ = 103 kPa ϕ′ = 17°	c′ = 178 kPa ϕ′ = 17°

[1]Uncertainty estimated using the “Three-Sigma Rule,” see Dai and Wang, 1992
[2]Uncertainty estimated using the statistical evaluation of direct shear data, see Duncan, 2000

Calculations using the variations in parameters given in Table 2 resulted in a calculated probability of a factor of safety less than 1.0, P_f, of slightly less than $1x10^{-3}$ (one in a thousand).

IMPLEMENTATION

Based on the results of the conventional, deterministic stability analyses and the probabilistic stability analysis, the planned reservoir draining and excavation were completed. The performance of the dam was carefully monitored and contingency plans were developed for implementation in the event of observed incipient slope instability. It was believed that, with the materials in the embankment and foundation at this site, slope instability, should it occur, would develop slowly enough that it very likely could be detected in time to take corrective measures.

A monitoring program was developed consisting of inclinometers, surface movement monitoring points, and visual monitoring. Contingency plans included partial refilling of Lake 3 and construction of a stability berm at the toe of the dam.

MONITORING PROGRAM AND PERFORMANCE

Inclinometers and surface movement points were installed along the east and west banks of Lake 3. These monitoring instruments were read once per day during construction. In addition, the lake banks were visually observed by qualified personnel on a full time basis during all construction working hours.

Throughout drawdown and excavation, the instruments indicated negligible movement, and visual observation did not detect any signs of slope instability. The excavation was completed and Lake 3 was refilled within the required schedule. None of the contingency plans needed to be implemented during construction.

CONCLUSIONS

For this project, a simplified probabilistic stability analysis method was used to supplement conventional stability analysis and guide the decision to proceed with the plan to drain Lake 3 and excavate from the bottom of the lake. Based on the results of the analysis, the planned project was implemented, subject to prudent monitoring and contingency plans. The project was successfully completed without development of any instability problems.

REFERENCES

Dai, S.H. and Wang, M.O. (1992) *Reliability Analysis in Engineering Applications*, Van Nostrand Reinhold, New York.

Dawson, E. and Roth, W. (2005) "3-D Slope Stability Analysis By Strength Reduction." 25th Annual U.S. Society on Dams Conference, Salt Lake City, UT, June 6-10, 2005.

Duncan, J.M. (2000) "Factors of Safety and Reliability in Geotechnical Engineering." *Journal of Geotechnical and Geoenvironmental Engineering*, Vol. 126 (4).

Itasca Consulting Group. (1999) *FLAC Version 4.0 – Fast Lagrangian Analysis of Continua, User's Guide.*

U.S. Army Corps of Engineers. (1998) "Engineering and Design Introduction to Probability and Reliability Methods For Use in Geotechnical Engineering." *Engineering. Technical Letter No. 1110-2-547*, Department of the Army, Washington, DC, (www.usace.army.mil/usace-docs), February 27, 1998.

U.S. Army Corps of Engineers. (1997) "Risk-Based Analysis in Geotechnical Engineering for Support of Planning Studies." *Engrineering Circular No. 1110-2-554*, Department of the Army, Washington, DC, (www.usace.army.mil/usace-docs), September 30, 1997.

U.S. Department of the Interior, Bureau of Reclamation. (1987) *Design Standards No. 13, Embankment Dams, Chapter 4, Static Stability*, U.S. Department of the Interior, Bureau of Reclamation, Denver, Colorado, August 3, 1987.

Wolff, T.F. (1994) "Evaluating the Reliability of Existing Levees." *Report, Research Proect.: Reliability of Existing Levees*, prepared for U.S. Army Engineer Waterways Experiment Station Geotechnical Laboratory, Vicksburg, MS.

Wright, S. (1999) "UTEXAS4 – A Computer Program for Slope Stability Calculations." Software Manual, Shinoak Software, Austin, Texas.

Analysis of Infinite Slopes with Spatially Random Shear Strength

D.V. Griffiths [1], F. ASCE, P.E., Giorgia F. deWolfe [2], Jinsong Huang [3], and Gordon A. Fenton [4], M. ASCE, P.Eng.

[1]Professor, Colorado School of Mines University,1610 Illinois Street, Golden, CO 80401; d.v.griffiths@mines.edu
[2]PhD candidate, Colorado School of Mines University, 1610 Illinois Street, Golden, CO 80401; gfulcher@mines.edu
[3]Research Professor, Colorado School of Mines University, 1610 Illinois Street, Golden, CO 80401; jhuang@mines.edu
[4]Professor, Dalhousie University, Halifax, NS, Canada, B3J 1Y9; gordon.fenton@dal.ca

ABSTRACT: The study investigates the role of spatially random soil on the stability of infinite slopes with application to landslides and other geohazards. The influence of the shear strength mean, standard deviation and spatial correlation length on the probability of failure is thoroughly investigated through parametric studies. The results show that the traditional "first order second moment" approach to this problem is inherently unconservative, due to its inability to allow the failure mechanism to "seek out" the critical depth below ground surface, which is frequently not at the base of the soil layer.

INTRODUCTION

One of the main objectives of this work was to create a powerful general framework for modeling statistically described parameters relating to long slopes. The method involves a combination of Random Field theory (e.g. Fenton and Vanmarcke, 1990) with infinite slope theory (e.g. Taylor, 1948; Lambe and Whitman, 1969; Bromhead 1992; Duncan, 1996). The method, applied in a Monte-Carlo framework, takes into account the mean, standard deviation and spatial correlation length of the input parameter. Repeated calculations using the same input statistics of soil parameters (e.g. undrained shear strength) eventually lead to stable output statistics of the design parameters (e.g. Factor of Safety). The paper then compares results from the Monte-Carlo analyses with those obtained using the first order second moment method (FOSM).

ANALYTICAL METHOD

The analytical method considers a slice of soil in the potential failure zone as shown in Figure 1. The slope is homogeneous with a ground water free surface and critical failure surface running parallel to the slope surface. The analytical solution includes the option of different heights of the ground water surface through the slope as well as a horizontal pseudo-acceleration.

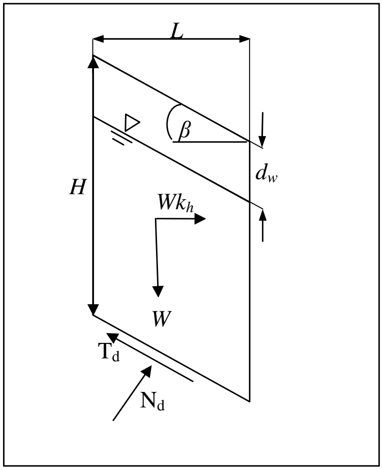

FIG. 1: Representation of forces acting on the infinite slope

Based on the key principles of infinite slope theory the factor of safety *FS* can be calculated as

$$FS = \frac{\tau_f}{\tau_d} \tag{1}$$

$$FS = \frac{c'}{\left((H-d_w)\gamma_{sat} + (d_w\gamma_m)\right)(\sin\beta\cos\beta + k_h\cos^2\beta)} + \frac{\left(\left((H-d_w)\gamma' + d_w\gamma_m\right)(\cos^2\beta - k_h\sin\beta\cos\beta)\right)(\tan\phi')}{\left((H-d_w)\gamma_{sat} + (d_w\gamma_m)\right)(\sin\beta + k_h\cos\beta)} \tag{2}$$

Assuming $\gamma_m = \gamma_{sat}$ we can obtain a simplified form of Eq. 2:

$$FS = \frac{c'}{H\gamma_{sat}(\sin\beta\cos\beta + k_h\cos^2\beta)} + \frac{\left(\left(H\gamma_{sat} - (H-d_w)\gamma_w\right)(\cos\beta - k_h\sin\beta)\right)(\tan\phi')}{H\gamma_{sat}(\sin\beta + k_h\cos\beta)} \tag{3}$$

The following symbols are used in the analytical solution of this problem:

c'	soil cohesion	β	slope inclination
d_w	depth of the water table	γ_{sat}	saturated unit weight
E'	Young's modulus	γ_w	unit weight of water
FS	factor of safety	γ_m	unit weight of material
H	depth of the soil layer	σ	normal total stress
k_h	horizontal pseudo acceleration coefficient	σ'	normal effective stress
L	width of slice	τ_d	developed shear stress
N_d	normal force component	τ_f	shear strength
T_d	shear force component	υ	Poisson's ratio
u	pore pressure	ϕ'	soil friction angle
W	weight of slice		

For variable soil strength profiles the classical infinite slope equation for homogeneous frictionless soil,

$$FS = \frac{c_u}{H\gamma \cos\beta \sin\beta} \tag{4}$$

should be written as:

$$FS = \frac{c_u}{z}\frac{1}{\gamma \cos\beta \sin\beta} \tag{5}$$

noting that the critical failure surface occurs at a depth where $\frac{c_u}{z}$ is a minimum.

In the random field approach, the input undrained shear strength is defined by its mean (μ_{c_u}), standard deviation (σ_{c_u}) and correlation length (θ). The spatial correlation length recognizes that soil samples "close" together are more likely to have similar properties than if they are "far apart". A visual example of a case of low and high correlation lengths is given in Figure 2.

In the results presented later in the paper, the spatial correlation length θ is expressed as a dimensionless parameter with respect to the soil depth as follows

$$\Theta = \frac{\theta}{H} \tag{6}$$

The issue of how many Monte-Carlo simulations are needed is addressed in Figure 3 for the case of $\Theta = 0.2$ and $V_{c_u} = 0.1$, where V_{c_u} is the coefficient of variation of the undrained shear strength. The probability of failure represents the proportion of Monte-Carlo realizations for which $FS \leq 1$. Five thousands simulations appear to give stable results.

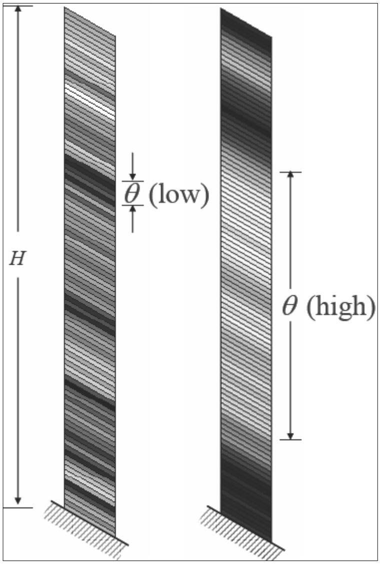

FIG.2: The grayscale represents varying shear strength values, with the light sections showing low strength areas. Both images represent a slope with same mean and standard deviation

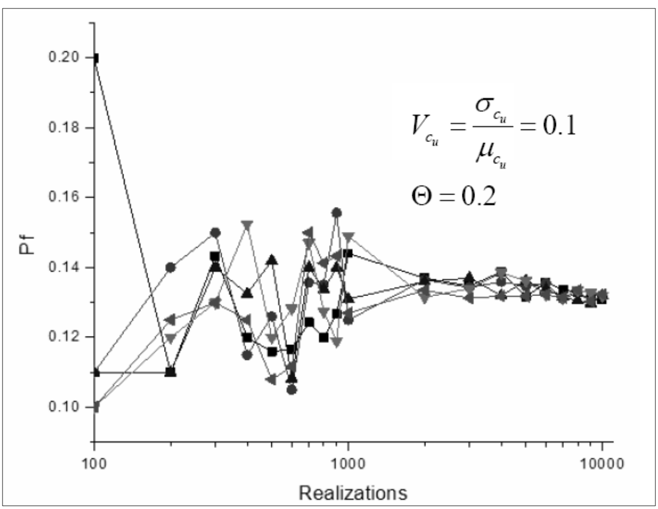

FIG. 3: Number of realizations vs. probability of failure.

FIRST ORDER SECOND MOMENT METHOD (FOSM)

The FOSM method for a single random variable is easily applied. For example, from Eq. 4 we get

$$\mu_{FS} = \frac{1}{\gamma H \sin\beta \cos\beta}\mu_{c_u} \tag{7}$$

and

$$\sigma_{FS} = \frac{1}{\gamma H \sin\beta \cos\beta}\sigma_{c_u} \tag{8}$$

It should be noted however that since no spatial variability is accounted for in this method (the soil is assumed to be variable but homogeneous) the failure mechanism is always assumed to act at a depth H.

Consider the particular case where $H = 2.5$ m, $\beta = 30°$, $\gamma = 20$ kN/m^3 with $\mu_{c_u} = 25$ kN/m^2 and $\sigma_{c_u} = 5$ kN/m^2 $(V_{c_u} = 0.2)$

From equations (7) and (8), FOSM gives $\mu_{FS} = 1.155$ and $\sigma_{FS} = 0.231$ $(V_{FS} = 0.2)$

If we assume a lognormal distribution of FS, then the mean and standard deviation of the underlying normal distribution of $\ln FS$ are given by

$$\mu_{\ln FS} = \ln \mu_{FS} - \frac{1}{2}\ln\left\{1 + V_{FS}^2\right\} = 0.124 \tag{9}$$

$$\sigma_{\ln FS} = \sqrt{\ln\left\{1 + V_{FS}^2\right\}} = 0.198 \tag{10}$$

To estimate the probability of failure, we need to estimate the probability that $FS < 1$, or in log-space, that $\ln FS < 0$

This is given by

$$\begin{aligned} P\left[FS < 1\right] &= \Phi\left[\frac{\ln 1 - \mu_{\ln FS}}{\sigma_{\ln FS}}\right] \\ &= \Phi\left[-\frac{0.124}{0.198}\right] = \Phi\left[-0.626\right] = 1 - \Phi\left[0.626\right] \\ &= 0.265 \end{aligned} \tag{11}$$

A similar procedure with an input $V_{c_u} = 0.4$ led to $P\left[FS < 1\right] = 0.428$.

If the distribution of FS is assumed to be normal in the above examples, FOSM gives $P\left[FS < 1\right] = 0.251$ and $P\left[FS < 1\right] = 0.369$ for input of $V_{c_u} = 0.2$ and $V_{c_u} = 0.4$ respectively.

RANDOM FIELD STUDIES WITH MONTE-CARLO

Numerous parametric studies have been performed, but in the interests of brevity only two of them are summarized in this paper. An undrained clay slope with $H = 2.5$ m, $\beta = 30°$, $\gamma = 20$ kN/m^3, and $\mu_{c_u} = 25$ kN/m^2 was considered with two different standard deviations of $\sigma_{c_u} = 5$ kN/m^2 and $\sigma_{c_u} = 10$ kN/m^2 corresponding to coefficients of variation of $V_{c_u} = 0.2$ and 0.4.

In both cases the dimensionless correlation length was varied in the range $0.1 < \Theta < 4$. This study used 5000 Monte-Carlo simulations which was sufficient to give statistically reproducible results for all the parametric combinations considered. The proportion that gave $FS < 1$ was calculated as the probability of failure p_f.

Figure 4 illustrates a typical histogram of FS values for $V_{c_u} = 0.2$ and $\Theta = 0.1$ generated by the Monte-Carlo simulations, together with both normal and lognormal fitted functions. The curve fits were based on the statistics of the factor of safety coming out of the Monte-Carlo analysis, which for this case were $\mu_{FS} = 0.92$ and $\sigma_{FS} = 0.11$

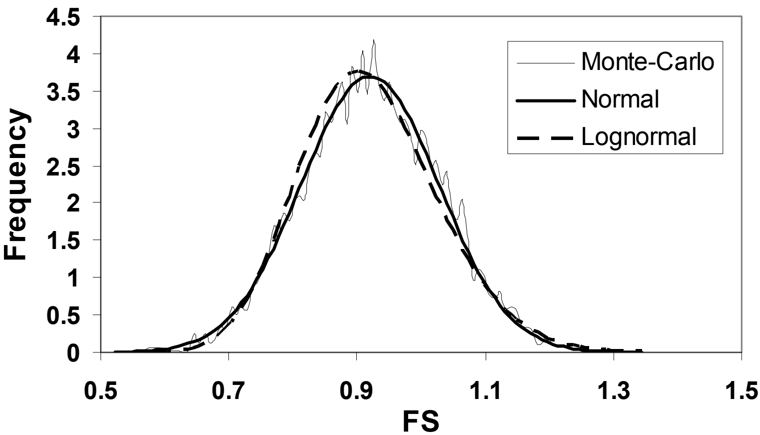

FIG.4: FS distribution from Monte-Carlo compared with normal and lognormal functions ($V_{c_u} = 0.2$, $\Theta = 0.1$)

Figure 5 and 6 gives plots of p_f vs. Θ from the Monte-Carlo simulations. The horizontal line in each case gives the probability of failure predicted by FOSM leading to $p_f = 0.264$ for $V_{c_u} = 0.2$ as computed earlier, and $p_f = 0.433$ for $V_{c_u} = 0.4$

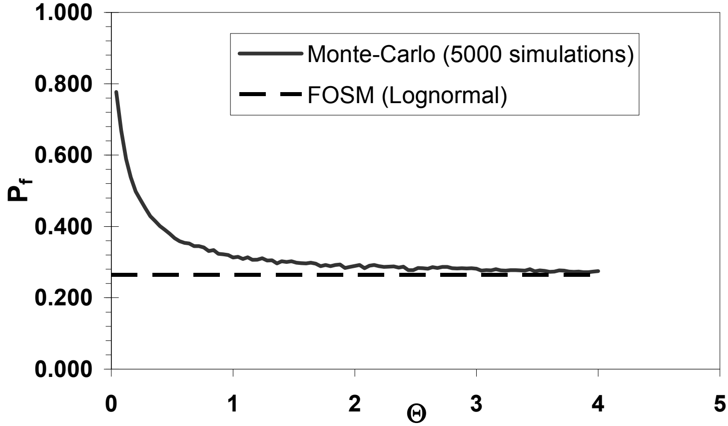

FIG. 5: Probability of failure vs. Spatial correlation length for $V_{c_u} = 0.2$

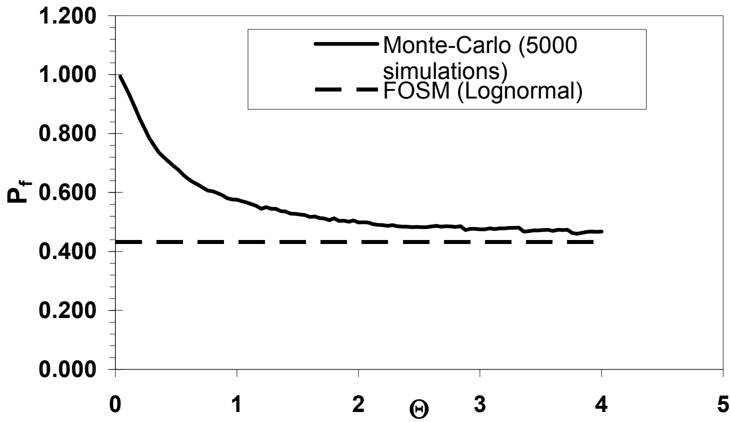

FIG. 6: Probability of failure vs. Spatial correlation length for $V_{c_u} = 0.4$

Clearly, FOSM is unconservative and is shown to be a special case of the random field results as $\Theta \to \infty$. The key reason for this is that the random field approach allows the slope to fail at its weakest point, while the FOSM method, being based on a classical formula, assumes the failure mechanism is at the base of the column which is not necessarily critical. Although not presented in this paper, similar conclusions are reached if c_u and FS are assumed to be normally distributed.

CONCLUSIONS

A novel analytical solution based on random properties has been developed and validated for the analysis of "infinite slopes" with the ability to model many different parametric variations. The classical analytical solution from infinite slope theory has been combined with random field theory to perform probabilistic infinite slope analyses in a Monte-Carlo framework. The method was compared with results obtained using the First Order Second Moment (FOSM) method. The FOSM lead in all cases to unconservative results because it is locked into the assumption that failure must occur at the base of the column. The random field approach has the key advantage that it "seeks out" the critical mechanism and is therefore a proper model of a spatially random soil. This phenomenon is also present in more conventional probabilistic studies of finite slope stability problems. Methodologies that resort to classical slope stability methodologies that do not allow the failure mechanism to "seek out" the most critical path are almost inevitably going to lead to unconservative results.

ACKNOWLEDGEMENT

The authors wish to acknowledge the support of NSF grant CMS-0408150 on "Advanced probabilistic analysis of stability problems in geotechnical engineering".

REFERENCES

Bromhead, E. N. (1992) "The Stability of Slopes." 2nd edition, Blackie Academic & Professional, New York: 135-137.

Duncan, J.M. (1996) "Slope stability analysis." Chapter 13 in "*Landslide Investigation and Mitigation.*", (Special report 247), TRB, National Research Council. National Academy Press, Washington, D. C.

Fenton, G.A. and Vanmarcke, E. H. (1990), "Simulation of random fields via local average subdivision." *J Eng Mech, ASCE,* Vol. 116, No. 8, pp. 1733-1749.

Lambe, T. W. and Whitman R. V. (1969), "Soil Mechanics." Wiley, New York: 553.

Taylor, D.W. (1948) "Fundamentals of Soil Mechanics." Wiley, Hoboken , New Jersey.

GIS Based Quantitative Risk Analysis Along Prithvi Highway Road Corridor During Extreme Events

Dr. Binod Tiwari[1], M. ASCE, Dr. Pankaj Bhattarai[2], and Mr. Carlos F. Garcia[3]

[1]Assistant Professor, Civil and Environmental Engineering Dept., California State University, Fullerton, 800 N State College Blvd, E-419, Fullerton, CA, 92834; btiwari@fullerton.edu
[2]Post Doctoral Research Fellow, Niigata University, Ikarashi 2-8050, Niigata, Japan
[3]Undergraduate Student, Civil and Environmental Eng. Dept., California State University, Fullerton

ABSTRACT: Geographic Information System (GIS) tools are widely used for the hazard mapping of slopes. However, quantitative slope instability mapping for a wide area is not commonly used. This study involves the evaluation of slope instability based on the three dimensional deterministic analysis. Various soil parameters that were measured from the field specimens were distributed according to the petrographic regions and slope instability mapping was prepared with the help of an automatic GIS algorithm. Estimated instability zones are verified with the field mapping and aerial photo interpretation. The study shows that the high hazard zone can increase up to 2.5 times of the current situation during the concurrent occurrence of rainfall and earthquake. The instability maps retrieved though this study can be effectively used for the maintenance of highways.

INTRODUCTION

Geographic Information System (GIS) is a useful tool in hazard mapping of slopes. However, quantitative hazard assessment is still not a common practice. With the development of the state-of-the-art GIS software, quantitative hazard assessment is possible. Automated slope stability analysis can be done easily and quickly for a large area if the required information is available.

Geological and geomorphologic investigation of an area and preparation of hazard susceptibility map are commonly performed before planning of infrastructure. Those maps ease in planning of infrastructures before construction. However, in many countries majority of the infrastructures, especially highway alignments are fixed considering various obligatory aspects, but not such hazard maps into consideration. Blockade of the highways due to mass movement obviously malfunction the transportation network and possess high risk of damage to lives and properties. "Deterministic hazard analysis" method based on shear strength of soil can be beneficially used in such area to plan the counter measures against the landslides and other mass movements. Considering such necessity, a slope instability mapping based on geomorphological characteristics and soil strength properties was carried out in Jogimara area, which covers about 16 Km length of Prithvi Highway, Nepal. This sector of the highway used to have numerous landslides every year as shown in figure 1.

The main objectives of this study are: to develop a simplified model for the stability analysis based on approximate 3D failure mechanism and estimate the potential mass movement area during concurrent occurrence of extreme events such as earthquake and heavy rainfall.

FIG. 1. One of the major landslides existing in the area

STUDY AREA

The Krishanabhir-Kurintar sector of the Prithvi highway of Nepal (Fig. 2) has been considered for this study. This sector is a part of two hundred kilometers long Prithvi highway of Nepal, which connects the capital city of Nepal to various other cities. Landslides and other mass movements block the highway every year. Due to the lack of information on potential failure sites, road clearance equipments are neither properly placed nor the pre-monsoon failure prevention strategies are well considered. Therefore, it is essential to prepare a database of slope instability parameters.

FIG. 2. Prithwi highway and the study area

SLOPE STABILITY MODEL

Because of the complex nature of mass movement, it is difficult to predict the exact configuration of the movement and its volume. However, depending on the ground condition and with some analytical assumptions, suitable theoretical models could be generated for the landslide analysis. In many investigations for natural slope stability, infinite slope analysis is used because of its relative simplicity, particularly when the thickness of the soil is much smaller than the length of the slope. However, for realistic modeling, three dimensional failure mechanisms should be considered. Use of GIS advantageously allows slope stability calculation for a square size grid. Three dimensional circular failure includes different depth of sliding surface throughout the slope failure mass. Therefore, some concept should be developed to allocate the equivalent depth of one dimensional (1D) plane failure which gives the same safety factor as with the three dimensional (3D) stability analysis method. This research was followed with this concept. To simplify the stability analysis process in GIS, geometry of more than 100 numbers of existing slope failures were recorded. The geometrical information of these slope failures were input in the GIS analytical tool. A one dimensional slope stability analysis was done for a depth of Z_{1D}. Likewise, a three dimensional slope stability analysis was done for a depth of Z_{3D} by modifying the two dimensional (2D) simple slice method to three dimensional analysis using effective stress condition. Those depths were grouped according to the geological and geomorphological conditions of the study area.

ACQUISITION OF THE SLOPE STABILITY PARAMETERS

The relationship given in the equation (1) is one dimensional translational failure equation. The relationship given in equations (2) and (3) are the equations used for one dimensional and two dimensional stability analyses, respectively, for dry condition (Bromhead, 1992). A three dimensional slope stability model was developed by modifying the two dimensional "method of slice" to a three dimensional "method of slice". "Slice" in the 2D method is replaced with "cylinder" in the 3D method. The necessary input parameters in the slope stability model are slope (β), the soil properties (cohesion, friction angle and unit weight), depth of failure surface and ground water depth/soil thickness ratio (m). Acquisition of slope stability parameters is briefly described below.

$$FS(Translational) = \frac{c + (\gamma - m.\gamma_w).z.\cos^2\beta.\tan\phi}{\gamma.z.\sin\beta.\cos\beta} \tag{1}$$

$$FS(Translational) = \frac{c + \gamma.z.\cos^2\beta.\tan\phi}{\gamma.z.\sin\beta.\cos\beta} \tag{2}$$

$$FS(Rotational) = \frac{c + \gamma.\tan\phi.\sum z.\cos^2\beta}{\gamma.\sum z.\sin\beta.\cos\beta} \tag{3}$$

Where,

c = cohesion of soil	ϕ = friction angle of soil	γ = unit wt. of soil
z = depth of sliding surface	β = slope angle	γ_w = unit wt. of water

The methodology of acquiring and setting the value of stability parameters are explained below.

Cohesion and internal frictional angle

Soil samples as well as rock pieces were collected from 100 different locations throughout the study area. All soil specimens were disturbed while sampling. As fully softened (remolded peak) and residual shear strengths were measured, sample disturbance did not have much effect on slope stability analysis. The study area is divided into equally spaced sampling grids. As the types of rock in the study area were briefly understood from the geological map, emphasis was given to collect the residual soil samples representing all of the soil types. At least one sample was collected from the recorded existing slope failure areas. Likewise, at least ten samples were collected from one petrological region. Shown in table 1 are peak and residual friction angles of soil specimen of study area. Fully softened (remolded peak) shear strength was measured with a simple shear device (ASTM D6528) whereas the residual shear strength was measured with a ring shear device (ASTM D6467). Samples could be clearly divided into 10 groups according to the type of rocks. There was good agreement between the values of cohesion and friction angles in each petrological region. Therefore, an average value of friction angle was calculated for each type of rock. From the available 1:250,000 scale geological map, distribution of each rock was identified and the friction angle distribution map was prepared by assigning the respective average value of residual friction angle (Fig. 3) to each type of rock. The distribution map of cohesion was also prepared in the similar way. To ensure a degree of conservatism, residual shear strengths were considered.

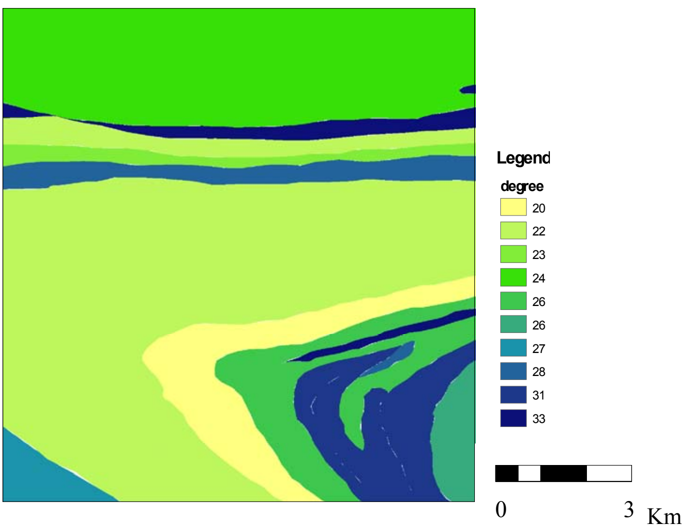

FIG. 3. Distribution of friction angle throughout the area

Soil Density (γ) and Density of water (γ_w)

The density of soil in the study area varies from place to place. Density of soil depends on the in situ condition. In this study, the value of unit weight of soil (γ) was distributed according to the γ of each sampling grid. Value of γ was also distributed according to the equi-γ line made using GIS technique. The unit weight of water was taken as 9.81 kN/m^3.

Slope Gradient (β)

The slope (β) was derived from digital elevation model (DEM). A 1:25,000 scale topographic map of the study area that has a 20 m contour interval was geo-referenced and digitized. This digitized contour map was then utilized to make DEM through the preparation of Triangulated Integrated Network (TIN) using Arc GIS 3D Analyst. The slope map of 1m x 1m grid size was then prepared directly from the Digital Elevation Model (DEM) using spatial analyst tool (fig. 4). This method is commonly used in generating a slope map using GIS.

Depth of terrain surface (Z)

Factor of safety using the "infinite slope stability analysis" for each 1m x 1m grid is widely used to conduct the large area deterministic analysis. However, such factor of safety calculated for 1m square grid may not represent the factor of safety of actual 3D failure surface. Therefore, a simplified approach has been considered by reducing 3D depth to 2D equivalent depth based on equal factor of safety. However, for automated calculation in a wide area, it is not simple to analyze a 2D rotational slide due to a variation in depth of sliding surface. Hence, depth of the 2D model that gives the same factor of safety as with the 1D model was calculated. Then 2D depth of rotational slide was then converted to equivalent translational depth keeping the same factor of safety.

Ground water/sliding surface depth ratio (m)

Groundwater plays a significant role in the occurrence of slope failures. Water decreases the stability by increasing the pore water pressure on the potential failure surface. However, there was no data available regarding the depth of ground water table in the study area. The ground water table is at very low level at the ridge of the mountain and it at the stream is assumed to be at water level of the stream. Cross sections were drawn for 15 slopes at different locations from the nearest ridge to the Trishuli River in perpendicular direction to observe the ground water level at about 2m deep slope failure. The ground water is 2m below ground level at the distance of 50m from the stream in case of 500m long slopes. This indicates that the remaining 450m portion always has water table below the sliding depth. The ratio of ground water depth and depth of sliding surface (m) was interpolated from 0 to 1 according to the distance from stream up to 10% slope length. The value of "m" was kept "0" for the remaining portion of slope. In order to define the slope unit, reverse DEM was prepared using the DEM data and GIS analysis tool. The watershed polygon made by using Arc Hydro for the DEM data had been dissected by the watershed polygon made from reverse DEM data. The divided polygons represent each slope units. Ground water analysis was done based on the buffering distance from the stream for each slope units separately.

Table 1. Residual & Remolded Peak Friction Angles For 10 Petrological Regions

Petrological zone	Peak friction angle (degree)	Residual friction angle (degree)
1	24	22
2	32	31
3	28	26
4	28	27
5	21	20
6	35	33
7	27	26
8	28	28
9	26	24
10	26	23

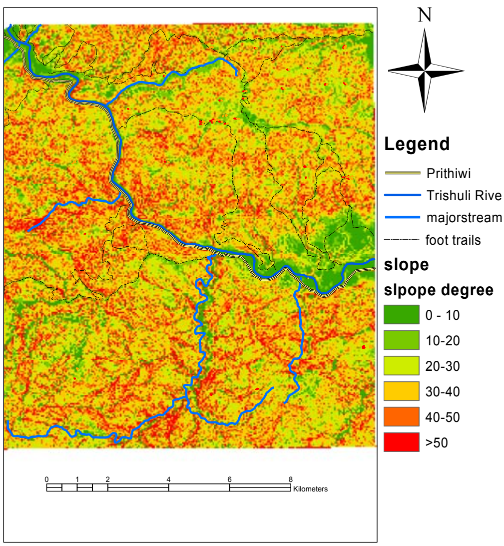

FIG. 4. Slope of the study area made from DEM

PREPARATION AND ANALYSIS OF INSTABILITY MAP

Using slope derived from Digital Elevation Model (Fig. 4), the tested shear strength parameters (Fig. 3), distance from stream (for m) and unit weight(γ), slope stability analysis were done for each 1m x 1m grid size using Arc GIS. The factor of safety for each 1m cell was calculated automatically. The GIS algorithm designed for the analysis is based on raster calculation of Arc GIS spatial analyst. Cohesion(c), friction angle(ϕ), ground slope(β), unit weight(γ), and ratio of depth of ground water and sliding surface(m), were used as input layers for the calculation. Based on the soil test results, zone for the value of c and ϕ was kept similar to the zone for each rock type. The slope instability map of the study area for 1m x 1m grid is shown in fig. 5. This map was prepared based on the factor of safety against sliding. Values of factor of safety were grouped into five different classes as: Fs < 1, Fs = 1-1.5, Fs= 1.5-2.5, Fs=2.5-3.5, and Fs >3.5. The proportions of area for those groups were 7%, 30%, 43%, 6%, and 3% respectively. 11% area contained no data, as they were either flat streams or flat lands at the ridge, which cannot be calculated by the proposed algorithm due to indefinite result.

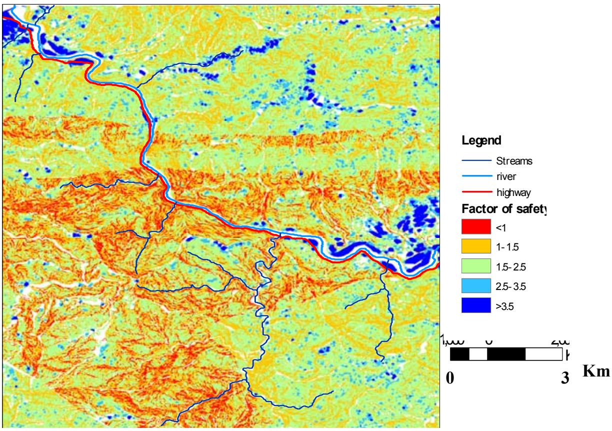

FIG. 5. Result of GIS based large area automated stability calculation

VARIFICATION OF THE INSTABILITY ZONES

The predicted instability maps were verified both through a distribution map of the slope failure and detailed field observations. More than 150 slope failures noted during field investigations were spatially arranged in the stability map to verify the analysis results. Likewise, the location of the collapsed sites recorded in photographs, which were close but inaccessible during the field study, were also compared with the calculated instability zones. The predicted instability zones were also compared with the small and large scale failures distributed in aerial photographs. For this, specific verification area was chosen and slope failures, which were clearly visible in 1:50,000 scale aerial photographs, were marked within the specified area (Fig. 6). Due to the small scale of available aerial photographs, small slope failures are hardly identified.

Almost 80% of the recorded slope failures were found in low stability zone (FS <1) and 20% were in medium stability zone (FS 1-1.5). These figures indicate that predicted instability areas correspond to the actually occurred slope failures except in a few cases. Existence of landslides at the area analyzed as low hazard zones, might be due to some other causes including geological and manmade. Both geological and man made causes are out of the scope of this study.

Analyses were performed for three other extreme cases: a) ground water level same as the ground level i.e. m =1 for all cases, b) earthquake causing a peak ground acceleration of 0.7 at the present ground water situation, and c) combination of a) and b). Shown in Table 2 are the % of areas calculated to be under different factor of safety zones.

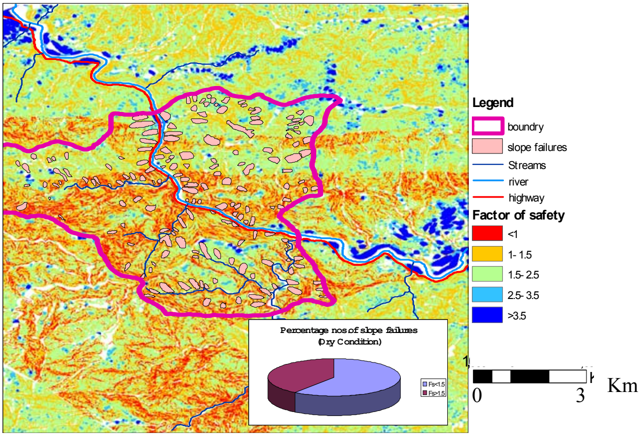

FIG. 6. Existing landslides at selected area within the slope instability map

Table 2. Percentage of Area Covered Under Different Fs for Various Conditions

Factor of Safety	Current Situation	Case (a)	Case (b)	Case (c)
< 1	7	34	21	47
1 – 1.5	30	35	33	41
1.5 – 2.5	43	17	30	1
2.5 – 3.5	6	1	3	0
> 3.5	3	2	2	0
No data	11	11	11	11

CONCLUSION

A comprehensive slope instability map of a large area can be prepared by using measured shear strength. The study shows that landslide hazard potential can increase by as high as 2.4 times during the concurrent occurrence of landslide and earthquake. Therefore it is necessary to evaluate long-term stabilities of slopes considering the effect of rainfall and earthquakes separately and in combination.

REFERENCES

Bromhead, E. N. (1992) "Stability of Slopes. 2nd edition", Surrey University Press, London, UK, pp 395.
Department of Survey, Nepal (1998) "Topographic map of Jogimara Area (1:25,000)".
Department of Survey, Nepal (1993) "Aerial photograph of Jogimara Area".
Department of Survey, Nepal (1950) "Land Capability map of Jogimara Area".
Department of Mines and Geology, Nepal (1984) "Geological Map of Central Region".

One-dimensional Probabilistic Uncoupled Consolidation Analysis by the Random Finite Element Method

Jinsong Huang[1], D.V. Griffiths[2] PE，F. ASCE
and Gordon A. Fenton[3] P. Eng., M. ASCE

[1]Research Professor，Division of Engineering, Colorado School of Mines,Golden, CO 80401, U.S.A.; PH (303)-273-3173; FAX (303)-273-3602; email: jhuang@mines.edu
[2]Professor，Division of Engineering, Colorado School of Mines, Golden, CO 80401, U.S.A.; PH (303)-273-3669; FAX (303)-273-3602; email: d.v.griffiths@mines.edu
[3]Professor，Department of Engineering Mathematics, Dalhousie University, P.O. Box 1000, Halifax, Nova Scotia, Canada B3J 2X4; PH (902) 494-6002; FAX (902) 423-1801; email: Gordon.Fenton@dal.ca

ABSTRACT: The influence of a spatially random coefficient of consolidation on one-dimensional uncoupled consolidation has been studied using the Random Finite Element Method. The results of parametric studies are presented, which describe the effect of the standard deviation and correlation length of the coefficient of consolidation on output statistics relating to the overall "effective" coefficient of consolidation. Three "effective" coefficient of consolidation are considered, namely harmonic mean, the log time method and the root time method.

INTRODUCTION

The Random Finite Element Method (RFEM) was pioneered by Griffiths, Fenton and co-workers in the early 1990s. Since then it has been applied to a wide range of geotechnical applications involving highly variable soils (see e.g., www.dalhousie.ca/engmath/rfem/rfem.html for a complete bibliography). This approach involves the generation of random fields of soil/rock properties with properly controlled spatial statistics (mean, standard deviation and spatial correlation). This spatial distribution of properties is then mapped onto quite refined finite element meshes taking proper account of local averaging over each element. A finite element analysis is then performed relating to the particular application under investigation. Monte Carlo simulations then follow, in which the finite element analysis is repeated numerous times, each with the same underlying statistics of the soil/rock properties, but different spatial locations of the soil/rock properties across the finite element mesh. Each new random field generation and the subsequent finite element analysis is termed a "realization". By generating a sufficient number of realizations, output quantities of interest can be assimilated and statistically analyzed to produce estimates of probability density functions.

Simpler probabilistic methods, such as First Order Second Moment (FOSM) and First Order Reliability Method (FORM), typically represent soil/rock property uncertainty by the use of a single "perfectly correlated" random variable (e.g., Schweiger *et al.* 2001, Nadim 2007). The use of RFEM represents an important refinement, by allowing the value of each soil/rock property assigned to each finite element to be itself a random variable, thus enabling spatial correlation to be accounted for in a systematic way. Recent studies (e.g. Griffiths *et al.* 2006) have shown that FORM and FOSM can be considered to be special cases of RFEM with perfectly spatially correlated random fields (infinite correlation length).

In the present works the RFEM has been used to examine one-dimensional uncoupled consolidation, with particular reference to the overall "effective" coefficient of consolidation. Three "effective" coefficient of consolidation are considered, namely the harmonic mean method, the log time method and the root time method.

TERZAGHI'S ONE-DIMENSIONAL CONSOLIDATION THEORY

Let u be the excess pore pressure within a thin layer of soil at any given depth z at any given time t. The excess pore pressure u can be calculated using the coupled equations (1) and (2).

$$\frac{\partial u}{\partial z}+\frac{1}{m_v}\frac{\partial^2 s}{\partial z^2}=0 \tag{1}$$

$$\frac{k}{\gamma_w}\frac{\partial^2 u}{\partial z^2}+\frac{\partial}{\partial t}\frac{\partial s}{\partial z}=0 \tag{2}$$

where m_v is the coefficient of volume compressibility, k is the soil permeability, γ_w is the unit weight of water and t is time.

The settlement variable s can be eliminated from (1) and (2) to give an uncoupled equation in terms of excess pore pressure only.

$$c_v\frac{\partial^2 u}{\partial z^2}=\frac{\partial u}{\partial t} \tag{3}$$

where c_v is the "Coefficient of Consolidation" as

$$c_v = \frac{k}{m_v \gamma_w} \tag{4}$$

If the initial (uniform) excess pore pressure is given by u_0 and the maximum drainage path by D, the analytical solution is given by the equation

$$u = u_0 \sum_{i=0}^{i=\infty} \frac{4}{(2i+1)\pi} \sin\left[\frac{(2i+1)\pi}{2}\frac{z}{D}\right] \exp\left[\frac{-(2i+1)^2\pi^2}{4}\frac{c_v t}{D^2}\right] \tag{5}$$

Defining the Average Degree of Consolidation as

$$U_{av} = 1 - \frac{1}{2}\int_0^2 \frac{u}{\Delta\sigma_z} dz \tag{6}$$

and substituting the analytical solution (5) into (6), we get

$$U_{av} = 1 - \sum_{i=0}^{i=\infty} \frac{2}{M^2} \exp\left(-M^2 T\right) \tag{7}$$

where $M = \frac{(2i+1)\pi}{2}$ and $T = \frac{c_v t}{D^2}$.

Hence U_{av} is a unique function of *T*. The relationship between U_{av} and *T* is often expressed in graphical form. The value of the coefficient of consolidation can be estimated by comparing the characteristics of the experimental and theoretical consolidation curves.

In the log time method, the coefficient of consolidation is determined by

$$c_{v0.5} = \frac{0.197D^2}{t_{0.5}} \tag{8}$$

where $t_{0.5}$ is the time corresponding to $U_{av} = 50\%$.

In the root time method, the coefficient of consolidation is determined by

$$c_{v0.9} = \frac{0.848D^2}{t_{0.9}} \tag{9}$$

where $t_{0.9}$ is the time corresponding to $U_{av} = 90\%$.

GENERATION OF COEFFICIENT OF CONSOLIDATION VALUES

The distribution type of the coefficient of consolidation is assumed to be log-normal as the coefficient of consolidation has no negative value. Essentially, the coefficient of consolidation field is obtained through the transformation

$$c_{vi} = \exp\{\mu_{\ln c_v} + \sigma_{\ln c_v} g_i\} \tag{10}$$

in which c_{vi} is the coefficient of consolidation assigned to the ith element, g_i is the local average of a standard Gaussian random field, g, over the domain of the i^{th} element, and $\mu_{\ln c_v}$ and $\sigma_{\ln c_v}$ are the mean and standard deviation of the logarithm of c_{vi} (obtained from the 'target' mean and standard deviation μ_{c_v} and σ_{c_v}).

The Local Average Subdivision (LAS) technique (Fenton and Vanmarcke 1990) renders realizations of the local averages, g_i, which are derived from the random field , g, having zero mean, unit variance, and a spatial correlation controlled by the spatial correlation length. As the spatial correlation length goes to infinity, g_i becomes equal to g_j for all elements i and j – that is the field tends to become uniform on each realization. At the other extreme, as the spatial correlation length goes to zero, g_i and g_j become independent for all $i \neq j$ – the coefficient of consolidation changes rapidly from point to point.

The overall "effective" coefficient of consolidation could also be estimated by evaluating the harmonic mean of coefficients of consolidation assigned to elements, namely

$$c_{vhm} = \frac{1}{\frac{1}{n}\sum_{i=1}^{n}\frac{1}{c_{vi}}} \tag{11}$$

where n is the number of elements and c_{vi} is the coefficient of consolidation of i^{th} element.

STOCHASTIC ANALYSIS

This is a qualitative study in which we have investigated the influence of a random coefficient of consolidation on one-dimensional consolidation rates. Normally, the unites are, m, kN and yrs, however, we have not included units in the results presented in this paper. Figure 1 shows a string of 100 elements attached end to end, representing a one-dimension layered saturated soil with a total depth of 1.0. The system is subjected to a uniform initial excess pore pressure distribution at $t = 0$ of 100.0 and is drained at the top only. The mean and standard deviation of the coefficient of consolidation are 1.0 and 0.5, respectively, and the spatial correlation length is assumed to be 0.5. Two thousand Mote-Carlo simulations were found to be sufficient to give statistically reproducible results and were used in this paper.

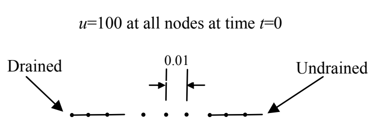

FIG. 1. One-dimensional layered consolidation

The highest excess pore pressure at the bottom at $t=1$ following 2000 simulations was 61.79 and the lowest was 0.13. The excess pore pressure at the bottom at $t=1$ is 10.81 if all the elements have a uniform coefficient of consolidation of 1.0. The various "effective" coefficients of consolidation are summarized in Table 1.

Table 1 "Effective" coefficients of consolidation

	Harmonic mean	Log time method	Root time method
Simulation with highest excess pore pressure	0.28	0.36	0.42
Simulation with lowest excess pore pressure	2.10	2.94	2.87

Figure 2 shows two typical distributions of excess pore pressure at $t=1$. One distribution corresponds to the highest excess pore pressure at the bottom and the other to the lowest. The distributions of excess pore pressure at $t=1$ for a uniform coefficient of consolidation is also shown.

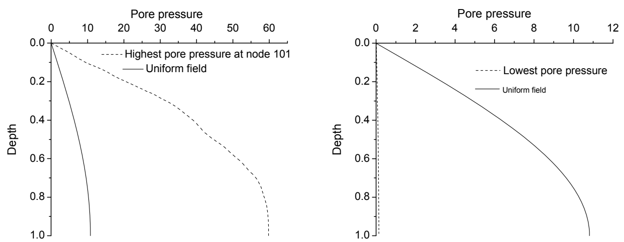

FIG. 2. Distributions of excess pore pressure after time 1

The randomly distributed coefficients of consolidation of the two typical simulations are displayed in Figure 3 in the form of a grayscale. The darker zones indicate lower coefficients of consolidation. The maximum and minimum coefficients of consolidation are also shown.

$c_{v\min}$ =0.12, $c_{v\max}$ =0.75 $c_{v\min}$ =0.70, $c_{v\max}$ =6.27

Highest pore pressure Lowest pore pressure

FIG. 3. Coefficient of consolidation distributions

PARAMETRIC STUDIES

Further parametric studies were performed using the model of the previous section to investigate the sensitivity of the "effective" coefficients of consolidation to the statistically defined input coefficient of consolidation.

The coefficient of variation is defined as

$$COV = \frac{\sigma}{\mu} \tag{12}$$

where σ and μ are the standard deviation and mean.

A dimensionless correlation length Θ is defined as

$$\Theta = \frac{\theta}{D} \tag{13}$$

where θ and D represent the spatial correlation length and maximum drainage path respectively.

The following parameters have been used for the parametric study.

COV=0.125, 0.25, 0.5, 1.0, 2.0, 4.0, 8.0

Θ=0.125, 0.25, 0.5, 1.0, 2.0

μ=1.0

The results of the parametric study are shown in Figures 4-9 in which the means and standard deviations of the three "effective" coefficients of consolidation are presented. The subscripts "hm", "0.9" and "0.5" mean harmonic mean, log time method and root time method respectively. It can be seen that all the effective mean values, μ_{hm}, $\mu_{0.5}$ and $\mu_{0.9}$ are lower than 1.0, decrease with increasing COV and increase with increasing Θ.

General speaking, an increase in Θ will result in a larger σ_{hm}, $\sigma_{0.5}$ and $\sigma_{0.9}$. When $\Theta \le 0.5$, there are indications of a maximum value of σ_{hm}, $\sigma_{0.5}$ and $\sigma_{0.9}$ in the curves of σ_{hm}, $\sigma_{0.5}$ and $\sigma_{0.9}$ vs. COV.

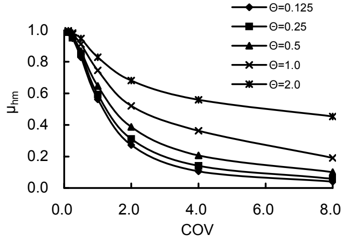

FIG. 4. μ_{hm} **vs. COV**

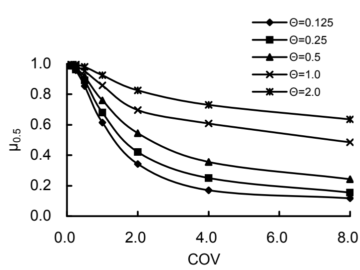

FIG. 5. $\mu_{0.5}$ **vs. COV**

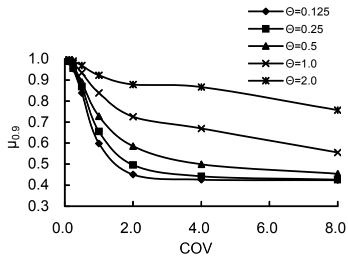

FIG. 6. $\mu_{0.9}$ **vs. COV**

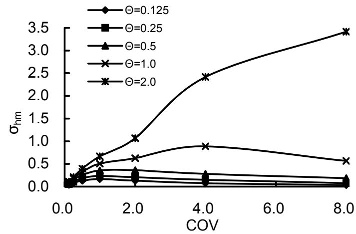

FIG. 7. σ_{hm} **vs. COV**

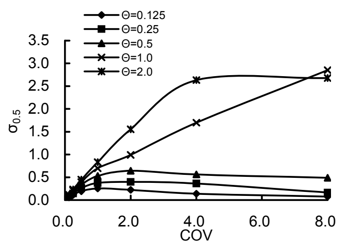

FIG. 8. $\sigma_{0.5}$ **vs. COV**

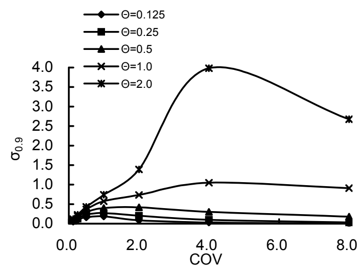

FIG. 9. $\sigma_{0.9}$ **vs. COV**

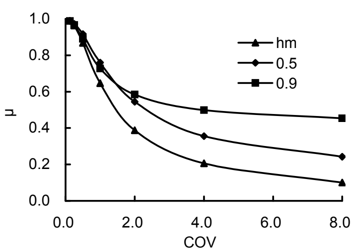

FIG. 10. μ_{hm}, $\mu_{0.5}$ **and** $\mu_{0.9}$ **(**Θ **=0.5)**

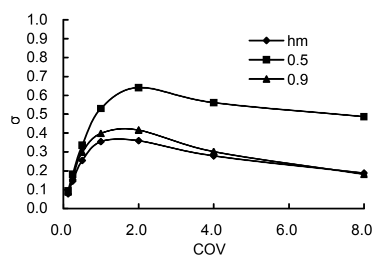

FIG. 11. σ_{hm}, $\sigma_{0.5}$ **and** $\sigma_{0.9}$ **(**Θ **=0.5)**

Figure 10 shows that for the case of Θ=0.5, $\mu_{hm} < \mu_{0.5} < \mu_{0.9}$ except for very low *COV* values, and Figure 11 shows that $\sigma_{hm} \approx \sigma_{0.9} < \sigma_{0.5}$.

CONCLUDING REMARKS

The influence of a spatially random coefficient of consolidation on one-dimensional uncoupled consolidation has been studied using the Random Finite Element Method. The effect of the standard deviation and correlation length of the coefficient of consolidation on three types of "effective" coefficients of consolidation were investigated. Parametric studies showed that the means of the "effective" coefficients of consolidation were always smaller than the input mean coefficient of consolidation, implying that soil variability results in slower consolidation that would be predicted in a traditional deterministic analysis. Furthermore, it was shown that the expected value of the coefficient of consolidation for a variable soil as predicted by the log-time method, is lower than that predicted by the root-time method. The results also demonstrate the deficiencies of one-dimensional consolidation analysis in highly variable soils, where low consolidation coefficient zones dominate the effective values. In practice it is known that consolidation typically proceeds faster than would be predicted by a one-dimensional analysis due to two-dimensional and three-dimensional effects, where the excess pressures can "seek out" the easiest escape paths from the system. The authors are continuing this work into higher dimensional analysis for both coupled and uncoupled consolidating systems.

ACKNOWLEDGEMENTS

The authors wish to acknowledge the support of NSF grant CMS-0408150 on "Advanced probabilistic analysis of stability problems in geotechnical engineering".

REFERENCES

Fenton, G.A. and Vanmarcke, E.H. (1990). "Simulation of random fields via Local Average Subdivision." *ASCE J. Engrg. Mech.*, Vol. 116(8):1733–1749.

Griffiths, D.V., Fenton, G.A. and Ziemann, H.R. (2006). "Seeking out failure: The Random Finite Element Method (RFEM) in probabilistic geotechnical analysis." *Proceeding of the GEOCONGRESS 2006, Atlanta. Mini-Symposium on Numerical Modeling and Analysis (Probabilistic Modeling and Design),* ASCE publication on CD

Nadim, F, (2007). "Tools and strategies for dealing with uncertainty in geotechnics" Chapter 2 in Probabilistic Methods in Geotechnical Engineering, eds. D.V. Griffiths and G.A. Fenton, Pub. Springer, Wien, New York.

Schweiger, H.F., Thurner, R. and Pottler, P. (2001). "Reliability analysis in geotechnics with deterministic finite elements." *Int J Geomech*, Vol. 1(4):389–413.

Potential Risk of Landslide Damming During Earthquakes

Dr. Binod Tiwari[1], M. ASCE, Dr. Gyanu R. Tuladhar[2], Dr. Hideaki Marui[3], and Mr. Carlos F. Garcia[4]

[1]Assistant Professor, Civil and Environmental Engineering Dept., California State University, Fullerton, 800 N State College Blvd. E-419, Fullerton, CA, 92834; btiwari@fullerton.edu.
[2]KOWA Consulting Group, Niigata, Japan.
[3]Professor, Research Center for Disaster recovery, Niigata University, Japan.
[4]Undergraduate Student, Civil and Env. Engineering Dept., California State University, Fullerton.

ABSTRACT: The Mid-Niigata earthquake occurred in 2004 and taught us a lesson about the possibility of landslide damming when the earthquake occurs after the softening of the ground by rainfall. Terano Landslide was considered stable before the earthquake. However, due to the earthquake, the landslide moved extensively and dammed the Imokawa River. A main landslide block was analyzed for a seismic loading condition using the observed peak ground acceleration. Soil samples were collected from numerous sliding surfaces, and fully softened and residual shear strengths were measured. Factor of safeties were calculated for the mobilization of fully softened and residual shear strengths during different peak ground accelerations (PGA) and different pore water pressure ratios. Quantitative risk to landslide damming was evaluated for different PGA and ground water level scenarios, using the Bishop's Simplified Stability Analysis Method modified for the dynamic loading. The study results showed that the landslide mass would fail even if the earthquake of PGA more than 0.4g occurred in a dry season.

INTRODUCTION

A M6.8 scale earthquake, known as Niigata Chuetsu Earthquake, occurred on October 23, 2004 in the Niigata Prefecture of Japan and triggered thousands of new and reactivated landslides. Chigira et al. (2005) described the preliminary geomorphological characteristics of those landslides. The earthquake killed 39 people and injured more than 3,000 people. The Epicenter of the earthquake was located at Kawaguchi Town, approximately 195 km North-west of Tokyo. This earthquake caused heavy damage at Yamakoshi Village (Fig. 1). Superimposition of peak ground acceleration (PGA) and distribution of landslides is shown in figure 2. Several aftershocks followed by the main earthquake triggered many landslides several of them dammed numerous streams and raised the stream water levels. Tuladhar et al (2007) completed an extensive review of Takezawa landslide, which is one of the major landslides that dammed the Imokawa River. They concluded that if the earthquake occurred in the dry season or a typhoon did not occur prior to the earthquake, activation of those landslides might not have happened. This study focuses on another landslide damming case at Terano landslide, which also dammed the Imokawa River. The length and width of the landslide in question are 390 m and 160 m, respectively. The landslide was the reactivation of an existing landslide. According to the preliminary investigation report (Chigira and Yagi, 2006), the landslide was triggered at the contact between two remarkably different geological layers. The upper layer consists of highly weathered sandstone with highly oxidized brown colored fine grained sandy soil, whereas the lower layer consists of siltstone/mudstone with inter-bedded sandstone layers. Though emergency efforts were implemented to breach the dam manually before over-topping occurs, it is necessary to design countermeasures for the stability of the slide mass. This report presents a preliminary seismic stability analysis enhanced by soil test results. This is helpful to clarify the mechanism of the earthquake.

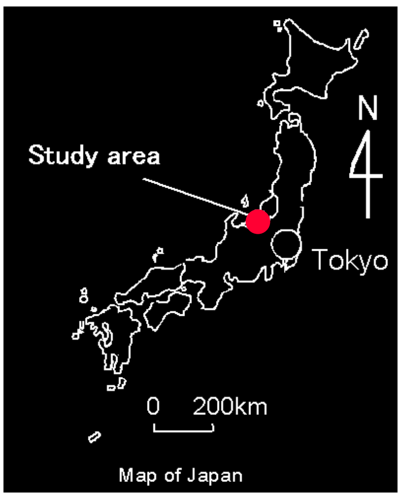

FIG. 1. Location map of the Mid Niigata earthquake affected area.

Geological map of the study area is shown in Figure 3, after modification on the map provided by the Geological Survey of Japan (Yanagisawa et al., 1986). The earthquake affected area covers a number of river corridors, and hilly to mountainous area. The landslide is located at an axial part of the South – South West plunging “Kajikane Syncline”. The strata that underlain the landslide consists of alternative beds of sandstone and siltstone or mudstone. Shown in Figure 4 is the mudstone layers sandwiched between the sandstone layers, which is the main cause of landslide.

Shown in figure 5 is an overall view of the landslide area. According to Chigira et al. (2005), the landslide mass is a reactivated mass and has multiple sliding surfaces.

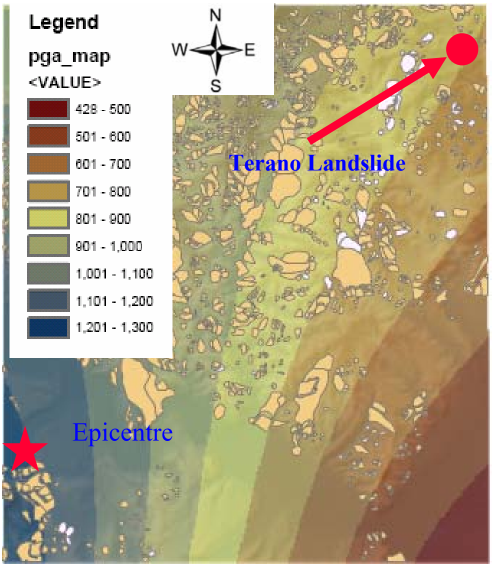

FIG. 2. PGA (gals) due to Mid Niigata Earthquake. (1 g = 980 gal) (source: Japan Landslide Society)

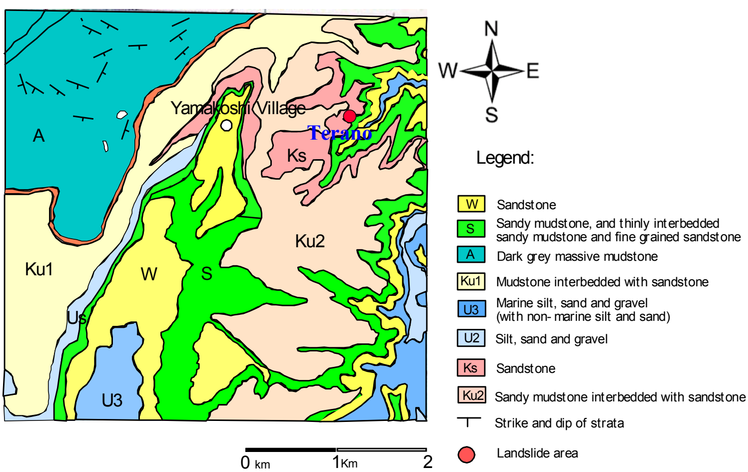

FIG. 3. Geological map of the study area

FIG. 4. Mudstone sandwiched between sandstones

FIG. 5. Overall view of the Terano landslide

FIELD INVESTIGATION

A field investigation was conducted to retrieve information about cross-section, ground water situation, and soil properties. Shown in Figure 6 is a cross-section of the landslide area. Our team conducted a field investigation a couple of weeks after the earthquake and collected six soil samples from the mudstone layers - three each from the head scarps and the deep sliding surfaces. All samples were disturbed soil samples.

LABORATORY TESTING PROGRAM

Our team conducted direct simple shear test and the ring shear test to measure the fully softened and residual shear strengths, respectively for all six specimens collected from the landslide area. While conducting shear tests, shearing speed of 0.01 mm/min was maintained. The main objective of this study was to get the value of static shear strength. As the value of excess pore water pressure during the earthquake could not be assessed, the "total stress analysis" approach was used for the analysis of landslides. The test results are presented in the following sections.

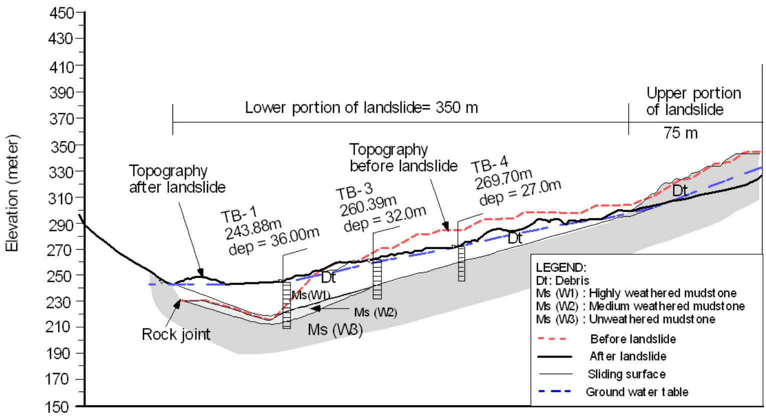

FIG. 6. Cross-section of Terano landslide.

SOIL TEST RESULTS

Shown in Table 1 are the fully softened and residual shear strengths of the collected specimens. According to the test results, average fully softened (or remolded peak) friction angle of soil was approximately 33.6º, and the average residual friction angle was approximately 22.5º. This friction angle is a typical value for mudstone having clay fraction less than 20%.

Table 1. Friction Angles (ϕº) of The Soil Samples

Sample No	residual	fully softened
1	25.2	35.1
2	21.6	34.0
3	23.9	34.7
4	21.6	31.8
5	22.4	32.5
6	23.9	33.1

DYNAMIC STABILITY ANALYSIS

To evaluate the stability of the slope during the earthquake, dynamic stability analysis was performed by modifying the Bishop's Simplified Stability analysis method for earthquake loading. Peak ground acceleration of the landslide area during the earthquake shaking was varied from 0.7 to 0.9 g (Fig. 2).

Dynamic stability of the slope was evaluated for the PGA ranging from 0.1 g through 0.9 g. Stability analysis was performed for the maximum value of shear strengths. The decrease in safety factor for increasing value of PGA for the observed ground water table right after the earthquake is shown in Fig. 7. The PGA of 0 is the static condition whereas PGA of 0.9g is the maximum PGA recorded during the earthquake. Even without the increase in excess pore water pressure, the landslide may start sliding due to the reduction in factor of safety (FS) from 1.72 to 1.0 at about 0.22 g of PGA. After sliding for about a meter, shear strength is supposed to decrease to the residual value. Shown in Fig. 8 is the factor of safety of the slope calculated with the residual shear strength of the interface and the fully softened shear strength. It is clear that after the reduction of the shear strength to residual, very small ground acceleration is enough to cause the mass to move.

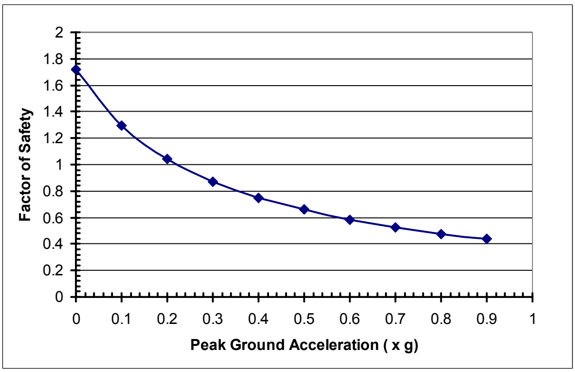

FIG. 7. Variations of FS with PGA.

For comparison purpose, dynamic stability analysis was conducted for the pore water pressure ratio (r_u) ranging from 0 (dry situation) through 0.43 (observed pore pressure ratio). The effect of excess pore water pressure during the earthquake was not considered for the analysis. Stability analysis results for those situations are presented in Fig. 9. The result shows that the landslide would move with the earthquake of that magnitude even in the dry season. Although the ground softening that was caused by the typhoon, 2 to 3 months prior, might have had significant impact on the Higashi Takezawa landslide (Tuladhar et al, 2007), it appears that the Terano landslide would have been moved in the dry season with a PGA of as low as 0.4 g. This result shows that landslide topographies like this are vulnerable to earthquake shaking even though ground water table is low. The only way to prevent movement might be geometrical or structural improvement of the slopes prior to the earthquake.

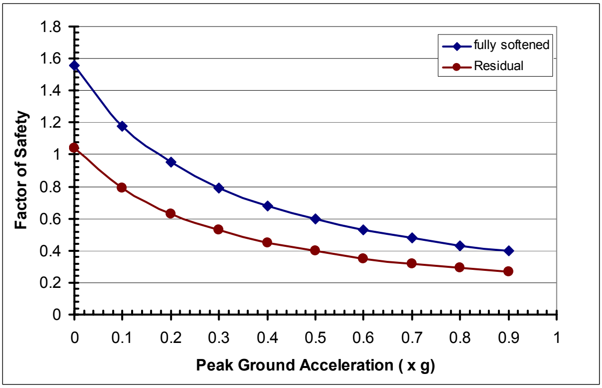

FIG. 8. Comparison of FS for residual and fully softened shear strength.

The dynamic stability analysis of the Terano landslide can be used as an example for the analysis of potential movement of landslide masses in other parts of Japan and other countries. It seems that a small magnitude of earthquake might be sufficient to cause concern and slope stabilizing measures need to be considered for critical water levels and earthquake loads. If the earthquake occurs during snow melt, when the value of r_u is relatively high, it would cause further damage. Therefore, to minimize large scale disasters in future, stability analysis of all potential landslides should be performed using the shear strength of the sliding surface soil and possible fluctuation of ground water table for different seasons.

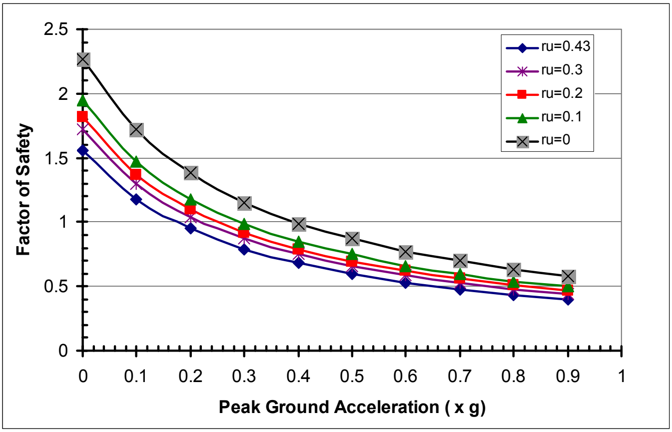

FIG. 9. Decrease in FS with PGA for different pore pressure ratios.

Dynamic stability analysis was also conducted for the existing stable slope after the movement for the PGA of 0.9 g. The safety factor is marginal if the earthquake of similar scale occurs during the snow melt season when the ground water table increases the pore pressure ratio to 0.5.

CONCLUSION

From this study, following general conclusions are made.

- Landslide mass would have failed even if the earthquake occurred in the dry season. This type of landslide topography is vulnerable to dynamic loading.
- Small ground vibration was enough to keep the mass moving after the mobilization of residual shear strength. The PGA of after-shock might have been sufficient.
- Countermeasures should be designed for all potential landslides using the residual shear strength and the dynamic stability analysis, before the occurrence of other similar disastrous event. This study can be considered as a basis for such designs.

REFERENCES

Chigira, M., and Yagi, H. (2006). “Geological and Geomorphological Characteristics of Landslides Triggered by 2004 Mid Niigata Prefecture Earthquake in Japan”, *Engineering Geology*, 82, 202-221.

Japan Landslide Society, Niigata (2004). “Urgent Report of the Landslide Disaster by the Nid-Niigata Prefecture Earthquake 2004”.

Tuladhar, G.R., Tiwari, B., and Marui, H. (2007). “Post earthquake evaluation of Higashi Takezawa landslide located at Niigata Prefecture of Japan”, Geotechnical Special Publication, ASCE, no. 160, pp 8 (1-10).

Yanagisawa,Y., Kobayashi, I., Takeuchi, K., Tateishi, M., Chihara, K., and Kato, H. (1986). “Geology of the Ojiya district”, Geological Survey of Japan, Quadrangle Series (scale 1:50,000), Niigata 7 (50).

Statistical risk analysis of groundwater pollution

Vincenzo Francani[1] and Paola Gattinoni[2]

[1]Full Professor of Applied Geology, D.I.I.A.R., Polytechnic of Milan, P.zza L. da Vinci 32, 20133 Milan (Italy); vincenzo.francani@polimi.it
[2]Researcher in Applied Geology, D.I.I.A.R., Polytechnic of Milan, P.zza L. da Vinci 32, 20133 Milan (Italy); paola.gattinoni@polimi.it

ABSTRACT: The phenomena that can affect the engineering works development and their impact on the quality of soil and groundwater are very complex and they are not easy to forecast through cause-effect relationships. Also, the knowledge of the social and environmental framework is often incomplete. Indeed, the aim of the study is to point out a methodology for forecasting and preventing the groundwater pollution risk arising from engineering works and to avoid environmental troubles coming from a lack of knowledge. The proposed risk analysis model consists of three steps: a first screening, aimed to identify the potential hazards and the possible lack of data; then, the statistical site characterization, aimed to describe the elements and the processes involved in the risk assessment; finally, the risk assessment. The study of a case history allowed to verify that the application of statistical techniques and quantitative risk analysis gives an objective description of the phenomena evolution for different project solutions.

INTRODUCTION

The traditional techniques of risk analysis are usually used to assess the damage arising from existing pollution then to prevent their development. On the contrary, some engineering works can bring a great impact on the quality of soil and groundwater. Hence, a preventive risk analysis is necessary to consider the sustainability of the project.

Indeed, the aim of the study has been to frame a risk analysis model able to solve these problems. That is to prevent pollution arising from engineering works and to avoid environmental troubles coming from a lack of knowledge. A case history, concerning an industrial site involved in an hydrocarbon pollution, illustrates the suggested risk analysis approach. The study has been developed through a statistical approach, based on the monitoring data analysis, and it has allowed the probabilistic assessment of: the pollution hazard, the groundwater vulnerability and the possible residual risk.

THE RISK ANALYSIS MODEL APPLIED TO A CASE HISTORY

First of all, the studied area has been split in four homogeneous sectors, with regard to the industrial activity and the related pollution danger. Then, the suggested risk analysis model has been applied in three steps:

1. a first screening, aimed to identify the potential hazards (as a function of the project and the environmental setting) and a possible gap in the data (for quantity, quality or structure), that has to be filled with the monitoring activity (Miles et Al., 1999);
2. the site characterization, aimed to describe the elements and the processes (through statistical analysis of data) involved in the risk assessment (Beretta, 2004);
3. the risk assessment, as the probability that a pollution occurs in the project area, also taking into account prevention and mitigation works.

ANALYSIS OF THE CURRENT STATE OF THE KNOWLEDGE: DANGER INDICES

The indices describing the hazard involved in the project can be classified as:

- informative indices: the monitoring network has to meet to minimal requirements, above all in terms of homogeneity with regard to the geological setting; for example Grath et Al. (2001) define an index for the homogeneity ot the monitoring network:

$$R_U = \frac{37.7}{dist_{ave}\sqrt{n / Area}}[\%] \tag{1}$$

  where n is the monitoring points number, $dist_{ave}$ the minimum average distance from a monitoring point; a monitoring network is suitable and homogeneous if $R_U \geq 80\%$ and $dist_{ave} \geq (Area)^{0.5}/10$;
- socio-economical indices: such as land use, economical trend (growing, stagnation or recession), state of implementation of the planning tools aimed to the water resources protection, any remediation works. These indices are very important for the assessment of both the vulnerability and the maximum acceptable concentration of the pollutants;
- technical indices: especially the effective vulnerability defined as:

$$V_e = \frac{c}{c_{\max}} \qquad if \quad c < c_{\max} \tag{2}$$

  where c is the input concentration of the pollutant and c_{max} is the maximum acceptable input concentration, depending on the groundwater quality. Actually, in the blending point between the uphill flow (having discharge Q and contaminant concentration C) and the input of the pollution (discharge q and concentration c), the contaminant concentration in groundwater C_0 is:

$$C_0 = \frac{cq + CQ}{q + Q} \tag{3}$$

This analysis of the current state of knowledge allows: to arrange the monitoring network, to identify the dangers and to assess the vulnerability.

For the studied area, the monitoring network has been operating since 1995 and it assures an adequate covering of the area, although the informative indices point out a lack of monitoring points in some sectors ($R_u < 80\%$, Table 1).

The analysis of the time series shows rising trends for the main contaminants (trichloroethylene *TCE* and tetrachloroethylene *PCE*), although with different rates (Fig. 1).

As for the vulnerability, the aquifer has a low trasmissivity ($T \cong 4*10^{-8}$ m^2/s) and a fair moderate gradient ($i \cong 0.1\%$); then, the unit discharge is quite low ($q_u \cong 4*10^{-8}$ m^2/s). Considering an effective infiltration equal to 10^{-8} m/s, the c_{max} of the different contaminants can be estimated. The obtained results point out a high vulnerability for manganese and a smaller one for iron and arsenic (Table 2).

Table 1. Surface covering of the different sectors of the studied area, according to the Garth's formula (2001).

Sector	A [m^2]	n	dist$_{ave}$ [m]	R$_u$
1	474000	14	87	80%
2	895000	19	134	61%
3	1574000	27	166	55%
4	1719000	26	164	59%

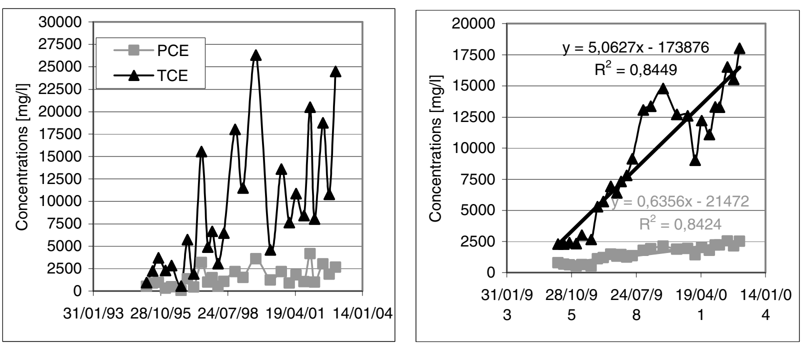

(a) (b)

FIG. 1. (a) Trends of the *PCE* and *TCE* concentrations and (b) their mobile averages.

Table 2. Values of the maximum acceptable input concentration c_{max} of some contaminant. C_m is the current average concentration and *CSC* is the concentration threshold (DL 152/06).

	CSC [μg/l]	C$_m$ [μg/l]	c$_{max}$ [μg/l]
Arsenic	10	0,02	49,92
Iron	200	4,86	980,56
Manganese	50	32	122,00

CHARACTERISATION OF THE POLLUTION

A probabilistic approach to the groundwater pollution study has to join the traditional techniques of analysis (aimed to identify the contamination sources and to forecast the pollution progress) with statistical tools such as kriging, association and correlation indices and Monte Carlo simulation.

Particularly, the statistical analysis of the monitoring data has to consider:

- the average concentrations and their variability in homogeneous areas, to describe the pollution (Vieira et Al., 1983);
- the relationships between contaminants, through the assessment of association and correlation indices, that are very important to identify the pollution source (See et Al., 1992);
- the spatial structure of the contamination (widespread, plumes, hot-spots), to map the most polluted areas and to point out their evolution (Beek et Al., 1992);
- the possible relation between piezometrical level and pollution, linked to a release of contaminants from the aquitard (Dhiman et Al., 2002).

The statistical analysis of the monitoring data allows the description of the current state of the groundwater pollution (intensity and size). Also, it points out the recurring phenomena and the possible dependence between the trends of different pollutants.

Particularly for the studied area, the analysis of the frequencies and the average concentrations in Sector 1 (Fig. 2 and 3) shows the predominance of the contaminants involved in the acetylene technology and their degradation products (mainly *TCE* and *PCE*, trichloroethane *TCA* and tretrachloroethane *PCA*, dichloroethylene *DCE* and vinyl chloride *CVM*). In Sectors 2, 3 and 4 both the frequencies and the average concentrations of dichloroethane *DCA*, *TCA* and hexachlorobutadiene *ExClBut* increase, whereas *TCE*, *DCE* and *CVM* decrease (Pouse et Al., 1992).

Subsequently, the pollution data for the different compounds have been compared to illustrate:

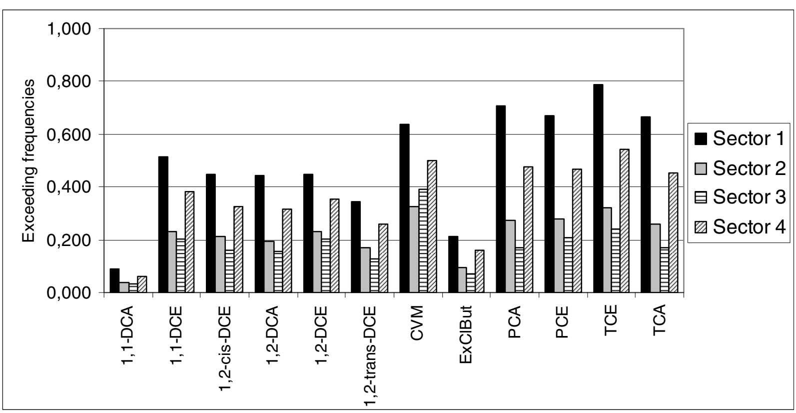

FIG. 2. Exceeding frequencies of the thresholds (DL 152/2006) for some contaminant in the different sectors of the studied area.

- the main sets and their relationships with the industrial activities of the area,
- the possible correlation between the different contaminants,
- the spatial data correlation, meaning possible plumes.

The analysis of the correlation indices (Fig. 4) can give very important information about pollution origin and processes. Particularly, the concentrations of *PCE-TCE* appear to be correlated, above all in the Sector 1 (correlation index ρ > 0.7). Moreover, the correlation between the *CVM* and the *DCE* is very significant ($\rho \approx 0.8$), with a decrease only in Sector 4 ($\rho < 0.35$). These results emphasize that the pollution originates from the acetylene technology used in the industrial activity of Sectors 1, 2 and 3 and from the consequent degradation processes. In confirmation of that, the *CVM* is never found without his harbingers; on the contrary, the *DCE*, *TCE* and/or *PCE* can be found also without the *CVM*, with different frequencies in the different sectors. Whereas the situation is quit different in Sector 4, where the source of the contamination has been found in a rubbish tip.

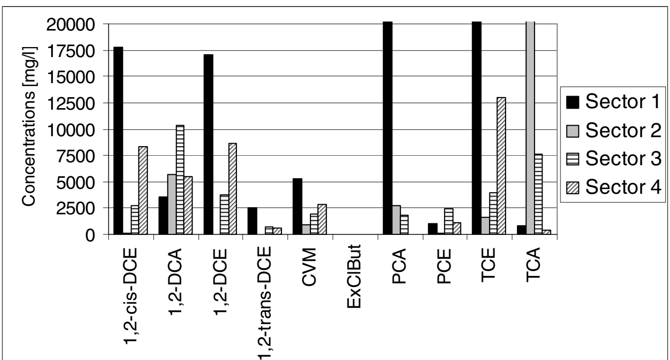

FIG. 3. Comparison between the groundwater concentrations of the most recurring contaminants.

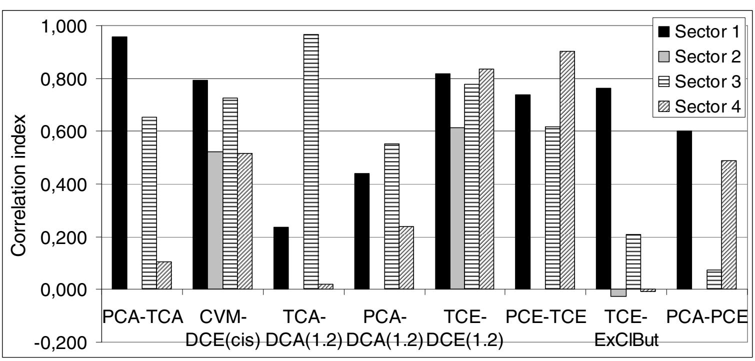

FIG. 4. Correlation indices between the concentrations of some contaminants in the different sectors of the studied area.

Finally, the geostatistical analysis shows that, in the groundwater, there are no plumes of contaminant. Precisely, the variograms of the main contaminants (for instance the *CVM*) show a nugget effect (Fig. 5a); such an effect is evidence of the great variability of the pollution and it points out that trends do not exist for small lag distances. Therefore, the structure of the pollution can be defined as “hot spots”, having size less than 200m (Fig. 5b).

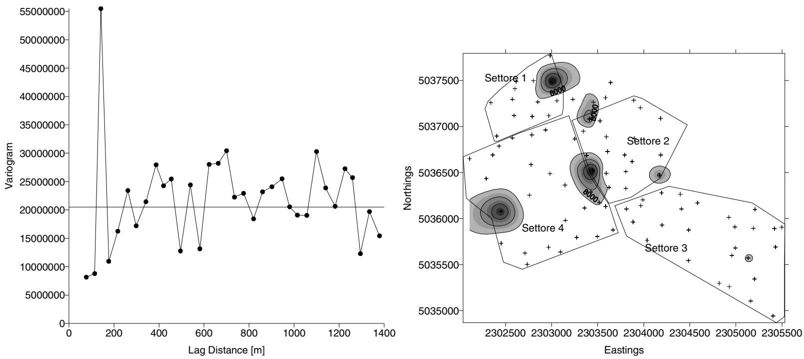

(a) **(b)**

FIG. 5. (a) Variogram of the *CVM* and (b) corresponding pollution map.

QUANTITATIVE ASSESSMENT OF THE POLLUTION RISK

A pollution risk assessment is generally based on a time series analysis of the pollution events and their triggering phenomena. Generally, it can be referred to:

- the current risk with regard to both a new contamination event and an existing pollution process,
- the future risk resulting from the development of an existing pollution process and with regard to remediation works.

The approach depends on the typology of the pollution event:

- single catastrophic event (instant phenomena);
- recurring events, with frequency depending on the pollution source and climatic characteristics;
- continuum and widespread pollution processes.

Concerning the rare events, there are problems collecting a significant set of data. If data are available, the risk analysis is based on the Poisson’s statistical model. In other words the number of events in a time unit follows the Poisson distribution ($\lambda=1/\beta$), whereas the waiting time for the next event follows an Exponential distribution (β), so that the waiting time for n events follows a Gamma distribution (n, β).

For continuum pollution processes, the analysis of the historical series of data allows to assess the recurrence time T of events exceeding an intensity threshold x_T:

$$P(x \geq x_T) = \frac{1}{T} = \frac{m}{n+1} \tag{4}$$

where m is the number of exceeding events among n observations. Then, the risk R

is the probability that the threshold value is exceeded in a specific time interval N:

$$R = 1 - [1 - P(x \geq x_T)]^N = 1 - \left(1 - \frac{1}{T}\right)^N \quad (5)$$

For the case study, the current pollution risk can be assessed on the basis of the frequency data, as the probability that the contaminant concentration exceeds a critical threshold. Figure 2 shows very high values of risk in Sector 1 for *TCE, PCE, TCA* and *PCA*.

Concerning the risk of a new pollution event, the example of the manganese has been analysed, assuming the possible bursting of a pipe. Considering a historical series of past events, the hazard H can be assessed with reference to a specific intensity I and interval space (Table 3). Since the risk R can be assessed from the product of the hazard H and the vulnerability V_e, the following variables have been assessed (Table 4) on the basis of the monitoring data:

- c_{max} with regard to the aquifer characteristics and the maximum suitable concentration (CSC = 0.05mg/l),
- the effective vulnerability V_e as a function of the bursting characteristics (outgoing discharge per unit of length and his contaminant concentration).

Because of the high vulnerability of the aquifer, the risk (even if it is always low) increases for events having less intensity and high hazard.

Table 3. Hazard *H* of a contamination event as a function of the intensity *I* and the interval space.

Space of time	H(I = 10 m^3)	H(I = 5 m^3)
1 year	0.066	0.117
2 years	0.125	0.209
5 years	0.261	0.378
10 years	0.390	0.440

Table 4. Annual risk *R* of contamination for the manganese with regard to events having intensity: a) 10 m^3; b) 5 m^3.

(a)

	Sector			
	1	2	3	4
c_{max} (mg/l)	0.08	0.08	0.07	0.09
c (mg/l)	0.1	0.1	0.1	0.1
V_e	1	1	1	1
R	**0.066**	**0.066**	**0.066**	**0.066**

(b)

	Sector			
	1	2	3	4
c_{max} (mg/l)	0.12	0.12	0.10	0.13
c (mg/l)	0.1	0.1	0.1	0.1
V_e	0.839	0.859	1	0.752
R	**0.098**	**0.101**	**0.117**	**0.088**

Actually, the intensity and the size of the pollution change, both for the natural flow of the groundwater and in consequence of possible remediation works. Then, the pollution evolution in space and time has to be studied through the implementation of a performance function, describing the limit state of the system. Generally, this performance function requires a Monte Carlo simulation, aimed to determine the probability distributions of the variables involved in the risk assessment. For instance, in the pollution risk assessment the performance function can be written as a contaminants mass balance or it can be simulated through a transport model; then the risk R is the probability that the contaminant concentration exceeds the threshold value, depending on the geological, morphological, climatic, etc. setting:

$$R = p[C(X_1, X_2, ..., X_n) < C_{threshold}] \tag{6}$$

CONCLUSIONS

The paper deals with a method for forecasting and preventing the groundwater pollution risk arising from engineering works and to avoid environmental troubles coming from a lack of knowledge. The study of a case history has verified that the application of statistical techniques points out the minimum requirements for number and uniformity of the monitoring data, useful for a probabilistic risk assessment. Moreover the statistical analysis of the monitoring data allows:

- the description of the groundwater pollution (in term of intensity and size);
- the detection of the recurring phenomena and the possible dependence between the trends of different pollutants;
- the individuation of the pollution sources and processes.

Finally the quantitative risk analysis gives an objective description of the phenomena evolution, useful for future projecting. Particularly the risk comes out to be high because of the existing pollution, whereas for the future development of the area the risk arises chiefly from the high vulnerability of the aquifer.

REFERENCES

Beretta, G.P. (2004). "Il trattamento e l'interpretazione dei dati ambientali." Pitagora Editrice, Bologna.

Beek, E.G., Stein, A. and Janssen, L.L.F. (1992). "Spatial variability and interpolation of daily precipitation amount." *Stochastic Hydrol. Hydraul*, 6, pp.209-221.

Dhiman, S.D. and Keshari, A.K. (2002). "GIS based correlation between groundwater quality parameters and geological units." *Map India 2002*.

Grath, J., Scheidleder, A., Uhlig, S., Weber, K., Kralik, T. and Gruber D. (2001). "The UE Water Framework Directive: Statistical aspects of the identification of groundwater pollution trends, and aggregation of monitoring results. Final Report." *Austrian Federal Ministry of Agriculture and Forestry, Environment and Water Management, European Commission*.

Miles, S. B. and Ho, C.R. (1999). "Application and issues of GIS as tool for civil engineering modelling." *Journal of computing in civil enginnering*, ASCE 13, 3, pp.144-161.

Poulse, M. and Keuper, B.H. (1992). "A field experiment to study the behavior of tetrachloroethylene in unsaturated porous media." *Environmental. Science and Technology*, 26, 5, pp. 889-895

See, R.B., Naftz, D.L. and Qualls, C.L. (1992). "GIS- assisted regression analysis to identify sources of selenium in streams." *Water Resources Bulletin*, AWRA 28, 2, pp.315-330.

Vieira, S.R., Hatfiled, J.L., Nielsen, D.R., and Biggar, J.W. (1983). "Geostatistical theory and applications to variability of some agronomical properties." *Hilgardia*, 51, 3, pp. 1-75.

Lessons from Catastrophic Dam Failures in August 1975 in Zhumadian, China

Yao Xu,[1] Limin Zhang,[2] and Jinsheng Jia[3]

[1]Research Assistant, The Hong Kong University of Science and Technology, HKSAR, China; xuyao@ust.hk
[2]Associate Professor, The Hong Kong University of Science and Technology, HKSAR, China; cezhangl@ust.hk
[3]Professor, China Institute of Water Resources and Hydropower Research, Beijing, China; jiajsh@iwhr.com

ABSTRACT: During 4-8 August 1975, an extreme storm occurred in Henan Province, China. The maximum 5-day rainfall reached a record of 1,631 mm. Two large dams (Banqiao Dam and Shimandan Dam), two medium dams (Tiangang Dam and Zhugou Dam), and 58 small dams failed from overtopping in the storm event. The breach peak flow rate was as high as 78,100 m^3/s from the Banqiao reservoir and 30,000 m^3/s from the Shimantan reservoir. The breaching of these dams caused an inundated area of 12,000 km^2, a death toll of over 26,000, and economic loss of more than RMB10 billion. This paper introduces 26 dam failures in a smaller region of Zhumadian, i.e., Banqiao Dam, Zhugou Dam, and 24 small dams. The catastrophic event is described in detail especially for Banqiao Dam and Zhugou Dam. The causes and mechanisms of the principal failures are discussed, as well as the influence of an upstream dam failure on the downstream dams. Lessons from the catastrophe are discussed.

INTRODUCTION

Henan Province is located in the central part of China, which is about 700 kilometers southwest of Beijing. It is flat in the east and mountainous in the west. During 4-8 August 1975, an extreme storm occurred in Henan; the maximum 5-day rainfall reached a record of 1,631 mm (Fig. 1). Two large dams (Banqiao Dam and Shimandan Dam), two medium dams (Tiangang Dam and Zhugou Dam), and 58 small dams failed from overtopping in the storm event. The breach peak flow rate was as high as 78,100 m^3/s from the Banqiao reservoir and 30,000 m^3/s from the Shimantan reservoir. The breaching of these 62 dams caused an inundated area of 12,000 km^2, a death toll of over 26,000, and economic loss of more than RMB10 billion. Many of those dams were rebuilt, e.g. Banqiao Dam in 1993 and Shimantan Dam in 1996.

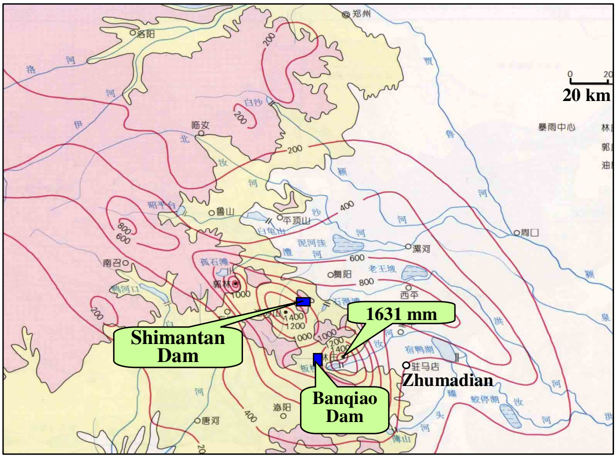

FIG. 1. Rainfall contours during 4-8 August 1975 in Henan Province, China.

In the August 1975 event, Zhumadian Prefecture of Henan suffered most from the floods. This paper introduces failure of 26 dams in Zhumadian, including Banqiao Dam, Zhugou Dam, and 24 small dams. The purpose of this study is to investigate the primary causes of the dam failures and the effect of failure of one or several dams on the safety of other dams in a system. The catastrophic event in Zhumadian is described in detail, especially for Banqiao Dam and Zhugou Dam. The causes and mechanisms of the principal failures are discussed, as well as the influence of an upstream dam failure on the downstream dams in a flood protection system. Finally, lessons from this catastrophe and recommendations regarding the dam safety are discussed.

OVERVIEW OF THE ZHUMADIAN REGION

Zhumadian is located in the south of Henan Province. Two major rivers, Hong River and Ru River, run east through Zhumadian and converge to Huai River. The Hong and Ru river basin is around 12,380 km^2, which covers most of the Zhumadian region. The average annual rainfall is in the range of 800-1000 mm, of which 60%-70% concentrates in the summer, particularly in July and August. It is noted that the eyes of rainstorms were always located at the upstream of Banqiao Dam in the history. Before the August 1975 event, 4 large reservoirs, 7 medium reservoirs, and 157 small reservoirs had been constructed in the Zhumadian flood protection system. The four large reservoirs were Songjiachang, Banqiao, Boshan, and Suyahu, of which the last three were on Ru River (Fig. 2). It is indicated in Fig. 2 that the failed medium dam, Zhugou Dam, was on Zhentou River, a tributary of Ru River. The small dams are not shown in Fig. 2, due to their far less importance in the whole system.

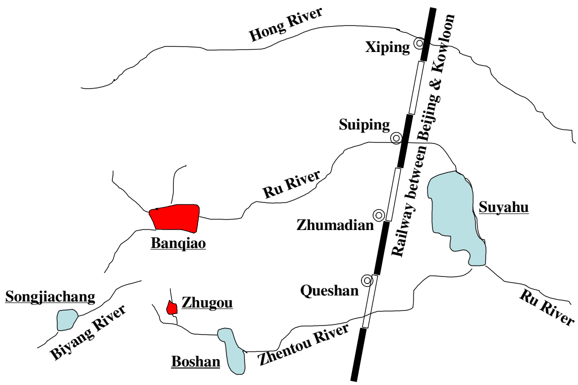

FIG. 2. Sketch of distribution of major dams in Zhumadian (Banqiao and Zhugou failed in the August 1975 event).

RAINSTORM CHARACTERISTICS

The rainstorm in Henan Province during 4-8 August 1975 lasted five days. Figure 1 shows the rainfall contours. The measured maximum rainfalls during different intervals of time are listed in Table 1. The maximum 1-day rainfall of 1060 mm even exceeded the average annual rainfall of 800-1000 mm. The rainstorm had two peaks on 5 and 7 August, respectively. For instance, the rainfall intensities at Banqiao Dam were 448 mm on 5 August, 190 mm on 6 August, and 748 mm on 7 August, respectively. The rainfall intensity changed from slight to heavy, with the precipitation being highly concentrated at the later stage. This disadvantageous feature undoubtedly increased the difficulty of dealing with flood protection problems. Two storm eyes appeared in the rainstorm, one close to the Banqiao reservoir and the other close to the Shimantan reservoir (See Fig. 1).

Table 1. Measured maximum rainfalls in different time intervals

Time interval	1 hour	6 hours	12 hours	1 day	3 days	5 days
Rainfall (mm)	190	830	954	1060	1606	1631

FAILURE OF BANQIAO DAM

Banqiao Dam was built in 1952 on Ru River, as part of a project for flood control for the Huai River basin. It was rebuilt in 1956 to raise the dam height and increase the reservoir capacity. The dam was designed to survive a 1-in-1,000-year flood (306 mm rainfall per day). This clay-core earthfill dam was 24.5 m high and had a storage capacity of 492 million m³, with 375 million m³ of it reserved for flood control. The dam crest was 6 m wide and 2020 m long, at elevation 116.34 m. The elevation of the parapet wall was 117.64 m. The total maximum discharge was designed as 3,092 m^3/s, of which 1,800 m^3/s was contributed from the primary spillway, 1,160 m^3/s from the supplemental spillway, and 132 m^3/s from the conduit. The general information of Banqiao Dam is presented in Table 2.

Table 2. General information of Banqiao and Zhugou and 24 small earthen dam failures in Zhumadian (Modified based on ZWRA 1997)

Name	Height (m)	Length (m)	Capacity (10^6 m^3)	Year built	Design flood frequency (year)	Failure mode	Average breach width (m)
Banqiao	24.5	2020	492	1952	1000	Overtopping	350
Zhugou	23.5	308	15.44	1970	500	Overtopping	159
Small1	20.5	532	7.4	1957	-	Overtopping	100
Small2	13.4	830	3.58	1957	-	Overtopping	30
Small3	14	225	2.06	1974	100	Overtopping	50
Small4	13.5	100	1.24	1969	-	Excavation	30
Small5	8	300	0.24	1965	50	Excavation	20
Small6	12	104	0.6	1970	100	Overtopping	40
Small7	14	110	0.105	1964	50	Overtopping	30
Small8	11	65	0.15	1957	100	Overtopping	15
Small9	15	250	0.5	1958	50	Overtopping	20
Small10	12	80	0.112	1968	50	Overtopping	60
Small11	9	100	0.1	1963	50	Overtopping	10
Small12	10	150	0.12	-	50	Overtopping	40
Small13	13	90	0.4	1973	-	Overtopping	30
Small14	10	170	0.2	1958	50	Overtopping	40
Small15	7	50	0.12	-	50	Overtopping	20
Small16	9	150	0.11	1974	-	Overtopping	22
Small17	8	140	0.12	1974	-	Overtopping	22
Small18	6	300	0.46	1973	-	Overtopping	20
Small19	12.1	120	0.18	1973	50	Overtopping	29
Small20	20	130	0.6	1968	100	Overtopping	70
Small21	7.5	100	0.2	1969	-	Overtopping	30
Small22	13	140	0.216	1972	-	Overtopping	30
Small23	8	500	0.84	1957	50	Overtopping	70
Small24	8	50	0.8	1969	50	Overtopping	21

As introduced in the former section, the rainfalls had two peaks near the Banqiao reservoir, 448 mm on 5 August and 748 mm on 7 August. Accordingly, two flood peaks flowed into the Banqiao reservoir before the dam failure with the maximum inflows of 7,500 m^3/s on 5 August and 13,000 m^3/s on 7 August. Correspondingly, the water levels in the reservoir rose very quickly on the two days. The water levels jumped from 107.87 m to 112.07 m during 19:00 pm on 5 August – 06:00 am on 6 August, and from 114.79 m to 117.94 m during 17:00 pm on 7 August – 01:00 am on 8

August. In total, a huge volume of flood, as large as 697 million m^3, flowed into the Banqiao reservoir, which exceeded the maximum capacity of 492 million m^3. Note that the Banqiao reservoir lost a certain capacity for flood control by an over storage of 32 million m^3 prior to the flood season. The processes of the inflow and the water level in the Banqiao reservoir are shown in Fig. 3.

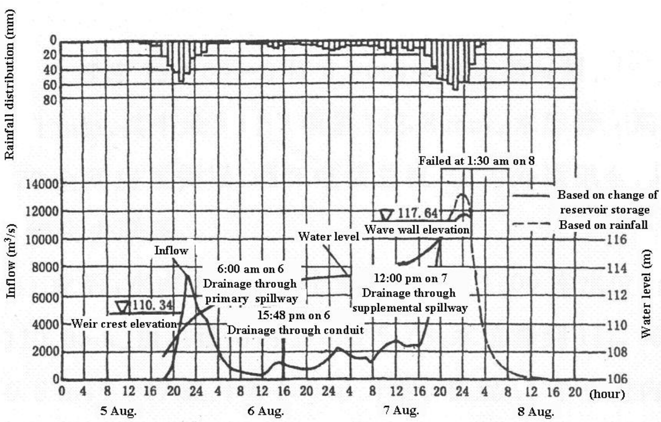

FIG. 3. Process of inflow and water level elevation in the Banqiao reservoir (Modified based on Ru & Niu 2001)**.**

The overtopping started at 23:30 pm on 7 August, when the reservoir water level reached 117.65 m. In terms of the definition summarized by Wahl (1998), the breaching of an earthen dam often includes two phases, the breach initiation phase and the breach formation phase. The breach initiation phase begins with the first flow over or through a dam, and ends at the start of the breach formation phase. The breach formation phase begins with the first breaching of the upstream face of the dam until the breach is fully formed. In this case, the first breaching of the upstream face started at 01:30 am on 8 August. It was followed by a rapid increase of the outflow and erosion, which led to the final failure. Therefore, the dam failure was considered to be initiated at 01:30 am on 8 August (See Fig. 3). The breaching of the dam ended at 07:00 am on 8 August, with the peak outflow of 78,100 m^3/s appearing at 02:57 am. At last, the reservoir was emptied at 10:00 am. The breach initiation time and the breach formation time were 2 hours (23:30 am on 7 August-01:30 am on 8 August) and 5.5 hours (01:30 am - 07:00 am on 8 August), respectively; the time to breach and empty reservoir proposed by Singh and Snorrason (1984) was 10.5 hours (23:30 am on 7 August-10:00 am on 8 August). The dam breach section after failure is shown in Fig. 4(a) and the corresponding simplified breach is presented in Fig. 4(b). The trapezoidal breach had a top width of 372 m at elevation 115.54 m and a bottom width of 210 m at elevation 86 m. The total volume of the eroded earthfill by overtopping was more than 1 million m^3. Note that the original foundation elevation was 91.84 m. It is noted that several initial small breaches developed firstly at the location which had not been reinforced in the 1956 re-build project. The weak location was symbolized by a thin clay corewall and a large settlement due to the sludge at the foundation being not completely cleaned.

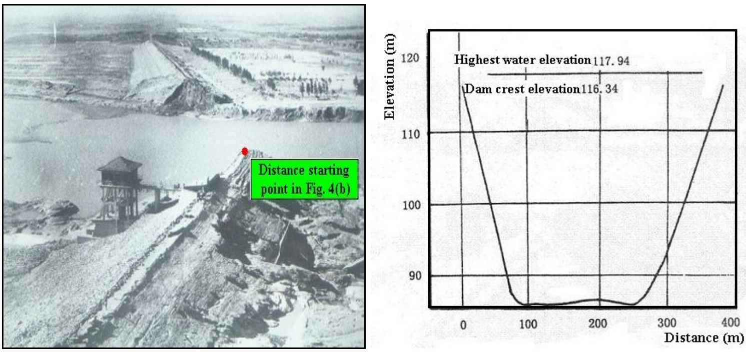

FIG. 4. (a) Banqiao Dam after failure; (b) Sketch of the dam breach (Modified based on Ru & Niu 2001)**.**

FAILURE OF ZHUGOU DAM

Zhugou Dam was built in 1970 on the Zhentou river (See Fig. 2). It was an earthfill dam with a clay corewall, which was designed to survive a 1-in-500-year flood (414 mm rainfall per day). The dam was 23.5 m high and had a storage capacity of 15.44 million m^3. The dam crest was 5 m wide and 308 m long, at elevation 186.5 m. The maximum design discharge of the spillway was 125 m^3/s. The general information of Zhugou Dam is shown in Table 2.

The rainfall and the water levels in the Zhugou reservoir during 4-8 August are shown in Table 3. The rainfall reached a peak value of 682.7 mm on 7 August, which produced a maximum inflow into the reservoir of 1,170 m^3/s. As a whole, a large volume of flood of 23.1 million m^3 flowed into the Zhugou reservoir before the dam failure. The dam failed at 22:34 pm on 7 August due to overtopping. The breaching was firstly located in the middle part of the dam, which was lower than the two sides by 0.3 m. This was due to the fact that the sand cover at the dam crest was not compacted, which caused significant settlement in the middle of the dam. The average width of the final breach was 159 m, 41% of the original dam length.

Table 3. Rainfall and water level elevation in Zhugou Reservoir during 4-8 Aug.

Date	4 Aug.	5 Aug.	6 Aug.	7 Aug.	8 Aug.
Rainfall (mm)	27.8	182.8	156.7	682.7	2.7
Water level (m)	172.53	172.58	177.36	186.5	-

FAILURE OF SMALL DAMS

In addition to Banqiao Dam and Zhugou Dam, 24 small earthen dams failed in the August 1975 event. The general information of the 24 small dams is shown in Table 2. All of those 24 dams failed due to overtopping, except two failures that were caused by man-made excavations on the dams for discharging. They all failed during the period from 16:00 pm on 7 August to 00:50 am to 8 August, after the heavy precipitation on 7 August. It is particularly interesting to find that 16 of 157 small dams in Zhumadian did not fail after being overtopped. It may be due to the active protection and fight against failure by the local people. This illustrates that a dam is likely to survive the overtopping condition if proper and timely actions are taken.

SAFETY OF A DAM SYSTEM

Many large dams and numerous small dams are built along the main channel and tributaries of a major river. Those dams form a dam system. In this study, a four-dam-system on Ru River is given in Fig. 2, including Banqiao, Zhugou, Boshan, and Suyahu Dams. During the August 1975 event, the former two dams failed while the later two dams survived. Failure of Banqiao Dam did cause a severe loading condition for the downstream Suyahu Dam. The Banqiao-breach flood flowed downstream at an average speed of 6 m/s. Six hours later, a large amount of the breach flood entered the Suyahu reservoir, the highest water level in the Suyahu reservoir being just 0.34 m below the dam crest. Boshan Dam made an invaluable contribution to the safety of Suyahu Dam by storing the flood from the breaching of Zhugou Dam. If Boshan Dam had failed, Suyahu Dam would have failed and brought about greater disasters.

Obviously, Banqiao Dam and Boshan Dam on the upstream played a key role in the dam system. The safety of Suyahu Dam on the downstream was significantly affected by the performance of Banqiao Dam and Boshan Dam. The failure probability of Suyahu Dam, $P_f(Su)$, is expressed as

$$\begin{aligned} P_f(Su) &= P_f(Su \mid Ba \,\&\, Bo)P(Ba)P(Bo) + P_f(Su \mid Ba \,\&\, \overline{Bo})P(Ba)P(\overline{Bo}) \\ &+ P_f(Su \mid \overline{Ba} \,\&\, Bo)P(\overline{Ba})P(Bo) + P_f(Su \mid \overline{Ba} \,\&\, \overline{Bo})P(\overline{Ba})P(\overline{Bo}) \end{aligned} \tag{1}$$

in which, Ba represents safe Banqiao; $\overline{Ba}$ represents failed Banqiao; Bo represents safe Boshan; $\overline{Bo}$ represents failed Boshan. Often, the fourth part can be neglected due to the very small product value of $P(\overline{Ba})P(\overline{Bo})$. In the August 1975 event, $P(\overline{Ba}) = 1$, $P(Ba) = 0$, and $P(\overline{Bo}) = 0$, $P(Bo) = 1$. Therefore, $P_f(Su) = P(Su \mid \overline{Ba} \,\&\, Bo)$. The failure probability of Suyahu Dam increased significantly due to the failure of Banqiao Dam. It is indicated that although a system of dams usually enhances the capacity of flood control, it can also impose larger risks in extreme events, especially if a dam on the upstream fails. Therefore, contingency plans should be prepared in advance for each potential scenario, such as the failure of Banqiao Dam in this study, when dealing with the safety of a dam system.

CONCLUSIONS

A review of the August 1975 event in Zhumadian of Henan Province was conducted, especially for Banqiao Dam and Zhugou Dam, and the safety of a four-dam system in the catastrophe was discussed. Several findings can be concluded:

(1) The primary cause for the 26 dam failures by overtopping is the insufficient flood control capacity. Banqiao Dam was designed to survive a 1-in-1,000-year flood; Zhugou Dam was designed to survive a 1-in-500-year flood; the other 24 small dams were designed to survive a 1-in-100-year or 1-in-50-year flood (See Table 2). However, the rainstorm during 4-8 August 1975 actually produced a flood larger than 1-in-10,000-year, far exceeded the flood control capacities of these failed dams.

(2) Poor management of the reservoirs also contributed to the dam failures. For instance, the Banqiao reservoir lost a certain capacity for flood control by an over storage of 32 million m^3 prior to flood season.

(3) In addition to the engineered dam safety, a powerful warning and emergency response system is also very important, which may prevent a dam failure or minimize the impact of a dam failure on the downstream region. A lack of an in-place emergency action plan or a warning system in the August 1975 event impaired the ability to minimize the losses from dam failures.

(4) Although a system of dams usually enhances the capacity of flood control, it can also impose larger risks in extreme events, especially if a dam on the upstream fails. Contingency plans should be prepared in advance for each potential scenario when dealing with the safety of a dam system.

ACKNOWLEDGMENTS

The authors acknowledge the support from the Ministry of Water Resources of the People's Republic of China (key research project "Study of reservoir dam failure prevention and mitigation"), the Research Grants Council of Hong Kong SAR (Project No. 622207), and the Hong Kong University of Science and Technology (Project RPC06/07.EG19).

REFERENCES

Ru, N. H. and Niu, Y. G. (2001). *Embankment Dam-Incidents and Safety of Large Dams*. Water Power Press, Beijing, China (in Chinese).

Singh, K. P. and Snorrason, A. (1984). "Sensitivity of Outflow Peaks and Flood Stages to the Selection of Dam Breach Parameters and Simulation Models." *Journal of Hydrology*, Vol. 68: 295-310.

Wahl, T. L. (1998). "Prediction of Embankment Dam Breach Parameters." *DSO-98-004, Dam Safety Research Report*, U.S. Department of the Interior Bureau of Reclamation, Dam Safety Office.

ZWRA (1997). *Log of the August 1975 storm event in Zhumadian*. Zhumadian Water Resources Authority (ZWRA), Henan Province, China (in Chinese).

Rapid Levee Assessment For Reliability And Risk Analysis

Hollie L. Ellis[1], Christopher B. Groves[2], P.E., A.M. ASCE, Gregory R. Fischer[3], P.E.

[1] Sr. Vice President, Shannon & Wilson, Inc., 400 N 34th St., Seattle, WA 98003-8600; hle@shanwil.com
[2] Sr. Vice President, Shannon & Wilson, Inc., 2043 Westport Center Drive, St. Louis, MO 63146-3564; cbg@shanwil.com
[3] Sr. Vice President, Shannon & Wilson, Inc., 1400 Blake St., Denver CO 80202-1488; grf@shanwil.com

Abstract: A rapid and comprehensive assessment of field conditions is an essential first step in the application of reliability and risk concepts to the analysis of levee safety. This paper presents a review of levee failure causes and mechanisms and describes methods that can be used to quickly and effectively incorporate reliability and risk into levee maintenance or repair decision-making processes. The methods include rapid field assessment of levee conditions; analysis of the causes and mechanisms of levee failure; and ranking levees by a first-order estimate of reliability. An example application of the methods is presented based on work currently underway on the Green River levee system in King County, Washington.

INTRODUCTION

Levee owners and managers are continually faced with difficult choices for the allocation of limited resources to levee maintenance and repair. One approach to addressing this dilemma is to apply the concepts of reliability and risk to help decision-makers and other stakeholders understand the causes, modes, and consequences of levee failure. This approach requires that decision-makers have some level of information that is common to all their levees in order to choose to repair Levee A instead of Levee B.

The general steps to be taken in applying the concepts of reliability and risk to levee assessment are a) identify the potential causes and modes of levee failure, b) assemble and review available information, c) complete a rapid assessment to identify and categorize specific problem areas and issues, and d) perform a detailed risk analysis. An important outcome of these steps is to identify and, to the extent possible, quantify the unknowns and uncertainties that may affect future levee performance. An understanding of the unknown and uncertain is often as important to the decision process as the explicit knowledge that may exist.

LEVEE FAILURE CAUSES AND MODES

To evaluate the condition and level of protection provided by a levee, it is necessary to understand the causes and modes of levee failure. Some of the failure causes and failure modes that should be considered in a levee evaluation program are presented below.

Levee Failure Causes

High Water Event

High water events are the most common reason for constructing levees and appear to be the most common cause of levee failures. The severity of the potential impact of a high water event will depend on height above normal level, degree of saturation of the levee and foundation, velocity, duration, and subsequent rate of drawdown. Although overtopping of a levee is the most obvious consequence of high water events, other effects at water levels less than overtopping level can result in levee failure. For example, scour or seepage effects can cause failures at water levels well below the top of a levee.

Rapid Drawdown

Rapid drawdown could be considered to be part of a high water event, but is addressed separately because it represents a distinct hazard to earth slopes and embankments. Rapid drawdown is a condition in which water next to a saturated embankment falls away quickly, resulting in excess pore water pressures in the embankment which leads to a reduction in safety or embankment failure.

Earthquake

Earthquake-induced levee failures are primarily a concern for 'wet' levees that protect against a persistent body of water. An earthquake can cause embankment or foundation failure, allowing the persistent body of water held by the levee to flood immediately. Although it is unlikely that an earthquake and high water event would occur simultaneously at a dry levee, it is possible that an earthquake could cause slope failure, basal sliding, settlement, or cracking that could lead to failure during subsequent high water events.

Seepage

Seepage is water flow through a levee (throughseepage) or under a levee foundation (underseepage) and is the result of differential water pressure from the water-side to the land-side of a levee. Seepage can occur in any soil but is generally more problematic in soils that are loosely compacted or at an interface between fine-grained and coarse-grained soil layers. Seepage can also be initiated in animal burrows and along plant roots or structures such as drain pipes that pass through or under a levee. Evidence of underseepage is sometimes seen as eruptions of soil and water on the land-side of the levee, also known as sand boils.

Channel Migration and Sedimentation

Channel migration and sedimentation create changes in geometry that may not have been anticipated in levee design. The effects of the geometric changes may include loss of levee freeboard or initiation of water-side toe scour.

Impacts

Water-borne objects with a potential to damage a levee include ships, barges, ice, logs, and debris. The effects of an impact range from surface damage that could lead to increased scour or seepage potential to complete failure of the levee depending on the magnitude and timing of the impact.

Levee Failure Modes

For purposes of evaluating future levee performance, it is necessary to understand the modes or mechanisms of potential failure. A levee failure mode (mechanism) is a description of the physical process or processes that result in unwanted water passing through or over a levee. Several attempts have been made to systematically categorize levee failure modes, for example Benjamin (1984) and Vriling (2003). The identified modes generally include variations of breaching, surface and internal erosion, slope movement, and mechanical failure of drainage or pumping systems as described below.

Overtopping and Breaching

Overtopping without additional structural failure of the levee embankment or wall is generally not considered a failure of the levee although the protected population may perceive it as a failure. A lack of sufficient levee height may be due to the rare and extreme nature of the event and, in this case, is not considered a design flaw. Other design or construction flaws, post-construction settlement of the levee, or post-construction channel changes that result in overtopping could be considered a levee failure.

Foundation Failure

Levee foundation conditions are critical to levee performance, but in many circumstances the location of the levee is not a matter of choice as it would be for most other structures. It is often necessary to build levees on weak, permeable, and otherwise undesirable foundation soils. An understanding of foundation conditions and the interaction among load, levee, and foundation is essential to predicting levee performance. Foundation failure, as opposed to failure of a levee embankment, can be initiated by underseepage, throughseepage, bearing capacity failure from the weight of the levee, and liquefaction or lateral spreading during an earthquake.

Slope Failure

Slope failures are mass soil movements on either the water-side or land-side of a levee. Slope failures reduce the thickness and, in some cases, the crest height of the levee. A slope failure by itself may not result in flooding, but it can affect the future ability of a levee to perform as intended. Slope failures can result from scour, rapid drawdown, throughseepage, underseepage, earthquake, impact, and wave action. Slopes can also fail after construction if the shear strength of the slope soil is inadequate to resist the slope weight. Earthquake forces can initiate inertial, liquefaction, or lateral spreading slope failures on either side of a levee.

Settlement Failure

Settlement failure of a levee occurs when the foundation and embankment settle under the weight of the embankment to a point where the design freeboard no longer exists. In addition to loss of freeboard, settlement of a levee can result in embankment cracking, increased opportunity for throughseepage, and, in some circumstance, slope failure.

RAPID ASSESSMENT METHODS

Rapid assessment is a form of applied research and is used to quickly develop a broad overview of conditions. It is a semi-quantitative, systematic approach to observation and data collection. Rapid assessment of levees is a step to be taken before more intensive, site-specific levee reliability and risk assessments are begun. The advantages of the method are that it can be completed quickly by relatively inexperienced, but well-trained, personnel, and is cost-effective. The method has been used in the social and health sciences as well as in engineering applications (Johnson 1999, 2006, Lee & Jones 2004) similar in scope and purpose to levee assessment. The method is especially well suited to linear projects such as roadways (Kelly, et al. 2005) and levees.

To be effective, a rapid assessment must use a disciplined, but straightforward, technique so that consistent and comparable results are obtained. The authors have used a technique based on the K-T analysis developed by C. H. Kepner and B. B. Tregoe (Kepner and Tregoe, 1981). A K-T analysis consists of a) defining relevant characteristics, b) assigning relative weights to all characteristics, c) assigning a score to each characteristic for a given case, and d) computing a total score for each case by summing the product of the weights and scores. The outcome is a ranking of all cases that, in the context of levee failure, could be correlated with a probability failure. Thus, the relationship between a rapid assessment and reliability and risk analysis is based on a comparison of relative ranking to relative reliability.

The first step in establishing a K-T analysis methodology is to identify the relevant characteristics and assign rational ranges to each characteristic, usually based on the expert judgment and experience. The next step is to assign relative scores to each range. For example, the levee geometry characteristics shown in Table 1 are assigned ranges and scores based on the influence of each characteristic on slope stability. In this example, the ranges and scores are ordered such that a high score is less favorable and a low score is more favorable. The system of scores could be ordered in the opposite way. The final step is to assign relative weights to each characteristic, again based on expert judgment and experience. In the example in Table 1, the riverside slope angle was given the greatest weight among the geometric characteristics based on expert opinion that this characteristic was most important in this situation. The process of establishing characteristics, ranges, scores, and weights is repeated for all characteristics that may contribute to understanding the reliability and risk of a levee system.

After establishing the complete set of characteristics, ranges, weights, and scores, observers are sent into the field to score each levee with respect to the characteristics and ranges. The observer needs only to record the appropriate range value for each characteristic. The field observations for each levee are then compiled and weighted scores are totaled. Ranking the levees by weighted score is then a semi-qualitative ranking of the levees according to their relative reliability.

Table 1. K-T Method Example, Levee Geometry

Characteristic	Weight	Score	Condition
Height	2	3	>10 feet
		2	5 to 10 feet
		1	<5 feet
Width	1	3	<10 feet
		2	10 to 20 feet
		1	> 20 feet
Riverside Slope	3	3	<1.5H:1V
		2	1.5 to 2H:1V
		1	>2H:1V
Landside Slope	1	3	<1.5H:1V
		2	1.5 to 2H:1V
		1	>2H:1V

GREEN RIVER LEVEES RAPID ASSESSMENT

The Green River watershed in King County in western Washington State covers approximately 1,270 square kilometers (490 sq. mi.). The major watershed drainage is provided by the Green River which runs about 120 kilometers (75 mi.) from the Cascade Range to Puget Sound. Prior to completion of the US Army Corps of Engineers' Howard Hanson Dam in 1961, flooding on the Green was an almost annual event (Shannon & Wilson, 2002). The dam, built near the headwaters of the river, is primarily a flood control facility.

The lower half of the river runs through the Kent Valley with a relatively flat floodplain. More than 30 levee facilities, mostly under the jurisdiction of King County, have been constructed in the valley. The levees were originally designed to protect land that was used predominantly for agriculture, but in the intervening years the valley has changed significantly to residential, commercial, and industrial uses. The development of major distribution centers and transportation corridors in the valley mean that flooding now has impacts well beyond the limits of the floodplain.

As part of an on-going evaluation of the river and levee facilities, King County has initiated a reliability and risk analysis of the levee facilities. Shannon & Wilson has completed the rapid assessment phase of the analysis for the County (Shannon & Wilson, 2007).

The procedures used for the rapid assessment phase were based on the K-T method. The major characteristic categories considered for each levee were levee geometry, presence of revetments or erosion, maintenance and inspection history, river hydraulics, geology and soils, and protected land use as shown in Table 2. Each characteristic was assigned scores similar to those shown in Table 1.

Table 2. Green River Levee Characteristics

Category	**Characteristic**
Levee Geometry	Height
	Top Width
	Riverside Slope
	Landside Slope
Revetments And Erosion	Revetments
	Slope Face
	Animal Signs
Land Use And Infrastructure	Property Protected
	Relative Value
Maintenance And Inspection	Repair History
	Current Condition
River Hydraulics	Channel Impingement
	Channel Depth
Geology And Soils	Foundation Soil
	Levee Soil

The field effort required to score levees on both banks of approximately 40 kilometers (25 mi.) of river took about ten working days and was accomplished by one individual. For purposes of managing the levee systems, the County has defined about 30 separate levee facilities, generally determined by the high ground to high ground extent of a levee. However, based on the unique characteristics observed during the field reconnaissance, the right bank levees were divided into 53 segments and the left bank into 47 segments for purposes of scoring and relative reliability ranking (Shannon & Wilson 2007). Vegetation, pavement, and riprap covered most levees and foundation soils preventing observation of their condition except in isolated cases. Consequently, these characteristics were not included in subsequent analysis of the data.

While reviewing the field data it was decided to eliminate the land use and infrastructure scores from the initial ranking of the levees. The team decided that ranking the levees without this characteristic would provide a better measure of relative levee reliability. The land use and infrastructure scores will be used as part of a future risk assessment.

The field scores were tabulated and summed using several different characteristic weighting schemes to evaluate the influence of the weights on the relative ranking of the levees. The different weighting schemes, which were based on expert judgment, tended to exaggerate or diminish the difference in individual levee scores, but left the overall relative ranking approximately unchanged. An example of the ranking based on weighted scores for the left bank levees of the Green River are shown in Figure 1, with a high score indicating a relatively less reliable levee.

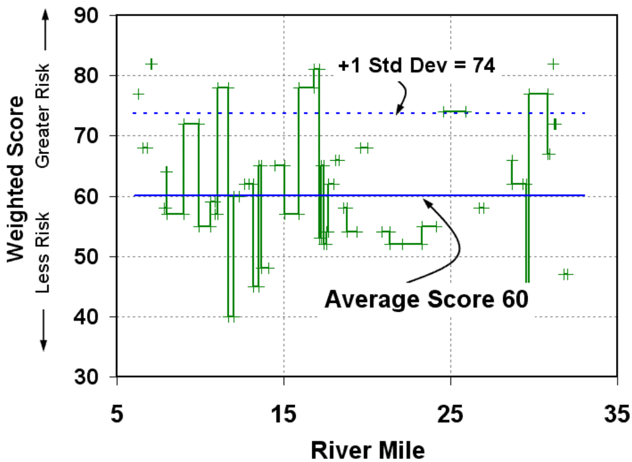

FIG. 1 Green River Left Bank Levee Scores

The levee segments with the highest scores are generally found in areas with greater levee height, lesser levee width, and steeper landside slopes. The location of past levee repairs were compared to the rapid assessment scores and appear to have some proximal relationship to levee systems having elevated scores. Although past levee repairs presumably are located in areas of the levee that previously had poor stability, one might presume that repaired sections of the levee should have relatively lower scores. While this is true in some areas, the majority of the repaired areas have higher scores, likely because the repaired segment of the levee is only a small portion of the entire levee facility.

The next phase of the Green River levee study will include more detailed analysis of levee system reliability based on the focus provided by the rapid levee assessment. The reliability analysis will be followed by a risk analysis using the US Army Corps of Engineers' Flood Damage Reduction Analysis (USACE 1998) software program

(USACE 1998). The County plans to use the risk analysis results in their levee repair and maintenance decision process.

CONCLUSION

Reliability and risk concepts have been successfully used to gain a preliminary understanding of the potential causes and modes of levee failure on the Green River in Washington. Rapid assessment methods have been used to develop a first-order ranking of the levee systems according to their relative reliability and will be used to guide more detailed risk analysis of the levee systems.

ACKNOWLEDGEMENTS

The authors wish to acknowledge Ms. Jeanne Stypula of King County's Water and Land Division and Mr. George Sills of the Engineering Research Development Center, US Army Corps of Engineers for their support and contributions to further understanding of levee reliability and risk.

REFERENCES

Benjamin, J. (1984) *Optimal reliability of lifeline levee systems under multiple natural hazards*, Benjamin & Associates

Johnson, P.A., Gleason, G., and Hey, R.D. (1999), *Rapid assessment of channel stability in the vicinity of a road crossing*, Journal of Hydraulic Engineering, American Society of Civil Engineers, 125(6), 645–652.

Johnson, P.A (2006), *Assessing stream channel stability at bridges in physiographic regions*, Federal Highway Administration Report No. FHWA-HRT-05-072

Kelly, A.J., Clifton, A.W., Antunes, P.J., and Widger, R.A. (2005), *Application of landslide risk assessment to the Saskatchewan highway network*, Landslide Risk Assessment, Hungr, Fell, Couture, and Eberhardt (eds.), Taylor & Francis Group, London

Kepner, C.H., and Tregoe, B.B. (1981), *The New Rational Manager*, Princeton Research Press, Princeton, NJ.

Lee, E.M. and Jones, D.K.C. (2004), *Landslide risk assessment*, Thomas Telford Publishing, London

Shannon & Wilson Inc. (2002), *Preliminary risk-based flood damage analysis Green River flood control zone district, King County, Washington*, report prepared by Shannon & Wilson, Inc., Seattle, WA, for King County, WA

Shannon & Wilson Inc. (2007), *Technical memorandum TM 900.10-1, field reconnaissance, Green River levee assessment, King County, Washington*, report prepared by Shannon & Wilson, Inc., Seattle, WA, for King County, WA

Shannon & Wilson Inc. (2007), *Technical memorandum TM 900.13-1, Summary of existing information, Green River levee assessment, King County, Washington*, report prepared by Shannon & Wilson, Inc., Seattle, WA, for King County, WA

US Army Corps of Engineers (1998), *HEC-FDA Flood Damage Reduction Analysis Users Manual*, Hydrologic Engineering Center, Davis CA

Vrjiling, J.K. (2003) *Probabilistic design and maintenance of water defense systems*, Proceedings, Risk-Based Maintenance of Civil Structures, Delft, Netherlands

Reliability Analysis of Rock Slope Involving Multiple Failure Mechanisms

Zhong Gui[1], Jian-Kang Chen[1], Zhen-Yu Wu[1], Han Zhang[1], and Yan-Lin Shi[1]

[1]College of Hydraulic Engineering, Sichuan University, Chengdu, Sichuan, 610065, China; e-mail: guizhong_2001_9@163.com

ABSTRACT: This paper deals with reliability analysis of a high rock slope in a hydropower project. The major slope failure modes are first identified by the finite-element strength reduction method. The performance function for a particular slip surface found by the finite element method is established by a response surface method and the corresponding failure probability is calculated by the Monte-Carlo method. The probability of failure for each failure mode that may contain several slip surfaces can be calculated based on series-parallel system assumptions. Finally, the resultant failure probability of the slope can be obtained using Ditlevsen's narrow limits method. With this new computational method, reliability analysis of a high slope in the Yaoheba Hydroelectric Station in the Nanya River is carried out as an engineering example. It shows that the new method is able to handle multiple failure mechanisms involved in the slope.

INTRODUCTION

In the long service process of a rock lope, rock is inevitably affected by environmental factors, such as weathering, earthquakes, groundwater and so on. Physical and mechanical properties of rock and soil in the shallow slope surface will gradually become weaker over time. When the rock strength reduces to a certain degree, slope failure may occur. That is to say the slope will fail in some time, and this failure possibility needs to be assessed.

In this paper, the failure probability of a slope behind a powerhouse is analyzed by structural system reliability theory, and the slope ability against failure is measured by a reliability index.

SEARCH FOR MAJOR SLOPE FAILURE MODES USING THE STRENGTH REDUCTION METHOD

Before slope failure analysis, we need first properly define slope instability modes and give a mathematical model of the slope failure. These are achieved through a shear strength reduction method. The basic idea of strength reduction method for slope stability analysis is that, in an ideal elastic-plastic finite element calculation, the shear strength parameters of the slope materials are reduced gradually until the materials reach the damaged state. Basing on elastic-plastic results, a destructive sliding surface (plastic strain and displacement mutation zone) can be found automatically. At that time, the reduction coefficient F is the safety factor of slope,

$$c'_e = \frac{c'}{F}, \quad \varphi'_e = \tan^{-1}\left\{\frac{\tan\varphi'}{F}\right\} \tag{1}$$

in which c'_e is reduced cohesion; c' is effective cohesion; φ'_e is reduced angle of internal friction; φ' is effective angle of internal friction.

In this paper, the Druker-Prager elastic-plastic constitutive model is used, whose functions are:

$$Z_i = \alpha I_1 + \sqrt{J_2} - k \begin{cases} < 0, & reliable \quad state \\ = 0, & disable \quad state \end{cases} \quad (i=1,2,\ldots,n) \tag{2}$$

where I_1 is first invariant of stress state, $I_1 = \sigma_1 + \sigma_2 + \sigma_3$; J_2 is secondary invariant of stress state, $J_2 = \left((\sigma_1 - \sigma_2)^2 + (\sigma_2 - \sigma_3)^2 + (\sigma_3 - \sigma_1)^2\right)/6$; α and k are constants related to the angle of internal friction and cohesion,

$$\alpha = \frac{2\sin\varphi}{\sqrt{3}(3-\sin\varphi)}, \quad k = \frac{6c\cos\varphi}{\sqrt{3}(3-\sin\varphi)} \tag{3}$$

In this paper, the criteria of slope instability in finite element calculation are: (1) an equivalent penetrating plastic strain region appears in the finite element model; (2) after a designated iterative step (in this paper taking as 1000), the stress and displacement are not convergent. If both of the two conditions are satisfied at the same time, it is considered that the slope instability has occurred, and then all elements in the plastic damaged channel should be found.

In the literature (Zheng 2004, Wu 2005, Sun 2003, Zhao 2002), the FEM strength reduction method has been used to find slope instability damaged channels that agree well with field observations, and the safety factor of slope is close to the one obtained by rigid limit equilibrium methods. Nonlinear stress-strain relationships for slope materials can also be considered in FEM, which can simulate complex terrain conditions and the geological structure in the slope. Thus the FEM strength reduction method reflects well the reality.

ANALYSIS OF SLOPE INSTABILITY PROBABILITY

When all the destructed channel elements fail, it could be considered that the instable slope has already failed. Therefore under the structural system reliability theory, the failure probability of the failure chain can be calculated assuming a parallel system, where Z_i is function, P_{fi} is failure probability.

$$P_{fi} = P\left(\bigcap_{j=1}^{n} Z_j = 0\right) = P(Z_1 = 0)P(Z_2 = 0|Z_1 = 0)\, P(Z_3 = 0|Z_1 = 0 \cap Z_2 = 0)\cdots$$

$$P(Z_n = 0|Z_1 = 0 \cap Z_2 = 0 \cap \cdots \cap Z_{n-1} = 0) \tag{4}$$

When all possible failure modes (destructed channel of FEM models) have been found, the joint probability of all failure modes can be calculated by,

$$P_f = P\left(\bigcup_{i=1}^{m} F_i\right) \tag{5}$$

where F_i represents failure of the ith failure mode.

Probability Network Estimation Method (PNET)

Equation (4) shows that, when calculating the probability of the main slope instability models, a series of high-dimensional probability functions is needed. So far the high-dimensional calculation of the conditional probability has not been satisfactorily resolved yet, so some approximate methods are often used to estimate the parallel system failure probability in engineering projects. In this paper we attempt to apply the PNET method (Wu 1990) for the parallel system failure probability calculation.

The method considers that all failure elements can be replaced by some so-called representative mechanisms. The selection of representative mechanisms follows that all failure mechanisms are divided into several groups, and in each group all mechanisms are correlative with a representative mechanism. The representative mechanism is in fact the minimal probability of all the failure mechanisms in the group. According to the correlative conditions, the probability that all failure mechanisms fail simultaneously can be represented by the probability of the representative mechanism. And the representative mechanisms in different groups are considered as statistically independent.

According to the principles above, assuming the failure probability of the ith body in m representative bodies is P_{fi}, then the disabled probability of the parallel system is:

$$P_f = \prod_{i=1}^{m} P_{fi} \tag{6}$$

Construction of the Element Functional and Calculation of Failure Probability

According to the PNET method, the failure probability of every element and correlation coefficient between two elements need to be calculated first; therefore the element function needs to be determined first. But according to the Druker-Prager yield criteria, the principal stresses in the function can only be obtained by a finite element method (FEM), and the element function cannot be expressed in an explicit form of basic random variables.

The Response Surface Method (Zhao 1996) developed in 1980s, is an effective method dealing with the problem involving implicit performance function in structural reliability analysis. The basic idea is: firstly using a comparatively simple function, which is expressed by basic random variables through statistical regression simulation, to replace the function that could not be expressed explicitly. When analyzing structural reliability with the finite element method, response surface methods design several groups of variables, and a pilot is composed of each group variables. Then using FEM to analyze the structure point-by-point, a series of corresponding numerical values of the function can be obtained. Finally using these variables and numerical values of function, we can simulate a comparatively simply specific function. Then this approximate function can be used to calculate structural failure probability and reliability index.

Currently, the common functions used for response surface are non-cross-term quadratic polynomial.

$$Z = a_0 + \sum_{i=1}^{n} b_i X_i + \sum_{i=1}^{n} c_i X_i^2 \tag{7}$$

where X_i ($i=1, 2, \ldots, n$) is basic random variables, a_0, b_i and c_i are parameters to be determined in response surface function, Z is the same as that in Eq.(4).

After constructing unit response surface function on damaged channel, we can use the Monte Carlo method (e.g. Zhao 2000) to calculate the failure probability and reliable indicators. The correlative coefficients between every two disabled elements can be calculated by the following formula.

$$\rho_{ij} = \frac{\sum (Z_i - \overline{Z}_i)(Z_j - \overline{Z}_j)}{\sqrt{\sum (Z_i - \overline{Z}_i)^2}\sqrt{\sum (Z_j - \overline{Z}_j)^2}} \tag{8}$$

where ρ_{ij} is the correlation coefficients between element i and element j; Z_i and Z_j are respectively numerical values of function of element i and element j; $\overline{Z}_i$ and $\overline{Z}_j$ are averages of numerical values of function.

Correlative Research of Main Instability Modes (Liu 1994)

After calculating the probability of the main failure modes, we can use Ditlevsen's narrow limits formula to estimate the joint probability of the main failure modes. The joint probability is namely the probability of failure. When using Ditlevsen's narrow limits formula, it needs to know the correlative coefficients of the main failure modes. Because a failure mode of slope is defined as the failure state that all elements on the damaged channel are disabled, equation (8) cannot be adopted to calculate the correlative coefficients of the main failure modes.

If the limit state surfaces of two failure modes are two planes in a n-dimensional space, the function can be defined as follows:

$$Z_1 = a_{10} + \sum_{i=1}^{n} a_{1i} X_{1i} \quad \text{and} \quad Z_2 = a_{20} + \sum_{i=1}^{n} a_{2i} X_{2i} \tag{9}$$

And the correlative coefficient of the two failure modes can be calculated by

$$\rho_{12} = \sum_{i=1}^{n} a_{1i} a_{2i} \tag{10}$$

Because failure modes in structural reliability FEM analysis are intersections of disabled elements, generally their limit state surfaces are not hyper planes but extremely complex surfaces. In order to calculate the correlation coefficients with equation (10), basing on an equivalent condition, a nonlinear equivalent limit state surface instead of the complex limit state surface of failure modes is used.

The limit state surface function can be written as

$$Z_E = \sum_{i=1}^{n} a_{Ei} X_i + \beta \tag{11}$$

where $a_{Ei} = \cos(\beta, X_i)$ ($i = 1, 2, \ldots, n$).

Broad reliability indicator β and cosine of coordinate axis in normal space can be calculated by

$$\cos(\beta, X_i) = \frac{\partial \beta}{\partial X_i} \Bigg/ \sqrt{\sum_{i=1}^{n} \left(\frac{\partial \beta}{\partial X_I} \right)^2} \tag{12}$$

Analysis and Evaluation of Probability of Failure

According to probability and statistical theory, the joint probability of the main failure modes can be calculated as a series-wound system model. At present, in the reliability of engineering risk analysis, Ditlevsen's narrow limits method (Wu 1990) is often used to estimate the failure probability of series-wound system,

$$P_{f1} + \sum_{i=2}^{m} \max\left(P_{fi} - \sum_{j=1}^{i-1} P_{fij}, 0 \right) \le P_f \le \sum_{i=1}^{m} P_{fi} - \sum_{i=2}^{m} \max_{j<i}\left(P_{fij}\right) \tag{13}$$

where, P_{fi} is the probability of the ith failure mode, P_{fij} is the probability of the ith failure mode and jth failure mode happening at the same time. It can take the average of the upper limit value and lower limit value of the failure probabilities, and then get corresponding broad reliability indicator,

$$\beta = \Phi^{-1}(P_s) = -\Phi^{-1}(1 - P_s) = -\Phi^{-1}(P_f) \tag{14}$$

where, $\Phi(\bullet)$ is the cumulative probability function of a standard normal variable.

ENGINEERING EXAMPLE

Yaoheba Hydropower Station is located in the north-south structural zone of Sichuan and Yunnan, where regional geological and seismic conditions are complex. In the area, Tiezhaizi fault runs along the left side of the river, and Anshunchang-Gongyi sea fracture (Moxi fracture) is through the diversion tunnel, belonging to an active fault where currently weak earthquake activity is frequent. Identified by the Sichuan Province, the seismic intensity in this area is 8^{th} degree. In the Yaoheba Powerhouse rock, weathering and relief load are significant and the geological conditions are poor. In the rock mass, there are three developed diabase rock dyke fracture zones trending to the mountains, which are propitious to overall slope stability. But there are rock mass in the low surface layer rock of slope crumbling and slackening, which makes it possible to lose stability partly. In addition, there are about 2 – 5 m thick cover layer of slope surface from 1441.00 m height to top, which is disadvantageous for the stability of the slope.

Search for Slope Failure Mode

According to the "Geotechnical engineering investigation specifications" (GB50021-2001), the Yaoheba Powerhouse Slope is a two-grade slope, and its design safety factor should be 1.15-1.30. For safety reasons, the damaged channel whose strength reduction coefficient is under 5.0 is selected as the main failure mode for slope reliability analysis. Through elastic-plastic plane finite element analysis, three main slope failure channels were found, as shown in Figure 1. In the figure, the shadow parts are failure channels, and their finite element strength reduction coefficients are 1.50, 2.50, and 5.00, respectively.

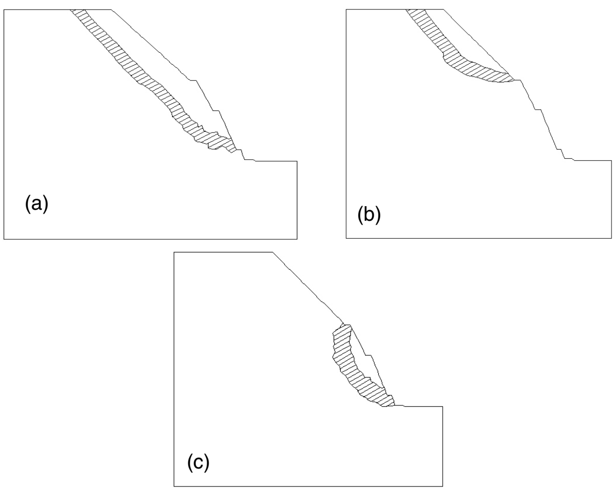

Figure 1. Main failure modes (strength reduction coefficients are 1.50, 2.50, and 5.00, respectively).

Calculation of Slope Failure Probability and Reliability Index

When constructing element function using the response surface method, the physical mechanics parameters of the weak to strong weathering and strong unloading zone in the low surface layer are treated as random variables. Among the mechanical parameters of rock, bulk density γ and Poisson's ratio μ are identified as deterministic values because of their little variability according to a large amount of statistical data. Then the elastic modulus E, cohesion c and internal friction angle φ are selected as the basic random variables for reliability analysis. Their distributions are assumed as normal, and the coefficient of variation is set as 0.3, as detailed in Table 1.

Table 1. Distributions types and parameters of basic random variables

Rock and Soil	Basic Random Variable	Symbol	Distribution Type	Average
Weak leaning to strong weathering and strong unloading zone	$c_1\,(MPa)$	X_1	normal	0.27
	φ_1 (°)	X_3	normal	27.7
	E_1 (GPa)	X_5	normal	0.84
Diabase rock dyke fracture zones	c_2 (MPa)	X_2	normal	0.2
	φ_2 (°)	X_4	normal	26.64
	E_2 (GPa)	X_6	normal	0.6

Using the former formulas, we can calculate the probabilities of the three main failure modes shown in Figure 1, which are 2.758E-05, 1.749E-05, and 2.936E-05 respectively. The correlation coefficients of the main failure modes can be calculated using equations (10) - (12), as detailed in Table 2.

Table 2. Correlation coefficients of the main failure modes of Yaoheba Powerhouse Slope

Number	1	2	3
1	1.00	0.06	-0.69
2	0.06	1.00	0.13
3	-0.69	0.13	1.00

Based on the probabilities of the main failure modes and the correlation coefficients, we can use equation (13) to work out the probability of slope instability. So its upper limit is 7.449E-05 while its lower limit is 7.443 E-05. Averaging the upper limit and lower limit and using equation (14), the reliability index is 3.8. According to the "Geotechnical engineering investigation specifications" (GB50021-2001), when the coefficients of variation of physical and mechanical parameters in the rock and soil selected as 0.3, the reliability index of the slope is selected as 3.8, which exceeds the required reliability index for first-class (important) structures; therefore, in long-term service process, the Yaoheba Powerhouse Slope is considered safe.

CONCLUSIONS

(1) According to the correspondence between probabilities of main failure modes and the strength reduction safety factors of the Yaoheba powerhouse slope, we can obtain the rule that the probabilities of main failure modes will become smaller when the strength reduction safety factors turn greater. It is possible to find the

main failure modes by the FEM strength reduction method.

(2) The results of the Yaoheba Powerhouse Slope prove that it is possible to calculate failure probability using serial-parallel systems and combining with reliability indicators.

(3) In this paper, the FEM strength reduction method is applied to the high slope stability analysis and broaden the scope of application. But it still needs in-depth study on how to apply the FEM strength reduction method to take into account other factors such as earthquake loads and large joints of slope.

REFERENCES

Zheng, Yinren (2004). "Application of strength reduction FEM in soil and rock slope." *Chinese Journal of Rock Mechanics and Engineering*, 23(19): 3381-3388.

Wu, Chunqiu (2005) "Dynamic method to assess critical state of slope stability." *Rock and Soil Mechanics*, 26(5): 784-788.

Sun, Wei (2003). "Strength reduction FEM in stability analysis of soil slopes." *Bulletin of Science and Technology*, 19(4): 319-322.

Zhao, Shangyi (2002) "Analysis on safety factor of slope by strength reduction FEM." *Chinese Journal of Geotechnical Engineering*, 24(3): 343-346.

Wu, Shiwei (1990). *Reliability Analysis for Structure.* Beijing: People's Communication Press.

Zhao, Guofan (1996). *Theory and Application in Engineering Structural Reliability*. Dalian: Dalian Technology University Press.

Zhao, Guofan (2000). *Structural Reliability Analysis.* M. Beijing: *Chinese Construction Industry Press.*

Liu, Nin (1994). "Relativity in three-dimensional structural failure modes research." *Transactions of Hohai University,* 22(5): 29-35.

Three-Dimensional Analysis of the Lodalen Landslide

Gilson Gitirana Jr.[1], Marcos A. Santos[2], and Murray D. Fredlund[3]

[1]Professor, School of Civil Engineering, Federal University of Goias, Goiania, GO, Brazil; gilsongj@eec.ufg.br
[2]Ph.D. student, Dep. of Civil and Environmental Engn., University of Brasilia, Brasilia, DF, Brazil; marcosairess@gmail.com
[3]President, SoilVision Systems Ltd., 202-640 Broadway Ave., Saskatoon, SK, Canada S7N 1A9; murray@soilvision.com

ABSTRACT: A convenient three-dimensional slope stability approach, presented in the accompanying paper, is applied to the analysis of the Lodalen landslide. Simple finite element stress and seepage analyses are employed to compute the three-dimensional factor of safety. The analysis shows that the three-dimensional factor of safety computed for the Lodalen landslide was 1.29 in average. The value obtained is 23% higher than that obtained using two-dimensional solutions. The hypotheses and procedures adopted in the analyses are discussed and the validity of rigorous three-dimensional computations is evaluated.

INTRODUCTION

The Lodalen landslide has been studied and analyzed by numerous authors. The early work by Sevaldson (1956) presents a thorough documentation of the slide. Sevaldson (1956) presented compelling results, indicating the power of the relatively new method of two-dimensional analysis proposed by Bishop (1954). Bishop's method provided factors of safety near 1, which are expected for a failed slope. However, the most significant result was the accurate prediction of the position of the actual slip surface along three chosen cross sections.

More recently, Pham and Fredlund (2004) and El-Ramly et al. (2006) present new analyses, using more elaborate methods of two-dimensional analysis. Pham and Fredlund (2004) have demonstrated that the dynamic programming method of analysis was able to reasonably predict the position of the actual slip surface. El-Ramly et al. (2006) presented a probabilistic analysis which demonstrated the high likelihood of a slide, which ended up occurring.

This paper presents a three-dimensional analysis of the Lodalen slide. The survey information and soil property data provided by Sevaldson (1956) are adopted herein.

The re-analysis is directed towards a better understanding of the advantages and of the method of analysis using three-dimensional procedures. The results of the three dimensional analysis are compared against those obtained using conventional two-dimensional analysis.

DESCRIPTION OF THE LODALEN LANDSLIDE AND THE PREVIOUS ANALYSES FOUND IN THE LITERATURE

According to Sevaldson (1956), the Lodalen slide occurred in the area of a marshalling yard, less than 2 miles east of the Oslo East railway station. The river Lo used to flow through the area of the slide and was conducted through a different path about 30 years prior to the slide.

Figure 1 presents the geometry and water table at cross-section 2, prior to the slide. This section was located approximately at the middle of the slide mass. The geometry of the slopes has been modified and trimmed a number of times prior the finl geometry presented in Fig. 1. The final inclination was 1V : 2H. Sevaldson (1956) indicated that the slide was a long-term stability problem, characterized by the reduction in shear strength due to the reduced overburden pressure.

The soil was determined to be sedimentary clay. The slopes were remarkably homogeneous. Numerous borings were done for sampling. Unconfined and triaxial tests were performed for determining the shear strength characteristics of the profile. The position of the water table was also determined.

Using the data collected, Sevaldson (1956) presented a detailed stability analysis of the landslide. Bishop's simplified method of limit equilibrium analysis was used in the original work. The slip surface shape and position was determined by surface inspection and the numerous test borings.

Three cross sections were analyzed by Sevaldson (1956) and the actual and theoretical critical slips surfaces were compared. The pore-water pressures used in the analyses where determined using a phreatic line. The phreatic line was obtained with piezometers. Artesian conditions where also observed. The unsaturated shear strength above the water table was not considered.

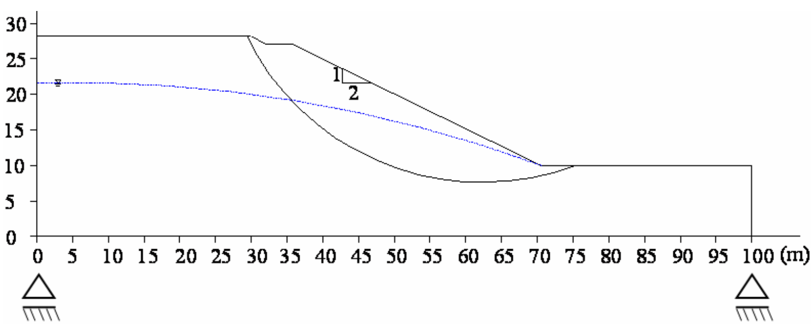

FIG. 1. Lodalen landslide: cross section 2.

The analysis performed by Sevaldson (1956) using Bishop's method provided factors of safety near 1 for the three cross sections analyzed. Sections 1, 2, and 3 resulted in factor of safety of 1.10, 1.00, and 1.19 respectively. The weighted average factor of safety was 1.05. The theoretical critical slip surfaces obtained matched the field data.

The good results obtained by Sevaldson (1956) using two-dimensional analyses could be considered surprising from the point of view of three-dimensional stress states and considering that the actual slip surface shape was not elongated across the slope face. Three-dimensional factors of safety are often 20 to 30% higher than the two-dimensional factors of safety. Moreover, the consideration of the unsaturated shear strength would further increase the theoretical, supposedly more rigorous, factor of safety. In summary, the factor of safety obtained by Sevaldson (1956) should, from that point of view, be considerably lower than 1.

THREE-DIMENSIONAL ANALYSIS OF THE LODALEN LANDSLIDE

The analyses presented herein were performed based on the theory presented in the accompanying paper and using the software SVOffice 2006 (SoilVision Systems Ltd., 2007). The formulation was programmed using FlexPDE (PDE Solution Inc., 2007), a general purpose partial differential equation solver. Problem setup time was approximately 20 minutes. The computation work usually took less than 7 minutes on a Core 2 Duo processor running at 2 GHz, with 1 Gb or RAM.

The parameters adopted herein for the stress analysis where as follows: a Young Modulus of 1500 kPa; Poisson's ratio varying from 0.1 to 0.49. An arbitrary value of Young modulus was adopted because it does not affect the factor of safety of homogeneous slopes. The shear strength and body load parameters of the problem are the same as those adopted by Sevaldson (1956): total cohesion of 10 kPa; friction angle of 27.1^{o}; and unit weight of 19.1 kN/m^3.

Figure 2 presents the problem geometry and mesh. The problem geometry was obtained using the survey data presented by Sevaldson (1956). A grid of elevation points was generated to describe the surface shape.

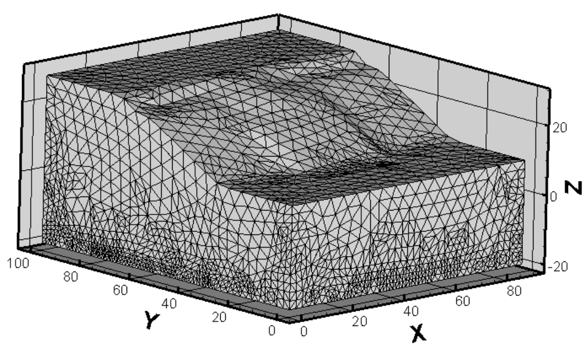

FIG. 1. Lodalen landslide: geometry and mesh.

Figure 3 presents the slip surface adopted herein. The shape of the actual slip surface observed in the field was matched using an ellipsoid. Figure 4 presents the pore-water pressure distribution. The data was generated by means of a steady state seepage analysis. The actual values used in the analysis were multiplied by a factor of 1.339 (El-Ramly et al., 2006), in order to account for artesian conditions observed right after the slide. The effect of negative pore-water pressure to the shear strength was neglected in the analyses presented in this paper.

Table 1 presents the results obtained herein and the original weighted factors of safety obtained by Sevaldson (1956) considering the average value of three cross sections and using three different methods of analysis. Comparing against Bishop's method, the three-dimensional factors of safety presented herein are 18 to 29% higher than the two-dimensional factors of safety obtained by Sevaldson (1956). Poisson's ratio had an effect on the factor of safety. Higher values of Poisson ratio result in higher factors of safety.

As discussed above, higher values of factor of safety were expected for the three-dimensional analysis. It is not possible to give a definite explanation, at this point, about why the three-dimensional analysis did not result in a factor of safety near 1. Similarly, the original two-dimensional analysis should provide values lower than 1. Additional studies are being carried out as an attempt to answer these questions.

Table 1. Lodalen landslide: factors of safety obtained by Selvadson (1956) and obtained in this study.

Sevaldson (1956)	Fs 2-D	This study, Fs 3-D				
		$\mu = 0.1$	$\mu = 0.2$	$\mu = 0.3$	$\mu = 0.4$	$\mu = 0.49$
Swedish method	1.010					
Ordinary method	0.850	1.237	1.260	1.289	1.323	1.359
Bishop's simplified	1.050					

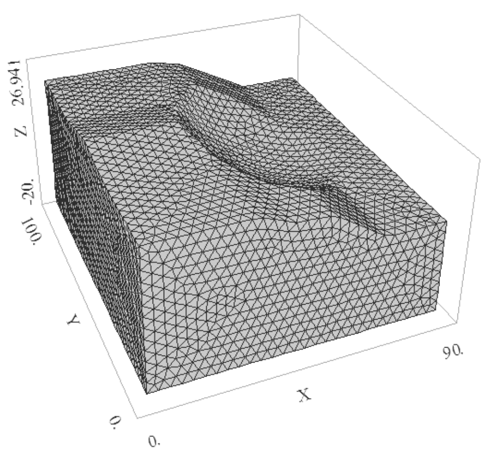

FIG. 3. Lodalen landslide: geometry and slip surface.

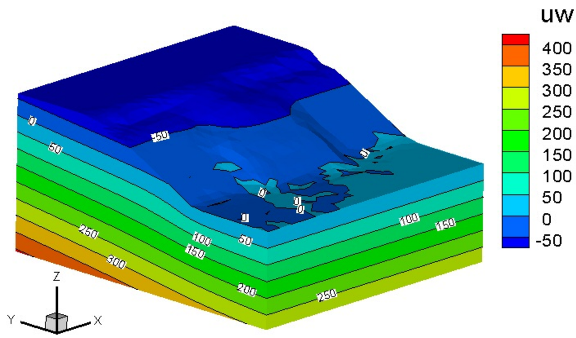

FIG. 4. Lodalen landslide: pore-water pressure distribution.

CONCLUSIONS

The Lodalen landslide was analyzed using the three-dimensional solution. The results were compared to those present but Sevaldson (1956). The three-dimensional factor of safety for the Lodalen landslide was 18-29% higher than that obtained with the two-dimensional solution. The differences observed between the three- and two-dimensional factors of safety are within expected ranges. However, further studies are needed in order to determine why the original two-dimensional analyses did not result in factors of safety lower than one.

ACKNOWLEDGMENTS

The authors would like to thank "Conselho Nacional de Desenvolvimento Científico e Tecnológico – CNPq, Brasil", for financial support and Jason Stianson for the discussions and for providing unpublished data from his PhD research.

REFERENCES

Bishop, A.W. (1954). The use of the slip circle in the stability analysis of slopes. Proc. European Conf. Stab. Earth Slopes, Stockholm, 1:1-13, and Géotechnique, V :1 :7.

El-Ramly, H., Morgentern, N.R. and Cruden, D.M. (2006). Lodalen slide: a probabilistic assessment. Can. Geotech. J. 43:956-968.

PDE Solutions Inc. (2007). FlexPDE 5.0 - Reference Manual, Antioch, CA, USA.

Pham, H.T.V. and Fredlund, D.G. (2003). The application of dynamic programming to slope stability analysis. Can. Geotech. J. 40:830-847.

Sevaldson, R.A. (1956). The Slide in Lodalen, October 6th, 1954. Geotechnique, 6: 167–182.

SoilVision Systems Ltd. (2007). "SVOffice 2006 User's and Theory Guide." Saskatoon, SK, Canada.

Three-Dimensional Slope Stability Model Using Finite Element Stress Analysis

Gilson Gitirana Jr.[1], Marcos A. Santos[2], and Murray D. Fredlund[3]

[1]Professor, School of Civil Engineering, Federal University of Goias, Goiania, GO, Brazil; gilsongj@eec.ufg.br
[2]Ph.D. student, Dep. of Civil and Environmental Engn., University of Brasilia, Brasilia, DF, Brazil; marcosairess@gmail.com
[3]President, SoilVision Systems Ltd., 202-640 Broadway Ave., Saskatoon, SK, Canada S7N 1A9; murray@soilvision.com

ABSTRACT: A practical three-dimensional slope stability approach is presented. Simple finite element stress and seepage analyses are employed in order to computer factors of safety. Benchmark problems are presented in order to verify the accuracy of the proposed method. Close agreement is observed when comparing the results obtained herein and those from the literature.

INTRODUCTION

Most slope stability problems are three-dimensional in nature. Few are the situation where a two-dimensional plane strain condition truly represents the field condition. Several field conditions can be better represented by three-dimensional models, such as excavation fronts, slope corners, dam shoulders, to name only a few geotechnical problems. Numerous advances in three-dimensional geotechnical analysis have been achieved in the last few decades, mostly due to the increase in computational power.

This paper presents how three-dimensional slope stability analyses can be undertaken using simple finite element stress and seepage analysis. Two benchmark problems are presented in order to demonstrate the accuracy of the method of analysis.

LITERATURE REVIEW

The methods of three-dimensional analysis of slopes are usually extensions of conventional two-dimensional approaches. Variational calculus, for instance, has been extended to three-dimensional conditions by Leshchinsky et al. (1985) and Leshchinsky and Baker (1986). Leshchinsky and Huang (1992) further extended their original work, but the method was limited to problems with symmetric geometry.

Michalowski (1989) presented a three-dimensional solution based on the upper-bound theorem. The solution was limited to homogeneous slopes. More recently, Farzaneh and Askari (2003) have extended the work by Michalowski (1989) to non homogeneous slopes. Chen et al (2001a, 2001b) have also presented an upper-bound solution for three-dimensional slope stability.

Lam and Fredlund (1993) have presented an extension of the GLE limit equilibrium method to three-dimensional conditions. The method is particularly interesting considering that the limit equilibrium is widely accepted in geotechnical engineering practice.

Other modeling approaches have been presented by numerous researchers in the last few years. The upper and lower-bound theorems have been applied along with the finite element method, in order to produce stress and strain fields (Lyamin and Sloan, 2002a and 2002b).

From the point of view of practicing geotechnical engineers, it becomes difficult to determine what three-dimensional method of slope stability analysis is the more adequate. A sound theoretical basis, a generalized approach that is capable of handling field conditions, and simplicity, are some of the requirements of a handy slope stability method. It appears that if a practical three-dimensional finite element tool for stress and seepage analysis is available, it becomes convenient to extend the two-dimensional enhanced method to three-dimensional conditions. Such method could be considered a practical tool for routine analyses.

THEORY

The factor of safety is usually defined as the ratio by which the shear strength must be reduced in order to bring the soil mass to a state of limit equilibrium. For a three-dimensional slip surface, the factor of safety may be computed by taking the total resisting shear force divided by the total shear force:

$$F_s = R/S = \int_A \tau_f \, dA \Big/ \int_A \tau_a \, dA \qquad (1)$$

where: R is the total resisting shear force; S is the total shear force; τ_f is the shear strength; τ_a is the shear stress; and A is the slip surface area.

The resisting and shearing stresses acting along a three dimensional slip surface must be determined. The state of stress and pore-water pressure at any point in the soil volume may be determined using the finite element method. Therefore, the method presented herein is an extension of the enhanced method to three-dimensional conditions. The computation of the factor of safety can be summarized as follows:

a) The distribution of stresses and pore-water pressures are determined using the finite element method. Appropriate boundary conditions, constitutive models, and constitutive parameters must be adopted;
b) The normal and shear stresses are computed for a grid of points located at the base of the slip surface. The normal stress depends on the position along the slip surface. The shear stress depends not only on the position at the slip surface but also on the direction of slippage projected on the horizontal plane;

c) Integration of the acting and resisting stresses is performed along the slip surface area.

Spherical and ellipsoidal slip surface shapes have been implemented and tested herein. The shape and position of a spherical slip surface are defined as follows:

$$z = z_{0s} - \sqrt{r_s^2 - (x - x_{0s})^2 - (y - y_{0s})^2} \tag{2}$$

where: x_{0s}, y_{0s}, and z_{0s} are the coordinates of the center of the sphere in the x, y, and z directions; and r_s is the radius of the slip surface. Only the bottom half of the sphere is taken by using the minus sign for the square root.

The shape and position of an ellipsoidal slip surface can be defined as follows:

$$z = z_{0e} - c\sqrt{1 - \frac{[(x - x_{0e})\cos\theta + (y - y_{0e})\sin\theta]^2}{a^2} - \frac{[(y - y_{0e})\cos\theta - (x - x_{0e})\sin\theta]^2}{b^2}} \tag{3}$$

where: x_{0e}, y_{0e}, and z_{0e} are the coordinates of the center of the ellipsoid; a, b, and c are the lengths of the semi-axes in the x, y, and z directions; and θ gives the orientation of the ellipsoid in the x-y plane, θ being 0 in the x-direction and increasing counter-clockwise.

The direction of a plane tangent to any point of the slip surface is defined by the angles its normal makes with x, y, and z. Such direction can be expressed in terms of the direction cosines:

$$a_{11} = \frac{\partial f/\partial x}{\|f\|}\,;\; a_{21} = \frac{\partial f/\partial y}{\|f\|}\,;\; a_{31} = \frac{\partial f/\partial z}{\|f\|} \tag{4}$$

where: f denotes the equation defining the geometric location of the slip surface (Eqs. 2 or 3) and $\|f\| = \sqrt{(\partial f/\partial x)^2 + (\partial f/\partial y)^2 + (\partial f/\partial z)^2}$. The first index "1" indicates the direction defined by the normal to the surface. The second indexes indicate the x, y, and z directions

For a spherical slip surface, the derivatives are as follows:

$$\partial f/\partial x = 2(x - x_{0s})\,;\; \partial f/\partial y = 2(y - y_{0s})\,;\; \partial f/\partial z = 2(z - z_{0s}) \tag{5}$$

For an ellipsoidal slip surface, the derivatives are as follows:

$$\partial f/\partial x = 2[(x - x_{0e})\cos\theta + (y - y_{0e})\sin\theta]\cos\theta/a^2 - 2[(y - y_{0e})\cos\theta - (x - x_{0e})\sin\theta]\sin\theta/b^2 \tag{6}$$
$$\partial f/\partial y = 2[(x - x_{0e})\cos\theta + (y - y_{0e})\sin\theta]\sin\theta/a^2 + 2[(y - y_{0e})\cos\theta - (x - x_{0e})\sin\theta]\cos\theta/b^2 \tag{7}$$
$$\partial f/\partial z = 2(z - z_{0e})/c^2 \tag{8}$$

The normal stress acting in a plane tangent to any point of the slip surface is given by the following equation:

$$\sigma_n = \sigma_x a_{11}^2 + \sigma_y a_{21}^2 + \sigma_z a_{31}^2 \\ + 2\tau_{xy} a_{11} a_{21} + 2\tau_{yz} a_{21} a_{31} + 2\tau_{zx} a_{31} a_{11} \tag{9}$$

Given the computed σ_n, the shear strength can be calculated using the Mohr-Coulomb criterion for saturated/unsaturated soils:

$$\tau_f = c' + (\sigma_n - u_a) \tan \phi' + (u_a - u_w) \tan \phi^b \tag{10}$$

where: c' is the effective cohesion; u_a is the pore-air pressure; ϕ' the angle of internal friction; u_w is the pore-water pressure; and ϕ^b is the angle of friction with respect to changes in matric suction. Equation 10 reduces to the conventional Mohr-Coulomb criterion when the soil becomes saturated.

In order to compute the acting shear stress, the direction of slippage movement must be known. The direction of the slippage movement may be determined as part of the optimization technique used in the determination of the critical slip surface. The slippage direction may also be adopted. For instance, the slippage movement could be assumed to be given by the average slope face direction.

The projection of slippage direction in the horizontal plane is given by a unit vector with components in the x and y direction, b_1 and b_2. The third component, b_3, indicates the direction normal to the slip surface and is orthogonal to b_1 and b_2:

$$b_3 = (-a_{11} b_1 - a_{21} b_2) / a_{31} \tag{11}$$

The direction cosines that indicate the slippage direction are as follows:

$$a_{12} = b_1 \Big/ \sqrt{b_1^2 + b_2^2 + b_3^2}\ ;\ a_{22} = b_2 \Big/ \sqrt{b_1^2 + b_2^2 + b_3^2}\ ;\ a_{32} = b_3 \Big/ \sqrt{b_1^2 + b_2^2 + b_3^2} \tag{12}$$

Finally, the shear stress acting at any point and slippage direction at the base of the slip surface is given by the stress state and direction cosines, defined by Eqs. 4 and 12:

$$\tau_a = \sigma_x a_{11} a_{12} + \sigma_y a_{21} a_{22} + \sigma_z a_{31} a_{32} \\ + \tau_{xy}(a_{11} a_{22} + a_{21} a_{12}) + \tau_{yz}(a_{21} a_{32} + a_{31} a_{22}) + \tau_{zx}(a_{31} a_{12} + a_{11} a_{32}) \tag{13}$$

Finite Element models usually employ procedures based on stresses that are computed at the integration points. Therefore, in order to compute the normal and shear stress at any point at the base of a given slip surface, the state of stress determined at the integration points must be used. If necessary, these stresses can be extrapolated to the nodes using simple mapping techniques.

The procedure presented above must be employed for each trial slip surface established during the optimization analysis. Several optimization techniques are available for the determination of the critical slip surface. This paper will not deal with these procedures. Instead, the computation of the factor of safety of three-dimensional slip surfaces with known shape and position is presented.

ANALYSIS OF BENCHMARK PROBLEMS

There are few numerical modeling tools available that are capable of performing three-dimensional analysis. Most of the available tools are not practical and efficient enough for routine use. The analyses presented herein were performed using the software SVOffice 2006 (SoilVision Systems Ltd., 2007). The formulation presented above was programmed using FlexPDE (PDE Solution Inc., 2007), a general purpose partial differential equation solver. For the benchmark analyses presented herein, problem setup time was less than 15 minutes. The computation work usually took less than 5 minutes on a Core 2 Duo processor running at 2 GHz, with 1 Gb or RAM.

Two benchmark problems have been selected for the verification of the three-dimensional slope stability analysis solution. The first problem corresponds to a simple and symmetric cohesive slope. The second problem corresponds to an asymmetric slope with friction and cohesion. Both problems have been frequently presented in the research literature for benchmark purposes.

Symmetric Cohesive Slope

Figure 1a presents the first benchmark problem. A spherical slip surface is employed. The simple geometry, boundary conditions and soil properties allowed for the development of analytical solutions. Baligh and Azzouz (1975) and Gens et al. (1988) present two different solutions. Hungr et al. (1989), Lam and Fredlund (1993) and Chen et al. (2001) have also analyzed this problem.

The parameters adopted herein for the stress analysis where as follows: a Young Modulus of 3500 kPa; Poisson's ratio that varied from 0.1 to 0.49; total cohesion of 0.1 kPa, friction angle equal to zero; pore-water pressure equal to zero; and unit weight of 1 kN/m^3.

Figure 1b presents the distribution of vertical stresses throughout the slope and at the base of the slip surface. The simple geometry and absence of external loads results in smooth contours for the distribution of stresses.

Table 1 presents the results of the analysis along with the factors of safety obtained by other researchers using different methods of analysis. It can observed that similar results where obtained when comparing the numbers provided by all authors. The factor of safety obtained previously ranges from 1.386 to 1.422. The GLE method (Lam and Fredlund, 1993) provided a factor of safety of 1.402 when using a relatively small number of columns, 540. The three-dimensional enhance method used herein provides factors of safety near 1.4. However, the results depend on the value of Poisson's ratio. Values of factor of safety as high as 1.438 were obtained when increasing Poisson's ratio near its maximum theoretical value of 0.5.

A variation of 0.05 in the factor of safety was obtained when subjecting the analysis to extreme variations in the number of nodes. The number of nodes was varied from approximately 5,000 to up to 300,000. The size of the problem domain could also affect the results if the boundaries are too close to the slip surface. Increasing of the problem size did not result in significant changes in the factor of safety (less than 2% of variation). Therefore, the original domain size, presented in Fig. 1, was deemed adequate.

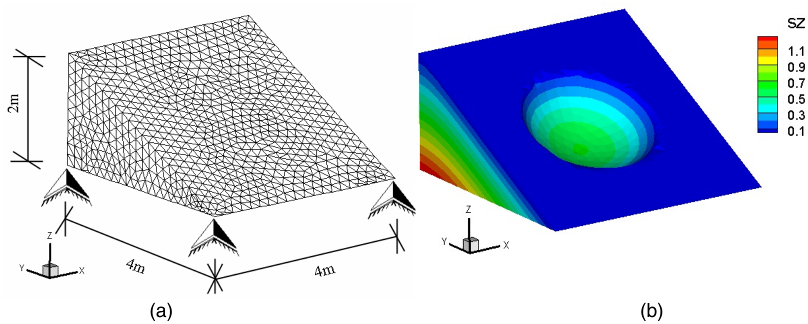

FIG. 1. Benchmark problem 1 - homogeneous cohesive slope with spherical slip surface: (a) geometry and boundary conditions; and (b) vertical stresses.

Table 1. Benchmark problem 1: factors of safety obtained by other research and obtained in this study.

Reference	Method of analysis	F_s 3-D
Baligh and Azzouz (1975)	Analytical solution	1.402
Gens et. al. (1988)	Analytical solution	1.402
Hungr et. al. (1989)	Method of slices (Bishop's simplified)	1.422
Lam and Fredlund (1993), 540 columns	Method of slices (GLE)	1.402
Lam and Fredlund (1993), 1200 columns	Method of slices (GLE)	1.386
Chen et, al. (2001)	Upper bound theorem	1.422
This study	Poisson's ratio = 0.1	1.396
	Poisson's ratio = 0.2	1.401
	Poisson's ratio = 0.3	1.409
	Poisson's ratio = 0.4	1.422
	Poisson's ratio = 0.49	1.438

Non-symmetrical slope with friction and cohesion

Leshchinsky et al. (1985) have proposed an analytical solution for three-dimensional slope stability problems using the logarithmic spiral. One of the examples presented by Leshchinsky et al. (1985) is re-analyzed herein, using a spherical slip surface approximation. The same problem was also analyzed by Hungr et al. (1989) and Stianson (2006), using different approaches.

The parameters adopted herein for the stress analysis where as follows: a Young Modulus of 3500 kPa; Poisson's ratio that varied from 0.1 to 0.49. The shear strength and body load parameters of the problem presented by Leshchinsky et al. (1985) are as follows: total cohesion of 0.116 kPa; friction angle of 15^o; pore-water pressure equal to zero; and unit weight of 1 kN/m^3.

Even though Leshchinsky et al. (1985) have used logarithmic spirals, a spherical shape approximates the shape of the original slip surface fairly well. Figure 2a presents the slip surface adopted herein. The radius and center were adjusted in order to match the original slip surfaces. Subtle differences in the position of the slip surfaces adopted by Hungr et al. (1989) and Stianson (2006) were matched.

Figure 2b presents the distribution of vertical stresses throughout the slope. Once again, the simple geometry and absence of external loads results in smooth contours for the distribution of stresses.

Table 2 presents the results obtained by the three previous researchers and those obtained in this study. The differences in factor of safety among the three previous researchers are due to differences in the method of analysis and, more importantly, differences in the position of the slip surfaces obtained. The factors of safety appear to be reasonably close when comparing those obtained by each author and the results presented herein. Poisson's ratio appears to have an effect on the factor of safety. Higher Poisson's ratios result in higher factors of safety.

CONCLUSIONS

A practical three-dimensional slope stability approach was presented, using simple finite element stress and seepage analyses. Benchmark problems were presented in order to verify the accuracy of the proposed method. Close agreement was observed when comparing the results obtained herein and those from in the literature. Higher values of Poisson's ratio resulted in higher values of factor of safety.

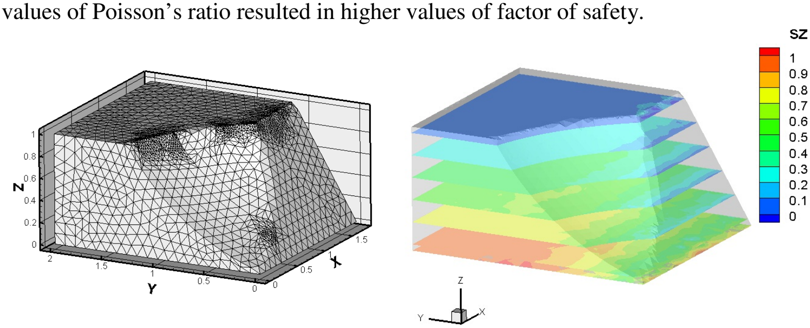

(a) (b)

FIG. 2. Benchmark problem 2: (a) geometry and slip surface shape matching that of Leshchinsky et al. (1985); and (b) distribution of vertical stresses.

Table 2. Benchmark problem 2: factors of safety obtained by other research and obtained in this study.

Reference	Fs 3-D	This study, Fs 3-D				
		$\mu = 0.1$	$\mu = 0.2$	$\mu = 0.3$	$\mu = 0.4$	$\mu = 0.49$
Leshchinsky et al. (1985)	1.250	1.209	1.221	1.234	1.246	1,258
Hungr et al. (1989)	1.230	1.239	1.247	1.256	1.265	1,277
Stianson (2006)	1.410	1.354	1.368	1.382	1.395	1,408

ACKNOWLEDGMENTS

The authors would like to thank "Conselho Nacional de Desenvolvimento Científico e Tecnológico – CNPq, Brasil", for financial support and Jason Stianson for the discussions and for providing unpublished data from his PhD research.

REFERENCES

Baligh, M. M. and Azzouz, A. S. (1975). End effects on stability of cohesive slopes. ASCE J. of the Geotech. Engng. Div., 101 (11): 1105-1117.

Chen, J., Yin, J.-H., and Lee, C.F. (2001). Upper Bound Limit analysis of slope stability using rigid finite elements and nonlinear programming Can. Geotech. J., 40: 742-752.

Chen, Z. Y., Wang, X. G., Haberfield, C., Yin, J. H. and Wang, Y. J. (2001a). A three-dimensional slope stability analysis method using the upper bound theorem. Part I: Theory and methods. Int. J. Rock Mech. Mining Sci. 38: 369–378.

Chen, Z. Y., Wang, J., Wang, Y. J., Yin, J. H. and Haberfield, C. (2001b). A three-dimensional slope stability analysis method using the upper bound theorem. Part II: Numerical approaches, applications and extensions. Int. J. Rock Mech. Mining Sci. 38: 379-397.

Farzaneh, O. & Askari, F. (2003). Three-dimensional analysis of nonhomogeneous slopes. J. Geotech. Geoenviron. Engng ASCE, 129(2): 137-145.

Gens, A., Hutchison, J.N., and Cavounidis, S. (1988). Three-dimensional analysis of slopes in cohesive soils. Géotechnique, 38 (1): 1-23.

Hungr, O., Salgado, F.M. and Byrne, P.M. (1989). Evaluation of a three-Dimensional Method of Slope stability analysis. Can. Geotech. J. 26: 679-686.

Lam, L. and Fredlund, D.G (1993). A general limit equilibrium model for three-dimensional slope stability analysis, Can. Geotech. J. 30: 905-919.

Leshchinsky, D., Baker, R. and Silver, M. L. (1985). Three dimensional analysis of slope stability. Int. J. Numer. Anal. Methods Geomech., 9: 199–223.

Leshchinsky, D. and Baker, R. (1986). Three-dimensional slope stability: end effects. Soil and Foundations, 26 (4): 98-110.

Leshchinsky, D. and Huang, C. C. (1992). Generalized three-dimensional slope stability analysis. J. Geotech. Engng ASCE 118 (11): 1748–1764.

Lyamin, A. V. & Sloan, S. W. (2002a). Lower bound limit analysis using nonlinear programming. Int. J. Numer. Methods Engng, 55 (5): 573–611.

Lyamin, A. V. & Sloan, S. W. (2002b). Upper bound limit analysis using linear finite elements and non-linear programming. Int. J. Numer. Anal. Methods Geomech., 26: 181-216.

Michalowski, R. L. (1989). Three-dimensional analysis of locally loaded slopes. Geotechnique, 39 (1): 27–38.

PDE Solutions Inc. (2007). FlexPDE 5.0 - Reference Manual, Antioch, CA, USA.

SoilVision Systems Ltd. (2007). "SVOffice 2006 User's and Theory Guide." Saskatoon, SK, Canada.

Stianson, J. (2006). Personal communication.

Using Helicopter Electromagnetic Surveys to Identify Potential Hazards at Coal Waste Impoundments

Richard Hammack[1]

[1]Research Group Leader, Geosciences Division, National Energy Technology Laboratory, Pittsburgh, PA 15236; richard.hammack@netl.doe.gov

ABSTRACT: In July 2003, helicopter electromagnetic surveys were conducted at 14 coal waste impoundments in southern West Virginia. The purpose of the surveys was to detect conditions that could lead to impoundment failure either by structural failure of the embankment or by the flooding of adjacent or underlying mine works. Specifically, the surveys attempted to: 1) identify saturated zones within the mine waste, 2) delineate filtrate flow paths through the embankment or into adjacent strata and receiving streams, and 3) identify flooded mine workings underlying or adjacent to the waste impoundment. Data from the helicopter surveys were processed to generate conductivity/depth images. Conductivity/depth images were then spatially linked to georeferenced air photos or topographic maps for interpretation. Conductivity/depth images were found to provide a snapshot of the hydrologic conditions that exist within the impoundment. This information can be used to predict potential areas of failure within the embankment because of its ability to image the phreatic zone. Also, the electromagnetic survey can identify areas of unconsolidated slurry in the decant basin and beneath the embankment. Although shallow, flooded mineworks beneath the impoundment were identified by this survey, it cannot be assumed that electromagnetic surveys can detect all underlying mines. A preliminary evaluation of the data implies that helicopter electromagnetic surveys can provide a better understanding of the phreatic zone than the piezometer arrays that are typically used.

INTRODUCTION

On February 26, 1972, a coal waste impounding structure on Buffalo Creek in West Virginia collapsed, releasing approximately 132 million gallons of water (Davies and others, 1972). The resulting flood killed 125 people, injured 1,100, and left more than 4,000 homeless. Factors contributing to the impoundment failure included heavy rainfall and deficiencies in the foundation of the dam that led to slumping and sliding of the waterlogged refuse bank. This disaster resulted in regulations that govern the design of embankment structures for new impoundments (National Research Council, 2002). Since the implementation of regulations, no new embankments have failed. However, other types of impoundment failure have released water and coal slurry into streams. Some of these involved the breakthrough of water and coal slurry from impoundments into underground mines. The most notable incident occurred on October 11, 2000 near Inez, Kentucky where 250 million gallons of water and 31 million gallons of coal slurry from an impoundment broke into an underground mine and flowed via mine workings into local streams (National Research Council, 2002). Aquatic life was destroyed along miles of stream and temporary shut downs were imposed on a large electric generating plant and numerous municipal water supplies. This incident caused Congress to request the National Research Council to examine ways to reduce the potential for similar accidents in the future. The findings and recommendations of the National Research Council were published in a book titled "Coal Waste Impoundments, Risks, Responses, and Alternatives" (National Research Council, 2002).

In response to the recommendations of the National Research Council, the Robert C. Byrd National Technology Transfer Center (NTTC) at Wheeling Jesuit University in Wheeling, West Virginia contracted Fugro Airborne Surveys to conduct helicopter electromagnetic (HEM) surveys of 14 coal waste impoundments in southern West Virginia. The Department of Energy, National Energy Technology Laboratory (NETL) was asked to process, interpret, and validate survey data. The surveys were part of a federally funded pilot project to help reduce the dangers of coal slurry impoundments by: 1) identifying saturated zones within the coal waste, 2) delineating the paths of filtrate flow beneath the impoundment, through the embankment, and into adjacent strata or receiving streams, and 3) identifying flooded mine workings underlying or adjacent to the waste impoundment. It was anticipated that HEM surveys could show the flow path of filtrate through the embankment or into adjacent strata. This information may be useful for predicting impoundment failures or detecting possible impoundment-related contamination of local streams and aquifers.

Survey Description

Site Selection

NTTC selected 14 impoundments for airborne FDEM surveys from a list of impoundments in southern West Virginia that were given a moderate or high hazard potential rating based on the height of the embankment, the volume of material impounded, and the downstream effects of an impoundment failure (MSHA, 1974, 1983). Impoundments with moderate hazard potential are in predominately rural areas where failure may damage isolated homes or minor railroads, disrupting services or important facilities. Impoundments with a high hazard potential are those where failure could reasonably be expected to cause loss of human life, serious damage to houses, industrial and commercial buildings, important utilities, highways, and railroads.

The list of selected impoundments was transferred to the National Energy Technology Laboratory where flight areas were determined by constructing a bounding rectangle that enclosed the impoundments and ancillary structures, and included approximately a 1-km wide buffer around the impoundments. An effort was made to include known underground mines in the surveyed areas. The corner coordinates for flight area boundaries were transferred to Fugro Airborne Surveys for final flight planning.

Data Acquisition

In July 2003, Fugro Airborne Surveys performed frequency domain electromagnetic (FDEM) surveys of the selected coal refuse impoundments using the RESOLVE electromagnetic data acquisition system. This system consists of five coplanar transmitter/receiver coil pairs operating at frequencies of 385 Hz, 1.70 kHz, 6.20 kHz, 28.1 kHz, and 116 kHz and one coaxial transmitter/receiver coil pair that operated at a frequency of 1.41 kHz. Separation for the five coplanar coil pairs was 7.9 m; separation for the coaxial coils was 9 m. A complete description of the RESOLVE data acquisition system is available at http://www.fugroairborne.com/service/resolve.php. An optically pumped cesium vapor magnetometer mounted within the RESOLVE sensor was used to acquire total field magnetic data concurrent with the collection of electromagnetic data.

The surveys were flown using an Ecureuil AS350-B2 helicopter with the RESOLVE sensor suspended about 30 m beneath the helicopter as a sling load. Survey information was acquired by flying parallel lines approximately 50 m apart while attempting to maintain the sensor at an altitude of 35 m. However, the average sensor height during these surveys was 45 m because the rugged terrain, trees, and numerous power lines necessitated flying higher in certain areas for safety. At an average flight speed of 90 km/hr, the 10 Hz data acquisition rate resulted in one reading every 2.5 m along the flight line.

Data Processing

Preliminary data processing, including leveling and digital filtering, was performed by Fugro Airborne Surveys. Electronic data were then transmitted to NETL for additional processing, analysis, and interpretation. These data included conductivity maps for six frequencies, a total magnetic field (TMF) map, and a comma separated value (CSV) file containing leveled in-phase and quadrature data, and navigational data.

At NETL, conductivity and TMF maps were incorporated into GIS projects constructed for each site. Within the GIS environment, the locations of conductivity anomalies were spatially related to specific attributes of each coal refuse impoundment and the locations of known underground mine workings. In-phase and quadrature data were used to construct conductivity/depth images (CDI) using EM1DFM software. CDI sections were related to features on maps and air photos using custom viewing software developed at NETL (Veloski and Lynn, 2005).

RESULTS AND DISCUSSION

Coal waste impoundments are predominantly constructed of both coarse and fine coal waste, which can contain varying amounts of water. Coarse coal waste is used to construct the embankment of the impoundment because it is relatively homogeneous in particle size and strength characteristics, and is therefore a predictable construction material (National Research Council, 2002). Slurry containing fine coal waste is hydraulically discharged into the decant pond behind the embankment where solids settle, the coarsest material closest to the discharge point. In the more distal parts of the settling basin, water is decanted and recycled to the processing plant. Water also filters through the coarse coal refuse in the embankment or infiltrates into adjacent or subjacent strata. In typical impoundment construction, lifts of coarse coal refuse may be juxtaposed or superposed with fine coal refuse depending on the type of embankment raising employed.

Magnetic Response of Coal Waste

Coal waste commonly contains fugitive magnetite from the coal cleaning process and, therefore, exhibits a magnetic response that contrasts sharply with that of surrounding strata. A map of the total magnetic intensity (Fig. 1) can be used to delimit the areal extent of coal waste. Furthermore, during the construction of a coal refuse impoundment, coarse and fine coal refuse are handled separately and differently, and this may result in different magnetic signatures. Fine coal waste is deposited from a slurry, which allows magnetite dipoles to orient with the earth's magnetic field (detrital remanent magnetism) prior to deposition. In contrast, the orientation of magnetite dipoles in coarse coal refuse is random because the material is mechanically emplaced using trucks or conveyers followed by grading and compaction. Magnetic signatures from both coarse and fine coal waste are expressed downstream from the crest of the embankment where coarse coal waste overlies fine coal waste. Fine coal waste predominates in the decant basin of the impoundment; the magnetic signature for slurry deposited coal waste is expressed in this area.

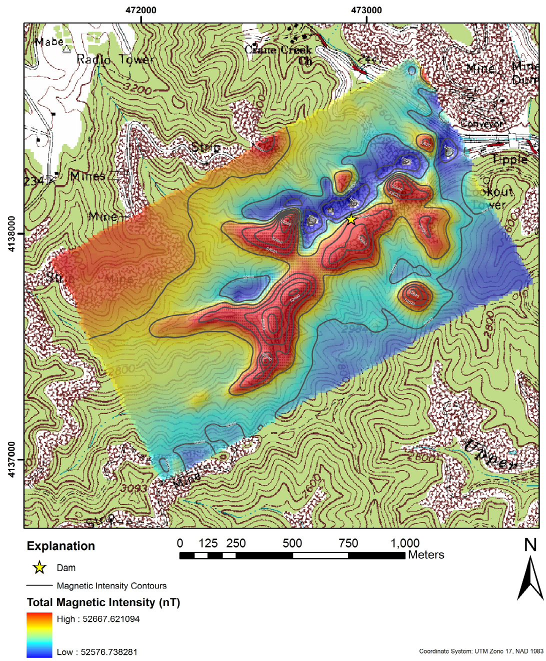

FIG. 1. Total magnetic field map of a coal waste impoundment in southern West Virginia.

Electromagnetic Mapping of Coal Waste Impoundments

The HEM response to different materials within the coal waste impoundment depends largely on the porosity of the material and the degree of water saturation, given that the electrical conductivity of impoundment water is much greater than the bulk conductivity of dry coal refuse. Saturated material with high porosity will be the most conductive. Saturated, well compacted material (lower porosity) will be somewhat less conductive. The least conductive material will be poorly compacted, coarse coal waste that is placed above the water table. Because of significant conductivity differences between saturated and unsaturated material, HEM can provide a clear demarcation between the vadose and phreatic zones within the embankment. When material is obviously below the water table, HEM provides an indication of porosity; more porous material will be more conductive. However, HEM does not provide an indication of permeability.

Figure 2 is a screen capture from custom NETL software that relates positions on a conductivity/depth image (CDI) to locations on a topographic map or georeferenced air photo. The CDI shows the EM1DFM model section for a flight line that crosses a coal waste impoundment. In the bottom left of the figure is an air photo of an impoundment with a colored, near-surface conductivity map and flight line map superimposed. Small, black-dotted crosshairs show coincident locations on the CDI and the air photo. Annotations point out major features of the coal waste impoundment including the decant basin and the crest and downstream parts of the embankment. The decant basin is the most conductive part of a coal waste impoundment because it often contains conductive, standing water several meters deep. In this case, the surface is less conductive than deeper areas of the decant basin, which may indicate that the conductive surface water has infiltrated or that lifts of coarse coal waste have been placed on the surface of the basin. The embankment crest is usually the least conductive area because it is composed of coarse coal waste placed high above the water table. The downstream embankment commonly contains conductive layers that represent the paths taken by water filtering through the embankment. Seeps are located where conductive layers are at or near the ground surface.

Figure 3 is a CDI and associated near-surface conductivity map that shows two conductive layers beneath parts of the decant basin and within the downstream embankment. Part of the decant basin's surface is conductive, which may indicate the location of standing water. The embankment crest is also conductive, probably from efflorescence, a deposit of soluble minerals brought to the surface by capillary action and evaporation. The downstream embankment contains two conductors, a near-surface conductor and a deeper conductor that is about 30 m below the surface. The presence of two strong conductors in the downstream embankment is unique to this impoundment. Other impoundments contain only one or sometimes no strong conductors in the downstream embankment. This impoundment has a downstream raised embankment, which afforded the operator the opportunity to incorporate blanket drains during embankment construction. The deep conductor beneath the downstream slope of the embankment probably depicts the location of a blanket drain. Conductive areas on or near the surface of the downstream embankment are seeps where filtrate water surfaces or concentrations of soluble minerals were deposited by evaporation.

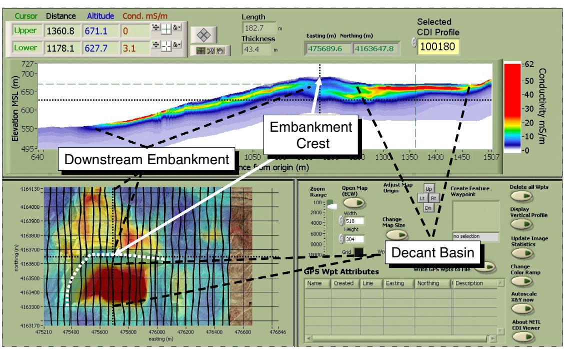

FIG. 2. CDI showing different areas of a coal waste impoundment and typical electromagnetic response.

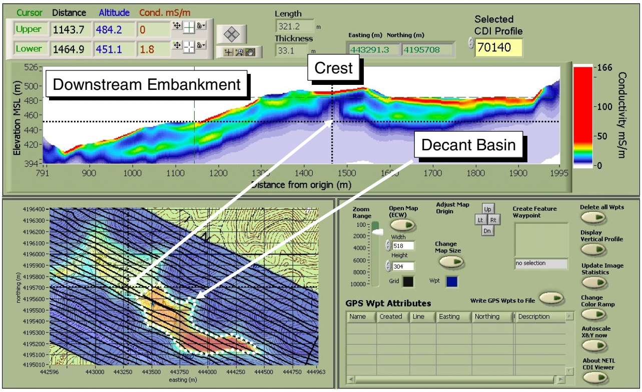

FIG. 3. CDI from a flight line that crosses an impoundment with a downstream raised embankment.

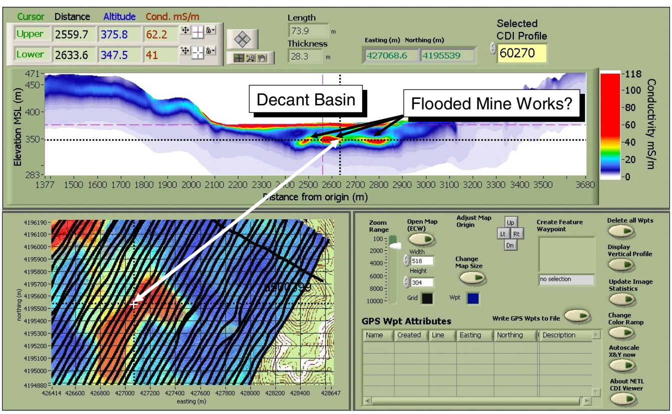

FIG. 4. CDI showing flooded mine workings beneath decant basin.

Figure 4 is a CDI from a flight line that crosses the decant basin of an impoundment thought to be leaking into underground mine workings. This figure depicts a discontinuous conductor about 30 m below the surface of the decant basin that may represent flooded underground mine workings. Resistivity surveys conducted as part of the ground verification activities confirmed the existence of this conductor (data not shown). Although there are no records of an underground mine at this location and elevation, there are permits on record to auger mine the Winnifrede Coal at this location. The Winnifrede Coal occurs at the same elevation as the conductive anomalies. We suspect that the Winnifrede Coal was auger mined from a strip bench now buried beneath the decant pond, and that the flooded auger bores are the source of the conductive anomalies. Although, HEM surveys of the 14 impoundments identified numerous flooded mine workings that are above drainage, this is the only CDI that may show flooded, underground mine workings beneath the impoundment.

The flowable nature of unconsolidated slurry is a potential cause of impoundment failure, especially when deeply buried within the embankment. Unfortunately, locating pockets of unconsolidated slurry is a hit-or-miss adventure when drilling is used for detection. HEM can quickly locate pockets of unconsolidated slurry so that drilling and monitoring activities can be concentrated on smaller areas. Figure 5 is a CDI that shows a pocket of unconsolidated slurry 38 m below the top of the embankment. The coordinates for this conductive anomaly can be imported into a GPS-equipped PDA with a moving map, which would allow the impoundment operator to walk to a location on the embankment that is directly over the anomaly. Drilling efficiency is increased when directed by HEM results because all holes would be on target.

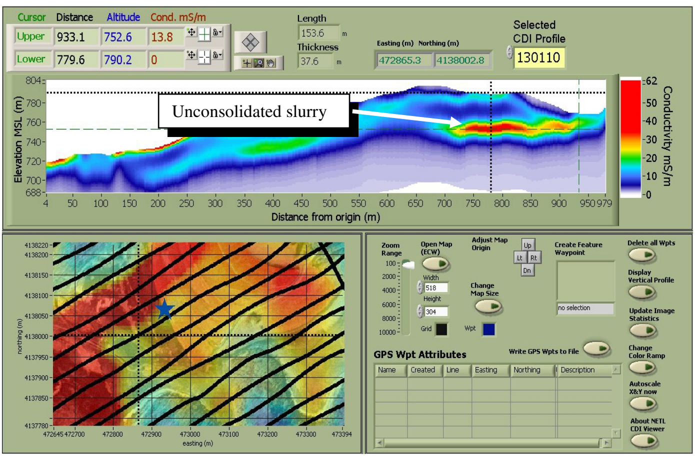

Figure 5. CDI showing a pocket of unconsolidated slurry buried 38 m deep in the embankment.

CONCLUSIONS

Helicopter electromagnetic surveys provide a 3-dimensional picture of the conductivity distribution within coal waste impoundments. NETL personnel have used ground resistivity surveys to confirm the accuracy of HEM results (ie. to corroborate the location, depth, thickness, and conductivity of conductors). For the purposes of this study, water is assumed to be the most conductive component of coal waste impoundments, and conductive areas are assumed to be areas of greater water content. Hydrologic interpretations that have been made using HEM data from 14 coal refuse impoundments appear to justify this assumption. However, if hydrologic interpretations based on HEM data are to be used for making regulatory decisions, the interpretations must be substantiated with results from accepted sources of hydrologic data. Currently, we suggest only that HEM results be used to target investigations that use conventional methods to directly measure physical or hydrological properties.

Results of this study suggest that conductivity/depth images generated from HEM data can be used to identify many hydrologic features of coal waste impoundments. For example, the pathways taken by filtrate through the embankment can be discerned easily by following conductors from the decant pond through the embankment until they emerge on the downstream face. One can predict areas prone to seepage by noting where conductors are at or near the surface. Also, HEM should be able to detect flooded mine workings that are adjacent to coal waste impoundments. Detection of flooded mine workings beneath the impoundment is less certain, however, because the exploration depth of HEM is limited by the conductive materials that comprise the impoundment. HEM appears to be able to identify pockets of unconsolidated slurry in the decant pond or beneath the embankment.

Hydrologic features detectable by HEM have been linked to past impoundment failures. For example, HEM should be able to depict the location of the phreatic surface between the decant basin and its emergence on the downstream slope of the embankment. This knowledge will help identify sites of internal erosion (piping) or surface erosion. HEM also can locate large areas of unconsolidated slurry beneath the embankment that may be subject to fluid-like flow under certain conditions. Finally, any flow of water or slurry from the decant basin into flooded mine workings or aquifers will be detected by HEM if within the exploration depth of HEM.

The 14 impoundments were chosen for HEM surveys because they were assigned a medium to high hazard potential indicating the amount of damage possible should they fail. Because HEM can identify some subsurface conditions that are linked to impoundment failure, the higher density of coverage provided by HEM surveys (versus conventional monitoring) gives added assurance that potential problems at these impoundments will be identified and corrected.

REFERENCES CITED

Davies, W. E., Bailey, J. F., and Kelly, D. B. (1972) "West Virginia's Buffalo Creek Flood: a study of the hydrology and the engineering geology." U.S. Geological Survey Circular 667.

MSHA (1974) "Design guidelines for coal refuse piles and water, sediment, or slurry impoundments, and impounding structures." Informational Report 1109, US Department of Labor, 29 p.

MSHA (1983) "Design guidelines for coal refuse piles and water, sediment, or slurry impoundments, and impounding structures." Amendment to Informational Report 1109, US Department of Labor, 6 p.

National Research Council (2002) "Coal waste impoundments; risks, responses and alternatives." National Academy Press, Washington, DC, USA, 230 p.

Veloski, G. A. and Lynn R. J. (2005) "Software for the visualization and interpretation of conductivity/depth images." in Proceedings of the 2005 Symposium for the Application of Geophysics to Engineering and Environmental Problems, Atlanta, GA, April 3-7, 2005.

Geophysical and Remote Sensing Characterization to Mitigate McMicken Dam

Michael L. Rucker[1], M. ASCE, P.E., Michael D. Greenslade[2], P.E.,
Ralph E. Weeks[3], P.G., Kenneth C. Fergason[4], P.G. and Bibhuti Panda[5], P.E.

[1]Senior Engineer, AMEC Earth & Environmental, Inc., 1405 West Auto Drive, Tempe, AZ 85284; michael.rucker@amec.com
[2]Dam Safety Engineer, Flood Control District of Maricopa County, 2801 West Durango Street, Phoenix, AZ 85009 mdg@mail.maricopa.gov
[3]Senior Geologist, AMEC Earth & Environmental, Inc., 1405 West Auto Drive, Tempe, AZ 85284; ralph.weeks@amec.com
[4]Project Geologist, AMEC Earth & Environmental, Inc., 1405 West Auto Drive, Tempe, AZ 85284; ken.fergason@amec.com
[5]Senior Engineer, AMEC Earth & Environmental, Inc., 1405 West Auto Drive, Tempe, AZ 85284; bibhuti.panda@amec.com

ABSTRACT: By 2002, earth fissures, open ground cracks in the subsurface induced by groundwater withdrawal from basin alluvium, had visibly propagated close to McMicken Dam west of Phoenix, Arizona. Using surface seismic measurements, these fissures were traced to and beyond the dam. Initial test pits and trenches at seismic fissure interpretations confirmed this otherwise undetectable piping erosion hazard at the dam. An investigation to characterize the hazard extent, mechanisms and predict future behavior for risk assessment and mitigation design was then implemented. Deep alluvial basin geometry and material properties characterization across the site was accomplished using surface geophysical gravity, large array surface resistivity and s-wave refraction microtremor seismic methods. Earth fissure presence and absence was further assessed using seismic refraction and test trenches; the results also assisted geotechnical characterization. Newly developed satellite interferometry by synthetic aperture radar (InSAR) provided historic differential subsidence information for the area back to 1992 when data collection began. Finite element modeling developed and calibrated using these results provided predictions for risk assessment and mitigation design. A new dam section avoiding fissures was designed and constructed. The monitoring program includes InSAR and GPS survey, tape extensometers and Time Domain Reflectometry (TDR) at the dam toe.

1. INTRODUCTION

In 1981, earth fissures induced by groundwater withdrawal from basin alluvium were discovered in the vicinity of McMicken Dam, a 9-mile long earthen flood retention structure located west of Phoenix, Arizona (Figure 1). Propagation of these fissures closer to the dam was observed in surface erosion features during a 2002 inspection. Using surface seismic measurements, the interpreted subsurface extent of these fissures was traced under and beyond the dam. Fissure detection was interpreted as sudden loss of signal or delayed arrival times in the seismic traces (Figure 2). Earth fissures can occur when differential subsidence induces significant horizontal tension in basin alluvium as a dropping water table causes the basin alluvium to consolidate. Less subsidence occurs where the alluvium is relatively thin (shallow bedrock), and alluvium with greater amounts of clay tends to consolidate more relative to the same thickness of coarser grained alluvium. Since open fissures under the normally dry dam could lead to piping erosion and possible failure, an extensive program to characterize and mitigate this hazard was initiated. The remedial response to earth fissure hazards at McMicken Dam is an expression of the Flood Control District's continuing mission to reduce the risk of flooding for the Citizens of Maricopa County, Arizona by providing well perceived and efficiently implemented management strategies. The McMicken Dam remedial project is part of an ongoing program of dam safety assessment and rehabilitation, designed to assure flood protection in a region of rapid population growth and associated infrastructure.

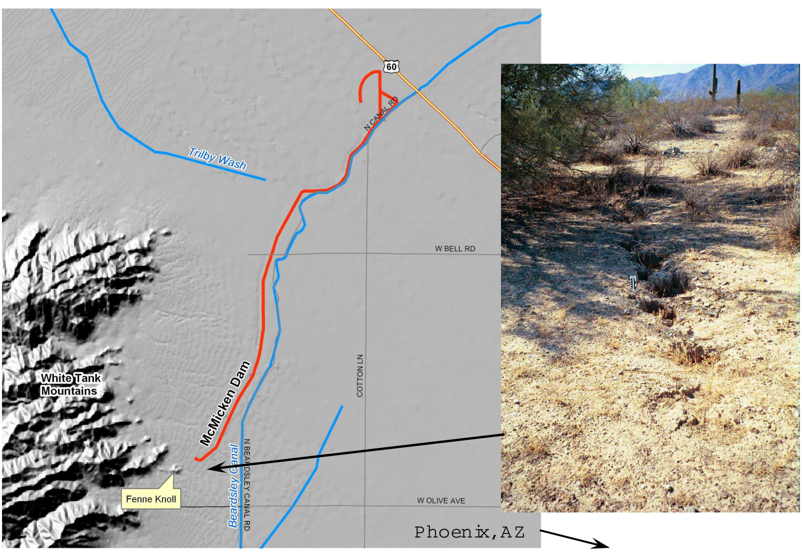

FIG. 1. Dam location relative to shallow bedrock and historic (1981) fissure.

2. DISCOVERY AND INITIAL TRACING OF NEW EARTH FISSURES

Earth fissures were originally in the area in 1981 during a previous rehabilitation of the dam. In 2002, expanded or new earth fissuring closer to the downstream dam toe was observed during inspection surface geologic reconnaissance. Initial subsurface evaluation consisted of three test pits (TP-1, -2, -3 in Figure 2) excavated across the new fissure features nearest the dam. No fissure feature was observed in TP-1 closest to the dam. Concerned that TP-1 missed the fissure, the geologists recommended surface geophysics to assist in locating further test pit activities.

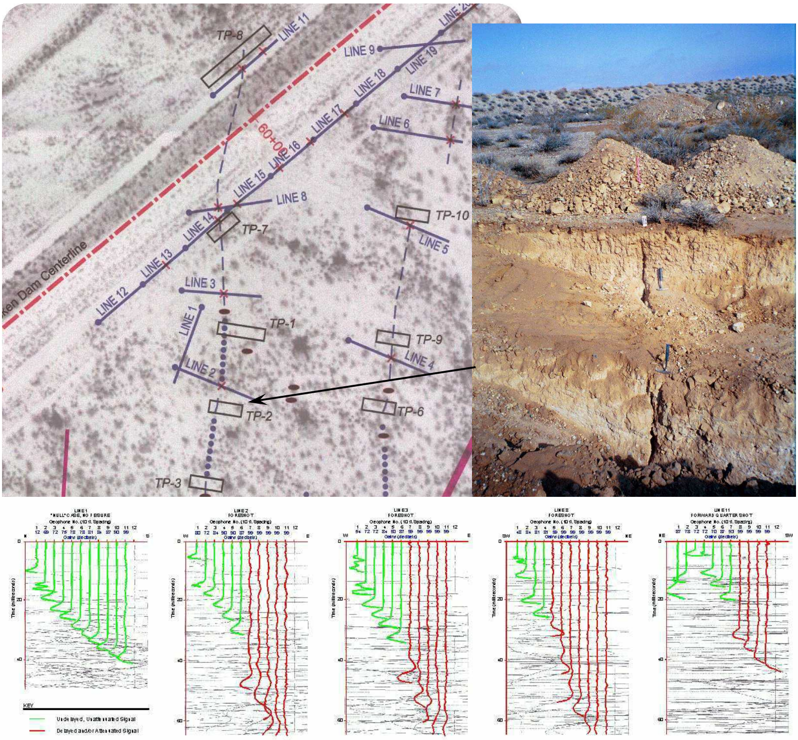

FIG. 2. Initial test pit and seismic refraction tracing of fissures at dam.

Rucker and Keaton (1998) and Rucker and Holmquist (2006) had developed seismic refraction methods for fissure tracing based on abrupt attenuation and time delays in first arrival seismic signals across a fissure-type feature; the methods were applied at the site. A 12-channel seismograph, 36-meter geophone array and sledge hammer energy source were used. Figure 2 includes example traces from Lines 1, 2, 3, 8 and 11 along what was traced as a fissure feature going under the dam. Line 1 was a null line that was parallel to and did not cross the fissure trend; first arrival traces through this seismic line were normal. Other traces showed abrupt, severe signal attenuation and anomalous time delays; interpreted anomaly locations are shown as red x's on seismic lines in Figure 2. Line 2 matched the known fissure at TP-2 (see photo in Fig. 2), and Line 3 identified that the fissure trend was located at the end of TP-1 where the pit was not sufficiently deep to locate the fissure.

3. QUANTIFICATION OF LAND SUBSIDENCE

Once the earth fissure risk was identified and the dam shown to be at risk, it was necessary to understand and quantify the hazard to guide and assist in the tasks of risk assessment and mitigation. Differential land subsidence was the mechanism of earth fissure development and location. Thus, quantification and understanding of the land subsidence at the site was the essential next step to abating the risk.

3.1 Historic Survey

The area of immediate concern was the southern end of the dam; nearby surface bedrock was evidence of deepening bedrock along the dam profile. Historical differential subsidence data was limited to crest elevation changes from 1955 to 1981, repeat surveys at benchmarks along the dam since 1985, and a few nearby National Geodetic Survey benchmarks. Although a reasonable and usable amount of historic elevation change data was available along the dam crest, no survey data existed off of the crest in the local area. Thus, only differential subsidence patterns near perpendicular to the dam axis could be effectively quantified, and differential subsidence patterns acute or sub-parallel to the dam axis could not be detected or quantified from available historic survey data.

3.2 Satellite Interferometry by Synthetic Aperture Radar (InSAR)

About this time results from a new satellite-based remote sensing technology radically expanded the potential to understand subsidence distribution and magnitudes throughout the region. Interferometry by synthetic aperture radar (InSAR) compares phase shift between time-separated radar data (typically separated in time by months or years) to measure relative elevation changes of 30 m by 30 m pixels to near-millimeter resolution, throughout typically 100 km by 100 km scenes. Radar data acquisition and archiving utilizing C-band radar with a 6 cm wavelength began in 1992 and continues; more satellites with additional frequency bands are coming on line. Phase shift in an interferogram is typically represented in cyclic color bands such as blue to pink to orange to yellow to green to blue shown in Figure 3. A complete phase cycle (360^{o} or 2pi radians), such as blue to blue (dark to dark) or yellow to yellow in a 6 cm reflected radar wave occurs with 3 cm of differential elevation change. Color bands can be considered equivalent to contour lines and intervals. An interferogram from radar data taken in December of 1996 and 1999 shows differential subsidence in part of the northwest Salt River Valley over that 36 month period. The White Tank mountains are in the left part, McMicken Dam is in the center part, and Sun City, Arizona is in the right part of the interferogram. Considerable differential subsidence, about 6 cm or more, is indicated in at least two color cycles in the Sun City area. Differential subsidence color banding is also apparent to the right (east) of Luke Air Force Base. Color banding in the White Tank Mountains is an artifact of processing an area with extreme topographic change. In agricultural areas, plowing and crop growth change the surface reflection elevation.

Similarly, surface changes occur in areas of new development and construction between radar images. Areas such as these that interfere with the radar signal phase change patterns show as decorrelated mottled colors as exemplified in the interferogram center.

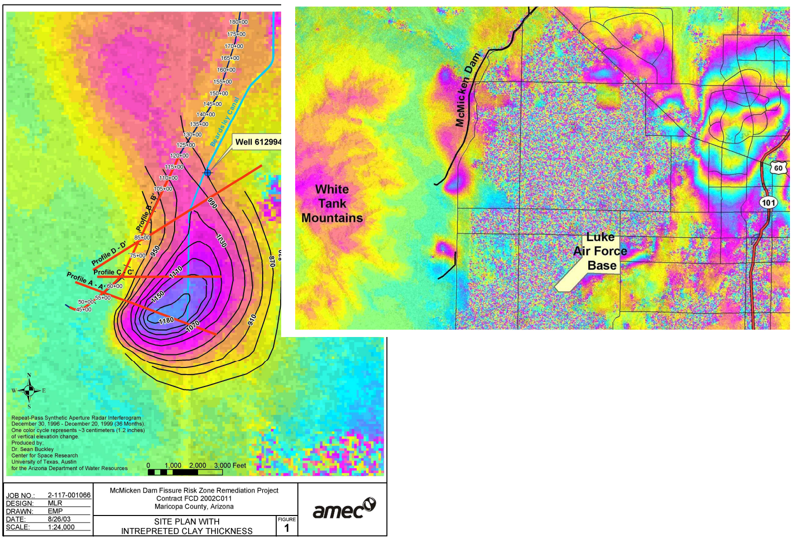

FIG. 3. 36-month InSAR interferogram showing elevation changes in area

Detailed InSAR results at the dam in Figure 3 document the presence of a feature of increased subsidence adjacent to the south end of the dam. Identified fissures in the area were located along the subsidence feature edge closest to the dam. That area is where subsidence induced ground tension strains would be anticipated to be greatest. InSAR also provided corroboration with survey of post-1992 differential subsidence measurements, and survey data provided confidence in the remote sensing results.

4. CHARACTERIZING BASIN ALLUVIUM

Having quantified subsidence, and with available historic well records for ground water decline trends, characterization of the basin alluvium geometry and material properties would make possible effective finite element modeling for future subsidence and earth fissure prediction. Three surface geophysical methods, gravity, resistivity and refraction microtremor seismic, were utilized (Rucker and Fergason, 2004). The variable depth to bedrock was generally interpreted through the area from gravity measurements made through the area generally shown in the Figure 3 detail on a 60 m by 120 m grid tied to bedrock at Fenne Knoll. No deep well data existed for gravity calibration bedrock depth. Bedrock depth calibration points for gravity were interpreted from seven deep refraction microtremor seismic (Louie, 2001) profiles using a 12-channel seismograph, 220-meter geophone array with 4.5 Hz geophones, and the field vehicle as a low frequency ambient energy source. Bedrock depths were interpreted in areas where bedrock depth was less than about 100 meters. Seven resistivity soundings were made using the Wenner 4-point method with electrode spacings ranging from 1.5m to 300m. Results from deep resistivity soundings were used to infer primarily clay, more compressible, very low permeability regions in the alluvium which would have different subsidence characteristics than the typical basin alluvium. These more clayey zones are associated with InSAR interpreted subsidence features as shown in Figure 3, and have considerably lower resistivities than typical basin alluvium. The subsurface profile shown in Figure 4 was derived from this geophysical data.

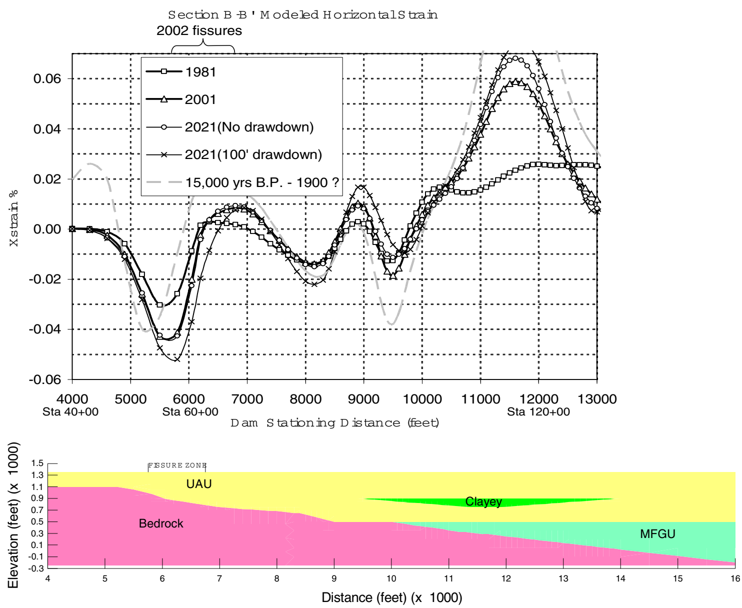

FIG. 4. Dam axis finite element model profile and modeled strain

5. MODELING SUBSIDENCE AND TENSILE STRAIN

Using the geophysically derived alluvium geometry and material distribution, survey and water level declines, 2-d finite element models were developed and calibrated (Weeks and Panda, 2004). Four finite element profiles are shown in Figure 3, with the AA-profile crossing the InSAR characterized subsidence feature and the BB-profile along the dam axis. The BB-profile subsurface model and modeled horizontal strains are shown in Figure 4; strains greater than about 0.02 percent were considered capable of initiating earth fissuring (Holzer, 1984). Once calibration was complete, forward predictions were made in 2003 to provide reasonable future subsidence and earth fissure scenarios to assist in selecting and designing mitigation and remediation.

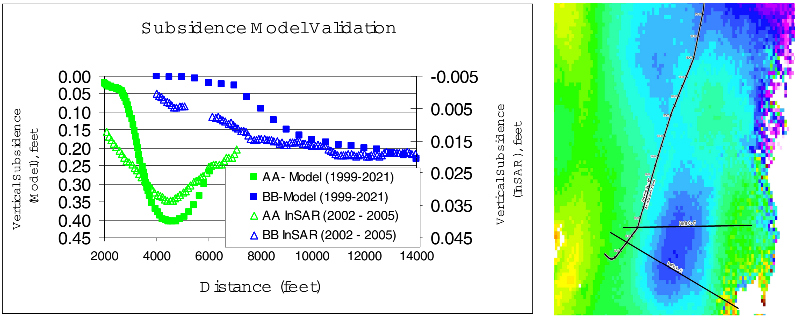

FIG. 5. Comparison of model subsidence prediction with 2002-2005 InSAR

A comparison of AA- and BB-profile modeled subsidence from 1999 to 2021 with actual InSAR measurements between 2002 to 2005 is shown in Figure 5. Although details vary, the general subsidence character and magnitude of the modeled 22 year prediction is similar to the 3 year InSAR measurement.

6. DAM MITIGATION AND MONITORING

Following the modeling effort, risk assessment, geotechnical investigation, and mitigation design, dam mitigation was accomplished. The south end of the dam area with earth fissures was abandoned, and a new section of dam constructed (Figure 6).

FIG. 6. Reconstructed dam section, TDR trench and tensile strain at Station 96

A monitoring program for the earth fissure area and the new and existing dam was designed and has been implemented. That program includes GPS survey and InSAR monitoring of subsidence, precision tape extensometer and rod extensometer measurements in the fissure zone and in select areas of modeled tensile strain, and 900 meters of trench with TDR cables encased in low strength concrete at the southernmost end of the old and new dam sections. Prior to TDR cable installation, the trenches were geologically logged. In the vicinity of dam Station 96+00, the ground showed visible indications of tensile strain (Figure 6) in the same area that the finite element modeling (Figure 4) indicated about 0.02 percent strain in 2001. No fissures have been observed in that area. Tensile strain is predicted to reduce in the future (Figure 4) at that location. Monitoring by GPS survey and tape extensometer will verify the accuracy of that prediction.

7. CONCLUSION

Task appropriate use of geophysical methods and application of new InSAR remote sensing technology were crucial to the identification, characterization and remediation of a significant geologic hazard impacting a major flood control dam.

ACKNOWLEDGEMENTS

The strong support and encouragement of the Flood Control District of Maricopa County was essential in the application of the new methods and technologies used in this project. The Arizona Department of Water Resources provided InSAR data for this project under an intergovernmental agreement with the Flood Control District.

REFERENCES

Holzer, T.L. (1984) “Ground failure induced by ground-water withdrawal from unconsolidated sediment.” *Reviews in Engrg. Geol.*, Vol. 6, GSA, Boulder, CO.

Louie, J.L. (2001) “Faster, better: Shear-wave velocity to 100 meters depth from refraction microtremor arrays,” *Bull. of the Seismological Soc. Am.,* 91: 347-364.

Rucker, M.L. and Fergason,K.C. (2004) “Role of practical geophysics to investigate and mitigate a distressed flood control dam,” Proceedings of the 24th Annual Conf. of the Assoc. State Dam Safety Officials, Phoenix, AZ, Sept 25-30.

Rucker, M.L. and Holmquist, O.C. (2006) “Surface seismic methods for locating and tracing Earth fissures and other significant discontinuities in cemented unsaturated soils and earthen structures.” *Unsaturated Soils* (GSP 147), ASCE, Reston/VA: 601-612.

Rucker, M.L. and Keaton, J.R. (1998) “Tracing an earth fissure using seismic refraction methods and physical verification.” *Land Subsidence Case Studies and Current Research: Proceedings of the Dr. Joseph F. Poland Symposium on Land Subsidence*, Spec. Publ. No. 8, AEG, Star Publishing Co., Belmont/CA: 207-216.

Weeks, R.E. and Panda, B.B. (2004) “Defining subsidence-induced earth fissure risk at McMicken Dam,” Proceedings of the 24th Annual Conf. of the Assoc. State Dam Safety Officials, Phoenix, AZ, Sept 25-30.

LNG Containment Dike Design and Monitoring at Southern LNG Elba Island Phase II Expansion

Guoming Lin[1], Jian Fang[2]

[1] Chief Engineer, WPC, Inc., 2201 Rowland Avenue, Savannah, GA 31404; Glin@wpceng.com
[2] Project Engineer, WPC, Inc., 2201 Rowland Avenue, Savannah, GA 31404; Jfang@wpceng.com

ABSTRACT:

The phase II expansion of the Southern LNG Elba Island terminal involved construction of a new storage tank and 3400 linear feet of earthen containment dikes. The dikes, classified as Category I structure, were designed and constructed to contain liquefied natural gas (LNG) in the event of a spill in accordance with the FERC requirements. The site features a layer of very soft clay in the upper 35 feet underlain by loose to medium dense sand layer. The design and construction had to overcome challenges in slope stability, settlement and potential liquefaction. This paper discusses the design considerations and the instrumentation and monitoring program performed during construction.

INTRODUCTION

Southern LNG Elba Island Terminal is one of the four LNG import terminals currently operating in the US. The terminal is located on an island within the Savannah River approximately five miles east of downtown Savannah. The facility was initially developed with three tanks in the 1970s, but only operated very briefly before it was shut down in 1978. The facility was re-commissioned in 2000. The phase II expansion, completed in 2005 with a total cost over $150 millions, included construction of a new 257 ft diameter double wall steel storage tank, 3400 linear feet of containment dikes, two docks in a dredged slip and various auxiliary equipments and pipelines.

A secondary containment dike is required to contain the liquefied natural gas on site in the event of a spill. Controlled by the area available, radial distance and impoundment volume required, the dike had a configuration of approximately 14 feet in height, five feet wide at top and a side slope of 3 to 1 (horizontal to vertical). The facility is permitted by the Federal Energy Regulatory Commission (FERC). The dike design was required to comply with various regulatory requirements, among those is to resist a safety shut down earthquake (SSE) which was defined as an earthquake with a probability of exceedance of 0.5% in 50 years (a 10,000 year event) in accordance with NBSIR 84-2833 and NFPA 59A (1996).

SITE AND SUBSURFACE CONDITIONS

`

Elba Island was formed by dredge material from the Savannah River and is known for very weak soils. A grassed area in front of the administration building has settled more 20 inches in the last 30 years and new steps had to be added in order to enter the pile-supported building from the paved sidewalk. A comprehensive geotechnical exploration was performed for the phase II expansion, including soil test borings, cone penetration test (CPT) soundings and flat blade dilatometer (DMT) soundings. The site is underlain by 35 feet of very soft clay and approximately 15 feet of loose to medium dense sand and the marl formation at approximately 50 feet below grade. Table 1 shows a generalized subsurface stratigraphy and soil density or consistency

TABLE 1. Generalized Subsurface Stratigraphy, Soil Density and Consistency

Layer No.	Soil Type	Elevation (ft, MLW)	Thickness (ft)	SPT N	CPT Tip Resistance (tsf)	DMT Modulus (tsf)
1	Surface crust	11 to 7	4	4 ~ 10	10 ~ 15	30 ~ 80
2	Soft clay	7 to -25	32	WHO ~ 4	3 ~ 5	10 ~ 30
3	Sand (SP)	-25 to -40	15	11 ~ 36	100 ~ 200	400 ~ 700
4	Marl	-40 to -95	55	9 ~ 44	30 ~ 80	200 ~ 400

The properties of Layer 2 (soft clay) are of primary concern from a settlement and stability standpoint. The soil has a natural moisture content of 40 to 160 percent, fines content over 90 percent and liquid limits of 130 to 250. The soil is considered highly compressible with compression ratios of 0.3 to 0.5. The soil would be considered normally consolidated based on the laboratory consolidation test results and empirical correlation between overconsolidation ratio (OCR) and CPT tip resistances. However, the fact that the grassed field has continued to settle in the recent years suggests the soils are actually underconsolidated. The layer exhibited increased consistencies with depths. The undrained unconsolidated triaxial tests yielded undrained shear strengths from 220 psf to 350 psf.

DESIGN CONSIDERATIONS

The presence of thick soft clay layer and stringent requirements in seismic design posed three challenges to the dike design and construction as outlined in the follow paragraphs.

Slope Stability Analysis

It was recognized at the beginning that slope stability would be a major concern for the containment dikes due to the thick soft clay layer beneath the surface crust. Slope instability, in the form of mudwave, had been observed on many sites east of downtown Savannah along the Savannah River. Slope sliding occurred during the initial development of the site in the 1970s, and a slope failure took place along a section of the dredged embankment during the slip dock construction in 2005. The undrained shear strengths of the soft clays generally increased with depth from 220 psf to 350 psf. The initial analysis indicated the dike slope would be stable with a factor of safety of 1.5 if the undrained shear strength was at least 350 psf.

Ground improvement with stone columns, deep soil mixing or pile supported embankment was considered, but deemed too costly. Fortunately, the construction schedule of this project was governed by tank construction, not dike construction. A prolonged construction schedule would allow the consolidation of the soft clays and increase of strength of the soft clay over time. Wick drains were used to accelerate the consolidation. To take advantage of the prolonged construction schedule, the design stipulated a fill placement rate of no more than one lift (8 to 10 inches) per week. The design incorporated an instrumentation program to verify the dissipation of pore water pressure within the soft clay layer and monitor the displacements of the soft clay layer in both vertical and lateral directions. Figure 1 shows the final section of the dikes with instrumentation layout.

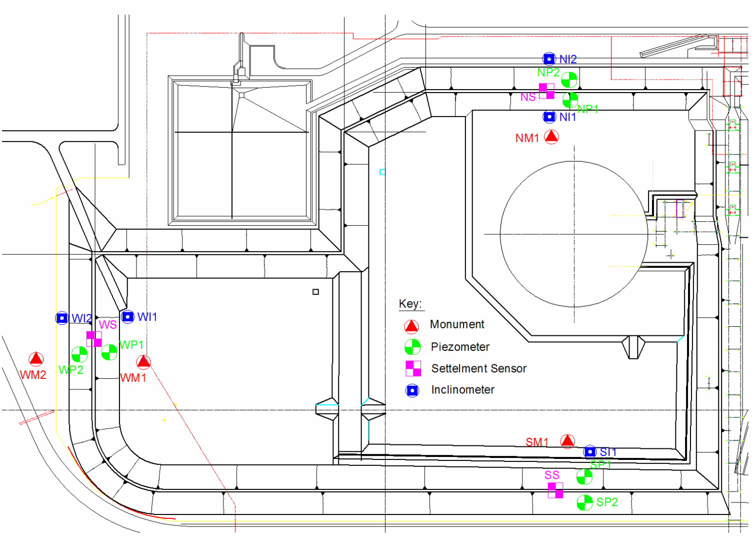

FIG. 1. Dike Layout and Monitoring System

Settlement Analysis

The sand and marl (layers 3 and 4) are practically incompressible relative to the soft clay layer. The compressibility of the soft clay was characterized by constrained modulus (M), which can be correlated to net cone tip resistance using a coefficient α_{nr} or DMT modulus. Senneset *et al.* (1989) proposed α_n ranging between 4 and 8 for normally consolidated clay. Kulhawy and Mayne (1990) suggested a more general relationship using α_n of 8.25. In general, the constrained modulus obtained from correlations with the in-situ testing methods compared favorably with those obtained from the laboratory consolidation tests. An average settlement of 30 inches was calculated for the dikes.

The use of wick drains and prolonged construction schedule would help increase the amount of settlement during construction and thus reduce post construction settlement. To maintain the free board and impoundment volume after post construction settlement, the dikes were required to be over-built to compensate the loss of height due to settlement. The amount of overbuild was determined near the end of dike construction and monitoring.

Liquefaction Analysis

Liquefaction analysis became an interesting topic because various regulatory requirements placed great emphasis on evaluation of seismic effects while the seismicity hazard in the area and the subsurface conditions rendered the site with low susceptibility of liquefaction. Liquefaction analyses were performed in accordance with the procedures outlined in the article "Liquefaction Resistance of Soils, Summary Report from the 1996 NCEER and 1998 NCEER/NSF Workshops on Evaluation of Liquefaction Resistance of Soils" by Youd and et al (2001). A comprehensive site-specific seismic hazard study was performed for this project to develop seismic design parameters (WPC, 2002). The peak ground acceleration and spectral accelerations increase significantly from the bedrock to the ground surface due to the amplification effect of the soft soil deposits. The potentially liquefiable soil layer is located at approximately 30 to 50 feet below existing grades. A site response analysis was performed using equivalent linear properties developed from the measured and estimated shear wave velocities to obtain mean peak ground accelerations in the center of the sand layer for liquefaction analysis. SPT blow counts after corrections of hammer energy and overburden stress, CPT tip resistance and shear wave velocities were used in the evaluation of liquefaction resistance. For a peak ground acceleration of 0.32g and a magnitude 7.6 (Mw) earthquake, only localized zones within the sand layer were found liquefiable.

The liquefaction potential was also evaluated considering the historical and geologic data. Based on worldwide data compiled by Ambraseys (1988), liquefaction has not been observed beyond 100 km from the epicenter for an Mw=7 earthquake. Savannah is located approximately 150 km from Charleston. Evidence of liquefaction was found in the Bluffton and Hilton Head Island areas from the 1886 Charleston earthquake, but no evidence of liquefaction was found in the Savannah area (Amick and Gelinas, 1991). Seismic settlement was calculated using procedures developed by Tokimatsu and Seed (1987), and a total settlement of 1 to 3 inches was estimated for all SPT boring and CPT sounding locations along the dikes. Unified methodology for seismic stability and deformation analysis developed by Kavazanjian et al (1997) was used in the stability analysis of the dike slopes under earthquake conditions.

Considering the low risk of liquefaction and small deformation from liquefaction in localized zone, we proposed to extend the wick drains into the sand layer as liquefaction mitigation measure. According to Dr. Jimmy Martin of Virginia Tech, a site with wick drain did not suffer liquefaction during the 1999 Turkey Earthquake while a comparable site without wick drains did liquefy. As such, the use of wick drains was proven to be effective in mitigating liquefaction.

INSTRUMENTATION AND MONITORING

Dike construction started in April 2004 and completed in June 2005. Wick drains were installed in a triangular pattern at five feet on centers. A relatively heavy rig was used for wick drain installations to ensure penetration into the sand layer, and the wick drains were cut off after penetration refusal or at the bottom of the sand layer. In lieu of a free draining sand layer, the contractor used a fabricated drainage blanket at the dike bottom. The wick drains were connected to the drainage blanket and a layer of geogrid was placed on top of the drainage blanket. Fill was placed at a controlled rate of one lift per week or slower. The fill was mostly silty fine sands (SM) or slightly clayey fine sands and compacted to 95 percent of the maximum dry density in accordance with the modified Proctor compaction tests.

Three sections of the dike were selected for monitoring. At each section, the monitoring system consisted of settlement sensors, piezometers, inclinometers and survey monuments as summarized in Table 2. Figure 1 shows the site layout of the monitoring system and Figure 2 shows the dike cross section and instrumentation scheme.

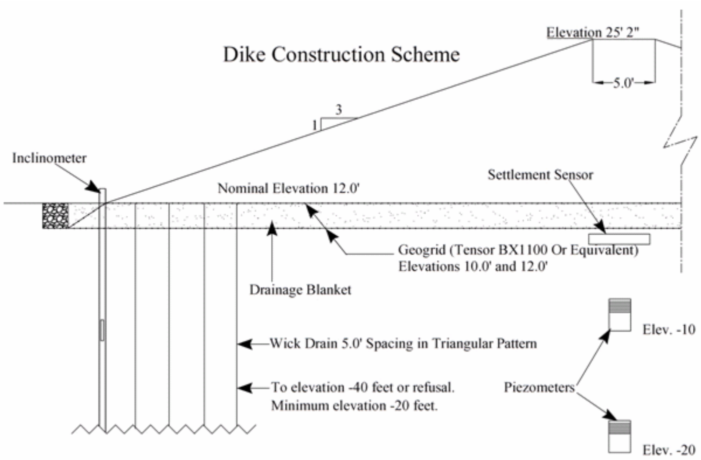

FIG. 2. Dike Construction and Instrumentation

TABLE 2. Instrumentation Installed on Tank D-4 Dike

Monitoring Section	North	South	West
Settlement Sensor	NS	SS	WS
Piezometer	NP1 (30’) NP2 (20’)	SP1 (30’) SP2 (20’)	WP1 (30’) WP2 (20’)
Inclinometer	NI1	SI1	WI1,WI2
Survey Monument	NM1	SM1	WM1, WM2

Figure 3 shows the measured settlements at three dike sections. The maximum measured settlements at the west and north dikes were between 23 and 32 inches, which were close to the predicted settlement of 30 inches based on average soil modulus derived from DMT soundings and laboratory testing. Settlement at the south dike was greater than 42 inches near the end of fill placement when the settlement sensor became damaged probably by cable disconnection due to the large settlement.

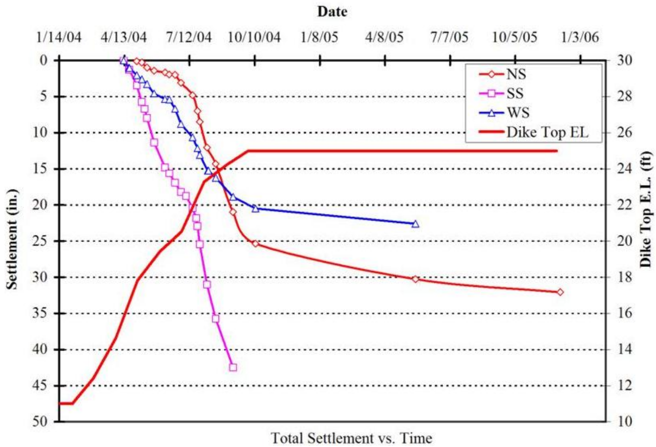

FIG. 3. Dike Settlement Monitoring Results

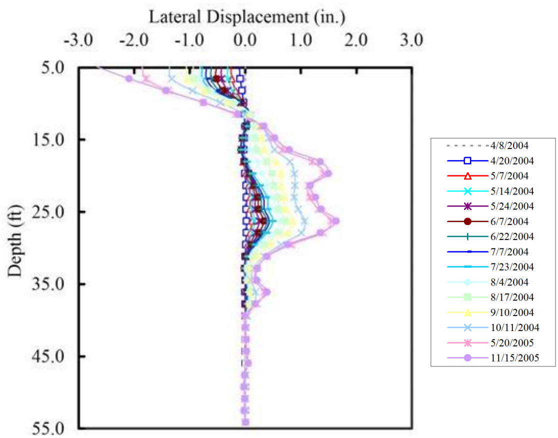

FIG. 4. Lateral Displacement vs. Depth at Different Time

The large settlement at the south dike can be explained from the inclinometer data shown in Figure 4. The inclinometer data indicated the foundation soils experienced little lateral movement (less than 0.25 inches) under the west dike and moderate deflection of approximately 1 inch under the north dike. The maximum lateral deflection was between 2 and 3 inches under the south dike (Figure 4). Apparently, the lateral deflection of the foundation soils had contributed to the dike settlement.

An effort was made to back-calculate the coefficient α_{nr} between constrained modulus (M) and net cone tip resistance using the measured settlements. The derived coefficient α_{nr} was less than 4 even for the west dike where little lateral deflection was detected in the foundation soils. This low coefficient may be caused by the fact the clays were actually under consolidated.

The two settlement sensors with long-term data indicated that a majority of the settlement was completed during construction. The post-construction settlement was less than six inches. These results suggest the wick drains were effective in accelerating the consolidation.

Figure 5 plots the measured pore pressure from three piezometers, NP1, NP2 and WP1. One shallower piezometer at 20 feet below grades recorded a maximum pore pressure of 5 psi while two deeper piezometers at 30 feet below grades had a maximum increase of approximately 2 psi. These results suggest the stress increase from the weight of fill decrease rather rapidly along the depth. With wick drains installed at five feet on center, the controlled fill placement rate of one lift per week was not slow enough to allow extra pore pressure to dissipate. Excess pore pressure was dissipated completely six months after the completion of fill placement.

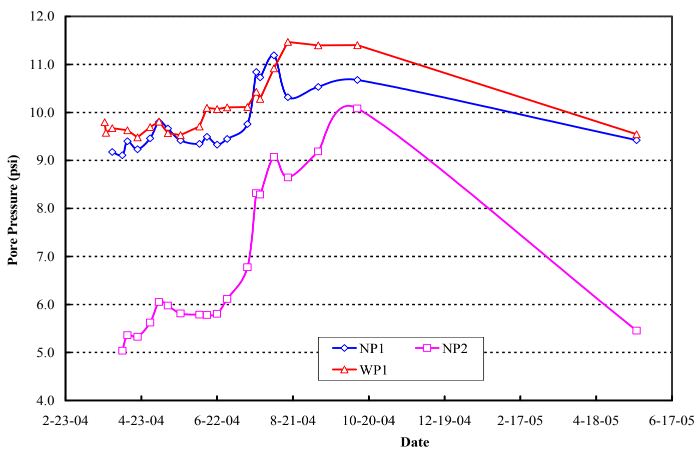

FIG. 5. Pore Pressure with Time from Piezometers

CONCLUSIONS

1. An LNG containment dike was successfully constructed on very soft ground using wick drains with elongated construction schedule to allow the soft clay to consolidate and gain strength during construction.

2. An instrumentation program was implemented during construction to permit the adjustment of fill placement rate based on the observed ground behavior such as pore pressure increase, settlement and lateral deflection.
3. The measured settlement was larger than predicted along the sections of dike where the ground experienced a significant amount of lateral deflection.
4. The existing empirical formula based on CPT and DMT tends to over-predict over consolidation ratios. The soft clay would be considered normally consolidated even though many observed conditions on the site suggest the clays were under-consolidated.

ACKNOWLEDGEMENT

The authors would like to acknowledge the following organizations and individuals for their help and support for this project: El Paso Energy, Southern LNG and Mr. Dan Tennison, CB&I and Messrs Mark McGahey, Joe Hoptay, Kevin Lanfried and Scott Paar, Dr. Felix Yokel, WPC and Mr. Wu Yang.

REFERENCES

Ambrasseys, N.N. (1988). "Engineering Seismology," Earthquake Engineering and Structural Dynamics, Vol. 17, pp. 1-105.

Kavazanjian, E. Jr., Matasovic, N., Haji-Hamour, T., and Sabatini P.J., (1997). " Design Guidance: Geotechnical Earthquake Engineering for Highways, Volumes I and II," Report No. FHWA-SA-97-076.

Kulhawy, F.H. and Mayne, P.H. (1990). "Manual on Estimating Soil Properties for Foundation Design." Electric Power Research Institute, ERPI, August, 1990.

Marchetti, S. (1980). "In Situ Tests by Flat Dilatometer." ASCE Journal GED, Vol. 106, No. 3: 299-321.

WPC, Inc. (2002). "Geotechnical Engineering Investigation Report" for Southern LNG Elba Island Expansion.

Youd, T.L., Idriss, I.M. with 20 other experts (2001). "Liquefaction Resistance of Soils: Summary Report from the 1996 NCEER and 1998 NCEER/NSF Workshops on Evaluation of Liquefaction Resistance of Soils," Journal of Geotechnical and Geoenvironmental Engineering, October 2001, pp. 817-833

Senneset, K., Sandven, R. and Janbu, N. (1989) "The Evaluation of Soil Parameters from Piezocone Tests". Transportation Research Record, No. 1235, 24-37.

Amick, D., Gelinas, R., (1991). "The Search for Evidence of Large Prehistoric Earthquakes along the Atlantic Seaboard," Science, v.251, p. 655-658.

Tokimatsu K. and Seed H.B. 1987. "Evaluation of settlements in sands due to earthquake shaking", J. Geotechnical Engineering, ASCE, 113(8), 861-878.

Marchetti, S. (1980) "In Situ Tests by Flat Dilatometer". Journal of the Geotechnical Engineering Division, ASCE, Vol. 106, No. 3: 299-321

NFPA 59A, "Standard for the Production, Storage, and Handling of Liquefied Natural Gas (LNG)", 1996 Edition.

"Data Requirements for the Seismic Review of LNG Facilities", NBSIR 84-2833

Dam Health Monitoring based on Dynamic Properties

Anun Patjawit[1], Chaiyuth Chinnarasri[2], and Worsak Kanok-Nukulchai[3]

[1]Assistant Professor, Department of Civil Engineering, Chulachomklao Royal Military Academy, Nakhon-nayok, Thailand; anun@mail.crma.ac.th
[2]Associate Professor, Department of Civil Engineering, King Mongkut's University of Technology Thonburi, Bangkok, Thailand; chaiyuth.chi@kmutt.ac.th
[3]Professor, School of Civil Engineering and Technology, Asian Institute of Technology, Pratumthani, Thailand; worsak@ait.ac.th

ABSTRACT: In order to execute dam safety planning, it is necessary to develop an index, which considers and simulates actual physical dam deterioration. The objective of this study is to monitor the behavior of dams by the experimental modal analysis. Ten model dams were tested by free drop of a steel ball to generate the different degree of damage to the dams. The experimental data was recorded in time domain. In each case of deterioration, the post processing was to transform these data to obtain the different natural frequencies, the global condition. Next, the local condition was further investigated using the finite element model, which was developed and calibrated using these obtained natural frequencies. The local dam deterioration could be evaluated and monitored from a number of the calibration parameters, i.e. boundary conditions and strength of dam materials. In addition, the different natural frequencies would be used as a simple index for the dam health monitoring.

INTRODUCTION

Failure of dams can cause devastated loss of human lives and properties downstream of the dams. The causes of dam damages include heavy rainfall, landslide, earthquake, settlement, etc. (Chinnarasri et al., 2004). The routine monitoring of dams is therefore necessary for the safety of the dams. It can provide early warning and protect the severe possible damage beforehand.

In the last two decades, few researches on the health monitoring of dams were conducted. New sensor and data collection technology has been developed recently for engineering proposes. Their application should be of interest to the health monitoring of dams. In the past, aerospace was the major field employing structural health monitoring based on structural vibration. In Civil Engineering, recent researches have been made on the development of health monitoring system for structures such as buildings and bridges. Among them were Aktan et al. (1993), Raghavendrachar and Aktan (1995), Yang et al. (2004) etc. These researchers used the change of mode frequencies and mode shapes to reflect the deterioration of the structural capacity. Recently, Patjawit and Kanok-Nukulchai (2005) proposed a global flexibility index (GFI) for monitoring the structural health of highway bridges. However, the development of similar structural health monitoring methods for dams was its early stage.

The objective of this study is to investigate a simple index through dynamic properties of model dams. The modal analysis is used to evaluate the apparent natural frequencies of the dam structure. Then, its finite element model can be developed and calibrated, and later used for examining the local conditions at sensitive areas of the dam structure.

THEORETICAL CONSIDERATION

In order to understand the modal analysis, a complete comprehension of single degree-of-freedom system is necessary. This approach is trivial from a modal analysis perspective, since no modal vectors exist. The multiple degrees-of-freedom case can be viewed simply as a linear superposition of single degree-of-freedom systems.

The general mathematical representation of a single degree-of-freedom system can be written as follows

$$m\ddot{r}(t) + c\dot{r}(t) + kr(t) = f(t) \tag{1}$$

where m is the mass constant, c is the damping constant, k is the stiffness constant, $r(t)$ is the harmonic variable in the time domain, t is the time variable. This differential equation yields a characteristic equation of the following form

$$ms^2 + cs + k = 0 \tag{2}$$

where s is the complex-valued frequency variable (Laplace variable). This characteristic equation of a single degree-of-freedom has two roots, λ_1 and λ_2 as follows:

$$\lambda_1 = -\sigma_1 + j\omega_1 \tag{3}$$

$$\lambda_2 = -\sigma_2 + j\omega_2 \tag{4}$$

where σ is the damping factor and ω is the damped natural frequency. Thus, the complementary solution of Eq. (1) is

$$x(t) = Ae^{\lambda_1 t} + Be^{\lambda_2 t} \tag{5}$$

in which A and B are complex-valued constants determined from the initial conditions imposed on the system at time $t = 0$. With reference to Eq. (2), this means that the two roots λ_1 and λ_2 are always complex conjugates. Also, the two coefficients, A and B are complex conjugates of each other. For an under-damped system, the roots of the characteristic equation can be written as

$$\lambda_1 = \sigma_1 + j\omega_1 \tag{6}$$

$$\lambda_1^{\,*} = \sigma_1 - j\omega_1 \tag{7}$$

Three methods have been widely used, which are the method of measuring frequency change, the method of measuring mode shape change and the method based on dynamic measurements of structural flexibility. These three damage-detection methods are examined in details (Patjawit and Kanok-Nukulchai, 2005). The structural damage detection based on the changes in the structure's dynamic properties will be presented in this study. This approach is recognized to be more effective for detection of structural health monitoring than the traditional methods. There is a large amount of literature related to the various methods used for this approach.

For any structure, modal frequencies reflect its global structural property. Currently, using frequency shifts to detect damage appears to be more practical in applications where such shifts can be measured very precisely in a controlled environment, such as for quality control in manufacturing. Based on the study by Osegueda et al. (1992) on the changes in dynamic properties of a scaled model of an offshore platform subjected to damage, the mode shape changes could not be correlated with the damage. In the meantime, another research by Fox (1992) showed that single-number measures of mode shape changes such as the Modal Assurance Criterion (MAC) are relatively insensitive to damage in beam-type structures.

EXPERIMENTAL PROCEDURE AND APPARATUS

The equipment for this experiment includes an accelerometer measurement PCB model 393A03 and a signal amplifier PCB Piezotronics model 483B17. The technical properties of PCB model 393A03 are: sensitivity 1V/g, range of amplitude ±2.5g with 0.0001 g resolution, and range of frequency 0.025 – 800 Hz with ±5% error. This equipment was attached on the structure to be measured. During the measurement of the vibration of the structure, the signal amplifier PCB Piezotronics model 483B17 was used for adjusting the output signal from the accelerometer to be suitable for the next transforming processes. The setup detail and the locations of the accelerometers are presented in Fig. 1.

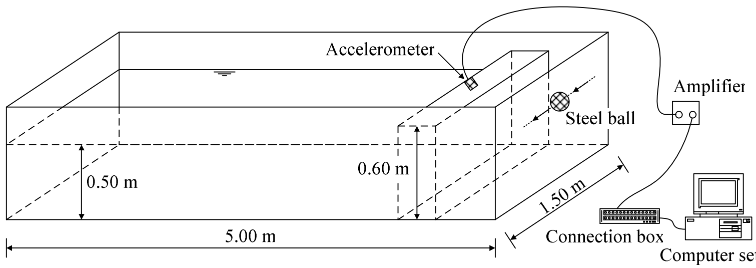

FIG. 1. Schematic diagram of the experimental setup.

The model dam was constructed at the nearly downstream of a basin of 1.50 m wide, 5.00 m long and 0.90 m high. The dimensions of the concrete dam were 0.60 m high and 0.08 m thick. At the front of the dam, water of 0.50 m high was filled served as a reservoir. The accelerometer was firmly fixed at the middle of the dam crest. At the downstream of the dam, a half circle pipe was installed and used as a rail for allowing a steel ball to attack the dam at its mid-height. The diameter of the steel ball was about 0.136 m. with weight 7.25 kg. The compressive strength of the cylindrical specimens at 28 days of the dams was about 180 kg/cm^2.

There were 10 experimental tests. To simulate the different degrees of deterioration on the dam madel, a steel ball was free drop on the rail at two different distances along the rail, i.e. 0.20 m and 1.00 m. measured from the mid-height of the dam. The first set of dropping was 10 times with distances 0.20 m. along the rail to make a small degree of deterioration on dam. Then, the vibration test was processed by exciting the dam with small magnitude of impact acting as simulation of ambient vibration. The second set of dropping was 10 times with distance 1.0 m. along the rail to force a larger degree of deterioration on dam. Then, the vibration test was further operated again as before. Totally, there were about 40 rounds of impacts with distance 1.0 m.

The experimental data was recorded in time domain. In each case of deterioration, the post processing was performed to transform these data for the different natural frequencies. This is the process to find the global condition of the dam.

FINITE ELEMENT ANALYSIS

Finite element analysis is performed on a numerical model of the dam with parameters to be calibrated from the results of the experiment. Generally, when studying a complex structure, it is a good idea to first model its finite element model for numerical analysis of the structure. From the preliminary finite element analysis, this not only indicates what types of motion and frequencies one might look for, but more importantly, it also helps identify good and bad locations for accelerometer placement for modal analysis. If an accelerometer is placed at a location on the structure that is not sensitive to a particular frequency, then a modal analysis may not yield useful data.

Finite element analysis in this study was used to inter-correlate between the experimental and the numerical models of dam in its modal analysis. At initial stage before planning the experimental program, the finite element analysis could be used togive a guideline. The preliminary finite element model was developed based on the previously known structural properties of dams. After completing of the experiments, the parameters in the finite element model were calibrated based on the experimental results. In this study, three-dimensional finite element model was used in the analysis to evaluate its dynamic responses. The local deterioration condition of the dam can be calibrated from a number of the calibration parameters, such as the changes in the boundary conditions and in the material properties of the dam.

RESULTS AND DISCUSSION

The results of the experimental studies can be divided into the pattern of the cracks for each test set and the natural frequencies of dam specimen as various state of deterioration. The crack pattern of the dam specimen is shown in Fig. 2. After the dam was hit by a steel ball 10 times, a hair-line crack on the middle of the specimen was observed as shown in Fig. 2 (a). When the dam was further impacted for 20 and 30 times, the crack was wider and longer as shown in Fig 2 (b) and (c). Finally, the broken part of the dam specimen was split out as shown in Fig. 2 (d).

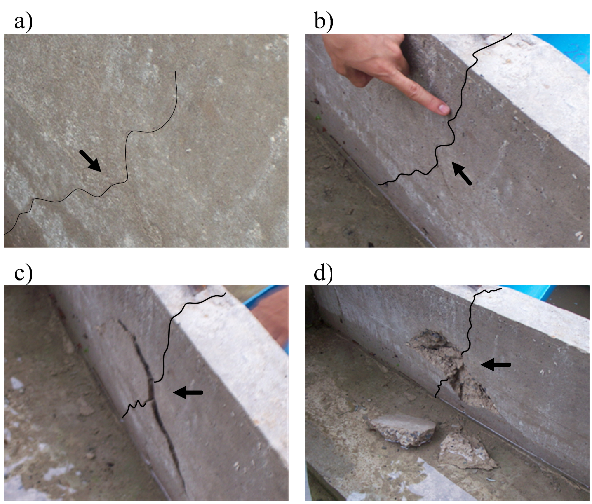

FIG. 2. Pattern of the cracking development.

The natural frequencies of the dam specimen as various states of deterioration are shown in Fig. 3. The x-axis represents the natural frequencies. The highest value of the graph identify the location of the natural frequency for each case. The y-axis represents the power of the signal which the accelerometer received from the vibration of the dam specimen. Normally, if the property of the structure has not changed, its natural frequency remains almost constant. Therefore, the relative magnitude of the signal power does not signify any change in the behavior of the dam structure. Only the change of the natural frequency implies change in the structural behaviors.

In this study, only the first mode of natural frequency was investigated. In Fig. 3(a), the natural frequency of the undamaged dam was found to be about 120 Hz. In Fig. 3(b) 3(c) and 3(d), the frequencies of the damaged dam, after hitting with a ball 10, 20 and 30 times, were observed to be about 90, 85 and 82 hz respectively.

The frequency reduces with the crack width. Some parts of dam were breaking out as shown in Fig. 2(d). The natural frequency of the dam specimen and the degree of deterioration in the form of the energy loss applied to the dam is shown in Fig. 4.

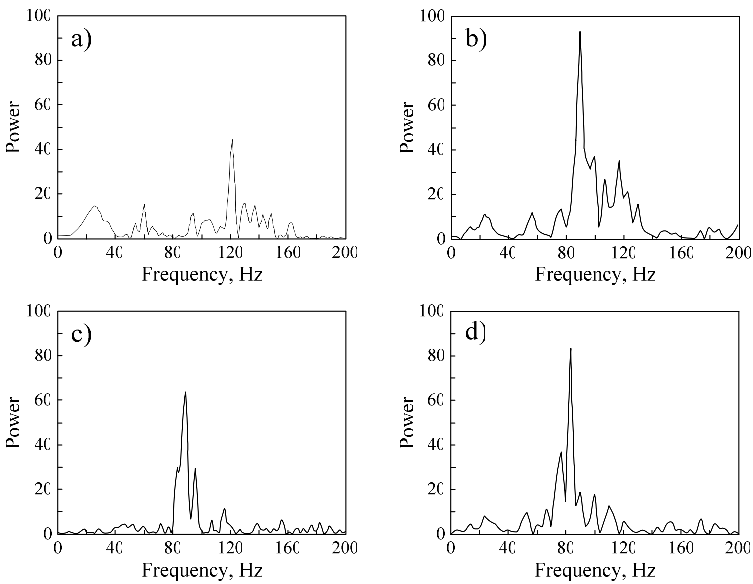

FIG. 3. Natural frequency of the dams at different phases of deterioration.

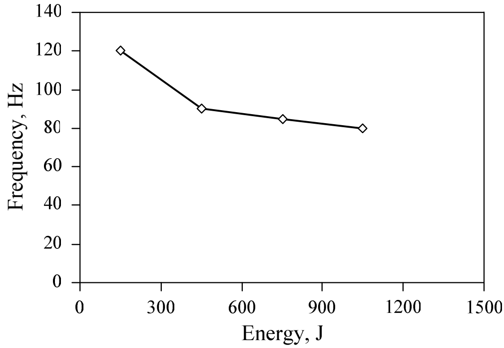

FIG. 4. Natural frequency vs energy used to damage the dam specimen.

From the preliminary finite element analysis, the fundamental frequency of the finite element model of the dam specimen is 118 Hz. Compared with 120 Hz from the experiment. This small difference show good agreement between the two methods. The finite element model was then calibrated to the experimental result by adjusting critical parameters including support and continuity conditions, modulus of elasticity, shear modulus and mass density of dam. This adjustment is able to bring the frequency of the finite element model to match with the experimental result of 120 Hz. The side view of the shape of the first mode is illustrated in Fig. 5.

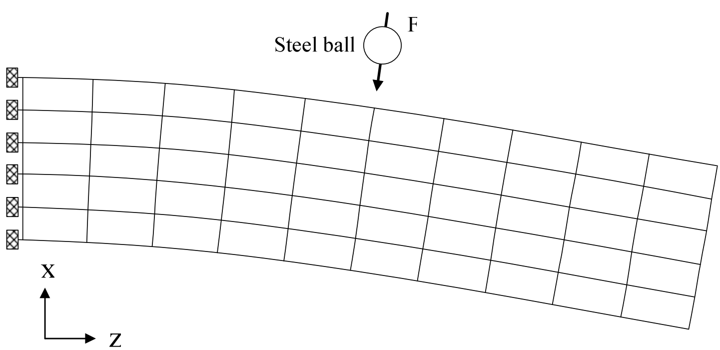

FIG. 5. The profile of the mode shape of the finite element dam model corresponding to the fundamental frequency of 118 Hz.

CONCLUSIONS

This study proposes a simple index to monitor the structural deterioration of dams. The simple index is the frequency deterioration of the aging dam, i.e., the difference between a base level and the present frequencies of the dam after undergoing aging process. Also by this method, a representative finite element model can be established after it is calibrated by the experimental result. This field test to obtain the fundamental frequency of the dam can be considered to be very simple and convenient for practicing engineers to monitor structural health of dams. This study can be further extended to a more rigorous health monitoring method in order to obtain the *global flexibility index* as proposed by Patjawit and Kanok-Nukulchai (2005)

ACKNOWLEDGEMENTS

The present study was partially supported by the Faculty of Engineering, King Mongkut's University of Technology Thonburi and the National Research Council of Thailand (NRCT).

REFERENCES

Aktan, A.E., Chuntavan, C., Lee, K., and Toksoy, T. (1993). "Structural identification of a steel stringer bridge." *Transportation Research Record.* 1393: 175-185.

Chinnarasri, C., Jirakidlert, S. and Wongwises, S. (2004). "Embankment dam breach and its outflow characteristics." *Civil Engineering and Environmental Systems.* 21 (4): 247-264.

Fox, C.H.J. (1992). "The location of defects in structures: a comparison of the use of natural frequency and mode shape data." *Proc. 10th Intl. Modal Analysis Conference*, Vol. 1, San Diego: 522-528.

Osegueda, R.A., Dsouza P.D., and Qiang Y. (1992). "Damage evaluation of offshore structures using resonant frequency shifts." *Serviceability of Petroleum, Process, and Power Equipment,* ASME PVP 239/MPC, 33: 31-37.

Patjawit, A. and Kanok-Nukulchai, W. (2005). "Health monitoring of highway bridges based on a Global Flexibility Index." *Engineering Structures*. 27 (9): 1385-1391.

Raghavendrachar, M., and Aktan, A.E. (1995). "Flexibility by multireference impact testing for bridge diagnostics." *Journal of Structural Engineering,* ASCE, 118 (8): 2186-2203.

Yang, J.N., Lel, Y., Lin, S. and Huang, N. (2004). "Identification of natural frequencies and damping of in situ tall building using ambient wind vibration data." *Journal of Engineering Mechcanics,* ASCE, 130 (5): 570-577.

An Evolving View of Geotechnical Engineering – A Focus on Geo-Risk Management

Ronald E. Smith[1], M. ASCE, PhD, P.E.
[1]Consulting Geotechnical Engineer, 38 Cliftwood Road, Palmyra, VA 22963

ABSTRACT: In December 2006, the GeoCouncil held a workshop examining a series of trends in the construction industry that will likely affect geotechnical engineering. Inherent in these trends is the ever increasing demand of the construction industry for geo-professionals to provide "Better, Faster, Cheaper" solutions to project geotechnical issues. The most inclusive and far reaching finding regarding these trends involved the need for active management of project geo-risks. The Workshop recommendations for dealing with project geo-risk management were: (1) involvement of geo-professionals over the full life of the project, (2) a project risk register for every project and (3) a geotechnical baseline report fashioned after such reports pioneered in the tunneling industry.

This paper reflects both the recommendations of the Workshop and the concepts of geo-risk management developed in Holland by GeoDelft. It retrospectively looks at three case histories of typical projects. The purpose of the case histories is to examine how these projects were, or might have been executed to provide Better, Faster, Cheaper project solutions using active geo-risk management.

INTRODUCTION

The construction trends the Workshop examined were:

- accelerated construction;
- innovative contracting;
- asset management;
- context-sensitive solutions;
- safety;
- cost analysis;
- research, development and training;
- extreme hazard mitigation; and
- risk management.

These issues were examined by a group of 50 geo-professionals (15% academics, 55% designers, 30% builders) tasked with making recommendations to the geo-community that could help them better meet the expectations of the construction industry.

The Workshop discussions raised serious concerns that the geo-profession faces both: the challenges of rapidly developing changes in the construction industry, and a simultaneous, serious deterioration in the current state of the practice. This later point had also been exposed during a recent G-I Task Force study where significant numbers of practitioner interviewees cited as a major challenge to the profession, the increasing commodization of geotechnical engineering services. One interview by this writer with a geotechnical specialty contractor noted the quality of geotechnical work he was seeing was so poor that over half of his work currently involved remediation of geo-construction features completed less than 12 months hence, a very sad, yet profitable business proposition from his point of view. In summary the requirements are getting tougher at the same the quality of geotechnical services are in decline; a real dilemma for the geo-profession.

CONSTRUCTION INDUSTRY EXPECTATION

The workshop was initiated Tuesday morning by presentation of white papers on each of the trends. By late afternoon Tuesday the group broke up into nine working groups to facilitate in depth examinations of each of the trends, working from the initial white papers. On Thursday morning the all participants reassembled to informally present the initial thoughts of the groups on the trends with feed back from all participants. Thursday afternoon was dedicated to finalizing positions, and Friday morning final presentations from each group were made.

As the workshop progressed, there was general agreement that the construction industry's expectation of the geo-community, represented in all nine trends, was that the geo-community must be an active participant in achieving Better, Faster, Cheaper (BFC) projects. In no way should this be interpreted to mean that the services of the geo-professional should be BFC. It is only the end result, i.e. the project, that should be the focus this expectation.

The fact that expectations are being expressed implies that the current performance of the geo-community is well below the expectations of the construction industry. This point was acknowledged by the participants as a situation that is bad and getting worse. Specific concerns developed during the workshop were:

- Commodization of the practice of geotechnical engineering – bad and getting worse
- Marginalization of the professional services provided by the geo-practitioners
- Preoccupation with exculpatory language by geo-practitioners
- Execution of geotechnical engineering services by other disciplines
- Slowness of the geo-practitioners to adapt to the client's needs
- Failure to educate clients and team mates as to how significantly geotechnical issues can affect their projects
- Failure of many geo-practitioners to educate themselves to the important drivers affecting the projects and other design team members
- A general lack of appreciation of and the necessity for at least a basic understanding of constructability of geo-design features

This latter point was strongly emphasized to this writer during an interview with the president of a major international geotechnical services firm, himself a geotechnical engineer. He was so concerned about this and an associated issue that he proposed that the practitioner community should work together to prevent universities from awarding of advanced degrees in geotechnical engineering if they did not have expertise to teach three critical geotechnical subject areas. Acceptable programs would include: theoretical geotechnical engineering that all programs possess; engineering geology, such as that proposed by Terzaghi (1961) and exemplified by the work of Deere at the University of Illinois, and an understanding of the interaction of engineering and construction, as exemplified by both Terzaghi and Peck. This writer agrees with this position.

In summary what the construction industry expects of the geo-community is that it makes significant contributions to the development of Better, Faster, Cheaper projects. Geotechnical services needed to support BFC projects should address at least the following issues:

- Long term, active involvement of the geo-professional from project conception into facility operation
- A focus on the total life cycle performance requirements of the facility
- A focus on the total life cycle costs of the facility
- Recognition that the geo-professional is providing services necessary to unite the owner's facility to the owner's site
- A subsurface investigation program that addresses both design and construction issues
- That the owner, design and builder be committed to equitable allocation of project geo-risks
- That the geo-professional provide to the project team recommendations for alternatives:
    - that address the functional, cost and schedule requirements of the project,
    - that are not unduly conservative as a result of the geo-professionals own risk avoidance strategy and
    - that allow for flexibility in implementation so as to promote innovation in design and construction.

The position the geo-community should take is that it can meet these expectations if it is provided the opportunity be select for service based on its knowledge, experience, and reasonable control of the scope and tenure of its services. The current level of generally poor services is largely the result of the long term effects of cost based selection with little more than lip service to the quality of the proposed services.

RISK MANAGEMENT PROCESS

Many workshop participants expressed the opinion that risk management, as a process, represented the best chance of meeting the BFC expectation in each of the trend areas. The ways by which geo-professional can influence Better, Faster, Cheaper projects are:

- by educating the project team to the significant impacts that geotechnical-related risks (geo-risks) can have on any land-based project, and
- By identifying, quantifying, mitigating and/or aid in equitable allocation of the foreseeable geo-risks associated with a specific project.

There are several outstanding references that address the management of project risk; the most relevant to the topic of geo-risk is vanStaveren's book(2006) that details the GeoQ process developed by GeoDelft. The GeoQ process involves six steps for each of six project phases, which speaks to the continuous and iterative nature of the process beginning at the feasibility phases and continuing through the maintinance phase of a project. This book is comprehensive in its coverage of the fundamentals of ground risk and the step by step management of risk through the life of a project. Early in this book vanStaveren addresses the key question as to what makes geo-risks so special in construction, namely the high cost of failing to properly manage these risks as manifest in overly conservative designs, high cost change orders, and differing site conditions claims. Differing site condition claims settlements alone have been documented lead to added project costs in the order of 10%-50% of the total cost of construction, orders of magnitude greater than the costs of top quality geotechnical services that may have prevented or reduced the impacts of such unpleasant surprises.

In addition to vanStaveren's book, the California Department of Transportation's (Caltrans) Office of Project Management Process Improvement has developed the Project Risk Management Handbook. Fundamental to this approach is the concept of a Risk Register. Such registers are initiated at the conception of each project and continually updated as new information and/or new actions are taken to modify the risk of that particular event. The objective of the register is to prompt the project team to identify and in some way address all foreseeable project risks.

While this handbook deals with all manners of project risks, it is very adaptable to handling geo-risks, including both geotechnical and geoenvironmental risks. Caltrans defines Risk as the product of Probability of occurrence of an event/hazard times an Impact factor rating. Probability is ranked on a relative scale as 1-5 (1-19%, …, 80-99%) and Impacts are ranked in the three categories of Time, Cost and Scope, with each described numerically by increasing severity as either 1-2-4-8-16. Assessment inputs are based on expert opinions. This book deals in detail with the Project Risk Register as a primary geo-risk management tool.

PROJECT GEO-RISKS MANAGEMENT PROCESS

There are three major actions for enabling the geoprofessional to deal with geo-risks in a way that assists the owner, designer, and builder in pursuing Better, Faster, Cheaper projects of all sizes. They are:

- Long-Term Involvement – To realistically identify and manage foreseeable project geo-risks, the project geo-professional and appropriate staff must be engaged with the project from the conceptual/feasibility phase continuously through construction and, for some projects such as dams, for the life of the facility. The risk management function of the geoprofessional is: to identify potential geo-risks, to identify actions to reduce the uncertainty associated with specific geo-risks, and to recommend actions for high risk events to either avoid, mitigate or allocate those geo-risks.
- Risk Register- The document that imparts discipline to the geo-risk management process is the Risk Register. Its function is to be the record of all foreseeable project risks, such as environmental, financial, social, subsurface, etc... Initial development of this document begins at the initiation of the project. Detailed discussions of the use of these documents and the risk management process are presented in both the Caltrans (2003) and the British RAMP (2006) documents. The Registers are a living record of the identification, evaluation, planned

response to the risk (further investigation/quantification, mitigation, avoidance) and the allocation of the residual risk. As steps are taken to address specific risk; those steps are recorded. While the Register becomes the responsibility of one person or a small team, the input to the Register involves the efforts of a numbers people familiar with the planned project and the key elements of its development that represent uncertainty and risk to the successful completion of the project. While the general reaction to the term "risk", is typically perceived as a negative, a more holistic approach is that there are some project uncertainties that could result in very positive outcomes for the project. For instance subsurface investigations could reveal that there is a high probability that onsite materials could be used for construction as opposed to the necessity of importing costly processed aggregates.

- Geotechnical Baseline Report (GBR) – The GBR is a document that has been developed in the underground construction industry over a period of 30+ years. In its current form, it is documented in a manual (Essex 1997) developed by the Underground Technology Research Council and published by ASCE. In its ultimate use it is an underground risk allocation statement that is included in the project contract documents. A typical GBR not only provides prospective bidders with baseline subsurface information, but they also provide baseline information as to what the design team, including the geoprofessionals, believes to be the interactions between the anticipated construction methods and the anticipated subsurface conditions. These reports do not direct construction means and methods but they do examine the factors, such as the volume of groundwater inflow, that are likely to affect the general constructability of the project. GBRs are written after the design is complete, and often necessitate additional subsurface investigation that focuses on information, such as excavatibility, that is important to the economics of constructing the facility.
  To be effective as a contract document, GBRs need to be accompanied in the contract with a Differing Site Condition (DSC) clause that allows the builder to recover if unforeseen conditions are encountered. In concert the GBR and the DSC clause form the basis for equitable allocation of the risk of unforeseen subsurface conditions.

CASE STUDIES

With the exception of large scale tunnel construction, the use of these three geo-risk management techniques is virtually nonexistent. The use of GBRs and more extensive site investigations have become more prevalent in tunneling industry during the last 30 years, and the value of the use of these techniques to owners and the industry was validated in a USNCTT report (1984). This report was based on a study of 84 major tunnel projects, mostly in North America, of which 55% experienced significant claims that were subsequently settled for an average of 12% of construction costs. The primary conclusion of this report was, "It is in the owner's best interests to conduct an effective and through site investigation and then make a complete disclosure of it to bidders."

In a study of claims related to subsurface conditions for a broader range of project types, Halligan, Hester and Thomas (1987) made a similar evaluation of over 600 large projects that had experienced "unforeseen site conditions." They concluded that contract disclaimer language was not an effective way for owners to attempt to pass responsibility for subsurface conditions on to contractors. Further, they recommend that interpretive geotechnical reports, such as the GBR, be used in contracts to equitably allocate subsurface geo-risks in order to minimize the cost of dealing with unforeseen subsurface conditions.

Because the three recommended geo-risk management procedures represent an evolving concept within the general geotechnical practice, there are few examples of projects that demonstrate the total concept. What the case studies given below do is examine two typical geotechnical projects from the perspective of what might have happened if a geo-risk management program had been in place.. The third project is one in which a geotechnical design summary report, an early version of the GBR, was used to effectively convey subsurface information to the contractor. In all three cases the writer believes that the impact of using geo-risk management concept could have or did have a significant effects on quality, schedule and/or cost of the project.

Case 1: Avoiding a Geo-Risk/Early Identification – This project involved construction of a large shopping center in the Mid-Atlantic Coastal Plain in the early 1970s. As the project evolved, the relevant geo-risk event that surfaced involved paving of the parking lots surrounding the facility. The paving was complicated by the "absolutely must make" scheduled opening date of the shopping center for Easter holiday shopping.

The pavement subgrade soils were predominantly silty clays, and to increase the probability of trouble, the grades surrounding the shopping center generally slope down to the facility entry level. Early spring in the Mid-Atlantic area is often cold and rainy, and the year of the opening was especially so. There was no question but that the facility had to open on schedule; not opening on schedule was totally unacceptable to the tenant stores.

Given the "must do" situation, the contractor adopted "heroic" measures to get the site paved under terrible conditions. He brought in several tractors pulling propane burner devices to dry the soils, Additionally he hired a helicopter to hover just above the subgrade to try to dry the subgrade enough to lay the asphalt pavement. In areas around the entrances to the facility, tons of crushed stone had to be placed to stiffen the subgrade. All in all, it was a very costly, unanticipated situation. To add to the cost, much of the area had to be removed and repaved the next summer.

If the proposed geo-risk management approach had been in place, the geotechnical engineer would have been access to the schedule and would have been tasked with managing this as an element of the project geo-risks. In all likelihood, this event was foreseeable and could have been avoided by a plan to proceed with paving at an earlier date or at least stabilizing the sensitive subgrade at time of year when that was more feasible; thus avoiding the large extra costs and the considerable mental anguish.

Case 2: A High Risk Situation of Common Occurrence and Disastrous Results – This case was selected because the writer has observed many similar events. It involves backfilling in a restricted yet critical area. This particular situation involved nearly all of the factors that played a role in the previous occurrences, namely: difficult schedule, difficult access, a lack of understanding of the need for separation of the QA and QC functions, and a construction supervisor with a "the lower part of a fill is self compacting" attitude.

The project was a luxury, midrise condominium complex with below grade basement parking, competent foundation materials, and a large interior courtyard with high-end landscaping and hardscape features. The high risk event involved the backfilling of the interior basement walls.

Shortly after completion of the interior courtyard, a fairly heavy rainstorm occurred. This was followed immediately by very large (1-3 feet) settlements that occurred over the 20 foot deep, wedge of backfill surrounding the courtyard. Complicating the situation was the fact that there were underground plastic water pipes from the basement servicing courtyard features. Nearly all of these were ruptured as a result of the large differential settlements at the interface where the pipes exited the concrete walls. This introduced additional water to the backfill zone. A forensic investigation revealed that, even after the settlements, the densities of the backfill were very low. The eventual solution to this problem cost over $500,000 to remediate, not counting the professional and legal fees resulting, in part, from the complexity of the project relationships.

Density testing of the backfill was contracted directly to the owner but on-call to the contractor. Very few tests were conducted in the lower 15 feet of the 20 backfill zone. (In simple terms this means there was minimal owner QA and no contractor QC.) In the writer's opinion, the poor backfill compaction was a foreseeable geo-risk. The settlement event could have been avoided by a proper QC/QA program.

<u>Case 3: Use of Geotechnical Baseline "type" Report in the Contract</u> – This project involved design and construction of a 90-foot high zoned earth and rock fill water supply dam to create a 500+ acre reservoir. Built in the early 1980s, the dam setting was an online stream valley in metamorphic rock, other elements of the facility included; a rock tunnel outlet works, spillways, and highway relocation across the lake involving a bridge and large approach fills.

The 1982 bid price for this facility was $12,000,000. The attorney/civil engineer partner for the design firm expressed his belief to the client that they would be best served with an equitable risk allocation approach that included a geotechnical baseline document and accompanying Differing Site Condition clause in the contract. The baseline document, known at that time as a Geotechnical Design Summary Report (predecessor to today's GBR), was prepared by the geotechnical engineer after completion of the design. It is the writer's opinion that that the lesson learned from this project was that the full disclosure/equitable risk allocation approach contributed to both competitive bids and no claims. The project had no differing site conditions claims and a total amount of all change orders for the project was less than 3% of the bid price.

CONCLUSIONS

The three primary implementation procedures listed above all have their roots in the tunneling industry. While the Risk Register, per se, is a relatively recent concept, basically all of these procedures were introduced because of the terrible cost overruns and claims that plagued tunnel construction until tunnel community came to grips with the need for better geotechnical services and equitable risk allocation. This effort began in the late 1960s when there was a crisis, namely the total project costs for tunnels had become so unpredictable that the National Academy of Science established a special committee of representatives from government, construction, design and consulting to find ways of preserving the tunneling industry in the USA, just as the major efforts in subway development were beginning (USNCTT, 1974).

If, as the GeoCouncil Workshop indicated, there are increased expectations of the geo-community, then there must be changes in the practice. The geo-community can provide services that supporting Better, Faster, Cheaper projects, as has been demonstrated in the tunnel construction industry. But, as has been the case in the tunnel industry, a higher level of profession practice must be accepted by the construction industry as necessary to achieve the desired expectation.

Since the early 1970s the general geotechnical practice has been constantly pressured by competitive bidding to trim services. This serves no ones long-term interests, especially the public interest. In all likelihood, some geoprofessionals will take this opportunity to upgrade the services they offer to include geo-risk management. If they are wise, they will begin to offer these services on a value pricing basis so that they can recruit the high quality talent necessary to support their critical work. Others may continue on the current path of selling themselves as a commodity. They are likely to be restricted to data gathering. With the transitioning to a “flat world” economy, it is quite likely that this part of the community will begin to lose analysts functions to parts of the world, say India, where highly educated analytical services can be obtained from high quality providers at much lower costs than in the USA.

ACKNOWLEDGEMENTS

The writer would like to thank all the participants in the December, 2006 GeoCouncil Workshop on “Trends Affecting the Geo-Community: What Does the Future Hold” for their stimulating discussions of issues critical to the geo-community. He owes a special debit of gratitude to fellow members of the Risk Management Working Group Bill Brumund (team leader), Barry Christopher and Allen Marr. It was the working group that articulated many of the ideas presented herein.

REFERENCES

Essex, R. J. editor (1997), *Geotechnical Baseline Reports for Underground Construction*, ASCE, New York.

Halligan, D.W., Hester, W.T., and Thomas, H.R. (1987), “Managing Unforeseen Site Conditions”, *J. Construction Engineering and Management 113(2): 273-287.*

Institution of Civil Engineers and the Actuarial Professions (2005), *RAMP – Risk Analysis And Management for Projects*, Thomas Telford, London.

Office of Project Management Process Improvement (2003), *Project Risk Management Handbook*, California Department of Transportation, Sacramento, CA.

Terzaghi, Karl (1961), “Engineering Geology on the Job and in the Classroom,” *Contributions to Soil Mechanics 1954-1962*, Boston Society of Civil Engineers. Boston.

U.S. National Committee on Tunneling Technology (1974), *Better contracting for Underground Construction*, National Academy of Sciences, Washington, DC.

U.S. National Committee on Tunneling Technology (1984), *Geotechnical Site Investigations for Underground Projects*, National Academy Press, Washington, DC.

vanStaveren, Martin (2006), *Uncertainty and Ground Conditions*, Elsevier, London.

DIKE BREACH REPAIR DESIGN IN INUNDATED, SCOURED CONDITIONS

Brian D. Benson[1], P.E., M.ASCE and Arlan H. Rippe[2], P.E., F.ASCE

[1]Senior Geotechnical Engineer, Kleinfelder, 62915 NE 18th Street, Suite 1, Bend, OR 97701; bbenson@kleinfelder.com
[2]Senior Principal Geotechnical Engineer, Kleinfelder, 15050 SW Koll Parkway, Suite L, Beaverton, OR 97006; arippe@kleinfelder.com

ABSTRACT: On June 7, 2006, the Geary Dike on the Upper Klamath Lake in Southern Oregon unexpectedly collapsed. The breach inundated 2800 acres of predominantly farmlands and recreational areas. An important highway link was closed and required emergency action and repair. The dike owner wanted to repair the breach prior to the summer season. This case study summarizes the investigation, design tasks, and breach closure construction. Subsurface conditions consist generally of very soft diatomaceous silt and clayey silt to an estimated 200 feet. A bathymetric survey revealed the breach scoured a long channel up to 24 feet below the original ground surface. The challenges that the design had to address were the difficulty in sampling and characterizing the foundation soils, the risk of foundation failure with single stage construction across the deep scour channel, and restricted construction access. The solution utilized lightweight volcanic cinders to reduce the embankment loading on the very soft, normally consolidated, weak foundation soils. This allowed it to be constructed in a single stage below the water surface.

INTRODUCTION

The Geary Dike breached in the afternoon of June 7, 2006. A 200-foot long section collapsed following a short period of effort to mitigate apparent through-dike seepage that had recently been noted. Eye witness accounts describe a one foot drop in the dike surface immediately prior to the actual dike breach. At the time of the breach, the lake level was at the annual high as revealed by U.S. Bureau of Reclamation gauging data. The breach inundated 2800 acres beneath up to 8 feet of water.

The 2.5-mile long dike was constructed before installation of the Link River Dam, circa 1921. This dam provides control of waters in the naturally occurring Upper Klamath Lake in south-central Oregon. We believe the dike was constructed primarily by placing silt and clay sediments dredged from the marsh / lake bottom adjacent to the dike alignment. Evidently, the dikes were constructed to convert the marsh to agricultural land after construction of the Link River Dam in order to increase storage capacity in the lake for irrigation purposes. As a consequence, over a significant portion of the water-year, the dike holds back up to 10 feet of lake water above the interior ground surface level. This distinguishes this structure from a flood protection levee.

The authors were retained by the owners of the Running Y Ranch Resort, who became owners of the breached dike and the inundated land subsequent to the breach. We were charged with developing a dike breach closure strategy as soon as possible to allow the inundated land to be un-watered. This was important to getting the Arnold Palmer designed golf course back in full service, removing from the resort a source of "swamp-conditions" and all of the negativity that suggests, and to provide satisfactory flood protection to adjacent areas.

SITE CONDITIONS

The project is located near the western margin of the Basin and Range Province of Western North America. Geologic structures within the Klamath Basin are typical of the Basin and Range Province and include down-thrown fault blocks (grabens) which form the Upper and Lower Klamath Basins (Klamath Graben), and adjacent, uplifted, steeply-dipping, fault-bounded blocks (horsts) which form the ridges and erosion-resistant upland areas of south-central Oregon. The oldest rocks exposed in the area are late Tertiary age, lacustrine and fluvial siltstone, sandstone, diatomite, welded tuff, volcanic breccia, and basalt flows (Orr, et. al., 1992). The Basin and Range is a tectonically young province. Beginning in the Miocene and extending into the Pliocene, the forces of crustal stretching and extension have triggered faulting, volcanism, and the development of the basin and fault block mountain topography that characterizes this province (Orr, et. al., 1992). Surficial geology in the vicinity of the dike consists of lacustrine sediments up to several hundred feet thick.

Recent seismicity in the Klamath Falls area also suggests that geologic structures within and/or bordering the Klamath Graben are active. The 1993 Klamath Falls earthquake sequence included two events (M 5.9 and 6.0) that occurred approximately several miles northwest of the site. Both earthquakes were caused by normal faulting on north to northwest-striking fault planes (Geomatrix, 1995).

Two 50-foot borings were drilled through the remaining dike, one on each side of the breach area. Standard penetration testing was performed along with obtaining Shelby tube samples for soil identification and testing. The borings revealed 12-inch surfacing of red cinder fill consisting of Sandy Gravel (GP). Then fill consisting of very soft to soft, low plasticity, gray Silt (ML) was encountered to approximately a depth 13 feet below top ground surface (bgs). This silt is the material that was placed for the embankment forming the existing dike. The moisture content of samples tested from this material ranged between 199 percent and 409 percent. These moisture contents, which were near the liquid limit, and non-plastic, are typical of organic lake bottom material (known locally as "lather muck") and diatomaceous earth. Diatomaceous earth (also known as, diatomite) is a naturally occurring, soft, chalk-like sedimentary rock that is easily crumbled into a fine white to off-white powder. This powder has an abrasive feel, similar to pumice powder and is very light, due to its high porosity. It is composed primarily of silica and consists of fossilized remains of diatoms, a type of hard-shelled algae (Wilson, 2000). Interestingly, when air-dried, this material can be observed to float. Beneath the dike fill, very soft to soft, gray-brown Silt (ML) was encountered to depths of about 28 feet bgs. This silt ranges between non-plastic to low plasticity. This lithologic soil unit contained occasional fibrous peat layers. The moisture content of samples tested in this material ranged between 173 percent and 520 percent. Also, the moisture contents and index properties of the soil indicate this material is diatomaceous. Very soft to soft, medium plasticity Clayey Silt (MH) was encountered below the Silt to the termination depth of both borings, 50.5 feet bgs. This soil unit is sensitive based on in-situ vane shear strength testing results. It contained sand lenses at various depths. The moisture content in this unit ranged between 82 percent and 111 percent.

Vane shear testing was accomplished to provide a shear strength profile of the subsurface soils. In-situ vane testing was performed at 2.5-foot intervals using a field vane device. Laboratory vane testing was also performed using a geovane testing device on the recovered Shelby tube samples. Peak vane shear strength test results are presented on Figure 1. The left side of the chart presents all peak vane shear strength test results and an average peak shear strength profile versus depth. All shear strength test values at each 2.5-foot interval were used to determine average values. The right side of the chart presents residual shear strength test results. It also presents a comparison of average residual shear strength and average peak shear strength versus depth. Shear strength loss indicated by the residual shear strength is related to sensitivity.

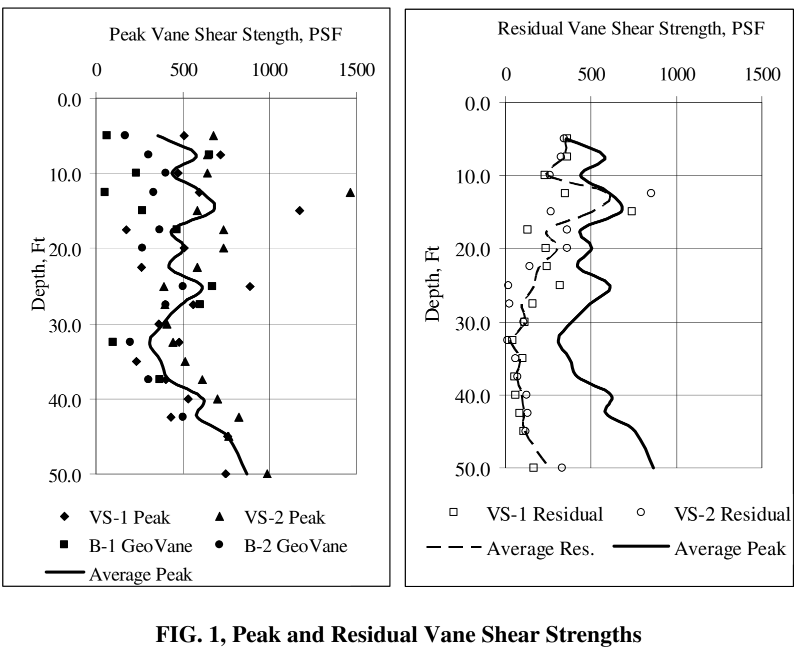

FIG. 1, Peak and Residual Vane Shear Strengths

Laboratory testing on selected soil samples was performed to determine their index and engineering properties. Grain size analysis, moisture content, Atterberg limits (plasticity), angle of repose, unit weight measurements, and consolidation tests were performed. Previously, the authors drilled several deep borings in the agricultural area away from the dikes to evaluate the subsurface conditions for other uses. Testing performed consisted of index tests, consolidation testing, and limited strength evaluations. These results were compared well to the test results from the borings completed from the top of the dikes.

Test results on the diatomaceous silt indicated it has a dry density of approximately 25 pounds per cubic foot (pcf). Two samples tested for Atterberg limits resulted in liquid limits of 149 and 318, and both samples were non-plastic. One undisturbed sample of diatomaceous silt tested for one dimensional consolidation resulted in modified compression and modified recompression indices of 0.52 and 0.02, respectively.

Post Breach Observations and Bathymetry

The authors' site observations after breach failure of the dike remnants at both sides of the breach indicate rotational-type ground failure occurred in conjunction with the breach. The rotational mechanism was especially evident at the north end of the breach. Although these observations have been somewhat obscured by the presence of water that had not yet been removed. At some point, the soil at the toe of the dike may have eroded sufficiently that the structure collapsed progressively, thereby resulting in a rotational-type failure, which led to catastrophic breach failure.

The breach scoured the soil below the interior ground surface (mudline) in the vicinity of the breached area. A bathymetric survey of the mudline surface surrounding the breach was performed. Bathymetry indicated up to 24-feet of scour at the breach location, and a long, channelized scour feature inland. The scour depth was approximately 18-feet deep at 500-feet inland, and 10-feet deep at 1000-feet inland.

DESIGN AND CONSTRUCTION METHODS

The owner's criteria for dike repair required that the breach be closed during fall 2006 to early winter 2007 such that the inundated lands could be dewatered during winter-spring 2007. Before site exploration and survey, conceptual design focused on relocating the dike inside of the breach area. Generally, levee breaches are expected to exhibit fan-shaped scour areas inside of the breach. Typically, dike repairs are located to avoid the scoured area. Also, locating it inside of the breach would avoid jurisdictional issues related to the Upper Klamath Lake Wildlife Refuge.

Figure 2, Site Plan, was originally prepared for expedited permit submittals and to initiate dike repair design. It schematically depicts relocating the dike repair around the breach and includes a construction turnaround and staging area. Cross Sections are presented in Figure 3. Section A-A' transects along the old dike and schematically depicts the scour through the dike breach area. Section B-B' transects

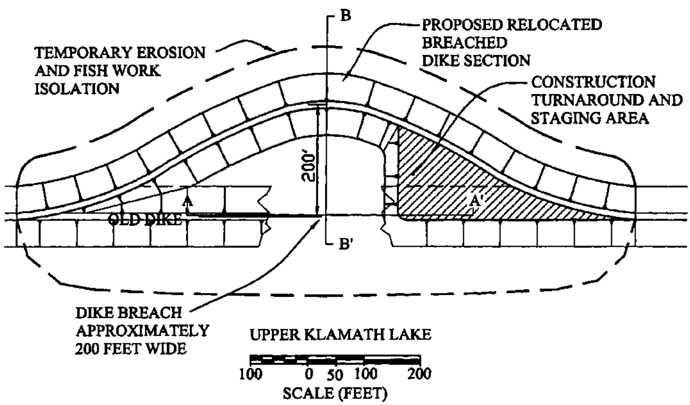

FIG. 2, Site Plan

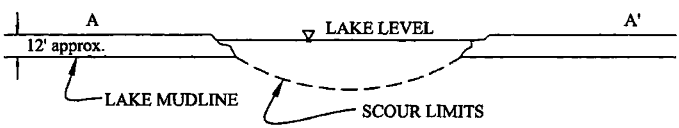

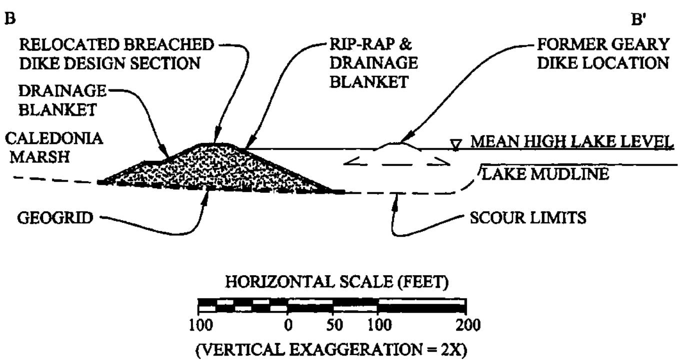

FIG. 3, Cross Sections

perpendicular to the old dike and is a schematic showing the washed out dike, the scour area, and the final configuration of the replacement dike section.

Once site explorations and surveys were completed, three significant design challenges became evident:

1. Constructing the dike repair in a single stage, to full height, might induce foundation failure of the very weak subsurface soils unless carefully controlled;
2. The scour feature exhibited a linear geometry, forcing the dike repair to cross a deeper scoured area than initially anticipated; and
3. Construction methods would be forced to work in relatively deep water within the scoured area.

Viable dike repair methods were reduced to earthen embankment, sheet piling, or a combination of these methods. Sheet piling potentially allowed construction in a single stage. However, constructability evaluation of piling indicated that very expensive marine operations would be required. Sheet piling installation was also deemed risky and difficult. Initial analyses suggested that an earthen embankment dike repair method might be potentially unstable when analyzed for construction in a single stage. The use of stabilization geo-grid was considered and found to be beneficial but insufficient by itself.

DESIGN ANALYSES

The authors pursued a design based upon the use of a light-weight fill embankment. This method reduced the foundation instability issues. However, the light-weight fill is highly susceptible to erosion and vulnerable to seismic liquefaction. The U.S. Army Corps of Engineers Design and Construction of Levees Manual (U.S. Army Corps of Engineers, 2000) was used to guide design. Major design elements are discussed below.

Constructability: Having eliminated placement from a barge, methods were considered to work from the fill being placed. If conventional dike sideslopes were used across the deeper portions of the scour channel, the required reach of placement equipment would exceed those locally and regionally available. For example, at a 4H:1V sideslope and a 25-foot high embankment, and the necessity to work above the water surface, the width of the sideslope would be 100 feet. This was deemed to be impractical. Furthermore, the amount of material required would be very large.

The authors believed that light-weight embankment material could be placed by pushing the material ahead of the leading edge of the embankment into the water. This would result in the material being placed uncompacted with sideslopes at the material's submerged angle of repose, which was determined in the laboratory to be about 32 degrees. Also, the dry unit weight of the loosely placed cinder fill was measured to be on the order of 80 pounds per cubic foot (pcf). The analyses indicated that sideslopes of the light-weight earthfill in the order of 1.5H:1V to 1.75H:1V were possible.

Embankment Stability: The scour resulted in steep mudline slopes on both the north and south sides of the resulting channel. Placing the earthfill embankment on steeply sloping sediments could result in localized instability. The dike-breach closure embankment is located downstream along the scour feature to where bathymetric slopes were no steeper than 2 horizontal to 1 vertical (2H:1V). At that location, the maximum embankment height ranged across the base between approximately 27 feet on the landside to 31 feet on the lakeside.

The earlier geotechnical work in the area, geologic reports, and research by others on diatomaceous earth, together with the current explorations and testing, were evaluated to select the material properties for stability analyses. Initial loading during construction and immediately following removal of the flood water were considered to be the worst case design conditions. Since the dike repair materials are predominately cohesionless and the slow rate at which dewatering was expected, rapid drawdown conditions within the dike were considered negligible. Slope stability analysis was performed by numerical modeling methods, using the slope stability function of the FLAC® program. Input parameters for the stability analyses are presented below.

Table 1. Material Properties for Embankment Stability Evaluation

Material Description	Moist Unit Weight (pcf)	∅ (degrees)	C (psf)
Cinder fill	100	32	0
Drainage blanket and rip-rap	135	42	0
Diatomaceous silt above Elevation 4116	86	0	350
Clayey silt, Elevation below 4116	86	0	330 - 520

The cohesion of the clayey silt was modeled to increase with depth at the rate of about 25 psf per foot of increasing depth. The resulting stability factor of safety during construction was unacceptably low without soil reinforcement. Consequently, geogrid reinforcement was added to the design embankment section. Further, within the scour area, the embankment's landside slope was benched to reduce the load onto the underlying weak subsoils. This was done by overfilling and then excavation to final configuration with an extended reach backhoe with a 55-foot arm. A geogrid placed at mudline yielded a minimum static factor of safety of 1.5 with Upper Klamath Lake at mean annual high water (4143 ft) and the landside dewatered to the ground surface (4136 ft).

Live loads from construction equipment and subsequent vehicular traffic were also considered in the stability analyses. This was an important consideration during the constructability evaluation in establishing working setbacks from the outside edges of the sideslopes because they will be constructed at the angle of repose. The factor of safety at the angle of repose is equal to 1.0. As the loading moves towards the center of the embankment away from the sideslope edges, the factor of safety increases. Consequently, construction mats were required to distribute equipment loads, no closer than 5 feet from the edges of sideslopes. The restrictions imposed provided an estimated minimum temporary factor of safety of 1.4 during construction.

Other Considerations: After the dike-breach closure is placed and dewatering begins, the lowered water level will result in seepage through it. Consequently, a drainage blanket was provided to collect seepage and to prevent erosion. Erosion protection is provided primarily by a non-woven geotextile placed directly upon the new embankment sideslopes and bench. The drainage rock blanket stabilizes the non-woven geotextile, and provides drainage to the embankment toe. Rip-rap was placed on the lakeside slope to protect the new embankment against wave erosion.

The dike repair was constructed on soft, compressible sediments that have not been preloaded. Thus, settlements will occur. Based on laboratory test results and design conditions, we estimate the embankment constructed on unscoured ground will settle up 2 feet. The embankment constructed on the deepest scour area is expected to settle two to three times that for unscoured locations. This will require ongoing addition of fill to maintain the desired dike top level.

The potential earthquake geohazards were also evaluated. Liquefaction is the primary geohazard risk of the breach closure embankment. The loosely placed embankment is susceptible to seismically induced liquefaction. Potential failure modes range from embankment deformation to slope collapse. Several soil improvement options have been considered, but none have been implemented to date.

CONCLUSIONS

Design of the dike breach repair required materials and techniques that could be constructed in the inundated, scoured conditions. Schedule, costs, and equipment availability dictated that land-based construction techniques be used. Use of lightweight fill, geogrid, and an embankment bench-cut provided acceptable stability to allow single-stage construction. Use of geotextile and a drainage rock blanket provided seepage collection and erosion protection.

Construction on the closure embankment was started in November, 2006, and was successfully completed December 29, 2006. A backhoe excavator with an extended arm with a 55-foot reach was used to place the initial geo-grid mat prior to end dumping the cinder fill. The extended-arm backhoe also was used to excavate the interior berm and place drainage rock blanket material along the long sideslopes in the scoured area.

REFERENCES

Geomatrix Consultants, 1995, *Seismic Design Mapping State of Oregon*: Final Report, prepared for Oregon Department of Transportation under personal services contract 11688.

Orr, E.L. Orr, W.N. and Baldwin, E.M., 1992, *Geology of Oregon*, Fourth Edition, Kendall/Hunt Publishing Co., DuBuque, Iowa.

U.S. Army Corps of Engineers, 2000, *Design and Construction of Levees*, Engineering Manual EM 1110-2-1913, Department of the Army, Washington, D.C.

Wilson, Sean Damian, 2000, *Geology and Slope Stability of the Borax Lake Hydrothermal Mound, Alvord Basin, Oregon*, A Thesis submitted in partial fulfillment of the requirements for the degree of Master of Science in Geology, Portland State University.

Viability Assessment of Terrestrial LiDAR for Retaining Wall Monitoring

Debra Laefer[1], M. ASCE and Donal Lennon[2]

[1] Director of Conservation Research, School of Architecture, Landscape and Civil Engineering, University College Dublin (UCD), Newstead, Room G25, Belfield, Dublin 4, Ireland debra.laefer@ucd.ie
[2] Senior Technical Officer, Urban Institute Ireland, UCD, Belfield, Dublin 4, Ireland dlennon@ucd.ie

ABSTRACT: The decreased cost and increased processing speed for terrestrial laser scanners have made this remote sensing procedure much more attractive. The approach has two major advantages over traditional surveying: (1) a registration of the survey instrument independent of any physical benchmarks. Thus, if the entire area is experiencing subsidence, the quality of the final results will not be compromised as they will be absolute measurements, as opposed to relative ones because they are based on a global positioning registration; (2) the ability of the technologies to highlight cracks in masonry. Unfortunately, despite major advances in the equipment and software, the technology is arguably not fully ready for the task of automated retaining wall monitoring. This paper will outline the challenges that remain with respect to registration and displacement monitoring.

INTRODUCTION

Retaining wall systems represent a two billion dollar a year industry of increasing complexity. As urban densification continues to grow and above ground space increases in value, retaining wall systems need to be installed deeper and under greater difficulty. The crowdedness of the sites, third-party permissions, and the installation geometries will increasingly complicate the use of traditional monitoring. Furthermore, the heightened risk of litigation has increased pressure to develop a more objective, permanent record regarding retaining system performance. As such, the attractiveness of terrestrial laser systems [usually referred to as light detection and ranging (LiDAR) systems] has gained increasing attention. This paper provides a technical overview of the current equipment and important installation and operating factors related to its potential application for retaining wall monitoring.

BACKGROUND

Lasers have been used for over a decade to detect defects in a wide variety of industries such as coke plants (Grosse-Wilde 1998) and petroleum facilities (Ogawa 1993), while LiDAR itself has been used for risk evaluation for a wide variety of

Civil Engineering subjects from predicting slope failures (Kwak and Jang 2006, Jones 2006) and selecting evacuation routes based on possible downed trees (Laefer and Pradhan 2006). LiDAR is potentially attractive for retaining wall monitoring as it provides the capability to rapidly make multi-point measurements over a large area. Typical equipment is shown in figure 1a along with an associated target in figure 1b.

(a) Scanning unit and laptop (b) Spherical target

FIG. 1. LiDAR equipment

Recent research-oriented work has advocated use of terrestrial LiDAR scanning for architectural documentation (English Heritage 2006), to integrate field data in a real-time manner (Oliveira Filho et al., 2005, Su et al. 2005, Hashash et al. 2005), to generate a more accurate permanent record of construction sequencing and performance (Su et al. 2006), and to improve the design quality and construction based on better performance monitoring (Hashash et al. 2005), in combination with digital photogrammetry (Hashash et al. 2006). Despite a significant decrease in the equipments cost coupled with major improvements in its flexibility and speed, the unit's price tag of over $100,000 has prevented a major marketing push into this area, but its enhanced use for condition assessment and bridge monitoring and generation of as-built drawings clearly show that it is simply a matter of time before retaining structures are seen as a viable market. Consequently, questions arise as to the benefits and drawbacks that terrestrial scanning offers today.

Terrestrial laser scanning, or LiDAR, is a non-contact method for making physical surface measurements, allowing visualizations of scanned surfaces in a digital 3D environment. The technique converts 'bounce-back' information [i.e. time of flight, and 2D angular components of the laser path with reference to a 0,0 position to fix a point in a 3D space for each laser pulse, thus building (in the form of a point cloud)] a 3D digital model of the surface being monitored. The technology is based on the facts that light travels in a straight line at a known speed.

The laser machine has an in-built digital camera that has two functions:

1) a digital image can be recorded during the scan to be “draped over” the point cloud resulting in a realistic 3D image of the scan subject.
2) the surveyor is aided in framing the scan area by the digital camera acting as the eyes of the machine, displaying an image of the scan area on the computer screen, while the surveyor frames the object to be scanned.

Provided the scan is carried out under suitable atmospheric conditions using adequate reference targets, it is possible to quantify measurements of surface features and orientation, with reference to surrounding features, such as a building or to reference targets placed within the scan area. The laser pulse is emitted in a controlled vertical sweeping motion as the machine rotates in the horizontal to sweep the scan area. The laser pulse bounces back from the first reflective surface that it encounters. Quality or intensity of laser bounce back depends on surface characteristics and atmospheric conditions. Dust and moisture in the atmosphere degrade feed back quality resulting in noise or rouge points, while moisture can result in void areas due to scatter.

Scanning requires that the laser is set up at the first location (station 1), the object to be monitored is framed, and the scan parameters are selected in terms of required accuracy and feature detail, and then the scan begins; the scanner cannot be moved from this position, until all the required data is collected. If further scans are to be conducted at a future time, as in the case of sheet piling monitoring, a number of reference targets must be established which are scanned in each subsequent survey. Subsequent scans are merged into one model using the reference points generated from these targets, and any alteration in sheet piling position can thus be visualized and measured. Reference targets are also used where a number of scan stations are required to build a complete image of a subject area.

CAPABILTIES AND CHALLENGES

There are several major companies in the terrestrial LiDAR market; some with multiple models. Each varies to some degree but can be categorized as very near range, mid-range, and far range. As most excavations of concern are within 100 m, this paper will focus on the capacities of units in that range. An exhaustive comparison of recent equipment is provided by Mechelke (et al., 2007), thus only a brief overview is herein provided. Data collection speeds are in the order of 5,000 points per second. This translates to a scanning time for 1m^2 at 5 x 5 mm point spacing (36,481 data points) of about 7.29 seconds. Speed is range dependent (i.e. long range scans reduces the data point collection rate). Thus, at a 100m stand-off distance from the object a data point at every 5mm vertical and horizontal (fig. 2),is returned where the unit is orthogonal to the monitored surface; degradation occurs with obliquity. If the scan was conducted at a third of the distance, point density would approximately triple. Alternatively, the scanner can be set for slower data collection, thus increasing the point density. Figure 2 shows a 2 x 2 mm point spacing at 100 m.

Selecting a scan density does not mean collecting the maximum data possible. Figure 3 shows the ability to detect cracks in a building at resolution of approximately 2 mm spacing. Collecting excessive quantities of data only make storage and processing problematic. A common error is in the framing of the object to be scanned. Unnecessary time, resources, and effort are expended, if unessential background elements are included, instead of only the objects of interest (FIG. 4). A sample field program at UCD showed that results were optimized, where the scanning occurred within 50 m of the object of interest.

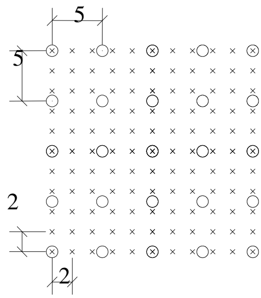

FIG. 2. Spacing of a 2mm x 2mm resolution scan overlaying a 5mm x 5mm resolution

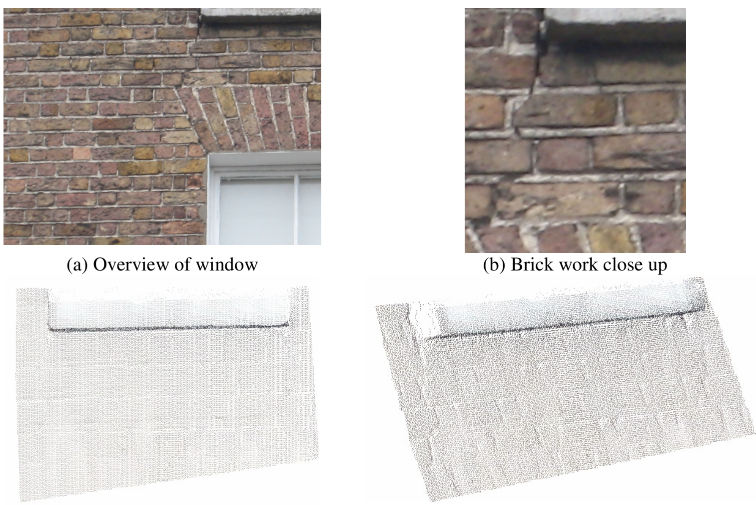

(a) Overview of window

(b) Brick work close up

(c) LiDAR image viewed orthogonally

(d) Rotated LiDAR image

FIG. 3. Damage detection for a brick building in Dublin, Ireland

Most units now provide a view 360˚ radially by 60˚ vertically, (40˚ above the horizontal centre line of the machine and 20˚ below), which provides significant flexibility in unit placement. Because of issues with obliquity, the unit should be positioned as perpendicular to as many of the main surfaces as possible (fig. 5). Multiple scans that can be integrated into a single composition are well within the capabilities of the technology, but each repositioning requires a semi-manual meshing of the scans, which are time consuming. Some of these issues are address by Ratcliffe and Myers (2006) in their comparison of LiDAR and photogrammetry for open pit mines.

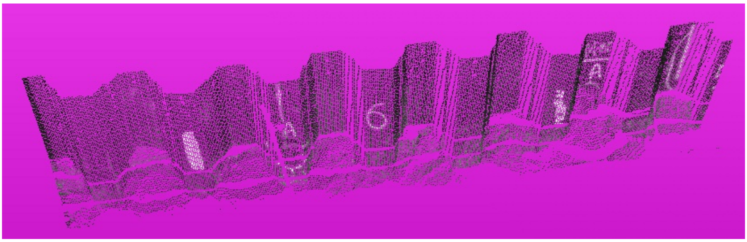

Fig. 4. Point cloud of a section of sheet piling.

The unit can be handled by one person, but a special transport box with wheels is recommended due to its weight. Additionally, in inclement conditions a van is strongly recommended as the unit can be operated from within the van despite the rain. Under heavy rain or without the protection of an external means, the unit cannot be used as the water interferes with the laser beam. Theoretically the unit can be used as a traditional survey instrument and is marketed as such (e.g. http://www.trimble.com/gs200.shtml).

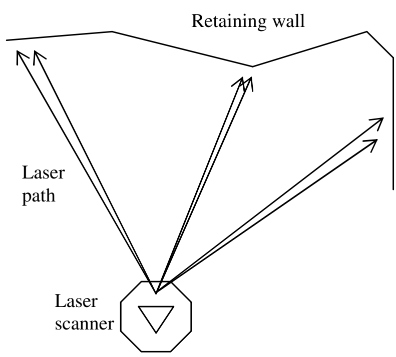

FIG. 5. Optimizing unit placement for a single scan approach to a complicated site

Since the laser scanning process is non-tactile, it need not interfere with ongoing earth works, especially since there is no need to install any monitoring equipment directly onto the retaining wall. Despite these advantages, the technology is not a panacea. To detect and measure movement in a sheet piling installation by the laser scanning method requires that a number of scans be recorded over a period of time. These scans are compared to detect and measure any movement in the sheet piling.

For this comparison to be made, each scan must contain common reference points that are not subject to subsidence or other earth movement effects on the site. Spherical targets (Fig.1b) are commonly used as reference points. The target must be placed in exactly the same place for each scanning operation. Ideally, the targets are left in situ for the duration of the monitoring program. However, this may not be possible and a method for accurately re-placing targets must be found (e.g. gluing a mounting in situ on the site onto which the target can be placed during scanning)

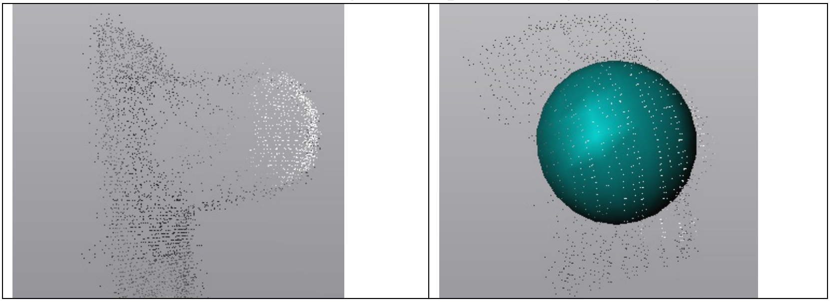

(a) Point cloud of spherical target (b) Post-process solid fitted to point cloud

FIG. 6. Scanner output

At least three fixed reference targets, for each scanner position, must be set up adjacent to the inspection site and within line of site of the laser scanner position, in such locations that are immune to any earth movements due to excavation works. However for improved accuracy and to mitigate against any of the target areas being compromised or occluded over the course of the monitoring program, it is advisable to use up to six reference target positions per scanner position (station). Only three reference points are required per scan, however the changing landscape of a busy site will result in the loss of line of sight to some targets locations over time and target reduncy will save time in such situation. For this to be viable, it is necessary to scan in all target points during the first scan of the site, and it is recommended to scan as many targets as possible in subsequent scans. Redundant targets, thus, prevent costly delays in having to wait to scan when lines of sight are free. Similar consideration is required when picking a location for the laser scanner. It is best to identify a number of possible laser scanner positions that provide line of sight to all or most of the six reference target positions, as well as line of sight to the subject area under consideration, if the site lay out allows it. To fully address this issue, the subsequent construction must also be considered. In all of this, however, what is foremost is that both the subject of the scan and the targets are recorded from the same zero position.

Additionally, when selecting the scanner position at a scan site it is best to select a site such that the spread of points on the surface to be measured will be as even as possible across the total length of the scan (FIG. 5). The laser scanning process is designed to register a point in a three dimensional space for every bounce back event during the scan. This is achieved through a calculation that includes the time of flight of the laser pulse and the vertical and horizontal angles of the laser path through the intervening space with reference to a zero position. The spread of points on the surface to be measured is an important consideration and is set by the surveyor when setting up the scan parameters. For example a setting of 50mm x 50mm at 100 meters while the scanner is true to a surface at 100m distance, the points collected that represent that surface will occur at 50mm intervals on the surface, vertically and horizontally. However as the distance to surface increases (as a result of the radial motion of the scanner), the points spread will increase. Equally as the angle of the laser path to the surface changes, the points spread also changes. Therefore, the laser scanner position should be selected to minimize the distortion of the point's matrix over the total scan. It may be necessary for the surveyor to use multiple scanner locations.

The normal sequence of events in a laser scanning exercise is to set up the equipment in the first scan position, 'scan station one'. The reference targets in line of sight of station one are scanned using manufacturer default parameter setting, the subject wall is then scanned at surveyor required density. If further scans from other vantage points are required, each pair of stations (scanner positions) must have line of sight of at least three common reference points to facilitate merging of the individual scans into one full three dimensional image of the whole sheet piling installation. The major disadvantage of multiple scan stations is the time needed to set-up the equipment in each location plus the time required to scan the reference targets (up to six) from each new scanner location. There is also some added processing time required in the office to 'register' each of the scans into one document. Accuracy can rival very high quality traditional surveying – the 2mm level for differential measurements.

Measurements of horizontal and vertical movement of a sheet piling installation are made by comparing initial scan results with subsequent scans using common reference targets to merge the scans as one document/model. Any out of position of the sheet piling in the subsequent scan with reference to the first will be apparent and can be measured by using the built-in measuring tools in the modeling software.

Use of a global position system (GPS) offers additional registration opportunities, but the canyoning effect in an urban environment has yet to be surmounted. Finally, temperature is a known source of error for all instruments as objects expand and contract diurnally, as well as seasonally (e.g. Buttry et al. 1996). As such, efforts should be made to take readings of the subject wall, when no movement is expected so that temperature related effects can be discounted as part of the baseline noise.

CONCLUSIONS

If set up with care, terrestrial LiDAR scanning can offer some additional benefits over traditional survey methods with respect to an objective permanent record that can be free from any large-scale subsidence that the area may be experiencing. Whether these advantages bear the high cost of the equipment and the more extensive need for a technically sophisticated survey crew remains an issue for the industry to judge.

ACKNOWLEDGMENTS

Support for this work was generously provided by Science Foundation Ireland, Grant 05/PICA/I830 GUILD: Generating Urban Infrastructures from LiDAR Data.

REFERENCES

Buttry, K.E., McCullough, E.S., and Wetzel, R.A. (1996). "Temperatures and related behavior in segmental retaining wall system." *Transportation Research Record*, National Research Council, n 1534, 19-23.

English Heritage (2006). Developing professional guidance: laser scanning in archaeology and architecture., 57 pp.

Grosse-Wilde, M. and Huhn, F. (1998)."Monitoring coke oven wall deformation by means of laser triangulation." *Revue de Metallurgie. Cahiers D'Informations Techniques*, 95 (3) Mar., 311-31.

Hashash, Y.M.A., Oliveira Filho, J.N., Su, Y.Y., Liu, L.Y. (2005). "3D laser scanning for tracking supported excavation construction.", *Geo-Frontiers 2005*, Jan 24-26, 2005, Austin, TX, Geo-Institute ASCE, 2013-22.

Hashash, Y.M.A., Liu, L., Su.Y.Y., Song, H. (2006). "Use of new technologies for tracking excavation progress." *GeoCongress 2006: Geotechnical Engineering in the Information Technology Age*, Feb. 26-Mar. 1, 2006, Atlanta, GA, ASCE, 70.

Jones, L.D. (2006). "Monitoring landslides in hazardous terrain using terrestrial LiDAR: An example from Montserrat." Q. *J. Engineering Geology and Hydrogeology*, Geological Soc. London 39 (4) Nov., 371-73.

Kwak, Y., Jang, Y. and Kang, I. (2006). "Web GIS management and risk evaluation of a road slope using a terrestrial LiDAR." *Lecture Notes in Computer Science*, Springer Verlag v 3833, 256-66.

Laefer, D.F. & Pradhan, A.R. (2006). "Evacuation Route Selection Based on Tree-Based Hazards Using LiDAR & GIS." *J. Trans. Eng*., ASCE, 132(4) 312-20.

Mechelke, K., Kersten, T.P., Lindstaedt, M. (2007). "Comparative Investigations into the accuracy behaviour of the new generation of terrestrial laser scanning systems." *Optical 3-D Measurement Techniques* VIII, (Eds.) Gruen/Kahmen, Zurich, July 9-12, Vol. I, 319-327.

Ogawa, S., Mizunuma, M. and Kuwano, H., (1993). "Sensing system for pipe innerwall inspection by laser-beam scanning." NTT R&D, v 42, n 7, p 923-932.

Oliveira Filho, J.N., Su, Y.Y., Son. H. Liu, L.Y. and Hashash, Y.M.A. (2005). "Field tests of 3D laser scanning in urban excavation." *Proc. of the 2005 ASCE Intl Conf. Computing Civil Eng*., Jul. 12-15, 2005, Cancun, Mexico ASCE, 563-572.

Ratcliffe, S. and Myers, A. (2006). "Laser Scanning in the Open Pit Mining Environment a Comparison with Photogrammetry." I-SiTE White Paper, 10 pp.

Su, Y.Y, Oliveira Filho, J.N., Liu, L.Y., Hashash, Y.M.A. (2005). "Integration of construction field data and geotechnical analyses." *Construction Research Cong. 2005: Broadening Perspectives*, Apr 5-7 2005, San Diego, CA, ASCE, 1129-36.

Su, Y.Y., Hashash Y.M.A., and Liu, L.Y. (2006). "Integration of construction as-built data via laser scanning with geotechnical monitoring of urban excavation." *J. Construction Engineering and Management*, ASCE 132 (12) 1234-41.

Trimble. (http://www.trimble.com/realworks.shtml) "RealWorks Survey Office Software for 3D Scanning in Surveying and Spatial Imaging." (August 20, 2007).

DEM Modeling of the Effect of Hydraulic Hysteresis on the Shear Strength of Unsaturated Granular Soils

U. El Shamy[1]

[1]Environmental and Civil Engineering Dept., Southern Methodist University, PO Box 750340, Dallas, TX 75275, E-mail: uelshamy@engr.smu.edu

ABSTRACT:

A micromechanical model for capturing the effect of hydraulic hysteresis on the behavior of unsaturated granular soils at low saturation (below 30%) is presented. The discrete element method is employed to model the solid particles. The capillary water is assumed to be in a pendular state and thus exist in the form of liquid bridges at the particle-to-particle contacts. The resulting interparticle adhesion is accounted for using the toroidal approximation of the bridge. Hydraulic hysteresis is accounted for based on the possible mechanism of the formation and breakage of the liquid bridges during wetting and drying phases. Shear test computational simulations were conducted at different water contents under relatively low net normal stresses. The results of these simulations suggest that capillary-induced attractive forces and hydraulic hysteresis play an important role on affecting the shear strength of the soil. These attractive forces produce a tensile stress that contributes to the apparent cohesion of the soil and increases its stiffness.

INTRODUCTION

Computational modeling of the coupled response of unsaturated soils has received a great deal of attention over the past two decades. Phenomenological models of partially saturated soils are highly sophisticated and refined (e.g., Muraleetharan and Wei, 1999; Laloui et al., 2003). Numerous constitutive models have been developed for partially saturated soils (e.g., Wheeler and Sivakumar, 1995; Russel and Khalili, 2005). All these models can be implemented in a continuum formulation to analyze the response of partially saturated soils. However, the drawback of continuum methods is that an appropriate constitutive law for the material may not exist, or the law may be excessively complicated with many obscure parameters.

The alternative would be the use of particle-based techniques such as the Discrete Element Method (DEM) (Cundall and Strack, 1979). DEM has been effectively used to qualitatively model the collapse behavior of unsaturated soils due to reduction in suction upon wetting using a 2D DEM-based model (Gili and Alonso, 2002; Liu and Sun, 2002). 2D DEM simulations were also conducted to characterize the shear response of unsaturated samples in a bi-axial testing environment (Jiang et al., 2004). While these studies provided useful information on the behavior of unsaturated soils, extrapolating the 2D response to the 3D real world experiments becomes rather difficult because of the kinematic constraints on particle movements in 2D (Thornton and Antony, 2000).

In this study, the response of unsaturated soils is explored based on micro-mechanical considerations. Attention is given to unsaturated coarse-grained soils or ‘wet’ granulates at low saturation (below 30%). The pore-fluid is assumed to exist in the form of pendular liquid bridges at the particle-to-particle contacts. These bridges induce attractive forces that are computed based on a toroidal approximation of the bridge (Lian et al., 1993). The soil grains are modeled as a randomly-packed assemblage of rigid spherical particles that are idealized using DEM. Using the developed model, a number of simulations were conducted to investigate the impact of hydraulic hysteresis during wetting and drying phases on the shearing behavior of wet coarse granular soils.

MICRO-MECHANICAL MODELING OF WET GRANULAR SOILS

Capillary force

The exact curvature of the bridge can only be obtained by numerical solution of the Laplace-Young equation (Lian et al., 1993). However, Lian *et al.* (Lian et al., 1993) showed that the difference between the numerical solution of the exact shape and a toroidal approximation is less than 10%. Considering the error of experimental measurements due to uncertainties of liquid bridge volume, surface tension, and particle roughness, this approximation is sufficiently accurate. The resulting force of a toroidal liquid bridge can be calculated either on the three-phase contact area (boundary method) or on the gorge (neck) of the bridge. The gorge method appears to be more accurate and it is therefore used in the present study. The method assumes that the capillary force consists of a contribution of the capillary pressure P_c as well as the surface tension T_s. The axial surface tension acting at the neck is:

$$F_1 = 2\pi T_s r_2 \tag{1}$$

and the hydrostatic force evaluated at the neck is given by:

$$F_2 = \pi {r_2}^2 P_c \tag{2}$$

Thus the total capillary force is:

$$F_l = F_1 + F_2 = \pi r_2 T_s \frac{r_1 + r_2}{r_1} \tag{3}$$

with the capillary pressure defined as:

$$P_c = T_s(\frac{1}{r_1} - \frac{1}{r_2}) \tag{4}$$

where r_1 and r_2 are the principal radii of the liquid meniscus. The capillary pressure ($P_c = u_a - u_w$) is often referred to as matric suction as it describes the difference between air pressure u_a and water pressure u_w (e.g., Lu and Likos, 2004). If the air pressure u_a is considered as a reference and equals to the atmospheric pressure, the pore-water pressure is negative and its absolute value is given by Eq. 4.

The liquid bridge volume can be determined analytically as it depends on the principal radii r_1 and r_2, as well as the half-filling angle β and the contact angle θ (Fig. 1). However, the half-filling angle β cannot be calculated explicitly. Therefore, to calculate β as a function of a given bridge volume, separation distance, and contact angle an iterative procedure is needed.

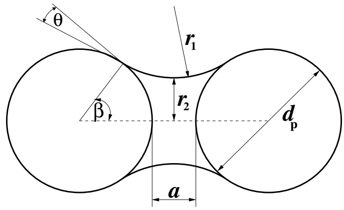

FIG. 1. Idealized liquid bridge between two identical spheres.

DEM formulation

Granular soils consist of an assemblage of discontinuous interacting particles which may be modeled effectively using the discrete element method (DEM). The motion of every grain follows Newton's second law:

$$m_i\dot{V}_i = F_{g_i} + \sum(F_{c_{ij}} + F_{l_{ij}}) \tag{5}$$

$$I_i\dot{\omega}_i = \sum R_i \times F_{c_{ij}} \tag{6}$$

where V_i and ω_i are translational and rotational velocity vectors (a superposed dot indicates a time derivative), m_i is particle mass, I_i is particle moment of inertia, $F_{c_{ij}}$ refers to inter-particle force of particle i due to particle j, $F_{l_{ij}}$ is the liquid bridge force between particles i and j, and R_i is vector connecting the center of particle i to the location of the contact point.

The particles are considered to be rigid, but can overlap. This overlap accounts for the deformations induced by the contact forces. A constitutive law provides the contact forces as a function of the relative position and displacement of the grains (El Shamy and Gröger, 2007). More specifically, the contact forces between two spherical particles consist of normal and shear components. Both components are functions of frictional, viscous, elastic and capillary effects. A contact force F_c between two particles consists of normal F^n and shear F^s components. The normal component of the force acting on particle i from particle j was idealized using a nonlinear Hertz model connected in parallel with a viscous dashpot:

$$F^n{}_{j\rightarrow i} = (k_nU_n - c_nV_n)e_n \tag{7}$$

where U_n and V_n are relative displacement and velocity at the contact along the line connecting the spherical particle centers, e_n is unit vector of normal direction at the contact, c_n is normal viscous damping coefficient, and k_n is normal contact stiffness (Mindlin and Deresiewicz, 1953):

$$k_n = \left(\frac{E\sqrt{d_\mathrm{p}}}{2(1-\nu^2)}\right)\sqrt{U_n} \tag{8}$$

in which E and ν are respectively particle Young's modulus and Poisson's ratio. The shear contact force was modeled using a linear elastic spring in series with a frictional slider:

$$F^s{}_{j\rightarrow i} = -c_sV_se_s - \mathrm{sign}(U_s)\min(ks|U_s|, \mu_p|F^n{}_{j\rightarrow i}|) \tag{9}$$

in which U_s and V_s are shear displacement and velocity at the contact, e_s is unit vector of tangential direction, c_s is shear viscous damping coefficient, μ_p is particle-to-particle friction coefficient, and k_s is shear contact stiffness. The shear and normal forces are related by a slip Coulomb model.

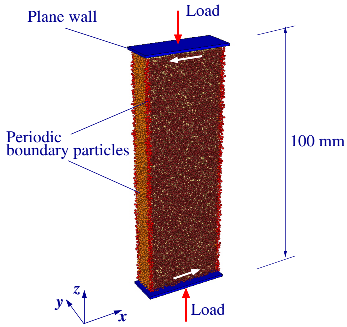

FIG. 2. Three-dimensional view of analyzed granular deposit and shear test setup.

Average suction

Suction plays an important role in unsaturated soil mechanics. Suction is a macro-scale quantity that reflects the average pressure difference between the air and water phases at their interfaces. Therefore, suction was calculated within the sample by averaging the capillary pressure computed for each liquid bridge that develops at a particle-to-particle contact (Eq. 4). That is, the average suction, $\overline{P}_c$, is given by:

$$\overline{P}_c = \frac{1}{M}\sum_{c}^{M} P_c \tag{10}$$

Hydraulic hysteresis

Hydraulic hysteresis has a significant impact on the behavior of unsaturated soils (Fredlund and Rahardjo, 1993). The response of a partially saturated soil sample during a drying stage would be different than that during a wetting stage. In this study, hydraulic hysteresis is accounted for by following the mechanism of liquid bridge formation during both stages. In case of wetting (i.e. starting from low saturation toward high saturation) the liquid bridge would form only between particles in body contact. In a drying scenario, water already exists between the particles not necessarily in body contact. Therefore, liquid bridges could exist at stretched contacts as long as the distance between the neighboring particles is less than the critical distance required to maintain a stable liquid bridge. Following this hypothesis, separate liquid bridge formation algorithms were used in the conducted simulations to resemble both scenarios.

SHEAR TEST SIMULATIONS

Numerical simulations were conducted to assess the shear strength of wet granular materials. A sample of mono-sized weightless particles was generated and use was made of periodic boundaries in the two lateral directions to reduce the number of particles in the simulation to a manageable size (El Shamy, 2004). Once particles are generated, they are consolidated through the movement of the top and bottom walls until the desired normal stress is achieved. The synthetic sample was then sheared in a manner similar to that used in a typical direct shear test. The external shear load was applied by moving the top and bottom platens in opposite direction at a constant shear strain rate of $5 \times 10^{-7} s^{-1}$ (Fig. 2). During shearing, the normal stress was maintained constant through a servo-mechanism (Itasca, 2005). Such mechanism would adjust

Table 1. Shear test simulation data.

Particles	
Diameter	1.0 mm
Young modulus	7×10^7 N/m^2
Poisson's ratio	0.15
Friction coefficient	0.5
Specific gravity	2.65
Number of particles	37,867
Initial height of solid particles	100 mm
Critical damping ratio	0.9
Water	
Surface tension	0.0727 N/m
Contact angle	0
Simulation	
Water content, w	0, 0.2, 2, and 5.2%
Degree of saturation, S	0, 1, 10, and 25%

the vertical velocity of the top and bottom platens (walls) such that the vertical normal stress within the sample is maintained at the desired value.

The simulations were conducted for degrees of saturation ranging from zero (dry) to about 25%. Throughout each simulation, the water content does not change but the sample can undergo volumetric deformations. For each water content considered, the sample was sheared under three different net normal stresses (250, 500, and 1000 Pa). The choice of these relatively low normal stresses was to illustrate the impact of the capillary forces on the response as it becomes negligible under large applied load (Cho and Santamarina, 2001). Table 1 provides a summary of computational details of the simulations. Average values of the solid phase parameters and state variables were monitored during the course of the simulation within spherical control volumes along the central vertical axis of the sample.

Soil-water characteristic curve

The present model was used to directly construct the soil-water characteristic curve for the soil under consideration using the methodology for computing the average suction (Eq. 10) and accounting for hydraulic hysteresis following the mechanism of liquid bridge formation described earlier. Using this approach, the SWCC was constructed (Fig. 3) as follows. During the drying phase, part (AB) of the curve was obtained by computing the average suction within the sample corresponding to degrees of saturation ranging from 0.01 to 30%.

Stress-strain response during drying and wetting stages

The shear stress-shear strain relations obtained from the conducted simulations for a state of drying are shown in Fig. 4. The failure envelopes of these tests are compiled in Fig. 5. As the degree of saturation increases, the maximum shear stress at failure, generally, increases. However, the failure envelopes and stress-strain curves for the $w = 2.0\%$ and $w = 5.2\%$ ($S \approx 10\%$ and $S \approx 25\%$, respectively) look almost identical. After a relatively low degree of saturation (small amount of water), the tensile stress reaches a constant value and does not increase with the increase of the amount of water in the pores. During the wetting stage, the same trend was observed as indicated in Figs. 4 and 5.

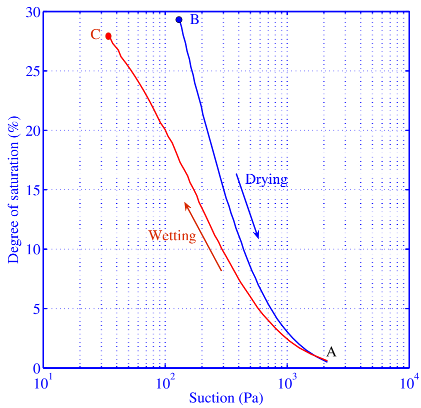

FIG. 3. Soil-water characteristic curves generated using proposed micro-scale model during drying and wetting stages.

The shear strength parameters corresponding to the failure envelops shown in Fig 5 can be backfigured using the Mohr-Coloumb failure criterion:

$$\tau = c_a + \sigma^{net} tan\phi \tag{11}$$

where c_a is apparent cohesion and ϕ is angle of internal friction. The angle of internal friction of a sample sheared during a drying phase is generally larger than that if sheared during a wetting phase. Note that the presence of water in the sample resulted in higher friction angle compared to the perfectly dry sample only if sheared during a drying phase (the ϕ angle for dry sample was 27.6^o). The apparent cohesion for samples tested during the drying stage is generally larger than that during the wetting stage except for at very low water content. The apparent cohesion also tends to increase as the amount of water increases up to the limit where the induced tensile stress becomes constant.

The volumetric strain of the sample during the conducted numerical experiments are shown in Fig. 6 for the drying and wetting phases respectively. At very low normal stresses, the sample tend to exhibit a loose-like response. As the normal stress increases, a dilative response was observed and was more pronounced at higher stress levels. This dilative response is mainly due to the mono-sized grain size distribution employed in the present study.

CONCLUSION

A micromechanical computational model for the analysis of wet granular soils at low saturation (below 30%) has been presented. The proposed model is capable of producing essential mechanical and hydraulic properties of the partially saturated granular soil. Hydraulic hysteresis is accounted for based on the possible mechanism of the formation and breakage of the liquid bridge during wetting and drying phases. Conducted shear test simulations suggest that capillary-induced attractive forces and hydraulic hysteresis play an important role on the shear strength of the soil. These attractive forces produce tensile stress that contributes to the apparent cohesion of the soil and increases its stiffness. During a drying phase, capillary-induced tensile stresses, and hence shear strength, tend to be larger than that during a wetting phase. These forces tend to be larger than that during a wetting phase.

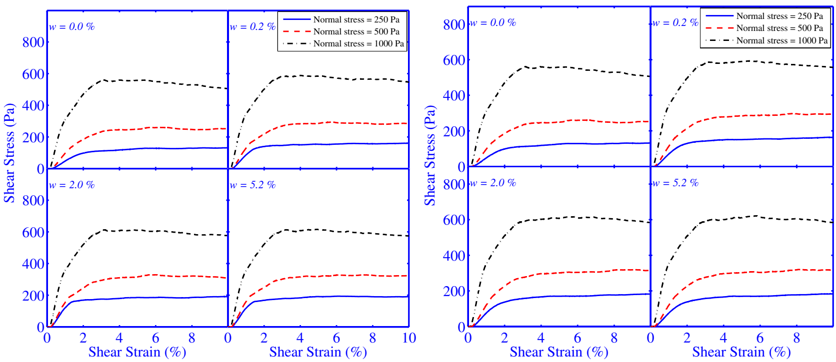

FIG. 4. Shear stress-shear strain relations for different water contents during a drying stage (left) and a wetting stage (right).

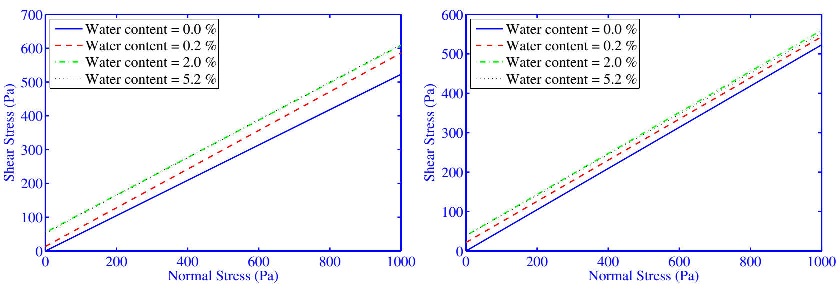

FIG. 5. Shear stress vs. net normal stress for different water contents during a drying stage (left) and a wetting stage (right).

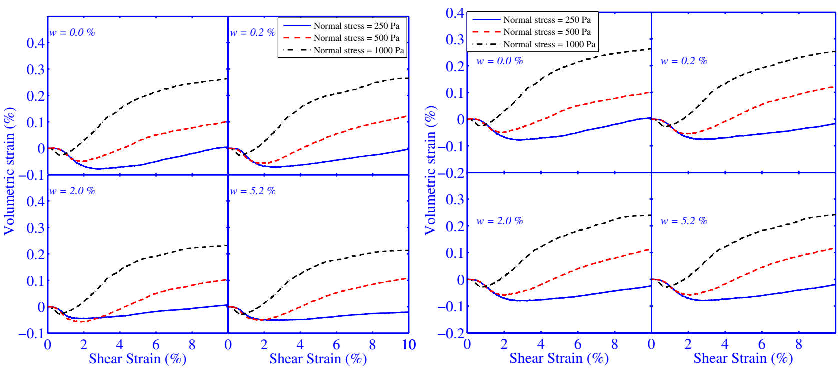

FIG. 6. Volumetric strain vs. shear strain for different water contents during a drying stage (left) and a wetting stage (right).

REFERENCES

Cho, G. and Santamarina, J. (2001). "Unsaturated particulate materials-particle-level studies." *Journal of Geotechnical and Geoenvironmental Engineering*, ASCE, 127(1), 84–96.

Cundall, P. and Strack, O. (1979). "A discrete numerical model for granular assemblies." *Geotechnique*, 29(1), 47–65.

El Shamy, U. (2004). "A coupled continuum-discrete fluid-particle hydromechanical model for granular soil liquefaction," PhD Thesis, Rensselaer Polytechnic Institute.

El Shamy, U. and Gröger, T. (2007). "Micromechanical aspects of the shear strength of wet granular soils." *International Journal for Numerical and Analytical Methods in Geomechanics*. Under revision.

Fredlund, D. G. and Rahardjo, H. (1993). *Soil Mechanics for Unsaturated Soils*. John Wiley and Sons, Inc., New York.

Gili, J. A. and Alonso, E. E. (2002). "Microstructural deformation mechanisms of unsaturated granular soils." *International Journal for Numerical and Analytical Methods in Geomechanics*, 26, 433–468.

Itasca (2005). *Particle Flow Code, PFC3D, release 3.1.* Itasca Consulting Group, Inc., Minneapolis, Minnesota.

Jiang, M., Leroueil, S., and Konard, J. (2004). "Insight into shear strength functions of unsaturated granulates by DEM analyses." *Computers and Geotechnics*, 31, 473–489.

Laloui, L., Klubertanz, G., and Vulliet, L. (2003). "Solid-liquid-air coupling in multiphase porous media." *International Journal for Numerical and Analytical Methods in Geomechanics*, 27, 183–206.

Lian, G., Thornton, C., and Adams, M. (1993). "A theoretical study of the liquid bridge forces between two rigid spheres." *Journal of colloid interface science*, 161, 138–147.

Liu, S. H. and Sun, D. A. (2002). "Simulating the collapse of unsaturated soil by DEM." *International Journal for Numerical and Analytical Methods in Geomechanics*, 26, 633–646.

Lu, N. and Likos, W. (2004). *Unsaturated Soil Mechanics*. John Wiley and Sons, Inc., Hoboken, New Jersey.

Mindlin, R. and Deresiewicz, H. (1953). "Elastic spheres in contact under varying oblique forces." *Journal of Applied Mechanics*, ASME, 20, 327–344.

Muraleetharan, K. and Wei, C. (1999). "Dynamic behavior of unsaturated porous media: Governing equations using the theory of mixtures with interfaces (TMI)." *International Journal for Numerical and Analytical Methods in Geomechanics*, 23, 1579–1608.

Russel, A. and Khalili, N. (2005). "A unified bounding surface plasticity model for unsaturated soils." *International Journal for Numerical and Analytical Methods in Geomechanics*, 23, 531–547.

Thornton, C. and Antony, S. (2000). "Quasi-static shear deformation of a soft particle system." *Powder Technology*, 109, 179–191.

Wheeler, S. J. and Sivakumar, V. (1995). "An elasto-plastic critical state framework for unsaturated soil." *Geotechnique*, 45(1), 35–53.

Geotechnical and Environmental Indicators for Characterizing Expansive Soils

Stanley M. Miller[1], M. ASCE, P.E. and Ryne C. Stoker[2], M. ASCE, P.E.

[1]Professor, Department of Civil Engineering, University of Idaho, Moscow, ID 83844-1022; smmiller@uidaho.edu
[2]Principal, GeoTek, Inc., 6835 South Escondido Street, Suite A, Las Vegas, NV 89119-3828; rstoker@geotekusa.com

ABSTRACT: The use of soil water tension (suction) is becoming increasingly important in the prediction of soil expansion and in the geotechnical design of post-tensioned, ground-supported slabs. To better understand expansive soils in the desert Southwest, recent field research in Las Vegas, Nevada, has emphasized insitu monitoring of temperature and water content, measuring soil suction and developing moisture characteristic curves (MCC) at various temperatures, and statistical modeling of expansive-soil indicators (e.g., percent fines, plasticity index, and expansion index). Initial results indicate that temperature can significantly affect the MCC slope; that the indicator properties with the greatest correlation with suction are liquid limit, plasticity index, and percent fines; that diurnal cycles of insitu soil temperature occur only at depths less than 0.3 m; and that evaporation and plant uptake of drip-irrigation water are significantly diminished during cool-weather periods. Thus, soil suction tests should be conducted at soil temperatures typical of summer. A critical period for soil-expansion impacts in landscaped areas is early autumn when soil temperatures generally are high but when air temperatures can drop, resulting in excess soil moisture due to an ongoing drip-irrigation cycle.

INTRODUCTION

Over the past 50 years, ground-supported reinforced concrete slabs have been used in residential and light commercial construction across the temperate southern region of the U.S. Specialized engineering adaptations have been developed to deal with expansive soils that react to natural climate cycles that influence soil moisture content. These engineering innovations have focused primarily on post-tensioned concrete slabs utilizing interior stiffening ribs (“ribbed foundation”), perimeter edge ribs (“California foundation”), or equivalent-stiffness uniform-thickness slabs as described by the Post-Tensioning Institute (2004).

Considerable work has been conducted in the past two decades to understand and characterize the particular soil properties associated with expansive soils and to predict their behavior for geotechnical design purposes (for example, see McKeen, 1992; Lytton, 1994; Covar and Lytton, 2001). Construction sites prone to expansive soil behavior have soils that meet at least one of the following two criteria (PTI, 2004): 1) Plasticity Index (PI) $\geq$ 15, and more than 10% of the particles are finer than the No. 200 sieve (0.075 mm), and more than 10% of the particles are smaller than 0.005 mm (according to ASTM D 422), and 2) the soil expansion index (EI) is greater than 20 (according to ASTM D 4829); see ASTM (2006).

Measurement of soil water tension (suction) also is critical for plotting the soil moisture characteristic curve (MCC), a graph of moisture content versus total soil suction, which is used in a special soil classification system to identify problem soils (McKeen, 1992). For our study, we assumed that measuring total soil suction is appropriate for this type of geotechnical evaluation and were not concerned directly with identifying two separate components: osmotic suction and matric suction.

Several soil properties are believed to influence expansive behavior, such as the liquid limit, plasticity index, and percent finer than the No. 200 sieve (Lytton, 1994; PTI, 2004). Thus, evaluation of such influences was the primary objective for our study of Las Vegas soils (the project also included two soil specimens from Phoenix, as well). Another goal was to investigate the influence of environmental conditions (e.g., moisture and temperature changes) on the expansive character of clayey soils.

DESCRIPTION OF SAMPLES

Soil specimens were collected from six different sites in Las Vegas and North Las Vegas, and also from two sites in Phoenix. Insitu moisture content was measured and laboratory testing included sieve analysis, Atterberg limits, expansion index (ASTM D 4829; see ASTM, 2006), and swell percent (adapted from a FHWA swell testing procedure; see FHWA, 1980). Laboratory testing results are summarized in Table 1.

Table 1. Descriptions of soil samples and summary of laboratory testing results.

Sample No.	USCS Classification	Insitu Mois.(%)	% minus #200	% - 2μ	LL (%)	PI (%)	Swell at 60 psf (%)	E.I.
LV0	lean clay with sand (CL)	2.2	83	19	43	24	7.3	38
LV1	sandy lean clay (CL)	13.2	81	36	41	23	5.3	37
LV2	sandy lean clay (CL)	7.9	68	9	35	22	7.3	51
LV3	clayey sand (SC)	13.2	44	5	32	19	6.9	50
LV4	sandy fat clay (CH)	10.7	87	68	54	41	23.2	48
LV5	sandy lean clay (CL)	11.1	82	24	47	32	24.0	68
Phx1	silt with sand (ML)	8.3	62	10	21	3	--	--
Phx2	clayey sand (SC)	5.2	48	17	25	10	--	--

LABORATORY SOIL SUCTION TESTING

A cooled-mirror dewpoint potentiameter (Model WP4-T from Decagon Devices, Inc.) was used in this study to measure soil suction in laboratory specimens at several different temperatures. This device initially was developed for agricultural and soil science applications, but recently has been accepted by geotechnical engineers as a tool to help assess the expansive character of active clays (for example, see Petry and Bryant, 2002; Campbell, 2005). It has a published accuracy of $\pm$ 0.1 MPa in the typical geotechnical range up to -10 MPa (pF = 5.01). Total suction is measured in stress units, with the following equivalence conversion: pF = log(MPa ·10,197) where pF is the log of the height of an equivalent column of water (cm) having the reference pressure at its base. Typical pF values for unsaturated soils are about 1.0 at the liquid limit of a clay soil, 3.5 at the plastic limit, and nearly 6.0 for extremely dry soils.

The suite of suction tests included four or five sub-samples prepared from each soil sample, such that estimated moisture contents varied from very low values (3-4%) to high values (20-28%). Each of the sub-samples then was tested at four different temperatures: 15°C, 20°C, 25°C, 30°C (i.e., ranging from 59°F to 86°F). Three trials were conducted for each sub-sample at each temperature to provide repeatability and greater confidence in subsequent regression analyses.

After plotting gravimetric water content (Y variable) as a function of suction in pF (X variable) for each soil, linear regression analyses provided estimates of the moisture characteristic curve (MCC) slope. This regression procedure was suggested by Campbell (2005), and the regression-line slopes are plotted as a function of temperature in Figure 1. Here, the reported values actually are the absolute values of the slopes, and the greater the value the more expansive the soil.

Repeatability tests were conducted using the WP4-T to assess the instrument's consistency in measuring the soil suction for a given soil specimen (at 20°C). The selected specimen was placed in the sampling tray of the WP4-T to obtain a suction reading, then withdrawn and re-inserted immediately to obtain a follow-up reading; four to six repeated trials were conducted for five different soils, some at natural moisture and some fairly dry. In units of pF, the standard deviation of each set of trials ranged from 0.005 to 0.020 for the dry soils and from 0.03 to 0.05 for the soils at natural moisture. Thus, the measured suction values for repeated measurements were quite close, and the instrument performed very well for these clayey soils.

ANALYSIS FOR PREDICTING EXPANSIVE BEHAVIOR

Based on an adaptation of McKeen's method (1992), Campbell (2005) presented a general characterization of soil-expansion behavior that includes five categories, based on the absolute value of MCC slope. Category 1 represents soils with a very high propensity for expansive behavior, while Category 5 represents non-expansive soils. Thus, the MCC slopes presented in Figure 1 can be used to provide a general classification for expansive soil behavior. This classification scheme is summarized below.

|MCC slope|	Soil Expansion Category	Description
< 0.05	5	non-expansive
0.05 – 0.08	4	low
0.08 – 0.10	3	moderate
0.10 – 0.17	2	high
> 0.17	1	very high

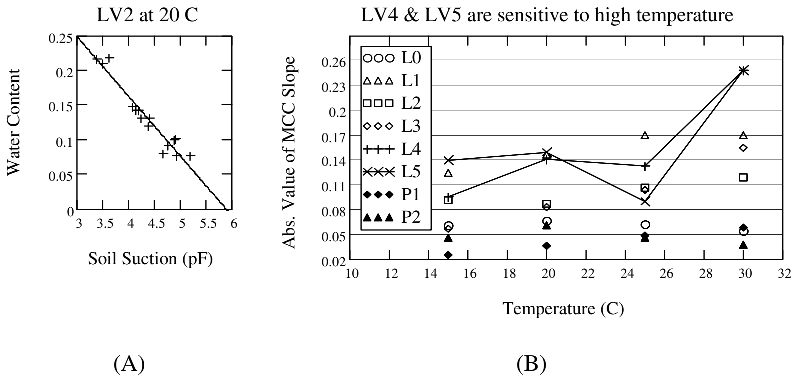

FIG. 1. Example MCC plot (A); MCC slope as a function of temperature (B).

Thus, the two soil samples from Phoenix can be rated as Category 4 or 5, and they should exhibit low or negligible expansion due to changes in moisture content. For the Las Vegas samples, only LV0 is rated as Category 4 (low) while the remaining five would be classified as Category 3 to 1 (moderate to very high), depending on which temperature level is used. Essentially, if a soil is classified as Category 3 or lower (i.e., moderate or higher propensity for expansion), special geotechnical considerations (such as the development of soil-suction profiles) likely are needed to provide prudent design and construction recommendations.

The suction test results reported above also indicate that MCC slope generally depends on the temperature of the soil samples, with a higher temperature often resulting in a steeper slope (and greater likelihood of expansive behavior). This is particularly noteworthy for samples LV4 and LV5, where the absolute value of MCC slope exceeds 0.24 for measurements at the 30°C temperature level.

To investigate the merit of using basic soil properties to predict expansive behavior of these soils, multiple regression equations for the absolute value of MCC slope were developed using several key soil attributes, including LL, PI, %–#200, %–2μ, and percent of fine clay (obtained from dividing %–2μ by %–#200, as per PTI, 2004). Each of these individual attributes generally showed higher linear-correlation influence on the value of |MCC slope| than other properties, such as swell percent and expansion index (the only exception was a high correlation for swell percent at a soil temperature of 30°C). Results of the multiple regression study are summarized below for soils at 20°C (note: R^2 is the coefficient of multiple determination and s_e is the standard error of the regression):

<u>MCC Slope $|\Delta w/\Delta pF|$ for soil temperature of 20°C</u>

S = .015963 + .000409(LL) + .002514(PI) + .000142(%-#200) $R^2 = 0.6806$ $s_e = .0266$

S = .019915 + .000654(LL) + .002094(PI) + .000267(%-2μ) $R^2 = 0.6871$ $s_e = .0263$

S = .014790 + .000800(LL) + .001989(PI) + .000253(%fc) $R^2 = 0.6898$ $s_e = .0262$

MCC Reciprocal Slope $|\Delta pF/\Delta w|$ for soil temperature of 20°C

$S = 24.0355 - 0.5917(LL) - 0.1887(PI) + 0.2178(\%\text{-}\#200)$ $R^2 = 0.7609$ $s_e = 3.83$

$S = 20.2474 + 0.2506(LL) - 0.8293(PI) + 0.0634(\%\text{-}2\mu)$ $R^2 = 0.7375$ $s_e = 4.01$

$S = 18.6998 + 0.3164(LL) - 0.8401(PI) + 0.0263(\%fc)$ $R^2 = 0.7272$ $s_e = 4.09$

The latter set of regression equations for absolute value of reciprocal slope is similar to the equation presented in the PTI manual (PTI, 2004, p. 14), which was based on earlier work by Lytton (1994) not using the absolute value:

$$S = -20.29 + 0.1555(LL) - 0.117(PI) + 0.0684(\%\text{-}\#200) \quad [\text{based on } \Delta pF/\Delta w]$$

This published expression predicts a slope of -10.7 for LV0 data (LL = 43, PI = 24, and %-#200 = 83), and the similar expression above for $|\Delta pF/\Delta w|$ predicts a slope of +12.1 (thus, the results are generally in agreement).

LONG-TERM FIELD MONITORING

A vertical array of soil sensors was installed at a field site in North Las Vegas in late August of 2006 to monitor soil temperature and volumetric moisture content. The insitu sensors were installed in a fairly uniform construction pad, which is part of a residential development area. Such pads (or compacted soil fills) are recommended at sites that contain clayey soils prone to expansive behavior. The primary goal is to produce a constructed building pad that is made more uniform (than native soils) through over-excavation and then controlled replacement as compacted fill under carefully monitored moisture and density conditions.

The sensors were installed to a maximum depth of 1.22 m (4 ft) below ground surface (BGS) in a pit excavated by a rubber-tired backhoe. This particular location was selected because drip-irrigation spigots for landscape shrubs are located about 1 m horizontally from the vertical sensor array. Soil samples were collected at depths of 0.5 and 1.2 m, and insitu moisture-density readings were obtained using a nuclear gage. Backfill soil was compacted in 180-mm lifts using a jumping-jack compactor. Sensor cables were routed into a PVC conduit, then to a metal utility box that housed a data logger. Conditions at the test site are summarized in Table 2. Note that this sandy clay is classified as expansion category 2 (high) because of its |MCC slope|.

Table 2. Soil sensors and conditions at North Las Vegas test site (sandy clay).

Depth		Sensor	Insitu		Laboratory	|MCC slope|	
(in.)	(m)	I.D.	γd (pcf)	w (%)	w (%)	at 25°C	at 30°C
48	1.22	P1 (T, W_v, E)*	97.6	18.9	14.8	0.125	0.138
36	0.91	P2 (W_v)					
24	0.61	P3 (T, W_v, E)					
16	0.41	P4 (W_v)	106.2	15.6	15.4	0.137	0.149
8	0.20	P5 (T, W_v, E)					

*T is temperature; W_v is volumetric water content; E is electrical conductivity.

The five soil sensors were labeled P1 through P5, corresponding to the five channels available on the data logger. The water content (W_v) recorded by these sensors is the soil's volumetric water content. This value can be converted to the more common geotechnical-based gravimetric water content by: $w = W_v\ (\gamma_w/\gamma_d)$; where w = gravimetric water content; W_v = volumetric water content; γ_w = unit weight of water; and γ_d = dry unit weight of the soil. As an example, consider a soil moisture sensor with a recorded W_v of 25% in a soil with an insitu dry density of 106.2 pcf: $w = 25\%\ (62.4/106.2) = 14.7\%$

Field data recorded during September at one-hour intervals for the soil sensor array installed at the field site are presented in Figure 2. Daily temperature cycles were clearly shown for sensor P5 (shallow depth), but were not observed by the deeper sensors P3 and P1. Likewise, a diurnal cycle in water content was recorded by the shallow sensor (P5), but not by the deeper sensors.

A closer look at these daily cycles reveals that the upper 0.3 m of the soil had a considerable lag time in regards to the air-temperature change (Fig. 2). That is, although the maximum air temperature in Las Vegas peaks at around 3 to 4 p.m. in September, the maximum soil temperature occurred around 11 p.m. Similarly, the minimum air temperature typically occurs around 4 to 5 a.m., while the minimum soil temperature was recorded around noon. The cooling trend that occurred September 16 and 17 resulted in subsequent increases in the soil water content in the upper sensors (P3, P4, P5), but very little change in the deeper ones (P1, P2). Apparently, the drip-irrigation schedule continued on as usual, but evapotranspiration losses were not as great due to the cooler air temperatures in the latter half of September.

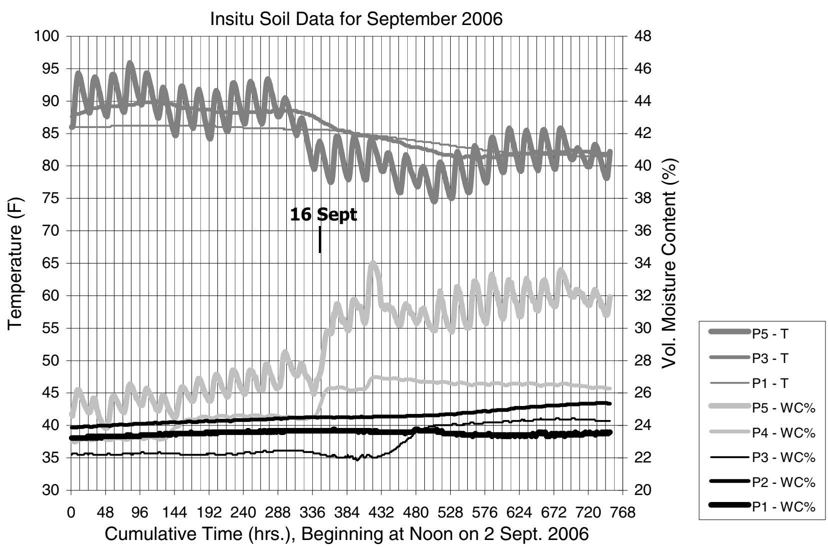

FIG. 2. Temperature and volumetric moisture data for September 2006.

Maximum and minimum daily temperatures recorded at the Las Vegas McCarran Airport (obtained from the NOAA website, 2007) also were plotted against soil temperatures to investigate the seasonal lag effect. Although the air temperatures reported in Fig. 3 are from the airport and not from North Las Vegas, we still see that the shallow soil sensor (P5) temperatures generally follow the daily maximums, while the deepest sensor (P1) temperatures follow the general trend of the air temperatures but typically lag behind by 3 to 4 weeks. This time lag is evident in April and May, where cool temperatures for deep soils cannot warm up nearly as fast as the air does. Soil temperatures are warmer than 21^{o}C (70^{o}F) for about 8 months out of the year.

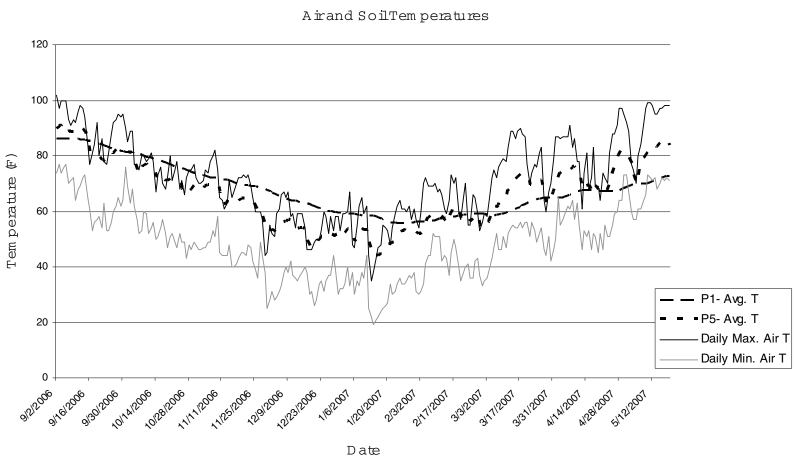

FIG. 3. Air and soil temperatures, Sept. 2006 through May 2007.

CONCLUSIONS

This initial testing program for clayey soils in the desert Southwest indicates that temperature can significantly influence soil suction measurements, which directly impacts the MCC slope and the subsequent expansive soil classification. In general, soil suction increased as soil temperatures were increased to 30^{o}C, and this behavior appears more prevalent for the more expansive soils. Thus, we recommend that soil suction testing in this region be conducted at around 30^{o}C (86^{o}F) for shallow soils in the upper 1.8 m (6 ft) and then at 25^{o}C (77^{o}F) for depths to 3.7 m (12 ft). Use of valid suction values with respect to temperature may significantly impact design values of differential soil movement, y_m, predicted by the PTI design method (PTI, 2004).

Indicator soil properties that showed the greatest correlation with suction were liquid limit, plasticity index, and percent fines. Multiple regression equations developed herein to predict the MCC slope appear to be similar to those previously presented by other investigators.

Long-term field monitoring at a site in North Las Vegas indicated that diurnal cycles of insitu soil temperature occur only at depths less than about 0.3 m; and that evaporation and plant uptake of drip-irrigation water are significantly diminished during cool-weather periods. Thus, soil suction tests should be conducted at soil temperatures typical to summer and early autumn. Also, a critical period for soil-expansion impacts in landscaped areas is early autumn when soil temperatures are high but when air temperatures can drop, resulting in less evapotranspiration which seems to cause excess soil moisture due to an ongoing drip-irrigation cycle**.**

For most of the year in Las Vegas, soil temperatures are greater than 21^{o}C (70^{o}F), and they tend to systematically lag behind seasonal air temperatures by about 3 to 4 weeks. Thus, soils can remain fairly warm until mid-November, and this should be remembered when developing soil-suction profiles for geotechnical design purposes.

The change in soil suction with depth (which is represented by a soil-suction profile) is a critical local characteristic that, in the past, was estimated when designing a foundation system to withstand expansive soil behavior. The concept that suction becomes constant at some depth is valid only in homogeneous soil. Our test results indicate that suction appears to depend on soil type and/or mineral classification zone (PTI, 2004, p. 16) and on temperature, as well. Thus, for design purposes, a constant suction value must correspond appropriately to the soil identified by layer (depth).

ACKNOWLEDGMENTS

The authors are grateful to the technical staff at GeoTek, Inc., for laboratory testing and data reduction, and to Astoria Homes® for permission to install the soil sensor array and the data logger.

REFERENCES

ASTM (American Society for Testing and Materials), 2006, Annual book of ASTM standards, Vol. 04.08 Soil and Rock (I), ASTM, West Conshohocken, PA.

Campbell, G.S., 2005, Classification of expansive soils using the WP4 dewpoint water potential meter, Decagon Devices Technical Note, available via internet at www.decagon.com/wp4.

Covar, A.P. and Lytton, R.L., 2001, Estimating soil swelling behavior using soil classification properties, Geotech. Publ. No. 115, ASCE, Reston, VA, p. 44-63.

FHWA (Federal Highway Administration), 1980, Technical guidelines for expansive soils in highway subgrades final report, Publ. No. FHWA-RD-79-51, FHWA, MacLean, VA.

Lytton, R.L., 1994, Prediction of movement of expansive clays, ASCE Geotechnical Special Publ. No. 40, Vol. 2, ASCE, Reston, VA, p. 1827-1845.

McKeen, R.G., 1992, A model for predicting expansive soil behavior, Proc. of 7th Intl. Conf. on Expansive Soils, Dallas, TX, Vol. 1, p. 1-6.

NOAA National Climate Data Center (or NOAA National Weather Service), 2007, internet website: www.weather.gov

Petry, T.M. and Bryant, J.T., 2002, Evaluation and use of the Decagon WP4 dewpoint potentiameter, Proc. of Fall 2002 Mtg., Texas Sec., ASCE, Waco, TX.

Post-Tensioning Institute, 2004, Design of post-tensioned slabs-on-ground, 3rd Ed., Post-Tensioning Institute (PTI), Phoenix, AZ, 106 p.

MITIGATION OF EXPANSIVE ELECTRIC ARC FURNACE SLAG IN BROWNFIELD REDEVELOPMENT

By Pieter J. DePree[1] M. ASCE and Charles T. Ferry[2] M. ASCE

ABSTRACT

A large brownfield redevelopment site in the Southeastern United States was known to be underlain by over 1,000,000 cubic meters of fill that contained significant amounts of slag. The site had been used for scrap steel smelting for nearly a century, including both open hearth furnace (OHF) and Electric Arc Furnace (EAF) operations. A byproduct of both of these smelting operations is slag which is derived from dolomite and limestone and contains Magnesium Oxide (MgO) and Calcium Oxide (CaO). Previous experience with slag from these types of furnaces both locally and worldwide has indicated potential for swell that can cause heave. However, heave often occurs only years after the slag placement. This time delay presents special difficulties in evaluating heave in the laboratory. This paper presents the results of investigation, laboratory testing, and analysis of the site and slag materials to assess the potential magnitude of swell and likely swell pressures, and to develop methods to mitigate the effects of potential slag swell in construction of foundations, slabs, pavements, and utilities. Various types of slag and slag containing mixtures were tested using autoclaves and pressure vessels to decrease the heave reaction time and allow evaluation of the swell properties.

BACKGROUND

Slag Definition and Origin

Slag is a byproduct of steel and iron smelting operations. In the steel making process, the raw material (iron ore or steel scrap) is heated to its melting point by various means. A fluxing agent, typically limestone ($CaCO_3$) or dolomite ($CaMg(CO_3)_2$) is added to the melting steel. The high temperatures in the smelting process “burns” the limestone and dolomite forming lime (CaO) and periclase (MgO) and releasing carbon dioxide (CO_2) to the atmosphere. The fluxing agent combined with impurities is less dense than the liquid steel, and floats to the top where it is removed, creating slag as the material hardens and cools. Slag was apparently created and used indiscriminately in the site fills considered herein.

[1] Principal Engineer, MACTEC Engineering and Consulting, Inc., 396 Plasters Avenue, NE, Atlanta, Georgia 30324

[2] Senior Principal Engineer, MACTEC Engineering and Consulting, Inc., 396 Plasters Avenue, NE, Atlanta, Georgia 30324

Volume Change and Swell Pressure

Slag swelling is thought to be caused primarily when lime (Calcium Oxide or CaO) and periclase (Magnesium Oxide or MgO) hydrate due to water or water vapor to form calcium hydroxide ($Ca(OH)_2$) and brucite ($Mg(OH)_2$) which result in volume change (Emery, 1984). Calcium Oxide is the principal ingredient of non-explosive demolition products sold under various trade names and advertised to produce pressures of 75 to 125 MPa (11,000 to 18,000 psi) (Manufacturer's Literature). Hence, under optimized conditions, potential swell magnitude and pressures of slag could be very great.

Literature Review and Experience with Steel Slag

Review of published literature and discussions with persons who have experience with projects involving steel slag, provide the following insights.
:

- Swell in excess of 10 percent has been reported(Collins & Ciesielski, 1994).
- Swell may not occur and/or may continue for some years or more after construction (Collins & Ciesielski, 1994).
- Swell primarily impacts lightly loaded areas, lifting slabs and pavements and tilting short retaining walls. (Crawford & Burn, 1969). No reports of heave of moderately loaded footings have been discovered.
- Various State DOT's have accepted use of some steel slags that meet certain test criteria and are treated prior to use as aggregate in asphalt pavement and/or as aggregate base beneath asphalt pavement; however, problems with cracking of pavements have caused some states to ban the use of steel slag in asphalt pavement (Collins & Ciesielski, 1994).
- Slag from other processes, notably blast furnace slag, does not present the same swell concerns. (Emery, 1984)

LABORATORY TESTING AND RESULTS

Program Elements

The laboratory testing program included the following:

1. Obtaining slag samples from test pits at various locations at the site
2. Crushing larger slag pieces to enable laboratory scale testing, thereby increasing surface area and breaking new faces.
3. Homogenization and division into portions for each of the various tests
4. Mixing of selected slag samples with soil
5. Autoclave concrete tests to screen swell potential (ASTM C151 with modifications)

6. Aggregate expansion tests (ASTM 4792 with modifications and PA TM-130 with modifications)
7. Chemical tests including wet chemistry and X-ray fluorescence to assess constitution of samples (ASTM-C141, with modifications)
8. Physical tests (grain size, specific gravity) for comparison of samples

Expansion of Aggregate

The expansion of aggregate test was used for direct measurement of swelling. The aggregate expansion test as modified consisted of placing the crushed slag in a 6-inch diameter metal cylinder with perforated base and top, compacting the slag with a predetermined effort, loading with a confining weight or a spring loaded plate on the top of the slag, then exposing the slag to water vapor in a low pressure steam boiler (about 100 KPa and 120^{o}C) to accelerate reaction and to simulate the anticipated field conditions in which the shallow slag will be exposed to water vapor.

Samples were placed in the boiler for one week periods after which they were removed, swell measured based on the single point swell plate, and then replaced in the boiler. The minimum period samples were left in the boiler was 2 weeks, but some samples were left for longer periods, up to 8 weeks. Limitations on schedule and equipment prevented longer exposure. Swelling rate of most samples significantly decreased after 2 weeks, although swell continued longer in some slag-soil mixtures, possibly due to the reduced permeability of the mix because of the silty soils used.

Chemical Tests

Several samples were submitted to chemistry laboratories for analysis. Samples were analyzed using various techniques, including wet chemistry, loss on ignition, and X-ray fluorescence. The chemical testing was conducted in an attempt to differentiate between hydrated or otherwise reacted calcium and magnesium compounds ($Ca(OH)_2$,$CaCO_3$, etc.) and potentially reactive forms (CaO, MgO). Variable crystalline forms, reaction during test preparation, and other interferences may have impacted the test results.

Slag swell is related to the hydration of CaO and MgO so the loss on ignition (LOI) test was used to assess the degree of hydration of samples. LOI involves drying the sample at relatively low temperature (105 ^{o}C) to remove free water and then burning the sample at much higher temperature to disassociate water and carbon dioxide from various calcium and magnesium compounds. Burning also removes organic matter and may cause oxidation of some compounds. The interpretation of the LOI results is complex, but is important in that it can give an idea of the degree of hydration of slag which indicates the amount of swelling that has already occurred and, hence, the potential for additional swelling.

X-ray Fluorescence and wet chemistry techniques were used to identify the slag composition. Chemical testing indicated that the slag composition was somewhat variable, but typically consisted of about 40 percent calcium species, 5 percent magnesium, and 50 percent iron, silica, aluminum, and manganese with traces of sodium, potassium, sulfur, titanium, strontium, and phosphorous. To assess the reaction of CaO and MgO, chemical tests were conducted on split samples of crushed cobble and cemented slag from before and after aggregate expansion tests in the low-pressure boiler for about 5 weeks (total 8 tests). The results are outlined in Table 1.

Prior to placement in the boiler, the apparent broken faces of slag particles created by the crushing appeared smooth and dark colored while the original slag surface was frequently rough and light gray. Following removal from the boiler, the outward appearance of the sample had changed significantly with a uniform, light gray, rough surface. However, when pieces of the post-boiler slag were broken, the inside of the fragments appeared similar to portions of the sample prior to introduction into the boiler with a smooth, dark surface (Figure 1).

Table 1 – Chemical Results of Pre- and Post – Boiler/Cemented and Cobble Slag

	Cobble Slag				Cemented Slag			
	Pre-Boiler		Post-Boiler		Pre-Boiler		Post-Boiler	
% by Dry Weight	%	%	%	%	%	%	%	%
Total Ca Species	45.6	44.1	45.0	45.5	33.7	35.0	32.2	33.5
Bound H_2O (LOI)	0.1	0.2	4.7	4.0	8.9	5.4	9.9	9.2
Free H_2O	0.4	0.3	3.0	2.4	1.1	1.0	4.7	4.7
CO_2	1.3	1.0	1.5	1.5	3.4	3.4	4.5	2.7
$CaCO_2$	2.8	2.3	3.3	3.4	7.8	7.7	10.2	6.2
$CaSO_4$	1.0	0.9	1.0	1.1	0.5	0.6	0.5	0.7
$Ca(OH)_2$	0.0	0.0	0.8	0.3	17.9	4.0	3.2	7.4
CaO	43.6	42.4	42.1	42.6	15.5	27.4	23.8	24.1
MgO	4.7	4.8	4.6	4.9	7.1	6.9	6.7	6.7
Total CaO+MgO	50.3	48.9	49.5	50.3	40.8	41.9	38.8	40.2
CaO, MgO Reacted	8	7	10	9	64	29	36	36
Swell %			1.3	2.9			0.4	0.9

Figure 1: Pre-Boiler Slag (Left) and Post Boiler Slag (Right)

CONCLUSIONS

Based on the results of the investigation related to site specific development plans, the following salient conclusions regarding slag were developed:

Swell Pressure and Magnitude

Under ideal conditions, swell pressures produced by CaO and MgO could be quite large (75+ MPa), as indicated by non-explosive demolition products. The magnitude of potential swell could also be large (200+ percent), based on simple calculations of changes in specific gravity and mass. Swell of these magnitudes and pressures would be difficult to address practically to allow construction over large volumes of slag fill.

However, experience with construction on slag and laboratory testing in this investigation suggest that swell is much lower, on the order of 50 to 75 KPa (1,000 to 1,500 psf) and 4 to 6 percent. Figure 2 shows envelopes of predicted swell of granular slag and slag-soil mixtures developed based on the laboratory testing conducted in this investigation.

Swell pressure and magnitude are impacted by many interrelated factors, including:

- Particle Size – Slag appears only to react at the surface of the particles, so larger particles, which have less surface area, should produce less swell than finely divided slag.
- Void Ratio – Lower sample void ratios correlate to higher swell suggesting that some swell is absorbed into voids in the slag or slag soil matrix.
- Weathering and Exposure – Although slag tested had been exposed to weathering or submerged below groundwater for over a decade, only a small percentage of the CaO and MgO in the samples had reacted and most samples showed additional reaction on testing. It appears from observation of slag particles before and after reaction that only the surficial portions of the slag

react and that the interior is protected. Thus, crushing of samples to gradations manageable in the laboratory would expose new surface area.

- Chemistry – CaO and MgO in the samples tested varied within a relatively narrow range. While the CaO and MgO reactions appear to explain the observed swell, the other variables (void ratio, heterogeneity, low reaction percentage) and the difficulties in defining the various species and crystalline forms make direct correlation difficult.
- Heterogeneity – The slag at this site was mixed with a variety of other materials. Aggregate expansion tests suggest significant differences in swelling behavior of particles crushed from apparently undifferentiated slag. Inert (non-swelling) materials appear to be intermingled within the slag and with the slag.

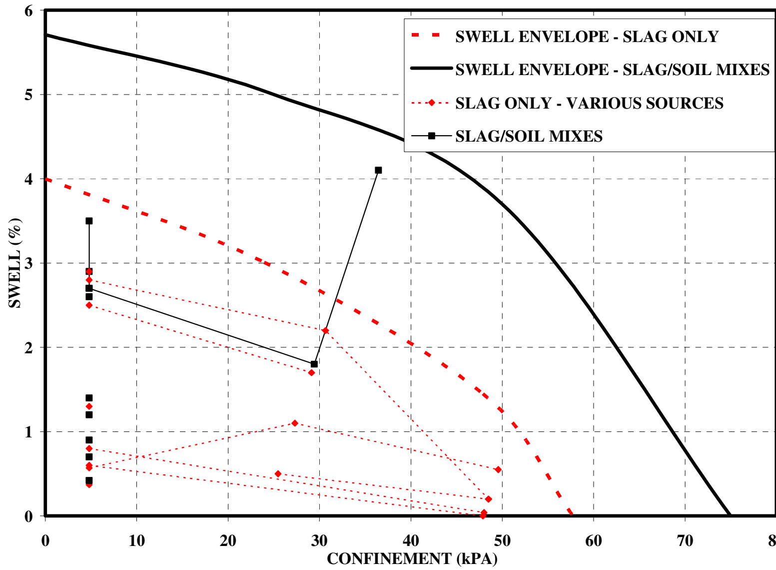

Figure 2 – Approximate Envelope of Measured Swell

Note: The upper (solid) line represents an envelope encompassing swell observed in slag-soil mixtures. The lower, (dotted) line represents an envelope encompassing measured swell in granular slag only. Individual points indicated individual laboratory tests on samples from various on-site locations and depths. Connected points are tests using split samples of slag from the same source.

Time Rate of Reaction

No correlation between the time in the boiler and the time in-situ was made. Many variables, including slag chemistry, environmental conditions, slag particle size, permeability of the slag or slag-soil mix, etc. would impact the rate of reaction. Given reports of slag swell occurring over some years (Collins & Ciesielski, 1994) and the indication that for granular slag swell largely ceases after a few weeks in the boiler in our lab tests, a rough correlation may be that a week in the boiler is similar to a year or more in-situ.

Ramifications of Potential Slag Swell in Site Development

The following were considerations in design of the redevelopment of this site:

- Crushing slag may expose reactive and expansive material. Therefore, crushing, handling, compacting, moving, or otherwise disturbing slag fills that have been in place for many years may increase swell potential.
- Lower void ratios appear to contribute to swell potential. Therefore, excessive compaction may be counter-productive. Poorly graded, granular slag may have less swell potential that well graded mixtures of slag and soil. Early plans to deliberately mix slag with soil in on-site fills were abandoned based on these test results.
- Slag swell impacts may be significant if even a relatively small proportion of a fill mass consists of reactive slag. Field characterization to identify swelling slag is impractical. Therefore, measures addressed all existing fill equally.
- Given the heterogeneity of the slag, slag swell is likely to occur in small, isolated pockets rather than uniformly over large areas.
- Measures to cause slag to react prior to use will likely require substantial reduction in particle size and long exposure times and are, therefore, unlikely to be practical.
- Given the slow reaction times, small intrusion or infiltration rates of water vapor or carbon dioxide may be sufficient to trigger swell. Therefore, sealing the slag to prevent such intrusion and limit swell is unlikely to be practical. The swell problems encountered by various DOT's for slag embedded in asphalt (Collins & Ciesielski, 1994) tend to confirm the impracticability of effective sealing.
- At a maximum swell pressure of 75 KPa (1,500 psf) and an average density of compacted slag of about 2,200 kg/M^3 (135 pcf), slag swell should occur in about the upper 3 meters (10 feet). At 4 to 6 percent swell, surface heave would be expected to be in the range of about 10 to 20 cm (4 to 8 inches).
- Swell pressures of 50 to 75 KPa can be confined by about 3 to 5 meters of non-slag fill or less overlying slag. The overlying fill will also buffer and distribute swell of isolated pockets of reactive slag.
- Appropriate safety factors should be adopted in designing around slag, recognizing the limitations of testing, heterogeneity of the slag, and the consequences of swell.

The swell magnitude and pressure identified could be addressed by relatively practical engineering measures, many similar to those used for natural materials with swelling properties, such as isolation, confinement, or structural flexibility. Based on the investigative findings, the following swell mitigation strategies were employed at the brownfield project site:

- A 3 meter zone of non-slag fill was placed beneath roadways dedicated to the local government to confine slag, distribute and buffer swelling pockets, and serve as a corridor for installation of shallow utilities. Non-slag fill zones were also employed under some lightly loaded structures and behind retaining walls.
- Heavily loaded structures, including high-rise and mid-rise buildings and parking decks, used isolation by means of deep foundations extending through the slag and framing of lower level slabs to leave void space to accommodate swell.
- Lighter structures used mat foundations or waffle slabs, to confine, resist, and absorb swelling.
- In less critical areas, such as the lowest level of parking decks, flexible or easily repaired pavements (asphalt or pavers) were used, accepting a greater risk of future distress and higher frequency of repair.

REFERENCES

Crawford, C.B. and Burn, K.N. (1969). "Building Damage from Expansive Steel Slag Backfill" *Journal of the Soil Mechanics and Foundations Division*, Vol. 95, No. 6, November/December 1969, pp. 1325-1334.

Collins, R.J. and Ciesielski, S.K. (1994). "Recycling and Use of Waste Materials and By-Products in Highway Construction" *Waste Materials In Hot Mix Asphalt*, ASTM, Easton, MD, pp. 17-38

Farrand, B. and Emery, J. (1995). "Recent Improvements in the Quality of Steel Slag Aggregate" *Transportation Research Record No. 1486, Environmental Testing and Evaluation of Stabilized Wastes, Performance of Stabilized Materials, and New Aggregate Tests*. Transportation Research Board, Washington DC. pp. 137-141

Test PTM 130–"Evaluation of Potential Expansion of Steel Slags" *ftp.dot.state.pa.us/public/pdf/BOCM_MTD_LAB/PUBLICATIONS/PUB_19/PTM-130.pdf*, Pennsylvania DOT, Harrisburg, PA

Standard Specification D4792-95, "Potential Expansion of Aggregates from Hydration Reactions," *Annual Book of ASTM Standards, Volume 04.03*, American Society for Testing and Materials. West Conshohocken, Pennsylvania. pp. 567-574

Emery, J. (1984) "Steel Slag Utilization in Asphalt Mixes" MF-*186* National Slag Association, Pleasant Grove, UT

Swell Potential of Near Surface Soils in Mississippi and Louisiana

David M. Coleman[1], M. ASCE, P.E. and S. Caleb Douglas[2], M. ASCE, P.E.

[1]Senior Geotechnical Engineer, Aquaterra Engineering, LLC, 859 Pear Orchard Road, Ridgeland, Mississippi, 39157; dcoleman@aquaterraeng.com
[2]Senior Geotechnical Engineer, Aquaterra Engineering, LLC, 859 Pear Orchard Road, Ridgeland, Mississippi, 39157; cdouglas@aquaterraeng.com

ABSTRACT: The near surface soils present throughout much of Mississippi and Louisiana consist of clayey soils that have liquid limits and plasticity indices that fall in a range that is near the upper limits of soils typically considered to have little expansive potential and the lower limits of soils typically considered to have some expansive potential. Climatic conditions in the South-Central United States since 1999, includes severe drought conditions in 1999 through 2001, dry summer and fall months in the past several years, and drought conditions throughout most of 2007 which have resulted in extremely low soil moisture contents within the upper 10 to 15 feet. Typical geotechnical engineering practice in the Mississippi and Louisiana areas has commonly not addressed these dry, lean clay soils as having expansive behavior, but rather has regarded them as "non-expansive". However, recent experience has indicated that dry lean clay soils can exhibit some expansive potential that can affect shallow foundation performance. This paper will present the results of a limited, preliminary study conducted to investigate the swell potential of near surface lean clay soils in the Mississippi and Louisiana areas.

INTRODUCTION

Near surface highly expansive clays have been well documented in the Mississippi and Louisiana areas. However, clayey soils with liquid limits ranging from 40 to 60 percent and plasticity indices from 20 to 40 are often encountered in this area. Although literature typically describes these lean clay soils as having a low to medium swell potential, many geotechnical engineers in the area typically regard these soils as "non-expansive" or having a "low potential" for expansive behavior. The expansive potential of these clayey soils has been increasingly evident in recent forensic studies. These soils have tended to be overlooked in the past since the thrust of most geotechnical investigations are to address the presence or absence of high plasticity clay (Unified Soils Classification System – CH) soils that are generally considered to be highly expansive and therefore more problematic.

Climatic conditions in the South-Central United States since 1999 include severe drought conditions in 1999 through 2001, lower than normal rainfalls in the past several years, and drought conditions throughout most of 2007, have resulted in extremely low soil moisture contents within the upper 3 to 4.5 meters (10 to 15 feet). Recent experience has indicated that dry, relatively lean clay soils can exhibit some expansive potential that can affect shallow foundation performance.

Soils are not homogeneous materials and each sample evaluated has a unique set of parameters which involve a complex set of variables including mineralogy, natural water content, suction and environmental factors. Geotechnical engineering is not an exact science and recommendations often include the influence of previous experience with similar soils. Based on our recent experience, the clayey soils typically not considered expansive have been the culprit in unacceptable movements in relatively new, lightly loaded structures. This paper will present the results of a limited study conducted to investigate the swell potential of near surface clayey soils that are generally considered to fall between "lean," low-plasticity clay and "fat," high-plasticity clay soils.

For this study, undisturbed samples of clayey soils collected at various locations throughout Mississippi and Louisiana were tested in the laboratory to determine the natural moisture content; liquid, plastic, and shrinkage limits; grain size distribution; percent swell/heave and swelling pressure. Correlations will be made between the plasticity index and percent swell. Data will be analyzed to evaluate the swelling potential of these clayey soils with comparison to generally accepted swell criteria and the potential for foundation movement.

COMMON ENGINEERING PRACTICE

The geotechnical engineering community in the Mississippi and Louisiana area have typically not recognized the potential for swelling of lean clay soils. Local practice has been to consider lean clay (CL) soils with a liquid limit less than 50 percent as either being non-expansive or having a low shrinking and swelling potential and soils having a liquid limit in the range of 50 to 65 percent having a moderate shrinking and swelling potential. Soils with a liquid limit greater than 60 percent are generally considered to be highly expansive. Thus, the thrust of most geotechnical investigation is to determine the presence or absence of any highly expansive clay soils. Practicing geotechnical engineers have typically considered the relationship between the natural water content and the plastic limit in estimating the likely swell potential. This estimating process is generally based on experience as most geotechnical investigations do not perform a rigorous evaluation of the swell potential of the lean clay soils. If the natural water content is well below the plastic limit for a highly expansive clay, the soil is typically considered to have an increased potential for swelling. As the moisture content increases and becomes greater than the plastic limit, the potential for swelling decreases. Recent experience indicates that relatively dry, natural moisture below the plastic limit, lean clay soils also have swell potential and this swell potential may be sufficient to result in problems with structures supported on shallow foundations.

Shallow foundations generally consist of either spread and continuous footings or a stiffened slab-on-grade with grade beams. Foundation designs generally have net allowable bearing capacities in the range of 96 to 120 kilopascals (kPa) (2,000 to 2,500 pounds per square foot) with typical anticipated movements of less than 2.5 centimeters (1 inch) with differential movements between points within the structure of less than 1.25 centimeters (0.5 inch). It should be noted that most lightly loaded structures which include residences and one-story, metal framed structures typically have applied bearing pressures in the range of 48 to 72 kPa (1,000 to 1,500 pounds per square foot). In the South-Central United States areas where significantly larger movements can be expected due to the presence of highly expansive clay soils, the soil conditions are often mitigated by overexcavation and backfill or the use of deep foundations.

COMMON EXPANSIVE CLAY IDENTIFICATION

Potentially expansive soils are usually identified by soil classification, mineralogy, swelling tests, Atterberg limits or a combination of these factors. Soils with a Unified Soil Classification System symbol of CH are commonly considered to be expansive. The soil's Atterberg Limits reflect the activity of the clay minerals present and are therefore widely used to help identify expansive soils (Rollings and Rollings, 1996). A summary of some of the typical expansive clay identifiers are presented in Table 1.

Table 1. Expansive Clay Identifiers

Potential Swell	Krebs and Walker (1971)	Holtz and Kovacs (1981)	Chen (1988)	Department of the Army (1983)		
	Plasticity Index	Plasticity Index	Plasticity Index	Liquid Limit	Plasticity Index	Swell Potential (%)
Low	<15	<18	<15	<50	<25	<0.5
Medium	15-24	15-28	10-35	50-60	25-35	0.5-1.5
High	25-46	25-41	20-55	>60	>35	>1.5
Very High	>46	>35	>35	- - -	- - -	- - -

MISSISSIPPI AND LOUISIANA GEOLOGY AND ENVIRONMENT

Geology. The most prominent geological features in the Mississippi and Louisiana areas are the Mississippi River Embayment and loessial soils. The Mississippi River extends down the western boundary of Mississippi and bisects the state of Louisiana. The Mississippi River delta is up to about 120 kilometers (75 miles) wide. On the eastern side of the Mississippi Embayment, loessial soils are found which typically extend approximately 100 miles from either the River or delta (Snowden and Priddy, 1968). Numerous other geologic formations are located at the ground surface across

Mississippi and Louisiana. However, this paper is focused at clayey soils with liquid limits that place them in the upper lean clay (CL) soils and lower high-plasticity clay (CH) soils. These soils are typically found in alluvial deposits and near the ground surface due to weathering of the natural soils.

Clayey soils swell with addition of water during the wet season or from external sources and shrink during the hot, dry summer months. Trees also extract a considerable amount of moisture from the soil through their root system from the underlying soil during the dry summer months. Sites that are heavily wooded often have very dry near surface soils due the extraction of moisture from the ground during the dry months.

Environmental Conditions. Mississippi and Louisiana have a very humid climate. According to the Natural Resources Conversation Service, Mississippi generally has a mean annual precipitation in the range of 127 to 152 centimeters (50 to 60 inches) (Viessman et. Al. 1996). A water surplus condition usually exists in the soil from around October through May, with a water deficiency occurring during the normal dry season from June through September. According to a study by Redus in 1962, the depth of the moisture active zone was found to be about 2.4 meters (8 feet). The moisture active zone is the depth below the ground surface which is subjected to seasonal wetting and drying cycles. Severe drought conditions occurred during the fall 1999 through spring 2001 period. Additionally, dry fall and winter months since 2005 and a severe drought throughout most of 2007 have resulted in soil moisture deficits throughout much of the South-Central United States.

FIELD AND LABORATORY INVESTIGATION

Samples selected for inclusion in this study were selected during the completion of geotechnical investigations across the study area. Samples having plasticity indices in the range of this study with relatively low moisture contents were selected from various investigations for additional testing.

Relatively undisturbed samples were obtained by Aquaterra drilling crews by pushing a three-inch diameter, Shelby tube sampler into the soil in general accordance with ASTM D 1587. After the Shelby tube was removed from the boring, the sample was carefully extruded in the field and visually classified. The undisturbed sample was placed in a protective container for transportation to the laboratory.

The laboratory testing for this study was completed at Aquaterra Engineering, LLC laboratories located in Jackson, Mississippi and Baton Rouge, Louisiana. The laboratories are both certified by their respective state highway departments and the testing was performed under the direction of senior engineering technicians with over 30 years experience.

Moisture content tests were performed to better understand the classification and shrink/swell potential of the soils evaluated. These tests were performed in general accordance with ASTM D 2216. Liquid limit (LL) and plastic limit (PL) determinations were performed to assist in classification by the Unified Soil Classification System. These tests were performed in general accordance with ASTM D 4318. The plasticity index (PI) was calculated as LL - PL for each Atterberg limit determination. Soil samples were tested to determine the particle gradation to aid in classification and to further understand the engineering characteristics. These tests were performed in general accordance with ASTM D 422. Swell pressure/volume tests were performed on selected soil samples in general accordance to ASTM D 4546, Method A. The samples were placed in a lever type dead weight consolidometer and loaded to a seating pressure of 12 kPa (250 pounds per square foot). The samples were then inundated and observations were made to record soil response to the free moisture. After swelling, the applied pressures were increased to determine the swell pressure which is the pressure required to return the sample to its original height.

LABORATORY RESULTS

For the purpose of this limited study, thirteen samples were evaluated from a collection of forty swell tests. The thirteen selected samples were chosen for Liquid Limits between 30 and 60, plasticity indices in the 15 to 35 percent range and natural moisture contents below or not greater than 1 percentage point above the plastic limit. Table 2 below presents a summary of the laboratory tests included in this limited study. For samples where less than 0.1 percent of swell was measured in the laboratory, the swell pressure was not determined.

Table 2. Summary of Laboratory Results

Atterberg Limits			Initial Moisture Content (%)	Free Swell* (%)	Swell Pressure (psf)	
Liquid Limit (%)	Plastic Limit (%)	Plasticity Index (%)			kPa	Pounds per Square Foot
32	17	15	17.8	0.02	ND**	ND**
34	14	20	16.1	2.70	82.8	1,730
35	16	19	15.7	0.1	ND**	ND**
35	15	20	11.7	2.3	65.8	1375
37	16	21	16.6	0.70	32.1	670
39	18	21	17.3	0.6	28.7	600
39	17	22	17.4	0.1	ND**	ND**
42	24	18	15.1	0.02	ND**	ND**
42	16	26	12.5	1.81	143.6	3,000
43	15	28	14.9	2.18	84.1	1,756
45	17	28	15.1	2.75	95.8	2,000
46	15	31	17.0	2.8	163.7	3,420
54	23	31	20.8	2.20	147.0	3,070

* Seating Load 12 kPa (250 pounds per square foot)
** (ND) Not Determined

From the data included with this study, correlations between swell potential and several of the test parameters were attempted. The correlation of swell potential to plasticity index is presented graphically on Figure 1. This correlation should only be considered valid where the natural moisture content of the lean clay soil is below or not more than 1 percentage point above the plastic limit. Other correlations to parameters such as the Liquid limit, Liquidity Index and Activity were also attempted, but meaningful relationships between these parameters were not obtained due to the small size of the data set.

From observation of the data, soils with liquid limits from 42 to 54 percent and plasticity indices of greater than 26, were found to have a swell potential in the range of 1.8 to 2.2 percent and swell pressures in the range of 84 to 164 kPa (1,750 to 3,400 pounds per square foot). Soils having a plasticity index of 25 or less were generally found to have volumetric swells of less that 1% with swelling pressures measured at less than 33.5 kPa (700 pounds per square foot).

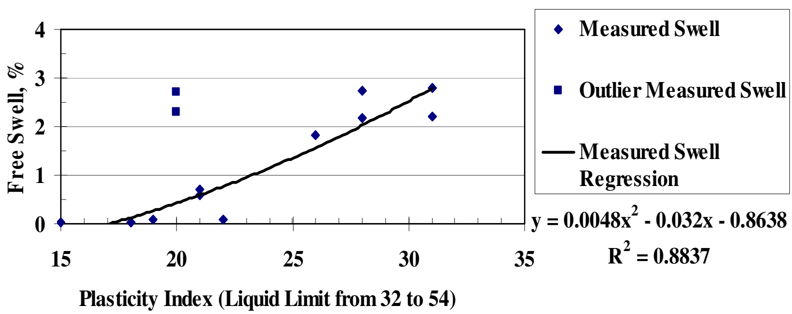

FIG. 1. Swell Potential vs. Plasticity Index

As expected, the test results generally indicate an increase in the free swell with an increase in the plasticity index. Two outlying tests were observed with one sample having a liquid limit of 34, a plasticity index of 20, a natural moisture content of 16.1% with a swell potential of 2.70 percent and another sample having a liquid limit of 35, a plasticity index of 20, a natural moisture content of 11.7% with a swell potential of 2.3 percent. Further evaluation of the two outlying data points revealed the two samples were from alluvial deposits, while the remaining tests were generally from older, more weathered deposits. The outlying data points are plotted on Figure 1, but were not used in the development of the regression that is shown. It is important to note that for liquid limits generally above 42 with a plastic index above 25, the swelling pressures are generally above 86 kPa (1,750 psf) with swelling pressures in these, by definition, lean clay soils of up to 164 kPa (3,420 psf).

CONCLUSIONS

The common practice in many areas of the South-Central United States is to ignore or discount the potential for lean (CL) clays to swell with increased moisture contents, and further, for these lean clays to swell with sufficient swelling pressures to result in foundation damage. The laboratory results from this limited study indicate that some lean clay soils with natural moisture contents near or below the plastic limit have the potential to swell with an increase in moisture. Specific conclusions that can be drawn from this limited laboratory study are:

- Lean clay soils with liquid limits up to about 40, plasticity indices of 25 or less, and moisture contents near or dry of the plastic limit generally have values of free swell that are less that 1% and swelling pressures that are less than 33.5 kPa (700 pounds per square foot).
- Clayey soils with liquid limits in the 40 to 54 range, plasticity indices greater than 26, and moisture contents near or below the plastic limit have the potential for free swell on the order of 1 to 3 percent with swelling pressures in the range of 84 to 164 kPa (1,750 to 3,400 pounds per square foot).
- These findings generally support the previously published expansive clay identifiers that are typically used as a "first cut" to identify the possibility of swelling in clayey soils.
- Structures founded in lean clay soils having liquid limits above 40, plastic limits greater than 25, and moisture contents that are near or below the plastic limit could be subject to magnitudes of swell and swelling pressures that are sufficient to result in foundation movement and damage.
- Our practice has shown that lightly loaded residential and commercial structures founded in what is by definition lean clays can be subject to swelling pressures and associated movements that are detrimental to the performance of the structures. This detrimental performance is usually evidenced in the form of floor slab movement; cracking of brick veneer, CMU walls, and drywall; and differential movements of up to several inches within the structure.
- Current geotechnical engineering practice in Mississippi and Louisiana should have an increased awareness of the swell potential of lean clay soils, include sufficient laboratory testing and analysis to verify the swelling potential of the materials as part of routine geotechnical investigations, and allow for mitigation of conditions that could result in foundation movement and damage.
- The laboratory study for this project was very limited in scope generally using data from geotechnical investigations that were currently underway and additional data from recent projects. This study should be considered preliminary and a basis for problem recognition that will lead to a more comprehensive and detailed research program.
- The data from this limited study are not sufficient to provide detailed evaluation of swelling potential in these lean clays. The complex interaction between mineralogy, plasticity characteristics, moisture content and swelling potential and pressure warrant more through study with a large amount of additional data used in the analysis. This study should consider the lean clay (CL) and lower plasticity fat clay (CH) clay soils generally having liquid limits

less than 60, plasticity indices in the 15 to 35 range, and moisture contents that are below or near the plastic limit.

ACKNOWLEDGMENTS

The authors of this paper would like to thank the management of Aquaterra Engineering, LLC for providing the personnel, laboratory, support and encouragement in completing the work for this paper. We would especially wish to recognize the efforts of Mr. Gomer Wallace, senior engineering technician with Aquaterra Engineering, LLC, who performed, compiled and resolved the bulk of the laboratory testing for this study.

REFERENCES

Chen, F.H. (1988). *Foundations on Expansive Soils*, American Elsevier Scientific Publications, New York.

Department of the Army (1983). "Foundations in Expansive Soils," TM 5-818-7: 1-5.

Krebs, Robert D. and Walker, Richard D. (1971). *Highway Materials*, McGraw-Hill Companies, New York, NY: 68-84.

Holtz, R.D. and Kovacs, W.G. (1981). *An Introduction to Geotechnical Engineering*, Prentice-Hall, Englewood Cliffs, NJ: 733.

Redus, J.F. (1962). "Experiences with Expansive Clay in Jackson, Mississippi," *Moisture, Density, Swelling and Swell Pressure Relationships*, Highway Research Board Bulletin No. 313: 40-46.

Rollings, Marian P. and Rollings, Raymond S. (1996). *Geotechnical Materials in Construction*, The McGraw-Hill Companies, New York, NY: 380-384.

Snowden, Jr., J.O. and Priddy, Richard R. (1968). *Loess Investigation in Mississippi*, Mississippi Geological, Economic and Topographical Survey, Bulletin 111: 40-46.

Viessman, Jr., Warren and Lewis, Gary L. (1996). *Introduction to Hydrology*, Fourth Edition, Harper Collins College Publishers, New York, NY: 22.

The Influence of Structure on One-Dimensional Wetting Induced Volume Change of Compacted Soil

Amy. B. Cerato[1], A.M.ASCE, Jumanah. A. Hajjat[2], and Gerald. A. Miller[3], P.E., M.ASCE

[1]Assistant Professor, University of Oklahoma, 202 W. Boyd Street, Room 334, Norman, OK 73019: email: acerato@ou.edu
[2]Graduate Research Assistant (graduated August 2007), University of Oklahoma, 202 W. Boyd Street, Room 334, Norman, OK 73019: email: jumanah.hajjat@ou.edu.
[3]Professor, University of Oklahoma, 202 W. Boyd Street, Room 334, Norman, OK 73019: email: gamiller@ou.edu

ABSTRACT: Volume changes due to soil wetting may occur in naturally deposited soils (i.e., unsaturated expansive soils) as well as earthen construction (i.e., compacted fills or embankments). Depending on the stress level, some soils exhibit increase in volume upon wetting (swell), while others may exhibit decrease in volume upon wetting (collapse). This paper focuses on wetting-induced volume changes in compacted soils. Even when soils are compacted to engineering specifications (i.e., minimum density and moisture content ranges), some earthen construction still exhibit problematic behavior under wetting conditions. Not only is this problematic behavior itself a concern, but the laboratory tests used to predict settlement of constructed facilities may not properly model the actual behavior of soil compacted under field conditions. A research study was conducted in the laboratory to investigate the influence of variations in structure on the one-dimensional wetting-induced volume change for three different fine-grained soils. The results of the study suggest that the influence of structure in one-dimensional oedometer tests depends on soil type. Soil with medium to high PI and large clay size fraction appears to be influenced more by differences in structure, whereas soil with low PI and low clay size fraction does not appear to suffer from structure effects in one-dimensional oedometer tests.

INTRODUCTION

Most compacted clayey soils will experience swelling under low confining stress and collapse under higher confining stresses; the degree of which depends on soil type and state. In general, all soils are susceptible to wetting-induced collapse when inundated with water under sufficient confining pressure. Precipitation, capillary water from foundation soils, and flooding may cause changes in the moisture content of soils and lead to collapse (Lim and Miller 2004). Several factors influence the amount of collapse potential: initial moisture content, initial dry density, soil type, and confining pressure (ie., Basma and Tuncer 1992, and Lim and Miller 2004). These factors, influencing collapse potential in the field, are taken into consideration when 1-D oedometer tests are performed in the laboratory in order to predict settlement behavior of a soil. To achieve relevant settlement information from 1-D oedometer tests, it is important to test "real" specimens from the field. However, compacted soils are generally evaluated in the laboratory prior to field construction and the engineering behavior of compacted fills in the field can be different from the engineering behavior predicted by laboratory tests. Therefore, an additional factor must be taken into consideration in 1-D oedometer test predictions in an attempt to model actual field compacted behavior.

This factor is the soil's 'structure,' which has been shown to influence the behavior of soils when subjected to either static or dynamic loads (Vallejo 1995). Consequently, evaluation of the soil structure and its changes as a result of loading is important in the field and the laboratory to understand the behavior of the soil. The term "soil structure" includes the combined effects of soil fabric and interparticle forces. "Fabric" generally refers to the geometric arrangement of particles whereas interparticle forces include physical and physico-chemical interactions between particles. The soil structure in this case, is associated with specimen preparation methods and is influenced by five factors: compaction method, clod size, clod size distribution at compaction, dry density or void ratio and compaction moisture content.

Research described herein is focused primarily on studying the influence of soil structure on one-dimensional behavior observed during oedometer tests for two natural soils from Oklahoma. The primary objectives of this research were to (1) examine the influence of sample preparation method on soil structure and (2) examine the influence of soil structure on collapse potential. Understanding these influences and how they can potentially impact predictions of fill behavior is important to appreciate long term behavior of earthen structures. Further, the understanding may impact the approach to design and quality control for important earthen structures.

BACKGROUND

Observations of soil volume change in the field may be different from predictions provided by one-dimensional (1-D) oedometer tests, even when the initial moisture content, initial dry density, soil type, and confining pressure are kept the same (e.g. Miller and Cleomene 2007). Therefore, the soil behavior under loading should be studied with consideration given to differences in structure between laboratory and field compacted specimens. It was found previously that the soil fabric strongly affects the collapsibility of soils (Rizkallah and Keese 1989); however, some soils may not exhibit variations in collapsibility by changing the internal fabric (i.e., silts).

Based on the compaction moisture content, there are two modes of soil fabric (Leroueil et al. 2002). When the soil is compacted at a moisture content lower than the optimum value, the soil fabric is aggregated; consequently, the soil exhibits more of a clod structure. On the other hand, when the soil is compacted at a moisture content higher than the optimum value, the soil fabric is homogenous and exhibits little to no clods (Benson and Daniel 1990, Leroueil et al. 2002). The soil clods compacted in the laboratory are often smaller than the soil clods compacted in the field. So, an important question arises: is it acceptable to predict volume change of compacted fills from standard 1-D oedometer tests?

Prior to the current study, Cleomene (2005) conducted research at the University of Oklahoma to examine differences in the 1-D volume change behavior of laboratory versus field compacted soil. Four soils from Oklahoma were used; three lean clays and one silty sand. Two compaction procedures were used to prepare standard oedometer samples in the laboratory: 1) air dried soil passing a #4 sieve was mixed with water, compacted in a standard Proctor mold, and then a sample was trimmed directly into the 60-mm oedometer ring; and 2) air dried soil passing a #10 sieve was mixed with water and then compacted (tamped) directly into an oedometer ring. The sample preparation methods did affect the behavior for the clayey soils, even though the samples had nominally similar dry density and moisture content. The fine sandy soil behavior was much less affected by preparation methods. Thus, it appeared that differences in the soil structure created during field and laboratory compaction could result in differences in the oedometer test results. Because only four similar soil types were tested, the results were somewhat inconclusive. Thus, the current study was developed to provide additional information on the influence of soil structure for a wider range of soil types..

METHOD OF INVESTIGATION

Test Soils

Three natural soils collected from Oklahoma were used in this work, including one lean clay (CL), one fat clay (CH) and one silt (ML). All the test soils were subjected to classification and physical property tests including: Atterberg Limits (ASTM D4318-00), grain size distribution (ASTM D422-00), specific surface area (Lutenegger and Cerato 2002), carbonate content (Dreimanis 1962), cation exchange capacity (Rhoades 1982), and standard Proctor compaction (ASTM D698-00) tests. Properties of the test soils are listed in Table 1.

Oedometer Sample Preparation

To create oedometer samples with different structure, two different methods of sample preparation were utilized in this study: 1) soil samples compacted directly into 63.5-mm diameter oedometer rings with a nominal maximum clod size of 2 mm, and 2) soil samples trimmed from soil compacted in a 101.6-mm diameter compaction molds with a nominal maximum clod size of 38 mm. The latter, while not the same as field-compacted soil, is more representative of larger clod sizes associated with field compaction. It was expected that if differences were observed in the behavior of soil prepared using these two different methods, then even greater differences may be possible between lab and field tests where clod sizes can be considerably larger than 38 mm (limited to 75 mm by specification but larger chunks are common).

Table 1: Properties of the Test Soils

Soil #	Soil Name	AASHTO	USCS	LL (%)	PI (%)	Fines (%)	Clay Fraction (%)	$\gamma_{d\max}$ (kN/m^3)	OMC (%)
3	Burford-Vernon Complex	A-6 (15)	CL	36	17	91	36	17	17.3
7	Devol Soil	A-4 (0)	ML	----	NP	80	7	17.6	14.7
10	Hollywood Soil	A-7-6 (45)	CH	65	43	93	61	15.2	24

Note: AASHTO: American Association of State Highway and Transportation Officials; USCS: Unified Soil Classification System; LL: Liquid Limit; PI: plastic index; OMC: optimum moisture content; CL: Inorganic clays of low to medium plasticity lean clays; CH: Inorganic high plasticity, fat clays; ML: inorganic silts; and SC: inorganic clayey sand.

Table 1. (cont.) Properties of the Test Soils

Soil #	Total SSA (m^2/g)	Ext. SSA (m^2/g)	Int. SSA (m^2/g)	CEC (meq/100g)	Activity (PI/CF)	Carbonate Content (%)	Dolomite Content (%)	Calcite Content (%)
3	92	29	63	23.6	0.47	3.9	0.5	3.5
7	54	10	44	16.5	---	5.2	1.6	3.6
10	220	44	176	50.0	0.7	4	0.9	3.1

Note: SSA: Specific surface area, CEC: Cation Exchange capacity

Oedometer Testing Procedures

All soil samples were subjected to single- and double-oedometer tests, although only the single-oedometer (collapse) method results will be presented herein due to page limitations. The single-oedometer method was performed in general accordance with American Society for Testing and Materials (ASTM) D 5333 "Standard test method for measurement of collapse potential of soils." It consists of incrementally loading a test specimen at its 'as-compacted' water content, up to a target stress level followed by inundation with water. Each loading increment is maintained for one hour or until no further significant deformation occurs. The sample is then inundated with water to induce collapse at a vertical stress of approximately 200 kPa. The collapse potential is determined when there is no more noticeable deformation in the specimen, which generally occurs overnight. The collapse index, I_e, is the collapse potential, or vertical strain change due to wetting the test specimen at an applied vertical stress of 200 kPa. Loads continue to be added after 200 kPa to determine the compression index and compare the results from the ring-compacted (RC) and Proctor-trimmed (PT) samples.

RESULTS

Soil #3 collapse test results are shown in Figure 1. Eight ring-compacted (RC) and two Proctor-trimmed (PT) tests were performed to study the repeatability of the procedure as well as to lend strength to the comparison of RC and PT structure influences on volume change behavior. As can be seen, there is some variability in collapsibility within RC tests performed with an I_e range from 0.5-2.9%, even though every effort was made to ensure the water content and dry density were initially the same. The differences in water content seen between the tests could be the cause in the I_e variability, thus only four of the eight tests were used to determine the average curve to compare with the PT tests, although the average curve using four tests was very similar to the overall average of eight tests. There were only two PT tests performed on Soil #3, and the average curve and range is shown along with the average curve and range for the RC tests.

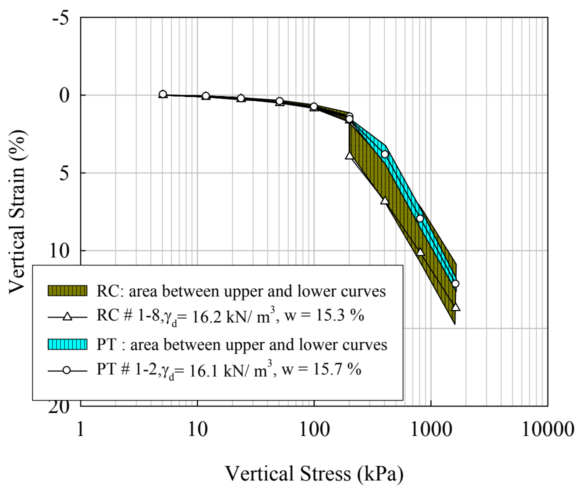

Figure 1. Soil # 3 - Comparison of test results from RC and PT specimens.

For Soil # 7, one RC and PT test were performed (Figure 2). There is no difference in collapse index between the RC and PT samples. Figure 3 shows the collapse test curves for Soil #10 (CH). The RC test showed a large collapse of 2.7% where the PT test showed swelling (-1.4%). This result was not expected, but can be somewhat explained by the slow movement of water inside the large clods in PT specimens causing a simultaneous slow loss of matric suction. This caused the soil particles inside the large clods in the PT specimen to swell and then occupy the large pores (inter-aggregate). Therefore, the overall behavior of the specimen was an expansion (swelling). It appears that the differences in soil structure of the two cases (RC vs. PT) influences behavior in clayey soils.

Comparison between average collapse indices for RC and PT specimens of all three soils are presented in Figure 4. As can be seen, there is a significant structure influence on collapse behavior in clayey soil, but not in silty soil, which exhibited very little collapse behavior. The lack of collapse and structure effect in the silty soil is most likely due to clod breakdown under both compaction methods that resulted in a similar structure. In both clayey samples, the RC specimens exhibited larger collapse than the PT specimens.

For the same moisture content and dry unit weight, the structure of clayey specimens compacted in a proctor compaction mold is different from the structure compacted directly in small rings. The differences in structure between the two cases are distinguished by clod size, pore size distribution and inter-particle forces. Because of the different clod sizes used in both approaches, different pore size distributions were formed. The soil clod consists of soil particles grouped in clusters and separated by individual or small pores (intra-aggregate). The number of the small pores in one clod in the PT specimens may be much higher than that in the RC specimens. Based on the pore size distribution in a compacted soil, the large pores (inter-aggregate) change in size and shape, whereas there are no significant changes in the size and shape of the smaller pores (intra-aggregate) (Vallejo 1995). Consequently, the clods in the PT specimens, where the small pores (intra-aggregate) remain unchanged, may deform less than those of the RC specimens (Cleomene 2005).

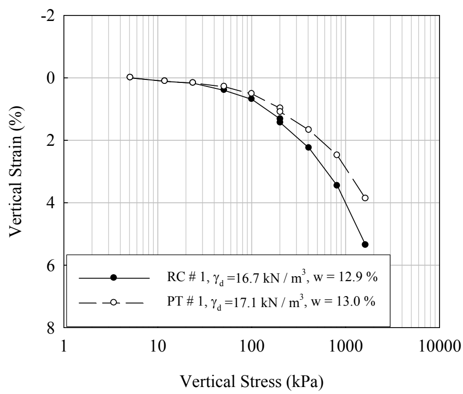

Figure 2. Soil # 7 - Comparison of RC and PT specimens.

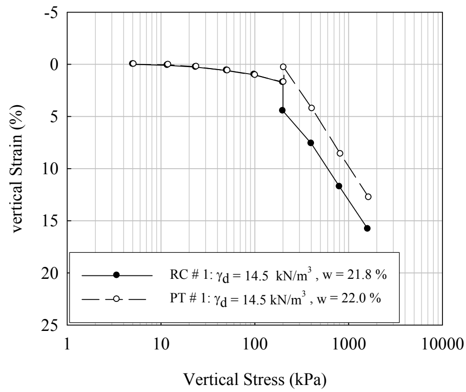

Figure 3. Soil # 10 - Comparison of RC and PT specimens.

In addition, it appears that the compactive effort used may affect the wetting-induced collapse behavior; the compaction effort used in the proctor-trimmed specimens was higher than that of the ring-compacted specimens. For the proctor-trimmed specimens, higher compaction effort may cause a change in the stress history of the soil particles. When a soil is compacted with a moisture content on the dry side of the OMC, it possess a flocculent structure where the diffuse double layer of ions surrounding the clay particles cannot be fully developed and interparticle repulsion forces are reduced. This results in a more random orientation of clay particles. At the same moisture content, higher compaction effort tends to give a more parallel orientation to the clay particles; consequently, the soil structure will be more dispersed. Therefore, the proctor-trimmed specimens exhibited smaller collapse indices compared to those of the ring specimens.

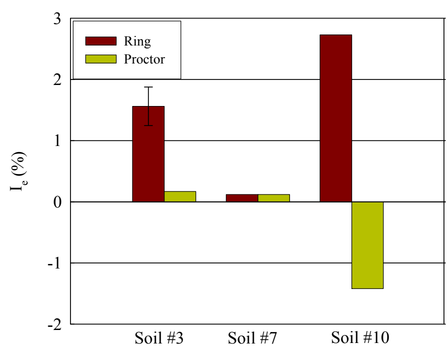

Figure 4. Comparison of Collapse from RC and PT Specimens.

CONCLUSIONS

Based on the comparison of results from RC and PT oedometer tests for three fine-grained soils, the following conclusions can be drawn:

1. Structure effects can be significant for some cohesive soils compacted on the dry side of the OMC.
2. Collapse potential was affected by clod size and initial specimen preparation method in clayey soils. Consequently, it is important to establish corrections between collapse indices in the laboratory and those in the field to predict real wetting–induced compression of embankments and compacted fills.
3. Cohesionless and low cohesive soils (non-plastic and low plastic) were not collapse susceptible and were not affected by sample preparation, and compaction method.

REFERENCES

Basma. A. A. and Tuncer. E. R. (1992) "Evaluation and control of collapsible soils," Journal of Geotechnical Engineering, Vol. 118, No.10, pp. 1491-1504.

Benson, C. H., and Daniel, D. E., (1990). "Influence of clods on hydraulic conductivity of compacted clay." Journal of geotechnical Engineering, ASCE, Vol. 116, No. 8, pp. 1231-1248.

Cleomene, E. (2005). "Scale and fabric effect on one-dimensional compression behavior of compacted soils". Master Thesis, University of Oklahoma., Norman.

Cerato, A.B. and Lutenegger, A.J. (2002), "Determination of Surface Area of Fine-Grained Soils by the Ethylene Glycol Monoethyl Ether (EGME) Method," ASTM, Geotechnical Testing Journal (GTJ), Vol. 25, No. 3, pp. 315-321.

Dreimanis, A. (1962). Quantitative Gasometric Determination of Calcite and Dolomite by Using Chittick Apparatus. Journal of Sedimentary Petrology. Vol. 32. No. 3. pp. 520-529.

Leroueil, S. (1988). "Tenth Canadian geotechnical colloquium: Recent development in consolidation of natural clays". Canadian Geotechnical Journal, Vol. 25, No. 1-2, pp. 85-107.

Lim, Y.Y.and Miller. G.A. (2004). "Wetting-induced compression of compacted Oklahoma soils", Journal of Geotechnical and Geoenviromental Engineering, Vol. 130, No.10, pp.1014-1023.

Miller, G. A. and Cleomene, E. (2007). "Influence of fabric and scale effect on wetting-induced compression behavior of compacted soils." GeoDenver: New Peaks in Geotechnics. GSP 162: Denver, CO, Feb. 18-21, 2007, pp. 1-10.

Rhoades, J.D. (1982). Cation Exchange Capacity. In AL. Page (ed.) Methods of Soil Analysis, Part 2, Second Edition. Agronomy Monograph 9, American Society of Agronomy, Madison, WI.

Rizallah, V. and Keese, K. (1989). "Geotechnical properties of collapsible soils." Proceedings of the 12th International conference on Soil Mechanics and Foundation Engineering, August, 13-19, Rio de Janeiro, Brazil. pp. 101-104.

Vallejo, L. E. (1995). "Fractal analysis of the fabric changes in a consolidating clay." Engineering Geology, Vol. 43, No. 4, pp. 281-290.

Performance of Expanded Clay Shale (ECS) as an Embankment Backfill

[1] Sireesh Saride, [2]Sunil K. Sirigiripet, [3]Anand J. Puppala, [4]Richard Williammee

[1] Post Doctoral Fellow, Department of Civil and Environmental Engineering, The University of Texas at Arlington, Texas 76019, sireesh@uta.edu
[2]Graduate Research Assistant, Department of Civil and Environmental Engineering, The University of Texas at Arlington, Texas 76019, sunil110@gmal.com
[3]Professor, Department of Civil and Environmental Engineering, The University of Texas at Arlington, Texas 76019, anand@uta.edu
[4]Materials Engineer, Texas Department of Transportation, Fort Worth, Texas 76137, rwillia@ @dot.state.tx.us

ABSTRACT: Light weight aggregates (LWA) have been extensively used throughout North America for more than 80 years in cast-in-place structural lightweight concretes for high-rise buildings and bridges. They are now being used for several geotechnical applications including as a backfill in the embankment laid over soft soils, or as a fill material in the retaining wall structures. A research study currently focuses on the use of LWA derived from the manufacturing of Expanded Clay Shale (ECS) as an embankment fill material along State Highway (SH) 360 in Arlington, Texas. This paper first presents the laboratory results obtained by testing Expanded Clay Shale (ECS) material to evaluate its function as embankment backfill. Both direct shear and consolidation tests were performed to evaluate its strength characteristics. This embankment was instrumented with vertical inclinometers to monitor fill movements. Based on the monitored data, it can be mentioned that the use of ECS resulted in less settlements of embankment at the site.

INTRODUCTION AND BACKGROUND

For nearly a century, expanded clay shale aggregates (ECS) have been used successfully around the world for various applications (Expanded Shale, Clay & Slate Institute (ESCS), 2004). ECS is a light weight aggregate prepared by expanding select minerals in a rotary kiln at temperature of over 1000ºC (Holm and Ooi, 2003). The production and raw material selection processes are strictly controlled to insure uniform, high-quality product that is structurally strong, stable, durable and inert, yet also lightweight and insulative (ESCS, 2004).

Millions of tons of ECS produced annually are used in many geotechnical applications. Its availability is currently widespread throughout most industrially developed countries. Consideration of ECS as a remedy to geotechnical problems stems primarily from the improved physical properties of reduced dead weight, high internal stability, and high thermal resistance (Stoll and Holm, 1985). These advantages arise from the reduction in particle specific gravity, stability that results from the inherent high angle of internal friction, the controlled open-textured gradation available from a manufactured aggregate which assures high permeability, and high thermal resistance due to high particle porosity (Holm and Valsangkar, 1993).

ECS lightweight aggregates are approximately half the weight of traditional fill materials. Because of the high internal friction angle of ECS materials, vertical and lateral forces can be reduced by more than one-half (Holm and Valsangkar, 1993). These materials have been used to solve numerous geotechnical engineering problems and to convert soft and unstable soil into usable property. Since ECS aggregate has high thermal resistivity, it provides durable, inorganic insulation around water and steam lines, and other thermally sensitive elements (Holm and Valsangkar, 1993). ECS aggregates provide a practical, reliable and economical geotechnical solution (DeMerchant and Valsanger, 2002). Table 1 shows the general engineering properties of ECS (after ESCS, 2004).

Table 1 General Properties for ECS (ESCS, 2004)

Aggregate property	Measuring method	Test method	Commonly specifications for ECS	Typical for ECS aggregates	Typical design values for ordinary fills
Soundness Loss	Magnesium Sulphate	AASHTO T 104	<30 %	<6 %	<6 %
Abrasion Resistance	Los Angeles Abrasion	ASTM C 131	<40 %	20 – 40%	10 – 45%
Compacted Bulk Density	Density Test	ASTM D 698	<70 lb/ft^3	40– 65 lb/ft^3	100-130lb/ft^3
Strength	Direct Shear Test & Triaxial (CD)	ASTM D 3080 & Corps of engineers EM 1110-2-1906	According to project	35º - 45º	30º - 38º (fine sand-sand & gravel)
Loose Bulk Density	Loose	ASTM C 29	Dry<50 lb/ft^3 Saturated<65 lb/ft^3	Dry 30-50 lb/ft^3	89-105 lb/ft^3
pH	pH meter	AASHTO T 289	5 – 10	7 – 10	5 - 10

The lightweight aggregates have been commonly used in case-in-situ structural lightweight concretes for high rise buildings and bridges for several years (Holm and Valsangkar, 1993). Their applications to geotechnical solutions are gaining popularity in recent years due to their promising engineering behavior. One such application of this material in alleviating the overburden pressure on soft clay subgrades is presented in this paper. The main intent of the research presented in this paper is to reduce the pressures exerted on the soft subgrades supporting the embankment and to reduce the settlement of the embankment fill. First, experimental studies including density, direct shear and consolidation tests on ECS were first carried out. The ECS material was then used as an embankment backfill on an embankment along state highway, SH-360 in Arlington, Texas. Figure 1 shows the typical cross section of the embankment with ECS backfill used at the project site. To evaluate the performance of ECS as an embankment fill material and to understand the fill movements and their patterns, vertical inclinometers were installed, one at the median (VI 1) and another at the exterior slope of the high rise embankment (VI2) as shown in Figure 1.

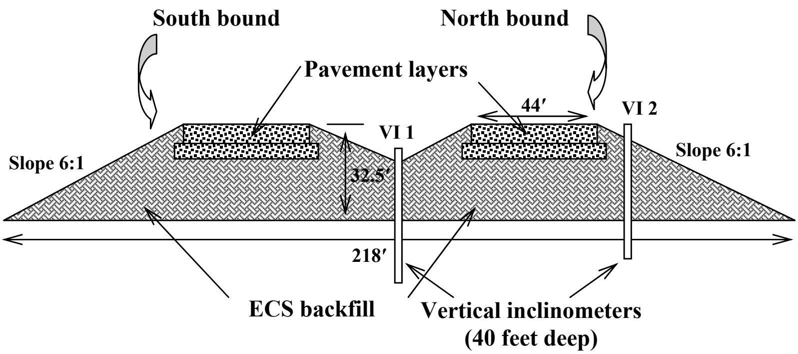

Figure 1 Typical cross section of ECS backfilled embankment, SH 360, Arlington, Texas

EXPERIMENTAL PROGRAM AND LABORATORY DATA

To evaluate the strength characteristics of ECS aggregates (Figure 2a), a series of direct shear tests was performed according to ASTM D 3080 method. ECS samples were well compacted in a 2.5 inch shear box. Normal stresses of 50, 100 and 200 kPa were applied to the samples and the sample was then sheared. Normal stresses were applied with the help of a loading ram. Shearing was applied with the help of a horizontal ram. This setup was connected to the computer where shear stress was plotted as a function of shear displacement. Figure 2b shows the graph between measured shear stress and applied normal stress. The calculated friction angle of the ECS was 49.5º.

Consolidation tests on ECS aggregate material were performed to address the compressibility of this recycled material. The test was conducted according to ASTM D2435. Sample was prepared in a 2.5 inch mould and was then placed in an oedometer for testing. An initial seating pressure of 40 kPa was applied to the sample to prevent swelling.

a) Photograph of ECS

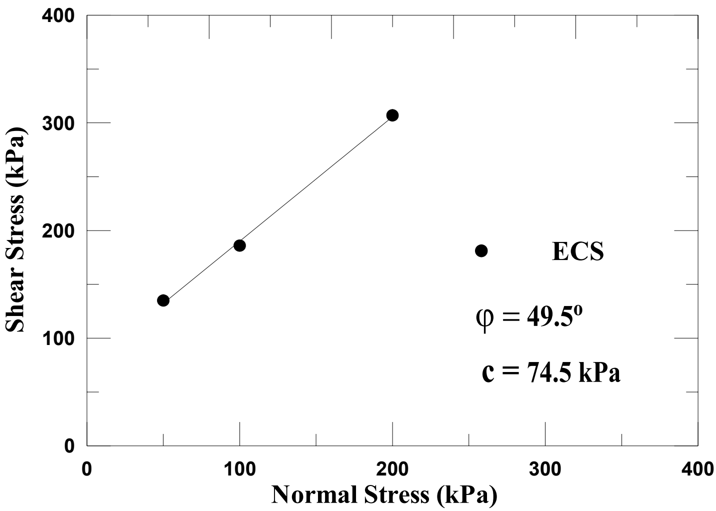

b) Direct Shear Test Results

Figure 2 Appearance and shear strength properties of ECS material

The load was allowed to stand till there was no change in the dial gauge reading. Dial gauge reading was noted under that pressure. The first increment of the load 40 kPa was applied to make the total load corresponds to 80 kPa and the readings were recorded at certain time intervals for 24 hours. The loading was doubled and hence successive pressures of 160, 320 and 640 kPa were applied during loading. After that, the final load was unloaded from 640 kPa to 40 kPa. Figure 3 shows the void ratio versus logarithm of the pressure of the ECS material. Compression index C_c was calculated from the normal compression line slope, which was found to be 0.05 for ECS material. Such number was expected for granular materials.

FIELD MONITORING DATA

The embankment section was constructed in the last summer months of 2006 and this section was then instrumented with vertical inclinometers that extended to a depth of 40 feet deep at two different locations. One inclinometer (VI 1) is located at the centre line of the median (in between the south and north bounds of SH 360) and another inclinometer (VI 2) is placed at the outer slope of the embankment. The main intent of the inclinometers is to understand the fill movements and their patterns. These inclinometers were regularly monitored once a month and on days when rainfall exceeds 1 in.

The 'e - log p' plot shown in Figure 3 was constructed from the laboratory test data. Although the monitoring period has been short, it is anticipated that most of the construction-induced settlement has already occurred and additional settlement may only occur during the next year due to traffic load application, long-term time and stress-dependent consolidation movements and time dependent creep settlements. These settlements will influence lateral soil movements and stability of the embankment slopes.

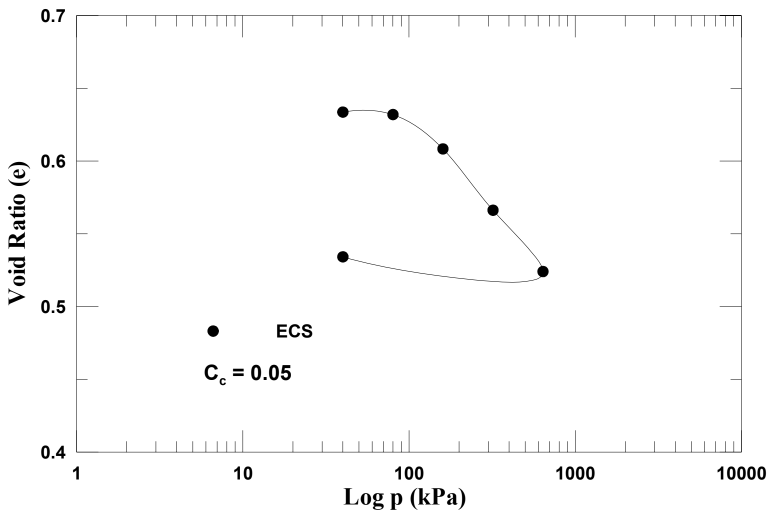

Figure 3 e-log p plot for ECS material

The magnitudes of settlement at which stability problems occur are not unique and they depend on site specific details of the projects including boundary conditions. Typically lateral movements that are beyond 1 in. are considered problematic. At such values, global stability assessments of the embankments are needed.

It can be seen that the lateral movements (deviations from the centre line) in the inclinometer (VR 1) are within the permissible limit of 1 in. The inclinometer located at the outside slope of the NB (VR 2) shows a slight rotation of the slope. It should be noted that the maximum movement recorded after January 2007. Figure 5 shows the cumulative displacement (inches) at the top end of the inclinometer casing with time (days). The embankment fill has started moving after 240 days (8 months) from the end of the construction.

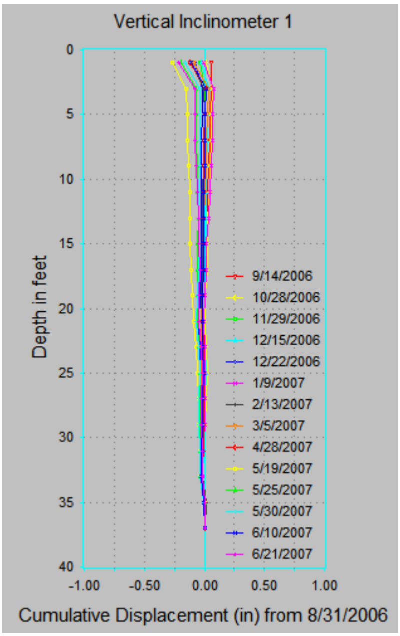

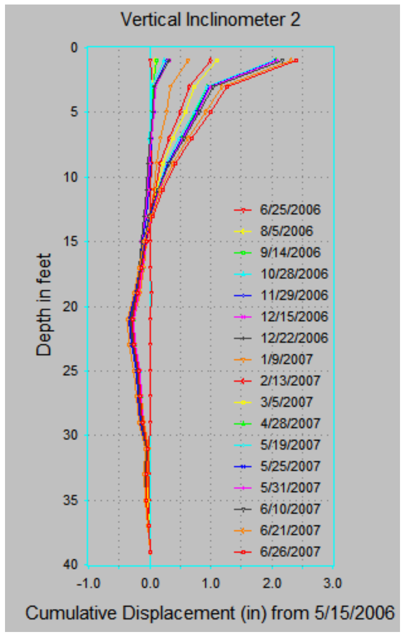

(a) Vertical inclinometer (median, VI 1) (b) Vertical inclinometer (outer slope, VI 2)
Figure 4 Vertical inclinometer readings: Cumulative displacement (in) versus depth of the embankment fill

Possible reasons for the soil movement could be attributed to recent heavy rainfall in early 2007 that might have induced lateral soil movements. The amount of rainfall recorded from the nearest weather station over the last one year is shown in Table 2. Table 2 indicates that an average monthly rainfall amount of 5.03 in. occurred at the test site over the last six months. Such high rainfalls might have contributed to the soil movements either from erosion or from later expansion. The top fill material used at the site is a local expansive soil and they generally undergo lateral movements when hydrated. Also, visual observations showed certain erosion of the fill material due to heavy rainfalls in a short time period. Continued monitoring of this site should provide better understanding of these soil movements and stability of ECS embankments.

Table 2 Details of rainfall data at the test site (SH 360, Arlington, TX) for the year 2006-2007 (Source: http://www.ncdc.noaa.gov/oa/ncdc.html)

Month /year	Amount of rainfall (inches)	Remarks
May/2006	2.68	Nominal rainfall
June/2006	1.24	
July/2006	0.55	
August/2006	1.46	
September/2006	2.23	
October/2006	4.70	
November/2006	1.80	
December/2006	4.69	
January/2007	5.06	Heavy rainfall
February/2007	0.83	
March/2007	5.35	
April/2007	2.66	
May/2007	10.10	
June/2007	8.87	

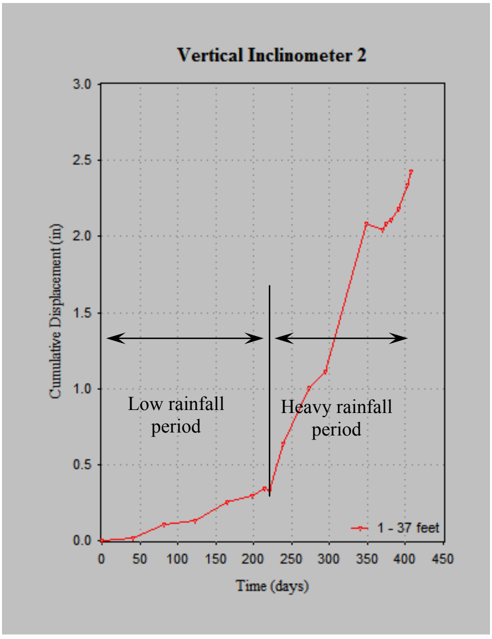

Figure 5 Variation of cumulative displacement of vertical inclinometer (VI 2) with number of days

SUMMARY

This paper presents the results of laboratory experiments on recycled expanded clay shale (ECS) material to evaluate its function as embankment backfill. Direct shear strength tests showed that these recycled material has high angle of internal friction and a nominal amount of cohesion component which offers a good stability to the embankment. The vertical inclinometer readings show a satisfactory performance of the ECS backfill, except the location outside slope of the embankment which shows a little rotation due to rainfall induced localized bulging of the fill. Overall, the laboratory testing results along with field monitoring data shows that this light weight aggregate material can be utilized successfully as an embankment backfill material.

ACKNOWLEDGMENTS

The authors would like to acknowledge the Fort Worth District and Jeff Seiders of the Construction Division of the Texas Department of Transportation (TxDOT) for providing financial support to this project under an interagency contract agreement.

REFERENCES:

ASTM International (2003) *ASTM Book of Standards, Vol. 4.13,* ASTM, Philadelphia, Pennsylvania.

DeMerchant, R. M and Valsangkar, A. J. (2002). “Plate load tests on geo-grid reinforced expanded shale lightweight aggregate”, Journal on Geomembrane and Geotextiles, Vol 20, Issue 3, pp172-190.

Holm, T. A., and Ooi, O. S. (2003) “Moisture dynamics in lightweight aggregate and concrete”. 6th International Conference on the Durability of Concrete, Thessaloniki, Greece.

Expanded Shale, Clay and Slate (ESCS) (2004). “Light weight aggregate for geotechnical applications” Information Sheet 6001 – www.escci.org

Stoll, R. D., and T. A. Holm, T. A. (1985). “Expanded shale lightweight fill: Geotechnical properties”, Journal of Geotechnical Engineering, ASCE, Vol. 111, No. 8.

Holm, T. A., and Valsangkar, A. J. (1993) “Lightweight artificial and waste materials for embankments over soft soils” Lightweight aggregate soils mechanics: Properties and Applications, Transportation Research Record, Issue 1422, Washington, D.C., pp 7-13.

Case Studies of Earthquake-Induced Ground Movement Effects on Concrete Channels

Craig A. Davis[1], A.M. ASCE, P.E., Jianping Hu[2], A.M. ASCE, P.E., and J.P. Bardet[3], A.M. ASCE

[1]Waterworks Engineer, Geotechnical Engineering Group, Los Angeles Department of Water and Power, 111 N. Hope Street, Room 1368, Los Angeles, CA 90012; Craig.Davis@ladwp.com
[2]Civil Engineering Associate, Geotechnical Engineering Group, Los Angeles Department of Water and Power, 111 N. Hope Street, Room 1368, Los Angeles, CA 90012; Jianping.Hu@ladwp.com
[3]Professor and Chair, Civil and Environmental Engineering Department, University of Southern California, Kaprielian Hall 230B, University Park, Los Angeles, CA 90089; bardet@usc.edu

ABSTRACT: Case studies are presented for two concrete lined channels shaken by strong ground motions during the 1994 Northridge earthquake, the High Speed (HSC) and Bypass Channels (BC), on the Los Angeles Department of Water and Power's Van Norman Complex. Performances of these two channels as they pass through different subsurface materials identify several important seismic aspects and the critical role of geotechnical earthquake engineering in assessing channel behaviors. Preliminary evaluations using detailed mapping of channel cracks, permanent ground movements, subsurface profiles, and nearby strong ground motion recordings from the 1994 earthquake show that the channel liners may have been damaged from both transient motions and permanent ground movements. Damage from permanent ground deformations is obvious by observation; therefore simplified analyses are presented only for transient movements. Site specific transient response analyses are performed to help provide an initial assessment of the differing effects from transient and permanent ground movements on HSC and BC liner damage. These case studies are helpful for introducing the potential for lifeline damage from transient movements within zones of permanent ground movement, a concept not well understood in the earthquake engineering community.

INTRODUCTION

The seismic performance of concrete lined channels is not easy to predict because their behaviors are strongly dependant on interactions between the concrete liner and the soil or rock they are constructed within. Channels constructed in stable ground are expected to perform well during strong earthquake shaking; however those in marginally stable ground are susceptible to earthquake damage. This generalized behavior pattern is similar to that of other lifeline components, such as pipelines, but channel damage resulting from transient and permanent ground deformations is much more difficult to predict than the typical pipe performance due to greater dependency on seismic ground response, construction methodology, and channel structure geometry. Fragility studies for water supply conduits (ALA, 2001) clearly identified this problem in predicting channel performance and also points out that a lack of case studies limits the ability to improve channel performance prediction.

To help improve the understanding of channel seismic performance, this paper presents case studies of two concrete lined channels, the High Speed Channel (HSC) and the Bypass Channel (BC), that were severely shaken by the M_w 6.7 January 17, 1994 Northridge Earthquake. The HSC and BC are located on the Los Angeles Department of Water and Power's (LADWP) Van Norman Complex (Complex), in the Northern San Fernando Valley.

HIGH SPEED CHANNEL (HSC) AND BYPASS CHANNELS (BC)

Figs. 1a and 1b show the HSC round-bottomed triangular and BC trapezoidal cross sections, respectively. Figs. 2 and 3 show HSC and BC profiles, respectively.

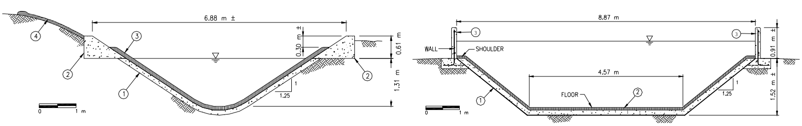

FIG. 1. (a) High Speed Channel cross-section. (b) Bypass Channel cross-section.

Subsurface Conditions

Soil profiles along the HSC and BC are presented in Figs. 2 and 3. These profiles were determined using results of Cone Penetration Testing (CPT) and boring logs obtained in the HSC and BC vicinity (Davis and Scantlin, 1997) with aid from the 1940 and 1913 (not shown) ground surface profiles. As seen in Figs. 2 and 3, the soil conditions vary along the HSC and BC. Much of the soils consist of interbedded sandy silts, silty clay, and clay alluvial deposits, underlain by stronger alluvial soils above Saugus formation bedrock. In a few places the channels were constructed in fill. There are two zones of very weak clays, one under the HSC as shown in Fig. 2, and one under the BC as shown in Fig. 3.

Groundwater around the HSC and BC is influenced by water seeping from the channels, which are not considered to be water tight. The natural groundwater has a general downward gradient to the south along the HSC and southwest along the BC. Fig. 2 shows the groundwater surface around the HSC measured from subsurface investigations within 10 m of the channel. Groundwater around to the BC was measured near the ground surface and is not shown in Fig. 3. Seepage influences the groundwater elevation locally around both channels, causing a mound in the groundwater surface. Away from the channels the natural groundwater is approximately 6 m deep. Seepage from the BC influences natural water levels in the soft clay soils at distances greater than 18 m. Seepage from the HSC dissipates rapidly within 10 m of the channel, except for a localized condition in soft clay soils where the groundwater is observed to remain near the ground surface.

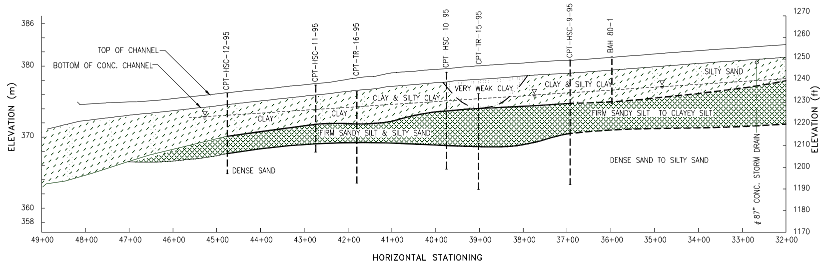

FIG. 2. High Speed Channel profile showing CPT locations and interpreted subsurface soil conditions. (1 station = 100 ft = 30.48 m)

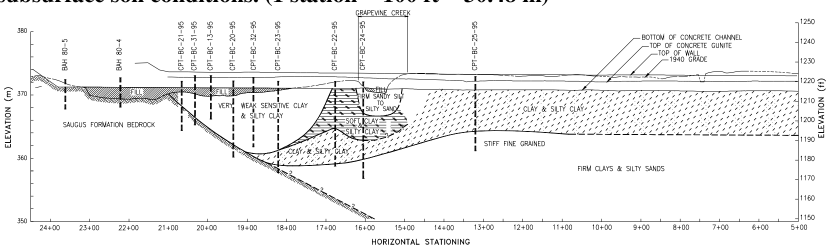

FIG. 3. Bypass Channel profile showing CPT locations and interpreted subsurface soil conditions. (1 station = 100 ft = 30.48 m)

CHANNEL PERFORMANCE DURING 1994 NORTHRIDGE EARTHQUAKE

Fig. 4 shows 1994 pipe and channel damage locations previously presented by Davis and Bardet (1995). As seen in Fig. 4, most 1994 pipe and all channel damage occurred on the Complex northern end where the HSC and BC are located.

Northridge Earthquake Strong Ground Motion Recordings

The January 17, 1994 Northridge Earthquake (M_w 6.7) occurred on an unmapped blind thrust fault (Wald & Heaton, 1994) at an epicentral distance of approximately 11 km south of the Complex. Seismic Stations 10 and 13 shown in Fig. 4, located at the Sylmar Converter Station a few meters east of the HSC and BC, are the most pertinent to this investigation (Bardet & Davis, 1996). Free-field Station 10 recorded 0.90g peak ground acceleration (pga), 130 cm/s peak ground velocity (pgv), and 41 cm peak ground displacement (pgd). The ground below Station 10 consists of approximately 10 m of firm silty sand to sandy silt soil having an average shear wave velocity $\beta = 263$ *m/s*. Station 13 is located in a concrete building basement and recorded a 0.58g pga, 116 cm/s pgv, and 38 cm pgd. The ground below Station 13 consists of approximately 14 m of weak clayey silt with average $\beta = 135$ *m/s*. Firm Saugus formation has estimated $\beta = 500$ *to* 600 *m/s*; weathered rock β is similar to firm soil at Station 10 (i.e., $\beta = 263$ *m/s*).

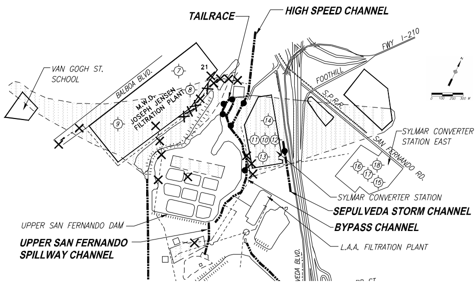

x - pipe damage
● - channel damage
Seismic recording stations are numbered and circled.

FIG. 4. Northern Van Norman Complex area showing channel locations, seismic stations, and regions bounding observed permanent ground movement (shaded).

Channel Damage

Figs. 5 and 6 present plots of crack density along the HSC and BC, respectively. The crack density is defined as the length of cracks per unit channel length. Crack locations were surveyed and identified as greater than or less than 0.63 cm wide, referred to herein as major or minor cracks. Davis and Scantlin (1997) show crack mappings and describe the methods used to obtain the crack data. The channels were routinely inspected on an annual or semi-annual basis prior to the earthquake with no signs of significant pre-earthquake cracking. The post-earthquake cracks in both channels were mostly transverse (perpendicular) or longitudinal (parallel) to the channel axes. Some of the damage to both channels was due to the continued water flow across broken sections immediately following the earthquake. As shown in Fig. 5c, the HSC sustained numerous transverse cracks. Many cracks extended through the original concrete liner and the gunite overlay that was placed in 1971. Most of the larger HSC longitudinal cracking identified in Fig. 5d occurred at the top of the gunite overlay, indicating separation between the top curb and the channel.

The BC cracked and separated in many locations and in some places the overlay began to delaminate from the original channel. Fig. 6 identifies the BC sustained numerous cracks. Davis et. al. (2002) described 7 transverse cracks greater than 0.63 cm wide. Two cracks over 0.63 cm wide occurred near the south end over soil fill. Many transverse cracks over the clay soils measured in excess of 1.3 cm wide. The greatest transverse cracking resulted above soft clayey soils between Stations 17+50 and 20+50 rupturing across the entire channel section displacing the lining and walls. The two transverse cracks between Stations 20+00 and 20+50 had a noticeable vertical offset, down to the north, and left lateral offsets having a minimum movement of 7.6 cm.

Permanent Ground Deformations

Figs. 5a and 6a show settlement profiles of the HSC and BC, respectively. All settlement measurements were taken on the concrete surfaces. In zones of large settlement, the channels could bridge the movement and create voids between the soil surface. As a result, settlement measurements reported in Figs. 5a and 6a are considered a lower bound of deformation in the underlying soil. As seen in Figs. 5a and 6a, the channels underwent large soil settlements with the greatest settlement resulting in the regions corresponding to soft clayey soils shown in Figs. 2 and 3. BC measurements showed differential settlements across the channel width of up to 0.15 m, indicating the liner tilted down to the west. Figs. 5 and 6 also show the approximate regions of observed greatest horizontal lateral permanent ground movement, which corresponds with greatest settlement.

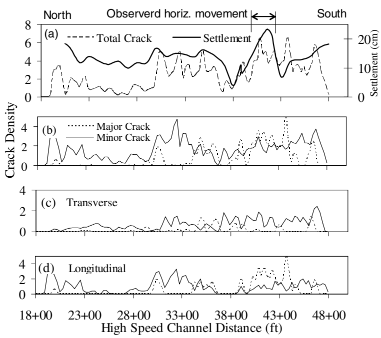

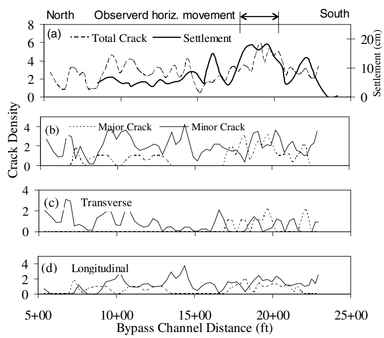

Fig. 5. HSC settlement and crack density. (1 station = 100 ft = 30.48 m)

Fig. 6. BC settlement and crack density. (1 station = 100 ft = 30.48 m)

EVALUATION

Channel Cracks

Figs. 5a and 6a present the calculated crack density using all cracks and show a general correlation of increased cracking with settlement, but no consistent pattern over the entire channel lengths. Figs. 5 and 6 also show that the crack density magnitudes for any crack subcategory are similar for the HSC and BC. Figs. 5b to 5d and 6b to 6d present the major and minor cracks and show a reasonably good correlation of major cracking with settlement, but no correlation of settlement with minor cracking. Longitudinal cracks in the HSC and transverse cracks in the BC have very good correlations with settlement and horizontal movement in Figs. 5d and 6c, respectively. However, the HSC transverse and BC longitudinal cracks do not correlate well with permanent ground movements.

The minor cracks cannot be correlated with permanent horizontal or vertical ground movements, soil conditions, or channel type. The major cracks do correspond somewhat with larger permanent ground movements; however there are a number of BC longitudinal and HSC transverse major cracks that do not directly correlate with the permanent ground movements. Cracks not resulting from permanent ground strains were presumably caused by transient strains. As a result, most of the minor cracks and some of the major cracks are hypothesized to have occurred from transient motions through: (1) shear distortions transverse to channel cross-section, (2) horizontal wave propagation ground strain, and/or (3) differential ground motion along the channel alignment. In addition, this raises questions as to whether some cracks within the greatest permanent ground deformation regions resulted from transient motions before the permanent ground deformations occurred, in a manner similar to that observed on a nearby large diameter pipe (Davis, 2001). To start addressing this problem simplified analyses are performed for the 3 strain conditions mentioned above, each independent of the other.

Simplified Transient Strain Analyses

Shear Distortions: Equivalent linear site response analysis using EERA (Bardet et al., 2000) was performed to better understand the horizontal shear distortion effects transverse to the channels. The analysis is performed at several HSC and BC locations. The subsurface profiles are defined in Figs. 2 and 3. The analysis uses standard G/Gmax and damping curves for sand (Seed & Idriss, 1970; Idriss, 1990) and clay (Sun et al., 1988; Idriss, 1990) to describe the variation in shear modulus and damping ratio with shear strain amplitude. In the calculations, soil layers were subdivided into sublayers of identical properties with the sublayer thickness d satisfying $d \leq \beta/5f_{max}$ (Bardet et al., 2000) where f_{max} is an acceptable higher cut-off frequency. The bedrock depth was estimated from limited field investigation information. The Station 10 free-field motion is deconvolved to represent a bedrock input motion below the channels. The site response at Station 13 was modeled and found to match closely with the earthquake recording.

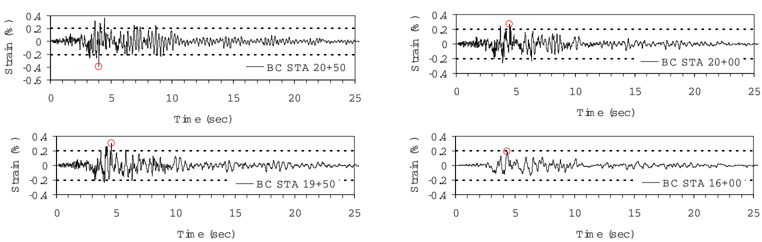

FIG. 7. Transient shear strain at BC STA 20+50, 20+00, 19+50 and 16+00.

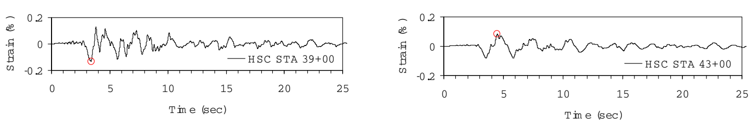

FIG. 8. Transient shear strain at HSC STA 39+00 and STA 43+00.

Figs. 7 and 8 show horizontal transient shear strain results transverse to and at different locations along the HSC and BC. These shear strain time histories are calculated, neglecting soil-structure interaction effects, at the depth between the ground surface and the channel bottom. As shown in Fig. 7, between BC STA 19+00 and STA 21+00, the maximum transient shear strains in the first 10 seconds of shaking exceed 0.2%, which is the minimum strain to initiate concrete cracking (USACE, 1990). This correlates well with the observed major crack and settlements at this portion of the channel. It also indicates that some of the BC major cracks within the greatest permanent ground deformation regions may have resulted from transient motions independent of permanent ground deformations. As shown in Fig. 8, similar transverse strain correlations cannot be made for the HSC.

Horizontal Wave Propagation: The horizontal wave propagation ground strain can be estimated similar to that of pipes (O'Rourke and Hmadi, 1988) from $\varepsilon_g = pgv/C$ where C is the apparent wave propagation velocity. The Station 10 and 13 pgv's were recorded nearly in line with the HSC and BC axes (Davis and Bardet, 2000). Assuming the pgv's result from Rayleigh surface waves and the apparent velocity $C = C_{ph} = 135$ *to* $500 m/s$, where C_{ph} is the phase velocity as described by O'Rourke and Hmadi (1988), then $\varepsilon_g = 1\%$ *to* 0.26% and is sufficient to cause channel cracking, especially on extensional wave cycles, anywhere along the HSC and BC alignment adequately bonded to the ground. ε_g will change along the channel with wave length and as the subsurface conditions change, resulting in non-uniform channel cracking. However, where relatively uniform conditions exist similar periodic crack patterns should appear. This may explain the periodic crack density patterns in Figs. 5 and 6.

Differential Ground Motion: A preliminary analysis to evaluate differential transient ground motion was also undertaken for the BC. The average transient strain γ between two points on the channel is $\gamma = (\Delta_1 - \Delta_2)/L$ where Δ_i is the ground surface displacement at location i and L is the distance between the two points. $\Delta_i = H * pgv_i/\beta_i$, where H is the depth over which strain is evaluated. Fig. 3 shows that the BC transitions from bedrock having shallow fill cover to the weak clay soils at STA 21+00. Bedrock site $i=1$ has β_1 ranging from *263* to *600 m/s (average 432 m/s) and* $pgv_1 = 130$ *cm/s* (estimated to be similar to Station 10). Site $i=2$ is over the 12 m deep clay deposit at STA 19+00 having $\beta_2 = 135$ *m/s*. Station 13 was recorded approximately over the deepest weak clay soils and is taken to represent motions at STA 19+00, providing $pgv_2 = 116$ *cm/s.* Evaluating sites 1 and 2 for $H = 12m$ gives $\Delta_2 = 3\Delta_1$. From the preceding information $\Delta_2 = 38$ *cm* at Station 13, $L = 61$ *m,* and $\gamma = 0.41\%$. The strain resulting from differential ground motion is sufficient to cause major cracking. Similar results are expected for the HSC.

Results from the three simplified strain evaluations provide initial indications that the HSC and BC were damaged from a combination of transient and permanent ground movements. Further work is needed to better understand how transient motions damage channels, appropriate methods for estimating damage for different channel types, and how to separate effects of transient and permanent movements.

CONCLUSIONS

Case studies of two concrete lined channels shaken by the 1994 Northridge earthquake were presented. Detailed investigations of subsurface conditions, earthquake damage, recorded site response, and permanent ground movements provide evidence that the channels were damaged by a combination of transient and permanent ground movements. Measured crack patterns do not consistently correlate with permanent ground movement locations or channel type. Simplified site specific response analyses were performed and provided initial indications that transient ground movements contribute to channel damage and combine with the permanent ground deformation in causing channel damage. The High Speed (HSC) and Bypass Channel (BC) evaluations also showed that additional studies are required to fully understand the problem. These case studies provide insight into different effects from transient and permanent movements, valuable information to improve the understanding of channel seismic performance, and help identify needed geotechnical and lifeline research.

REFERENCES

American Lifelines Alliance (ALA), 2001, "Seismic Fragility Formulas for Water Systems," Parts I and II, ASCE and FEMA, www.americanlifelinesalliance.org.

Bardet, J.P. and C.A. Davis, 1996, "Engineering Observations on Ground Motion at the Van Norman Complex after the Northridge Earthquake," *Bull. Seism. Soc. Am.*86, 1B, pp. S333-S349.

Bardet, J. P., Ichii, K. and Lin, C. H. (2000). "EERA: A Computer Program for Equivalent-linear Earthquake Site Response Analysis of Layered Soil Deposits," USC, Department of Civil Engineering, http://geoinfo.usc.edu/gees.

Davis, C.A., 2001, "Retrofit of Large Diameter Trunk Line Case Study of Seismic Performance," *Proc. 2nd Japan-U.S. Workshop on Seismic Measures for Water Supply,* AWWARF/JWWA, Tokyo, Aug.

Davis, C.A., and J.P. Bardet, 1995, "Seismic Performance of Van Norman Water Lifelines," *Proc. 4th U.S. Conference on Lifeline Earthquake Engineering,* ASCE, San Francisco, Aug., pp. 652-659.

Davis, C.A., and J.P. Bardet, 2000, "Responses of Buried Corrugated Metal Pipes to Earthquakes," *Journ. Geotech.Engr. Div*., ASCE, 126(1), pp. 28-39.

Davis, C. A., Bardet, J. P., and J. Hu, (2002). "Effects of Ground Movements on Concrete Channels." *Proc. 8th US–Japan Workshop on Eq. Resistant Design of Lifeline Facilities and Countermeasures Against Soil Liquefaction, MCEER.*

Davis, C.A., and P.S. Scantlin, 1997, "Response of High Speed and Bypass Channels to 1994 Northridge Earthquake and Recommended Repairs," *LADWP Rpt. AX 215-47*.

Idriss, I. M. (1990). "Response of Soft Soil Sites during Earthquakes", *Proc., Memorial Symposium to honor Professor Harry Bolton Seed*, Berkeley, CA, Vol. II, May.

Seed, H. B. and Idriss, I. M. (1970). "Soil Moduli and Damping Factors for Dynamic Response Analysis", *Report No. UCB/EERC-70/10, Earthquake Engineering Research Center*, University of California, Berkeley, December, 48p.

Sun, J. I., Golesorkhi, R., and Seed, H. B. (1988). "Dynamic Moduli and Damping Ratios for Cohesive Soils." *Report No. UCB/EERC-88/15, Earthquake Engineering Research Center*, University of California, Berkeley, December, 42p.

O'Rourke, M.J. and K.E. Hmadi, 1988, "Analysis of Continuous Buried Pipelines for Seismic Wave Effects," *Earthquake Engr. and Soil Dyn.*, 16, pp. 917-929.

U.S. Army Corp of Engineers (USACE), 1990, "Engineering and Design Settlement Analysis," *Department of the Army*, EM 1110-1-1904, p. 2-5.

Wald, D.J., and T.H. Heaton, 1994, "A Dislocation Model of 1994 Northridge, Earthquake Determined from Strong Ground Motions," *USGS,* Open-File Report 94-278.

Centrifuge Modeling of Explosion Craters Formed Over Underground Structures

Anirban De, P.E., M.ASCE

Assistant Professor, Department of Civil & Environmental Engineering, Manhattan College, Bronx, NY 10471, anirban.de@manhattan.edu

ABSTRACT: Crater formation due to surface explosions immediately above underground structures were studied through geotechnical centrifuge model tests. The underground structures include tunnels and pipelines, located close to the ground surface. The crater formed by a surface explosion removes a portion or all of the cover material over the underground structure.

Strains developed at various locations on the model underground structure due to the explosion were measured during the centrifuge model tests. The strains varied with the thickness and nature of the cover material.

Results related to crater formation from this study are compared with those available from published literature and are expected to provide an understanding of the nature of crater formation due to surface explosion. These results will be useful in designing new underground structures as well as for developing protective retrofits for existing structures.

INTRODUCTION

Explosions on the ground surface, caused due to terrorist activities, can cause significant damage to underground structures located below the explosion. The research reported here is part of a study to investigate the effects of surface blasts on underground structures, such as tunnels and pipelines. Geotechnical centrifuge testing was utilized to study the effects of explosions on scale models of underground structures.

The effects of an explosion are volumetric in nature and are related to the third power of the gravitational acceleration and model scale. Thus a relative small mass of explosives in a model, detonated at a proportionately higher gravitational acceleration will have the same effects as a full-scale prototype explosive detonated under the earth's normal gravitational field [Taylor, 1995]. Researchers, such as Schmidt and Holsapple [1980] and Kutter, et al. [1988], have previously reported on the scale effects of blasting, through both dimensional analyses and centrifuge model testing. Details regarding the current project have been presented by De and Zimmie [2006 and 2007].

The centrifuge tests reported in this paper all utilized models constructed to 1:70 scale and were all conducted at 70 g, on board a 150 g-ton geotechnical centrifuge located at Rensselaer Polytechnic Institute, Troy, New York. In each test, charges with TNT equivalent of approximately 2.6 grams, were utilized under 70 g acceleration. Following the centrifuge scaling relationship mentioned previously, this amount of charge created the same effects as 888 kg or 8.7 kN of TNT equivalent under normal gravity.

CENTRIFUGE MODELING OF CRATER FORMATION

The crater formed on the ground surface due to an explosion has different definitions. A true crater is one that is formed by the initial detonation. Following the explosion, the material that is uplifted from the crater area, as well as from the surrounding ground, is deposited back into the newly-formed crater. These materials are termed ejecta and fallback. The final resultant crater, after ejecta and fallback has deposited in the crater, is termed the apparent crater. The dimensions of a crater measured after an explosion has occurred are those of the apparent crater. It is almost impossible to make a direct physical measurement of a true crater.

Kutter et al. [1988] noted that an explosion causes damage to underground structures through two principal mechanisms. The first is through a direct loading by a shock wave created due to the explosion. The second mechanism of damage is large soil displacements in and surrounding the crater. The effects of these mechanisms were studied in this research through readings of strain gages installed at various locations of the underground structures that were monitored and acquired in real time, before, during and after each explosions and through measurements of apparent crater dimensions after each explosion.

At the end of each test, a symmetric, circular crater was formed as a result of the explosion. The size of the crater was measured in three-dimensional coordinates using a profilometer. It should be noted that the measurements were taken for the apparent crater, i.e., the crater that was observed at the end of the test. The crater initially formed during the explosion, the true crater, is deeper than the apparent crater. The average crater had a diameter of approximately 12 m and maximum depth of approximately 1.25 m, both in prototype scale. The photograph of a typical crater from a centrifuge model test is shown in Figure 1.

FIG. 1. Photograph of a crater from a typical centrifuge model test, taken after the test was completed. Average crater diameter: 12 m, average crater depth: 1.25 m (prototype scale)

EFFECTS OF COVER THICKNESS AND COVER MATERIAL

Cover refers to the intervening material which is present between the ground surface and the top (or crown) of the underground structure. The impact of an explosion on the ground surface passes through this cover material before reaching the underground structure. Therefore, the nature and thickness of the cover material influence the level of stress and strain experienced by the structure. These effects were studied through centrifuge model tests where covers of different thicknesses and comprising of different material were utilized.

Effects of Cover Thickness

Tests were conducted on identical models of underground structures, with two different thicknesses of soil cover, compacted to approximately the same relative density. The thicknesses of soil cover used in the tests were 1.8 m and 3.6 m, both in prototype scale. As expected, the thicker soil cover (3.6 m) appeared to provide greater protection, in the form of reduced strains measured at different locations on the structures. For example, plots of axial strains measured at the top, quarter span are shown in Figure 2. These results have previously been presented and discussed in De & Zimmie [2007].

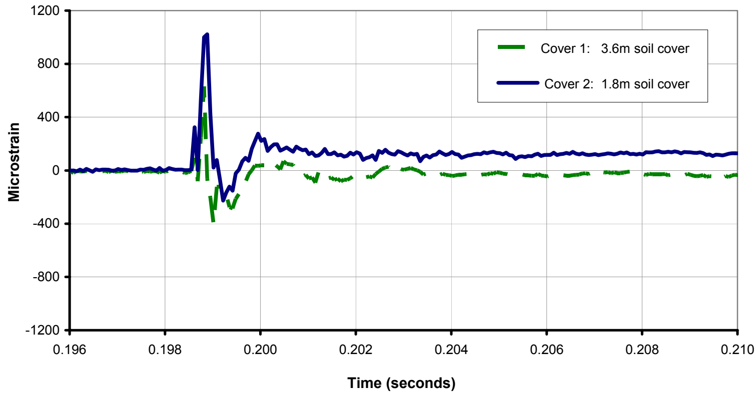

FIG. 2. Plots comparing effects of soil covers of 3.6 m and 1.8 m on axial strains measured at quarter-span on the top of the underground structure

Effects of Cover Material

The possible mitigating effects of a compressible inclusion barrier (CIB), made of polyurethane geofoam, were investigated. These tests were conducted with total cover thicknesses of either 1.8 m or 3.6 m (both in prototype scale). Interesting differences were observed in the axial strains recorded on the model structures in the two cases.

The case with a total cover thickness of 3.6 m included two different configurations of covers:

Cover 1: 3.6 m of compacted soil

Cover 4: 2.7 m of compacted soil and 0.9 m of geofoam CIB, with the geofoam in intimate contact with the structure and the soil extending to the ground surface

Comparison of axial strains recorded at different locations of the underground structure indicated that the presence of geofoam CIB appeared to mitigate the impact of the explosion, since smaller magnitudes of strains were recorded when Cover 4 was utilized. This is shown in the plots of axial strains measured at the top, quarter span are shown in Figure 3. These results have previously been presented and discussed in De & Zimmie [2007]. It is noted that there is no significant permanent strain in either case.

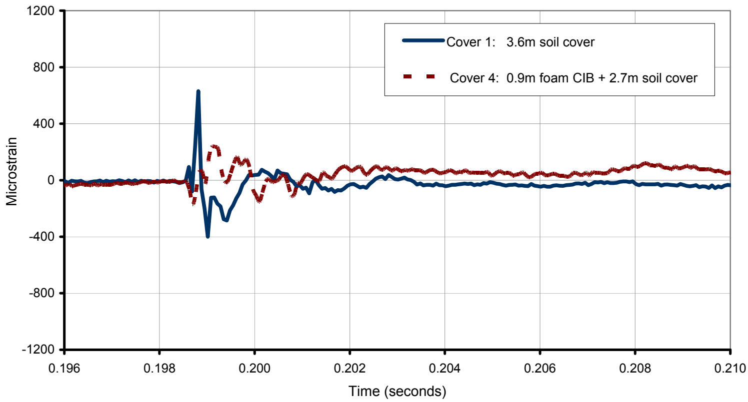

FIG. 3. Plots comparing effects of soil cover with soil plus geofoam cover, both to total thickness of 3.6 m, on axial strains measured at quarter-span on the top of the underground structure

The case with a total cover thickness of 1.8 m included two different configurations of covers:

Cover 2: 1.8 m of compacted soil

Cover 5: 0.9 m of compacted soil and 0.9 m of geofoam CIB, with the geofoam in intimate contact with the structure and the soil extending to the ground surface

In this case, the axial strains recorded at different locations on the model structure for the two conditions (Covers 2 and 5) were found to be comparable. For example, as shown in the plots of axial strains measured at the top, quarter span, shown in Figure 4 indicate similar magnitudes of strains in the two cases. In this case, the presence of the geofoam CIB does not appear to have any mitigating effect on the impact of the explosion on the underground structure. Also, there appears to be some permanent strains at the end of the period shown in the plots.

A comparison of plots on Figures 3 and 4 points to possible limitations of the mitigating effects of a geofoam CIB, placed in intimate contact with the underground structure. In the case of tests with a total cover thickness of 3.6 m, the presence of the geofoam CIB appears to mitigate the impact, with the recorded strains with Cover 4 significantly lower than those with Cover 1. However, in the case of tests with a total cover thickness of 1.8 m, the presence of the geofoam CIB appears to make no difference, with recorded strains of comparable magnitudes with Cover 2 and Cover 5. A possible explanation of this observation is presented in the next section.

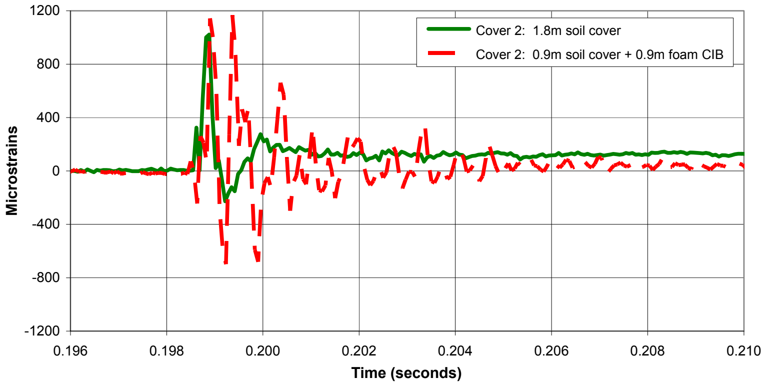

FIG. 4. Plots comparing effects of soil cover with soil plus geofoam cover, both to total thickness of 1.8 m, on axial strains measured at quarter-span on the top of the underground structure

DISCUSSION OF RESULTS

Crater Formation in Covers of Different Material over Underground Structures

For the tests reported here, the depth of the apparent crater, measured at the end of each test, was found to be between 1.1 m and 1.6 m, with an average depth of approximately 1.25 m, all dimensions in prototype scale. The true crater, formed at the time of the explosion, is larger than the apparent crater, since material ejected due to the explosion get a chance to settle into the crater (as “fallback”) before the apparent crater can be measured. There is no convenient means of measuring the depth of the true crater; however, this depth is of importance when studying the strains generated on the underground structure.

Crater Formation with Total Thickness of 3.6 m (Covers 1 and 4)

In the case where the total cover thickness was 3.6 m (Covers 1 and 4), the thickness of soil cover was 3.6 m (Cover 1) or 2.7 m (Cover 4). In both of these cases, the soil cover thickness exceeded the depth of the apparent crater (1.25 m depth) and likely that of the true crater (unknown depth, greater than 1.25 m). Observation of the model structure at the end of the tests indicated there was no visible damage (such as a dent) on the surface of the model structure closest to the crater. The strain gage measurements recorded during the tests also do not indicate any appreciable permanent strain on the model structure.

Crater Formation with Total Thickness of 1.8 m (Covers 2 and 5)

In the case where the total cover thickness was 1.8 m (Covers 2 and 5), the thickness of soil cover was 1.8 m (Cover 2) or 0.9 m (Cover 5). In both of these cases, the soil covers were either close to or less than the depth of the apparent crater (1.25 m depth). The depth of the true crater (greater than 1.25 m) most likely exceeded the soil cover thickness in each case.

A visible dent was observed on center top of the model structure, immediately below the location of the explosion, where Cover 2 (1.8 m of soil cover) was used. The strain gages recorded permanent strains on the model structure during these tests. The strain gages installed at the center top of the structure were permanently damaged due to the explosion. This indicates the possibility that the soil cover above the model structure was either completely or partially removed when the true crater was formed due to the explosion.

In the case of Cover 5 (0.9 m of soil cover and 0.9 m of geofoam cover), the apparent crater was 1.25 m deep, which exceeded the depth of the soil cover. After the test, a hole was observed in the geofoam CIB cover, exposing the model structure, immediately below the explosion location. This is shown in the photograph on Figure 5, taken after the test on Cover 5 was completed.

FIG. 5. Visible deformation on the model underground structure after test on Cover 5 (0.9 m of compacted soil and 0.9 m of geofoam CIB, dimensions in prototype scale)

CONCLUSIONS

Results from centrifuge model tests indicate important characteristics related to the effects of surface explosions on underground structures for various thicknesses and types of cover material. When the soil cover above the underground structure was well in excess of the depth of the apparent crater (e.g., 2.7 m of cover for 1.25 m deep apparent crater), no visible damage (such as dent) was observed on the model structure and no appreciable permanent strain was recorded. The presence of a geofoam CIB in intimate contact with the model structure appeared to mitigate the impacts of the explosion, as evidenced by reduced strains recorded at different locations on the model structure.

When the thickness of the soil cover above the underground structure was comparable to the depth of the apparent crater (e.g., 1.8 m of cover for 1.25 m deep apparent crater), a visible damage (dent) was observed on the model structure and the structure experienced permanent strains. In these cases, the explosion likely created a true crater which removed the soil cover (i.e., all of the soil cover was temporarily blown off), exposing the model structure. The presence of a geofoam CIB did not appear to have any mitigating effect in these cases and, where present, the geofoam cover appeared to have been easily penetrated by the crater.

The results presented here indicate that a soil cover of thickness well in excess of the maximum depth of the apparent crater provides protection against surface explosion. The presence of a compressible inclusion barrier (CIB), such as a geofoam layer, in intimate contact with the model structure mitigates the impact of the explosion by reducing strains, only when such barrier is located beyond the crater depth. When located within the crater depth, the geofoam CIB appears to be easily removed and provides no more protection than a soil cover.

ACKNOWLEDGEMENTS

The work reported in this paper was funded through an SGER grant and supplementary ROA grant provided by the Civil and Mechanical Systems Program of the National Science Foundation (NSF). The centrifuge experiments were conducted with the assistance of technical personnel at the Geotechnical Centrifuge Research Center at RPI, Troy, NY.

REFERENCES

De, A., and Zimmie, T. F. [2006], “Modeling of Surface Blast Effects on Underground Structures”, *Proceedings of GeoCongress 2006*, ASCE, Atlanta, Georgia.

De, A., and Zimmie, T. F. [2007], “Centrifuge Modeling of Surface Blast Effects on Underground Structures”, *Geotechnical Testing Journal*, ASTM, Vol. 30, No. 5.

Kutter, B.L., O’Leary, L.M., Thompson, P.Y., and Lather, R. (1988). “Gravity-scaled Tests on Blast-induced Soil-structure Interaction”, *Journal of Geotechnical Engineering*, American Society of Civil Engineers, Vol. 114, No. 4, pp. 431-447.

Schmidt, R. M. and Holsapple, K. A. (1980). “Theory and Experiments on Centrifuge Cratering”, *Journal of Geophysical Research*, Vol. 85, No. 1, pp. 235.

Taylor, R.N. (editor) (1995). *Geotechnical Centrifuge Technology*, Blackie Academic & Professional, Chapman and Hall, Glasgow.

Effect of Non-Plastic Fines on Cyclic Behaviour of Sandy Soils

T.G. Sitharam[1] and H.K. Dash[2]

[1] Professor, Department of Civil Engineering, Indian Institute of Science, Bangalore, INDIA -560 012; sitharam@civil.iisc.ernet.in
[2] Research Scholar, Department of Civil Engineering, Indian Institute of Science, Bangalore, INDIA - 560 012; hkdash@civil.iisc.ernet.in

ABSTRACT: This paper presents the results of the detailed studies on stress – controlled cyclic triaxial tests on sandy soils from Ahmedabad, Gujarat, India subjected to a loading frequency of 0.1 Hz in cyclic triaxial equipment. Undrained stress controlled cyclic triaxial tests were carried out on cylindrical samples of size 50 mm diameter and height 100 mm with different cyclic stress ratios. Laboratory evaluations were carried out to compare the cyclic resistance of clean sand to that of sand with various fines contents at a constant gross void ratio. The gross void ratio considers the voids formed by sand particles and fines. The effects of gross void ratio with and without fines on pore water pressure build up and liquefaction potential of sandy soils in stress controlled tests are presented. The results obtained from this study provide direct evidence that the limiting silt content plays an important role in the cyclic resistance of sandy soils. Below the limiting silt content the cyclic resistance decreases until the limiting silt content is reached and then the cyclic resistance increases.

INTRODUCTION

It is well established that the occurrence of liquefaction under seismic loading conditions is due to the generation of excess pore water pressure. Many investigators have studied the effects of different parameters on the pore water pressure buildup in saturated sands, liquefaction potential and dynamic properties of sandy soils subjected to cyclic loading in cyclic stress controlled triaxial tests. In stress-controlled triaxial tests, liquefaction and cyclic behavior of sandy soils are evaluated based on the earthquake-induced shear stresses and the shear stresses required to cause liquefaction. Most of the previous researchers have focused on the cyclic behavior of clean sands. However, sand deposits with fines may be as liquefiable as clean sands. The presence of fines generally is considered to resist the development of high pore water pressures during earthquake loading. However, the literature indicates that no clear conclusions can be drawn on the effect of fines content on the excess pore water pressure generation characteristics under cyclic loading, and in turn the liquefaction behavior.

Both clean sands and sands containing silt have been shown to be liquefiable in the field (Seed and Lee, 1966; Youd and Bennett, 1983), and also in laboratory (Lee and Seed, 1967; Casagrande 1975; Koester 1994; Polito and Martin, 2001). Non plastic silts, most notably mine tailings, have also been found to be liquefiable (Dobry and Alvarez, 1967; Garga and McKay, 1984). Though many laboratory studies have been performed world wide, the reported results appear to be conflicting. Several studies have reported that increasing the silt content of a sandy soil will either increase its resistance to liquefaction (Dezfulian, 1982; Amini and Qi, 2000) or decrease its resistance to liquefaction (Finn et al1994; Vaid, 1994 Lade and Yamamuro 1997; Yamamuru and Lade 1997; Zlatovic and Ishihara 1997). Some studies have reported that the resistance to liquefaction of sandy soils initially decreases with increase in silt content until some minimum resistance is reached and then increases as the silt content increases further (Koester, 1994). Finally, several other studies (Troncoso and Verdugo, 1985; Vaid, 1994) have reported that the liquefaction resistance of silty-sand is more closely related to its sand skeleton void ratio than to its silt content. In our work, we have carried out a detailed study evaluating cyclic resistance considering constant gross void ratio of the mixture, constant sand skeleton void ratio and constant relative density of the sand-silt mixtures. However, in this paper we present the results of the cyclic resistance of clean sand to that of sand with various fines contents at a constant gross void ratio.

SOIL TESTED

The sands in Bhuj, Ahmedabad and other areas in Gujarat, India contain large amounts of non-plastic fines. The grain size distribution of original Ahmedabad sand (Base Sand) and the clean sand are presented in Fig.1, which clearly highlights the presence of non-plastic fines of about 9.2%. To understand the effect of non-plastic fines on the cyclic resistance of sandy soils, the sand used in this study was Ahmedabad sand. This sand has 37% of medium sand, 53.8% of fine sand and 9.2% of silt. The clean sand was prepared by removing the silt portion by wet sieving the base sand using a 75 micron IS sieve. The clean sand had a mean grain size D_{50} of 0.3mm and its grains are sub-angular to sub-rounded in shape. Its specific gravity is 2.65. The sand mixtures were prepared by adding non-plastic quarry dust (<75micron) in different percentages (10%, 20%, 30%, 40%, 50% and 75%). The quarry dust used in this investigation as a substitute for silt consists of the fine grained portion of quarry dust from aggregate crusher plants in and around Bangalore(<75 micron). Quarry dust is a byproduct of rubble crusher units. It has a specific gravity of 2.67 and plasticity index of 1.57 and is non-plastic.

Six combinations of sand and silt were created using Ahmedabad clean sand with varying silt (quarry dust) contents from 10 to 75%. Additional tests were also performed on clean sand. Index properties including grain size distribution, specific gravity, and maximum and minimum index void ratios were determined for each soil mixture. Maximum void ratio was evaluated by loosely filling the mould (used for the vibratory table method) and then the vibratory table method was used to determine the minimum void ratio of the sand quarry dust mixtures as per the specification of IS: 2720 (Part 14)-1983. A plot of the maximum and minimum void ratios versus quarry dust content for the Ahmedabad sand mixtures is presented in Fig. 2.

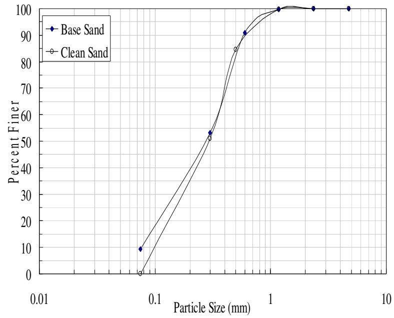

FIG. 1. Grain size distribution of soils used in the investigation

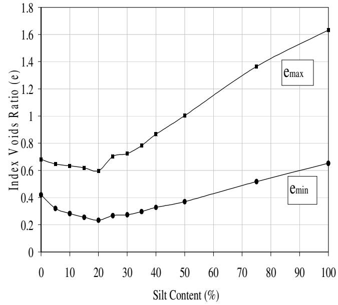

FIG. 2. Variation in index void ratios with silt content

CYCLIC TRIAXIAL TESTING

The cyclic resistance of the sand-quarry dust mixtures was determined using cyclic triaxial tests performed on reconstituted specimens. Testing was carried out using state of the art cyclic triaxial testing equipment. The equipment consists of a submersible load cell, an LVDT, and four transducers to detect chamber pressure, pore water pressure and lateral deformations. The triaxial cell is built with a low friction piston rod seal to which a submersible load cell of 5kN capacity is fitted. The loading system consists of a load frame and hydraulic actuator capable of performing strain-controlled as well as stress-controlled tests, with a frequency range of 0.01Hz to 10Hz, employing built-in sine, triangular and square wave forms. The equipment is computerized and servo-controlled.

The soil specimens tested were 50mm in diameter and 100mm in height. Samples were formed by the dry deposition method. The oven dried soil (quantity by weight) is filled into the rubber membrane lined split mould, which is fixed to the pedestal of the base plate, by means of a funnel having a nozzle of 12mm diameter with a long spout. To maintain uniform density over the entire range of the soil height, the soil was prepared in five layers and gently tamped in a symmetrical pattern to the sides of the sample mould. The number of tamping blows for each layer was pre-assessed for a particular density. The lower layers were prepared at a lesser density than the higher layers to maintain the uniform density throughout. Relative density was varied by 1% per layer.

After sample preparation was complete and the specimen was formed, CO_2 was passed through the specimen followed by de-aired water. Once a desired volume of water was collected, the specimen was saturated with sufficient back pressure to ensure Skempton's B parameter was greater than 95%. The specimens were then consolidated to an effective confining pressure of 100kPa. All void ratios reported here are post-consolidation void ratios, and relative densities are also based on the post-consolidation void ratios.

After the consolidation process was complete which took about 4 minutes (for clean sands) to 1 hour (for 75% quarry dust – sand mixture) and was dependent upon the nature of the soil and percentage of silt content, the drainage lines were closed and the LVDT was initialized to zero. The specimens were loaded with stress controlled cyclic loading (using a repeating uniform sine wave) and a constant peak deviator stress at the appropriate cyclic stress ratio (CSR), until they liquefied. Initial liquefaction was defined as the state at which the excess pore pressure in the specimen becomes equal to the initial effective confining pressure, or corresponding to 5% double amplitude axial strain. In this investigation, cyclic resistance was defined as the cyclic stress ratio required to cause initial liquefaction corresponding to 20 cycles of uniform loading.

Results of a typical cyclic triaxial test are presented in Fig. 3. The plots presented are from a test on Ahemdabad clean sand with an average post consolidation void ratio of 0.54 and Relative Density of 55%. In the figures, deviator stress (q), axial strain, pore pressure ratio (Ru) and mean effective stress (p') are plotted against cycles of loading. The deviator stress (q) is plotted against axial strains to show the hysteresis loop. A typical effective stress path is also presented. The specimen shown was loaded at a cyclic stress ratio (CSR) of 0.179 and has reached initial liquefaction at the 26th cycle.

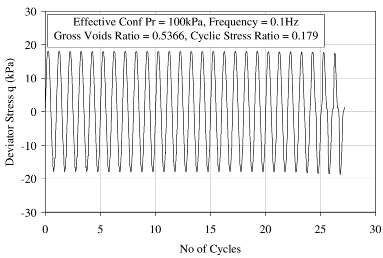

FIG. 3(a). Deviator stress vs. number of cycles

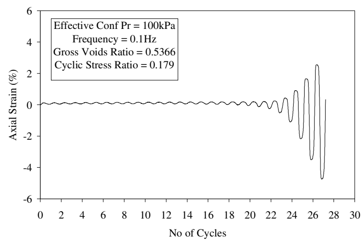

FIG. 3(b). Axial strain vs. number of cycles

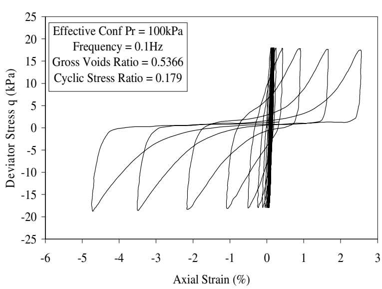

FIG. 3(c). Deviator stress vs. axial strain

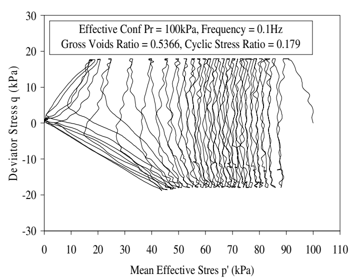

FIG. 3(d). Effective stress path

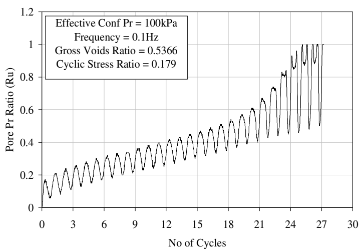

FIG. 3(e). Pore pressure ratio vs. number of cycles

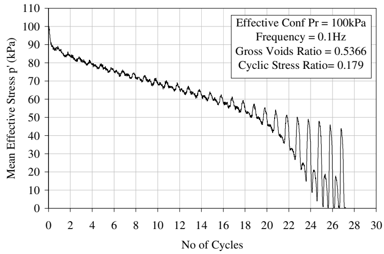

FIG. 3(f). Mean effective stress vs. number of cycles

FIG. 3. Typical cyclic triaxial test data

A set of curves showing the cyclic stress ratio (CSR) versus number of cycles to initial liquefaction is presented in Fig. 4 for different clean sand and quarry dust mixtures. The results of various tests on Ahemdabad clean sand, which had an average post consolidation void ratio of 0.54 and relative density (RD) of 55% is presented in Fig. 4. Corresponding to 20 uniform cycles, the cyclic resistance of clean sand is determined to be 0.185. Similarly, the cyclic resistances corresponding to 20 cycles for every combination of clean sand and silt up to a silt content of 75% have been determined and the results have been reported as CSR (in brackets) corresponding to each mixture in Fig. 4**.**

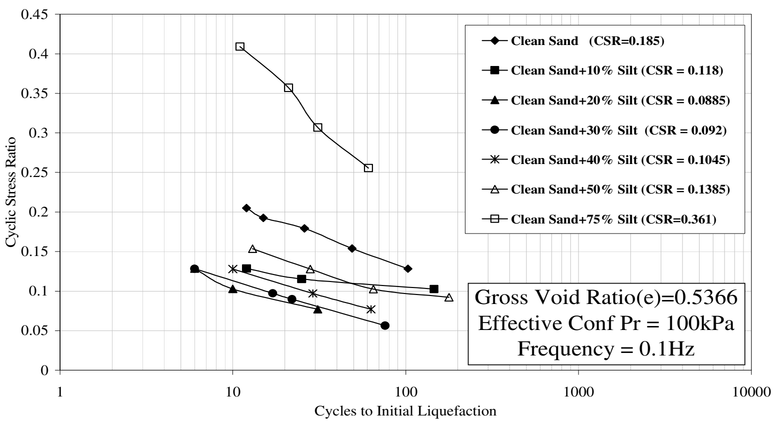

FIG .4. Cyclic resistances with various silt contents for a constant gross void ratio

RESULTS AND DISCUSSION

The cyclic resistances of various combinations of Ahemdabad clean sand and silts were evaluated using the techniques described earlier. Cyclic resistances were evaluated in terms of their void ratios. The void ratio of the specimens tested was found to be essentially independent of the silt content, except for the small effect that the amount of silt present has on the specific gravity of the sand silt mixtures. The void ratio solely depends on the weight of the soil used and volume of the specimen.

Initially, the effect of altering silt content on the cyclic resistance of soil specimens prepared to constant void ratio was examined. For the Ahemdabad sand an average post-consolidation void ratio of 0.54 (0.5366) was used. This void ratio was chosen since it was possible to prepare specimens over the entire range of silt contents investigated. All the tests were conducted using an effective confining pressure of 100kPa and a frequency of 0.1Hz. Fig. 5 plots the cyclic resistance versus the percentage of silt content in the clean sand-silt mixtures at a constant gross void ratio.

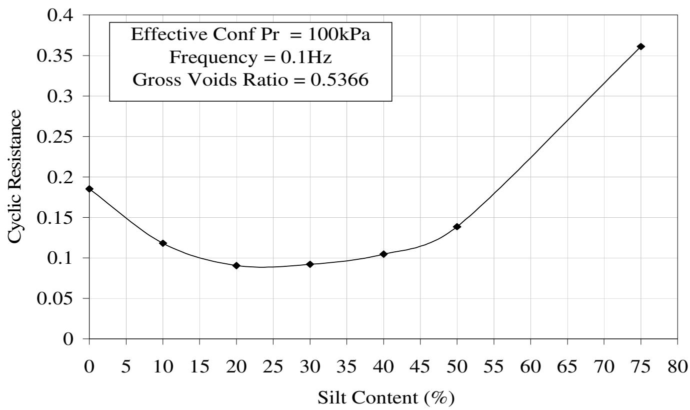

FIG.5. Cyclic resistance of Ahemdabad sand at constant gross void ratio vs. % silt content

As may be seen in Fig. 5, the cyclic resistance of the mixture of Ahemdabad clean sand and silt mixtures decreases rapidly as the silt content increases until a minimum cyclic resistance of 0.0905 is reached, corresponding to a silt content of 20%. With further increase in silt content, the cyclic resistance increases up to 50% silt content. Beyond this point there is a drastic increase in cyclic resistance. The cyclic resistance corresponding to 75% silt content is almost twice that of the cyclic resistance of clean sand at the same gross void ratio. The decrease and increase of cyclic resistance can also be attributed to changes in relative densities in the constant gross void ratio approach. The relative density of sand-silt mixtures decreases below the limiting silt content (26%) and relative density increases after this limiting silt content (can be seen in figure 2 in terms of e_{max} and e_{min}). The sharp rise in cyclic resistance may be due to the sharp rise in relative density (up to about 97% for 75% silt and clean sand mixture) beyond the limiting silt content (26% in this case). Also, it should be noted that it is difficult to prepare silt-sand mixture samples containing more than 75% silt at this gross void ratio. Secondly, the cyclic resistance of each combination of sand and silt was tested at various void ratios (which are not reported here). It was found that, for a given silt content, when the void ratio is varied, the cyclic resistance decreases as the void ratio increases. This behavior is similar to clean sands.

In summary, for specimens prepared to a constant gross void ratio, the cyclic resistance decreases as the silt content increases until some minimum value is reached, then increases with further increase in silt content. For a given silt content, when the void ratio is varied, the cyclic resistance decreases as the void ratio increases. This was found for both clean sand and sand-silt mixtures.

CONCLUSIONS

Two distinct behavioral patterns were observed from this study of sands with varying percentage of silt content at constant gross void ratio. Below the limiting silt content, where the sand matrix is generally a sand dominated structure, there is less resistance to dynamic loads. As the silt content increases the liquefaction resistance of sandy silt decreases until the amount of silt reaches a limiting fines content. Beyond the limiting fines content, the sand structure gradually transforms from a sand dominated to a silt dominated matrix, the cyclic resistance increases to about 50% silt content. Beyond 50% silt content, there is a drastic increase in cyclic resistance. For example the cyclic resistance at 75% silt content is almost twice the cyclic resistance of clean sand at the same gross void ratio.

ACKNOWLEDGEMENT

We acknowledge the Department of Science and Technology (DST), Seismology Division, Govt. of India, New Delhi, India for sponsoring the work presented in this paper.

REFERENCES

American Society for Tests and Materials (ASTM). “Standard test method for load controlled cyclic triaxial strength of soil” ASTM D 5311-92 (Re-approved 1996) ASTM, West Conshohoken, Pa.

Amini, F. and Qi, G. Z. (2000). “Liquefaction testing of stratified silty sands”. *J. Geotechnical and Geoenv. Engrg*., ASCE, Vol.126(3): 208-217.

Casagrande, A. (1975). “Liquefaction and cyclic mobility of sands. A critical review.” *Proc. 5th pan American conference on Soil Mechanics and Foundation Engrg*., Vol. 5: 80-133.

Dezfulian, H. (1982). “Effects of silt content on dynamic properties of sandy soils”. *Proc., 8th world conference on Earthquake Engrg*.: 63-70.

Dobry, R. and Alvarez, L. (1967). “Seismic failure of Chilean tailings dams” *J. of Soil Mechanics and Foundations Divn*., ASCE, Vol. 93(6): 237-260.

Garga, V. K. and McKay, L. D. (1984). "Cyclic triaxial strength of mines tailings." *J. of Geotechnical Engrg*, ASCE, Vol. 110(8): 1091-1105.

Ghionna, V. N. and Porcino, D. (2006). "Liquefaction resistance of undisturbed and reconstituted samples of a natural coarse sand from undrained cyclic triaxial tests." *J. Geotechnical and Geoenv. Engrg.*, Vol. 132(2): 194-202.

Govindaraju, L. (2005). "Liquefaction and dynamic properties of sandy soils." *PhD thesis* submitted to Indian Institute of Science, Bangalore in the Faculty of Engrg.

IS 2720(Part 14)-1983. "Method of test for soils: determination of density index (relative density) of cohesionless soils. *Bureau of Indian Standards*.

Koester, J. P. (1994). "The influence of fine type and content on cyclic resistance." *Ground Failures Under Seismic Conditions*, (GSP 44), ASCE, New York: 17-33.

Ladd, R. S. (1974). "Specimen preparation and liquefaction of sands." *J. Geotechnical Engineering Divn.*, ASCE, Vol. 100(10): 1180-1184.

Lade and Yamamuro (1997). "Effects of non-plastic fines on static liquefaction of sands." *Canadian Geotech J.*, Ottawa, Vol. 34: 918-928.

Lee, K. L. and Seed, H. B. (1967). "Cyclic stress conditions causing liquefaction of sand." *J. Soil Mechanics and Foundations Divn*, ASCE, Vol. 93(1): 47-70.

Polito, C. P. and Martin II, J. R. (2001). "Effects of nonplastic fines on the liquefaction resistance of sands." *J. Geotechnical and Geoenv. Engrg.*, Vol. 127(5): 408-415.

Ravishankar, B. V., (2006). "Cyclic and monotonic undrained behavior of sandy soils." *PhD thesis* submitted to Indian Institute of Science, Bangalore in the Faculty of Engineering.

Sitharam, T. G., Govindaraju, L. and Srinivasa Murthy, B. R. (2004). "Evaluation of liquefaction potential and dynamic properties of sandy soil using cyclic triaxial testing." *ASTM Geotechnical Testing J.*, Vol. 27(5): 427-429.

Troncoso, J. H. and Verdugo, R. (1985). "Silt content and dynamic behavior of tailing sands." *Proc., 12th Int Conf on Soil Mechanics and Foundation Engrg.*: 1311-1314.

Vaid, V. P. (1994). "Liquefaction of silty soils." *Ground Failure Under Seismic Conditions*, (GSP 44), ASCE, New York: 1-16.

Vaid, V. P., Sivathayalan, S. and Stedman, D. (1999). "Influence of specimen reconstituting method on the undrained response of sands." *Geotechnical Testing J.*, Vol. 22(3): 187-195.

Yamamuro, J. A. and Lade, P. V. (1997). "Static liquefaction of very loose sands." *Canadian Geotechnical J.*, Ottawa, Vol. 34: 905-917.

Liquefaction Susceptibility of Fine-Grained Soils in Charleston, South Carolina Based on CPT

Hossein Hayati[1], S.M. ASCE, and Ronald D. Andrus[2], M. ASCE, P.E.

[1]Graduate Research Assistant, Dept. of Civil Engineering, Clemson Univ., Clemson, SC 29634-0911; hhayati@clemson.edu
[2] Associate Professor, Dept. of Civil Engineering, Clemson Univ., Clemson, SC 29634-0911; randrus@clemson.edu

ABSTRACT: The liquefaction susceptibility of four fine-grained soils in Charleston, South Carolina was examined primarily using cone penetration test (CPT) measurements. Ages of these four soils range from <6,000 years to about 30 million years. The liquefaction susceptibility criteria by Robertson and Wride appear to be adequate for the three younger soils, which are estuarine deposits. However, as noted previously by Li et al., the criteria incorrectly predict liquefaction susceptibility for the oldest soil, called the Cooper Marl. The Cooper Marl is a deep marine deposit that consists of 60-80% calcium carbonate and often classifies as MH to CH, based on the Unified Soil Classification System. The results illustrate the usefulness of also measuring pore water pressure during cone testing in fine-grained soils, for classification and liquefaction evaluation. A new CPT-based liquefaction susceptibility chart for screening out non-susceptible fine-grained soils is proposed.

INTRODUCTION

A major cause of damage in the 1886 Charleston, South Carolina earthquake was liquefaction-induced ground deformation. From the report of Dutton (1889), numerous liquefaction craterlets and lateral spreads occurred throughout the epicentral region. Talwani and Schaeffer (2001) suggested a recurrence rate of about 500 years for similar magnitude 7+ earthquakes near Charleston, based on paleoliquefaction evidence.

To develop next-generation liquefaction hazard maps, as well as other seismic hazard maps of Charleston and the surrounding region, numerous cone penetration test (CPT) and small-strain shear-wave velocity (V_s) measurements have been compiled (Fairbanks et al. 2004; Andrus et al. 2006; Mohanan et al. 2006). The measurements were performed primarily by four different testing organizations (i.e., ConeTec, Gregg In Situ, S&ME, and WPC). All CPT measurements are from electrical cones with pore water pressure measurements, called piezocones.

Presented in this paper for the first time is a detailed discussion of the CPT-based characteristics of four fine-grained soil deposits beneath the peninsula of Charleston. From the discussion, criteria for identifying layers that are too clay rich to be susceptible to liquefaction are proposed. These criteria were adopted in the recent liquefaction potential mapping work by the authors (Hayati and Andrus 2008).

GEOLOGY

The peninsula of Charleston is located on the eastern seaboard of the United States. It is bounded on the east by the Cooper River and on the west by the Ashley River. Much of the low-lying tidal marsh areas of the peninsula adjacent to the rivers (designated as Qht on the geologic map by Weems and Lemon 1993) have been built up with artificial fill (af) during the past 300 years. The natural higher ground areas consist of two units of Pleistocene age. The older Pleistocene unit (Qws) is the barrier-island facies of the Wando Formation. The younger Pleistocene unit (Qhes) is beach deposits that flank the Wando Formation. Other Pleistocene sediments present in the subsurface include Holocene to Pleistocene estuarine deposits (Qhec) and estuarine to fluvial facies of the Wando Formation (Qwc). Underlying these Quaternary sediments is the Tertiary-age Cooper Group, locally known as the Cooper Marl. Brief descriptions of each geologic units are presented in Table 1.

Table 1. Description of near-surface geologic units beneath Charleston peninsula (adapted from Weems and Lemon 1993; Hayati and Andrus 2008).

Unit	Age (years)	Soil type	Typical cone tip resistance, q_t (MPa)	Typical shear-wave velocity, V_s (m/s)	Typical soil behavior type index, I_c	Typical pore pressure ratio, u_2/u_0
af	< 300	sand to clayey sand	3.1	160	not available	not available
Qht	< 5 k	clayey sand to clay, organic	0.5	100	3.2	3
Qhec	6-85 k	silty to sandy clay, sand	1.1	140	3.0	5
Qhes	33-85 k	fine-grained sand	2.6	140	not available	1
Qws	70-130 k	fine-grained sand	6.2	210	not available	1
Qwc	70-130 k	clayey sand to clay	1.6	180	3.0	6
Cooper Marl	~30 M	silty clay to clayey silt	3.6 top 25 m	400 top 25 m	2.4	10

Representative CPT, V_s, and geologic profiles are presented in FIG. 1. CPT tip resistances (q_t) have been corrected to account for the effect of pore pressure acting behind the cone tip (u_2). The friction ratio (*FR*) is defined as the cone sleeve resistance (f_s) measurement divided by q_t. Values of *FR* are usually much greater (over 1 %) in clayey soils than sandy soils. Thus, the materials at depths of 3-6.5 m, 10-12.5 m and 13.5-18 m are clayey soils of increasing ages. Between 7 m and 9 m, lower values of *FR* and values of u_2 near the hydrostatic line (u_0) indicate freely draining material, which are likely sand mixtures. Lower values of q_t and V_s indicate softer material.

At depths greater than 18.0 m in FIG. 1, the high u_2 and V_s values are distinct indicators of the Cooper Marl. The Marl is a well-compacted calcarenite with 60-80% calcium carbonate that classifies as silty clay to clayey silt. It is characterized by fairly uniform q_t profiles, u_2 values that typically exceed 1 MPa, and V_s values on the order of 400 m/s. The Marl is generally recognized to be non-susceptible to liquefaction (Li et al. 2007).

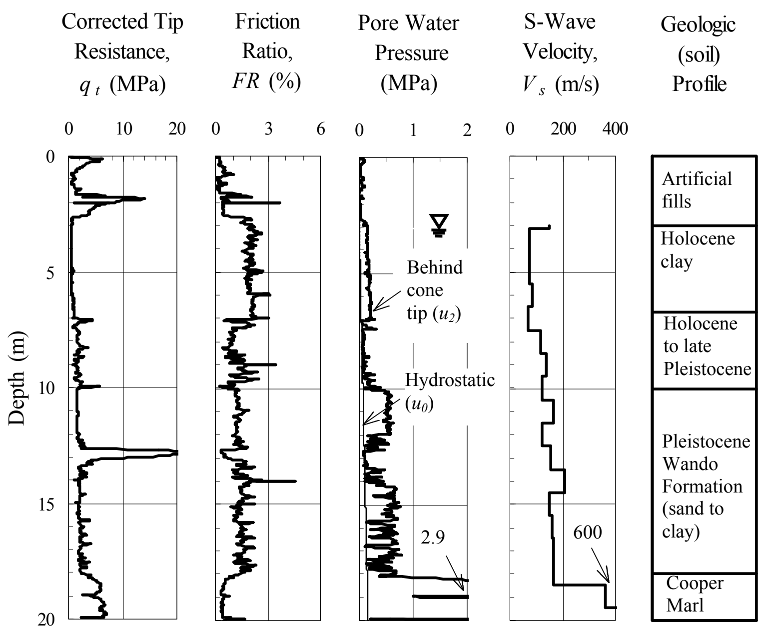

FIG. 1. Representative profiles of cone, V_s and geology from CPT site S01369-A5 (Fairbanks et al. 2004).

SOIL BEHAVIOR TYPE

Because soil samples are usually not collected as part of CPT investigations, soil type is often estimated from the two charts shown in FIG. 2. Lunne et al. (1997) suggested using the chart in FIG. 2a when u_2 measurements are not available. This chart is based on the normalized cone tip resistance, $Q_t = (q_t - \sigma_v)/\sigma'_v$, and the normalized cone friction ratio, $F_N = f_s/(q_t - \sigma_v)$ x100%, where σ_v is the in situ total vertical stress and σ'_v is the effective vertical stress. In FIG. 2b, the chart is based on Q_t and the normalized cone pore pressure ratio, $B_q = (u_2 - u_0)/(q_t - \sigma_v)$. When u_2 measurements are available, the use of both charts to classify the soil was recommended by Lunne et al. (1997).

Plotted on the soil behavior type charts in FIG. 2 are 79 data points from four fine-grained deposits in Charleston, consisting of 15, 5, 29 and 30 data points for Qht, Qhec, Qwc and Marl, respectively. The data are picked from layers with thickness of at least 1 m, lie below the ground water table, and exhibit uniform measurements with depth. In addition, to ensure that the material is fine grained, all 79 data points are for soils with mean $FR > 2\%$ or $u_2 > u_0$. The Marl data are from Li et al. (2007). The Quaternary data (i.e., Qht, Qhec, Qwc) are compiled as part of this study.

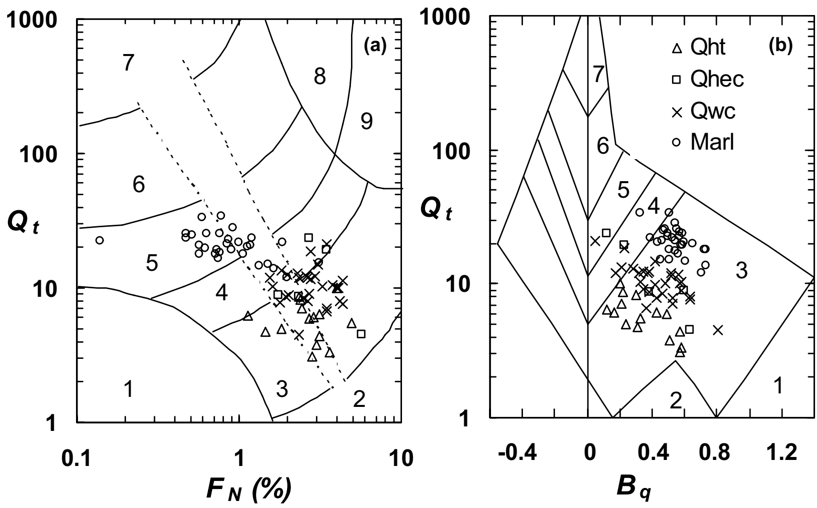

Zone	Soil behavior type
1.	Sensitive, fine grained;
2.	Organic soils, peats;
3.	Clays: clay to silty clay;
4.	Silt mixtures: clayey silt to silty clay;
5.	Sand mixtures: silty sand to sandy silt;

Zone	Soil behavior type
6.	Sands: clean sands to silty sands;
7.	Gravelly sand to sand;
8.	Very stiff sand to clayey sand;
9.	Very stiff fine grained.

FIG. 2. Soil behavior type classification charts by Robertson (1990) with data from four fine-grained soils in Charleston (modified from Li et al. 2007).

As noted by Li et al. (2007), 80% (23/30) of the Marl data lie in Zone 5 (sand mixture: silty sand to sandy silt) in the Q_t-F_N chart (see FIG. 2a); and 93% (28/30) of the Marl data lie in Zone 3 (clays: silty clay to clay) in the Q_t-B_q chart (see FIG. 2b). Laboratory Atterberg limit tests indicate that about 90% of the Marl in the top 25 m beneath the peninsula classifies as MH (sandy elastic silt) to CH (fat clay with sand), based on the Unified Soil Classification System. The classification of MH to CH is most consistent with Zones 3 and 4 (silt mixtures: clayey silt to silty clay) materials. Thus, the correct soil type for the Marl lies between the predictions provided by the two charts.

Concerning the Quaternary data, both charts provide similar predictions of soil type, as shown in FIG. 2. All of the Qht data plot in Zone 3 of both charts. For the Qhec data, 60% (3/5) lie in Zone 4 in the Q_t-F_N chart (see FIG. 2a) and 60% (3/5) lie in Zone 3 in the Q_t-B_q chart (see FIG. 2b). For the Qwc data, 72% (21/29) of the points lie in Zone 3 in the Q_t-F_N chart and 86% (25/29) lie in Zone 3 in the Q_t-B_q chart. Although Atterberg limit test information is not available for these soil deposits, the consistency between predictions by the two charts suggests an accurate assessment.

It is interesting to note that the data for the four units are separated best in the Q_t-B_q chart (see FIG. 2b). The data points of Qht and Marl, which are the youngest and the oldest units, fall in two distinct zones and are separated by the Qhec and Qwc data points. The distinct separation in Qht and Marl data is likely due to the significant differences in their age, chemistry, and overconsolidation ratio (OCR). The OCR is around 1 for Qht and 3-6 for the Marl (Camp 2004). The overlap of the Qhec and Qwc data may be attributed to more similar age, chemistry, and OCR.

SUSCEPTIBILITY CRITERIA

Soils that are too clay rich are generally considered not susceptible to liquefaction (e.g., Seed and Idriss 1982; Robertson and Wride 1998; Youd et al. 2001; Idriss and Boulanger 2004; Bray and Sancio 2006). Robertson and Wride (1998) suggested soils with F_N > 1.0 % and "soil behavior type index" > 2.6 and are not likely to liquefy. The soil behavior type index, I_c, is defined by (Lunne et al. 1997):

$$I_c = \left[\left(3.47 - \log_{10} Q_t\right)^2 + \left(\log_{10} F_N + 1.22\right)^2 \right]^{0.5} \tag{1}$$

An I_c value of 2.6 approximately represents the circular boundary separating Zones 4 and 5 in FIG. 2a. Youd et al. (2001) noted that the cutoff of I_c > 2.6 was overly conservative for some soils and recommended that soils with I_c of 2.4-2.6 be tested to assess their liquefaction susceptibility.

Represented in FIG. 3a are the CPT-based liquefaction susceptibility criteria recommended by Robertson and Wride (1998) and Youd et al. (2001). Plotted on this chart are the Marl data compiled by Li et al. (2007) and the Quaternary data compiled as part of this study. About 53% (16/30) of the Marl data lie in the zone of "susceptible." All of the Quaternary data plot in the zone of "not susceptible."

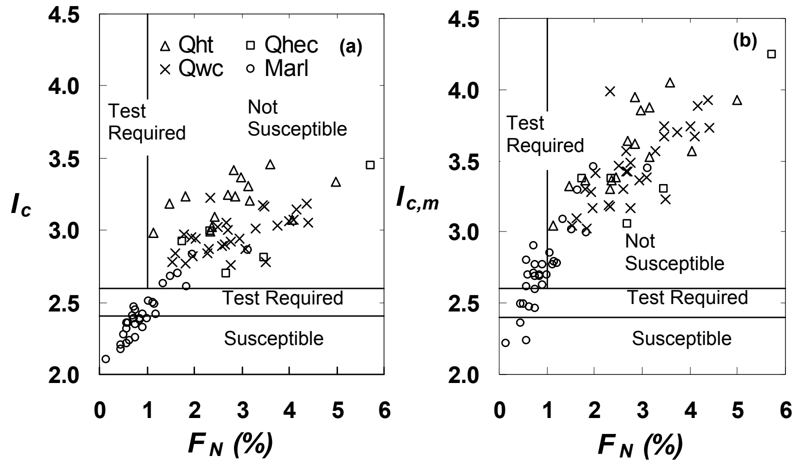

FIG. 3. CPT-based liquefaction susceptibility charts based on (a) I_c versus F_N and (b) $I_{c,m}$ versus F_N with data from four fine-grained soils in Charleston (modified from Li et al. 2007).

In an attempt to improve the prediction for the Marl, Li et al. (2007) considered a modified soil behavior type index developed by Lewis and his colleagues at the Savannah River Site, South Carolina. This modified soil behavior type index, $I_{c,m}$, is expressed as:

$$I_{c,m} = \left[\left(3.25 - \log_{10}\left[Q_t(1-B_q)\right]\right)^2 + \left(1.5\left[\log_{10} F_N + 1\right]\right)^{2.25} \right]^{0.5} \quad (2)$$

Presented in FIG. 3b is the CPT-based susceptibility chart based on $I_{c,m}$ with the Charleston data re-plotted. It can be seen that only 10% (3/30) of the Marl data lie in the susceptible zone. However, a limitation of the prediction shown in FIG. 3b is that 53% (16/30) of the Marl data still lie in the zone of "test required." This number is much greater than the 16% (6/37) that lie in the "test required" (or "moderately susceptible") zone using the criteria by Bray and Sancio (2006) based on Atterberg limit tests (Li et al. 2007).

As an alternative, the criteria of Robertson and Wride (1998) can be modified to $I_c > 2.6$ or $B_q > 0.5$ for identifying soils that are non-susceptible to liquefaction. Soils with $I_c < 2.4$ and $B_q < 0.4$ are considered susceptible. In between these limits soils are considered moderately susceptible and, therefore, another test may be required. Concerning sensitive fine-grained soils (Zone 1), they can be identified by $I_c > 5.7\text{-}2.3B_q$. These limits are based on the classification charts shown in FIG. 2 and the soil data for the four fine-grained soils. They are expressed graphically in FIG. 4. With this new chart (FIG. 4), 23% (7/30) of the Marl data lie in the "susceptible" or "test required" zone, which agrees well with the 22% predicted by the Atterberg-based assessment presented in Li et al. (2007).

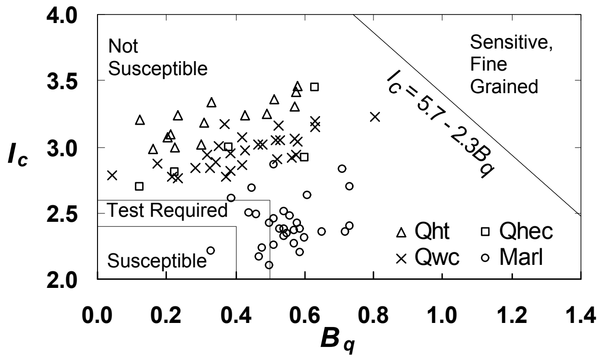

FIG. 4. Proposed CPT-based liquefaction susceptibility based on I_c and B_q.

CONCLUSIONS

The cutoff I_c value of 2.6 suggested by Robertson and Wride (1998) appears to be adequate for identifying the three Quaternary-age, fine-grained estuarine soils as non-susceptible to liquefaction. However, as previously noted by Li et al. (2007), the deep marine sediments of the Cooper Marl have typical I_c values around 2.4 and are incorrectly predicted to be susceptible by the Robertson and Wride (1998) criteria. It is proposed that the criteria be modified to $I_c > 2.6$ or $B_q > 0.5$ for identifying soils that are too clay rich or plastic to liquefy; and $I_c > 5.7\text{-}2.3B_q$ for identifying sensitive fine-grained soils. These modified criteria are expressed graphically in FIG. 4.

ACKNOWLEDGMENTS

This research was supported by the United States Geological Survey, Department of the Interior, under grant number 06HQGR0058, and the National Science Foundation, under grant number CMS-0556006. Any opinions, findings, and conclusions or recommendations expressed in this material are those of the authors and do not necessarily reflect the views of the United States Geological Survey or the National Science Foundation. The authors also thank the many individuals who assisted with data collection, in particular, William Camp and Timothy Cleary of S&ME; Thomas Casey and William Wright of WPC; and Cedric Fairbanks, Nisha Mohanan and the late Aniket Shrikhande former students at Clemson.

REFERENCES

Andrus, R. D., Fairbanks, C. D., Zhang, J., Camp, W. M. III, Casey, T. J., Cleary, T. J. and Wright, W. B. (2006). "Shear-wave velocity and seismic response of near-surface sediments in Charleston, South Carolina," *Bulletin of the Seismological Society of America*, Vol. 96 (5): 1897-1914.

Bray, J. D. and Sancio, R. B. (2006). "Assessment of liquefaction susceptibility of fine-grained soils," *J. Geotechnical & Geoenv. Engrg.,* Vol. 132 (6): 1165-1177.

Camp, W. M., III (2004). "Site characterization and subsurface conditions for the Cooper River Bridge," *Geotechnical Engrg. for Transportation Projects* (GSP 26), M. K. Yegain and E. Kavazanjian, eds., ASCE, Reston, VA: 347-360.

Dutton, C. E. (1889). "The Charleston earthquake of August 31, 1886," *USGS Ninth Annual Report 1887-1888*, U.S. Geological Survey, Washington, D.C., 203-528.

Fairbanks, C. D., Andrus, R. D., Zhang, J., Camp, W. M., Casey, T. J. and Clearly, T. J. (2004). "Electronic files of shear-wave velocity and cone penetration test measurements from the Charleston quadrangle, South Carolina," Data report to U.S. Geological Survey, Clemson Univ., Clemson, SC.

Hayati, H. and Andrus, R. D. (2008). "Liquefaction potential map of Charleston, South Carolina based on the 1886 earthquake," *J. Geotechnical & Geoenv. Engrg.,* accepted for publication.

Idriss, I. M. and Boulanger, R. W. (2004). "Semi-empirical procedures for evaluating liquefaction potential during earthquakes," *Proc., 11th Int. Conf. on soil Dynamics and Earthquake Engrg. (SDEE) & 3rd Int. Conf. on Earthquake Geotechnical Engrg. (ICEGE),* Berkeley, CA: 32-56.

Li, D. K., Juang, C. H., Andrus, R. D. and Camp. W. M. (2007). "Index properties-based criteria for liquefaction susceptibility of clayey soils: a critical assessment," *J. Geotechnical & Geoenv. Engrg.,* Vol. 133 (1): 110-115.

Lunne. T., Robertson, P. K. and Powel, J. J. M. (1997). *Cone Penetration Testing in Geotechnical Practice*, Blackie Academic and Professional, London.

Mohanan, N. P., Fairbanks, C. D., Andrus, R. D., Camp, W. M., Clearly, T. J., Casey, T. J. and William B. Wright (2006). "Electronic files of shear wave velocity and cone penetration test measurements from the greater Charleston area, South Carolina," Data report to U.S. Geological Survey, Clemson Univ., Clemson, SC.

Robertson, P. K. (1990). "Soil classification using the cone penetration test," *Canadian Geotechnical J.*, Vol. 27 (1): 151-158.

Robertson, P. K. and Wride, C. E. (1998). "Evaluating cyclic liquefaction potential using the cone penetration test," *Canadian Geotechnical J.*, Vol. 35(3): 442-459.

Seed, H. B. and Idriss, I. M. (1982). "Ground motions and soil liquefaction during earthquakes," EERI Monograph, Oakland, CA.

Talwani, P. and Schaeffer, W. T. (2001). "Recurrence rates of large earthquakes in the South Carolina Coastal Plain based on paleoliquefaction data," *J. Geophys. Res.*, Vol. 106: 6621-6642.

Weems, R. E. and Lemon, E. M. Jr. (1993). "Geology of the Cainhoy, Charleston, Fort Moultrie, and North Charleston Quadrangles, Charleston and Berkley Counties, South Carolina," *USGS Misc. Investigation Map I-1935, scale 1:24,000*, Department of the Interior, U.S. Geological Survey, Reston, VA.

Youd, T. L., Idriss, I. M., Andrus, R. D., Arango, I., Castro, G., Christian, J. T., Dobry, R., Finn, W. D. L., Harder, L. F. Jr., Hynes, M. E., Ishihara, K., Koester, J. P., Liao, S. S. C., Marcuson, W. F. III, Martin, G. R., Mitchell, J. K., Moriwaki, Y., Power, M. S., Robertson, P. K., Seed, R. B. and Stokoe, K. H. II (2001). "Liquefaction resistance of soils: summary report from the 1996 NCEER and 1998 NCEER/NSF workshops on evaluation of liquefaction resistance of soils," *J. Geotechnical & Geoenv. Engrg.*, Vol. 127 (10): 817-833.

LOW STRAIN SHEAR MODULUS OF SAND-CLAY MIXTURES

S.V.Dinesh,[1], A.M. ASCE, S.Yamada[2] and M. Hyodo[3]

[1]Professor, Department of Civil Engineering, Siddaganga Institute of Technology, Tumkur, India: NPEEE Postdoctoral research fellow, Yamaguchi University, Japan; dineshsv2004@yahoo.com
[2]Assistant Professor, Department of Civil Engineering, University of Tokyo, Japan; suguru@geot.t.u-tokyo.ac.jp
[3]Professor, Department of Civil Engineering, Yamaguchi University, Japan; hyodo@yamaguchi-u.ac.jp

ABSTRACT: This paper presents the results of hollow cylindrical torsion shear tests of remoulded sand-clay mixtures presented in terms of equivalent shear modulus. The clay samples were obtained from six different sites covering river deposits and marine sites, with wide range of plasticity. Two types of sand-clay mixtures with different plasticity were prepared by mixing sand in different proportions. Hollow cylindrical torsion tests were carried out on remoulded clays, remoulded sand-clay mixtures and undisturbed clays & sand-clay mixtures. The objective of this experimental investigation is the low strain shear modulus of sand-clay mixtures. The results of initial shear modulus are reported. The effect of fines content, plasticity index and confining pressure are examined.

INTRODUCTION

Dynamic deformation characteristics of soil namely shear modulus and damping are input parameters for soil dynamic problems such as ground response analysis, soil structure interaction problems, response of marine sediments and marine structures to wave induced cyclic loading. Several researchers have carried investigations and empirical relationships have been proposed for the dynamic properties of clays, such as Hardin and Black (1968, 1969), Marcuson and Wahls (1972), Kokusho et al. (1982) and Vucetic and Dobry (1991). These relationships hold good for clays and clays with negligible amount of sand. In practice, in-situ deposit consists of sand, silt and clays in different proportions. It is expected that for clays of low plasticity containing substantial amount of sand, may show increased stiffness with increase in the percentage of sand fraction. Therefore, it is difficult to generalize the above relationships for predicting dynamic properties of sand-clay mixtures.

In the present work, a series of undrained hollow cylindrical torsion shear tests have been carried out on remoulded soil samples to determine the shear modulus of sand-clay mixtures. Clay samples with wide range of plasticity were obtained from different sites. The clay was mixed with silica sand in various proportions. The results were compared with the existing empirical relationship proposed by Zen et. al., (1987).

MATERIALS AND EXPERIMENTAL METHOD

For the present investigation, natural clay samples were obtained from six different sites designated as Ariake A, Ariake B, Ariake C (samples from river deposits), Itsukaichi, Onoda and Dejima clays (samples from marine origin obtained from ports) in Japan. Table 1 shows the physical properties and figure 1a shows the grain size distributions of these natural soil samples. Ariake C and Onoda clay deposits were used to prepare sand-clay mixtures. Silica sand was mixed in the range of 0 to 70%. Figures 1b, 1c and 1d show the grain size distributions of Ariake C, Onoda and undisturbed Dejima sand-clay mixtures. Table 2 shows the physical properties of remoulded sand-clay mixtures. The values (100, 80, 60, 40 and 30) indicated besides the sample name in figures and table refers to the ratio of dry weight of clay with respect to the total weight of the mixture. These mixtures have wide range of plasticity from I_P = 16 to 111 and fines content varying from 25 to 100%.

Table 1. Physical properties of natural soil samples.

Name of sample		**Properties**				
Type of sample	**Name of source**	**Specific gravity (Gs)**	**Fines content (%)**	**Liquid limit (%)**	**Plastic limit (%)**	**Plasticity Index (Ip)**
Remoulded clay	Ariake A	2.60	98.3	89.09	41.36	47.7
	Ariake B	2.72	87.9	83.47	39.87	43.6
	Ariake C	2.59	100.0	155.34	44.33	111.0
	Onoda	2.60	84.5	84.04	34.58	49.5
	Itsukaichi	2.69	98.6	109.59	34.54	75.1
Undisturbed Dejima clay	C-5 T-4	2.59	99.1	116.75	34.53	82.2
	C-5 T-12	2.67	96.6	134.10	36.70	97.4
	C-8 T-2	2.68	99.9	113.80	29.32	84.5
	C-8 T-11	2.70	43.0	38.08	22.04	16.0

Sample Preparation and Hollow Cylindrical Torsion Shear Test

Remoulded samples were prepared with initial water content twice that of liquid limit. The slurry was consolidated in a perspex cell of 30cm diameter and 40 cm height to a pressure of 10 and 20 kPa. Each pressure increment was maintained for 24 hours. The sample was then subjected to a one dimensional consolidation of 50 kPa and subsequently test specimens were prepared. The testing was performed using hollow cylindrical torsion shear test equipment. Hollow cylindrical specimens of 7.5

cm outer diameter, 3.5cm inner diameter and 10 cm height were cut from a block of clay prepared as explained above.

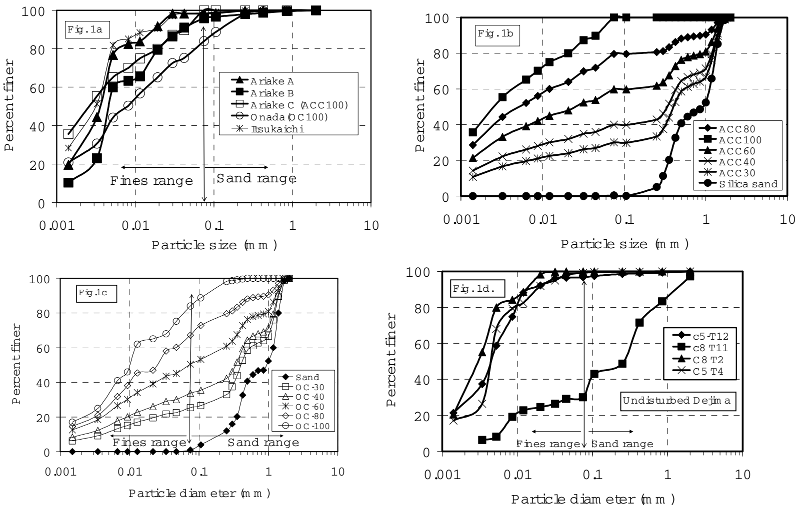

FIG. 1. Grain size distribution curves of natural and remoulded sand-clay soil samples.

Table 2. Physical properties of remoulded sand-clay mixtures.

Name of sample		**Properties**				
Type and source of sample	**Sample designation**	**Specific gravity (Gs)**	**Fines content (%)**	**Liquid limit (%)**	**Plastic limit (%)**	**Plasticity Index (Ip)**
Remoulded Onoda clay mixtures	OC-100	2.60	84.5	84.0	35.7	48.3
	OC-80	2.61	67.0	69.2	24.4	44.8
	OC-60	2.62	50.0	63.2	22.6	40.6
	OC-40	2.63	32.5	55.4	21.4	34.0
	OC-30	2.63	25.3	47.0	20.6	26.4
Remoulded Ariake C mixtures	ACC-100	2.59	100.0	155.3	44.33	111.0
	ACC-80	2.60	79.5	138.4	40.1	98.3
	ACC-60	2.61	59.7	124.3	36.0	88.3
	ACC-40	2.62	39.9	108.5	31.5	77.0
	ACC-30	2.63	29.8	95.5	28.1	67.3

Hollow cylindrical specimens were subjected to a confining pressure of 30 kPa and a back pressure of 100kPa. The saturation time was maintained till the Skempton's pore pressure coefficient exceeds 0.95. Then the specimens were anisotropically consolidated with Ko=0.5, corresponding to a mean effective stress of σ'_{mc} = 66.7, 100, 133.3 kPa (σ'_{vc}=100, 150, 200 kPa). Hollow cylindrical torsional tests were carried out as per JGS-2000. All the specimens were subjected to sinusoidal cyclic loading at a frequency of 0.1Hz and 11 cycles were applied in each loading stage. The dynamic properties were calculated from the 10^{th} cycle data. There were 270 data points per load cycle at 0.1Hz frequency.

EQUIVALENT SHEAR MODULUS (G_{eq}) CHARACTERISTICS:

The equivalent shear modulus of remoulded clays, remoulded sand-clay and undisturbed soil samples are shown in figure 2 corresponding to a mean effective principal stress of 66.7 kPa at a frequency of 0.1 Hz for a wide range of single amplitude shear strain (γ_{SA}) from 0.00001 to 1%. The solid lines represent the hyperbolic relationship as per Hardin and Drnevich (1972) given by Eq.1.

$$\frac{G_{eq}}{G_0} = \frac{1}{1+(\gamma)_{SA}/\gamma_r} \tag{1}$$

Where, G_{eq} is the equivalent shear modulus, G_o is the initial shear modulus corresponding to a strain level of γ_{SA}=0.0001% and γ_γ is the reference strain. Figure 2a shows the equivalent shear modulus versus single amplitude shear strain for remoulded natural clays from various sources. Onoda clay has 85% fines while all other samples have close to 100%. The results are in agreement with the general trend of increase in the equivalent shear modulus with reduction in plasticity. Figures 2b and 2c show the equivalent shear modulus variation for Ariake C (river sediment) and Onoda (port clay) mixtures respectively. Higher equivalent shear modulus is observed in samples with low fines content, the magnitude of increase is more than double as the fines content is reduced to 30%. This indicates stiffening of the sample due to sand matrix. Similar trend is observed in figure 2d for undisturbed Dejima clay samples. Three samples (C8T2, C5T12 and C5T4) are pure clays with fines content of nearly 100% with high plasticity and one sample (C8T11) has 43% fines content with low plasticity.

The results of undisturbed and remoulded samples follow the general trend, that clays of low plasticity and soil samples with substantial amount of sand have higher initial shear modulus. The equivalent shear modulus of all samples begins to show degradation from 0.01% single amplitude shear strain level. However, at large strains beyond 0.1% strain level, the effect gets nullified and all samples show the same stiffness irrespective of the variation in fines content.

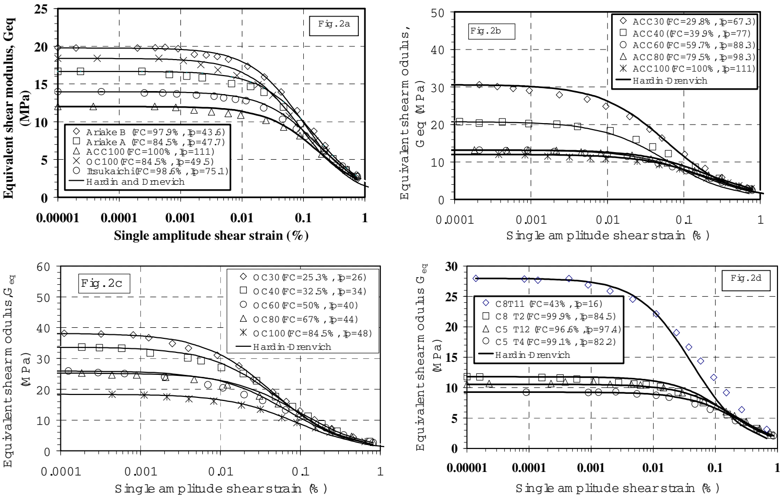

FIG. 2. Equivalent shear modulus versus single amplitude shear strain.

Effects of Fines Content and Plasticity

Figure 3 shows the relationship between equivalent shear modulus and fines content for all the sand-clay mixtures considered in the present investigation corresponding to σ'_{mc} = 66.7 kPa and f = 0.1 Hz. At low strain levels, fines content has significant influence on the equivalent shear modulus. All remoulded soils which have large fines content close to 100% show low initial shear modulus depending on the plasticity whereas for Onoda and Ariake C mixtures containing substantial amount of sand, initial shear modulus increases with reduction in fines content. It is clearly observed from fig. 3 that when fines content is around 50% or less the initial shear modulus is more than twice when compared with its value for soils containing close to 100% fines. The initial shear modulus versus fines content relationship shows distinct separate curves for each of these mixtures. At the same fines content, Onoda mixtures show higher initial shear modulus when compared to Ariake C mixtures owing to low plasticity index. Even the undisturbed Dejima clay with 43% fines content shows the same trend.

It is reported in literature that the initial shear modulus depends to a large extent on the plasticity index for soils containing significant fines (Zen et. al., 1987 and Kokusho et. al., 1982). Figure 4 shows the plot of initial shear modulus versus plasticity index for sand-clay mixtures considered in the present experimental investigation. Also the predictive relationship proposed by Zen et. al., (1987) is shown. The predictive relationship shows a linear trend and gives a lower shear modulus than the present experimental results. The Zen et.al., (1987) relationship is predominantly developed for soils with large amount of fines with plasticity index greater than 30. Sand-clay mixtures of different origin show distinctly separate curves.

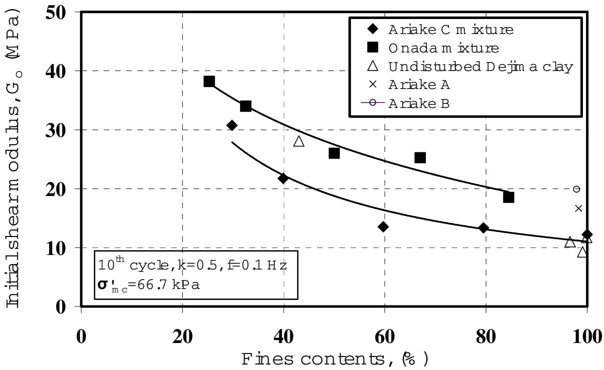

FIG. 3. Initial shear modulus versus fines content.

It is clearly observed that there is no unique relationship between initial shear modulus and plasticity index for sand-clay mixtures. However, clays with large fines content with large plasticity index show initial shear modulus close to the predictive relationship of Zen et. al., (1987). The initial shear modulus of undisturbed Dejima soil samples and Itsukaichi samples with higher plasticity index are close to the predictive relationship and the Zen et. al., (1987) relation serves as lower bound values. This clearly brings out the fact that the plasticity index doesn't correlate well with the initial shear modulus of sand-clay mixtures and there is clearly a need to develop an empirical relationship to predict the initial shear modulus of sand-clay mixtures.

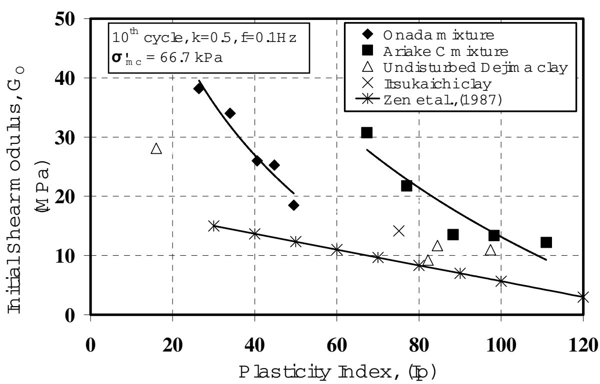

FIG. 4. Initial shear modulus versus plasticity index

Figure 5 shows the initial shear modulus versus effective mean principal stress for Onoda sand-clay mixtures. Initial shear modulus increases with increase in confining pressure. The magnitude of increase is higher with confining pressure for samples with increase in sand content and low plasticity. Similar trend is observed for Ariake C mixtures and remoulded natural soil samples.

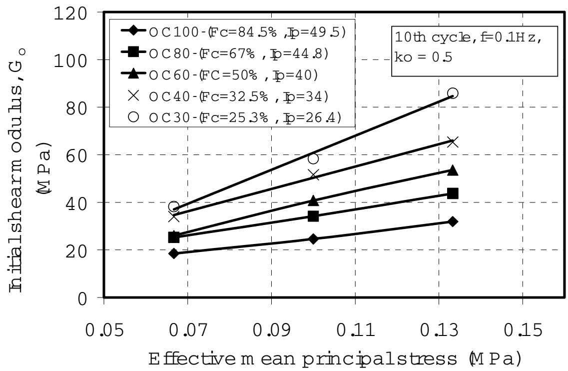

FIG. 5. Initial shear modulus versus effective mean principal stress.

CONCLUSIONS

This paper presents the dynamic properties of remoulded sand-clay mixtures of both river bed and marine origin with a wide range of plasticity obtained by conducting hollow cylindrical torsion shear tests. The results of shear modulus is analyzed in terms of fines content, plasticity and confining pressure. The results were compared with the existing empirical relationship. The important findings from the study are summarized below.

1. The experimental equivalent shear modulus corresponds well with the Hardin and Drnevich recommendations for the entire range of strain amplitude.
2. The initial shear modulus of sand-clay mixtures increases with decrease in fines content and shows a strong dependence on the fines content.
3. The predictive relation of Zen et. al (1987) can serve as lower bound values for soils with large fines content and plasticity.
4. There is no unique relationship between the conventional plasticity index and initial shear modulus for sand-clay mixtures.
5. The initial shear modulus increases with increase in confining pressure and the magnitude of increase is more with increase in the amount of sand and low plasticity.

ACKNOWLEDGEMENTS

The first author acknowledges the help and support of Prof. Masayuki Hyodo of Yamaguchi University, Japan, during his postdoctoral research program and also thank the Department of Science and Technology, Govt. of India for funding the research project No. DST/23(534)/SU/2005.

REFERENCES

Hardin, B.O. and Black, W.L. (1968). “Vibration modulus of normally consolidated clay.” *Journal of the Soil Mechanics and Foundation Engineering Division,* ASCE, Vol.94, SM2: 353-369.

Hardin, B.O. and Black, W.L. (1969). “Closure to vibration modulus of normally consolidated clay.” *Journal of the Soil Mechanics and Foundation Engineering Division,* ASCE, Vol.95, SM6: 1531-1537.

Hardin, B.O. and Drnevich, V.P. (1972). “Shear modulus and damping in soils: Design equations and curves,” *Journal of the Soil Mechanics and Foundation Engineering Division,* ASCE, Vol.98, SM7: 667-692.

Japanese Geotechnical Society (2000). “Cyclic tests for deformation characteristics.” *Soil Testing Methods and Explanation*, First Revised Edition, Vol. 7, Chapter 7: 678-697 (in Japanese).

Kokusho, T. Yoshida, Y. and Esashi, Y. (1982). “Dynamic properties of soft clay for wide strain range.” *Soils and Foundations*, Vol.22, No.4: 1-18.

Marcuson, W.E. and Wahls, H.E. (1972). “Time effects on dynamic shear modulus of clays.” *Journal of the Soil Mechanics and Foundation Engineering Division,* ASCE, Vol.98, SM12: 1359-1373.

Vucetic, M. and Dobry, R. (1991). “Effect of soil plasticity on cyclic response.” *Journal of Geotechnical Engineering*, ASCE, Vol.117, No.1: 89-107.

Zen, K. Yamazaki, H. and Umehara, Y. (1987). “Experimental study on dynamic properties of soils for use in seismic response analysis.” *Report of Port and Harbour Research Institute*, Vol. 26, No. 1.

Seismic Passive Earth Pressure Coefficients by Pseudo-Dynamic Method using Composite Failure Mechanism

B Munwar Basha[1] and G L Sivakumar Babu[2]

[1]Research Scholar, Department of civil engineering, Indian Institute of Science, Bangalore, 560012, Karnataka, India, basha@civil.iisc.ernet.in

[2]Associate Professor, Department of Civil Engineering, Indian Institute of Science,Bangalore-560012 India, Email:gls@civil.iisc.ernet.in, Tel.: + 91-80-22933124, fax:+ 91-80-23600404

ABSTRACT: The paper presents a new formulation for the use of pseudo-dynamic method to compute the passive earth pressure coefficients of bridge abutment gravity retaining walls by using composite (combination of log-spiral and planar) failure mechanism in the framework of limit equilibrium method when subjected to seismic loads. Numerical optimization of passive earth pressure coefficients is performed using the “improved Nelder-Mead simplex method” which is a direct search algorithm in the optimization of nonlinear functions and also accounts for variable bounds. Predictions by the present method are compared with those given by other authors. It is shown that the pseudo-static methods overestimate the passive earth pressure coefficients due to non-consideration of the effect of time and phase difference due to finite shear wave and primary wave velocities.

1. INTRODUCTION

The conventional method for the calculations of seismic passive earth pressure is the Mononobe and Okabe method. Based on the classical limit equilibrium theory, this method is a direct modification of the Coulomb wedge method where the earthquake effects are replaced by a pseudo-static inertia forces (Kramer 1996). But in the pseudo-static method, the dynamic nature of earthquake loading is considered in a very approximate way. The phase difference due to finite shear wave propagation behind a retaining wall can be considered using a simple and more realistic pseudo-dynamic method, proposed by Steedman and Zeng (1990). Choudhury and Nimbalkar (2005) considered the case of passive earth pressure behind a retaining wall by a pseudo-dynamic method using planar failure surface.

Terzaghi (1943) reported that planar rupture surfaces seriously overestimate the passive pressures for higher wall friction angles. Curved rupture surfaces result in more acceptable values of passive pressures. Duncan and Mokwa (2001) reported the experimental results and concluded that the logarithmic spiral earth pressure theory provides more accurate estimates of passive pressures for conditions where the interface friction angle is more than about 40% of the angle of internal friction of backfill. Morrison and Ebeling (1995) reported that the Mononobe and Okabe equation assumes a planar failure surface, which is not the most critical mode of failure for determining the passive failure load. Soubra (2000) and Kumar (2001) used the limit analysis method along with curved rupture surfaces for the computation of passive earth pressures. But the case of passive earth pressure behind a retaining wall by the pseudo-dynamic method using curved rupture surface has not received any attention so far. Hence, in this paper, the pseudo-dynamic method is applied to determine the seismic passive resistance behind a rigid retaining wall by considering composite failure mechanism in the framework of limit equilibrium method.

2. COMPOSITE FAILURE MECHANISM

As suggested by Terzaghi (1943), the developing failure surface can be realistically represented by a logarithmic spiral and a straight line as shown in Fig. 1. Logarithmic spiral portion of the failure surface (GJ) is governed by height of the retaining wall (H_1G) and the location of centre of the logarithmic spiral arc (A). As shown in Fig.1, The logarithmic spiral starts at the initial radius AG joins the conjugate failure surface of wedge MNJ. AJ lies on a ray of the logarithmic spiral zone that must pass through the center of the logarithmic spiral arc. As a result, the location of the center of the log-spiral curve (A) can be accurately defined based on the subtended angle 'θ_1' as shown in Fig. 1.

The present pseudo-dynamic method considers finite shear and primary wave velocities within the backfill soil. The phase and the magnitude of horizontal and vertical accelerations are varying along the depth of the wall. Consider the rigid gravity wall bridge abutment of height $= H$ supporting horizontal cohesionless backfill as shown in Fig. 2. The present method considers finite primary wave velocity (v_p) and shear wave velocity (v_s) within the backfill soil. As the primary wave and shear wave approach the ground surface, the vibrations are also amplified. The amplified motions with in the backfill soils and retaining wall may have devastating effects on bridge abutments. It is assumed that the horizontal and vertical seismic accelerations in soil vary linearly from the input seismic acceleration at the base to the higher value at the top of the wall.

3. COMPUTATION OF PASSIVE EARTH PRESSURE

In the present analysis it is assumed that the base of the wall is subjected to both the horizontal and vertical harmonic vibrations with amplitude of accelerations $k_h g$ and $k_v g$ respectively, where g is the acceleration due to gravity. Similar to Choudhury and Nimbalkar (2007) analysis, it is also assumed that both the horizontal and vertical vibrations start at exactly the same time and there is no phase shift between these two vibrations. The horizontal and vertical accelerations at any depth (z) below the top of the wall and any time (t) with soil amplification factor (f) are given by,

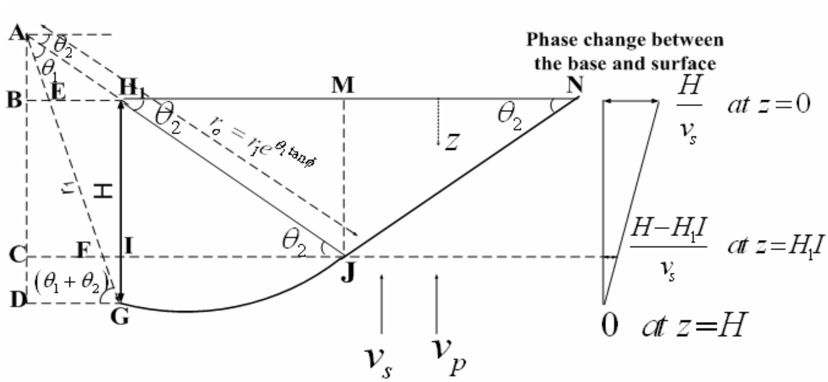

FIG. 1. Composite failure mechanism

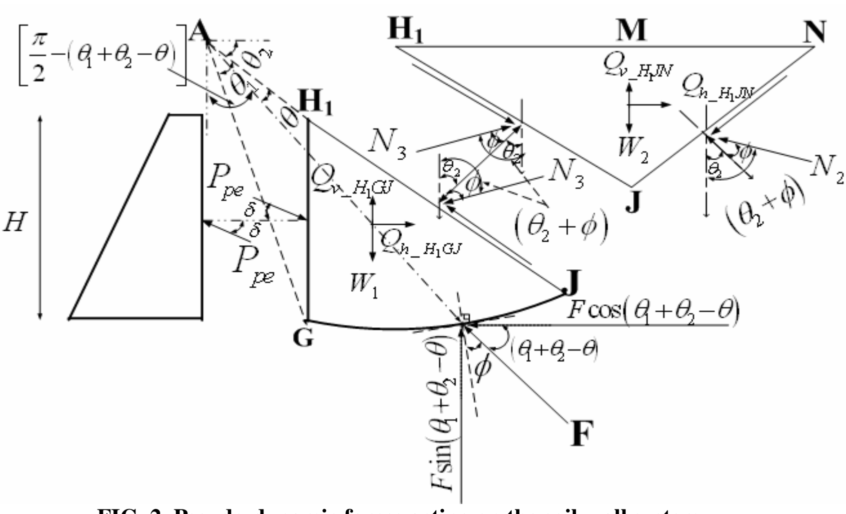

FIG. 2. Pseudo-dynamic forces acting on the soil-wall system

$$a_h(z,t) = \left(1 + \frac{H-z}{H}(f-1)\right) k_h g \sin\omega\left(t - \frac{H-z}{v_S}\right) \tag{1}$$

$$a_v(z,t) = \left(1 + \frac{H-z}{H}(f-1)\right) k_v g \sin\omega\left(t - \frac{H-z}{v_p}\right) \tag{2}$$

The principle of superposition is assumed to be valid and total horizontal and vertical inertial forces acting on the part of logarithmic spiral wedge H_1GJ can be expressed as follows: The total horizontal inertial force acting on H_1GJ is given by,

$$Q_{h\_H_1GJ} = Q_{h\_H_1IJ} + Q_{h\_IGJ} \tag{3}$$

The total vertical inertial force acting on H_1GJ is given by,

$$Q_{v\_H_1GJ} = Q_{v\_H_1IJ} + Q_{v\_IGJ} \tag{4}$$

where $Q_{h\_H_1IJ}, Q_{v\_H_1IJ}, Q_{h\_IGJ}$ and Q_{v_IGJ} are horizontal and vertical inertial forces acting on H_1IJ and IGJ respectively. These inertial forces can be calculated as discussed below (the details of integration are given in Figs. 3(a), 3(b) and 4)

$$Q_{h\_H_1IJ}(t) = \int_0^{H_1I} \frac{\gamma}{g} z\cot\theta_2 \left[f + \frac{z}{H}(1-f) \right] k_h g \sin\omega\left(t - \frac{H-z}{v_S} \right) dz \tag{5}$$

After integration, Eq. (5) is reduced to

$$\frac{Q_{h\_H_1IJ}(t)}{0.5\gamma H^2} = 2k_h \cot\theta_2 \left\{ \begin{array}{l} f\left[\left(\frac{1}{2\pi}\frac{\lambda}{H} \right)^2 \{\sin 2\pi\xi_1 - \sin 2\pi\xi_2\} - \left(\frac{1}{2\pi}\frac{\lambda}{H} \right)(hi)\cos 2\pi\xi_1 \right] \\ +(1-f)\left[\begin{array}{l} -\left(\frac{1}{2\pi}\frac{\lambda}{H} \right)(hi)^2 \cos 2\pi\xi_1 + \left(\frac{1}{2\pi}\frac{\lambda}{H} \right)^2 2(hi)\sin 2\pi\xi_1 \\ +2\left(\frac{1}{2\pi}\frac{\lambda}{H} \right)^3 (\cos 2\pi\xi_1 - \cos 2\pi\xi_2) \end{array} \right] \end{array} \right\} \tag{6}$$

In Eq. (6) the terms ξ_1, ξ_2, H_1I, hi and H are defined as follows:

$$\xi_1 = \left(\frac{t}{T} - \frac{H}{\lambda}(1-hi) \right);\ \ \xi_2 = \left(\frac{t}{T} - \frac{H}{\lambda} \right);\ H_1I = r_o \sin\theta_2 \left[1 - e^{-\theta_1\tan\phi} \frac{\cos(\theta_1+\theta_2)}{\cos\theta_2} \right] \tag{7}$$

$$hi = \frac{H_1I}{H} = e^{\theta_1\tan\phi} \frac{\sin\theta_2\cos\theta_2}{\sin\theta_1} \left[1 - e^{-\theta_1\tan\phi} \frac{\cos(\theta_1+\theta_2)}{\cos\theta_2} \right];\ H = \left(\frac{\sin\theta_1}{\cos\theta_2} \right) r_1 \tag{8}$$

The vertical inertial force acting on the wedge H_1IJ can be written as follows:

$$Q_{v\_H_1IJ}(t) = \int_0^{H_1I} \frac{\gamma}{g} z\cot\theta_2 \left[f + \frac{z}{H}(1-f) \right] k_v g \sin\omega\left(t - \frac{H-z}{v_p} \right) dz \tag{9}$$

Similar to the derived equation of horizontal inertial force, $Q_{h\_H_1IJ}(t)$, final equation for vertical inertial force, $Q_{v\_H_1IJ}(t)$ can be obtained by replacing k_h and λ by k_v and η in Eqn (6) respectively.

Various parameters in the above equations are defined as follows: r_1 = initial radius of the log-spiral wedge (AGJ), r_o = final radius of the log-spiral wedge (AGJ), θ_1 = subtended angle of log-spiral wedge (AGJ), θ_2 = the angle of the failure plane with the horizontal ground surface, γ = unit weight of the backfill soil, ϕ = friction angle of the backfill soil, t = time, T = period of lateral shaking ($= 2\pi/\omega$), $\lambda = Tv_s$ is the wavelength of the vertically propagating shear wave through the backfill, $\eta = Tv_p$ is the wavelength of the vertically propagating primary wave through the backfill and ω = angular frequency of the base shaking. The horizontal inertial force acing on IGJ is given by,

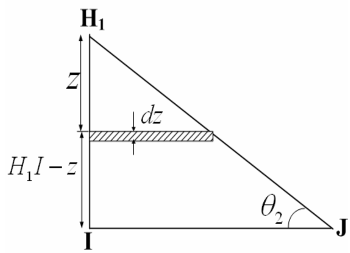

FIG. 3(a). Integration details of wedge H_1IJ

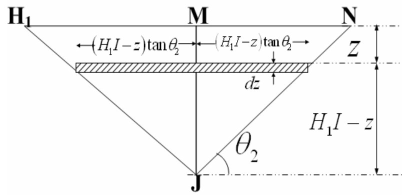

FIG. 4. Integration details of wedge H_1NJ

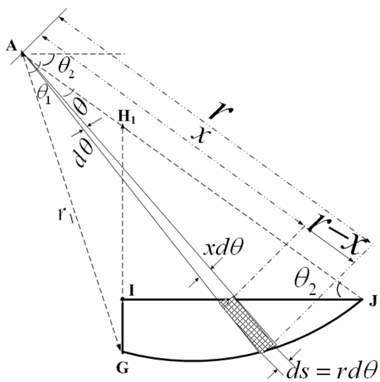

FIG. 3(b). Integration details of wedge IGJ

$$Q_{h\_IGJ}(t) = \int_{H_1I}^{GI} m(\theta)\, a_h(\theta,t)\, d\theta \tag{10}$$

where $m(\theta)$ is mass of elemental strip in the wedge IGJ as shown in Fig. 3(b) is

$$m(\theta) = \frac{\gamma}{g}\frac{1}{2}\left(r.rd\theta - x.xd\theta\right) = \frac{\gamma}{2g}\left(r^2 - x^2\right)d\theta, \text{ where } x = \frac{r_o \sin\theta_2}{\sin\left(\theta_2 + \theta\right)} \tag{11}$$

$a_h(\theta,t)$ is the horizontal acceleration in the wedge IGJ is given by

$$a_h(\theta,t) = \left\{1 + \frac{H - H_1I - (r-x)\sin(\theta_2+\theta)}{H}\left(f-1\right)\right\}k_h g \sin\omega\left(t - \frac{H - H_1I - (r-x)\sin(\theta_2+\theta)}{v_s}\right) \tag{12}$$

Similar to the derived equation of horizontal inertial force, $Q_{h\_IGJ}(t)$, the vertical inertial force, $Q_{v\_IGJ}(t)$ can be obtained by replacing k_h and v_s by k_v and v_p in Eqn (12) respectively. The horizontal and vertical inertial forces $Q_{h\_IGJ}(t)$ and $Q_{v\_IGJ}(t)$ are computed in Mathematica (Wolfram Research, Inc. 2007) by converting the trigonometric sine function into Taylor's series expansion (see equation 12). The horizontal inertial forces acting on the wedge H_1NJ can be computed as follows:

$$Q_{h\_H_1NJ}(t)=\int_0^{H_1I}\frac{\gamma}{g}z\cot\theta_2\left[f+\frac{z}{H}(1-f)\right]a_h\sin\omega\left(t-\frac{H-z}{v_S}\right)dz \qquad (13)$$

after integration, we obtain the following final form of Eq. (15) as given below:

$$\frac{Q_{h\_H_1NJ}(t)}{0.5\gamma H^2}=4k_h\tan\theta_2\left\{\begin{array}{l}\left(\frac{1}{2\pi}\frac{\lambda}{H}\right)^2(\sin 2\pi\xi_2-\sin 2\pi\xi_1)+\left(\frac{1}{2\pi}\frac{\lambda}{H}\right)(hi)\cos 2\pi\xi_2\\ +(1-f)\left[-2hi\left(\frac{1}{2\pi}\frac{\lambda}{H}\right)^2\sin 2\pi\xi_1+2\left(\frac{1}{2\pi}\frac{\lambda}{H}\right)^3\left[\cos 2\pi\xi_2-\cos 2\pi\xi_1\right]\right]\end{array}\right\} \qquad (14)$$

The vertical inertial force acting on the wedge H_1NJ can be expresses as follows:

$$Q_{v\_H_1NJ}(t)=\int_0^{H_1I}\frac{\gamma}{g}z\cot\theta_2\left[f+\frac{z}{H}(1-f)\right]k_v g\sin\omega\left(t-\frac{H-z}{v_p}\right)dz \qquad (15)$$

Similar to the derived equation of horizontal inertial force, $Q_{h\_H_1NJ}(t)$, final equation for vertical inertial force, $Q_{v\_H_1NJ}(t)$ can be obtained by replacing k_h and λ by k_v and η in Eqn. (14) respectively.

3.1. Derivation of Passive Resistance

The passive earth pressure $P_{pe}(t)$ can be obtained by resolving the forces on the two wedges H_1GJ and H_1NJ as explained below. By considering the horizontal equilibrium condition ($\sum H=0$) for the log-spiral wedge H_1GJ, we get,

$$-Q_{h\_H_1GJ}+F_H+N_3\sin(\theta_2+\phi)=P_{pe}\cos\delta \qquad (16)$$

where F_H can be estimated as

$$F_H=\int_0^{\theta_1}F\cos(\theta_1+\theta_2-\theta)d\theta = F\left[\sin(\theta_1+\theta_2)-\sin\theta_2\right] \qquad (17)$$

F = resultant force acting along the radial line of the logarithmic spiral and δ = wall friction angle. By considering the vertical equilibrium condition ($\sum V=0$) for the log-spiral wedge H_1GJ we get,

$$F_V-P_{pe}\sin\delta=N_3\cos(\theta_2+\phi)+\left(W_1-Q_{v\_H_1GJ}\right) \qquad (18)$$

where N_3 = resultant force acting between the log-spiral and triangular wedge, W_1 = weight of the log-spiral wedge H_1GJ.

and F_V can be estimated as

$$F_V=\int_0^{\theta_1}F\sin(\theta_1+\theta_2-\theta)d\theta = F\left[\cos\theta_2-\cos(\theta_1+\theta_2)\right] \qquad (19)$$

the horizontal equilibrium condition ($\sum H=0$) for the wedge H_1NJ, results in

$$N_2\sin(\theta_2+\phi)-Q_{h\_H_1JN}=N_3\sin(\theta_2+\phi) \qquad (20)$$

the vertical equilibrium condition ($\sum V=0$) for the wedge H_1GJ, results in

$$N_2 \cos(\theta_2 + \phi) + N_3 \cos(\theta_2 + \phi) = \left(W_2 - Q_{v\_H_1JN}\right) \tag{21}$$

where N_2 = resultant force acting on linear plane JN of triangular wedge H_1NJ , W_2 = weight of the triangular wedge H_1NJ . By solving the above four equations, passive earth pressure is obtained as follows:

$$P_{pe} = \frac{\left[\begin{array}{l}\left[0.5\left(W_2 - Q_{v\_H_1NJ}\right)\tan(\theta_2 + \phi) + 0.5Q_{h\_H_1NJ}\right]\left[\cot(\theta_2 + \phi)\cot(\theta_1/2 + \theta_2) + 1\right] \\ + \left(W_1 - Q_{v\_H_1GJ}\right)\cot(\frac{\theta_1}{2} + \theta_2) - Q_{h\_H_1GJ}\end{array}\right]}{\left[\cos\delta - \sin\delta\cot(\theta_1/2 + \theta_2)\right]} \tag{22}$$

Seismic passive earth pressure coefficient is given by,

$$K_{pe} = \left(2P_{pe}\left(t\right)\right)/\left(\gamma H^2\right) \tag{23}$$

3.2 Determination of the critical failure surface

The purpose of optimization is to locate the critical failure surface in order that K_{pe} achieves a minimum. In this paper, numerical optimization of passive earth pressure coefficients is performed using the "improved Nelder-Mead simplex method" (Luersen and Riche 2004).

Table 1. **A comparison of static and seismic passive earth pressure coefficients**

Static passive earth pressure coefficients ($k_h = 0$ and $k_v = 0$)						
ϕ (in degrees)	$\delta = 0$			$\delta = \phi$		
	Kumar and Subba Rao (1997)	**Soubra (2000)**	**Present**	**Kumar and Subba Rao (1997)**	**Soubra (2000)**	**Present**
15	1.70	1.70	1.68	2.22	2.25	2.26
25	2.46	2.46	2.44	4.42	4.51	4.44
35	3.69	3.69	3.69	10.76	11.13	10.80

Seismic passive earth pressure coefficients for k_v = 0							
ϕ (in degrees)	k_h	$\delta = 0$			$\delta = \phi$		
		Kumar (2001) (Pseudo-static)	**Soubra (2000) (Pseudo-static)**	**Present (Pseudo-dynamic)**	**Kumar (2001) (Pseudo-static)**	**Soubra (2000) (Pseudo-static)**	**Present (Pseudo-dynamic)**
40	0.0	5.83	5.83	5.83	36.95	38.61	36.97
	0.15	5.49	5.46	5.43	34.08	35.56	28.80
	0.30	5.05	5.07	5.06	31.02	32.33	20.12

3.3 Comparison of K_{pe} *Values*

Table 1 presents a comparison of K_{pe} values obtained in the present study and the values obtained on the basis of limit equilibrium technique by employing the composite logarithmic failure surface both for static (Kumar and Subba Rao 1997) and the pseudo-static cases (Soubra 2000 and Kumar 2001) for typical values of friction angles, ϕ = 15°, 25°, 35° and δ/ϕ = 0 and 1.0. It can be seen from the Table 1 that the three approaches compare reasonably well for static case. It confirms the validity the present formulation. The values of K_{pe} predicted by the pseudo-dynamic method are lower than pseudo-static methods reported in Soubra (2000) and Kumar (2001) and the difference increases for higher values of δ.

Conclusions

The study proposes a new formulation and computation of passive earth pressure coefficients using pseudo-dynamic method considering the composite failure mechanism for the design of gravity wall bridge abutments. Pseudo-static methods overestimates the passive earth pressure coefficient (K_{pe}) values due to the limitations of pseudo-static analysis such as non-consideration of the effect of time and phase difference due to finite shear wave and primary wave velocities.

References

Choudhury, D., and Nimbalkar, S. (2005). “Seismic passive resistance by pseudo-dynamic method.” *Geotechnique*. 55(9): 699–702.

Choudhury, D., and Nimbalkar, S. (2007). “Seismic rotational displacement of gravity walls by pseudo-dynamic method: passive case.” *Soil Dynamics and Earthquake Engineering*, 27, 242–249.

Duncan, J.M., and Mokwa, R.L. (2001). ‘Passive earth pressures: theories and tests.” *J. Geoechnical and Geoenvironmental Engrg. ASCE*, 127 (3) 248 – 257.

Kramer, S. L. (1996). *Geotechnical earthquake engineering*. Upper Saddle River, NJ: Prentice Hall.

Kumar, J. (2001). “Seismic passive earth pressure coefficients for sands.” *Canadian Geotech. J.* 38: 876–881.

Luersen, M.A., and Riche, R.L. (2004). "Globalized Nelder–Mead method for engineering optimization." *Computers and Structures*, 82, 2251-2260.

Morrison, E.E., and Ebeling, R.M. (1995). “Limit equilibrium computation of dynamic passive earth pressure.” *Canadian. Geotech. J.* 32: 481–487.

Steedman, R.S. and Zeng, X. (1990). “The influence of phase on the calculation of pseudo-static earth pressure on a retaining wall.” *Geotechnique*. 40(1): 103–112.

Soubra, A. H. (2000). “Static and seismic passive earth pressure coefficients on rigid retaining structures.” *Canadian. Geotech. J.* 37: 463–478.

Terzaghi, K. (1943). “Theoretical soil mechanics.” Wiley, New York.

Wolfram Research, Inc. (2007). “*Mathematica tutorial for Integration*.” http://reference.wolfram.com/mathematica/tutorial/Integration.html.

Analysis of Alternatives to Mitigate Erosion of Sacramento River Levee

Rebecca L. Money[1], M. ASCE and Ali Porbaha[2], M. ASCE

[1]Project Engineer, Kleinfelder Inc., Sacramento, California, bmoney@kleinfelder.com
[2]Geotechnical Eng. Faculty, Department of Civil Engineering, California State University, Sacramento, 6000 J Street, Sacramento, California 95819-6029, porbaha@ecs.csus.edu

ABSTRACT: This study presents a series of analyses performed to evaluate various construction alternatives to mitigate the erosion affecting a portion of Sacramento River levee. Engineering analyses include evaluation of seepage potential, analysis of the slopes for stability, settlement and cost analysis. The mitigation alternatives that are being considered include adding rock on the waterside of the existing levee, widening the existing levee slopes with imported soil, or constructing a new levee inland of the existing levee (a setback levee). Based on the engineering and cost analyses it is concluded that a setback levee using on-site soils constructed with 4H:1V slopes, a 10.7 m (35 ft) deep slurry cutoff wall, and internal drains is the most cost effective and environmentally conscious solution that fulfills all required mitigation needs.

INTRODUCTION

Flooding is an event that can cause millions of dollars in damage to farms, houses, and businesses. Many government agencies are given the task of preventing flooding to the best of their ability. A few years ago the Sacramento Area Flood Control Agency (SAFCA) evaluated the levees that surround the Sacramento River in Sacramento and Sutter Counties. Erosion of portions of riverbank adjacent to these levees was noticed in a stretch at the southern portion of Sutter County. The erosion was so significant that SAFCA determined that some kind of remediation would need to be performed in order to prevent a levee break that could flood the new growth area of Natomas in the Sacramento valley.

The objective of this study is to analyze various construction alternatives to mitigate the riverbank erosion affecting an existing portion of the Sacramento River levee. Engineering analyses include evaluation of seepage potential, slopes stability, settlement, and construction costs. The mitigation alternatives that are being considered include adding rock on the waterside of the existing levee, widening the existing levee slopes with imported soil, or constructing a new levee inland of the existing levee (a setback levee). Details of other issues and impacts of these alternatives are presented by Money (2006).

PROJECT BACKGROUND

Erosion is occurring along the outside of a bend in the Sacramento River passing the south of the Natomas Cross Canal in Sutter County, California. At this location the current is swift and has more potential to impact the river channel and possibly the levee. If the water rises out of the river channel the levee will be subjected to the forces of the river. The raise in water level will increase the size of the existing eroded area and if the erosion expands into the levee, failure would be highly likely. A levee failure along this portion of the Sacramento River would send an uncontrolled amount of water raging toward the thousands of new homes in Natomas, the Sacramento International Airport, and inundate portions of four major highways. The ramifications of a levee failure at this location would be catastrophic not only for Natomas residents but for all residents and traffic in Northern California.

The discovery of advanced erosion conditions led to a fast paced investigation of the site that included geotechnical studies, laboratory testing, and engineering analyses to determine what needed to be done to improve this portion of the levee in order to prevent a potential failure. Based on these findings, various construction alternatives were recommended. However, during preliminary analysis of erosion mitigation alternatives two of the three alternatives, riprap placed along erosion area and levee widening, were discarded due to environmental issues discussed in Money (2006).

The third alternative, setback levees are a method used to strengthen portions of existing levees experiencing various forms of degradation. Degradation usually includes erosion of the existing levee or riverbank from the river along a curved section. Setback levees allow an increase in flow area of the river channel. This provides more room for the river to meander before it contacts the levees and causes problems. Some advantages to setback levees are that they provide riparian habitat and an opportunity to construct new levees according to modern day standards of design and construction; however the cost to construct a new levee is often too expensive.

ANALYSIS OF ALTERNATIVES

Table 1 summarizes the main benefits and impacts associated with each main mitigation alternative based on the engineering and cost analyses described below and additional project challenges discussed in Money (2006).

This comparison shows that constructing a setback levee costs more, but provides a long term solution to mitigate for the current riverbank erosion. The rock placement and levee widening may save money in the short term, however they may not provide a lasting solution depending on how aggressive the bank erosion and river channel migrate. Rock placement also negatively impacts the river channel by affecting the salmon-spawning habitat. Construction of a setback levee will allow for additional riparian habitat to be formed between the new levee and the existing levee. During high water flows the area will fill up with water and during normal river flows it will serve as a marshy area for fish and wildlife.

TABLE 1. Summary of construction alternatives

Alternative	Benefit	Impact
Rock Placement	Inexpensive, but may fail during the life of the levee	Significant environmental concerns
Widen Levee	Inexpensive, but may fail during the life of the levee	Temporary solution and traffic impact
Setback Levee – 3H:1V	Provide long term solution and riparian habitat	Very expensive, environmental issues
Setback Levee – 4H:1V	Provide long term solution and riparian habitat	Moderately expensive and environmental issues

ENGINEERING ANALYSES

A set of analyses were performed to aid in selection of the most appropriate alternative for the setback levee. The engineering analyses included potential seepage analysis of the existing ground with a new levee, slope stability analysis of the proposed levee, and settlement calculations. Laboratory tests were performed to obtain site-specific soil parameters pertaining to grain size and strength using direct shear and triaxial shear tests to be used in the slope stability analysis.

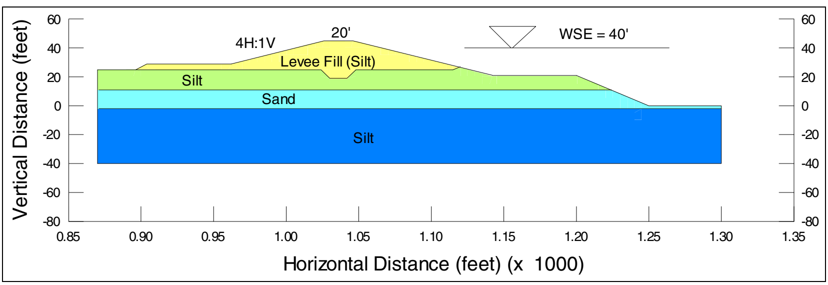

FIG. 1. Cross section and soil profile of setback levee mitigation alternative for seepage analysis (1ft=0.3m)

Seepage Analysis

Seepage analysis was required in order to determine if seepage under the existing levee had the potential to occur. It is important to make sure new construction does not produce more of a problem than the existing conditions. A computer program SEEP/W, developed by Geo-Slope International (1998), was used to perform steady state condition seepage analyses. Input parameters included soil permeabilities, anisotropy, and boundary conditions. Figure 1 shows the cross section and soil profile of the setback levee used for the analyses. The results generated by the computer model were compared with values published by the US Army Corps of Engineers (USACE). The first seepage analysis determined that the new levee design had a potential underseepage problem and that seepage mitigation alternatives needed to be analyzed.

Mitigation alternatives using a seepage berm and a cutoff wall were analyzed in order to meet the USACE criteria. The seepage berm alternative analysis included adding either a 61 or 106.7 m (200 or 350 ft) long, 1.5 to 2.1m (5 to 7 ft) thick berm on top of the ground immediately at the landside toe of the levee. The cutoff wall alternative analysis included adding a 0.6m (2 ft) wide slurry cutoff wall from the centerline of the levee through the embankment fill and keyed 1.5m (5 ft) into a lower permeable material 9.1 m or 15.2 m (30 or 50 ft) deep. Cutoff walls add a semi-impervious material into the ground to impede the flow of water under or through the levee. The results of the seepage analyses indicate that without any mitigation the new levee may experience dangerous seepage conditions driven by a flood event. Figure 2 shows typical results from the analysis. Further details about seepage analysis were discussed by Money and Porbaha (2006a).

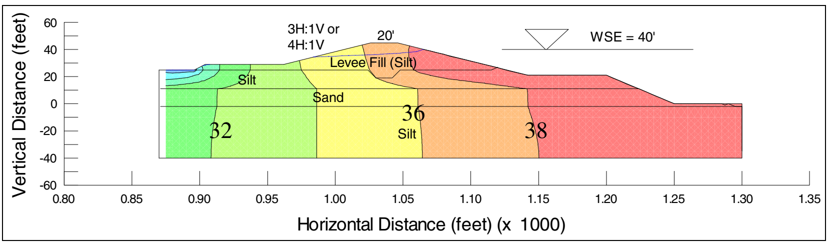

FIG. 2. Typical results of seepage analysis showing total head contours (1ft=0.3m)

Slope Stability Analysis

Slope stability analysis was performed using a computer program, SLOPE/W, to determine if the proposed levee design slopes would fail during high water events. Input parameters included soil unit weight, cohesion, and friction angle (phi). The analysis utilized the Spencer method. An estimated phreatic surface was input into the stability model to reflect potential seepage conditions. The cross section analyzed for the stability analysis was a proposed new construction configuration while the cross section for the seepage analysis was the current existing levee configuration. Analyses were performed for the proposed levee construction geometry with 4 to 1 horizontal to vertical slopes using native soil and 3 to 1 slopes for imported levee fill soil. Two different levee material properties were analyzed (on-site soil and imported soil). The computed factors of safety were compared to a published value of 1.4 from the USACE EM 1110-2-1913 for steady seepage condition on a new levee. The results from this analysis indicate that the levee construction provides adequate safety against slope failure during a flood event. Figure 3 shows a typical result from slope stability analysis. Further details about stability analysis were discussed by Money and Porbaha (2006b).

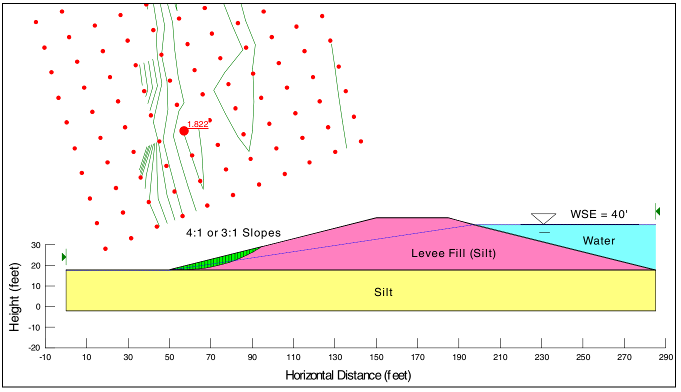

FIG 3. Typical result of slope stability analysis showing a potential failure surface (1 ft=0.3m)

TABLE 2. Summary of anticipated consolidation induced settlement

Cause of Settlement	Estimated Range of Settlement, m (ft)	Estimated Time to Reach 75% of Primary Consolidation (years)	Estimated Time to Reach 90% of Primary Consolidation (years)	Estimate Time to Reach 100% Primary Consolidation (years)
Primary Consolidation	0.34-0.84 (1.10-2.76)	0-6	0-10.5	0.5-24.4
Secondary Consolidation	0.07-0.18 (0.23-0.59)	--	--	--
Total	0.41-1.02 (1.33-3.35)	--	--	--

Settlement Analysis

Settlement rates and quantities were calculated using results from eleven time-rate consolidation tests from one-dimensional laboratory consolidation tests. The range of values calculated during the settlement analysis show that the materials tested ranged from over-consolidated to under-consolidated. The depth of the sample plays a factor in this determination, however the locally high groundwater and fluctuating water table due to irrigation practices in the area have also contributed to the range of consolidation experienced by the near surface soils. Consolidation induced settlement during construction was estimated to range between 0.41 m and 1.02 m (1.3 ft and 3.3 ft). Table 2 shows a summary of the estimated settlement.

COST ANALYSIS

Cost analysis includes evaluation for construction of three alternatives, riprap, levee widening, and setback levee. The following items are included in this cost analysis:

- Land acquisition (if applicable)
- Site grading and excavation
- Purchase, excavate, load, and haul select fill material (if applicable)
- Construction of levee, cutoff wall, and seepage berm
- Construction and/or relocation of Garden Highway

Description of Construction Alternatives

Three construction alternatives were considered for cost analyses:
(a) Alternative 1: Riprap Rock Revetment along 1950 m (6,400 ft) of levee.
(b) Alternative 2: Widen existing levee 4.6 m (15 ft), with 3H:1V side slopes, to the landside, for 1950 m (6,400 ft) of levee.
(c) Alternative 3: Construct a 2743 m (9,000 ft) long setback levee 7.6 m (25 ft) tall, with a 6 m (20 ft) wide crown, located 152 m (500 ft) landward of the existing levee. This alternative was analyzed with either (a) 3H:1V side slopes using imported select fill and (b) 4H:1V side slopes using on-site fill.

Costs for each of these alternatives were estimated using three different seepage mitigation measures:

- 60 m (200 ft) long seepage berm tapering from 2.1 m (7 ft) thick to 5 ft thick,
- 106.7 m (350 ft) long seepage berm tapering from 2.1 m (7 ft) thick to 5 ft thick, and
- 10.7 m (35 ft) deep SCB slurry cutoff wall, 0.76 m (2.5 ft) wide.

Estimation of Construction Costs

Construction costs were estimated by first designing the proposed levee mitigation cross sections. These cross sections were utilized to determine cross sectional areas and volumes to be used for costing. Unit costs for demolition, site preparation, purchase, excavation, loading, and hauling of fill materials, construction of alternatives, and land acquisition were referenced from a preliminary analysis by Parsons Brinckerhoff performed for the project (Parsons Brinckerhoff, 2004). These areas and volumes were inputted into an Excel spreadsheet to calculate the total cost for each proposed mitigation alternative. Total costs were then reduced to a linear value for comparison purposes. Table 3 summarizes the estimated cost for each alternative. Further details about cost analysis were presented by Money (2006).

TABLE 3. Summary of estimated construction costs for seepage mitigation alternatives

Construction Mitigation	Total Cost ($M)	Cost Per Linear Meter ($)
Widen Existing Levee	3.96	189
Rock Riprap to Waterside Bank	19.25	917
Setback Levee 3H:1V Slopes	23.24	786
Setback Levee 3H:1V Slopes with 10.7 m (35 ft) Deep Slurry Cutoff Wall	24.50	829
Setback Levee 3H:1V Slopes with 60 m (200 ft) Wide Seepage Berm	32.00	1085
Setback Levee 3H:1V Slopes with 106.7 m (350 ft) Wide Seepage Berm	38.57	1307
Setback Levee 4H:1V Slopes	11.61	393
Setback Levee 4H:1V Slopes with 10.7 m (35 ft) Deep Slurry Cutoff Wall	12.87	435
Setback Levee 4H:1V Slopes with 60 m (200 ft) Wide Seepage Berm	20.38	691
Setback Levee 3H:1V Slopes with 106.7 m (350 ft) Wide Seepage Berm	26.95	911

Costs are a significant engineering consideration in the comparison of mitigation alternatives. As shown above, the cost for the 4H:1V levee ($393/m) is less than the cost for the 3H:1V levee ($786/m), despite the large volume of material placed. This is because seepage mitigation measures necessary for the 3H:1V levee are considerably higher than for the 4H:1V levee.

CONCLUDING REMARKS

Recent bank erosion along the Sacramento River East Levee just south of the Natomas Cross Canal in Sutter County, California has resulted in a condition that may eventually compromise the integrity of the levee. The engineering and cost analyses results discussed here serve as an effective tools to systematically evaluate various mitigation alternatives.

The seepage analysis has shown that construction of a setback levee is feasible with the use of an additional mitigation method. The geometry of the setback levee is shown to significantly impact the project cost. Utilizing on-site non-select soils saves the project approximately $4265 per meter ($1,300 per linear ft) of levee, despite having to use flatter levee slopes and more material. The mitigation alternatives shown to reduce the exit gradients to acceptable levels include a cutoff wall at least 10.7 m (35 ft) deep and a 60 m (200 ft) wide seepage berm for the 3H:1V levee and between a 60 to 106.7 m (200 to 350 ft) wide seepage berm for the 4H:1V levee. Addition of these seepage berms also significantly increase the project cost by over $3280 per meter ($1,000 per ft), whereas the slurry cutoff wall only adds approximately $656 per meter ($200 per linear ft).

Results of the stability analyses illustrate that acceptable factors of safety can be achieved by modifying levee design based on the quality of levee fill materials. However, determining a successful design does not end with stability results. The cost to construct the levee using imported soils is almost twice as much as utilizing on-site soils. Since the stability analysis showed acceptable results for both construction alternatives and there are substantial cost savings when using the on-site soils, this is the more likely option for final design.

Based on the engineering and cost analyses it is concluded that a setback levee using on-site soils constructed with 4H:1V slopes, a 10.7 m (35 ft) deep slurry cutoff wall, and internal drains is the most cost effective and environmentally conscious solution that fulfills all required mitigation needs.

ACKNOWLEDGEMENTS

The authors would like to appreciate the Sacramento Area Flood Control Agency (SAFCA) for providing project information and background. Appreciation is extended to Mr. Ray Costa of Kleinfelder for his review and sharing of technical information.

REFERENCES

2003 CESPK Levee Task Force (2003) Recommendations for seepage design criteria, evaluation and design practices, July.

Geo-Slope International (1998) SEEP/W software, Version 4, Calgary, Alberta, Canada.

Money, R. L. (2006) Analysis of alternatives to mitigate erosion of Sacramento River setback levee, Department of Civil Engineering, California State University, Sacramento, Master's project.

Money, R.L., and A. Porbaha (2006a) Seepage analysis of Sacramento River setback levee, *Danube-European Conference on Geotechnical Engineering*, Ljubljana, Slovenia.

Money, R.L., and Porbaha, A. (2006b) Stability analysis of Sacramento River setback levee, Proceedings of Geo-Congress 06, *Geotechnical Engineering in the Information Technology Age*, ASCE Geo-Institute, Atlanta, Georgia, February.

Parsons Brinckerhoff (2004) Administrative Draft, Preliminary Cost Estimates, Natomas Setback Levee, Sacramento East Levee, August 9, 2004.

USACE (2000). Design and construction of levees, *Engineering Manual EM 1110-2-1913*, April 2000, U.S. Army Corps of Engineers.

DEM Simulation of Flood-Induced Piping Including Soil-Fluid-Structure Interaction

U. El Shamy[1] and F. Aydin[2]

[1]Environmental and Civil Engineering Dept., Southern Methodist University, PO Box 750340, Dallas, TX 75275, E-mail: uelshamy@engr.smu.edu
[2]Former graduate student at the Civil and Environmental Engineering Dept., Tulane University, 6823 St. Charles Ave, New Orleans, LA 70118.

ABSTRACT

In this paper, flood-induced piping under river levees is simulated using a three-dimensional transient fully-coupled hydromechanical model and taking into account the effects of soil-fluid-structure interactions. The porous soil medium is modeled as a mixture of two interpenetrating phases, namely the fluid phase (water) and the particulate solid phase. The fluid is idealized as a continuum by using averaged Navier-Stokes equations that accounts for the presence of the solid particles. The Discrete Element Method (DEM) is employed to model the assemblage of these particles. The interphase momentum transfer is modeled using established relationship that accounts for the dynamic change in porosity and possible occurrence of nonlinear losses. The hydraulic structure (levee) is modeled as an impervious rigid body and its motion is dictated by the combination of external and internal forces from the surrounding fluid and solid particles. A computational simulation is conducted to investigate the response of a granular deposit when subjected to a rapidly increasing head difference. The conducted simulation provided information at the micro-scale level for the solid phase as well as at the macroscopic level for the pore-water flow. The proposed computational framework for analyzing river and flood-protection levees would provide a new dimension to the design of such vital geotechnical systems.

INTRODUCTION

Flood-induced piping and subsequent formation of sand boils is a major cause of severe damage to river levees and earth dams. Most of the analytical work found in the literature considers piping under steady state conditions (Sellmeijer and Koenders, 1991; Ojha et al., 2003). While these models can be used for design of levees against piping, they do not account for intergranular stresses, stresses due to weight of the hydraulic structure and any subsequent deformation of the soil system. Application of computational methods in modeling of piping is widely used. Griffiths and Fenton (1997, 1998) employed two and three-dimensional finite element models to study seepage in spatially random soil with statistically variable soil permeability and steady state flow. Unsteady ground water flow models using finite element method were also presented (e.g., Nath, 1981; Koo and Leap, 1998). Lu and Zhang (2002) used the finite difference technique that accounts for heterogeneous soils.

Flow conditions that would result in piping encompass several issues that have to be accounted for when developing a computational model for fluid flow through a deforming porous medium. In the case of flood-induced piping, transient analysis has to be considered since flooding of a river results in a rapidly increasing hydraulic head that a steady flow regime is unlikely to occur. Furthermore, under such extreme flow conditions, soil particles may undergo large displacements leading to significant changes in porosity. Variations in porosity affect the soil hydraulic conductivity and deformation characteristics. The effects of the weight of the hydraulic structure on the developed stresses within the soil mass during water flow have to be taken into account.

Conceptually, in presented computational simulation, the mixture of solid particles and pore fluid is viewed as two interpenetrating media, namely the solid phase and the fluid phase. The fluid is idealized as a continuum by using a homogenized form of Navier-Stokes equations that accounts for the presence of the solid particles. These particles are modeled at a micro scale using the DEM. The inter-phase momentum transfer is modeled using established relationship. The soil-structure interaction is maintained by generating a clump which behaves as a rigid body. A recent computational simulation of piping was achieved by the authors using a transient fully-coupled continuum-discrete hydromechanical model to analyze the pore-fluid flow and solid phase deformation of saturated granular soils when subjected to seepage conditions (El Shamy and Aydin, 2007a).

COMPUTATIONAL MODEL

Fluid Phase

Most energy dissipation associated with water flow through granular soils occurs at fluid-particle interfaces. Furthermore, the volumetric deformation of water is typically negligible compared to changes in pore volumes. The pore fluid was therefore considered to be inviscid and incompressible. The averaged Navier-Stokes continuity and momentum equations are then given by (e.g., Jackson, 2000):

$$\frac{\partial n}{\partial t} + \nabla \cdot (n\overline{\mathbf{v}}_{\mathrm{f}}) = 0 \tag{1}$$

$$\rho_{\mathrm{f}}\left(\frac{\partial(n\overline{\mathbf{v}}_{\mathrm{f}})}{\partial t} + \nabla \cdot (n\overline{\mathbf{v}}_{\mathrm{f}}\overline{\mathbf{v}}_{\mathrm{f}})\right) = -n\nabla\overline{p}_{\mathrm{f}}\boldsymbol{\delta} - \overline{\mathbf{f}}_i + n\rho_{\mathrm{f}}\mathbf{f}_g \tag{2}$$

where $n = n(\mathbf{x},t)$ is porosity (in which $\mathbf{x}$ and t are space and time coordinates), $\overline{\mathbf{v}}_{\mathrm{f}} = \overline{\mathbf{v}}_{\mathrm{f}}(\mathbf{x},t)$ is averaged fluid velocity vector, $\overline{p}_{\mathrm{f}} = \overline{p}_{\mathrm{f}}(\mathbf{x},t)$ is averaged fluid pressure, ∇ is gradient operator, ρ_{f} is fluid density, $\mathbf{f}_g$ is gravitational acceleration vector, and $\overline{\mathbf{f}}_i = \overline{\mathbf{f}}_i(\mathbf{x},t)$ is averaged fluid-particle interaction vector. The associated boundary conditions consists of fluid velocity and/or pressure constraints.

Averaged fluid-particle interactions may be quantified using a number of semi-empirical relationships. In this study, the semi empirical equation developed and calibrated by Ergun (1952) was employed.

Solid Phase

The discrete element method (Cundall and Strack, 1979) was used to idealize the assemblage of soil particles using distinct spheres. The motion of a particle p is dictated by the momentum equations:

$$m_p \dot{\mathbf{v}}_p = m_p \mathbf{f}_g + \sum_c \mathbf{f}_c + \mathbf{f}_d \tag{3}$$

$$I_p \dot{\boldsymbol{\omega}}_p = \sum_c \mathbf{r}_c \times \mathbf{f}_c \tag{4}$$

where $\mathbf{v}_p$ and $\boldsymbol{\omega}_p$ are translational and rotational velocity vectors (a superposed dot indicates time derivative), m_p is particle mass, I_p is particle moment of inertia, $\mathbf{f}_c$ refers to inter-particle force at contact c ($c = 1, 2, \cdots$), $\mathbf{r}_c$ is vector connecting the center of the particle to the location of the contact c, and $\mathbf{f}_d$ is drag force exerted by the fluid on the particle p which includes buoyancy and fluid-particle interaction terms. The inter-particle forces are dictated by contact laws which are direct functions of grain stiffness properties and relative movements at the contacts. The normal component was idealized using a linear spring stiffness which is connected in parallel to a viscous dashpot. The shear contact force was modeled using an elastic spring in series with a frictional slider. The shear and normal forces are related by a slip Coulomb model (Itasca, 2005).

COMPUTATIONAL SIMULATION

The proposed approach was used to conducted a computational simulation of seepage through a deforming granular medium. A hydraulic structure with a length of 5.0 m is constructed over a 9.7 m deep deposit of cohesionless soil. The total number of particles that can be used reasonably in a DEM simulation using current state-of-the-art serial computers is small in comparison to the number of grains comprised in an actual deposit. Therefore, the high-g level concept commonly implemented in centrifuge modeling was utilized. Uniformly graded spherical soil particles with a uniformity coefficient of 1.4 were generated and settled under 1 g until there was no further movement of particles. Then a 100 g gravitational field was applied until a submerged state condition is maintained (Fig. 1). In order to compensate for the employed high g-level, viscous fluid was used in the simulation (Kutter, 1992).

Modeling the Hydraulic Structure

The hydraulic structure was generated using clumped spherical particles which behave as a rigid body. That is, regardless of the forces acting upon it, the structure will not break apart. The contact forces between the clump particles are not taken into account. However, the interactions between the clump particles and soil particles are considered. The spherical clump particles were assembled to resemble near-realistic conditions between the hydraulic structure and the soil particles. The stress applied by the structure on the underlying soil resembled that due a structure that is 6.5 m high, 5 m wide and with 2000 kg/m^3 material density. Only a 5 m strip was considered in the normal direction to analyze the presumably infinite structure.

Forces that act on the structure were calculated analytically and were taken into account during the whole simulation (Fig. 2). In this figure, L, H, B represent respectively the length, height and width of the structure and H_w is the height of the water level.

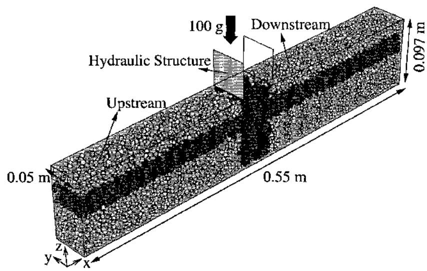

FIG. 1. Three-dimensional view of the particulate deposit in the conducted simulation.

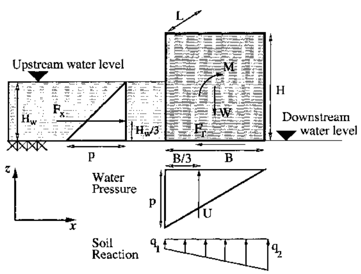

FIG. 2. Free body diagram of the forces acting on the hydraulic structure.

W is the self weight of the structure, p is the water pressure for corresponding H_w, U is the uplift force, F_x is the horizontal force due to water pressure, F_r is the frictional force between the hydraulic structure and the soil particles and M is the moment created on the centroid of the structure as a result of these forces. In the simulation, forces acting on the structure as well as their turning moments were calculated as the water level increased and carried to the centroid of the structure. The frictional force F_r was obtained from the contact forces of particles in contact with the base of the structure and was automatically accounted for by PFC^{3D}. Since the clump in PFC^{3D} behaves as a rigid body, translational and rotational motion equations are sufficient to describe its motion (Itasca, 2005).

After generating the particles composing the structure, the deposit was allowed to come to equilibrium. The initial conditions were chosen to correspond to an initial head difference of approximately 1.0 m and the fluid flow was allowed to reach steady state under these conditions. The deposit was then subjected to a head increase at a rate of 100 Pa per second. Multiple solid and pore-fluid state variables were monitored during the course of the simulation. Table 1 summarizes the computational data for the

TABLE 1. Characteristics of conducted numerical simulation in model units.

Particles	
Diameter	1.7 mm to 8.5 mm
Normal/Shear Stiffness	1e5 N/m
Critical damping ratio	0.10
Friction coefficient	0.5
Density	2650 kg/m^3
Number of particles	22,303
Initial average porosity of soil	0.39
Structure	
Width (y-dir.)	0.05 m
Height (z-dir.)	0.065 m
Length (x-dir.)	0.05 m
Number of clump particles (n_{cl})	5764
Density of a clump particle (ρ_{cl})	12922.4 kg/m^3
Volume of a clump particle (V_{cl})	4.2×10^{-9} m^3
Fluid	
Density	1000 kg/m^3
Viscosity	0.1 Pa s
Boundaries	
Width (y-dir.)	0.05 m
Depth (z-dir.)	0.097 m
Length (x-dir.)	0.55 m
Computation parameters	
Time steps for DEM	4×10^{-6} s
Time steps for fluid	2×10^{-5} s
Number of fluid cells (x, y, z)	$44\times3\times8$
Applied 'g' level	100

solid and fluid phases as well as other computational details. Results are presented in prototype units exclusively.

Fluid Flow Characteristics

Several response patterns of the pore fluid flow are discussed herein as the upstream water level increased gradually with time. The progressive increase of the head in the upstream side is shown in Fig. 3. These flow patterns are consistent with what is commonly obtained using any analytical solution of the seepage equations.

Investigation of the evolution of seepage velocity as the water level kept rising in the upstream indicates progressive increase in the amplitude of seepage velocity vectors. High seepage velocities were observed in the zone surrounding the structure. The highest velocity was always next to the toe of the structure in the downstream side and next to the heel of the structure in the upstream side (Fig. 3). The amplitude of the

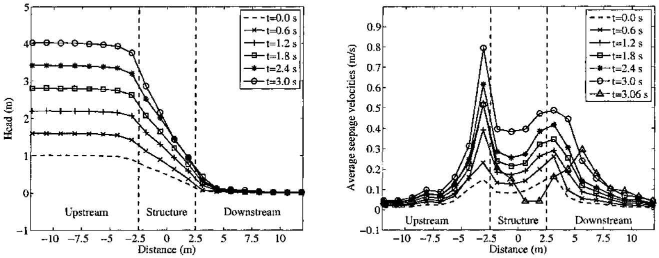

FIG. 3. Water head vs. distance in meters (left) and average seepage velocities vs. distance at 0.61 m below the ground level (right).

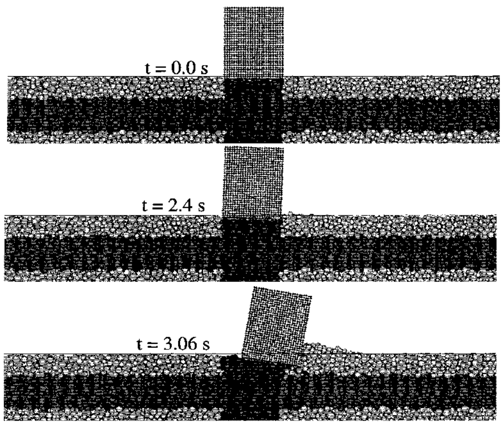

FIG. 4. Snapshots of particles and hydraulic structure at selected time instants.

seepage velocity increases as the water level in the upstream increases gradually and decreases significantly as the distance from the structure increases in both directions. As shown below, the structure experienced significant settlement and tilting causing it to fail (Fig. 4). As a result of this movement, the amplitude of seepage velocity decreased significantly in the upper layers of the deposit directly underneath the downstream side and the toe of the structure, as can be seen from the seepage velocity at 3.06 s (Fig. 3).

Solid Phase Response

Investigation of the changes in porosity of the solid phase at different locations shows that the area near the toe of the hydraulic structure on the downstream side

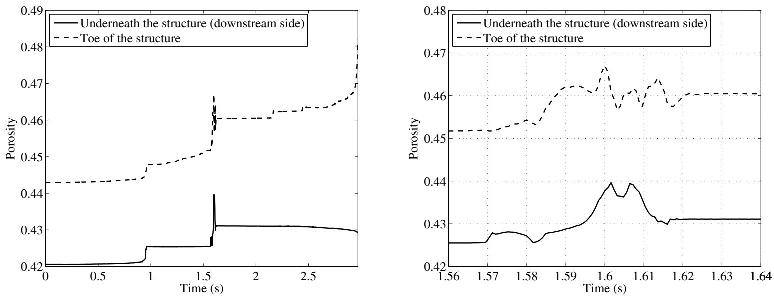

FIG. 5. Porosity vs. time at 0.61 m below the ground level near the toe of the structure (left) and at $t = 1.6\ s$ failure instant (right).

sustained significant increase in porosity. At the instant of first significant settlement (at 1.6 s) there is a high jump in porosity, since particles left the cells that they were occupying and subsequently new particles occupied their place. This can be better observed in Fig. 5, which shows the porosity at the failure instant in details. In Fig. 5, the increase in porosity at the toe of the structure reflects the effect of particles leaving that region. The movement of these particles resulted from the coupled effects of flow-induced drag forces and the weight of the structure. Just after the 1.59 s time instant, the particles under the structure experienced large deformation causing the structure to settle and subsequently fail. More results of the conducted simulation are presented in El Shamy and Aydin (2007b).

CONCLUSIONS

This paper examines the potential of a three-dimensional fully-coupled fluid-particle-structure model to simulate large soil deformations resulting from extreme flow conditions. The mesh-free nature of DEM allows particle movements to be tracked as they respond to the seepage forces. The conducted simulation captured the movement of soil particles and the subsequent displacement of the hydraulic structure showing the trend of failure. This approach appears to be a very effective tool to model saturated granular deposits when subjected to high seepage forces such as those encountered during flooding of a river. The approach accounts for soil-structure interaction, transient flow conditions, spatial and time variations in porosity and subsequent changes in the permeability of the soil.

ACKNOWLEDGEMENT

This research was supported by the Louisiana Board of Regents Support Fund, grant number LEQSF(2005-07)-RD-A-32. This support is gratefully acknowledged.

REFERENCES

Cundall, P. A. and Strack, O. D. L. (1979). “A discrete numerical model for granular assemblies.” *Géotechnique*, 29(1), 47–65.

El Shamy, U. and Aydin, F. (2007a). "A Micro-Scale Model for the Analysis of Flood-Induced Piping in River Levees." Geo-Denver 2007, Denver, CO. Geotechnical Special Publication (GSP161).

El Shamy, U. and Aydin, F. (2007b). "Multi-Scale Modeling of Flood-Induced Piping in River Levees." *Journal of Geotechnical and Geoenvironmental Engineering*, ASCE. Under revision.

Ergun, S. (1952). "Fluid flow through packed columns." *Chemical Engineering Progress*, 43(2), 89–94.

Griffiths, D. V. and Fenton, G. A. (1997). "Three-dimensional seepage through spatially random soil." *Journal of Geotechnical and Geoenvironmental Engineering*, ASCE, 123(2), 153–160.

Griffiths, D. V. and Fenton, G. A. (1998). "Probabilistic analysis of exit gradients due to steady seepage." *Journal of Geotechnical and Geoenvironmental Engineering*, ASCE, 124(9), 789–797.

Itasca (2005). *Particle Flow Code, PFC3D, release 3.1*. Itasca Consulting Group, Inc., Minneapolis, Minnesota.

Jackson, R. (2000). *The dynamics of fluidized particles*. Cambridge, U.K.; New York: Cambridge University Press. London, UK.

Koo, M. H. and Leap, D. I. (1998). "Modeling three-dimensional groundwater flows by the body-fitted coordinate (BFC) method: II. free and moving boundary problems." *Transport in Porous Media*, 30(3), 345–362.

Kutter, B. (1992). "Dynamic centrifuge modeling of geotechnical structures." *Transportation research record*, (1336), 24–30.

Lu, Z. and Zhang, D. (2002). "Stochastic analysis of transient flow in heterogeneous, variably saturated porous media: The van Genucten-Mualem constitutive model." *Vadose Zone Journal*, 1, 137–149.

Nath, B. (1981). "A novel finite element method for seepage analysis." *International Journal for Numerical and Analytical Methods in Geomechanics*, 5, 139–163.

Ojha, C. S. P., Singh, V. P., and Adrian, D. D. (2003). "Determination of critical head in soil piping." *Journal of Hydraulic Engineering*, ASCE, 129(7), 511–518.

Sellmeijer, J. B. and Koenders, M. A. (1991). "A mathematical model for piping." *Applied Mathematical Modeling*, 15(6), 646–651.

Experimental Investigation of Piping Potential in Earthen Structures

Kevin S. Richards[1], P.E., and Krishna R. Reddy[2], P.E., Ph.D.

[1]Department of Civil and Materials Engineering, University of Illinois, Chicago, 2095 Engineering Research Facility, 842 W. Taylor Street (M/C 246), Chicago, Illinois 60607-7023, PH (847) 615-0076; email: kricha3@uic.edu
[2]Department of Civil and Materials Engineering, University of Illinois, Chicago, 2095 Engineering Research Facility, 842 W. Taylor Street (M/C 246), Chicago, Illinois 60607-7023, PH (312) 996-4755; email: kreddy@uic.edu

ABSTRACT: Current methods for evaluation of piping potential have not been successful in preventing piping failures. The initiation of classic backwards-erosion piping failure is currently assessed from the anticipated hydraulic gradient at the point of seepage exit, using a theoretical method originally developed by Karl Terzaghi in 1922. Recently, some researchers suggested that there may be a relation between effective stress and the critical hydraulic gradient and recommended further investigations. To date, there has been little research performed to evaluate constitutive behavior of soil that relate to the initiation and progression of backwards erosion piping. In order to evaluate piping potential, a series of laboratory experiments were conducted. A true-triaxial load cell was developed and used for the testing. The load cell was designed to provide the flexibility to modify loading conditions along three orthogonal axes, and to permit loading the cell with pressurized water. The parameters investigated with respect to pipe initiation are: (1) pipe initiation behavior under variable stress tensors; (2) effect of exit geometry on piping potential; (3) effect of load path on piping potential, (4) pipe initiation behavior under variable seepage stress rates. Preliminary test results confirm that there is an energy component in pipe initiation that currently is not adequately considered in piping evaluations and that the exit velocity is a better predictor of piping potential than the hydraulic gradient. Hydraulic exit losses were found to play a key role in pipe initiation. The critical hydraulic gradients determined in these horizontal flow tests are lower than standard theory would predict. A weak relationship between confining stresses and critical hydraulic gradients was observed at higher confining stresses.

INTRODUCTION

Piping causes approximately 46% of all dam failures (Foster et al. 2000), with the backwards erosion mode of piping in perhaps 31% of all these piping cases (Richards and Reddy 2007). While the majority of these piping failures may be attributed to poor design or construction of features that penetrate dams, piping failures due to backwards erosion also make up a large percentage of these failures. Hence, it is important for engineers to have a better understanding of the mechanics of backwards erosion piping, as well as proper designs for dam penetrations. The current understanding of processes contributing to backwards erosion, and methods used to evaluate dams that may be prone to this type of failure, are inadequate in that they do not consider conservation of energy or the critical states of soil. The authors are currently conducting a comprehensive research study to explain the detailed behavior of soil that contributes to backwards erosion and the factors that may contribute to these types of failures. The research required development of a true-triaxial load cell with permeameter capabilities. Preliminary results of tests on uniform quartz silica sand are presented, which helped to identify the critical parameters that affect piping potential.

PREVIOUS WORK

Richards and Reddy (2007) provided a comprehensive review of previous work related to piping. Karl Terzaghi (1943) defined piping as being due to heave, and offered a theoretical basis for evaluation based on the effective stress method. He also defined backwards erosion piping and indicated that this mode of piping failure defied solution by theoretical methods available at the time. His theory for heave was later adapted to assess 'critical' exit gradients that may lead to piping failures in dams. A new theory for behavior of soils, critical state soil mechanics (Schofield & Worth, 1968) considers another independent variable that influences soil behavior (void ratio). Critical state soil mechanics has been used to evaluate piping potential in dams. Sasiharan et al. (2006) explained the Teton Dam piping failure using critical state soil mechanics. Muhunthan and Schofield (1999) also used critical state soil mechanics to explain failure of Teton, Fort Peck and the Baldwin Hills dams. Tomlinson and Vaid (2000) studied the influence of confining pressure on piping gradients through unstable filters and found that confining stresses influence the critical gradient that causes pipe initiation, and that the rate of increase in hydraulic forces also influences the critical gradient for piping.

The results from these few past studies support a theory that critical piping gradients are sensitive to confining stresses, void ratio, and energy considerations inherent in the rate of hydraulic loading. However, no constitutive model exists presently that adequately considers these factors in pipe initiation. Hence, a comprehensive study is being performed by the authors to further define this behavior.

TRUE-TRIAXIAL LOAD CELL

To the author's knowledge, no studies have evaluated the piping behavior of soils in a three dimensional stress regime, which would be necessary to develop a reasonable constitutive model for pipe initiation. Hence, a true triaxial load cell was developed in this study that is capable of applying three dimensional stress states on soil samples. The load cell was constructed of 1-inch thick Lexan and aluminum plate with three pneumatically inflated bladders to apply confining stresses into the soil. The bladders were inflated to move steel plates into the sample, compressing it from three orthogonal directions (σ_1, σ_2, σ_3). An inlet port and outlet port are provided to apply water pressures and allow flow through the load cell.

Parameters measured during the testing were outlet (back-pressure) and inlet pressure, total pore pressure, confining stresses σ_1, σ_2, and σ_3, differential water pressure between inlet and outlet, and mass of water flowing from the outlet.

The inlet flow rate was controlled during the experiment by gradually increasing the flow rate until piping was initiated. A flow-through turbidimeter was used to determine when soil began piping into the outlet. Total pore pressure was measured with a pressure transducer located just below the outlet, and one located in the gravel drain beneath the inlet. The amount of water exiting the load cell was measured using either an Ohaus scale taking readings every second or with a graduated cylinder (for tests with small backpressures). A schematic of this device is shown in Figure 1.

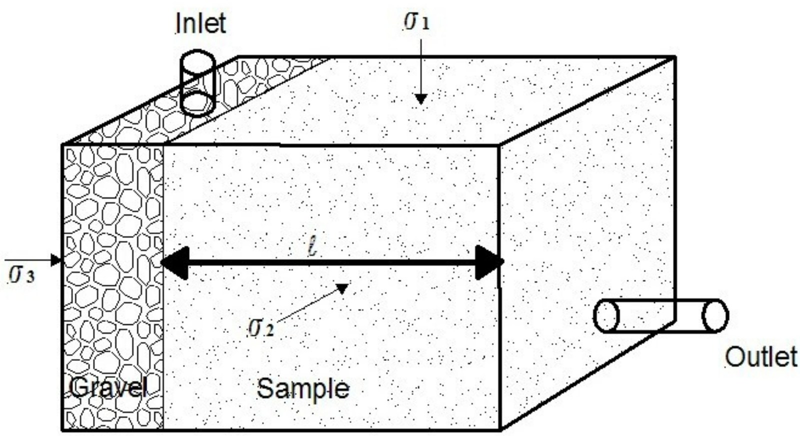

FIG.1. Schematic diagram of true-triaxial test chamber.

A clear flow tube conveys water from the test cell out of the outlet. The clear flow tube enabled easy visual detection of piping sand. In all tests, piping was defined as the initial flow of sand into the outlet. When piping initiated, sand would gradually migrate through the clear flow tube in a very regular and repeatable fashion.

TESTING PROCEDURE

Tests were conducted using commercially available silica sand. The sand was U.S. Silica sand, F-series. The gradation is 99.9 percent passing the No. 20 sieve with only 3.0 percent passing the No. 40 sieve, and only 0.06 percent passing the No. 60 sieve. It contains less than 0.005 percent fines (passing the No. 200 sieve).

Hence, the material is extremely uniform with good internal stability.

Four tests were conducted; 1) trigger piping with no applied confining stress and the saturated soil at rest, 2) trigger piping during application of stress in only the $\sigma 1$ direction, varying it from 5.2, 9.9, to 17.9 psi (35.6, 68.0, and 123.3 kPa), 3) trigger piping during application of stresses in all three principle axes, 4) trigger piping during application of all three stresses using a different load path. Confining stresses were applied prior to application of pore pressure in the last test to simulate the different loading path. As can be seen in Table 1, the tests were performed using a lateral earth pressure coefficient (K) of either 0.25 or 0.50. For the at-rest cases, a K value of 0.50 was assumed in the computations. Two sizes of outlet openings were used in the tests. Sand was placed in its loosest state into the load cell using a funnel in accordance with the placement method of ASTM D4254 (Method A) Minimum Index Density. Figure 2 shows the test setup prior to loading with a soil sample.

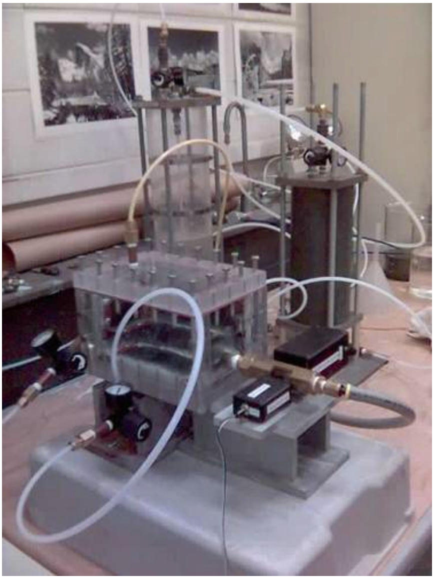

FIG. 2. True triaxial test cell (center of picture), inflow and outlet reservoirs (background), and clear flow tube (equipped with a flow-through turbidimeter).

TEST RESULTS

The discharge rate (Q) was controlled during the experiments and used to initiate piping. The hydraulic conductivity (k) at the outlet was computed using the critical hydraulic gradient (i_{crit}) across the cell and the cross sectional area (A) of the outlet ($k=Q/i_{crit}A$). Values for p' and q' were computed ($p' = [\sigma_1' + \sigma_3']/2$, $q' = [\sigma_1' - \sigma_3']/2$), as was the critical velocity of water flowing through the outlet ($v_{crit} = k i_{crit}$). The initial void ratios and dry density were computed for each test in tests 1 through 7. Since the placement method was consistent throughout all the tests, the initial void ratios were estimated in tests 7 through 11 based on the average void ratios obtained from the first two series. Tables 1 and 2 summarize the results for the silica sand experiments.

Table 1. Summary of test data[1].

Test No.	Outlet Hole Area (cm^2)	Rate of Increase (cm^3/sec/min)	Pore pressure (kPa)	Applied Stresses			h_{crit} (cm)	γ_{sat} (kN/m^3)
				σ_1 (kPa)	σ_2 (kPa)	σ_3 (kPa)		
1	1.27	0.11	3.3	1.9	0.9	0.9	8.6	19.86
2	1.27	0.02	3.3	1.8	0.9	0.9	10.2	19.19
3	1.27	0.02	3.3	1.8	0.9	0.9	3.3	18.88
4	0.52	0.02	28.5	1.4	0.7	0.7	7.1	19.68
5	1.27	0.11	24.4	35.6	17.8	17.8	2.3	19.86
6	1.27	0.11	24.4	68.0	34.0	34.0	2.8	20.41
7	1.27	0.11	28.0	123.3	61.6	61.6	7.1	19.68
8	0.52	0.02	25.8	35.9	18.0	18.0	8.1	19.68
9	0.52	0.02	25.8	35.9	9.0	9.0	7.4	19.68
10	0.52	0.02	28.0	35.9	9.0	9.0	6.6	19.68
11	0.52	0.02	28.7	35.9	18.0	18.0	2.5	19.68

Table 2. Summary of test data continued.

Test No.	Outlet Hole Area (cm^2)	p' (kPa)	q' (kPa)	Q_{crit} (cm^3/sec)	v_{crit} (cm/sec)	i_{crit}	k (cm/sec)	e_o
1	1.27	-1.89	0.47	0.89	0.70	0.56	1.27	0.61
2	1.27	-1.94	0.45	0.79	0.62	0.66	0.95	0.72
3	1.27	-1.96	0.44	0.79	0.62	0.21	2.92	0.78
4	0.52	-27.44	0.36	0.37	0.29	0.53	1.34	0.64
5	1.27	2.32	8.91	0.95	0.75	0.15	5.12	0.64
6	1.27	26.67	17.02	0.95	0.75	0.18	4.14	0.61
7	1.27	64.42	30.82	1.10	0.87	0.46	1.90	0.52
8	0.52	1.09	8.98	0.37	0.29	0.60	1.18	0.64
9	0.52	-3.40	13.47	0.37	0.29	0.55	1.30	0.64
10	0.52	-5.54	13.47	0.37	0.29	0.49	1.45	0.64
11	0.52	-1.80	8.98	0.42	0.33	0.19	4.30	0.64

[1] h_{crit} is the head at which piping initiates, γ_{sat} is the saturated unit weight of the soil, p’ and q’ were defined above, Q_{crit} is the flow rate through the cell at which piping initiates, v_{crit} is the computed critical velocity through the outlet hole, i_{crit} is the computed critical hydraulic gradient at which piping initiated, k is the hydraulic conductivity of soil in the outlet area, and e_o is the initial void ratio at the beginning of the test.

DISCUSSION OF RESULTS

There is good reproducibility in the tests 1-3; however the size of the exit opening area has a strong influence on critical discharge rate and critical velocity. Piping initiated in these tests at a critical hydraulic gradient of 0.21 to 0.66. The hydraulic gradient of 0.21 was resulted in the test that was affected by an additional force due to suction produced by accidental siphoning through a plastic tube that led to a graduated cylinder being used to measure the volume of discharged fluids during the test, and this result is probably erroneous. The method for measuring the amount of flow passing through the cell was modified in subsequent tests. The other tests conducted in the first series yielded critical hydraulic gradients ranging from 0.53 to 0.66, which are comparable. Test sample 1, with the highest critical discharge, corresponds to the densest sample and the sample with the slowest rate of loading in the first series. The standard theory for piping would predict a critical hydraulic gradient of 1.0 for this material. The standard theory is based largely on tests conducted with flow being vertically oriented in opposition to gravity. Hence, the affect of gravity is magnified. The actual gradients measured in these experiments indicate piping may initiate at significantly lower gradients when piping is oriented horizontally rather than vertically. The amount of work required to move particles is less with this orientation, since the particles can move in a generally downhill direction rather than straight up. The initial relative density and rate of loading of the soil also influenced the critical gradient and critical discharge.

The second series of tests yielded some interesting results. In these cases, the confining stresses exceeded pore pressure by a significant amount. Even though the applied principle stresses varied, in all three cases piping initiated at a very similar discharge rate, falling within a narrow range of 0.95 to 1.1 cm^3/sec. The critical hydraulic gradients varied systematically from a low of 0.15 for the 5.2 psi (35.6 kPa) test to a high of 0.46 for the 17.9 psi (123.3 kPa) test. The apparent systematic variation in critical hydraulic gradients is more pronounced at these higher confining stresses, where the effective stress is positive. These results indicate the principle stress, acting orthogonal to the flow direction, has an influence on the critical hydraulic gradient. The computed hydraulic conductivity is inversely proportional to the critical hydraulic gradient. The hydraulic conductivity was lowest for the highest confining stress; this requires a higher hydraulic gradient to initiate piping since the critical velocity is approximately constant.

The third series of tests (tests 8 through 10) evaluated the influence of the minor principle stresses. In test 8, the lateral earth pressure coefficient (K) was set at 0.5. The resulting critical hydraulic gradient was only slightly larger than in tests 9 and 10, which were run with K set at 0.25. The most striking result is that the critical discharge and critical velocities are identical in all three tests. In fact, all tests run with the 0.52 cm^2 opening have very similar critical discharge. The tests conducted with the 1.27 cm^2 opening also have very similar critical discharge, with only minor variation with values ranging from 0.79 to 1.1 cm^3/sec. These minor variations can be explained by either the different confining stresses, rate of loading, or initial void ratios for these samples. The consistency of critical discharge for the third series of tests suggests the minor principle stress has less influence in piping potential than the major principal stress. The size of the exit opening had a dramatic affect on the critical discharge rate. Tests conducted with openings of 1.27 cm^2 generally fell around 0.8-1.1 cm^3/sec, while those with a smaller opening (0.52 cm^2) began piping at a critical discharge rate of 0.37 to 0.42 cm^3/sec. The last test would seem to indicate the load path may have an influence on piping potential; however, more tests are needed to confirm this result. The relationships between various key parameters are plotted in Figures 3 and 4 (tests run at a slower rate of 0.02 cm^3/sec/min are shown in solid colors, tests shown by open symbols were run at 0.11 cm^3/sec/min).

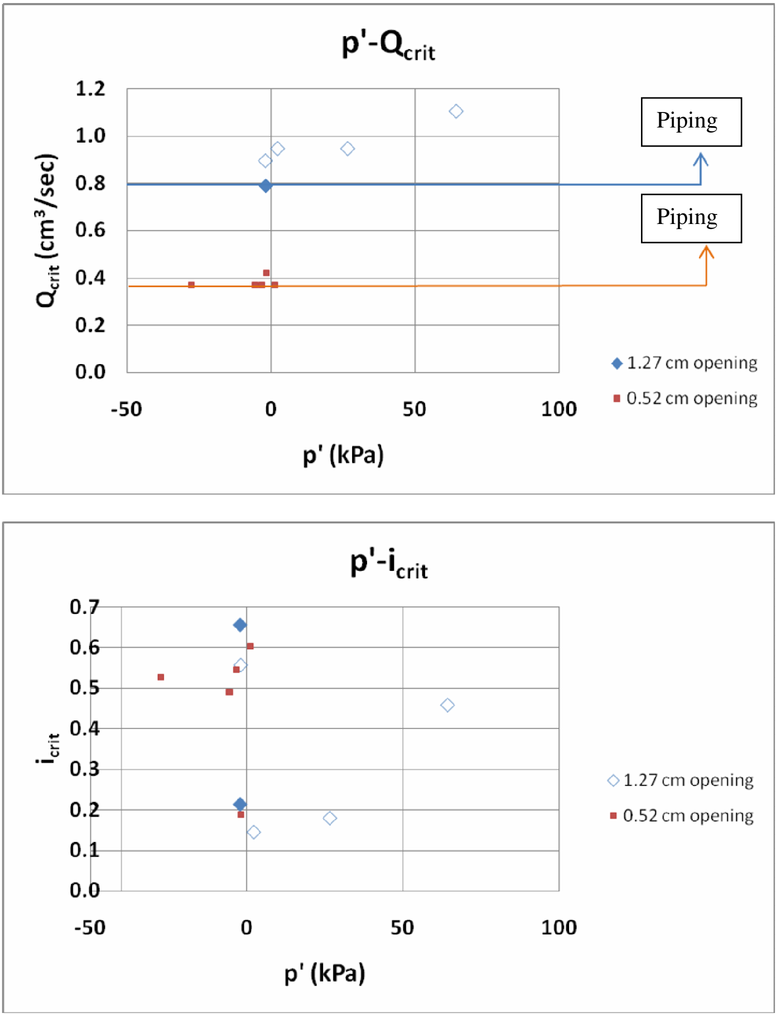

FIG. 3. Effect of p' on piping parameters. Discharge above lines results in piping.

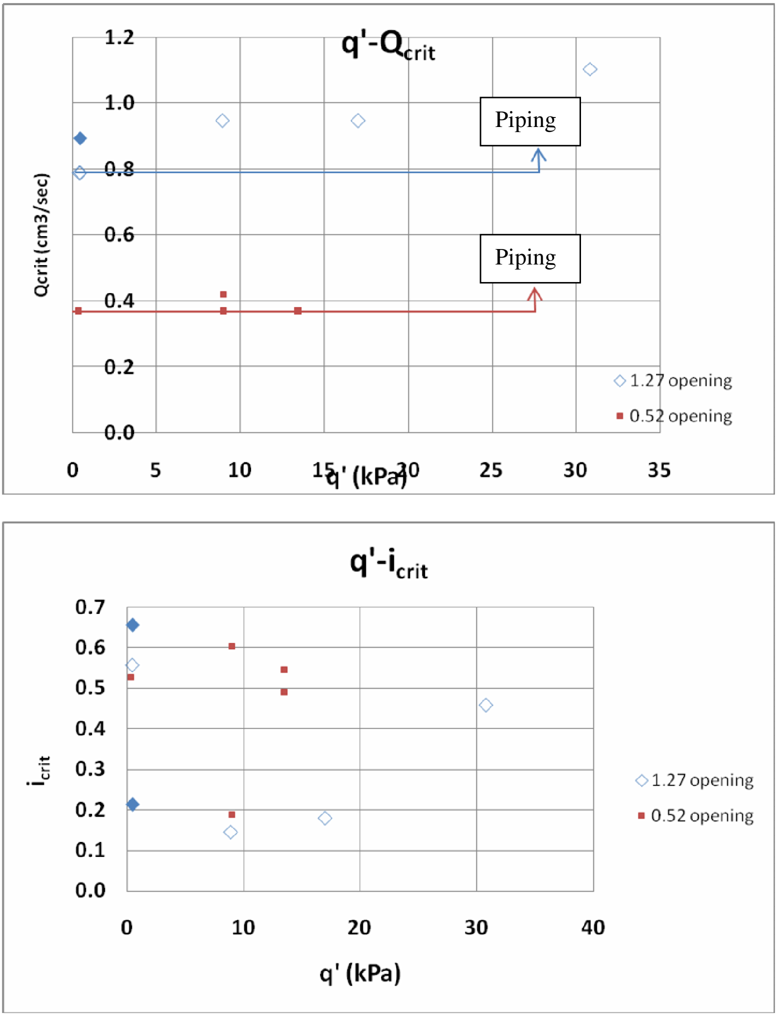

FIG. 4. Effect of q' on piping parameters.

A significant result from these tests is the apparent consistent initiation of piping at similar critical discharge rates rather than under similar critical hydraulic gradients. The second important finding is that the exit losses, demonstrated by the change in critical discharge rates for the two outlet opening sizes, also strongly influence pipe initiation. These phenomena indicate that shear stresses induced by the exit velocity are a much more fundamental parameter controlling backwards-erosion pipe initiation than the critical hydraulic gradient, which can be influenced by changes in the state of the soil. In this experiment, the critical hydraulic gradient (i_{crit}) and hydraulic conductivity (k) of the soil are constrained by the critical discharge rate (Q) and Darcy's law, since the cross sectional area (A) of the outlet is constant. For noncohesive materials, the hydraulic conductivity is prone to change during the piping process due to changes in void ratio. Terzaghi and Peck (1948) noted similar phenomena of dynamic hydraulic conductivity during pipe initiation. If Darcy's Law is considered (Q=kiA), a lower critical gradient will require a larger increase in the hydraulic conductivity to initiate piping at a constant critical discharge rate. This coupling of hydraulic conductivity and critical hydraulic gradient at the point of pipe initiation is responsible for the variations observed. The hydraulic conductivity at pipe initiation can be considered the "critical" hydraulic conductivity, and it is representative of a critical state of the soil. Due to this coupling effect, it may be incorrect to only consider a critical hydraulic gradient without giving consideration to the critical hydraulic conductivity.

The hydraulic gradient required to induce piping was noticeably smaller when confining stresses are applied only in the σ_1 direction (tests 5 and 6). A likely explanation is that the smaller critical hydraulic gradients are the result of the increased rate of hydraulic loading in tests 5-7. If this is substantiated, it would indicate that there is an energy component to pipe initiation that is currently not being considered.

CONCLUSIONS

The true-triaxial apparatus used for conducting experiments appears to provide good reproducibility as evidenced by the consistent relationship between piping and critical discharge. The primary parameter controlling pipe initiation and progression appears to be the shear forces induced by the velocity of flow through an open exit. The geometry of this exit plays an important part in the critical discharge that is needed to induce piping. Preliminary indications are that confining stress may be a factor in pipe initiation, especially at higher stresses. However, this relationship is not true for the critical discharge, which is not significantly affected by confining stress. Due to the coupling of the critical hydraulic gradient to the critical hydraulic conductivity, the effect of the critical hydraulic gradient is mitigated by change to the critical hydraulic conductivity upon pipe initiation. The results of these horizontal flow-tests indicate piping may be induced at much lower hydraulic gradients than current theories would indicate. Piping may be aided by increased rate-of-change of velocity of flow, as indicated by the unusually low hydraulic gradients in some of the tests that were conducted with higher rates of change.

Further work is needed to better define these relationships. If internal stresses do influence the critical hydraulic gradient for piping, a means to predict the critical hydraulic conductivity is needed. Additional testing is now being conducted to help resolve these issues.

REFERENCES

ASTM D 4254-00 (2006). "Standard Test Methods for Minimum Index Density and Unit Weight of Soils and Calculation of Relative Density" ASTM International.

Foster M., R. Fell, and M. Spannagle (2000). "The statistics of embankment dam failures and accidents", *Canadian Geotechnical Journal*, 37(5): 1000-1024.

Muhunthan, B., and A.N. Schofield, (1999). "Liquefaction and Dam Failures", in *Slope Stability 2000*, Geotechnical Special Publication No. 101, eds. D.V. Griffiths, G.A. Fenton, T.R. Martin, ASCE, Reston, VA., pp. 266-280.

Richards, K. and K. Reddy (2007). "Critical appraisal of piping phenomena in earth dams", *Bulletin of Engineering Geology and the Environment*, 66(4):381-402.

Sasiharan, N., B. Muhunthan, and V.S. Pillai, (2006). "Failure report – the case of Teton dam", *Water Power & Dam Construction*, http://www.waterpowermagazine.com, 16 August 2006.

Schofield, A.N., and P. Worth (1968). *Critical State Soil Mechanics*, McGraw Hill.

Terzaghi, K. (1943) *Theoretical Soil Mechanics*, John Wiley and Sons, Inc., New York, pp. 1-510.

Terzaghi, K., and R. Peck. (1948). *Soil Mechanics in Engineering Practice*, 2nd Edition, J. Wiley & Sons.

Tomlinson, S, and Y. Vaid (2000). "Seepage forces and confining pressure effects on piping erosion", *Canadian Geotechnical Journal,* Vol. 37(1):1-13.

Rainfall Erosion Resistance of Various Compost Soils on Roadside Embankment

Ming Xiao[1], M. ASCE,
Christopher Abela[2], Keith Mortensen[2], Michael Beltran[2], Aaron Oliver[2]

[1]Assistant Professor, Department of Civil and Geomatics Engineering and Construction, M/S EE94. California State University, Fresno, California 93740. Email: mxiao@csufresno.edu
[2]Graduate students, Department of Civil and Geomatics Engineering and Construction, California State University, Fresno, California 93740.

ABSTRACT: Compost use in landscaping and erosion control applications has become widespread. Various types of composts have been utilized on highway embankments. Erosion resistance could vary with different compost materials. The objective of this study is to investigate the erosion resistance of three types of widely used composts. Rainfall simulators were constructed to simulate natural rain of 3.0 in/hr. Soil boxes were designed and built to simulate inclined embankments. Bench scale experiments were first conducted to test the erosion of natural base soils (sand, silt, and sandy clay) under 1 hr rainfall. Excessive soil losses were observed in all base soils, and silt slope failed during the test. Then repeated rainfall erosion tests were performed on sandy slopes with three types of composts covers (green compost, manure compost, and biosolid and green material co-composts). The co-compost slope retained stability and the other two compost slopes failed. Chemical and biological constituents in the runoff were analyzed. The concentrations of the analyzed constituents were high in the initial rainfall event and reduced with sequential rainfalls. Most of the toxic metal concentrations in the runoff were less than the EPA criteria.

INTRODUCTION

Surface erosion of roadside embankments due to rainfall can lead to embankment failure and possible contamination of a downstream water body by surface runoff. Compost, an erosion control material made from readily available and inexpensive waste, can reduce erosion and runoff and allow quick establishment of roadside landscaping. Compost use by state Departments of Transportation (DOTs) in landscaping and erosion control applications has become widespread (Composting Council Research and Education Foundation (CCREF) and US Composting Council (USCC), 2001). Various types of composts have been utilized on highway embankments, including 1) green material compost made from yard trimmings, clippings, and agricultural byproducts, 2) manure compost such as from dairy and poultry manures, and 3) co- compost material such as bio-solids and green material co-compost, 4) wood chips and forestry residual composts. Food scraps and municipal solid waste composts have also been used for erosion control (CCREF and USCC, 2001).

Compost, as a manufactured soil from a wide array of original materials, varies significantly in physical, chemical, and biological characteristics, and thus could perform differently in an engineering application. Iowa State University along with Iowa DOT compared the performance of three types of compost (biosolid compost, yard trimmings compost, and bioindustrial compost) and revealed that the coarsest yard trimmings compost performed the best and the biosolids and bioindustrial composts showed more vulnerability to rill erosion (Glanville et al., 2003). Another field study by Faucette et al. (2005) tested four types of composts (biosolids compost, yard waste compost, municipal solid waste compost with mulch, and poultry litter compost with mulch and gypsum), and the study revealed all the compost treatments significantly reduced total solids loss compared to bare natural soils during storm events. Although composts have been widely used in field applications on erosion control, the mechanisms behind the different erosion resistance have been less explored and discussed. The main objective of this research work is to study the erosion control performance of three common composts through bench scale rainfall erosion experiments. The second objective of this paper is to compare and document the runoff constituents of the three composts.

MATERIALS AND EXPERIEMENTAL SETUP

Bench scale rainfall erosion tests were conducted on the campus of California State University, Fresno from August to December 2006. Three types of natural soils (sand, silt, and sandy clay) were tested. Their grain size distributions were plotted in Figure 1. Three types of commercial composts were used as erosion control blankets. The composts are (1) green compost made of road clippings, yard trimmings and other municipal green waste, (2) manure compost made of 100% dairy manure, and (3) co-compost made of 50% (by volume) biosolids and 50% (by volume) green waste. Biosolids are nutrient-rich organic materials resulting from the treatment of domestic sewage in a wastewater treatment facility. The grain size distributions of the three composts were also shown in Figure 1.

A rainfall simulator (Figure 2) was constructed to simulate natural rainfall, based on the theory by Humphry et al. (2002). The rainfall simulator consisted of a spray nozzle, a pressure regulator, a pressure gauge, PVC pipes, hoses, and a supporting frame. The simulator provided heavy rainfall with intensity of 7.6 cm/hr (3.0 inch/hr) at a pressure of 28 kPa (4.1psi). A soil box (30cm wide × 91cm long, 18cm deep) (1ft wide × 3ft long, 7inch deep), also shown in Figure 2, was built to simulate an inclined embankment. The slope angle was 1:2 (V:H), or 27 degrees. A metal screen was installed at the end of slope to prevent the soil from sliding; meanwhile, the screen opening was large enough to allow the eroded soil to pass. A hose connected the soil box to a runoff collector outside of the rainfall pattern, so that runoff could be collected for soil loss and constituent analysis. Rainfall gauges were mounted on the sides of the soil box to measure the precipitation. Three rainfall simulators were built and positioned side by side (Figure 2), so that three erosion tests could be conducted simultaneously. Tarps were used between the rainfall simulators to prevent interference of raindrops.

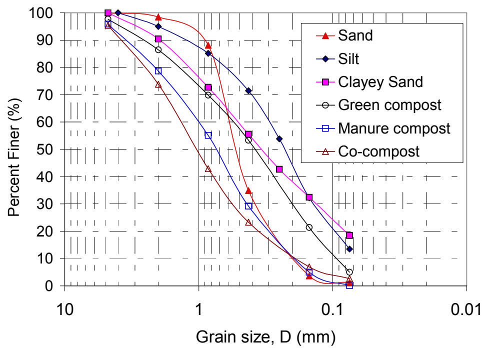

FIG. 1. Grain size distributions

FIG. 2. Erosion test setup

RAINFALL EROSION TESTS

The aforementioned three types of base soils were first tested for erosion. The soils were compacted in the soil boxes to 85% of their maximum dry density at the optimum moisture content based on the standard Proctor compaction tests. The thickness of the compacted soil is 2.54 cm (1.0 inch). Then 1hr rainfall erosion tests were conducted. At the end of the tests, the solids in the runoff were collected and oven dried. The soil losses for the three base soils were listed in Table 1. The natural slopes immediately after the tests were shown in Figure 3. The silt slope failed during the rainfall test and also suffered significant soil loss. Both the sand and clay slopes retained stability, but the clay soil had much more soil loss and small rills formed at the end of the slope.

Based on the soil erosion tests, sand was selected as the base soil for the following compost erosion tests. The sand was prepared and compacted as aforementioned. Composts (green, manure, and co-compost) were loosely applied on the compacted sand in the three soil boxes, respectively. The composts were loosely laid on the sand to simulate the application of compost onto highway embankment using pneumatic blowers. The application rate (thickness of compost blanket) was 1.27 cm (0.5 inch). Then 1hr rainfall erosion tests were conducted on the three composts. The soil loss measurement followed the same method as in the base soil erosion tests, and the results were also listed in Table 1. Figure 4 shows the compost-covered slopes immediately after the 1hr erosion tests. The previously stable sandy slope (in the base soil erosion tests) failed when coupled with green compost blanket during the rainfall, while the other two compost-covered slopes were stable. During the test, as the saturated green compost slid, it pulled the base soil with it, resulting in even more soil loss than that measured in the base soil erosion test.

Many pilot erosion control projects demonstrated that compost blankets promoted and sustained vegetation growth on roadside embankments (California EPA, 2000; Barkley, 2004). Before vegetation is established, however, bare compost blanket could be subjected to repeated rainfalls. In order to test the long-term erosion resistance before the vegetation establishment, manure compost and co-compost, which did not fail during the initial 1hr rainfall test, were subjected to repeated

(a) Sand, after 1hr rain. (b) Silt, after 1hr rain. (c) Sandy Clay, after 1hr rain.

FIG. 3. Base Soil Rainfall Erosion

(a) Green compost failed, after 1hr rainfall. (b) Manure compost failed, after 2 events of 1-hr rainfall. (c) Co-compost was stable, after 4 events of 1hr rainfall.

FIG. 4. Compost Soil Rainfall Erosion (the base soil is sand)

rainfalls (sequential tests), each with 1hr in duration and 1week in interval. The manure compost slope failed at the upper slope during the second erosion test, asshown in Figure 4 (b). The co-compost retained stability after the fourth erosion test (Figure 4 (c)), after which the sequential rainfall test was terminated. The soil losses in the sequential tests were listed in Table 2. A spike in the soil loss of the co-compost covered slope was observed in the third sequential test. During the collection of the eroded soils from the co-compost slope, more sand was noticed in the collected runoff compared to that in Tests 1 and 2. It was speculated that internal erosion beneath the compost cover occurred in Test 3, causing the sudden increase of soil loss. Then the internal erosion stabilized and the soil loss went back to minimum (11 g) in Test 4. More replicate tests are in progress to verify the speculation and to study the cause of possible internal erosion.

Table 1. Soil Losses in Single Rainfall Erosion Tests

Soil Type	Sand	Silt	Clay	Green Compost	Manure Compost	Co-Compost
Soil Loss (g)	235	2813	866	591	61	12
Soil Loss (g/m^2)	843	10093	3107	2120	219	43

Table 2. Soil Losses of Compost-covered Slopes in Repeated Rainfall Tests

Compost Type	Soil loss (g)			
	Test 1	Sequential Test 2	Sequential Test 3	Sequential Test 4
Green Compost	591 (failed)			
Manure Compost	61	53 (failed)		
Co-Compost	12	9	150	11 (stable)

Effect of compost size distributions on erosion was reported by Buchanan et al. (2000) – a diverse particle size distribution reduced erosion more than either small or large particles. This study showed that coarse grains (co-compost) are more erosion resistant than the fine particles of the green compost. Soil organic matter also affects erosion resistance. Organic molecules can be adsorbed on to mineral surface or mineral particles can be adsorbed onto living structure cells, so that an enmeshment of primary mineral particles is created due to the presence of soil organic components (Huang et al., 2002). The organic matter contents, in terms of mass percentage, of the composts used in this study were: 42.6% for co-compost, 30.5% for manure compost, and 26.3% for green compost. The less degree of enmeshment of particles due to less organic matter content is another reason for more soil loss in green compost.

Table 3. Runoff Analysis from Compost Blankets in Sequential Rainfall Erosion Tests

ANALYTE	UNITS	EPA CWA	Green	Manure Compost		Co-Compost			
		Criteria	Test 1	Test 1	Test 2	Test 1	Test 2	Test 3	Test 4
Specific Conductance (EC)	µS/cm		2600	1600	400	2500	770	480	670
pH	pH Units	6.5~9.0	8.0	7.9	8.0	8.1	8.4	8.2	7.7
Total Suspended Solids	mg/L		2400	400	650	110	73	320	52
Total Nitrogen	mg/L		130	79	17	360	96	51	63
Total Kjeldahl Nitrogen	mg/L		31	27	12	350	94	48	39
Nitrate as Nitrogen	mg/L	90	100	52	4.5	6.6	1.9	1.6	5.9
Nitrite as Nitrogen	mg/L	5	ND	ND	ND	ND	ND	1.3	18
Orthophosphate as P	mg/L	0.05	6.1	8.9	1.8	13	13	11	5.8
Phosphorus	mg/L		9.3	4.5	3.4	14	15	15	6.8
Potassium	mg/L		450	280	60	72	25	22	19
Aluminum	mg/L	0.75	55	10	10	2.8	1.4	2.3	0.77
Arsenic	mg/L	0.34	0.021	0.015	0.017	0.038	0.027	0.018	0.016
Cadmium	mg/L	0.0043	0.0029	0.0011	0.0011	0.0011	ND	ND	ND
Chromium	mg/L	0.57	0.068	0.022	0.018	0.014	0.0092	0.0088	0.0058
Copper	mg/L	0.013	0.50	0.083	0.053	0.26	0.17	0.12	0.079
Iron	mg/L	1	73	14	14	6.2	3.8	4.6	2.0
Lead	mg/L	0.065	0.032	0.065	0.039	0.0064	0.0059	0.0058	ND
Magnesium	mg/L		N/A	N/A	15	N/A	6.6	8.5	21
Manganese	mg/L		1.7	0.55	0.46	0.14	0.092	0.10	0.050
Molybdenum	mg/L		0.026	0.012	0.0098	0.082	0.037	0.018	0.019
Nickel	mg/L	0.47	0.054	0.027	0.023	0.026	0.015	0.0087	0.0076
Selenium	mg/L	0.005	ND	ND	ND	ND	ND	ND	ND
Silver	mg/L	0.034	ND	ND	ND	0.033	0.015	0.0059	ND
Titanium	mg/L		2.98	0.692	0.562	0.180	0.0664	0.143	0.0435
Zinc	mg/L	0.12	0.64	0.34	0.30	0.31	0.31	0.19	0.19
Chloride	mg/L	860	260	160	20	62	17	12	15
Biochemical Oxygen Demand (BOD)	mg/L	10~20	<29	<10	4.6	<95	39	18	23
Total Organic Carbon	mg/L		75	50	27	530	160	70	61
E. Coli	MPN/100 mL	235	< 2	< 2	< 2	N/A	< 2	< 2	< 2
Fecal Coliforms	MPN/100 mL		< 2	< 2	< 2	N/A	< 2	< 2	< 2

RUNOFF CONSTITUENTS ANALYSIS

One runoff sample was collected in each of the compost erosion tests, following the proper sampling and chain of custody procedures. The samples were immediately sent to an environmental lab for physical, chemical, and biological analysis. One sample for green compost, two samples for manure compost, and four samples for co-compost were analyzed. The results are listed in Table 3. The Clean Water Act (CWA) (EPA, 1999) and the Stormwater Effects Handbook (Burton and Pitt, 2001) were referred to when evaluating the runoff constituent concentrations. The CWA's ambient freshwater quality criteria were also included in Table 3.

All the constituents had high concentration in the initial flush. Compared with the CWA's criteria, the runoff contained low concentration of priority toxic pollutant except for copper and zinc. Biochemical oxygen demand (BOD) in the runoff was in the approximate range (10 to 20 mg/L) specified by the CWA, and E. Coli bacteria concentrations were well below the allowable limit for designated beach, indicating most of the coliform bacteria and pathogens were killed in the composting process. For non-priority toxic pollutants (Al and Fe), concentrations in the runoff were initially much higher; then they gradually decreased with more rainfall events. For co-compost, Al and Fe concentrations were close to (albeit slightly higher than) the recommended values at the end of Test 4. It is also noted that copper, an EPA regulated priority toxic pollutant, has higher concentration in the runoff of all the three composts. The runoff contained much elevated phosphate, which could stimulate excessive or nuisance growth of algae and other aquatic plants.

CONCLUSIONS

In this preliminary research project, bench scale erosion tests using simulated rainfalls were conducted in order to investigate the differences in erosion resistance of three commonly used composts before vegetation establishment. Runoff analysis was conducted to quantify the physical, chemical and biological constituents. EPA regulations were referred to for the environmental impact evaluation. Based on the results and analysis, the conclusions can be summarized as follows:

1) Different compost soils with different particle size distributions and organic matter contents may vary significantly in erosion resistance. Erodible compost cover can trigger the failure of an entire slope that would be otherwise stable without compost.
2) Compost covers usually release high concentrations of nutrients and chemicals in the first rainfall event, then the constituent concentrations quickly decrease in the following rainfall events. Some chemical and nutrients concentrations (aluminum, iron, copper, and phosphate) in the compost runoff are higher than the EPA regulated limits.

ACKNOWLEDGMENTS

The authors appreciate the support of Steve Scherer, Research Technician of the Department of Civil and Geomatics Engineering at CSU Fresno, for designing and building the rainfall simulators and soil boxes. The authors also thank Ronald Boquist, corporate manager of Moore Twining Associates, Inc., for his input in the runoff testing and analysis. This research was funded by the California State University, Fresno. The sponsorship is greatly appreciated. The authors also thank the anonymous reviewers for their constructive help in improving this paper.

REFERENCES

Barkley, T. (2004). "Erosion control with recycled materials." US DOT, FHWA, Public Road, March/April 2004. Available at http://www.tfhrc.gov/pubrds/04mar/03.htm. Accessed 3 July 2007

Buchanan, J.R., Yoder, D.C., and Smoot, J.L. (2000). "Controlling soil erosion on construction sites with steep slopes with wood chips." *American Society of Agriculture Engineers Annual International Meeting*, Milwaukee, Wisconsin. 2000.

Burton, G.A. and Pitt, R.E. (2001). "*Stormwater Effects Handbook: a textbook for watershed managers, scientists, and engineers*." Lewis Publishers, 2001.

California EPA, Integrated Waste Management Board. (2000). "Compost demonstration project, Placer County: Use of Compost and Co-compost as a Primary Erosion Control Materials." January, 2000.

Composting Council Research and Education Foundation (CCREF) and US Composting Council (USCC) (2001). "Compost use on state highway applications." Available at http://www.epa.gov/epaoswer/non-hw/compost/highway/. Accessed 29 June 2007

Faucette, L.B., Jordan, D.F., Risse, L.M., Cabrera, M., Coleman, D. C., and West, L.T. (2005). "Evaluation of stormwater from compost and conventional erosion control practices in construction activities." *Journal of Soil and Water Conservation*, Vol. 60 (6): 288-297.

Glanville, T.D., Richards, T.L., and Persyn, R.A. (2003). "Evaluating performance of compost blankets." *BioCycle.* Vol. 44 (5): 48-54.

Huang, P.M., Bollag, J.-M., and Senesi, N. (Ed.). (2002). "Interactions Between Soil Particles and Microorganisms: Impact on the Terrestrial Ecosystem." *IUPAC Series on Analytical and Physical Chemistry of Environmental Systems*, Vol. 8. John Wiley and Sons.

Humphry, J.B., Daniel, T.C., Edwards, D.R., and Sharpley, A.N. (2002). "A portable rainfall simulator for plot-scale runoff studies." *Applied Engineering in Agriculture* Vol. 18 (2): 199-204.

US EPA. (1999). Clean Water Act, EPA 822-Z-99-001, Washington, D.C., June 1999.

Simplified Method for Estimating Scour at Bridges

A. V. Govindasamy[1], J.-L. Briaud[2], H.-C. Chen[1], J. Delphia[3], K. Elsbury[1], P. Gardoni[1], G. Herrman[3], D. Kim[1], C.C. Mathewson[1], M. McClelland[3], F. Olivera[1]

[1]Texas A&M University, College Station, Texas 77843-3136 [2]Zachry Dept. of Civil Engineering, Texas A&M University, College Station, Texas, 77843-3136; briaud@tamu.edu [3]Texas Department of Transportation, Austin, Texas

ABSTRACT: Scour at bridges is a major cause of bridge failure in the United States. Current available methods of bridge scour evaluation rely upon two categories of assessment methods. The first category is an initial evaluation process that is based on field observations and is primarily qualitative in nature. This method does not utilize actual measured scour data. The second category involves calculations of maximum scour depth based on flume tests on sand. The first method does not provide realistic results in many cases due to its reliance on a more qualitative form of assessment. The second method is often conservative in the case of clays, which are known to erode at a much slower rate than sand. A simplified method for estimating the scour risk of a bridge has been developed. The proposed method comprises three phases presented in decision tree format. The first phase utilizes measured scour data and observed or estimated flow parameters at a bridge to evaluate the scour risk. The second and third phases involve simple calculations to obtain maximum scour depth and time dependent scour depth, respectively. Phases two and three do not require site specific erosion testing of bridge foundation soils. The proposed method will provide more realistic scour risk estimates due to the fact that it utilizes measured data and accounts for time dependent scour depth for clays. The elimination of site specific erosion testing reduces the effort and cost associated with evaluating a bridge for scour.

INTRODUCTION

Out of the approximately 600,000 bridges in the United States, 500,000 are over water (National Bridge Inventory 1997). In the last 30 years more than 1,000 of the 600,000 bridges have failed. Of those failures, 60% were caused by scour, with earthquakes accounting for only 2% (Shirole and Holt 1991). The average cost for flood damage repair of highways on the federal aid system is $50 million per year (Lagasse et al. 1995). From a collective evaluation of bridges over waterways carried out by state Departments of Transportation (DOT) in the United States, it was found that 62.4% of these bridges have a low risk of scour failure, 13.5% are scour susceptible, 20.0% have unknown foundations, 0.6% are left to be screened, and 3.5%

or about 17,000 bridges are scour critical, which means that they are likely to fail if subjected to a 100-year flood (Pagan-Ortiz 1998). These statistics give a clear indication of the significance of the bridge scour problem and highlight the need of a proper bridge scour assessment program.

The methods currently available for bridge scour evaluation rely upon two categories of assessments. The first category is an initial evaluation process that is qualitative in nature and is based on the bridge inspector's field observations. This method does not utilize actual measured scour data. The second method is a quantitative assessment that involves calculations of maximum scour depth based on flume tests on sand. The first method does not provide realistic results in many cases due to its reliance on a more qualitative form of assessment. The second method is often conservative in the case of clays, which are known to erode at a much slower rate than sand.

This paper presents a simplified method for estimating the scour risk of a bridge which has and is being developed by the authors. The proposed method consists of three phases termed Bridge Scour Assessments 1, 2 and 3 (BSA 1, BSA 2 & BSA 3) presented in decision tree format. BSA 1 utilizes measured scour data and observed or estimated flow parameters at a bridge to evaluate the scour risk. BSA 2 and BSA 3 involve simple calculations to obtain maximum scour depth and time dependent scour depth, respectively. BSA 2 and BSA 3 do not require site specific erosion testing of bridge foundation soils, but instead utilize an erosion chart to determine the erodibility and erosion function of geologic material.

CURRENT PRACTICE

Scour can be divided into general scour (general erosion of the stream bed without obstacles), local scour (scour generated by the presence of obstacles such as piers and abutments), and channel migration (lateral movement of the main stream channel) (Briaud et al. 1999).

Initial scour evaluation procedures have been developed by/for several state DOT's. These methods are either qualitative in nature, or rely on simplified scour depth – hydraulic parameter relationships that are mainly based on flume tests in sand. These methods, unlike the BSA 1 do not make use of measured scour depths in the field. For example, the Montana DOT, in collaboration with the United States Geological Survey (USGS), developed a rapid scour evaluation process that relies upon calculated scour depth – measured hydraulic parameter relationships (Holnbeck and Parrett 1997). A similar method has also been adopted by the Missouri DOT (Huizinga and Rydlund 2004). The Tennessee DOT uses an initial evaluation process that utilizes a qualitative index based on field observations to describe the potential problems resulting from scour (Simon et al. 1989). Similar qualitative methods have been adopted by the California, Idaho and Texas DOTs and the Colorado Highway Department for their initial assessment of bridges for scour. Johnson (2005) developed a preliminary assessment procedure that individually rates 13 stream channel stability indicators, which are then summed to provide an overall score that places a bridge in one of four categories: excellent, good, fair and poor.

Current practice for more detailed scour evaluation is heavily influenced by two FHWA hydraulic engineering circulars called HEC-18 and HEC-20 (Richardson and Davis 2001; Lagasse et al. 1995). These methods regroup the work of many investigators and are known to be overly conservative in the case of clays and some types of rock due to the fact that they are based on flume tests in sand and do not account for time-dependent scour. Briaud et al. (1999, 2005) at Texas A&M University developed models to calculate scour depths due to pier and contraction scour that are capable of accounting for time-dependent scour in clays. However, these methods require site specific erosion testing.

BRIDGE SCOUR ASSESSMENT 1 (BSA 1)

BSA 1 makes use of existing data collected either from bridge records maintained by the authorities or by site visit. Figure 1 shows the BSA 1 flowchart. BSA 1 essentially is aimed at determining the probability that the scour depth corresponding to the 100-year flood (Z_{100}) exceeds the scour depth leading to a foundation safety factor of one ($Z_{threshold}$). The value of $Z_{threshold}$ can be obtained from simple foundation bearing capacity calculations. Z_{100} is obtained from the following equation:

$$(Z_{mo}/Z_{100}) = (V_{mo}/V_{100})^{\beta} \qquad (1)$$

where Z_{mo} = maximum observed scour depth in the field
V_{mo} = maximum flow ever experienced by the bridge
V_{100} = flow velocity corresponding to the 100-year flood, Q_{100}
β = 1 for flow velocities within the range of 0.1 to 3.5 m/s

Equation (1) is based on the work being carried out by the authors on the relationship between calculated scour depth and flow velocity. Preliminary findings indicate that the value of the β is around 1 for velocities ranging from 0.1 m/s to 3.5 m/s. This velocity range is well within the range of velocities in rivers in the Unites States. Once the required parameters are obtained, the probability of Z_{100} exceeding $Z_{threshold}$, $P(Z_{100} > Z_{threshold})$ is determined. If $P(Z_{100} > Z_{threshold})$ is below a pre-determined operating risk level, R, the bridge is found as “Minimal Risk (Regular Monitoring).” The term “Regular Monitoring” refers to the routine bridge inspections carried out by relevant authorities. If the bridge is not found as “Minimal Risk (Regular Monitoring)” at the end of BSA 1, BSA 2 needs to be undertaken.

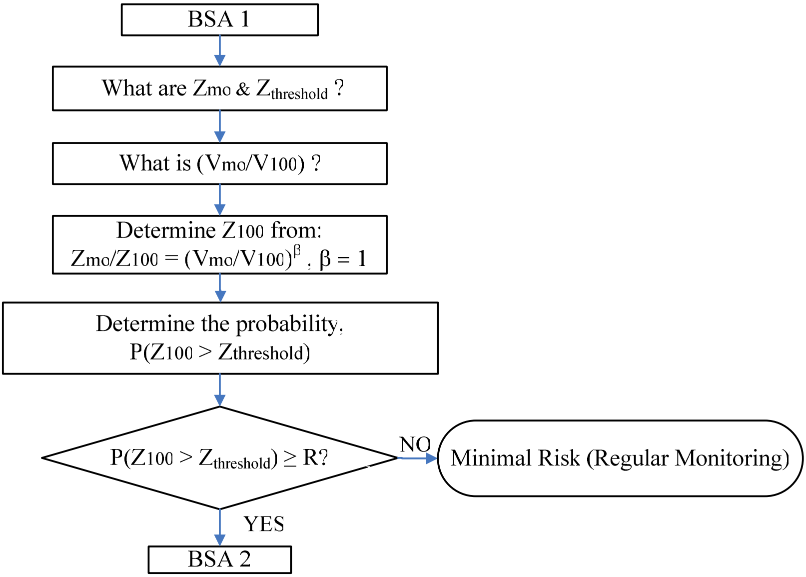

FIG. 1. Bridge Scour Assessment 1 Flowchart.

BRIDGE SCOUR ASSESSMENT 2 (BSA 2)

The BSA 2 flowchart is shown in Figure 2. BSA 2 consists of two parts. The first part is essentially a simple filtering process that utilizes the critical velocity of the soil present at the bridge (V_c) and local velocities at the pier, contraction or abutment ($V_{max,p}$, $V_{max,c}$ and $V_{max,a}$, respectively). The critical velocity is obtained by an Erosion Chart developed on the basis of a database of more than 500 Erosion Function Apparatus (EFA) tests (Briaud et al. 1999) and on the experience of the authors (Figures 3a and 3b). The Erosion Chart shows erosion categories for various soils and the bridge inspector can determine the relevant critical velocity. This chart essentially eliminates the need for site specific erosion testing. Work on the Erosion Chart is on-going and the chart presented herein is based on preliminary findings. The following equations for local velocities are derived from the authors experience and numerical simulations results:

$$V_{max,p} = 1.5\ V_{appr} \tag{2}$$

$$V_{max,c} = V_{appr} / R_c \tag{3}$$

$$V_{max,a} = 1.5\ V_{max,c} \tag{4}$$

where V_{appr} = approach velocity upstream of the bridge and R_c = contraction ratio (the ratio of the contracted width of the channel to the uncontracted width of the channel).
If the local velocities exceed the soil critical velocity, then the second part of BSA 2 is required to be carried out. Otherwise, the velocities at the obstruction are less than the velocity required to initiate significant erosion and the bridge is categorized as "Minimal Risk (Regular Monitoring)."

In the second part of BSA 2, simple calculations for maximum scour depth are carried out. The calculations for maximum pier scour and contraction scour are adopted from Briaud et al. (1999, 2005). Calculations for maximum abutment scour are based on HEC-18. The maximum local scour depth, $Z_{max,l}$ is a summation of all three scour components:

$$Z_{max,l} = Z_{max,p} + Z_{max,c} + Z_{max,a} \tag{5}$$

where $Z_{max,p}$, $Z_{max,c}$ and $Z_{max,a}$ are the maximum pier scour, contraction scour and abutment scour, respectively.

If $Z_{max,l}$ does not exceed $Z_{threshold}$, the bridge is deemed as "Minimal Risk (Regular Monitoring)". Otherwise, BSA 3 needs to be undertaken.

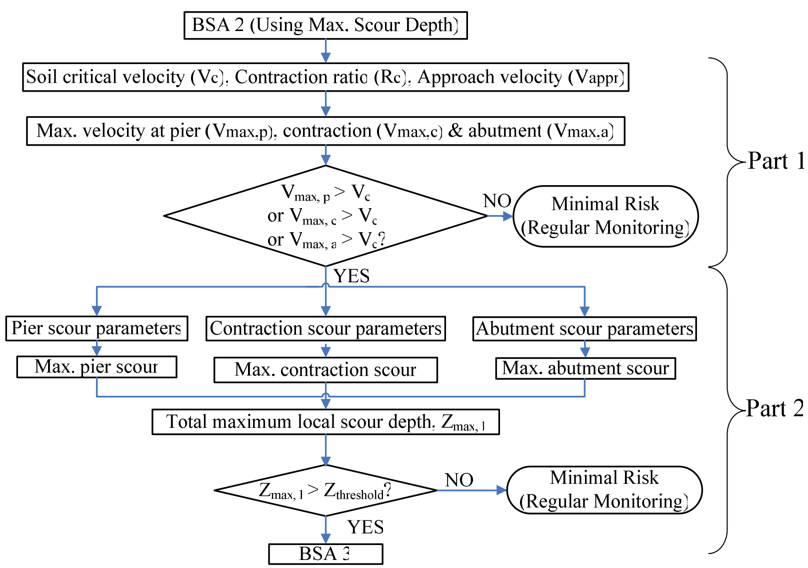

FIG. 2. Bridge Scour Assessment 2 Flowchart.

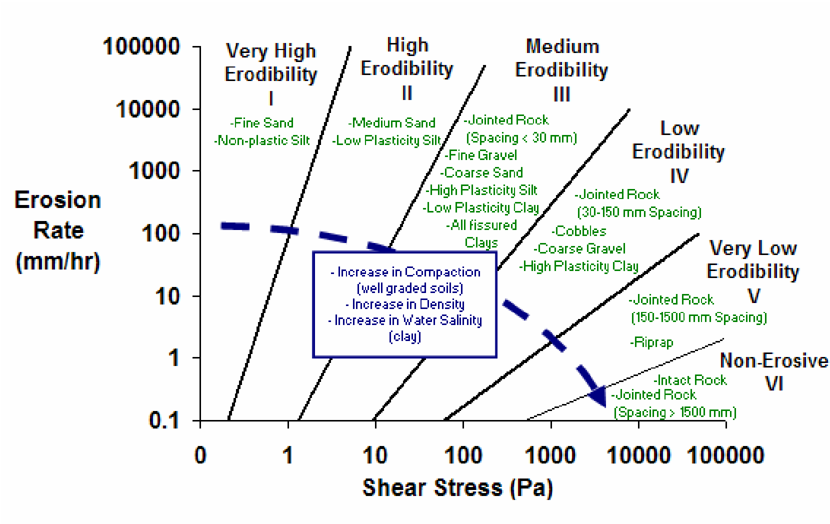

FIG. 3(a). Erosion Chart (Shear Stress)

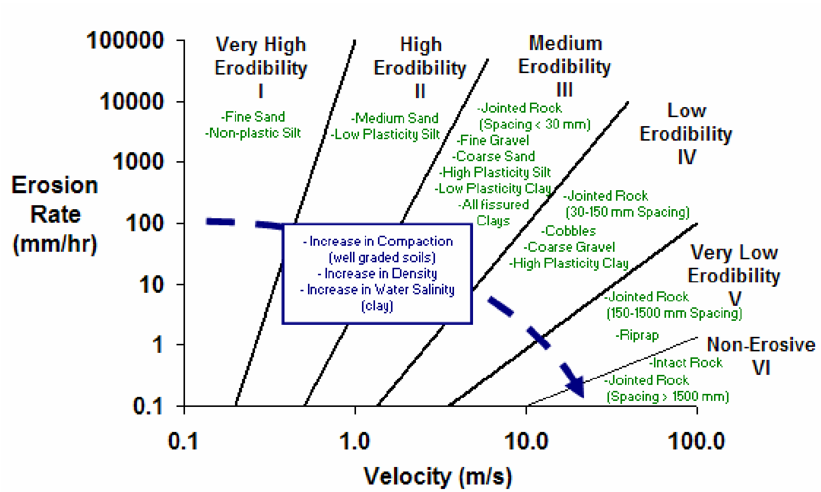

FIG. 3(b). Erosion Chart (Velocity)

BRIDGE SCOUR ASSESSMENT 3 (BSA 3)

The BSA 3 flowchart is shown in Figure 4. BSA 3 involves the calculation of time dependent scour depth, $Z_{fin,l}$ which is a summation of the three scour components:

$$Z_{fin,l} = Z_{fin,p} + Z_{fin,c} + Z_{fin,a} \tag{6}$$

where $Z_{fin,p}$, $Z_{fin,c}$ and $Z_{fin,a}$ are the pier scour, contraction scour and abutment scour after a specified time, respectively.

BSA 3 utilizes the hyperbolic model determine to $Z_{fin,l}$ (Briaud et al. 1999 and 2005):

$$z_{fin,\,p} = \frac{t}{\dfrac{1}{\dot{z}_i} + \dfrac{t}{z_{max,\,p}}} \tag{7}$$

$$z_{fin,\,c} = \frac{t}{\dfrac{1}{\dot{z}_i} + \dfrac{t}{z_{max,\,c}}} \tag{8}$$

where $\dot{Z}_i$ is the initial scour rate.

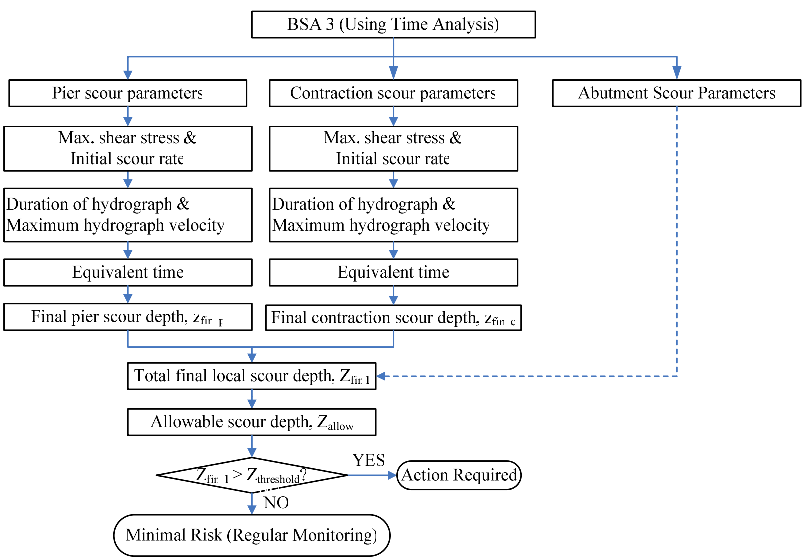

FIG. 4. Bridge Scour Assessment 3 Flowchart.

$\dot{Z}_i$ is the scour rate on the Erosion Chart (Figure 3) which corresponds to the shear stress at the initiation of scour, τ_{max}. t is the equivalent time which is the time required for the maximum velocity in the hydrograph to create the same scour depth as the one created by the complete hydrograph (Briaud et al. 1999).

The process of determining the time dependent abutment scour, $Z_{fin,a}$ is ongoing. At this point in time, the reader is referred to HEC-18 for maximum abutment scour depth calculations. If $Z_{fin,l}$ does not exceed $Z_{threshold}$, the bridge is deemed as "Minimal Risk (Regular Monitoring)". Otherwise, action is required.

ONGOING RESEARCH AND FUTURE IMPROVEMENTS

The method presented in this paper is a result of ongoing research work at Texas A&M University lead by Dr. Jean-Louis Briaud. Several additions to the material presented herein are in the development stage and it is envisioned that the final product will be a comprehensive method for bridge scour assessment. Some of the planned additions are the simplified determination of the V_{mo}/V_{100} ratio from bridge flow data as well as rainfall data. Work is also underway to improve and verify the Erosion Chart. Additionally, the probability $P(Z_{100} > Z_{threshold})$ in BSA 1 will incorporate a Bayesian statistical procedure that updates the probability of exceedence based on observed scour depth (Z_{mo}). The final product will also be subjected to verification with field data.

CONCLUSION

A new method for evaluating bridges for scour has been developed and divided into three Bridge Scour Assessments (BSA). BSA 1 is based on a relatively new idea of incorporating actual scour measurements into a preliminary assessment for bridge scour before more detailed scour calculations are carried out if required. BSA 2 and BSA 3 involve simple calculations for maximum and time dependent scour depth, respectively and do not require site specific erosion testing.

ACKNOWLEDGEMENTS

This project was sponsored by the Texas Department of Transportation.

REFERENCES

Briaud, J.-L., Ting, F.C.K., Chen, H.C., Rao G., Perugu, S. and Wei, G. (1999). "SRICOS: prediction of scour rate in cohesive soils at bridge piers." *Journal of Geotechnical and Environmental Engineering*, Vol. 125, (4): 237-246.

Briaud, J.-L., Chen, H.C., Li, Y., Nurtjahyo, P. and Wang, J. (2005). "SRICOS-EFA method for contraction scour in fine-grained soils." *Journal of Geotechnical and Geoenvironmental Engineering*, Vol. 131, (10): 1289-1294.

Holnbeck, S.R. and Parrett, C. (1997). "Method for Rapid Estimation of Scour at Highway Bridges Based on Limited Site Data", *U.S. Geological Survey, Water-Resources Investigations Report* 96-4310, Helena, Montana. pp. 79.

Huizinga, R.J. and Rydlund, P.H. (2004). "Potential-Scour Assessments and Estimates of Scour Depth Using Different Techniques at Selected Bridge Sites in Missouri", *Scientific Investigations Report 2004-5213,U.S. Geological Survey*, pp 41.

Johnson, P.A. (2005). "Preliminary Assessment and Rating of Stream Channel Stability Near Bridges." *Journal of Hydraulic Engineering*, Vol. 131, (10): 845-852.

Lagasse, P.F., Shall, J.D., Johnson, F., Richardson, E.V., and Chang, F. (1995). "Stream stability at highway structures." U.S. Federal Highway Administration Publication, Rep. No. FHWA-IP-90-014, Hydraulic Engineering Circular No. 20, Washington, D.C., pp 195.

National Bridge Inventory. (1997). Bridge Management Branch, Federal Highway Administration, Washington, D.C**.**

Pagan-Ortiz, J. E. (1998). ''Status of scour evaluation of bridges over waterways in the United States.'' *Proc., ASCE Conf. on Water Resour. Engrg.*, ASCE, Reston, Va., 2–4.

Richardson, E. V., and Davis, S. M. (2001). "Evaluating scour at bridges." *Publication No. FWHA-IP-90-017, HEC-18*, U.S. Dept. of Transportation, Washington, D.C.

Shirole, A. M., and Holt, R. C. (1991). ''Planning for a comprehensive bridge safety assurance program.'' *Transp. Res. Rec. No. 1290*, Transportation Research Board, Washington, D.C., 137–142.

Simon, Andrew, Outlaw, George. S., and Thoman, Randy. (1989). "Evaluation, modeling and mapping of potential bridge scour, West Tennessee," *Proceedings of the Bridge Scour Symposium*, Subcommittee on Sedimentation, Interagency Advisory Committee on Water Data, co-sponsored by Federal Highway Administration and U.S Geological Survey: 112-139.

The Ground Reaction Curve due to Tunnelling under Drainage Condition

Young-jin Shin[1], Byoung-min Kim[2], Shin-in Han[3], In-mo Lee[4], and Daehyeon Kim[5]

[1]School of Civil Engineering, Purdue University, West Lafayette: iamyjshin@gmail.com
[2] Underground Space Construction Technology Centre, Seoul, Korea
[3] Department of Civil Engineering, Korea University, Seoul, Korea
[4] Department of Civil Engineering, Korea University, Seoul, Korea: inmolee@korea.ac.kr
[5]Indiana Department of Transportation, West Lafayette

ABSTRACT: When a tunnel is excavated below the groundwater table, water flows into the excavated wall of tunnel and seepage forces are acting on the tunnel wall. Such seepage forces significantly affect the ground behavior. The ground response to tunnelling is understood theoretically by the convergence-confinement method, which consists of three elements: longitudinal deformation profile, ground reaction curve, and support characteristic curve. The seepage forces are likely to have a strong influence on the ground reaction curve which is defined as the relationship between internal pressure and radial displacement of the tunnel wall. In this paper, seepage forces arising from the ground water flow into a tunnel were estimated quantitatively. Magnitude of seepage forces was determined based on hydraulic gradient distribution around tunnel. To estimate seepage forces, different cover depths and groundwater table levels were considered. Using these results, the theoretical solutions for the ground reaction curve (GRC) with consideration of seepage forces under steady-state flow were derived.

INTRODUCTION

When a tunnel is excavated below the groundwater table, groundwater may flow into the tunnel and, consequently, seepage forces may develop in the ground seriously affecting the behavior of the tunnel. Ground response to tunnelling can be understood theoretically by the convergence-confinement method. This method is based on the principle for which a tunnel is stabilized by controlling its displacements after installation of a support near the tunnel face. The convergence-confinement method is based on three elements: the longitudinal deformation profile, the ground reaction curve, and the support characteristic curve. The longitudinal deformation profile assuming no support shows the radial displacement of the tunnel cross-section in the longitudinal direction from the tunnel face. The support characteristic curve describes the increasing pressure that acts on the supports as the radial displacement of the tunnel increases. Lastly, the ground reaction curve shows the increasing trends of radial displacement as the internal pressure of the tunnel decreases. Tunnelling below the ground water table induces additional seepage stresses (Shin et al., 2007), and the seepage forces are likely to have a strong influence on the ground reaction curve.

Previous studies on the ground reaction curve by Stille (1989), Wang (1994), Carranza-Torres(2002), Sharan (2003), and Oreste (2003) did not consider seepage forces. The effects of seepage forces on the tunnel face or the support system were studied by Muir Wood (1975), Curtis (1976), Atkinson (1983), Schweiger (1991), Fernandez and Alveradez (1994), Fernandez (1994), Lee and Nam (2001), Bobet (2003), Shin et al. (2005). A simplified analytical solution of the ground reaction curve was suggested by Lee et al. (2007); however, mathematical solutions of ground reaction curves influenced by seepage forces have not been suggested.

In this study, based on these previous studies, the theoretical solutions of the ground reaction curve considering seepage forces due to groundwater flow under steady-state flow were derived.

THEORETICAL SOLUTION OF GROUND REACTION CURVE WITH CONSIDERATION OF SEEPAGE FORCES

Theoretical solution for stress

It is assumed that a soil-mass behaves as an isotropic, homogeneous and permeable medium. Also, an elasto-plastic model based on a linear Mohr-Coulomb yield criterion is adopted in this study, as indicated in Figure 1.

$$\sigma_1' = k\sigma_3' + (k-1)a \tag{1}$$

Here σ_1' indicates the major principal stress, σ_3' is the minor principal stress, $k = \tan^2(45 + \frac{\phi}{2})$, $a = \frac{c}{\tan\phi}$, where k and a are the Mohr-Coulomb constants, c is the cohesion, and ϕ is the friction angle.

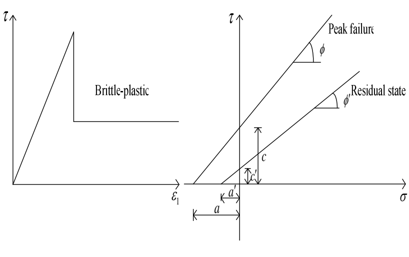

FIG. 1. Elasto-plastic model based on Mohr-Coulomb yield criterion

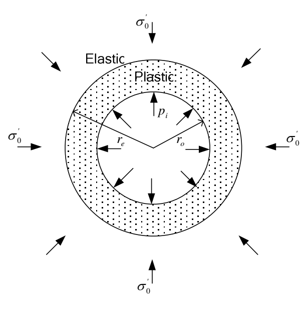

FIG. 2. Circular opening in an infinite medium

Figure 2 shows a circular opening of radius r_0 with $k_0 = 1$ in an infinite soil-mass subject to a hydrostatic in situ stress, σ_0' . The opening inner surface is subject to the outward radial pressure to the tunnel surface, p_i (k_0 means the ratio of effective vertical stress and horizontal stress).

Considering all the stresses on an infinitesimal element *abcd* of unit thickness during excavation of a circular tunnel in Figure 3, when $\partial\theta$ is small, the equilibrium of radial forces with respect to r and θ can be expressed as follows:

$$\frac{\partial\sigma_r'}{\partial r}+\frac{1}{r}\frac{\partial\sigma_{r\theta}}{\partial\theta}+\frac{\sigma_r'-\sigma_\theta'}{r}+F_r=0 \tag{2}$$

$$\frac{1}{r}\frac{\partial\sigma_\theta'}{\partial\theta}+\frac{\partial\sigma'_{r\theta}}{\partial r}+\frac{2\sigma'_{r\theta}}{r}+F_\theta=0 \tag{3}$$

If the tunnel is excavated under the groundwater table, then it acts as a drain. The body force is the seepage stress, as illustrated in Figure 3.

$$F_r=i_r\gamma_w \tag{4}$$

$$F_\theta=i_\theta\gamma_w \tag{5}$$

In this state, i_r and i_θ are the hydraulic gradients in the r and θ directions, respectively, and γ_w is the unit weight of the groundwater.

Therefore, (2) and (3) can be rewritten as follows:

$$\frac{\partial\sigma_r'}{\partial r}+\frac{1}{r}\frac{\partial\sigma'_{r\theta}}{\partial\theta}+\frac{\sigma_r'-\sigma_\theta'}{r}+i_r\gamma_w=0 \tag{6}$$

$$\frac{1}{r}\frac{\partial\sigma_\theta'}{\partial\theta}+\frac{\partial\sigma'_{r\theta}}{\partial r}+\frac{2\sigma'_{r\theta}}{r}+i_\theta\gamma_w=0 \tag{7}$$

If the stress distribution is symmetrical with respect to the axis O in Figure 3, then the stress components do not vary with angular orientation, θ, and therefore, they are functions of the radial distance r only. Accordingly, (6) reduces to the single equation of equilibrium as follows:

$$\frac{d\sigma_r'}{dr}+\frac{\sigma_r'-\sigma'_\theta}{r}+i_r\gamma_w=0 \tag{8}$$

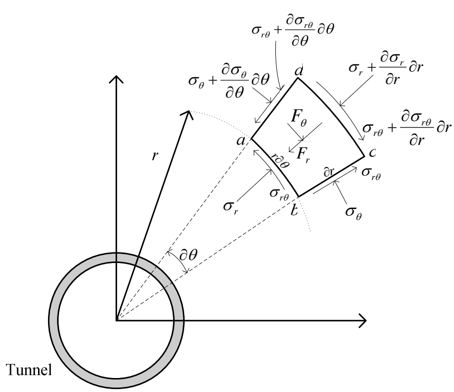

FIG. 3. Body forces under the groundwater table

For the plastic region, (1) can be modified as follows:

$$\sigma'_\theta = k_r \sigma'_r + (k_r - 1)a_r \tag{9}$$

where $k_r = \tan^2(45 + \frac{\phi_r}{2})$, $a_r = \frac{c_r}{\tan\phi_r}$, k_r and a_r are the Mohr-Coulomb constants, c_r is the cohesion, and ϕ_r is the friction angle in the plastic region.

Substituting (9) into (8) and solving it with the boundary conditions $\sigma'_r = p_i$ at $r = r_0$. Then, the radial and circumferential effective stresses in the plastic region are as follows (Shin et al., 2007):

$$\sigma'_{rp} = \left(\frac{r_0}{r}\right)^{1-k_r}(p_i + a_r) - a_r - \frac{\gamma_w}{r^{1-k_r}}[\int_{R_0}^{r} \xi^{1-k_r} i_r(\xi)d\xi - \int_{R_0}^{r_0} \xi^{1-k_r} i_r(\xi)d\xi] \tag{10}$$

$$\sigma'_{\theta p} = k_r\left(\frac{r_0}{r}\right)^{1-k_r}(p_i + a_r) - a_r - k_r\frac{\gamma_w}{r^{1-k_r}}[\int_{R_0}^{r} \xi^{1-k_r} i_r(\xi)d\xi - \int_{R_0}^{r_0} \xi^{1-k_r} i_r(\xi)d\xi] \tag{11}$$

where, R_0 is the distance from ground to the center of tunnel.

In this equation, p_i is all the support pressure developed by in situ stress and seepage. Subscripts rp and θp are the radial and tangential effective stresses in the plastic region, respectively.

In order to estimate the effective stress in the elastic region, the superposition concept is used. As shown in Figure 4, the effective stress considering the seepage force can be assumed as a combination of the solution of the equilibrium equation for the dry condition and the effective stress only considering seepage.

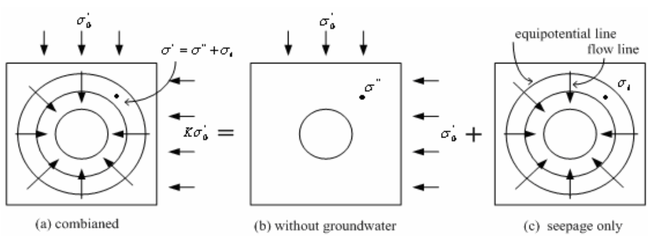

FIG. 4. Concept of superposition in elastic region.

The Kirsch solutions are applied to solve the effective stresses in the elastic region under dry condition (Timoshenko and Goodier, 1969).

For the seepage condition, Stern (1969) suggests effective stresses in the elastic region with consideration of the seepage force as follows:

$$\sigma'_{rei} = -\frac{C}{r^2} - \frac{A}{4}\left[2\log(r) - 1\right] - \frac{B}{2} - \frac{1}{2(v-1)}I(r) - \frac{2v-1}{2(1-v)}J(r) \tag{12}$$

$$\sigma'_{\theta ei} = \frac{C}{r^2} - \frac{A}{4}\left[2\log(r) + 1\right] - \frac{B}{2} - \frac{1}{2(v-1)}I(r) + \frac{2v-1}{2(1-v)}J(r) \tag{13}$$

where $I(r)=\gamma_w\int_{R_0}^{r} i_r(\xi)d\xi$, $J(r)=\frac{\gamma_w}{r^2}\int_{R_0}^{r}\xi^2 i_r(\xi)d\xi$, C, A and B are constants defined by the boundary conditions.

(12) and (13) can be solved by using the boundary conditions $\sigma'_{rei}=0$ at $r=r_0$, $\sigma'_{rei}=0$ at $r=R_0$, and $\sigma'_{\theta ei}=0$ at $r=R_0$.

Here, subscript i represents the term related to seepage.

Consequently, the radial and tangential effective stresses with consideration of the seepage forces in the elastic region can be obtained by the superposition of both of solutions as follows:

$$\sigma'_{re}=\frac{-Z}{\frac{-1}{r_0^2}+\frac{2\log R_0-2\log r_0+1}{R_0^2}}\frac{1}{r^2}-\frac{Z}{\frac{-1}{r_0^2}+\frac{2\log R_0-2\log r_0+1}{R_0^2}}\frac{1}{R_0^2}\left[2\log(r)-1\right]$$
$$+\frac{Z}{\frac{-1}{r_0^2}+\frac{2\log R_0-2\log r_0+1}{R_0^2}}\frac{2\log R_0}{R_0^2}-\frac{1}{2(v-1)}I(r)-\frac{2v-1}{2(1-v)}J(r)+\sigma'_0-(\sigma'_0-p_i)\left(\frac{r_0}{r}\right)^2 \tag{14}$$

$$\sigma'_{\theta e}=\frac{Z}{\frac{-1}{r_0^2}+\frac{2\log R_0-2\log r_0+1}{R_0^2}}\frac{1}{r^2}-\frac{Z}{\frac{-1}{r_0^2}+\frac{2\log R_0-2\log r_0+1}{R_0^2}}\frac{1}{R_0^2}\left[2\log(r)+1\right]$$
$$+\frac{Z}{\frac{-1}{r_0^2}+\frac{2\log R_0-2\log r_0+1}{R_0^2}}\frac{2\log R_0}{R_0^2}-\frac{1}{2(v-1)}I(r)+\frac{2v-1}{2(1-v)}J(r)+\sigma'_0+(\sigma'_0-p_i)\left(\frac{r_0}{r}\right)^2 \tag{15}$$

Here, $Z=\frac{1}{2(v-1)}\gamma_w\int_{R_0}^{r_0} i_r(\xi)d\xi+\frac{2v-1}{2(1-v)}\frac{\gamma_w}{r_0^2}\int_{R_0}^{r_0}\xi^2 i_r(\xi)d\xi$

(16) is derived from (14) and (15) and the Mohr-Coulomb yield criterion at the stress state in the elastic region.

$$\sigma'_{r_e}=\frac{1}{1+k}\left(2\sigma'_0\right)+\frac{1-k}{1+k}a+\frac{1}{1+k}(-A\left[\log(r_e)\right]-B-\frac{1}{(v-1)}I(r_e)) \tag{16}$$

Where,

$$A=\frac{Z}{\frac{-1}{r_0^2}+\frac{2\log R_0-2\log r_0+1}{R_0^2}}\frac{4}{R_0^2}\quad B=\frac{-Z}{\frac{-1}{r_0^2}+\frac{2\log R_0-2\log r_0+1}{R_0^2}}\frac{4\log R_0}{R_0^2}$$

Finally, at the interface between the plastic and elastic regions, $r=r_e$, the radial stress calculated in the plastic region must be identical to that in the elastic region. Consequently, (10) should be equal to (16) since the radial stress should be continuous over the boundary. The radius of the plastic zone, r_e, can be derived as follows:

$$r_e=r_0\left[\frac{1}{p_i+a_r}\left\{\begin{array}{l}\frac{1}{1+k}\left(2\sigma'_0\right)+\frac{1-k}{1+k}a+a_r+\frac{1}{1+k}(\frac{-1}{(v-1)}\gamma_w\int_{R_0}^{r_e} i_r(\xi)d\xi\\ -A\left[\log(r_{ec})\right]-B)\\ +\frac{\gamma_w}{r_e^{1-k_r}}[\int_{R_0}^{r_e}\xi^{1-k_r}i_r(\xi)d\xi-\int_{R_0}^{r_0}\xi^{1-k_r}i_r(\xi)d\xi]\end{array}\right\}\right]^{\frac{1}{k_r-1}} \tag{17}$$

Theoretical solution for displacement

The radial displacement for a circular tunnel can be worked out based on the elasto-plastic theory. The strains in the plastic region are composed of elastic and plastic strains, and are expressed as Eqn. (18) and (19), respectively. The superscripts e and p represent the elastic and plastic parts, respectively. By considering compressive strains and radially inward displacements to be positive, the relationship between strain and displacement at any point in a soil-mass can be written as follows:

$$\varepsilon_r = \varepsilon^e{}_r + \varepsilon^p{}_r \tag{18}$$

$$\varepsilon_\theta = \varepsilon^e{}_\theta + \varepsilon^p{}_\theta \tag{19}$$

$$\varepsilon_r = \frac{-du_r}{dr} \tag{20}$$

$$\varepsilon_\theta = \frac{-u_r}{r} \tag{21}$$

The plastic strain can be represented by using the plastic flow rule. When the volume expansion effect is important in plastic strain, generally the non-associated flow rule is valid; otherwise, the associated flow rule is valid. The plastic potential function, Q, when using non-associated flow rule, is as follows:

$$Q = f(\sigma_r, \sigma_\theta) = \sigma_\theta - k_\psi \sigma_r - 2c\sqrt{k_\psi} = 0 \tag{22}$$

where $k_\psi = \dfrac{1+\sin\psi}{1-\sin\psi}$, the parameter ψ is the dilation angle.

The plastic parts of radial and circumferential strains can be related as follows:

$$\varepsilon^p_r = -k_\psi \varepsilon^p_\theta \tag{23}$$

Eqn. (20) ~ (23) lead to the following differential equation.

$$\frac{du_r}{dr} + k_\psi \frac{u_r}{r} = f(r) \tag{24}$$

where $\varepsilon^e_r + k_\psi \varepsilon^e_\theta = f(r)$ (25)

Eqn. (24) can be solved by using the following boundary condition for the radial displacement, $u_{r(r=r_e)}$, at the elasto-plastic interface (Brady and Brown, 1993).

$$u_{r(r=r_e)} = \frac{-b}{2G}(\sigma_{vo} - \sigma_{r(r=r_e)}) \tag{26}$$

where G is the shear modulus of the soil-mass.

Eqn. (24) - (26) lead to the following expressions for the radial displacement:

$$u_r = r^{-k_\psi} \int_{r_e}^{r} r^{k_\psi} f(r)dr + u_{r(r=r_e)} \left(\frac{r_e}{r}\right)^{k_\psi} \tag{27}$$

In order to evaluate the integral in the above equation, expressions for ε^e_r and ε^e_θ can be obtained by the following equation (Brady and Brown, 1993):

$$\varepsilon^e_r = \frac{1}{2G}[(1-2\upsilon)C + \frac{D}{r^2}] \tag{28}$$

$$\varepsilon_\theta^e = \frac{1}{2G}[(1-2\upsilon)C - \frac{D}{r^2}] \tag{29}$$

Here $C = \dfrac{(\sigma'_{r(r=r_e)} - \sigma'_0)r_e^2 - (p_i - \sigma'_0)r_0^2}{r_e^2 - r_0^2}$, $D = \dfrac{(p_i - \sigma'_{r(r=r_e)})r_0^2 r_e^2}{r_e^2 - r_0^2}$, and υ is the Poisson`s ratio of the soil-mass.

Eqn. (26) can be solved by using Eqn. (28) and (29). The expression for the radial displacement in the plastic region at the opening surface $r = r_0$ is given by Eqn. (30).

$$u_{r(r=r_0)} = \frac{1}{2G} r_0^{-k_\psi}[C(1-2\upsilon)(r_e^{k_\psi+1} - r_0^{k_\psi+1}) - D(r_e^{k_\psi-1} - r_0^{k_\psi-1})] + u_{r(r=r_e)}(\frac{r_e}{r_0})^{k_\psi} \tag{30}$$

The ground reaction curve is estimated by using the theoretical solutions for the cases in which the cover depth of the tunnel, C, and water height, H, are 10 times the diameter of tunnel, D. As shown in Figure 5, the ground reaction curve with consideration of seepage force shows larger radial displacement than the ground reaction curve for the dry condition; this result means that there is no ground water when the cover depth of the tunnel, C, is 10 times the diameter of the tunnel, D. This is due to the fact that even if the effective overburden pressure can be decreased by the arching effect during tunnel excavation, seepage forces still remain.

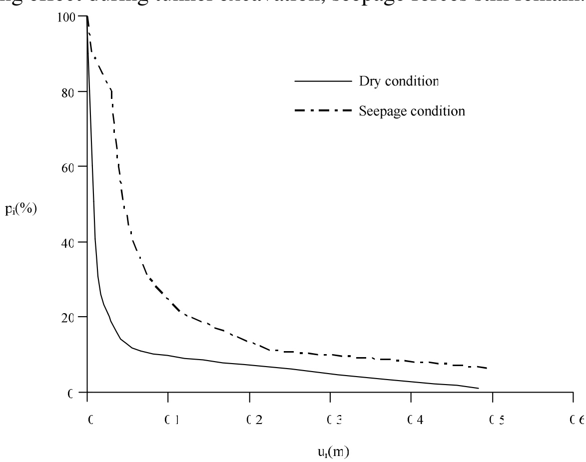

FIG. 5. The ground reaction curve ($C/D = 10$, $H/D = 10$)

CONCLUSIONS

The flow of groundwater has a significant effect on the radial displacement of a tunnel wall. While the effective overburden pressure is reduced slightly by the arching effect during tunnel excavation, seepage forces still remain. Therefore, the presence of groundwater induces larger radial displacements of the tunnel wall than those in the case of dry condition.

ACKNOWLEDGMENTS

This paper was supported by the Underground Space Construction Technology Center under the Ministry of Construction and Transportation in Korea (Grant C04-01).

REFERENCES

Atkinson, J.H. and Mair, R.J. (1983). "Loads on leaking and watertight tunnel lining, sewers and buried pipes due to groundwater." *Geotechnique*, Vol. 33(3): 341-344.

Brady, B.H.G. and Brown, E.T. (1993). “Rock mechanics for underground mining.” London; Chapman and Hall.

Carranza-Torres, C. (2002). "Dimensionless Graphical Representation of the Exact Elasto-plastic Solution of a Circular Tunnel in a Mohr-Coulomb Material Subject to Uniform Far-field Stresses." *Rock Mechanics and Rock Engineering*, Vol. 36(3): 237-253.

Fernandez, G. and Alvarez, T.A. (1994). "Seepage-induced effective stresses and water pressures around pressure tunnels." *J. Geotechnical Engineering*, Vol. 120(1): 108-128.

Lee, S.W., Jung, J.W., Nam, S.W. and Lee, I.M. (2007). "The influence of seepage forces on ground reaction curve of circular opening." *Tunnelling and Underground Space Technology*, Vol. 21: 28-38.

Oreste, P.P. (2003). "Analysis of structural interaction in tunnels using the convergence-confinement approach.", *Tunnelling and Underground Space Technology*, Vol. 18: 347-363.

Schweiger, H.F., Pottler, R.K. and Steiner H. (1991). "Effect of seepage forces on the shotcrete lining of a large undersea cavern." *Computer Method and Advances in Geomechanics*, Beer, Booker & Carter (eds), pp. 1503-1508.

Sharan, S.K. (2003). "Elastic-brittle-plastic analysis of circular openings in Hoek-Brown media." *International J. of Rock Mechanics and Mining Sciences*, Vol. 40: 817-824.

Shin, J.H., Potts, D.M. and Zdravkovic, L. (2005). "The effect of pore-water pressure on NATM tunnel lingings in decomposed granite soil." *Canadian Geotechnical J.*, Vol. 42: 1585-1599.

Shin, J.H., Lee, I.M. and Shin, Y.J. (2007). "Seepae-induced Stress due to Tunnelling under Drainage Condition.", *Canadian Geotechnical J.*, (Submitted).

Stille, H., Holmberg, M. and Nord, G. (1989), "Support of Weak Rock with Grouted Bolts and Shotcrete", *International J. of Rock Mechanics and Mining Sciences & Geomechanics Abstracts*, Vol. 26, No. 1, pp. 99-113.

Hydraulic Characteristics of the Hurricane Surge in the Mississippi Delta and Implications for Geotechnical Design of Coastal Protections

Hassan S. Mashriqui [1], M. ASCE and Radhey Sharma [2], M. ASCE

[1]Assistant Extension Professor – Coastal Engineering, Department of Biological and Agricultural Engineering, LSU Agricultural Center, 105 E.B. Doran Building, Baton Rouge, LA 70803. hmashriqui@agcenter.lsu.edu
[2]Associate Professor, Department of Civil and Environmental Engineering, Louisianan State University, Baton Rouge, LA 70803, rsharma@lsu.edu

ABSTRACT: Low lying coastal areas in the Mississippi River delta are susceptible to damage caused by surge, currents and waves as tropical cyclones make landfall. A fully parallel, 2-dimensional ADvanced CIRCulation model (ADCIRC) was used to simulate storm surge characteristics during hurricane Katrina. We have found that storm surge builds up over a large area but reaches its highest elevations when it encounters a steep shore face or is trapped against levees and floodwalls as it was around New Orleans. Our research showed that man-made canals have increased current velocities 2 to 3 times in the vicinity of earthen hurricane protection levees and allowed about 6 to 8 times more surge to propagate into the many coastal cities near New Orleans. Dynamic loads of the surge and waves along with the surge heights appear to be a significant factor in designing coastal structures.

INTRODUCTION

Low lying coastal areas with in the Mississippi River delta are susceptible to extensive inland flooding and to damage caused by surge, currents and waves as hurricanes make landfall. Louisiana coast has a large, shallow and gradually sloping shelf that enhances storm surge generation by preventing water going back to the Gulf and accumulating water against the coast. Local coastal features such as rivers, bayous and levees govern storm surge build up; helps amplify and channel the surge to a particular community (Mashriqui et al, 2006).

Primary concerns of many traditional storm surge analysis were to determine maximum height of the surge obtained from several days of hurricane event. While static water levels are important, storm surges have additional critical characteristics and impacts. For example, surge speed could be a factor in transporting large volume of water per unit time. During a breach high speed surge or rapid flow could inundate a community rapidly leading to higher fatality. Surge elevations have received the most attention to date (IPET, 2006) but current velocities could play a role in loss of life and property damage (Mashriqui et al, 2006).

Here, we focus on the spatial distribution of surge velocity and transport capacity of dredged channels, in addition to height, in an effort to better explain the dynamics that led to widespread rapid flooding on the east side of the city during Hurricane Katrina.

METHODS

In this research we have used the fully-parallel ADCIRC S08 bathymetry grid developed by Westerink et al. (2004) and Feyen et al. (2002). It consists of 314,442 finite element nodes in a domain large enough to reduce boundary effects that includes the western half of the Atlantic Ocean, the Caribbean Sea and the Gulf of Mexico (Figure 1 top). Computational mesh elements were large in deep water and very small and refined in the area around Louisiana. About 85 percent of these nodes are concentrated within Louisiana's wetlands and estuaries to reproduce the complex geometry of natural and manmade channels and levee systems (Figure 1 bottom).

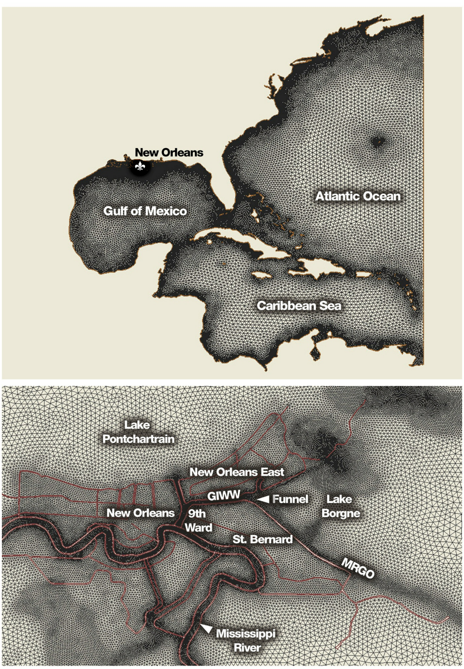

Fig. 1. ADCIRC "S08" computational model domain (top) and detailed mesh outlines around New Orleans area (for S08 grid reference see Feyen et al. 2002).

Dynamic hurricane wind stress and pressure fields are generated with a U.S. Army Corps of Engineers (USACE) version of the Planetary Boundary Layer model (Thompson and Cardone, 1996) using interpolated track and storm information derived from advisories issued by the National Hurricane Center (NHC). ADCIRC predicted storm surge elevations during hurricane Katrina to within 15-20 percent of observed values (van Heerden, 2007a,b).

Figure 2 shows the general location of the area of interest within the Greater New Orleans (GNO) area and simulated surge and velocity hydrograph developed at several key locations. Highest surge build ups were along the south side of St. Bernard levee and in the triangular area between the Gulf Intracoastal Waterway (GIWW) and the Mississippi River Gulf Outlet (MRGO). The MRGO is a deep draft ship channel that provides a path for surge that builds up in Lake Borgne area to move into the Inner Harbor Navigation Canal (IHNC) (Figure 2).

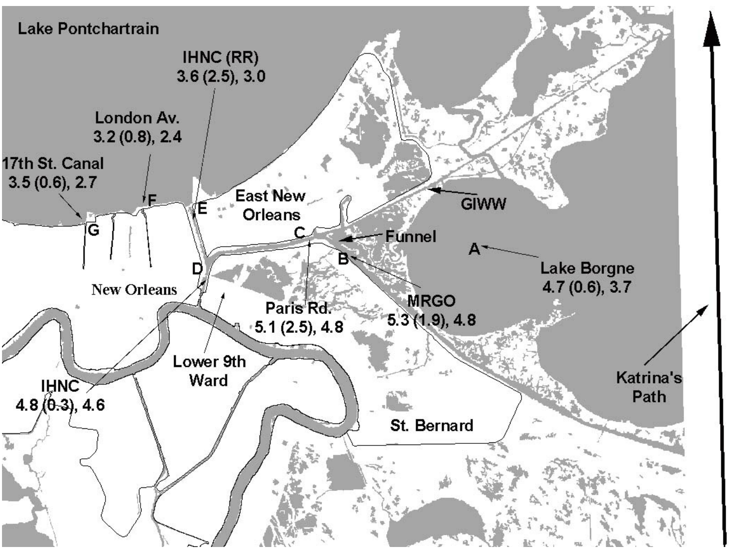

Fig. 2. Predicted ADCIRC maximum surge elevation and current velocity based on NHC Advisories 31 and 18. The arrow indicates the point at which the surge and velocity is reported. The first number under the name indicates the surge elevation (m, NGVD 29) predicted from the Advisory 31 postcast. The second number in parentheses is the maximum current velocity (m/s). The final number is the surge elevation (m) forecast 39 hours prior to landfall.

In the early 1920s, before the dredging of the GIWW, New Orleans was protected by cypress swamps and did not have a direct connection to the Gulf of Mexico. During the World War II, GIWW was dredged (width 38.1 m and depth of 3.7 m or width 125 ft and depth of 12 ft) and later MRGO (width 182.9 m and depth of 11.6 m or width

600 ft and depth of 38 ft) channel was created to connect the Port of New Orleans to the Gulf of Mexico. MRGO connected New Orleans to the Lake Borgne and inadvertently provided 12 fold increased cross sectional area (compared to the GIWW section) for surge propagation during any storm (fig 3).

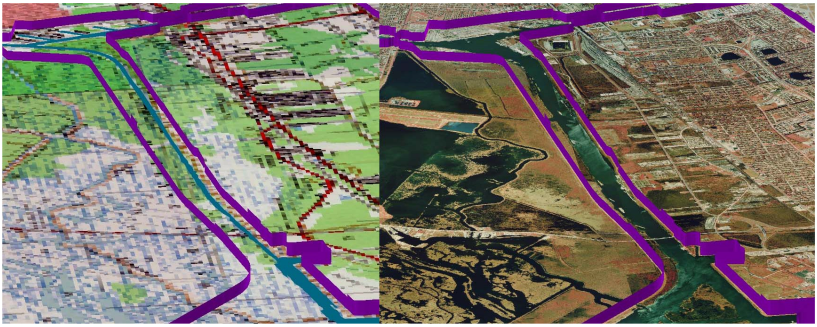

Fig. 3. Aerial Photographs showing the landscape near New Orleans in the 1920s (left) and after the construction of the MRGO (right).

Figure 4 shows the surge and velocity hydrograph developed in the east west portion of the MRGO near the Paris Road Bridge (Point C, Fig. 2), near the Bayou Bienvenue (Point B, Fig. 2) on the Northwest-Southeast oriented section and on the near by marsh area (fig. 2) between the MRGO and the Lake Borgne. We used ADCIRC produced surge heights and velocities to estimate representative flow depth, flow areas and average velocity for each area of interest. Capacity of surge flow through a channel was estimated using the formula: flow = velocity x cross-sectional area (or Q = VA) as suggested by Chow (1983).

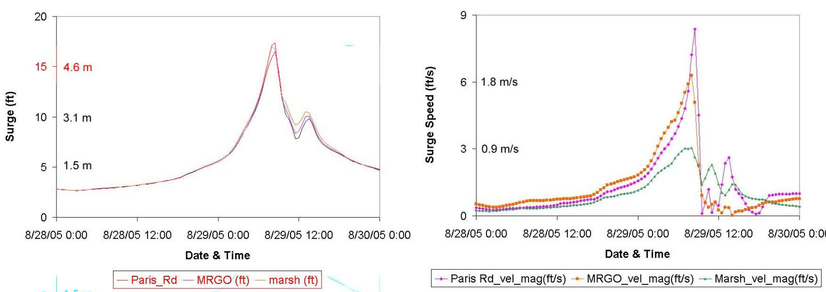

Fig. 4. ADCIRC simulated surge height (left) and velocity (right) hydrographs on MRGO near the Paris Road, Bayou Bienvenue and on the near by Marsh for hurricane Katrina.

RESULTS AND DISCUSSION

Along the south shore of Lake Pontchartrain, near the 17^{th} street and London Avenue canal, maximum surge levels were computed to range between 3.5 m (11.4 ft) to 3.2 m (10.5 ft) and about 3.0 m (10 ft) near the IHNC (fig. 2). Adjacent to the levees along the MRGO, maximum computed surge levels were 4.9 m (16 ft) to 5.2 m (17 ft). Maximum surge elevation in the GIWW near the Paris Road was 5.1 m (16.7 ft). Surge elevations varied from 4.8 m (15.7 ft) at the IHNC lock to 3.6 m (11.7 ft) near the Lake Pontchartrain. There was a steep gradient of surge elevation from the south to the north in the IHNC indicating two separate surge events; one in the Lake Pontchartrain and the other one in the Lake Borgne.

The east side of the city of New Orleans that faces Lake Borgne experienced a higher level of storm surge than the metro center south of Lake Pontchartrain (Figure 2). The surge from Lake Borgne propagated through the MRGO to the IHNC causing water levels in that canal to rise above 4.6 m (15 ft), while surge along the lakefront to the west was 1.2 m to 1.5 m (4 ft to 5 ft) lower (Fig2). Therefore, Lake Borgne surge through the MRGO contributed to about 40% rise at the IHNC near New Orleans when compared to the Lake Pontchartrain surge. This surge rise could have been reduced to about 3.2 m (10.5 ft) Lake Pontchartrain surge by closing the funnel (MRGO) with a gate or similar structure. Some of those funnel closure options are being considered now.

Maximum current velocities toward New Orleans were greater than 2.4 m/s (8 ft/s) at Paris Road in the MRGO channel that connects to the IHNC (Fig. 2). Surge velocity in the Lake Borgne was about 0.7 m/s (2.5 ft/s). In general, model simulated surge speed suggests surge velocity in the channel were two to there time faster than that of the over marsh areas. If the simulated time-series of velocity and surge in the MRGO channel are compared, it can be seen that velocity increases proportionally with surge (fig. 4). Surge velocity drops quickly as winds change direction and the surge begins to fall.

Estimated flow hydrograph (fig 5 top) shows that the surge propagated toward New Orleans days before the land fall until 1030 am local time on Monday August 29. Peak surge flow through the Paris Road reach was about 9,915 cms (350,000 cfs). When surge flow rate was estimated using the original GIWW section (38.1 m x 3.7 m) for the same surge and velocity, peak surge was reduced to about 1,275 cms (45,000 cfs). Similarly, peak flow through the MRGO reach near the Bayou Bienvenu section was 6,516 cms (230,000 cfs) with the MRGO section in place. Whereas, same surge would have produced 992 cms (35,000 cfs) peak discharge with out the MRGO channel and marsh in place. In this case, peak flow rate reduction was due to the decrease of the channel cross section as well as reduced flow velocity through the marsh. There was about 6 to 8 fold increase in peak surge flow through the MRGO channel and was directly related to the increase in transport area. Old GIWW section would have delivered far less water than what was actually propagated through the MRGO.

As several reports indicated levees on the south (west side) bank of the MRGO failed more completely than any others during Katrina (IPET, 2006 & Seed et al, 2006). In addition, floodwalls and levees along the IHNC also experienced extensive overtopping and breaching. While concerns about erosions of earthen levee faces are warranted around the MRGO, the high speed surge estimated in this paper also

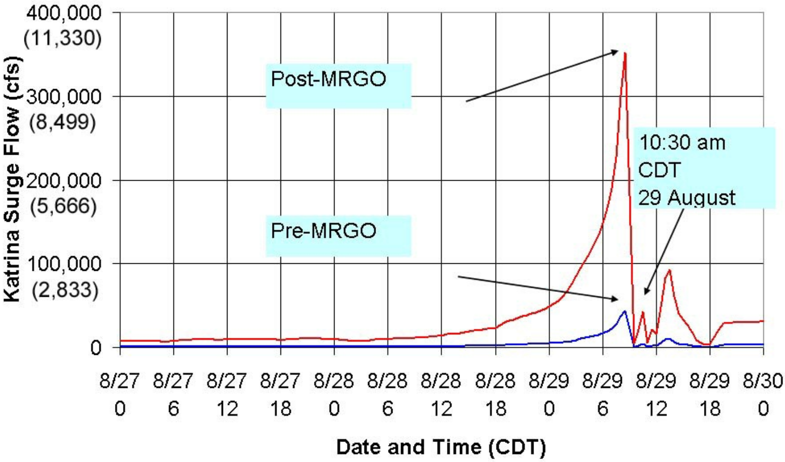

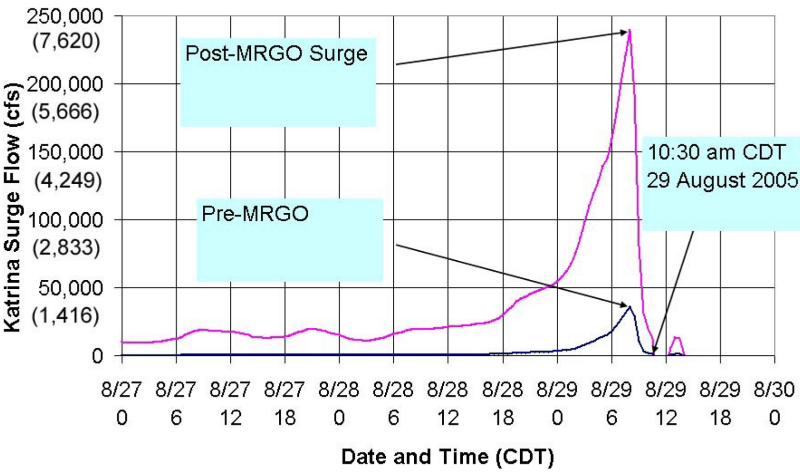

Fig. 5. ADCIRC simulated surge flow hydrographs on MRGO near the Paris Road (left) and Bayou Bienvenue (right) with and with out the MRGO in place. (Numbers with in the parenthesis indicates flow in cms)

suggests a potential to produce dynamic loads on the I-walls and other levee structures. Waves and surge currents can cause significant erosion on un-armored levees and walls, causing failure of critical infrastructures. The soils that make up the levees, rather than only those that comprise the foundation, assume greater importance. Waves and currents operate primarily on levee faces rather than foundations, and have received less attention to date, but were primarily responsible for the collapse of many miles of earthen levees on the east side of the City (Seed et al, 2006). Breaches scoured deeply into the levee base to establish a direct connection to the high velocity channel flow and were estimated to have transmitted nearly 84 percent of the observed GNO flood volume (van Heerden et al, 2007a,b). Because of this rapid channel flow, breaching before the peak surge greatly influenced the volume of water introduced into the Lower 9th Ward and the St. Bernard parish.

CONCLUSIONS

This paper showed that simulated surge could be used to provide a reliable estimate of surge velocity and flow rate during a storm event and could be used to determine the increase of peak surge due to increase of the cross sectional areas in critical locations. In future, a 3D-model or measuring device could be used to refine or to improve estimate of the surge flow through any cross section of a channel.

An in-depth analysis of all critical characteristics of storm surge (height, velocity and flow rate) is needed to analyze surge propagation. In case of channel flow, added cross sectional areas could increase risk of fatality rate in case of breaching or over topping. Surge heights, as well as flow velocities and flow rates and dynamic impacts of surge on the levees and walls need to be part of a comprehensive structural design.

ACKNOWLEDGEMENTS

This research was supported by the Louisiana Department of Transportation and Development, as well as by the Center for the Study of Public Health Impacts of Hurricanes, a Louisiana Board of Regents Health Excellence Fund Center, and by the McKnight Foundation. Drs. Ivor van Heerden and G. Paul Kemp of the LSU Hurricane Center provided data collection and analysis assistance.

REFERENCES

Chow, V.T. 1983. Open Channel Hydraulics, 20th Printing, 1983, McGraw-Hill Book Company, New York, NY. 680 pp.

Feyen, J.C., J.H. Atkinson and J.J. Westerink, 2002: GWCE-Based Shallow Water Equation Simulations of the Lake Pontchartrain - Lake Borgne Tidal System. Computational Methods in Water Resources XIV, S.M. Hassanizadeh et al. Eds., Volume 2, Developments in Water Science, 47, Elsevier, Amsterdam, 1581-1588.

IPET (Interagency Performance Evaluation Task Force), 2006. Performance Evaluation Plan and Interim Status, Report 1 of a Series: Performance Evaluation of the New Orleans and Southeast Louisiana Hurricane Protection System. U.S. Army Engineers MMTF 00038-06, January 10, 2006. 165 pp + Apps.

Luettich, R.A., Jr., and Westerink, J.J., 1995. Continental Shelf Scale Convergence Studies with a Barotropic Tidal Model, Quantitative Skill Assessment for Coastal Ocean Models, D. Lynch and A. Davies [eds.], Coastal and Estuarine Studies series, vol. 48, pp. 349-371, American Geophysical Union press, Washington, D.C.

Mashriqui, H.S., Kemp, G.P., van Heerden, I. Ll., Ropers-Huilman, B.D., Hyfield, E., Young, Y., Streva, K., and Binselam, 2006. Experimental Storm Surge Simulations For Hurricane Katrina, in "Coastal Hydrology and Water Quality", Xu, Y. J. & Singh, V. J., (editors), Proceedings of the AIH 25th Anniversary Meeting & International Conference, American Institute of Hydrology (AIH), May 21-24, 2006, Baton Rouge, Louisiana, USA. pp 481-489.

Seed, R., et al., "Preliminary Report on the Performance of the New Orleans Levee Systems in Hurricane Katrina on August 29, 2005" (Report No. UCB/CITRIS – 05/01, November 17, 2005).

Thompson, E. F., and Cardone, V. J., 1996. Practical modeling of hurricane surface wind fields. Journal of Waterway Port Coastal and Ocean Engineering - ASCE 122(4): 195-205.

van Heerden, I. Ll., Kemp, G.P., Mashriqui, H.S., 2007a. "Use of the ADCIRC Storm Surge Model for Hurricane Katrina Surge Predictions and Levee Forensic Studies," in Proceedings of the American Society of Civil Engineers (ASCE), Organized by the Geo-Institute (G-I), February 18-21, 2007, Denver, Colorado, USA.

van Heerden, I. L., G. P. Kemp, H. Mashriqui, R. Sharma, B. Prochaska, L. Capozzoli, A. Theis, A. Binselam, K. Streva, and E. Boyd, 2007b. The Failure of the New Orleans Levee System during Hurricane Katrina. TEAM LOUISIANA Final report for Louisiana Department of Transport and Development.

Westerink, J.J., Luettich, R.A., Jr. and Muccino, J., 1994. Modeling Tides in the Western North Atlantic Using Unstructured Graded Grids. Tellus 46a(2):178-199.

Westerink, J.J., Feyen, J.C., Atkinson, J.H., Richard A. Luettich, R.A., Dawson, C.N., Powell, M.D., Dunion, J.P., Roberts, H.J., Kubatko, E.J., Pourtaheri, H., 2004. A New Generation Hurricane Storm Surge Model for Southern Louisiana, University of Notre Dame, Notre Dame, IN 46556, http://www.nd.edu/~adcirc/index.htm.

Meeting Post Katrina Geotechnical Challenges

G. Rai Mehdiratta, M.ASCE, Ph.D., P.E.

Program Director, FFEB J.V., L.L.C., 6100 Hillcroft, Houston, TX 77081; rmehdiratta@fugro.com

ABSTRACT: This paper describes one of the largest field and laboratory geotechnical investigation programs currently underway in the United States for flood protection systems in Louisiana. The work is being performed by FFEB JV, L.L.C. (FFEB) under a contract signed in January 2007 with the U.S. Army Corps of Engineers, New Orleans District (USACE, N.O.D.). Storm protection measures being engineered and constructed embody one of the largest infrastructure programs currently underway in the United States. Geotechnical studies for this program focus on 560 kilometers (350 miles) of federal levees; hundreds of kilometers of supplementary levees; and a multitude of pump stations, floodwalls, floodgates, and erosion armor. The paper highlights key logistic and managerial challenges in equipping and mobilizing field exploration and laboratory testing equipment within strenuous time constraints. Within two weeks of receiving notice to proceed, FFEB mobilized 22 drill rigs and 4 Cone Penetrometer Testing Units; expanded local laboratory facilities to accommodate routine and sophisticated testing; and dedicated more than 100 people to the immediate effort.

INTRODUCTION

In January 2007, a joint venture of Fugro Consultants, Inc. (Fugro), Fuller Mossbarger Scott & May (FMSM), Eustis Engineering, Inc. (Eustis), and Burns Cooley Dennis (BCD), herein referred to as FFEB, was awarded a $100 million Indefinite Delivery/Indefinite Quantity (ID/IQ) contract by the U.S. Army Corps of Engineers, New Orleans District (USACE, N.O.D.). This paper describes highlights of this major geotechnical investigation program which has been underway since January 2007 to meet a very demanding schedule required by USACE, N.O.D.

The geotechnical investigation program includes drilling of several hundred borings, cone penetrometer testing (CPT), installation of piezometers, extensive laboratory testing and engineering analyses. This paper focuses only on the field and laboratory phases of the program. A rigorous Quality Assurance/Quality Control (QA/QC) program was implemented both by the USACE, N.O.D. and FFEB. Comprehensive Health and Safety (H&S) Plan and a Design Quality Control Plan (DQCP) were developed to meet USACE, N.O.D. and Mississippi Valley Division requirements.

Changing priorities and special N.O.D. requirements for drilling, transportation of samples, and laboratory testing made this investigation unique and challenging. Massive amounts of data generated during the field, laboratory, and engineering phases of the study are organized and stored on an FTP site which is accessible by the N.O.D. through use of a password system.

New design criteria partly based on the findings of the Interagency Performance Evaluation Taskforce (IPET) and the American Society of Civil Engineers' (ASCE) Hurricane Katrina External Review Panel are currently being developed by the N.O.D. Interim design criteria addressing slope stability, seepage and overtopping have been established by N.O.D. and are currently being used to analyze the stability of the existing levees and to provide recommendations to upgrade the existing levee system.

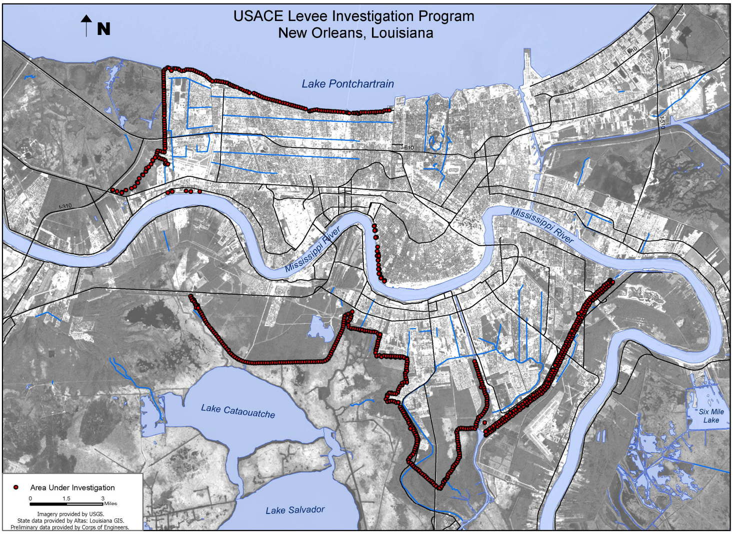

FIG. 1. Representative Area of Investigation

SCOPE OF WORK

The overall mission of the USACE, N.O.D. is to design, upgrade and build a system of levees, gated structures and pump stations to provide protection to New Orleans and vicinity from hurricanes. An enhanced hurricane protection system is being implemented in several phases. Damage to Greater New Orleans levee system and Mississippi River flood protection levees have already been repaired. The next phase of the work involves upgrading the hurricane protection system to pre-Katrina authorized grade followed by upgrading the system to 100-year storm event. FFEB was selected by USACE, N.O.D. to provide geotechnical field, laboratory and design services to assist in accomplishing N.O.D.'s mission.

Current assignments have included soil borings; cone penetrometer testing;

piezometer installation and monitoring; laboratory soil testing; surveying; geotechnical studies entailing stability analyses of levees, and excavations; selection of design parameters for pile foundation systems and flood walls. Future assignments are anticipated to include pile load testing, vibration/noise monitoring, construction material testing, project management, and construction assurance and construction quality (QA/QC) services.

Services requested under this contract have required equipment and expertise to work in extremely soft soils with difficult access conditions; conformance with rigorous, technical protocols and safety standards; high capacity to meet tight deadlines; familiarity with local suppliers and small businesses; and ability to deliver innovative solutions.

To date, most of the effort has focused on field exploration (drilling of undisturbed soil borings and performance of Cone Penetrometer Tests), laboratory testing of soil samples and data reporting. Engineering task orders have increased considerably over the past few months and are expected to be the major focus as the field and laboratory data become available. Future assignments are expected to focus on remediation and construction of the levees, instrumentation and QA/QC during construction of the Hurricane Protection System (HPS).

FIELD INVESTIGATION

As of June 2007, the N.O.D. had authorized eleven separate task orders for field and laboratory work covering a large area within the N.O.D. boundaries (see Fig. 1). Most of the work has been concentrated in and around New Orleans, although borings have been drilled as far as 100 km (62 miles) north of New Orleans and 160 km (100 miles) west of New Orleans. As of June 2007, a total of approximately 690 borings (5-inch undisturbed sample borings) amounting to approximately 16,310 linear meters (53,500 feet) of drilling and approximately 700 CPT tests amounting to approximately 16,040 linear meters (52,600 feet) had been completed. Fieldwork and laboratory testing is still continuing at a brisk pace along with increasing engineering assignments.

FIG 2. Track-mounted drilling rig at USACE, N.O.D. facility.

The Notice-to-Proceed (NTP) for the first three task orders was received on January 29, 2007. Within two weeks of NTP, FFEB mobilized 22 drilling rigs, 4 CPT rigs and approximately 100 personnel consisting of surveyors, drillers, helpers, technicians, cone operators, field managers, management and office personnel.

In addition to meeting the equipment requirements (over 1000 sampling tubes, 2000 inner plugs and caps, 30 piston samplers), there were numerous challenges in coordinating the activities of these large numbers of rigs, transporting soil samples, hiring of subcontractors, as well as boarding and lodging of personnel in a city which is still recovering from the aftermath of Katrina. Most of the personnel worked 12 to 18 hours/day for an extended period of time to meet a very demanding schedule.

The N.O.D. requires drilling 127mm (5-inch) diameter undisturbed sample borings using a 1.37m (54-inch) long fixed piston sampler. Most of the drilling companies had little experience in operating the piston samplers, soil sampling using 127mm (5-inch) diameter tubes, or handling of the tubes (each tube weighs roughly 27kg [60 lbs.] when full of soil). The drilling companies came from various regions of the country and from as far away as Michigan. Most of the companies had not worked together on a project of this magnitude and complexity. Senior experienced drillers were assigned as “team leaders” to train less experienced personnel.

FIG 3. Barge-mounted drilling rig.

FIG 4. Cone Penetrometer Testing.

USACE N.O.D., as well as personnel from other Districts and the Division conducted frequent field QA audits and checks. Their comments were addressed by FFEB by developing a detailed QA/QC checklist, which was provided to each drilling crew. The most experienced FFEB member company conducted internal QA/QC checks on all drilling rigs and the reports were circulated internally as well as to N.O.D. At the same time, detailed Health and Safety Plans and Design Quality Control Plan (DQCP) were developed in conformance with the N.O.D. requirements.

The fieldwork was conducted on Protected Side (PS), Flood Side (FS) and Center Line (CL) of the levees. The drilling of the borings required use of truck-mounted, all-terrain vehicles (ATVs), and track-mounted (Fig. 2) and skid-mounted drilling equipment. Several of the borings were drilled over water using barges (Fig. 3) and lift boats. Transportation of the samples offered unique challenges because of the weight and sheer number and size of the sampling tubes. Four-men drilling crews were utilized to handle the sampling tubes in a safe and efficient manner. From the onset of the project, FFEB committed to place safety as a top priority. Cone penetrometer testing was also performed using truck-mounted (see Fig. 4) units, ATVs and skid-mounted units.

During the course of the project, N.O.D. instructed FFEB to transport tubes in a vertical orientation as opposed to the normally accepted practice of horizontal transportation of tubes. FFEB complied with N.O.D. instructions by purpose-built boxes to carry the samples in a vertical position. A specialty transportation truck with a dedicated forklift was used to lift the sample boxes from each drilling site and deliver the boxes to the laboratory. Forklifts were used to unload and to move the samples to the extruding area in the laboratories. Frequently changed drilling priorities to meet the rigorous demands of the project required shifting resources on short notice. These are just a few examples of the challenges that were faced to meet the special requirements of this project.

LABORATORY TESTING

Laboratory testing of the samples required a different set of challenges than the field program. A major reason for this was the unique nature of this project, i.e., Indefinite Delivery/Indefinite Quantity (ID/IQ) meaning that FFEB did not know when and how much work will be authorized. FFEB leased about 745 square meters (8,000 SF) of office building space in New Orleans a week before receiving the NTP. The remodeling of the office space was initiated immediately along with setting up a new geotechnical laboratory per N.O.D. contract requirements. Specialty built sample extruders (see Fig. 5) and working areas were set up at two locations to extrude, classify and run moisture contents while the rest of the space was remodeled to set up a state-of-the-art high production geotechnical laboratory. At the peak of the fieldwork, the laboratory was handling 244 linear meters (800 ft) of samples every day, which meant extruding, classifying, waxing (see Fig. 6) and keeping track of 800 individual samples on a daily basis. Within the first two weeks of fieldwork, FFEB realized that it was running out of warehouse and storage space. FFEB scrambled to lease another 460 square meters (5,000 SF) of warehouse space that was also fully used up within another month. Currently, FFEB has over 930 square meters (10,000 SF) of warehouse space to store the samples generated during the first five months.

FIG. 5. Soil extrusion at the FFEB Lab.

FIG. 6. Waxed samples.

The geotechnical laboratory is now fully validated by USACE and has a staff of over 40 personnel. The laboratory currently has the following testing capacity:

Table 1. Laboratory Testing Capacity

Type of Test	Number of Tests per Week
Sample Extrusion and Classification (ASTM D 2216/2488)	610 meters (2000 linear feet)
Moisture Content (ASTM D 2216/2488)	1,250
Organic Content (ASTM D 2974)	60
Sieve Analysis (ASTM D 422)	60
Liquid and Plastic Limit (ASTM D 4318)	450
Unconfined Compression (ASTM D 2166)	350
Unconsolidated-Undrained Triaxial (series of 3 tests) (ASTM D 2850)	350
Specific Gravity (ASTM D 854)	20

Type of Test	Number of Machines
Incremental Consolidation Test (ASTM D 2435)	20 machines
Direct Shear Test (ASTM 3080)	2 machines
Consolidated-Undrained Triaxial (ASTM D 4767)	2 machines

The approximate number of laboratory tests performed is given in the table below:

Table 2. Approximate Number of Laboratory Tests Performed (March – June 2007)

Type of Test	Approximate Number of Tests Completed
Moisture Content	32,000
Organic Content	600
Sieve Analysis	450
Liquid and Plastic Limit	4,800
Unconfined Compression	2,400
Unconsolidated-Undrained Triaxial (series of 3 tests)	2,400

To produce logs per N.O.D. format, FFEB personnel required training on the use of GBORE and UBORE programs and the Geosystem software. On average it takes about 4 hours per boring to process, interpret and perform QA/QC after completion of the tests. FFEB has dedicated several engineers to perform these functions.

FIG. 7. Unconsolidated-Undrained Triaxial Testing

FIG. 8. Consolidation Testing

FFEB continues to provide services to the USACE, N.O.D. on its 3-year ID/IQ contract.

ACKNOWLEDGEMENTS

The author wishes to acknowledge the strong commitment and dedication of USACE, N.O.D. and FFEB professionals in addressing the post Katrina design and construction challenges. The assistance of other FFEB professionals in preparing this paper is also appreciated and acknowledged.

Reduction of Landfill Waste by Recycling Spent Blast Abrasives in Hot Mix Asphalt in New Orleans

Norma Jean Mattei[1], Ph.D., P.E., M. ASCE and Amer Khanfar[2]

[1]Associate Professor, University of New Orleans, Department of Civil and Environmental Engineering, New Orleans, LA 70148; nmattei@uno.edu
[2]Ph.D. candidate, University of New Orleans, Department of Civil and Environmental Engineering, New Orleans, LA 70148; amerkhanfer@hotmail.com

ABSTRACT: Using spent abrasive blast material (ABM) in hot mix asphalt to replace part of the fine aggregates used in the production of conventional hot mix asphalt has environmental benefits (e.g., reduction of dust, minimization of disposal and potential contamination of adjacent waterways). Usually these wastes are disposed of in landfills. Reuse is especially beneficial to southeast Louisiana, where massive amounts of hurricane debris and reconstruction wastes require vast landfill space. This paper is concerned with recycling the spent ABMs that are generated at two shipyards in New Orleans, Bollinger Shipyards, and Northrop-Grumman Avondale, as opposed to onsite storage and disposal in non-hazardous landfills. A feasibility study, including mechanical and environmental tests, was performed to evaluate if the waste can be used as part of a modified hot mix asphalt. The Marshall Method was used for evaluating the performance of the modified mix. Preliminary mechanical and environmental test results indicate that the modified hot mix asphalt will perform similarly to conventional hot mix asphalt. One of the major findings of this study is that the recycling and reuse option is a more desirable waste management option. Waste minimization credit may be given to the shipyard generator of the recycled spent ABM.

INTRODUCTION

Abrasive blasting is the use of abrasive material to clean or texturize a material such as metal or masonry. Many types of ABM are used to remove paint, coatings, and/or corrosion from industrial structures. Sand is the most widely used blasting abrasive. Other abrasive materials include coal slag, smelter slag, mineral abrasives, metallic abrasives, and synthetic abrasives. Industries that use abrasive blasting include the shipbuilding industry, automotive industry, and other industries that involve surface preparation and painting. When the ABM no longer functions as desired, this material is referred to as “spent” and is often handled as waste (Ahmed, 1993).

Background

Typically, asphaltic concrete is 4%-10% bitumen mixed with graded aggregate. The aggregate is a mixture of specific proportions of particles ranging in size from fine sand to medium-diameter gravel or coarse aggregate (1/2" – 1"). Depending on the mix design and strength and durability requirements, the fine particles may comprise 35-45% of the asphaltic concrete. Total aggregate portion in a mix may be as high as 90-96% by weight of the paving mixture. This makes the quality (size, gradation, cleanliness, toughness, shape, surface texture, absorptive capacity and affinity for asphalt), cost and availability of aggregate a critical factor for possible pavement use. Although the bitumen makes up the smallest percentage in the mixture, it is by far the most costly ingredient in the asphaltic concrete. Consequently, a good aggregate should not be too absorptive.

When using spent ABMs as a substitute for normal aggregate in hot mix asphalt, the aggregate must comply with both performance and environmental standards. ABM containing solvents should not be used. ABM with high metals concentrations may pose health risks to asphalt plant personnel due to dust inhalation and to the general public due to metals leaching. The presence of sulfate or metallic iron should be avoided; upon oxidation, detrimental swelling will occur. High silt or very fine particles are undesirable, as their portion allowed in a hot mix is limited because it causes poor wetting capabilities in the bitumen matrix. Finally, and most importantly, aggregate particle shape is very important for good vehicular traction and pavement durability. Angular particles result in the best hot mix asphaltic concrete performance. Round particles should be avoided.

The reported production rate of spent ABM from eight US shipyards is in the range of 75,000 – 100,000 tons per year. The spent ABM generally contains low levels of metals from paints and other coatings that are applied to ships. Most US shipyards dispose of this waste in nonhazardous waste landfills, if the spent ABM contains relatively low concentrations of metals. If metal concentrations are too high, disposal in a hazardous landfill is required. Disposal is costly and uses valuable landfill space. Costs to dispose of spent ABM in a permitted landfill include transportation costs (this varies with shipyard and landfill) and tippage costs at the landfill ($50-$250 per ton). There is also a growing emphasis on waste minimization and reuse of resources, in part due to regulations such as the Resource Conservation and Recovery Act, RCRA.

The recycling of spent ABM in asphaltic concrete has been found to be an effective and inexpensive way to manage waste material in other parts of the country (Medford, 1990) and (Weyand and Sutton, 1990). This type of recycling has a track record in states such as California, Maine, North Carolina and Ohio. A project involving recycling of spent ABM must be qualified on a case-by-case basis because each spent ABM has different physical and chemical characteristics. The mixes provided by an asphalt producer are highly dependent on aggregate cost and availability in the specific locality. Environmental regulations also vary from state to state.

The follow lists some advantages pertaining to recycling ABM's in hot mix asphalt (Heath *et. al.*, 1996):

- The cost of recycling is usually lower than the cost of disposal.
- The recycling and reuse option is a more desirable waste management option.
- A waste minimization credit may be given.
- Recycling does not consume valuable landfill space.
- The cost of the spent ABM is lower than the cost of normal virgin aggregate, thus the cost of the asphaltic concrete is reduced.

The disadvantages of using spent ABM as a portion of the aggregate in asphaltic concrete are now listed:

- If the spent ABM is deemed hazardous, the material must be handled as such and compliance with transportation, storage, handling and reporting regulations is required.
- A high portion of very fine material, sulfate/metallic iron particles, or organic material in the spent ABM will adversely affect the strength and performance of the pavement.
- Bench-scale (small specimen) testing is required for each combination of bitumen, normal aggregate, and spent ABM in order to optimize the asphalt content of the modified mix and predict performance.

There are several recent examples of asphalt recycling projects involving similar spent ABM. Black Beauty™ (coal slag) spent ABM from ship-cleaning operations at Bath Iron Works in Bath, Maine has been successfully recycled into hot mix asphalt since 1990, with mix designs having a 5% spent ABM by weight concentration. On the opposite coast of the US, beach sand spent ABM contaminated with a portion of paint chips from ship-cleaning at the Naval Station at Hunters Point, California (considered hazardous because of highly leachable concentrations of copper, zinc and lead in the spent ABM) was successfully recycled into hot mix asphalt, again at the 5% by weight concentration level.

Spent ABM in the New Orleans Area

Local Louisiana shipyards generate spent ABM as result of ship-cleaning and surface-preparation operations. Onsite storage of spent ABMs negatively impact neighboring properties because the fine materials are a source of airborne debris and dust. Use of tarps as curtains only reduces this hazard. Storage piles are situated near canals, waterways and the Mississippi River. Future storms may carry these waste products into neighboring waterways. Many shipyards are willing to consider reuse options for their spent ABM for environmental reasons. In order for reuse to have the greatest economic impact for Louisiana, the spent ABM materials must be consumed in large quantities. The largest user of hot mix asphalt in the State is the Louisiana Department of Transportation and Development (LaDOTD). LaDOTD uses hot mix asphalt to build flexible pavements: streets, road and bridge overlays, parking lots and other parts of public works projects. Barriere Construction Company (Barriere) is one of the large producers of hot mix asphalt in Louisiana.

In this research, two New Orleans area shipyards were considered: Bollinger Shipyards, Inc and Northrop-Grumman Avondale (Avondale). The spent abrasives from these shipyards are now classified by the Louisiana Department of Environmental Quality, (LADEQ), as non-hazardous waste materials. Bollinger and Avondale presently use these spent ABMs as fill on site or dispose of them in State landfills. Both shipyards use curtains to minimize the impact of wind-blown spent ABMs from onsite storage piles on the air quality of surrounding neighborhoods and adjacent shipyard operations.

Avondale produces spent Black Beauty™ ABM and Bollinger produces silica sand spent ABM. The reported production rate of spent ABM from the two shipyards is in the range of 400-600 tons/month. Disposal costs, including tippage and transportation, are estimated to be over $300,000 per year. LaDOTD uses approximately 3.25- 3.5 million tons of asphalt annually in various public works. Most of this asphalt consists of aggregate (~90%). Barriere purchases about 700,000 tons of aggregate annually. Barriere estimates that a minimum of 100,000 tons can be replaced with spent ABM, for a savings of $550,000 annually. This study evaluates the feasibility of using these two types of spent ABMs in hot mix asphalt in the New Orleans area.

ABM Applicability

The acceptability of spent ABM in highway applications is evaluated based on test results and specifications as shown in Figure 1. This evaluation process ensures the desirable level of performance of the chosen material, in terms of its impact on the product's permeability, volume stability, strength, hardness, toughness, fatigue, durability, shape, viscosity, specific gravity, purity, safety, and temperature susceptibility. The work plan used included consultation with LADEQ and LaDOTD personnel, creation and use of a sampling plan for acquisition of the spent ABM material from each shipyard, physical testing of virgin conventional materials as well as spent ABM materials, design of trial mixes for both regular (Marshall) and Superpave hot mixes, optimization of mix design, and environmental/chemical testing of the optimum mixes.

MATERIAL CHARCTERISTICS

Basic information about the spent abrasive's physical characteristics is required in order to determine if it is feasible to recycle the material in asphalt. Gradation is one of the most important properties of an aggregate used in an asphalt mix. Thus, gradation determines the percentage of spent ABM that can be used in the mix before the mix properties are negatively impacted. Specific gravity and moisture content are also important parameters. The presence of debris such as wood, metal, or cloth in the spent ABM is common and detrimental. Debris can easily be removed by screening or by modification of shipyard practices.

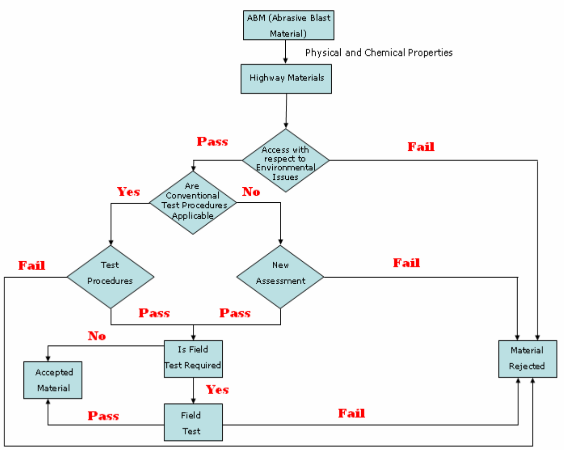

Figure 1. Evaluation process for determination of suitability of spent ABM in highway applications

Debris was an issue in spent abrasive received from both shipyards. As the spent abrasive was previously considered waste, other waste materials were often combined in the stockpiles. Material received from Avondale was restricted to come only from two specific blasting locations within the shipyard. The procedures for gathering and stockpiling spent abrasives were modified in the two areas. Subsequent materials were acceptable. Material from Bollinger was restricted to abrasives used in blasting for surface preparation of new steel. Spent abrasives from the blasting of tanker interiors contained rust. Shipyard stockpile procedures were also modified at Bollinger so that other waste material was kept separate from the spent abrasive piles. Once revised modified stock piling procedures at the shipyards were in place, specific gravity, gradation, and other physical test results of materials from both yards were found to be acceptable and comparable to pump sand used by Barriere in many conventional hot mix designs.

MIX DESIGN, EVALUATION AND OPTIMIZATION

Barriere has several standard conventional mix designs used in asphaltic concrete production. All mixes in this research were either for a conventional incidental wearing course or a conventional binder course with a reuse modification. The modification was that one of the spent ABM replaced a portion of the conventional fine aggregates ordinarily used. Concentrations of spent ABMs used in similar recycling in other states range from 5-10 % by weight with, theoretically, a maximum of 25-35%. Table 1 lists Marshall Test results for two example hot mix designs containing 7% coal slag spent ABM and 10% silica sand ABM, respectively. Three trial mix designs were tested, with the Percent Asphalt Content (%AC) parameter varied in order to obtain the optimum amount of asphalt. Three tests were run per %AC and the results averaged and shown in the table. Both mixes are for a Type 8 binder course. Both contain conventional aggregates: pump sand, sandstone, limestone and recycled asphaltic concrete (RAP). Acceptable Marshall Stability Test results are 1800 lbs. minimum and 2680 recommended. Both mixes met these requirements using the optimum asphalt content of 4% for the coal slag mixes and 4.5% for the silica sand mixes.

Table 1. Marshall Test results for asphalt with ABM (average of three tests per %AC)

Marshall Test Results	7% coal slag spent ABM mix			10% silica sand spent ABM mix		
% AC	3.5	4.0	4.5	4.0	4.5	5.0
Specific Gravity	2.341	2.360	2.381	2.330	2.362	2.379
Density (lbs/ft^3)	146.1	147.3	148.6	146.0	147.4	149.0
Marshall Stability (lbs)	2362	2775	2594	3429	3775	3693

ENVIRONMENTAL TESTING

Environmental testing is required in order to ascertain if the modified hot mix asphalt is hazardous. If so, an assessment of the risks posed to human or ecological receptors by the recycling process or by the product itself is required (Means, 1995). Usually hot mix asphalt with recycled abrasives has metal concentrations similar to those found in native soils (Table 2).

Table 2. Typical total metal RCRA test results for native soils (US EPA, 1983)

Metal	Common Range (mg/kg)	Typical Average in Soils (mg/kg)
Arsenic	1-50	5
Barium	100-3000	430
Cadmium	0.01-0.7	0.06
Chromium	1-1000	100
Lead	2-200	10
Mercury	0.01-0.3	0.03
Selenium	0.1-2	0.3
Silver	0.01-5	0.05

Both shipyards periodically have Toxicity Characteristic Leaching Procedures (TCLPs) done in order to ensure that the spent abrasives are not hazardous in nature. Historically, the shipyards' spent abrasives TCLP results indicated that it was safe to dispose the wastes in nonhazardous landfills.

Total and leachable metal concentrations were determined using applicable EPA methods for samples of conventional, 5% coal slag and 10% silica sand hot mix asphalt. As shown in Table 3, total metal concentrations for all three types of samples are at or below average concentrations found in native soils.

Table 3. Total metal RCRA test results

Metal	USEPA Physical Chemical Method	Practical Quantitation Limit, PQL (mg/kg)	Conventional Mix (mg/kg)	Spent 5% Coal Slag Mix (mg/kg)	Spent 10% Silica Sand Mix (mg/kg)
Arsenic	6010B	3.0	below PQL	below PQL	below PQL
Barium	6010B	5.0	21.7	437	33.0
Cadmium	6010B	0.5	below PQL	below PQL	below PQL
Chromium	6010B	2.0	6.3	11.5	10.4
Lead	6010B	5.0	below PQL	below PQL	below PQL
Mercury	7470-1A	0.014	below PQL	below PQL	below PQL
Selenium	6010B	5.0	below PQL	below PQL	below PQL
Silver	6010B	1.0	below PQL	below PQL	below PQL

Table 4 lists the results of TCLP tests run on the three types of samples. All concentrations are well below regulatory levels.

Table 4. TCLP test results, USEPA Method 1311

Metal	Practical Quantitation Limit (mg/l)	Regulatory Level (mg/l)	Conventional Mix (mg/l)	Spent 5% Coal Slag Mix (mg/l)	Spent 10% Silica Sand Mix (mg/l)
Arsenic	0.03	5.0	below PQL	below PQL	below PQL
Barium	0.05	100.0	0.21	0.10	0.08
Cadmium	0.005	1.0	below PQL	below PQL	below PQL
Chromium	0.010	5.0	below PQL	below PQL	below PQL
Lead	0.010	5.0	below PQL	below PQL	below PQL
Mercury	0.020	0.2	below PQL	below PQL	below PQL
Selenium	0.05	1.0	below PQL	below PQL	below PQL
Silver	0.010	5.0	below PQL	below PQL	below PQL

CONCLUSIONS

A feasibility study, including mechanical and environmental tests, was performed to evaluate if spent ABM from two New Orleans shipyards could be used as part of a modified hot mix asphalt. Results of Marshall Stability Tests, a standard test used to predict hot mix asphalt performance, indicated that hot mix asphalt modified with 5-7% coal slag ABM or 10% silica sand ABM yield acceptable mixes. Environmental testing of the modified asphalts show that total and leachable metal concentrations are well below regulatory limits for mixes using either spent ABM. It is concluded that the reuse of the two spent ABMs tested in this study as part of hot mix asphalt is feasible in the New Orleans area. Use of this recycling option in other areas is dependent on the characteristics of the spent ABM, normally used materials, and economics of the specific locale. The study also identified that shipyard ABM stockpiling procedures required modification to control and prevent debris from being included in the ABM stockpile.

ACKNOWLEDGEMENTS

The authors would like to thank the staff of Bollinger Shipyards Inc, and Northrop-Grumman Avondale for their support in the acquisition of spent ABMs and Barriere Construction Company for the use of their asphalt laboratory. They would especially like to thank John Victory and Mike Bittner of Barriere Construction Company for their expert advice.

REFERENCES

Ahmed, I. (1993). *Use of Waste Materials in Highway Construction*, Noyes Data Corp, Park Ridge, NJ.

Heath, J.C., L.A. Smith, J.L. Means, and K.W. Nehring (1996). *"Technology Transfer Report on Recycling Spent Sandblasting Grit into Asphaltic Concrete*", Tech Memorandum TM-2179-ENV, Naval Facilities Engineering Service Center, Port Hueneme, CA.

Means, J.L., K.W. Nehring, and J.C. Heath (1995). "Abrasive Blast Material Utilization in Asphalt Roadbed Material", *3rd International Symposium of Stabilization of Hazardous Radioactive and Mixed Wastes*, ASTM 1240, Eds. T.M. Gilliam and C.C. Wiles, ASTM, Philadelphia, PA.

Medford, W.M. (1990). "Containment and Beneficial Reuse of Blasting Sand in Asphalt Concrete: A Case History", *Journal of Protective Coatings and Linings*, January, pp. 36-44.

U.S. EPA (1983). *"Hazardous Waste Land Treatment"*, Environmental Protection Agency Manual SW-874.

Weyand, T.E., and W.F. Sutton (1990). *Identification of Acceptable Beneficial Reuses for Spent Bridge Painting Blast Material*, FHWA-PA-89-037+89-02, prepared by Pittsburgh Mineral and Environmental Technology for PennDOT, Harrisburg, PA.

Sediment Contaminants Inside New Orleans, LA Homes Following Hurricane Katrina

Nicholas A. Ashley[1], Kalliat T. Valsaraj[2], Louis J. Thibodeaux[3]

[1]Ph.D. Candidate, Cain Department of Chemical Engineering,
Louisiana State University, Baton Rouge, LA 70803 nashle1@lsu.edu
[2]Charles and Hilda Roddy Distinguished Professor and Department Chair, Cain Department of Chemical Engineering, Louisiana State University, Baton Rouge, LA 70803 valsaraj@lsu.edu
[3]Jesse Coates Professor of Chemical Engineering and Interim Department Chair, Department of Geology and Geophysics, Louisiana State University, Baton Rouge, LA 70803 thibod@lsu.edu

ABSTRACT: The flooding of residential areas of New Orleans following hurricane Katrina resulted in suspended bottom sediments from Lake Pontchartrain invading neighborhoods, homes, and businesses. As a result of a selective winnowing/filtering process, only particles of the smallest size, dominated by silts and clays, made their way inside homes and other structures, where they eventually settled out during the stagnation of the floodwaters in the week after Katrina's landfall. Small particles are winnowed from larger ones because water to flood the home must seep through small cracks in doors and windows, thereby preventing all but the finest (< 63 μm) particles from entering the home. These fine particles are often associated with the highest loading of metal and organic contaminants. Key pollutants detected in interior deposited sediments include the heavy metals arsenic, cadmium, lead and vanadium as well as semi-volatile organics dieldrin, chlordane (pesticides), and fluoranthene. The contaminated sediment particles have consequences both for exposure of returning residents and first-responders to hazardous and toxic materials, as well as for disposal of the contaminated debris, resulting in long-term environmental consequences for the residents of New Orleans.

INTRODUCTION

The flooding caused by failure of levees in and around the city of New Orleans during hurricane Katrina in August 2005 has raised many questions as to the long-term environmental consequences for the city and its residents. Initial reports after the storm have characterized the contaminants associated with floodwater, exterior sediments, and biota(Pardue 2005; Presley 2006). A recent study presents the analysis of contaminated sediment deposited inside the homes following hurricane Katrina flooding(Ashley 2007).

Floodwaters that entered the homes must first seep through small cracks in doors and windows, thereby preventing larger particles from entering the home. Additionally, stagnation of the floodwaters inside the home provides a quiescent environment whereby the fine particles can settle out on floors and other surfaces. When floodwaters are pumped out of the flooded neighborhoods, settled particles remained behind in the homes. The particle entry and settling process is shown graphically in Figure 1. The concentration of metal and organic pollutants often increases with decreasing sediment particle size (Kleineidam 1999; Vulava 2007), thus the concentration of these contaminants found inside the homes has the potential to be much greater than those seen outside the home due to the particle fractionation process which concentrates fine particles indoors. The high loadings of pollutants from in-home sediments also present consequences for the disposal of contaminated debris when the home is either gutted or torn down, and the material to be disposed of ends up in one of the city's landfills.

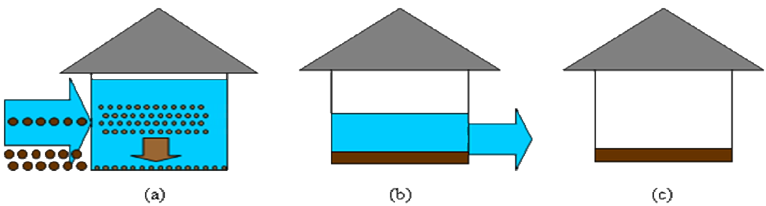

Figure 1. Particle winnowing/settling process from Katrina floodwaters. (a) floodwaters with suspended sediments enter homes where large particles are prevented from entering the home because floodwaters must seep through small cracks in doors and windows; small particles inside the home then settle out of the water column. (b) floodwaters are pumped out of the homes, but particles that have settled out inside the home remain behind. (c) homes are no longer submerged but now contain a thin layer of sediment on the floors and other horizontal surfaces which contained high loadings of metal and organic pollutants.

MATERIALS AND METHODS

Samples were collected from inside two Katrina-flooded homes in the Lakeview subdivision of New Orleans. Metals were determined using EPA methods 3051 and 6020; semi-volatile organics were quantified using EPA methods 3550B and 8270C. Further details on the sampling locations, analytical techniques, and quality control measures are provided in Ashley et al. 2007.

RESULTS AND DISCUSSION

Indoor Sediment Contaminant Concentrations

Analysis of the particle size distribution for sediments collected from both homes appears to confirm the particle winnowing hypothesis. For both homes, greater than 92 and 99% of particles, respectively, had diameters of less than 63 µm, the commonly accepted cutoff value for silt and clay particles(Ashley 2007; Duester 2007).

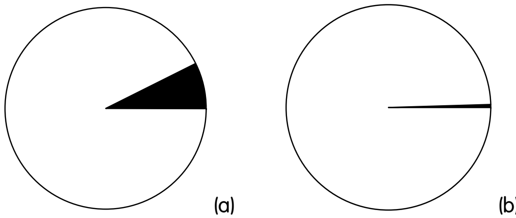

Figure 2. Particle size distributions for the two homes sampled: (a) home # 1; (b) home # 2. White is silt and clay (fine particle) fraction and black is sand (coarse particle) fraction.

Silt and clay particles are associated with a greater number of adsorption sites and higher organic matter content than coarser particles (sand), and thus it is no surprise that contaminant loadings are often found to be quite high in this fraction (Kleineidam 1999; Talley 2002). Results for selected key metals and organic contaminants are shown in Figure 2. The bar graphs present the concentrations measured inside the home (Ashley 2007), at an outdoor location between the two homes sampled (EPA 2005), as well as the corresponding U.S. EPA and Louisiana Department of Environmental Quality (LA DEQ) screening standards. For the pollutants arsenic, cadmium lead and fluoranthene, concentrations measured inside the home are 2-100 times greater than those reported in samples taken from the outdoor location. The pesticides chlordane and dieldrin are present in concentrations two orders of magnitude greater than the applicable EPA and LA DEQ screening standards. Other key organics detected include C_{20}-C_{30} alkanes, phthalates, the pesticide diethyltoluamide (DEET), along with the volatiles trimethyl benzenes and 1-ethyl-2-methyl benzene(Ashley 2007).

The specific pollutants seen are the result of a combination of contaminants found in the Lake Pontchartrain bottom sediments, as well as local sources from within the neighborhood itself. Water to flood the two homes sampled must travel nearly 1.6 km from the levee breach before reaching the homes. During that time, floodwaters will travel across yards, roads, playgrounds, and other open areas, and metal and organic materials that are in an available form can be incorporated into the floodwaters. Materials that would have obvious local sources include arsenic from herbicides and CCA-treated wood, lead which is well-known to have accumulated in high concentrations in New Orleans soils (Mielke 1994), cadmium from automobiles and consumer electronics, alkanes and fluoranthene from motor vehicle fuel, and dieldrin from pesticide and termite control use.

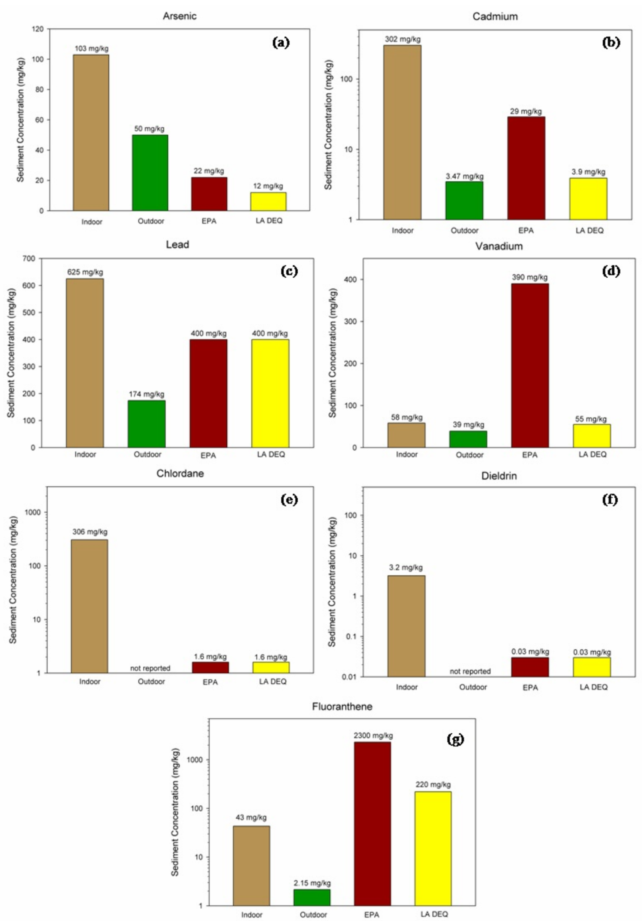

Figure 2. Selected metal and organic contaminants found inside homes sampled in New Orleans, LA post-Katrina. Bars shown are for measured indoor concentrations (tan), measured outdoor concentrations (green), EPA screening standard (red), and Louisiana Department of Environmental Quality screening standard (yellow).

Indoor Sediment-Water Partitioning of Organic Pollutants

A sediment-water partition model has been employed to assess the concentrations of key organic pollutants in the floodwaters while inside the homes. Determining the quantity and types of pollutants present in the floodwaters in the vicinity of the two homes is important for two reasons. First, floodwater contaminants can be absorbed into materials inside the home, such as furniture, upholstery, drywall, and many other soft goods. Returning residents can be exposed to the organic compounds when handling these materials upon return to their previously flooded homes. Additionally, such items will most likely be unsalvageable, and will end up in the landfill along with the contaminated sediment, further exacerbating the disposal issues, as will be discussed in greater detail below. Second, floodwater contaminants pose a direct risk to rescue workers and other first responders who traveled the New Orleans residential areas by boat in the weeks after the storm in an effort to save human and animal lives.

Sediment-water partitioning was quantified by use of the octanol-water partition coefficient (K_{ow}) for key organic pollutants, the fraction of organic carbon in the sediment, and correlations to convert the K_{ow} to K_{oc}, the organic carbon partition coefficient, for each class of compounds. The sediment-water partition coefficient, K_{sw}, is then calculated by (Valsaraj 2000):

$$K_{sw} = K_{oc} \bullet f_{oc} \quad (1)$$

Once K_{sw} is known, the floodwater concentration can be calculated from the sediment concentration by:

$$C_{aq} = \frac{w_s}{K_{sw}} \quad (2)$$

where C_{aq} is the floodwater concentration (mg/L), w_s is the sediment loading (mg/kg), and K_{sw} the sediment-water partition coefficient (L/kg).

Results of the sediment-water partitioning study for selected contaminants in the floodwaters inside the home are given in Table 1. While all concentrations shown are below EPA screening limits for these compounds, contaminated floodwaters still remain a portion of the overall exposure to rescue workers, and disposal of materials inside the home which may have absorbed pollutants from the floodwaters contributes to the disposal problems encountered in the city’s landfills.

Table 1. Calculated floodwater concentrations(mg/L) inside two homes based on sediment-water partitioning. ND = not detected in sediment samples.

Contaminant	Home # 1	Home # 2
Diethyltoluamide (DEET)	2.3	1.0
Diethyl phthalate	1.2	ND
Fluoranthene	0.01	0.01

Consequences of Landfill Disposal

As previously mentioned, contaminated sediments from inside homes along with other unsalvageable contaminated household materials (clothing, furniture, upholstery, etc.) will be disposed of in the Gentilly and Chef Mentur landfills in New Orleans. The sheer magnitude of the debris to be removed is unprecedented and has resulted in numerous political, economic, and social challenges in addition to the obligation to provide for the long-term care of the environment and residents of New Orleans.

Landfills are dynamic environments, and pH, redox, and moisture conditions are constantly changing. pH and redox are the primary parameters affecting metal speciation, and metal transport and bioavailability are strongly influenced by the metal's oxidation state. Arsenic is one such heavy metal. It has been demonstrated that iron-bound arsenic can be freed by reducing conditions, while sulfur-bound arsenic can be mobilized by oxidizing conditions (Keimowitz 2005). Because landfills ultimately reach strongly reducing conditions (evidenced by the large quantity of methane gas evolved), arsenic from sediments inside two homes sampled in this study, which was found to be overwhelmingly iron-controlled (Ashley 2007), is expected to be mobilized into the landfill leachate. Other metals, such as cadmium and vanadium that are found predominantly in the mineral-bound phase in sediments, can also be expected to be mobilized by the reducing conditions encountered within the landfill.

Rainwater can be expected to affect all of the material disposed of in landfills, and with annual rainfall amounts of nearly 60 inches per year in New Orleans, rainwater will generate a leachate which must then be pumped out of the landfill into a containment/treatment facility. Water interacts with the contaminated sediment particles by effectively competing with organics for adsorption sites on the clay minerals (Valsaraj 1997). Mineral-bound organic substituents may then be forced from the particle surface by competing water molecules. However, many of the organic contaminants are likely not mineral-bound but rather complexed with the humic materials that make up the organic matter content of the sediment. Organic matter likely blocks mineral adsorption sites from water (Karimi-Lotfabad 1993), thereby reducing the effectiveness of this mechanism for driving organic contaminants from the particle into the leachate. Humic substances are by nature a complex mixture of many different functional groups; the role of redox conditions and pH in oxidizing/reducing these functional groups is unclear, and may result in the mobilization of semi-volatile contaminants from the sediment organic matter. Materials with a high aqueous solubility limit, such as some phthalates, pesticides, aldehydes and ketones should be monitored in the landfill leachate to ensure that large quantities of these materials are not being freed from the sediment matrix. Volatile species, such as the trimethyl benzenes and 1-ethyl-2-methyl benzene will volatize to the air rapidly upon disposal, due to the high temperature and relative humidity encountered in south Louisiana.

CONCLUSIONS

A number of metal and organic pollutants have been quantified in elevated concentrations in sediments deposited inside flooded homes compared to the same compounds measured outside the home. Exposure to contaminated sediments and materials inside flooded homes is a primary concern to residents and first responders, and creates additional complications in the long-term destruction and disposal of debris from the hundreds of thousands of destroyed homes in the New Orleans area. The potential exists for long-term environmental impacts to the area which will occupy the efforts of environmental scientists for years to come.

ACKNOWLEDGEMENTS

The authors are grateful to the homeowners, Ms. Deweylene B. Schneider and Ms. Leatrice J. Burr for allowing them to collect samples from inside their homes. Nick Ashley is supported by a Donald W. Clayton Graduate Fellowship by the LSU College of Engineering. This work was funded by the Cain Department of Chemical Engineering at Louisiana State University.

REFERENCES

Ashley, N. A., Valsaraj, K.T. and Thibodeaux, L.J. (2007). "Elevated in-home sediment contaminant concentrations—the consequence of a particle settling winnowing process from Hurricane Katrina floodwaters." *Chemosphere*: In Press. doi: 10.1016/j.chemosphere.2007.07.010.

Duester, L., Hartmann, L.M., Luemers, L. and Hirner, A.V. (2007). "Particle size distribution of organometal(loid) compounds in freshwater sediments." *Appl. Organomet. Chem.* Vol. 21: 441-446.

EPA, U. S. (2005). "FLOODWATER : Sediment Chemical Testing Results for 9548: September 18, 2005." Retrieved 1/22/2007, from http://oaspub.epa.gov/storetkp/storet_wme_pkg.Station_Sediment_Chem_Results?pstation_id=9548& p_org_id =KATRINA6&p_sample_date=09-18-2005.

Karimi-Lotfabad, S., Pickard, M.A., and Gray, M.R. (1993). "Reactions of Polynuclear Aromatic Hydrocarbons on Soil." *Environ. Sci. Technol.* Vol. 30:1145 -1151.

Keimowitz, A. R., Zhang, Y., Chillrud, S.N., Mailloux, B., Jung, H.B., Stute, M., and Simpson, H.J. (2005). "Arsenic Redistribution between Sediments and Water near a Highly Contaminated Source." *Environ. Sci. Technol.* Vol. 39: 8606-8613.

Kleineidam, S., Rugner, H., Grathwohl, P. (1999). "Impact of grain scale heterogeneity on slow sorption kinetics." *Environ. Toxicol. Chem.* Vol. 18(8): 1673-1678.

Mielke, H. W. (1994). "Lead in New Orleans soils: new images of an urban environment." *Environ. Geochem. Hlth.* Vol. 16(3/4): 123-128.

Pardue, J. H., Moe, W.M., McInnis, D., Thibodeaux, L.J., Valsaraj, K.T., Maciasz, E., van Heerden, I., Korevec, N. and Yuan, Q.Z. (2005). "Chemical and Microbiological Parameters in New Orleans Floodwater Following Hurricane Katrina." *Environ. Sci. Technol.* Vol. 39(22): 8591-8599.

Presley, S. M., Rainwater, T.R., Austin, G.P., Platt, S.G., Zak, J.C., Cobb, J.P., Marsland, E.J., Tian, K., Zhang, B., Anderson, R.A., Cox, S.B., Abel, M.T., Leftwich, B.D., Huddleston, J.R., Jeter, R.M., Kendall, R.J. (2006). "Assessment of Pathogens and Toxicants in New Orleans, LA Following Hurricane Katrina." *Environ. Sci. Technol.* Vol. 40(2): 468-474.

Talley, J. W., Ghosh, U., Tucker, S.G., Furey, J.S., Luthy, R.G. (2002). "Particle-Scale Understanding of the Bioavailability of PAHs in Sediment." *Environ. Sci. Technol.* Vol. 36(3): 477-483.

Valsaraj, K. T. (2000). Elements of Environmental Engineering: Thermodynamics and Kinetics. Boca Raton, Lewis Publishers.

Valsaraj, K. T., Choy, B., Ravikrishna, R., Reible, D.D., Thibodeaux, L.J., Price, C.B., Brannon, J.M. and Myers, T.E. (1997). "Air emissions from exposed, contaminated sediments and dredged materials 1. Experimental data in laboratory microcosms and mathematical modeling." *J. Hazard Mater.* Vol. 54: 65-87.

Vulava, V. M., McKay, L.D., Driese, S.G., Menn, F-M. and Sayler, G.S. (2007). "Distribution and transport of coal tar-derived PAHs in fine-grained residuum." *Chemosphere* Vol. 68: 554-563.

Case History of the June 1, 2005 Bluebird Canyon Landslide in Laguna Beach, California

Hannes H. Richter[1], PE, M. ASCE, and Kevin A. Trigg[2], CEG
Geofirm/Stoney-Miller Consultants, Inc.

[1]Registered Civil Engineer/Geotechnical Engineer, Geofirm/Stoney-Miller Consultants, Inc., 801 Glenneyre St., Laguna Beach, CA 92651; hrichter@geofirm.com
[2]Registered Geologist/Engineering Geologist, Geofirm/Stoney-Miller Consultants, Inc., 801 Glenneyre St., Laguna Beach, CA 92651, ktrigg@geofirm.com

ABSTRACT: This paper presents the geotechnical findings and describes the remedial construction activities for the June 1, 2005 Bluebird Canyon Landslide in Laguna Beach, California. The failure occurred in bedrock terrain, and was initiated by an elevated groundwater level from the 2004-2005 Winter's high rainfall. The resulting risks to the public improvements and the community included downstream flood hazard, headscarp retreat, potential mudflow-debris flow hazards along the landslide margins, and the potential loss of three more public streets. The emergency mitigation and the eventual public infrastructure repair was conducted in two Phases. Phase I consisted of winterization of the slope by removal of the destroyed homes, surface regrading and drainage control, dewatering, removal of slide debris in the Bluebird Canyon drainage, installation of a storm drain, construction of a gravity buttress in the canyon, and stabilization of the headscarp with a temporary tieback /shoring wall. This work was fast-tracked and required constant coordination between the design and contracting teams to respond to difficult field conditions. Phase II included removal of the majority of the landslide mass, construction of two soil-cement shear keys, placement of a subdrain network, and placement of engineered fill to rebuild the slope.

INTRODUCTION

Site Description and Recent Landslide

The failure involved an area of about three hectares on the northern flank of Bluebird Canyon, bounded by Madison Place to the north, Bluebird Canyon Drive to the south, Oriole Drive to the west, and Didrickson Way to the east (Figure 1). Nineteen residences were destroyed or damaged, Flamingo Road was severed, and all utilities were severed. The Bluebird Canyon drainage was dammed by 18 meters of landslide debris. The landslide extended south-southeast from an east-west trending ridgeline to the canyon bottom adjacent to Bluebird Canyon Drive. Flamingo Road, which traversed the upper portion of the landslide, moved downslope horizontally approximately 15 to 25 meters and vertically approximately 6 to 9 meters. The landslide mass was approximately 245 meters feet long, 130 meters wide, up to 30 meters deep, and involved an estimated 445,000 cubic meters of material.

Figure 1. Aerial view northward of the 2005 failure. Limit of failure indicated by dotted line. Direction of movement is toward the viewer.

FIELD INVESTIGATION

The subsurface investigation was conducted from June 7 to July 2, 2005. The program consisted of the drilling of ten, 75 cm diameter borings and eleven, 15.2 cm diameter air rotary borings within and around the landslide. The maximum depth of exploration was 35 meters below grade. Large diameter borings provided down-hole physical inspection and structural measurements. The air-rotary borings were conducted to install slope inclinometer casings for monitoring of potential deep ground movement. The inclinometer monitoring program began on June 8, 2005 and continued through the first phase of construction, until July 2006.

Monitoring data indicated the landslide remained nominally active and translated at a rate of up to 6.5 mm per month during the investigation program.

Geologic Setting

Bluebird Canyon is located in the seaward slope of the San Joaquin Hills in Orange County, southern California. These hills are composed of Miocene-Age Topanga Formation bedrock strata that were uplifted by tectonic forces during the late Pliocene and Pleistocene. Numerous canyons, including Bluebird Canyon, were deeply incised and eroded into the San Joaquin Hills during this uplift.

Earth Materials

The bedrock strata in this area typically consist of thickly-bedded marine sandstone and silty sandstone units, interrupted with thinly bedded to laminated siltstone and claystone beds. The sandstone units vary from a meter to several meters thick, are weakly to strongly cemented, and commonly exhibit high strength. The siltstone and claystone beds can occur as very thin continuous seams and laminations, and these finer-grained seams typically exhibit low strength.

The bedrock directly underlying the landslide consists of an uncharacteristic 5 to 6 meter thick layer of clayey siltstone and claystone that is softened, chaotically sheared, and brecciated due to tectonic activity. The basal rupture surface occurs at the top of this layer in a particularly weak claystone bed.

The central portion of the landslide mass consists of a 20 to 27 meter thick, essentially intact block of bedrock material. This material is composed of thinly to thickly bedded silty sandstone and sandstone that appears undisturbed in the boring exposures. The upper and side margins of the failure consist of rock significantly disrupted by the landslide movement, with large open fractures between brecciated material and chaotic internal structure. The composition of the toe of the landslide consists of ground rock and soil, mixed with uplifted alluvium from the canyon bottom.

Geologic Structure

Overall, the bedding beneath the landslide is inclined to strike approximately east-west and dip southerly at 12 to 39± degrees from horizontal. This structural orientation is consistent with regional trends. The local topographic-structural relationship is essentially a dip-slope.

Two sub-parallel northwest trending ancient faults/shears were mapped to transect the bedrock in this area (CDMG, 1976), dipping at moderate to high angles to the northeast and southwest. One of these structures was exposed and mapped to form the eastern margin/scarp of the landslide.

The second fault forms the western margin, and is interpreted to be the control for the oblique, south 30± degrees east direction of movement with respect to the south-southwest dipping bedding orientation. This interpretation was supported by the bulging pressure ridge adjacent to the western failure margin and later confirmed by direct examination during grading.

A third fault transects the ridgeline south of the Madison Place cul-de-sac between the two side margin faults and is exposed in the cut slope behind Flamingo Drive. This fault appears to provide the structural control to the northern limit of the failure, with deformed and warped bedding or as a structural discontinuity.

A cross-section through the central portion of landslide depicts generalized subsurface conditions and the proposed repair configuration (Figure 2).

Groundwater

The groundwater surface is closely coincident with the former canyon bottom elevation at the south and rises to the north within the landslide. While some minor seepage was observed emanating from the rock, the majority of the groundwater flow was observed through secondary permeability in various fractures. The maximum cumulative seepage flow rates from fractures within the landslide below the 12 meter depth interval ranged from 230 to 380 liters per minute in one of the investigation borings. However, the sustained flow rate during construction dewatering was about 27 liters per minute.

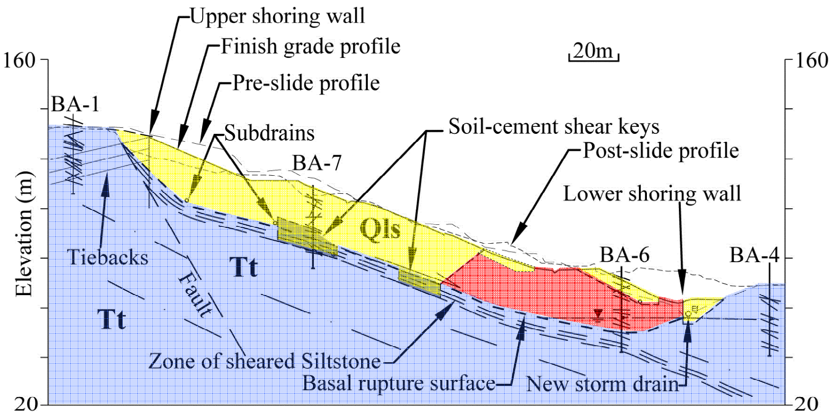

Figure 2. Geotechnical Cross Section

CAUSATION

The City of Laguna Beach receives an average annual rainfall of approximately 315 mm. Historically the majority of this rainfall occurs from November to April, but is concentrated in the months of January to March. The recorded 2004-2005 rainfall approximately follows this pattern. However, the rainfall totals for October, December, January, and February significantly exceed the monthly averages, resulting in 627 mm of the total 759 mm this season. Specifically, the rains of January and February combined accounted for over half the season total. Review of the daily rainfall totals indicates these events were long and consistent, allowing greater infiltration and less runoff. Because of the extraordinary rainfall in January and February, two separate national disasters were declared in several southern California counties, including Orange County.

It is important to note a 4-month delay occurred between the end of significant rains and the initiation of the landslide, as the rate of water penetration into the landslide mass is slow and the resulting pore-pressure build-up is not immediate.

Other potential sources of landslide causation, such as seismic activity, canyon erosion, site development, or leaking infrastructure were reviewed, but found not to be a factor in the failure.

ENGINEERING ANALYSES

Laboratory Testing Program

Our laboratory testing program was conducted on samples collected during the drilling of the bucket-auger borings. The testing of representative ring and bulk samples included in-situ moisture and density determinations, soil and rock strength properties through direct and torsional ring shear testing, and classification testing with atterberg limits determinations and particle size analysis. Strength parameters determined from the laboratory testing of remolded, consolidated drained rupture surface samples by both direct and ring shear methods for fully softened and residual strength conditions are presented in Figure 3.

Rupture surface materials exhibited liquid limits ranging from 52 to 88, and clay fractions ranging from 17 to 42 percent.

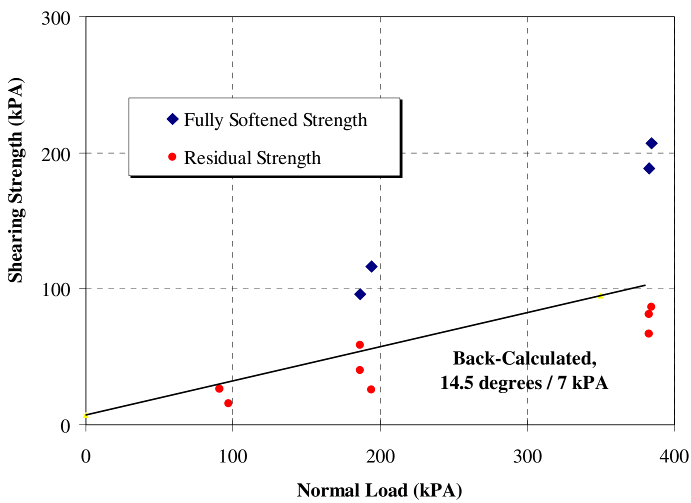

Figure 3. Rupture Surface Shear Strengths (Consolidated, Drained)

Engineering Stability Analysis

Engineering stability analyses were performed to determine measures needed to stabilize the landslide headscarp, to maintain stable excavations needed to restore drainage through the canyon, and to stabilize the overall landslide mass. The headscarp stabilization was intended to function both as temporary stabilization and for shoring during the grading planned for the landslide area. The toe area stabilization was intended as a temporary measure to facilitate storm drain installation and a canyon gravity buttress.

Strength parameters utilized for the analyses were based upon back-calculation of the existing failure conditions, results of shear testing of onsite samples, review of testing for nearby projects, as well as local experience in similar soils and engineering judgment. The back-calculation indicated a composite rupture surface strength could be defined having a cohesion of 7 kPa and a friction angle of 14.5 degrees. These back-calculated values are consistent with a composite of the shear strength obtained from laboratory testing.

Analyses were performed on the geometries depicted on various cross sections using a computer program (GSTABL7) based upon the limit equilibrium method and generally implementing the simplified Janbu method. Analyses were also performed using Spencer's and three-dimensional methods (CLARA) to verify the analyses. A 1.25 temporary factor of safety was targeted, while a 1.5 factor-of-safety was utilized for the permanent overall landslide stabilization.

REPAIR PROGRAM

Repair of the 2005 Bluebird Canyon Landslide was implemented in two phases. Phase I of the repair focused on reducing the threat to the infrastructure in the area. This Phase I repair included placement of a storm drain and buttress fill in Bluebird Canyon, mitigating against retreat of the headscarp supporting Madison Place through the winter season, and winterizing the landslide by surficial remedial grading, drainage control, and debris fencing. Phase I work was performed on an emergency basis, with construction 12 hours a day, seven days a week. All of the Phase I repair objectives were completed in August 2006.

A summary of the main geotechnical issues during the Phase I repair are presented as follows:

- Dewatering: This was attempted through the drilling and installation of a series of 11 eductor and standard pump dewatering wells. These efforts proved marginally successful, as 27 liters/minute was the average output of the system. A total of about 14 million liters was extracted.
- Trench Excavation for Storm Drain and Buttress Construction: Due to the 9 to 11± meter depth of required removal and potential for instability, the toe portion of the landslide required shoring with a caisson/tieback wall system. Excavations were limited to maximum 30-meter long sections, and some sections were as short as 6 meter in order to control landslide movement. (Inclinometer monitoring recorded approximately 200 mm of landslide displacement during the canyon grading.)
- Headscarp Stabilization: This system included a 12± meter high caisson/tieback wall and twin grade beam/tieback system, extending behind the headscarp and penetrating into competent bedrock.
- Remedial Grading: Remedial grading included the removal of the slide material and alluvium, and buttress fill placement in the canyon. The work included installing the new water, storm drain, and sewer lines.

Phase II of the repair consisted of landslide removals and re-grading, construction of soil-cement shear keys, and installation of sub-drainage within the failed area. The intent of the Phase II plan was to restore the road and hillside to approximately the original configuration with current grading code factors of safety. Modifications to the original landform were necessary, however, to satisfy current code requirements for 2:1 (horizontal:vertical) ratio slopes and surface drainage improvements.

The main geotechnical issues in achieving the Phase II design include:

- <u>Soil-Cement Treated Fill</u>: The 5 to 6 meter thick layer of softened claystone rock underlying the failure required buttressing. In order to minimize the key volume required to stabilize the material, 5 percent cement by weight was added to soil to increase the key material strength to 250 kPa.
- <u>Earthwork Logistics and Stockpiling</u>: The remedial grading, soil-cement preparation, and stockpiling had to be conducted within the three hectare site, while maintaining temporary stability during excavations. This was accomplished by geotechnically coordinating and pre-planning the earthwork into three sub-phases using AutoCad to balance the required excavation volumes with the available stockpile and preparation area.
- <u>Local Stability</u>: For each sub-phase landslide removals and key excavations extended to depths of up to 27 meters below grade. To limit internal instability within the grading area, the key excavation grading was performed in an upper and lower segment, utilizing 1:1 ratio cut slopes with excavation and backfilling of the 6 meter deep shear keys in 30 meter wide slots. This was successful in limiting the backcut failures to relatively minor volumes.
- <u>Internal Subdrainage</u>: In order to reduce the potential for future pore pressure build-up, a network of fabric-wrapped gravel and pipe subdrains were installed at regular vertical intervals within shear key excavations and landslide removal area.
- <u>Final Surface Stability</u>: Stabilization fill key excavations and placement of compacted fill to design grades was conducted over the remainder of the landslide area.

The Phase II earthwork began in May 2006 with the export of 45,000 cubic meters of excess material. The first upper key excavation began in August 2006, with completion of all remedial grading in October 2007(Figure 4).

Figure 4. Completed Regrading of the Landslide

CONCLUSIONS

1. The landslide is a block-glide type bedding plane failure that occurred in a formerly intact ridgeline. Our findings indicate that the slide is based at the top of an unusually thick, tectonically disturbed layer of unoxidized claystone and siltstone, and is structurally influenced to the north, east, and west by ancient bedrock faults.
2. The elevated groundwater pore pressures associated with the 2005 seasons above-normal rainfall was the initiating factor responsible for the landslide.
3. The geotechnical design and construction pre-planning in AutoCad allowed the consultant to control site stability during grading. This method was critical to maintaining the earthwork program within the limits of the confined site.
4. The construction dewatering program at this site proved only marginally beneficial. The temporary factor of safety during canyon slot-cutting was therefore near 1.0 and almost 200 mm of landslide movement occurred during the Phase I work.
5. Construction monitoring with slope inclinometers and wall survey targets was crucial in evaluating landslide movement and controlling the excavation sequencing. The landslide movement proved useful, however, in verifying the initial modeling of the landslide.
6. The difficulties involved with earthwork logistics, excavation sequencing, and controlling landslide movement required constant coordination with the contracting team. Good communication and cooperation was essential in being able to complete the work in a safe and efficient manner.

ACKNOWLEDGEMENTS

The writers sincerely appreciate the unequivocal support from the City of Laguna Beach, especially from council member and (former) Mayor Elizabeth Schneider, City Manager Ken Frank, and Community Recovery Coordinator Bob Burnham. The writers also recognize the extraordinary efforts of The Moote Group, Inc. (construction manager), Zamborelli Enterprises, Inc. (caissons and tiebacks), Bubalo Construction, Inc. (grading and utilities), Fuscoe Engineering, Inc. (civil engineer), Earth Support Systems, Inc. (shoring engineer), and KDM Meridian (surveyor).

REFERENCES

CDMG, 1976, "Geology and Engineering Geologic Aspects of the Laguna Beach Quadrangle, Orange County, California" Special Report 127.

Fuscoe Engineering, 2005, "Conceptual Grading Plan, Bluebird Canyon," Plan Projects 378/05/Eng/Exhibits/ 37805-XH-CON-GRD-SK.DWG, dated July 15, 2005.

Leighton and Associates, Inc., 1978, "Bluebird Canyon Landslide, City of Laguna Beach, California, Summary of Emergency Repair Measures."

Leighton and Associates, Inc., 1979, "Final Geotechnical Report of Emergency Repair Operations, Bluebird Canyon Landslide of October 1978," Project No: 178515-05, dated August 24, 1979.

Geotechnical Evaluation of Subdivision Setback from River Valley Slopes

Vishnu Diyaljee, F. ASCE, P. Eng.

Managing Director, GAEA Engineering Ltd, 2408 -113A Street, Edmonton, Alberta, T6J 4Y2; diy001@gaeaeng.com

ABSTRACT: This paper addresses a geotechnical study to determine the desirable setback of housing lots from the crest of a valley slope for a 160-acre subdivision bordered on its east by a 30 m deep river valley and a Canadian National Rail (CNR) track, and on its south by a 20 m deep ravine. This study was prompted by observations from aerial photos of past slope instability along the east valley slope above and below the rail track, and along the ravine slopes. Historic geotechnical reports from the CNR indicated significant instability with the east slope and railway track twenty-eight (28) years before and proved invaluable to the overall study.

INTRODUCTION

Houses constructed close to the crest of slopes have been known to be associated with settlement, distortion, and on occasions, loss of property and life. This paper addresses a geotechnical study of the proposed Valleyview subdivision to ensure that housing lots would be setback a safe distance from the crest of a deep river valley and ravine slope. This subdivision, Fig.1, is situated within the City of Camrose, Alberta. At the inception of its planning and development study in 2002, a review of aerial photos showed evidence of isolated shallow slumping along the slopes of the Camrose Creek and a No-Name ravine. A site review in 2002 showed that along the east valley slope there were shallow slumps in grassed areas and in over-steepened slopes in treed areas, as well as isolated slumps along the north slope of the ravine, Figs.2-5.

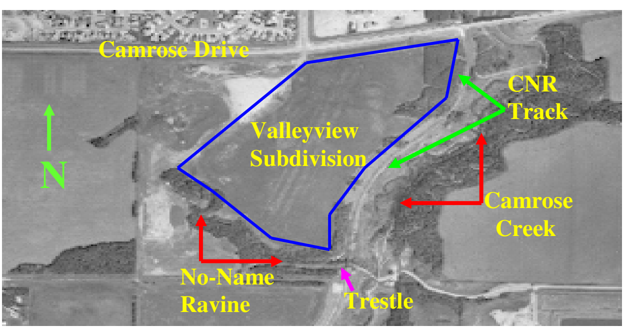

FIG. 1. Proposed Subdivision and Other Site Features

FIG.2. Overview of East Slope

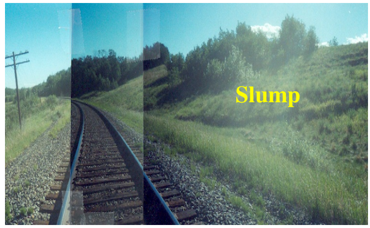

FIG. 3. Grassed East Slope (Slump)

FIG.4. Treed East Slope (Slump)

FIG. 5. North Slope (Slump)

REVIEW OF HISTORIC GEOTECHNICAL INFORMATION

Based on the observations and findings of the site review concerns were raised about past stability of the CNR rail. This led to a review of the CNR project files whereby seven (7) reports were found on studies initiated in November 1974 relevant to the Valleyview Subdivision (Thurber Consultants, 1975). These studies were undertaken when several rail-track embankment slope instabilities occurred following a severe flood in 1974 resulting from excessive snowfall in the winter of 1973. The following are some pertinent findings.

1. The Camrose creek was realigned in 1950 to eliminate creek meanders responsible for eroding the track embankment and causing instability.
2. Earth berms were constructed to stabilize movements of the track embankment.
3. Flattening of the slope of the east valley was undertaken to prevent slumping. Perforated pipes were recommended for installation along and at the toe of the slope to remove subsurface seepage. However, during the 2002 site review, these pipes could not be found.
4. A catchwater ditch was constructed at the top of slope to collect surface runoff from the farmland discharging on the east slope. This discharge was determined as a primary reason for possible slope slumping.

GEOTECHNICAL STUDIES TWENTY EIGHT (28) YEARS AFTER

Phase 1 Study

On July 4 and 5, 2002, a conventional geotechnical investigation of the site was undertaken (DK Consulting and GAEA Engineering Ltd, 2002). Four (4) deeper holes were drilled to a maximum depth of 10 m in areas along the east and south boundaries of the subdivision. Bentonitic clay was encountered at a depth of about 9 m below ground in two of the holes, one along the east boundary and the other along the south boundary. Standard Penetration Tests (SPT) were done in these holes and standpipe piezometers installed after drilling.

Preliminary slope stability analyses were undertaken using the G-Slope Software Program (www.mitresoftware.com) to provide some initial guidelines for planning the subdivision layout. The values of soil parameters used for the till were Ć=0 and Ǿ=35º, and unit weight of 20.4 kN/m^3, while for the bentonitic shale values used were Ć=0, Ǿ=10º and unit weight of 18.86 kN/m^3 (Hardy Associates (1978) Ltd, 1993). The analyses examined the stability of the east valley slope with a 9 m (shallow) and a 28 m (deep) bentonitic layer, respectively. The cross-section used for the slope stability analyses was obtained from contour mapping of the slope shown in Fig. 2.

Figs. 6 and 7 show the Factor of Safety (FOS) versus Setback Distance for water levels at 3 and 6 m below ground, which represented the range of monitored water levels 15 days after the investigation. For a desirable FOS of 1.5, setback distances for the upper slide plane were 15 and 25 m for the 6 m and 3 m water levels, respectively, and 68 and 78 m for the lower slide plane with reference to the crest of slope.

From site observations, and engineering judgment, a 30 m minimum setback was considered reasonable, but a 60 m setback appeared to be more desirable for the site. Since the study was preliminary in nature and several assumptions were made, a further study was undertaken to obtain definitive recommendations as the magnitude of the setback could also have an impact on the subdivision layout and land use.

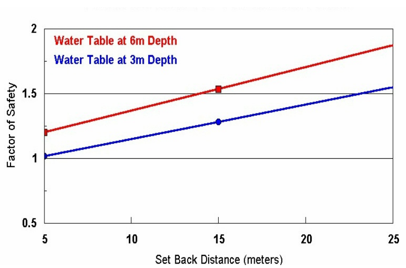

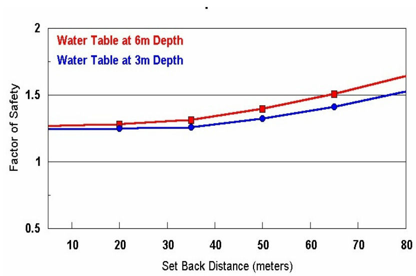

FIG. 6. Slide on Shallow Bentonitic Seam **FIG.7. Slide on Deep Bentonitic Seam**

Phase 2 Study

This study, undertaken in February 2003, included the installation of slope indicators and piezometer instrumentation, testpitting, and topographic surveys (GAEA, 2004). Slope indicators were installed close to the locations of the deep boreholes drilled in the Phase 1 study and at an estimated setback distance of 30 m from the crest of slope. Three (3) pneumatic piezometer tips were installed between SI's 3A and 3B, Fig. 8, in the same hole at depths of 9, 12 and 21 m, where seepage was noted during the drilling operations. This drilling revealed the presence of bentonitic sandy clays, and dispersed coal. A continuous coal seam encountered in all testholes was consistent with the findings from testholes done in 1974. Fig.9 shows a cross-section and soil stratigraphy from the 1974 and 2003 topographic surveys and testhole data.

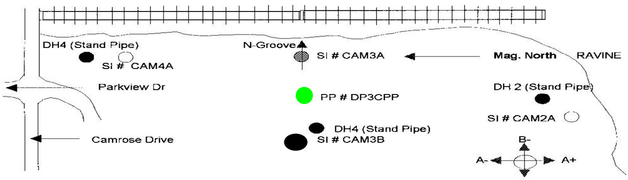

FIG. 8. Sketch Plan Showing the Location of SI's and Piezometers

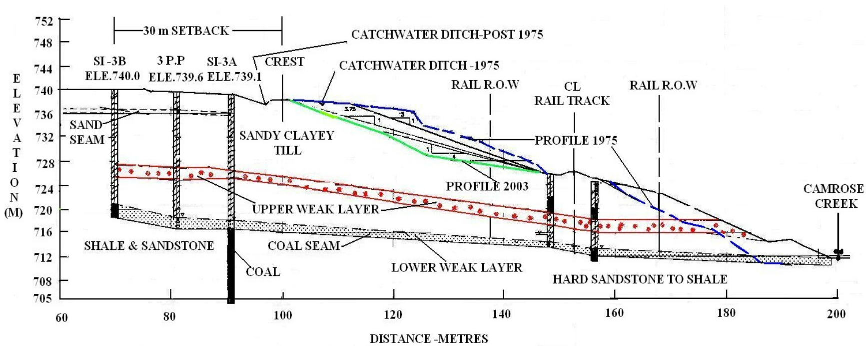

FIG. 9. Cross-Section Used in Slope Stability Analyses – Phase 2 Study

RESULTS OF INSTRUMENTATION MONITORING

Slope Indicator Results

The slope indicators (SI) were monitored over a period of 7 months from March to September 2003. Possible movement zones were inferred at 2, 17, 22, 24, and 25 m for SI 2A along the ravine slope, 2, 10, 21 and 35 m for SI 3A, 2, 8, and 16 m for SI 3B and 6, 20, 25 and 27 m for SI 4A. Movement along these zones was downslope and varied from 2 to 10 mm. These small movements were anticipated since the slope indicators were not located in visually active slumping areas.

Standpipe, Pneumatic Piezometer and Testpit Water Levels

The testholes from the 2002 and 2003 drilling program showed saturated sand seams about 0.3 to 1 m thick between SI 3A and SI 3B (Fig. 9). These seams were about 3 m below ground. While the standpipes did not show water at the 3 m level, this was considered a likely upper level that could be attained by water at the site. The pneumatic piezometer tip at the 9 m depth showed water levels comparable to that of the corresponding standpipe piezometer suggesting that the soil above and below the sand layer was influenced by the water in the sand seams. The presence of a hard layer from about 9 to 12 m was also considered to influence the piezometer water levels for slope stability analyses. The piezometer tip at the depth of 21 m in the coal layer showed no appreciable rise in water pressure indicating, as suspected, that this coal layer was free draining to the river and would be influenced only by a significant rise in water level in the Camrose Creek. Four (4) of six (6) testpits were dug between the SI 3 and SI 4 locations within the catch water ditch parallel to the crest of the valley slope. Wet sand seams were encountered between 2 and 7 m in these pits with water breaking into one of the pits at a depth of 6.5 m from a sand seam. Isolated bentonitic material was also encountered in all pits. The bentonitic material was not very wet and did not show signs of being reworked or slickensided.

SLOPE STABILITY EVALUATIONS

General

Numerous slope stability runs were undertaken to examine the FOS of a number of feasible slope instability scenarios to assist in defining a setback distance for the housing development. From the site investigations, the ground could be discretized into an upper and lower zone for stability considerations. As shown in Fig.9, the upper zone is separated from the lower by a weak layer at around 12 m depth below the crest. The lower zone is bounded by the more or less continuous weak coal seam at a depth varying from about 20 to 23 m below the crest location. The weak layers defined the locations where sliding was most likely to occur and these were used primarily in undertaking the stability analysis.

The subsurface stratigraphy was modelled for the upper slide plane as a till layer overlying bentonitic material followed by an infinitely strong till overlying bentonitic shale material. For the lower slide plane, the lower shale was modelled as infinitely strong with the strength and density characteristics of the overlying till layer the same as the initial till layer. The values of the soil parameters were the same used in the Phase 1 study. The water levels used were 3, 6 and 7 m below ground.

Initially, slope stability analyses were undertaken using piezometric heads affecting two (2) and four (4) layers of the subsurface stratigraphy to assess how variations in the piezometric levels would influence the stability of the site. The results of the slope analyses for the upper slide plane yielded FOS's varying from 0.64 to 1.04 for the stated water levels. For piezometric levels affecting the lower slide plane, the FOS varied from 0.75 to 1.22 for all water levels with four (4) soil layers affected and from FOS of 1.25 to 1.76 for corresponding water levels with two (2) soil layers affected.

From observations of the results of the standpipe and pneumatic piezometers the piezometric head affecting two (2) soil layers was considered more representative of the action of the water on the lower slide plane, despite that the coal seam is water bearing. It was decided to use the piezometric head affecting two (2) layers in subsequent analyses. On this basis, the lower slide plane was considered stable.

Based on the above, the continuing instability of the track backslope was attributed to groundwater flows/seepage toward the backslope. The obvious solution would be to prevent the water from reaching the slope. The solution is often one of providing drainage measures. Subsurface trench drains traditionally allow this to be achieved. Slope stability analyses were undertaken for the condition of a subsurface drain and with the existing ground level, and the condition of a subsurface drain with a 2 m cut (offloading) of the existing ground. The results obtained are discussed below.

Subsurface Drain with Original Ground Level

A number of slope stability runs were undertaken with water levels depressed 6 and 7 m below the ground surface with a geotextile lined subsurface drain parallel to the crest of the valley slope. The FOS's for the upper slide plane were below 1.0 and slightly higher than 1.0 at the 21 m setback from the crest. The lower slide plane provided a FOS close to 1.5, for a 40 m setback and 1.75 for a 65 m setback.

Subsurface Drain with 2m Cut (Offloading)

Two scenarios were examined, one with the slide plane going across the tracks, and the other with the slide plane exiting around the ditch location on the uphill side of the tracks. For the slide plane, exiting the tracks, the analyses showed that failure occurs for all setback distances. This condition, however, was not considered as realistic as a slide exiting at the ditch location. For this scenario and a 6 m piezometric head with a geotextile lined subsurface drain, the FOS varied from 1.23 to 1.35. With a geomembrane and geotextile composite lined subsurface drain with the geomembrane on the downslope side (modified drain), the FOS varied from 1.47 to 1.58 for a 7 m deep drain. The modified drain was conceived to prevent seepage to the slope due to the presence of the geomembrane. This prevention would not be expected with the geotextile lined drain. The results for the lower slide plane provided FOS's of 1.5 to 1.78 for setbacks of 9 m and greater from the crest indicating that failure is not likely to occur along the lower slide plane with the 7 m deep modified drain.

Effect of River Flooding On Slope Stability

The 1973 heavy snow precipitation resulted in significant run-off causing water levels to rise significantly in the Camrose Creek. The scenario was analyzed in relation to the upper and lower slide surfaces, with floodwaters attaining an elevation of 715 m. When four (4) layers are affected as a result of flooding, the FOS for the lower slide plane varied from 1.23 to 1.35 for zero and larger setbacks with the 7 m modified drain. These results indicate that although a desirable FOS of 1.5 was not achieved, a slope failure through the lower slide plane would not occur under those conditions. For the case of two (2) layers, a FOS of 1.54 was achieved at a setback of 21 m for the lower slide plane with a 7 m deep geotextile lined drain.

SUMMARY OF STABILITY AND SETBACK EVALUATIONS

Numerous slope stability analyses were undertaken to assess the existing stability and to determine the effect of preferred remedial measures for arresting further slope failures along the backslope. The evidence from site observations, testpitting, water level determinations, monitoring and subsurface stratigraphy, and slope stability analyses indicates that subsurface seepage is responsible for the failures that have occurred along the backslope prior to over the past 30 years. This slope sloughing has occurred despite that the backslope was flattened and an interceptor ditch constructed at the crest of the backslope. This confirms the opinion expressed in the Thurber (1975) report that the backslope flattened to 3:1 would be stable if subsurface seepage was not significant.

Treatment of the slope by flattening would still lead to slope sloughing and the incidence of movement closer to the crest. This often occurs because of blocked seepage paths causing a build up of pore pressure at varying locations in the slope and resulting in retrogression of failure surfaces. Based on the overall evaluation and assessment of the results, it was determined that the best stability conditions of the site would be attained with a setback of 30 m minimum, Fig. 9, in conjunction with a geomembrane and geotextile composite lined drain and a 2 m offloading at the crest location. This scenario would provide a FOS of 1.54, which satisfies the stability criterion for slopes forming part of subdivisions containing buildings and their infrastructure. This recommendation includes the understanding that the lots will be graded to direct all surface runoff away from the slope

EFFECT OF FAILURE OF CNR TRACK EMBANKMENT ON BACKSLOPE

Slope stability was examined for the recommended setback and associated conditions. The results showed that the backslope will fail along the upper slide plane if the track embankment suffers a failure. For the lower slide plane the FOS exceeds 3.36 and hence the possibility of failure at this level is remote. Failure of the track embankment would then lead to a failure of the backslope despite the remedial measures that were proposed. This failure could be promoted because of loss of toe support. Since this event would result in an unwelcome situation for both the CNR and subdivision, it is important that stable conditions persist at the track level. This suggests that the CNR would have to be involved in the exercise of ensuring that stable conditions persist at the track level at all times in the future.

CONCLUSIONS, FINDINGS AND RECOMMENDATIONS

The planning and development of a 160-acre subdivision bounded on the east by a 30 m deep river valley slope and on the south by a 20 m deep ravine slope was studied extensively by site reviews, investigations and slope stability analyses to determine the most appropriate setback distance for the proposed subdivision from the crest of the slopes.

The scope and extent of the study was largely influenced by aerial photo and site reviews, and the discovery of historic geotechnical reports of previous instabilities associated with the CNR rail along the east valley slope some twenty eight (28) years previously. Without this historic geotechnical information significant site features would not have been readily recognized and understood. This study apart from allowing sound decisions to be made regarding setback and site development points up the importance of undertaking an aerial photo review and thorough search for historic site information not only from records but through people discussions before undertaking a geotechnical study of any site.

The following are some pertinent recommendations and findings resulting from this study:

1. Lot boundaries should be setback a minimum of 30 m from the crest, Fig. 9.
2. Site grading shall be undertaken to direct surface runoff from the subdivision away from the east and south slopes.
3. The continuation of sloughing of the backslope uphill of the tracks is primarily caused by subsurface seepage. Instability caused by this seepage is most likely to result in slope instability along the upper slide zone.
4. Slope instabilities along the weak coal layer is not likely to occur because of its free draining characteristic and its more or less flat topographic disposition.
5. Sand seams within the subsurface stratigraphy are water bearing and contribute to the seepage conditions that exist along the slope and the resulting instability condition.
6. Flattening the slope alone without drainage measures would not prevent further sloughing of the slope.
7. The use of a modified subsurface drain of a geotextile – geomembrane wrapped conventional trench drain would be better suited to preventing seepage transverse to the drain and improve the stability of the slope.
8. Off loading the crest by a 2 m cut and installation of a 5 m deep subsurface drain along the crest of the slope between SI 3 and 4 over a distance of about 100 m would ensure that backslope instability in these areas would not occur in the future.
9. A flood event similar to that in 1974 is not expected to result in the failure of the slope along the upper or lower slide zones.
10. Failure of the track embankment will result in failure of the backslope along the upper slide zone.
11. Stability concerns of the east valley slope likely to occur as a result of possible failures along the track embankment need to be addressed with the CNR.
12. Further investigation through testpitting along the north valley slope of the subdivision needs to be undertaken to confirm whether the proposed 30 m setback distance along this slope would also be applicable.

REFERENCES

DK Consulting Ltd and GAEA Engineering Ltd. (2002). “Geotechnical Investigation, Valleyview Subdivision, Camrose, Alberta.

GAEA Engineering Ltd.(2004). “Slope Stability Considerations” Valleyview Subdivision, Camrose, Alberta.

Hardy Associates (1978) Ltd (1993). “Geotechnical Investigation For Proposed South Ring Road and Overpass/Bridge Structure, City of Camrose, Camrose, Alberta.

Thurber Consultants Ltd (1975). “Grade Stabilization, Mile 50 to Mile 50.8, Camrose, Alberta, Volume 1, General; Volume 2, Hydraulics Report; Volume 3, Mile 50.1, Volume 4, Mile 50.15; Volume 5, Mile 50.2; Volume 6, Mile 50.3; and Volume 7, Mile 50.4. Reports to Canadian National Railway.

**Landslide Stabilization along the Ohio River
Using Cantilevered Stub Piers**

Swaminathan Srinivasan, P.E.[1], M. ASCE and Jess A. Schroeder[2], P.E., M. ASCE

[1] Chief Engineer, Senior Principal, H. C. Nutting Company, A Division of Terracon Consultants, 611 Lunken Park Drive, Cincinnati, OH 45226, ssrinivasan@terracon.com
[2] Office Manager / Principal Engineer, Senior Principal, H. C. Nutting Company, A Division of Terracon Consultants, 611 Lunken Park Drive, Cincinnati, OH 45226, jaschroeder@terracon.com

ABSTRACT: Landslide activity along U.S. 50 in Cincinnati, Ohio has caused roadway damage for decades. After a necessary closure of 3 lanes due to slope movements, emergency stabilization measures were undertaken to protect the roadway by providing a short-term solution necessitated by ODOT budget constraints.

The deep shear plane was near the top of a sloping bedrock surface. Drilled shafts were installed 12 m downslope of the roadway shoulder. The shafts were heavily reinforced across the shear plane but steel reinforcing did not extend the full length of the shafts and was stopped well short of the ground surface. The goal was to provide shear resistance across the failure plane, forcing the theoretical failure surface higher into the overburden soils. These “Stub Piers” were installed and found to meet all of the project goals.

The stub piers and surrounding ground were instrumented and preliminary analysis of collected data showed earth pressures and horizontal deflections were highly over-predicted in the original design. However, time-related effects have yet to be evaluated. Indications after a year suggest this option offers much more than a short-term solution to the problem and may in fact, offer long-term support.

INTRODUCTION

Landslide activity has occurred along U.S. Rt. 50 in western Cincinnati, Ohio. The slope rises more than 75 m above the roadway. On the downhill side, grade slopes down about 5 to 6 m at about 3H:1V to a railroad right-of-way before continuing down to the Ohio River’s edge. This area is located on a “cutting bank” of the river. Slope and road movements have required periodic repairs over recent decades. The railroad tracks downslope of the roadway also show signs of horizontal displacement and periodic repair. Visual evidence suggests the shear plane extends below the roadway at deep levels and extends out into the Ohio River.

H. C. Nutting Company was retained by the Ohio Department of Transportation (ODOT) to perform a geotechnical study that included test borings and inclinometer monitoring. After only a few weeks of monitoring, the inclinometer casings sheared off about 15 m below grade, near the soil/bedrock interface. Soon after, roadway distress worsened, causing ODOT to close 3 of the 4 lanes to traffic and reroute traffic onto the remaining lane and shoulder. HCN was asked to develop a stabilization design under emergency repair conditions. However, funds were limited at the time, necessitating a direction by ODOT that the solution be at least short-term.

GEOLOGIC SETTING

The overburden profile consists of cohesive embankment fill, alluvium, colluvium, and residuum. Fill ranges from 3 to 7.6 m deep and is underlain by alluvium that is interbedded with and sometimes lying atop colluvium. Colluvial clays are formed by action of gravity and have slickensides with random orientation. Residuum is also present in some areas at a thickness of about 1 m Residuum is a soil formed from the in-place weathering of the underlying parent bedrock.

Bedrock lies between 10 to 15 m deep. Typically, gray shale and limestone occurs. However, about 1 m of brown weathered shale with limestone occurs in some locations above the gray shale. The horizontally-bedded shale and limestone belongs to the Kope Formation (Ordovician System) and includes shale that rates as very soft to soft in terms of bedrock hardness. There are numerous documented landslides in this local geologic setting. Shale comprises about 90% of the Kope's mass. Very hard limestone makes up the remainder, occurring in layers up to about 4 cm thick (refer to Figure 1). The Ohio River in this area has a normal pool elevation of 138.7 m and official flood elevation of 147.8 m. The 100-year flood elevation is 152.7 m while the highest recorded river level in Cincinnati occurred during the 1937 flood at elevation 156.1 m. With the U.S. 50 roadway elevation at 154.8 to 157.3 m and the railroad at 149.4 m, at least the lower portions of this slope are subject to periodic flooding and river drawdown conditions. These conditions worsen the overall slope instability.

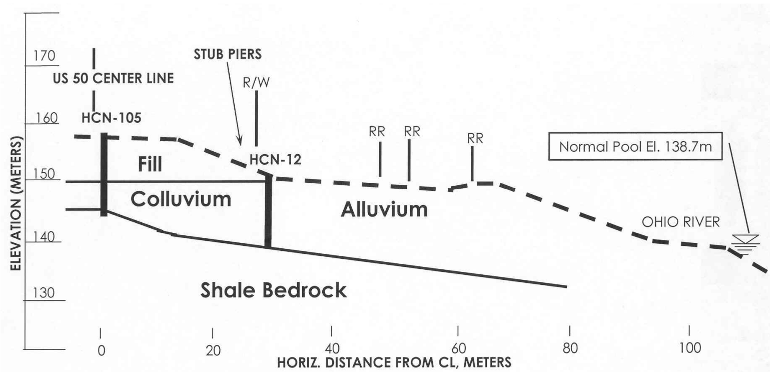

FIG. 1. Typical Subsurface Profile

DESIGN APPROACH

Working under ODOT's direction to develop a somewhat short-term solution using limited funds, HCN ruled out some potential options. For example, a more permanent repair using tieback anchors was ruled out due to cost and constructability considerations and the fact that the shear plane was so deep. Tieback installations would have been extensive and possibly involved temporary excavations and multiple anchor levels.

The design goal was to provide shear resistance along the deep failure plane, thus pushing the theoretical failure envelope higher into the overburden profile. The selected design consisted of a single row of cantilevered drilled shafts located within the right-of-way about 12 m downslope of the roadway shoulder. The shafts would be socketed into bedrock. The innovative and cost-effective aspect of this scheme involved the steel-reinforcing length. Only the zone near the deep shear plane would be heavily reinforced, thus creating shear pin behavior. Steel would be terminated as much as 10.5 m short of the ground surface. For presentation purposes, these units were termed "Stub Piers."

From an analytical point, the short-term solution criteria was quantified by slope stability analyses. Laboratory tests were conducted and soil parameters were then adjusted slightly for the failed slope condition (safety factor of 1.0) and observed shear plane depths. Then, the shear plane was forced upward to the planned top-of-steel elevation of the stub piers. This process resulted in a theoretical safety factor increase from the original 1.0 to about 1.2 (see Figure 2). ODOT was conferred with and they agreed with this potential improvement, as a short-term solution.

Stub pier design details were then developed. The lateral earth pressure was estimated assuming triangular pressure distribution from the ground level to the shear plane. This resulted in a trapezoidal-shaped earth pressure diagram acting on the piers. For potential arching effects above the steel, it was assumed that the contributing pressure extended to one pier diameter above the top-of-steel. This estimated earth pressure was also checked using slope stability analysis to compute the resisting pressure required to generate a safety factor of 1.2. Refer to Figure 3 for a schematic of the assumed earth pressure diagram.

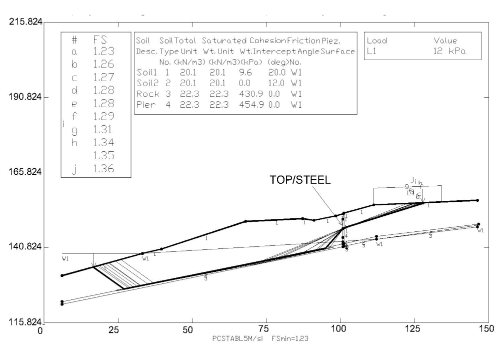

FIG. 2. Slope stability schematic.

Stub pier design was developed using the LPILE computer program. The eventual design included 154 stub piers on 1.5 m centers. Both 76 and 91.4 cm diameter shafts were to be socketed 3 to 4.6 m into bedrock and have total lengths of 13.7 to 18.3 m. Steel reinforcement consisted of HP14X73, W18X119, and W24X117 rolled steel sections. In some cases, additional bending resistance was added by welding a steel stiffening plate to the uphill face of the beam. The steel extended to the bottom of the hole; however, it was only extended about 6.1 m above the top-of-rock. Therefore, steel beams ranged from 9.1 to 10.7 m long and stopped well short of the ground surface. The shaft opening above the steel was backfilled with either structural concrete or a low-strength flowable fill. In some cases during construction, the contractor elected to use concrete backfill above the steel instead of flowable fill due to convenience (partial truck loads already on site). A schematic of a typical stub pier is shown on Figure 3.

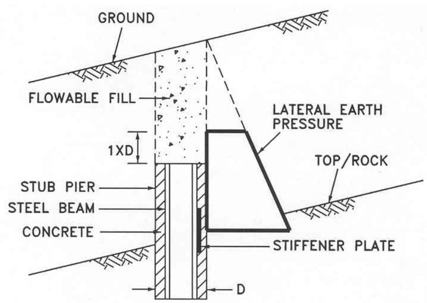

FIG. 3. Stub Pier Schematic

CONSTRUCTION

Construction began in July 2005 under an emergency repair contract. The 154 Stub Piers were installed from July to September 2005. The roadway was repaved on October 6 and 7, 2005, adding upwards of 0.6 m of asphalt in some areas to relevel the road. Traffic was reopened on October 7, 2005.

The 2005 construction cost for stub pier installation as supplied by ODOT was about $500,000.00. This cost included drilling, reinforcing, and backfilling 154 stub piers (2556.1 m of shaft drilling, 1135 cubic meters of concrete backfill, 423 cubic meters of flowable fill backfill, and 247,660 kg of steel). The cost does not include those for site preparation, paving, and other miscellaneous items. The stub pier material and drilling costs were therefore on the order of $200 per linear meter of drilled length, or $325 per linear meter of steel-reinforced stub pier length.

INSTRUMENTATION

ODOT approved a recommended instrumentation program to order to monitor the slope, verify that the stub piers were meeting design goals, and to help confirm design assumptions. This program began shortly after construction was underway.

Locations for instrumentation devices were selected for their critical locations, as well as to coordinate with the contractor's activities and schedule.

The instrumentation program consisted of the following:

1. Five Inclinometers installed within selected Stub Piers.
2. Six Inclinometers installed both upslope and downslope of selected Stub Piers.
3. Three Push-In Earth Pressure Cells (Geokon Model 4830) installed within boreholes just upslope of the row of stub piers.
4. Arc weldable Strain Gages (Geokon Model 4000) on both the uphill and downhill faces of the steel beams embedded within 2 of the Stub Piers. Six strain gages were installed per pier (four on the tension side and two on the compression side). The depths of the strain gages were approximated in order to encompass the assumed zone where the maximum bending moment would occur (near top-of-rock).

Pieces of angle iron were welded over the strain gages to prevent damage during concrete placement. The cables were extended up the stub piers to the ground surface and routed about 12 m laterally to a terminal box.

INSTUMENTATION DATA REVIEW AND ANALYSIS

Strain gages were installed on Stub Pier steel at Piers 96 and 110. The measured or "apparent" strain was converted to bending strain by subtracting the calculated compressive strain due to the weight of the pier above (carried by steel and concrete) from the measured apparent strain. The bending stress and bending moment were then computed from the bending strain value at each strain gage location.

The earth pressures that would cause bending moments calculated from the strain gage data were also generated.

Conventional earth pressure theory was followed to develop design lateral earth pressure distribution on the stub piers. LPILE analyses were conducted to determine the required pier size and steel reinforcement during design. Comparisons between the maximum bending moments and average earth pressures between the original design analyses and those estimated from measured strain gage data indicated strain gage data-generated results for both moment and earth pressure were well below the design values.

Measured horizontal earth pressures near the soil/rock interface and 3 stub piers ranged from 24.8 to 129.3 kPa. Two of the devices may have rotated before being seated at the bottom of the borehole and therefore, may not have measured full stress exerted perpendicular to the slope contours. However, measurements at one location showed 129.3 kPa comparing closely with conventional earth pressure theory assumptions.

At the two instrumented Piers, the measured maximum horizontal deflections were about 0.71 and 0.89 cm at the ground surface, respectively. At the top-of-steel elevation, the measured lateral deflections were 0.38 and 0.51 cm, respectively. For comparison, horizontal deflection was predicted during design using the computer program LPILE. The predicted value at the top-of-steel was about 4-inches and thus, well above values measured from the inclinometers embedded within the piers.

The five inclinometers installed within the stub piers collectively showed the shear plane had indeed been cut off and well-supported. Representative inclinometer data is plotted on Figure 4. Figure 4.a. shows an inclinometer before construction. Figure 4.b. shows an inclinometer installed within a stub pier and Figure 4.c. shows an inclinometer installed during construction and located downslope of the Stub Piers. Therefore, this inclinometer location was in an area left unsupported and data suggests slight creep movement on the downhill side of the stub piers, toward the river.

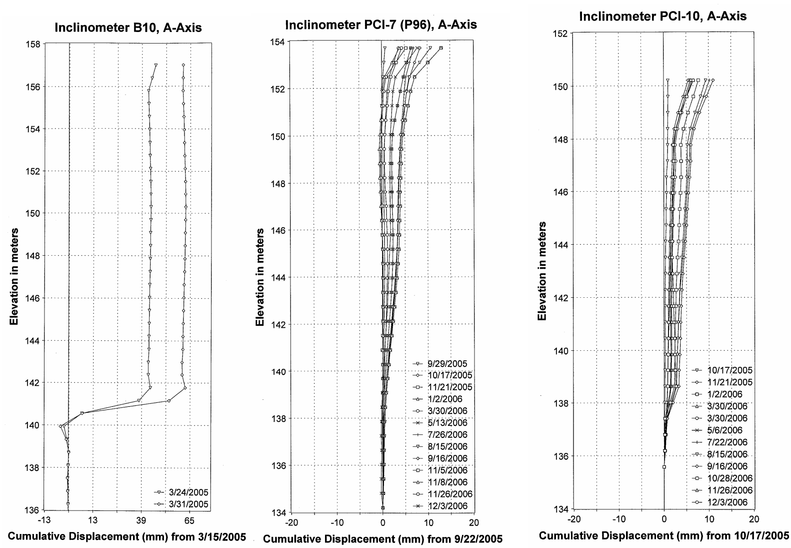

a. Pre-construction **b. Within Stub Pier** **c. Downslope of Stub Pier**

FIG. 4. Typical inclinometer results showing horizontal displacement before and after construction.

In summary, these observations suggest that the Stub Pier approach achieved the goal of creating short-term stabilization of the roadway embankment and may in fact provide much longer-term stabilization of this slope. Measured horizontal deflections indicate only a fraction of a centimeter.

RIVER STAGE AND PRECIPITATION ANALYSIS

Hagerty (1983) studied combined effects of elevated river stage and precipitation on riverbank stability along the Ohio River. He suggested looking at a 10-day cumulative rainfall combined with river stage. Figure 5 applies to the subject site and shows date versus both Ohio River elevation and 10-day-cumulative precipitation over a 2.5-year period. The 10-day cumulative precipitation was computed by adding daily precipitation for that day plus the previous 9 days. Any recorded snowfall was assumed to be equivalent to rainfall depth at a ratio of 10%. In other words, a snowfall of say, 1.1 inches was assumed to equal 0.11 inches of rain, as an approximation.

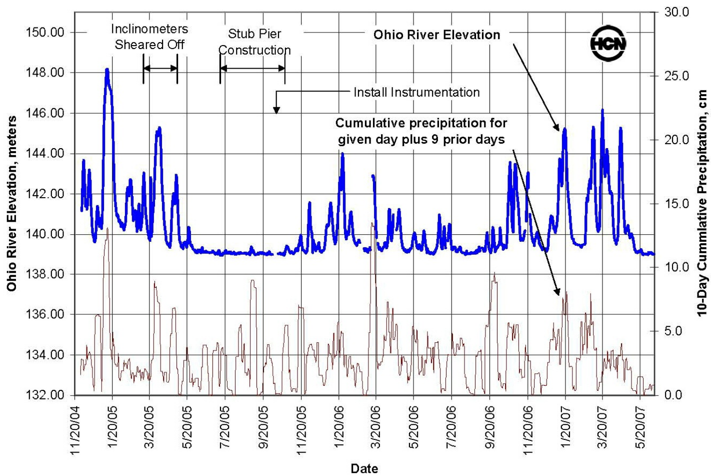

FIG. 5. Ohio River Stage in Cincinnati vs. 10-Day Cumulative Precipitation

When both the river elevation and 10-day cumulative precipitation curves are reviewed in unison, some rather significant events become evident. For example, Figure 5 suggests the following potential events:

1. Event No. 1: Approximate period between 1/6/05 and 1/14/05.
2. Event No. 2: Approximate period between 3/27/05 and 4/6/05.
3. Event No. 3: Approximate period between 4/22/05 and 5/3/05.
4. Event No. 4: Approximate period between 3/11/06 and 3/21/06.

It is interesting that these events correlate rather well to observed slope movements during the course of this study. For example, the inclinometer casings installed during the initial study sheared off in a relatively short period about March or April, 2005, corresponding to both events 2 and 3 listed above. Event No. 1 was just prior to that time period and may have actually set the whole slope in motion at the time the initial test borings were being drilled. Event No. 1 appears to be the most significant during the 2 (+) years of data shown on Figure 5.

As shown, the river and rainfall behaviors were more normal during the time of construction (Summer 2005). The new instrumentation program began in October 2005. Collected data from some of the devices suggested a slight acceleration in movements and earth pressure build-up during a period of about March / April 2006. Event No. 4 corresponds to the beginning of this time period.

This analysis has shown reasonably good comparison between observed accelerated slope movements and a combination of elevated river stage (and associated drawdown) and elevated events of cumulative 10-day precipitation.

CLOSING

The owner (ODOT) realized a successful repair solution because the repair was designed and constructed quickly, where the stub piers were installed and the roadway repaved in under 3 months time. The costs were significantly less than the alternative of a tieback-anchored drilled pier arrangement. Such a program may have involved excavating and installing multiple rows of tiebacks due to the 17 m depth between ground level and the shear plane. Excavation materials would likely have had to be removed from the site to avoid stockpile loads, only to be returned later for burying the deeper tiebacks. A much longer construction period would have been required at significant inconvenience to roadway users. Finally, a tieback anchor and drilled pier approach cost was estimated to be at least 3 to 4 times the cost of the constructed stub pier approach. Finally, the stub pier approach appears to be functioning well and may provide many years of support, exceeding the original goal of providing a “short-term” solution.

ACKNOWLEDGEMENTS

The writers wish to express their appreciation for the assistance and collaboration during this project by Mr. Joseph Smithson, P.E., ODOT District 8 Geotechnical Engineer and Mr. Andrew Bodocsi, P.E., PhD, H. C. Nutting Company Senior Geotechnical Consultant.

REFERENCES

Hagerty, J. D., Sharifounnasab, M, and Spoor, M. F., (1983). “Riverbank Erosion – A Case Study.” *Bulletin of the Association of Engineering Geologists*, Vol. XX, No. 4, pp. 411 – 437.

U. S. Geological Survey Web Site, Ohio River at Cincinnati, No. 03255000: http://waterdata.usgs.gov/oh/nwis/dv?cb_00065=on&cb_00060.

National Oceanic and Atmospheric Administration Web Site, Local Climatological Data for Cincinnati: http://www.erh.noaa.gov/er/iln/climo/cvg.

Non-frame method combining with tree root to stabilize natural slope

Iwasa Naoto [1], P.E., Nghiem Minh Quang[1], PhD., Ikeda Takashi[1] and Noda Ryu[2].

[1] Nippon Steel & Sumikin Metal Products Co., Ltd SA bldg., 2-7-12 Kiba Koto-Ku Tokyo, Japan 135-0042: Niwasa@ns-kenzai.co.jp, Nghiem@ns-kenzai.co.jp and tikeda@ns-kenzai.co.jp
[2] Forest Civil Engineering Facilities Research Institute 1-7-12, Bunkyo-Ku, Tokyo, Japan 112-0004

ABSTRACT: Tree root is known as a kind of reinforcement material on natural slopes by fixing unstable soil into the bedrock. This paper introduces a new soil nail method named Non-frame that has the same reinforcement mechanism as of tree root. Non-frame consists of a number of soil nails with fixed plates at their heads and connected together by a wire net system. There are three reinforcement components: 1) axial component born by effects of skin friction of nail body and vertical settlement of fixed plate, 2) shear reinforcement occurs at slip surface and 3) tension occurs at connecting wire between nail heads. A theoretical model was applied to analyze the reinforcement of Non-frame. The calculated results of soil nail had good agreement with that of experiment data. The efficiency of tension of connecting wire to avoid partial failures was confirmed by other experiment in highly saturated soil. Results of shaking experiments as well as stabilized natural slopes after earthquake in observation field shows the effectiveness of wire net against earthquake.

INTRODUCTION

Natural slopes are those which are not disturbed by human action. Trees can grow on the natural slope with top soil. Tree roots are found to be distributed up to 2m of soil depth (Abe and Iwamoto, 1986). It is one of main reasons why in Japan total percentage of slope failure with slip surface shallower than 2.0m is about 80% of all slope failures (Japan Public Work Research Institute, 1985).

FIG. 1 shows a scenario where a slip surface (red line) is created on the natural slope with below the tree root reinforcement. The root reinforcement is effective only above the depth of penetration of roots (yellow zone) of the landslide. The slip surface occurs below the yellow zone in the figure due to lack of root reinforcement. To stabilize such slopes, concrete structures are often applied.

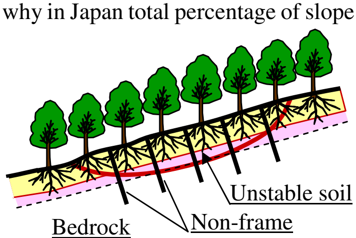

FIG. 1. Soil nails stabilize a natural slope.

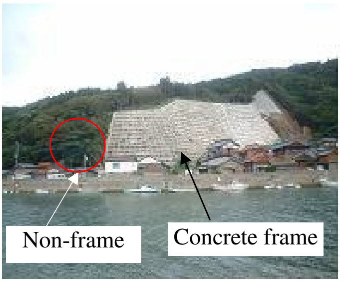

Photo 1. Non-frame and Concrete

However, for such structures trees needs to be cut off which deprives the slope from the root reinforcement. On the other hand, Abe K. & Iwamoto M., 1986 and Gray D. H. & Sotir R. B., 1996 found that tree root played important role in slope stabilization. To make use of the root reinforcement and to protect the trees, a new soil nail method named Non-frame is proposed in the present paper. Non-frame adds more reinforcement at deep zone of the landslide where root reinforcement is not available, FIG. 1. It avoids deforestation, fulfills the conservation requirements of landscape or cultural heritage sites (see Photo 1).

REINFORCEMENT MECHANISM OF TREE ROOT AND NON-FRAME

The mathematical model of tree root and soil nail is illustrated in FIG. 2. When the unstable soil layer is moving down, tree roots or soil nails deform. The longer the displacement of slope, the larger will be the deformation of the root or soil nail. This deformation produces shear force, axial force and bending moment in the tree root and soil nail which acts against the slope movement. Equations 1, 2 (Nghiem et al, 2003) show the relation (p-y) between shear force, axial force and deformation of material (root or Non-frame).

$$EI_i \frac{d^4 y}{dx^4} + Es_i(y_i - p_i \cdot \sin\alpha) = P_{xi} \frac{d^2 y}{dx^2} \qquad (1)$$

$$P_{xi} = Es_i \int_0^x (y_i \cdot \cot an\,\alpha - p_i \cdot \cos\alpha) \cdot dx \qquad (2)$$

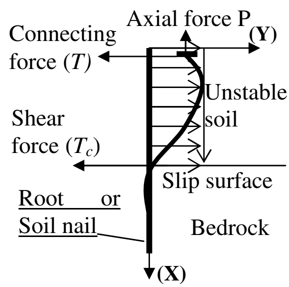

FIG. 2. Reinforcement of tree root or soil nail

Where: α is inclination of root, i^{th} soil layer has Young's modulus Es_i and displacement p_i. Reinforcing material has a deformation y_i, axial force P_{xi}, Young's modulus E_i and bending stiffness EI_i at i^{th} soil layer.

Connecting force T is born by the horizontal root connecting the stumps or wire with soil nail heads that reinforce the slope by reducing the partial failure. The sum of shear force T_c and connecting force (see FIG.2) must be equal to the total horizontal reaction of unstable soil acting on reinforcement material. We have Equation 3:

$$T + T_c = E_s \int_o^{L_1} (p - y)dx \qquad (3)$$

Where: p is soil displacement, E_s is elastic modulus of unstable soil, y is deflection of reinforcement material, P is axial force and L_1 is thickness of unstable soil layer.

By equations 1, 2 and 3, three components of reinforcement $T_{c,}$ P and T were calculated.

AXIAL AND SHEAR COMPONENT OF NON-FRAME REINFORCEMENT

The simplest test of reinforcement of soil nail includes two soil boxes, a model of two-soil layer slope (see FIG. 3). The upper box containing soil is the model of unstable soil layer and the lower one containing soil-cement is the model of bedrock (properties of soil in Table 1). The reinforcement material was a aluminum nail 5mm wide, 2mm thickness and 500mm length with a fixed plate 50×50mm^2 at head. It was inserted into lower box through upper box. When the upper box was forced to slip, soil nail deformed and fixed plate settled (see FIG. 3). Axial reinforcement caused by plate settlement combined with skin friction between soil and nail, and shear reinforcement caused by nail bending reduces soil movement that make slope become stable. A good agreement was observed between the calculated bending moments from Equations (1) and (2) and those recorded during of experiment as seen in FIGS. 4 and 5.

Table 1. Properties of soil

Properties of soil		Unit
Grain diameter	< 4.75	mm
Unit weight of soil	15	kN/m3
Moisture	24	%
Cohesion	0	kN/m2
Shear resistance angle	34.7	degree

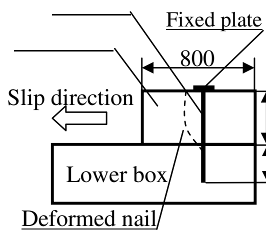

FIG. 3. Shear test of soil nail

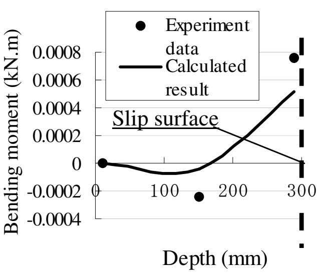

FIG. 4. Distribution of bending moment in depth (Dis. 10mm)

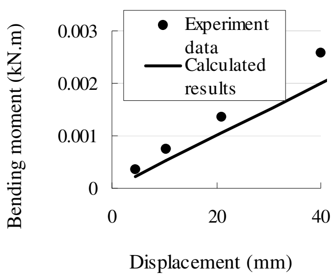

FIG. 5. Bending moment at slip surface

WIRE TENSION COMPONENT OF NON-FRAME REINFORCEMENT

Wire tension prevents nail and consequently soil from moving and thus reduces the partial failure of slope that occurs very often in rainy season or after earthquake. The efficiency of wire tension in high rainfall condition was tested by conducting an experiment with highly saturated soil (saturation 85%). Two sets of experiments were conducted 1) case1 with only fixed plate and 2) case 2 with fixed plate connected together by wire net (Photo2, table 2). The box containing soil was placed at 25 degree to facilitate sliding with time. In the case 1(no connecting wire), the bottom and mid part of slope started to slip away from the top part (FIG. 6). It simulates the natural slope which experiences partial failure developed from foot to the top. In case 2, the connecting wire kept three parts of slope together as a block (FIG. 7) and whole the block slid together. Wire net reduced partial failure making the slope more stable. The slope in case 2 failed after 130sec compared to 100sec in case 1.

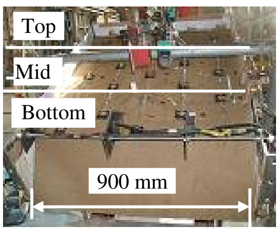

Photo 2. Highly saturated soil test

Table 2 Conditions of soil-steel in rainfall test

Bedrock	Gravel diameter D>0.85mm, moisture 5%, γ=18.1kN/m3.
Topsoil	Sand, Saturation85%, γ=15.9kN/m3.
Soil nail	D=3mm, cupper
Fixed plate	Size 50x50mm^2, t=5mm
Wire	D=0.81mm, SUS304

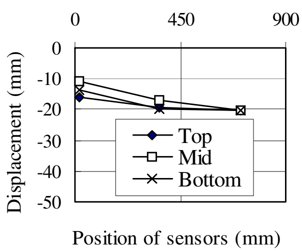

FIG. 6. Slope movement (Case 1)

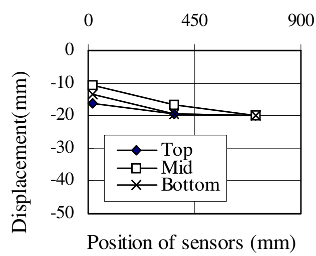

FIG. 7. Slope movement (Case 2)

NON-FRAME REINFORCEMENT DURING EARTHQUAKE

The reinforcement capacity of Non-frame during earthquake was simulated by 4 shaking table experiments (see FIG. 8). Non-frame slope was modeled by a steel box containing soil and reinforced with soil nails. The horizontal table was shaken while increasing the horizontal acceleration by 50gal, frequency by 50Hz and duration by 10 sec for each step. Table 3 shows the conditions and results of 4 cases. In case2, slope had no reinforcement; it slowly slipped down while acceleration increasing and was failed by acceleration 295 gal. In case1, slope was reinforced by Non-frame but soil nail ends were not fixed into bottom

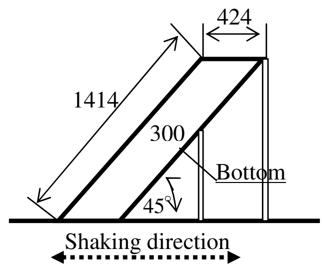

FIG. 8. Shaking experiment

of the steel box. The sliding progress in case 1 was similar to case 2 except the condition at failure. In case 1, the failure occurred at 650gal which was much greater than that of case 2 that is 295gal. Case 3 and 4 were carried out with fixed end bar. In case 4 the connecting wire net with pretension of 3N was used. Pretension of wire provided extra resistance due to which critical acceleration increased from 911 to 947gal.

Table 3 Conditions of test on shake table

<table>
<tr><th></th><th>End of soil nail</th><th>Soil properties</th><th>Plate (square) L x B (mm^2), t (mm)</th><th>Pretension of wire</th><th>Critical Acc. (gal)</th></tr>
<tr><td>1</td><td>Not fixed</td><td rowspan="4">γ= 15kN/m^3,
W = 11.5%,
Dc=70.8%</td><td>50 x 50 mm^2, 5mm</td><td>-</td><td>650</td></tr>
<tr><td>2</td><td>-</td><td>-</td><td>-</td><td>295</td></tr>
<tr><td>3</td><td>Fixed</td><td rowspan="2">50 x 50 mm^2, 5mm</td><td></td><td>911</td></tr>
<tr><td>4</td><td>Fixed</td><td>3 (N)</td><td>947</td></tr>
</table>

Photo 3 shows the slope failure in case 1, 2 and 4. By carefully excavating the failed slope in case 2, the slip surface was found to be at about 100mm depth from the slope surface. In case 1, the slope failed at its foot where there was no soil nail reinforcement. The failure at foot of slope caused upper slope slip down. No slip surface occurred inside the slope with soil nail. It means that the soil nail reinforcement kept soil slope stable. However, without being fixed at the bottom of steel box, the slipping occurred at the bottom of steel box. In case 3 and 4, soil nails were fixed into the bottom which kept the slope stable until the acceleration exceeded 900gal. In this way extra reinforcement was achieved by fixing the slope to the bottom of steel box.

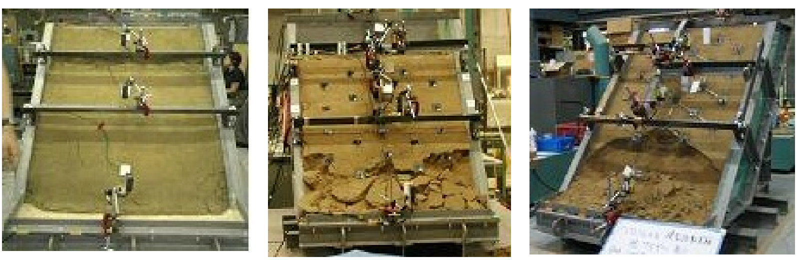

(a) Case 2 (b) Case 1 (c) Case 4

Photo 3. Failed slope at critical acceleration

MODEL OF FOREST SLOPE STABILIZATION BY NON-FRAME DURING RAINFALL AND EARTHQUAKE

FIG. 9 shows four graphs. The first one shows a conceptual graph of variation of rainfall or earthquake acceleration with time. For an unprotected slope the safety factor (*Fs*) would reduce with increase in GWL or the acceleration and failure occur when the *Fs* falls below 1.0, after time t_1 in the graph.

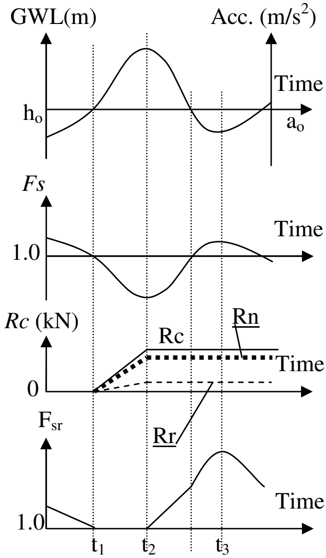

FIG. 9. Variation of reinforcement and Fs during earthquake/rainfall

In case of slope reinforced with the Non-frame, the reinforcement is zero when the GWL or earthquake acceleration is below critical. With the increase in GWL (or acceleration) deformation occurs and consequently the reinforcement increases as seen in the third graph. As the GWL (or acceleration) reaches the maximum, reinforcement also reaches the maximum. But the reinforcement due to Non-frame remains even after the subsidence of GWL (or acceleration) because the slope remains displaced. Thus a factor of safety is achieved due to the reinforcement of Non-frame (*Rn*) and the tree root (*Rr*). To design Non-frame, the maximum allowable displacement with respect to the permissible stress of material is considered to determine the reinforcement capacity of material *Rc* (*Rn+Rr*). The factor of safety can be calculated using these parameters. Nghiem et al, 2004 introduced a case study, where factor of safety Fs of natural slope was increased from 1.0 to 1.2 using tree root in combination with Non-frame. Tree roots provided about 17% of reinforcement while the remaining 83% of reinforcement was provided by Non-frame (Rn). Tree root used was Japanese cedar (Sabo technical center, 2000) and soil nails of Non-frame had 50mm diameter and 3m (average) length, which is the most common type of soil nail in Japan.

APPLICATION OF NON-FRAME

(a) Slope stabilized by Non-frame
(b)A Shallow landslide
Photo 4. Non-frame fields in Niigata

This chapter introduces landslides in the aftermath of Chuetsu earthquakes in Niigata Prefecture of Japan which from Oct.20 to Dec.24, 2004. The earth quake followed just after typhoon (No.0423) of Oct.20. The slopes were soaked and weakened due to heavy rainfall. As a consequence, the following earthquakes caused many slope failures. In Yamakoshi village (epicenter of the earthquake) only, about 800 slope failures with accumulated volume of more than 60 million m^3 were reported (Ozuka, 2005). Photo 4.b shows a shallow landslide with depth of slip surface at about 1.0～3.0m caused by Chuetsu earthquake. Photo 4.a shows a natural slope stabilized by Non-frame. Photo 5 shows other soil slope in Niigata that was saturated due to heavy rain of Typhoon No.0423. Both of these slopes are located about 60km northwest from the center of earthquake. The rainfall and earthquake did not damage the slope (Photo 4.a). It is a good example of successful stabilization of slope by Non-frame. Niigata prefecture has 17,023m^2 of Non-frame and all of them are reported to be safe.

Photo 5. Saturated soil around Non-frame head

Another example is Izuinatori slope, Izu peninsula, Shizuoka Pref. which partly failed due to rainfall of Jun.1998 (see FIG. 10 and Photo 6). This slope is located right above the Izu Express railway and prefectural route and its failure directly threatened the safety of local people. Moreover, Izuinatori is famous for its beautiful landscape and cultural heritage that has to be protected (see Photo 7a). By these reasons, Non-frame was applied to protect Izuinatori slope (see Photo 7).

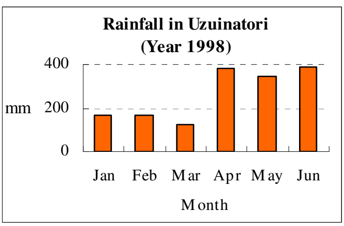

FIG. 10. Rainfall in Izuinatori

Photo 6. Slope failure, June 1998

On 23rd July 2005, earthquake magnitude smaller than M5 occurred in Izu peninsula. Three days later, 27th July, typhoon No.0507 landed with 97mm/day rainfall. During the site survey of the Izuinatori slope after 3 days of Earthquake-Typhoon, the slope stabilized by Non-frame was found to be in stable condition(Photo 7b) while a lot of natural slopes (away 3km in SW) had failed. According to the local people, all slopes had failed due to

(a) Izuinatori landscape *(b) Non-frame on Izuinatori slope*

Photo 7. Izuinatori slope

Photo 8. Kawazu slope

rainfall from 15^{th} to 19^{th} July, prior to the earthquake. So, we can understand that the earthquake on 23^{rd} was not the reseaon. Photo 8 shows a shalow landslide at Kawazu near Izuinatori slope that occurred only ten days (20 July) before the observation. The depth of Kawazu landslide is about 2.0m which is deeper than the penetration of tree roots. The right side (looking from toe) of Kawazu landslide had also become unstable and was later stabilized by Non-frame.

CONCLUSIONS

Non-frame method preserves the vegetation on natural slopes and makes use of tree roots as a kind of reinforcement material. The reinforcement of Non-frame is similar to tree root that increases according to the slope displacement. A theoretical model (p-y) and three experiments were used to analyze axial component, shear component and wire tension of Non-frame reinforcement. The axial and shear reinforcement of Non-frame were calculated by the theoretical model and the calculated results compared quite well with data of a direct shear test. The efficiency of wire tension to avoid partial failure of slope was clearly shown by an experiment with soil slope in 85% saturation. The efficiency of wire tension was proved by shaking experiment too. These experiments and models helped authors to propose a new reinforcement mechanism of Non-frame which can be used for the design of natural slope against failure due to rainfall or earthquake. Two examples of field observations show the successful application of Non-frame against earthquake and rainfall.

REFERENCES

Abe, K. and Iwamoto, M. (1986) “An evaluation of tree root effect on slope stability by tree root strength”, *Japan Forestry Society J.*, Vol. 68: 505-510.

Japan Public Work Research Institute (1985) “Situation of Japan slope failures”, *Report number 3651 of Japan Public Work Research Institute*, *Tsukuba, Japan. (Japanese)*

Gray, D. H. and Sotir, R. B. (1996) “Biotechnical and Soil Bioengineering Slope Stabilization: a Practical Guide for Erosion Control”, *John Wiley & Sons, Inc.*

Nghiem, M. Q., Nakamura, H., Siraki K. (2003) “Analysis of Root Reinforcement at Slip Surface”, *Japan Landslide Society J.*, Vol.40: 44-52.

Nghiem, M. Q., Nakamura, H., Siraki K. (2004) “Slope stability of forested slopes considering effect of tree root and steel bar reinforcement”, *Japan Landslide Society J.*, Vol.41: 264-272.

Ozuka, S. (2005) “Slope and river disaster caused by heavy rain in Niigata”, *JSNDS J.*, Vol. 24:107-162. *(Japanese)*

Sabo Technical Center (2000) “Pullout tree root, experiment in fields”, *Report of Japan Sabo Technical Center*, *Tokyo, Japan. (Japanese)*

Simplified Approach For Estimating Caisson Spacing And Post Construction Loads In a Caisson Wall

Seungwoon Han, M. ASCE, Ph.D., P.E.[1] and Gabriel W. Lang, M. ASCE, P.E.[2]

[1] Geotechnical Engineer, North Carolina Department of Transportation, 1570 Mail Service Center, Raleigh, NC 27699-1570; shan@dot.state.nc.us
[2] Sr. Geotechnical Engineer/Manager, Tierra, Inc., 2736 Rowland Road, Raleigh, NC 27615; glang@tierraeng.com

ABSTRACT: The paper presents the results of post construction monitoring of a caisson wall system used to stabilize a landslide that impacted a roadway on a steep alluvial bank along the Ohio River in eastern Ohio. From the post construction monitoring, a simplified approach for evaluating the spacing of the wall system and estimating current loads on the caissons, within the pre-defined failure surface, has been developed. The approach includes the development of site specific design charts, which can be readily utilized to evaluate the above criteria.

INTRODUCTION

Drilled caisson wall systems are a common remediation system for landslide failures involving deeper seated slides or slides at the soil/rock interface. The walls are designed with spaced caissons and provide passive restraint through embedment into rock as well as lateral stability through embedded H-beams. Soil arching is considered in the wall design and is utilized to equally distribute the load between adjacent caissons. However, methods for evaluating the post construction performance of these systems are not readily available and do not allow the designer to verify the assumptions used in their design. Such post construction evaluation systems may include the installation of slope inclinometer casings within and behind the wall and embedded strain gauges. The methods proposed herein are intended to assist the designer in evaluating the post construction performance of the system as well as providing design methodologies to enhance future designs.

SITE CONDITIONS

A caisson wall system was installed at a site located in eastern Ohio, along the Ohio River, in Fall/Winter 2005 (e.g. Lang and Han 2007). The wall system consisted of 3 feet diameter caissons, installed approximately 6 feet center to center throughout the limits of the slide area (Fig. 1).

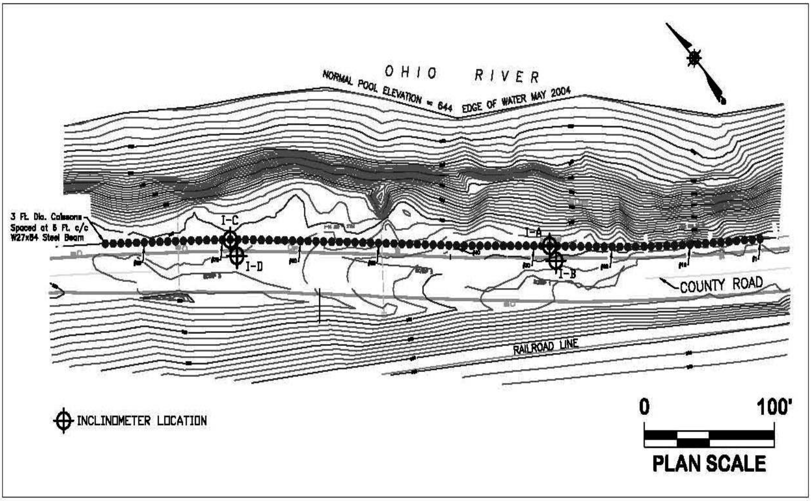

FIG. 1. Caisson Wall/Inclinometer Location Plan

The caissons were designed to retain up to 26 feet of fill/alluvial soil and were embedded a minimum of 10 feet into weathered rock and rock. A W27X84 beam was installed throughout the full length of the caisson to control deflection and resist the moment. During construction, a total of four (4) slope inclinometer casings (I-A thru I-D) were installed within the caissons as well as behind the caisson wall system. The inclinometers have been monitored over an approximately 2 year period following construction in Winter 2005 until Fall 2007 and have shown movements of 0.1 to 0.2 inches at the top of the caisson.

NEW APPROACH

Limit equilibrium methods have been used for the design of pile/drilled caisson wall systems successfully in the past (e.g. Liang 2002 and Nethero 1982). In that approach, loadings resulting from earth pressures, developed along the pile, due to soil movement are estimated based on conventional Rankine earth pressure theory, with the assumption that two dimensional earth pressures are developing along a continuous surface. However, research has also been performed to estimate earth pressure loads on the pile/caisson wall utilizing Mohr-Coulomb’s yield criterion (e.g.

Ito et. al. 1981). A method was also proposed to estimate earth pressure loads on the pile/caisson using p-y curves, which represent the soil reaction on the pile/caisson (e.g. Reese et. al. 1992). However, the approaches mentioned above do not consider pile/caisson head deflection as part of their criteria.

Therefore, a new simplified approach is proposed herein to limit the caisson head deflection using the well known beam-column differential equation as follows (e.g. Ensoft 1997) (Fig. 2):

$$EI\,\frac{d^4y}{dx^4} + Q\,\frac{d^2y}{dx^2} - p + w = 0 \tag{1}$$

Q = axial load on the caisson
x = length coordinate
y = lateral deflection of the caisson at a point x
p = soil reaction per unit length (ky)
k = soil modulus
EI = flexural rigidity of the caisson
w = distributed earth pressure load along the caisson

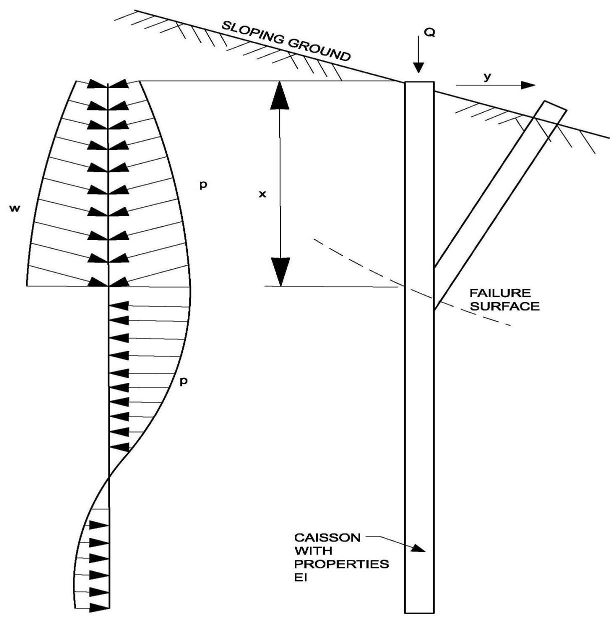

FIG. 2. Forces Acting on Caisson

Assuming that axial load on the caisson is negligible; the following two equations are rewritten:

$$EI\ \frac{d^4y}{dx^4} - p + w = 0 \text{ (above shear failure surface)} \qquad (2)$$

$$EI\ \frac{d^4y}{dx^4} - p = 0 \text{ (below shear failure surface)} \qquad (3)$$

In conventional LPILE analysis, the soil is considered fixed versus a moving caisson. However, in the case of landslide stabilization, the soil is moving in relation to the fixed caisson. As described previously, w is typically estimated using Mohr-Coulomb's yield criterion or Rankine Earth Pressure Theory. However, in this design method, w is estimated by developing site specific p-y curves for varying soil types above the failure surface and applied as a external boundary force as shown in Fig. 2 (e.g. Ensoft 1997). Therefore, w can be estimated as the soil modulus (k) times the soil movement (u_{soil}) above the pre-defined failure surface. Assuming that sufficient soil movements will occur above the failure surface, w will reach its ultimate value (w_{ult}) at the point of ultimate soil reaction (p_{ult}). However, it should be noted that in this case, only a single caisson element is considered and therefore, no soil arching.

To consider the reduction of the earth pressure load (w) along the caisson as a result of soil arching and limited soil movement from the caisson spacing, a normalized parameter (α) is introduced in the w term. Typical soil arching effects are noted to range from 2 to 3 times the caisson diameter (B) (e.g. Nethero 1982 and Liang 2002). The procedures and terminology are presented in the following section.

DESIGN CHARTS

In order to solve the beam-column differential equation and to develop p-y curves, a series of LPILE analysis was performed to develop the site specific p-y curves. The site specific soil parameters utilized for the LPILE analysis are provided in Table 1 and were based upon a slope stability back calculation analysis and correlations with published data (Lang and Han 2007).

Table 1. Soil Parameters

Soil/Rock Description	Saturated Unit Weight (pcf)	Angle of Internal Friction (ϕ) (degrees)	Cohesion (c) (psf)
Fill Material	120	24	0 to 50
Alluvial Clays and Sands	110	26	0

P-y curves were developed for the full depth of the failure surface (i.e. 26 feet). Sample results for the site specific p-y curves at various depths are presented in Fig. 3.

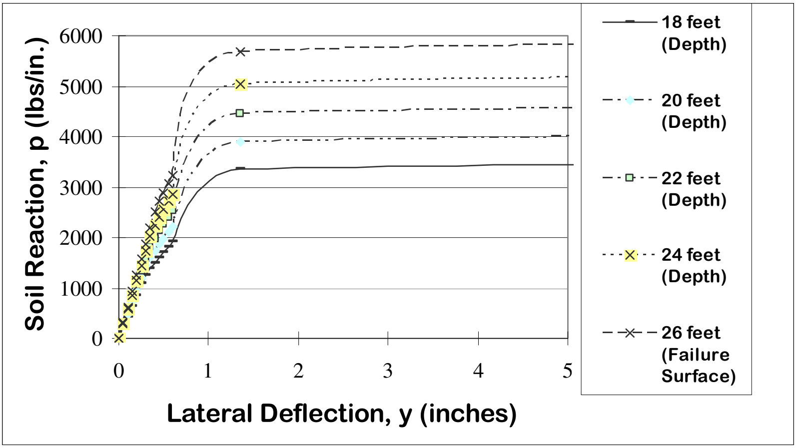

FIG. 3. Soil Reaction vs. Lateral Deflection (p-y curves)

Utilizing the above p-y curves, the ultimate soil reaction (p_{ult}) is determined for each depth increment above the failure surface. The values of p_{ult} are then plotted versus the depth of the caisson and used to determine the ultimate distributed load (w_{ult}) acting along the caisson as a result of the soil movement. However, as stated previously, this does not consider the effects of soil arching. The values of w_{ult} versus the caisson depth are presented in Fig. 4.

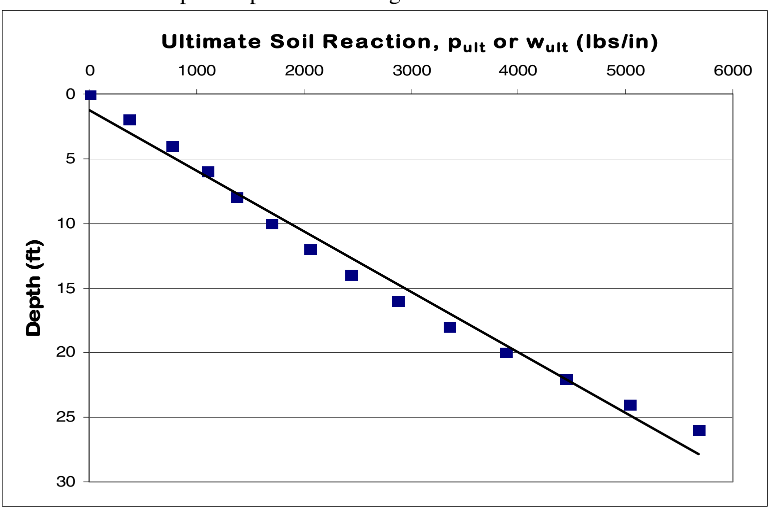

FIG. 4. Ultimate Soil Reaction vs Depth

From Fig. 4, it is observed that w_{ult} is linearly distributed along the caisson above the failure surface. As mentioned briefly above, the earth pressure load will vary depending on the caisson spacing (earth pressure load will decrease with reduced caisson spacing). The reduced spacing is considered by introducing a normalized parameter (α) in Eq. 2, leading to the following equation:

$$EI\,\frac{d^4y}{dx^4} - p + \alpha w_{ult} = 0 \qquad (4)$$

Where,

$$\alpha = \frac{w}{w_{ult}}$$

Applying α values ranging from 0 to 0.55, w is estimated and applied in LPILE to determine caisson top deflections for the various values of α (Fig. 5). Of note in Fig. 5 are the values of α corresponding to the design case (1 inch deflection) and post-construction monitoring (0.2 inch deflection) of the caisson.

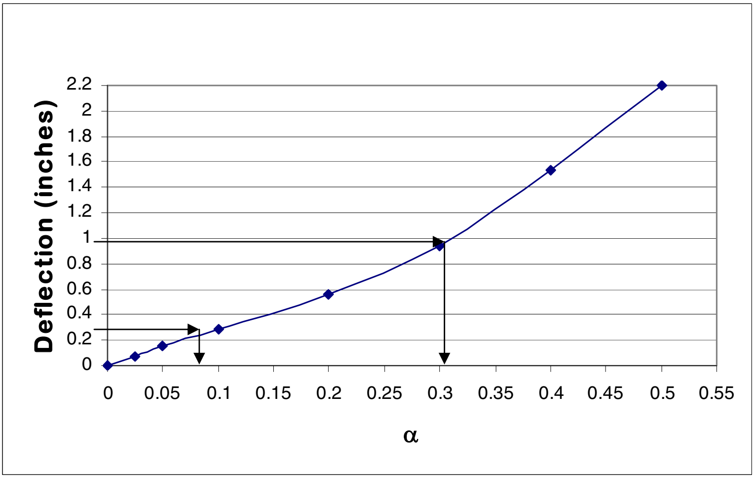

FIG. 5. Caisson Head Deflection vs. α

Note: In Fig. 5, 1 inch deflection represents the design case and 0.2 inches post-construction.

In order to compare the results of the LPILE analysis with slope stability calculations for determining the required force on the caisson, α can be redefined as shown in Eq. 5. Based on the distribution diagram of w_{ult} (Fig. 4), w is also assumed to have a linear distribution along the caisson. Therefore, with this assumption, α can also be expressed as follows:

$$\alpha = \frac{F_e}{W_{ult}} \tag{5}$$

F_e = total reduced earth pressure load, which is estimated by integrating w with respect to depth.

W_{ult} = total ultimate earth pressure load, which is estimated by integrating w_{ult} with respect to depth.

The total reduced earth pressure load F_e is then calculated for a desired deflection using Fig. 5 and compared with required resistance of the caisson, $F_{caisson}$ estimated from the slope stability analysis and the following equation (Elias and Christopher 1996).

$$F_{caisson} = (FoS_{reinf}/FoS - 1) \times F_R \times S \tag{6}$$

$F_{caisson}$ = Required resistance of the caisson
FoS = Factor of Safety for unreinforced slope (1.0)
FoS_{reinf} = Factor of Safety for reinforced slope with the caissons (1.5)
F_R = Resistance force of unreinforced slope
S = Caisson Spacing

The resistance of the caisson estimated from Eq. 6 is based on the pre-defined failure surface observed in the slope inclinometers, which is assumed to remain at its present location and not be impacted as a result of the introduction of the caissons for stabilization.

If F_e estimated from Fig. 5 is less than $F_{caisson}$, from slope stability analysis and Eq. 6, the caisson diameter or caisson spacing should be adjusted to limit caisson head deflection (i.e. $F_e/F_{caisson}<1$). By limiting the caisson head deflection, it is likely that the bending moment will be within tolerable limits as well.

For this project, caisson spacing of two (2) times the caisson diameter were used and, as represented in Fig. 5, were limited to 1.0 inch caisson head deflection. This deflection corresponds to a α value of 0.31. Using this α value, and a W_{ult} of 774 kips, F_e is estimated to be 230 kips. From the slope stability analysis, $F_{caisson}$ is estimated to be 110 kips. Considering that Fe is almost two times greater than $F_{caisson}$ the design is satisfied and has a deflection less than 1.0 inch. For design optimization, the caissons may be spaced wider. However, due to the long term movements associated with landslides, long-term monitoring of the inclinometers should be performed to verify that the post-construction deflections do not exceed 1 inch.

The chart (Fig. 5) may also be used to estimate the current loads applied along the caisson from the measured deflections in the slope inclinometers installed within the caissons. Based upon a measured deflection of 0.2 inches, it is estimated that F_e of 52 kips is currently developed on the caissons. This load is less than ¼ the load (F_e = 230 kips) used in our design.

CONCLUSIONS

The above discussions lead to the following step by step procedure:

Step 1. Determine the location of the shear failure surface using monitoring data or slope stability analysis.

Step 2. Prepare site specific p-y curves for the site using LPILE and the site soil conditions determined from residual shear testing, backcalculation or other methods (Fig. 3). Estimate a site specific ultimate earth pressure distributed load (w_{ult}) along the portion of the caisson above the failure surface from the p-y curves (Fig. 4).

Step 3. To account for the caisson spacing, generate a caisson head deflection vs. normalized parameter (α) graph using a series of LPILE analysis (Fig. 5). Caisson head deflection is calculated for each α value, by reducing w with α values from 0 to 1.

Step 4. Determine the design α value for the allowable caisson head deflection from the caisson head deflection vs. normalized force graph (Fig. 5) in Step 3.

Step 5. Calculate W_{ult} by integrating w_{ult} (Fig. 4) with respect to depth. Estimate the resistance for caisson ($F_{caisson}$) to satisfy the required factor of safety using slope stability analysis and Eq. 6.

Step 6. If $F_{caisson}$ is greater than a value of α times W_{ult}, go to Step 3 either increasing pile diameter or decreasing pile spacing. The iteration should be continued until $F_{caisson}$ is equal to or less than Fe estimated as α times W_{ult} .

From the results of the analysis for the project and post-construction measurements, the caissons are designed and sized conservatively to provide sufficient factor of safety. The design total earth pressure load is calculated to be approximately four times higher than measured, resulting in significantly less caisson head deflection. However, a longer term monitoring program is suggested to verify post construction deflections and loads. In addition, it is noted that if the subsurface conditions within the proposed caisson wall area are not uniform, the development of several design charts may be required.

REFERENCES

Elias, V and Christopher, B. R (1996). "Mechanically Stabilized Earth Walls and Reinforced Soil Slopes, Design and Construction Guidelines". FHWA-SA-96-071.

Ensoft, Inc. (1997). Technical Manual of Documentation of Computer Program LPILE ^{PLUS}3.0 For Windows.

Ito, T., Matsui, T. and Hong, W.P. (1981). "Design Method for Stabilizing Piles Against Landslide – One Row of Piles". *Soils and Foundations.* Vol. 21, No. 1: 21-37.

Lang, G.W. and Han, S. (2007). "Stabilization of a Roadway on a Steep Alluvial Bank Using Drilled Caissons". Proceedings from GeoCongress 2008: pages not available.

Liang, R.Y. (2002). Drilled Shaft Foundations for Noise Barrier Walls and Slope Stabilization. FHWA/OH-2002/038.

Nethero, M.F. (1982). "Slide Control By Drilled Pier Walls". ASCE Special Publication: Applications of Walls to Landslide Control Problems: 61-75.

Reese, L.C., Wang, S.T., Fouse, J.L. (1992). “Use of Drilled Shafts in Stabilizing a Slope”. ASCE Proceedings from Specialty Conference on Stability and Performance of Slopes and Embankments:1318-1331.

Stabilization of A Roadway On a Steep Alluvial Bank Using Drilled Caissons

Gabriel W. Lang, M. ASCE, P.E.[1] and Seungwoon Han, M. ASCE, Ph.D., P.E.[2]

[1] Sr. Geotechnical Engineer/Manager, Tierra, Inc., 2736 Rowland Road, Raleigh, NC 27615; glang@tierraeng.com
[2] Geotechnical Engineer, North Carolina Department of Transportation, 1570 Mail Service Center, Raleigh, NC 27699-1570; shan@dot.state.nc.us

ABSTRACT: The paper presents a case history for using a drilled caisson wall to stabilize a landslide that impacted a roadway on a steep alluvial bank along the Ohio River in eastern Ohio. A subsurface exploration which included: drilling SPT borings, installing and monitoring slope inclinometers and a monitoring well, and laboratory testing of the soil and bedrock was performed to explore the geotechnical and geologic characteristics of the failed area. Based upon these results, a back-calculation slope stability analysis was performed with a pre-defined shear failure surface to determine the residual strength characteristics of the slope. Simplified design methods were then utilized to determine spacing, diameter and embedment for the caisson wall system and the resultant factor of safety. To evaluate the performance of the system and the design methods, a post-construction monitoring program was initiated, which included the installation of inclinometer casings within and behind the caissons.

INTRODUCTION

Landsliding and slope movements along the alluvial banks of the Ohio River are a common occurrence in the region. Previous studies have suggested several mechanisms for failure such as: high porewater pressures and/or piping resulting from riverward groundwater flow, rapid river rise and drawdown, scour, and man's activity including fill placement on unstable alluvial banks (e.g. Hamel 1988). Common remediation methods for these slopes include overexcavation and replacement, riprap/rock buttressing, subsurface drainage and filters and driven piles.

However, for the site in question, right-of-way limitations, an adjacent railroad and a deep failure surface necessitated a remediation technique that would not require excavation and that would provide structural stability for the roadway. Drilled caisson wall systems are a common remediation system for landslide failures involving deeper seated slides or slides at the soil/rock interface. These systems have the advantage of being rigid structural elements and are constructed using top down construction techniques that do not require excavations into unstable slopes. The walls are designed with spaced caissons and provide passive restraint through embedment into rock as well as lateral stability through embedded H-beams. Soil arching is considered in the wall design and in some cases, shoring systems may be installed between the elements to prevent erosion.

SITE CONDITIONS

Site Location and Description

The site is located on a county road adjacent to the Ohio River in eastern Ohio (Fig. 1). The slopes to the east of the roadway, slope downward moderately to steeply towards the Ohio River, with portions as steep as one (1) horizontal to one (1) vertical (1H:1V). To the west of the roadway, the site slopes upward to an existing railroad track, with a maximum vertical rise of about 6 to 8 feet. Beyond the railroad tracks, the site continues sloping upward to a rock slope, with a vertical rise of about 100 feet.

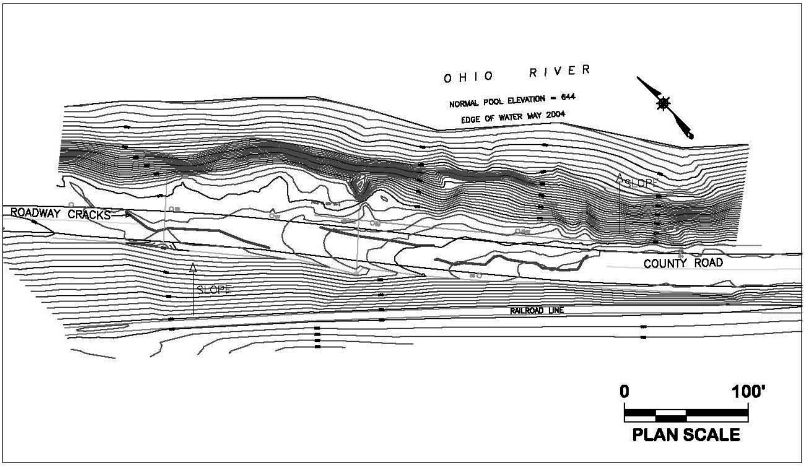

FIG. 1. Overall Site Topography, Ohio River at Top of Page and Railroad at Bottom.

Slope movements in the site vicinity were reported to have occurred in the late 1980's and early 1990's. However, by the Spring of 2004, significant distress had occurred in the roadway. Longitudinal cracking was noted to extend over a distance of approximately 550 feet, was over one foot wide in some areas, and traversed both lanes of the roadway. In addition, three distinct scarps were observed in the roadway, as well as numerous depressions, and resulted in temporary closure of the road (Figs. 1 and 2).

FIG. 2. Photo of Roadway Distress and Scarp, Existing Railroad on Right Hand Side and Slope to Ohio River on Left.

Utility poles and trees located on the downslope side of the roadway were leaning downslope toward the Ohio River (Fig. 2). Indications of riverbank erosion and hillside seepage were also noted at the toe of the slope.

Test Borings and Laboratory Testing

A geotechnical evaluation of the site was performed by drilling nine (9) Standard Penetration Test (SPT) borings, rock coring, and laboratory testing on the soil and rock samples (Fig. 3). Test borings were drilled at the site using hollow stem augers and NQ-sized core barrels and collecting samples at 3 feet intervals.

The soil conditions at the site generally consisted of variable man-placed fills underlain by alluvial deposited soils, weathered rock and unweathered rock (bedrock). Although common to the area, colluvial type soils were not encountered at the site. The fill materials consisted of black gravel sized slag, ash, coal and organic silt/clay with root fragments; the alluvial soils from an orange and brown silty clay to gravel sized sandstone fragments with silty sand; the weathered rock from brown to gray weathered shale to weathered sandstone and the bedrock from a gray to dark gray shale, carbonaceous shale and siltstone (Fig. 4). The bedrock units at the site are part of the Allegheny Group of the Pennsylvanian System and cyclic sequences of shale, sandstone, limestone and coal are present within this group. Rock core operations conducted in the bedrock resulted in recoveries ranging from 93 to 100 percent and Rock Quality Designation (RQD) values ranging from 8 to 75 percent. The condition of the bedrock was variable and ranged from slightly to highly weathered, very broken to massive, and soft to hard.

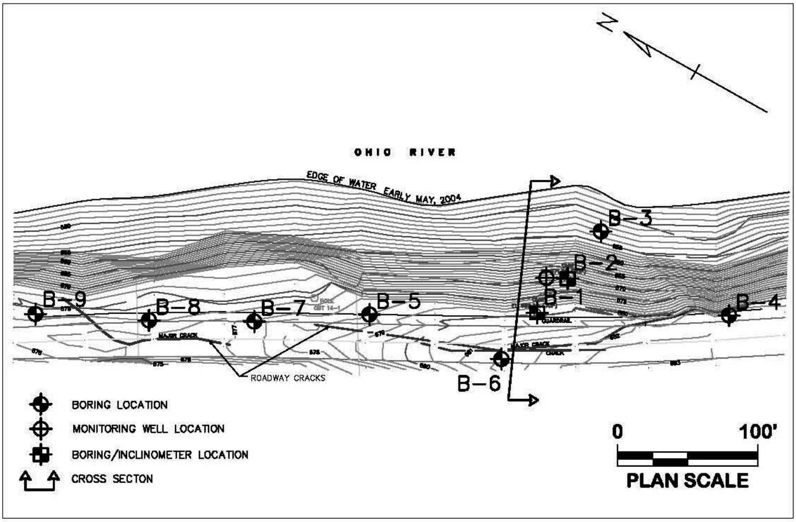

FIG. 3. Boring Location Plan

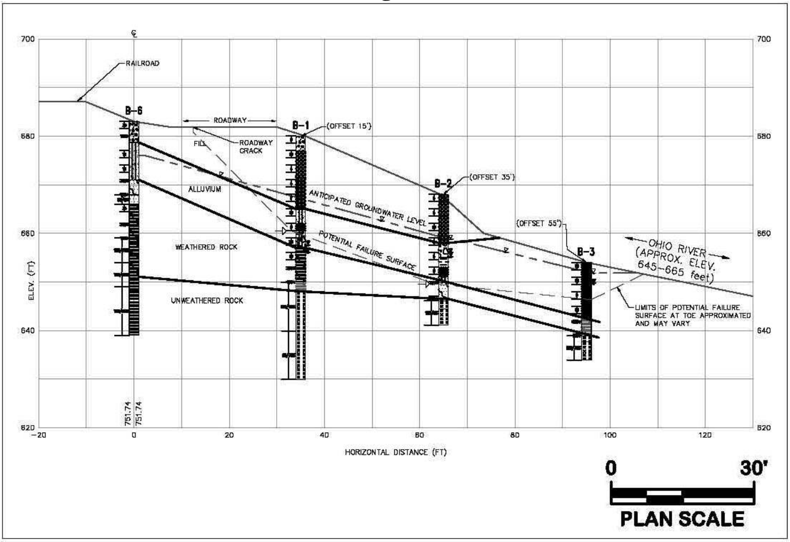

FIG. 4. Typical Subsurface Profile

Field and laboratory testing procedures were performed on both soil and rock samples obtained from the site. Cohesive soils samples were subjected to field pocket penetrometer testing as well as laboratory grain size analysis, Atterberg limits and natural moisture content. Due to the variable nature of the soils and presence of non-cohesive materials, laboratory residual direct shear testing was not performed.

Samples of the unweathered rock were tested for unconfined compressive strength. A summary of the properties of the soil and bedrock as tested in the field and laboratory are presented in Table 1.

TABLE 1. Summary of Laboratory Test Results

Geologic Descriptor	Material Description	Soil Classification (USCS)	Grain Size Analysis Minus #200 Sieve (%)	Atterberg Limits (%)		Moisture Content (%)	Unconfined Compressive Strength (psi)
				Liquid Limit	Plasticity Index		
Fill	Ash and Silty Sand with Slag, Coal and Fat Clay Lenses	SM	13.5 - 44.5	NP-72	NP-14	18-54	--
Fill	Organic Silt and Silty Clay	OL	--	43	15	24	3.5-35*
Alluvium	Silty Clay	CL	54-59	25-27	4-9	20-22	3.5-35*
Bedrock	Unweathered Siltstone	--	--	--	--	--	9,550-11,220
* From Pocket Penetrometer.							

Instrumentation

A preconstruction monitoring program with slope inclinometer casings and a monitoring well was performed to determine the location of the failure surface and elevation of groundwater within the landslide. A total of two slope inclinometer casings were installed at boring locations B-1 and B-2 to depths of about 36 and 26 feet, respectively and one monitoring well adjacent to boring B-2 to a depth of about 22 feet (Fig. 3). The monitoring well was constructed with a 2 inch diameter PVC pipe and ten feet of slotted (screened) sensing section. Slope movements in excess of 1.5 inches occurred over a two month monitoring period and a shear surface developed at a depth of about 20 feet below top of casing (Elevs. 650 to 660 feet).

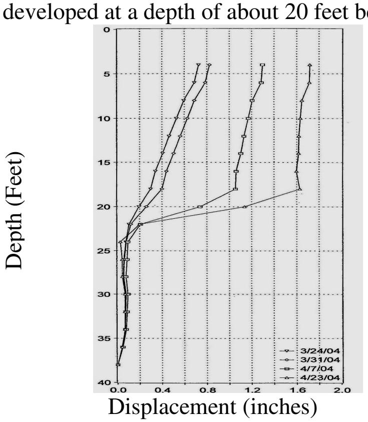

FIG. 5. Inclinometer at B-1

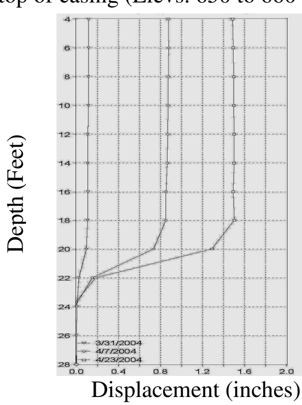

FIG. 6. Inclinometer at B-2

The depth of the shear surface, at the inclinometer locations, corresponds approximately with the soil/weathered rock interface between the alluvial soils and weathered rock (Fig. 4). Attempts were made to obtain additional readings on the slope inclinometers prior to construction, however, slope movements resulted in permanent damage to the casings. In addition, water levels in the monitoring well varied from 9.5 to 10 feet below ground surface (Elev. 658 feet), well above the normal pool elevation of the Ohio River of 644 feet.

ENGINEERING EVALUATIONS

Based upon our visual observations, field explorations, monitoring, analysis and review of previously published papers and reports, it did appear that there were several mechanisms or combinations thereof, causing the slope movements. These mechanisms include: the riverward flow of groundwater, resulting from rapid river rise and drawdown, as well as the presence of potential hillside springs from the vertical rock face slope above the site which may result in piping of the soils and the buildup of porewater pressure, each reducing the shear strength of the soils. Secondly, the erosion of the toe of the slope as a result of flood scour and riverwater rise and drawdown would decrease the amount of stabilizing material at the toe and reduce the stability of the slope. Finally, the placement of uncompacted, variable fill materials on low strength alluvial deposits which increases the driving forces and reduces the stability of the slope. Additionally, the uncompacted, low strength nature of the fill material also increases the potential for localized slope failures in the fill.

Slope Stability Analysis

A back calculation slope stability analysis was performed, using the computer program STABL5 developed by Purdue University, on the typical slope section utilizing the results of the test borings, slope inclinometers and field surveying. Based upon the failure surface defined by the slope inclinometers and location of the surface scarp in the roadway, a sliding block type failure surface was utilized in the analysis (Fig. 4). The phreatic surface was defined by water levels measured in the monitoring well and test borings. Additionally, the phreatic surface was adjusted to reflect impacts associated with riverwater rise and drawdown from the Ohio River. The parameters utilized in the analysis were either determined by the back calculation analysis, or were based upon previous experience and correlations with published data (e.g. Mesri and Shahien 2003, and Stark et. al. 2005).

Table 2. Soil/Rock Parameters for Slope Stability Analysis

Soil/Rock Description	Saturated Unit Weight (pcf)	Angle of Internal Friction (ϕ) (degrees)	Cohesion (c) (psf)
Fill Material	120	24	0 to 50
Alluvial Clays and Sands	110	26	0
Weathered Rock/Alluvial Gravel	130	30	750
Rock	140	40	4,000

Caisson Wall Analysis

Considering the subsurface conditions at the site, location of the failure surface at the soil/rock interface, and limited right-of-way, a drilled caisson wall with embedded soldier beams was considered a feasible option. Additional analyses were performed to determine the caisson spacing, embedment and reinforcement. The analyses were based upon the typical profile presented in Fig. 4 and included approximately 26 feet of soil, 5 feet of weathered rock and 5 feet of rock. Additional slope stability analyses were performed incorporating the back calculation analysis described above. A drilled caisson wall was incorporated in the slope at the right-of-way limits for the roadway, which was essentially at the top of the slope. From the analysis, resisting forces were calculated for the vertical element based upon a global factor of safety of 1.5 for the slope. To provide stability for overturning, penetration into rock for each element was determined using the AASHTO method for permanent flexible walls embedded into rock (e.g. AASHTO 1998). A distributed load from the retained landslide soils was applied along each element to determine deflection, moment and reinforcing requirements utilizing the computer program LPILE (e.g. Reese et. al. 1992).

From the analysis, the wall system consisted of 3 feet diameter caissons, installed approximately 6 feet center to center throughout the limits of the slide area (Fig. 7). Although typical caisson spacing's in caisson walls range from 2 to 3B (B=diameter) between the outer edge of each element, smaller spacings were required to provide stability and prevent soil migration in the loose granular fills and alluvial soils (e.g. Nethero 1982 and Liang 2002). The caissons were embedded a minimum of 10 feet into weathered rock and rock. A W27X84 beam was installed throughout the full length of the caisson to control deflection and resist the moment.

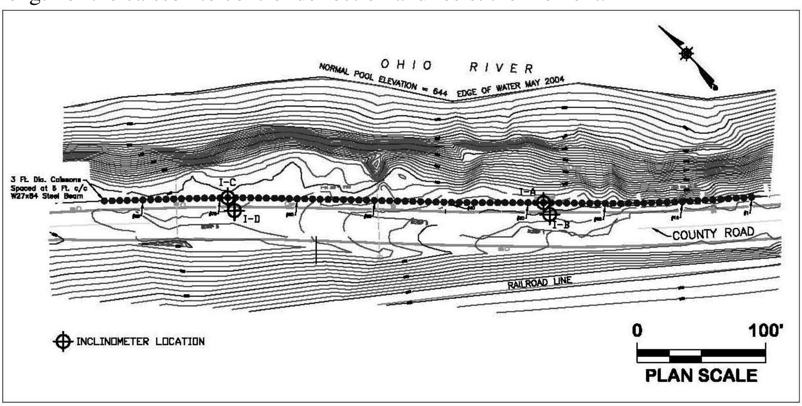

FIG. 7. Caisson Wall/Inclinometer Location Plan

Post Construction Monitoring

During construction, a total of four (4) slope inclinometer casings (I-A thru I-D) were installed within the caissons as well as behind the caisson wall system (Fig. 7). To date, the inclinometers have been monitored over an approximately 2 year period following construction in Fall/Winter 2005. Inclinometers I-C and I-D have not shown any measurable deflection to date, while inclinometers I-A and I-B, which are located in the main portion of the slide area, have shown movements of 0.1 to 0.2 inches at the top of the caisson as reflected in Figs. 8 and 9.

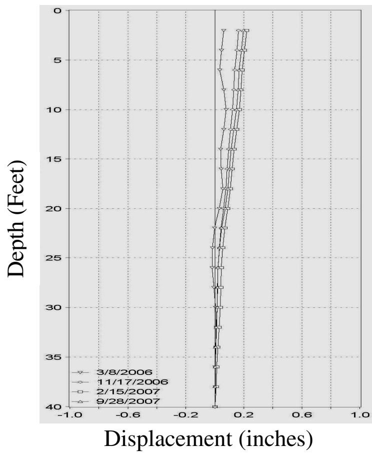

FIG 8. Incl. I-A (Inside Caisson)

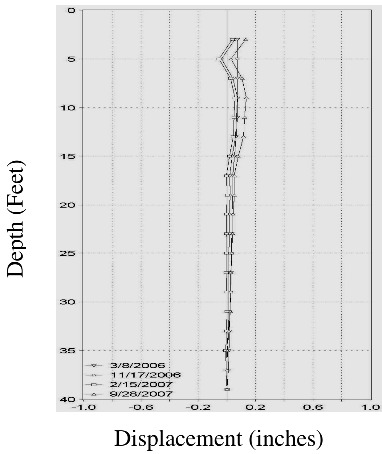

FIG 9. Incl. I-B (Behind Wall)

CONCLUSIONS

Based upon the results of the post construction monitoring program to date, movements within the caissons as well as behind the caisson wall have been limited to 0.2 inches or less. Following caisson wall construction in Fall/Winter 2005, the roadway was reconstructed and has been open to traffic and not shown indications of distress. The installation of a caisson wall system has proven to be an effective solution to stabilizing a landslide on an alluvial bank with limited right-of-way.

ACKNOWLEDGEMENTS

The authors wish to express their appreciation to Professional Service Industries, Inc. (PSI), Tierra, Inc. and the NCDOT for allowing us the time and resources to prepare this paper. It should be noted that the conclusions and discussions contained within this paper are solely those of the authors and do not represent those of the companies listed above.

REFERENCES

AASHTO (1998). 1998 Interim Revisions to the Standard Specifications for Highway Bridges, Sixteenth Edition, 1996: 129-130.

Hamel, J.V. (1988). "Geotechnical Failure Mechanisms in Alluvial Banks," *Mechanics of Alluvial Channels*, Proceedings of 3rd U.S. – Pakistan Symposium on Mechanics of Alluvial Channels:359-386.

Liang, R.Y. (2002). Drilled Shaft Foundations for Noise Barrier Walls and Slope Stabilization. FHWA/OH-2002/038.

Mesri, G. and Shahien, M. (2003). "Residual Shear Strength Mobilized in First-Time Slope Failures," *J. Geotechnical and Geoenvironmental Engrg.* 129 (1): 12-31.

Nethero, M.F. (1982). "Slide Control By Drilled Pier Walls". ASCE Special Publication: Applications of Walls to Landslide Control Problems: 61-75.

Reese, L.C., Wang, S.T., Fouse, J.L. (1992). "Use of Drilled Shafts in Stabilizing a Slope". ASCE Proceedings from Specialty Conference on Stability and Performance of Slopes and Embankments:1318-1331.

Stark, T.D., Choi, H., McCone, S. (2005). "Drained Shear Strength Parameters for Analysis of Landslides". *J. Geotechnical and Geoenvironmental Engrg.* 131 (5): 575-588.

Analysis and Rehabilitation of a Failed Submarine Slope Cut in Soft Clay

Shuwang Yan[1], Cui Wang[2] and Jian Chu[3]

[1]Professor, Director of Institute of Geotechnical Engineering, Tianjin University, Tianjin, China, 300072. email: yanshuwang@tju.edu.cn
[2]PhD Candidate, Institute of Geotechnical Engineering, Tianjin University, Tianjin, China, 300072. email: wangcui_tju@126.com
[3]School of Civil and Environmental Engineering, Nanyang Technological University, Singapore 639798. email: cjchu@ntu.edu.sg

ABSTRACT: This paper presents a case study of a slope failure and its rehabilitation works. A submarine slope cut in soft soil failed during construction in Tianjin Harbor, China. A post-failure analysis was carried out using in-situ testing and back analysis to identify the causes of the failure and assess the changes in soil properties and geological conditions at the site. Based on the investigation, the factors that might have caused the slope failure are identified. These include: excessive excavation, violation of construction procedure, generation of excessive pore water pressure by earlier piling work nearby, and sudden water-level fluctuation in front of the slope. Methods that could be used to rehabilitate the failed slope are discussed. The slope was repaired by reinforcing the slope using sand compaction piles and dividing the excavation into four steps.

INTRODUCTION

A slope in Tianjin New Harbor, China, failed in 1997. The slope formed part of a construction for a port. The sliding body of the soil slope was about 210 m long and 190 m wide. Thousands tons of soil as well as some temporary shelters for the construction workers were sliding into the sea. Fortunately, there were no casualties. Some deep cracks had occurred few hours before the slope collapsed. This served as a warning signal to people working there and all managed to escape just before the slope failed.

The slope sliding started at about 10 am and lasted for about 40 minutes. It was a typical progressive failure case. A smaller sliding body first collapsed into the sea, which triggered immediately another slide. This process continued until a new equilibrium condition was established in the remained soil.

In this paper, the failure process was described. The details for constructing the port, including the soil properties, the designed and the actual profiles of the slope and the construction management were provided. The stability of the slope was back analyzed with in situ vane test results. The rehabilitation works for the slope are also described.

BACKGROUND

The design of the port and the slope is shown in Fig. 1. The slope was formed by cutting into clayey soil which was deposited recently for land reclamation. The construction work commenced in 1997 when the hydraulic filling for reclamation was completed. The reclamation was carried out using soft clay dredged from the sea which could be consolidated under vacuum preloading. A sand blanket of 0.5 m was placed on the surface to facilitate the vacuum preloading work. However, vacuum preloading had not been carried out at the time when the slope was excavated.

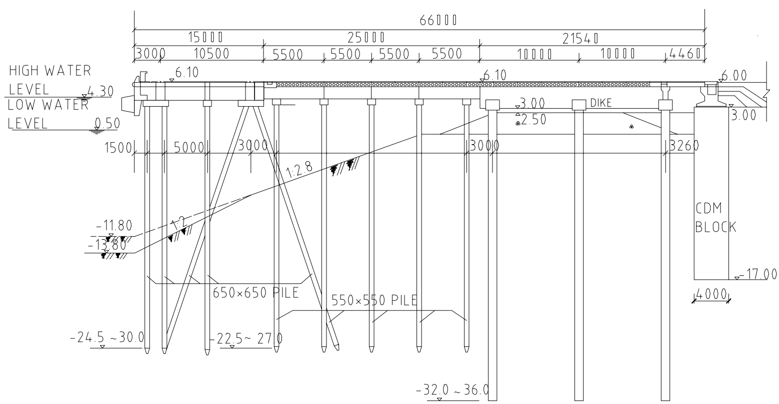

FIG. 1. Design sketch

Following the original construction process, piling works for constructing the port should only be performed after the soft clay has been consolidated. However, to catch the best construction season, piling works started before the schedule. In order to allow the pile driving vessel to go near to the top of the slope to install piles, some part of the slope was over excavated. As a result, a slope angle of the slope near the toe was 1V:2H, instead of 1V:2.8H, as indicated in Fig. 1. More than 40 piles had been driven into the slope before the slope failed.

Table 1 Soil profile and description of soils in each layer

Soil layer		Elevation (m)	Description	LL %	PL %	W %	γ (kN/m^3)	Void ratio	c' (kPa)	φ' (°)	Avg. N value
Fill		4.0 – 0.0	Silty clay consolidated from dredged slurry	43.7	21.3						
Sea bed soil	Upper layer	0.0 – -5.0	Soft silty clay layer with thin sandy silt.	30.7	16.3	41.7	17.9	1.15	19.5	29.2	<1
		-5.0 – -11	Soft silty clay with organic matters.	49.3	23.7	58.2	16.5	1.66	18.0	18.0	<1
		-11 – -14	Soft silty clay layer with thin sandy layer and organic matters.	42.9	20.9	46.6	17.5	1.30	15.5	26.5	1.6
	Intermediate layer	-14 – -15	Clay with sand and shells	28.8	16.1	25.4	19.6	0.75	-	-	3.5
	Lower layer	-15 – -17	Clay with sandy silt or silty sand.	29.1	18.0	26.1	19.7	0.74	36.0	34.0	11.8
		-17 – -20	Clay with silt sand and shell debris.	41.0	20.3	34.7	18.7	0.98	31.0	24.0	6.7
		-20 – -23	Clay with silty sand.	25.9	19.8	21.9	20.2	0.62	-	-	34.9
		Below -23	Hard silty sand layer.								>50

Note: LL = liquid limit; PL = plastic limit; W = water content; γ = unit weight of soil; N = SPT N value
c' = effective cohesion & ϕ' = effective friction angle were determined by isotropic consolidated undrained tests.

SOIL CONDITIONS

The Port was located along a mud coastal plain. A thick Holocene soft soil stratum forms the seabed of the shoreline. This soil stratum consists of mainly marine deposits with some thin alluvial deposits.

The slope mainly consisted of a layer of consolidating clay fill formed by land reclamation and the original seabed soil. The seabed soil can be further classified into 4 layers, an upper layer, an intermediate layer, a lower layer, and a hard silty sand layer. A description of the soil in each layer along with average soil properties is given in Table 1. It can be seen from Table 1 that the water content of the seabed soil in the upper layer was higher than the liquid limit. The effective cohesion and effective friction angle, as measured by consolidated undrained (CU) triaxial tests are also given in Table 1. The undrained shear strength profiles measured by field vane shear tests at two typical locations are shown in Fig. 3. It can be seen that the undrained shear strength increased with depth. The sensitivity of the soil as measured by the vane shear tests ranged from 3 to 4. At the toe of the slope, the undrained shear strength was about 40 kPa.

FAILURE EDSCRIPTION

The slope failure occurred on September 17, 1997, when the highest and the lowest tide occurred on the same day. The head difference between the highest and the lowest water level was about 3 m. The sudden water-level fluctuation in front of the slope had been one of the factors contributing to the failure.

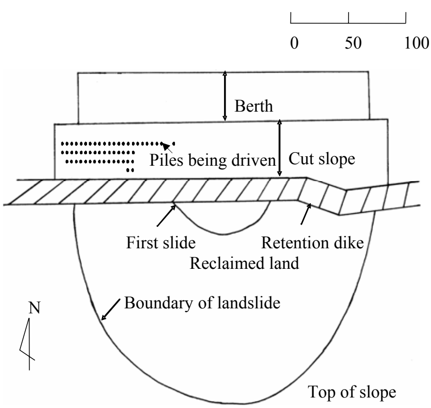

FIG. 2 A plan view of the failed area

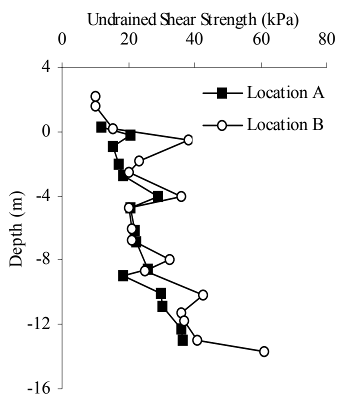

FIG. 3 The field vane shear test results conducted before landslide

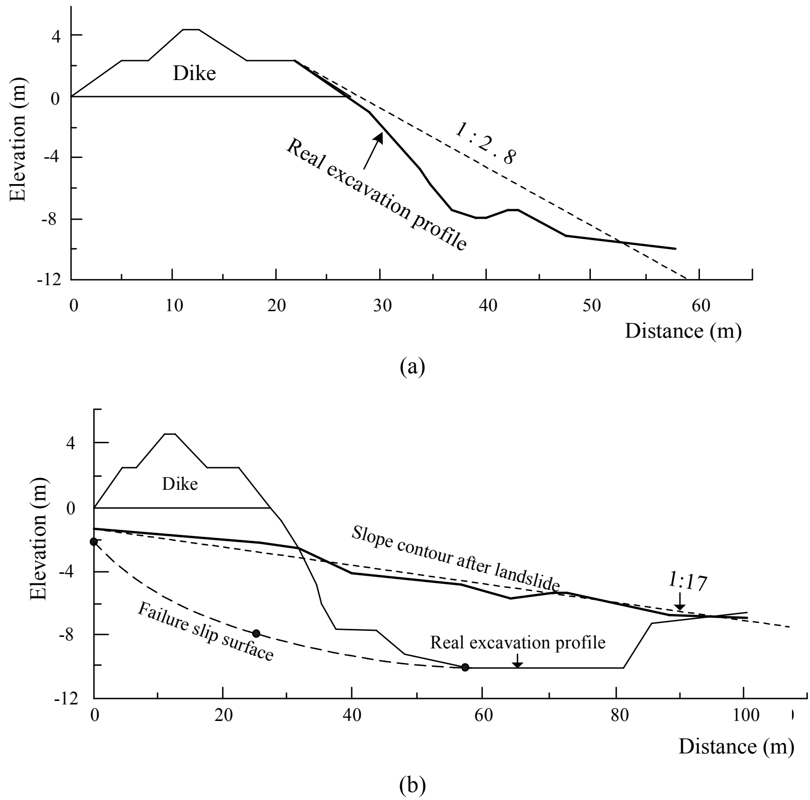

FIG. 4 Slope profiles (a) before failure and (b) after failure

The failure occurred at around 9:00 am and lasted for about an hour. It was a multiple retrogressive failure comprised of a number of small circular slides. A few hours before the first slide slipped into the sea, several deep tension cracks were observed on the ground surface and the dike. The first slide, in the form of a wedge, appeared at a position 10 to 20 m behind the dike (see Fig. 2). This was followed by subsequent slips. The failure developed retrogressively for about an hour until a stable condition was established in the remaining soil mass. The failed area was in a fan shape (Fig. 2) covering an area of 200 m long and 140 m wide on the average, or a total area of about 28,000 m^2. A volume of 240,000 m^3 was estimated to have slipped into the sea. Forty out of the 55 piles installed were pushed down into the sea. The remaining 9 standing piles titled at different angles in the direction of sliding. The slope profiles before and after the landslide is shown in Fig. 4. The slope angle after the landslide had become very flat with an overall slope angle of 17:1 (3.4^{o}).

FIG. 5 The failed slope crashed into the sea

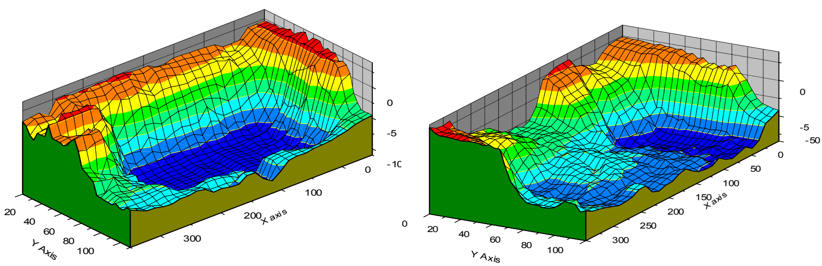

(a) Before failure (b) After failure

FIG. 6 Slope contours based on underwater survey

The reclaimed area after the landslide is shown in Fig. 5. Cracks were observed on the ground surface. These cracks were about 0.5 to 0.6 m wide and formed a set of arcs of circles with the concave side facing the sliding direction. Based on the underwater surveying data, the pre- and post-failure slope contours were shown in Fig. 6a and 6b. The mode of failure is quite similar to the flow slide cases reported by Andresen and Bjerrum (1968), Hadala and Torrey (1989), and Hight et al. (1999), although the soil conditions in those cases are different from the conditions in this case.

POSSIBLE FACTORS AFFECTING THE FAILURE

Based on the investigations, the landslide could be caused by the followings:

1) *Excessive excavating of the slope.* As shown in Fig. 1, the slope at a section was excessively excavated to facilitate pile-driving, which reduced the stability of the slope;

2) *Violation of construction procedure.* Piling and excavating activities were carried out before soil improvement works, which violated the proposed constructing procedure.

3) *Inducing of excessive pore water pressure by piling*. Pile driving works generated excessive pore water pressures in the slope as shown by Massarsch and Broms (1981). This in turn reduced the shear strength of soil.

4) *Sudden drawdown in front of the slope.* The tide level happened to change from the highest to the lowest before failure occurred. The sudden drawdown in water level affected the stability of the slope.

The failure of the discussed slope was likely caused by a combination of localized over-steep cutting of the slope, pile driving near the slope, and water drawdown.

RECONSTRUCTION OF THE FAILED PORT

The failed slope was reconstructed in 1999. The following steps were taken for the reconstruction works:

1). Strengthening the failed slope using sand compaction piles (SCPs). The landslide area was smoothed before the SCPs were installed. The SCPs were formed from –14.0 m (the bottom of the soft clay layer) to –3.7 m (the average elevation of the remained ground surface of the failed slope). The diameter of the SCPs was 0.5m and the spacing was 1.0 to 1.4 m. The quality of the SCPs was controlled with the SPT number greater than 18.

2). Filling up the crushed stone layer. After the installation of SCPs, a crushed stone layer was laid on the ground to up to +3.0 m. The crushed stone layer acted as a surcharge load to consolidate the subsoil. Settlements at several places were observed and the results are given in Table 2. A degree of consolidation of 85% was achieved.

3). Excavation. The excavation was then carried out in four steps, i.e., from the surface to –4.0 m, from –4.0 to –10.0 m, from -10.0 to -11.5 m, and from –11.3 to –13.8 m. The debris of the failed slope was cleared during excavation and the slope was kept at 1V:2.8H.

4). *Piling.* Piles were installed at an interval of three times pile spacing in order to avoid the accumulation of excess pore water pressures. The onshore piles were driven during high tide and the offshore piles were during low tide period.

The above remedy measures were successful. The failed slope was stabilized and the port has been functioning well till today.

TABLE 2. Observed Settlement

Gauge no.1		Gauge no.2		Gauge no.3		Gauge no.4	
Date	Settlement (m)	Date	Settlement (m)	Date	Settlement (m)	Date	Settlement (m)
17/12/98	0	24/12/98	0	24/12/98	0	5/1/99	0
25/5/98	0.486	25/5/99	0.372	25/5/99	0.658	25/5/99	0.470
1/10/99	0.513	26/9/99	0.434	13/8/99	0.722	25/9/99	0.506

CONCLUSIONS

The failure of the discussed slope was likely caused by a combination of localized over-steep cutting of the slope, pile driving near the slope, and water drawdown. The mode of failure was in the form of a series of slides that developed retrogressively. Pile driving in soft clay near or along a slope induces a destabilizing effect on the slope. This effect has to be taken into consideration in both design and construction. When analyzing the stability of a water front slope, the variation in the water table and tide activities, in particular the effect of quick drawdown, should be taken into consideration.

REFERENCES

Andresen, A. and Bjerrum, L. (1968). "Slides in subaqueous slopes in loose sand and silt." *Publication No. 81*, Norwegian Geotechnical Institute.

Hadala, P. F. and Torrey V. H. (1989). "Mississippi riverbank flowslides." *The Art and Science of Geotechnical Engineering*, Prentice-Hall, 12-30.

Hight, D. W., Geogiannou, V. N., Martin, P. L. and Mundegar, A. K. (1999). "Flow slides in micaceous sands." *Problematic Soils*, Eds Yanagisawa, Moroto & Mitachi, Balkema, Rotterdam, 945-958.

Massarsch, R. K. and Broms, B. B. (1981). "Pile driving in clay slopes." *Proc. 10th Int. Conf. Soil Mech. Found. Eng.*, 3, 469-474.

Estimate of Cliff Recession Rates for a US Highway Located on a Sandstone Cliff over Lake Superior

Alexander Williams[1] and Stan Vitton[2], A.M. ASCE, Ph.D., P.E.

[1]Graduate Student, Michigan Technological University, Civil & Environmental Engineering, 1400 Townsend Drive, Houghton, MI 49931; alwillia@mtu.edu
[2]Associate Professor, Michigan Technological University, Civil & Environmental Engineering, 1400 Townsend Drive, Houghton, MI 49931; vitton@mtu.edu

ABSTRACT: Coastal cliff erosion is a problem in many coastal regions including the Great Lakes of Canada and the United States. While data exists on the recession rates for oceanic cliffs, there is limited data for the fresh water cliff erosion. Currently, cliff recession is threatening a US highway (US-41) located on a 30 m sandstone cliff on the south shore of Lake Superior. The recession has advanced to a point where it is undercutting the guardrail system for the highway. A research program was conducted to determine the regression rate and when the highway should be relocated or if alternative methods of slope remediation can be performed allowing the scenic highway to remain in its current position. The cliff regression analysis includes investigating variations in shore platform widths, freeze thaw cycling, and other environmental factors, in addition to rock characteristics. Laboratory tests include point load testing, uniaxial compressive testing, rock quality designation (RQD), rock mass rating (RMR), and freeze-thaw durability. It was found that the following factors control the rate of the cliff regression, which was found to be about 0.15 feet/year: (1) deposition of mine waste at the base of the cliffs during the early 20th century and the subsequent removal by long shore currents; (2) rock weathering and water migration above low permeability layers accessing the cliff face; and (3) the development of the talus slope at the base of the cliff, which acts as a barrier to further regression.

INTRODUCTION

Cliffs are a major feature along coastlines throughout the world and have been studied extensively. However, they are also a feature along larger inland lakes, such as the Great Lakes. The Great Lakes cover 95,000 sq. miles, with 10,000 miles of shoreline, almost as long as the total coastal length of the United States including Alaska. Lake Superior, the largest of the lakes both in volume and area, is bounded on a part of its' southern shore by the Jacobsville Sandstone where a small section of this sandstone forms moderately high cliffs on the order of 30 m (100 ft). In the mid-1950's the Michigan Department of Transportation created a scenic overlook and roadside park by rerouting a portion of US Highway 41 to a location on top of a cliff for a distance of about 800 m (0.5 miles). However, cliff erosion is now threatening the highway. This section of highway is located in northern Michigan in Keweenaw Bay area as shown in Figure 1. Views of the cliffs from on top and from the water are shown in Figure 2.

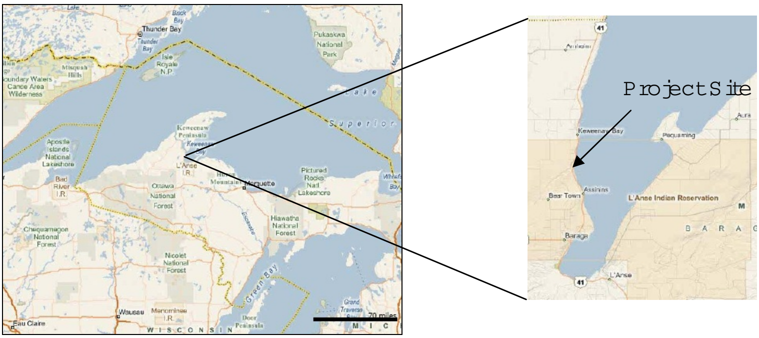

Figure 1: Location of Jacobsville Cliffs threatening US-41

Figure 2: View of the cliffs from the top and from the water.

In order to determine the rate of cliff recession for the Keweenaw Bay cliffs both historical information and the cliff rock properties were investigated to develop a predictive model. As with most cliff regression studies, the determination of cliff recession was difficult due to the shoreline cliff erosion process and long term lake level fluctuations. In addition, since rock is not homogeneous, erosion is not consistent from one location to another. For example features such as seasonal streams can drastically affect the erosion of the cliff as seen in Figure 3. However, the Keweenaw Bay cliff erosion is similar to coastal cliff erosion, in that it is made up of both regular small losses, and rapid larger losses (Hall 2002).

Figure 3: Disparity of erosion between locations caused by seasonal runoff stream

Coastal erosion models for ocean environments have been presented by de Lange and Moon, 2005; Budetta et al., 2000; Hall, 2002; Lee et al., 2001; Davies et al., 1998 as well as others. These studies are valuable in studying cliff regression environment of Lake Superior where it has been shown that in all but the softest materials cliff erosion is more a consequence of the strength of the cliff materials than the wave action and long shore currents processes (Lahousse and Pierre, 2003; Stephenson and Kirk, 2000). Selby (1993) has estimated the relative contribution of various factors affecting cliff regression. These factors are listed in Table 1. By using a combination of the methods from previous research, a regression estimate for the Jacobsville Sandstone cliffs is currently under developed. This paper will present the primary processes investigated along with historical research in providing an estimate of cliff regression rate for the Keweenaw Bay cliffs on Lake Superior.

Table 1: Erosion factors affecting cliff stability (after Selby, 1993)

Erosion Factor	Contribution
Intact rock strength	20%
Discontinuity characteristics	
Spacing	30%
Orientation	20%
Width	7%
Continuity & infill	7%
Water	6%
Weathering	10%

GEOLOGY AND CLIMATE

The cliffs are composed of Jacobsville Sandstone a thick sequence (+900 m) of fluvial feldspathic (matrix) and quartzose (highly rounded) sandstone, siltstone, shale and conglomerate. The formation of the Jacobsville is associated with the Lake Superior segment of the Midcontinent Rift System as it began to subside relative to the edges of the rift zone during the Early and Middle Cambrian age. The sediments are fluvial in nature and vary considerably in size and composition (Kalliokoski 1982). The upper portion of the Jacobsville in which the cliffs are composed is primarily of sandstone layers interbedded with thinner silt and clay layers. These sandstone layers are a very attractive reddish-brown stone with some sections having leaching with alternating oxidized (red) and reduced layers (white). The Jacobsville sandstone has been used as a architectural building stone throughout the Midwest United States and as far east as New York City.

The climate of the Keweenaw Bay area has average seasonal temperatures that range from -9°C (15F) in the winter to 21°C (70°F) in the summer with maximum low of -37°C (-35°F) and a high of 39°C (102°F). Total annual precipitation is around 90 cm (34 in) with the average seasonal snowfall about 5.2 m (208 in) inland but is considerably less at the Lake Superior shoreline. The average number of days with at least 2.54 cm (1 in) of snow on the ground is 150 days.

BACKGROUND

Previous Studies

An important location for coastal cliff recession studies is the coastal cliffs of Auckland, New Zeeland where significant land development is occurring. Assessment of the risks posed by the cliff is a high priority. In order to accomplish this assessment research has been conducted on the short and long term coastal cliff recession rates along the Auckland coast. The cliffs around Auckland are comprised of two rock types, volcanic basalt lava flows, and a soft flysch, from the Miocene Waitemata Group. This latter rock, though much softer than the Jacobsville Sandstone, was considered as a benchmark for this study.

The methods employed to model recession of the Auckland cliffs, include the following:. (1) Aerial photography performed by both (Brodnax, 1991) and a followup by (Glassey et al., 2003); (2) Cadastral surveys (Glassey et al., 2003) using historical land surveys along the coast; (3) Structure surveys (Brodnax, 1991; Glassey et al., 2003; (4) Geologic/geomorphic markers (Glassey et al, 2003); (5) Cliff profile surveys (Glassey et al, 2003); (6) Cliff face surveys (Gulyaev and Buckeridge, 2004); (7) Spot shore platform width measurements (Paterson and Prebble, 2004); and (8) Full shore platform width measurements (de Lange et al., 2005)

From these methods aerial photography and platform width measurements were used to create a model for the Jacobsville Sandstone cliffs. In addition, historical photographs, estimates from residents, rock cores, and an inclinometer were also used.

Methods Employed

Aerial photographic surveys have been made throughout the United States since as early as the turn of the century. In Michigan these photographs are stored at local Department of Natural Resources centers. The cliff area has high quality photographs from 1962 up through 1997 available.

A survey of the shore platform width along the extent of the cliff was conducted in the summer of 2007. It was accomplished using a *Garmin GPSMap 720c Sounder* attached to a laptop running *Windmill* data acquisition software, in conjunction with a video camera and digital camera to establish a connection between bathymetric data and the cliff face.

Several historic photographs were found that showed the cliffs or surrounding area. These historic photographs helped explain the historic anthropogenic impacts on the cliff and the rate at which it is receding.

Residents who live on or near the cliffs have been very helpful in giving estimates as to how far the cliffs adjoining their properties have receded in the time that they have lived there. This information has been shown to be quite accurate, and with some of the residents having been there for over 25 years, short term estimates for the recession of the cliff can be made.

In 2006, rock cores were obtained from three drill holes made from the top of the cliff. These drill holes extended below the current water surface and several. Rock testing included, rock quality designation (RQD), rock mass rating (RMR), uniaxial unconfined compression, point load, and freeze-thaw.

Concerns about overburden slippage and possible movement of the rock mass caused for an inclinometer tube to be placed inside one of the drill holes. This tube was monitored regularly throughout 2006 and 2007.

RESULTS AND DISCUSSION

Aerial photography of the cliffs showed that a beach, comprised of mine tailings, protected the cliffs from long-shore currents but had been rapidly removed over the forty year period of the photographs. The recession of the beach is shown below in Figure 4, with traces of the beaches extent in 1962 in green, 1968 in red, 1986 in blue, overlaid on a photograph taken in 1997.

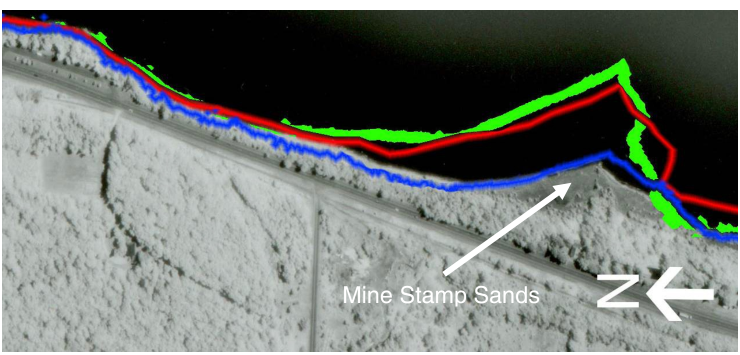

Figure 4: Protective Beach Recession

The shore platform was surveyed in the summer of 2007, from this survey a computer model of the shoreline was created as seen below in Figure 5. The method outlined by de Lange et al. (2005) was used to estimate the recession of the cliff. The method utilizes the assumption that the shore platform has not been eroded since the water level rose above it to its current level and that at the time that the water was low enough to erode the shore platform the cliff and platform edge were a continuous slope. Thereby simply dividing the width of the shore platform by the length of time since water levels were, in this case, fifteen feet below current levels. The U.S. Geologic Survey (1996) fact sheet on the state of Michigan concludes that lake levels have not dropped that low since 7,000-8,000 years ago. This would place the recession rate at approximately 0.15 ft/year.

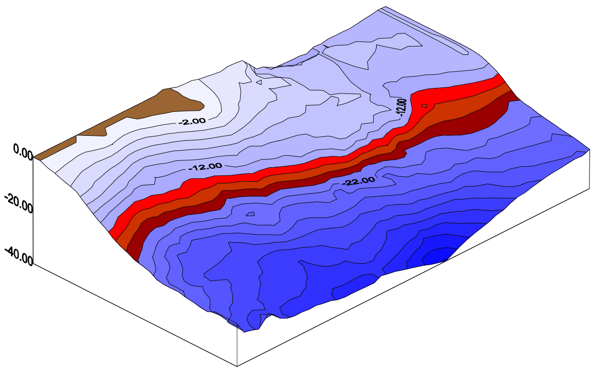

Figure 5: Computer model of shore platform and shoreline

Archival photographs and articles concerning the cliffs and surrounding area were found in the Copper Country Archives (Arch.) located at Michigan Technological University in Houghton, Michigan. This information referenced a stamp mill at the southern end of the cliffs. A stamp mill is a mining ore processing facility used to separate copper ore from waste. This process produces a large amount of material called “stamp sands” which are waste materials (tailings). These materials were simply dumped wherever it was most convenient in this case off the cliff into Lake Superior. Consequently, a large amount of tailings were deposited at the base of the cliff. Over time long-shore currents eroded the stamp sands as shown in Figure 3. The U.S. Army Corps of Engineers has been involved in a project south of the cliffs location to rehabilitate an area where a majority of these sands have migrated. They estimate the amount of stamp sands deposited at more than six billion pounds (KBIC, 2006). The stamping facility operated from 1900 to 1919. Since the aerial photographs are from some forty years later it can be assumed that nearly double the quantity shown in the photograph from 1962 was originally there. This large sand barrier would have protected the cliff from erosion for nearly the last hundred years.

Residents that live along a section of Jacobsville Sandstone cliffs approximately three miles north of the cliffs being studied have given estimates for the speed of recession for the cliffs along their property. Most residents have put fences along the cliff face and these can act as fairly accurate measures of the rate of erosion. Based on an informal survey of residents and measurements taken on their properties a general estimate of one foot per decade can be made.

In the fall of 2006 three cores of rock, sixty feet in length were taken from the top of the cliff. These samples had very high RQD values, between 80 and 100 percent. Almost all fractures occurring due to silt and clay lenses which occurred irregularly within the overall stratigraphy of the formation. Random samples were tested both uniaxial compression and corresponding point load testing. The results showed a uniaxial compressive strength of about 5000 psi, similar to concrete with a standard deviation of 2000 psi. The average RMR for the cliff based on the cores and general condition of the cliff is approximately 65. Eight samples are undergoing freeze-thaw testing for approximately 300 cycles to determine the susceptibility of the rock to ice jacking.

Early on in the investigation, an inclinometer tube was installed at the southern extent of the cliff at the request of the Michigan Department of Transportation. The inclinometer was monitored regularly through the fall of 2006 and spring of 2007. Though no movement was detected this installation would have given vital warning of an impending total failure of the cliff face.

ANALYSIS and CONCLUSIONS

The cliffs appear to have two distinct modes of recession. The first mode is characterized by a virtually vertical cliff face that recedes consistently at the top and base in sections where no talus slope protects the cliff. The talus slope is prevented from developing by wave action and long shore currents as well as freeze-thaw weathering of the talus materials. The second mode is differentiated by the development of a talus slope that protects the toe of the cliff and allows the top of the cliff to continue to recede until a “stable “ slope is developed and rapid recession ceases. In this case the talus slope was able to form due to the sand bench deposited by the stamping facilities. Once the talus slope had been allowed to form, it protected the foot from further weathering and the slope continued to grow. It is possible that higher lake levels could remove the slope and return the cliff to its former mode of recession; however this is unlikely given the extent to which the slope has been allowed to form and vegetate. The long term estimate of between one and one and a half feet per decade may not be seen any longer for the highway. Once the talus slope has reached the top of the cliff, overall recession may slow dramatically due to the increased stability of the slope. However, long shore currents and wave action will continue to remove sediment from the base of the slope and cause some recession unless armor stone is placed to protect the toe of the slope from these forces. An additional issue for the Great Lakes is variations in long term lake levels which will also have an impact on cliff regression.

REFERENCES

Archival Material, Michigan Technological University Archives, Mills-Stamp-Mi.

Belliveau, L.P., 1991. Fractures in the Jacobsville Sandstone and the Precambrian "W" rocks in eastern Marquette County, MI. MSc Thesis, Western Michigan University, Kalamazoo. 82 pp.

Brodnax, R.C., 1991, Cliff erosion in the Waitemata Harbour and Hauraki Gulf. MSc Thesis, University of Auckland, Auckland. 145 pp.

Budetta, P., Galietta, G., Santo, A., 2000. A methodology for the study of the relation between coastal cliff erosion and the mechanical strength of soils and rock masses. Engineering Geology 56, p. 243-256

Davies, P., Williams, A.T., Bomboe, P., 1998. Numerical analysis of coastal cliff failure along the Pembrokeshire coast national park, Wales, UK. Earth Surface Processes and Landforms 23, p. 1123-1134

de Lange, W.P., Moon, V.G., 2005. Estimating long-term cliff recession rates from shore platform widths. Engineering Geology 80, 292-301

Glassey, P., Gibb, J.G., Hoverd, J., Jongens, R., Alloway, B.V., Coombes, K., Benson, A.P., 2003. Establishing a methodology for coastal cliff hazard mapping: an East Coast Bays, Auckland pilot study. In: Kench, P., Hume, T. (Eds.), Coasts and Ports Australasian Conference, Auckland, Paper 49, p. 1-12.

Gulyaev, S.A., Buckeridge, J.S., 2004. Terrestrial methods for monitoring cliff erosion in an urban environment. Journal of Coastal Research 20, 871-878

Hall, J.W., 2002. Stochastic simulation of episodic soft coastal cliff recession. Coastal Engineering 46, p. 159-174.

Kalliokoski, J. (1982). Jacobsville Sandstone: An Up-Date. 1988. p. 127-136.

Keweenaw Bay Indian Community. "Sand Point Project" 2006, Baraga, MI, <http://www.ojibwa.com/html/NR/ERP/SANDPOINT.htm>

Lahousse, P., Pierre, G., 2003. The retreat of chalk cliffs at Cap Blanc-Nez (France): Autopsy of an erosional crisis. Journal of Coastal Research 19, p. 431-440

Lee, E.M., Hall, J.W., Meadowcroft, I.C., 2001. Coastal cliff recession: the use of probabilistic prediction methods. Geomorphology 40, 253-269

Selby, M.J. 1993, Hillslope Materials and Processes. Oxford University Press, Oxford. 451 pp.

Stephenson, W.J., Kirk, R.M., 2000. Development of shore platforms on Kaikoura Peninsula, South Island, New Zealand, II: the role of subaerial weathering. Geomorphology 32, p. 43-56

U.S. Department of the Interior, U.S. Geological Survey. Fact Sheet FS-022-96, 1996, Lansing, MI, < http://pubs.usgs.gov/fs/FS-022-96/>

A Case Study of Safety Factor Comparison of Different Slope Stability Methods for Levee Design in New Orleans

Therese Koutnik[1], M. ASCE, P.E., Lei Wei[2], M. ASCE, P.E. and Jaskaran Singh[3]

[1]Geotechnical Department Manager, HNTB Federal Services Corporation, 9100 Bluebonnet Centre Blvd, Suite 301, Baton Rouge, LA 70809; tkoutnik@hntb.com
[2]Geotechnical Engineer, HNTB Federal Services Corporation, 9100 Bluebonnet Centre Blvd, Suite 301, Baton Rouge, LA 70809; lwei@hntb.com
[3]Geotechnical Engineer, HNTB Federal Services Corporation, 9100 Bluebonnet Centre Blvd, Suite 301, Baton Rouge, LA 70809; jsingh@hntb.com

ABSTRACT: Factors of safety are of the primary design criteria used in most slope stability analysis. Various analytical methods have been developed to assess factors of safety based on limit equilibrium theory, such as Janbu Simplified, Bishop Simplified and Spencer Methods. For decades, US Army Corps of Engineers, Mississippi Valley District (MVD), has been using a wedge-shape based approach called the Method of Planes. By analyzing one typical cross section in the New Orleans area, factors of safety calculated from different methods were compared assuming both circular and wedge-shaped failure surfaces. The calculations were performed utilizing commercial slope stability software SLOPE/W by GEO-SLOPE International Ltd. and program "Stability with Uplift" by US Army Corps of Engineers, MVD. It was found that for the same failure surfaces, Method of Planes tends to yield exactly the same factor of safety as Janbu Simplified Method when in cohesive soils using total stress strength parameters. In general, Method of Planes and Janbu Simplified Method usually have factors of safety lower than those calculated by Bishop Simplified and Spencer Methods for the same assumed failure surfaces. However, the actual difference significantly depends on the method's assumptions, soil properties and stratification, loading, geometry, pore water pressures, and methods of searching. This paper has limited these differences to major differences in soil properties and search mechanisms.

INTRODUCTION

The purpose of slope stability analysis is typically to determine a factor of safety (FS) against slope failure. Numerous methods based on limit equilibrium (LE) theory have been developed over the last century. The first was the Ordinary Method of Slices developed by Fellenius in 1936, which ignores interslice shear and horizontal forces, employs circular failure surfaces, and satisfies only moment equilibrium.

In the early to mid 1950s, Janbu Simplified Method (Janbu) and Bishop Simplified Method (Bishop) were introduced, which incorporate interslice forces and employ either circular or wedge-type failure surfaces. The major difference between the two methods is that Janbu satisfies only force equilibrium whereas Bishop satisfies only complete moment equilibrium. For these earlier methods, searching for the most critical failure surface was done by trial and error and hand-calculations (Duncan, 2005, and USACE, 2003).

In the 1960s, at the time computers were invented, methods with more rigorous search routines and more complex assumptions were introduced such the Spencer Method. At the same time, the Mississippi Valley District (MVD) adopted a modified approach to Fellenius's method called the Method of Planes (MOP) which has been used solely in the New Orleans area. MOP combined with local experience and significant database of subsurface information has been effectively used for decades. MOP satisfies force equilibrium and employs a wedge-shaped potential failure surface consisting of three blocks, an active (ABC), central (CBED) and passive wedges (DEF), as shown in Fig. 1 (Caver, 1973). The failure surface of the central block of the wedge is assumed to be along the bottom of each soil layer, and the controlling, weaker shear strength along the failure surface is selected. The inclination angles from the horizontal, α_1 and $\alpha_{2,}$ are assumed to be equal to 45+ϕ/2 and 45-ϕ/2 for the active and passive wedges, respectively, as shown in Fig.1, with ϕ as the friction angle.

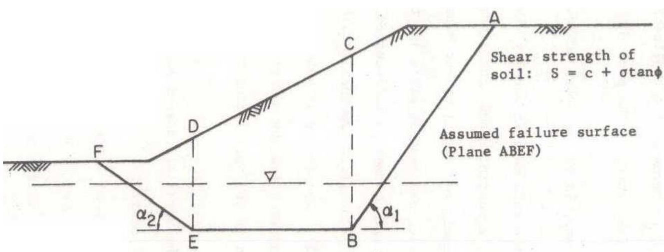

FIG. 1. Analysis of Slope Stability by Method of Planes (Caver, 1973)

Due to the three-wedged approach, the FS in MOP can be easily calculated by hand for simple models such as new levees or embankments on relatively flat surfaces, where the stratigraphy is generally horizontally-bedded and failures are primarily translational, as found typically in the New Orleans area. This slip surface is also applied to a relatively strong levee embankment founded on weaker, stratified alluvial soils. Differences between MOP and other popular LE methods are listed in Table 1. Overall, differences between the LE methods correspond to the static equilibrium equations, interslice force assumptions, unknowns, and types of failure surfaces. Based on previous research, significance of interslice forces on FS results depends on the shapes of the failure surfaces. For wedge-type surfaces, interslice normal and shear forces affect both moment and force equilibrium. For circular slip surfaces, moment equilibrium will be independent of the interslice shear forces; however, force equilibrium is dependent.

Table 1. Comparison of Assumptions using Different Slope Stability Methods

Method	Equilibrium			Interslice Forces		Inclination of Interslice Force	Unknowns (#) and Type	Failure Surface
	M	F_H	F_V	Normal	Shear			
Ordinary Method of Slices	✓			No	No	None	(1) FS	Circular
MVD Method of Planes		✓	✓	No	No	None	(1) FS	Wedge
Janbu Simplified		✓	✓	Yes	No	Horizontal	(2n) FS, N, Z	Circular or Wedge
Bishop Simplified	✓		✓	Yes	No	Horizontal	(n + 1) FS and N	Circular or Wedge
Spencer	✓	✓	✓	Yes	Yes	Constant	(3n) FS, Φ, N, Z, L	Circular or Wedge

Notes: M = Method satisfies Moment Equilibrium, F_H = Method satisfies Horizontal Force Equilibrium, F_V = Method satisfies Vertical Force Equilibrium,* = Satisfies only Horizontal Force Equilibrium, FS = Factor of Safety; N = Normal Force at the base of slices; Z = Interslice Force Resultant, Φ = Interslice Inclination, and L = Location of Side Forces

Besides the differences in slope stability methods, numerous other parameters such as soil properties, stratification, pore pressures, loading, and geometry affect the FS and how to properly model a site. Because of the numerous efforts that have been launched to rebuild New Orleans after Hurricane Katrina, evaluations of existing and raised levees are certainly of the highest importance. A case study is presented in this paper to compare FS calculated by the aforementioned different methods.

ANALYSIS MODEL

One typical cross section in St. Bernard Parish is selected, and both circular and wedge-shaped failure surfaces are investigated. The existing top of levee elevation of the section is approximately El 5.7 meters as shown in Fig. 2. (All elevations noted in this paper are in meters.) The design high water level used is El 7.9. To account for settlement during the service period of the levee, the existing levee is to be raised to a proposed El 8.8, assuming 1.1 meters of overbuild. The proposed levee has a wave berm on the flood side and a 4H:1V side slope on the protected side. Slope protection consisting of 0.5 meters of riprap is proposed along the levee surface from levee toe to toe, making the top of the riprap at El 9.4. As this study only focuses on FS calculations, no remedial measures for the proposed levee will be discussed.

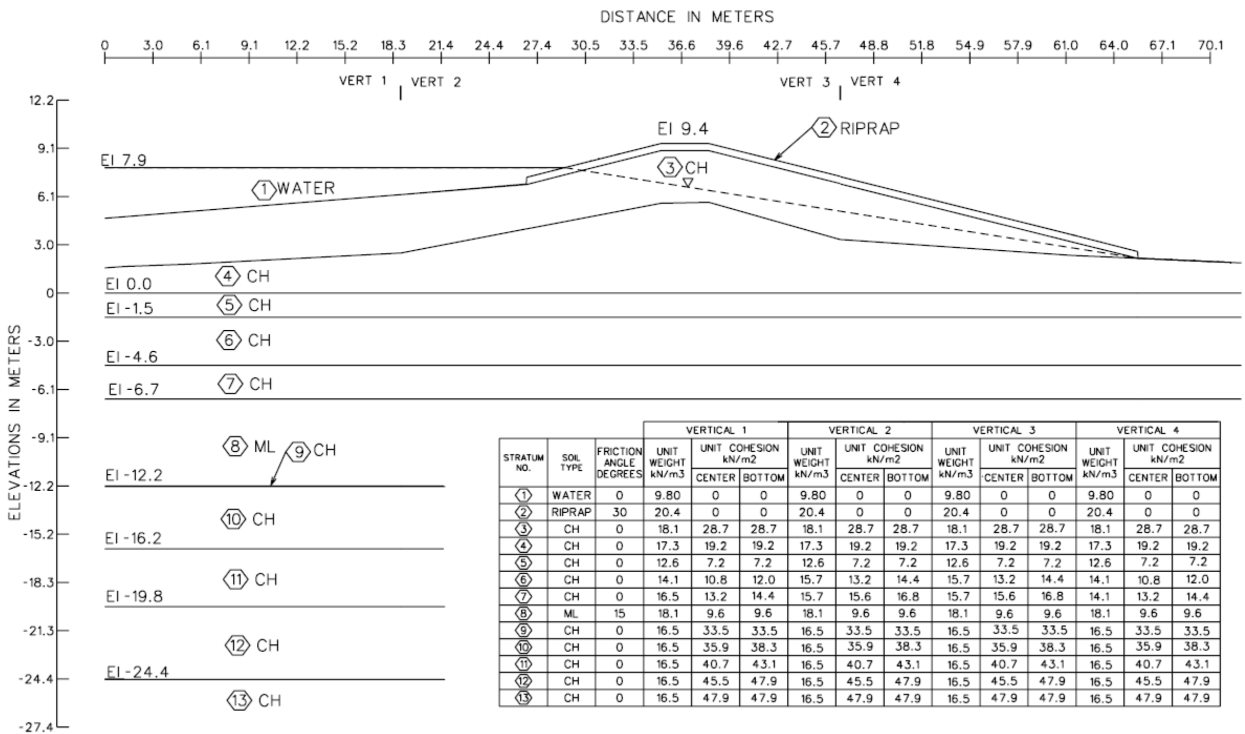

STRATUM NO.	SOIL TYPE	FRICTION ANGLE DEGREES	VERTICAL 1 UNIT WEIGHT kN/m3	VERTICAL 1 UNIT COHESION kN/m2 CENTER	VERTICAL 1 UNIT COHESION kN/m2 BOTTOM	VERTICAL 2 UNIT WEIGHT kN/m3	VERTICAL 2 UNIT COHESION kN/m2 CENTER	VERTICAL 2 UNIT COHESION kN/m2 BOTTOM	VERTICAL 3 UNIT WEIGHT kN/m3	VERTICAL 3 UNIT COHESION kN/m2 CENTER	VERTICAL 3 UNIT COHESION kN/m2 BOTTOM	VERTICAL 4 UNIT WEIGHT kN/m3	VERTICAL 4 UNIT COHESION kN/m2 CENTER	VERTICAL 4 UNIT COHESION kN/m2 BOTTOM
1	WATER	0	9.80	0	0	9.80	0	0	9.80	0	0	9.80	0	0
2	RIPRAP	30	20.4	0	0	20.4	0	0	20.4	0	0	20.4	0	0
3	CH	0	18.1	28.7	28.7	18.1	28.7	28.7	18.1	28.7	28.7	18.1	28.7	28.7
4	CH	0	17.3	19.2	19.2	17.3	19.2	19.2	17.3	19.2	19.2	17.3	19.2	19.2
5	CH	0	12.6	7.2	7.2	12.6	7.2	7.2	12.6	7.2	7.2	12.6	7.2	7.2
6	CH	0	14.1	10.8	12.0	15.7	13.2	14.4	15.7	13.2	14.4	14.1	10.8	12.0
7	CH	0	16.5	13.2	14.4	15.7	15.6	16.8	15.7	15.6	16.8	14.1	13.2	14.4
8	ML	15	18.1	9.6	9.6	18.1	9.6	9.6	18.1	9.6	9.6	18.1	9.6	9.6
9	CH	0	16.5	33.5	33.5	16.5	33.5	33.5	16.5	33.5	33.5	16.5	33.5	33.5
10	CH	0	16.5	35.9	38.3	16.5	35.9	38.3	16.5	35.9	38.3	16.5	35.9	38.3
11	CH	0	16.5	40.7	43.1	16.5	40.7	43.1	16.5	40.7	43.1	16.5	40.7	43.1
12	CH	0	16.5	45.5	47.9	16.5	45.5	47.9	16.5	45.5	47.9	16.5	45.5	47.9
13	CH	0	16.5	47.9	47.9	16.5	47.9	47.9	16.5	47.9	47.9	16.5	47.9	47.9

FIG. 2. Typical Cross Section

Based on the subsurface information, weak fat clays (CH) are predominately encountered below the existing ground surface. Peat is noted from El 0 to -1.5, and silt (ML) is encountered from El -6.7 and -12.2. A summary of soil profiles along with the engineering properties are shown in Fig. 2. As anticipated, shear strengths beneath the centerline of the levee are higher than the shear strengths beyond the toes. To model horizontal shear strength variations, the toe strengths are represented by Verticals 1 and 4 as shown in Fig. 2, and the centerline strengths are indicated between Verticals 2 and 3 in Fig.2. The vertical variation in shear strength is shown by the center and bottom shear values and can be linearly interpolated with depth.

RESULTS AND DISCUSSIONS

Wedge-Shaped Failure Surface

A full search for the active and passive wedge locations was implemented by using "Stability with Uplift" program provided by MVD of USACE program for the MOP. The most critical failure surfaces at each specified elevation from MOP were imported into commercial software SLOPE/W (GEO-SLOPE 2007) in order to directly compare FS for all other LE methods, including Janbu, Bishop and Spencer methods. The calculated FS are summarized in Table 2. The critical failure surfaces for each layer determined from the MOP analysis is shown on Fig. 3.

Table 2. Comparison of Factor of Safety for Wedge-Shaped Failure Surface

Central Block Bottom El	Method of Planes	Janbu Simplified	Bishop Simplified	Spencer
0	0.87	0.87	0.90	0.90
-1.5	0.73	0.73	0.74	0.74
-4.6	0.70	0.70	0.76	0.76
-6.7	0.68	0.68	0.75	0.75
-12.2	0.96	0.96	1.27	1.33
-16.2	1.03	1.03	1.40	1.52
-19.8	1.09	1.09	1.52	1.59
-24.4	1.20	1.21	1.71	1.78

The FS are exactly the same when comparing MOP and Janbu at corresponding elevations, except at El -24.4 where there is a 0.01 difference. This slight difference is believed to be attributed to numerical rounding. Having the exact FS indicates that these two methods have essentially the same approach and assumptions (no shear forces between slices, equivalent wedge inclination angles, and satisfaction of force equilibrium) when calculating the FS for the same assumed failure surface.

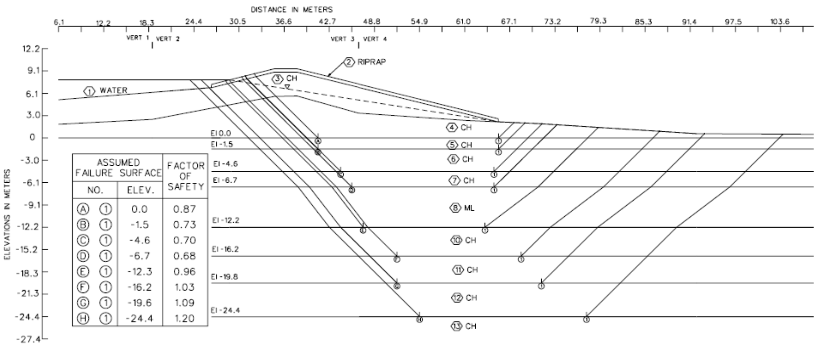

FIG. 3. Critical Failure Surfaces determined from Method of Planes

Based on Table 2, the FS in the upper layers (El 0, -1.5, -4.6 and -6.7) that consist of pure clay ($\phi=0^{o}$) are exactly the same between Spencer and Bishop for the same failure surface. For the lower layers (El -12.2, -16.2, -19.8 and -24.4) that consist of clay and silt, the FS determined by Spencer are, on average, about 5.5% and 44.8% higher than Bishop and Janbu (or MOP), respectively. This indicates that the actual difference between the methods greatly depends on the soil properties.

Duncan and Wright (1980) pointed out that for $\phi=0^{o}$ conditions, Spencer and Bishop yield the same FS for the same circular failure surface. Based on the findings in the case study, it appears that this conclusion can be further extended to include non-circular failure surfaces, too. That is, for $\phi=0^{o}$ conditions, as long as the overall moment equilibrium is satisfied, different methods will give the same FS regardless of what other equilibrium conditions it does or does not satisfy. Again, this is because shear strength in $\phi=0^{o}$ condition does not rely on the normal stress on the slip surface. For $\phi=0^{o}$ conditions, FS from Spencer or Bishop will be slightly higher than those from Janbu or MOP. When silt or sand are present, FS from Spencer is slightly higher than Bishop and significantly greater than FS from Janbu or MOP. This indicates that the different assumptions in static equilibrium conditions play a more significant role in granular materials ($\phi\neq0^{o}$) than in pure clays ($\phi=0^{o}$).

Circular Failure Surface

Since MOP cannot employ circular failure surfaces, this method will not be discussed in this section. Commercial software SLOPE/W was used to perform Janbu, Bishop and Spencer methods by assuming circular failure surfaces. The program automatically searched the most critical failure surface by identifying the location for lowest FS, as shown in Fig. 4. The calculated FS are 0.69, 0.71 and 0.71 with Janbu, Bishop and Spencer methods, respectively. The FS are identical for Spencer and Bishop methods and very close to the Janbu method FS, which is similar to what was found with wedge-shaped failure surfaces.

Considering the different assumptions between the methods listed in Table 1, the study appears to indicate that ignoring interslice shear forces will not affect the FS derived based on moment equilibrium for a circular failure surface in pure clays ($\phi=0^o$). The fact that the reported Spencer FS is about 3% higher than Janbu means that ignoring interslice shear forces when only horizontal force equilibrium is satisfied for a circular failure surface in pure clays ($\phi=0^o$) will result in a slightly lower FS (<5% in this case study) than when all the static equilibrium equations are satisfied. The difference in FS between Spencer and Janbu is even smaller for a circular failure surface than a wedge-shaped failure surface.

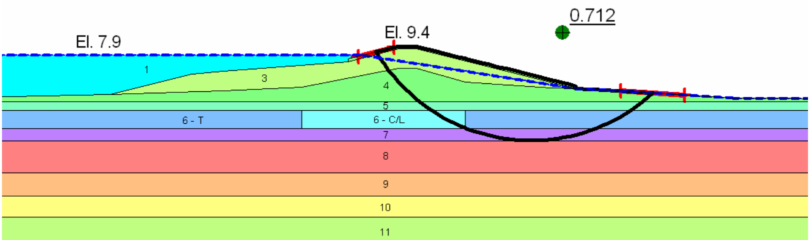

FIG. 4. Analysis of Slope Stability Based on a Circular Failure Surface

CONCLUSIONS

This paper presents a case study of slope stability analysis using different methods, namely MOP, Janbu, Bishop and Spencer. By comparing the calculated FS, the following conclusions may be drawn.

1) MOP and Janbu method are essentially the same method when considering the same wedge-shaped failure surface. This is due to the same inherent assumptions (interslice forces and satisfaction of static equilibrium conditions). However, Janbu can be used for any shaped failure surfaces while MOP can only be applied to wedge-shaped failure surfaces. The advantage of MOP over Janbu Simplified Method is that in MOP, it is not necessary to divide the failure zone into slices as required in Janbu and can easily be performed by hand.
2) Janbu or MOP tends to yield the lowest FS among those methods, while Spencer or Bishop, in most cases, tend to yield the highest FS using the same critical failure surfaces. The difference in FS results depends on the assumptions of the method.
3) In cohesive soils using $\phi=0^o$, Bishop and Spencer methods tend to yield the same FS for both circular and wedge-shaped failure surfaces. When silts or sands are present, Spencer tends to report a slightly higher FS than Bishop Method.
4) In cohesive soils using $\phi=0^o$, Janbu tends to yield a slightly lower FS than Spencer for both circular and wedge-shaped failure surfaces. When silts or sands are present with clays, Spencer tends to report a significantly higher FS than Janbu for a wedge-shaped failure surface.

5) In the authors' opinion, the "correct FS" to be used in design differs depending on the situation, risk and what the acceptable FS is for design. If one acceptable FS is selected, independent of the method, then for simple geometry with horizontal bedding in cohesive soil using $\phi=0^o$, any of the methods appear appropriate as they yield very similar results. For more complicated stratigraphy, geometry, and combined silt, sand and clay soils, the Spencer method appears to be the most appropriate because overall force and moment equilibrium are satisfied. However, it may be appropriate to use other methods if the acceptable FS is dependent on what method is utilized. For instance, Spencer may require a higher acceptable FS than Janbu.

The above conclusions are only based on this specific case study and some of the conclusions may not be general; however, numerous studies on this subject related to the Janbu, Bishop, and Spencer methods show similar conclusions ((Duncan and Wright, 1980 & 2005 and Pockoski and Duncan, 2000). Additional research effort may be needed to validate or generalize some of the findings in this paper.

ACKNOWLEDGMENTS

The authors would like to thank the New Orleans District of USACE for providing the program "Stability with Uplift" to conduct slope stability analysis using MOP.

REFERENCES

Caver, W.W., Jr. (1973). "Slope Stability in Soft Layered Soil Systems." *Master Thesis*, Oklahoma State University, Stillwater, OK.

Duncan, J.M and Wright, S.G. (1980). "The Accuracy of Equilibrium Methods of Slope Stability Analysis." *Engineering Geology*, Vol 16, pp 5-17.

Duncan, J.M and Wright, S.G. (2005). "Soil Strength and Slope Stability." John Wiley & Sons, Inc., Hoboken, NJ.

GEO-SLOPE International Ltd. (2007). "Stability Modeling with SLOPE/W 2007, An Engineering Methodology." Calgary, Alberta, Canada..

Pockoski, M. and Duncan, J.M. (2000). "Comparison of Computer Programs for Analysis of Reinforced Slopes."Virginia Tech, Blacksburg, VA.

US Army Corps of Engineers. (2003). "Engineering and Design: Slope Stability." *EM 1110-2-1902*, Department of the Army, US Army Corps of Engineers, Washington, DC.

New Approaches to Stability Analysis of Steep Coastal Bluffs

Brian D. Collins[1], M. ASCE, P.E., Ph.D. and Nicholas Sitar[2], M. ASCE, P.Eng, Ph.D.

[1]Research Civil Engineer, U.S. Geological Survey, Western Coastal and Marine Geology, 345 Middlefield Rd, MS999, Menlo Park, CA 94025, bcollins@usgs.gov
[2]Professor, University of California, Berkeley, Dept. of Civil and Environmental Engineering, 449 Davis Hall, Berkeley, CA 94710, sitar@ce.berkeley.edu

ABSTRACT: We present a discussion on the limitations and needed improvements for existing slope stability analysis methods to accurately model steep coastal bluff failures resulting from both direct wave action at the toe in weakly cemented sands and precipitation-induced seepage failures in moderately cemented sands. Using a case-study detailing over 5 years of observations of coastal bluff erosion and landsliding in northern California, we show that existing analysis methods over-predict the observed crest retreat and mis-predict the field-measured failure geometry. In response, we propose new analysis methods for evaluating stability in these settings.

INTRODUCTION

Predictions of cliff failure and associated crest retreat in coastal environments provide a continuing challenge to engineers and geologists. Very often, coastal bluffs (i.e. sea-cliffs or coastal cliffs) are composed of weakly lithified sediments (e.g. weakly to moderately cemented sands – Fig. 1) that are difficult to characterize and still harder to analyze in terms of failure mechanism and failure mode. While many analysis methods do exist, our research has found that they typically over-predict the expected crest retreat, as measured at the top of the cliff or bluff. This quantity is often the factor of greatest importance when planning for coastal hazard mitigation. Further, the timing of failure and overall stability of these cliffs is generally mis-predicted by existing methods, highlighting the need for both an examination of these methods and suggestions for development of new methods.

Failures of steeply inclined slopes and vertical cliffs are typically modeled using limiting equilibrium techniques. The relative ease of analysis and the ability to analyze the development of shear planes from changing geometric (slope) conditions lends itself to these techniques. In some cases however, and particularly those associated with more well-cemented lithologies, the reduction of tensile strength from wetting is dominant in the failure behavior and is more easily modeled with deformation-based criteria, or at a minimum, those methods that can model the transition of tensile to compressive stresses throughout the soil mass. In this paper, we discuss the limitations of each of these methods, with regard to modeling the slope behavior of weakly lithified sand coastal bluffs and make suggestions on necessary improvements.

(a)

(b)

FIG. 1. Typical (a) weakly and (b) moderately cemented sand coastal bluffs in Pacifica, California

STABILITY METHODS FOR WEAKLY CEMENTED SAND COASTAL BLUFFS

Bluffs composed of weakly cemented sands, with unconfined compressive strength (UCS) values between 5 kPa and 30 kPa, very often fail due to steepening of the overall slope profile from wave action-induced erosion at the cliff toe. Development of failures over bluff-high shear planes is typical in response to an increasingly unstable steep cliff geometry.

Culmann (1866) was among the first to develop an analysis method for the stability of steep slopes. However, Francais (1820) also developed a similar methodology independently from Culmann some 46 years earlier. Both methods were based on even earlier work by Coulomb (1773) and were developed to calculate the maximum excavation depth, H in steep cut-slopes at angle β. The methodologies presented a static solution for a rigid body of soil moving along a shear plane.

In general, this method predicts reasonable results when the slope angle is near-vertical, becoming more exact as the slope approaches vertical (Taylor, 1948). However, in the application of this analysis to typical sea-cliffs, we have found that the magnitude of crest retreat is grossly over-predicted, by up to 200% of its expected value, and that the failure plane inclination is under-predicted by up to 10°. Hampton (2002) found similar discrepancies with the predicted cliff height and slope inclination using the Culmann method as well.

A slope stability model that more correctly simulates evolving cliff geometries, particularly those with vertical toes, was investigated by Carson (1971) for actively down-cutting streams, and later refined by Sunamura (1992) for wave action-induced failures in coastal settings. These methods assume a variable vertical toe height (H_t) and appropriately adjust the standard Culmann expression through use of an effective inclination angle (i).

While this expression provides a slight improvement in the prediction of actual crest retreat in sea-cliffs and better simulates the true geometric conditions, we also found that it introduced less realistic predictions of the slope and failure plane inclinations in case-study trials for typical weakly lithified sea-cliffs.

To properly predict these competing factors (crest retreat, slope inclination, failure plane inclination, and toe geometry), we suggest that a new approach be taken which more correctly models the failure plane geometry. Our observations show that the failure plane is typically parallel to the slope in these types of failures, which in turn suggests that an infinite slope analysis be used for stability analyses. Unfortunately, infinite slope analysis also requires that either the slope angle or failure plane depth be known a priori, which is not the case in typical coastal settings – it is these characteristics that we are trying to determine, and that constantly evolve with continued wave action at the toe of the slope. We therefore suggest that infinite slope analysis assumptions be used within an evolving toe, Culmann–type finite slope framework so that stability can be assessed for coastal bluffs of known height under evolving slope inclination and toe height conditions (Fig. 2). An analysis technique following this suggestion, and which includes a term for a vertical slope and tension crack at the crest of the slope (H_{tc}) has been developed and is presented by Collins (2004) and Collins and Sitar (in prep.). The governing formula is:

$$\frac{c}{F_s} = \frac{\gamma}{2\tan\beta(H_s + H_t)}\left(H^2 - (H_s + H_{tc})^2\right)\cdot\left(\sin^2\beta - \sin\beta\cos\beta\frac{\tan\phi}{F_s}\right) \tag{1}$$

where H_t, H_s, and H_{tc} are as defined in Fig. 2, H is equal to the sum of H_t, H_s, and H_{tc}, F_s is the factor of safety, β is the slope inclination angle, γ is the unit weight and φ and c are the Mohr-Coulomb strength parameters. Stress-path controlled, triaxial strength testing on undisturbed samples is recommended to obtain reasonable estimates of φ and c.

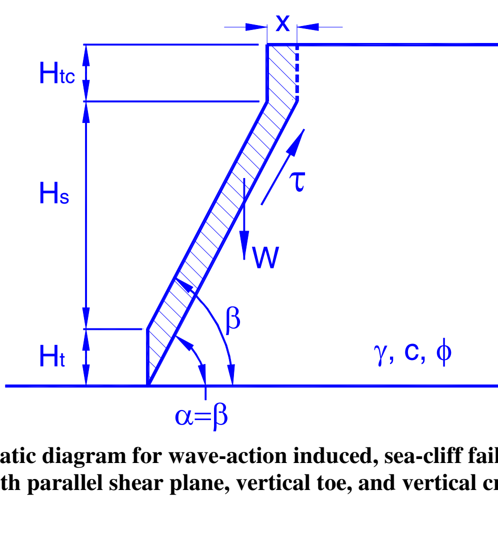

FIG. 2. Schematic diagram for wave-action induced, sea-cliff failure finite slope formulation with parallel shear plane, vertical toe, and vertical crest.

To test this method, we performed slope stability analysis for a typical coastal bluff located in northern California along the coast south of San Francisco (Fig. 1a). Here, the slope height H is 24 m, with a toe height from wave action erosion of H_t = 2 m , and a vertical crest section of H_{tc} = 2 m. Geotechnical parameters used in all analyses are those taken from site-specific testing by Collins (2004) and are: γ = 17 kN/m^3, φ' = 39°, and c' = 6 kPa.

The results from the Culmann (1866) method, the Sunamura (1992) method, and the proposed methodology (Eq. 1) are shown in Table 1. Of most importance is the more realistic prediction of the crest retreat (1.4 m) compared with the existing methods and the steeper failure plane inclination angle, which also agrees with our case study observations (Collins, 2004). In general, typical crest retreat of single failures are on the order of 1 to 2 meters, although total crest retreat of an entire winter season may be up to 10 or more meters.

TABLE 1. Comparison of Analysis Results for Typical Weakly Cemented Coastal Bluff Failures

Analysis Method	Slope angle, β	Failure plane angle, α	Crest retreat, x (m)
Conventional Culmann	57°	48°	6.1
Culmann w/ vert. toe (i.e. Sunamura, 1992)	53°	48°	4.7
Finite slope Culmann (Eq. 1)	55°	55°	1.4

STABILITY METHODS FOR MODERATELY CEMENTED SAND COASTAL BLUFFS

Our observations have shown that bluffs composed of moderately cemented sands (typical UCS up to 400 kPa) do not often fail as a direct result of bluff toe erosion by wave action, but rather due to the effects of precipitation-induced ground and surface water seepage. Whereas toe erosion by wave action does maintain cliffs in steep geometries, it does not directly lead to the majority of failures (Collins, 2004; Collins and Sitar, in press). Our observations, along with those of other coastal research engineers (i.e. Hampton, 2002) have shown that failures more often occur as 0.5 to 1.0-meter-thick slabs of material failing from nearly vertical cliff faces as a result of a loss of tensile strength. The reduction of tensile strength is typically either from stress-release of supporting, seaward material, or due to the flow of groundwater seepage through the bluff profile towards the bluff face (Fig. 3).

The brittle nature and exfoliation type fracture pattern of typical failures in moderately cemented sand coastal bluffs does not lend itself to analysis with limiting equilibrium techniques. These types of analyses can not predict the timing, crest retreat, or failure plane geometry correctly, since they utilize improper methodologies from the beginning.

We therefore propose a finite element based analysis method that implements a tensile component of slope stress and soil strength. Our analyses (Fig. 4), along with

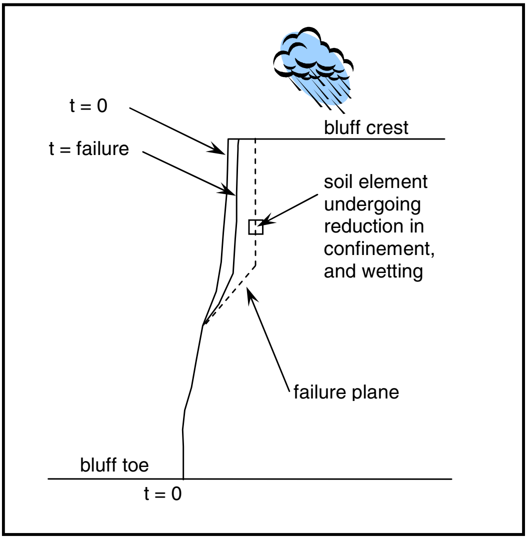

FIG. 3. Failure schematic for exfoliation fractures in strongly cemented sand coastal bluffs.

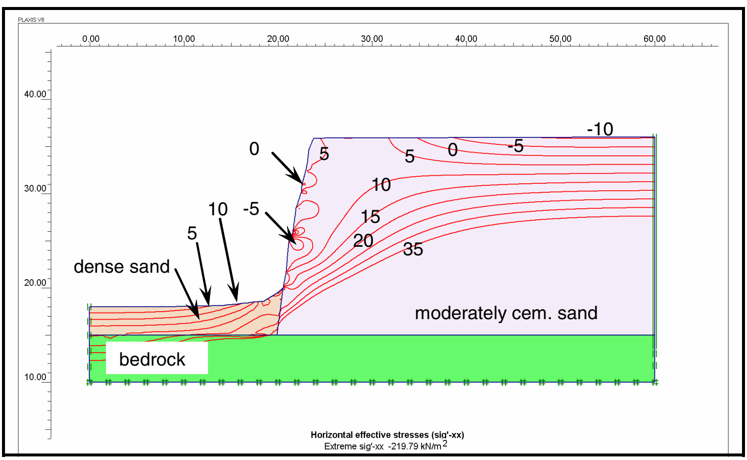

FIG. 4. Distribution of minor principal stress (σ_3) at the bluff face in typical moderately cemented slope. All stresses are in kPa.

those performed independently in previous studies (Sitar and Clough, 1983; Ashford and Sitar, 2001) show that the middle third of a typical near-vertical cliff face exists in a state of tension. Further, Brazilian tensile testing of typical moderately cemented sands from our study area in northern California (Fig. 1b) indicates that the material undergoes a dramatic reduction in tensile strength upon wetting (Collins, 2004), from 32 kPa at in-situ water content (~12.6%) to 5 to 10 kPa when wetted (~22.1%). By comparison to the FEM results (Fig. 4) and our field observations, we generalize this data to indicate that when the bluff face becomes wetted or saturated, the tensile strength of the soil is reduced such that tensile fracture occurs:

$$\sigma_{t-insitu} > \sigma_3 \text{ (STABLE)} \tag{2}$$

$$\sigma_{t-wetted} < \sigma_3 \text{ (UNSTABLE)} \tag{3}$$

Failure will therefore occur where this criteria holds true, typically in the mid-bluff region, where we have observed a majority of failures to occur. Although this simple comparison of tensile strength to tensile stress does not provide an indication of the magnitude of bluff crest retreat resulting from mid-bluff failure, it does more correctly model the mode of failure which can be considered an improvement over existing analysis methods with regard to failure timing. This method has the potential to identify incipient failure conditions more correctly.

CONCLUSIONS

Existing methods of slope stability analysis for steep coastal bluff failures were investigated. To overcome limitations in these methods to properly predict the mode and magnitude of failures, new slope stability methodology is proposed. The methodologies – a finite slope with parallel shear plane for weakly cemented sand coastal bluffs, and a tensile strength-stress comparison for moderately cemented sands show improvements over existing methods. In the former, the conventional method of analysis is preserved, but improvements on the prediction of failure slope geometry and resulting crest retreat are made. In the latter, conventional methods are disregarded and a comparison of in-situ and wetted tensile strength to the existing bluff tensile stress configuration appears to more correctly model the failure mode.

ACKNOWLEDGEMENTS

Funding for this research was provided by grants from the U.S. Geological Survey, Western Region Coastal and Marine Geology Program, the University of California, Coastal Environmental Quality Initiative, and the U.S. Geological Survey, Mendenhall Postdoctoral Program. This support is gratefully acknowledged. Reviews by Robb Moss (California Polytechnic State University), Diane Minasian (USGS), and two anonymous reviewers are gratefully acknowledged.

REFERENCES

Ashford, S. A., and Sitar, N. (2001). "Effect of element size on the static finite element analysis of steep slopes." *International Journal for Numerical and Analytical Methods in Geomechanics*, 25, 1361-1376.

Carson, M. A. (1971). *The Mechanics of Erosion*, Pion Limited, London.

Collins, B.D. (2004). *Failure Mechanics of Weakly Lithified Sand Coastal Bluff Deposits*, University of California, Berkeley, Dept. of Civil and Envir. Eng. Doctoral dissertation, 278p.

Collins, B.D. and Sitar, N. (in press). “Processes of coastal bluff erosion in weakly lithified sands, Pacifica, California, USA.”, *Geomorphology*, El Sevier.

Collins, B.D. and Sitar, N. (in preparation). “Slope stability of wave-action induced sea-cliff failures in weakly lithified sediments.”, *Journal of Geotechnical and Geoenvironmental Engineering*, ASCE.

Coulomb, C. A. (1773). "Essai sur une application des regles de maximis et minimis a quelques problemes de statique, relatifs a l'architecture." *Memoires de L'Academie des Sciences*, Vol. 7, 343-382.

Culmann, K. (1866). *Die Graphische Statik*, Von Meyer & Zeller, Zurich.

Francais, J. F. (1820). "Recherches sur la pousee des terres, sur la forme et les dimensions des murs derevetement et sur les talus d'excavation." *Memoires de L'office d Genie*, Vol. 4, 157-193.

Hampton, M. (2002). "Gravitational failure of sea cliffs in weakly lithified sediment." *Environmental and Engineering Geoscience*, 8(3), 175-192.

Sitar, N., and Clough, G. W. (1983). "Seismic Response of Steep Slopes in Cemented Soils." *Journal of Geotechnical Engineering*, 109(2), 210-227.

Sunamura, T. (1992). *Geomorphology of Rocky Coasts*, John Wiley and Sons, New York.

Taylor, D. W. (1948). *Fundamentals of Soil Mechanics*, John Wiley and Sons, New York.

Research on Risk Assessment for Talus Slope of Freeway in Mountain Area

Huang Hong-wei[1], Liu Zhong-qiang[2]

[1, 2] Department of Geotechnical Engineering, Tongji University, Shanghai 200092
[1] huanghw@mail.tongji.edu.cn [2] zqliu1982@163.com

ABSTRACT: Talus slopes have poor stability on both sides of freeways, which usually lead to landslides and result in great damage. In order to assess these damages, fuzzy comprehensive evaluation systems for hazard and vulnerability assessment of talus slope were set up based on the basic principles and methods of the fuzzy mathematics. Weights of factors were evaluated by formulas method or Delphi method. Through the evaluation of hazard and vulnerability, we established a sort of risk assessment system for landslides based on the theory of risk matrix. The rating of risk was divided into five levels. Using the system of risk evaluation, a case study was presented.

1. INTRODUCTION

Due to rainy climatic conditions and complex geological conditions in mountain areas, slopes on both sides of a freeway frequently become unstable, causing significant casualties and economic losses. By analyzing causes of formation, freeway landslides usually occur in the process of construction (Fang, 2003).

As a special geological slope, a talus slope is susceptible to sliding under the influence of environment and artificial disturbance during the construction period of a freeway. Therefore, it is of great significance to understand the sliding mechanism of talus slopes. In this paper, risk assessment of talus slopes is discussed from two aspects, hazard assessment and vulnerability assessment.

2. HAZARD ASSESSMENT FOR TALUS SLOPE

Landslide hazard usually includes two kinds as either history hazard or potential hazard. History hazard refers to the activity intensity of the disaster which had occurred before, while the potential hazard involves active degree of the potential disaster which has not yet occurred. Due to the difficulty of collecting historical data, hazard assessment in this paper only considers potential hazard. The primary and secondary levels, as well as the criteria for rating are established basing on the productions of former experts (Zhang et al., 2000; Jia et al. 2004) and the manual (Code for investigation of geotechnical engineering, 2002). The weights of factors are evaluated by experts, sees in Table1 (weights in parenthesis). Hazard rating for a talus slope can be calculated by fuzzy math.

Table 1. The Weights of Factors and Hazard Levels for Talus Slope

Primary level	**Secondary level**	**Criteria for rating**				
		Very low(I)	**Low (II)**	**Medium (III)**	**High (IV)**	**Very high (V)**
Geology (0.15)	Condition of faulting(0.20)	none	Inactive, >50m	Inactive, <50m	active, >50m	active, <50m
	development of cross bedding /group(0.25)	zero or one		two to three		more than three
	Condition of leading edge /°(0.25)	<15	15~30	30~45	45~60	>60
	degree of gully cut/m(0.15)	<30	30~45	45~60	60~80	>80
	Weathering grade/%(0.15)	<5	5~10	10~20	20~30	>30
Structure (0.30)	Base rock strength/ q_u , kg/cm^2(0.15)	very strong (>1000)	strong (500~ 1000)	medium (250~500)	weak (100~ 250)	very weak (<100)
	Condition of base rock plane (0.15)	very coarse	coarse	slightly coarse	smooth	very smooth
	Degree of slope/°(0.15)	<15	15~25	25~35	35~45	>45
	Friction angle/°(0.1)	>33	29~32	19~28	13~18	<13
	Cohesion/ k_{pa} (0.1)	>21	21~13	13~9	9~5	<5
	Composition of talus(0.2)	covered by clay soil		covered by little clay soil		composed of rock and soil
	Cemented degree (0.15)	very compact	compact	loose	very loose	no

Table 1. (Continued) The Weights of Factors and Hazard Levels for Talus Slope

Primary level	Secondary level	Criteria for rating				
		Very low(I)	Low (II)	Medium (III)	High (IV)	Very high (V)
Hydro-geology (0.35)	Seepage of ground water(0.25)	dry	occa-sionally damp	always damp	dripping	flow
	Erosion of surface water(0.15)	no	very weak	weak	intense	very intense
	Average annual precipitation /mm (0.4)	<100	100~200	200~250	250~350	>350
	Drainage facility(0.20)	multiple (vertical and horizon-tal)	two(vertical and horizon-tal)	one catch drain (vertical)	one catch drain (hori-zontal)	none
Envi-ronment (0.20)	Type of vegetation(0.2)	grass	trees> grass	trees> grass	trees	No cover
	Density of vegetation/% (0.2)	>30	30~20	20~15	15~5	<5
	Earthquake intensity/°(0.2)	<3	3~4	5~6	7~8	>8
	Type of land use(0.1)	forest	pasture, orchard, place of enter-tainment	residential district, school	roads, protection facility	pipeline
	Activity of human being(0.3)	No	Very weak	weak	Strong	Very strong

Considering the fuzziness between each level, the membership function and membership can be determined by formulas method and Delphi method. Taking the character of data distribution into account, the memberships of continuous indices are calculated by "drop-ladder" distributing (equation (1) - (5)), while the memberships of discrete indices are calculated by Delphi method (Table 2).

$$U_{\mathrm{I}}(x)=\begin{cases}1 & x\le V_1\\ \dfrac{V_2-x}{V_2-V_1} & V_1<x\le V_2\\ 0 & x>V_2\end{cases} \quad (1)$$

$$U_{\mathrm{II}}(x)=\begin{cases}0 & x\le V_1 \ or\ x>V_3\\ \dfrac{x-V_1}{V_2-V_1} & V_1<x\le V_2\\ \dfrac{V_3-x}{V_3-V_2} & V_2<x\le V_3\end{cases} \quad (2)$$

$$U_{\mathrm{III}}(x)=\begin{cases}0 & x\le V_2 \ or\ x>V_4\\ \dfrac{x-V_2}{V_3-V_2} & V_2<x\le V_3\\ \dfrac{V_4-x}{V_4-V_3} & V_3<x\le V_4\end{cases} \quad (3)$$

$$U_{\mathrm{IV}}(x)=\begin{cases}0 & x\le V_3 \ or\ x>V_5\\ \dfrac{x-V_3}{V_4-V_3} & V_3<x\le V_4\\ \dfrac{V_5-x}{V_5-V_4} & V_4<x\le V_5\end{cases} \quad (4)$$

$$U_{V}(x)=\begin{cases}0 & x\le V_4\\ \dfrac{x-V_4}{V_5-V_4} & V_4<x\le V_5\\ 1 & x\ge V_5\end{cases} \quad (5)$$

Where V_1, V_2, V_3, V_4 and V_5 are standard values of the five levels of talus slope hazards (for interval indexes, using their means); x represents measured values. For continuous indices, U_{I}, U_{II}, U_{III}, U_{IV} and U_{V} are values of membership when x is in different ranges. For discrete factors, they are values calculated by Delphi method.

Table 2. Membership for Discrete Factors

Criteria for rating	Membership				
	U_{I}	U_{II}	U_{III}	U_{IV}	U_{V}
I (very low)	0.75	0.25	0.00	0.00	0.00
II (low)	0.15	0.70	0.15	0.00	0.00
III (medium)	0.00	0.15	0.70	0.15	0.00
IV (high)	0.00	0.00	0.15	0.70	0.15
V (very high)	0.00	0.00	0.00	0.25	0.75

3. VULNERABILITY ASSESSMENT

Vulnerability refers to the degree of potential loss for a given element at risk, or set of such elements, resulting from the occurrence of landslide. For risk assessment of freeway talus slopes, due to long route of freeways in mountain area and the complex situation of slopes, the elements at risk are also very complicated, so elements at risk can be divided into different categories, and then evaluated. The elements at risk in freeway involve loss of life, roads, lifeline, bridges, dwellings and land category (R.Anbalagan et al. 1996) (Table 3). Their weights are determined by Analytic Hierarchy Process, which are 0.28, 0.22, 0.15, 0.15, 0.1 and 0.1 separately. The selection of membership function and membership are consistent with assessment of hazard.

Table 3. Vulnerability Assessment for Talus Slope

Types of elements at risk	Rating of vulnerability				
	Very low(I)	Low(II)	Medium (III)	High(IV)	Very high(V)
Loss of life or injured	MI≤3	SI≤1or MI>3	1<SI≤3	1≤F<3 or SI>3	F≥3
Length for damage for roads(m)	<100	101~500	501~1000	1001~ 2000	>2000
Lifeline	no or slight damage, normally use	slight damage, need small repair	relatively serious damage, need special repair	serious damage, need massive repair	total damage, need rebuilding
Length of damage for bridges (m)	<10	11~30	31~60	61~100	>100
No. of dwellings likely to be damaged	<2	2~5	6~10	11~50	>50
Land category	barren	sparsely vegetated	moderately vegetated/ agricultural land	thickly vegetated	very thickly vegetated

Note: F=loss of life (missing included), SI= Serious injuries, MI= Minor injuries

4. THE SYSTEM FOR RISK ASSESSMENT OF TALUS SLOPE

Landslide risk assessment began in the 1970s. Although landslide assessment methods vary widely in different countries, all methods have some things in common, to take all the actions of geological factors to assess the possibility of landslides for particular geological conditions into full account (Xie et al., 2004).

Landslide risk assessment is becoming a means to reduce landslide disaster. Based on the hazard and vulnerability assessment, the risk assessment matrix method (Guidelines for Tunneling Risk Management, 2004) is adopted to assess the risk of talus slopes (Table 4 and Table 5).

Table 4. Risk Assessment Matrix

Risk		**Rating of vulnerability**				
		1.very low(I)	**2.low(II)**	**3.medium(III)**	**4.high(IV)**	**5.very high(V)**
Rating of hazard	A: very low(I)	1A	2A	3A	4A	5A
	B: low(II)	1B	2B	3B	4B	5B
	C: medium(III)	1C	2C	3C	4C	5C
	D: high(IV)	1D	2D	3D	4D	5D
	E: very high(V)	1E	2E	3E	4E	5E

Table 5. Color and Label for Rating of Risk

Rating of risk	**I**	**II**	**III**	**IV**	**V**
Color	Green	Blue	Yellow	Orange	Red
Label					

5. CASE STUDY

The talus slope is located in Shuima freeway, Yunnan province. Based on the theoretical framework aforementioned, risk of this talus slope is assessed.

5.1 Hazard Assessment

(1) Geology

The faulting of this landslide is not developed; Cross bedding has two groups of joints. There is a high steep face at the bottom of slope. The slope degree of the face is above 60°. The gullies are cut into v-type. The degree of weathering is high.

(2) Structure

The condition of structure is poor: the strength of base rock is medium; the surface condition of base rock is smooth; the terrain is extremely steep and the degree of slope is above 28°. Also, obtaining from experiment in laboratory, we got that the friction angle is 33.8° and the cohesion is 20.78kpa. The talus slope is accumulated by rock and soil. Talus bonding is mainly mud cementation and compact.

(3) Hydrogeology

The section is located in the upper slopes of the Shangqing River, which flows from the south to the north. In the rainy season, the surface water erosion is strong. An average annual precipitation is 1200mm. But there are no drainage facilities in the survey stage.

(4) Environment

On top of the slope vegetation is developed, most of which are shrubs and trees. In the lower part of the slope vegetation is not developed, with only a small amount of trees. The coverage of vegetation is about 20%~30%. Earthquake intensity is 7 degrees. The land is used to construct freeways. Activity of human being is intense.

From the analysis above, the membership of hazard is computed as follows (Table 6). Basing on the principle of largest membership, the hazard of the slope belongs to class V.

Table 6. The Computed Membership of Hazard

Criteria for rating	Very low(I)	Low (II)	Medium (III)	High (IV)	Very high (V)
membership	0.0996	0.1207	0.1658	0.2540	0.3570

5.2 Vulnerability Assessment

According to the field research, we can perform vulnerability analysis. In ancient landslides there is a house with ten residents. The average length of the slope is about 155m with a medium coverage of vegetation. Taking into account residents and the construction of freeway, if landslide occurs, casualties will reach more than three. The damage length of road is more than 100m. Lifeline will be suffered seriously damage and the house in the slope will be seriously damaged.

So the membership of vulnerability is computed as follows (Table 7). Based on the principle of largest membership, the vulnerability of the slope belongs to class II.

Table 7. The Computed Membership of Vulnerability

Criteria for rating	Very low(I)	Low (II)	Medium (III)	High (IV)	Very high (V)
membership	0.2205	0.2540	0.2080	0.1075	0.2100

Based on the Risk Assessment Matrix in Table 4, we can obtain that the risk of slope belongs to class III.

CONCLUSION

The risk analysis of talus slope in freeway involves many uncertainties. Based on hazard and vulnerability assessment, the system of risk assessment was established. The factors involved in the hazard assessment amount to 21 items. A quite comprehensive analysis of their mutual relations and a fuzzy comprehensive evaluation were also established. This evaluation system was used to assess the risk of a talus slope in Shuima freeway in Yunnan Province, and the result of risk rating is class III. The system of risk assessment presented in this paper, can be used simply and easily in engineering. However the values of some hazard indexes as well as elements at risk were empirical. With further study of the mechanism and richer information we get, the method will be improved and more practical.

REFERENCES

Fang Xiangchi. (2003). "Studying on the prevention and treatment of the landslide calamity of highways in mountain area." *J. Yunnan Communication Science and Technology*. Vol.19 No.1:14-17.

Guidelines for Tunneling Risk Management (ITA,2004)

Jia Houhua, He Huaijian. (2004). "Analysis of fuzzy-random reliability of slope stability." *J. Rock and Soil Mechanics.* Vol.24 No.4:657-670.

Ministry of Construction of the People’s Republic of China. (2002). "Code for investigation of geotechnical engineering." China Architecture & Building Press.

R.Anbalagan, Bhawani Singh. (1996). "Landslide hazard and risk assessment mapping of mountainous terrains-a case study from Kumaun Himalaya." India. *Engineering Geology* 43: 237-246.

Xie Quanmin, Liu Peng and Xia Yuanyou. (2004). "Study on Risk Evaluation of Landslide Hazard." *J. Metal Mine.* Series No. 333:58-61.

Zhang Xiaohui, Wang Hui, Dai Fuchu, Ma Wei. (2000). "Comprehensive Evaluation of Slope Stability Using Interaction Matrix and Fuzzy Sets." *J. Chinese Journal of Rock Mechanics and Engineering.* Vol.19 No.3:346-351.

The Effects of Basal Resistance and Hydroplaning on the Initial Kinematics of Seismically Induced Tsunamigenic Landslides

Oliver-Denzil S. Taylor[1] S.M. ASCE, Aaron S. Bradshaw[2], M. ASCE, P.E., Christopher D.P. Baxter[3], M. ASCE, P.E., and Stephan T. Grilli[4], M. ASCE

[1] Graduate Student, Department of Civil and Environmental Engineering, University of Rhode Island, Kingston, RI, USA; otaylor@mail.uri.edu
[2] Assistant Professor, Department of Civil Engineering, Merrimack College, North Andover, MA, USA; bradshawa@merrimack.edu
[3] Associate Professor, Departments of Ocean / Civil and Environmental Engineering, University of Rhode Island, Narragansett, RI, USA; baxter@oce.uri.edu
[4] Professor and Chair, Department of Ocean Engineering, University of Rhode Island, Narragansett, RI, USA; grilli@oce.uri.edu

ABSTRACT: According to current landslide tsunami generation models, the initial acceleration time history of a submarine mass failure is an important factor influencing the source characteristics of tsunami waves. Translational models developed thus far typically simulate rigid or deforming bodies sliding down an inclined plane, assuming either negligible basal resistance or an idealized basal resistance, with or without the inclusion of hydrodynamic forces. However no known models incorporate realistic basal resistance, hydrodynamic forces, and hydroplaning together to quantify their effects on the initial kinematics of submarine failures. In all current models it is assumed that the maximum initial acceleration occurs nearly instantaneously after the moment of failure. Here, we propose a new rigid body model that incorporates hydrodynamic drag, with realistic basal resistance and hydroplaning effects. Utilizing the post failure shear strength of the sediment, this new model investigates the initial kinematics and time histories of the slide event in relation to tsunami generation over varying slope angles and idealized hydroplaning conditions. The current work is restricted to seismically induced submarine landslides in normally consolidated clay. The modeling results indicate a decrease in the magnitude of the peak slide acceleration by 27% to 47% and significant delays in the acceleration time histories of the sliding mass. The results also show an exponential increase in the delay of the acceleration time histories as the slope angle decreases, suggesting a greater influence of basal resistance and hydroplaning effects on typical submarine failures, for slopes of less than 5°. Further research is necessary to determine the influence of using the refined basal resistance models on predicted initial landslide tsunamis wave heights, lengths, and subsequent costal run-up elevations.

INTRODUCTION

The 1998 Papua New Guinea tsunami and the 2004 Indian Ocean tsunami, that caused the death of over 200,000 people in several countries, has focused even more the interest of various scientific communities on such geohazards. Tsunamis can be generated by volcanic eruptions, co-seismic ocean bottom motion, gas hydrate phase change, subaerial and submarine landslides, and oceanic meteorite impacts (Watts 2004). Until recently, submarine landslides have been the least studied of these tsunami generation mechanisms, mainly due to the complexity of slide failure dynamics, center of mass kinematics and landslide deformation (Locat and Lee 2002; Watts 2004). The majority of tsunamigenic submarine landslides investigated have occurred at slope angles of less than 5^{o}, with the most common trigger being seismic activity (Canals et al. 2004). Extreme seismic events are not required to induce tsunamigenic landslides. Frequent, moderate earthquakes can potentially trigger tsunamigenic submarine failures with resulting wave heights greater than those generated solely by the vertical displacement of the seismic ground motion (Watts 2003), thus justifying the importance of investigating seismically induced submarine failures.

Unlike subaerial landslides, submarine landslides tend to propagate for very large distances, starting as rigid blocks and then sometimes transitioning to debris flows. While research advances have been made in the past decade in the kinematics of submarine landslides, particularly in the behavior of debris flows and run-out distances, very little research has focused on the initial kinematics of these events, especially relating to tsunami generation. The transition of cohesive slides to turbidity currents, for instance, indicates that significant remolding and strength reduction can occur, which earlier research suggests, may be explained in part by the entrainment of water beneath the failed mass, causing *hydroplaning*. Recent investigations relate hydroplaning of liquefied debris flows to a critical densimetric Froude number (Fr_{crit}=0.3) that relates to a critical velocity of between 4 to 18 m/s, depending on the thickness of the failed mass (De Blasio et al. 2004 and others). In the present investigation, the critical velocity for hydroplaning to occur was taken as 6 m/s, which corresponds to Fr_{crit}=0.28, in keeping with laboratory findings. The extent to which hydroplaning occurs under the failed mass, however, is uncertain, as it depends on the rheological properties of the sediment and the geological setting of the slide, greatly complicating modeling techniques (Locat and Lee 2002).

Recent numerical modeling of tsunamigenic landslides has considered the translation (sliding) or rotation (slumping) of initially rigid bodies, moving down a plane slope with specified kinematics and deformation rate (e.g., Grilli and Watts, 2005). In such cases, results show, typical translational slides tend to produce relatively higher initial tsunami amplitudes than slumps, and a strong deformation will enhance tsunami generation, particularly in the far field. Other non-rigid slide models often assumed that the sliding mass is a liquefied debris flow from the onset of failure (e.g., Watts and Grilli, 2003). However, evidence from past failures show debris fields with large outrunner blocks where the moving sediment has remained intact giving validity to the assumption that, at least initially, the failed sediment, especially in the case of clay sediment, does not liquefy and behaves as a rigid body. Therefore, in this study of initial kinematics, initial slide failure was modeled as and compared to other rigid body models.

A major assumption made by Grilli and Watts (2005) and others is that the influence of basal resistance is negligible on slide kinematics, as compared to the hydrodynamic drag. However, since the parameter of greatest influence on tsunami generation has been shown to be the initial acceleration of the center of the failed mass (Haugen et al. 2005; Watts et al. 2005; and others), elimination of basal resistance (i.e., soil behavior) may result in a potentially overestimated acceleration time history that is not representative of actual slide motion. Accordingly, Bradshaw et al. (2007) developed a modified solid body model, extending the work of Grilli and Watts (2005), to include effects of basal resistance on translational failures triggered by non-seismic events (i.e., rapid sedimentation and overpressures). This paper presents a further refinement of that analysis of initial slide kinematics with a model for a seismically induced slide, that accounts for effects of basal resistance, slope angle, and hydroplaning on the time history of slide acceleration.

DESCRIPTION OF SLIDE MODEL

Based on a balance of gravity, buoyancy, inertia, hydrodynamic drag and added mass, and Coulomb friction forces, Grilli and Watts (2005) expressed the center of mass motion of a rigid 2-D Gaussian-shaped body moving down an inclined plane, as (Fig. 1):

$$(\gamma + C_m)\ddot{s} = (\gamma - 1)(\sin\theta - C_n\cos\theta)g - C_d\frac{2}{\pi \cdot B}\dot{s}^2 \qquad [1]$$

where γ = ratio of the bulk density of the sediment to the density of water, θ = slope angle, g = gravitational acceleration, B = slide length (for an equivalent semi-ellipse), C_m = added mass coefficient, C_n = Coulomb friction coefficient, C_d = hydrodynamic drag coefficient, $\ddot{s}$ = slide acceleration, and $\dot{s}$ = slide velocity (the upper dots denoting time derivatives of the slide displacement [s]).

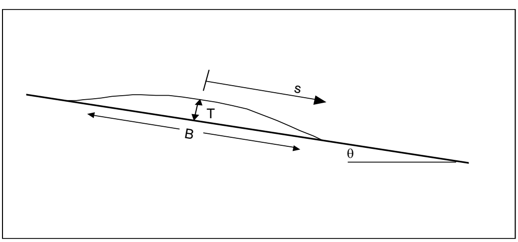

FIG. 1. Semi-elliptical rigid body utilized in modeling slide motion.

For translational failures, Grilli and Watts (2005) and Watts et al. (2005) assumed that C_n was nearly zero, once motion was initiated, thus eliminating any role of soil behavior on the kinematics of the failed mass. Bradshaw et al. (2007) extended Eq. 1 to include basal resistance as a function of *s* and *B*:

$$(\gamma + C_m)\ddot{s} = (\gamma - 1)g \sin\theta - \frac{S(s,B)}{\rho_w \frac{\pi}{4} BT} - C_d \frac{2}{\pi \cdot B}\dot{s}^2 \qquad [2]$$

where $S(s,B)$ = basal resistance function, ρ_w = density of water, and T = slide thickness.

As the focus of this study is on the initial slide kinematics, only the initial post failure conditions are considered and any deformations occurring before failure and the exact initial stress state of the slope are neglected. For a seismically induced failure, a combination of increasing pore pressures and driving stresses continue to act until the critical or yield acceleration is reached and slope instability occurs under undrained conditions. Since the duration of earthquakes is relatively short as compared to typical characteristic times of slide motion, the lateral forces induced by ground shaking (i.e., horizontal seismic accelerations) are assumed to cause failure but do not have to be considered in the post failure kinematics (Kvalstad et al. 2005).

For the nearly semi-elliptical body shown in Figure 1 the post failure motion is assumed to be initiated when the driving stress equals the peak undrained shear strength (S_u) of the clay within the weak shear zone, given by the following expression:

$$\tau_f = \rho_w \frac{\pi}{4} T \cdot (\gamma - 1) g \sin\theta = S_u \qquad [3]$$

Given the results of undrained ring shear testing by Stark and Contreras (1996) on normally consolidated Drammen clay, the undrained residual shear strength (S_{ur}) is defined by the following:

$$S_{ur} = 0.55 \cdot \tau_f = 0.55 \cdot S_u \qquad [4]$$

Based on Stark and Contreras's ring test results, Bradshaw et al. (2007) modeled the complete sediment strain softening behavior from peak to residual shear strength. However, given the small displacements (~ 2 cm) required to mobilize the residual strength in this sediment, it was thought that perhaps the strength behavior could be simplified to use a constant residual shear strength for all displacements. To investigate this, the present slide model was run successively with the inclusion of strain softening behavior and without. For the cases tested, no significant changes were observed in the magnitude of the peak slide acceleration and a small (0.35 s) difference occurred in the time histories. Thus, it was inferred that for these cases, strain softening at small displacements does not play a significant role in the initial acceleration time history of the slide and that the undrained residual shear strength can be assumed constant from the onset of slide movement.

In addition to residual shear strength, the other aspect considered in this study, with respect to basal resistance, is the degree of slide hydroplaning during motion. Despite recent advances, the mechanics of slide hydroplaning are not fully understood. It is known, however, that hydroplaning can occur under varying lengths of the frontal wedge, where a water layer can become entrained, thereby decreasing the shearing resistance (De Blasio et al. 2004). Accordingly, in this study we assume, for large enough slide speeds (greater than 6 m/s here) hydroplaning occurs over a specified percentage of slide length, for which a zero basal resistance is set in the model. Note, for the hydroplaning length, we only consider the portion of the slide that overrides the sediments located down-slope from the initial failure location. Therefore, the basal resistance function, that includes soil strength and hydroplaning effects, is given by the following set of equations:

$$S(s,B) = S_{ur} \cdot (B); \qquad \{\dot{s} \le 6\,m/s \tag{5}$$

$$S(s,B) = S_{ur} \cdot (B - s); \qquad \begin{cases} s \le B \cdot H_y \\ \dot{s} \ge 6\,m/s \end{cases} \tag{6}$$

$$S(s,B) = S_{ur} \cdot B \cdot (1 - H_y); \qquad \begin{cases} s \ge B \cdot H_y \\ \dot{s} \ge 6\,m/s \end{cases} \tag{7}$$

where H_y = fraction of the slide length susceptible to hydroplaning [0,1].

SENSITIVITY OF SLIDE KINEMATICS

A finite difference approach was used to solve the equation of motion (Eq. 2) utilizing the refined basal resistance (Eqs. 5-7), the undrained residual shear strength (Eqs. 3 and 4), slide properties, and varying the slope angle from 1^{o} to 10^{o}. The values modeled for the slide properties (T = 60 m, B = 4 km, and γ = 1.8) are in the typical ranges for known submarine landslides investigated in the COSTA Project (Canals et al. 2004). To analyze the effects of hydroplaning on the kinematics, H_y was varied from 25% to 100% to simulate slides that undergo partial to full hydroplaning. Coefficients C_m and C_d were taken as unity, assuming a slender and streamlined slide geometry (Grilli and Watts, 2005). These results were then compared to values obtained when assuming a zero basal resistance, as in Grilli and Watts (2005).

As could be expected, results show that as more contact exists between the slide and the sediments down slope (i.e., the smaller H_y), the greater the decrease in peak acceleration and velocity, and the effects on the time histories of slide kinematics, due to a given basal resistance (Fig. 2). Looking at Fig. 2, we see, as H_y decreases, the peak acceleration occurs earlier in the time history, but always significantly later than in the zero basal resistance model.

While Fig. 2 only shows the time histories for two slopes of 2^{o} and 5^{o}, it illustrates that as the slope angle decreases the time to peak acceleration increases for all values of H_y. The time to peak acceleration is plotted in Figure 3 over the full range of investigated slope angles (1^{o} to 10^{o}), and for the selected values of H_y. Figure 3 further indicates that for slope angles above 4^{o} there is no significant change in the time to peak acceleration with respect to slope angle. However, for slopes less than 4^{o}, the time to peak acceleration increases exponentially. This emphasizes the importance of basal resistance on slide kinematics for shallow slopes, which is critical considering that the majority of studied tsunamigenic submarine failures occur at slope angles of less than 5^{o} (Canals et al. 2004 and others).

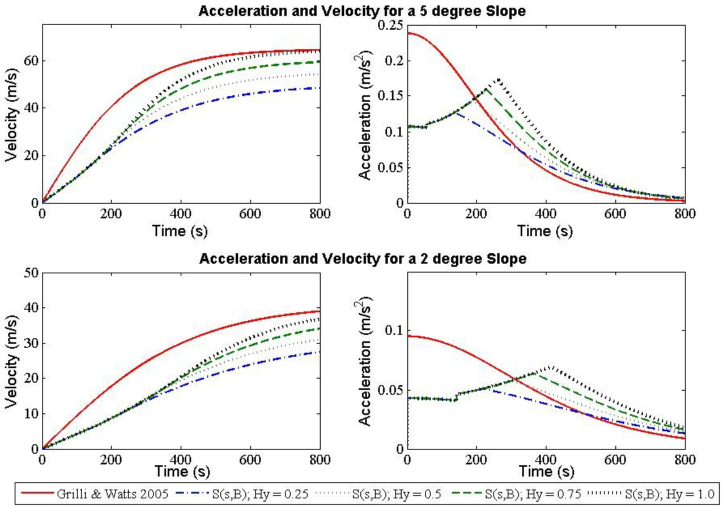

FIG. 2. Influence of hydroplaning effects for the proposed basal resistance model, at various degrees of hydroplaning H_y, on slide velocity and acceleration time histories as a function of slope (2 and 5 deg). The solid line is the zero basal resistance solution of Grilli and Watts (2005).

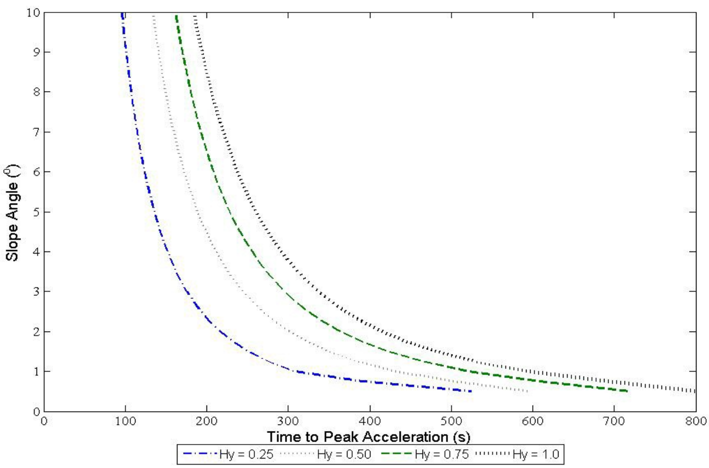

FIG. 3. Influence of failure slope angles and hydroplaning on the time to peak acceleration of the failed mass.

In addition to delaying the occurrence of the acceleration peak, Fig.2 and Table 1 show, basal resistance also significantly decreases its magnitude for all H_y cases, as compared to the zero basal resistance case. In addition, for all slope angles, reducing the portion of the slide that hydroplanes (i.e., decreasing H_y) decreases the peak acceleration. The decrease in peak acceleration, relative to the zero basal resistance case, varies from 27% for 100% hydroplaning to approximately 47% for 25% hydroplaning.

Table 1. Influence of Basal Resistance on Peak Slide Acceleration

	Peak Acceleration (m/s²)				
Slope Angle (degrees)	**Without Basal Resistance** Grilli and Watts (2005)	**With Basal Resistance**			
		$H_y = 1.0$	$H_y = 0.75$	$H_y = 0.50$	$H_y = 0.25$
10	0.474	0.345	0.317	0.287	0.252
8	0.38	0.276	0.254	0.23	0.202
6	0.285	0.208	0.191	0.173	0.152
5	0.238	0.173	0.159	0.144	0.127
4	0.19	0.139	0.128	0.115	0.101
3	0.143	0.104	0.096	0.086	0.076
2	0.095	0.069	0.064	0.058	0.051
1	0.048	0.035	0.032	0.029	0.026

CONCLUSIONS

The results of the refined slide kinematics model reported here indicate an increasing effect of basal resistance on the initial kinematics of underwater landslides as slope angles decrease. To complicate matters, as the percentage of the slide subjected to hydroplaning decreases, the influence of basal resistance on slide kinematics also increases. In particular, the acceleration time histories are significantly affected by basal resistance, which in turn would affect tsunami generation. Based on numerical modeling, Grilli and Watts (2005) and Watts et al. (2005) show that both the magnitude and time to the peak acceleration influence the initial tsunami wave height and inundation distances. For instance, these authors report that the initial landslide tsunami maximum surface depression is roughly proportional to initial peak acceleration, which in turn similarly affects the magnitude of coastal runup. As the peak acceleration occurs later in the time history, the frontal slide wedge will also have traveled to deeper water, which will potentially further decrease the amplitude of the generated wave.

Specifically, for slopes less than 10 deg, the refined basal resistance function yields a 27% to 47% reduction in the magnitude of the peak acceleration relative to the case where basal resistance is neglected. For the mildest slopes (1 to 5 deg), which represent the majority of observed slides, the combined effects of these parameters on the initial kinematics of the failed mass would be most significant. This suggests that the assumption that basal resistance is negligible, previously made by others, may not be accurate and yield unrealistic and overestimated time histories.

These results warrant further investigations into the effects of these refined time histories on tsunami wave generation and propagation, tsunamigenic landslide case studies, and hazard assessment models. To precisely quantify the effects of the new slide kinematics derived here on tsunami amplitude and runup, new landslide tsunami generation simulations will have to be performed. This will be the object of future work.

ACKNOWLEDGMENTS

Financial support for a portion of this work was provided by a grant from FM Global, Inc. and the National Science Foundation under Grant No. 0530203. This support is greatly appreciated.

REFERENCES

Bradshaw, A.S, Baxter, C.D.P., Taylor, O-D.S., Grilli, S.T. (2007) Role of soil behavior on the initial kinematics of tsunamigenic slides. *Submarine Mass Movements and Their Consequence,s 3rd Int. Symp., Santorini, Greece* (in press).

Canals, M., Lastras, G., Urgeles, R., Casamor, J.L., Mienert, J., Cattaneo, A., De Batist, M., Haflidason, H., Imbo, Y., Laberg, J.S., Locat, J., Long, D., Longva, O., Masson, D.G., Sultan, N., and Bryn, P. (2004) Slope failure dynamics and impacts from seafloor and shallow sub-seafloor geophysical data: case studies from the COSTA project. *Marine Geology*, 213: 9-72.

De Blasio, F.V., Engvik, L., Harbitz, C.B., Elverhøi, A. (2004) Hydroplaning and submarine debris flows. *J. Geophys. Res.,* 109:C01002.

Grilli, S.T., and Watts, P. (2005) Tsunami Generation by Submarine Mass Failure. I: Modeling, Experimental Validation, and Sensitivity Analyses. *J. Waterways, Ports, Coastal, and Ocean Engng.*, 131(6): 283-297.

Haugen, K.B., Løvholt, F., and Harbitz, C.B. (2005) Fundamental mechanisms for tsunami generation by submarine mass flows in idealized geometries. *Marine and Petroleum Geology*, 22: 209-217.

Kvalstad, T.J., Nadim, F., Kaynia, A.M., Mokkelbost, K.H., Bryn, P. (2005) Soil conditions and slope stability in the Ormen Lange area. *Marine and Petroleum Geology* 22: 299-310.

Locat, J., and Lee, H. (2002) Submarine landslides: advances and challenges. *Canadian Geotechnical Journal*, 39: 193-212.

Stark, T.D., and Contreras, I.A. (1996) Constant volume ring shear apparatus. *Geotechnical Testing Journal*, 19(1): 3-11.

Watts, P., (2004) Probabilistic analysis of landslide tsunami hazards. *In: Submarine Mass Movements and their Consequences*. Locat, J., Meinert, J. (Eds.), Kluwer Academic Press, Netherlands, 1st Int. Symp. 163-170

Watts, P., and Grilli, S. T. (2003) Underwater landslide shape, motion, deformation, and tsunami generation. *Proc., 13th Offshore and Polar Engineering Conf., Intl. Soc. of Offshare and Polar Engineers*, Cupertino, Calif., 3: 364–371.

Watts, P., Grilli, S.T., Tappin, D.R., and Fryer, G.J. (2005) Tsunami Generation by Submarine Mass Failure. II: Predictive Equations and Case Studies. *J. Waterways, Ports, Coastal, and Ocean Engng*. 131(6): 298-310.

Comparison of Geotexile and Geogrid Reinforcement on Unpaved Road

Jingyu Zhang[1], ASCE and Gary Hurta[2], ASCE, P.E.

[1]Geotechnical Engineer, ASCE, PhD, Golder Associates, 200 Century Parkway, Mt. Laurel, NJ 08054; PH (856)793-2005; FAX (856)793-2006; jzhang@golder.com
[2]Geotechnical Engineer, ASCE, P.E., Golder Associates, 200 Century Parkway, Mt. Laurel, NJ 08054; (856)793-2005; FAX (856)793-2006; ghurta@golder.com

ABSTRACT: Geosynthetics, such as geotextile and geogrid, are commonly used for the reinforcement of unpaved roads. The geosynthetics can reduce the thickness of aggregate required above soft subgrade and improve the durability of the unpaved road. Both geotextile and geogrid perform similar functions and often equivalently. However, the similar functions come from different reinforcement mechanisms. The reinforcement by geogrid mainly results from lateral constraint provided by interlocking between aggregate and geogrid. In contrast, geotextile functions through a number of ways, including reinforcement through interaction friction, separation between subgrade soil and base course material, filtration, and drainage. Several methods are available to design unpaved road using these two reinforcements. The focus of this paper is to review and discuss the reinforcement mechanisms from geotextile and geogrid, as well as methods used for the design of unpaved roads with the two reinforcements.

1. INTRODUCTION

Haul roads and temporary access roads are often unpaved. Unpaved roads generally are a two-layer system consisting of a subgrade and a base course. The base course is comprised of engineered fill, typically coarse aggregate. The subgrade is the original soil on site upon which the roadway is constructed. There are many cases when soil making up the existing subgrade is too weak to support the traffic loads. Conventional measures used to address soft subgrade soils include excavation and replacement with more competent fill material; consolidation of cohesive soils by preloading; deep dynamic compaction of loose, granular fill; and soil improvement by chemical mixing. These methods are effective, but could be cost prohibitive or require lengthy construction periods. The introduction of geotextile, geogrid, and geocell, led to an approach to the problem that is frequently more cost-effective than the traditional methods of subgrade improvement. By placing a geosynthetic at the interface of the subgrade and base course, not only will the performance of original subgrade be improved, but the required base course thickness can often be significantly reduced. It also is recognized that the geosynthetic reinforcements lead to low maintenance and good durability by observation of the performance and exhumed geosynthetics. As a result, reinforcement with geosynthetics has become common practice for stabilizing unpaved roads. Among the three geosynthetic reinforcements, geocell is different because it is a triplanar product, compared with the biplanar geotextile and geogrid, which indicates different mechanisms and applications. Numerous studies on the use of geotextile and geogrid in unpaved roads have been conducted during the past several decades. The similarity in function and cost makes it difficult to choose between the two reinforcements. It is the purpose of this paper to discuss the similarity and difference in them as the reinforcement, and the design methods in the unpaved roads.

2. COMPARISON OF FUNCTION OF GEOTEXTILE AND GEOGRID

2.1 Function of Geotextile in Unpaved Roads

When used in the construction of unpaved roads, geotextile can serve one or more of the following functions: separation, reinforcement, drainage and filtration.

Separation is the predominant function of the geotextile when the underlying subgrade is medium to firm (usually California Bearing Ratio or CBR greater than 3). The geotextile prevents the migration of the aggregate into the relatively soft subgrade ("stone loss") and the intrusion of subgrade soils into the aggregate. This intermixing of the two layers decreases the bearing capacity of the aggregate and reduces the thickness of base course. Yoder (1959) found that the bearing capacity of a mixture of 20 percent (by weight) subgrade with aggregate could be as low as that of subgrade.

The ability of the geotextile to provide reinforcement becomes more significant when the subgrade soil is very soft soil (CBR less than or equal to 3). By placing a geotextile at the interface of the subgrade and aggregate, the geotextile restrains lateral displacement of both upper aggregate and lower subgrade through interfacial frictional resistance. The restraint of aggregate can contribute to the reduction of the vertical deformation of base course and improved distribution of the load onto the subgrade ("slab effect").. Similarly, the restraint of subgrade can improve performance of subgrade by confinement and improved load distribution. Confinement can reduce the vertical deformation of subgrade, increase the bearing capacity from elastic limit to ultimate state (i.e. plastic limit). As a result, the failure mode changes from local shear to general shear failure. Furthermore, the inward stress at the interface introduced the geotextile can also contribute to the increase of bearing capacity. Studies (Giroud and Noiray 1981) showed that both the tangents of distribution angles for unreinforced and geotextile reinforced are in an approximate range of 0.5 to 0.7, and the difference considered minor. "Membrane support" occurs when subgrade deforms under traffic load. Geotextile will conform to the wavy shape and is stretched. It is known that stress on concave face is larger than that on the convex face. The difference in the stress is carried by the geotextile. By comparing several commercial geotextiles, Raumann (1982) indicated that use of a geotextile with a high modulus (greater than 1000 kN/m) is important for reducing the required aggregate thickness, especially for deep rutting. It was reported (Chew, et al, 2005) that pretensioning of geotextiles could improve the reinforcement by increasing the tensile modulus. However, the benefits gained by pretensioning would have to be weighed against considerations of survivability and constructability.

Filtration and drainage are secondary functions provided by a geotextile in unpaved road construction. By acting as a filter, pore water in the subgrade soils can flow into the aggregate base layer without transport of the fine subgrade soils (Hausmann, 1987), allowing subgrade soils can consolidate more quickly.

2.2 Function of Geogrid in Unpaved Roads

Reinforcement is commonly considered to be the single function of geogrid in unpaved roads. However, through selection of properly sized, well-graded aggregate, geogrid can also provide separation of aggregate and subgrade (Giroud et. al, 1985). Similar to geotextile, a geogrid provides reinforcement to the soil-aggregate system by restraint and membrane support. Two mechanisms contribute to the restraint: friction between geogrid ribs and passive resistance between transverse ribs and soil in front of them. The latter mechanism is often termed as interlocking.

2.3 Comparison of Geotextile and Geogrid Function

Compared to geotextile, the performance of geogrid is considered superior because it can provide more confinement due to interlocking mechanism and higher material modulus (Milligan and Love, 1985, Giroud et. al, 1985, Guido et. al 1986, Giroud and Han, 2004). Giroud and Han (2004) quantified the increase of bearing capacity reinforced by geogrid by using a bearing factor of 5.71 compared 5.14 for geotextile. The interlocking mechanism is thought to maximize the inward stress at the interface than pure friction provided by geotextile. Both reinforcements could improve distribution angles. Giroud et al (1985) indicates that the difference on the distribution angle on the aggregate is negligible. However, Giroud and Han (2004) embraced the difference in the equations they developed. They also indicated that the membrane effect from both geogrid and geotextile is minor if the rut depth is small. Membrane effect becomes significant only when a very large rut depth is reached. For example, for a design rut depth of 150mm, an approximate 10 percent decrease in aggregate thickness may be observed when comparing roads reinforced with geogrids with the unreinforced roads (Giroud et al, 1985).

3. DESIGN METHODS OF UNPAVED ROAD

3.1 History of Unpaved Road Design Method

The target of the unpaved design is to achieve acceptable rut depth under repeated traffic load by placing minimum thickness of base course. For most of the unpaved roads, rut depth of 50-100 mm is acceptable, although a depth up to 150 mm may be allowed in some cases. Common choice for design standards is a rut depth of 75 mm. With or without reinforcement, adequate aggregate needs to be placed so that the distributed stress on the subgrade is less than the bearing capacity of subgrade. Hammit (1970), Barenberg (1980), and Giroud and Noiray (1981) proposed different empirical equations to determine aggregate thickness without reinforcements. The concept of using geotextile as reinforcement started from the study by Barenberg et al. (1975), and Kinney (1978) at University of Illinois, Urbana-Champaign. Other early studies included Steward et al (1977), Giroud and Noiray (1981), Raumann (1982), Sellmeijer et al. (1982), to name a few. The design using geogrid reinforcement in unpaved roads appears to start about one decade later. Key studies include Milligan et al. (1985), Giroud et al. (1985), and Giroud and Han (2004). Design equations and charts are usually developed from these studies. Design charts can also be found from some manufactures. Usually, these approaches treat geotextiles and geogrids, respectively. However, Giroud and Han (2004) developed a comprehensive design equation that can embrace both two reinforcements.

3.2 Comparison of Different Methods

To compare the design methods and reinforcements, four well-used design methods are discussed: (1) Barenberg (1980), (2) Giroud and Noiray (1981), (3) Giroud et al. (1985), and (4) Giroud and Han (2006). Among them, (1) and (2) are methods for geotextile only, (3) is for geogrid only, and (4) is for both geotextile and geogrid.

Method (1) is based on the study of soil-fabric-aggregate (SFA) using Mirafi® 140, Barenberg et al. (1975), and Bender and Barenberg (1978). Barenberg (1980) revised the procedure by incorporating the fabric tension model developed by Kinney (1979). This method is the earliest approach for unpaved road design. It considered the confining effect of geotextile on the increase of bearing capacity, and membrane effect. But it does not evaluate the effect of traffic passes and based on limited tests and specific geotextiles.

Method (2) developed by Giroud and Noiray (1981) is a two-step procedure to derive the required aggregate thickness. First, the reduction of aggregate thickness, Δh, assuming no traffic (quasi-static analysis) is calculated. Then, the required thickness, h', without geotextile reinforcement under design traffic is achieved. The design thickness is the difference between h' and Δh. It is a step further compared to Method (1) because it takes the traffic load into account, although applicable only to light-medium volume (1-10,000 passages). It should be noted that the assumptions are made in the two-step procedures, i.e., Δh do not depend on traffic and h_0' does not depend on geotextile, which should be justified.

Method (3) developed by Giroud et al. (1985) might be the first procedure to design an unpaved road with geogrid. The approach is very similar to Method (2). The procedure involves two steps, with the second step to find a thickness ratio instead of the difference. The mechanisms of confinement and load distribution are accommodated in this method. It was concluded that these two mechanisms contribute equally to the reduction of the aggregate thickness. This conclusion is very different from that of Method (2), which assumed load distribution contributed by reinforcement is negligible. Furthermore, the membrane effect is considered negligible in Method (3).

Method (4) by Giroud and Han (2004) is a step forward to previous theories. They developed a comprehensive equation applicable to non-reinforced, geotextile and geogrid reinforced unpaved road.

$$h = \frac{1}{\tan\alpha}\left(\sqrt{\frac{P}{\pi r^2 m N_c c_u}} - 1\right) r \tag{1}$$

$$\frac{1}{\tan\alpha} = \frac{0.868 + (0.661 - 1.006 J^2)(r/h)^{1.5} \log N}{1 + 0.204(R_E - 1)} \tag{2}$$

$$m = (s/f_s)\left\{1 - 0.9\exp\left[-(r/h)^2\right]\right\} \tag{3}$$

Where,

h= required base course thickness (m);
$\tan\alpha$ = tangent of load distribution angle;
P = wheel load (kN);
r = radius of the equivalent tire contact area (m);
m = bearing capacity mobilization coefficient
Nc = bearing capacity factor, 3.14, 5.14, and 5.71 for unreinforced, geotextile, and geogrid-reinforced cases, respectively;
c_u = undrained cohesion of subgrade soil (kPa);
J = geogrid aperture stability modulus (mN/^{o}), 0 for unreinfocement and geotextile;
N = number of axle passages;
R_E = limited modulus ratio;
s = allowable rut depth (mm); and
fs = factor equal to 75 mm.

Using a unity equation is achieved by reducing the design into two parts: (1) distribution angle improvement by introducing a new parameter, aperture stability modulus (ASM), J. ASM is the in-plane stiffness and stability of the geogrid ribs and junctions. There is no ASTM standard for measuring this property, but can be tested by methods described by Kinney (2000), and GRI (2004). For geotextile and unreinforcement, ASM is treated as zero. (2) Bearing capacity improvement by applying proper bearing capacity factors, Nc, (Nc of 3.14, 5.14, and 5.71, are used in the equation for unreinforced, geotextile-reinforced, and geogrid-reinforced, respectively). The single step approach is straightforward and easy to use. On top of the design parameters considered by other methods, Method (4) accommodated additional design parameters that include geosynthetic stiffness, interlock between geosynthetic and base course material, strength of base course material, etc. Also, it was calibrated by a large number of laboratory cyclic plate loading tests and field wheel load tests. Therefore, it appears to be the most reliable design method. Method (4) ignores membrane effect because it is considered insignificant when rut depth less than 100mm. However, the method assumes all geotextile performs exactly the same, therefore unable to differentiate geotextiles. The equation appears to be too conservative for geotextile design because geotextile-reinforced road is treated the same as unreinforced road except an increase of bearing capacity. It is considered by some researchers that tensile modulus of geotextile could replace the ASM in order to incorporate the effect of geotexitile on distributing the stresses and to differentiate the capacity among them as well. Another reason for the conservatism of geotextile reinforcement comes from adoption of the bearing factor of

5.14, which is conservative compared to the theoretical value provide by Cox et al. (1961).

Due to the empirical or semiempirical nature of all these methods, attentions must be paid to the units used in each equation.

4. DESIGN EXAMPLE

To compare the methods presented above, an example is presented: Assume an unpaved road that will be built on subgrade soil with CBR of 1. Available aggregate has CBR of 30. Either Tensar® geogrid BX1100, BX1200 or Mirafi® geotextile 500X will be used as reinforcement. The road will be designed for both 1,000 and10, 000 passages under a 40kN wheel load with tire pressure of 550kPa. Table 1 shows the required calculated aggregate thickness by the four methods.

Table 1. Required Aggregate Thickness Calculated by Different Design Methods

Design Methods	Aggregate Thickness (m) (N=1,000)			Aggregate Thickness (m) (N=10,000)		
	Unreinforced	GT	GG	Unreinforced	GT	GG
Method (1)	0.49	0.26	N/A	0.49	0.26	N/A
Method (2)	0.53	0.4	N/A	0.7	0.57	N/A
Method (3)	0.56	N/A	0.31 (BX1100)	0.72	N/A	N/A
			0.23 (BX1200)			0.32 (BX1200)
Method (4)	0.47	0.33	0.27 (BX1100)	0.52	0.38	0.32 (BX1100)
			0.16 (BX1200)			0.19 (BX1200)

All methods show that geosynthetics are very effective at reducing required aggregate thickness. However, the results derived from these methods show large differences, especially at high traffic volume. This appears to correspond to that most research and methods are relevant to low to medium traffic volume only. It is interesting to note that there is significant difference in required aggregate thickness among the methods when no reinforcement is used. This indicates significant discrepancy exists among the design methods for unreinforced unpaved roads, which is beyond the scope of this paper. All calculation procedures show that contribution from load distribution or membrane effect is minor compared to that from improved bearing capacity at given design rut depth.

The example also shows geogrid is generally more efficient than geotextile in terms of reinforcement. Method (4) shows that the geogrid can reduce the aggregate thickness by over 60% by BX1200 and about 40% by BX1100 geogrids, compared to less than 30% induced by geotextile. The significant difference confirms superior reinforcement by interlocking mechanism provided by geogrid than shear friction from geotextile. It also shows Method (4) is the least conservative for geogrid-reinforced road design. Given the fact that all design methods served the industry satisfactorily; it appears that both Method (2) and (4) are too conservative for geotextile-reinforced design compared to Method (1).

It should be noted that all the design methods do not consider other functions (mainly separation) that are in favor of geotextile. To choose between geotextile and geogrid, reinforcement efficiency, cost, and site condition should be considered. Geogrid is more efficient than geotexile, but with relatively higher cost. As to site condition, geotextile is preferred to geogrid for medium to stiff subgrade (usually CBR>3) when separation becomes the primary function. If cost could be justified, the combination usage of both geotextile and geogrid is possible.

5. SUMMARY AND CONCLUSION

Geotextile and geogrid have been satisfactorily used on unpaved road reinforcement for decades. Geotextile could improve unpaved roads through a number of ways, i.e., separation, reinforcement, filtration and drainage. Geogird can be used only for reinforcement. Both reinforcements could contribute by increasing bearing capacity, increasing load distributing angle, and membrane effect. Geotextile improves the bearing capacity by interface friction while geogrid is mainly through interlocking mechanism. Interlocking is more efficient than interface friction. Several methods are available for the design of unpaved roads using geosynthetics. Most design methods deal with either geogrid or geotextile. Giroud and Han (2004) method can accommodate both reinforcements, and is considered the most reliable because it embraces the most design parameters and calibrated by laboratory and field tests. It appears that it is the least conservative for geogrid-reinforced design, but too conservative for the geotextile-reinforced design. Also, the equation fails to differentiate the effect from different geotextiles. The design example shows that for relatively shallow rut depth, membrane effect and load distribution effect are minor compared to improvement of bearing capacity by reinforcements. Choosing between geotextile and geogrid should depend on reinforcement efficiency, cost, and specific site condition. Generally, geogrid is more efficient in reinforcement but with higher cost.

REFERENCES

Ashmawy, A,K., and Bourdeau, P.L. (1995) "Geosynthetic-Reinforced Soils Under Repeated Loading: A Review and Comparative Design Study", *Geosynthetic International*, V. 2. N. 4, 643-668

Barenberg E.J. et al (1975) "Evaluation of Soil Fabric-Aggregate Systems with Mirafi Fabric", Civil Engineering Studies

Barenberg, E.J. (1980) "Design Procedures for Soil-Fabric-Aggregate Systems with Mirafi 500X", University of Illinois Transportation Engineering Series No. 30, UILU-ENG-80-2019

Bearden, J., and Labuz, J. (1997) "Interim Report: Fabric for Reinforcement and Separation in Unpaved Roads", Minnesota Department of Transportation

Bernder, D., and Barenberg, E.J. (1977) "Analysis of Soil-Fabric-Aggregate System", *Transportation Research Record 671*, pp.64-75

Burd, H.J., (1995) "Analysis of Membrane Action in Reinforced Unpaved Roads", *Canadian Geotechnical Journal*, V.32, 946-956

Chew, S.H., et al (2005) “Performances of Geotextile-Stabilized Unpaved Road Systems Subjected to Pretensioning”, *Geo-Frontier 2005*.

Giroud, J.P., Noiray, L. (1981) “Geotextile-Reinforced Unpaved Road Design”, ASCE, *Journal of the Geotechnical Engineering*, V. 107, I. 9, 1233-1254

Giroud, J.P., et al, (1984) “Design of Unpaved Roads and Trafficked Areas with Geogrids”, *Polymer Grid Reinforcement*, 116-127

Giroud, J.P., and Han, J. (2004) “Design Method for Geogrid-Reinforced Unpaved Roads I. Development of Design Method”, *Journal of Geotechnical and Geoenvironmental Engineering*, 775-786

Giroud, J.P., and Han, J. (2004) “Design Method for Geogrid-Reinforced Unpaved Roads II. Calibration and Application”, *Journal of Geotechnical and Geoenvironmental Engineering*, 787-797

Giroud, J.P., and Han, J. (2004) “Design Method for Geogrid-Reinforced Unpaved Roads I. Development of Design Method”, *Journal of Geotechnical and Geoenvironmental Engineering*, 775-786

Giroud, J.P. and Han, J. (2006) “Closure to ‘Design Method for Geogrid-Reinforced Unpaved Roads I. Development of Design Method’ by J.P. Giroud and Jie Han”, *Journal of Geotechnical and Geoenvironmental Engineering*, 549-551

Guido, V.A., et al, (1986) “Comparison of Geogrid and Geotextile Reinforced Earth Slabs”, *Canadian Geotechnical Journal*, V. 23, 435-440

Hausmann, M.R. (1987) “Geotextile for Unpaved Roads - A Review of Design Procedures”, *Geotextiles and Geomembranes* 5, 201-233.

Holtz, R.D., and Silvakugan, N., (1987) “Design Charts for Roads with Geotextiles”, *Geotextiles and Geomembranes* 5, 191-199

Koerner, M.R., (2005) “Designing with Geosynthetics”, fifth edition

Lapuz, J.F., and R. J.B. (2000) “Geotextile-Reinforced Unpaved Roads: Model Tests”, *Geotechnical Fabric Report*, 28-34

Leu, W. and Tasa, Luane, (2001), “Applications of Geotextiles, Geogrids, and Geocells in Northern Minnesota”, *Geosynthetics Conference*, 809-821

Love, J.P., et al (1987), “Analytical and Model Studies of Reinforcement of A Layer of Granular Fill on A Soft Clay Subgrade”, *Canadian Geotechnical Journal*, V. 24, I. 4, 611-622

Milligan, G.W.E., and Love, J.P. (1985) “Model testing of Geogrids Under an Aggregate Layer on Soft Ground”, *Polymer Grid Reinforcement*, 128-138

Oloo, S. et al, (1997) “Bearing Capacity of Unpaved Roads”, *Canadian Geotechnical Journal*, V. 34, 398-407

Simac M.R., et al, J. (2006) “Discussion of ‘Design Method for Geogrid-Reinforced Unpaved Roads I. Development of Design Method’ by J.P. Giroud and Jie Han”, *Journal of Geotechnical and Geoenvironmental Engineering*, 547-549

Steward, J., Williamson, R., & Mahoney, J. (1977) “Guidelines for Use of Fabrics in Construction and Maintenance of Low-Volume Roads,” USDA, Forest Service Report PB-276 972

Yorder, E.J. (1959) “Principal of Pavement Design”, John Wiley and Sons, Inc. New York, 21-23.

Evaluation of road subsurface drain performance by geophysical methods

Joan M. Larrahondo[1], Fikret Atalay[2], Alexander V. McGillivray[3], and Paul W. Mayne[4], M. ASCE, P.E.

[1]Graduate Research Assistant, School of Civil and Environmental Engrg., Georgia Institute of Technology. 790 Atlantic Dr, Room 252, Atlanta GA 30332. email: joan.larrahondo@gatech.edu
[2]Project Engineer, Ardaman and Associates, Inc., 3925 Coconut Palm Drive, Suite 115, Tampa, FL 33619. email: fatalay@ardaman.com
[3]Graduate Research Assistant, School of Civil and Environmental Engrg., Georgia Institute of Technology. 210 Technology Circle, Savannah, GA 31407. email: alec@gatech.edu
[4]Professor, School of Civil and Environmental Engrg., Georgia Institute of Technology. 790 Atlantic Dr, Room 241, Atlanta GA 30332-0355. email: paul.mayne@ce.gatech.edu

ABSTRACT: Infiltrated water from precipitation runoff and freeze-thaw cycles is a detrimental climatic factor affecting pavement stability. To collect and remove excess free water from pavements, road subsurface drains in the form of underdrains and edgedrains are extensively used. One objective of this study was to evaluate the performance of road subsurface drain systems by estimating water contents in pavement and subgrade via two geophysical methods. At three road locations in the State of Georgia, volumetric water contents were calculated from the results of ground penetrating radar (GPR) and low-frequency electromagnetic induction (EM). Water contents were estimated assuming that pavement materials, subgrade characteristics, and water ionic concentration were constant throughout each site area. Thus, contour maps of infiltrated water content in each finite ground volume were prepared. The majority of pavement sections where road subsurface drains were clogged or damaged showed high water contents and vice versa. These results suggest the effectiveness and quickness of geophysics to capture the variability of infiltrated water content during site investigations.

INTRODUCTION

Excessive moisture in pavement structures has been recognized as a major cause of many types of pavement failures, such as extensive cracking due to loss of subgrade support in flexible asphalt pavements and faulting and associated pumping in rigid concrete pavements (Christopher & McGuffey, 1997). To prevent these failures, road subsurface-drain systems are constructed to capture, conduct and dispose of infiltrated water. These systems are typically edgedrains and underdrains. Edgedrains are corrugated perforated high-density polyethylene (HDPE) pipes embedded in a clean-aggregate packing, which in turn is wrapped in geotextile filter. Edgedrains can run either along the edge of pavement or under the shoulder or curb. Underdrains include transverse drains and other permeable-base systems. (Christopher, 2000)

Subsurface drains can fail either structurally or functionally. Structural failures occur when components of the system are physically damaged, e.g., mowers cutting off edgedrain outlets, or pipes crushed by heavy equipment. Functional failures develop when one or more components of the system are not performing their intended operation, e.g., clogged pipes, or siltation of aggregates.

Traditional subsurface-drain assessment has been based upon direct excavation to see whether a drain is structurally or functionally damaged. However, these procedures are time-consuming, and often costly, as the drain system must be reconstructed after examination, thus disrupting traffic and accessibility.

Few studies have attempted to use non-invasive, non-destructive techniques such as Ground Penetrating Radar (GPR) prospection to correlate underdrain offset and clogging in highways (Maser and Weigand, 2005). Also, GPR has been extensively employed during non-destructive locating and testing of tubes (e.g., Daniels and Schmidt, 1995). In this study, a different subsurface-drain assessment approach is explored whereby results from GPR and EM (electrical-conductivity meter) are used to estimate water contents in the base layer and subgrade of pavement. Then, a failure criterion is defined such that relatively-high water contents in pavement sections with drains indicate drainage problems. Finally, these results are correlated to actual subsurface drain conditions.

GEOPHYSICAL METHODS

Two geophysical testing methods were applied to three pavement sections in Georgia: Ground Penetrating Radar (GPR) and Low-frequency Electromagnetic Induction (EM).

The GPR was an air-launched, PulseEkko IV device (Sensors and Software, Inc.) with a pair of 200-MHz antennae. A constant 5-cm off-the-ground distance and a constant 0.5-m antennae spacing were kept during all the surveys. Signal stacking was set at 16 to improve the signal-to-noise ratio. The vertical resolution was about 12.5 cm which was acceptable enough for the objective of this study, though not for estimating accurate pavement layer thicknesses. Volumetric water-content calculations followed the method proposed by Maser and Scullion (1991).

The EM was a Geonics-Limited EM31 conductivity meter, able to measure electrical conductivities between 10^1 and 10^3 mS/m at both 3-m and 6-m depth ranges. To get volumetric water-contents, a modified version of Archie's Law was invoked following the procedures by McNeill (1980) and Rhoades et al. (1976).

It is paramount to note the following two facts: first, water contents were estimated assuming that everything else remained constant throughout each site, i.e., pavement materials, subgrade characteristics, and water ionic concentration. Second, both GPR- and EM-based volumetric water contents are not necessarily exact due to the absence of actual electrical-conductivity and water-content measurements at the depth range of the equipments, which are indeed variables of the models employed. Nevertheless, the results are sufficient to map out the hydraulic behavior of a given road drain site.

STUDY SITES, RESULTS AND DISCUSSION

Three road subsurface drain locations in the State of Georgia were selected for study near the cities of Cairo, Macon, and Waycross. All three sites were maintained by the Georgia DOT District and were located in the Atlantic Coastal Plain. The sites contained flexible-asphalt pavement in semi-rural environments and had shown either pavement distress and/or excess-water conditions. Also, in all cases, in-situ data were obtained after slight-to-moderate rain events, typically the night before the test day. Thus, sufficient time was allowed for the infiltrated water to be captured by the subsurface drains. For additional site details, refer to Larrahondo et al. (2007).

Location 1: District 4 (Tifton), Area 7 (Cairo)

In this road section near Cairo GA, severe pavement distresses were first reported before the subsurface-drain installation. The section was then reconstructed and provided with edgedrains, though the road pavement failed again. The approximate distressed area is 1000 m^2. Seismic cone penetration test (SCPT) and flat dilatometer test (DMT) were also performed at the site for geotechnical characterization purposes, yielding that the top 3 m of the soil subgrade correspond to clay to clayey silt. The site coordinates are 30.88288°N, 84.31785°W.

The interpreted water content results from GPR and EM for this site are shown in FIG. 1 (all contour maps were plotted using Surfer V.8 by Golden Software). The GPR and EM obtain data at very different depth ranges. GPR-based water contents represent the conditions at the top layers, i.e., surface and base layers, up to about 0.3 m of depth. Meanwhile, EM-based water contents represent either a 3-m or a 6-m depth, adjustable depending upon the application. Thus, EM results are an “average” of the conditions of the top 3 m or 6 m of subgrade soil. This approach including two depth ranges allows one to study the whole pavement-and-soil profile of interest.

The GPR-based results (FIG. 1a) show zones of relatively low water content of the pavement base along the edge of the curb where the edgedrain is. This observation suggests adequate functioning of the subsurface drains in this rather narrow region. However, this figure also indicates relatively high water content beneath the patched area of the westbound lanes where severe pavement distresses have occurred in the past. This result suggests that either the current capacity of the subsurface drains may be insufficient to serve the site (and possibly transverse drains are needed), or that there are fines clogging the base material, thus preventing water from being captured by the edgedrain. Furthermore, water contents decrease away from the patched zone.

The EM water-content map (FIG. 1b), averaging up to 3 m of depth, basically shows a continuous increase of volumetric water content towards the west end of the section. This possibly corresponds to topographic change since elevation decreases towards the west. This indeed affects the groundwater regime on a local fashion.

Location 2: District 3 (Thomaston), Area 4 (Macon)

This Macon GA road section showed evidence suggesting that the pavement was working under water-saturated conditions due to possible drain clogging and/or capillarity, as free water was emanating from the asphalt surface. (see FIG. 2)

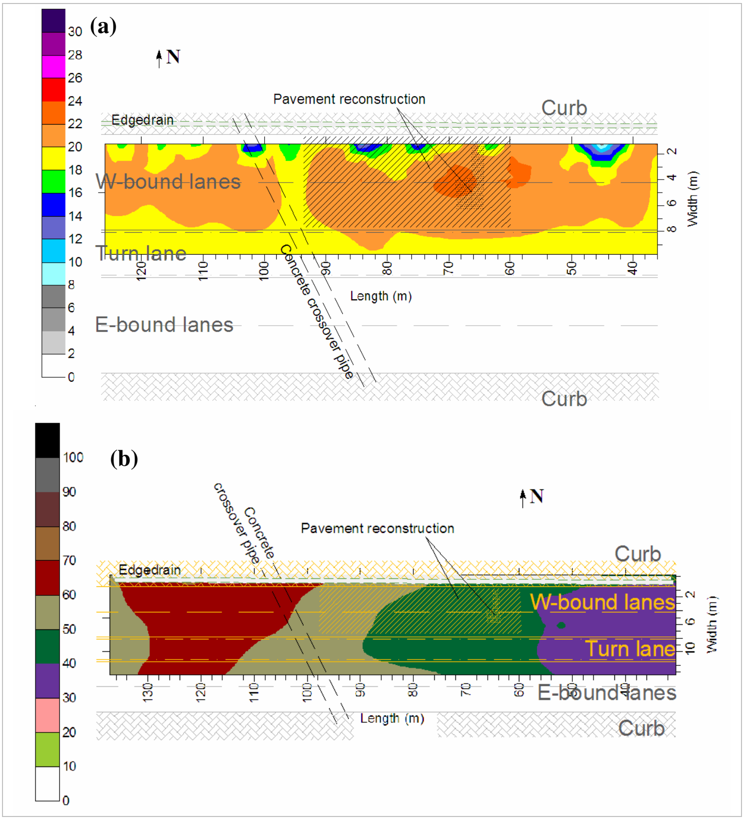

FIG. 1. Volumetric water-content maps at Cairo, GA site: (a) GPR-based, (b) EM-based (3-m induction depth). Color bar represents %

FIG. 2. Left: Macon GA site view. Right: Old GDOT pavement sampling hole ejecting underground water. This suggests water saturation of the pavement.

Interestingly, when this was observed, no water was simultaneously flowing in the actual subsurface drain system. (Mayne et al, 2006) A clay wall also exists running under the edge-of-pavement. The SCPT-interpreted soil types suggest primarily clays to a depth of 2.6 m at this site, underlain by sandy clayey silts to a final exploration depth of 3.2 m. The site coordinates are 32.89947° N, 83.70798°W. See FIG. 3.

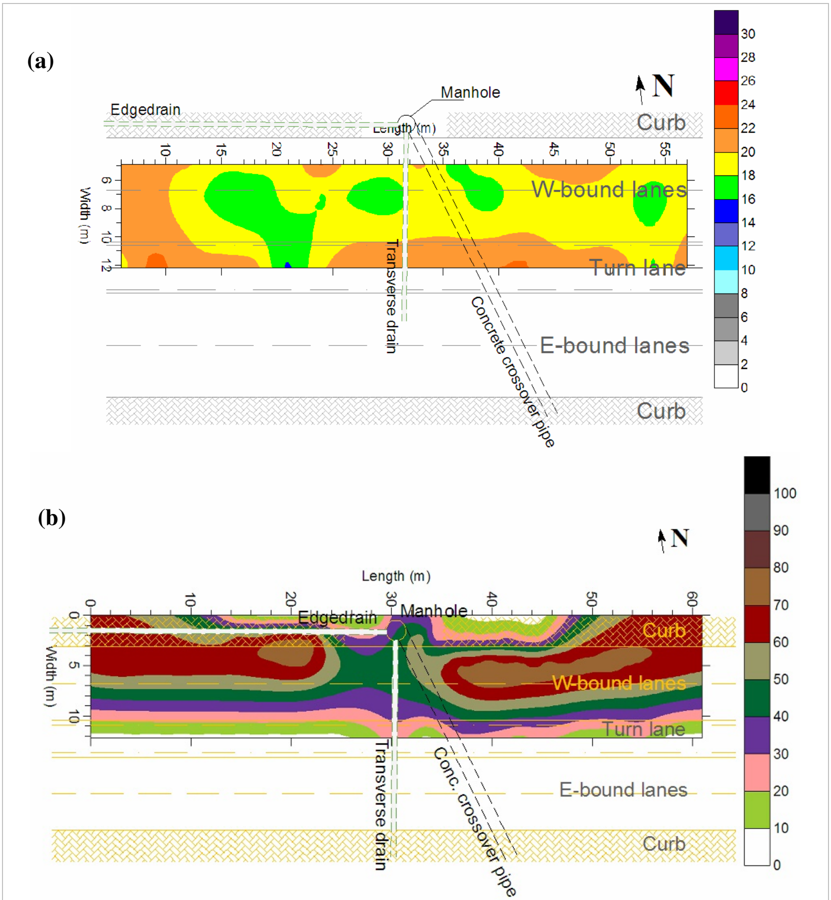

FIG. 3. Volumetric water-content maps at the Macon GA location: (a) GPR-based, (b) EM-based (3-m induction depth). The color bar represents %.

The GPR-based map (FIG. 3a) indicates relatively high water contents in the base course near the curb. Water content also increases toward the west side of the section and on the turn lane. These moisture increments can be correlated to drain clogging, and are indeed consistent with the findings of a drain video inspection of the site (see

Larrahondo et al., 2007). This video inspection showed clogging of the transverse drain towards the turn lane as well as slight clogging of the longitudinal edgedrain.

The EM-based water-content map (FIG. 3b) represents up to 3 m of depth, showing peaks of water content underneath the next-to-curb lane. Moisture then decreases towards the curb and the turn lane. These results suggest water accumulation because of the edge-of-pavement clay wall. This accumulated water can eventually reach the top layers and is likely to contribute to saturate the overlying pavement structure.

Location 3: District 5 (Jesup), Area 2 (Waycross)

This road section near Waycross and Nahunta GA failed before subsurface drains were installed. Upon reconstruction, edgedrains were provided. This location is next to a retention pond. SCPT and DMT investigations on the top 3 m suggest a mainly sandy soil profile with some thin silty layers. The site coordinates are 31.19636°N, 81.98241W°.

The GPR-based map (FIG. 4a) shows contrast between the drier east and the wetter west pavement sections. Two facts can support these observations (note the position of the edgedrain): the edgedrain showed clogging related to lack of maintenance; also, capillary rise is possible due to the water table imposed by the retention pond.

The EM-based map (FIG. 4b) basically represents the hydraulic gradient generated by the nearby pond and other external sources of water. At the left-hand side of this map, water content decreases towards the north, away from the pond. Also, there appears to be a high hydraulic head coming from the east.

CONCLUSIONS AND LIMITATIONS

Series of GPR and EM geophysical tests conducted at three distressed or saturated pavement sites in Georgia demonstrate that these methods are able to infer the variability of subsurface water content at road subsurface drain locations. Geophysics thus appear viable for assessing the behavior of drain systems indirectly, depending on resolution and depth range. In fact, it is expected to find relatively high water contents beneath pavement sections provided with underdrains that may not be performing properly.

A trenchless, contour-map-based approach for road drain-system assessment was presented to facilitate visual interpretation and implementation of remedial measures. Geophysics allows for quick evaluation without the need to either dismantle the operations or disrupt traffic flow and accessibility.

The volumetric water contents interpreted from the geophysical GPR and EM surveys presented herein deserve further calibration and validation. The value of the approach is in the display of the variability and relative contrast of their readings. It is indeed recognized that additional factors affect the water contents beneath a pavement system and/or the geophysical interpretation of GPR and EM data. These factors include soil type, fines content, capillary suction of the layers, degree of saturation, and salinity of the underground water. Some of these factors are beyond the scope of this study and should be the topic of further research, particularly via sensitivity analyses.

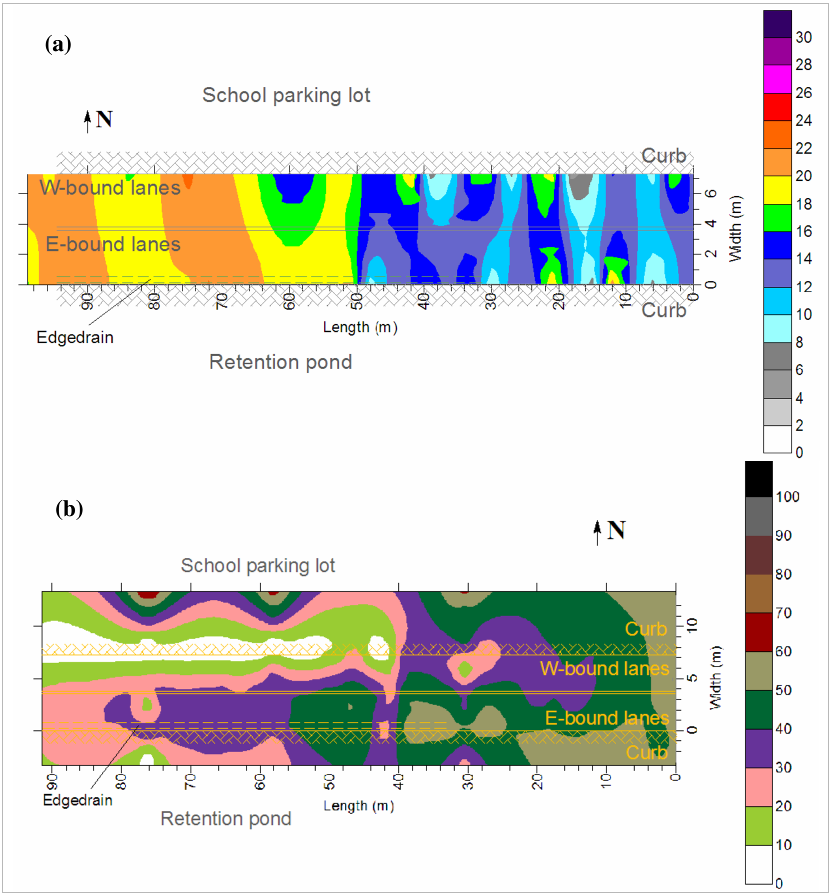

FIG. 4. Volumetric water-content maps at Waycross location: (a) GPR-based, (b) EM-based (3-m induction depth) The color bar represents percentage.

ACKNOWLEDGMENTS

The authors appreciate the support of the Georgia Department of Transportation and the Georgia Transportation Institute.

REFERENCES

Christopher, B.R., and McGuffey, V.C. (1997). *Pavement Subsurface Drainage Systems*, NCHRP Synthesis of Highway Practice 239, Transportation Research Board, National Research Council, Washington, D.C.

Christopher, B.R. (2000). *Maintenance of Highway Edgedrains*, NCHRP Synthesis of Highway Practice 285, Transportation Research Board, National Research Council, Washington, D.C.

Daniels, D. and Schmidt, D. (1995). “The use of ground penetrating radar technologies for non-destructive testing of tubes”. *International Symposium on Non-Destructive Testing in Civil Engineering*. Berlin, Springer Netherlands, Dordrecht, pp. 429-436

Larrahondo, J. M., Atalay F., McGillivray, A.V., and Mayne, P.W. (2007). *Assessing Highway Drain Performance in Georgia. Technical Report on Primary Drain Sites,* GDOT Project No. B-02-662. GTI Fund No. R6038, CEE Project No. E-20-K86. Atlanta, GA, Georgia Dept. of Transportation, Office of Materials & Research, R&D Branch, Forest Park, Georgia,188 pages.

Maser, K.R. and Scullion, T. (1991). “Automated Detection of Pavement Thicknesses and Subsurface Moisture Using Ground Penetrating Radar”, *Proc. of the Fifth International Conference on Ground Penetrating Radar*, Vol. 2, 423-432.

Maser, K.R., and Weigand, R.S. (2006). “Ground Penetrating Radar Investigation of a Clogged Underdrain on Interstate I-71”. Paper presented at the 85th Annual Meeting of the Transportation Research Board, Washington, DC.

Mayne, P. W., Larrahondo, J. M., Atalay F., McGillivray, A., and Ashiqueali, B. (2006). *Assessing Highway Underdrain Performance in Georgia. Interim Report on Reconnaissance Visits*. GDOT Project No. B-02-662. GTI Fund No. R6038, CEE Project No. E-20-K86. Atlanta, GA, Georgia Dept. of Transportation, Office of Materials & Research, R&D Branch, Forest Park, Georgia, 165 pages.

McNeill, J. D. (1980). “Electrical conductivity of soils and rocks.” Geonics Limited, Mississauga, ON, Canada. http://www.geonics.com/pdfs/technicalnotes/tn5.pdf

Rhoades, J.D., Raats, P.A.C., and Prather, R.S. (1976). “Effects of liquid-phase electrical conductivity, water content, and surface conductivity on bulk soil electrical conductivity”. *Soil Sci. Soc. of America Jour.*, 40, pp. 651-665.

Evaluation of Surface Infiltration Rate of Permeable Sidewalks under Rainfall

Fen Ye[1], Xiao-yang Jia[1], and Jie Han[2]

[1] Key Laboratory of Road and Traffic Engineering of the Ministry of Education, Tongji University, Shanghai 200092, China, yefen@mail.tongji.edu.cn

[2] Associate Professor, Department of Civil, Environmental, and Architectural Engineering, the University of Kansas, Lawrence, KS 66045, USA, jiehan@ku.edu

ABSTRACT: Sidewalks are the important part of city streets and their performance greatly influences the convenience and safety of pedestrians. To ensure the safety of the pedestrians under rainfall and prevent sidewalk and driveway structures from being eroded by water, sidewalk structures must be well designed and constructed, such as the use of permeable sidewalks. This paper discusses a pavement structure with an inner drainage system, which can allow the rainwater to infiltrate through sidewalk cracks, joints, and/or slab pores. One important parameter, which controls the performance of such a sidewalk, is the surface infiltration rate. Limited studies have been conducted in the past on this parameter and no definite method is available in terms of how to evaluate the surface infiltration rate of permeable sidewalks. In this study, different laboratory tests were conducted on permeable interlocking brick sidewalks and test data were analyzed for the surface infiltration rate. In addition to the laboratory study, one permeable sidewalk was constructed in the field and monitored for one and half years to measure its surface infiltration rate. The test results indicate that the surface infiltration rate of permeable sidewalks should always be higher than $7cm^3/h\cdot cm$ so that the sidewalks can drain freely under rainfall.

INTRODUCTION

An Environment-Friendly (EF) sidewalk should have nice appearance, excellent functions and safety, and a friendly environment to pedestrians. To ensure reasonable performance, the sidewalk should have a good drainage system, which can drain out water immediately after rainfall. Any unacceptable drainage system would reduce the service life of the sidewalk and cause inconvenience to pedestrians. If water enters the sidewalk structure and remains in the system for a long time period, it will erode or soften subgrade and subbase of the sidewalk, and eventually reduce the load-bearing capacity of the sidewalk.

Surface infiltration rate is one of the important parameters used to evaluate the drainage capability of the sidewalk. However, limited studies have been conducted in the past on this parameter and no definite method is available in terms of how to evaluate the surface infiltration rate of permeable sidewalks. In this study, three experimental methods were adopted to measure the surface infiltration rate: infiltrometer test, indoor, and field rain simulation tests.

BASIC THEORIES FOR THE ABILITY OF SIDEWALK DRAINAGE

Velocity of Filtration

The velocity of filtration is an average rate of water flow through a cross section of a test specimen within a certain time period, which is commonly used to quantify the drainage capacity of a pavement. The velocity of filtration can be expressed as:

$$v_{pr} = \frac{Q}{At} \tag{1}$$

where v_{pr} is the velocity of filtration, Q is the total quantity of filtration, A is the cross-section area of the specimen, and t is the seepage time.

The velocity of filtration can be used to describe the drainage capacity of a permeable sidewalk or an ordinary pavement. This parameter is suitable for a pavement without any joint, such as flexible pavements but it can also be used to evaluate the drainage capacity of a permeable brick sidewalk.

Darcy's Law

Suppose that water flow in soil is laminar, the quantity of water flow can be calculated based on Darcy's law as follows:

$$q = kA\frac{\Delta h}{d} = kAi \tag{2}$$

where k is the permeability, i is the hydraulic gradient, A is the discharge area, and Δh is the head loss.

The study done by National University of Singapore (NUS) (Fwa et al., 1999) showed that water flow in the permeable asphalt mixture is turbulent; therefore, a modified Darcy's equation should be used:

$$v_{pr} = ki^m \tag{3}$$

where k is the permeability and $k = -89.1 + 5.840e$ (cm/s), e is the void ratio of the mixture, and m=0.696. However, the index, m, depends on the type of drainage material. Therefore, Eq. (3) should be further evaluated based on the actual condition. It is assumed herein that the dimension of each sidewalk brick is same and the head loss for each brick is equal. Under these conditions, the hydraulic gradient is a constant. As a result, the velocity of infiltration through brick joints can be estimated through an indoor experimental study.

Considering the possible turbulent flow in permeable pavements or sidewalks, the modified Darcy's equation should be used to evaluate the drainage capacity of pavements or sidewalks. Even though modified Darcy's law is more appropriate from the theoretical point of view, it is more convenient to use a surface infiltration rate to evaluate the drainage capacity of sidewalks.

Surface Infiltration Rate

The surface infiltration rate can be determined using different experimental methods. The rate measured by an infiltrometer can be calculated as follows:

$$I_c = \frac{Q \times 3600}{t \cdot l} \tag{4}$$

where I_c is the surface infiltration rate (cm^3/h·cm), Q is the quantity of water flow during the time t (ml), t is the time of infiltration (s), and l is the length of a joint that the infiltrometer covers.

In this study, the surface infiltration rate was determined through experimental tests based on the drainage capacity in unit length. This parameter is suitable for pavements with regular joints, such as PCC and permeable pavements. In addition, it can be used to evaluate the pavements with permeable bricks.

Maximum Allowable Intensity of Rainfall

In order to design permeable pavements, it is also needed to know the maximum allowable intensity of rainfall. Based on the condition of a road, the maximum allowable intensity of rainfall can be estimated using the following equation (Yan, 2001):

$$r = \frac{3600 \times v_c \times d}{L} \tag{5}$$

where r is the intensity of rainfall (mm/h); v_c is the velocity of water flow in the drainage layer (mm/s), d is the thickness of drainage layer (m), and L is the width of the road (m).

This relationship can also be used to determine the allowable velocity of water flow in the permeable sidewalk based on the predicted maximum intensity of rainfall.

INTERLOCKING PERMEABLE SIDEWALKS

In this study, interlocking permeable sidewalks were used for experimental studies. They consist of five components:

(1) Interlocking brick pavement. Generally, the thickness of interlocking bricks is approximately 6 - 8cm. In this study, 6cm thick anti-skiing interlocking bricks were used.
(2) Sand layer. The sand layer has three functions: to provide a smooth surface for bricks, allow the bricks to sink into the sand layer, and act as a drainage layer. In this study, the width of joints was 3mm and the thickness of the sand layer was 3cm.
3) Stone chip filter course. To prevent fine particles from migrating into the permeable base, a filter layer was needed. At the same time, it was used as the leveling course. This filter layer was 3cm thick in this study.
4) Supporting layer. The supporting layer used in this study was a cement treated permeable base (CTPB) or semi-rigid permeable concrete base. The thickness of this layer was 6cm.

INDOOR SIMULATION TEST

As discussed earlier, the surface infiltration rate is suitable for interlocking permeable sidewalks and can be directly and quickly measured. Therefore, it was selected as a parameter to be measured in this study. Three different indoor simulation tests were conducted in this study and are presented below.

Infiltrometer Method

An infiltrometer with an inner diameter at the base of 15 cm was used in this study. The test section with an area of 80.9cm x 101.5m included a 3cm thick stone chip layer, a 3cm thick sand bed course, and 40 bricks (19.8 cm long × 9.8cm wide and placed with the joint width of 0.3cm) as shown in Figure 1. The test section was bordered with timber beams.

The surface infiltration rate can be calculated using Eq. (4). The length of joints covered by the infiltrometer was 30cm, which is 2 times the inner diameter of the infiltrometer base. During the tests, the center of infiltrometer was at the intersection point of two joints. The calculated surface infiltration rates based on test data and Eq. (4) are listed in Table 1.

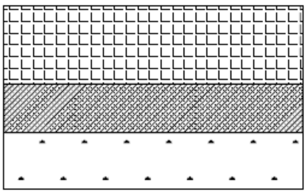

FIG. 1. Cross section of the sidewalk for testing

Table 1. Test results from the infiltrometer tests

Test method	Point	Quantity of seepage (ml)	Time of seepage (s)	Infiltration rate (cm^3/h·cm)	Average value of infiltration rate (cm^3/h·cm)
No.1	1	400	59.27	810	679
	2	400	74.66	643	
	3	400	73.98	649	
	4	400	78.15	614	
No.2	1	400	38.49	1871	1928
	2	400	29.6	2432	
	3	400	48.59	1482	

There were two test methods, in which test method No.1 followed the procedure discussed above. During the tests, however, it was found that water flew out of the joints, which differ from the real situation. A modified method, i.e., test method No.2, was added. In these tests, 3cm thick sand layer was placed on a geotextile sheet and 32 pieces of bricks were placed after. The total brick area was 80.9cm×81.3cm, each brick having its dimensions of 19.8 cm long × 9.8cm wide and the joint width of 0.3cm. It is shown in Table 1 that the average infiltration rate from test method No. 1 was approximately 1/3 that from test method No.2.

Indoor Rainfall Simulation Test

The results obtained by the above two infiltrometer tests show large deviation. This deviation may result from the small measurement area, excessive water head, and sealing of the infiltrometer. Therefore, an indoor rainfall simulation test was also used to measure the surface infiltration rate of sidewalks. The pavement structure in the indoor rainfall simulation test is the same as that used in method No.2 as discussed earlier. Clark et al. (1979) obtained good test results on measuring the infiltration rate of interlocking brick pavements using a water spray method. A water spray system controlled by a valve was used in this study to simulate different rainfall intensities. Equation (5) was modified to calculate the surface infiltration rate as follows:

$$I_c = \frac{q \times t_q \times 3600}{t \cdot l_A} \tag{6}$$

where I_c is the surface infiltration rate (cm^3/h·cm), q is the flow rate of the water spray system simulating rainfall (ml/min), t_q is the time of spraying (min), t is the time of seepage (s), and l_A is the length of brick joints (equal to 1134.6cm). The results of this test are listed in Table 2.

Table 2. Results of indoor rainfall simulation test

Point	Flow rate of spray (ml/min)	Time of spraying (min)	Time of seepage (s)	Infiltration rate (cm^3/h·cm)	Average value of infiltration rate (cm^3/h·cm)
1	1000	3	380	25	25
2	1000	3	390	25	
3	4000	3	1614	24	

The surface infiltration rate measured in the rainfall simulation test is much closer to that in the field situation than the infiltrometer method because this rainfall method can simulate the field condition much better.

FIELD SIMULATION

Test Procedures

An actual pavement was selected for the field simulation test. The following test procedures were used:

1) Cleaned the surface of the sidewalk and joints between bricks with high pressure water;
2) Built a temporary dam to form a measuring area of $13.66m^2$;
3) Filled water into a measuring area for approximately 20 minutes. The deepest water depth was 10.2 cm at Point 1; the water depth at the edge of the vegetated area (Point 2) was 8.6cm, and the water depth at the edge of the sidewalk (Point 3) was 1.9cm; and
4) Measured the rate of water flow from the collection pipe after the flow was stable for 5 minutes.

Measured Surface Infiltration Rate

The surface infiltration rate was obtained based on the water depth at each control point and the flow rate in the collection pipe. The surface infiltration rate was calculated using the following equation:

$$I_c = \frac{q_c \times 60}{l_A} \qquad (7)$$

where I_c is the surface infiltration rate ($cm^3/h \cdot cm$), q_c is the flow rate of water seeping into the sidewalk (ml/mim), and l_A is the total joint length of the brick sidewalk (cm), which can be calculated as $13.66m^2 \times 17.13m/m^2 \approx 2.34 \times 10^4 cm$.

The test results are listed in Table 3, which shows that the measured surface infiltration rate from this field test was less than that from the indoor rainfall simulation test ($25cm^3/h \cdot cm$). The lower infiltration rate from the field test may result from the blocked joints of bricks by soil during the service. Based on the rainfall intensity in Shanghai (2.0mm/min for 10 minutes per every 5-year chance), the required surface infiltration rate is approximately $7cm^3/h \cdot cm$ assuming rainwater only draining through brick joints. Therefore, the tested pavement had slightly lower surface infiltration rate than the required.

Table 3. Test results from the field simulation test

No.	Depth of water in control point(cm)			Time (hh:mm)	Flow in PVC (ml/min)	Flow in sidewalk q_c(ml/min)	Measuring time (s)	Infiltration rate (cm^3/h·cm)	Average infiltration rate (cm^3/h·cm)
	1	2	3						
1	10.2	8.6	1.9	14:06					
2	10.1	8.6	1.9	14:08	150	2277	60	5.84	6.23
3	10.0	8.5	1.8	14:13	150	2732	60	7.01	
4	9.9	8.4	1.8	14:17	150	2277	60	5.84	

CONCLUDING REMARKS

The infiltrometer tests and the indoor simulation test on the same pavement show that significant difference existed in the measured surface infiltration rate between these two test methods. The indoor and field rainfall simulation tests yielded close surface infiltration rates to the required rate based on the rainfall condition in Shanghai, China. Based on the rainfall intensity and pavement structures in Shanghai, it is recommended that the surface infiltration rate of a permeable sidewalk should remain higher than 7cm^3/h·cm during a service period. Under these conditions, a permeable sidewalk should be able to satisfy the drainage requirement to be an environment friendly one in Shanghai.

REFERENCES

China Architecture and Building Press (1998). *Specifications for Construction and Acceptance of Interlocking Brick Pavements* (CJJ 79-98), Beijing, in Chinese.

Clark, R.A., Ferziger, J.H., and Reynolds, W.C. (1979). "Evaluation of Subgrid-Scale Models using an Accurately Simulated Turbulent Flow." Journal of Fluid Mechanics, 91, 1-16.

Fwa, T.F., Tan, S.A., and Guwe, Y.K. (1999). "Laboratory Evaluation of Clogging Potentials of Porous Asphalt Mixtures." *Transportation Research Record*, 1681, 43-49.

Shanghai Municipal Engineering Administration (1999). *Specifications for Construction and Acceptance of Color Sidewalks* (SZ-05-99), in Chinese.

The People's Communications Press (1997). *Specifications of Drainage Design for Highways* (JTJ 018-97), Beijing, in Chinese.

Yan, Jun (2001). *Research on Performance of Porous Asphalt Mixtures*, Tongji University, in Chinese.

Numerical Simulation of Influence of Climatic Factors on Concrete Pavements Built on Expansive Soil

Xiong Zhang[1], A.M. ASCE and Juanyu Liu[2], A.M. ASCE

[1]Assistant Professor, Department of Civil and Environmental Engineering, University of Alaska, Fairbanks, AK 99775-5900, Email: ffxz3@uaf.edu
[2]Assistant Professor, Department of Civil and Environmental Engineering, University of Alaska, Fairbanks, AK 99775-5900, Email: ffjl@uaf.edu

ABSTRACT: Expansive soils beneath the concrete pavements can cause distresses in pavements under the influence of climatic factors. This article presented a complete system aimed at simulating the soil-rigid pavement system and its responses to daily weather conditions. The weather data included rainfall, solar radiation, air temperature, relative humidity and wind speed, all of which are readily available from a local weather station or the internet. These data were used to determine the flux boundary conditions for the simulation. A coupled hydro-mechanical stress analysis was used to simulate the volume change of expansive soils due to both mechanical stress and water content variations. Coupled hydro-mechanical stress jointed elements were used to simulate the interaction between the soil and the concrete slab, contour integral evaluation was used to determine the possibility of cracking occurrence. These models were combined to a single system to predict the rigid pavement behavior for which some conclusions were derived.

INTRODUCTION

The volume of an unsaturated expansive soil changes significantly when the soil is subjected to moisture variations. Cyclic swelling and shrinking of soils in response to seasonal weather variations often causes distress in both concrete and asphalt pavements due to lane/shoulder dropoff (as shown in Fig. 1), resulting in substantial discomfort, safety hazard and vehicle damage. This problem has been reported worldwide, including the United States, Australia, Canada, China, India, Israel, and South Africa, among others (Chen 1988). In Texas, more than half of the total damage due to the highways and streets is caused by expansive soils, which costs the Texas Department of Transportation millions of dollars in repairs every year (Prozzi and Luo 2007). Hence it is of significant importance to investigate the influence of climatic factors on the behavior of pavements. Predicting the behavior of pavements built on expansive soils under the influence of climatic factors requires knowledge in disciplines such as agricultural engineering, hydraulic engineering, unsaturated soil mechanics, structural engineering and fracture mechanics. In the past

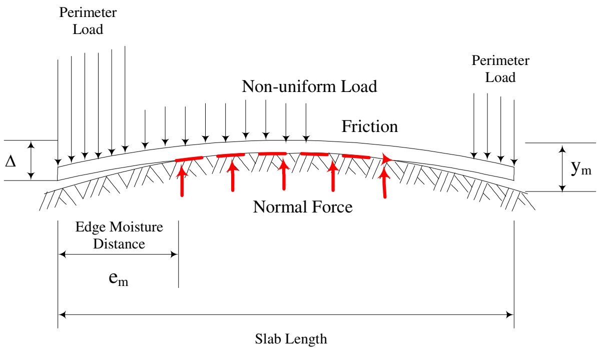

Fig.1. Typical Damage Modes Caused By Expansive Soils

thirty years great progress had been achieved in all these disciplines. However, most researchers worked independently in their own fields and the theories had not been combined to solve this problem. Researchers still lack a quantitative understanding of soil and structure behaviors in a given climate. Zhang (2004) utilized simple and readily available historic weather data such as daily temperature, solar radiation, relative humidity, wind speed, and rainfall as the input. Accurate three dimensional predictions are obtained by integrating a number of different analytical and numerical techniques: different simulation methods for different boundary conditions such as trees, grass, and bare soils, coupled hydro-mechanical stress analysis to describe deformation of saturated-unsaturated soils, coupled hydro-mechanical stress jointed elements simulation of soil-structure interaction, analysis of structure stress by general shell elements, and assessment of structure damage by the smeared cracking model. The proposed system can also be used for the simulation of behavior of rigid pavements built on expansive soils. This research is undertaken to study the effect of climatic factors on possibility of cracking occurrence in a rigid pavement constructed on expansive soils using the proposed system.

A COMPLETE SYSTEM OF INFLUENCE OF CLIMATIC FACTORS ON CONCRETE PAVEMENTS BUILT ON EXPANSIVE SOIL

The soil near the ground surface is greatly influenced by the environment. A soil gains water through rainfall infiltration and loses water by direct evaporation from the soil surfaces or transpiration from trees or vegetation. The infiltration rate can be estimated from the rainfall data while the evaporation and/or transpiration are determined by the weather conditions. Two steps are involved in the evapotranspiration, the first step is water vaporization and the second is vapor removal. Energy is required to change the state of the molecules of water from liquid to vapor. Direct solar radiation and the ambient temperature of the air provide energy required for changing the state of the molecules of water from liquid to vapor. The driving force to remove water vapor from the evaporating surface is the difference between the water vapor pressure at the evaporating surface and that of the surrounding atmosphere determined by the relative humidity in the air. The replacement of the saturated air with drier air depends greatly on wind speed. Hence, radiation, air temperature, air humidity and wind terms must be considered to estimate evapotranspiration. Other factors such as the soil permeability, soil water salinity (which is related to osmotic suction), and the characteristic of tree and vegetation also influence the evapotranspiration rate significantly. Zhang (2004) proposed the use of the FAO 56 (Food and Agriculture Organization of the United Nations) Penman-Montieth method (Allen et al. 1998) to determine the boundary conditions for the simulation of the influence of climatic factors on foundation on expansive soils. The FAO 56-PM method is a method to predict an hourly or daily evapotranspiration (ET). In a first step, it makes use of an ET equation for a reference grass surface. The FAO 56 PM equation is:

$$ET_0 = \frac{0.408\Delta\left(R_n - G\right) + \gamma \dfrac{900}{T+273} u_2 \left(e_s - e_a\right)}{\Delta + \gamma\left(1 + 0.34u_2\right)} \tag{1}$$

Where ET_0 =reference evapotranspiration (mm day^{-1}); R_n =net radiation at the crop surface (MJ m^{-2} day^{-1});G =soil heat flux density (MJ m^{-2} day^{-1});T= air temperature at a 2 m height (°C);u2 =wind speed at a height of 2 m (m s^{-1}); e_s =saturation vapor pressure (kPa); e_a =actual vapor pressure (kPa); Δ =slope of saturation vapor pressure versus temperature curve (kPa °C^{-1}); and γ =psychrometric constant (kPa °C^{-1}).

If the real conditions such as vegetation types, ground cover, canopy, aerodynamic resistance, are different from the reference grass conditions, the evapotranspiration will be different. In addition, the actual evapotranspiration in the field may be lower than the maximum possible evapotranspiration if the vegetation are under non-optimal conditions or the total suction in the soil is too high. The actual evapotranspiration , $ET_{c\ adjusted}$, is therefore determined by the following equation:

$$ET_{c\ adjusted} = Ks \times Kc \times ET0 \tag{2}$$

Where K_c = crop coefficient (dimensionless)for different vegetation types and K_s = water stress coefficient for different soils.

The volume of an expansive soil at a certain depth is mainly influenced by the mechanical stress and moisture (pore water pressure) variation whereas the other factors such as temperature, salt concentration and pore air pressure usually remain constant and their influences are negligible. If the evapotranspiration process at the soil-atmosphere interface can be determined, the soil behavior can be simulated by a coupled hydro-mechanical stress analysis. The governing differential equations for the volume change of an expansive soil, which is a fully coupled hydro-mechanical stress problem, are as follows (Zhang and Briaud. 2006):

$$\left(\lambda + G\right)\frac{\partial \varepsilon_v}{\partial x} + G\nabla^2 u - \left(3\lambda + 2G\right)\alpha \frac{\partial\left(-u_w\right)}{\partial x} + X = 0 \tag{3a}$$

$$\left(\lambda + G\right)\frac{\partial \varepsilon_v}{\partial y} + G\nabla^2 v - \left(3\lambda + 2G\right)\alpha \frac{\partial\left(-u_w\right)}{\partial y} + Y = 0 \tag{3b}$$

$$\left(\lambda + G\right)\frac{\partial \varepsilon_v}{\partial z} + G\nabla^2 w - \left(3\lambda + 2G\right)\alpha \frac{\partial\left(-u_w\right)}{\partial z} + Z = 0 \tag{3c}$$

$$\frac{k}{\rho_w g}\left(\frac{\partial}{\partial x}\left(\frac{\partial u_w}{\partial x}\right)+\frac{\partial}{\partial y}\left(\frac{\partial u_w}{\partial y}\right)+\frac{\partial}{\partial z}\left(\frac{\partial u_w}{\partial z}+1\right)\right)=\rho_d C_w\frac{\partial u_w}{\partial t}-m_1^w\frac{\partial(\sigma_m)}{\partial t}+S' \tag{3d}$$

where u, v, and w = displacements in x-, y-, and z-directions, respectively; X, Y, and Z = Body forces in x-, y-, and z-directions, respectively; $\lambda = E\nu/((1+\nu)(1-2\nu))$; $G = E/(2(1+\nu))$; E= Young's modulus of the soil, ν = Poisson's ratio of the soil, =coefficient of expansion due to matric suction variation; ε_v = volumetric strain; u_w =pore water pressure; k = hydraulic conductivity; ρ_d = dry mass density of the soil;C_w= the specific water capacity of the soil (the volume of water expelled from a unit mass of soil by one kPa of matric suction); m_1^w =material parameter related to the ability of mechanical stress to squeeze water out of the soil; and S'= water source term.

As can be seen in Fig. 1, if the weather conditions are too severe, there might be separation between the slab and the soils. If the load is not symmetric or there is relative movement between the soil and the slab due to shrinking or swelling, there will be shear forces between the slab and the ground. Therefore, a model which can simulate both the normal (contact and separation) and tangential (friction) behaviors between the soil and the slab is needed. Zhang and Briaud (2006) proposed the use of coupled jointed elements to simulate the soil-structure interaction of the slab built on expansive soils. The coupled effect was included in order to simulate behavior of the soil and the slab in a unified system. The behavior of the slab can be simulated by conventional three dimensional finite elements. The governing differential equations are the same as those in Equations 3a through 3d.

A damage model is also needed to determine if there is cracking occurrence in the pavement structure. Stress intensity and fracture toughness (or critical stress intensity factor) are key fracture mechanics parameters used by materials engineers. By comparing these two parameters directly based on fracture criteria for unstable growth, one can then determine the crack stability of the material under given loading conditions. In this study, a K_I - K_{IC} based model was proposed to predict the occurrence potential of cracking in concrete pavements. The criterion is that cracking occurs when K_I exceeds KI_C. The contour integral method is proposed for the evaluation of stress intensity factors. This means that in a finite element model each evaluation can be thought of as the virtual motion of a block of material surrounding the crack tip. Each block is defined by contours: each contour is a ring of elements completely surrounding the crack tip or crack front from one crack face to the opposite crack face.

All the above models are synthesized in one single program to simulate the influence of climatic factors on the performance of a concrete slab built on expansive soils. The thermodynamic analogue and the pseudo moisture variation simulation are special techniques used to implement the proposed system (Zhang 2004). An example is given in the following section to illustrate the application of the proposed system.

NUMERICAL SIMULATION

Fig. 2(a) shows an example of a typical configuration of the pavement section studied, and the mechanical boundary conditions are also shown. In the example described as follows, the concrete slab was 0.25-meter (10-in) thick. Those concretes were made with gravel aggregates from Victoria, Texas, 0.45 of water-cementitious ratio (w/cm). The concrete has a Young's Modulus of $E = 2\times10^7$ kPa, Poisson's ratio $\nu = 0.15$, and hydraulic conductivity of $K = 1\times10^{-9}$ m/s. The K_{IC} measurement was facilitated by a variable-notch one-size split-tensile test method (15) developed at the Texas Transportation Institute (TTI) which is about 700 kPa $m^{1/2}$.. Due to the symmetry of the pavement structure, a 5-meter (16.4-ft) of width was chosen. The concrete slab was built on an expansive soil foundation with two soil layers: a dark gray silty clay from 0-1.50m and a brown silty clay from 1.5-6.0m. The ground surface was assumed to be covered by grass with a root depth of 0.35m. K_s and K_c for the grass are assumed to be 0.4 and 0.6, respectively. The suction at a depth of 6.0 m was constant and assumed to be equal to 100 kPa (pF=3). The concrete slab was assumed to rest on the soil and coupled contact elements were used to simulate the soil-structure interaction between the concrete slab and the foundation. For the left and right sides of the structure, only vertical displacements were allowed due to symmetry. A shallow notch of 0.005m in width and 0.025m in depth shown in Fig. 2(b) was set in order to initiate the cracking in the concreter slab at the center of the slab along the longitudinal direction.

The pavement was assumed to be at Arlington, Texas and the soil has an initial suction condition of 100 kPa everywhere at August 1, 1999. The soil moisture changed with the weather conditions shown in Fig. 3. Fig. 3 shows the daily rainfall and potential evapotranspiration calculated from Equation 1. The former is related to water gain and the latter is associated with water loss. These data was used to determine the boundary conditions using the FAO-56 Montieth Penman method.

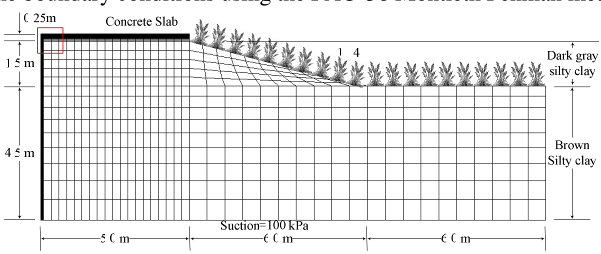

(a) Configuration of pavement section

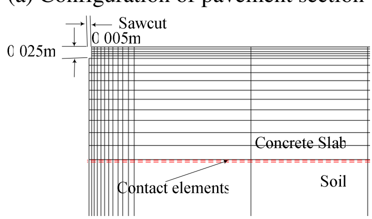

(b) Configuration of notch for cracking initiation

FIG. 2. Representative graphics embedded within the format of the paper.

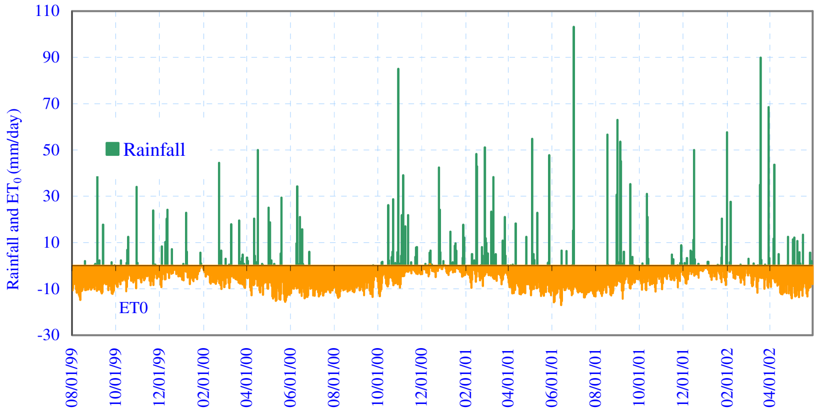

FIG. 3. Weather Conditions **at Arlington, Texas for a Period of Two Years.**

The finite element analyses were conducted using the ABAQUS program. The finite element mesh has a total of 1140 four-node bilinear displacement and temperature elements (CPE4T), which are sufficient for the analysis for this problem. The shrinkage and expansion due to drying and wetting of the concrete were not considered and the coefficient of drying shrinkage was taken as zero. For soils, the material properties needed for the analysis (as shown in the governing differential equations 3a through 3d) can be found in Zhang (2004). The Poisson's ratios for the two soils were assumed to be 0.4. Three user subroutines (i.e., USDFLD, UMAT, and UMTHT) were developed to facilitate the numerical analysis. Since all material properties used in the analysis were stress state variable dependent, USDFLD was used to obtain stress, strain, and suction from a previous calculation step. UMAT was used to update the stiffness matrix and UMTHT was used to update the corresponding moisture flow matrix during the simulation.

SIMULATION RESULTS AND DISCUSSIONS

The proposed method was used to simulate the performance of the concrete with the changes in climatic factors. A simulation was performed for every day of the two year period. The daily cumulative rainfall and potential evapotranspiration calculated by the FAO-56 PM method and were used to determine the flux boundary condition for the simulation. Fig. 4 shows the displacements at different locations of the model.

As can be seen from Fig. 4, the movements of the soil and the slab at the center of the simulated domain (point A in Fig.2) are the same at any, indication the slab and the soil were in good contact throughout the period of two years. The movements at the soil and the slab at the edge of the slab were however different, indicating there were separations between the soil and the slab. In the first three months from 08/01/1999 to11/09/1999, there were settlements everywhere, which was due to the shrinkage of a relatively wet initial soil profile. From 11/09/1999 to 06/24/2000, there were relatively small settlements everywhere and the curves were relatively flat, which was mainly attributed to the fact that the rainfall and evapotranspiration during this period were relatively evenly distributed as shown in Fig. 3d. From 06/24/2000 to 10/14/2000, there were dramatic settlements for both the slab and the soils, which was consistent with the long dry summer with no rainfall during this period shown in Fig. 3d. After that there was a rainy winter and spring from 10/13/2000 to 04/01/2001, which caused the soil and the slab to go up to their original positions. The deflection of the slab, which is the difference between curves at the center and the edge of the slab, increased during the whole period. The increase in the slab defection was caused by the interruption to the evapotranspiration process caused by the construction of the concrete pavements. In a long run, the soil underneath center of the slab was wetter than soils close to the edge of the slab. Consequently, there was moisture flow out of the center of the slab. The gap between the soil and slab at the edge of the slab, which was the difference between the curves for soil and slab at the edge of the slab, varied with climatic conditions. It had a peak value on June 24, 2000 decreased after that due to the swell of the soil at the edge of the slab caused by the following rainy winter and spring seasons. The deflection of the slab kept decreasing after June 24, 2000, indicating that soils between the edge and center of the slab were drying during a rainfall season. This lag in soils' response to climatic factors was reasonable considering the low permeability of the high plasticity expansive soils in this simulation.

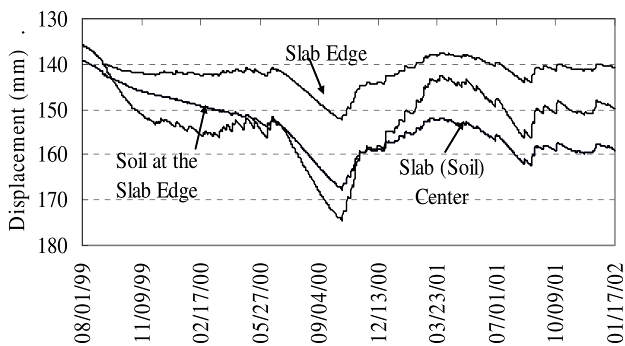

FIG. 4. Vertical displacements for different locations at different times.

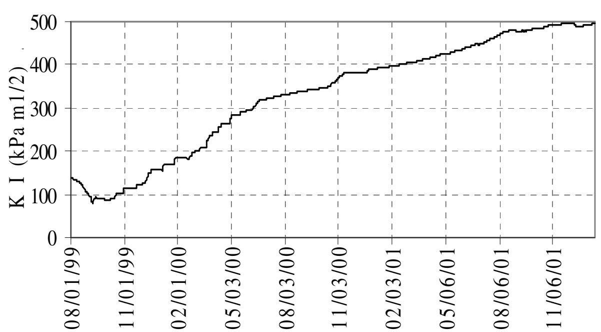

FIG. 5. Stress intensity factors at the tip of the notch at different times.

Fig. 5 illustrates the results of stress intensity factors at the notch at different time using the contour integral method. Initially the stress intensity factors at the notch was about 136 kPa $m^{1/2}$, which was induced by the non-uniform settlements resulted from the initial conditions. After three months of equilibrium, the stress intensity factor kept increasing until the end of the simulation, which was caused by the increase in the slab deflection as shown in Fig. 4. The maximum the stress intensity factors at the notch was about 500 kPa $m^{1/2}$, smaller than the fracture toughness of the concrete, which was about 700 kPa $m^{1/2}$. Therefore, there was no crack occurrence.

CONCLUSIONS

This paper presented a complete system aimed at simulating the soil-rigid pavement system and its responses to daily weather condition. The weather data included rainfall, solar radiation, air temperature, relative humidity and wind speed, all of which are readily available from a local weather station or the internet. These data were used to determine the flux boundary conditions for the simulation. A coupled hydro-mechanical stress analysis was used to simulate the volume change of expansive soils due to both mechanical stress and water content variations. Coupled hydro-mechanical stress jointed elements were used to simulate the interaction between the soil and the concrete slab, contour integral evaluation was used to determine the possibility of cracking occurrence. These models were combined to a single system to predict the rigid pavement behavior. The predicted movements of the slab and soils as well as the stress intensity factor with time were consistent with the historic weather conditions.

REFERENCES

ABAQUS/Standard User's Manual (2002). Vol. I, II, and III, Version 6.3, Hibbit, Karlsson and Sorenson Inc., 1080 Main Street, Pawtucket, RI02860-4847, U.S.A.

Allen, R.G., Periera, L.S., Raes, D., and Smith, M. (1998). *Crop Evapotranspiration: Guidelines for Computing Crop Requirements.* Irrigation and Drainage Paper No. 56, FAO, Rome, Italy

Chen, F. H.(1988). *Foundations on Expansive Soils*. Elsevier Science Publishing Company Inc.,New York.

Prozzi, J. and Luo, R. (2007). "Using Geogrids to Minimize Reflective Longitudinal Crackingon Pavements Over Expansive Soils." Proceedings of Transporation Research Board Annual Meeting, Washington D.C.

Brown, D.Z. and Vinson, R.J. (2006). "Stiffness parameters for a strong and colorful aeolian soil." G*eomaterial Characterization* (GSP 199), ASCE, Reston/VA: 12-22.

Cimponella, G.R. and Rubertsen, K.P. (1999). "Common problems with conventional testing." *J. Geotechnical & Geoenv. Engrg.*, Vol. 181 (9): 1193-1199.

Zhang, X. (2004) Consolidation theories for saturated-unsaturated soils and numerical simulations of residential buildings on shrink-swell soils. *Ph.D. Dissertation*, Department of Civil Engineering, Texas A&M University, College Station, TX.

Zhang, X. and Briaud, J. L. (2006) "Mandel-Cryer Effect for Unsaturated Soils." *Proceedings of the Fourth International Conference on Unsaturated Soils*, April 2006, Carefree, AZ, Geotechnical Special Publication No.147, pp. 2063-2074.

Soil Damage Models for Off-Road Vehicles

James Hambleton[1], S.M. ASCE and Andrew Drescher[2], M. ASCE

[1]Graduate Research Assistant, Department of Civil Engineering, University of Minnesota, 500 Pillsbury Drive SE, Minneapolis, MN 55455; hamb0025@umn.edu
[2]Professor, Department of Civil Engineering, University of Minnesota, 500 Pillsbury Drive SE, Minneapolis, MN 55455; dresc001@umn.edu

ABSTRACT: Off-road vehicles such as ATVs, SUVs, dirt bikes, and hauling trucks cause damage to soft soils in unpaved areas within parks, forests, wetlands, and tundra. These vehicles can form deep ruts which result in destruction of vegetation, changes in water absorption/retention, and reduction in aesthetical land values. Large areas of particularly vulnerable soils are becoming increasingly common in northern regions, where permafrost is disappearing as a result of climate change. In this paper, theoretical models that predict the effect of material properties, wheel geometry, and wheel load on wheel penetration and rutting in cohesive soils are presented. The effects of tire flexibility are considered, as well. The models are approximate, yet predict similar response as that obtained from comprehensive numerical simulation.

INTRODUCTION

The growing usage of off-road vehicles (ORVs) like ATVs, dirt bikes, SUVs, and hauling trucks is resulting in damage to soil in parks, forests, and wetlands and stimulating growing societal concerns. Excessive use of these vehicles leaves scars to soil, visible as deepening grooves or ruts negatively affecting vegetation, water infiltration and runoff characteristics, and aesthetics. As a consequence of global climate change, the extent of frozen regions is decreasing and the depth of the permafrost active layer is increasing, exposing vast areas of soft, saturated or partly saturated soils for which bearing capacity is very low. Hauling trucks sink and become difficult to operate, and the land is destroyed.

Notwithstanding the significance of educational and regulatory efforts to minimize the negative impacts of ORVs, limited knowledge exists as to a quantifiable relationship between vehicle characteristics and the degree to which the soil is damaged. This paper is an attempt to arrive at such a relationship by proposing theoretical, soil mechanics-based models. The interaction between vehicle wheels and soil has been of interest in the field of terramechanics, as exemplified in a number of sources (cf. Bekker 1960; Wong 2001). Accurate prediction of rutting, however, has been of secondary importance in this field, and empirical methods predominate.

The objective of this paper is to relate the force exerted on a wheel to the depth to which the wheel sinks when being indented or rolled. The analysis is limited to wheels not transmitting torque, examples being towed wheels and front wheels of dirt bikes, trucks, and some ATVs. This paper is an extension of work on test rolling, a quality assessment technique used in road construction (Hambleton 2006; Hambleton and Drescher 2007, 2008). The results pertain only to purely cohesive soils, which are likely to be encountered in thawing northern regions of land where fine-grained soils may have large water content. Hambleton and Drescher (2008) include results for frictional/cohesive soils.

Modeling the problem of wheel-induced damage to soil is difficult, due primarily to the three-dimensional nature of the problem. The wheel is fully or partly surrounded by soil that is pushed forward and sideways, leaving a permanent, narrow rut and berms. Rigorous solutions to three-dimensional problems are very scarce, and two-dimensional approximations are often introduced. In the approach presented in this paper, the three-dimensional character of the problem is fully preserved, albeit several approximations are made. The models presented are semi-analytic and should be viewed as first approximations to more accurate predictions based on numerical simulations (Liu and Wong 1996; Chiroux *et al*. 2005; Hambleton 2006; Hambleton and Drescher 2007, 2008).

THEORETICAL MODELS

The theoretical models proposed are based on the assumption that indentation can be regarded as a sequence of plastic states in the soil, induced by an increasing load (force) on the wheel, equivalent to plastic states beneath shallow, rigid, rectangular footings. Likewise, rolling is regarded as a steady plastic state analogous to a footing with inclined loading. It is further assumed that the load can be evaluated by using the generalized bearing capacity equation of Meyerhof (1963), which is based on the well-known formula proposed by Terzaghi (1943). Meyerhof's approximate equation accounts for the depth and shape of a footing, as well as load inclination, by introducing depth, shape, and inclination factors. For frictionless soils with cohesion c and with the factors as in Das (2005), the equation becomes

$$q_u = \left(1 - \frac{2\beta}{\pi}\right)^2 \left[5.14c\left(1 + 0.19\frac{B}{L}\right)\left(1 + 0.4\frac{D}{B}\right)\right] \tag{1}$$

where q_u is the average ultimate stress acting on the footing, L is the footing length, $B < L$ is the footing width, $D < B$ is the embedment depth, and β is the load inclination angle. Soil unit weight is unimportant for very shallow footings in cohesive soil and is therefore disregarded.

Expression (1) gives the average stress acting over the footing-soil contact area. When applied to wheel indentation/rolling, proper choice of the contact area is the key aspect of the model. First, it is assumed that the contact region is rectangular, with the resulting force calculated as

$$Q = q_u BL \tag{2}$$

Next, the dimensions B and L are taken as corresponding to the projection of the wheel at sinkage s, with the latter defined as the vertical distance between the soil undisturbed by the wheel and the lowest point of the wheel (Fig. 1). As contributions of elastic (small) deformation are disregarded, the sinkage s is equivalent to rut depth.

Indentation

When the stiffness of a wheel is sufficiently large to prevent noticeable wheel deformation in relation to induced soil deformation, the wheel can be regarded as rigid. Highly inflated and stiff tires satisfy this condition (Bekker 1960), although their shape and tread arrangement differ significantly. In the following, the shape of tires is approximated by a right cylinder (Fig. 1).

For a rigid, right-cylindrical wheel, the contact length h is related to the wheel diameter d and sinkage s by

$$h = 2\sqrt{sd - s^2} \tag{3}$$

and the equivalent footing lengths B and L (see Fig. 1c) are

$$\left.\begin{array}{l} B = h \\ L = b \end{array}\right\} \text{ for } h \le b \;\; ; \;\; \left.\begin{array}{l} B = b \\ L = h \end{array}\right\} \text{ for } h > b \tag{4}$$

where b is the width of the wheel. The volume displaced by the indented wheel V, and the resulting depth of the uplifted material D, can be approximated by

$$V = 2bhD \;\; ; \;\; D = \frac{s}{6} \tag{5}$$

Eqs. (3)-(5) are substituted into Eqs. (1) and (2) to find that the vertical indentation force, denoted Q_V, is given as a function of s, b, d, and c by

$$Q_V = 10.28bc\sqrt{ds - s^2}\left(1 + 0.39\frac{\sqrt{ds - s^2}}{b}\right)\left(1 + \frac{0.03s}{\sqrt{ds - s^2}}\right) \text{ for } 2\sqrt{sd - s^2} \le b \tag{6a}$$

$$Q_V = 10.28bc\sqrt{ds - s^2}\left(1 + \frac{0.1b}{\sqrt{ds - s^2}}\right)\left(1 + 0.07\frac{s}{b}\right) \text{ for } 2\sqrt{sd - s^2} > b \tag{6b}$$

When the wheel is flexible, its deformation depends on how the soil deforms. The sinkage, too, is therefore affected. The problem is coupled and cannot be solved accurately without knowing the inflation pressure and deformability characteristics of the tire itself, with the latter often being proprietary. Motivated by the work of Fujimoto (1977), Karafiath and Nowatzki (1978), and Qun *et al.* (1987), a simplified approach is proposed, in which the shape of the portion of the tire in contact with the

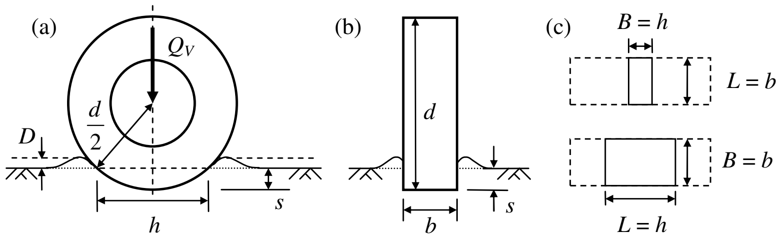

FIG. 1. Schematic of rigid wheel indentation: (a) cross section in plane of wheel diameter; (b) cross section in plane of wheel width; (c) evolution of contact area.

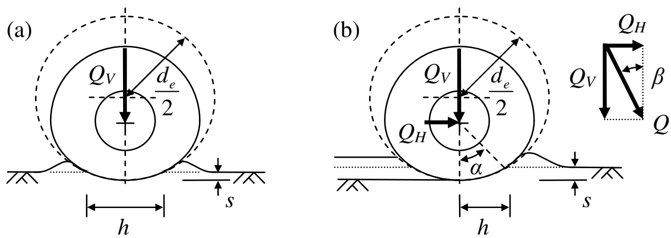

FIG. 2. Schematic of flexible wheel: (a) indentation; (b) rolling.

soil is approximated by a circle of diameter d_e larger than the tire diameter d (Fig. 2). It is assumed that flattening of the wheel only affects the contact length h.

A linear relationship is postulated between the diameter d_e and d

$$d_e = d + \lambda_i Q \tag{7}$$

where λ_i, is the wheel flexibility coefficient; λ_i = 0 implies a rigid wheel. One can expect that λ_i decreases with increasing inflation pressure, increasing carcass stiffness, or decreasing soil strength. The resulting length of contact is then

$$h = 2\sqrt{d_e s - s^2} = 2\sqrt{s\left(d + \lambda_i Q\right) - s^2} \tag{8}$$

With h as in Eq. (8), the resulting expressions for Q_V in the flexible wheel case are

$$Q_V = 10.28bc\sqrt{s\left(d + \lambda_i Q_V\right) - s^2}\left(1 + 0.39\frac{\sqrt{s\left(d + \lambda_i Q_V\right) - s^2}}{b}\right) \times \left(1 + \frac{0.03s}{\sqrt{s\left(d + \lambda_i Q_V\right) - s^2}}\right) \quad \text{for } h \le b \tag{9a}$$

$$Q_V = 10.28bc\sqrt{s\left(d+\lambda_i Q_V\right)-s^2}\left(1+\frac{0.1b}{\sqrt{s\left(d+\lambda_i Q_V\right)-s^2}}\right)\left(1+0.07\frac{s}{b}\right) \quad \text{for } h>b \tag{9b}$$

As a reflection of the coupling between wheel deformation and soil deformation in the flexible wheel case, Eqs. (9a) and (9b) are implicit with respect to Q_V.

Rolling

In the steady state of rolling, the contact area is reduced, and the total force Q is inclined at angle β. The angle β is assumed to bisect the angle α subtending the arc of the wheel in contact with the soil (Fig. 2b). This assumption is supported by experimental results (Onafeko and Reece 1967), which indicate that the distribution of normal contact stresses is close to symmetrical and that of the shear stresses is roughly antisymmetrical. The deformability of the wheel is modeled by (7), with the coefficient λ_i replaced by λ_r, as the apparent flexibility of a wheel in rolling is, in general, different than in indentation. The resulting expression for β is then

$$\beta = \frac{\alpha}{2} \approx \sqrt{\frac{s}{d_e}} = \sqrt{\frac{s}{d+\lambda_r Q}} \tag{10}$$

The contact length h is assumed to be half of that for indentation, resulting in the expression

$$h = \sqrt{d_e s - s^2} = \sqrt{s\left(d+\lambda_r Q\right)-s^2} \tag{11}$$

Combining Eqs. (1), (2), (4), (5), (10), and (11) results in the following expressions for the inclined force Q in the case of a rolling, flexible wheel:

$$Q = 5.14bc\sqrt{s\left(d+\lambda_r Q\right)-s^2}\left(1+0.19\frac{\sqrt{s\left(d+\lambda_r Q\right)-s^2}}{b}\right)\left(1+\frac{0.07s}{\sqrt{s\left(d+\lambda_r Q\right)-s^2}}\right) \times\left(1-0.64\sqrt{\frac{s}{d+\lambda_r Q}}\right)^2 \quad \text{for } h\le b \tag{12a}$$

$$Q = 5.14bc\sqrt{s\left(d+\lambda_r Q\right)-s^2}\left(1+0.19\frac{b}{\sqrt{s\left(d+\lambda_r Q\right)-s^2}}\right)\left(1+0.07\frac{s}{b}\right) \times\left(1-0.64\sqrt{\frac{s}{d+\lambda_r Q}}\right)^2 \quad \text{for } h>b \tag{12b}$$

Again, expressions (12a) and (12b) are implicit in Q; however, both Q and its vertical component $Q_V = Q\cos\beta$ can be easily calculated numerically.

DAMAGE/RUTTING PREDICTIONS

The theoretical models presented allow for construction of response curves relating wheel sinkage/rut depth to the weight (Q_V) exerted on a wheel. To demonstrate the correctness of the models, a comparison is made in Fig. 3a with results from three-dimensional numerical simulation using the finite element code ABAQUS. The numerical simulations were performed as described in Hambleton (2006) and Hambleton and Drescher (2007). A three-dimensional wheel declared as an analytical, rigid body was indented, or rolled under the condition of constant wheel weight, on an elastoplastic soil bed defined by the von Mises material model. Elastic properties in the simulations were such that elastic effects could be considered negligible. Frictional interaction was declared on the soil-wheel interface.

Fig. 3a compares the sinkage-weight response from ABAQUS with Eqs. (6) and (12), using the dimensionless quantities s/d and Q_V/cd^2. Numerical results for rolling are given as discrete points corresponding to sinkage at steady state under constant weight. The qualitative agreement between the formulas and the numerical results is surprisingly good, given the approximate nature of the analytic approach. Clearly, the response curves are strongly nonlinear (roughly quadratic), and it is evident that for a given wheel weight, rolling results in much greater sinkage than indentation.

Fig. 3b gives the theoretical predictions of sinkage as a function of wheel weight, in indentation and rolling, for a wheel with a size representative of those on SUVs and light trucks operating on a medium consistency soil (c = 50 kPa). For such a wheel size and soil type, Figs. 4 and 5 reveal how sinkage is affected by changes in cohesion, flexibility, and wheel geometry. Results are shown for two weights: 6 kN and 10 kN. The former might represent an empty full-sized SUV or truck, and the latter may be the same vehicle carrying cargo.

Fig. 4a plots sinkage against cohesion (holding b, d, and Q_V fixed) for the case of a rolling, rigid wheel, showing that sinkage increases rapidly when the cohesion is low; again, the relationship is strongly nonlinear. Fig. 4b shows sinkage versus the wheel flexibility coefficient λ_r (holding b, d, and Q_V fixed). Flexibility of the wheel clearly reduces sinkage, which agrees with a well-known fact that deflated tires are less prone to sinking. Fig. 5 similarly plots the variation in sinkage with changing wheel diameter and width. Expectedly, a decrease in the wheel diameter increases the sinkage, and narrow wheels sink more than wide.

CONCLUSIONS

As demonstrated in the paper, the theoretical models proposed capture the expected dependence of soil damage, identified as sinkage/rut depth, on soil strength and wheel weight, geometry, and flexibility. By incorporating the varying contact area and shape factors, the models account for three-dimensionality of the wheel-soil interaction. The results presented are limited to wheels whose geometry can be approximated by a right cylinder, which seems warranted for SUV and hauling truck tires. As shown in Hambleton (2006), the models can be extended to toroidal tires, such as those used on ATVs and dirt bikes, by modifying the prescription for how the contact area at the soil-wheel interface evolves with sinkage.

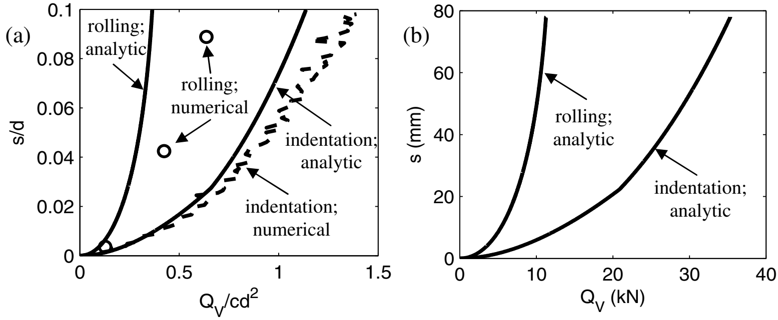

FIG. 3. Sinkage *vs* weight for indenting and rolling rigid wheels: (a) dimensionless analytic and numerical results; (b) dimensional analytic results for *b* = 0.26 mm, *d* = 0.78 m, and *c* = 50 kPa.

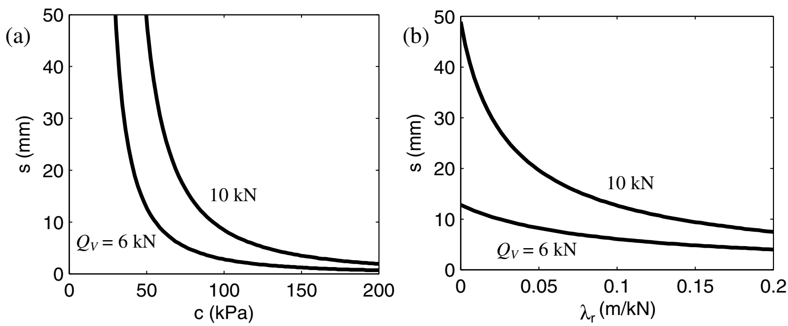

FIG. 4. Sinkage of rolling wheel (*b* = 0.26 m and *d* = 0.78 m) for varying (a) cohesion ($\lambda_r = 0$) and (b) varying wheel flexibility coefficient (*c* = 50 kPa).

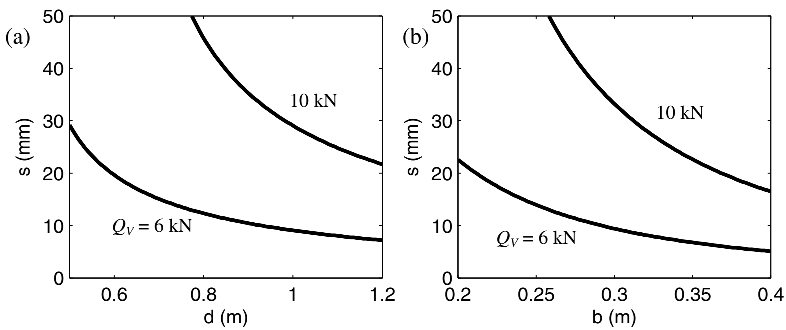

FIG. 5. Sinkage of rolling, rigid wheel (*c* = 50 kPa): (a) effect of diameter (*b* = 0.26 m); (b) effect of wheel width (*d* = 0.78 m).

The models are approximate; however, numerical studies support the findings. Improvements to the approach leading to better agreement are discussed in Hambleton (2006) and Hambleton and Drescher (2008). With proper improvements, the theoretical models have potential to form the basis for load restrictions and appropriate tire selection for minimizing the negative impacts of off-road vehicles.

ACKNOWLEDGEMENTS

The authors acknowledge the support provided by the Minnesota Local Road Research Board and the Shimizu Corporation. This work was supported in part by the University of Minnesota Supercomputing Institute.

REFERENCES

Bekker, M.G. (1960). *Off-the-Road Locomotion*, University of Michigan Press, Ann Harbor.

Das, B.M. (2005). *Fundamentals of Geotechnical Engineering*, Thomson, Toronto.

Fujimoto, Y. (1977). "Performance of elastic wheels on yielding cohesive soils." *J. Terramech.* 14(4): 191-210.

Hambleton, J.P. (2006). Modeling test rolling in clay. *MS Thesis*, University of Minnesota, Minneapolis.

Hambleton, J.P., and Drescher, A. (2007). “Modeling test rolling on cohesive subgrades.” *Proc. Intl. Conference. on Advanced Characterisation of Pavement and Soil Engrg. Matls.*, Vol. 1., Athens: 359-368.

Hambleton, J.P., and Drescher, A. (2008). "Development of improved test rolling methods for roadway embankment construction, final report.” Minnesota Department of Transportation, St. Paul. (In preparation).

Karafiath, L.L., and Nowatzki, E.A. (1978). *Soil Mechanics for Off-Road Vehicle Engineering*, Trans. Tech. Pub., Clausthal.

Liu, C.H., and Wong, J.Y. (1996). "Numerical simulations of tire-soil interaction based on critical state soil mechanics." *J. of Terramech.* 33(5): 209-221.

Meyerhof, G.G. (1963). "Some recent research on bearing capacity of foundations." *Canadian Geotech. J.* 1(1): 16-26.

Onafeko, O., and Reece, A.R. (1967). "Soil stresses and deformations beneath rigid wheels." *J. of Terramech.* 4(1): 59-80.

Qun, Y., Sunrong, G., and Guyuan, Y. (1987). "On the modelling and simulation of tire-soil systems." *Proc. 9th Intl. Conference of the Intl. Society for Terrain-Vehicle Systems*, Barcelona: 257-266.

Terzaghi, K. (1943). *Theoretical Soil Mechanics*, Wiley, New York.

Liu, C.H., and Wong, J.Y. (1996). "Numerical simulations of tire-soil interaction based on critical state soil mechanics." *J. of Terramech.* 33(5): 209-221.

Chiroux, R.C., Foster, W.A., Johnson, C.E., Shoop, S.A., and Raper, R.L. (2005). “Three-dimensional finite element analysis of soil interaction with a rigid wheel.” *Appl. Math. and Comp.* 162(2): 707-722.

Wong, J.Y. (2001). *Theory of Ground Vehicles*, Wiley, New York.

Variation in Moduli of Base and Subgrade with Moisture

Soheil Nazarian[1], M. ASCE and Deren Yuan[2]

[1] Director, Center for Transportation Infrastructure Systems, The University of Texas at El Paso, El Paso, TX 79968-0516, nazarian@utep.edu
[2] Research Specialist, Center for Transportation Infrastructure Systems, The University of Texas at El Paso, El Paso, TX 79968-0516, dyuan@utep.edu

ABSTRACT: The modulus of each layer in a pavement system is one of the primary parameters that affect the performance of the pavement. The determination of the layer moduli under different moisture regimes is an essential task in any pavement design. Seismic nondestructive testing technology based on the use of stress waves has been shown to be a useful tool in achieving this goal. Based on these studies, laboratory tests have been developed to quantify the moisture susceptibility of base and subgrade materials. These suggested methods are also described.

INTRODUCTION

To successfully implement a mechanistic pavement design procedure or to develop realistic performance-based specifications, moduli of different layers in a pavement should be accurately measured and their seasonal variations should be well-quantified. Large research programs, such as the Federal Highway Administration (FHWA) long-term pavement performance (LTPP) monitoring program, have seriously focused on these issues for some time.

This paper provides methods for quantifying the variation in modulus with moisture using seismic nondestructive testing (NDT) technology. Procedures to measure the modulus of base and prepared subgrade materials both in the laboratory and in the field are briefly discussed. Examples that exhibit the use of these methods for quantifying the impact of moisture are included. Laboratory test protocols for developing project-specific modulus-moisture relationships are proposed. Typical results that may be obtained and the issues that have yet to be resolved are addressed.

BACKGROUND

The remaining life of the flexible pavement is mainly based on predicting the strains or stresses at the interfaces of different layers. These critical strains are strongly related to the moduli of all pavement layers. A practical means of quantifying the variations of these moduli with environmental parameters such as moisture will enhance the capabilities of these algorithms to predict the performance of pavements more realistically.

The determination of the variation in modulus with moisture can be carried out either in the laboratory or in the field. Deflection-based devices such as the Falling Weight Deflectometer (FWD) are typically used in the field for this task. An impressive body of data has been collected under the LTPP and from other regional programs that can be used to study the impact of moisture on the moduli of different layers. Briggs and Lukanen (2000) showed an excellent example of how trends can be established. However, they indicate that uncertainties in the backcalculated moduli along with spatial variations may impact some of the relationships developed.

In the laboratory, resilient modulus (M_R) tests are the primary means of determining the variation in modulus of base and subgrade materials with moisture (Barksdale et al., 1997). These laboratory tests are comprehensive, usually time-consuming, and sometimes not very robust. As such, they are not suitable for testing a large number of specimens.

OVERVIEW OF METHODS USED IN THIS STUDY

Based on the background information provided, the goal of this study is to develop site-specific modulus-moisture relationships. In the next section several alternatives based on seismic methods to obtain the low-strain linear elastic modulus are presented. The low-strain linear elastic moduli are greater than those measured either by FWD or by other laboratory, such as M_R testing. Abdallah et al. (2002) have developed an algorithm that provides the appropriate design modulus for a given layer based on the seismic modulus, load level applied, the nonlinear parameters obtained from M_R testing and the pavement structure.

A simplified laboratory test, the free-free resonant column (FFRC) test is used in this study. This test method is comprehensively described in Nazarian et al. (2003). A schematic of the test set-up is shown in Figure 1a. An accelerometer is securely placed on top of the specimen placed on a pedestal, and the specimen is impacted with a hammer instrumented with a load cell. The signals from the accelerometer and load cell are used to determine the longitudinal resonance frequency, f_L. Once the frequency, mass density, ρ and the length of the specimen, L, are known, the low-strain modulus, E_{ff}, can be found from

$$E_{ff} = \rho(2\, f_L\, L)^2, \quad (1)$$

Since the method is nondestructive, the specimens to be tested in the resilient modulus device can be used before they are placed in the loading frame. Based on tests on more than three dozen base and subgrade materials, Williams et al. (2007) describe a method to relate the modulus obtained in this manner to the resilient modulus of the same specimens.

The seismic modulus of a base or subgrade layer is nondestructively measured by using the high-frequency surface waves (a.k.a. ultrasonic surface waves, USW or SASW) before it is covered during construction. The theoretical and experimental background behind this method can be found in detail in Celaya and Nazarian (2006). A device called the portable seismic pavement analyzer or PSPA (Baker et al., 1995, shown in Figure 1b) can be used to perform this test, in the field, in less than one

FIG. 1 - Free-free Resonant Column FFRC) Test (left) and Portable Seismic Pavement Analyzer (right)

minute per point. The surface of the medium is impacted and the transmitted waves are monitored with the receivers. By conducting a spectral analysis, a so-called dispersion curve (a plot of velocity of propagation of surface waves with wavelength) is obtained. The average modulus of the layer, E_{USW}, can be simply obtained from the average phase velocity of the layer, V_{ph}, using

$$E_{USW} = 2\,\rho(1+\nu)[(1.13 - 0.16\nu)V_{ph}]^2 \tag{2}$$

MODULUS-MOISTURE RELATIONSHIP

The use of the seismic modulus in QA/QC of bases and subgrades was extensively described by Nazarian et al. (2003). Based on the results from that study, extensive laboratory and field work was carried out to determine the parameters that impact the modulus of the bases and subgrades. One of the most important parameters is, of course, moisture. The results from several of such experiments are included here.

Moisture-Modulus Relationship under Constant Compaction Effort

The first study was to determine the variation in modulus with moisture content under a constant compaction effort. An experiment very similar to that carried out to determine the moisture-density curve with the Proctor method was used. The FFRC set up shown in Figure 1 was used to measure the modulus. The modulus-moisture relationship under constant compaction effort exhibits two patterns. As shown in Figure 3a, for a fine-grained material the relationship resembles that of a typical moisture-density curve. The maximum modulus occurs at a moisture content of about 13% which is less than the optimum moisture content of about 18% for this type of material. For moisture contents greater than the value at which the peak modulus occurs, the modulus decreases with an increase in moisture. Also a sharp drop in modulus for moisture contents less than that of the peak modulus is observed.

Clean, coarse-grained material, with an optimum moisture content of about 8%, demonstrates a trend as reflected in Figure 3b. The modulus increases with a decrease in moisture content until a point, say, about 3%. Below that moisture content, the specimens are so fragile that they could not stand with out cracking. As such, their measured moduli are quite low. For a typical base, which usually contains some fine-grained materials, the trend is somewhat in between the two.

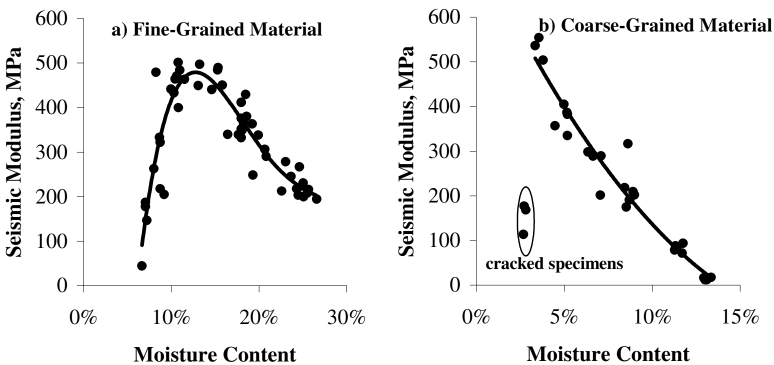

FIG. 3 - Variation in Seismic Modulus with Moisture Content under Constant Compaction Effort

In summary, under constant compaction effort, the maximum modulus is obtained at a moisture content lower than the optimum one. The difference between the optimum moisture content and the moisture content at which the maximum modulus occurs depends on the fine content of the mixture. For the materials with high clay content, the difference between the two varies from 1% for about 15% fine content to about 8% for pure fat clays. For clean sands, the modulus increases until the specimens become too fragile. Independent of the type of material, a decrease in modulus with progressive increase in the moisture content is inevitable. The dropping rate in modulus depends on the type of material.

Moisture-Modulus Relationship due to Moisture Infiltration

After the compaction of a layer is completed, the layer will be exposed to environmental factors that could impact its behavior. One of the major concerns with most fill materials is its water retention potential and the impact of a change in moisture content on the strength and stiffness parameter of the layer. At this time, there is no convenient method for addressing this issue. We have adapted tests that will potentially allow the engineer to quantify the moisture sensitivity of a material.

Laboratory Tests

A cylindrical specimen (150-mm by 300-mm for coarse-grained materials or 100-mm by 200-mm for fine-grained material) is prepared. A PVC concrete mold is retrofitted within a compaction mold for this purpose. Several small holes are drilled at the bottom of the mold so the specimen can absorb water. The specimen is prepared at the optimum moisture content as per Proctor method. The prepared specimen is then placed in an oven normally set at 40°C and dried for four days. The specimen is weighed, and the FFRC test is performed on it daily. Since the test is nondestructive, the same specimen can be used over and over. After four days, the specimen is placed in a pan filled with water. The gain in weight of the specimen and the change in modulus with time are then monitored for another 10 days. By inspecting the change in modulus with moisture content, the behavior of the material can be judged.

Typical results from one base material from El Paso area is shown in Figure 4. The modulus immediately after the specimen is prepared (day zero) is quite low. About an order of magnitude increase in modulus can be detected for the drying cycle. The drying cycle can be potentially associated with the change in the properties of the exposed soil during hot summer days after the completion of compaction in the field. A significant drop in modulus is observed during the first two days of soaking, after two days the drop in modulus becomes less rapid.

The change in moisture with time is also shown in Figure 4. During the drying cycle, the specimen loses a significant portion of water. However, during the first two days of soaking, the specimen rapidly absorbs a significant amount of water. The gain in water slows down after two days of soaking.

A more practical way of using the modulus-moisture data in Figure 5 is shown in Figure 6. This modulus-moisture curve may be used to adjust the seasonal variation in the modulus of the material by simply measuring the change in moisture content at

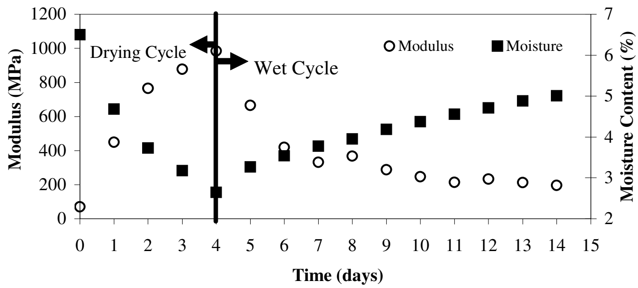

FIG. 4 – Variations in Modulus and Moisture with Time in Soak Test

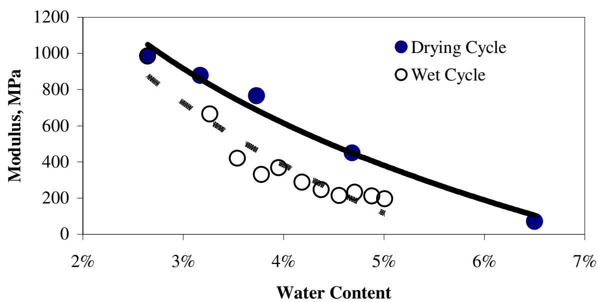

FIG. 5 - Variation in Modulus with Moisture during Soak Test

regular time intervals. The modulus-moisture trends from the drying cycle and wetting cycle are different.

Based on tests on about several dozen distinct materials, the experience gained, several general comments can be made. The moisture-modulus relationships can be developed for all materials. However, the relationships are material-specific. Practically speaking, for each material tests should be carried out to develop the appropriate relationship. The sensitivity of modulus to moisture content increase as the fine content in the material increases. Almost all materials, except clean coarse-grained materials, exhibit different patterns between drying and wetting cycles. The greater the fine content is, the more distinct the two patterns will become.

Large-Scale Model Tests

Finally, to verify the variation in modulus with moisture in a field setting, two 1 m-wide and 1.3 m-long boxes were filled with a subgrade material and a base material, respectively. The schematic of the box is shown in Figure 6. About 150 mm of coarse-grained sand was placed on the bottom of each box to act as a free-draining material. An outlet pipe was embedded inside the sand. The other end of the pipe was connected to a water bottle. The density and moisture content were controlled to ensure uniformity and consistency. To achieve this, the material was dried first.

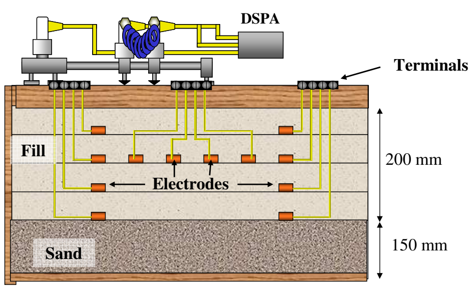

FIG. 6 - Schematic of Experimental Boxes for Moisture Study

Appropriate amount of the dry material was placed in a cement mixer, and water was added gradually for uniformity in the mixture. The mixture was then placed and tamped to achieve a 50-mm thick layer. Several electric probes were placed at the interface of two adjacent layers to monitor the change in electric resistivity caused by the moisture regime within the box. This process was repeated until a 200-mm thick layer of base or subgrade material was placed in each box. At the completion of this task, the top of each box was covered with plastic to inhibit the loss of moisture.

The modulus of the base or subgrade was measured with a PSPA as shown in Figure 1. The resistivity was measured by using AC current of about 100 Hz to reduce the effects of electrode polarization. It was easy to detect changes in moisture content with the resistivity probes, but it was difficult to accurately measure the moisture content during wetting and drying periods. For this reason, the results from resistivity measurements are not discussed here.

Base Material

The base material is a standard one used extensively in the El Paso County. The composition of the material is approximately 44% gravel, 48% sand and 8% fines with a top aggregate size of 20 mm. The variations in modulus and the approximate water intake as a function of time are shown in Figure 7a. The material absorbed water quite rapidly for the first day, and at a moderate rate up to day 21. The material's surface looked reasonably dry at the beginning of the experiment, and quite moist around day 21. The excess water was drained from the specimen at day 21. In addition, the plastic cover was removed so that the material could dry out. Overall, the material absorbed about 2.5% more than the initial moisture content of about 6.5%.

Even though the material absorbed nearly 15 kg of water during the first day, the modulus did not noticeably change until 1.5 days, when a rapid reduction in modulus was observed. The reduction in the rate of absorption of water coincided with a decrease in the rate of reduction in modulus. After day 21, the modulus was about 200 MPa (about 1/6 of the initial modulus). After 10 weeks of drying, the modulus increased about 1.5 times its initial modulus. Unfortunately, the rate of discharge of the water from the material could not be measured. Based on inspection of the dispersion curve from the PSPA, the modulus started to increase from the top of the material, mainly due to evaporation.

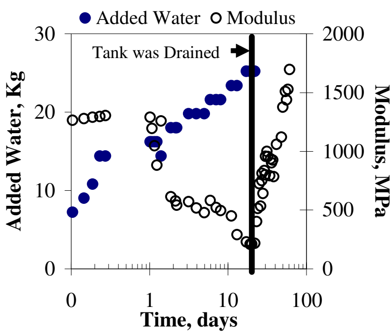

a) Base Material

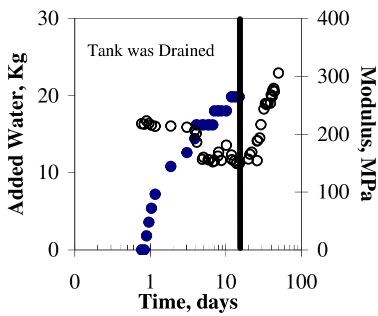

b) Subgrade Material

FIG. 7 - Variation in Modulus with Moisture for Large-Scale Models

Subgrade Material

The subgrade was a uniform fine sand with about 3% fine content. The initial water content at compaction was about 12%. This material did not absorb as much water as the base material, as shown in Figure 7b. The time lag between the absorption of water and the reduction in modulus was also further delayed. The maximum drop in the modulus was about 30% as opposed to 6 times for the base. This is anticipated because of a lack of fines in the material. At the completion of the drying cycle, the modulus was again about 1.5 times the original one.

This experiment demonstrates the importance of the material type, especially the fine content, to the moisture susceptibility of the material. However, a more accurate means of measuring the moisture content in the field should be implemented so that the results from the laboratory and the field can be compared.

CONCLUSIONS

The feasibility of directly quantifying the moisture dependency of base and subgrade materials in the field and in the laboratory with different types of nondestructive methods and devices are discussed and summarized. Seismic methods measure the engineering properties of pavement materials. Seismic testing both in the laboratory and in the field is rapid and repeatable.

For the base and subgrade, the seismic modulus is sensitive to the variation in moisture content. The level of moisture susceptibility can be identified by laboratory tests. The impact of moisture can also be measured in the field. Work is in progress to bring together the field and laboratory procedures.

ACKNOWLEDGMENTS

This work was supported by the Texas Department of Transportation. The authors would like to express their sincere appreciation to Mike Arellano, Mark McDaniel, Stephen Smith and David Head, for their ever-present support and valuable advice.

REFERENCES

Abdallah, I., Meshkani, A., Yuan, D. and Nazarian, S. (2002) “An algorithm for determining design moduli from seismic methods.” Research Report 1780-4, Center for Highway Materials Research, Univ. of Texas, El Paso/TX, 67 p.

Baker M. R., Crain K., and Nazarian S. (1995), "Determination of pavement thickness with a new ultrasonic device." Research Report 1966-1, Center for Highway Materials Research, Univ. of Texas at El Paso, El Paso/TX, 53 p.

Barksdale, R.D., Alba, J., Khosla, P.N., Kim, R., Lambe, P.C. and Rahman, M.S. (1997) “Laboratory determination of resilient modulus for flexible pavement design.” NCHRP Web Document 14, Federal Highway Administration, Washington/DC, 486 p.

Briggs, R.C. and Lukanen, E.O. (2000),”Variation in backcalculated pavement layer moduli in LTPP SMP Sites,” STP 1384, ASTM, West Conshohocken/PA: 113-128.

Celaya, M. and Nazarian, S. (2006) “Seismic testing to determine quality of hot -mix asphalt.” Transportation Research Record 1946, Washington,/DC: 113-122.

Nazarian S., Yuan D., and Williams R.R. (2003), “A Simple Method for Determining Modulus of Base and Subgrade Materials,” STP 1437, American Society for Testing and Materials, West Conshohocken, PA (accepted for Publication).

Williams, R. R. and Nazarian, S. (2007), “Correlation of resilient and seismic modulus test results.” *J. Materials in Civil Engrg.*, (accepted for publication).

Zhou H. (2000), “Comparison of backcalculated and laboratory measured moduli on AC and granular base layer materials,” STP 1384, ASTM, West Conshohocken/ PA: 161-174.

Construction of an embankment using vacuum consolidation and surcharge fill

Richard Kelly[1], John Small[2], M ASCE and Patrick Wong[3], M. ASCE

[1] Senior Geotechnical Engineer, Coffey Geotechnics, Sydney, Australia, richard_kelly@coffey.com.au:
[2]Visiting Senior Principal, Coffey Geotechnics and Professor, University of Sydney, Australia, john_small@coffey.com.au
[3] Senior Principal, Coffey Geotechnics, Sydney, Australia, patrick_wong@coffey.com.au

ABSTRACT: Vacuum consolidation, in the form of suction applied beneath a membrane, in conjunction with additional surcharge filling has been used to construct an embankment on top of a 25m deep soft clay layer. Design of the combined vacuum and surcharge fill system and construction of the embankment is described. Field monitoring data is presented showing how the embankment performed during construction. A comparison of the performance of the vacuum system with that of an adjacent area constructed using standard surcharge fill highlights the benefits of vacuum consolidation.

INTRODUCTION

The Pacific Highway is the major road connecting Sydney and Brisbane on the east coast of Australia and is progressively being upgraded. Part of these works involves bypassing the town of Ballina in the far north of the state of New South Wales. The preferred route traverses a floodplain associated with the Richmond River for a distance of approximately 6km. A number of bridges and other flood relief structures will be constructed along this section of the highway and stringent post-construction settlement limits have been specified for the approach embankments to these structures.

Conventional methods of soft soil treatment, such as staged construction using surcharge with or without wick drains, are not capable of consolidating the deeper soft clay deposits to the required level within the time allocated to construct the bypass. Consequently, alternative methods capable of accelerating construction of the bridge approach embankments were sought.

Vacuum consolidation, in the form of suction applied beneath a membrane, was selected for trial at the southern approach to Emigrant Creek, north of Ballina. The generic system is described by Masse *et al* (2001). Vacuum consolidation had not previously been used in Australia and part of the scope of work was to assess the performance of the system. Some results from the assessment are presented in this paper.

SITE DETAILS

The geology at the site of the vacuum consolidation trial comprises a uniform deposit of soft to firm silty clay overlying residual soil and bedrock. The depth of the silty clay varies from near zero at the southern end of the site to 25m at the northern end of the site, adjacent to Emigrant Creek.

A plan of the embankment is shown in Figure 1. The area treated by vacuum consolidation extends from SP3 to the north (near I5 and I6). Conventional surcharge and wick drains were used in the area to the south of SP3. Tensile fabric and berms were included in the embankment, as the client insisted on conservative design to ensure the success of the trial. However, a fibre optic telephone cable was discovered running along the northern boundary of the embankment, which resulted in the berm width being reduced to 5m in that area. A power pole was also incorrectly relocated further to the south resulting in an area without berms near I2.

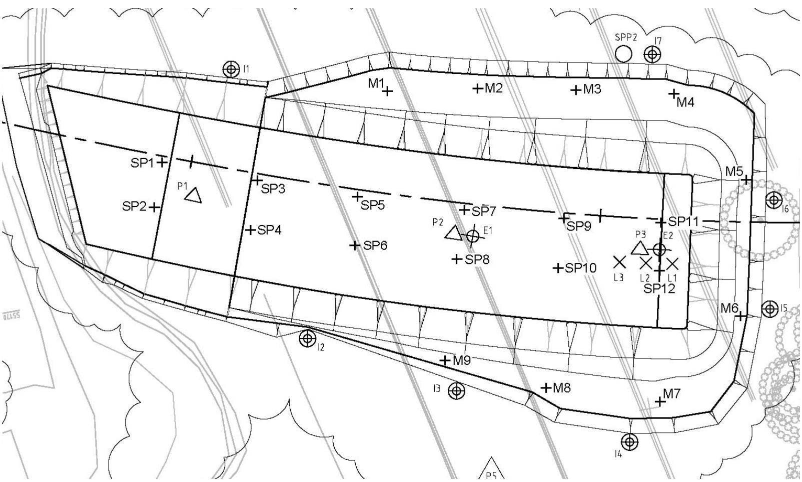

FIG. 1 Embankment footprint and location of instrumentation

The design embankment height was about 4.3m at the bridge abutment where the thickness of the soft clay layer was about 25m. At the bridge abutment, the required preload thickness was assessed to be 11.2m (for conventional preloading with surcharge fill weight of $20kN/m^3$) to limit post-construction settlement to 50mm. Assuming that an effective vacuum pressure of 70kPa could be maintained over a sufficient period of time, this vacuum pressure would be equivalent to approximately 3.5m of preload fill. Therefore, the total required fill thickness with vacuum consolidation was assessed to be 7.7m. The anticipated primary consolidation was about 4.2m, and assuming 90% primary consolidation was to be achieved during preloading, settlement during preloading was expected to be about 3.8m.

The location of the instrumentation is also shown in Figure 1. Settlement plates (SP), permanent monuments (M), magnetic extensometers (E), inclinometers (I), vibrating wire piezometers (P), vacuum pressure gauges, standpipes (SPP) and load cells (L) attached to the tensile fabric were used. One vibrating wire piezometer (P3e) was installed inside one of the vertical transmission pipes to a depth of 19.4m below original ground surface level. The remaining piezometers were installed approximately at the centre of the square vertical drain spacing pattern, and therefore record the maximum pore pressures in the clay.

The original groundwater level recorded in the standpipes was about 0.2m below ground level.

PERFORMANCE

Settlements recorded by the settlement plates and permanent monuments are shown in Figure 2. Day zero is 20 November 2006, which is just prior to the settlement plates being read for the first time. Part of the drainage layer had been placed prior to this date and settlements associated with this filling prior to 20 November have not been recorded. Data from the permanent monuments start at day 84. The permanent monuments were placed on the berms where no additional surcharge fill was added. The vacuum pumps were started about day 100 and the settlements accelerated rapidly to a maximum of 45mm per day at this time. The rate of settlement reduced to 20mm per day between 140 to 180 days. Additional surcharge fill was placed from day 119 to a maximum thickness of about 8.5m, which was greater than the specified design thickness. A comparison with rate of settlement in the standard surcharge area (SP1 and SP2) between 100 and 119 days clearly shows the effects of the vacuum.

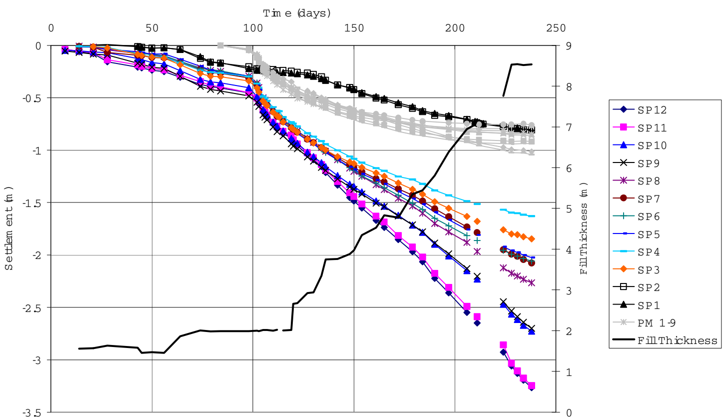

FIG 2. Recorded settlements

Inferred excess pore pressures recorded by the vibrating wire piezometers (VWP) are shown in Figure 3. Suction pressures recorded at the vacuum pumps and beneath the membrane are also shown. In the calculations to estimate excess pore pressures, the groundwater table was assumed to rise 1m to the underside of the horizontal transmission pipes when the vacuum was applied and then to lower with settlement of the horizontal transmission pipes. Estimated settlements of the VWPs were also included in the calculations.

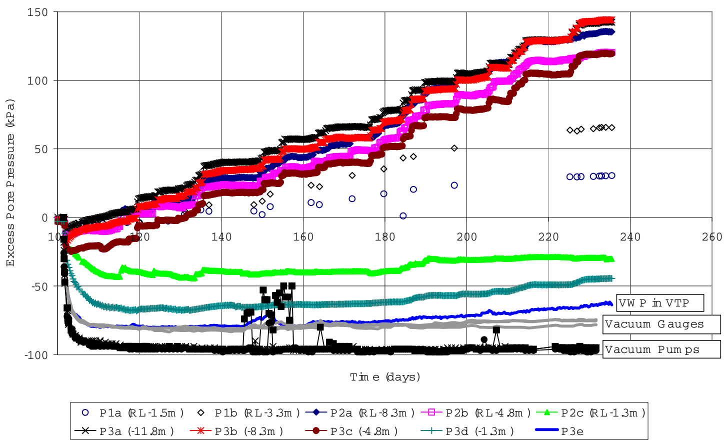

FIG. 3 Inferred excess pore pressures

A suction pressure of -80kPa was rapidly attained beneath the membrane and most of this pressure was transmitted down the vertical transmission pipe (VTP) to a depth of RL-19.4m (P3e). The VWPs at shallow depth (RL-1.3m) developed significant suction pressures shortly after starting the vacuum pumps. Vertical drainage in conjunction with horizontal drainage is likely to have affected the response of the shallow VWPs. The permeability of the upper 5m of soil may also have been greater than the lower soils due to the effects of desiccation. In contrast, the VWPs below RL-4.8m only slightly responded to the application of vacuum as the permeability of the clay is very low and there is a substantial delay before the negative pressure imposed at the drain boundary is transmitted to the location of the piezometers. In contrast, surcharge-induced increases in pore pressure after day 115 were instantly transmitted to the deeper VWP's.

A summary of lateral deformations recorded by inclinometer I3 is shown in Figure 4. The lateral displacements progressed through three distinct phases. There was an initial outward (positive) deformation caused by placement of the drainage layer prior to application of the vacuum. This outward deformation was confined to the upper 6m of clay. Application of vacuum pressure caused the soil to displace inwards to 14m depth. Subsequent surcharge fill placement caused the soil to displace outwards again. However, in contrast to the initial loading, outwards displacement occurred over the full depth of the clay.

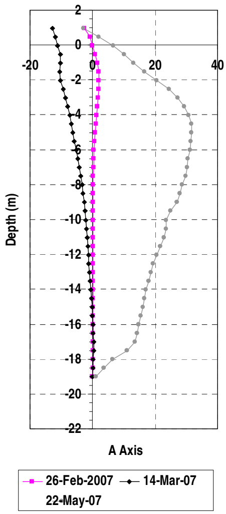

FIG. 4 Summary of lateral displacements of I3

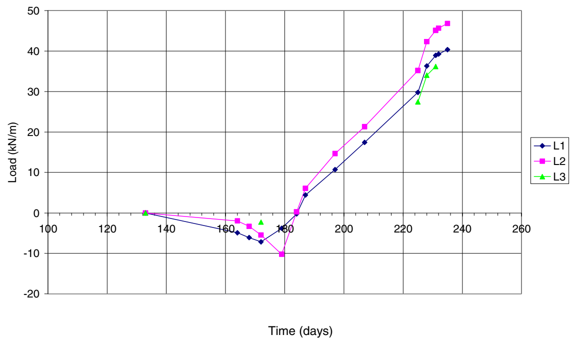

FIG. 5 Loads induced in tensile fabric

Loads induced in the tensile fabric during placement of surcharge fill are shown in Figure 5. The negative load is caused by relaxation of the preload applied to the load cells during installation. A maximum load of 46kN/m was measured by load cell L2 when the fill thickness reached its final thickness of about 8.5m. The tensile fabric has an ultimate capacity of 600kN/m and was assigned a design capacity of 200kN/m. The loads induced in the fabric are much smaller than were anticipated during design, which is judged to be a result of ignoring the strengthening effect of the vacuum on the sand drainage layer.

Treatment of the groundwater extracted from the vacuum system was an issue at this site because of the presence of acid-sulphate soils and naturally occurring heavy metals. The water was held in ponds and treated with Electrobind™ to remove the heavy metals and increase the pH of the water to between 6 and 8. The water was then pumped into Emigrant Creek. Treatment of the groundwater was a hidden cost to the client not considered prior to commencement of the works.

ANALYSIS FOR DEGREE OF CONSOLIDATION

Deformation parameters adopted for the analyses were obtained from in-situ and laboratory tests. Compression, recompression and creep ratios ($CR=C_c/(1+e_0)$, $CRR=C_r/(1+e_0)$, $C\alpha=\alpha/(1+e_0)$) were obtained from one-dimensional oedometer tests. Compression ratios of 0.35 and 0.3 were obtained for the soft clay to 15m depth and firm clay from 15m to 25m depth respectively. A recompression ratio of 0.05 was adopted for the entire clay depth as was a creep ratio of 0.015. The coefficient of horizontal consolidation (c_h) was determined from the results of piezocone dissipation tests and a value of $4m^2/yr$ adopted. The coefficient of vertical consolidation (c_v) was taken to be half the horizontal value ($2m^2/yr$), in spite of the oedometer test results indicating c_v ranged between $0.5m^2/yr$ to $1m^2/yr$, to take account of macro fabric (eg silt lenses) that were not captured in small scale laboratory tests.

Data from settlement plate SP12 was assessed to estimate the degree of consolidation. A comparison between SP12 and back-figured settlement is shown in Figure 6. Also shown is the rate of filling and the fill profile used in the analysis.

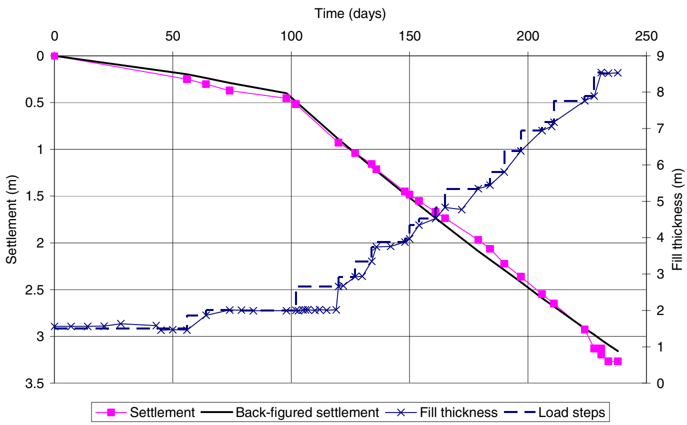

FIG. 6 Measured and computed settlements

The back-figured curve was computed using the following expression:

$$\frac{s}{s_{100}} = 1 - \exp\left(\frac{-8c_h t}{\mu d_e^2}\right) \qquad (1)$$

In Equation 1, s is settlement, s_{100} is the settlement at 100% consolidation, t is time, d_e is the diameter of influence, and μ is the smear factor. Vacuum pressure was considered to act like a surcharge load in the calculation of settlement at 100% consolidation. A vacuum pressure of 80kPa, a unit weight of the fill of $21.5kN/m^3$, a diameter of influence of 1.028m and $c_h = 4m^2/yr$ were used. The smear factor incorporated a smear radius to well radius ratio of 5 as well as a ratio of smeared to virgin soil permeability. The computed settlement was matched to the measured settlement using the least-squares method. The ratio of smeared to virgin soil permeability was varied to achieve the minimum error and was found to be 4.3. The resulting value of the smear factor was 8.0. These values are similar to the design values of 5 and 9.19 respectively. If smear is not explicitly taken into account, the average coefficient of horizontal consolidation required to match the recorded settlements is about $1.38m^2/yr$. The back analysis suggested that the degree of consolidation was about 62% at day 230. From Equation 1, the difference in time between 62% and the target 90% consolidation is about 150 days, which indicates that the vacuum pumps need to be running for a further 5 months.

This method of back analysis has its limitations as it is always possible to fit the measured settlement data by varying one of the smear radius ratio, the permeability ratio or the coefficient of consolidation. As the smear radius and permeability ratios are not measured parameters it is possible to convince oneself that the back analysis is representative of the observed embankment behaviour. A more sophisticated back analysis would attempt to match the measured pore pressure data as well as the settlement data.

STABILITY DURING CONSTRUCTION

Assessment of the embankment stability, and by implication the rate of surcharge filling, was performed using the method described by Tavenas and Leroueil (1980). The maximum lateral deformations recorded by the inclinometers are compared with the settlement at the centre-line of the embankment. Impending instability is indicated by the ratio of lateral displacement increment to settlement increment, δy/δs approaching unity. Tavenas and Leroueil (1980) suggest that a ratio of 0.15 to 0.2 indicates a low risk of instability. Maximum lateral displacements are plotted against settlement in Figure 7. Inclinometer I1 lies adjacent to the standard surcharge area while the other inclinometers ring the vacuum area. Negative increments in lateral displacement are possible and reflect vacuum-induced inward movement of the clay.

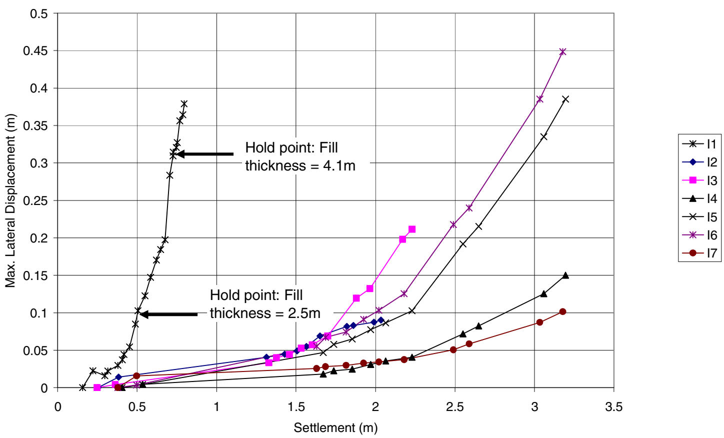

FIG. 7 Lateral displacement to settlement plots

Around the vacuum area, the ratio of δy/δs did not exceed 0.13 when the surcharge fill was less than 5.3m thick and increased to 0.3 once the fill thickness reached 7m. The ratio was greatest in the areas where the berm widths were least. As the width of the berms increased the ratio decreased. However, the data indicates that the embankment was stable in all areas, which implies that stability berms are not required. In contrast, the ratio δy/δs in the standard surcharge area approached one after a fill thickness of only 2.5m had been placed. A hold point preventing further filling in the standard surcharge area was invoked until the ratio dropped below 0.6. Subsequent filling to 4.1m increased the ratio to one again and a second hold point was applied. Stability berms would have allowed a faster rate of filling in this area. This comparison shows clearly the beneficial effects of vacuum consolidation. More fill can be placed more rapidly on top of the vacuum consolidation area than can be placed using standard surcharge filling methods.

Tavenas and Leroueil's (1980) method was developed from data obtained from the construction of stable and unstable conventionally constructed embankments as opposed to vacuum assisted construction. A question arises whether a vacuum-induced inward component of the total lateral deformation would disguise an outward lateral displacement that otherwise could be considered an indication of impending instability. To address this question, a stability assessment was performed by the contractor once the ratio of lateral displacement to settlement increments passed 0.3 (fill thickness of 6.5m). The factor of safety against instability was assessed to be 1.7. This relatively high factor of safety was caused by the rapid consolidation that had occurred immediately below the drainage layer.

CONCLUSIONS

The following conclusions regarding the design, construction and performance of the vacuum consolidation system were drawn from the trial:

- The design methods adopted to assess settlement and rate of settlement adequately predicted total settlement and rate of consolidation.
- It is likely that stability berms and tensile fabric are not required to maintain stability in the presence of vacuum. The monitoring data indicates that construction could have proceeded more rapidly but it is unclear what the maximum rate of construction could have been.
- Construction of the vacuum system was relatively straight-forward. Treatment of the extracted groundwater added to the final cost of the trial.
- Embankments constructed using a vacuum consolidation system are able to be built more rapidly and to greater heights than embankments constructed using standard surcharge filling methods because the vacuum pressure enhances the stability of the embankment.

ACKNOWLEDGMENTS

The authors appreciate the support of the Roads and Traffic Authority of New South Wales, Australia and of Austress-Menard.

REFERENCES

Masse, F., Spaulding, C.A., Wong. I. C. and Varaskin, S. (2001), "Vacuum Consolidation: A Review of 12 years of Successful Development", *Geo-Odyssey* ASCE Virginia Tech.

Tavenas, F. and Lerouiel, S. (1980), "The behaviour of embankments on clay foundations", Can. Geotech. J., Vol. 17, 236-260

Vacuum Preloading Techniques - Recent Developments and Applications

Jian Chu[1], Shuwang Yan[2], and Buddhima Indraranata[3], F. ASCE

[1] School of Civil and Environmental Engineering, Nanyang Technological University, Blk N1, 50 Nanyang Ave, Singapore 639798, Singapore, cjchu@ntu.edu.sg.
[2] Geotechnical Research Institute, Tianjin University, Tianjin, China, shuwangyang@tju.edu.cn .
[3] School of Civil, Mining and Environmental Engineering, Faculty of Engineering, University of Wollongong, Wollongong City, NSW 2522, Australia, indra@uw.edu.au.

ABSTRACT: In this paper, an overview on the mechanisms, techniques and applications of the vacuum preloading method are presented. Some recent developments in the vacuum preloading techniques, including the use of new materials, the expansion of the method, and new analysis or numerical modeling methods are briefly summarized.

INTRODUCTION

It has been 56 years since the idea of vacuum preloading was proposed by Kjellman (1952). Since then, the vacuum preloading method has evolved into a mature and efficient technique for the treatment of soft clay. This method has been successfully used for soil improvement or land reclamation projects in a number of countries (Holtz 1975; Chen and Bao 1983; Bergado et al. 1998; Chu et al. 2000; Indraratna et al. 2005). With the merging of new materials and new technologies, this method has been further improved in recent years. A brief overview of this technique and the recent developments and applications is given in this paper. In adopting this technique, sand drains and recently prefabricated vertical drains (PVDs) have often been used to distribute the vacuum pressure and discharge pore water. A nominal vacuum load of 80 kPa is normally used in design although a higher vacuum pressure of up to 90 kPa may be achieved sometimes. When a surcharge load higher than 80 kPa is required, a combined vacuum and fill surcharge can be applied. For the treatment of very soft ground, the vacuum preloading method is faster than the fill surcharge method, as the 80 kPa vacuum pressure can be applied almost instantly, without causing stability problem. The vacuum preloading method is also cheaper when compared with the fill surcharge method for an equivalent load (Chu et al. 2000). The vacuum preloading method has also been incorporated in the land reclamation process when clay slurry dredged from seabed is used as fill material for land reclamation. As the clay slurry fill is too soft for fill surcharge to be applied, the vacuum preloading method is ideally used for the consolidation of the clay slurry. Thousands of hectares of land have been reclaimed in Tianjin, China, using this method (Chen and Bao 1983; Yan and Chu 2005). In recent years, a similar vacuum technique has also been used for site remediation works (Lindhult et al. 1995). A variation of this technique has also been adopted for the stabilization of retaining structures (Miyazaki et al. 2005). Various applications of the vacuum preloading and the combined vacuum and fill surcharge preloading methods have been presented in Chu et al. (2000); Tang and Shang (2000); Indraratna et al. (2005); and Yan and Chu (2005). The mechanisms of vacuum preloading and conventional and innovative techniques related to equipment, materials, monitoring, analysis and numerical simulations are discussed in the followings.

MECHANISMS

The principles and mechanism of vacuum preloading have been well explained in the literature, e.g., Kjellman (1952), Holtz (1975), Chen and Bao (1983), Chu et al. (2000), and Indraratna et al. (2004). As a comparison with the fill surcharge preloading, the pore water pressure and effective stress change processes in vacuum preloading can be further examined as follows.

The consolidation process of soil under surcharge load has been well understood and can be illustrated using the spring analogy as shown in Fig. 1(a). For the convenience of explanation, the pressures in Fig. 1 are given in absolute values and p_a is the atmospheric pressure. As shown in Fig. 1a, the instance when a surcharge load, Δp, is applied, it is the excess pore water pressure that takes the load. Therefore, for saturated soil, the initial excess pore water pressure, Δu_0, is the same as the surcharge Δp. Gradually, the excess pore water pressure dissipates and the load is transferred from water to the spring (i.e., the soil skeleton) in the model shown in Fig. 1(a). The amount of effective stress increment equals to the amount of pore water pressure dissipation, $\Delta p - \Delta u$ (Fig. 1(a)). At the end of consolidation, $\Delta u = 0$ and the total gain in the effective stress is the same as the surcharge, Δp (Fig. 1(a)). It should be noted that the above process is not affected by the atmospheric pressure, p_a.

The mechanism of vacuum preloading can also be illustrated in the same way using the spring analogy as shown in Fig. 1(b). When a vacuum load is applied to the system shown in Fig. 1(b), the pore water pressure in the soil reduces. As the total stress applied does not change, the effective stress in the soil increases. The instance when the vacuum load, $-\Delta u$, is applied, the pore water pressure in the soil is still p_a. Gradually the pore pressure is reducing and the spring starts to be compressed, that is, the soil skeleton starts to gain effective stress. The amount of the effective stress increment equals to the amount of pore water pressure reduction, Δu, which will not exceed the atmospheric pressure, p_a, or normally 80 kPa in practice.

TECHNIQUES

A typical vacuum preloading system is shown in Fig. 2 (Chu et al. 2000). PVDs and the horizontal pipes are used for the distribution of vacuum pressure and the dissipation of pore water. The horizontal pipes and the top ends of the PVDs are buried in a sand blanket made of coarse sand which transmits the vacuum to the

PVDs. Corrugated flexible pipes (50 to 100 mm in diameter) are normally used as horizontal pipes. These pipes are perforated and wrapped with a permeable fabric textile to act as a filter layer as shown in Fig. 3(a). The horizontal pipes are connected to the main vacuum distribution pipes. Three layers of thin PVC membranes are often used to seal the area to be improved by vacuum preloading. The membranes are buried into a trench at the four boundaries of the area. For this reason, the entire soil improvement area often needs to be subdivided into small areas to facilitate the installation of the membranes. Vacuum pressure was applied using vacuum pumps continuously for the whole duration of preloading.

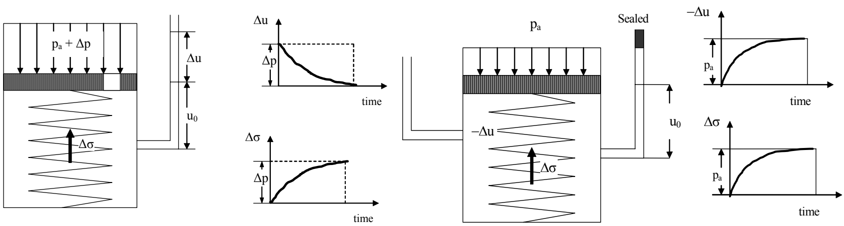

$u_0 = p_a$
$\Delta\sigma = p_a + \Delta p - (u_0 + \Delta u) = \Delta p - \Delta u$

(a)

$u_0 = p_a$
$\Delta\sigma = p_a - (u_0 - \Delta u) = \Delta u$

(b)

FIG 1. Spring analog of consolidation process (a) under fill surcharge; (b) under vacuum load

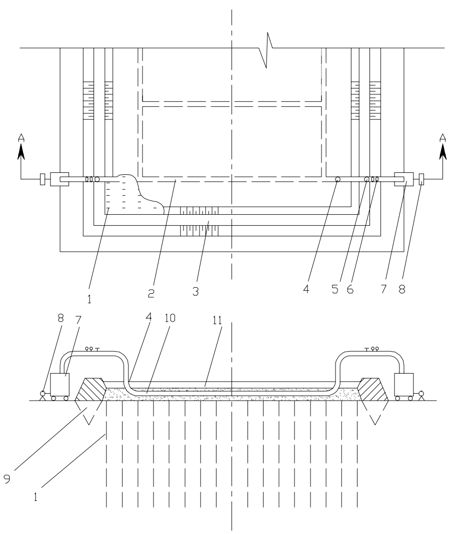

1 PVDs; 2 horizontal pipes; 3 revetment; 4 water outlet; 5 valve; 6 vacuum gauge; 7 jet pump; 8 centrifugal pump; 9 trench; 10 main vacuum pipes; 11 sealing membrane.

FIG 2 A Schematic illustration of the vacuum preloading system

NEW DEVELOPMENTS

Use of Drain Panels

Several improvements to the vacuum preloading technique presented in Fig. 2 have been made in the recent years. The first is the use of drain panels as shown in Fig. 3(b), instead of the pipes. This is to ensure the drainage channels will still function well under a high surcharge pressure, as in the case of combined fill and vacuum preloading. The drainage panels also provide better channels for distributing vacuum pressure and discharging water. Some drainage panels also have slots for direct connection with PVDs and thus improve the efficiency of the system.

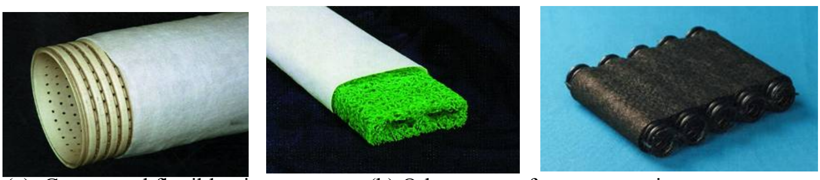

(a) Corrugated flexible pipes (b) Other types of geo-composites

FIG 3 Horizontal pipes used for vacuum preloading

Membrane Free Techniques

When the total area has to be subdivided into a number of sections to facilitate the installation of membrane, the vacuum preloading can only be carried out one section after another. This may not be efficient when the vacuum preloading method is used for land reclamation over a large area. One way to overcome this problem is to connect the vacuum channel directly to each individual drain using a tubing system as shown in Fig. 4. In this way, the channel from the top of the PVD to the vacuum line is sealed. Hence a sand blanket and membranes are not required. This system has been used for the construction of the new Bangkok International Airport (Seah, 2006). However, as such a system does not provide an airtight condition for the entire area, high efficiency may be difficult to be achieved. The vacuum pressure applied can be only 50 kPa or lower (Seah, 2006). This method also only works when the soil layer to be improved is dominantly low permeability soil.

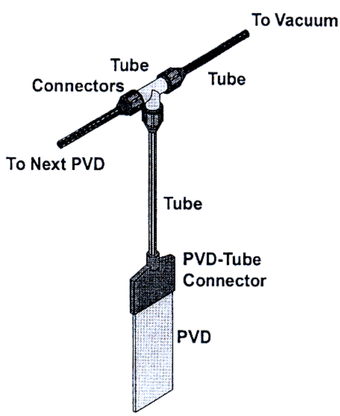

FIG. 4 PVD and tubing for vacuum preloading (after Seah, 2006)

Another method to do sway with the membrane is to use the so-called low level vacuum preloading method (Yan and Cao, 2006). This method is schematically illustrated in Fig. 5. When clay slurry is used as fill for land reclamation, the vacuum pipes can be installed at the seabed or a level a few meters below the ground surface. In this way, clay slurry fill can be placed on top of the vacuum pipes. As clay has a low permeability, the fill material will provide a good sealing cap and membranes will not be required. However, this method is not free of problems. Tension cracks will develop in the top layer when dried under sunlight. The vacuum pressure may not be distributed properly unless a drainage blanket is used at the level where the drainage pipes are installed or the individual drains are connected to the vacuum pipes directly. It is also difficult to install drainage pipes or panels underwater. Nevertheless, this method does not require the construction of inner dikes for subdivision and thus cuts down the project costs and duration substantially.

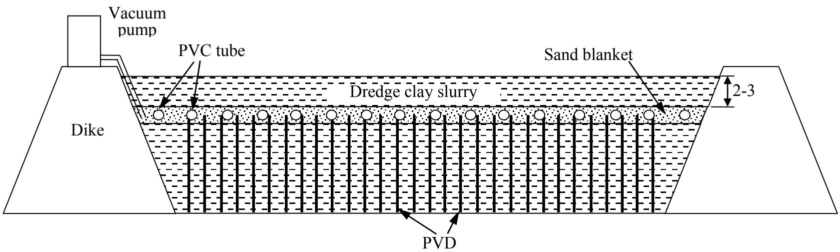

FIG. 5 No membrane vacuum preloading method

Dealing with Inter-bedded Permeable Layers

The vacuum preloading method may not work well when the subsoil is inter-bedded with sand lenses or permeable layers that extend beyond the boundary of the area to be improved, such as the improvement of soft soil below sand fill for reclaimed land. In this case, a cut-off wall is required to be installed around the boundary of the entire area to be treated. One example is given by Tang and Shang (2000), in which a 120 cm wide and 4.5 m deep clay slurry wall was used as a cut-off wall in order to improve the soft clay below a silty sand layer. However, installation of cut-off walls is expensive when the total area to be treated is large. An alternative method is to use PVD with impermeable plastic sleeve for the section of the PVD that passes through the permeable layer. However, this is workable only when we know fairly accurately the thickness of the permeable layer, which is often the case for reclaimed land.

Drainage Enhanced Dynamic Compaction Method

One shortcoming of the vacuum preloading or the surcharge preloading method in general is that it is time consuming. One way to overcome this problem is to combine vacuum preloading with dynamic compaction. The basic idea is to use dynamic compaction with low impact energy to generate excess pore pressure which can be then dissipated quickly under the vacuum action (Chu et al. 2005). The quick dissipation of pore pressure in turn improves the efficiency of dynamic compaction. This method has been used in a number of projects in China (Xu et al. 2003). However, more research is required to develop this method into a mature technique.

FIELD MONITORING AND DATA INTERPRETATION

Field monitoring is essential for projects using vacuum preloading as it is the only way to assess the effect of soil improvement using vacuum preloading. Normally, settlements of different soil layers, pore water pressure and lateral displacement at different elevations are measured. The average degree of consolidation (DOC) can be evaluated based on either the settlement or pore pressure data. The DOC estimated using settlement is affected by the methods used for predicting the ultimate settlement. Using the monitored pore water pressure data, the pore water pressure distribution versus depth profiles can be plotted for the initial, final, and any intermediate states. The DOC can be estimated based on the pore water pressure profile using the method suggested by Chu and Yan (2005). One example is shown in Fig. 6. As shown by Chu and Yan (2005) using case studies, the DOC estimated using settlement data is generally greater than that using pore water pressure data. This can be partially explained by the fact that when only limited instruments are used, settlement and pore water pressure gauges will be installed only at the locations where the maximum settlement and pore water pressure will likely be developing. As a result, the DOC tends to be overestimated when settlement data are used and underestimated when pore water pressure data are used. It has been suggested by Chu and Yan (2005) that for contracting purpose, it is necessary to specify the method used to calculate the DOC and indicate clearly whether the DOC is to be estimated using settlement or pore water pressure data.

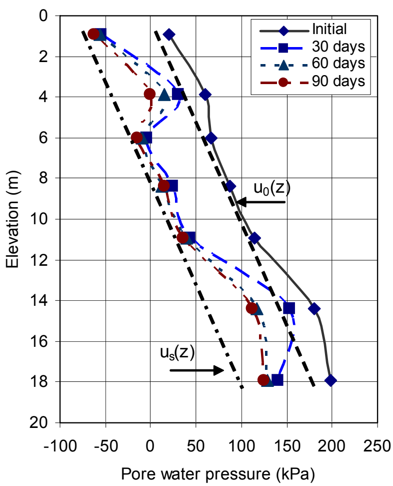

FIG. 6 Pore pressure profiles used for the calculation of DOC.

NUMERICAL MODELLING

A case study of a combined vacuum and surcharge load through prefabricated vertical drains (PVD) at a storage yard at Tianjin Port, China was investigated using a finite element analysis (Rujikiatkamjorn et al. 20007). At this site, a combination of 80 kPa vacuum pressure and 40 kPa of fill surcharge was required to improve the soft soil condition and avoid any instability problems. Figure 7 presents soil profile with its relevant soil properties. The vertical cross section and the locations of field instrumentation are shown in Fig. 8a. This included settlement gauges, pore water pressure transducers, multi-level gauges, inclinometers and piezometers. PVDs of 20 m in length (Section: 100 mm × 3 mm) were installed in a square pattern at 1 m spacing. The finite element mesh contained elements having 8-node bi-quadratic displacement and bilinear pore pressure shape functions (Fig. 8b).

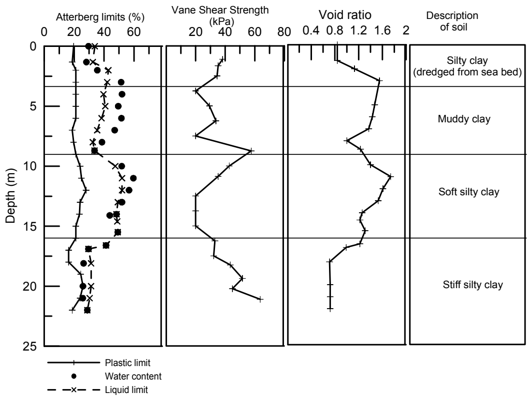

FIG. 7 General soil profile and properties at Tianjin port (adopted from Rujikiatkamjorn et al. 2007)

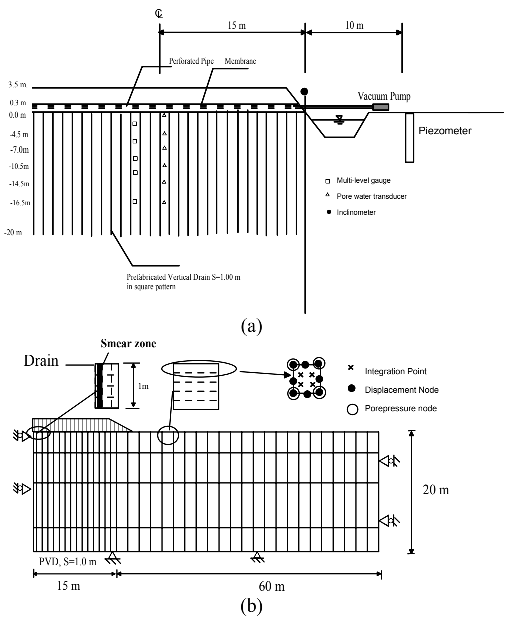

FIG. 8 (a) Vertical cross section A-A and locations of monitoring instruments and (b) Finite element mesh for plane strain analysis (adopted from Rujikiatkamjorn et al. 2007)

Figures 9 and 10 show a comparison between the predicted and recorded field settlements and excess pore pressure, respectively. The predicted consolidation settlement and excess pore pressure are in accordance with the measured results. The mean excess pore pressure is negative (suction), avoiding any potential undrained failures (Indraratna et al., 2005). Figure 11 illustrates the comparison between the measured and predicted lateral movements at the toe of embankment after 180 days. The negative lateral displacement denotes an inward soil movement towards the centerline of the embankment. The predictions at shallow depth (i.e., 0-5m) agree well with the field data, but they slightly underestimate the field results at 5-10 m depth (middle of the soft clay layer). As vacuum consolidation induces an inward and fill surcahrge an outward movement, a combined vacuum and fill surcharge preloading can be used as a method to control or minimise soil lateral movement to enhance stability of embnkment or reduce the effect to adjacent buildings (Yan and Chu 2005).

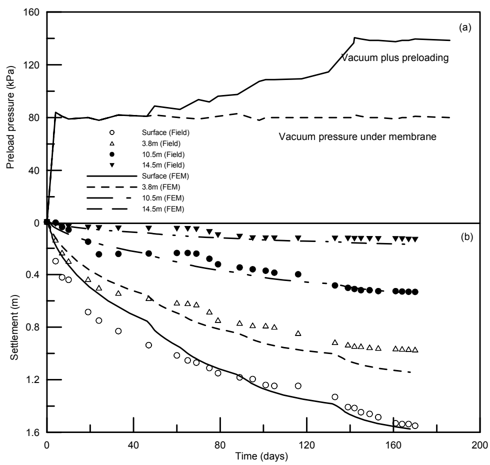

FIG. 9 Section II: (a) Loading history and (b) Consolidation settlements (adopted from Rujikiatkamjorn et al. 2007)

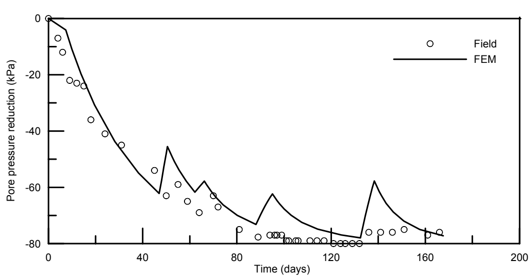

FIG. 10 Excess pore pressure predictions at 0.25m away from the embankment and at 5.5m depth (adopted from Rujikiatkamjorn et al. 2007)

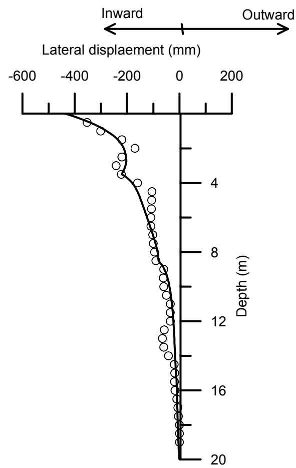

FIG. 11 Lateral displacement after 180days at the embankment toe (adopted from Rujikiatkamjorn et al. 2007)

CONCLUDING REMARKS

Some applications and new developments of the vacuum preloading method are summarized. The main advantage of vacuum application is that the surcharge height of embankments on very soft clays can be reduced to prevent any undrained failure. The review presented in this paper has shown that the vacuum preloading method is still evolving and can be further improved. While the membrane-based method of vacuum application has been conventional, membrane free techniques that apply vacuum pressure directly through PVDs and other improvements to the conventional method have been developed. There is still much potential to expend the capacity of the vacuum preloading methods into new applications by combining them with other ground improvement techniques.

REFERENCES

Bergado, D.T., Balasubramaniam, A.S., Fannin, R.J., and Holtz, R.D. (2002). “Prefabricated vertical drains (PVDs) in soft Bangkok clay: a case study of the new Bangkok International Airport project.” *Canadian Geotechnical Journal*, Vol. 39, No. 2, 304-315.

Chen, H. and Bao, X.C. (1983). “Analysis of soil consolidation stress under the action of negative pressure.” *Proc. 8th European Conf. on Soil Mech. and Found. Eng.*, Helsinki, Vol. 2, 591-596.

Chu, J., Yan, S.W., and Yang, H. (2000). "Soil improvement by vacuum preloading method for an oil storage station". *Geotechnique*, Vol. 50, No. 6, 625-632.

Chu, J. and Yan, S.W. (2005). “Estimation of degree of consolidation for vacuum preloading projects." *International Journal of Geomechanics*, *ASCE*, Vol. 5, No, 2, 158-165.

Chu, J. Yan, S.W. and Zheng, Y.R. (2006). "Three soil improvement methods and their applications to road construction." *Ground Improvement,* Vol. 10, No. 3, 103-112.

Holtz, R.D. (1975). "Preloading by vacuum: current prospects." *Transportation Research Record*, No. 548, 26-79.

Indraratna, B., Bamunawita, C. & Khabbaz, H (2004). "Numerical modelling of vacuum preloading & field applications." *Canadian Geotechnical Journal,* Vol. 41, 1098-1110.

Indraratna, B., Rujikiatkamjiorn, C. and Sathananthan, I. (2005). "Analytical and numerical solutions for a single vertical drain including the effects of vacuum preloading." *Canadian Geotechnical Journal*, Vol. 42, NO. 4, 994-1014.

Indraratna, B., Rujikiatkamjorn, C., Balasubramaniam, A.S. and Wijeyakulasuriya (2005). "Prediction and observations of soft clay foundations stabilized with geosynthetic drains and vacuum surcharge." *Ch. 7, Ground Improvement Case Histories*, Eds. Indraratna, B. and Chu, J., Elsevier, 199-230.

Kjellman, W. (1952). "Consolidation of clayey soils by atmospheric pressure." *Proc. of a Conf. on Soil Stabilization*, Massachusetts Institute of Technology, Boston, 258-263.

Lindhult, E.C., Tarsavage, J.M. and Foukaris, K.A. (1995). "Remediation in clay using two-phase vacuum extraction." *Proc. National Conference on Innovative Technologies for Site Remediation and Hazardous Waste Management,* Pittsburgh, Pennsylvania, July 23-26, Eds. R.D. Vidic and F.G. Pohland, *New York: ASCE*.

Miyazaki, K., Hagiwara, T. and Imamura, S. (2005). "Ground improvement of soft marine clay layer by super well point method." *Proc. Int. Conf. Geot. Eng. for Disaster Mitigation and Rehabilitation*, Singapore, 12-13 Dec, Eds. J. Chu et al., World Scientific, 466-471.

Tang, M. and Shang, J.Q. (2000). "Vacuum preloading consolidation of Yaoqiang Airport runway." *Geotechnique*, Vol. 50, No. 6, 613-623.

Seah, T.H. (2006). "Design and construction of ground improvement works at Suvarnabhumi Airport." *Geot. Eng, J. of Southeast Asian Geot. Society*, Vol. 37, 171-188.

Rujikiatkamjorn C., Indraratna, B. and Chu, J. (2007). "Numerical modelling of soft soil stabilized by vertical drains, combining surcharge and vacuum preloading for a storage yard." *Canadian Geotechnical Journal*, Vol. 44, 326-342.

Xu, S.L., Lu, X.M., Liu, C.M. and Liu, Y.Y. (2003). "Field trials of the vacuum compaction method for soil improvement." *Proc. 9th National Geot. Conf.*, Beijing, China, Vol. 2, 736-739.

Yan, S.W. and Chu, J. (2005). "Soil improvement for a storage year using the combined vacuum and fill preloading method." *Canadian Geotechnical Journal,* Vol. 42, No. 4, 2094-1104.

Yan, H.S. and Cao, D.Z. (2005). "Application of low-level vacuum preloading technique in offshore projects." *Ocean and River Hydraulics, No. 3, 41-43.*

Effects of Partially Penetrating Prefabricated Vertical Drains and Loading Patterns on Vacuum Consolidation

Buddhima Indraratna[1], F. ASCE, and Cholachat Rujikiatkamjorn[2]

[1] Professor of Civil Engineering, School of Civil, Mining and Environmental Engineering, University of Wollongong, Wollongong City, NSW 2522, Australia. PH: (61-2)-4221 3046; FAX: (61-2)-4221 3238; email: indra@uow.edu.au

[2] Research Associate, School of Civil, Mining and Environmental Engineering, University of Wollongong, NSW 2522, Australia

ABSTRACT: In this study, numerical modeling of a multi-drain system is employed to determine the optimum penetration depth of prefabricated vertical drains (PVDs) and the vacuum pressure that provides the maximum consolidation settlement and less lateral displacements. The plane strain analysis using an equivalent permeability with transformed unit cell geometry was considered for varying drain length and vacuum load. The effects of the vertical drain length and vacuum pressure on soft clay consolidation were examined through time for 90% degree of consolidation, associated settlement and lateral displacement.

1. INTRODUCTION

Much of Australian railway tracks traverse coastal areas containing soft soils and marine deposits. Pre-construction stabilization of soft formation soils by applying a surcharge load alone often takes too long. The installation of prefabricated vertical drains (PVDs) and vacuum pressure can reduce the preloading period significantly by decreasing the drainage path length, sometimes by a factor of 10 or more (Chu et al. 2004). Beneath railway tracks, the loaded area is significantly small in comparison with the thickness of the soft soil layer. The increase in vertical stress is usually sustained within the first several metres of the formation (Runnesson et al., 1985; Jamiolkowski, et al. 1983). In this context, there is no need for improving the entire depth of the soft clay deposit, hence, relatively short PVDs without any prolonged preloading may still be sufficient to support the load with acceptable track deformation. Vacuum pressure can act as an apparent surcharge load and ensure a reduction of the outward lateral displacement (Bergado et al. 2002). Due to the complexity of the problem, the consolidation due to partially penetrating drains is only analysed using a unit cell approach (Hart et al., 1958; Tang and Onitsuka, 1998). An advantage would be gained if it were possible to optimize the vertical drain configuration and vacuum pressure to minimize consolidation time and effectively control lateral displacement (Indraratna et al. 2005).

In this study, the effects of partially penetrating vertical drains and the vacuum pressure are numerically investigated through settlement and corresponding lateral displacements.

2. THEORETICAL BACKGROUND

A simplified plane strain (2-D) finite element analysis can be readily adopted to most field situations, in order to accurately predict the soil behaviour underneath a long embankment that has a compatible geometry for plane strain conditions (Indraratna and Redana, 2000; Chai et al. 2001). Indraratna et al. (2005) have shown that equivalent soil parameters are needed when a plane strain analysis is employed. A summary of the theoretical background for conversion from the axisymmetric to the equivalent plane strain model is presented below for the readers' benefit.

According to Figure 1, the ratio of the smear zone permeability to the undisturbed zone permeability is obtained by (Indraratna et al., 2005a):

$$\frac{k_{s,ps}}{k_{h,ps}} = \beta / \left(\frac{k_{h,ps}}{k_{h,ax}} \left[\ln\left(\frac{n}{s}\right) + \frac{k_{h,ax}}{k_{s,ax}} \ln(s) - \frac{3}{4} \right] - \alpha \right) \tag{1}$$

In the above, $\alpha = 0.67 \times (n-s)^3 / n^2(n-1)$ and $\beta = \frac{2(s-1)}{n^2(n-1)} \left[n(n-s-1) + \frac{1}{3}\left(s^2+s+1\right) \right]$

where, $n = d_e/d_w$, $s = d_s/d_w$, d_e = equivalent diameter of cylinder of soil around drain, d_s = diameter of smear zone and d_w = diameter of drain well, k_h = average horizontal permeability in the undistrubed zone (m/s), and k_s = average horizontal permeability in the smear zone (m/s). The subscribes ps and ax describe plane strain and axisymmetric conditions

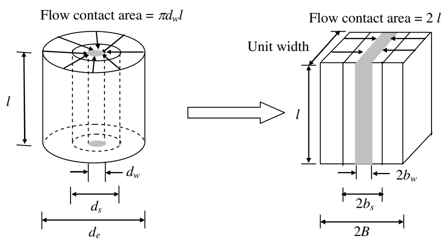

(a) **(b)**

FIG. 1 Geometric conversion between (a) axisymmetric condition and (b) equivalent plane strain condition (after Indraratna et al., 2005a).

3. PROBLEM CHARACTERIZATION

A 2D finite element program (ABAQUS) was employed to simulate multi-drain analysis (Hibbitt et al., 2006). A total of 2000 elements of eight-node tri-linear displacement node with 8 pore pressure nodes (C3D8P) were used (Fig. 2). The dense mesh beneath the embankment is the zone of soil stabilized by PVDs. The equivalent plane strain model (Equation 1) was incorporated in the finite element code (ABAQUS) adopting the modified Cam-Clay theory (Roscoe and Burland, 1968). It is assumed that the clay is uniform and normally consolidated. The relevant soil parameters are: λ = 0.14, κ=0.014, M= 1.2, e_0=1.1, k_h= 1.18×10^{-9} m/s. Vertical drain spacing is 1m, and the values of k_h/k_s and d_s/d_w ratios are 3 and 4, respectively. The impermeable boundaries are located at the centerline, bottom and right side of the embankment.

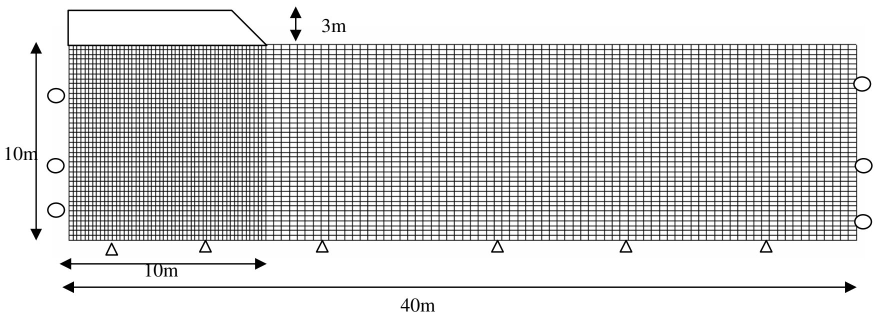

FIG. 2 Mesh discretization

4. NUMERICAL MODEL

4.1. Vertical Drains with Equal Length

Figure 3 presents vertical drain installation with varying depths of penetration. In the zone of PVD installation, the radial flow is predominant, whereas vertical flow occurs mainly below the PVD installation zone. In this section, the effect of drain length to the overall soil thickness (l_1/H) on consolidation is investigated numerically.

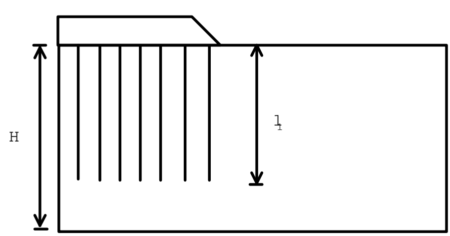

FIG. 3 Partially penetrating vertical drains of equal length

Figure 4 illustrates the effect of partially installed vertical drains (i.e. different l_1/H ratios) on the overall degree of consolidation (Fig. 4a) and lateral displacements (Fig.4b). The degree of consolidations was calculated, based on the settlement at the centerline and the lateral displacement at the embankment toe. It can be seen that the drain length may be reduced up to 90% of the entire soft clay thickness without significantly affecting the degree of consolidation. The lateral displacements are almost the same when drain lengths are more than 50% of the clay layer thickness. The maximum lateral displacement when drains are installed can be reduced by 15%.

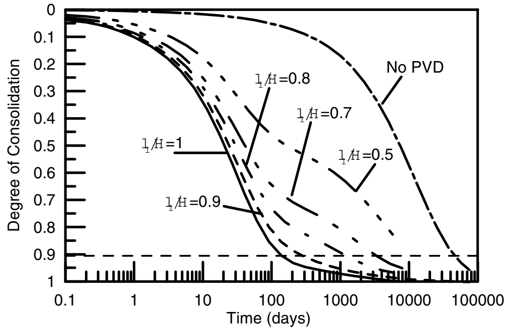

(a)

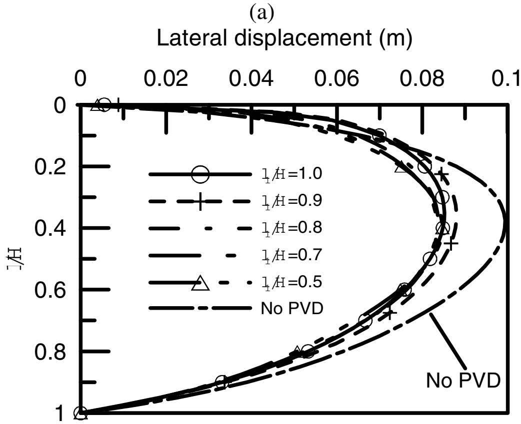

(b)

FIG. 4 Effects on partially penetrating drains (equal pattern) on (a) degrees of consolidation and (b) lateral displacement

4.2. Vertical Drains with Alternating Length

As shown in Fig. 5a, vertical drains are assumed to be installed to a depth l_2, while the drains in between these are installed to the entire depth of soft clay (*H*). It can be seen that l_2 can be reduced up to 0.6H without any significantly increase in the time for 90% consolidation. As expected, this installation is more effective compared to the equal length installation (Fig. 4a). The calculated lateral displacements are almost the same in all cases and only 15% less than the "no PVD" case, therefore, the results are not plotted here.

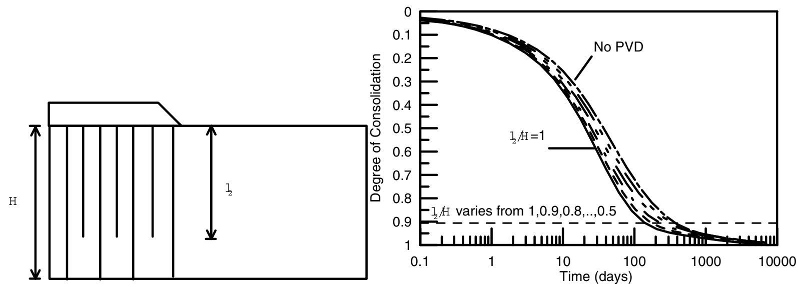

(a) (b)

FIG. 5 (a) Vertical drains with alternating length and (b) effects on the degree of consolidation

4.3. Effect of short vertical drains on narrow strip load

In this section, the vertical drain length is varied beneath narrow 2m strip load (e.g. railway tracks) to determine the required time for 90% degree of consolidation and associated lateral displacement. Vertical drains were installed at 1m spacing (Fig. 6a). The numerical analysis shows that the applied load propagates up to a depth of about 4m.

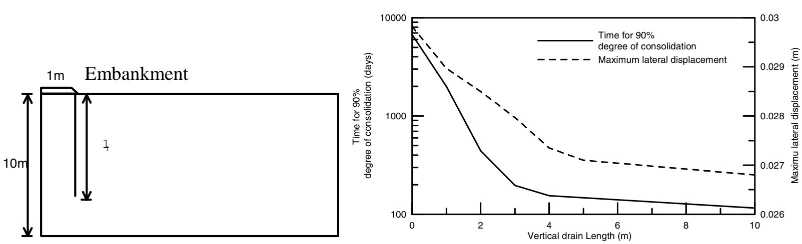

(a) (b)

FIG. 6 (a) Vertical drains beneath narrow embankment (b) Required time for 90% degree of consolidation and associated maximum lateral movement

In terms of required time, the vertical drains installed to a depth exceeding 4m have insignificant effect on the consolidation time, however, at least 5m long vertical drains are required to reduce the generation of lateral movement. It can be concluded that the effects of vertical drains are marginal when drains are installed beyond the influence zone of the applied load, as shown in Fig. 6b (4-5m).

4.4. Vacuum pressure ratio

Rujikiatkamjorn et al. (2007) has discussed the benefits of vacuum pressure combined surcharge load in terms of counterbalancing the excessive lateral displacements. The outward lateral compressive strain due to surcharge can be reduced by suction (vacuum preloading). However, this inward lateral movement may sometimes generate tension cracks in the adjacent areas. The variation of vacuum and preloading pressure to obtain a given required settlement will be considered in the numerical model to optimise the lateral displacement at the embankment toe, while identifying any zones of tension.

The variation of lateral displacement at the embankment toe due to different preloading pressures (total preloading pressure 150 kPa) is illustrated in Fig. 7a. The negative lateral displacement represents an inward soil movement towards the centerline of the embankment. As expected, the vacuum application alone can create the maximum inward lateral movement, whereas preloading without any vacuum pressure may contribute to the maximum outward lateral movement. For a uniform soil layer, the combination of 40% surcharge preloading stress with 60% vacuum pressure seems to maintain the lateral displacements close to zero axis. Fig. 7b shows the variation of surface settlement profiles with increasing % surcharge loading. The effect of vacuum pressure alone may create settlements up to 10m away from the embankment toe. Also, due to the outward lateral displacement, soil heave can be observed beyond the toe.

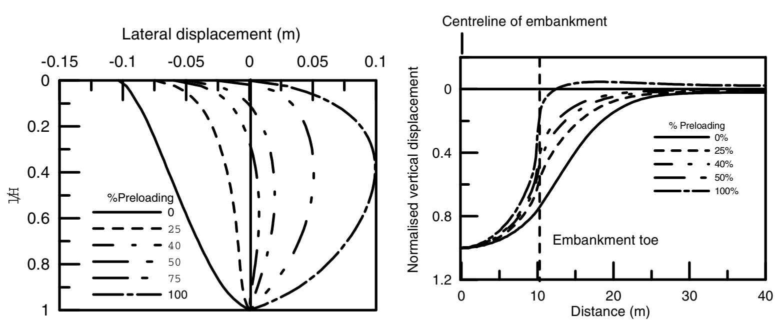

(a) (b)

FIG. 7 (a) Lateral displacements and (b) Surface settlement profiles

4.5. Effects of Vacuum Preloading on Consolidation Time

Since soft clays have low undrained shear strengths, most surcharge embankments cannot be raised beyond 2-3m without causing failure. The minimum required height to eliminate primary settlement and compensate for secondary consolidation is at least 3-4m (Hansbo, 1981). To overcome these problems, special precautions such as multi-staged construction and/or vacuum-preloading combined with PVDs, may be considered in design. In this section, the consolidation time due to multi-staged construction and vacuum-surcharge preloading is examined. It is assumed that the required preloading stress is σ_t. For a multi-staged loading, there are 2 stages of applied stress denoted by σ_1 and σ_2. The construction of the 2nd stage is assumed after 50% degree of consolidation is achieved during the 1st stage. For combined vacuum-surcharge preloading, both vacuum and surcharge pressures are applied together in a single stage. The time required for 90% consolidation can be determined by (Hansbo, 1981):

$$t_{v+p} = -\mu d_e^2 \ln(0.1)/8/c_h \quad \text{for vacuum and surcharge preloading} \tag{2}$$

$$t_{multi} = -\mu d_e^2 \ln(0.5)/8/c_h - \mu d_e^2 \ln\left(\frac{0.1}{8(0.5\sigma_1/\sigma_t + \sigma_2/\sigma_t)c_h}\right) \quad \text{for multi-stage} \tag{3}$$

Table 1 shows that with a single stage loading of combined vacuum and surcharge consolidation time can be reduced up to 25% for the above case. It is clear that vacuum preloading can be used effectively in a very soft clay, where a relatively high surcharge embankment cannot be raised because of potential undrained failure.

Table 1. Time reduction due to vacuum and surcharge preloading

σ_1/σ_t	σ_2/σ_t	t_{multi}/t_{v+p}
0.25	0.75	1.24
0.50	0.50	1.17
0.75	0.25	1.09

5. CONCLUSIONS

The current study of consolidation of a uniform soil with partially penetrating vertical drains and vacuum preloading has led to the following conclusions.

(a) For vertical drains with equal length beneath large embankment, the length of the drains can be shortened up to 90% soil thickness without seriously affecting the time for a given degree of consolidation. In contrast, the length of the drains with alternating length can be reduced up to 40% of the entire soil thickness.

(b) For a narrow embankment, installation of vertical drains deeper than the loading propagation zone has insignificant effect on consolidation time and lateral displacement reduction.

(c) The combination of vacuum and surcharge preloading can be used to avoid any excessive lateral displacements. Based on this simulation, almost zero lateral displacement can be obtained when using 40% preloading and 60% vacuum pressure.

(d) The application of vacuum pressure can substantially decrease the required height of the embankment and, therefore, the need for staged construction may be eliminated. Moreover, the height of temporary surcharge embankment can be reduced.

6. REFERENCES

Bergado, D.T., A.S. Balasubramaniam, R.J. Fannin and R.D. Holtz (2002). "Prefabricated vertical drains (PVDs) in soft Bangkok Clay: a case study of the new Bangkok International Airport project." *Canadian Geotechnical Journal*, 39(2), 304-315.

Chu, J., M.W. Bo and V. Choa (2004). "Practical considerations for using vertical drains in soil improvement projects." *Geotextiles and Geomembranes*, 22(1-2 February/April), 101-117.

Chai, J.C., Shen, S.L., Miura, N. and Bergado, D.T. (2001). “Simple method of modeling PVD improved subsoil.” *J. Geot. Engg*, ASCE, 127 (11), 965-972.

Hart EG, Konder RL, and Boyer WC. (1958). “Analysis for partly penetrating sand drains.” *JSMFD* (ASCE) 84(SM4), 1812–1815.

Hibbitt, Karlsson and Sorensen (2006). *ABAQUS/Standard User's Manual*, Published by HKS Inc.

Indraratna, B., and Redana, I. W. (2000). "Numerical modeling of vertical drains with smear and well resistance installed in soft clay." *Canadian Geotechnical Journal*, 37, 132-145.

Indraratna, B., Rujikiatkamjorn C., and Sathananthan, I. (2005). “Analytical and numerical solutions for a single vertical drain including the effects of vacuum preloading”. *Canadian Geotechnical Journal*, 42, 994-1014.

Jamiolkowski, M., R. Lancellotta and W. Wolski (1983). "Precompression and speeding up consolidation." *Proc. 8th European Conference on Soil Mechanics and Foundation Engineering*, Helsinki, 1201-1226.

Roscoe, K.H., and Burland, J.B. (1968). “On the generalized stress strain behavior of wet clay”. *Engineering plasticity*, Cambridge Univ. Press; Cambridge, U.K., 535-609.

Rujikiatkamjorn C., Indraratna, B. and Chu, J. (2007). “Numerical modeling of soft soil stabilized by vertical drains, combining surcharge and vacuum preloading for a storage yard” *Canadian Geotechnical Journal*, 44, pp. 326-342.

Runesson, K., S. Hansbo and N.E. Wiberg (1985). "The efficiency of partially penetrating vertical drains." *Geotechnique*, 35(4), 511-516.

Tang, X.W. and Onitsuka, K. (1998) “Consolidation of ground with partially penetrated vertical drains.” *Geotechnical Engineering Journal* 29(2), 209-231.

Calibration of an Elastoplastic Model for the Prediction of Stone Column Ultimate Bearing Capacity

Wissem Frikha[1], Mounir Bouassida[1] and Jean Canou[2]

[1]Unité de Recherche Ingénierie Géotechnique, ENIT- BP 37 Le Belvédère 1002, Tunis. Tunisia. mounir.bouassida@enit.rnu.tn; frikha_wissem@yahoo.fr
[2] ENPC, CERMES 6-8 Av. B. Pascal, Marne-La-Vallée, Champs Sur Marne Cedex, France; canou@cermes.enpc.fr

ABSTRACT: The ultimate bearing capacity of an isolated stone column is studied. The soil surrounding the column is modeled by a constitutive law of plastic potential with variable flow. This recent model permits the calculation of the limit pressure of an expanded cylindrical cavity from which the ultimate bearing capacity is derived. Using recorded in situ data from load tests performed on thirteen isolated column models, the model parameters are identified. Comparison between experimental data and predictions by several models is discussed.

INTRODUCTION

Reinforcing soft clays by stone columns is becoming more successful thanks to the use of advanced procedures of column installation as well as higher interest by researchers on this topic. The efficiency of this improvement technique consists in settlement reduction and increase of bearing capacity of soft soils. Further, the rapid process of installation and inexpensive cost make this technique quite competitive compared to other types of foundations. Several investigations were conducted for determining the bearing capacity of an isolated column by considering several methods which are classified in three categories (Bouassida and Hadhri, 1995). In the first approach, the state of stress is considered (Aboshi et al, 1979). Second, a failure mechanism is combined with a state of stress (Greenwood, 1970), Hughes et al. (1975), Datye (1982), Balaam and Booker (1985), Van Impe and De Beer (1983), Priebe (1995). In the third type of approach a failure mechanism only is used (Bouassida and Jellali, 2002). In this work, the second approach will be considered to compute analytically the bearing capacity of an isolated column. The column installation is modeled similarly as pressuremeter lateral expansion.

During the column expansion, in the plastic zone, a ring of soft soil around the column, with small thickness, is assumed to behave in drained condition due to the presence of drained column material. In this zone, especially, the plastic volume variation is not negligible, while an undrained behavior is assumed (then plastic volume variation is zero) in the exterior zone due to the rapidity of column installation. The aimed prediction of bearing capacity, stated above, is undertaken on the basis of an analytical result detailed in Frikha and Bouassida (2006).

THE PROBLEM OF EXPANDED CYLINDRICAL CAVITY

The problem of cylindrical cavity expansion was treated by several authors who adopted several constitutive models: Gibson and Anderson 1961, Ladanyi 1963, Salençon 1966, Vésic 1972, Wroth and Windle 1975, Baguelin et al 1978, Carter et al. 1986, Yu and Houlsby 1991 among others.

Recently, Frikha and Bouassida (2006) generalized the contribution of Salençon (1966) related to expanded cylindrical cavity within a medium governed by a constitutive law with variable flow. This problem was solved by dividing the medium around the cavity in two zones. The first zone, close to the cavity border, is assumed plastic with variable flow law. The second zone is assumed elastic. The plastic zone is divided into "n" flow zones, each one being characterized by its own plastic radius c_i and coefficient of compressibility k_i (i = 1, n). This formulation complies with continuity of radial displacement and stress vector between all zones.

In the present contribution, the plastic zone only comprises two flow zones (Fig. 1). In addition, in the external zone (II), the condition of no volume variation at infinity is assumed (Salençon, 1966), then no plastic volume variation, hence $k_2 = 1$. However, the interior plastic zone (I) is defined by its potential flow ($k_1 = k$).

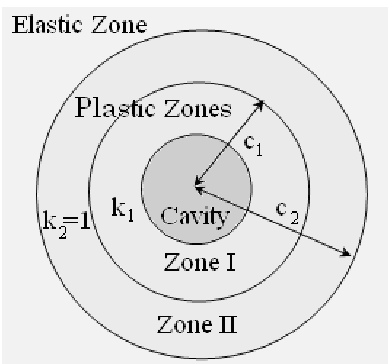

Fig. 1. Definition of different zones around the cavity subjected to radial expansion

Further, it is assumed that the ratio of the variation in time of plastic radii (denoted $\alpha = c_1 / c_2$) is constant. According to these assumptions, in case of purely cohesive soil, the limit pressure is (Frikha and Bouassida, 2006):

$$p_l = p_0 + c_U\left(1 + \frac{2}{1+k} Log\left(\frac{E}{4.\alpha^{k-1} c_U\left(1-\nu^2\right)}\right)\right) \tag{1}$$

p_0 = at rest pressure; c_U = undrained shear strength; E = Young's modulus ν = Poisson's ratio. In the case where deformation occurs without volume variation ($k_1 = k = 1$), from Equation (1), the limit pressure established by Salençon (1966) is then obtained:

$$p_l = p_0 + c_U\left(1 + Log\left(\frac{E}{4c_U\left(1-\nu^2\right)}\right)\right) \tag{2}$$

In this paper, the volume variation is taken into account; the coefficient of compressibility will depend on the angle of dilatancy denoted ψ. Further, assuming a non associated plastic flow, the plastic potential used by Monnent and Khlif (1994) is considered: $G(\underline{\underline{\sigma}}) = (\sigma_3 - \sigma_1) + \sin\psi(\sigma_3 + \sigma_1)$. In this case, the coefficient of compressibility, only depending on dilatancy angle in zone (I), is written:

$$k = \frac{1-\sin\psi}{1+\sin\psi} \tag{3}$$

ULTIMATE BEARING CAPACITY OF AN ISOLATED COLUMN

Depending on the type of column, based on earlier work of Datye (1982), three modes of failure can be foreseen as detailed in Soyez (1985): lateral expansion, generalized shearing in case of end-bearing column, and punching failure in the case of floating column. The ultimate bearing capacity of an isolated column is investigated here by combining a state of stress with a failure mechanism of lateral expansion in cylindrical cavity) which reproduces the stone column installation in a purely cohesive soft soil. The isolated column is subjected to passive triaxial compression; hence the ultimate bearing capacity as vertical stress is (Soyez, 1985):

$$q_U = K_p . p_l \tag{4a}$$

$K_p = \tan^2(\pi/4 + \varphi/2)$ = coefficient of passive pressure.

p_l = Limit pressure in surrounding soil.

Otherwise it can be written:

$$q_u = K_p\left(p_0 + Lc_U\right) \tag{4b}$$

L = a multiplier which value can be derived from Hughes and Withers (1974), who proposed the following expression of the limit pressure due to radial expansion:

$$p_l = p_0 + c_U\left(1 + Log\left(\frac{E}{2c_U(1+\nu)}\right)\right) \tag{5a}$$

Identifying Eqs (4b) with Eq (5a), it comes:

$$L = \left(1 + Log\left(\frac{E}{2c_U(1+\nu)}\right)\right) \tag{5b}$$

The model can be considered with two laws of plastic flow described above. Substituting Equation (1) into Equation (4a) yields the following expression for the ultimate bearing capacity:

$$q_u = K_p\left(p_0 + c_U\left(1 + \frac{2}{1+k}Log\left(\frac{E}{4.\alpha^{k-1} \times c_U \times (1-\nu^2)}\right)\right)\right) \tag{6}$$

In the following, the calibration of the model with two plastic flow zones is undertaken, for determining the bearing capacity of an isolated stone column.

CALIBRATION OF THE SUGGESTED MODEL

Bergado and Lam (1987) tested thirteen (13) in situ stone column models (G1 to G13); each model of column was characterized by specified grain size column material and process of installation. Table 1 presents the recorded ultimate bearing capacity of all column models and angle of friction of column material.
The calibration aims at determining the constant values α and k appearing in Eq (6). Then, for each column model, the recorded ultimate bearing capacity is identified to that predicted by the analytical solution. Whereas p_0 value is calculated (at depth equals two column diameter) from full scale data recorded on isolated column models.

Table 1. Ultimate bearing capacity of column models (Bergado & Lam, 1987)

Column models	**G1**	**G2**	**G3**	**G4**	**G5**	**G6**	**G7**	**G8**	**G9**	**G10**	**G11**	**G12**	**G13**
φ (degrees)	39.1	38.4	37.2	37	36	37.6	35.1	36.2	35.6	37.4	37.9	42.5	44.7
Bearing capacity (kN)	35	32.5	32.5	32.5	30	30	22.5	22..5	20	32.5	30	35	37.5

The calibration of coefficients α and k, under necessary condition $\alpha \succ 0$, was carried out by using KaleidaGraph software. Successive iterations, by increments equal to 0.1, for α in interval (0.1, 1) were performed to fit as close as possible the experimental ultimate bearing capacity. Then, the interval of variation for parameter k was identified that is $0 \prec k \leq 0{,}75$. Figure 2 illustrates the evolution of parameter α versus parameter k as result of the best calibration of suggested model which led, after linear regression with coefficient of correlation $R^2 = 0.98$., to:

$$\alpha = -0.1812\,k + 0.1408 \tag{7a}$$

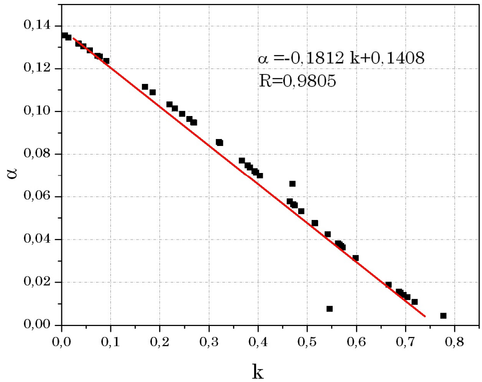

Fig. 2. Calibration result of α and k parameters from KaleidaGraph software

Otherwise, in terms of dilatancy angle, substituting Eq (3) in Eq (7a) it comes:

$$\alpha = -0.1812\,\frac{1-\sin\psi}{1+\sin\psi} + 0.1408 \tag{7b}$$

Figure 3 illustrates the variations of α and k parameters, according respectively to Eqns (3) and (7b), versus ψ. Substituting Eq (7a) in Eq (6) and by setting ($\nu = 0.5$, in the case of saturated incompressible medium), it comes:

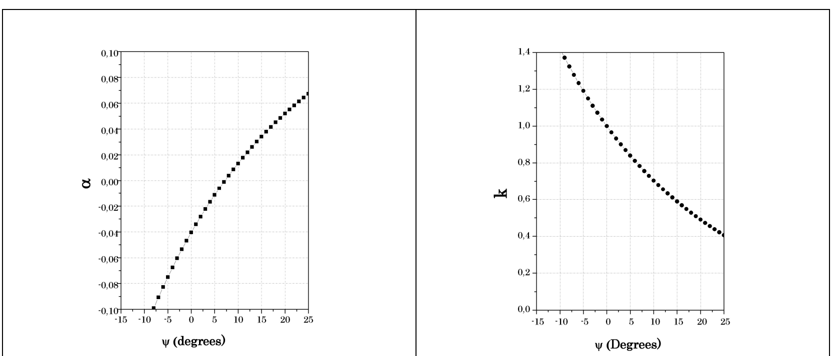

Fig. 3. Variation of the parameters α and k versus angle of dilatancy

$$q_u = K_p\left(p_0 + c_U\left(1 + \frac{2}{1+k}Log\left(\frac{E}{3(-0.1812k+0.1408)^{k-1}\times c_U}\right)\right)\right) \tag{8}$$

Eq (7b) which holds for $0 \prec k \leq 0{,}75$ leads to: $0 \leq \alpha \leq 0.14$. Further, from condition $\alpha \succ 0$ it follows $\psi \geq 8°$ ($k \leq 0.75$). The angle of dilatancy which usually ranges in [-5°; 15°] shall be measured from undrained triaxial shear test. Thus, the calibration margins are $0.4 \leq k \leq 0.75$ and $8° \leq \psi \leq 15°$. For extreme values ψ = 8° and 15° (i.e. $k = 0.75$ and $k = 0.4$) it corresponds: $\alpha = 0.005$ and $\alpha = 0.068$, respectively.

After Equations (3) and (7a) note if the dilatancy angle increases the ratio of plastic radii increases too. Applying Equation (8) for the two extreme cases $k = 0.75$ and $k = 0.4$ gives:

$$q_u(k = 0{,}75) = K_p\left(p_0 + c_U\left(1 + 1.14.Log\left(\frac{E}{11.28c_U}\right)\right)\right) \tag{9a}$$

$$q_u(k = 0{,}4) = K_p\left(p_0 + c_U\left(1 + 1.43.Log\left(\frac{E}{15.05c_U}\right)\right)\right) \tag{9b}$$

Figure 4 shows the variation of (q_u / c_U) ratio, versus the friction angle of column material, predicted by various models with recorded measurements and those derived from Equations (9a) and (9b).

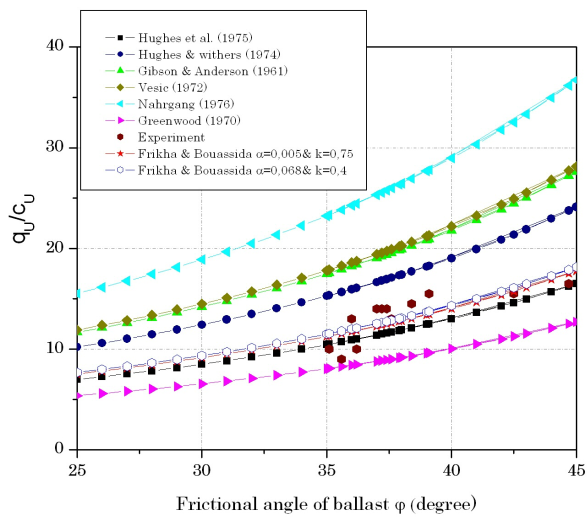

Fig. 4. Normalized ultimate bearing capacity versus the friction angle of column material

Compared to in situ measurements, it appears that the two proposed models lead to reliable estimates of ultimate bearing capacity of isolated column model.

The parametric study shows that the suggested model is suitable for $\alpha = 0.005$ and $\alpha = 0.068$. It is then noticed that the volume variation, characterized by a high coefficient of compressibility, occurs at a maximum about 6.8 % of the radius of the plastic zone surrounding the column. Further, the radial expansion occurs in undrained condition, and then involves negligible volume variation. In conclusion the plastic behavior accompanied by high dilatancy, even if occurring in small area of soft clay, played a positive role in efficient prediction of bearing capacity of an isolated stone column after comparison with recorded in situ measurements.

CONCLUSION

In this paper, a recent theoretical formulation based on lateral expanded cavity study has been presented for estimating the bearing capacity of an isolated stone column installed in purely cohesive soft clay. The soft soil is modeled as an elastoplastic medium governed by a thin dilatant zone around the column and exterior zone where plastic volume variation is neglected.

The calibration of the proposed model has been then carried out by comparing analytical predictions of bearing capacity with recorded measurements on full scale isolated stone column models. The reliability of the model proposed has been verified, with respect to previous contributions. Meanwhile, it is recommended to discuss the validity of the model by using other experimental results in the literature.

REFERENCES

Aboshi, H., Ichimoto, E., Harada K. and Enoki, M. 1979, “The Compozer: A Method to Improve Characteristics of Soft Clays by inclusion of Large Diameter Sand Columns”. Proc. Inter. Symp « Reinforcement of soils », ENPC-LCPC, 211-216, Paris.

Baguelin, F., Jézéquel, J.F. and Shields, D.H. (1978). “The pressuremeter and foundation engineering”. *Series on Rock and Soil Mechanics* Vol.2 n°4, (Trans. Tech. Publications), first edition.

Balaam, N.P. and Booker, J.R 1985. “Effect of stone column yield on settlement of rigid foundations in stabilized clay”. *Int J. Num. Anal Meth. Geom.* Vol. 9, (4), 331–351.

Bergado, D.T. and Lam, F. L. (1987). “Full scale load test on granular piles with different densities and different proportions of gravel and sands on soft Bangkok clay”. *Soils and foundations*, Vol. 27 (1), 86-93.

Bouassida, M. and Hadhri, T. (1995). “Extreme load of soils reinforced by columns: The case of an isolated column”. *Soils and Foundations*. Vol. 35, (1) 21-36.

Bouassida, M. and Jellali, B. (2002). « Capacité portante d’un sol renforcé par une tranchée ». *Revue Française de Génie Civil*. Vol. 6 (7 and 8) 1381-1395.

Carter, J. P., Booker, J.R. and Yeung, S. K. (1986). “Cavity expansion in cohesive frictional soils”. *Géotechnique*. Vol. 36, (2), 349–358.

Datye, K.R. (1982). “Settlement and bearing capacity of foundation system with stone columns.” Proc. Symp Soil and Rock Improvement Techniques including

Geotextiles, reinforced earth and modern piling methods. AIT–Bangkok, A1 1-27.
Dhouib, A. and Blondeau, F. 2005. « Colonnes ballastées. Techniques de mise en oeuvre, domaine d'application ». Presses de l'école nationale des ponts et chaussées Paris.
Frikha, W. and Bouassida, M. (2006). "Analytical determination of the limit pressure during the expansion of a cylindrical cavity in an elastoplastic medium governed by a variable plastic potential of flow". First Euro Mediterranean in Advances on Geomaterials and Structures – Hammamet 3-5 May Tunisia. 251-256.
Gibson, R.E. and Anderson, W.F. (1961). "In situ measurement of soil proprieties with the pressuremeter". Civil Engineering and Public Review. 56. No 658.
Greenwood, D.A. (1970). "Mechanical improvement of soils below ground surface". Proc. of Ground Eng. Conf. Institute of Civil Engineering, London, 9–20.
Hughes, J. M.O., Withers, N. J. (1974). "Reinforcing soft cohesive soil with stone columns". *Ground Engineering*, May, 42-49.
Hughes, J.M.O., Withers, N.J. and Greenwood, D.A. (1975). "A field trial of reinforcing effects of stone columns in soil". *Géotechnique*, Vol. 25, (1), 31-44.
Ladanyi, B. (1963). "Expansion of a cavity in saturated clay medium". *Journal of Soil Mechanics and Foundation Engineering Division*. ASCE. July, 89 SM 4. 127-161.
Monnent, J. and Khlif, J. (1994). "Etude théorique de l'équilibre élasto-plastique d'un sol pulvérulent autour du pressiomètre ». *Revue Française de Géotechnique*, n°65, 71-80.
Nahrgang, E. (1976). "Untersuchung des Tragverhaltens von eigrüttelten Schottersäulen anhand von Modellversuchen". *Baumaschine und Bautechnik*, Vol. 23, (8). 391-404.
Priebe, J. H. (1995). "The design of vibro replacement". *Ground Engineering*. December.
Salençon, J. (1966). "Expansion quasi-statique d'une cavité à symétrie sphérique ou cylindrique dans un milieu élastoplastique ». *Annales des Ponts et Chaussées* Vol. 3, May-June, 175-187.
Soyez, B. (1985). « Méthodes de dimensionnement des colonnes ballastées ». *Bull Liaison Lab. Ponts & Chaussées*, 135, Jan–Feb, 35–51.
Van Impe, W and De Beer, E. (1983). "Improvement of settlement behaviour of soft layers by means of stone columns". Proc., 8th European conference on soil Mechanics and foundation engineering, Helsinki, (1). 309-312.
Vesic, A.S. (1972). "Expansion of cavities in infinite soil mass". *Journal of Soil Mech. and Found. Division. ASCE*, Vol. 2 (3), 451-457.
Wroth, C.P., Windle, D. (1975). "Analysis of the pressuremeter test allowing for volume change". *Géotechnique* Vol. 25, (3), 589-604.
Yu, H.S. and Houlsby, G.T. (1991). "Finite cavity expansion in dilatant soils: loading analysis". *Géotechnique* Vol. 41, (2), 173–183.
www.synergy.com; KaleidaGraph: graphic and data analysis for macintosh and windows.

Bridge Approach Embankments Supported on Concrete Injected Columns

Jeff Hsi, MIEAust, CPEng, MICE, CEng

Chief Technical Principal - Geotechnics, SMEC Australia Pty Ltd, Level 6, 76 Berry Street, North Sydney, NSW 2060, Australia; jeff.hsi@smec.com.au

ABSTRACT: Bridge approach embankments constructed on soft ground are prone to long term settlements which could potentially lead to unacceptable differential settlements at bridge abutments. Foundation treatments are therefore required to control and minimize such differential settlements in order to satisfy the functionality of the road. A special technique involving installation of concrete injected columns (CIC's) based on the soil displacement pile technique (Bauer BG-System) to support bridge approach embankments of the Brunswick Heads to Yelgun Upgrade of the Pacific Highway in New South Wales, Australia, has been proved to be effective. These piles are cast in-situ concrete piles without reinforcement. The method has offered significant cost, environmental and program benefits to the project.

INTRODUCTION

The Brunswick Heads to Yelgun Upgrade of the Pacific Highway in the northern region of New South Wales, Australia, involved construction of several embankments and structures over flood plains. The subsurface mainly comprised very soft and loose alluvial soils, imposing significant geotechnical constraints on the construction of the road embankments.

Without adoption of specific foundation treatments, the road embankments constructed over soft ground would be prone to embankment instability, excessive ground settlement, prolonged construction time and large post-construction settlement.

This paper presents the use of Concrete Injected Columns (CIC's) to control settlements of bridge approach embankments. The treatment measures included surcharging, geotextiles, CIC's and piles which were complex systems with interaction between all the working components. The discussion includes the various components of the system and how spacing and depth were optimized to give zones of CIC's with different residual settlement characteristics in order to control the change of grade at bridge approaches. It also describes the process to limit the impacts of lateral loading on the bridge piles as well as quality control and compliance testing of the CIC's. In addition, instrumentation and monitoring results are discussed to demonstrate the performance of this technique.

BRIDGE APPROACH TREATMENT

Criteria

In accordance with the project requirements, the pavement is required to achieve specific settlement design targets at each location, together with performance criteria of 100mm residual settlement and a change in grade of 0.3% in any direction over the 40 year design life of the pavement. The amount of lateral load that could be tolerated by the bridge abutment piles was limited to satisfy the structural design requirements for the piles at each bridge.

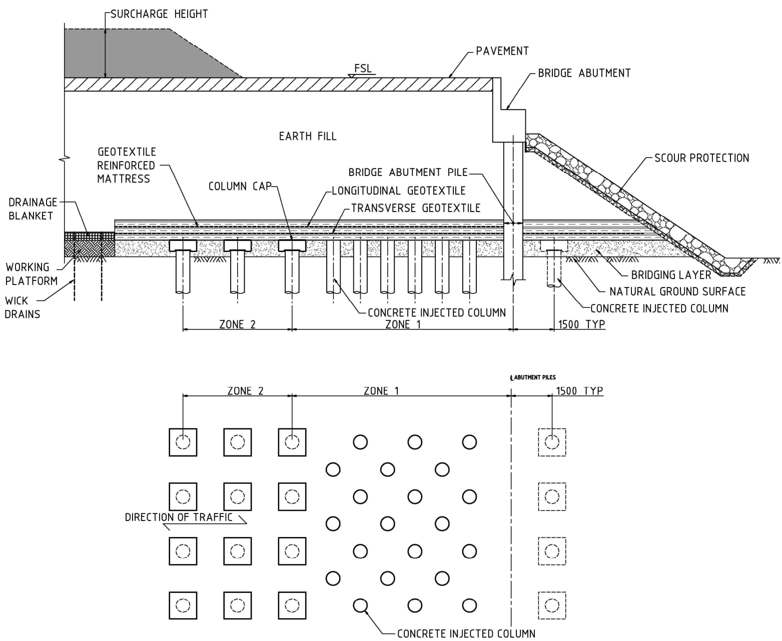

Fig. 1. Bridge Approach Treatment

Arrangement

Fig. 1 shows the arrangement of the bridge approach treatment which eliminates the impact of embankment settlement on the abutment/structure piles and minimize the differential settlement at the interface between the piled structures and non-piled embankments. The following system of treatments has been adopted:

- Bridge approach foundation treatment comprises Concrete Injected Columns (CIC's) installed in two different patterns, i.e. Zone l and Zone 2 as shown in Fig. 1.

- Zone 1 is provided for ground improvement. The extent is related to the fill height and subsurface condition. The CIC's are installed into a relatively incompressible or rigid stratum at a spacing (c/c) of 1.4m.
- Zone 2 is for settlement transition between the abutment and the embankment. CIC's are installed to a specified depth to allow for some long-term settlement. The spacing of these CIC's is 2m. Due to the presence of Zone 1, the horizontal soil movement in Zone 2 is reduced to within the manageable level for the CIC's.
- For Zone 1, as CIC's are installed in close spacing, pile caps are not required. Within Zone 2, pile caps of 1m x 1m are required. For both Zones 1 and 2, a reinforced mattress is required to distribute the embankment loading onto the CIC's

The layer of geotextile reinforced mattress, placed over the CIC's forms an effective bridging layer to transfer the embankment loads onto the CIC's. These CIC's then carry the full embankment loading and hence no significant ground settlement would occur due to compression of the soft ground. This method enables earlier construction of the abutment piles and hence earlier completion of the bridge to enable haulage and construction traffic through the alignment.

Installation

Typically, to install CIC's, a displacement tool is lowered into the ground by rotating and pushing the tool. The soil is loosened by the auger starter and then pushed into the surrounding soil by the displacement body. Upon reaching the final depth, concrete is pumped through the hollow stem of the tool during extraction of the tool. In addition, a reinforcement cage may be installed into the fresh concrete of CIC's by assistance of vibratory action to form a reinforced CIC. However, the depth to which a reinforcement cage can be installed into a CIC is limited. On this project, no reinforcement was required for CIC's.

The CIC's have been installed to form a nominal 500mm diameter column extending to competent soils at depth of the weathered rocks. The required founding level was determined by assessment of the ground conditions from boreholes at a particular location. The termination level of the CIC's in areas where rock head varied significantly was determined by the torque based on the ground conditions in an adjacent borehole. However, the torque must be limited to practicable values i.e. less than 300 bars to avoid damaging the installation equipment. By correlation of torque with adjacent boreholes, it was established that a torque of 230 bars was sufficient for the CIC to toe into the competent strata. Fig. 2 shows the drilling bit of the Bauer BG-System provided by Piling Contractors.

The CIC's installation technique has advantages as follows:

- Increased bearing capacity of the CIC's because the installation method results in densification of surrounding soils.
- Vibration-free installation process.
- Minimisation of drilling spoil. The soil is displaced into the surrounding soil mass during installation in displaceable soils. When drilling into non-displaceable soils, the excavated material is transported by the shape of the tool into the upper layers.
- High productivity.

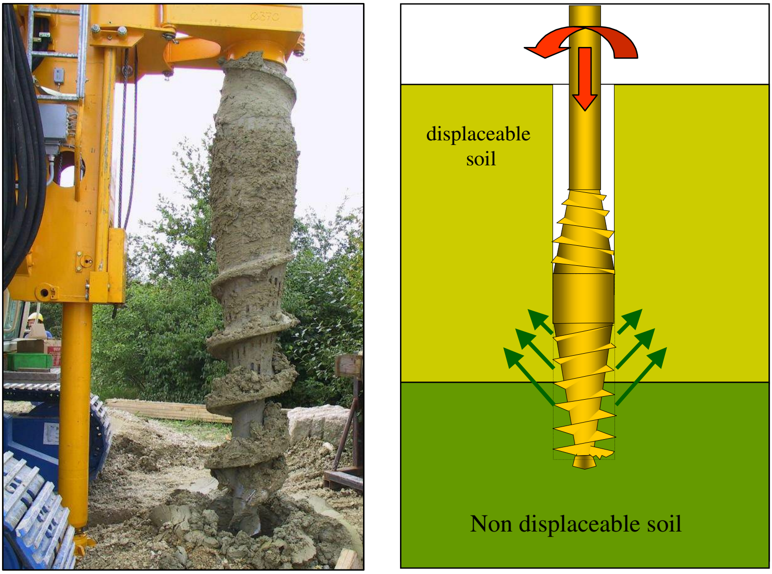

Fig. 2. Drilling Bit of Bauer BG-System (courtesy of Piling Contractors)

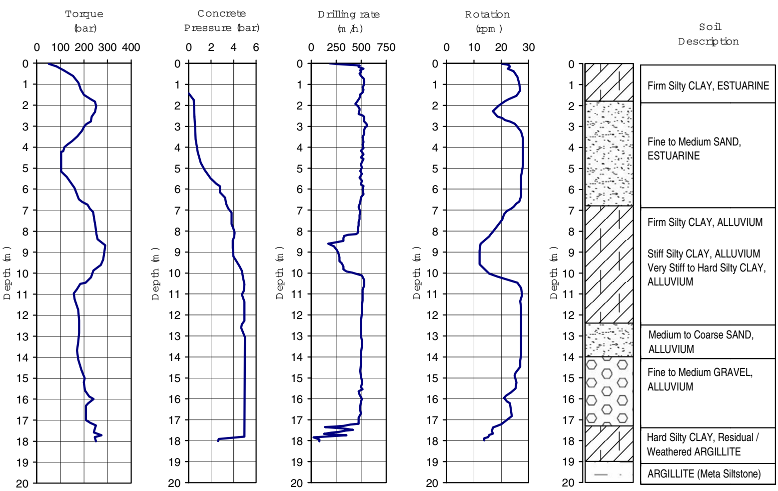

Note: 1 bar = 100 kPa

Fig. 3. Typical CIC Installation Process Record

- Variable length of CIC's readily provided.
- Minimisation of concrete consumption.

Quality Control

The primary quality control during installation comprises the operation parameters. The computerised data collection, visualisation and storing system during installation are available along with continuous real-time observations. Throughout the construction process, the operation parameters are automatically controlled and monitored. Typical controlled operation parameters during the CIC's installation process are as follows:

- Depth
- Torque and crowd force
- Crowd speed
- Deviation
- Concrete pressure and concrete volume.

These data collected during construction are analyzed and printed as production records and quality control sheets. A typical production record is shown in Fig. 3.

Properties

The strength and stiffness properties of CIC's were obtained from unconfined compressive tests (UCS) on core samples taken from the installed CIC's. The bulk density of CIC's was normally between 23.2kN/m^3 to 24.2kN/m^3. Generally, the CIC's compressive strength achieved an average of 20MPa to 25MPa after 7 days. The CIC's compressive strength increases to 35MPa to 40MPa after 28 days.

DESIGN APPROACH AND METHODOLOGY

The bridge approach analyses involve modelling of surcharging, geotextiles, CIC's, piles, which are complex systems with interaction between all the working components. This requires sophisticated numerical modelling using finite elements. The program PLAXIS was adopted to analyze the effectiveness of the system.

The impacts of soil movements on the bridge abutment piles have been assessed using the soil-structural interaction program PALLAS (Hull, 1998), which requires the soil movement profile at the pile location as input. The green field soil displacements at the location of the piles as predicted by PLAXIS are used as input to PALLAS. From the inputted displacement profile the PALLAS program then calculated the bending moment profile based on the stiffness of the pile or CIC.

The same approach as above using PALLAS has been adopted in ensuring the structural capacity of the CIC's is met when considering the induced loading in the transverse direction to model the effects of the embankment edges. Differential lateral displacement due to bending over the length of the column has been practicably limited to 50mm in both the transverse and longitudinal directions.

GEOTECHNICAL MODEL

The geotechnical model adopted for the design included subsurface stratigraphy and geotechnical parameters. The subsurface stratigraphy was derived from the field investigation comprising electric friction cone test (CPT), piezocone test (CPTU), borehole, and trial pit records. The geotechnical parameters were determined from interpretation of the field and laboratory test results. Based on the interpretation of geotechnical data, typical geotechnical parameters for Fill 8 (Station 48 200 to 49 530) are shown in Table 1.

Table 1. Typical Soil Parameters for Fill 8

Depth (m)	Soil type (USC)	Consistency /density	m_v (m^2/MN)	e_o	$C_c/(1+e_o)$	OCR	$C_\alpha/(1+e_o)$	c_h (m^2/yr)	S_u (kPa)
0.0 - 4.0	CL	VS	-	~ 1	0.1 - 0.2	1 - 2	0.010	2 - 10	10 - 20
4.0 - 6.0	CL	VS	-	~ 1	0.1 - 0.2	1 - 2	0.010	2 - 10	10 - 20
6.0 - 8.5	CL	ST	0.093	-	-	-	0.002	10 - 40	50
8.5 - 10.0	SC	L	0.074	-	-	-	-	-	-
10.0 - 11.5	CL	S	-	~ 1	0.1 - 0.2	1 - 2	0.005	5 - 10	10 - 20
11.5 - 16.0	GP	L	0.074	-	-	-	-	-	-
16.0 - 18.0	CL	ST	0.093	-	-	-	0.002	10 - 40	100

Notes: m_v, coefficient of volume change; c_h, horizontal coefficient of consolidation; USC, Unified Soil Classifications; S_u, undrained shear strength; C_c, coefficient of primary compression; C_α, coefficient of secondary compression; e_o, initial void ratio; OCR, over consolidation ratio.

FIELD PERFORMANCE

The performance of bridge approach during construction was assessed based on extensive field instrumentation and monitoring, including:

- Settlement of the embankment showing the rate and magnitude of consolidation of embankment at the bridge approach.
- Lateral deformation of soil at the bridge pile location due to bridge approach embankment settlement showing the magnitude of lateral soil movement impact on bridge piles.

Fig. 4 illustrates a typical instrumentation and monitoring plan at the northern approach of Bridge INFRA 9. At this location an inclinometer at approximately STN 48,842m was installed in front of the heads of the bridge abutment piles at approximately STN 48,843m. Further north behind the CIC's area, a settlement plate was installed at approximately STN 48,861m. The settlement plates recorded the settlements due to general embankment load while the inclinometer monitored the lateral deflection at the bridge pile location due to the embankment settlements.

The measured settlement history below the base of the embankment at STN 48 861m is shown in Fig. 5 and the measured lateral deflection profiles at the inclinometer at STN 48 842m due to the embankment settlement is shown in Fig. 6. The inclinometer was installed on 15th November 2005 after the CIC's were installed at Bridge INFRA 9. The bridge piles were installed between 4th December 2005 and 12th December 2005. The final fill thickness is approximately 5m. The measured settlement is approximately 700mm whilst the lateral displacement of the inclinometer adjacent to the bridge piles has been limited to approximately 12mm.

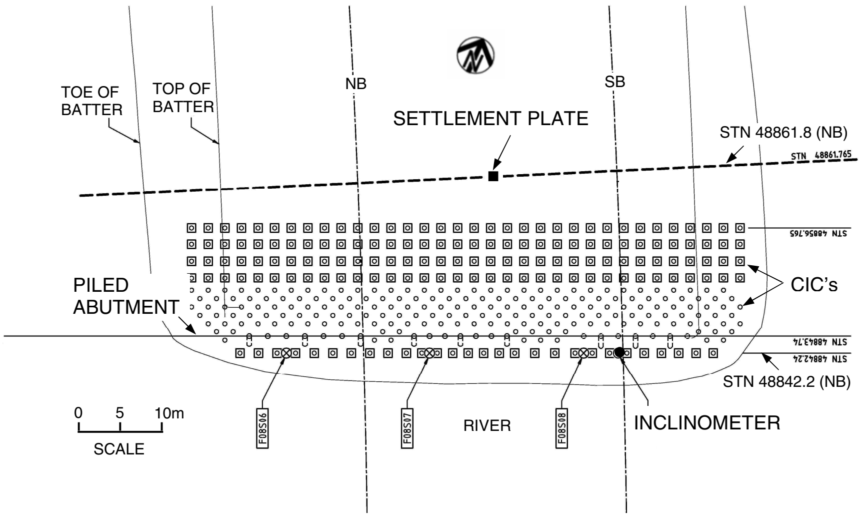

Fig. 4. Instrumentation and Monitoring Plan at INFRA 9

CONCLUSIONS

The use of Concrete Injected Columns (CIC's) is described as a means to support the embankment at bridge approaches and control the pavement settlements, in order to limit the change in grade from unsupported embankment to the hard spot formed by the bridge structures. The design methodology is described, together with requirements for installation and the results from measured performance. It is demonstrated that the CIC's provide an effective system to control the pavement settlements and limit the lateral loading on bridge piles.

This method enables the bridge piles to be installed prior to preloading of embankments which has significant benefits in terms of programming the works and overall construction cost in comparison to other methods e.g. timber piles or heavier reinforced concrete piles.

REFERENCES

Hull, T.S. (1998). "Piles And Lateral Loading Analysis (PALLAS)." Centre for Geotechnical Research, Department of Civil Engineering, University of Sydney.

PLAXIS (2002). "Finite element code for soil and rock analyses." Version 8, PLAXIS B. V., Netherlands.

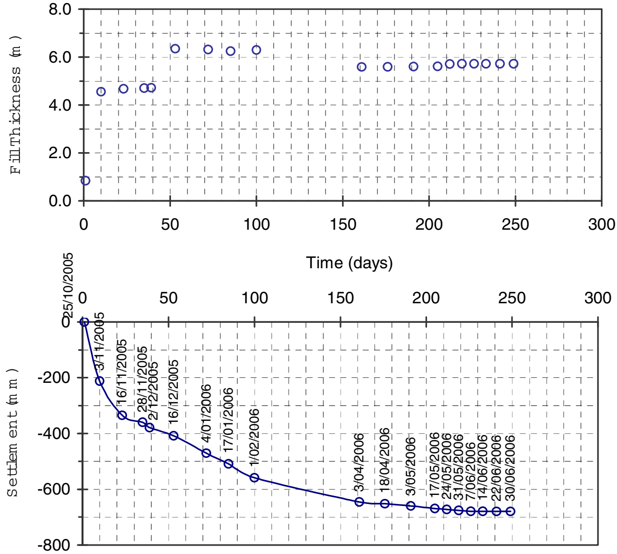

Fig. 5. Measured Settlement Profiles at Station 48 861.765m

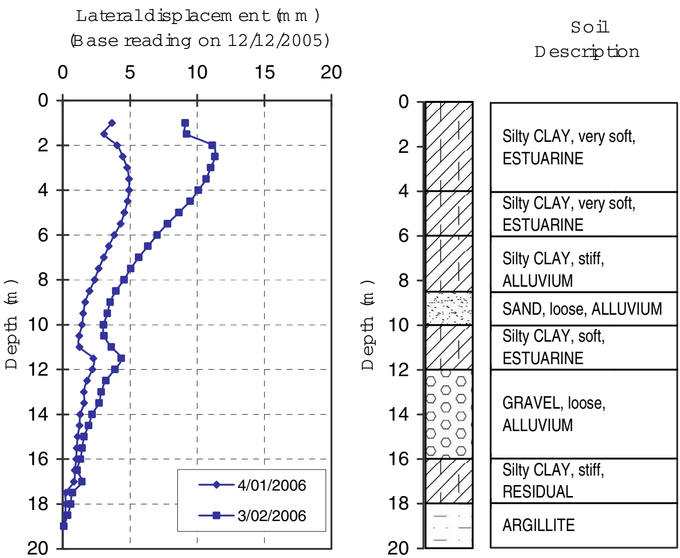

Fig. 6. Measured Lateral Deflections at Station 48 842.2m

Consolidation Calculation of Soft Ground Improved by T-shape Deep Mixing Columns

Lei Chen[1] and Songyu Liu[2]

[1]Ph.D Candidate, Institute of Geotechnical Engineering, Southeast University, Nanjing 210096, China; clove.chenlei@gmail.com

[2]Professor, Ph.D, Institute of Geotechnical Engineering, Southeast University, Nanjing 210096, China; Liusy@seu.edu.cn

ABSTRACT: T-shape deep mixing (TDM) method is a new method for soft ground improvement, which was developed from a dry jet mixing (DJM) method. A simplified consolidation calculation model for the ground improved by T-shape columns is presented based on one dimensional consolidation of layered soils. By using the method of separation of variables, the formulas of pore pressure and consolidation degree were deduced which can consider the consolidation of both composite ground and underlying layer. The consolidation behavior of T-shape columns composite foundation was analyzed, and the results show that the variation of excess pore water pressure, consolidation degree, and settlement of embankments are reasonable and consistent with the measured data in the field.

INTRODUCTION

T-shape deep mixing (TDM) method is a new method of soft ground improvement, which was developed from the DJM method (Xi and Liu 2006). The cross section along T-shape deep mixing columns varies. Near the ground surface, the column diameter is relatively larger than the rest. As a result, the load transfer, the interaction between columns and the surrounding soil, and the drainage path of pore water are quite different from those for ordinary DJM columns. Obviously, generation and dissipation of excess pore water pressure in the soil around TDM columns under the embankment would also be different from that of the ordinary DJM composite foundation. It is necessary and meaningful to study on the consolidation characteristics of the composite foundation improved by TDM. Based on the field observation and the existing consolidation theories, a consolidation calculation method applicable for the composite foundation improved by TDM is presented in this paper.

CONSOLIDATION CALCULATION MODEL

Assumptions

A simplified cross-section of the TDM composite foundation is shown in Fig.1. In order to establish the consolidation equations, assumptions were made as follows:

(1) The ground can be simply divided into three layers: the layer with enlarged

columns, h1; the layer with normal columns, h2; and the underlying layer, h3. (2) Only one dimensional compression in the vertical direction is taken into account. Column and soil have equal strain at any depth. (3) Lateral movement, soil arch effect, and disturbance of soil induced by construction are not considered. (4) At the moment of the load being applied, all the load is carried by in the excess pore water pressure in the surrounding soil. (5) Other assumptions are the same as those used in Terzaghi's one dimensional consolidation theory.

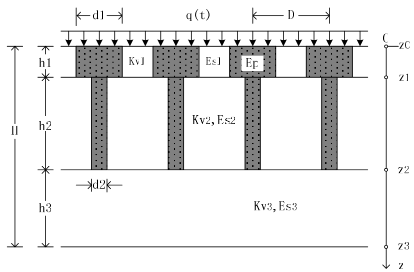

FIG.1. Simplified cross-section of TDM composite foundation

Equations and solution

Define the original point of z coordinate on the ground surface (Fig.1).The thickness of each layer is divided as the assumption (1) as: $z_0 = 0$, $z_i = \sum_{j=1}^{i} h_j$, $i = 1,2,3$, $z_3 = H$. Based on Terzaghi's one dimensional consolidation theory, the surrounding soil satisfies the following equation:

$$-\frac{k_{vi}}{\gamma_w}\frac{\partial^2 u_{si}}{\partial z^2} = \frac{\partial \varepsilon_{vi}}{\partial t} \tag{1}$$

At any time, both TDM columns and the surrounding soil share the applied load, i.e., $M_i\sigma_{pi} + (1-M_i)\sigma_{si} = q \qquad i = 1,2,3$ (2)

The equal strain assumption between the column and the surrounding soil yields

$$\partial\varepsilon_{vi} = m_{vsi}\partial\sigma'_{si} = m_{vpi}\partial\sigma_{pi} \tag{3}$$

where $\sigma_{si}, \sigma'_{si}$, and u_{si} are the total stress, the effective stress, and the pore water pressure in the surrounding soil in layer i, respectively, σ_{pi} is the stress on the column in layer i, q is the total load applied on the composite foundation, m_{vpi}, m_{vsi} are the coefficients of volumetric compressibility of TDM (If i=1, it represents the enlarged part and if i=2, it represents the normal part) and soil, k_{vi} is the vertical permeability of soil, γ_w is the unit weight of water, ε_{vi} is the volumetric strain of element, M_i is the area replacement ratio in layer i (i.e., the ratio of the column cross-sectional area to the soil area, when i=3, $M_3 = 0$).

The rate of the soil volumetric strain change with time can be expressed as:

$$\frac{\partial \varepsilon_{vi}}{\partial t} = m_{vsi} \frac{\partial \sigma'_{si}}{\partial t} \tag{4}$$

Combining Eqs.(2) and (3) and the relationship $\sigma_{si} = \sigma'_{si} + u_{si}$ yields,

$$\sigma'_{si} = \frac{\sigma_{pi}}{N_i} = \frac{q - (1 - M_i)(\sigma'_{si} + u_{si})}{M_i N_i} \tag{5}$$

where $N_i = m_{vsi} / m_{vpi}$.

Considering the assumption that the applied load is maintained constant during the consolidation, i.e., $\partial q / \partial t = 0$, the following equation can be obtained.

$$\frac{\partial \sigma'_{si}}{\partial t} = -\frac{1 - M_i}{1 + M_i(N_i - 1)} \frac{\partial u_{si}}{\partial t} \tag{6}$$

Substituting Eq.(6) into Eqs.(4) and (1) yields:

$$\frac{k_{vi}}{\gamma_w} \frac{\partial^2 u_{si}}{\partial z^2} = m_{vsi} \frac{1 - M_i}{1 + M_i(N_i - 1)} \frac{\partial u_{si}}{\partial t} \tag{7}$$

Equation (7) can be simplified as:

$$(1 - M_i) \frac{\partial u_{si}}{\partial t} = C_{vi} \frac{\partial^2 u_{si}}{\partial z^2} \qquad i = 1,2,3 \tag{8}$$

where C_{vi} is the vertical consolidation coefficient of the composite foundation,

$$C_{vi} = [1 + M_i(N_i - 1)] \frac{k_{vi}}{\gamma_w m_{vsi}} = [1 + M_i(N_i - 1)] C_{vsi} \tag{9}$$

where C_{vsi} is the vertical consolidation coefficient of the soil in layer i.

Equation (8) is the one dimensional consolidation differential equation for the TDM composite foundation. In order to obtain the solution for Eq.(8), boundary conditions and initial conditions are necessary as follows:

① $z = 0 : u_{s1} = 0$, ② $z = z_i : u_{si} = u_{si+1}, i = 1,2$, ③ $z = z_i$: $(1 - M_i)Q_i = (1 - M_{i+1})Q_{i+1}$, it can also be described as $(1 - M_i)k_{vi} \frac{\partial u_{si}}{\partial z} = (1 - M_{i+1})k_{vi+1} \frac{\partial u_{si+1}}{\partial z}$, $i = 1,2$, Q_i is the quantity of vertical water flow in layer i, ④ $z = H$: $\frac{\partial u_{s3}}{\partial z} = 0$ (permeable bottom side), $u_{s3} = 0$ (un-permeable bottom side), ⑤ $t = 0 : u_{si} = u_0$.

Define

$$a_i = \frac{k_{vi}}{k_{v1}}, b_i = \frac{[1 + M_i(N_i - 1)]m_{vsi}}{[1 + M_1(N_1 - 1)]m_{vs1}}, \quad \rho_i = \frac{h_i}{H}, \mu_i = \sqrt{\frac{(1 - M_i)C_{v1}}{C_{vi}}} = \sqrt{\frac{(1 - M_i)b_i}{a_i}} \quad i = 1,2,3 \tag{10}$$

The solution for Eq.(8) can be presented as follows:

$$u_{si} = \sum_{m=1}^{\infty} C_m g_{mi}(z) T_m(t) \qquad i = 1,2,3 \tag{11}$$

where $T_m(t) = u_{s0} e^{-\beta_m t}$ (12)

$$\beta_m = \lambda_m^2 C_{v1} / H^2 \tag{13}$$

$$g_{mi}(z) = A_{mi} \sin(\mu_i \lambda_m \frac{z}{H}) + B_{mi} \cos(\mu_i \lambda_m \frac{z}{H}) \tag{14}$$

From boundary conditions ①, ②, ③, there are

$A_{m1}\cdot 0+B_{m1}\cdot 1=0$, it means $B_{m1}=0$ (15)

$A_{m1}\cdot A_1+B_{m1}\cdot B_1=A_{m2}\cdot C_1+B_{m2}\cdot D_1$ (16)

$\frac{(1-M_1)k_{v1}}{(1-M_2)k_{v2}}\cdot\frac{\mu_1}{\mu_2}\cdot\left(A_{m1}\cdot B_1-B_{m1}\cdot A_1\right)=A_{m2}\cdot D_1-B_{m2}\cdot C_1$ (17)

where $A_1=\sin(\mu_1\lambda_m\frac{z_1}{H})$, $B_1=\cos(\mu_1\lambda_m\frac{z_1}{H})$, $C_1=\sin(\mu_2\lambda_m\frac{z_1}{H})$, $D_1=\cos(\mu_2\lambda_m\frac{z_1}{H})$.

Define $d_1=\frac{(1-M_1)k_{v1}}{(1-M_2)k_{v2}}\cdot\frac{\mu_1}{\mu_2}=\frac{(1-M_1)^{\frac{3}{2}}\sqrt{a_1b_1}}{(1-M_2)^{\frac{3}{2}}\sqrt{a_2b_2}}$. From Eqs.(16) and (17), there is

$[A_{m2}\quad B_{m2}]^T=\begin{bmatrix}C_1 & D_1\\ D_1 & -C_1\end{bmatrix}^{-1}\begin{bmatrix}A_1 & B_1\\ d_1B_1 & -d_1A_1\end{bmatrix}[A_{m1}\quad B_{m1}]^T$ (18a)

Define $S_2=\begin{bmatrix}C_1 & D_1\\ D_1 & -C_1\end{bmatrix}^{-1}\begin{bmatrix}A_1 & B_1\\ d_1B_1 & -d_1A_1\end{bmatrix}$ (19a)

Equation (18a) can be described as $[A_{m2}\quad B_{m2}]^T=S_2\cdot[A_{m1}\quad B_{m1}]^T$ (18b)

where S_2 can be expressed as $S_2=\begin{bmatrix}A_1C_1+d_1B_1D_1 & B_1C_1-d_1A_1D_1\\ A_1D_1-d_1B_1C_1 & B_1D_1+d_1A_1C_1\end{bmatrix}$ (19b)

Similarly, from boundary conditions ②, ③, it is

$[A_{m3}\quad B_{m3}]^T=S_3\cdot[A_{m2}\quad B_{m2}]^T$ (20)

where $S_3=\begin{bmatrix}A_2C_2+d_2B_2D_2 & B_2C_2-d_2A_2D_2\\ A_2D_2-d_2B_2C_2 & B_2D_2+d_2A_2C_2\end{bmatrix}$ (21)

and $A_2=\sin(\mu_2\lambda_m\frac{z_2}{H})$, $B_2=\cos(\mu_2\lambda_m\frac{z_2}{H})$, $C_2=\sin(\mu_3\lambda_m\frac{z_2}{H})$, $D_2=\cos(\mu_3\lambda_m\frac{z_2}{H})$,

$d_2=\frac{(1-M_2)k_{v2}}{k_{v3}}\cdot\frac{\mu_2}{\mu_3}=\frac{(1-M_2)^{\frac{3}{2}}\sqrt{a_2b_2}}{\sqrt{a_3b_3}}$.

From the boundary condition ④, Eq.(22) can also be obtained:

$$\begin{cases}A_{m3}\cos(\mu_3\lambda_m)-B_{m3}\sin(\mu_3\lambda_m)=0 & (unpermeable-bottomside)\\ A_{m3}\sin(\mu_3\lambda_m)+B_{m3}\cos(\mu_3\lambda_m)=0 & (permeable-bottomside)\end{cases} \quad (22)$$

Define $S_4=\begin{cases}[\cos(\mu_3\lambda_m)\quad -\sin(\mu_3\lambda_m)] & (unpermeable-bottomside)\\ [\sin(\mu_3\lambda_m)\quad \cos(\mu_3\lambda_m)] & (permeable-bottomside)\end{cases}$ (23)

λ_m can be obtained by equation below as a positive root,

$S_4\cdot S_3\cdot S_2\cdot S_1=0$ (24)

where $S_1=[1\quad 0]^T$.Substituting Eq.(11) into Eq.(8) yields the following equation:

$f(z)=\sum_{m=1}^{\infty}(1-M_i)C_m g_{mi}(z)=1$ (25)

From Schiffman(1970), the eigenfunction can be established as follows:

$G_{mi}(z)=(1-M_i)m_{vi}g_{mi}(z)$ (26)

Thus, the value of C_m can be determined as

$$C_m = \frac{\sum_{i=1}^{3}(1-M_i)m_{vi}\int_{h_{i-1}}^{h_i} g_{mi}(z)dz}{\sum_{i=1}^{3}(1-M_i)m_{vi}\int_{h_{i-1}}^{h_i} g_{mi}^2(z)dz} = \frac{\sum_{i=1}^{3}(1-M_i)b_i\int_{h_{i-1}}^{h_i} g_{mi}(z)dz}{\sum_{i=1}^{3}(1-M_i)b_i\int_{h_{i-1}}^{h_i} g_{mi}^2(z)dz} \tag{27a}$$

Substituting the formula of $g_{mi}(z)$ into the above equation yields

$$C_m = \frac{\sum_{i=1}^{n} 2\sqrt{(1-M_i)a_i b_i}[-A_{mi}(B_i - D_{i-1}) + B_{mi}(A_i + C_{i-1})]}{\sum_{i=1}^{n}\sqrt{(1-M_i)a_i b_i}[\rho_i\mu_i\lambda_m(A_{mi}^2 + B_{mi}^2) + (B_{mi}^2 - A_{mi}^2)(A_i B_i - C_{i-1}D_{i-1}) + 2A_{mi}B_{mi}(A_i^2 - C_{i-1}^2)]} \tag{27b}$$

where $C_0 = \sin\mu_1\lambda_m \dfrac{0}{H} = 0$, $D_0 = \cos\mu_1\lambda_m \dfrac{0}{H} = 1$, $A_3 = \sin\mu_3\lambda_m \dfrac{H}{H} = \sin\mu_3\lambda_m$, $B_3 = \cos\mu_3\lambda_m \dfrac{H}{H} = \cos\mu_3\lambda_m$.

Substituting Eqs.(12), (14) and (27) into Eqs.(11) can obtain the value of excess pore water pressure. The consolidation degree of the soil layers can be calculated,

$$U_{si} = \frac{1}{u_0 h_i}\int_{z_{u-1}}^{z_i}[u_0 - u_{si}]dz \tag{28}$$

The average consolidation degree is

$$U_{sp} = \frac{u_0 - \overline{\mu}_s}{u_{0c}} = 1 - \frac{1}{u_0 H}\sum_{i=1}^{3}\int_{z_{i-1}}^{z_i} u_{si}dz = \sum_{i=1}^{3}\rho_i U_i \tag{29}$$

The degree of consolidation can also be obtained based on settlement as follows:

$$U_s = \frac{S_{st}}{S_{s\infty}} = \frac{\sum_{i=1}^{3} m_{svi}\int_{z_{i-1}}^{z_i}(u_0 - u_{si})dz}{u_0\sum_{i=1}^{3} m_{svi}h_i} = \frac{\sum_{i=1}^{3} b_{si}\rho_i U_i}{\sum_{i=1}^{3} b_{si}\rho_i} \tag{30}$$

where $b_{si} = m_{svi} / m_{sv1}$.

When the values of M_i ($i = 1,2$) in Eq.(7) are all set as zero, the solution is the same as Terzaghi's one dimensional consolidation formula for natural soil. Therefore, the consolidation of natural soil can be considered as the special case of the TDM composite foundation consolidation model in this paper.

CALCULATION FOR A CASE STUDY

Parameters

Table 1. Physical and mechanical properties of soil

Layers	Depth (m)	w_0 (%)	e_0	γ(kN/m3)	m_{vs} (MPa^{-1})	k_v (10-7cm/s)
Crust layer	0-4	40.9	1.121	18	0.094	1.05
Soft soil layer	4-17	53.8	1.533	16.6	0.461	0.152
Underlying layer	17-34	25.6	0.691	20.2	0.05	2.55

To verify the applicability of the above method for the TDM composite foundation, a case study was selected here. The parameters shown in Table 1. and Table 2. are from the TDM test site for the Hu-Su-Zhe Highway in China.

Table 2. Physical and mechanical properties of T-shape deep mixing columns

Parts	Length of column (m)	Diameter (mm)	Space (m)	Cement content (kg/m)	m_{vp} (MPa^{-1})
Enlarged part	4	1000	2	260	0.00833
Normal part	13	500	2	65	0.00833

Results and analysis

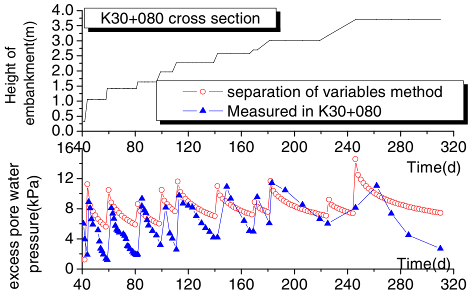

FIG. 2. Variation of excess pore water pressure at the depth of 5m

Figure 2 compares the calculated excess pore water pressure at the depth of 5m with the measured data. Both of them showed that pore water pressure generated and dissipated obviously with each loading.

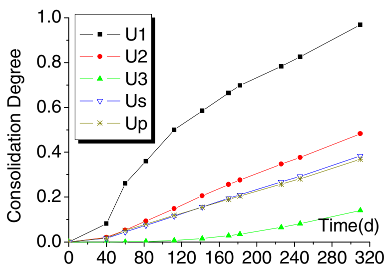

FIG. 3. Variation of consolidation degree of TDM improved foundation

The calculated degree of consolidation is shown in Fig.3, which shows that the degree of consolidation of the layer with enlarged columns (U1) is much higher than that of two other layers for its short draining path from the ground surface. The layer with normal columns consolidates slightly slower (U2) than its upper layer but quicker than the underlying layer (U3). Consolidation degree calculated by Eq.(24) (Up) is close to that by Eq.(25) (Us). All these results prove that the TDM method can accelerate the soil consolidation. The consolidation property of the underlying soil should not be ignored and need to be further studied.

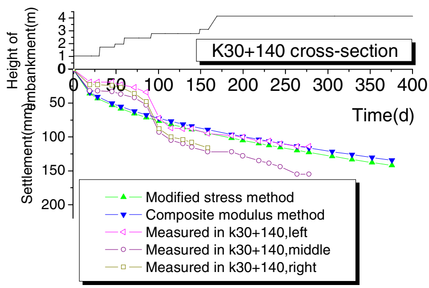

FIG .4. Variation of settlement of TDM improved foundation with time

Since the consolidation degree of the ground is known, the settlement under the embankment with time can be determined if the final settlement is known. Figure 4 shows these settlement curves by analytical methods or field measurements. The final settlements used in the calculation are from the modified stress method and the composite modulus method which both introduced by Gong (2002). Based on Eq.(31) and the calculated consolidation degree at a certain time, the settlement at a certain time can be obtained using the following formula:

$$S_t = U_t \cdot S_\infty \quad (31)$$

where S_t and S_∞ are the settlement at time t and the final settlement, respectively, and U_t is the degree of consolidation of the foundation at time t.

In Fig. 4, the calculated results from both the modified stress method and the composite modulus method are close to the measured settlements on the left side of the embankment. The measured settlements in the middle and on the right of embankment are slightly larger. Figure 4 also shows that the traditional methods underestimate the settlements. A factor valued of 1.3 may be applied or a new method specifically for the TDM improved ground is needed.

In addition, explanations are required for the difference in calculated and measured data from 10 to 100 days. As show in Fig.4, the measured settlements are smaller than calculated ones. That is because the observed area once preloaded as a pile site for construction materials, and the soil behaves a slight over consolidation property at the beginning of embankment loading.

CONCLUSIONS

The consolidation of the TDM composite foundation, a new type of soil improvement technique was investigated in this study. This paper presents a calculation method and the following conclusions can be made:

(1) This study established the differential equations which can describe the consolidation of the ground varying with depth. They consider the effect of geometrical properties of the T-shape columns on load transfer and drainage of pore water. The decomposition method was adopted to obtain the numerical solution.

(2) A case study was selected and analyzed. The calculated excess pore water pressure at the depth of 5m is consistent with the measured.

(3) The degree of consolidation at a certain time is the highest for the layer with enlarged columns, and followed by the layer with normal columns and the underlying layer. The TDM method can accelerate ground consolidation. The consolidation property of the underlying soil should not be ignored.

(4) The calculated settlement under the embankment is close to the measured one. A modification factor or a settlement calculation method specific to the TDM improved ground is required for a more rigorous solution.

ACKNOWLEDGMENTS

The authors appreciate the support of the Specialized Research Fund for the Doctoral Program of Higher Education of China under Grant No.20060286031.

REFERENCES

Xi, P.S. and Liu, S.Y. (2006). "Analysis of Cement-soil Deep Mixing Method Strengthening Soft Foundation." *Construction Technology*, 35 (1):2-5, in Chinese.

Xie, K.H. and Pan Q.Y. (1995). "One Dimensional Consolidation of Layered Soils Under Arbitrary Loading." *Chinese Journal of Geotechnical Engineering,* Vol.17 (5):80-85, in Chinese.

Xie, K.H. (1994), "Theory of one dimensional consolidation of double-layered ground and its applications." *Chinese Journal of Geotechnical Engineering*,Vol.16(5): 24–35, in Chinese.

Schiffman, R.L., and Stein, J.R.(1970). "One-dimensional Consolidation of Layered Systems". *JSMFD, ASCE*, Vol.96(4):1499-1504.

Gong, X.N. (2002). "Composite foundation theory and engineering application." *China Architecture & Building Press*:150-156, in Chinese.

Han, J. and Ye, S. L. (2002). "A theoretical solution for the rate of consolidation of a stone column reinforced foundation accounting for smear and well resistance." *International Journal of Geomechanics*, 2(2):135-151.

PERFORMANCE OF REINFORCED LOAD TRANSFER PLATFORMS FOR EMBANKMENTS SUPPORTED BY DEEP CEMENT MIXING PILES

D. T. Bergado, P. Jamsawang, T. Tanchaisawat and Y.P. Lai
School of Engineering and Technology, Asian Institute of Technology, Bangkok, Thailand ; bergado@ait.ac.th

G.A. Lorenzo
Department of Civil Engineering, Mindanao State University, Marawi City, Philippines

ABSTRACT: A 6 m high reinforced embankment was supported by Deep Cement Jet Mixed Piles on Soft Bangkok clay. Each clay-cement pile (or soil-cement column) had diameter of 0.50 m and length of 9.0 m and were installed at 1.5 m center to center spacing in square pattern. The performance of the full scale test embankment was observed for a period of one year until 90% consolidation was achieved. Subsequently, analytical analyses were performed and the results were compared with the measured data. Consequently, the relevant geotechnical parameters were back-calculated including the permeability ratio, compressibility ratio, and the coefficients of consolidation of the pile and surrounding clay. Since the actual load transfer mechanism is neither equal strain nor equal stress, weighting factors were utilized to obtain the average degree of consolidation. The results demonstrated that at any time, the overall load transfer mechanism can be taken as 80% equal strain condition plus 20% equal stress condition. Furthermore, the deep mixing piles has resulted in 70% settlement reduction in the improved foundation.

1. INTRODUCTION

Ground improvement by cement stabilization can be broadly divided into shallow stabilization and deep stabilization. Shallow stabilization, which includes stabilization of subgrade for roadways and airfields and other similar structures, normally employs “low water content” mixing. The deep stabilization, on the other hand, includes deep mixing method (DMM) using either slurries or powder of cement to form columns of improved soil in the ground. The improved column of soil is considered to act as reinforcement or as a pile, transferring the load to the skin and to the bottom-end of the improved column of soil. The methods of mixing are broadly divided in to two: either mechanical mixing or high pressure jet mixing (Kamon and Bergado, 1991; Porbaha, 1998). In the mechanical mixing the chemical admixtures are mixed into the soil by mixing blades, while in the jet mixing the same are mixed into the soil through jet of water or slurries of admixtures. The slurry deep mixing and jet mixing methods would normally produce high water content cement-admixed clay; besides, the soft clay deposit normally has high water content.

The technique of reinforcing earth has been extensively used for construction of earth retaining wall and embankment slopes, and in stabilization of embankments placed on soft ground. The reinforced soil mass is generally called Mechanically Stabilized Earth (MSE). MSE structures can be divided into three main parts:

(1) *facing elements*, which act like an armor to prevent erosion of retained, fill materials, (2) *reinforcing elements*, which add tensile strength in the soil mass, and (3) *engineering fill*, which make the bulk of the structure.

A full scale deep mixing improved soft clay foundation supporting a six-meter high reinforced embankment was constructed within the soft Bangkok clay area in Thailand, and it was monitored in order to study its consolidation and deformation behavior. The jet mixing technique having a jet pressure of 20 MPa was utilized in the installation of deep mixing piles. Based on the results of the instrumentation of this full scale test, the compression mechanism of deep mixing pile improved ground overlain by reinforced embankment are discussed in this paper.

2. TEST EMBANKMENT ON SOFT GROUND IMPROVED WITH DMM

2.1. Site and description of the test embankment

A 6m high Test Embankment reinforced with PVC-coated hexagonal wire mesh reinforcement was constructed at Wangnoi District, Ayuthaya, Thailand (Bergado and Lorenzo, 2003). The foundation soils and their properties at the site of the test embankment are shown in Fig. 1. Prior to embankment construction, the foundation subsoil was first improved with soil-cement columns which were installed in situ by jet mixing method employing a jet pressure of 20 MPa. Soil-cement piles were installed at 1.5 m spacing in square pattern, except for the perimeter soil-cement piles which were installed at 2.0m spacing (Figs. 2a,b). The water-cement ratio (W/C) of the cement slurry and the cement content employed for the construction of deep mixing piles were 1.5 and 150 kg/(m^3 of soil), respectively. Each deep mixing pile has a diameter of improvement of 0.5 m and a length of 9.0m, penetrating down to the bottom of the soft clay layer, as shown in the section view of the embankment (Fig. 2b). The deep mixing piles were allowed to cure while the dissipation of excess pore water pressure was monitored until about 80 days prior to the embankment construction (Bergado and Lorenzo, 2003).

The embankment was made of well-compacted silty-sand backfill reinforced with PVC-coated hexagonal wire mesh. The backfill soil has compacted unit weight of 18.20 kN/m^3, cohesion of 7.70 kPa and angle of internal friction of 22^o, and it has maximum dry density and optimum water content of 16.1 kN/m^3 and 15%, respectively. During construction, the embankment filling was done at 0.375 m lift thickness and was compacted to at least 98% of the maximum dry density of the fill material (Bergado and Lorenzo, 2003). To support the vertical side of the embankment, concrete facing with dimensions of 1.50 m x 1.50 m x 0.15 m were installed, each being held by two layers of hexagonal wire mesh reinforcements resulting to a vertical spacing of the reinforcements of 0.75 m (Fig. 2b). All reinforcements were 4m long and were laid horizontally behind the concrete facing. The finished embankment is 6 m high. The embankment construction was completed within 15 days, started on 28 January 2002 and ended on 12 February 2002.

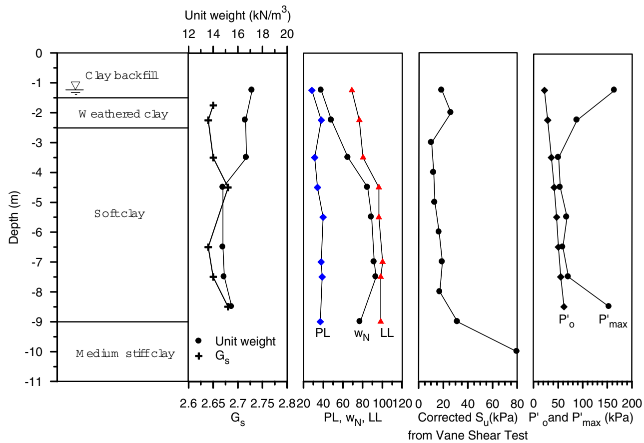

Fig. 1. Soil profiles under the hexagonal wire reinforced test embankment

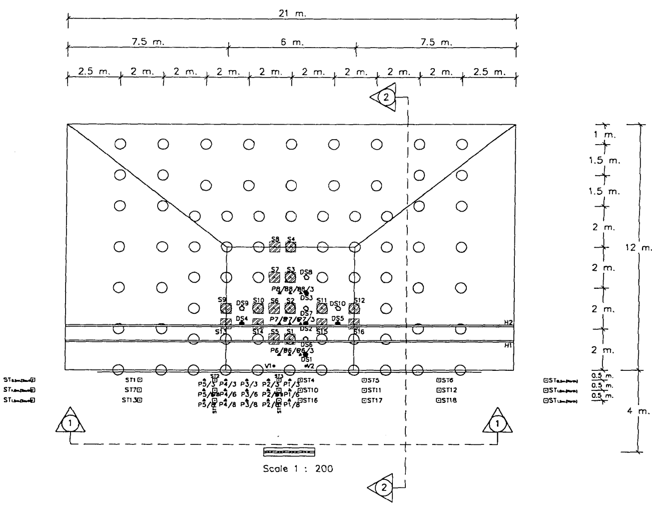

Fig. 2a. Plan view of the test embankment on DMM piles showing the locations of surface settlement plates (Si) and deep settlement plates (DSi)

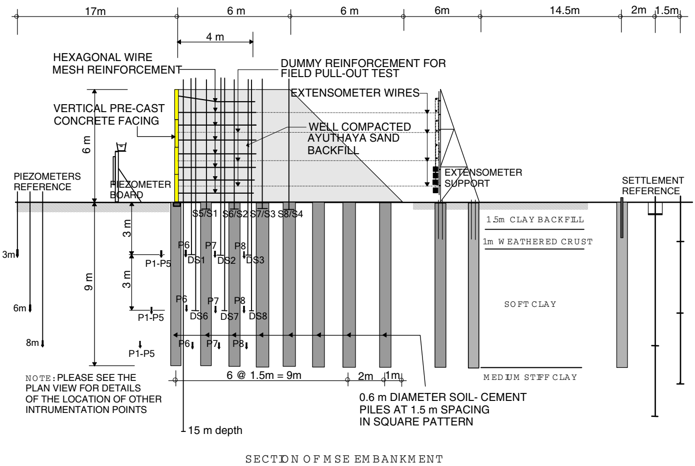

Fig. 2b. Centerline elevation of the test embankment on deep mixing piles

2.2. Settlement behavior of soil-cement piles improved soft clay foundation

Figure 3 shows the settlements on top of deep mixing piles and on the surface of surrounding clay during and after construction up to one year of full embankment loading. From these actual observed data, the average settlements on deep mixing pile and on clay amounted to about 122 and 162 mm, respectively, after embankment construction. One year after embankment construction, the average settlements on deep mixing pile and on clay amounted to about 285 and 335 mm, respectively. Hence, the corresponding average settlement at the bottom of the reinforced soil is about 310 mm one year after embankment construction. Using the method of Asaoka (1978), the average total settlements of deep mixing pile and of the surrounding soil were predicted using the data recorded from settlement plates S11 and S15, which demonstrated the average settlement of the deep mixing piles and the surrounding soil, respectively. The maximum total settlements of deep mixing pile and of the surrounding soil amounted to 340 and 440 mm, respectively. Thus, about 40% of the total settlement occurred during the construction of test embankment (Lai et al, 2006).

Moreover, if there had been no improvement in the foundation soil, the settlement of embankment one year after construction could have been greater than 1000 mm (Bergado and Lorenzo, 2003). Thus, the embankment load (weight of embankment) has been transferred to the deep mixing piles, thereby not only reducing the intensity of pressure on the surrounding clay, hence the magnitude of its settlement, but also increasing the bearing capacity of the improved foundation. The deep mixing piles have, therefore, transferred the load down to their bottom ends and, consequently, effected a settlement reduction in the soft clay foundation by about 70%.

The deep mixing piles also promoted faster rate of consolidation of the improved foundation. The consolidation settlement of the improved ground was almost 90% one year after construction, as can be calculated from the predicted total settlement and the settlement after one year. For S11 and S15 for example, the settlement of pile and clay were 298 and 362, respectively, one year after embankment construction; hence, the corresponding degree of consolidation of the improved ground was about 86% on the average, which is almost 90%. Besides, the settlement-time plot in Fig. 3 also confirmed this observation. If there had been no improvement in the 6.5 m thick soft clay (Figs. 1 and 2b), the 90% consolidation settlement could have been attained 9 years after construction (assuming actual coefficient of consolidation of soft clay, C_v = 4 m^2/yr). Moreover, the time-settlement plot obtained from deep settlement plates installed at 3 m and 6 m depth (Fig. 4) also confirmed the faster rate of consolidation settlement of the deep mixing improved ground. Figure 3 demonstrated that both settlements at the surface, at 3 m depth and at 6 m depth indicated the same pattern of consolidation behavior, which implied that the rate of consolidation was almost uniform over the entire depth of improvement due to the presence of deep mixing piles.

2.3. Local differential settlement between deep mixing pile and surrounding clay

The local differential settlements between pile and adjacent clay range from 25 mm to 60 mm (Fig. 3) when the average settlement of deep mixing piles amounted to 285 mm after one year of full embankment loading. This implies that the local differential settlement between the deep mixing pile and the surrounding clay under the hexagonal wire reinforced embankment can range from 8% to 20% of the average settlement. However, this amount of local differential settlement was almost eliminated at the surface of embankment due to the combined effect of compaction as well as reinforcement stiffness and arching of overlying reinforced soil. Significantly, Fig. 3 also demonstrated that the magnitude of local differential settlements between piles and surrounding clay has been almost fully attained just after one month of full embankment loading. This practically implies that, for road embankment constructed on deep mixing piles, the final surfacing could be better done at least one month after embankment construction, giving time to compensate the differential settlement.

3. ANALYTICAL BACK-ANALYSIS OF THE RATE OF SETTLEMENT

To obtain the basic consolidation properties of DMM piles installed by jet mixing method, analytical simulations of the observed settlement of the test embankment was performed. The analytical simulation was done using the technique of Lorenzo and Bergado (2003) for the consolidation analysis of deep mixing improved ground, together with the Asaoka's observational method to estimate the total settlement (Asaoka, 1978).

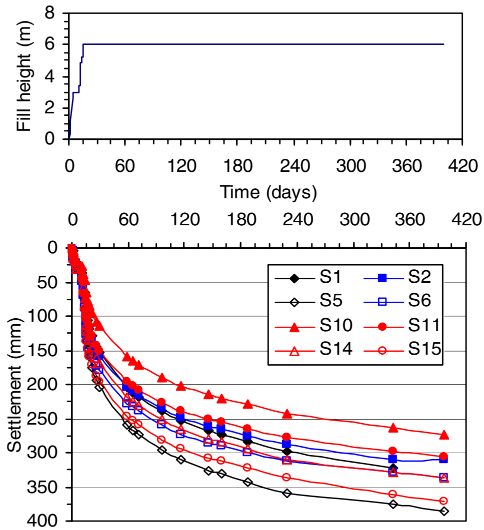

Fig. 3. Surface settlement "on clay" and "on piles" near the center of test embankment (solid symbols=on piles; hollow symbols=on clay)

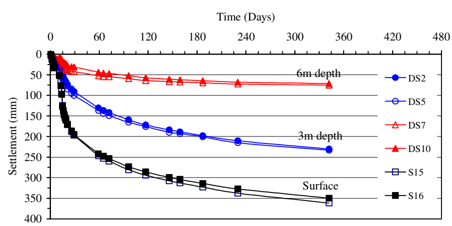

Fig. 4. Comparison of settlements at designated depths below the embankment

3.1. Analytical model for the rate of settlement of deep mixing improved ground

To calculate the average degree of consolidation of the soil-cement pile improved ground, the following modified time factors obtained from the analytical model of Lorenzo and Bergado (2003) must be substituted to the standard solution (or chart) or to any approximate solutions (e.g., Sivaram and Swamee, 1977) of one-dimensional consolidation equation:

Equal stress condition between DMM pile and soil:

$$T_{v,\sigma} = \left(\frac{\left(\frac{m_{v,p}}{m_{v,c}}\right)}{\left(\frac{m_{v,p}}{m_{v,c}}\right) + \left(n^2 - 1\right)\left(\frac{C_c}{C_s}\right)_p} \right)\left(\frac{c_{v,p}t}{H_p^{\ 2}}\right) \tag{1}$$

Equal strain condition between DMM pile and soil:

$$T_{v,\varepsilon} = \left(\frac{1}{1 + \left(n^2 - 1\right)\left(\frac{C_c}{C_s}\right)_p} \right)\left(\frac{c_{v,p}t}{H_p^{\ 2}}\right) \tag{2}$$

where: $(C_c/C_s)_p$ = is the ratio of the compression and swelling indices of the DMM pile at stress level corresponding to loading condition (if the DMM pile does not reach to its yield stress, this constant can be taken as unity);
$c_{v,p}$ = coefficient of consolidation of the DMM pile material as obtained from oedometer test;
$m_{v,p}/m_{v,c}$= ratio of the coefficient of volume change of the DMM pile and the surrounding clay;
$n = (D_e/d_p)$ = ratio of the equivalent diameter of the unit cell to the diameter of the pile; where D_e = 1.03S and 1.13S corresponding to triangular and square pattern of the piles, respectively, S is the center-to-center spacing of the piles, d_p is the diameter of pile.
H_p = is the effective longest drainage path of the consolidating soil-cement pile;
t = time when a particular degree of consolidation is desired.

The actual load transfer mechanism is neither equal strain nor equal stress; however, it would surely fall within these two extreme conditions. The actual average degree of consolidation can be better estimated by applying appropriate weighting factor to each average degree of consolidation from the two extreme conditions, equal stress and equal strain conditions. Thus, the actual average degree of consolidation of the improved ground, $\overline{U}$, will be predicted using the following relationship:

$$\overline{U} = \alpha_\varepsilon\left(\overline{U}_{v,\varepsilon}\right) + \alpha_\sigma\left(\overline{U}_{v,\sigma}\right) \tag{3}$$

where α_ε and α_σ are the weighting factors of the average degree of consolidation corresponding to equal strain and equal stress conditions, respectively; $\overline{U}_{v,\varepsilon}$ is the average degree of consolidation under equal strain condition calculated using the standard solution (or chart) or to any approximate solutions (e.g., Sivaram and Swamee, 1977) of one-dimensional consolidation equation with the time factor, $T_{v\varepsilon}$, given in Eq. (2); and $\overline{U}_{v,\sigma}$ is the average degree of consolidation under equal stress condition calculated using the time factor, $T_{v\sigma}$, given in Eq. (1). Obviously, the sum of these two weighting factors, α_ε and α_σ, must be equal to unity.

3.2. Input soil parameters for the analytical model

The consolidation parameters as well as the strength parameters of soil-cement piles used in the back-analyses were estimated based from the test piles, which were installed few meters away from the embankment. Petchgate *et al.* (2003) reported the following properties of the tested soil-cement piles: water content = 160%, γ_{wet} =1.30t/m^3; q_u =300~700 kPa and E_{50}= 60,000~120,000 kPa. From laboratory test, the specific gravity of the cement-admixed clay composing the pile is about 2.65. Accordingly, the after-curing void ratio of cement-admixed clay composing the soil-cement pile can be obtained as 4.3, which is almost twice the void ratio of the natural clay. At this magnitude of after-curing void ratio of soil-cement piles, the coefficient of vertical permeability, $K_{v,p}$, ranges from 150 to 200 x 10^{-10} m/sec and the corresponding coefficient of consolidation, $C_{v,p}$, ranges from 200 to 400 m^2/yr (Lorenzo and Bergado, 2003). In addition, for the surrounding clay, the coefficient of vertical permeability, $K_{v,c}$, ranges from 3 to 6 x 10^{-10} m/sec and the corresponding coefficient of consolidation, $C_{v,c}$, ranges from 1 to 3 m^2/yr (Lorenzo and Bergado, 2003).

4. RESULTS OF BACK-ANALYSIS

4.1. Results from analytical back-analysis

Figure 5 shows the predicted settlement-time plots together with the corresponding measured settlement-time plots from settlement plates S1 vs. S5 respectively (refer to Fig. 2a for their locations). As mentioned, two adjacent settlement plates on pile and on the adjacent clay, respectively, were paired accordingly. In the analysis, the immediate settlement and the consolidation settlement were first obtained by trial until the actual settlement just after embankment construction and one year after construction (last observed data) agreed to the predicted or projected ones. The behavior of the settlement against time reflects the consolidation properties such as permeability ratio ($k_{v,p}/k_{v,c}$), compressibility ratio ($m_{v,p}/m_{v,c}$), and the coefficient of consolidation of the deep mixing pile ($c_{v,p}$).

The good agreement between the measured and the predicted settlements using the method of Lorenzo and Bergado (2003) shown in Fig. 5 was obtained using the coefficient of consolidation of the pile ($c_{v,p}$) of 800 m^2/yr and coefficient of consolidation of surrounding clay ($c_{v,c}$) of 2.0 m^2/yr. Bergado et al. (1999) also utilized coefficient of consolidation of surrounding clay ($c_{v,c}$) of 2.0 for the back-analysis of Bangna-Bangpakong Highway embankment which was also improved by deep mixing method. Moreover, the compressibility ratio ($m_{v,p}/m_{v,c}$) of 0.10 was used, which also confirmed to the back-analysis of another case study done previously by Lorenzo and Bergado (2003). Consequently, the permeability ratio ($k_{v,p}/k_{v,c}$) was derived as 40, which is twice to what was obtained by Bergado et al. (1999) and Lorenzo and Bergado (2003) for the Bangna-Bangpakong Highway embankment. Moreover, the predictions using the sand drain technique of Barron (1948) overpredicted while the predictions using the technique of Hansbo (1979) underpredicted the settlements as shown in Fig. 5.

Furthermore, the weighting factors of the average degree of consolidation, α_ε and α_σ, as mentioned in Eq. (3) corresponding to "equal strain" and "equal stress" conditions, respectively, that were utilized in the analysis and simulated closely to the actual rate of settlement of the improved ground are 80% for equal strain and 20% for equal stress. This means that at any time the overall degree of consolidation of the improved ground was taken equal to 80% of the average degree of consolidation under equal strain condition plus 20% of the average degree of consolidation under equal stress condition (Lai et al, 2006).

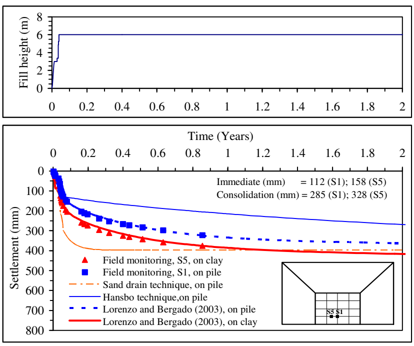

Fig. 5. Back-analysis of settlement with time for S1 vs. S5

5. CONCLUSIONS

1. The deep mixing improvement in the soft clay foundation has effectively reduced the settlement of reinforced test embankment by 70%. Just after embankment construction, the settlement of the improved ground already amounted to 40% of the total settlement.
2. The local differential settlement between piles and the adjacent surrounding soil amounted to 25 to 60 mm, which were about 8% to 20% of the average settlement. The local differential settlement, however, was not obvious at the top surface of the embankment due to the combined effect of compaction as well as reinforcement stiffness and arching of the reinforced soil.

3. The jet mixing method can create soil-cement piles with higher after-curing void ratio and, hence, higher coefficients of permeability and consolidation.
4. The higher permeability ratios, $K_{v,p}/K_{v,c}$, of 30 and 40 were confirmed from numerical and analytical analyses, respectively. In addition, in the analytical back-analysis the following parameters were obtained: compressibility ratio ($m_{v,p}/m_{v.c}$) of 0.10; coefficients of consolidation of the deep mixing pile ($c_{v,p}$) and of the surrounding clay ($c_{v,c}$) of 800 and 2.0 m^2/yr, respectively.

6. REFERENCES

Asaoka, A. (1978). "Observational procedure of settlement prediction." *Soils and Foundations*, 18(4):53-66.

Barron, R.A. (1948). "Consolidation of fine-grained soils by sand drain wells." *Trans. ASCE*, 113:1718.

Bergado, D.T. and Lorenzo, G.A. (2003). "Behavior of reinforced embankment on soft ground with and without jet grouted soil-cement piles." *Proc. 12th Asian Regional Conference on Soil Mechanics and Foundation Engineering*, Singapore: 1311-1316.

Bergado, D.T., Ruenkrairergsa, T., Taesiri, Y. and Balasubramaniam, A.S. (1999). "Deep soil mixing used to reduce embankment settlement." *Ground Improvement*, 3:145-162.

Hansbo, S. (1979). "Consolidation of clay by bandshaped prefabricated drains." *Ground Engineering*, 12(5):16-25.

Kamon, M and Bergado, D.T. (1991). "Ground Improvement Techniques." *Proc. of the 9th Asian Regional Conference on Soil Mechanics and Foundation Engineering*, Bangkok, Thailand, 2:526-546.

Lai, Y.P., Bergado, D.T., Lorenzo, G.A. and Duangchan, T. (2006). "Full-scale reinforced embankment on deep jet mixing improved ground." *Ground Improvement*, 10(4):153-164.

Lorenzo, G.A. and Bergado, D.T. (2003). "New consolidation equation for soil-cement pile improved ground." *Canadian Geotechnical Journal*, 40(2):265-275.

Lorenzo, G.A. and Bergado, D.T. (2004). "Fundamental parameters of cement-admixed clay – new approach." *Journal of Geotechnical and Geoenvironmental Engineering, ASCE*, 130(10):1042-1050.

Petchgate, K., Jongpradist, P. and Panmanajareonphol, S. (2003). "Field pile load test of soil-cement column in soft clay." *Proc. of the International Symposium 2003 on Soil/Ground Improvement and Geosynthetics in Waste Containment and Erosion Control Applications*, 2-3 December 2003, Asian Institute of Technology, Thailand:175-184.

Porbaha, A. (1998). "State of the art in deep mixing technology. Part I: Basic concepts and overview." *Ground Improvement*, 2:81-92.

Sivaram B. and Swamee, P. (1977). "A computational method for consolidation coefficient." *Soil and Foundations*, Tokyo, Japan, 17(12):48-52.

Critical Height of A Deep Mixed Column-Supported Embankment under An Undrained Condition

Jie Huang[1] and Jie Han[2], M. ASCE

[1]Staff Engineer, Kleinfelder Inc., 7802 Barton, Lenexa, Kansas 66214; jhuang@ku.edu (former Ph.D. student at the University of Kansas)
[2]Associate Professor, Civil, Environmental, and Architectural Engineering (CEAE) Department, the University of Kansas, 1530 W. 15th Street, Lawrence, Kansas 66045-7609; jiehan@ku.edu

ABSTRACT: Deep mixing technology has been increasingly used to support embankments over soft soil. Deep mixed (DM) columns and soft soil form a composite foundation. Similar to other foundation systems, the DM foundation has a limit to support a certain height of the embankment. After this critical height, the columns and/or the soil between the columns start to yield and result in significantly increased settlement, which is often intolerable. In this study, a numerical study was conducted to investigate the influence of four key factors including strength, size, and spacing of DM columns and strength of soft soil on the critical height of the embankment under an undrained condition. The soft soil, the embankment fill, and DM columns were modeled as linearly elastic perfectly plastic materials with Mohr-Coulomb failure criteria. The embankment was constructed by lifts with equal thickness. The critical height was determined corresponding to a sudden nonlinear increase on the maximum settlement versus the embankment height plot. Empirical correlation was developed to estimate the critical height of the embankment built over DM foundations. In addition, a formula was proposed to estimate the bearing capacity of a DM foundation under an embankment.

INTRODUCTION

Columns have been used to improve the overall bearing capacity and reduce the settlement of various embankments (such as, roadway and railway embankments) since early 1960s (Magnan 1994). The benefits associated with the use of a column-support embankment are as follows: (1) to build the embankment in a single stage without prolonged waiting time, (2) significantly reduce total and differential settlements, (3) reduce earth pressures, and (4) avoid excavation and refill employed in many situations. Different types of columns have been used in column-supported embankments, such as deep-mixed (DM) columns, rammed aggregate piers, stone columns, sand columns, vibro-concrete columns (VCCs), etc. Terashi (2003) pointed out that nearly 60% of Japanese on-land applications and 85% of Nordic applications of DM columns were used to reduce settlements and increase stability of embankments. In recent years, deep mixing has also been considered one of the promising ground improvement technologies in the United States.

DM columns are installed in the soft soil to form a composite foundation with the soft soil. Similar to other foundations, this composite foundation has a limited bearing capacity. Kitazume et al. (1996) and Broms (1999) both indicated that lateral force from the embankment would reduce the bearing capacity of the composite foundation. Therefore, embankments can be safely built to a certain height, called the critical height in this paper, to avoid intolerable settlement. So far, no method is available to properly predict or estimate this critical height. To investigate the influence of various factors on the critical height, a numerical analysis was conducted in this study. Two-dimensional finite difference software - FLAC version 5.0 (Itasca Consulting Group, Inc. 2006) was used to fulfill the objective.

NUMERICAL MODELING

Prior to the numerical study, a baseline case was selected based on the typical configuration in the field as a reference. The cross-section of the baseline case is presented in Fig. 1. Since it is a symmetric problem, only half of the embankment was modeled to improve the computing efficiency. The in-situ soil profile included a 10m thick soft soil and a 2m thick firm soil. High strength and modulus were assigned to the firm soil to ensure no failure and significant deformation in that layer. DM columns were modeled as walls and installed to penetrate to the half depth of the firm soil. A 5m high embankment with 2:1 slope was built over DM columns and the soft soil. The width of the embankment at the crest was assumed to be 10m to simulate a two-lane roadway plus a shoulder in one direction. The DM columns, the soft soil, the firm soil, and the embankment fill were modeled as linearly elastic and perfectly plastic materials with Mohr-Coulomb failure criteria. An undrained condition was assumed, therefore, the undrained shear strengths, c_u, were employed for the soft soil, the firm soil, and the DM columns. The groundwater table was assumed to be at the ground surface. The DM walls were assumed to have a tensile strength equal to 20% of the undrained shear strength of the DM columns as typical. The elastic moduli of DM columns and the soft soil were determined based on commonly accepted correlation: $E=200c_u$ (Bruce 2001). The construction consequence was simulated by ten lifts of fill with equal thickness. The properties of the materials of the baseline case are summarized in Table 1.

Table 1. Properties of Materials in the Baseline Case

Material	Properties
DM Columns	γ = 18kN/m^3, c_u = 100kPa, E = 20MPa, c_t = 20kPa
Soft Soil	γ = 18kN/m^3, c_u = 10kPa, E = 2MPa, c_t = 0kPa
Firm Soil	γ = 18kN/m^3, c_u = 500kPa, E = 100MPa, c_t = 0kPa
Embankment Fill	γ = 18kN/m^3, c' = 0kPa, ϕ' = 30^o, E = 30MPa, c_t = 0kPa

Note: γ = unit weight, c_u = undrained shear strength, E = elastic modulus, and c_t = tensile strength.

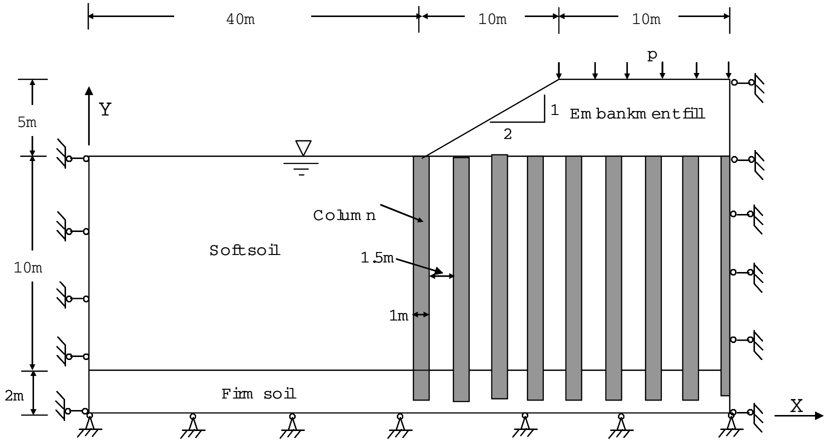

FIG. 1. Cross-section of the baseline case.

On the completion of the baseline case, a parametric study was conducted by changing a parameter individually from the baseline case to investigate the influence of that specific factor. The properties of DM columns and the soft soil were chosen based on their typical ranges used in practice (Budhu 2000; Bruce 2001), which are listed in Table 2. Typically, the material properties of the embankment fill do not vary significantly, therefore, its properties were assumed to be constant in this study.

Table 2. Parameters Investigated

Properties	Values
DM column modulus (MPa)	10, 20, 100, 200
DM column size (m)	0.5, 1.0, 1.5
DM column spacing (m)	1.5, 2.5, 3.0, 3.5, 4.5
Soft soil modulus (MPa)	1, 2, 4

RESULTS AND ANALYSIS

As mentioned earlier, intolerable settlement would develop if the embankment is built beyond a critical height. Maximum settlement of the embankment is expected to be a good indicator whether the critical height has been reached or not. The maximum settlement at the base of the embankment was plotted against the embankment height to help identify the critical height for each case. The curve of the maximum settlement versus the embankment height for the baseline case is presented in Fig. 2 as a representative. It can be seen that this curve consists of two linear portions connected by an arc. When the embankment height is below a certain value, the maximum settlement increases gradually with the embankment height and the linear portion has a gentle slope. However, as the embankment height exceeds a certain value, the maximum settlement increases much faster and turns into another linear portion, which has a much steeper slope. In this study, the critical height is determined by extending the two linear portions to intersect at one point as illustrated in Fig. 2.

The critical heights of all cases were obtained in the same way. For some cases that the critical height could not be reached even after the construction of the 5m high embankment, a distributed load was applied and increased to pass the critical height. The applied distributed load was converted to the equivalent embankment height to generate a maximum settlement versus embankment height plot. The conversion of the traffic load to the additional equivalent embankment height was based on the formula $\Delta H = p/\gamma$, where ΔH is the converted additional equivalent embankment height, p is the traffic load, and γ is the unit weight of the embankment fill (i.e., 18kN/m^3).

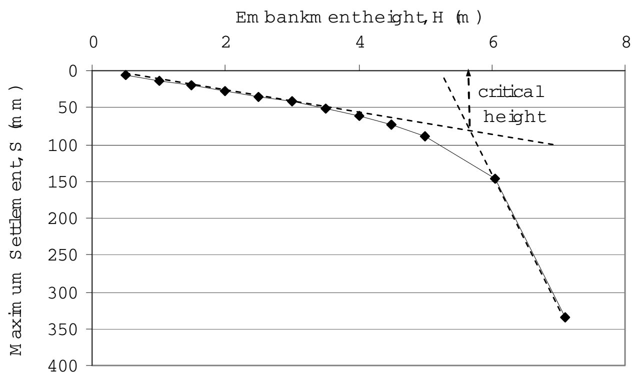

FIG. 2. Maximum settlement vs. embankment height.

Influence of Column Modulus on Critical Height

The influence of the column modulus on the critical height is presented in Fig. 3. The higher column modulus leads to a higher critical height. Keep in mind that the column modulus is proportional to the column undrained shear strength in this study. The higher column modulus means a higher column undrained shear strength and in turn a higher undrained shear strength for the composite foundation. As a result, the embankment can be built higher. However, it can also be seen that the influence of the column modulus on the critical height flattens out as the column modulus continues to increase. This phenomenon is attributed to the fact that the soft soil and the DM columns do not yield at the same strain level and the DM columns do not fully mobilize their strength when the soft soil reaches its strength limit.

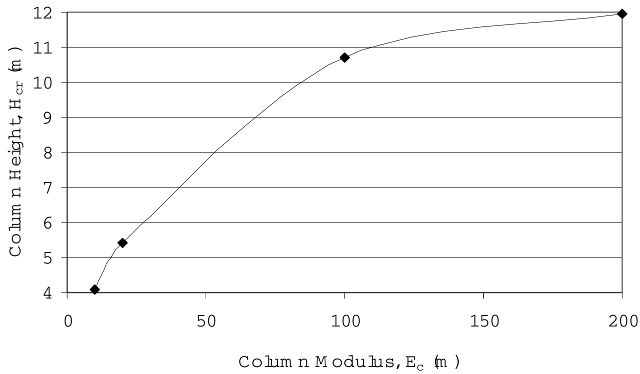

FIG. 3. Influence of column modulus on critical height.

Influence of Column Size on Critical Height

The influence of the column size (actually the wall width in this study) on the critical height is presented in Fig. 4. The larger column size yields a higher critical height. This effect is attributed to the increase of the undrained shear strength of the composite foundation. When the column spacing remains unchanged, the larger column size would lead to a higher area replacement ratio, which is defined as the column size to the column center-to-center spacing in the two-dimensional condition. As a result, the composite foundation has a higher bearing capacity or critical height.

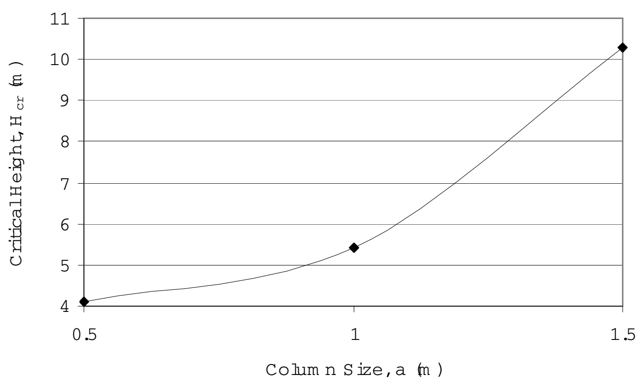

FIG. 4. Influence of column size on critical height.

Influence of Column Spacing on Critical Height

Opposite to the influence of the column size on the critical height, the increase of the column spacing leads to a lower critical height. The reason is that the larger column spacing produces a smaller area replacement ratio, and consequently a weaker composite foundation, as the column size remains unchanged. It is worth mentioning that the spacing used herein is the center-to-center spacing.

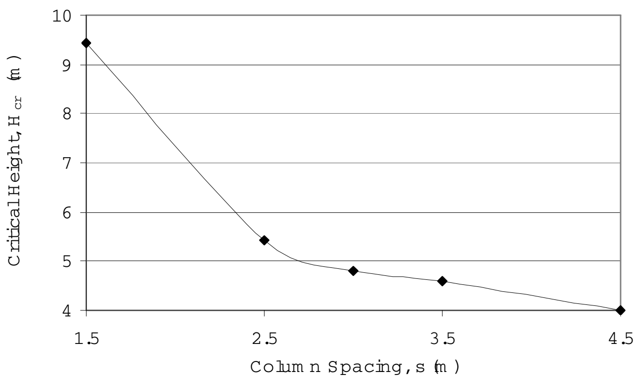

FIG. 5. Influence of column spacing on critical height.

Influence of Soil Modulus on Critical Height

The influence of the soil modulus on the critical height is shown in Fig. 6. The critical height increases almost linearly with the soil modulus. The reason for this relationship is similar to what has been stated for the effect of the column modulus on the critical height.

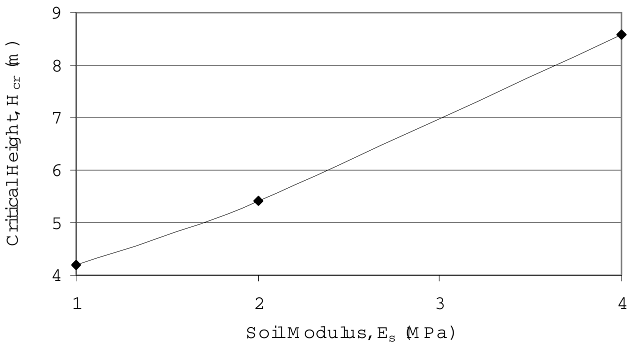

FIG. 6. Influence of soil modulus on critical height.

Empirical Relationship for Critical Height

As discussed above, the factors influence the critical height through their influence on the undrained shear strength of the composite foundation. In other words, the change of the undrained shear strength of the composite foundation changes the critical height accordingly. A correlation is expected between the undrained shear strength of the composite foundation and the critical height of the embankment. The area-weighed average undrained shear strength of the composite foundation is used herein to develop this correlation, which can be expressed as follows:

$$c_{ucom} = c_{uc} a_s + c_{us} (1 - a_s) \tag{1}$$

where c_{ucom} = the undrained shear strength of the composite foundation; c_{uc} = the undrained shear strength of the DM columns; c_{us} = the undrained shear strength of the soft soil; and a_s = the area replacement ratio.

The critical height is plotted against the undrained shear strength of the composite foundation in Fig. 7. Considering that the strength of DM columns may not be fully mobilized as the DM columns become much stronger than the soft soil, the undrained shear strength of the columns was limited to 20 times that of the soft soil in order to generate the highest R^2 in the plot. In other words, if the column strength was more than 20 times the soil strength, it was assumed to be 20 times the soil strength. A satisfactory linear relationship was found between the critical height of the embankment and the undrained shear strength of the composite foundation. In practice, Fig. 7 can be used to estimate the critical height of the embankment if the undrained shear strength of the composite foundation is known or estimated using Eq. (1). In practice, embankments are built to support loads, such as traffics. Attention should be paid that the critical height determined from Fig. 7 includes the actual height of the embankment and the equivalent additional height of the load.

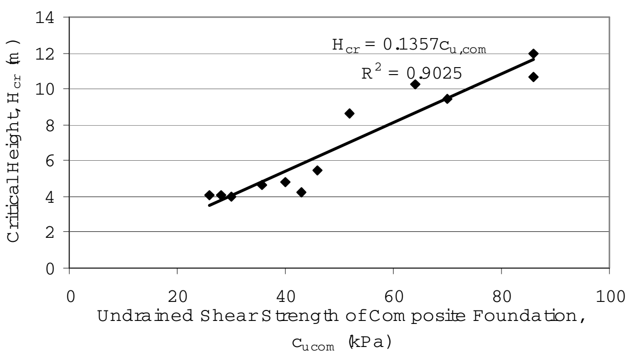

FIG. 7. Critical height of the embankment versus undrained shear strength of the composite foundation.

According to the linear correlation shown in Fig. 7, the allowable bearing capacity of the DM composite foundation can also be determined in form of $N_c \cdot c_{ucom}$, in which N_c is the allowable bearing capacity factor. Expressing the linear correlation shown in Fig. 7 with a unit weight of fill equal to γ = 18kN/m^3 can yield N_c = 2.44, i.e.

$$\gamma H_{cr} = N_c c_{ucom} \tag{2}$$

In any circumstance, the embankment weight plus the traffic load, p, should not exceed the allowable bearing capacity of the composite foundation, i.e.,

$$\gamma H + p \leq N_c c_{ucom} \tag{3}$$

Consequently, the allowable embankment height can be easily estimated from Eq. (3). In addition to the bearing capacity, the settlement of the embankment should also be checked against the serviceability requirement, which is beyond the scope of this study.

CONCLUSIONS

Based on this study, it can be concluded that the critical height of an embankment increases linearly with the undrained shear strength of the deep-mixed composite foundation. Under an undrained condition, the allowable bearing capacity of the composite foundation under the embankment can be estimated as 2.44 times the undrained shear strength of the composite foundation. To avoid excessive settlement, the embankment weight plus the traffic load should not exceed this allowable bearing capacity of the composite foundation.

REFERENCES

Broms, B.B. (1999). "Can lime/cement columns be used in Singapore and Southeast Asia?" *3rd GRC Lecture*, Nov. 19, Nanyang Technological University and NTU-PWD Geotechnical research Centre, 214p.

Bruce, D. A. (2001). *An Introduction to the Deep Mixing Methods as Used in Geotechnical Applications – Volumne III: The Verification and Properties of Treated Ground*. FHWA-RD-99-167, 455p.

Budhu, M. (2000). *Soil Mechanics and Foundations*. New York: John Wiley, 586p.

Itasca Consulting Group, Inc. (2006). *FLAC/Slope User's Guide*, Version 5.0, 84p.

Kitazume, M., Ikeda, T., Miyajima, S., and Karastanev, D. (1996). "Bearing capacity of improved ground with column type DMM." *Grouting and Deep Mixing*, Yonekura, Terashi, and Shibazaki (eds), Balkema, Rotterdam, 503-508.

Magnan, J. (1994). "Methods to reduce the settlement of embankments on soil clay: a review." *Foundations and Embankment Deformations*, ASCE, Geotechnical Special Publication No. 40, 77-90.

Terashi, M. (2003). "The state of practice in deep mixing methods." *Proceedings of the 3rd International Conference on Grouting & Ground Treatment*, 1-15.

Combined Lime and Cement Treatment of Expansive Soils with Low to Medium Soluble Sulfate Levels

[1] Chakkrit Sirivitmaitrie, [2]Anand J. Puppala, [3] Vivek Chikyala, [4]Sireesh Saride, [5]Laureano R. Hoyos

[1]Graduate Research Assistant, The University of Texas at Arlington, Department of Civil and Environmental Engineering, Box 19308, Arlington, TX 76019, sschakkrit@hotmail.com
[2] Professor, The University of Texas at Arlington, Department of Civil and Environmental Engineering Box 19308, Arlington, TX 76019, anand@uta.edu, (Corresponding Author)
[3] Former Graduate Research Assistant, The University of Texas at Arlington, Department of Civil and Environmental Engineering, Box 19308, Arlington, TX 76019
[4] Research Associate, The University of Texas at Arlington, Department of Civil and Environmental Engineering, Box 19308, Arlington, TX 76019, sireesh@uta.edu
5 Associate Professor, The University of Texas at Arlington, Department of Civil and Environmental Engineering Box 19308, Arlington, TX 76019, lhoyos@uta.edu

ABSTRACT: Expansive soils are considered as one of the major natural hazards causing billions of dollars of damage annually to various civil infrastructures built over them. Several methods have been attempted to stabilize expansive soils with some success. One method using combined lime and cement additives shows some promise, with initial lime treatment improving the workability and the subsequent cement treatment improving the strength and resilient properties of the same subsoil. However, the efficiency of this method has not yet been extensively studied. Hence, an attempt is made in the present research to evaluate the suitability of combined lime and cement treatment in stabilizing expansive clays of the city of Arlington, Texas. This paper covers two of the test pavement sections built on combined lime and cement treated subgrades. Laboratory test results including unconfined compression strength, free swell tests and linear shrinkage tests were first conducted to evaluate the property enhancements. Field sections built on combined treated subsoils were monitored and surveyed to study the heave related movements and cracking.

INTRODUCTION

Expansive soils are a worldwide problem. The estimated damage to buildings, roads and other structures built on expansive soils exceeds 15 billion dollars in the US annually (Azam et al. 2003). The expansive soils are considered natural hazards that pose challenges to civil engineers. The volumetric changes of expansive soils rely on moisture content fluctuations. Arid climate, alkaline environment, and local geology are responsible for volumetric changes in expansive soils (Azam et al. 2003).

The aim of pavement construction is to provide safety and comfort riding condition to the travelers. Expansive clay soil has always been a challenge to pavement structures since the clay movements often distress pavements. Hence, it is essential to improve the expansive clay properties, prior to pavement construction (Croney, and Croney, 1997).

Lime and cement stabilization methods are traditional treatment methods used to modify problematic soils. Lime has the ability to improve workability and reduce volumetric changes of soils. Cement has the ability to improve strength and also lower the volume changes of soils. Lime modification is more effective on a treatment of high-plasticity clays. On the other hand, cement stabilization is more effective on granular and moderately effective on cohesive soils (Chavva et al. 2005).

At present, it has long been seen that the majority of works done for stabilization of problematic soils involve either using lime modification or using cement stabilization. Lime stabilizer is mostly preferred since it can reduce volume change related soil movements and also due to cost consideration. Recent research showed the potential of cementitious stabilizers that are proven effective on plastic clays. The concept of using combined lime and cement stabilization has been explored, but not extensively reported in the literature, primarily due to high initial cost and lack of long term field monitoring (Prusinski and Battacharja. 1999).

Researchers at The University of Texas at Arlington have been attempting to investigate the effectiveness of combined lime and cement treatment method for enhancing properties of local clay subgrades with low sulfate levels and thereby improve pavement riding conditions in Arlington, Texas. For comparisons, data from the same soil treated by control method of standard lime treatment was used. This paper presents test data and comparisons of two expansive clayey soils. This paper also discusses specifications for field treatments and construction sequence details followed in the field. Test results from field samples are also compared with laboratory results to understand the property variations. Four soil properties such as Plasticity Index or PI (workability), unconfined compressive strength, free swell potential, and linear shrinkage strain potentials are addressed.

LABORATORY TESTS AND RESULTS

The sites used for the present research are located in the city of Arlington, Texas. The north Texas climatic condition is in an arid zone and the local geology indicates that the subsoils are composed of Marl and Montmorillonite clay minerals, which have high plasticity characteristics and hence these soils tend to absorb water. Such soils often undergo swelling or shrinking due to moisture fluctuations (Azam et al. 2003).

Two construction sites selected for this research are Southmoor and International Street pavements, which were constructed on expansive soils with low to medium soluble sulfate levels. These pavements were designed for a low to medium traffic volume conditions. In order to verify the effectiveness of the combined lime-cement stabilization method on these site soils, laboratory tests were first carried out on the soil specimens collected from the project site. Tests conducted include Atterberg Limits, Unconfined Compressive Strength (UCS) tests, Vertical Swell and Linear Shrinkage Bar tests. Soils were treated with lime (12% by dry weight of soil) and combined lime-cement (6% of lime and 6% cement) and then soil specimens were compacted to a size of 10.2 cm diameter and 11.4 cm height. The specimens were then cured in controlled humidity environment for seven (7) days. The curing time of seven days was selected since the City would like to complete the pavement construction in a fast track mode. The following sections describe test results.

Atterberg Limits

Figure 1 and Figure 2 show individual results of Atterberg limits of both sites. Tests on control or untreated soils from various bore holes (one sample per every four bore holes) from both locations yielded an average liquid limit (LL) of 59 with an average plasticity index (PI) of 38. In contrast, lime treated soils from both locations yielded an average liquid limit of 42 with an average plasticity index of 10. Combined lime and cement treated soils yielded even better average liquid limit of 40 and an average plasticity index of 7.

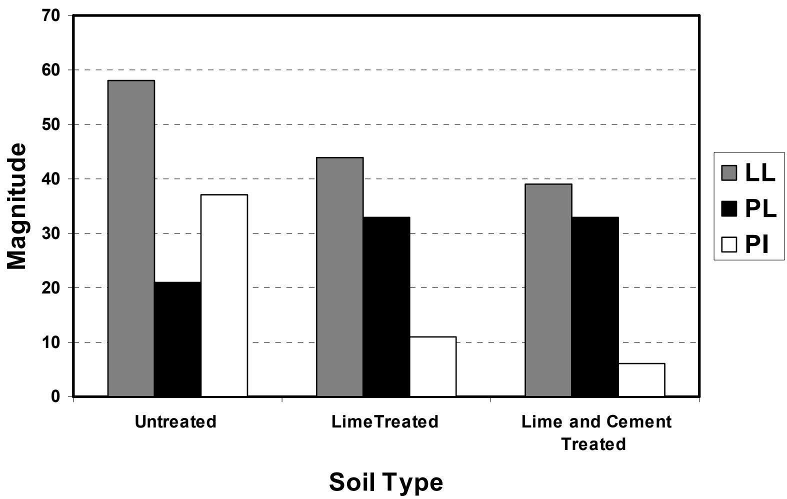

Figure 1. Atterberg Limits of Untreated and Lime-Cement Treated Clays in International Street

There was a considerable decrease in Atterberg Limits of the treated soils, which is attributed to the decrease in the thickness of the diffused double layer as a result of cationic exchange reactions by the calcium ions from lime and cement binders. Overall, an increase in plastic limit and a decrease in plasticity index indicate enhancement in the workability of the soil when treated with both lime and lime-cement treatments.

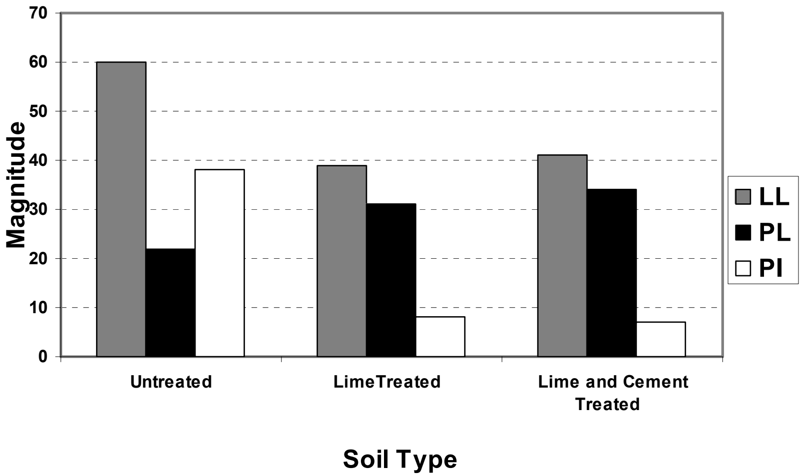

Figure 2. Atterberg Limits of Untreated and Lime-Cement Treated Clays in Southmoor Street

Strength, Swell and Shrinkage Strain Test Results

The quality control of the lime and cement stabilized specimens is often assessed in term of strength improvement that the stabilizers made to the soil specimens. Hence, the most popular test used is Unconfined Compression Strength (UCS) test. UCS tests were carried out on both treated and untreated soil specimens in order to compare their strength variations with respect to lime and combined cement-lime treatments. Cement treatments were not considered as cement treatment method is not used by the City of Arlington on high PI clays. Summary of the UCS test results are shown in figure 3.

For the untreated soil specimens, the average UCS of both sites are 22.9 psi (157.89 kPa), whereas both lime and combined lime-cement treated soils exhibited higher UCS strengths in the range of 200 psi (1378.95 kPa) to 270 psi (1861.58 kPa), giving a tenfold increase in the UCS of untreated soil. This strength increase meet the UCS criterion often used in soil cement materials for low volume traffic conditions.

The compressive strength of untreated soil specimens is considerably enhanced after both treatments. The combined lime and cement treatment has resulted in slightly higher compressive strength than the isolated lime treatment. Strength enhancements are attributed to pozzalonic compounds formed due to chemical reactions between stabilizers and soil in the presence of moisture. The effect of curing period on strength of the treated soils is explained by comparing UCS results obtained at two curing periods, 2 and 7 days respectively (Table 1). As expected, the 7-day UCS is three times the UCS of a 2-day UCS of the combined treated soils, indicating strength enhancements are dependent on early curing periods.

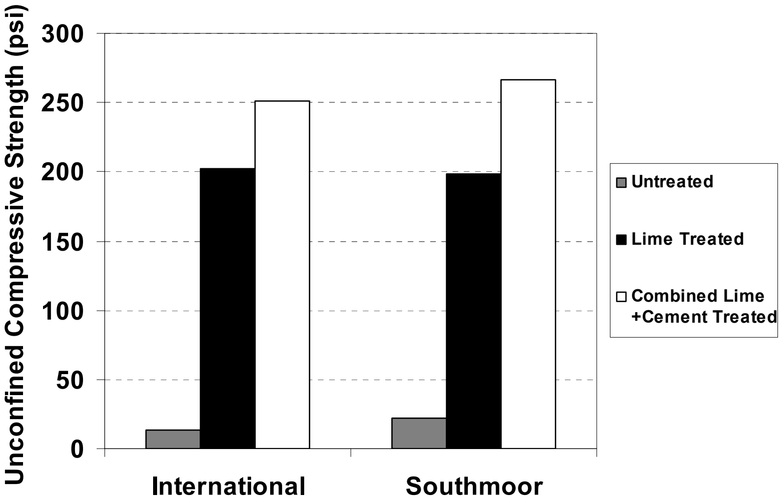

Figure 3. Summary of UCS Test Results

Linear shrinkage bar tests were also conducted as per TxDOT standard method to evaluate the improvements in linear shrinkage strain properties of treated soil with respect to untreated soil. Untreated soils showed a linear shrinkage strain of 20.2% and 18.3% for International and Southmoor Street respectively, whereas treated soils showed minute or very small shrinkage strains due to the formation of hairline cracks. Swell and shrinkage strains on 2-days and 7-days cured specimens showed no volume changes in the treated soils, which was attributed to plasticity decrease and reductions of moisture affinity of treated soil particles due to ionic exchange reactions.

FIELD CONSTRUCTION AND SPECIFICATIONS

The construction sequences starts with an excavation down to the in-situ material to be stabilized. Then, the imported stabilizer is placed on the subbase. This method is known as "Mix-in-place stabilization". In this method, the stabilizer is spread before pulverization and mixing of the soil and stabilizer. The sequences consist of initial lime modification, followed by cement stabilization. The equal amounts of lime and cement were used at a rate of 42 lb per square yard (15.93 kg per square meter) each and to a depth of 9 in (22.86 cm). below the ground surface. The content of lime and cement used is approximately 6% separately (Sherwood. 1993).

Lime modification is relatively simple as to compare to cement stabilization. This is because lime has much lower bulk density than cement and it is possible to achieve a more uniform distribution. Prior to the modification, the subgrade is prepared in accordance with the specification. The proper amount of lime is then spread over the soil by the mechanical spreader. Pulverization and mixing are used to combine lime and soil thoroughly in an appropriate depth (Little et al. 1998).

Cement binder is either in the form of slurry or in the form of a powder. Lime treated subgrade and cement binder in dry form are thoroughly mixed with a pulvimixer. After mixing, the cement, lime and soil mixture is compacted with a sheep foot roller to a density not less than 95% of maximum dry density as determined by ASTM D698 moisture/density relationships. Figure 4 shows the sequence of combined lime and cement treatment of subgrade.

Table 1. Summary of Laboratory Test Results of Both Sites

Sample Type	Curing Period	UCS in psi (kPa)	Free Swell Strain (%)	Linear Shrinkage Strain (%)
INTERNATIONAL				
Untreated (Field Cores)	-	13.7 (94.46)	6.27	20.2
Lime (Laboratory)	2 Days	74.2 (511.59)	0.0	0.0
	7 Days	202.3 (1394.81)	0.0	0.0
Combined Lime and Cement (Laboratory)	2 Days	83.0 (572.26)	0.0	0.0
	7 Days	250.9 (1729.89)	0.0	0.0
Combined Lime and Cement (Field Cores)	7 Days	128.0 (882.53)	0.0	0.0
SOUTHMOORE				
Untreated (Field Cores)	-	22.1 (152.37)	5.08	18.3
Lime (Laboratory)	2 Days	68.9 (475.05)	0.0	0.0
	7 Days	198.6 (1369.30)	0.0	0.0
Combined Lime and Cement (Laboratory)	2 Days	86.1 (593.64)	0.0	0.0
	7 Days	266.4 (1836.76)	0.0	0.0
Combined Lime and Cement (Field Cores)	7 Days	133.0 (917)	0.0	0.0

Field Specifications

The combined lime-cement treatment specifications in the field are as follows: For lime modification, a 100% of all material should pass through a 2 in (50.8 mm). sieve after initial mixing pulverization in order to allow uniform mixing of cement stabilization in the next phase. A minimum mellowing period of 48 hrs should be allowed after mixing and pulverization of lime. The average in-situ moisture content of stabilized soil from both streets is 29%. Water content in lime treated soil should be maintained at least +2% above the optimum moisture content

For cement treatment, cement is mixed with soil as thoroughly as possible. The water content of cement treated soil is to be maintained at a minimum of two percent above the soils optimum moisture content. Pulverization of lime treated subgrade should be such that 100 % should pass a 1-1/2 in. (38.1 mm) sieve and a minimum of 60% should pass a No.4 sieve (4.75mm). A curing period of 7 days should be allowed for the treated subgrade to gain their full strength after final compaction. The water content is kept at least 4% above optimum moisture content thorough out the curing.

(a)

(b)

(c)

(d)

Figure 4. (a) Lime Slurry Placement, (b) Re-scarification, (c) Final Mixing of Soil with Lime and Cement, (d) Final Compaction

QC/QA Issues

During the construction process, quality control or QC checks need to be made in order to ensure that the stabilization follows all the requirements of the specification. In situ gradation was performed to check for the specifications regarding treated materials passing through the sieves. Compaction densities measured with a nuclear gauge were also within the field targeted moisture content – dry unit weight specification.

Quality assessment QA studies were performed by collecting Shelby tubes specimens from the stabilized subgrade and then subjecting them to Unconfined Compressive Strength, Swell and Linear Shrinkage tests. The results of these tests are shown in table 1. For swell and shrinkage test, the results of field specimens show consistency to the laboratory prepared specimens. Whereas, the strength of field specimen is lower than laboratory prepared specimens. The lower strength is subjected to sampling method which may reduce strength of specimens due to breaking of cementation bonds.

SUMMARY AND CONCLUSIONS

From the experimental program of the effect of combined lime and cement treatment on low to medium sulfate content subgrade, the following conclusions have been made: Combined lime modification and cement stabilization enhanced the strength, and reduced swell and shrinkage strain behaviors of treated subgrades. Swell and shrinkage behaviors are also enhanced in the way that treated specimens show less water absorbing capacity. The volume change of zero magnitude is also observed in both swell and shrinkage test. The quality assessment tests show that swell and shrinkage potential of cored specimens and laboratory tests are consistent. The treated core specimens showed lower strength when compared with laboratory tests, and certain amount of this variation was attributed to the sampling process which might have resulted in the breaking of cementation bonds.

ACKNOWLEDGEMENTS

Authors would like to acknowledge the City of Arlington's Public Works Department for providing financial assistance to this research. Also, TEAM consultants, Inc. of Arlington, Texas assisted with the field sampling support to this research.

REFFERENCES

Azam S., S.N. Abduljauwad and S.B. Al-Amoudi (2003), "Volume change behavior of arid calcareous soils", *Natural hazards review, ASCE, 2003.*

Chavva P.K., S.K. Vanapally, A.J. Puppala and L.Hoyos (2005), "Evaluation of strength, resilient moduli, swell, and shrinkage characteristics of four chemically treated sulfate soils from north Texas", *GSP 136.,* ASCE Special Publication, Geofrontiers, Austin, 2005.

Croney, D. and Croney, P. (1997). "Design and performance of road pavements." Third Edition. *McGraw-Hill*, London

Kitazumi M., M. Nakamura, M. Terashi, and K.Ohishi (2003), "Laboratory tests on long term strength of cement treated soil." *Proc. 3rd Int. Conference on grouting and ground improvement*. New Orleans, Louisiana.

Little, D.N., E.H. Males, J.R. Prusinski and B.Stewart, "Cementious stabilization." *Transportation Research Board, Millenium Paper,* 1998.

Prusinski J.R. and S.Battacharja (1999), "Effectiveness of Portland cement and lime in stabilizing clay soils." *Transportation Research Record*, v 1, n 1652, pp. 215-217.

Sherwood P.T (1993), "Soil stabilization with cement and lime." *Transport Research Laboratory*, Department of Transport, London, 1993.

Egyptian Collapsible Soils and their Improvement

Mohamed Sakr[1], M.ASCE; Mohsen Mashhour[2], M.ASCE and Adel Hanna[3], F.ASCE.

[1]Director, Geotechnical Engineering Research Laboratory, Tanta University, EGYPT; mamsakr@yahoo.com
[2]Professor of Geotechnical Engineering, Zagazig University, EGYPT; mmashhour@access.com.eg
[3]Professor of Geotechnical Engineering, Concordia University, Canada; hanna@civil.concordia.ca

ABSTRACT: Large expansion in constructing new cities in the desert outside the traditionally inhibited Nile Delta and Valley has been going on since the reopening of the Suez Canal in June 1975. Since then Egyptian geotechnical engineers have the challenge of dealing with totally new types of problematic soils in such arid and semi arid environment; of which collapsible soils represent a major and most common type. Today a valuable experience has been achieved in classifying, testing and constructing on Egyptian collapsible soils. In this paper the geotechnical and geological properties of Egyptian collapsible soils are introduced. A comparative analysis between these soils and the resembling types in other parts of the world is presented. Actual failure cases are also presented and discussed.

INTRODUCTION

In Egypt, recent extensions of urban communities towards the desert have exposed Egyptian geotechnical engineers to relatively new challenges, among which is the collapsible soil. Intensive research and data collection and compilation in the past three decades have resulted in valuable results that might worth consideration when dealing with similar soils in other parts of the world. These include studying the effect of geological and petrographic factors on collapse characteristics, construction of a large data base with zonation maps in addition to the analysis of classical physical and mechanical properties. Failure case studies with adopted treatment methods have also been reported.

OCCURRENCE OF COLLAPSIPLE SOIL IN EGYPT

Collapsing soils are observed in many areas in Egypt. Most of these areas are situated towards the western desert which covers about 65% of the area of Egypt.

Many researchers have recognized various locations of collapsing soils in Egypt. The geology of these locations were described within the work of Radwan and Gabr (1980), El-Sohby et al (1985 & 1988), El-Saadany (1986), Mahmoud (1989) and Sakr et al (1999). From the previous studies, it could be concluded that most of the collapsing soils in Egypt were deposited in shallow water depths in a loose structure of high void ratio. Rivers, flood streams and rainfalls are responsible for these formations.

Some geological features and occurrence of collapsing soils in some locations in Egypt are; (1) Interridges areas parallel to the north coast of the Mediterranean, (2) Six October Plateau which lies between Cairo-Alexandria desert road and Cairo-El-Fayoum road area, and (3) Inter dune areas which rest along Cairo-Ismailia desert road and Cairo-Bilbeis desert road and includes the 10th of Ramadan city.

GEOLOGICAL FACTORS AFFECTING COLLAPSING BEHAVIOR OF SOILS

For the purpose of providing the essential explanation to the engineering characteristics and behavior of collapsing soil, tools like geology, petrography, mineralogical analysis and environmental factors are employed. The main geological factors that control the behavior of collapsing soils could be summarized as; (1) Age, as a time factor, which is related to the time of rock formation and the history of alteration and changes, (2) Rock type (Origin), (3) Depositional environment, (4) Post - depositional changes such as cementation, dissolution, corrosion and formation of new minerals, and; (5) Post-uplift changes, such as weathering processes, fracturing and rock-surface water interaction. Each of these factors interacts with each other in such a way that forms the final soil product.

ZONATION MAPS FOR POTENTIALLY COLLAPSIBLE SOILS IN EGYPT

The Egyptian geotechnical engineers have always suspected the structural stability of desert dry sand formations that contain appreciable amounts of fines to be potentially collapsible (GEE 2003). The literature, however, recognizes Aeolian fluvial and highly saline soils (sabkha) as naturally occurring collapsible soils. Aeolian deposits, which are mainly in the form of sand dunes, are located south of Siwa Oasis. Fluvial deposits extend from the southwest region of Egypt to the north of Sudan. Sabkhas are located in northern delta, along the Red Sea coastal Plain, northwestern coast of Egypt, coastal regions of Sinai Peninsula, and Qattara and Siwa depressions (Mosaad et al. 2006).

Geotechnical zonation maps for potentially collapsible soils in Egypt have been developed (GEE 2003) as part of a full and detailed geotechnical data base utilizing both Expert Systems and GIS techniques. These zonation maps were developed based on actual boreholes and laboratory and field tests.

PETROGRAPHIC ANALYSIS

The soil texture can help interpreting the collapse behavior and characteristics. For this purpose, an extensive petrographic study has been undertaken on representative thin sections. As an example, A detailed micro-texture analysis of undisturbed soil samples from; (I) the 10th of Ramadan, (II) New Ameriyah city, (III) New Borgel-Arab city, (IV) KM (32.00)-Cairo-Bilbeis desert road, and (V) El-Goreizat-Sohag. (Figure 1).

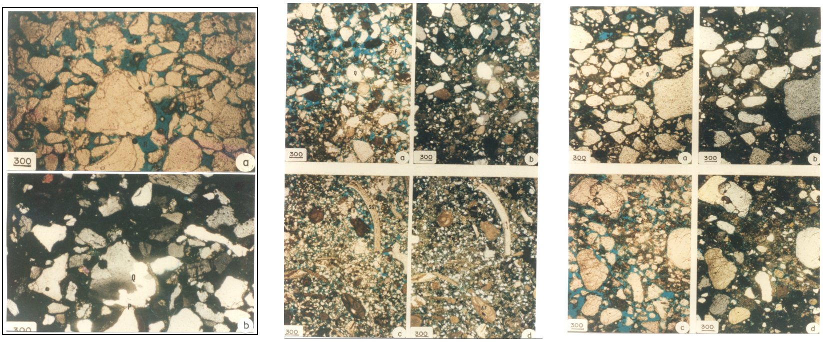

Plate (1)
a, b: 10th of Ramadan city

Plate (2)
a, b: New Ameriyah city
c, d: New Borgel-Arab city

Plate (3)
a, b: kM (32.00)-Cairo-Bilbeis desert road
c, d: El-Goreizat-Sohag

FIG.1 Petrography of the studied samples at different sites of Egyptian collapsing soils

It can be concluded that these samples could be classified into three main types. The first type which existed in locations (I) & (IV) is quartz arenite. In location (I), this type is slightly silicious and ferruginous, while in location (IV), it is dolomitic and calcareous. The second type which existed in locations (II) and (III) is quartz litharenite. The third type which recorded in location (V) is calcareous sublitharenite.

From the geological point of view, these types are of transported soils as they have no relation with the underlying bed formations. The soil at location (I) is transported by fluvial action, while the soil at other four locations are near shore marine deposits.

GEOTECHNICAL PROPERTIES OF EGYPTIAN COLLAPSIBLE SOILS

The collapse potential (Cp) is calculated at 200kN/m^2 wetting (inundating) pressure, according to Jenning and Knight's formula (1975). Table (1) shows the results compared with those for other parts of the world, for the case of sand content more than 50%. From this table, it can be observed that despite their geographical and geological separation the collapsing soil deposits from Egypt and other parts of the world have some similarity in some physical properties such as plasticity and the natural unit weight. On the other hand, no similarity in other physical and mechanical properties of collapsing soils from Egypt and other parts of the world are shown. Those are: (1) Collapsing soils in Egypt have silt content lower than those of the world by about 25 percent (in average); (2) The natural moisture content of collapsing soils in the world is 3 to 3.5 times of that of Egyptian soils; (3) Collapsing soils in the world have sand content lower than that of Egyptian soils by about 20 percent; (4) The clay content of collapsing soils in the world is double as much as that of Egyptian soils; and (5) The average collapse potential (Cp) of collapsing soils in the world is about 6.5 percent, where Cp of Egyptian soils is about 8.5 percent (in average).

Table 1. Geotechnical and geological properties of Egyptian collapsing soils and some other countries (Soils containing more than 50% sand)

Property	**Continent**	**South America**	**Asia**		**Africa**	
	Country	Brazil	Thailand	Turkey	South Africa	Egypt
Gradation	Sand%	60-63	65-70	66-69	55	60-88
	Silt%	15-26	15-20	------	38	7-30
	Clay%	5-25	15	10-18	2	2-10
Physical properties	γ_b kN/m^3	16-18	15.7	19-20	14-15	16-20
	W %	5-10	6-9	5-6	6-9	1-3
	Wl	23-30	12	-----	-----	22-37
	Wp	12-16	12	-----	-----	13-25
	PI	9-14	-----	-----	-----	9-18
Mechanical properties, Cp		6-7	12.5	-----	-----	3-9.7
Geological features	Soil type	Clayey & silty sand	Silty clayey sand	Clayey sand	Silty sand	Silty clayey sand
	Method of Decomposition	Alluvial & colluvial	Aeolian Deposits	Alluvial Deposits	Aeolian Deposits	Old rivers & stream rivers
	Geological period	Tertiary sediments	-----	-----	Gamblian pluvial Era	Oligocene & pleistocene
Severity of problem	According to Jenning & Knight (1975)	Trouble	Severe trouble	-----	-----	Moderate to Trouble
References		Ferreira& Teixeria (1989)	Phien et al (1992)	Ordemir &Ozkan (1985)	Barrett& Wrench (1984)	***

*** El-Gindy (1991), El-Saadany (1986), El-Sohby et al (1985 & 1988) and Mansour(1992).

This non-similarity is attributed to three factors; (1) The existence of Egyptian collapsing soils in elevated areas and in arid and semi-arid climates, whereas most of collapsing soils in the world exist in alluvial plains and rainfalls areas in some countries, (2) Occurrence of most of Egyptian collapsing soils in desert areas which contain high amount of sand and less amount of silt and clay, and, (3) Collapsing soils in Egypt mostly occurred and precipitated in old geological ages, whereas most of the soils in other parts of the world occurred and formed in recent ages (Holocene and Pleistocene).

SHEAR STRENGTH CHARACTERISTICS OF EGYPTIAN COLLAPSING SOILS

Shear strength tests included direct shear box and triaxial tests. Data of collapse potential (Cp) from oedometer tests were also provided. Two cases of inundation were used. The first is inundation before shearing and the second is inundation at 50% of maximum shear at natural condition. The collapse potential was measured in the two cases at 200 kN/m^2 inundation pressure as per the standard codes (Egyptian Code, 2001 and ASTM, 2003). It was aimed from these tests to evaluate the shear strength of the Egyptian collapsing soils from different locations before and after inundation. The method of inundation and the effect of the used apparatus type were also considered.

From these test results it is concluded that, (1) The shear parameters C & Φ decreased greatly after inundation, about 82 and 29 percent respectively of the corresponding values at NMC, (2) Inundating the sample at 50 percent of maximum shear caused tremendous reduction in C & Φ, about 98 and 88 percent less than the corresponding values at NMC. With the progress in shear strain, peak shear resistance was reached where C & Φ were 85 and 35 percent less than the corresponding values at NMC, (3) The type of apparatus had insignificant effect on the reduction in shear strength in case of inundation before testing, and; (4) When the sample was inundated after being subjected to shear (50 percent of maximum shear), the collapse potential (Cp) increased by about 1.5 times of the corresponding value at inundation before applying shear, at an inundation pressure of 200 kN/m^2.

CASE STUDIES

This part is concerned with the study of sabkha soil along the northern coast of Egypt, in Al-Gharbaneyat area, 60 km west of Alexandria where several sinkholes have been developed. These sinkholes are of different shapes and sizes but mostly exhibit an elliptical shape with diameters vary between 10 and 20m and extend down to a depth ranging from 3 to 5m (Fig. 2). The Egyptian Railway Authority initiated a project to monitor risks and hazards due to the formation of large sinkholes in and around Al-Gharbaneyat railway station. The corrective measures to the problem are presented and discussed.

Subsurface investigation of soil in the area was carried out in accordance with the standard codes in order to obtain samples from boreholes and open pits for classification and laboratory testing.

From this subsurface investigation the soil can broadly be divided into three layers. The top layer (sabkha) consists mainly of brown, laminated, very fine quartz and carbonate sand of wind blown origin, with various quantities of small lenticular gypsum and elongated celestite crystals. Detrital corroded dolomite rhombs and fine-grained calcite are also present. The sediments beneath the sabkha can be divided into two lithologic layers, mostly without sharp boundaries. The lowest layer is composed of brown sandy silt with fragments of limestone and algal-bored bivalves with scattered glauconitic grains suggesting marine or lagoonal origin. This layer is overlain by a thick layer consisting of brown silty sand with coarse-grained gypsum nodules and overlain by a thin bed (few centimeters) of brown silty sand that contains nodules of very fine-grained crystals of gypsum. Both layers represent a supratidal sabkha facies.

The study of geotechnical properties of Al-Gharbaneyat soil has indicated that the sabkha soil can be classified as calcareous sandy silt type. The soil varies from stiff to hard soil depending on the natural water content. The collapse potential increases with decreasing water content until the soil reaches its dry state and becomes collapsible. Some large cavities were found during soil exploration reaching about 2.0m thickness at different levels from the ground surface. Groundwater was encountered at a depth ranging from 2.5m to 5.0m from the ground surface at the time of investigation.

Bearing in mind all the possible causes of the problem, it was necessary to gather all the available information and question the residents in the area and the persons who faced the problem when it started to take place. These observations were of great value as any data obtained from the subsurface investigations. Both field and laboratory investigations revealed that the subsidence was due to the rise of groundwater table. In other areas the subsidence was related to surface and domestic use of water that has led to substantial dissolution of gypsum nodules and the development of subsurface cavities and large sinkholes.

Following the Problem, a rehabilitation program was proposed right after this investigation to improve the soil by filling the voids or cavities by grouting (Fig. 3). This method proved to be efficient, as it was important to keep the railway line in a working condition without disturbance when dealing with the problem. In other site, it was necessary to use a deep compaction method to improve the soil as the situation of the site allows to do so.

FIG. 2. General view of concentric joints with successive vertical displacement around sinkholes indicating continuous subsidence adjacent to railway station

FIG.3. Filling the voids by grouting as soil improvement

Different case histories where severe structural damages were observed in a buildings that were constructed in the same area. The first case is a 2-story skeleton building (Fig. 4). The second case is for one storey bearing wall type building suffered from Significant and uneven settlements seriously damaged the structure (Fig. 5). It was evident that no point of remedy for both buildings and finally both were totally removed.

FIG. 4. Case of 2-storey skeleton building suffered from severe structural damage due to foundation on collapsing soil

FIG. 5. Case of 1-storey bearing wall type building suffered from severe structural damage due to the presence of collapsing soil and occurrence of sinkholes

CONCLUSIONS

The main geological and geotechnical properties of Egyptian collapsible soils are introduced, with a reference to the locations of potential occurrence. A comparison between Egyptian collapsible soils and those in other parts of the world is illustrated. A case study of the impact of sinkholes on the safety of structures and foundations at Al-Gharbaneyat area is presented. This article is devoted to throw light on the nature of collapsing soil in the region, in a trial to monitor risks and hazards due to the development of large sinkholes in the area. Geotechnical constrains that can be faced during construction on this type of soil were regarded as severe problems due to the presence of such sinkholes.

The sabkha soil in Al-Gharbaneyat area is characterized by the presence of many surface and subsurface zones of weakness represented by large solution cavities and major sinkholes. The rise of water table in the area, as a result of wet seasons and increased population, has led to substantial dissolution of subsurface gypsum nodules and the development of subterrainean cavities and large sinkholes. These underground cavities are variable in size, shape and stability, and each one requires individual assessment, if it is relevant to engineering works.

REFERENCES

Annual Book of ASTM Standards Designation: D 5333-03 (2003). *Standard test method for measurement of collapse potential of soils, Vol. 04.09*

Barrett, A. T. and Wrench, B. P. (1984). "Impact rolling trial on collapsing Aeolian sand". Proceedings of the 8th ARCSMFE, Harare, Vol. (1).

Egyptian Code for Soil Mechanics and Design and Construction of Foundations (2001), *Vol.5: Foundations on Problematic Soils*, No. 202/5.

El-Gindy, A. A. (1991). "Collapsibility of three Egyptian desert formations", CERM, Al-Azhar University, 13(7).

El-Saadany, M. M. (1986). "Some factors affecting engineering behavior of light weight dry soil". *M. Sc. Thesis*, Faculty of engineering, al-Azhar University.

El-Sohby, M. A. et al (1985). "Comparative study of Problematic Soils in two areas around Cairo". *Proceedings of the Symposium on environmental geotechnics & problematic soils and rocks*, Bangkok, Pp525-526.

El-Sohby, M. A. et al (1988). "Stress-strain characteristics of two calcareous arid soils". *Conference on calcareous sediments* , Perth, Pp17-24.

Erol, M. A. and El-Ruwaih, I. A. (1982). "Collapse behaviour of desert loess". *Proc. of 5th Congress Int. Assoc. of Engineering Geology*, New Delhi, Vol.(1).

Ferreira, S. R.M. and Teixeria, D. C. L. (1989). "Collapsible soil- A practical case in construction". Proceedings of 12th ICSMFE, Reo De Janiro, 1(7).

Geotechnical Encyclopedia of Egypt (GEE,2003). Published by the General Authority of Educational Building, Egypt, ISBN 977-6079-23-7.

Jenning, J. E. and Knight, K. (1975). "A guide to construction on or with materials exhibiting additional settlement due to collapse of grain structure", *Pro. of the 6th ARCSMFE*, Durban, South Africa.

Mahmoud, M. A. (1989). "Stabilization of Egyptian collapsible soils with hydrated lime". *Al-Azhar Engg. Conference-AEC'89*, Vol.(4).

Mansour, S. A. (1992). "Geotechnical characteristics of some Egyptian collapsing soils", *Ph. D. Thesis*, Zagazig University, 296P.

Mossaad, M. E. et al (2006). "A study on collapsing soils in Egypt." Internal *Research Report*, Academy for Scientific Research & Technology (ASRT), Egypt.

Ordemir, I. and Ozkan, Y. (1985). "Compression of alluvial deposits due to wetting", *Proc. of 11th ICSMFE*, San Fracisco, 4(8c).

Phien-Wej, N. et al (1992). "Collapse and strength characteristics of loess in Thailand", *Engineering Geology* (32).

Radwan, A. M. and Gabr, A. W. (1980). "Geotechnical Studies at new Ameriyah city". *Civil Engg. Research Magazine*, Al-azhar University, Egypt, Vol.(2), Pp1-21.

Sakr, M. A. M. et al (1999). "Geoenvironmental impact of sinkholes in sabkha soil along the Mediterranean coast of Egypt". *EGS Jl.*, V.10, Part 2, Pp. 41-49.

The treatment of collapsible loess soils using cement materials

Ian Jefferson[1], Dimcho Evstatiev[2] and Doncho Karastanev [3]

[1] Senior Lecturer in Geotechnical Engineering, Civil Engineering, University of Birmingham, UK; I.Jefferson@bham.ac.uk
[2] Professfor of Engineering Geology, Bulgarian Academy of Sciences, Sofia, Bulgaria; dimcho_e@geology.bas.bg
[3] Senior Engineering Geologist, Bulgarian Academy of Sciences, Sofia, Bulgaria; doncho@geology.bas.bg

ABSTRACT: Loess is a metastable collapsible soil, whose collapse can cause significant distress to the built environment across the world. This paper presents a case history illustrating how with proper pre-treatment assessment and careful selection, a cement based treatment approach was used successfully to improve a collapsible loess soil. This case history illustrates that even for structures when very tight specifications for post treatment performance exist, it is still possible to build safely on a problematical loess soil.

INTRODUCTION

Loess consists essentially of silt-sized primary quartz particles that form as a result of high-energy earth-surface processes. This has resulted in the almost continuous deposit from the North China plain to south-east England, for example, with other notable deposits found in North America, South America and New Zealand, equating to some 10% of the world's landmass. The formation processes has produced an open metastable structure, which can often collapse upon the application of load and/or water; a process known as collapse or hydro-collapse. As such loess soils present a significant challenge to engineers. A suite of improvement approaches are available to mitigate the collapse potential of these soils and these include pre-construction treatment or methods to treat loess post construction, (see Jefferson et al. 2005 for further details).

The treatment used depends on the requirements for an individual project and the characteristics of the loess ground – first of all the total collapsibility of the loess ground and the depth of the collapsible zone. One such loess treatment technique that has been successfully applied for many years is cement stabilization. This paper illustrates the effectiveness of cement treatment of collapsible loess by a case history. It shows how a very sensitive structure, which required a strict ground specification was safely built on a collapsible loess formation in Northern Bulgaria.

GROUND IMPROVEMENT AND ASSESSMENTS

Prior to any ground improvement, an effective site investigation must be first performed (Charles and Watts, 2002). This is especially true for notoriously difficult ground such as a collapsing loess soil. Jefferson et al. (2005) discussed the various stages involved when dealing with collapsible loess soils. It should, however be noted that collapsibility of a loess deposit can be very variable even across a small site. A preliminary assessment of the lateral and vertically collapse variability can be achieved by the use of validated geophysical techniques, calibrated to physical testing both in the laboratory and in the field (Northmore et al. 2008). Failure to do this can lead to severe consequences especially if the structure is sensitive to collapse. An example was the Atommash (an abbreviation of atom machinery) factory in Volgodonsk, in the Ukraine, which suffered a sudden wall failure in 1983 when ground water levels rose, causing the sub-grade loess soils to collapse (Jefferson et al., 2001)

Pretreatment assessment is essential when the improvement process is chemical. The gathering of insufficient data of the chemical composition of a soil has in the past caused problems, e.g. lime stabilization and adverse expansions in sulfate bearing soils (Hunter, 1988). Although, there is a considerable literature on the subject of chemical interactions and soils (e.g. Mitchell 1991), mistakes are still being made, e.g. post lime treatment heave along A10 road in England in 2004, (Parker, 2004). However, there are many examples of successful treatment of a number of sensitive structures, built on collapsible loess soils.

CEMENT TREATMENT OF LOESS

Cement based treatment of loess to mitigate collapse has been used around the world e.g. Li et al. (2007) in China and Bell et al. (1990) in New Zealand. Other researchers have looked at cement type treatments, e.g. the use of fly ash to treat loess in the USA (Zia and Fox, 2000); treatment of loess with waste cement kiln dust (Sreekrishnavilasam et al., 2007), and the use of fly ash and rice husk ash to improve loess in Thailand (Gasaluck and Nantasarn 2002). In addition, Evstatiev et al. (2002) demonstrated how carefully constructed soil cement cushions (mixed with 3 to 7% Portland cement by weight) have allowed a 50m tall administrative tower to be built on collapsible loess in Rousse, Northern Bulgaria. In Bulgaria alone some 100 building have been successfully built on collapsible loess soils using this technique (Jefferson et al., 2005).

Thus it is clear with careful assessments a variety of cement with additive or other cementations materials can be used to significant enhance the properties of loess soils to successfully mitigate its collapse potential. To illustrate this, a case history from Bulgaria will now be presented, where cement treated collapsible loess soil was successfully used as the foundation sub-grade material for a highly sensitive structure, namely a nuclear power plant at Kozlody, north Bulgaria, where any ground related failure/collapse would have posed an acute and very serious problem.

CASE STUDY: TREATMENT AT KOZLODUY NUCLEAR POWER PLANT

The Kozloduy Nuclear Power Plant (NPP) was built on the first non-flood loess terrace of the Danube River. The loess thickness under the first four NPP units (I, II, III and IV) was 10-12 m, overlaying Quaternary alluvial and Pliocene lacustrine deposits. The deposits of loess in this region are described in detail in Jefferson et al. (2005) and the reader is referred to this text for further details.

The main structures of the NPP were founded at a depth of 4.5 m below the surface For shallow foundation a loading of 0.3-0.4 MPa in the machine room and 0.5-0.6 MPa in the reactor building were expected. The loess at this depth was found to have a slight loaded collapsibility (classed as type I collapsibility). Jefferson et al. (2005) provide a detailed discussion on this type of classification of loess collapse, which is a method commonly used in Eastern Europe and central Asia.

Initially it was envisaged that removal of collapsible loess and its replacement with compacted ballast would be required. However, this proved very expensive and would have caused unpredictable ecological consequences. An alternative also considered was the removal re-compaction of loess to form a soil-cushion. However, this requires close control of water contents which can prove difficult especially with soils of relatively low plasticity indices such at loess. Other alternatives considered included silicate grouting, but costs prohibited most the alternatives assessed. Finally loess-cement cushions a technique that had been found to be effective in the treatment of collapsible loess in Bulgaria was used.

Loess-cement cushions have been shown from previous experience of treating collapsible loess soils, to combine the high bearing capacity of the ballast cushion and silicate grouted loess with the impermeability of the compacted soil-cushions, (Minkov and Evstatiev, 1970). Moreover, loess-cement cushions are relatively independent of climatic conditions.

All units at the NPP (units I – IV) were built on loess-cement cushions (LCC). In some locations this was supplement by heavy compaction to ensure integrity of the final treatment. For the power units the foundation soils consisted of loess with an average thickness of 12-14 m. The foundations to the main plant were on loess which had type II, unloaded collapsibility, which is defined in detailed in Jefferson et al. (2005).

The soil under the power units (V and VI) had to meet much higher specification in comparison to the other units I-IV. The average loading on the soil base in the reactor building of units V and VI ranged from 0.6 MPa to up to 1.2 MPa in the periphery of the foundation zone. Due to the large foundation area (66mx66m) stresses transferred to a considerable depth. However, it was essential that the settlements were limited and uniform, with little tolerance for differential settlement, due to the nature of the specific high sensitivity of the final building. The final soil based and treated zone is shown in Fig. 1.

The construction of the foundations consisted of an excavation 4-7m below the foundation base, with complete removal of the loess soils under the reactor building, the machine building and other equipment, where the settlement specification was particularly strict. For the foundation of the reactor buildings of units V and VI, the loess was excavated to benchmark 20-22m (benchmark 0 is at 35m). Then, a compacted gravel cushion (bedding) was made up to benchmark 26m. A soil-cement cushion was built on the top of the gravel to benchmark 28m (see Table 1). In this way the collapsible loess was entirely replaced by improved soil. Alluvial gravel and sand, overlain on Pliocene deposits (Broussartsi Formation with predominating dense clays), were situated under the artificial soil layer. The final foundation plate was placed on a soil-cement cushion (Fig. 1).

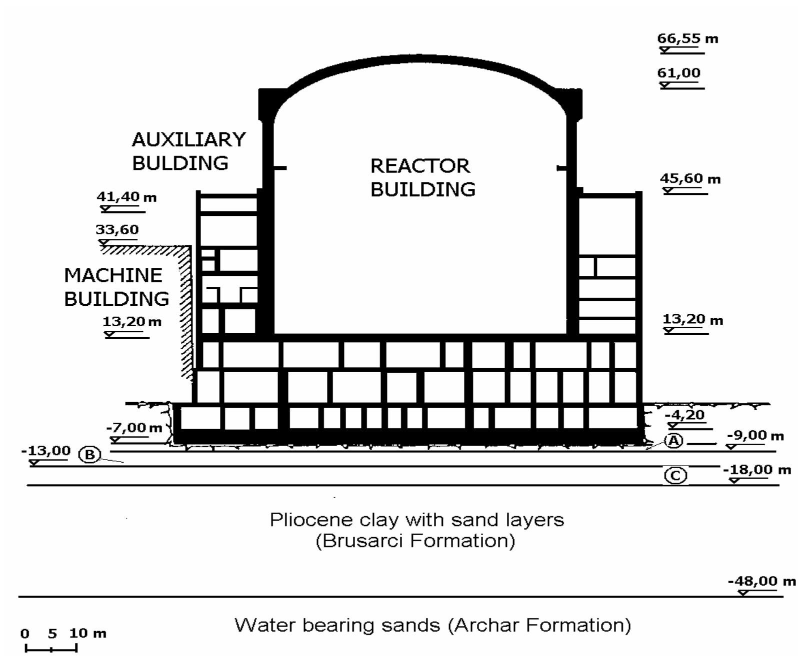

FIG. 1. Cross section of the Unit V reactor building and soil base: A- soil-cement cushion; B-gravel cushion; C-alluvial sand, gravel and clay

For the other structures where lower ground stresses occurred, the collapsible loess was excavated from foundation benchmark 30.1 m to 26.5 m. A LCC was built from this benchmark to the foundation base. For the deeply founded retaining walls of the pump house – intake structures only a smaller gravel cushion (GC) was used due to the small additional loading that occurred.

The main concern for the reactor building was settlement due to its high foundation stresses. Thus, the deformation zone included the alluvial gravel and sands with modulus of total deformation (determined from standard plate bearing tests), E_o = 30-40 MPa and also the Pliocene clays with $E_{o,\ average}$= 50-70 MPa (Bojinov and Markov, 1985). Due to the thickness of the two cushions used, the effect on settlements was small and any subsidence depended mainly on the deformation parameters of the Pliocene clays and the alluvial materials.

TABLE 1. Soil base improvement methods for the equipment of Units V and VI

Equipment	Foundation depth, m	Treatment measures		Soil type under the cushion
		LCC thickness, m	GC thickness, m	
Machine building	6.10	1.60	4.80	Alluvial sand Pliocene clay
Auxiliary building	7.00	4.0	-	Clayey loess
Reactor building	7.00	2.0	4.00	Alluvial sand
Diesel generator building	5.00	3.5	-	Clayey loess Alluvial sand & gravel
Spray ponds	4.35	0.70	-	Compacted loess
Retaining walls of the pump station	7.00 to 11.50	-	1.10	Clayey loess Alluvial sand & gravel

Main Characteristics of the Loess-cement Cushion (LCC)

The soil-cement cushion represents a strengthened layer of the soil base, situated immediately under the foundation. It is constructed with the aim of increasing the bearing capacity of the foundation as well as of preventing ground water pollution. The cushion is performed under the whole area of each NPP building and its thickness varied from 1.5 to 5 m. Loess from the excavations was used for the construction of the cushion. It was mixed with Portland cement (by weight) in the amount of 3 % for the lowest one third, 4 % for the middle one third and 6 % - for the top one third. The soil-cement cushions were found to operate elastically for relatively high stresses. In addition the filtration coefficient of the LCC k_f is less than 10^{-9} m/s. The single layers of the cushion exhibited mechanical parameters for various cement quantities as shown in Table 2.

TABLE 2. Design parameters of the loess-cement cushion

Cement %	**Unconfined compressive strength σ_c** MPa	**Apparent Cohesion c** MPa	**Angle of internal friction φ** deg	**E_o** MPa
2	0.5	0.17	26	65
3-4	0.7	0.22	27	85
5-6	1.3	0.32	28	110

Construction Details for LCC

Construction of the LCC consisted of excavation to the required level, spreading cement, mixing cement into loess adding water to achieved the desired density as required, followed by compaction until the dry density was between 1.74 - 1.77 Mg/m^3. After this, the process was repeated to build up subsequent layers. The layer thickness of in the compacted state was 130 mm and so required 15-16 layers for a 2m cushion thickness. The construction of the cushion in thin layers guarantees the high-quality homogenization of cement and high compaction of the mixture.

Quality assurance undertaken at the site included: control on the quantity of the cement; control on the mixture quality; control on the optimal water content the dry density according; assessment of the deformation modulus of the cushion, and assessment foundation settlement by means of precise geodetic measurements. This ensured full control throughout the construction sequence.

Radionuclide Migration Insulation Properties

Another important criterion to be fulfilled by the LCC was as a protective engineering barrier against radionuclide migration to the underlying groundwater. This was achieved due to the LCC high density and low hydraulic conductivity coupled with the cushion's ability to retard radionuclide propagation. Observation boreholes have confirmed that in 35 years no recorded trace of radioactive pollution of underlying groundwater has occurred. This demonstrates the effectiveness of LCC as a barrier medium.

The Behavior of LCC Under Seismic Conditions

An additional concern was raised after the Vrancea earthquake in 1977. Minkov and Evstatiev (1979) showed that the most badly affected buildings in North Bulgaria had been built on natural loess, other weak soils and landslides material, where no supporting and strengthening had been carried out. By comparison all buildings erected on improved loess suffered considerably less damage. The seismic intensity was considered to be VII degree according to the MSK scale for the buildings in the region around the NPP.

The LCC demonstrates considerable benefit in seismic risk mitigation avoiding the liquefaction of the loess situated immediately under the cushion and the risk of plastic deformations in the base. In addition the cushion receives and redistributes to the soil base the increased stresses in the foundations caused by the swinging of rigid structures, thus contributing to the reduced hazard of arising of shear forces in them.

Potential Uncertainties with a LCC

To overcome initial uncertainty associated with the use of LCC, large-scale testing was carried out during the design and construction stages to prove its bearing capacity (Minkov and Evstatiev, 1975), while a conservative approach has been applied to its thickness determination (Minkov et al. 1981). In addition durability issues have also been assessed. Samples have also been tested after continuous storing, including samples from real structures. It has been established that the structural changes in loess-cement in the course of time lead to the increase of its strength. In addition there are more than 100 buildings in Bulgaria built on LCC. Some of these structures have been in operation for more than 35 years and no unfavorable strength changes in the cushions have been established.

CONCLUSIONS

The operation of the Kozloduy NPP for more than 35 years proves the effectiveness of the foundations in loess using loess-cement cushion. The soil base treatment not only eliminates the hazard of loess collapse but also reduces the settlement, tending to make it uniform. The LCC has further performed well even during extreme seismic events and has maintained its high performance since, including acting as an effective barrier to radionuclide migration to underlying groundwater.

Thus LCC not only offers mechanical benefits for building founded on collapsible loess soils but has added controls were aggressive environments may be encountered. Therefore a LCC built up in layers of controlled cement mixing (between 4 % to 7% cement typically) with strict compaction can provide an excellent pre-construction treatment when building on collapsible loess conditions.

REFERENCES

Bell, D.H., Glassey, P.J., and Yetton, M.D. (1990). "Chemical stabilization of dispersive loessial soils, Banks Peninsula, Canterbury, New Zealand." *Proc. 5th Intl. Assoc. of Engrg Geology Congress*. Vol. 4, Balkema, Rotterdam: 2193-2208.

Bozhinov, B., and Markov, G. (1985). Investigations on Soil Base and of Pliocene Clay

Properties under the Reactor Buildings of Blocks V and VI. *Archive of Exploration* Department of Energoproekt. (*in Bulgarian*).

Charles, J.A., and Watts, K.S. (2002). Treated ground engineering properties and performance, *CIRIA Report C572*, CIRIA, London, 168p.

Gasaluck, W., and Nantasarn, R. (2002). "The stabilization of Khon Kaen Loess by means of fly ash and rice husk ash." *Proc. 4th Intl. Conf. Ground Improvement Techniques*, Vol. 1., Kuala Lumpur: 357-362

Evstatiev, D., and Minkov. M. (1970). A Method for Performing the Foundations of Buildings and Equipment. *Authors' License No 16 276*. (*in Bulgarian*).

Evstatiev, D., Karastanev, D., Angelova, R., and Jefferson. I.F. (2002). "Improvement of collapsible loess soils from eastern Europe: lessons from Bulgaria." *Proc. 4th Intl.. Conf. Ground Improvement Techniques*, Vol. 1., Kuala Lumpur: 331-338

Hunter, D. (1988). "Lime-induced heave in sulfate-bearing clay soils." *J. Geotechnical Engrg*. 114 (2): 150-167.

Jefferson, I.F., Rouaiguia, A., and Smalley, I.J. (2001). "Improvement of Collapsible ground for Construction." *Proc. 7th Intl. Conf. Inspection, Appraisal, Repairs & Maintenance of Buildings & Structures*, Nottingham: 339-346.

Jefferson, I., Evstatiev, D., Karastanev, D., and Rogers, C.D.F. (2005). "Treatment of metastable loess soils: lessons from Eastern Europe." *Ground Improvement case histories*. Oxford, Elsevier:727-766.

Li, J.J., Qui, S.Z., and Wang, T.H. (2007). "Research on the properties of the cement-loess." *Industrial Construction*. 7: 25-28 *(in Chinese).*

Minkov, M., Evstatiev, D., Karachorov, P. Slavov, P., Stefanov, G., and Jelev. J. (1981). "Stresses and Deformations in Stabilised Loess." *Proc. 10th Intl Conf. on Soil Mechanics and Foundation Engrg.,* Vol. 2, Stockholm: 193-197

Minkov, M., and Evstatiev. D. (1975). "Foundations, Linings and Screens of Improved Loess Soils." *Tehnika,* Sofia, 189 p. *(in Bulgarian).*

Minkov, M., and Evstatiev, D. (1979). "On the seismic behavior of loess soil foundations." *Proc. 2nd US National Conf. on Earthquake Engrg,* Stanford University: 988-996.

Mitchell, J.K. (1991). "Conduction phenomena: from theory to geotechnical practice." *Geotechnique.* 41 (3): 297-340.

Northmore, K.J., Jefferson, I, Jackson, P.D., Entwisle, D.C., et al. (2008). "On-Site Characterisation of Loessic Brickearth Deposits at Ospringe, Kent, UK." *Geotechnical Engineering, Proc. on the ICE. (in press)*

Parker, D. (2004). "Undetected sulphates blamed for A10 heave." *New Civil Engineer.* 11 November 2004: 8

Sreekrishnavilasam, A., Rahardja, S., Kmetz, R., and Santagata, M. (2007). "Soil treatment using fresh and landfilled cement kiln dust." *Construction and Building Materials.* 21: 318-327.

Zia, N., and Fox, P.J. (2000). "Engineering properties of loess-fly ash mixtures for roadbase construction," *Trans. Research Record.* 1714: 49-56.

Investigating Erosional Behaviour of Chemically Stabilised Erodible Soils

Buddhima Indraratna[1], FASCE, Thevaragavan Muttuvel[2], and Hadi Khabbaz[3]

[1]Professor of Civil Engineering, Faculty of Engineering, University of Wollongong, NSW 2522, Australia. Indra@uow.edu.au
[2]PhD Candidate, Faculty of Engineering, University of Wollongong, NSW 2522, Australia. tm996@uow.edu.au
[3]Lecturer in Civil Engineering, Faculty of Engineering, University of Wollongong, NSW 2522, Australia. khabbaz@uow.edu.au

ABSTRACT: Chemical stabilisation is a popular technique to improve the erosion resistance of soils. In this study, two chemical stabilisers, namely lignosulfonate and general purpose Portland cement were tested on two different soils, a silty sand and dispersive clay. A series of erosion tests were performed to study the effectiveness of the stabilisation on increasing the erosion resistance. Results showed that an increase in the critical shear stress of the silty sand with only 0.6% lignosulfonate treatment was equivalent to that with around 2.5% cement treatment. However, the stabilisation of the dispersive clay with 0.6% cement was more effective than 0.6% lignosulfonate. The findings of this research also indicated that the coefficient of soil erosion decreased as a power function of the critical shear stress.

INTRODUCTION

Erosion through internal cracks leading to piping and surface erosion are the most common erosion modes, which cause failures of earthdams and embankments. Hence, it is very important to improve the erosion resistance of soils using appropriate and cost effective techniques. Use of chemical admixtures is one way of increasing the erosion resistance of soil in earth structures. In the past, various stabilisers such as lime, cement, fly ash and milled slag were used as stabilising agents. The erosion of dispersive soils was controlled by adding lime and gypsum especially at the foundation-embankment interface and on the slope of the embankment (Biggs and Mahony 2004; Cole *et al.*1977; Phillips 1977). Lime, milled slag, and fly ash can be used to reduce the erodibility of dispersive and colluvial soils (Indraratna 1996; Indraratna *et al.* 1991). However, limitations such as corrosion of steel structures adjacent to gypsum treated soils, and adverse effects on vegetation in the vicinity of lime treated soils due to high pH levels (Biggs and Mahony 2004; Perry 1977) have encouraged researchers to find alternative stabilisers.

Several studies were conducted in the past to understand the erosion mechanism and its dependability on different factors such as soil properties, and the properties of pore and eroding fluids. Wan and Fell (2004) performed erosion tests by applying a hydraulic gradient across a 6-mm soil hole to investigate the erosion characteristics of unsaturated soil in cracks of embankment dams. They concluded that the erosion rate is directly influenced by the degree of compaction and placement water content. Sherard *et al.* (1976) developed the standard pinhole test to study the erosion characteristics of soil by pushing eroding fluid through a 1-mm crack.

In this study, a process simulation apparatus for internal crack erosion was designed and built at the University of Wollongong to evaluate the effectiveness of chemical treatment on the erosional behaviour of different soils (a silty sand and a dispersive clay) treated with two chemical stabilisers, lignosulfonate and general purpose Portland cement. The details of the experimental investigation are discussed in the following section.

EXPERIMENTAL INVESTIGATION

Properties of Soil and Chemical Stabilisers

A silty sand collected from the area near Wombayen caves in New South Wales (NSW), Australia, and a dispersive clay collected from Wakool in NSW, Australia were selected for this study. According to the standard pinhole test (ASTM D4647), the silty sand and the dispersive clay are classified as D1 and D2, respectively. General purpose Portland cement manufactured in Australia, and lignosulfonate were selected for the experimental investigation. The lignosulfonate mixture is a completely soluble, dark brown liquid having a pH value of approximately 4. This stabiliser is inflammable, does not corrode metals, and is not classified as hazardous according to the National Occupational Health and Safety Commission (NOHSC) criteria (CHEMSTAB 2003).

Sample Preparation

Four dosages of lignosulfonate, 0.1%, 0.2%, 0.4%, and 0.6% by dry weight of soil were selected to treat both soils. However, 0.5%, 1.0%, 1.5%, 2.0%, and 3.0% of cement were chosen to stabilise the silty sand, while 0.2%, 0.4%, and 0.6% dosages were selected to treat the dispersive clay. Each soil was mixed with the selected chemical additives and then it was compacted inside a 72mm diameter by 100mm long copper mould. After a seven-day curing, the samples were immersed in the eroding fluid (tap water) until they absorbed the maximum amount of water to become saturated. Erosion tests were carried out using newly built Process Simulation Apparatus for Internal Crack Erosion (*PSAICE*). A schematic diagram of the experimental set up is shown in Fig. 1. All tests were conducted by pushing the eroding fluid through a 10-mm soil crack formed at the centre of the samples. The eroding fluid was pumped into the moving constant head tank during testing. Two pressure transducers were connected to both ends of the sample to measure any difference in pressure across the crack. To continuously measure the erosion rate, an in-line process turbidity meter was connected next to the downstream side of the soil sample to constantly monitor the effluent turbidity during the erosion test. The turbidity values were then used with the relationship developed by the authors between the concentration of solids (kg/m^3) and turbidity (NTU) of the selected soil to calculate the erosion rate. In order to continuously measure the flow rate, the effluent was weighed with an electronic balance. As shown in Fig. 1, all pressure transducers, the turbidity meter, and the electronic balance were connected to a data acquisition system.

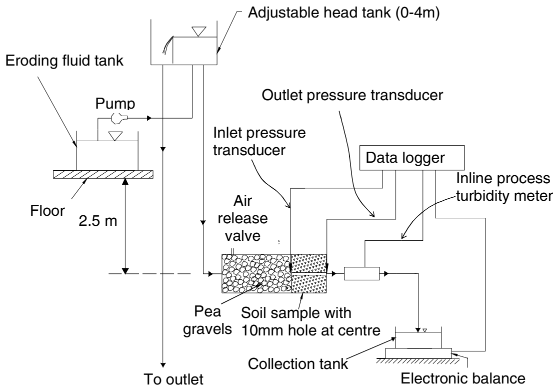

Fig. 1. Schematic diagram of process simulation apparatus for internal crack erosion

Interpretation of Observations

The observed flow rate and turbidity, and the relationship between concentration and turbidity for 0.4% lignosulfonate treated dispersive clay are given Fig. 2 (a) and (b), respectively.

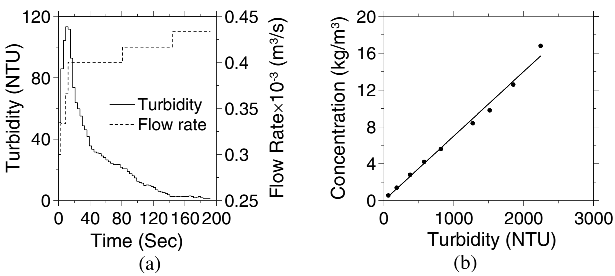

Fig. 2. (a) Observed turbidity and flow rate, and (b) relationship between concentration and turbidity for 0.4% lignosulfonate treated dispersive clay

Based on the observations, the amount of soil eroded in a selected time interval δt is determined by:

$$\delta m = kQT \times \delta t \quad (1)$$

where, δm (kg) is the amount of dry soil eroded during a selected time interval δt, Q (m^3/s) is the average flow rate through the soil crack at time interval δt; T (NTU) is the average turbidity of the effluent at δt; and k (kg/m^3/NTU) is the empirical factor relating turbidity to the soil solids concentrated in the flow. The value of k for untreated and cement treated silty sand, determined based on the linear relationship, was 0.013

kg/m^3/NTU. A slightly smaller value of k (0.011 kg/m^3/NTU) was obtained for lignosulfonate treated silty sand. However, a range of k values (0.002-0.011) was obtained for treated and untreated dispersive clay. When the diameter of the soil crack changes by $\delta\phi_t$ in a time interval δt, the amount of soil eroded during this time will be:

$$\delta m = \frac{\pi \phi_t l \rho_d}{2} \times \delta\phi_t \tag{2}$$

where, ρ_d (kg/m^3) is the dry density of compacted soil; l (m) is the length of the soil crack; and ϕ_t (m) is the diameter of the soil crack at time t.

Combining Equations (1) and (2) yields:

$$\delta\phi_t = \frac{2kQT}{\pi \phi_t l \rho_d} \times \delta t \tag{3}$$

Equation (3) can be used to calculate the change in diameter of the soil crack during erosion for each time interval using the flow rate, turbidity of effluent, and initial diameter of the soil crack. The erosion rate, $\dot{\varepsilon}$ (kg/s/m^2), can then be calculated using Equation (4):

$$\dot{\varepsilon} = \frac{kQT}{\pi \phi_t l} \tag{4}$$

The hydraulic shear stress, τ (Pa), on the soil crack surface can be calculated from:

$$\tau = \frac{\rho_w g\, i\, \phi_t}{4} \tag{5}$$

where, ρ_w (kg/m^3) is the density of the eroding fluid; g (m/s^2) is the gravitational acceleration; and i is the hydraulic gradient across the soil crack.

RESULTS AND DISCUSSION

The predicted erosion rate against the hydraulic shear stress for 0.4% lignosulfonate treated dispersive clay compacted at 95% of the maximum dry density is plotted as shown in Fig. 3, where the erosion rate increases almost linearly with the hydraulic shear stress. Similar behaviour has also been reported by other researchers (Arulananthan *et al.* 1975; Sargunan 1977). In this study, the critical shear stress, τ_c, is defined as the minimum hydraulic shear stress necessary to initiate erosion. It will therefore be determined by extrapolating a straight line to the zero erosion rate. The slope of this straight line is presumed to be the coefficient of soil

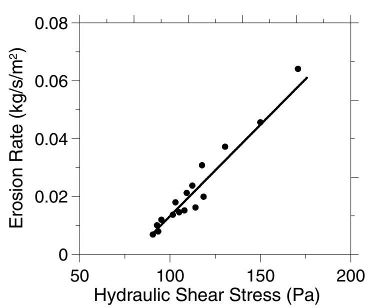

Fig. 3. Erosion rate versus hydraulic shear stress for 0.4% lignosulfonate treated dispersive clay

erosion. Hence, the predicted critical shear stress and the coefficient of soil erosion for 0.4% lignosulfonate treated dispersive clay are 79.1 Pa and 0.00063, respectively. It was observed that the variation of erosion rate with the hydraulic shear stress is linear for all other treated and untreated soil samples compacted at 95% and 90% of the maximum dry density.

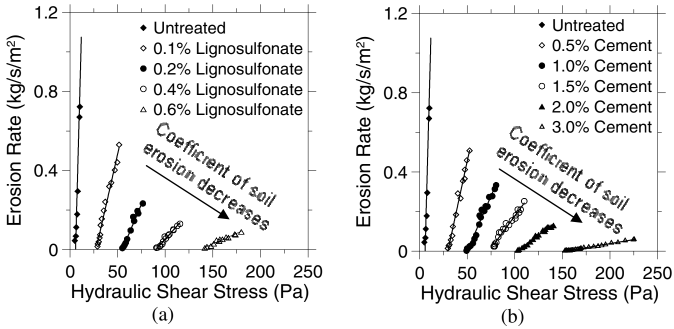

Fig. 4. Erosion rate versus hydraulic shear stress for (a) lignosulfonate treated and untreated (b) cement treated and untreated silty sand

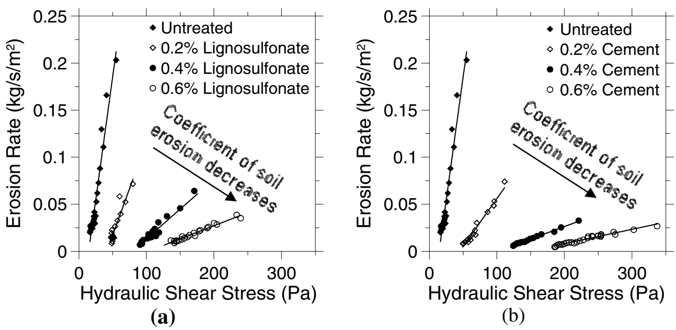

Fig. 5. Erosion rate versus hydraulic shear stress for (a) lignosulfonate treated and untreated (b) cement treated and untreated dispersive clay

Fig. 4 indicates the variation of the erosion rate with the hydraulic shear stress for the silty sand treated with two chemical stabilisers (compacted at 95% relative density). With increased levels of chemical additives, the coefficient of soil erosion decreases, as expected. It is noted that the critical shear stress also increases with the amount of chemical additives. Since untreated silty sand is non-cohesive and all treated and untreated soils were compacted at the same dry density and kept under the same curing conditions, it could be argued that the only possible cause for an increase in the erosion resistance of treated silty sand compared to untreated was the enhancement of cohesion attributed to cementation. For the silty sand, significantly less amount of lignosulfonate compare to cement is required to achieve a given increase in the critical shear stress.

The behaviour of lignosulfonate and cement treated dispersive clay is shown in Fig. 5. It illustrates that 0.6% cement treatment increases the critical shear stress of the dispersive clay more than 0.6% lignosulfonate treatment. This behaviour differs from that was observed for the silty sand. If cement behaved as a binder (as in the case of silty sand), the increase in the critical shear stress with 0.6% of cement treatment would not be greater than that with 0.6% lignosulfonate treatment. It appears that the stabilisation mechanisms of lignosulfonate and cement on the dispersive clay are different. Cement can alter the mineralogy of the clay with its ion exchange capacity to form a stable clay structure, which is sufficiently resistant to erosion. Hence, it can be concluded that altering the clay mineralogy of dispersive clay with cement is more effective than binding the clay particles with lignosulfonate.

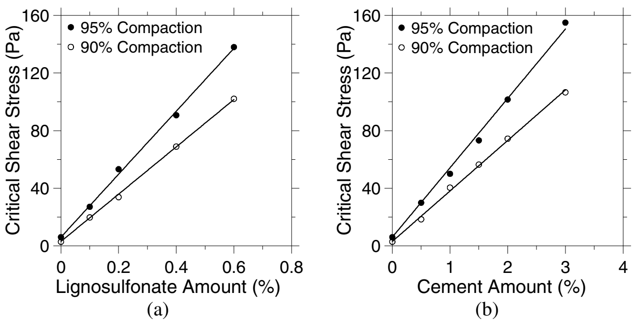

Fig. 6. Variation of critical shear stress with the amount of (a) Lignosulfonate and (b) Cement for silty sand

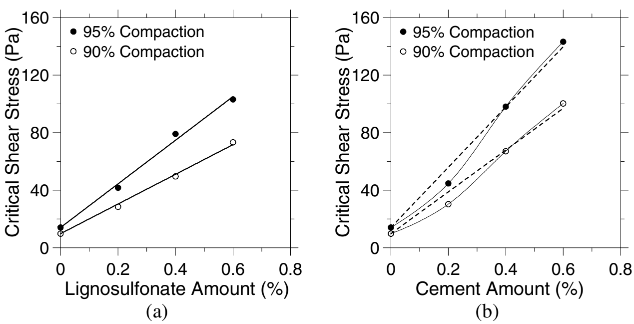

Fig. 7. Variation of critical shear stress with the amount of (a) Lignosulfonate and (b) Cement for dispersive clay

As shown in Fig. 6, the critical shear stress changes linearly with the stabiliser dosage of both cement and lignosulfonate for the silty sand. A similar trend was observed for lignosulfonate treated dispersive clay (Fig. 7(a)). However, the increase in the critical shear stress is not quite linear for cement treated dispersive clay (Fig. 7(b)). Figures 6 and 7 also indicate that the critical shear stress of all soils compacted to 95%

is more than those compacted to 90%. In addition, the difference between the critical shear stress of soil compacted to 95% and 90% shows a continuously increasing trend as the amount of cement and lignosulfonate increase. To determine a simple expression for estimating the erosion rate of stabilised soils, an attempt was made to develop an empirical relationship between the critical shear stress and the coefficient of soil erosion. It was found that all data points for treated silty sand fall on a best fit line following a power function as shown in Fig. 8(a). A similar trend was observed for the treated dispersive clay as illustrated in Fig. 8(b).

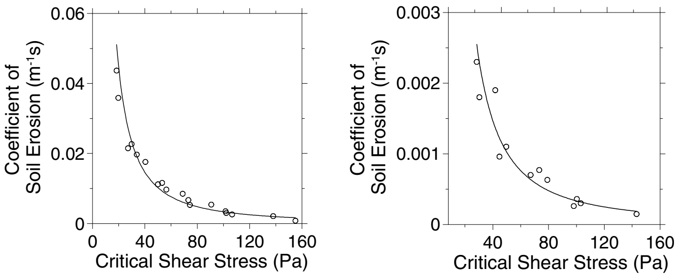

Fig. 8. Variation of coefficient of soil erosion with critical shear stress for treated (a) silty sand and (b) dispersive clay

Thus corresponding empirical expression for the erosion rate of chemically treated soils can be determined by:

$$\dot{\varepsilon} = \frac{a}{\tau_c^b}\left[\tau - \tau_c\right] \tag{6}$$

where, *a* and *b* are constant parameters. Values of *a* and *b* are 5.6 and 1.61, respectively, for treated silty sand, while they are 0.6 and 1.62 for treated dispersive clay.

Based on the results given in Fig. 6 and Fig. 7, the critical shear stress of treated soil can be calculated using:

$$\tau_c = \tau_{co} + m(CP) \tag{7}$$

where, τ_{co} (Pa) is the critical shear stress of untreated soil; and *m* is the proportionality coefficients as tabulated in Table 1. Values of *m* for cement treated dispersive clay were calculated using estimated straight lines (doted lines in Fig. 7(b)).

Table 1. Values of *m* and critical shear stress of untreated soil

Stabiliser type	Degree of compaction (%)	Silty sand		Dispersive clay	
		(m)	(τ_{co})	(m)	(τ_{co})
Lignosulfonate	95	217.8	6.0	151.6	14.1
	90	166.0	2.8	103.1	9.8
Cement	95	48.2	6.0	209.2	14.1
	90	35.2	2.8	145.2	9.8

CONCLUSIONS

This paper recaps an experimental method for evaluating the critical shear stress and the coefficient of soil erosion of chemically stabilised, two erodible soils from New South Wales, Australia. It was found that these stabilisers reduced the coefficient of soil erosion and significantly increased the critical shear stress. The increase in the critical shear stress of the silty sand with only 0.6% lignosulfonate treatment was equivalent to that with around 2.5% cement treatment. However, the stabilisation of dispersive clay was more effective with 0.6% cement than 0.6% of lignosulfonate. The critical shear stress increased with an increase in degree of compaction from 90% to 95% of the maximum dry density. It was also found that the difference between the critical shear stress of 95% and 90% compacted soil increased continuously with an increase in the amount of cement and lignosulfonate. The results of this study indicated that the coefficient of soil erosion had a strong relationship with the critical shear stress following a decaying power function.

REFERENCES

ASTM standards, (2004). “Identification and classification of dispersive clay soils by the pinhole test.” *Section 4, Construction*, Vol. 04.08: 826-833.

Arulananthan, K., Loganathan, P., and Krone, R.B. (1975). “Pore and eroding fluid influences on surface erosion of soil.” *Journal of the Geotechnical Engineering Division*, ASCE, Vol.101 (GT1): 51-66.

Biggs, A.J.W. and Mahony, K.M. (2004). “Is soil science relevant to road infrastructure?” *13th International Soil Conservation Organization Conference (ISCO)* – Brisbane, Paper No 410.

Chemstab, (2003). “*Technical Manual*”, CHEMSTAB Consulting Pty Ltd, Horsley, NSW Australia.

Cole, B.A., Ratanasen, C., Maiklad, P., Liggins, T.B. and Chirapunthu, S. (1977). “Dispersive clay in irrigation dams in Thailand.” *ASTM Special Technical Publication*, 623: 25-41.

Indraratna, B. (1996). “Utilisation of lime, slag and fly ash for improvement of a colluvial soil in New South Wales, Australia.” *Journal of Geotechnical & Geological Engineering*, Vol. 14: 169-191.

Indraratna, B., Nutalaya, P. and Kugamenthira, N. (1991). “Stabilisation of a dispersive soil by blending with fly ash.” *Quarterly Journal of Engineering Geology*, Vol. 24: 275-290.

Perry, J.P. (1977). “Lime treatment of dams constructed with dispersive clay soils.” *Transactions of the ASA*E, Paper No: 76-2093: 1093-1099.

Phillips, J.T. (1977). “Case histories of repairs and designs for dams built with dispersive clay.” *ASTM Special Technical Publication*, 623: 330-340.

Sargunan, A. (1977). “Concept of critical shear stress in relation to characterization of dispersive clays.” *ASTM Special Technical Publication*, 623: 390-397.

Sherard J.L., Dunnigan L.P., Decker R.S., Steele E.F. (1976). “Pinhole test for identifying dispersive soils.” *Geotechnical special publication,* ASCE, No: 32: 280-296.

Wan, C.F. and Fell, R. (2004). “Investigation of erosion rate of soils in embankment dams.” *Journal of Geotechnical and Geo-environmental Engineering*, ASCE, Vol. 130 (4): 373-380.

An Approach to Estimate the Optimum Depth of Floating Type Columns for Embankment Stability

Shui-Long Shen[1], Jie Han[2], M.ASCE, and Zhen-Shun Hong[3]

[1]Professor, Department of Civil Engineering, School of Naval Architecture, Ocean, and Civil Engineering, Shanghai Jiao Tong University, Shanghai 200030, China, slshen@sjtu.edu.cn
[2]Associate Professor, The University of Kansas, Civil, Environmental, & Architectural Engineering Department, Lawrence, Kansas 66045-7609, jiehan@ku.edu
[3]Professor, Institute of Geotechnical Engineering, Transportation College, Southeast University, Nanjing 210096, P. R. China, zshong@seu.edu.cn

ABSTRACT: Deep mixed (DM) columns are usually used to ensure the stability of embankments on soft deposit. However, for a thicker soft deposit, especially when the soil strength linearly increases with depth, since the lower part of the deposit is strong enough, the use of floating type (FT) DM columns is more economical. In the design of the FT columns, the length and rows of FT columns are often obtained through trial calculations using a slice-type stability analysis method, which is time consuming. Generally, this trial calculation approach needs much iteration. This paper presents an effective method using the tangential limit equilibrium analysis to estimate the depth of floating columns.

INTRODUCTION

DM columns are widely used to improve soft clay foundations of road embankments, river dikes, and other geotechnical structures. In the design of embankments over improved foundations, limit equilibrium stability analysis is often used to calculate the safety factor under undrained conditions. So far, the stability analysis assumes that the deformation or strain in the composite ground is unique. It is thought that the columns and the original soft soil reach the critical state at the same time (Takeo Office, 1996). To ensure stability, it is preferred that end bearing (EB) columns are used. However, full-scale field tests indicated that the use of the floating (FT) columns with a length equal to two thirds that of the EB columns not only guaranteed the stability but also controlled the deformation of the embankment (Sakai et al., 1991, Takeo Office, 1996). In the design of the FT columns, the length and rows of FT columns are often obtained through trial calculations using the slice-type stability analysis method. Generally, this trial calculation needs many iterations. Engineers' personal experience and judgment are needed for the final decision. Also, this process is time consuming. This paper presents an approach to determine the length of the FT columns using the tangential limit equilibrium method (Low, 1989).

VARIATION IN THE MINIMUM SAFETY FACTOR FOR A POTENTIAL SLIP CIRCLE TANGENTIAL TO A GIVEN DEPTH

Embankments constructed on soft clay foundations may have a potential failure in the form of an approximately circular slip surface extending into the soft foundation. The safety factor corresponding to a given potential slip surface (A) with depth D, as shown in Fig. 1, can be computed based on the geometry and force/moment equilibrium. One can draw an infinite number of slip circles (A, B, C...), which are all tangential to a given trial limiting horizontal tangent at depth D (Fig. 1). Among all these possible slip circles passing through the soft foundation tangential to the horizontal line at a given depth D, there is a circle with the minimum safety factor ($FS_{min(D)}$), which is called the $FS_{min(D)}$ slip circle herein. By varying the depth D of the trial limiting tangent (TLT), there exists another $FS_{min(D)}$ slip circle with $FS_{min(D)}$. The actual failure, if occurs, will follow a path along which the safety factor is the minimum among all of the TLT depths. This path is represented by the critical slip circle (CSC). Low (1989) provided a procedure and equations to calculate the minimum safety factor $FS_{min(D)}$ corresponding to a trial limiting tangent (TLT).

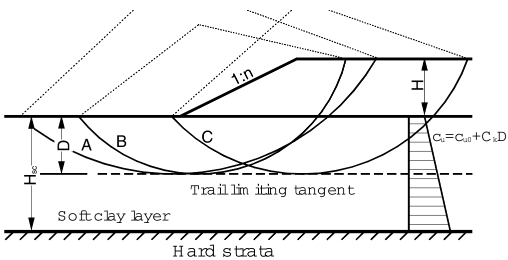

FIG. 1. Trial limiting tangent (TLT) and potential slip circle (based on Low, 1989)

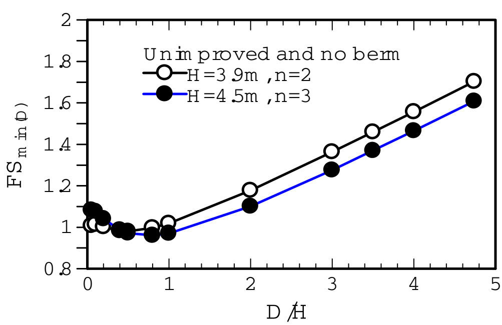

FIG. 2. Variation of the minimum safety factor for a given sliding depth

When the shear strength of soft soil linearly increases with depth, the value of $FS_{min(D)}$ will increase with depth of TLT after deeper than a certain depth. Figure 2 gives the $FS_{min(D)}$ and D/H (H is the height of the embankment) relation calculated using Low's equation (Low, 1989), in which the strength of soft clay is a typical Ariake clay value determined by the relation c_u=7+12D (kPa) (Miura et al., 1998). The parameters of the embankment material are γ=18kN/m^3, C=10kN/m^2, ϕ=25°. As shown in the figure, $FS_{min(D)}$ increases with the increase of D/H after D/H > 0.5 to 0.9. If the desired minimum safety factor is 1.3, there is no need for ground improvement in terms of stability when D/H is greater than a certain value corresponding to this $FS_{min(D)}$. In other words, floating type (FT) DM columns can be used to improve the soft ground. Moreover, all the embankment crests have a limited width B_c. Thus, the use of FT columns is feasible.

UPPER LIMIT DEPTH OF FT COLUMNS FOR A GIVEN EMBANKMENT WITH CREST WIDTH B_C

For the natural Ariake clay, because of its high sensitivity, high compressibility, and low shear strength (Miura et al., 1998; Hanzawa et al., 1990), constructing only a 2~3m high embankment could result in a slip failure. To ensure the stability of the embankment on the soft Ariake clay during a staged construction and lower the maintenance cost, DM columns are commonly constructed (Takeo Office, 1996). The issue with the stability analysis of the FT column improved ground is whether the critical slip circle (CSC) passes under the bottom of the FT columns. Since the strength of soft soil generally increases with depth, $FS_{min(D)}$ increases with the given depth of the sliding surface. The following analysis shows how the possible maximum depth of slip surface can be determined.

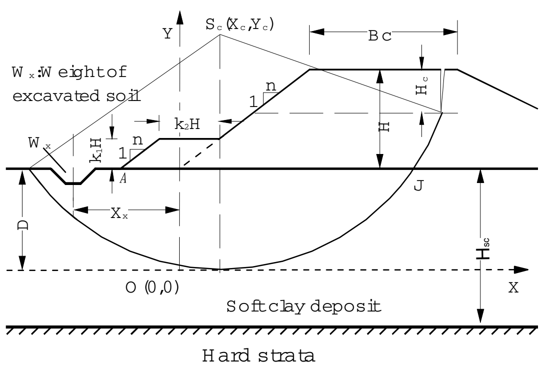

FIG. 3. Maximum depth of TLT of the embankment with complicated geometry

Conditions of Maximum TLT Depth

Figure 3 illustrates a typical slip failure for an embankment with or without cracks on the crest. The embankment has a height of H and a crest width of B_c. Therefore, the center coordinates (X_c, Y_c), with respect to the minimum safety factor corresponding to a tangential depth D, are calculated as follows, using the tangential limit equilibrium analysis method (Low, 1989; Kaniraj, 1994)

For a base failure with the CSC passing through the crest, we have

$$nH \le X_{I'} \le nH + B_c \tag{1}$$

and

$$\left(X_{I'} - X_c\right)^2 + \left(Y_c - D - \beta H\right)^2 = Y_c^2 \tag{2}$$

Let $X_{I'} = nH + B_c$ and substitute it into Eq. 2, the maximum depth of TLT can be calculated by the following formulae:

$$\frac{D}{H} = \frac{Y_c}{H} - \beta - \sqrt{\left(\frac{Y_c}{H}\right)^2 - \left(n - \frac{X_c}{H} + \frac{B_c}{H}\right)^2} \tag{3}$$

where the coordinates of the center of the slip circle (X_c, Y_c) are given by the following equations (Kaniraj, 1994):

$$\frac{X_c}{H} = \frac{n}{2} - k_1 k_2 + \frac{W_x}{\gamma H^2} \tag{4a}$$

$$\frac{Y_c}{H} = 1.5638\alpha_1 \tag{4b}$$

where

$$\alpha_1 = \frac{\alpha_1^{'}}{\frac{D}{H} + \beta - \frac{\beta^2}{2}} \tag{5}$$

$$\alpha_1^{'} = \beta^2\left(1 - \frac{2\beta}{3} - \frac{D}{H}\right) + 2\beta\frac{D}{H} + \left(\frac{D}{H}\right)^2 + \frac{n^2}{12} + \mu - \frac{W_x}{\gamma H^2}\left[\frac{W_x}{\gamma H^2} + n + 2\left(\frac{X_x}{H} - k_1 k_2\right)\right] \tag{6}$$

where μ is a term called the berm factor and given by

$$\mu = k_1 k_2\left(n + k_2\right)\left(1 - k_1\right) \tag{7}$$

The value of μ increases as the size of the berm increases and μ=0 for the embankment without any berm. β is the ratio between the uncracked height and the total height of the embankment, and is given by

$$\beta = 1 - \frac{H_c}{H} \tag{8}$$

For a full-height tension crack, β=0; if there is no tension crack and the failure surface passes through the fill height of the embankment, β=1. Other notations are illustrated in Fig. 3.

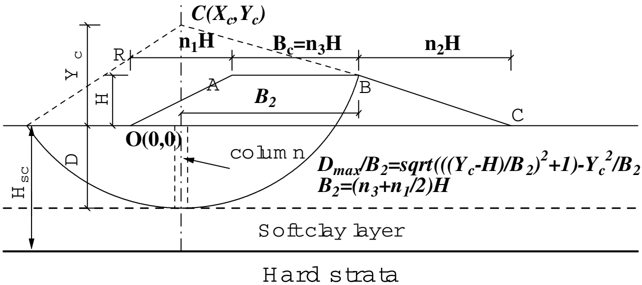

FIG. 4. Maximum depth of TLT for embankment without cracks

Figure 4 shows an embankment without any tension crack (β=1) on soft clay with a height of H and crest width of B_c. As a result, Eq. 3 can be simplified as follows:

$$\frac{D}{H}=\frac{Y_c}{H}-1-\sqrt{\left(\frac{Y_c}{H}\right)^2-\left(n-\frac{X_c}{H}+\frac{B_c}{H}\right)^2} \tag{9}$$

where X_c and Y_c are the coordinates of the center of the slip circle with respect to the minimum safety factor corresponding to a tangent depth D. Their solution is given as follows (Low, 1989):

$$\frac{X_c}{H}=\frac{n}{2} \tag{10a}$$

$$\frac{Y_c}{H}=0.1303\frac{1+n^2}{\left(\frac{D}{H}+\frac{1}{2}\right)}+1.5638\left(\frac{D}{H}+\frac{1}{2}\right) \tag{10b}$$

For an embankment with a simple geometry and without any crack, the relationship between the maximum D/H and B_c/H is shown in Fig. 5. When the width of the embankment crest ranges from 1 to 3 times its height H, the maximum depth of TLT varies from 0.8 to 2.6 times the embankment height (H). If the soft ground is not stable under the embankment, the soft ground needs to be improved by DM floating columns. The calculated depth, using Eq. 3 or 9, can be treated as the upper limit depth of the floating columns. After the determination of the depth, the stability analysis can be conducted by the use of computer programs, and the minimum safety factor, corresponding to the selected TLT, can be checked, in which the slip circle is allowed to pass through and under the columns.

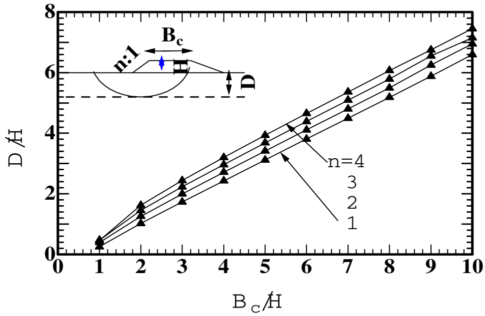

Fig. 5. Relationship between maximum depth of TLT and width of the crest

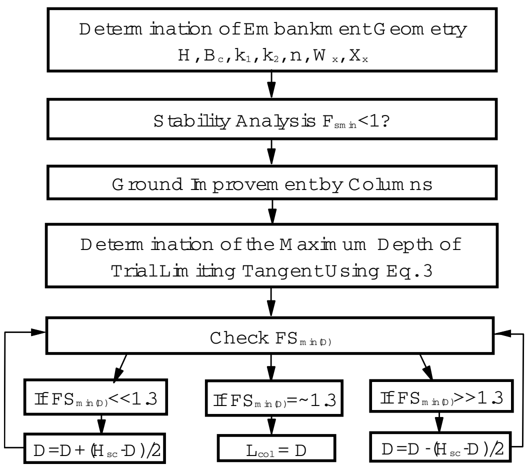

FIG. 6. Flowchart for obtaining the length of the floating columns

Calculation Procedure for Obtaining Optimum Depth of FT Columns

This calculated maximum depth of the possible slip surface D_{TLT}, using Eq. 3, can be considered as the upper limit of the column length. In other words, the improved FT DM columns should be deeper than this value. The optimum depth D_{opt} should be between D_{TLT} and the thickness of the soft clay layer H_{sc}. In practical design, if B_c is less than 2H, the calculated D_{TLT} using Eq. 3 can be used as the initial design depth of the columns. Then, the minimum safety factor $FS_{min(Dupp)}$ corresponding to the slip circle passing under the bottom of columns is examined. If the calculated $FS_{min(Dupp)}$ is greater than 1.3, then, this depth D_{TLT} is the design depth, and if $FS_{min(DTLT)}$ is less than 1.3, and let D_i=(D_{TLT}+H_{sc})/2, check $FS_{min(Di)}$, until $FS_{min(Di)}$>1.3. This procedure for the iteration calculation is illustrated in Fig. 6.

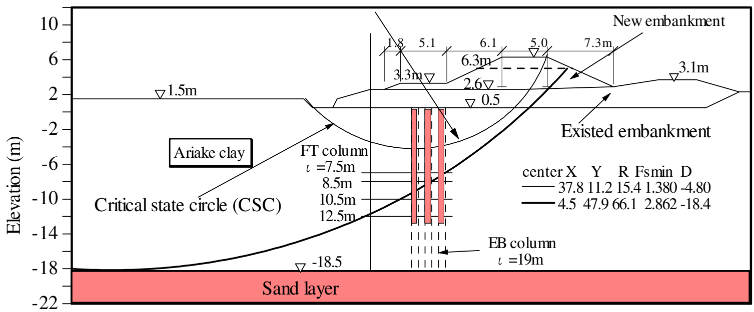

FIG. 7. Relationship between CSC for a given depth and FT columns at Fukuyoshi

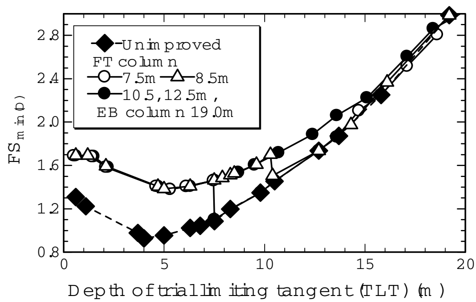

FIG. 8. Variation of the minimum safety factor with respect to a given depth

EXAMPLE FOR SEARCHING OPTIMUM DEPTH OF FT COLUMNS

The test embankment at Fukuyoshi (Fig. 7) was selected as an example and analyzed as follows. As shown in Fig. 7, the design parameters are as follows: H=5.8m, k_1=0.375, k_2=1.438, n=2.03, B_c=5.0m, weight of excavated soil mass W_x=17.75kN/m, and X_x=8.5m. The tension crack is considered occurring at the full-height of the embankment, then, β=0. The calculated $FS_{min(D)}$, with the TLT depth, is shown in Fig. 8. In the stability analysis, the shear strength of the soft ground above G.L.-12 m was set as $c_u = 7 + 1.1D$ (kPa), below G.L.-12.0m was set to $c_u = 30.2 + 2.0D$ (kPa). The procedure to obtain the optimum depth of the columns is as follows:

From Eq. 3, the initial value D_{TLT} equals to 6.1 m and the corresponding minimum safety factor ($F_{smin(D)}$) is 1.02, which is much less than 1.3.

Let $D_i = [6.1 + (20.0 - 6.1)/2] = 13.05$ m, we have $FS_{min(Di)}$=1.72>>1.3; $D_i = [13.05 - (20.0 - 13.05)/2] = 9.58$ m; we have $FS_{min(Di)}$=1.32≅1.3. Therefore, the length of improved columns is selected as 10.0 m. This is the optimum depth for 3 row DJM improved columns.

As shown in Fig. 8, when the depth of columns is greater than 10.0 m, no difference in $FS_{min(D)}$ exists between using FT columns and using EB columns in terms of stability. However, the improved soil volume for FT columns is only 53% that for EB columns. Consequently, it is much more economical to use FT columns than EB columns.

CONCLUSIONS

As presented above, the following conclusions can be drawn:

(1) For a thicker soft deposit, especially when the soil strength linearly increases with depth, the use of the floating type DM columns is an economical and effective way.

(2) Based on Low's tangential limit equilibrium method on stability, the approach presented in this paper can estimate the depth of the floating columns.

(3) To determine the optimal depth of the columns, the following procedures should be followed: (i) determining the maximum depth of a trial limiting tangent; (ii) checking the minimum factor of safety along the maximum depth using Low's equation; and (iii) determining the optimal depth of the columns to ensure that the minimum factor of safety is approximately equal to the required value. Iterations may be necessary if the calculated minimum factor of safety is much different from the required.

ACKNOWLEDGEMENTS

This work was undertaken with the financial support from the National Nature Science Foundation of China (Grant No. 50779035) and the Science and Technology Commission of Shanghai Municipality (Grant No. 05PJ14069). This research is also supported by Shanghai Leading Academic Discipline Project (Project Number: B208).

REFERENCES

DJMRG, DJM Research Group (2006). Manual of Dry Jet Mixing Method, pp55-56, (in Japanese).

Hanzawa, H., Fukaya, T. and Suzuki, K. (1990). "Evaluation of engineering properties for an Ariake clay." *Soils and Foundations*, 30(4): 11-24.

Kaniraj, S.R. (1994). "Rotational stability of unreinforced and reinforced embankments on soft soils." *Geotextiles and Geomembranes*, Vol.13(4): 707-726.

Low, B. K. (1989). "Stability analysis of embankments on soft ground." *Journal of Geotechnical Engineering*, ASCE, Vol.115(2): 211-227.

Miura, N., Chai, J.C., Hino, T., and Shimoyama, S.(1998). "Depositional environment and geotechnical properties of soft deposit in Saga Plain." *Indian Geotechnical Journal*, Vol. 28(2): 121-146.

Sakai, A., Miura, N., Aramaki, G., and Koga, K. (1991). "Deformation analysis of improved soft ground under embankment." *Proc. 7th International Conference on Computer Methods and Advances in Geomechanics*/Cairns, by Beer, Booker and Carter (eds.), A. A. Balkema, Rotterdam: 193-198.

Takeo Office, the Ministry of Construction (1996). Research Report on Construction Countermeasures of Soft Clay Foundation of Dyke Embankment along the Bank of Rokkaku River, Saga, Japan, p.229, (in Japanese).

Enhanced Stabilization of Dikes and Levees Using Direct Current Technology

J. Kenneth Wittle, Ph.D[1], Lawrence M. Zanko[2], Falk Doering, Ph.D[3], and James Harrison[4]

[1]Vice-President, Electro-Petroleum, Inc., 996 Old Eagle School Rd., Wayne, PA 19087; kwittle@electropetroleum.com
[2]Research Fellow, Natural Resources Research Institute, University of Minnesota Duluth, 5013 Miller Trunk Highway, Duluth, MN 55811; lzanko@nrri.umn.edu
[3]President, electrochemical processes, llc, 996 Old Eagle School Rd., Wayne, PA 19087
[4]Harrison Marine Electronics, 7801 East Superior Street, Duluth, MN 55804; jimmyoh@warmerbythelake.com

ABSTRACT: A demonstration study conducted between late July and early October, 2006, at the Erie Pier Confined Disposal Facility (CDF) in Duluth, MN, suggests that direct current technology can simultaneously dewater and retard water movement through a leaking dike. Four electrode (anode and cathode) configurations/combinations were tested between late July and early October, 2006, but the most significant effects took place within the first 14 days of operation, when measured dike leakage dropped by more than 70 percent and dike settlement/consolidation reached 50 percent of its final value. The results indicate that direct current technology can be an effective method for reducing water flow through a dike and physically stabilizing a dike structure via electrokinetic dewatering and through the in-situ electrolytic introduction of aluminum to the dike soil using aluminum anodes. Other indicators of the technology's impact include: changing piezometer levels over time; visible movement of water to both the horizontal and vertical cathodes; and significant electrochemical deterioration of the aluminum-donating anodes. It is recommended that these technologies be further applied and evaluated at "real world" sites where dewatering and consolidation of saturated soils and sediments is needed, accompanied by more rigorous and quantitative monitoring and measurement of project variables.

INTRODUCTION

Dikes and levees at CDFs and river banks can be structurally stabilized, and their permeability to water reduced, by the use of electrokinetics and electrochemistry. Electrokinetics is used to reduce water content of the soil, and electrochemistry is used to cement the soil structure through ion exchange. This technology has been successfully used in Europe and elsewhere.

Electro-Petroleum, Inc. (EPI), electrochemical processes, llc (ecp), the University of Minnesota Duluth's Natural Resources Research Institute (NRRI), and Harrison Marine Electronics had previously demonstrated that fine silt could be stabilized and water could be removed from fine silt using direct current (Wittle et al., 2006). EPI had also used direct current to remove water from mud pits generated by oil well drilling operations in the oil patch, aiding in the solidification of the mud for final disposal; this work is covered under a US Patent, No. 4,382,341. The use of electrokinetics as a dewatering/consolidation method is reported many times in the literature and a review will not be covered in this paper. However, a few examples are included for reference: Casengrande (1983); Burnotte et al. (2004); and Mikic et al. (2001).

Based on their prior experiences, EPI and ecp proposed to demonstrate electrokinetic stabilization technology to the United States Army Corps of Engineers (USACE) at one of the Confined Disposal Facilities (CDFs) the Corps operates. Two sites were suggested: the Black Lagoon CDF near Detroit, Michigan, and the Erie Pier CDF in Duluth, Minnesota, although other sites could also have been used. For example, a location near New Orleans may have been of interest to the Corps in the wake of Hurricane Katrina.

Following a series of discussions between NRRI, the Duluth Seaway Port Authority (owner of the Erie Pier CDF), the Detroit and Duluth Offices of the U.S. Army Corps of Engineers, and EPI for choosing an appropriate location to conduct the dike demonstration, a decision was reached to build a dike and conduct the demonstration within the confines of the Erie Pier CDF. A test site at Erie Pier has been in use since 2002 to evaluate an emerging technology, Electrochemical Geo-Oxidation (ECGO), for in- and ex-situ remediation of contaminated sediments (Zanko and Oreskovich, 2004). Consequently, much of the infrastructure and equipment needed for conducting the electrokinetic test was already in place on-site.

TEST AND TEST METHODOLOGY

The Demonstration Site

The Erie Pier Confined Disposal Facility (CDF) is located in Duluth, Minnesota, at the western tip of Lake Superior, and is the repository for sediments dredged from the Duluth-Superior harbor (Fig. 1). An aerial view of the CDF is also shown, and two identified items are pertinent to this study. The first is the location at the top (north) corner of the CDF where the demonstration took place. The second is the perimeter berm that surrounds the CDF and contains the dredged material placed in the CDF. The road girdling the CDF is at the outside base of the containment berm. An on-site visit the previous winter showed considerable ice build-up at the base of this berm; during the summer, seepage water was observed along the road at the same location. Direct current technology was suggested as a possible method of plugging this leak; however, building a dike and conducting the demonstration within the confines of the Erie Pier CDF under more controlled and protected conditions, within a pre-existing test site, was recommended to be a better option.

FIG. 1. Erie Pier CDF, Duluth-Superior Harbor, and demonstration location (map and photograph courtesy David Bowman, USACE, Detroit District).

Dredged material that filled a control cell used during a previous demonstration project (Fig. 1) was excavated, and a dike was constructed across the cell. The same material used in the construction and maintenance of the berm around the CDF was used to build the test dike. The dike was constructed so that a pool of water could be placed behind it, ensuring that a constant water head provided water to the dike and sufficient head pressure to drive water leakage. The dike material had a silty-sandy-clayey (loamish) composition and was built up by successively dumping bucket loads across the width of the cell with a small loader. Following construction, the pool behind the dike was filled with water and allowed to sit for several days until the dike began to "leak". The completed dike measured approximately 13 meters (40 feet) long, 2 meters (6.5 feet) wide at the top, 6 to 7 meters (18 to 20 feet) wide at the base, and almost 2 meters (6 feet) high. The dike material's angle of repose was approximately 40°. Figure 2 shows the completed dike and pool, with the loader in the background. Actual moisture content and compaction densities were not measured during dike construction. The pool volume was determined to be about 22.6 cubic meters (800 cubic feet), or 22,600 liters (6,000 gallons), based on an average constant pool elevation of 185.9 meters (610 feet) above sea level. As constructed, the dike was anticipated to have sufficient water seepage for the test, and it did. The pool was equipped with a float valve that controlled a water supply pump to maintain a nearly constant water level on the pool side of the dike.

FIG. 2. Completed dike and pool

Test Configurations

Three primary test configurations (four electrode combinations, total) were proposed and tested; Test 1 and Test 2 (Fig. 3) are highlighted in this paper. Each configuration served a specific purpose and had its own advantages.

- **Test 1:** Three aluminum anodes, spaced about 1 meter apart, installed vertically at each end of the dike, and a single steel cathode driven horizontally approximately one-half of the way into the base of the dike at its midpoint. In this configuration, water was to be drawn to (and drained through) the cathode, while aluminum ions donated by the anodes further stabilized the dike material.
- **Test 2:** Vertical aluminum anodes placed along the center line of the dike with a set of vertical steel cathodes placed on the wet (pool) side of the dike. In this configuration the water would be retarded from flowing through the dike. Prior to the start of this test, five PVC piezometer wells were installed along the sump side of the dike to monitor the change in water level (hydraulic head) in the dike itself.
- **Test 3:** The same vertical anode configuration as in Test 2 (placed along the centerline of the dike), but with:
  - **a)** two rows of cathodes placed along both edges of the dike. This configuration would dewater the dike from the center outward to the two sides; and
  - **b)** the same configuration as Test 3a, but with only the sump side row of cathodes connected. This configuration would dewater the dike from the center outward to the sump side.

By using aluminum anodes throughout the demonstration project, additional dike stabilization could be achieved by aluminum exchange with cations in the soil to form an environmentally safe soil matrix.

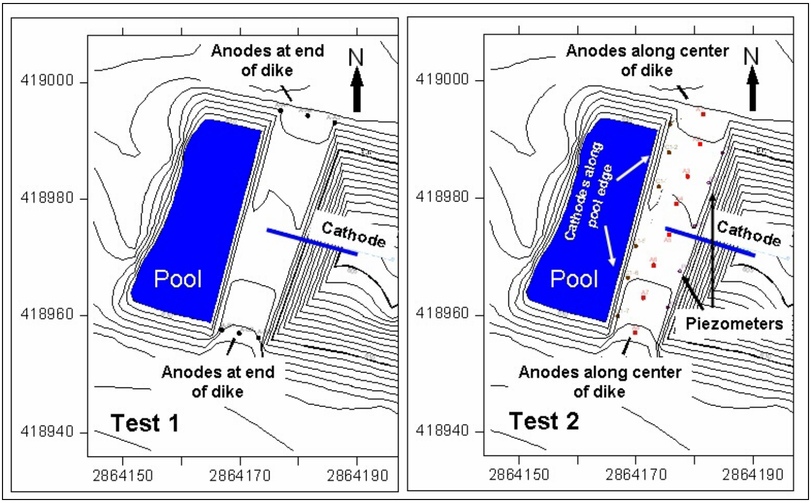

FIG. 3. Test 1 and Test 2 configurations (shown coordinates are State Plane, Minnesota North, U.S Feet, NAD 83; contour interval is 0.5 feet, i.e., 0.15 meters).

Measured test parameters

- In all tests the following parameters were measured: leakage rate; power input; current distribution to the electrodes; and total settling (subsidence) of the dike. Piezometer measurements were added after Test 1 was complete. The piezometers allowed for monitoring the hydraulic head in the dike and the influence of the respective electrode arrays on the height of that head.

RESULTS

Test 1 (July 28 to August 1) and Test 2 (August 2-August 27) had the most significant and discernible effect during the study period, especially within the first two weeks of operation, i.e., by August 11. The remainder of this paper focuses on results from this period.

Test 1 and Test 2 results

Average daily dike leakage measured during the five-day Test 1 period dropped from 1,890 ml/min (720 gal/day) prior to startup on July 28, to 660 ml/min (250 gal/day) by August 1 - a 65% reduction. The most significant reduction occurred within two days of power-up, i.e., by July 30. Between July 29 and July 30, the dike leakage rate dropped from 1,570 ml/min (596 gal/day) to 845 ml/min (321 gal/day) – a single-day reduction of 46%. At the same time, average daily drainage from the horizontally installed cathode doubled (increased by 100%) from a 70 ml/min (27 gal/day) rate just prior to the 9:50AM startup on July 28 to 143 ml/min (54 gal/day) by mid-afternoon the same day. Cathode drainage stayed at a maximum through July 30, and dropped steadily through August 1, back to 70 ml/min. At a minimum, the rates confirm electro-osmotic movement of water to the cathode. Furthermore, the increased rate of flow through the cathode was visually obvious almost immediately after power was applied to the system on July 28. Second, the decreased rate of dike leakage and cathode drainage suggests consolidation (tightening) of the dike material via the combined effects of electro-osmotic water movement toward the cathode and electrochemical addition of aluminum ions to the soil matrix from the anodes, especially by the 2nd and 3rd days of operation.

Average daily dike leakage measured during the 25-day Test 2 period fell from 656 ml/min (250 gal/day) on August 2, to 475 ml/min (181 gal/day) by August 27 - a 28% reduction. During this period, leakage decreased at a relatively steady rate. Drainage through the horizontal cathode was not measured during this or subsequent tests, as its flow slowed to a single drip every 2 to 4 seconds.

It is also worth noting that by August 3 (just six days after project startup), the dike had already reached 45 percent of the *total* settlement that would be measured as of the final (October 2) project survey (66 days after startup). By the end of Test 2 (August 27), the dike had reached over 70 percent of its total settlement. Average leakage (ml/min) and cumulative dike settlement are plotted against each other in Figure 4, and indicates a potential relationship between the two variables. The plot also suggests that the most significant electrokinetic and electrochemical effects (dewatering, and consolidation via aluminum ion addition) took place relatively quickly, by the early days of Test 2.

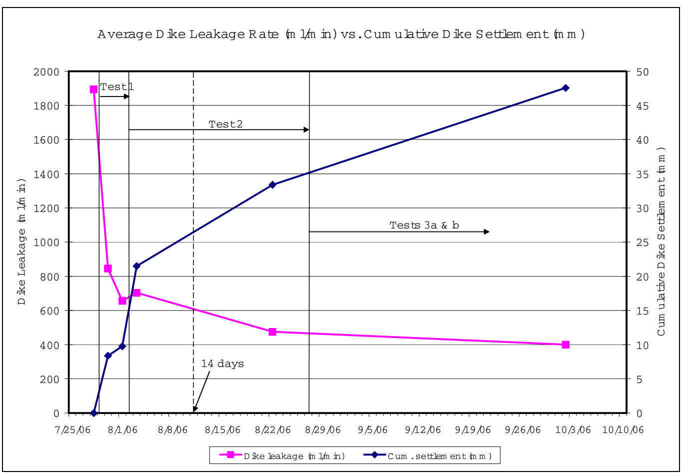

FIG. 4. Plot of dike leakage and settlement from project start to end.

OBSERVATIONS

If time and resources permitted, up to 2 weeks should have been devoted to establishing baseline leakage rates, piezometer levels, and dike settling after the dike was constructed but before electricity was applied; unfortunately this was not possible. Likewise, additional parameters should have been monitored and recorded, such as the amount of water needed to maintain the pool level behind the dike; this would have been a useful additional measure of dike leakage. A rain gage would also have been useful to have on-site throughout the project as a direct measure of water input due to precipitation. It must be noted that over 5 inches of rain fell during the initial test period. Lastly, chemical and/or mineralogical analysis of the dike soil would have shown to what degree aluminum was delivered to the dike by the anodes, because significant electrochemical depletion (deterioration) of the aluminum anodes occurred.

CONCLUSIONS

The demonstration showed how electrokinetics can simultaneously dewater (and retard water movement through) a leaking dike. The most significant demonstration effects took place within the first 14 days of operation. During those first two weeks, measured dike leakage dropped by more than 70 percent, and dike settlement/consolidation reached 50 percent of its final project total of 47.5mm (0.156 feet), or 2.6 percent of the original dike height of 6 feet.

An additional illustration is appropriate to reference at this time. Figure 5 shows the overall power into the system over the three test periods and the leakage rate during the three tests, indicating that the highest effectiveness for stopping a leak is in the initial phases of the treatment.

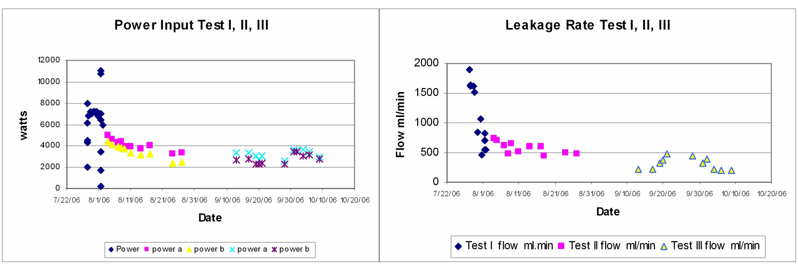

FIG. 5. Power inputs (watts) and leakage rate (ml/min) for Tests 1, 2, and 3.

Despite the limited availability of time and resources, the test program provided some important information about the technology's viability, and a sufficient amount of the project's reported quantitative and observational information supports the occurrence of a positive technology effect. Other indicators and evidence of the technology's impact include: changing piezometer levels over time; clearly visible movement of water to both the horizontal and vertical cathodes; and significant electrochemical deterioration of the aluminum anodes. Therefore, it is recommended that the technology be further applied and evaluated at one or more “real world” sites where dewatering and consolidation of soils or sediments is needed. It is also recommended that future application and evaluation of the technology have built into it even more rigorous and quantitative monitoring and measurement of project variables.

ACKNOWLEDGEMENTS

The authors gratefully acknowledge the Duluth Seaway Port Authority, for providing continued access to the Erie Pier test site; Harrison Marine Electronics, Duluth, for major operational assistance; and the U.S. Army Corps of Engineer’s (USACE) Detroit District and Duluth Area Office, and its Waterways Experiment Station (WES), Engineer Research and Development Center (ERDC), Vicksburg, MS, for project oversight and logistical support; with special thanks going to David Bowman, Tommy Myers, Ph.D., and David Gent of the Corps for their advice and critiques.

REFERENCES

Casagrande, L., 1983, Stabilization of soils by means of electroosmosis — State of-the-art, *Journal of the Boston Society of Civil Engineers*, 69(2): 255–302.

Burnotte, F., Lefebvre, G., and Grondin, G., 2004, A case record of electroosmotic consolidation of soft clay with improved soil–electrode contact, *Can. Geotech. J*. 41: 1038–1053.

Micic, S., Shang, J.Q., Lo, K.Y., Lee, Y.N., and Lee, S.W., 2001, Electrokinetic strengthening of a marine sediment using intermittent current, *Can. Geotech. J*. 38: 287–302.

Wittle, J.K., Zanko, L.M., Doering, F., and Harrison, J., September 2006, Innovative technology demonstration pilot study: electro-kinetics dewatering and consolidation of Erie Pier fine silts: draft report

Zanko, L.M., and Oreskovich, J.A., August 2004, Emerging technology demonstration at the Erie Pier Confined Disposal Facility, draft NRRI Report of Investigation (unpublished).

Geo-Bag Method for Levee Construction and Rehabilitation

Shuwang Yan[1] and Jian Chu[2]

[1] Geotechnical Research Institute, Tianjin University, Tianjin, China, shuwangyang@tju.edu.cn .
[2] School of Civil and Environmental Engineering, Nanyang Technological University, Blk N1, 50 Nanyang Ave, Singapore 639798, Singapore, cjchu@ntu.edu.sg.

ABSTRACT: A method of using clay slurry filled geotextile bags (or geo-bag) to construct levees is introduced in this paper. A case study of using this method to construct an offshore levee is presented. A method to use cast-in-situ concrete mat to protect the slopes of levees is also introduced. These methods can also be used for disaster mitigation and rehabilitation of damaged levees.

INTRODUCTION

The importance of costal protection has been highlighted by the flooding in New Orleans caused by Hurricane Katrina. As a large amount of resources are required to construct costal defense or protection facilities, the selection of the most cost-effective costal protection structures and the construction techniques becomes important in reducing the overall cost of the project. This is particularly the case when the levees or other types of costal protection structures are long. Therefore, it is beneficial to develop new levee construction methods. In this paper, the geotextile bag method which uses either sand or clay to fill geotextile tubes or bags to form levees or breakwaters is introduced.

The traditional method of constructing shoreline structures is to use rock or precast concrete units. In recent years, several methods have been developed to use geotextile materials for the construction of coastal structures such as breakwaters and levees. One of the methods is to use geotextiles acting as formwork for cement mortar units cast in situ (Silvester and Hsu, 1993). The mortar mix needs to be only of sufficient compressive strength to support the weight above, plus the moment from the side force of the waves. Since the flexible membrane is required to hold the mixture in place until it sets, any subsequent deterioration due to UV rays or other conditions is of little concern. Thus, the method tends to be cheaper than the conventional methods. Details of these methods are referred to Silvester and Hsu (1993).

When levees are to be built to cross a river or a lake for flood control or for making a small reservoir, water or air filled rubber tubes have been used to form the so called rubber dam. One example is shown in Fig. 1. The advantage of this method is that the height of the levee can be adjusted easily. However, the disadvantage is that the height of the levee is limited. The height of the inflated rubber tube ranges from 1 to 3 m. The highest rubber dam that has ever been built in China (or probably Asia) is 6 m, in Enshi, Hubei Province. This rubber dam is 96 m long and the longest has well exceeded 1000 m. The rubber tube used for the dam is prefabricated using high strength synthetics, such as macromolecule compound materials (Chu and Yan, 2007).

FIG. 1 Small Levee made of water inflated geotextile tubes

Similar methods, but using sand or dehydrated soil as the fill material to inflate the geosynthetic tube, or geo-tube, have also been used for levee construction (Kazimierowicz, 1994; Leshchinsky et al., 1996; Miki et al., 1996). Sand or sandy soil is the most ideal fill material for this purpose. For near shore or offshore project, a suction dredger can be used to pump sand from the seabed or a sand pit directly into the geotextile tubes. In case sand is not readily available, silty clay or soft clay may also be used. In this case, the clayey fill would have to be in a slurry state in order to be pumped and flow in the tube. The slurry would have to be dewatered in the geotextile tubes under an ambient pressure. Then the selection of the geotextile used for the tubes becomes important. The geotextile has to be chosen to meet both the strength and filter design criteria. Some analytical methods have been developed to estimate the required tensile strength for the geotextile (Kazimierowicz, 1994; Leshchinsky et al., 1996; Miki et al., 1996). The apparent opening size (AOS) of the geotextile needs to be selected to allow the pore pressure to dissipate freely and yet retain the soil particles in the bags.

The geo-tubes are normally like sausages with a more or less circular cross-section. One disadvantage of the sausage like geo-tube is that it is difficult to stack one on top of another without lateral support or forming a broad base, as one can image with stacking sausages. To overcome this problem, a method to use geotextile bags is presented in this paper. These geotextile bags are not like sausages, but more like mats with its horizontal dimensions much longer than the vertical dimension. For this reason, it will be called the geotextile bag or geo-bag in this paper.

GEO-BAG METHOD

The typical dimension of the geo-bag after inflation with slurry is 20 to 30 m long and 0.5 to 1.0 m tall. Its width varies with the width of the levees. The bags can be made onsite by sewing geotextile sheets using a sewing machine. When forming a levee, the geo-bags are inflated onsite by pumping slurry into the bags. When the seabed is soft, a layer of geotextile can be laid on the seabed before the geo-bags are placed. To facilitate the construction, the first layer of geo-bags can also be filled with sand so that the geotextile layer can be quickly held in position.

As an example, the cross-section of an offshore levee constructed along the coast of Tianjin, China, is shown in Fig. 2. A picture showing the alignment of the bags along its axis is given in Fig. 3. The designed height of the levee was 4.8 m with base and top elevations at 0.7 m and 5.5 m respectively. The top width of the levee was 2.43 m. The water levels were at 4.7 m elevation during high tide and at nearly 0.7 m elevation during low tide. The outer and inner slopes of the levee were chosen to be 2H:1V and 1.5H:1V, respectively. For the bottom bag, the dimension used was 30 m in circumference. Clay slurry was dredged from the seabed of a selected area and pumped directly into the bags through an injection hole. The height of the bag after consolidation was around 0.5 m. Nine layers of geotextile bags were used.

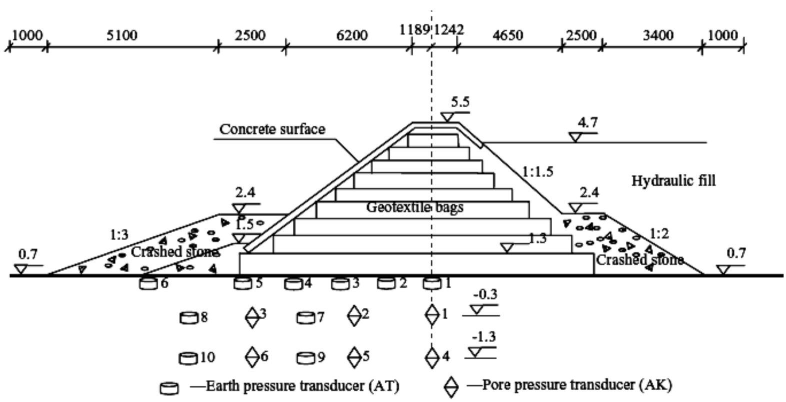

FIG 2 Design of levee constructed using clay slurry filled geotextile bags

The soil used to fill the bags had it physical properties as shown in Table 1. It had a low plasticity index of 8.9. The fines content of the soil was 55%. According to the Unified Soil Classification System (USCS), the soil is classified as a borderline case of SC-CL, that is, between clayey sand and low plasticity clay.

Table 1. Physical properties of the soil used for the geo-bags

Soil Type	Plastic Limit (%)	Liquid limit (%)	Plasticity Index (%)	Unit weight (kN/m^3)	Fines Content (<75 μm)	Permeability (m/sec)
SC-CL	11.5	20.4	8.9	20.0	55%	3.4×10^{-7}

FIG. 3 Levee constructed using clay slurry filled geotextile bags

FIG. 4 Leveling the slope formed by geo-bags using small geotextile bags.

The levee built with the large size geo-bags forms stepped slope as shown in Fig. 3. Small geotextile bags filled with cement mixed clay were used to fill the gaps and remove the steps, as shown in Fig. 4. The smoothened slope surface is then protected by casting a 25 mm thick concrete mat on top of the surface, as shown in Fig. 5. The cast-in-place concrete mat was formed by pumping lean concrete into a mould made of geotextile, a technique that is commonly used in China (Chi, 1991). The levee constructed using geo-bags and covered with the cast-in-place concrete mat is shown in Fig. 6.

FIG. 5 Cast in-situ concrete mat

FIG. 6 Levee made of geo-bags and covered with cast in-situ concrete mat

LEVEE REHABILITATION

The techniques presented above can also be used as quick and convenient methods for levee rehabilitation. One major advantage of the geo-bag method is that the geo-bag fits uneven ground surface and can even be placed to cover a slope surface without causing any stability problem to the bags or the slope. The bags can be filled with a variety type of soils ranging from sand to low plasticity clay. The levee or embankment made of geo-bags can also tolerate a large amount of settlement. Therefore, the geo-bag method can be conveniently used to elevate the height of a levee or construct temporary levees for disaster mitigation and rehabilitation purpose.

For quick repair of a damaged levee, the cast-in-situ concrete mat method can be used. The thickness and strength of concrete mat can be adjusted easily by adjusting the size of the mat, the geotextile material and the type of concrete used. It can be adopted wither above or below water. It can also be installed rapidly by using quick setting concrete.

CONCLUSIONS

A method of constructing levees using clay slurry filled geo-bags is presented. The method is workable for levees or breakwaters that are less than 10 m high. This method differs from the geo-tube method in that the geo-bags are more like a mat with its horizontal dimensions much larger than the vertical one along a cross-section, rather than like a sausage. This offers the advantages of stacking the geo-bags easily without causing stability problem. A cast-in-situ concrete mat method is also introduced. Both methods can be used for levee rehabilitation and disaster mitigation.

REFERENCES

Chi, J. K. (1991). *Technical Report on the Technique of Pumping Concrete into Geotextile Mould*. Shanghai Geotechnical Research Institute (in Chinese).

Chu, J. and Yan, S. W. (2007). "Ground improvement in disaster mitigation and rehabilitation works." *Invited Special Lecture, Proc. 16 Southeast Asian Geotechnical Conference*, 8-11 May, Kuala Lumpur, 163-170.

Kazimierowicz, K. (1994). Simple analysis of deformation of sand-sausages. *Proc. 5th Int. Conf. Geotextiles, Geomembranes and Related Products*, Singapore, 5-9 Sept., **2,** 775-778.

Leshchinsky, D., Leshchinsky, O., Ling, H.I., and Gilbert, A. (1996). "Geosynthetic tubes for confining pressurized slurry: some design aspects." *J. Geot. Eng, ASCE*, 122(8), 682-690.

Miki, H., Yamada, T., Takahashi, I., Shinsha, H., and Kushima, M. (1996). Application of geotextile tube dehydrated soil to form embankments. *Proc. 2nd Int. Conf. on Environmental Geotechnics*, Osaka, 5-8 Nov., 385-390.

Silvester, R. and Hsu, J.R.C. (1993). *Costal Stabilization – Innovative Concepts*, Prentice-Hall Inc.

Yan, S. W. and Chu, J. (2005). Methods for using natural or synthetic materials for dike construction. *Proc. Int. Symp. On Tsunami Reconstruction with Geosythetics,* 8-9 Dec. Bangkok, 183-191.

Laboratory Model Study on Densification of Hydraulically-Filled Fine Sands by Vibro-compaction

Jian Zhou[1], Jie Han[2], Min-Cai Jia[1], and Xiaobin Lin[1]

ABSTRACT Levees, ports, and other water-front structures have been commonly constructed on hydraulically-filled fine sands, which are typically loose, compressible, and susceptible to liquefaction. Densification and treatment of these sands are necessary prior to the construction of levees and other structures. Since these hydraulically-filled fine sands are often uniform and/or contain a relatively high fine content, backfill materials such as aggregates are commonly needed during the densification by vibroflotation. The use of aggregates increases the cost of a project.

The focus of this paper is to investigate the effectiveness of densification of hydraulically-filled fine sands by vibroflotation without any backfill material. This investigation was done in the laboratory through model tests using a vibro-probe to simulate the densification of fine sands in the field. A multi-phase (up to 7) densification technique was adopted. Excess pore water pressures were monitored in the sand at different locations. Cone penetration tests were performed before and after the densification to evaluate the improvement of the soil properties. Soil samples were also exhumed before and after the densification to evaluate the change of the relative density of the fine sand. Test results showed that the degree of densification of fine sands depended on the location (depth and horizontal distance), the phase of densification, and time.

INTRODUCTION

Levees, ports, and other water-front structures have been commonly constructed on hydraulically-filled fine sands, which are typically loose, compressible, and susceptible to liquefaction. Densification and treatment of these sands are necessary prior to the construction of levees and other structures (Zhou et al., 2003). Vibroflotation is one of the most commonly used ground improvement methods for this application.

Vibroflotation has been commonly adopted in China for ground improvement since late 1970s (Han, 1992). It is often referred as vibro-compaction if no backfill is

[1] Department of Geotechnical Engineering, Tongji University, Shanghai, P.R. China

[2] Department of Civil, Environmental, and Architectural Engineering, the University of Kansas, Lawrence, KS 66045, USA

used or vibro-replacement if backfill is used. Vibro-compaction has been successfully used to densify medium or coarse sands, however, it is controversial whether it can be used for fine sands, especially when they are uniform and/or have more than 10% fine particles. As shown in Figure 1, Thorburn (1975) recommended a wide range of soils suitable for vibrocompaction. However, Mitchell (1981) recommended the ranges suitable and unsuitable for vibrocompaction in more detail. He indicated that vibrocompaction is best suitable for soils having the gradation Range B. However, densification becomes difficult if the soil gradation is within Range C due to excessive fine contents. On the other hand, vibro-probes are difficult to penetrate and even damaged by large particles within the gradation Range A.

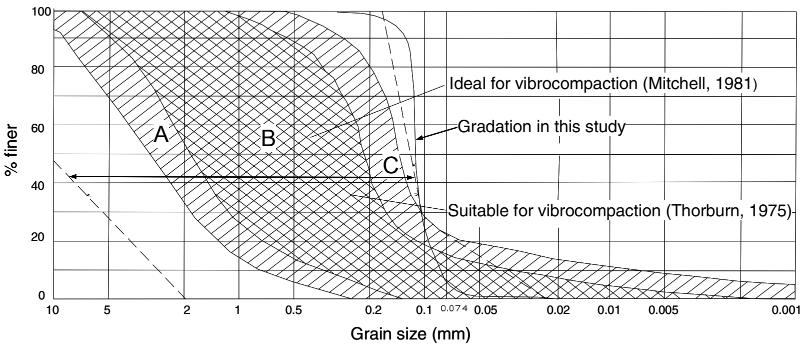

FIG. 1. Suitability of Soil Types for Vibroflotation

Since hydraulically-filled fine sands are often uniform and/or contain a relatively high fine content (greater than 10%), backfill materials such as aggregates are commonly needed during the densification by vibroflotation. The use of aggregates increases the cost of project, which can become very significant if the improved area is large. Therefore, it becomes an attractive option if no backfill is needed during densification of hydraulically-filled fine sands, i.e., vibrocompaction.

This study is to investigate the effectiveness of densification of hydraulically-filled fine sands by vibrocompaction. The gradation of the soil used in this study is also shown in Figure 1, which is out of the range suitable for vibrocompaction recommended by Thorburn (1975) and Mitchell (1981). This investigation was done through laboratory model tests to simulate the densification of fine sands in the field.

MODEL INSTALLATION TESTS

Test Box

The model test consisted of three components, the box, the probe, and the monitoring system as shown in Figure 2. The model box, made of steel plates, has internal dimensions of 1.2m x 1.2m x 1.5m high. On top of the box, a steel frame was made for the operation of the probe for vibro-compaction. To minimize the boundary effect on vibration, 10mm thick expanded polystyrene foam was placed at the bottom and around the internal sides of the box.

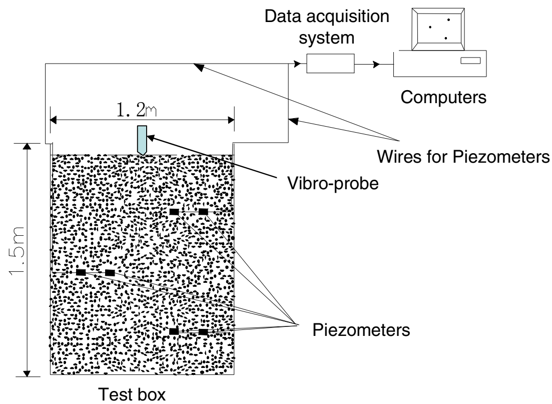

FIG. 2. Model Test Box and Monitoring System

The vibro-probe used in this study has the same working mechanism as probes in the field. Vibration is generated through the high-speed rotation of an eccentric weight. The vibro-probe had a diameter of 51mm and length of 150mm, power of 1.1kW, rate of rotation of 2840r/min (equivalent to a frequency of 7Hz), magnitude of free vibration of 1.15mm, and electric current of 2.52A.

Six piezometers were placed at three depths (0.4m, 0.8m, and 1.2m) and two distances from the center of the probe (0.2m and 0.4m) to monitor the variations of excess pore water pressures during and after each densification. Unfortunately, the piezometer at the depth of 1.2m and distance of 0.2m from the center of the probe was mal-functional prior to the densification so that no data was recorded.

Sand Properties and Sample Preparation

Sand used in this study was obtained from a project site in the Shanghai Waigaoqiao Port, which is hydraulically filled. The gradation of this air-dried sand is shown in Figure 1, which is out of the range suitable for vibrocompaction recommended by Thorburn (1975) and Mitchell (1981). This sand is poorly graded and has a mean grain size of 0.126mm, coefficient of uniformity of 1.58, and 7% fine content (< 0.075mm). Specific gravity of sand particles is 2.68. The maximum and minimum dry densities are 1.725g/cm^3 and 1.176g/cm^3, respectively.

To simulate hydraulically filling, sand was placed in lift in the box by free falling in water at a height of 0.5m. Each lift had thickness of 0.20m. Piezometers were placed during the filling of sand. After the placement of sand, it was set for two days before any test or installation of the probe. The measured average dry density after the placement was 1.415g/cm^3, which is equivalent to relative density of 53%.

Densification

Before the densification, the vibro-probe was mounted on the steel frame set on top of the test box to ensure the verticality of its penetration. The vibro-probe was pushed into sand at a rate of 1m/min and then withdrawn to the surface at the same rate. This installation process was repeated once as the whole densification process for one phase. For the initial densification, the vibro-probe remained at the bottom for 30s while for the repeated densification, it remained at the bottom for 15s. To avoid fine sand particles being flushed away, no water jetting was applied during the densification. The variations of excess pore water pressures during and after each densification were monitored through the pre-placed piezometers. The following phases of densification were performed after the complete dissipation of excess pore water pressures, which typically took 24 hours. To investigate re-densification effects by subsequent phases of densification, the sand condition prior to densification was considered as the initial one for the subsequent phase of densification. The multi-phase densifications are referred herein as Vibro1, Vibro2, Vibro3 … for the first, second, third … phases of densification. Before and after each phase of densification, CPT tests were performed at distances of 0.2m and 0.4m from the center of the probe to evaluate the effectiveness of densification. The diameter of the CPT cone is 25mm. After CPT tests, samples were taken from two depths at 0.2m and 0.6m using ring cutters (60mm in diameter and 20mm thick) to evaluate the relative densities of sand. CPT and relative density tests were performed at distributed locations around the center for each phase but at desired radius distances to the center. The holes left by CPT cones and ring cutters were backfilled with the same fine sand.

Pore Water pressure Monitoring and Analysis

It is well known that saturated sand under dynamic loading can be liquefied due to the generation of excess pore water pressure. The distribution of excess pore water pressure in the sand can be used to evaluate the influence range of the vibro-compaction. Therefore, it is important to investigate the generation and dissipation of excess pore water pressure during and after each phase of densification.

Figure 3 presents the measured excess pore water pressures at five different locations during the penetration, vibration at the bottom, and withdrawal of the probe. It is shown that the excess pore water pressure increased from the shallow to the deep depths and from the close to far distances when the vibro-probe penetrated into the sand. As a result of horizontal and rotational vibrations of the probe, the excess pore water pressure at the same depth almost increased at the same pace. However, the time to reach the maximum excess pore water pressure was different at different depths. As shown in Figure 3, the excess pore water pressure at the depth of z = 0.4m first reached the peak, which was followed by those at the depths of 0.8m and 1.2m subsequently. Figure 3 also shows that the fine sand at the distance of r = 0.2m to the center of the probe was liquefied during the densification. However, the fine sand at the distance of 0.4m was not liquefied except that at the depth of 1.2m, which may be due to the boundary effect. Even though the fine sand at the distance of 0.4m was not liquefied, high excess pore water pressure was generated at that distance as well. These results confirm that the vibro-probe used in this model study can generate high excess pore water pressure in fine sand.

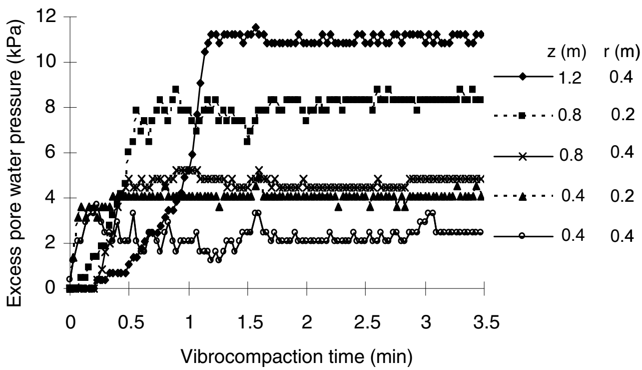

FIG. 3. Measured Excess Pore Water Pressures with Time during Densification

As shown in Figure 3, the variation of the excess pore water pressure during the densification can be divided into three stages: (1) when the probe entered the sand, the probe was distant to the piezometers so that the excess pore water pressure increased gradually; (2) when the probe approached the piezometers, the excess pore water pressure increased suddenly and reached the peak value when the probe at the same depth as the piezometer; and (3) After that, the excess pore water pressure maintained the same level during the remaining densification.

The dissipation of the excess pore water pressure started after the vibrocompaction stopped for 6 minutes. Figure 4 presents the dissipation of the excess pore water pressure at different depths and distances.

The excess pore water pressure after the vibrocompaction can be approximately expressed in the following format:

$$u_d = a \cdot \exp(b \cdot t) \tag{1}$$

where u_d = the excess pore water pressure at time, t (min); a = the initial excess pore water pressure after vibrocompaction, u_{d0}; and b = the dissipation rate.

From this study, the regression analysis yields the results shown in Table 2. The parameter, b, ranges from – 0.021 to – 0.036. The higher absolute b value shows the higher rate of excess pore water dissipation. At a distance of 0.4m, the absolute b value decreases with an increase of depth. This result implies that the sand close the top surface dissipates faster than that deep from the surface, which is reasonable as the top surface is the only drainage surface. Table 2 also shows that at the same depth, the absolute b value increases with the distance away from the center. This phenomenon results from the fact that the sand away from the center is looser and has a higher permeability after densification.

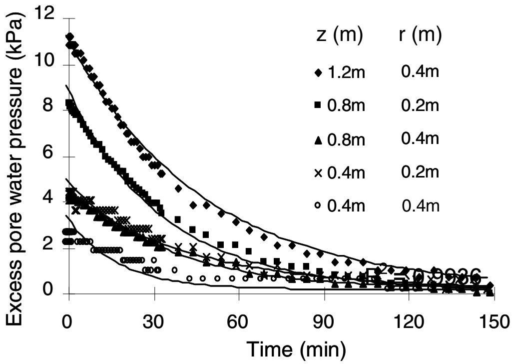

FIG. 4. Dissipation of Excess Pore Water Pressures with Time after Densification

Table 2. Excess Pore Water Pressure Parameters

Depth, z(m)	Distance, r(m)	a (kPa)	b (1/min)	R^2
1.2	0.4	10.922	-0.0207	0.9898
0.8	0.2	8.832	-0.0256	0.9196
0.8	0.4	4.771	-0.0278	0.8685
0.4	0.2	4.281	-0.0263	0.9778
0.4	0.4	3.199	-0.0358	0.8898

EVALUATION AFTER DENSIFICATION

CPT Tests

CPT tests were performed at distances of 0.2m and 0.4m from the center before and after vibrocompaction to evaluate the effectiveness of densification and re-densification. As shown in Figure 5, the sand at the distance of 0.2m was densified at the first densification (Vibro1) and further densified at the subsequent densifications (Vibro2, 3, and 4). However, the sand at the distance of 0.4m was not obviously densified at the first densification but gradually densified at the subsequent densifications. This phenomenon can be explained below. For the first densification at the distance of 0.2m, the sand is liquefied as shown in Figure 3 so that the sand was densified after the dissipation of excess pore water pressure. Since the sand near the vibro-probe was liquefied, the vibration and energy could not be effectively transmitted to the sand at the surrounding area (for example, at the distance of 0.4m). As a result, the sand at that distance was not effectively densified. For the re-densifications (Vibro2, 3, and 4), since the sand near the probe had been densified, no or less liquefaction occurred, the vibration and energy could be transmitted to a farther area so that the sand at 0.4m distance was gradually densified.

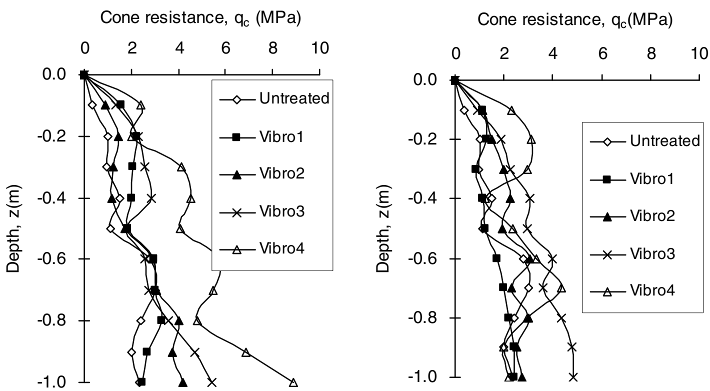

(a) r = 0.2m (b) r = 0.4m

FIG. 5. CPT Profiles

Relative Density Tests

Relative density is a commonly used index for evaluating the density of cohesionless soil, such as sand. Samples were taken from the model tests before and after each phase of densification (up to 7 phases). Figure 6 shows the relative density of sand at two different depths and two different distances. It is shown that the sand at the close distance of 0.2m was densified more than that at the farther distance of 0.4m and the sand at the deep depth of 0.6m was densified less than that the shallow depth of 0.2m. These results are intuitively reasonable because the sand closer to the probe had more energy to be densified and the sand at a deeper location needed to overcome more overburden stresses. Figure 6 also shows that the sand at the shallow depth (z = 0.2m) had more obvious contraction and dilation behavior during the densification. This phenomenon can also be observed from the CPT test results as shown in Figure 5.

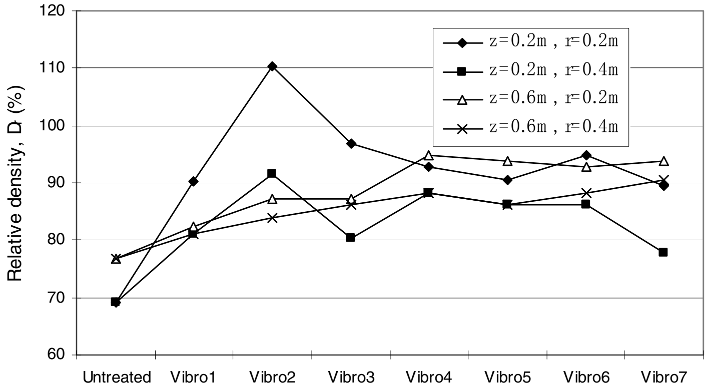

FIG. 6. Influence of Densification on Relative Density of Sand

CONCLUSIONS

Based on the model tests of vibrocompaction in the hydraulically filled fine sand, the following conclusions can be made:

(1) The model tests demonstrated that vibrocompaction can be used to densify uniform fine sand.
(2) Measurements showed that the excess pore water pressures were generated in three stages during the densification, depending on the depth, distance, and time.
(3) The dissipation of excess pore water pressure with time after densification can be expressed in an exponent formula.
(4) CPT and relative density results show that the sand close to the probe can be densified at the first couple of densifications while the sand farther from the probe requires more re-densification processes. The sand at a shallow depth experienced contraction and dilation cycles during re-densifications.

REFERENCES

Han, J. (1992). “Stone column techniques - general report.” Invited speaker, *Proc. of 3rd Chinese Soil Improvement Conference*, Qengwangdao, China, in Chinese.
Mitchell, J. K. (1981). "Soil improvement - State-of-the-Art." Proceedings, 10th ICSMFE, Stockholm, 4, 509 - 565.
Thorburn, S. (1975). “Building structures supported by stabilized ground”. Geotechnique, 25, 83-94.
Zhou, J., Jia, M.C., and Chi, Y. (2003). “Vibroflotation compaction of silty fine sands with additional backfill materials.” Chinese Journal of Rock Mechanics and Engineering, 8.

Stability Analyses of a Levee on Deep-Mixed Columns, Plaquemines Parish, Louisiana

Tiffany E. Adams[1], M. ASCE, P.E., George M. Filz[2], Ph.D., F. ASCE, P.E., Peter R. Cali[3], Ph.D., M. ASCE, P.E., and Mark L. Woodward[4], P.E.

[1]Via Fellow and IGERT Trainee, Department of Civil and Environmental Engineering, Virginia Tech, Blacksburg, VA 24061; teadams@vt.edu
[2]Professor, Department of Civil and Environmental Engineering, Virginia Tech, Blacksburg, VA 24061; filz@vt.edu
[3]Geotechnical Engineer - Contractor, U.S Army Corps of Engineers, Hurricane Protection Office, P.O. Box 60267, New Orleans, LA 70160, peter.r.cali@mvn02.usace.army.mil
[4]Supervisory Geotechnical Engineer, U.S Army Corps of Engineers, P.O. Box 60267, New Orleans, LA 70160, mark.l.woodward@mvn02.usace.army.mil

ABSTRACT: The U.S. Army Corps of Engineers recently completed reconstruction of a section of flood protection levee known as the P24 project, which included installation of shear walls along a portion of the alignment. The shear walls were created using the dry method of deep mixing. Two-dimensional stability analyses were performed using limit-equilibrium and numerical methods to evaluate the factor of safety of the structure and assess the potential for racking. Ordinary limit equilibrium analyses do not account for potential failure modes other than shearing; whereas, numerical stress-strain analyses can account for other failure modes, such as racking of the deep mixed material due to slipping along vertical joints between adjacent columns in the shear panels. Numerical analyses were completed for varying numbers of weak joints as well as for a range of joint strength values to evaluate the sensitivity of the results to these factors. The results show that, for the conditions used to represent this project, the racking failure mechanism ceases to control performance at vertical joint efficiencies greater than or equal to 30%.

INTRODUCTION

The U.S. Army Corps of Engineers (the Corps) recently completed reconstruction of a section of flood protection levee known as the P24 project along the Mississippi River in Plaquemines Parish, Louisiana. The new levee structure is constructed on the protected side of an existing levee and floodwall system. Reconstruction included installation of deep-mixed columns in the foundation of the levee segment between stations 408+00 and 427+00, where a narrow levee footprint was needed due to the close proximity of an existing roadway. For this segment of the levee, shear walls were constructed perpendicular to the levee alignment by overlapping dry-mixed, single-axis columns installed by the deep mixing method (DMM). The shear walls are 12.2 m deep, 10.7 m long, and positioned at a 2.13 m center-to-center spacing in the direction of the levee alignment. The columns are 80 cm diameter, and the specified overlap between adjacent columns is 15.2 cm, which produces a center-to-center spacing of 64.8 cm and a chord length of 47 cm at the overlap.

The depth, length, and spacing of the shear walls, as well as the required strength of the improved ground, were established by the Corps to achieve a factor of safety of 1.3 using limit-equilibrium stability analyses by means of the “Method of Planes.” The levee geometry and the subsurface conditions are described below.

The purpose of this study was to evaluate stability of the design section using limit-equilibrium and numerical methods, under the same conditions as analyzed by the Corps. Our comparative analyses were completed using the design section provided by the Corps, as discussed below, which may differ from as-built conditions.

ANALYSIS SECTION AND MATERIAL CHARACTERIZATION

The geometry of the design section was established by the Corps, and it includes the configuration of the soil-cement columns. The design section is shown in Figure 1, in which “Stratum 1” is the floodwater on the left-hand side, “Stratum 2” is a flood-side stability berm, “Stratum 3” is the levee, and “Stratum 4” through “Stratum 13” are existing layers of soil at the site. The location of the DMM columns that comprise the shear panels is also shown in Figure 1.

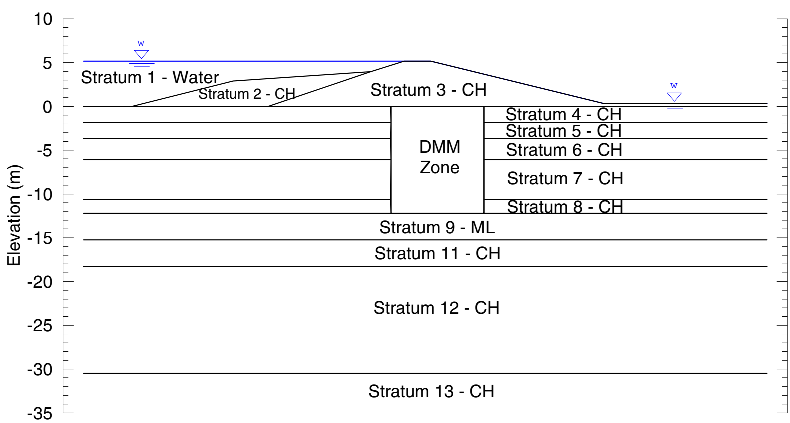

FIG 1. Design Cross-Section

The material property values for the limit equilibrium analysis were provided by the Corps. Additional material property values were required for the numerical analyses. Values for Young’s Modulus, E, were estimated from published correlations for soil modulus based on soil plasticity and undrained shear strength (Barker et al. 1991). Poisson’s ratio values for the subsurface soils and the material property values for the dry-mix columns were estimated based on information provided in Filz and Navin (2006). The material property values used in the analyses are listed in Table 1.

Table 1. Summary of Material Property Values

Stratum	γ_t (kN/m³)	c (kN/m²)	ϕ (deg)	E (kN/m²)	ν
Stratum 1	9.8	0	0	--	--
Stratum 2	15.7	9.6	0	2873	0.45
Stratum 3	17.3	19	0	9576	0.45
Stratum 4	17.3	19	0	9576	0.45
Stratum 5	14.1	9.6	0	2873	0.45
Stratum 6	15.7	9.6	0	2873	0.45
Stratum 7	15.7	9.6 to 17[b]	0	2873 to 5028[d]	0.45
Stratum 8	15.7	17 to 19[b]	0	5028 to 5746[d]	0.45
Stratum 9	18.4	9.6	15	9576	0.40
Stratum 11	17.3	24 to 29[b]	0	7182 to 8619[d]	0.45
Stratum 12	17.3	29 to 48[b]	0	8619 to 14365[d]	0.45
Stratum 13	17.3	48+ [b]	0	14365+ [d]	0.45
DMM Zone	Varies[a]	110[c]	0	55064	0.45

[a] The unit weight equals that assigned to the corresponding existing soil layers.

[b] Cohesion increases with depth at a rate of 1.57 kN/m^2/m.

[c] Representative cohesion within the DMM Zone is based on the DMM strength and geometry. The design shear strength of the DMM material is 345 kN/m^2, the average width of the panels is 70.1 cm, and the center-to-center spacing of the panels is 213 cm. Ignoring the soil strength within the DMM zone because of strain compatibility considerations, the composite strength of the DMM zone is (70.1 cm)(345 kN/m^2)/(213 cm) = 114 kN/m^2, which is approximately equal to the value of 110 kN/m^2 assumed by the Corps.

[d] Young's Modulus, E, increases with depth at a rate of 471 kN/m^2/m.

LIMIT EQUILIBRIUM ANALYSES

Limit equilibrium stability analyses were completed by the Corps using the Method of Planes to analyze a series of three-wedge failure surfaces. Subsequently, Spencer's Method in UTEXAS3 (Wright 1991) was used to search for critical circular and non-circular failure surfaces.

Limit-Equilibrium Analyses using the Method of Planes

Limit equilibrium stability analyses were completed by the Corps for over 20 different wedge failure surfaces using in-house software that computes factors of safety for wedge surfaces using the Method of Planes. This method of slope stability analysis is a force-equilibrium method that divides the failure mass into active, passive, and central blocks, and it assumes horizontal earth forces between blocks. The critical surfaces that were identified for shallow and deep failure modes by the Corps' limit equilibrium stability analyses are shown in Figure 2, and the values of the factor of safety are 1.32 for the critical shallow surface and 1.31 for the critical deep failure surface.

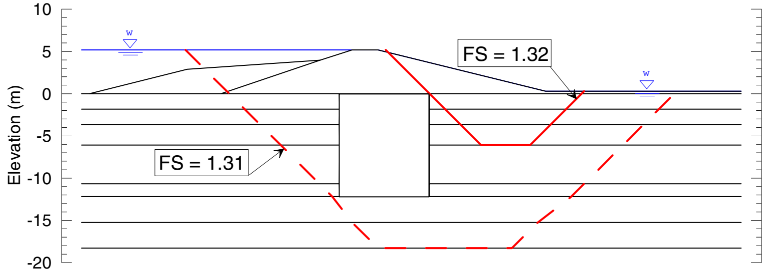

FIG 2. Limit-Equilibrium Results, Method of Planes Critical Surfaces

Limit-Equilibrium Analyses using Spencer's Method

The computer program UTEXAS3 was used to search for critical circular and non-circular surfaces. The analyses were performed using Spencer's Method, which satisfies both force and moment equilibrium and allows for non-horizontal inclination of the interslice forces. For circular surfaces, the minimum calculated factor of safety is 1.53 for a shallow failure surface located downstream of the DMM columns. For a deeper mode involving the DMM columns, the minimum computed factor of safety is 1.65. For non-circular surfaces, the minimum calculated factor of safety values are lower than for circular surfaces: 1.32 for a shallow failure downstream of the DMM columns and 1.51 for a deeper failure surface below the DMM treated zone. The critical non-circular surfaces, which represent the lowest factors of safety identified for shallow and deep failure modes using Spencer's Method, are shown in Figure 3.

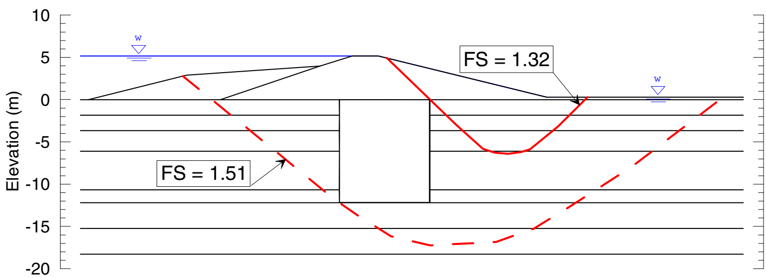

FIG 3. Limit-Equilibrium Results, UTEXAS3 Critical Surfaces

NUMERICAL ANALYSES

Numerical analyses were completed using the finite difference computer code FLAC (ITASCA 2005). Factors of safety were calculated using an automated procedure in the FLAC program, which reduces the shear strength of all of the materials in the model by a uniform reduction factor until the program is not able to satisfy convergence criteria in a limited number of iterations. The factor of safety is the smallest reduction factor at which convergence is not achieved.

Vertical joints were included in the DMM improved zone in order to model potential weak joints between columns. The possibility of weak vertical joints at column overlaps is discussed in the Japanese and Scandinavian literature (CDIT 2002, Broms 2003) and is also recognized in U.S. practice (Allen Sehn, personal communication, 2005). In addition to a reduction in the composite strength due to the reduced width of the wall at the overlap locations, the strength at the column overlap could be further reduced by misalignment during construction. The influence of strength achieved at the column overlap on stability of the system was evaluated by varying the joint strength over a range extending from that corresponding to the full design mixture strength applied to the full design column overlap (100% efficiency) and that corresponding to no overlap between the columns (0% efficiency).

The vertical joint strength corresponding to 100% efficiency was determined based on the width of the shear wall at the location of the design column overlap (47 cm chord length for 80 cm diameter columns at a 64.8 cm center-to-center spacing). Because peak strengths in the DMM treated ground would be expected to develop at much smaller strains than those corresponding to peak strength in the existing site soils between the DMM panels, the strength of the existing site soils was neglected in establishing composite vertical joint strength for 100% efficiency. Based on a design shear strength for the DMM mixture of 345 kN/m^2, the composite strength on vertical planes at the column overlaps for 100% efficiency is 76 kN/m^2, determined as follows: (47 cm)(345 kN/m^2)/(213 cm) = 76 kN/m^2.

The joint strength corresponding to 0% efficiency is the representative soil strength of 13.4 kN/m^2 in the DMM treated zone. This condition corresponds to no overlap between columns. The vertical joint strength for intermediate efficiencies is obtained by interpolation between the values for 0% and 100% efficiencies.

The joints were modeled by assigning FLAC's "Ubiquitous Joint" model to selected columns of elements within the DMM improved zone and assigning a vertical orientation for the reduced strength. On any other plane within the Ubiquitous Joint elements, the full composite strength of 110 kN/m^2 applies. The DMM improved material between vertical joints was modeled using the full composite strength of 110 kN/m^2 in all directions. Analyses were performed using 5 and 8 equally spaced vertical joints to investigate the influence of the number of such weak joints on values of factor of safety.

100% Efficiency of Vertical Joints at all Locations

For 100% efficiency of vertical joints, the computed factors of safety are summarized in Table 3, and shear strain contours that illustrate the failure modes are shown in Figure 4. As indicated in Table 3 for 100% efficiency, the numerical analyses resulted in computed factors of safety similar to those calculated using limit equilibrium analyses. For the shallow failure surface that passes downstream of the DMM columns, the shape of the failure surface in Figure 4a is similar to the shallow failure surface determined by limit-equilibrium analyses in Figure 3. For a deep failure mode, the numerical analyses indicate a more complex failure mode in Figure 4b than the deep failure surface determined using limit-equilibrium analyses in Figure 3, with rotation and translation of the DMM treated zone occurring in the numerical analyses. Nevertheless, the values of factor of safety for the deep failure mode from limit equilibrium and numerical analyses are the same for this case.

Table 3. Comparison of FS from Limit-Equilibrium and Numerical Analyses

	Minimum Factor of Safety	
Analysis Case	**Limit-Equilibrium**	**Numerical Analyses**
100% Efficiency of Vertical Joints:		
Shallow Failure Surface	1.32	1.33
Deep Failure Surface[a]	1.51	1.51
0% Efficiency of Vertical Joints:		
Shallow Failure Surface	1.32	1.29
Deep Failure Surface[a]	1.51	1.37

[a] "Deep Failure Surface" refers to failure surfaces that involve significant translation, rotation, and/or racking of the DMM treated zone.

0% Efficiency of Vertical Joints at Five Locations

For 0% efficiency of vertical joints, i.e., only the native soil strength due to no overlap between columns, at five locations, the computed factors of safety are summarized in Table 3, and shear strain contours that illustrate the failure modes are shown in Figure 4. For the shallow failure mode shown in Figure 4c, the results of the numerical analyses show a slightly reduced value of factor safety, and a relatively minor influence of racking of the columns. For the deep failure mode shown in Figure 4d, the numerical analyses show significant racking of the columns, and a more significant decrease in the value of the factor of safety, compared to the case with 100% efficiency of vertical joints.

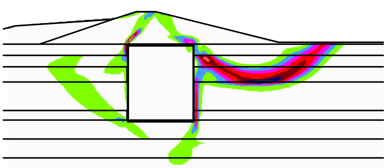

FIG 4a. Shallow Surface (FS=1.33) 100% Efficiency of Joints

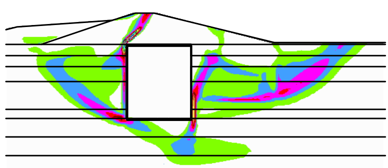

FIG 4b. Deep Surface (FS=1.51) 100% Efficiency of Joints

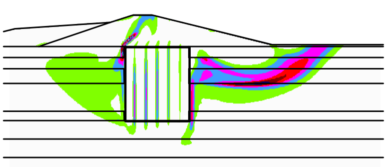

FIG 4c. Shallow Surface (FS=1.29) 0% Efficiency, 5 Vertical Joints

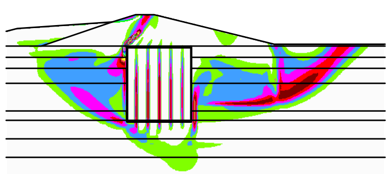

FIG 4d. Deep Surface (FS=1.37) 0% Efficiency, 5 Vertical Joints

FIG 4. Numerical Analyses Results, FLAC Failure Modes

Sensitivity Analysis for Efficiency of Vertical Joints

Sensitivity analyses of the factor of safety for deep failure modes were completed for vertical joint strengths corresponding to different efficiencies ranging from 0% to 100%. The results are summarized in Figure 5, and they show a decrease in the calculated value of factor of safety with decreasing efficiency of the vertical joints. This occurs because racking failure becomes more likely as the vertical joint efficiency decreases. The racking failure mechanism ceases to control performance at vertical joint efficiencies greater than or equal to 30%. It can also be seen that there is very little difference between the results for 5 and 8 vertical joints.

Sources in the literature suggest that vertical joint efficiencies on the order of 50% should be considered in design (CDIT 2002, Broms 2003). The results in Figure 5 indicate that, for the conditions used to represent the P24 levee project, there is no reduction in the value of factor of safety due to a reduction in the joint efficiency from 100% to 50%.

Figure 5 also shows the minimum values of factor of safety for deep failure surfaces obtained from limit equilibrium analyses using the Method of Planes and Spencer's Method. It can be seen that the results of the numerical analyses with vertical joint efficiencies greater than 30% are in exact agreement with Spencer's Method. It can also be seen that the Method of Planes produces a value of factor of safety less than the numerical analyses, even with a vertical joint efficiency of 0%.

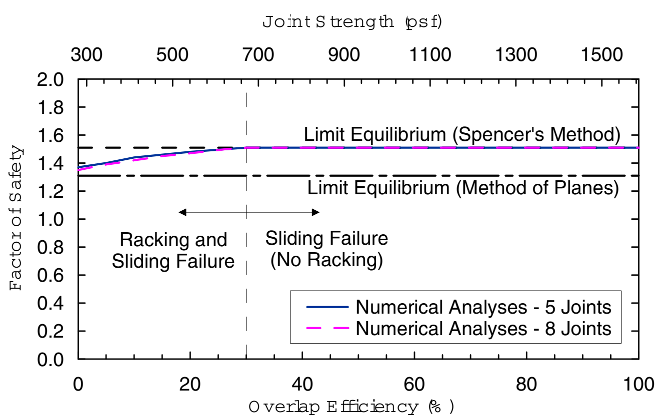

FIG 5. Factor of Safety Versus Joint Overlap Efficiency

CONCLUSIONS

The following conclusions can be drawn from the analyses described above, for the conditions used to represent the P24 levee project:

- The Corp's minimum factor-of-safety value of 1.32 using the Method of Planes for shallow failure surfaces is in exact agreement with the minimum value found by the non-circular search routine in UTEXAS3 using Spencer's Method.

- The Corp's minimum factor-of-safety value of 1.31 using the Method of Planes for deep failure surfaces is substantially less than the minimum value of 1.51 from the non-circular search routine in UTEAXS3 using Spencer's Method.
- Numerical analyses using FLAC show that the factor of safety values for predominantly shallow failure surfaces are only slightly dependent on the efficiencies of vertical joints between columns and are in good agreement with the results of the limit equilibrium analyses.
- For deep failure modes, the factor of safety from numerical analyses is in exact agreement with the results of the limit equilibrium analyses using Spencer's Method when the efficiency of vertical joints between columns is at least 30%. For joint efficiencies smaller than 30%, the factor of safety decreases with decreasing joint efficiency due to increasing influence of racking failure mode on the results. The deep mixing literature indicates that a vertical joint efficiency of about 50% should be used for design. At this efficiency, the factor of safety from numerical analyses is unaffected by the racking failure mode.
- The minimum factor-of-safety value of 1.31 from the Method of Planes for deep failure surfaces is less than the minimum factor-of-safety value from numerical analyses for deep failure surfaces, even for a vertical joint efficiency of 0%.
- Overall, it can be concluded that the Method of Planes produced conservative results for the conditions used to represent the P24 levee project in the limit equilibrium and numerical analyses described here. This conclusion is specific to the P24 project, and it should not be generalized to other projects.

ACKNOWLEDGMENTS

The authors acknowledge the important contributions of Mike Navin. The information presented in this paper is based on work supported by the U.S. National Science Foundation under grant No. DGE-0504196. Any opinions, findings, conclusions, and recommendations in this paper are those of the authors and do not necessarily reflect the views of the U.S. National Science Foundation.

REFERENCES

Barker, R. M., Duncan, J. M., Rojiani, K. B., Ooi, PSK, Tan, C. K., Kim, S. G. (1991). *Manuals for the Design of Bridge Foundations: Shallow Foundations,* NCHRP Report 343, Transportation Research Board, Washington, D.C.

Broms, B.B. (2003). *Deep Soil Stabilization: Design and Construction of Lime and Lime/Cement Columns*, Royal Institute of Technology, Stockholm, Sweden.

CDIT, Coastal Development Institute of Technology. (2002). *The Deep Mixing Method: Principle, Design and Constructions*, A.A. Balkema: The Netherlands.

Filz, G.M. and Navin, M.P. (2006). *Stability of Column-Supported Embankments*, Virginia Transportation Research Council Report No. 06-CR13, Richmond.

ITASCA Consulting Group (2005). *FLAC2D Fast Lagrangian Analysis of Continua, ITASCA Consulting Group*, Minneapolis.

Wright, S.G. (1991). *UTEXAS3: A Computer Program for Slope Stability Calculations,* Users Manual, Shinoak Software, Austin.

Stability of Levees over Soft Soil Improved by Deep Mixing Technology

Jie Han[1], ASCE Member, Zhenshun Hong[2], and Shuilong Shen[3]

[1] Associate Professor, Department of Civil, Environmental, and Architectural Engineering, the University of Kansas, Lawrence, KS 66045, USA, jiehan@ku.edu
[2] Professor, Institute of Geotechnical Engineering, Southeast University, Nanjing, Jiangsu Province 210096, China, zshong@seu.edu.cn
[3] Professor, Department of Civil Engineering, School of Naval Architecture, Ocean, and Civil Engineering, Shanghai Jiao Tong University, Shanghai 200030, China, slshen@sjtu.edu.cn

ABSTRACT: Stability of levees is critical to the safety of human and structures, especially at high water levels. Levees may fail due to the existence of soft soil foundations or seepage of water through the levees. Deep mixing technology has been considered one of the good alternatives to solve these problems. Studies have shown that deep mixed columns can increase the stability of highway embankments over soft soils. In those studies, however, no ponding water exists on either side of the embankment, which is not the case for levees. Experimental studies have shown that deep mixed columns under a combination of vertical and horizontal force could fail due to shear or bending or rotation. A finite difference method, incorporated in the FLAC (Fast Lagrangian Analysis of Continua) Slope software, was adopted in this study to investigate the stability of the levee with ponding water. In this study, deep mixed columns were installed in continuous wall patterns, which were modeled as 2-D deep mixed walls. Mohr-Coulomb failure criteria were used for the levee, the soft soil, and the deep mixed walls. The stability of a levee at different stages (end of construction, average service condition, and high water surge) was examined. The study clearly demonstrated that the deep mixed walls can enhance the stability of the levee by providing shear/moment resistance and hindering seepage through the levee.

INTRODUCTION

The recent levee breakage caused by Hurricane Katrina in August 2005 killed more than 1,000 people and were estimated to cost the U.S. Federal Government more than $200 billion (Cristo, 2005). Preliminary investigation concluded that levee breaches due to Hurricane Katrina were caused by the water overflow and erosion of the levee and seepage under the levee and weakening of underlying soil (Cristo, 2005). Hess et al. (2006) indicated that "a major flood or earthquake and resulting levee failure in the capital region of Sacramento alone would put at risk more than 400,000 people and 170,000 structures, with estimated potential damage of between $7 and $15 billion". The Sacramento Area Flood Control Agency (SAFCA) warns that Sacramento has a higher risk of flooding than most U.S. cities including New Orleans. SAFCA stated that "each year Sacramento has approximately a 1-in-100 chance of experience flood disaster". The combination of earthquake and high-tide may cause more severe damage to levees than it happens alone.

Ground improvement technologies, such as deep mixing (DM), vibrocompaction, compaction grouting etc., have been used to mitigate potential damage to levees. Deep mixing is an in situ ground improvement technique which mixes in situ soil with a cementitious agent (mainly cement slurry or powder) by augers to improve the engineering characteristics of the soil. Earlier studies have demonstrated that DM columns can increase the stability of highway embankments over soft soils (Han et al., 2005; Navin and Filz, 2006). Experimental studies have also showed that deep mixed columns under a combination of vertical and horizontal force could fail due to shear or bending or rotation (Kitazume et al., 2000). To date, however, there are no well recognized guidelines or design procedures available to design deep mixing for mitigating levee failures due to ponding water in front of levees, which is a critical situation as demonstrated by the recent levee breakage caused by Hurricane Katrina.

This paper presents a numerical study to demonstrate how DM technology can enhance the stability of levees at end of construction, average service condition, and high water surge.

NUMERICAL MODELING

Problems for Analysis

Levees at four different stages as listed in Table 1 and shown in Figure 1 were investigated in this study. In the analysis, the soft soil and the levee are either untreated or treated by a DM wall. The thickness of the DM wall is assumed to be 3m, which is the same as the width of the crest. In practice, it can be formed by DM columns in wall or grid patterns. The 3m thick DM wall is considered as a composite wall treated by deep mixing. This ground improvement approach can be used for the construction of new levees but is more feasible for the mitigation of existing levees if they are determined as unstable under an untreated condition. The water at the mid-height of the levee with steady seepage is considered as the average service condition in this study. The surging water at the full height of the levee but with steady seepage still at the previous average service stage is considered as a special event in which water rises suddenly from the mid-height to the full height due to flood, hurricane, etc. The water at the full height of the levee with steady seepage established at the current condition is considered as the situation in which the surging water is maintained at the highest level for a certain period. The time needed to reach this stage directly depends on permeability and cross-section of the levee, the core material, and the drainage system if any. The DM wall in the core of the levee and the foundation can act as a barrier to slow down the establishment process of a new steady seepage line because the permeability of soil-cement mixture is typically one order or more lower than untreated soil (Han et al., 2002b).

Table 1. Stages Considered in the Analysis

Stage	Condition	Description
1	End of Construction	No water involved and no consolidation of soft soil considered during the construction
2	Average Service Condition	Water at the mid-height of the levee (steady seepage established)
3	Water Surge to Top	Surging water at the full height of the levee (steady seepage still at Stage 3)
4	Highest Water Level Service	Water at the full height of the levee (steady seepage established at the current condition)

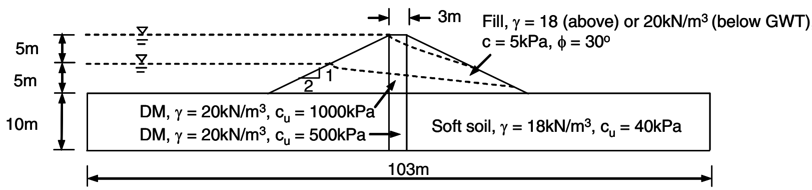

FIG. 1. Levee for Analysis

The free surface lines shown in Fig. 1 were determined based on a theoretical solution for seepage through an earth dam on an impervious base, which can be found in many geotechnical engineering textbooks, such as Das (2001). It was assumed that the soft soil had much lower permeability than the levee fill, therefore, the theoretical solution can be applied.

Geometry and Material Properties

Figure 1 presents the geometry and dimensions of a selected levee for analysis in this study. The cross-section of the levee meets the basic requirements by US Army Corps of Engineers (2000). The 10m high levee was built on the 10m thick soft soil underlain by a firm soil layer or bedrock. The levee had 2:1 slopes on both sides. The crest of the levee was 3m.

The physical and mechanical properties of the soft soil and the levee fill are presented in Figure 1. The soft soil was considered failing under an undrained condition. The fill below or above the ground water table had a different unit weight but the same strength values. Due to the difference in the properties of the soft soil and the fill, the DM wall within the soft soil and the fill had different strength values. These strength values will vary from project to project, however, they are used herein for demonstration purposes.

Factor of Safety

In recent years, numerical methods have been increasingly used for analyzing slope stability including the computation of its factor of safety (FoS). Dawson et al. (1999) indicated that the FoS value of unreinforced slopes obtained using the finite difference method in the FLAC software were in good agreement with those using the limit equilibrium method with a log-spiral slip surface. Han et al. (2002a) used the same finite difference software (FLAC) to obtain the identical corresponding FoS values of unreinforced and geosynthetic-reinforced slopes as the Bishop's simplified method. However, Han et al. (2005) found that the limit equilibrium method may overestimate the factor of safety for embankments over soft soil improved by DM walls, especially when the DM walls fail due to bending or rotation rather than shear. Therefore, the numerical method incorporated in the FLAC Slope 5.0 can be used for this analysis (Itasca Consulting Group, Inc., 2006).

In the finite difference program, a shear strength reduction technique was adopted to solve for the FoS value of slope stability. Dawson et al. (1999) exhibited the use of the shear strength reduction technique in this finite difference program. In this technique, a series of trial FS values were used to adjust the cohesion, c and the friction angle, ϕ, of soil as follows:

$$c_{trial} = c / FoS_{trial} \tag{1}$$

$$\phi_{trial} = \arctan\left(\tan\phi / FoS_{trial}\right) \tag{2}$$

Adjusted cohesion and friction angle of soil layers were used in the model for equilibrium analysis. The factor of safety was determined by adjusting the cohesion and friction angle to make the slope become unstable from a verge stable condition or verge stable from an unstable condition.

ANALYSIS OF NUMERICAL RESULTS

Stage 1 – End of Construction

Figure 2 presents the maximum shear strain rates and the factors of safety for levees at end of construction over untreated and treated foundations calculated by FLAC. It is shown that the untreated case had typical circular slip surfaces. Two slip surfaces formed the bearing capacity wedge failure mode. For the treated case, however, there was no continuous slip surface, which was also found by Han et al. (2005) and Navin and Filz (2006) when they analyzed embankments over soft soils. The existence of the DM wall stopped the development of a continuous slip surface. Figure 2 also shows that the factor of safety increased from 1.43 for the untreated case to 1.65 for the treated case. US Army Corps of Engineers (2000) recommended that new levees should have an FoS greater than 1.3 at end of construction and 1.4 for long term (steady seepage). Therefore, the factors of safety for both untreated and treated cases are satisfactory at end of construction.

Stage 2 – Average Service Condition

Figure 3 presents the numerical results for levees at an average service condition (i.e., water at mid-height) over untreated and treated foundations. In both untreated and treated cases, steady seepage was assumed for a long-term condition. For the untreated case, a clear circular slip surface can be identified and the slide was towards the landside. For the treated case, no continuous slip surface can be identified, however, there was a tendency for a slide developing in front of the DM wall towards the landside. Figure 3 also shows that the factor of safety increased from 1.38 for the untreated case to 1.58 for the treated case. The factors of safety for both cases meet the requirements for long term recommended by US Army Corps of Engineers (2000). Comparing Fig. 3 with Fig. 2, it is clearly shown that the factors of safety at the average service condition are less than those at end of construction due to the rise of the water table at the riverside and the seepage through the levee.

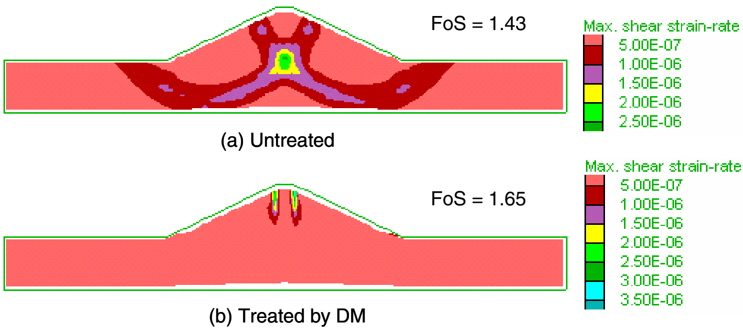

FIG. 2. Stability at the End of the Levee

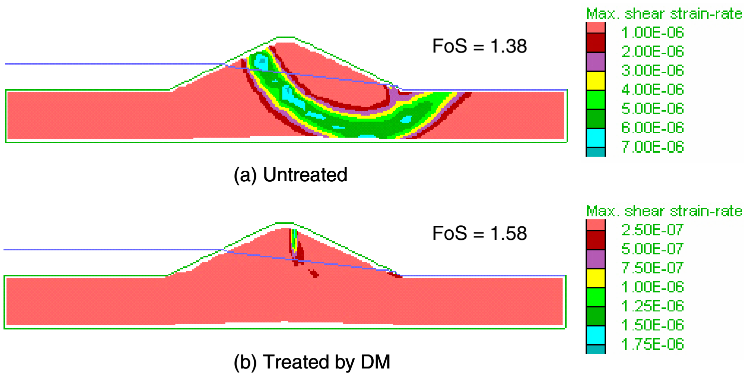

FIG. 3. Stability at the Average Service of the Levee

Stage 3 – Water Surge to Top

Water surge typically occurs during a special event, such as flood, hurricane, etc. so that the rise of water table is within a very short period. In this analysis, the water table at the riverside was assumed to rise from the mid-height to the full height but the water table under the crest and at the landside was assumed to remain at the same elevation as that in Stage 2. Similar to Stage 1 and Stage 2, a clear circular slip surface can be identified for the untreated case but not for the treated case. As shown in Fig. 5, large shear zones developed in front and behind the DM wall and tension developed behind the DM wall, which indicates the development of a bending or rotation failure of the DM wall. As Han et al. (2005) pointed out, however, shear failure may develop through the DM wall if the strength of the DM wall is relative low. The factors of safety for the untreated and treated cases at this stage are 1.17 and 1.27, respectively. This comparison confirms that the DM wall still plays a role in stabilizing the levee. It is obvious that water surge reduced the factors of safety for the levee. US Army Corps of Engineers (2000) did not specify the requirements for a water surging condition, however, the required factor of safety for a rapid drawdown case is 1.0 to 1.2. Therefore, the factor of safety for the untreated case in Fig. 4 should be high enough to ensure the temporary stability of the levee during the water surge.

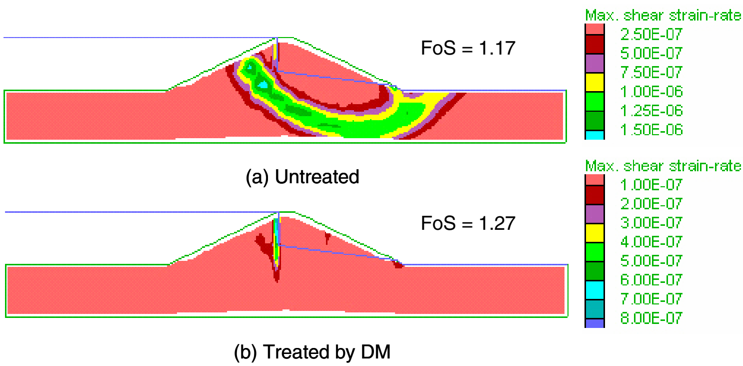

FIG. 4. Stability at the Water Surge to Top of the Levee

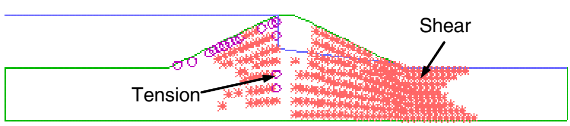

FIG. 5. Plasticity Indicators for the Treated Case

Stage 4 – Highest Water Level Service

Stage 6 represents a condition under which the highest water level is maintained long enough to develop steady seepage in the levee. This condition may happen for the untreated case but unlikely for the treated case if the DM wall is properly designed, constructed, and maintained since the DM wall can be much impermeable than the levee. However, if the DM wall is not well constructed, such as leaking, or rupture due to soil movement, it may lose its function as a barrier. In addition, water overflow may saturate the fill on the landside. Under these circumstances, the ground water table at the landside for the treated case may also rise to that high elevation. Figure 6 shows that the untreated and treated cases had almost identical factor of safety (note: the marginal difference in FoS is within the numerical error) since the failure mostly developed in front of the DM wall. It is also shown that the high water table due to seepage at the landside drove the factor of safety below 1.0. In other words, the levee at the landsite would fail first and then the whole levee would break. The rise of the water table in the levee due to seepage and overflow was one of the key factors causing the failure of the levee in New Orleans during Hurricane Katrina (Cristo, 2005).

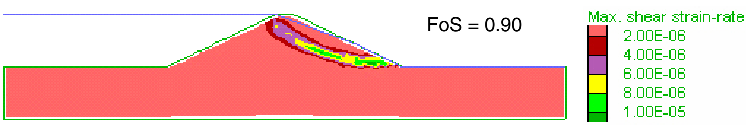

(a) Untreated

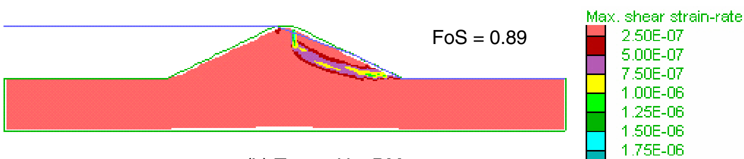

(b) Treated by DM

FIG. 6. Stability at the Highest Water Level Service of the Levee

CONCLUSIONS

This numerical analysis clearly shows that deep mixing (DM) technology can enhance the stability of the levee above the soft soil. The main contributions of the DM wall in the core of the levee and the foundation are to provide shear/moment resistance and hinder/slow down the rise of water table in the landside due to seepage. No continuous slip surface could be identified in numerical results for the treated case and the DM wall might fail under bending or rotation when the DM wall is strong.

REFERENCES

Cristo, R. (2005). “Researchers learn from Katrina disaster.” *The Record - News*, October 19.

Das, B.M. (2001). *Principles of Geotechnical Engineering*, 5th edition, Thomson Learning, 589p.

Dawson, E.M., Roth, W.H., and Drescher, A. (1999). “Slope stability analysis by strength reduction.” *Geotechnique* 49(6), 835-840.

Han, J., Leshchinsky, D., and Shao, Y. (2002a). “Influence of tensile stiffness of geosynthetic reinforcements on performance of reinforced slopes.” *Proceedings of Geosynthetics – 7th ICG*, Delmas, Gourc & Girard (eds), Swets & Zeitlinger, Lisse, 197-200.

Han, J., Parsons, R.J., Sheth, A.R., and Huang, J. (2005). “Factors of safety against deep-seated failure of embankments over deep mixed columns.” *Proceedings of Deep Mixing 2005 Conference*, Sweden, Vol. 1.2, May 23-25, 231-236.

Han, J., Zhou, H. T., and Ye, F. (2002b). “State of practice review of deep soil mixing techniques in China.” *Journal of the Transportation Research Board*, No. 1808, Soil Mechanics 2002, Transportation Research Board of the National Academies, 49-57.

Hess, J.R., Sills, G.L., Costa, R., Shewbridge, S. (2006). “California’s levees at risk.” *Geo-Strata*, November/December, 24-28.

Itasca Consulting Group, Inc. (2006). *FLAC/Slope User’s Guide*, Version 5.0, 84p.

Kitazume, M., Okano, K., and Miyajima, S. (2000). “Centrifuge model tests on failure envelope of column type deep mixing method improved ground.” *Soils and Foundations*, 40(4).

Navin, M.P. and Filz, G.M. (2006). “Numerical Stability Analysis of Embankments Supported on Deep Mixed Columns.” ASCE Geotechnical Special Publication, Ground Modification and Seismic Mitigation, Proceedings of GeoShanghai International Conference, 1-8.

US Army Corps of Engineers (2000). *Design and Construction of Levees*. Engineering Manual (EM 1110-2-1913), 77p.

A Case Study: Levee Geotextile Reinforcement to Reduce ROW Acquisition and Borrow Quantity

John M. Siwula[1], P.E., Member ASCE and Scott A. Breen[2], P.E., Member ASCE

1 Principal Geotechnical Engineer, HNTB Corporation, 11414 W. Park Place, Suite 300, Milwaukee, WI. 53224-3526, PH (414) 410-6857;FAX (414) 359-2315; email:jsiwula@hntb.com
2 Geotechnical Engineer, HNTB Corporation, 11414 W. Park Place, Suite 300, Milwaukee, WI. 53224-3526, PH(414) 410-6706; FAX (414) 359-2315; email:sbreen@hntb.com

Abstract: Post-Katrina levee enlargement in greater New Orleans, LA is required to provide increased storm protection. Hero Canal levee in Plaquemines Parish is part of an improvement plan that will include levee enlargement, new levee and floodwalls. Typically, levee improvements in the area are accomplished using non-reinforced earthen embankments extended beyond existing levees. The existing grades will need to be raised and levee stability issues develop due to the underlying low strength soil. The resulting levee cross-sections without geotextile reinforcement were wider than the current design alignment and required additional Right of Way (ROW). Acquisition of ROW is expensive and normally expands the time needed for levee construction. Obtaining suitable borrow material is more difficult since Katrina. The enlarged levee sections needed substantial borrow quantities. Geotextile reinforcement was incorporated in the levee design to reduce the lateral extent of levee enlargement, which lessened the ROW acquisition and borrow quantity. Single and multiple layers of geotextile were used to maintain stability. Use of geotextile reinforced levees resulted in a savings of approximately 121,410 square meters (30 acres) of ROW and 11,553 cubic meters (408,000 cubic yards) of borrow.

Introduction

Levee enlargements are required in post-Katrina New Orleans, LA to provide increased protection during storm events. A United States Army Corps of Engineers (USACE) feasibility report in 1994 examined additional hurricane surge protection to areas of Jefferson, Orleans, and Plaquemine parishes. For the area to the east of the Algiers Lock, the report recommended raising the existing protection along the Algiers and Hero Canals and the construction of a new levee near Oakville to connect to the Hero Canal levee and to the existing Plaquemines Parish levee.

Project Description

The project location is shown on the Vicinity Map as Figure 1. The Hero Canal levee has a length of 5,822 meters (19,100) feet and will be enlarged to satisfy grade increases associated with revised Hydrology and Hydraulic analyses. Initial designs indicated that additional ROW and large quantities of earth borrow would be needed for the improvements. It was desired to reduce borrow and ROW for the levee enlargement. Storm events for 2007 and 2057 are the basis of the design. The existing levee was last upgraded (1st Lift) around 1998, to a project design grade at EL.2.1 meters (7.5 feet). This current project repairs and upgrades the Hero Canal 1st Lift by increasing the project grade elevations. The new design grade for 2007 is EL.4.0 meters (EL. 13.0 feet) and a corresponding construction grade at EL. 4.3 meters (EL. 14.0 feet) to counteract expected settlement. The 2057 design grade is EL. 4.6 meters (EL. 15.0 feet) and a construction grade at EL.4.9 meters (EL.16.0). The authorized design section of the levee is 1 vertical on 3 horizontal on both of the side slopes with a 3.05 meter (10 feet) wide crown. A wave berm with an approximate side slope of 1 vertical on 6 horizontal was used on the flood side throughout the length of the levee. The final levee location was determined using the existing levee centerline as the desired enlargement centerline and then adjusting the new centerline towards the protected side in order to optimize the use of the existing ROW.

Subsurface Conditions

Sixteen soil borings were drilled and twelve Cone Penetration Test (CPT) probes were advanced for this project. The borings and probes extended to 24 meters (80 feet) below the ground surface. The borings generally encountered fat clay (CH) with medium stiff to soft consistency. Layers of lean clay (CL), silt (ML), and silty sand (SM) were also present. Relatively thin layers of organic peat (PT) deposits were encountered in three borings generally between 4.3 and 6.7 meters (14 and 22 feet) below the surface. Wet unit weights ranged between 11.93 and 16.33 kN/m ^{3} (76 and 104 pounds per cubic foot (pcf)) in the upper 21 meters (68 feet) and increased up to 19.0 kN/m ^{3} (121 pcf) below that depth. Cohesion values ranged between 5.5 to 46.4 kPa (113 to 950 pounds per square foot (psf)). Figure 2 is a typical design shear strength profile.

The CPT reported soil conditions were generally consistent with the boring information. Organic material was reported in four locations at variable depths. The CPT cone tip resistance values varied from less than 97 kPa (2000 psf) to approximately 17,035 kPa (350,000 psf). The CPT sleeve friction values and undrained shear strength values ranged from approximately 9.7 kPa to greater than 58 kPa (200 to1,200 psf).

Water was not encountered during drilling. Based on the water content test data along with the CPT data, the water table was considered to be at approximately 0.3 to 3 meters (1 to 10 feet) below the surface (EL+1.07 to -1.22 meters) at the time of the exploration.

Stability Analysis

For the embankment slopes, the design criteria required use of the Mississippi Valley Division (MVD's) Method of Planes (MOP) Slope Stability with Uplift Computer Program that uses a Block and Wedge force equilibrium solution. The computed factor of safety (FS) was determined by summing the horizontal resisting forces and dividing by the horizontal driving forces.

Input for the analysis included geometry of the cross-section, soil stratification, and soil parameters of each stratum as determined by HNTB and reviewed by the USACE. The geometry of the ground surface, including the levee profile, was surveyed at each cross-section location.

The new embankment fill section was variable in height to meet the 3.3 meter (10-feet) crown, and the final side slopes as provided by the USACE. The system was checked for a minimum factor of safety for the Flood Side and Protected Side with sections including stability berms if required, for the following three cases; High Water Level, Still Water Level and Low Water Level. Design water surface elevations were provided by the USACE and are presented in Table1.

Table 1 – Design Water Surface Elevations

Location	High Water Level (HWL)	Still Water Level (SWL)	Flood side Low Water Level (Hero Canal Side)
2007 Enlargement	4.0	2.3	0.0
2057 Enlargement	4.6	2.3	0.0

If the new levee cross-sections had factors of safety below the minimum required FS for the respective analysis condition for the 2007 or 2057 design water levels using the short term soil strength parameters, then the cross-sections were modified with the addition of a geotextile reinforcement to improve stability. Single or multiple layers of geotextile were used to satisfy the stability requirements with geotextile strengths ranging from 2.95 to 14.75 kN/meter (4,000 to 20,000 pounds per foot). If the addition of geotextile reinforcement alone did not provide the minimum safety factor, then additional embankment fill (stability berm) was added for an acceptable factor of safety. SLOPE/W software (GeoStudio 2004®) was initially used in a force equilibrium analysis mode to demonstrate agreement with the Corps MOP Program and then in a moment equilibrium analysis mode (Spencer's method) to check the geotextile reinforced embankment stability. The stability runs for the 2057 enlargement were also performed to evaluate the effect on ROW, so that acquisition of ROW can be planned in the future. In analyzing both the 2007 and the 2057 design water levels, geotextile reinforcement design was developed to satisfy the more stringent of the two design year conditions. If a higher strength geotextile was required for the 2057 design, that geotextile was incorporated in the 2007 design to gain efficiency in the initial construction process. Additional field investigation and stability analyses will be required in the future for the 2057 design as the subsurface conditions will change after the 1st enlargement in 2007 is completed. Table 2 summarizes the safety factors obtained from the SLOPE/W analysis with a geotextile. The factor of safety for the MOP analysis without the geotextile was typically on the order of 1 before the addition of the geotextile was used to increase the safety factor.

Geotextile reinforcement was utilized in all locations to reduce the extent of ROW to be purchased and borrow material for the project. In order to get the most efficient use of geotextile reinforcement, the geotextile material needs to have sufficient embedment in the embankment. Therefore, the geotextile was placed generally at the base of the existing levee for increased overburden pressure. A minimum of 0.91 meter (3 feet) of soil cover on the geotextile is also needed per COE New Orleans District guidelines.

TABLE 2 – Slope Stability Safety Factors

Cross Section Analyzed and Design Year	Case A: HWL; SLOPE/W Software (w/Geofabric)	Case B: SWL; SLOPE/W Software (w/Geofabric)	Case C: Floodside Check; SLOPE/W Software (w/Geofabric)
	Calculated FS (1.2 req.)	Calculated FS (1.3 req.)	Calculated FS (1.3 req.)
Sta 106+30/2007	N/A	N/A	1.31
Sta 106+30/2057	1.22	1.43	1.30
Sta 136+30/2007	1.28	1.30	1.56
Sta 136+30/2057Berm	1.33	1.41	1.43
Sta 156+30/2007	1.21	1.35	N/A
Sta 156+30/2057	1.23	1.33	N/A
Sta 216+30/2007	1.38	1.42	N/A
Sta 216+30/2057Berm	1.29	1.48	N/A
Sta 236+30/2007	1.26	1.50	N/A
Sta 236+30/2057	1.33	1.33	N/A

Figure 3 indicates a typical lateral extent of the levee improvements for the 2007 and 2057 design cases. The use of geotextile typically did not require a stability berm and therefore the extent of ROW needs for the improvements was reduced. For the 2057 condition, the geotextile reinforced levee had a significantly reduced section compared to the nonreinforced levee.

ROW and Borrow Quantity Impacts

The use of geotextile reinforcement beneath the levee enlargement results in a reduced width of the levee and in some instances did not require a stability berm at the toe of the levee. If a stability berm was needed, the geotextile resulted in a reduced extent of the stability berm. The use of geotextile reinforcement reduced the lateral extent of the levee by approximately 8 to 43 meters (24 to 140 feet). This reduced levee section resulted in economy for the design. The information presented in Table 3 presents the additional ROW and borrow required for the case where the levee was enlarged and a geotextile was not used.

Table 3 ROW and Borrow for NonGeotextile Reinforced Levee

Additional ROW Area Needed for Levee without geotextile	Additional Borrow Quantity for Levee without geotextile
121,410 square meters (30 acres)	11,553 cubic meters (408,000 cubic yards)

Conclusions

Based on the analysis performed, use of geotextile reinforcement for the Hero Canal levee improved the slope stability safety factors to acceptable values compared to factors of safety without reinforcement. The reinforcement resulted in savings of approximately 121,407 meters (30 acres) of additional ROW and 11,553 cubic meters (408,000 cubic yards) of clay borrow material. The reduction in ROW will reduce the amount of time required for the ROW acquisition and the cost associated with the levee enlargement. This allows increased protection to Plaquemines Parish in a reduced timeframe.

Acknowledgements

The authors acknowledge the New Orleans District of the United States Army Corps of Engineers for giving permission to present on this project. Additionally, Mr.Shung Chiu and Mr. Ellsworth Pilie of the USACE were helpful in the course of the project.

References

Stability with Uplift Computer program, 2001, U.S. Army Corps of Engineers, New Orleans District, by Robert Jolissaint

SLOPE/W Slope Stability software program by GeoStudio 2004®

Appendix I. Conversion to SI Units

1 foot (ft) = 0.3048 meters (m)
1 acre = 4046.856 square meters (m^2)
1000 pounds per square foot = 47.88 kilopascals (kPa)
2000 pounds = 8.896 kilonewtons (kN)

Appendix II, Figures

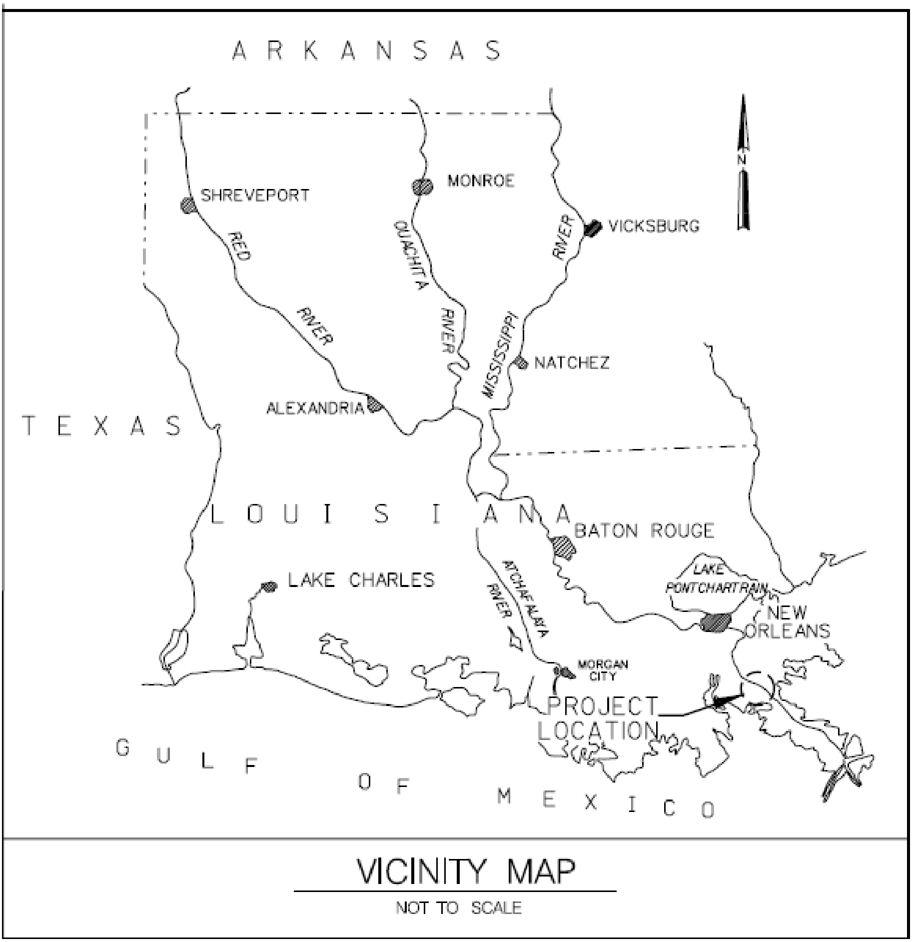

Figure 1 – Vicinity Map

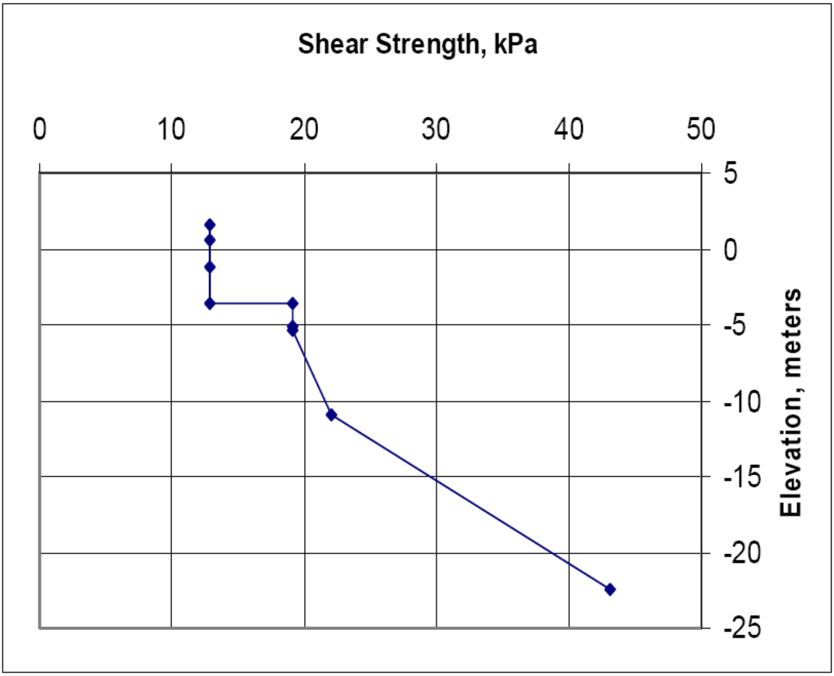

Figure 2 – Design Shear Strength Profile

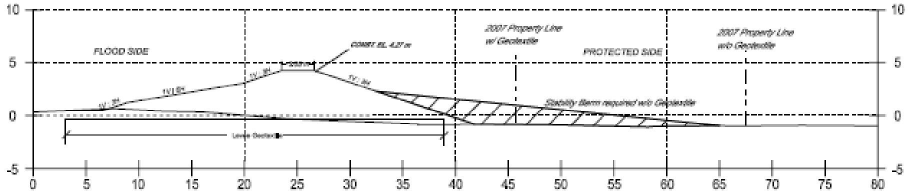

2007 Condition

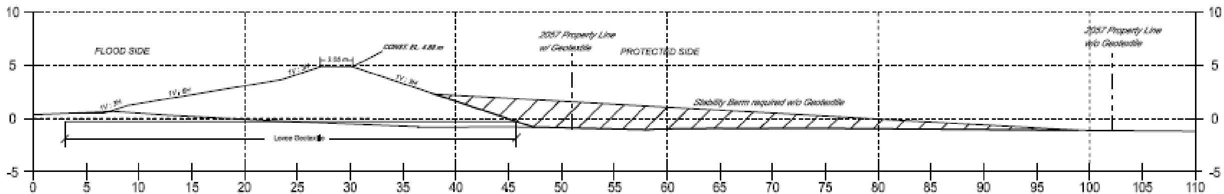

2057 Condition

Figure 3 - Levee Improvements with and without Geotextile Reinforcement

Analytical modelling of pull-out tests on geosynthetic straps

Abdelouhab A.[1-2], Dias D.[1], Freitag N.[2], Bourdeau Y.[1], Kastner R.[1]

[1] Laboratory of Civil Engineering, Inst. Natl. Sci. Appl. Lyon, Domaine Scientifique de la Doua, F-69621 Villeurbanne cedex – France
[2] Terre Armée Internationale, 1 bis, rue du Petit-Clamart – 78140 Vélizy-Villacoublay – France

ABSTRACT: The reinforcements used in Reinforced Earth structures are most commonly made of ribbed steel strips or of geosynthetic straps. The behaviour of the later is more complex, due to their extensibility. However, the design methods used for the geosynthetic straps are based on a classical friction model. This simple model considers the same design assumptions for the geosynthetic straps as for inextensible reinforcements and does not take into account the strap progressive mobilization. If this is justified for the justification of the structure stability, the detailed behaviour is supposed to be different. To highlight the influence of the synthetic reinforcement extensibility, several pull out tests were carried out on Geostraps developed by *Terre Armée Internationale*. These tests allow us to monitor the imposed tension as well as the displacements of several points along the strap. Then, back analyses of these results using an analytical model allowed to define the interaction parameters between the soil mass and the synthetic reinforcements.

1 INTRODUCTION

In aggressive environments, geosynthetic straps based on high-tenacity polyester, which exhibit some relative elongation, are used for the Reinforced Earth® structures. The design methods created for the structures reinforced by metallic reinforcements and thus inextensible were brought to be extrapolated to extensible materials. The difference in behaviour of these two types of reinforcement induces the definition of elongation limits beyond which the behaviour of the structure may be different. In order to adapt and to improve these methods, a better knowledge of the interaction between the soil mass and the reinforcement strips seems necessary.

Most of the design methods used for the structures reinforced by geosynthetic straps are developed from the friction models based on the soil/geosynthetic interface friction model (Cambefort type, Fig. 2) and on the tensile-load linear elasticity of the inclusion (resulting from the Hooke's law, Fig. 1). This article presents an analytical method for analysing the pull-out tests on synthetic straps. This method is based on the classic friction laws (Schlosser & Guilloux 1981, Segrestin & Bastick 1996) and permits to reproduce the variation of tensile-load and displacements along the reinforcement strip. Back analysis of the analytical model on the experimental results allows us to validate this analytical development.

2 ANALYTICAL FRICTION MODELS DEVELOPMENT

The friction model permits to determine the tensile-load/displacement relationship and the mobilized deformation along a pulled-out reinforcement. The determination of the friction model requires the knowledge of the tensile-load model T - ε of the constitutive material and of the local friction model τ - U.

The tensile-load relation is supposed to satisfy the Hooke's law T = J ε (Fig. 1). The parameters of this model are the tensile-load T, the deformation ε, and the inclusion stiffness J. These parameters are supposed to be identical over the entire length of the reinforcement. The ground-inclusion interface friction relation is assumed to be of Cambefort's type (Fig. 2). Limit friction τ*, displacement U* are the parameters which characterize this constitutive model.

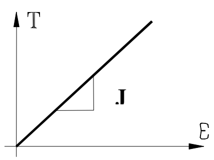

FIG. 1. Tensile-load model.

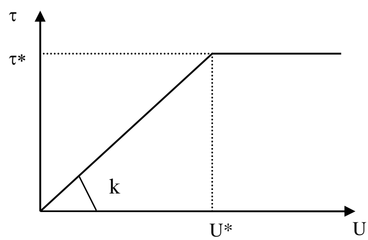

FIG. 2. Local friction model.

2.1 Analytical description of the delayed extension mechanism starting from the friction model and the tensile-load model

To consider the dilatancy in the tensile strain calculation (shear stress), Schlosser (1981), Segrestin and al. (1996) and other authors represented the friction model by the graph f - U (f is the friction parameter, $f = \dfrac{T}{\sigma_v pl}$). Then, starting from this point, the analytical development for pull-out test and displacements has been adapted to the synthetic straps.

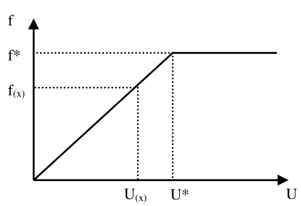

FIG. 3. Local friction law.

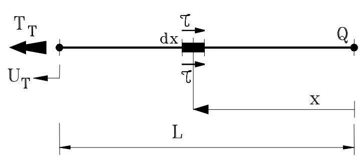

FIG. 4. Strip modelling.

The mobilization of a reinforcement subjected to head loads is divided into three stages. For each stage, one can calculate the tension and the displacement along the strip (Segrestin and Bastick, 1996).

1st stage $U_T < U^*$: the strap is in a mobilization state.

The inclusion is positively directed from the end Q towards the head T (Fig. 4). Along an element length dx, the elementary tensile-load is given by equation (0).

$$dT(x) = pf(x)\sigma_v dx \qquad \textbf{(0)}$$

From Fig. 3, we deduce the relation (1).

$$\frac{dT(x)}{dx} = \frac{pf^*\sigma_v}{U^*}U(x) \qquad \textbf{(1)}$$

The local deformation ε(x) at the position x is calculated from the inclusion tensile-load model (Fig. 1).

$$\frac{dU(x)}{dx} = \frac{T(x)}{J} = \varepsilon(x)$$

$$\frac{d^2T(x)}{dx^2} = \frac{1}{\rho^2}T(x) \qquad \textbf{(2)}$$

with $\rho = \sqrt{\dfrac{JU^*}{pf^*\sigma_v}}$

The general solution of differential equation (2) leads to equation (2bis).

$$T(x) = Ash(x/\rho) + Bch(x/\rho) \qquad \textbf{(2bis)}$$

Applying the initial conditions, for x = 0, T = 0 we obtain B = 0 (2ter).

$$T(x) = Ash(x/\rho) \qquad \textbf{(2ter)}$$

At the reinforcement head x = l, $T = T_T$; we can write equations (3) and (4).

$$T_T = Ash(l/\rho) \quad \text{hence } A = \frac{T_T}{sh(l/\rho)}$$

$$T(x) = T_T\frac{sh(x/\rho)}{sh(l/\rho)} \qquad \textbf{(3)}$$

$$U(x) = \frac{\rho T_T}{J}\frac{ch(x/\rho)}{sh(l/\rho)} \qquad \textbf{(4)}$$

2nd stage $U_T > U^*$, $Uq < U^*$:

In this stage, the reinforcement is divided in two parts (Fig. 5), a part at the head (x > x *) where the friction is completely mobilized and a part at the rear (x < x *), the friction is in mobilization state.

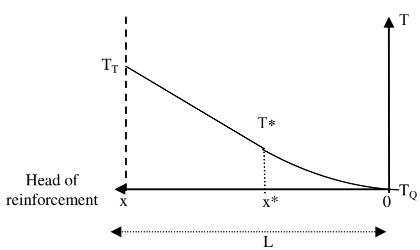

FIG. 5. Tensile-load variation along the reinforcement.

<u>Zone 1. x >x*</u> T* and x* evolve with the evolution of the pull-out load and with displacement at the head, these two variables are determined by the equations (6bis) and (6ter).	$dT(x) = pf * \sigma_v dx$ and $\frac{dU(x)}{dx} = \frac{T(x)}{J}$ $T(x) = T * + pf * \sigma_v (x - x*)$ **(5)** $U(x) = U * + \frac{T*}{J}(x - x*) + \frac{pf * \sigma_v}{J}(x - x*)^2$ **(6)** $T* = \frac{JU*}{\rho} th(x*/\rho)$ **(6bis)** $\frac{pf * \sigma_v}{J}(l - x*)^2 + \frac{U*}{\rho}(l - x*) th(x*/\rho)$ **(6ter)** $-(U_T - U* = 0$
<u>Zone 2. x < x*</u> In this zone (see Fig. 5), we can apply the equations developed in the 1st stage, where the reinforcement length would be l = x* and the head tensile-load $T_T = T*$.	$T(x) = T * \frac{sh(x/\rho)}{sh(x*/\rho)} = \frac{JU*}{\rho}\frac{sh(x/\rho)}{ch(x*/\rho)}$ **(7)** $U(x) = \frac{\rho T*}{J}\frac{ch(x/\rho)}{sh(x*/\rho)} = U * \frac{ch(x/\rho)}{ch(x*/\rho)}$ **(8)**
<u>3rd stage Ui > U*, Uq < U*:</u> The strap is entirely released.	
$T(x) = pf * \sigma_v x$ **(9)** $U(x) = U_T - \frac{pf * \sigma_v}{J}(l^2 - x^2)$ **(10)** with $U_T = \frac{pf * \sigma_v l^2}{J} + Uq$	

3 EXPERIMENTAL TESTS

The tests were carried out on Geostraps anchored in a test tank filled with sand (Fig. 6). The test tank has large inner dimensions: 1.10 m width, 1.10 m height and 2.0 m length. To apply a surcharge on the sand, an air cushion is used between the top of sand and the cover plate. The reinforcements are made of geosynthetic strips containing high-tenacity polyester yarns protected by a low density polyethylene sheath. The dimensions of these strips are: 50 mm width and 2 mm thickness. In these tests, two parallel Geostraps of 1.9 m length spaced by 50 mm are anchored in the tank. *Terre Armée Internationale* makes use of these straps for the fully synthetic Omega® system. The advantage of this system lies in the fact that it does not make use of any structural metallic elements at the connection (thus corrodible) between the concrete facing and the reinforcement strips, for applications in aggressive environments, which are outside the standard limits of galvanised steel applicability.

The material used in the tests is fine dense sand known under the name of Hostun RF. Its principal characteristics are: granulometry (mm) 0.16-0.63, density 1.32 - 1.59 and friction angle 38°. Various authors have studied this sand (Gay 2000, Gaudin 2002).

Two types of incremental position sensors were used, wire sensor and LVDT sensors. They allow measuring displacements of the strip. To measure the tensile force, an annular load sensor is placed at the end of the pull out jack.

In order to control the density of the sand set up and to simulate the reconstitution of a sandy ground formed by sedimentation, a pluviation method is used (Fig. 7). It is defined as a technique of granular sample reconstitution by material discharge.

FIG. 6. Test tank.

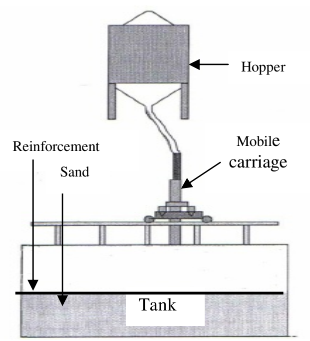

FIG. 7. Pluviation system.

4 THEORETICAL METHODS APPLICATION ON THE EXPERIMENTAL TESTS

To apply the theoretical method on experimental tests, it is necessary to know the characteristics of the reinforcements (stiffness of the reinforcement J and friction law). We deduce U^* and f^* from the experimental curve of the displacements versus tensile-load at the head of the strap (Fig. 8). Then, this model allows us to determine displacements along the strip (Fig. 9) by applying analytical equations.

Several tests were carried out with a different vertical stress and the analytical method was applied to these experimental tests. The results presented in this paper have been obtained from pull-out tests where the applied vertical stress is equal to 100 kPa. They allow us to determine the tension load, the maximum friction parameter mobilized as well as the displacements in several points of the strips.

The reinforcement behavior analysis shows that the tension in the strip is gradually mobilized as the tension applied at the strip's head increases. Friction is thus mobilized gradually along the strip and a displacement at the head is requested at the beginning for low tensile stresses (see experimental results, Fig. 8 and 9). This behaviour is anticipated by Segrestin & Bastick (1996).

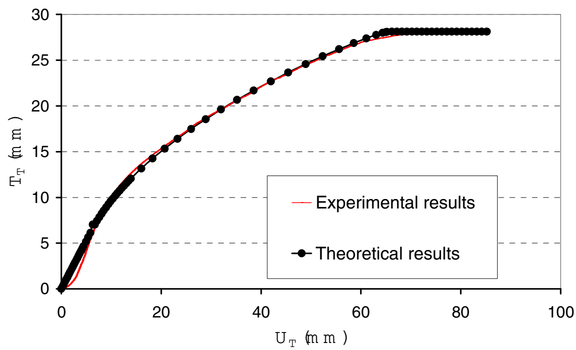

FIG. 8. Displacements versus tensile-load at the head of the strap.

In order to check the validity of the analytical method, we have compared the analytical results with the experimental values (Fig. 8 and 9). First, the curves of head displacements versus tensile-loads (Fig. 8) show that the analytical values are in good agreement with the experimental results. The analytical method thus allows us to model correctly the displacements at the inclusion head. Then, displacements along the strip versus displacement at the head show that the analytical method reproduces well the progressive mobilization of the reinforcement. However, this method considers a mobilization of the entire strip at the beginning of tension (see curves UT-UQ, Fig.9). That does not correspond to the experimental results, where the rear point only moves when friction is saturated around the head of the tested strip.

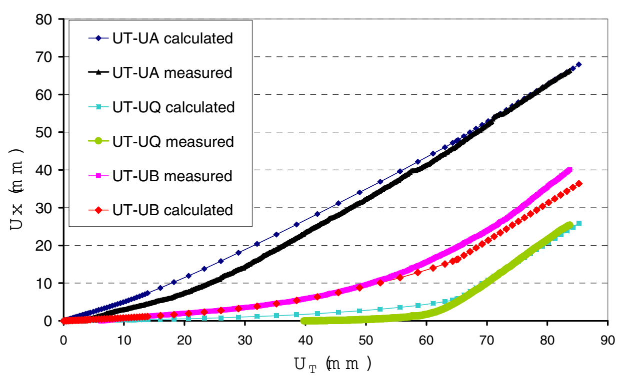

FIG. 9. Comparison between experimental results and modelling of the displacements along the strip.

Figure 9 shows that there is some discrepancy in the experimental results and the analytical model. Indeed, this difference is related to the fact that the behaviour of the synthetic strap is supposed to be elastic linear. This assumption does not correspond to reality.

The stiffness J chosen in the theoretical calculations does not exactly correspond to the real stiffness given by the manufacturer. We chose the more adapted one to have better theoretical curves. It is necessary also to note that the theoretical stiffness changes according to the applied vertical stress in the test. For the test presented in this paper (applied vertical stress equal to 100 kPa), the calculation stiffness taken is equal to 450 kN whereas the real stiffness given by the manufacturer is equal to 560 kN. A higher theoretical stiffness (650 kN) was selected for a pull-out test under a vertical stress equal to 75 kPa. The value of the theoretical stiffness is thus variable, it is necessary to carry out an experimental study which permits to determine the real stiffness J according to the imposed strain.

In addition, the tests results show that for an applied vertical stress equal to 100 kPa, the measured friction parameter f* is equal to 0.74 knowing that for the same conditions that parameter used in structures design is close to 0.7.

5 CONCLUSIONS

The design methods used for the structures reinforced by the synthetic reinforcements are based on classical friction models (developed from models like "Cambefort" type and the linear elastic tensile-load model). These relations allow us to model correctly the displacements at the inclusion head and the progressive mobilization of the reinforcement as we have showed in this article. However, the theoretical model shows a friction mobilisation on the entire length of the geosynthetic reinforcement and a non-null displacement at the rear at the beginning of the head loading. The results of the pull-out tests on synthetic straps are not in agreement with this assumption and show a null displacement at the rear's strap at the beginning of the pull out test. The analytical method used here seems then to be too simple to take into account all the complexity of the interaction between the ground and the synthetic reinforcement.

Back analysis of the analytical models on the experimental results shows that the theoretical friction model permits to well reproduce displacements at the head. That is not the same for the local displacements case. Thus, it is necessary to measure local displacements in each test to check the validity of a new model to be developed and which can describe the progressive mobilization of a strap.

Several laboratory tests on synthetic reinforcements are planned for the current year. These tests will permit to finely study the synthetic reinforcement behavior subjected to a tensile-load. The tests will be carried out under various vertical stresses. They allow us to simulate the vertical stresses applied in various depths of a real earth reinforced structure. Then an instrumentation of these types of structures will be carried out to validate the laboratory tests. Finally, a numerical part of the research will allow us to better understand the influence of various parameters and to use a new structure safety approach.

6 NOTATION

J : geosynthetic stiffness (N/m)
L : reinforcement length (m)
L* : length of reinforcement embedded in resistance zone (m)
T_T : applied tensile force at the head of reinforcement
T_x : applied tensile force at x point of reinforcement
U : local displacement
U* : reinforcement displacement corresponding to total mobilisation of friction
U_T : displacement at the head of reinforcement
U_Q : displacement at the rear of reinforcement
U_A : displacement of the point located at 0.4 m from the head of reinforcement
U_B : displacement of the point located at 1.2 m from the head of reinforcement
dx : infinitesimal element length along soil-reinforcement interface (m)
p : reinforcement perimeter (m)
σ_v : vertical stress applied on the reinforcement (kPa)
γ : bulk unit weight (N/m3)
τ : interface shear stress (N/m2)
τ^* : maximum of sol/reinforcement interface shear stress (N/m2
ε : local deformation
ε_0 : initial deformation threshold

7 REFERENCES

Alimi, Bacot, Lareal, Long, Schlosser, (1977). "Etude de l'adhérence sol-armature." *Proc. of the 9th Int. Conf. on Soil Mechanics and Found. Eng*. Tokyo.

Bollo-Kamara, N. Bourdeau, Y. Bahloul, F. and Ogunro, V. (1995). "A study of friction mobilization at a soil/geotextile interface using a bi-dimensional analogic model." *Geosynthetics Conference*, Nasshville, USA V.3 :1071-1082.

Bourdeau, Y. Kastner, R. Bollo-Kamara, N. and Bahloul, F. (1990). "Comportement en ancrage d'un géosynthétique enfoui dans un matériau bidimensionnel." *5ème colloque Franco-Polonais de Mécanique des sols Appliquée*, 4-7 septembre 1990.

Frank, R. and Zhao, S.R. (1982). "Estimation par les paramètres pressiométriques de l'enfoncement sous charge axiale de pieux forés dans les sols fins." *Bulletin de liaison des Laboratoires des Ponts et Chaussées,* 1982, N° 119 : 17-24.

Lo, S.R. (2003). "The influence of constrained dilatancy on pullout resistance of strap reinforcement." *Geosynthetics international*, 10, No. 2: 47-55.

Martinez, L. Novelli, B. (2006). "Renforcement des sols par inclusions souples, approche expérimentale de laboratoire." *Projet d'initiation à la recherche et développement, LGCIE, INSA Lyon,* p. 52.

Schlosser, F. Guilloux, A. 1981, "Le frottement dans le renforcement des sols", *Revue française de géotechnique*, n° 16, pp. 65-77.

Segrestin, P. and Bastick, M. (1996). "Comparative Study and Measurement of the Pull-Out Capacity of Extensible and Inextensible Reinforcements." *Earth Reinforcement, Ochiai*: 81-86.

Enhancement in the Interface Shear Resistance
Achieved by a Novel Geogrid with In-Plane Drainage

Brendan C. O'Kelly[1] and Patrick J. Naughton[2]

[1]Lecturer in Civil Engineering, Department of Civil, Structural and Environmental Engineering, Trinity College Dublin, Dublin 2, Ireland; bokelly@tcd.ie
[2]Lecturer, School of Engineering, Institute of Technology, Sligo, Ireland; naughton.patrick@itsligo.ie

ABSTRACT: The enhancement in the interface shear strength achieved in the short-term by a novel geogrid, which combines both reinforcement and in-plane drainage functions, was studied. Marginal fill material (wet gravelly clay) was standard Proctor compacted to achieve 92% of its maximum dry unit weight and tested in the large shearbox apparatus under consolidated-undrained conditions. Overall, the interface shear resistance ($\tau_{s\text{-}g}$) values mobilized for the novel geogrid were similar to the undrained shear strength of the test soil itself. In contrast, the $\tau_{s\text{-}g}$ values mobilized for a conventional geogrid, which had similar physical and tensile strength properties, were between only 82 and 85% of the undrained shear strength of the test soil. The benefit is that the increase in the interface friction angle (achieved by in-place drainage along the novel geogrid) will facilitate the use of some marginal fills, which may already be readily available onsite, in the construction of earth structures.

1. INTRODUCTION

Earth structures (embankments and slopes) are traditionally constructed using suitable fill material that is placed and compacted to within 95% of its maximum dry unit weight achieved under standard Proctor compaction. Free-draining, high shear strength materials including gravel and sand are acceptable for use under any circumstances. Soils that contain less than 15% fines (percentage by weight passing the 0.063-mm sieve) are generally considered as suitable fill since these materials can be pre-drained if their water contents are too high. The fill material is generally placed and compacted in lifts, between 0.25 and 0.30 m in thickness, with at most 1.0-m depth of fill being placed in any given 24-hour period.

There is an economic benefit in using marginal fill (wet cohesive fill) that may already be readily available onsite rather than importing suitable fill material.

Marginal fill is defined as a predominantly granular material that includes high silt and/or clay fractions, and often has high water contents (typically only 90 to 95% of its maximum dry unit weight can be achieved under standard Proctor compaction).

The shear strength of the marginal fill may be reduced during the construction phase (short-term) due to the increase in the excess pore water pressure (generated during compaction of the poorly draining fill) and the increase in the total applied stress due to its self-weight. Geosynthetics can be included in the embankment core to provide reinforcement (geogrids) and/or preferential drainage channels (geosynthetics) thereby increasing its factor of safety against global and local instability. It is generally accepted that geogrids reinforce mainly through interlocking with adjacent soil. However, the angle of interface friction value mobilized by conventional geogrids is lower than the angle of shearing resistance value of the soil itself. Hence, in analyzing the factor of safety against slope instability where potential slip surfaces can align themselves along the soil-geosynthetic interface, the lower shear resistance value mobilized along the soil-geosynthetic interface must also be considered.

This paper studies the enhancement in the interface shear resistance that is achieved in the short-term (critical case in for example embankment construction) for a wet gravelly, clay fill material using a novel geogrid that combines both reinforcement and in-plane drainage functions. Kempton et al. (2000) and Zornberg and Kang (2005) reported the experimental results of dissipation and pullout tests on the novel geogrid in English China Clay (for σ_v = 50 kPa) and wet gravelly clay (σ_v = 41 kPa), respectively, which indicated that the mobilized interface shear resistance was about 30% greater than that mobilized for a conventional geogrid with similar physical and tensile strength properties. A series of consolidated-undrained large shearbox tests were conducted in the present study over the range of applied normal stresses typically associated with earth embankments between 5 and 10 m in height.

2. MATERIALS

2.1 Soil

The test soil was Brown Dublin Boulder Clay (Skipper et al., 2005); a gravelly clay of low plasticity (liquid limit of 31%, plastic limit of 16%, and plasticity index of 15%) that had a natural water content value of about 11%, and a specific gravity value of 2.70. Standard Proctor compaction tests, carried out on the material using a CBR compaction mould, indicated a maximum dry unit weight of 1.84 tonne/m^3, which corresponded to an optimum water content for compaction of about 13.0% (Fig. 1).

2.2 Geosynthetics

The novel geogrid (Paradrain^{TM}) comprised two elements, namely: (i) flexible reinforcement straps that had been profiled to provide in-plane drainage channels; and (ii) drainage elements (non-woven geotextile that had been bonded to the shoulders of the drainage channels (Fig. 2). The reinforcement straps (33-mm wide and 2.5-mm thick in cross-section, and 75-mm pitch in the reinforcing direction) comprised polyester fibers that were enclosed in a smooth polyethylene sheath that had a characteristic tensile strength of 150 kN/m (main reinforcement). It should be noted that there are other products available that simultaneously serve both reinforcement and drainage functions.

A conventional smooth biaxial geogrid (Paragrid™) that had the same physical and tensile strength properties was also tested in the shearbox apparatus as a basis for comparison. Further details on the properties of these geosynthetics are available from the manufacturer, Linear Composites Limited (2007), or in the literature (Kempton et al. 2000; Zornberg and Kang 2005).

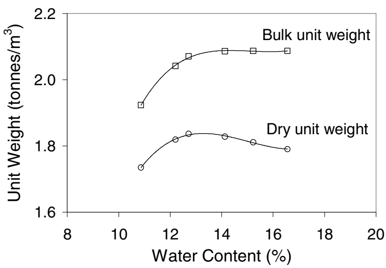

FIG. 1. Standard Proctor compaction.

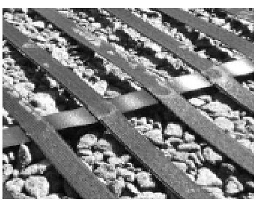

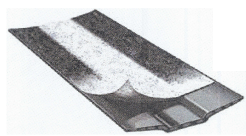

(a) Conventional geogrid (Paragrid™) (b) Novel geogrid (Paradrain™)

FIG. 2. Geogrid test materials (Linear Composites Limited, 2007).

3. EXPERIMENTAL METHOD

3.1 Test Program

A series of consolidated-undrained tests were conducted using the large shearbox (300 by 300-mm in plan and 150-mm in depth) in accordance with ASTM D5321 (2002) in order to measure the development of the shear resistance over a range of applied normal stresses (σ_v = 111–222 kPa), including:

- Five tests on the soil alone;
- Five tests shearing the soil over conventional geogrid attached to aluminum plate;
- Five tests shearing the soil over the novel geogrid attached to an aluminum plate;
- Five tests shearing the soil over an aluminum plate.

3.2 Specimen Preparation

The geogrid specimens were attached to a smooth aluminum plate (300 by 300-mm in plan) that was located flush with the shear plane at the mid-height of the shearbox, and with its main reinforcement straps aligned in the direction of shear (Fig. 3). Both the novel and conventional geogrids were essentially fully fixed (bonded to the aluminum plate using a water-proof adhesive and fixed at one end of the plate using three screw fasteners) which prevented elongation of the geogrid specimens. The novel geogrid specimens were secured such that their drainage (geotextile) element was in contact with the soil that was contained in the upper half of the shearbox (Fig. 3). The screw fasteners were necessary since some of the geogrid specimens became detached during trial shearing tests when only the adhesive had been used to form the bond.

The straps of the novel and conventional geogrid specimens covered about 56 and 58% of the plate surface area, respectively (greater than the 50% coverage recommended by Koerner (1998)). The soil was in direct contact with the aluminum plate over the remaining areas. New geogrid specimens were prepared and secured to the aluminum plate at the start of each test.

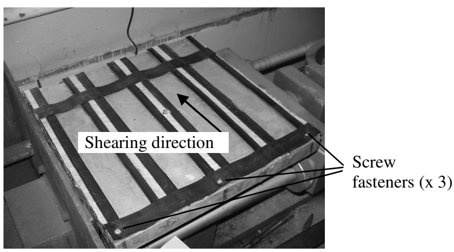

FIG. 3. Novel geogrid straps secured to aluminum plate.

The gravelly clay material was disaggregated to pass the 20-mm sieve size and the larger-sized solid particles were removed, which accounted for about 11% of its bulk mass. Distilled water was added to the soil, increasing its water content to about 16.5% (exceeding the optimum water content for compaction by 3.5%), and the mixture was allowed to equilibrate overnight. In this state, the test soil is categorized as a marginal fill material. All of the shearbox specimens had the same initial water content value and were imparted the same level of compaction during specimen preparation. A known mass of the wet soil was placed and compacted in the upper half of the shearbox in three layers of equal thickness, with each layer being imparted 25 blows of a steel tamper (75 by 100-mm in face area) to obtain a dry unit weight of 1.68 tonne/m^3 (92% of the maximum dry unit weight achieved under standard Proctor compaction), and an air voids content of 8%.

3.3 Shearbox Tests

A normal stress was applied to the specimen via the serrated loading platen in contact with the top of the soil specimen. The soil was allowed to consolidate under the applied stress over a period of between 18 and 24 hours before shearing commenced to simulate in the geotechnical laboratory the construction sequence whereby the fill material is placed and compacted in stages onsite, and allowed to consolidate during the intervening periods.

The consolidation properties of the soil could not be determined by applying curve-fitting techniques to the measured compression versus time responses since the soil was in a partially saturated state ($S_r \cong 78\%$). However, drainage and hence dissipation to the pore-air voids of the excess pore water pressure that had been generated under the applied stress would have been substantially complete for the novel geogrid by the end of the 18 to 24 hour consolidation period. This has been shown experimentally by Kempton et al. (2000) by continuous measurement of the excess pore water pressure response during dissipation and pullout tests on the novel geogrid in English China Clay.

The specimens were then sheared quickly in order to determine the shear resistance values mobilized over the different interfaces under undrained conditions. The soil contained in the upper half of the shearbox was displaced relative to the geogrid specimen that had been fixed to the aluminum plate, which was located flush with shear plane) in the bottom half of the shearbox. Although the soil specimens were in a partially saturated state, the displacement rate of 0.25 mm/minute effectively produced undrained shear conditions (Koerner (1998), Koutsourais et al. (1991), amongst others). Reinforced earth embankments are typically 5 to 10 m in height so the different interfaces were tested in the shearbox apparatus under applied normal stresses in the range σ_v = 111–222 kPa.

4. EXPERIMENTAL RESULTS AND ANALYSIS

The shearbox results were analyzed in terms of the total stress condition since the pore pressure response was unknown during the shearing stage. However, drainage and hence the dissipation of the excess pore pressures to the pore-air voids resulted in increasing shear resistance with increasing applied normal stress. The Mohr-Coulomb failure line of best fit for the soil itself gave c = 35 kPa and $\phi = 26^o$ (peak values mobilized at between 7 and 9% strain); where c is the apparent cohesion and ϕ is the angle of shearing resistance (total stress condition). Similar analysis for the soil-aluminum plate interface, and using the shear resistance values mobilized at 8% strain gave a = 5 kPa, and $\delta = 20^o$; where a is the apparent adhesion and δ is the angle of interface friction (total stress condition).

Figure 4 shows the plots of the shear resistance mobilized against the horizontal displacement for the combined soil-geogrid-aluminum plate interface. The tests were be terminated at the limiting horizontal displacement of 45 mm (15% strain) of the shearbox apparatus The plots have a characteristic shape with most of the interface shear resistance was mobilized by about 9 mm horizontal displacement (3% strain), although the shear resistance continued to increase steadily without reaching a peak value. Zornberg and Kang (2005) reported similar constitutive behavior from pullout tests on the novel geogrid in a wet gravelly clay.

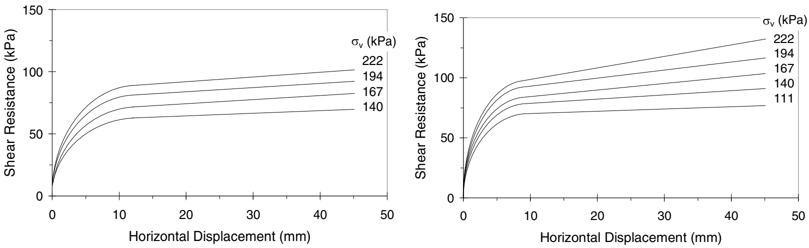

(a) Conventional geogrid. (b) Novel geogrid.

FIG. 4. Shear stress versus horizontal displacement for soil-plate-geogrid interface.

Figure 5 shows the undrained interface shear resistance ($\tau_{s\text{-}g}$) that would have been mobilized for the soil-geogrid combination (more representative of the in-service field conditions). The interface resistance plots in Fig. 4 were adjusted using Eq. (1) which takes into account that over the shear plane, the soil specimen had been in contact with the aluminum plate on 42 or 44% of the shear area instead of the soil shearing on itself, as occurs in the in-service field condition. The contribution of interface interlock (gravelly clay particles and geogrid straps) to the mobilized shear resistance was not significant since the shearing occurred in the direction of the main reinforcement straps.

$$\tau_{s\text{-}g} = \tau_{s\text{-}p\text{-}g} + [(\tau_{s\text{-}s} - \tau_{s\text{-}p})(1 - A_g)] \quad (1)$$

where $\tau_{s\text{-}p\text{-}g}$ is the shear resistance mobilized along the combined soil-plate-geogrid interface; $\tau_{s\text{-}s}$ is the shear resistance of the soil itself; $\tau_{s\text{-}p}$ is the shear resistance mobilized along the soil-aluminum plate; and A_g is the fraction of the plate surface area that had been covered by the geogrid reinforcement straps.

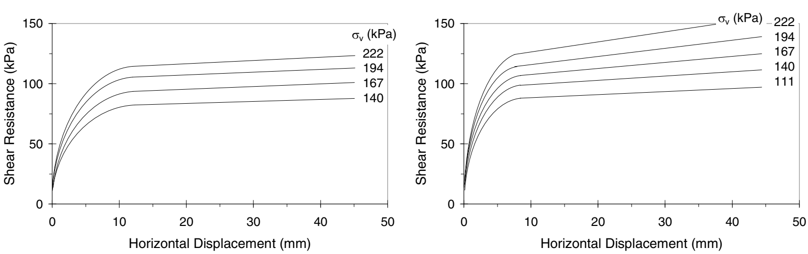

(a) Conventional geogrid. (b) Novel geogrid.

FIG. 5. Interface shear resistance versus horizontal displacement for soil-geogrid.

Figure 6 shows the $\tau_{s\text{-}g}$ interface resistance values calculated for the novel and conventional geogrids at 5, 7.5 and 10% strains (relative horizontal displacements of 15, 22.5 and 30 mm). The $\tau_{s\text{-}g}$ values have been normalized by the corresponding shear resistance values of the soil itself ($\tau_{s\text{-}s}$). The 5 to 10% strain range was chosen since the undrained shear strength of the soil had been fully mobilized by about 8 to 9% strain.

The $\tau_{s\text{-}g}$ interface shear resistance for the novel geogrid was dependent both on the stress and strain levels, reducing slightly with increasing applied normal stress (Fig. 6), Overall, the $\tau_{s\text{-}g}$ values mobilized at 10% strain were for practical purposes the same as the undrained shear strength of the soil. However, the ratio of the $\tau_{s\text{-}g}$ to $\tau_{s\text{-}s}$ values mobilized for the conventional geogrid at 10% strain was only about 82%. This indicates that for the in-service field condition, slippage along the interface between the soil and conventional geogrid is more likely to occur rather than shear failure of the soil itself, and this failure mechanism must be considered in analyzing the factor of safety against slope instability where potential slip surfaces can align themselves along the soil-geosynthetic interface. Figure 6 also indicates that the ratio of the $\tau_{s\text{-}g}$ to $\tau_{s\text{-}s}$ values is somewhat strain level dependent, with the ratio reducing slightly with increasing strain.

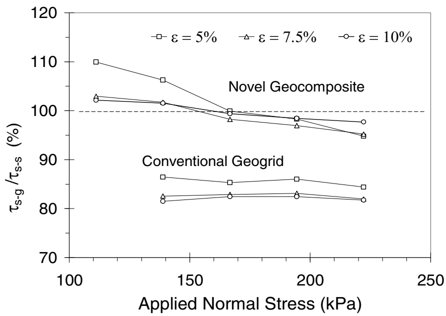

FIG. 6. Normalized undrained interface shear resistance.

5. DISCUSSION

The novel geogrid performed considerably better than the conventional geogrids (which had similar tensile strength properties) for the wet marginal fill material tested, in agreement with other studies by Zornberg and Kang (2005) and Kempton et al. (2000). The excess pore pressures generated in the vicinity of the geogrid reinforcement straps dissipate rapidly along its in-plane drainage channels (Kempton et al. 2000). A higher state of effective stress, and hence a higher shear resistance, is achieved in the immediate vicinity of the shear zone, thereby enhancing geotechnical stability particularly in the short term. Furthermore, the construction of earth structures (embankments and slopes) using wet marginal fill material becomes feasible with the inclusion of the novel geogrid. The novel geogrid significantly reduces the time required for primary consolidation of the wet fill material to occur, thereby reducing the construction time. In contrast, the interface shear resistance of the conventional geogrid reduces to only about 82 to 85% of the undrained shear strength of the soil itself due to the build up in the excess pore pressure that occurs during shearing, and the smoother geogrid surface.

6. SUMMARY AND CONCLUSIONS

The enhancement in the short-term interface shear strength achieved by a novel geogrid, which combines both reinforcement and in-plane drainage functions, was studied. The test soil (marginal fill) was a wet gravelly clay (c = 35 kPa and $\phi = 26^o$ from large shearbox tests) that had been compacted to obtain 92% of its maximum dry unit weight achieved under standard Proctor compaction, and its water content value exceeded the optimum water content for compaction by 3.5%. The soil specimens were consolidated over a period of between 18 and 24 hours in the large shearbox apparatus and sheared quickly (undrained condition).

Overall, the shear resistances values ($\tau_{s\text{-}g}$) mobilized along the novel geogrid-soil interface were similar to the undrained shear strength of the soil itself. The excess pore pressures (generated on applying the normal stress and subsequent shearing) dissipated rapidly along the in-plane drainage channels in the geogrid reinforcement straps, thereby achieving a high shear resistance in the immediate vicinity of the shear zone. In contrast, the $\tau_{s\text{-}g}$ values mobilized for the conventional geogrid (with similar physical and tensile strength properties) were only between 82 and 85% of the undrained shear strength of the soil. The benefit of the novel geogrid is that the increase in the interface friction angle achieved by its in-place drainage capability facilitates the use of some marginal fills in the construction of earth structures.

7. ACKNOWLEDGEMENTS

The authors would like to acknowledge Martin Carney, John Kenna and Paul Creaven who performed the shearbox tests at the Geotechnical Laboratories, Trinity College Dublin. This paper was written by the lead author while on sabbatical leave at the Urban Institute Ireland, University College Dublin.

8. REFERENCES

ASTM D5321 (2002). Standard test method for determining the coefficient of soil and geosynthetic or geosynthetic and geosynthetic friction by the direct shear method. ASTM International, Pennsylvania, USA.

Kempton, G.T., Jones, C.J.F.P., Jewell, R.A. and Naughton, P.J. (2000). "Construction of slopes using cohesive fills and a new innovative geosynthetic material." *Proc. 2nd European Geosynthetics Conference (EuroGeo 2)*, 15–18 October, Bologna: 825–828.

Koerner, R.M. (1998). Designing with Geosynthetics, Prentice Hall.

Koutsourais, M.M., Sprague, C.J., and Pucetas, R.C., (1991). "Interfacial friction study of cap and liner components for landfill design." *Geotextiles and Geomembranes* 10 (5–6): 531–548.

Linear Composites Limited (2007). Product Data sheets. Available at www.linear composites.co.uk

Skipper, J., Follett, B., Menkiti, C.O., Long, M., and Clark-Hughes, J. (2005). "The engineering geology and characterization of Dublin Boulder Clay." *Quarterly J. Engineering Geology and Hydrogeology* 38 (2): 171–188.

Zornberg, J.G. and Kang, Y. (2005). "Pullout of geosynthetic reinforcement with in-plane drainage capability." *Proc. ASCE Geo-Frontiers*, 24–26 January, Austin, Texas (available on CD).

Performance of Geogrid Load Transfer Platform over Vibro-Concrete Columns

Raymond Mankbadi[1], P.E., M. ASCE, Jack Mansfield[2], P.E., M. ASCE and Aravinda Ramakrishna[3], P.E., A. M. ASCE.

[1] Director of Geotechnical Engineering, Hardesty & Hanover, LLP., 850 Bear Tavern Road, suite 206, West Trenton, NJ 08628.
[2] Manager, Geotechnical Unit, New Jersey Department of Transportation, 1035 Parkway Avenue, Trenton, NJ 08625.
[3] Geotechnical Engineer, Hardesty & Hanover, LLP., 850 Bear Tavern Road, suite 206, West Trenton, NJ 08628.

ABSTRACT: A case history involving the use of geogrid transfer platforms over Vibro-Concrete Columns (VCC) to support approach embankments on soft ground is presented The Route 52 Causeway reconstruction project in Ocean City, New Jersey involves the replacement of existing bridges, approximately two miles long, which cross Great Egg Harbor between Somers Point on the New Jersey mainland and Ocean City on the barrier island. Proposed reconstruction involves staged construction of the two-mile long crossing, which will replace the existing four structurally deficient and geometrically obsolete bridges with new bridges and roadway embankments on tidal-marsh islands with a complex depositional history.

The project involves the installation of VCC that support approximately 8-m-high (24-ft-high) mechanically stabilized earth walls underlain by a geogrid reinforced-sand platform. The design concept of the embankment supporting system is outlined. A comparison between two methods (British Standard vs. Collin's) for the design of the platform is discussed. The result of a Statnamic Load Testing performed on one VCC is also presented. The performance of the embankment supporting systems is assessed based on monitoring data obtained from various instruments installed during construction including settlement platforms and inclinometers. In addition, a comparison of case histories between geogrids and geotextile load transfer platforms is presented, drawing from a similar experience in a former project. Finally, conclusions are presented regarding the design aspects of the geosynthetic-reinforced load transfer platform and VCC.

INTRODUCTION

This paper describes the case history of roadway-embankment construction on tidal-marsh islands with a complex depositional history in the Route 52 Causeway Project. Furthermore, this paper presents a comparison of case histories between the performance of geogrid and geotextile load transfer platform based on our similar experience in a former project.

The existing Route 52 Causeway is located between Somers Point on the New Jersey mainland and Ocean City on the barrier island. See Figure 1: Project Location Map. The existing structures are increased in height and widened to accommodate the anticipated 100-year flood conditions and future traffic. This entails constructing MSE walls on the tidal-marsh islands.

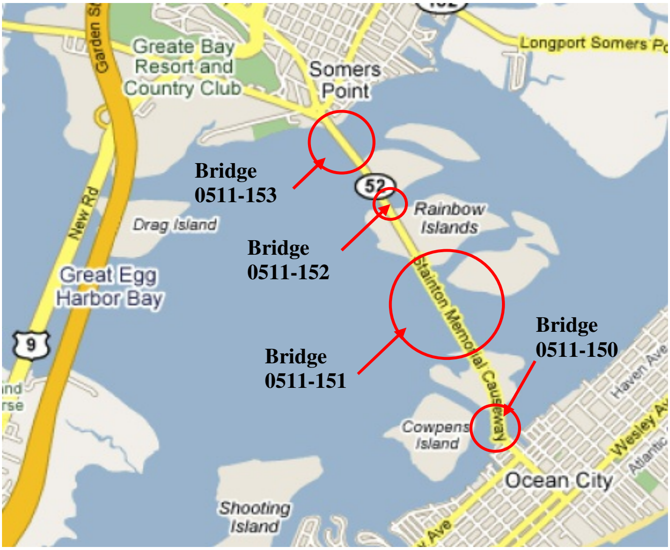

FIG. 1. Project Location Map

The construction of the project is separated into two contracts. Construction Contract A1 comprises the construction of the low-level portions of the proposed replacement structure on the Rainbow Islands and across Elbow Thorofare and Rainbow Channel, as well as the construction of appurtenant ramps, bulkheads and miscellaneous structures. The remaining two bridges will be constructed in Contract B. Construction of Contract A1 started in July 2006 and is ongoing.

The tidal-marsh islands in the area consist of 6 to 12 meter-thick soft cohesive deposits. Accordingly, ground improvement was necessary to support the proposed high embankment at Rainbow Island embankments. Different ground improvement techniques were evaluated and it was concluded that the Vibro-Concrete Column (VCC) technique, in conjunction with an overlaying geo-synthetic reinforced-sand platform, was the most appropriate solution.

The high embankment at the rainbow island location consists of 8-m-high by 12.2-m-wide back-to-back mechanically stabilized earth walls (MSE walls). The walls are supported by a 1.2-m-thick geosynthetic reinforced-sand platform. The fill load is transmitted to a firm foundation through a reinforced-sand platform and a VCC.

The overall performance of the foundation system for the high embankment of Rainbow Island, and in particular the high-strength geosynthetic component, is addressed based on system performance, which is monitored by a field instrumentation program.

SUBSURFACE CONDITION AND DESIGN PARAMETERS

The typical soil profile encountered along the VCC area is given in Figure 2. In general, the stratigraphy illustrated in Figure 2 may be described as mostly soft cohesive soils overlaying deeper Cohansey dense sand with interbedded clay lenses, although the depositional history is more complex.

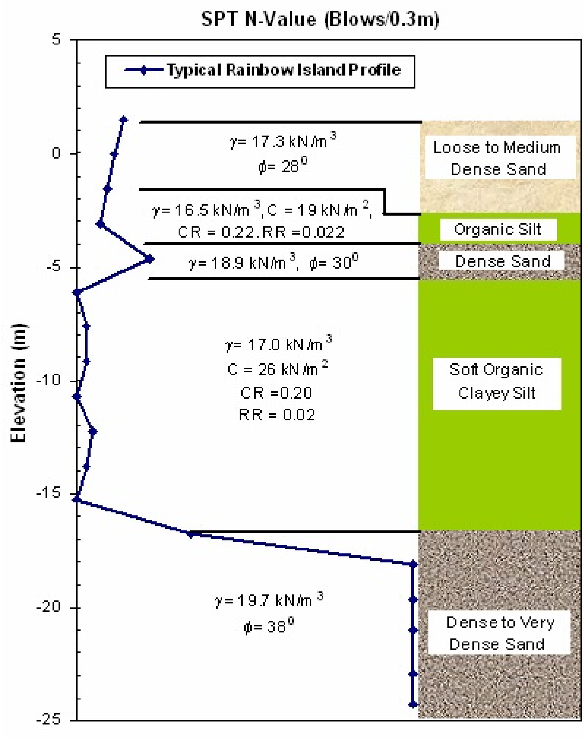

FIG. 2. Typical Soil Profile at Water and Land Test Site

Along the proposed alignment, the upper cohesive soils were encountered between the existing ground surface and depths ranging from approximately 15 m to 17 m. These soils consist of both high-plasticity organic silt and clay, and low-plasticity silt and clayey silt. Moisture contents range from 20% for the low plasticity silt to over 120% for the highly organic deposits. Plasticity indices are generally less than 12 for the low plasticity silt and range up to 50 for the more plastic silt and organic soils, with occasional higher values recorded. The liquidity indices are generally lower than 1 but greater than zero, consistent with normally consolidated deposits that are not sensitive. These soils are compressible but not highly compressible unless a high organic content is present. The consistency of these deposits ranges from very soft to medium based on the field Standard Penetration Test (SPT) data.

The deeper non-cohesive soils consist of poorly graded fine and fine-to-medium sand, typically containing less than 5% fines. The relative density of these deposits generally ranges from medium-dense to very dense based on the field SPT data. Many of the field-measured SPT blow counts are recorded as exceeding 100 blows per foot.

Soil samples recovered from selected borings and all undisturbed tube samples were incorporated into a laboratory-testing program to evaluate index properties, shear strength and compressibility parameters.

Based on the results of the subsurface exploration program and the laboratory-testing program, design soil parameters were determined. Settlement and stability analyses were performed at several locations along the alignment of Rainbow Island. The engineering analyses results indicated that the differential settlement problem may cause downdrag on the abutment foundations and would yet cause constructability and performance issues that would affect the MSE walls, the roadway drainage, and the maintenance of traffic during stage construction. In addition, the maximum height of the fill resulted in the potential for lateral squeeze within the underlying soft clayey silt stratum that would result in additional lateral thrust on the foundation piles. Accordingly, ground improvement and treatment were required.

DESIGN CONCEPT AND THEORETICAL CONSIDERATIONS

Vibro Concrete Column Design

The design concept for the vibro-concrete columns involves constructing a pattern of grout columns in situ using the vibro-displacement method. The columns are constructed to bear on the dense sand strata underlying the cohesive strata that would otherwise consolidate under applied loading. An expanded diameter is formed at the top and bottom of the columns to improve load transfer and increase bearing capacity. A load transfer mat, consisting of approximately 914 mm (3.0 ft) of well-graded fill with multiple layers of geosynthetic reinforcement, is constructed immediately above the tops of the columns to improve the transfer of the embankment area loading to the columns.

The typical concept for the embankment fill and the underlying reinforced-sand platform and VCC is illustrated in Figure 3. As shown in the drawing, the selected design diameter for the VCC is 457 mm (18.0 in) with 609 mm (24.0in) upper and bottom bulbs. VCC at the perimeter of the load transfer platform (LTP) are belled to 914 mm (36 in) at the upper portion. The general contractor; George Harms Construction, Inc slightly modified the initial design by forming the top bulb and adding a reinforcement steel bar for the cold joint.

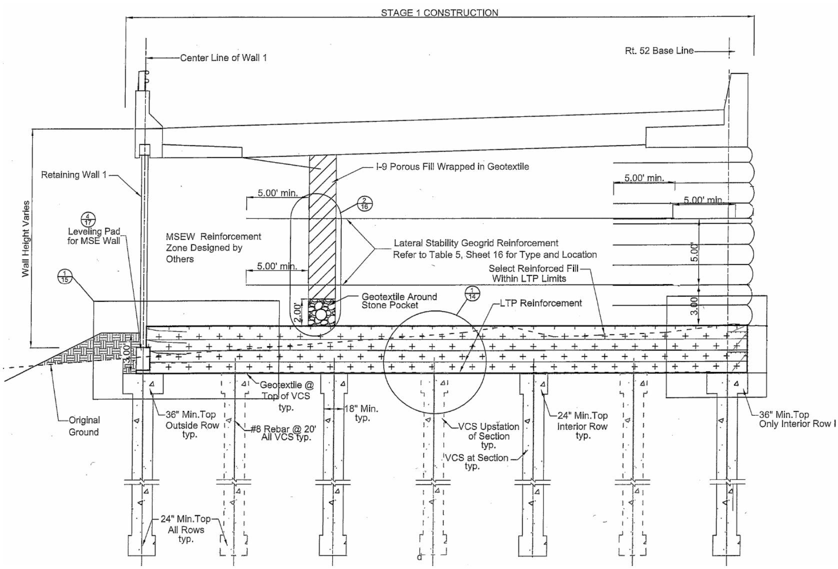

FIG. 3. Typical Cross Section

The main advantage of this system is that it combines advantages of in-situ ground-improvement vibro-systems with the load-carrying characteristics of piles. The VCC can be installed with a relatively large-diameter bottom bulb in order to increase its load-carrying capacity. An enlarged head can also be formed with the purpose of reducing the exposed area of the weak soil below the embankment fill. This would lead to a better load transfer of the fill weight to the VCC through an overlaying reinforced-sand platform.

Since the method of installation for the VCC involves densification of the sandy soil during the formation of the bottom mushroom, the end bearing capacity can be closer to that of a driven pile than that of a drilled shaft (Mankbadi et al. 2004). A value of 50 for the baring capacity factor, Nq, which is given in D.M-7.2 (Nav, 1986) for a soil friction angle of 36 degrees, was assumed in the calculations. It involves an arbitrary reduction of 15 % from the value of 62 given in DM-7.2. The resulting ultimate capacity was 1984 kN (466 kips), neglecting skin friction. The VCC was chosen such that the maximum load on the column does not exceed 867 kN (195 kips), which corresponds to a factor of safety greater than 2.0 against bearing capacity failure. Since the column tips are placed on firm material, anticipated post-construction settlement is less than 25.4 mm (1.0 in).

Load Transfer Platform (LTP)

The load transfer platform is used to efficiently distribute the embankment load onto the series of vibro-concrete columns below. The design concept for the load transfer platform is based on the use of multiple layers of reinforcement to create a stiff reinforced soil mass and the load transfer is achieved through soil arching (Collin et al, 2005). The geogrid reinforcement is included as an integral part of the load transfer platform. The reinforcement increases the lateral confinement of the selected fill in the transfer platform. This confinement enhances the ability of the soil to create an arch. The embankment load induces tensile stress in the load transfer platform, which should be considered in determining the required mechanical properties of the geotextile reinforcement. There are two fundamentally different approaches to the design of the load transfer platform, the British Standard and the Collin method.

According to the British Standard, the approach-fill load is transferred to the column below through catenary tension in the reinforcement. Essentially, the reinforcement behaves as a structural element and any benefit achieved by the creation of a composite soil mass is ignored. According to the Collin method, the reinforcement soil mass acts as a beam to transfer the load from the fill to the column below. For this project, the final design utilized the British Standard approach to design the load transfer platform. However, the general contractor (GHC) submitted an alternative design, which utilized the Collin method. The alternative design was approved and utilized in the construction. Based on the Collin method, four layers of geogrid reinforcement are required to reinforce the platform and the load transfer platforms are required to be 1067 mm (42 in) thick.

VCC LOAD TESTS

Accurate design and prediction methods for ultimate column resistance and load deformation characteristics are limited. The main unknown parameters are related to the installation procedures, which have a significant effect on altering and/or changing the initial in-situ properties for the cohesive and cohesionless soils encountered. Therefore, a load-testing program was essential (Mankbadi et al., 2004). The load-testing program called for a Statnamic Load Test on a production shaft with the goals of the test being to:

1. Establish an installation procedure based on the performance of the column
2. Verify that the VCC is capable of sustaining the applied axial load

During the test, load and displacement were monitored to obtain the foundation response. The ultimate capacity was determined using the Unloading Point method (Middendrop, 1993). This method was used in conjunction with a rate reduction factor based on the soil condition as suggested by National Cooperative Highway Research Program (NCHRP) Project Report: NCHRP 21-08.

Loading was applied to the VCC foundation in three cycles. Table 1 presents a summary of the derived static capacity and displacement response during testing for the individual load cycles. Table 2 presents a summary of derived static capacity and displacement response during testing for all load cycles combined based on the loading history.

Table 1. Load and Displacement Summary for Individual Load Cycles

Cycle	Maximum Derived Capacity	Displacement at Maximum Derived Static Capacity	Maximum Displacement	Permanent Displacement
1	885 kN (199 kips)	5.8 mm (0.23 in)	5.8 mm (0.23 in)	2.3 mm (0.09 in)
2	1597 kN (359 kips)	16.0 mm (0.63 in)	18.3 mm (0.72 in)	9.9 mm (0.39 in)
3	1784 kN (401 kips)	16.3 mm (0.64 in)	17.5 mm (0.69 in)	9.9 mm (0.39 in)

Table 2. Load and Displacement Summary for All Load Cycles Combined Based on Loading History

Cycle	Maximum Derived Capacity	Total Displacement at Maximum Derived Static Capacity	Total Maximum Displacement	Total Permanent Displacement
1	885 kN (199 kips)	5.8 mm (0.23 in)	5.8 mm (0.23 in)	2.3 mm (0.09 in)
2	1597 kN (359 kips)	17.8 mm (0.70 in)	20.1 mm (0.79 in)	11.7 mm (0.46 in)
3	1784 kN (401 kips)	27.4 mm (1.08 in)	28.7 mm (1.13 in)	18.8 mm (0.74 in)

The VCC was loaded to a maximum derived static capacity of 1784 kN (401 kips), or twice the design load. The corresponding total measurement was 28.7 mm (1.13 in) with a corresponding total permanent displacement of 18.8 mm (0.74 in). Therefore, it was concluded that a VCC could support the applied design load with a factor of safety of 2.0.

INSTRUMENTATION AND PERFORMANCE EVALUATION

Settlement platforms and slope inclinometers were utilized to monitor the VCC system performance. The field instrumentation readings indicated that the MSE wall supported by the VCC had experienced a maximum lateral deflection of 8 mm (0.3 in) and a vertical settlement of 15 mm (0.6 in).

It may be noted that the maximum predicted settlement is less than 25.4 mm (1.0 in). No prediction was made for the lateral deformation. However, it is assumed that this value is negligible given the stability of the system. Based on field instrumentation readings, it can be concluded that the VCC solution is adequate for supporting the MSE wall.

COMPARISION STUDY

The performance of the geogird-reinforced LTP in this project was compared to the performance of the geotextile-reinforced LTP from the nationally acclaimed Route 9 over Nacote Creek project in New Jersey (Mankbadi et al., 2004) for better understanding of the behavior and performance of LTP.

The Nacote Creek project LTP was designed as per the recommendation of the British Standard BS 8006. The reinforced LTP overlying the VCC was designed with three high-strength geotextile layers embedded in a granular blanket. Table 3 summarizes the LTP information and the performance for both projects.

Table 3. Summary of LTP information and performance of LTP

Project	LTP Design Method	Height of Embankment	Approximate Thickness of Weak Bearing Stratum	Geosynthetic Reinforced Used	Maximum Lateral Deflection Observed	Maximum Settlement Observed
Route 52 Causeway	Collin method	8 m (26.25 ft)	6 to 12 m (20 to 40 ft)	High Strength Geogrid	15 mm (0.6 in)	31 mm (1.2 in)
Rt 9, Nacote Creek	British Standard	10 m (32.80 ft)	3 to 6 m (10 to 20 ft)	High Strength Geotextile	13 mm (0.5 in)	40 mm (1.6 in)

Hence, it was concluded that both geotextiles and geogrids are very effective for reinforcing the load transfer platform, and will enhance the ability of the soil to create an arch through lateral confinement.

CONCLUSIONS

The vibro-concrete column solution is an effective and viable solution where approach embankments are to be constructed over soft ground within a limited right-of-way.

Vibro-concrete columns can be designed in a similar fashion to driven piles, relying on their end bearing capacity. A load test program is essential since the installation procedure governs the ultimate axial resistance of pile.

Instrumentation-monitoring data indicated that the vibro-concrete column solution, in conjunction with either geogrid or geotextile reinforced-sand platforms, can successfully support high embankments.

A load transfer platform designed by either the British Standard or the Collin approach are effective with respect to the transfer of the fill load to the column below.

The British Standard approach generally requires higher-strength reinforcement for the same design condition as opposed to the beam method. The Collin method will generally allow for larger column-to-column spacing than the British Standard approach for standard geosynthetic. Hence, the Collin method is a more cost effective method.

ACKNOWLEDGEMENT

This paper is based on the design and construction work of Michael Baker, Jr Inc. (the prime designer), Hardesty & Hanover, LLP., NJDOT, and George Harms Construction Co, Inc. We are grateful to Kuang-yu Yang and Dave Lambert of NJDOT for their support and dedication. We are also grateful to Glen Schetelich, Andy Coates and Lori Ruggiero from Hardesty & Hanover, Inc., John Pizzi from STV, Inc., and Dr. James G. Collin from The Collin Group Ltd for their valuable comments and suggestions.

REFERENCES

British Standard BS 8006 (1995) "*Code of Practice for strengthen/reinforced soils and other fills*", BSI, London.

Collin, J.G.; Han, J. and J. Huang, "*Geosynthetic-reinforced column-support embankment design guidelines*." Proceedings, the North America Geosynthetics Society Conference, 2005.

Elias, V., Lukas, R., Bruce, D., Collin, J.G., and Berg, R.R. (2004). "*Ground Improvement Methods Reference Manual"*. Federal Highway Administration FHWA NHI-04-001, July 2004.

Fahmy, R. W, Hanna, S, Mankbadi, R (2005). "*Approach Embankment Supported by Geotextile Reinforced Sand Platform over Vibro Concrete Column-A Case Study*". NAGS / GRI-19 Cooperative Conference Proceedings.

Hardesty & Hanover, LLP. "*Geotechnical Engineering & Foundation Report: Route 52 Causeway Construction Contract A*", March 2006.

Mankbadi, R, Mansfield, Fahmy, R. W., Hanna, S, and Krstic, V. (2004). "*Ground Improvement Utilizing Vibro-Concrete Columns*" GeoSupport Conference: Innovation and Cooperation in the Geo-Industry, Jan. 29-31, 2004.

Middendrop, P (1993). " *First Experience with Statnamic Load testing of Foundation piles in Europe"*, Proceeding 2nd International Geotechnical seminar on Deep Foundations on Bored and Auger Piles, Gent, p. 265-272.

NAVFAC Design Manual DM-7.2 (1986). " *Foundation and Earth Structure*".

Seismic Response of Rigid Faced Reinforced Soil Retaining Walls

G. Madhavi Latha[1], and A. Murali Krishna[2], S. M. ASCE

[1]Assistant Professor, Indian Institute of Science, Bangalore 560 012, India; madhavi@civil.iisc.ernet.in
[2] Research Scholar, Indian Institute of Science, Bangalore 560 012, India; amurali@civil.iisc.ernet.in

ABSTRACT: This paper presents the results of shaking table tests on rigid faced reinforced soil retaining walls. Construction of model retaining walls in the laminar box mounted on shaking table, instrumentation and results of model tests are discussed in detail. The reinforcement materials of different tensile strength are used in different model tests. It is observed from these tests that the horizontal face displacement response of the rigid faced retaining walls is significantly affected by the inclusion of reinforcement. Even low strength polymer reinforcement is found to be efficient in significantly reducing the face deformations. However, acceleration amplifications are observed to be less affected by reinforcement parameters.

INTRODUCTION

Reinforced retaining walls have gained extensive popularity over the past three decades and their performance under static loading conditions is well documented. In recent times, post earthquake observations of several reinforced retaining walls all over the world revealed that these walls have more resistance to earthquake induced damage even under the conditions where unreinforced walls were completely collapsed. This aspect led several researchers to focus on the seismic vulnerability of retaining walls and the design of reinforced walls to withstand earthquakes (Richardson and Lee 1975; Ling et al. 1997; El-Emam and Bathurst 2007 etc.). Studying the performance of models of reinforced retaining walls under cyclic base shaking conditions in laboratory helps in understanding how these walls actually perform during earthquakes.

In this paper, some of the important behavioral aspects of rigid faced reinforced soil retaining walls under dynamic conditions are studied through shaking table tests. A series of shaking table tests are conducted on rigid faced retaining walls reinforced with different types of geosynthetic reinforcement to study the effect of reinforcement type on the accelerations, horizontal face displacements and soil pressures under seismic condition. Results from these tests will be helpful in selecting the reinforcement type for earthquake resistant design of retaining walls.

Models of retaining walls are constructed in a laminar box with different reinforcing materials (bi-axial geogrids, uni-axial geogrids and geonet) and dry sand backfill. The test walls are constructed to a size of 750 × 500 mm in plan and 600 mm height. The models are instrumented with ultra sonic displacement transducers, accelerometers and soil pressure sensors at different locations. The effects of type of reinforcement material on acceleration response at different elevations, horizontal soil pressures and face deformations for the reinforced retaining wall are presented and also compared with those for unreinforced wall.

EQUIPMENT AND MATERIALS

A computer controlled hydraulically driven single degree of freedom (horizontal) shaking table with loading platform of 1000 mm × 1000 mm size and payload capacity of 1 ton is used in the experiments. Models of retaining walls are constructed in a laminar box of size 500 mm × 1000 mm and 800 mm deep, consisting fifteen rectangular hollow aluminum laminas, using dry sand backfill with reinforcing layers placed at regular intervals. More details of the shaking table and laminar box and construction of model walls are discussed by Madhavi Latha and Murali Krishna (2006).

Locally available dry sand is used as the backfill material. Figure 1 shows the grain size distribution of the sand. The sand is classified as poorly graded sand with letter symbols SP as per the Unified Soil Classification System. The sand has achieved maximum dry density of 18 kN/m^3 in vibration test and the minimum dry density observed in loosest state is 14.3 kN/m^3. Specific gravity of the sand is tested to be 2.64 and the other index properties determined are shown in Table 1.

Three different reinforcement materials are used in different tests; a bi-axial geogrid (BX) made up of polypropylene, a uni-axial geogrid (UA) made up of HDPE and a low strength geonet. Ultimate tensile strength properties of the geogrids obtained from standard multi-rib tension test (as per ASTM: D 6637-01) are shown in Figure 2. Wide range of tensile strength is adapted from lowest tensile strength of 7.6 kN/m for geonet material, through 26 kN/m for BX, to 40 kN/m for UA material.

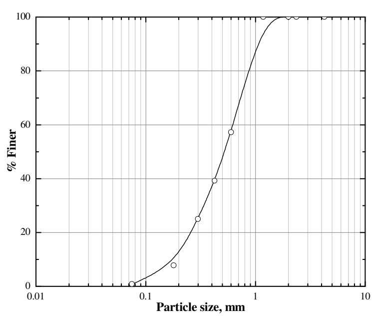

FIG. 1 Grain size distribution of the test sand

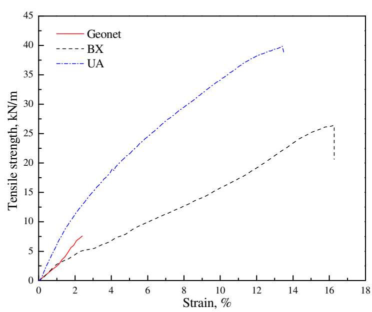

FIG. 2 Tensile strength properties of reinforcement materials

Table 1. Index properties of the test sand

Specific Gravity	2.64
e_{max}	0.846
e_{min}	0.467
D-10, mm	0.1742
D-30, mm	0.3372
D-60, mm	0.619
Coefficient of curvature (C_c)	1.054
Uniformity coefficient (C_u)	3.553

Each model retaining wall is instrumented with accelerometers and pressure sensors at different locations within the backfill soil. Four accelerometers are used in each model test. Accelerometers are of analog voltage output type with a full-scale acceleration range of ± 2g in both the X and Y axes, within the bandwidth of 1Hz-2 kHz. Pressure sensors are of strain-gauge type with up to 100 kPa measuring capacity. To measure horizontal displacement, three non-contact ultrasonic displacement transducers (USDT), U1, U2 and U3 are positioned at different elevations along the facing.

MODEL CONSTRUCTION AND TESTING PROCEDURE

Model retaining walls are constructed in laminar box to a size of 750 mm × 500 mm in plan and 600 mm height. The model is constructed in lifts of equal height (s_v) while reinforcing each lift with a layer of reinforcement material. The facing is constructed from 12 hollow steel box sections of 50 mm height each, bolted together to form 600 mm high rigid panel with a thickness of 25 mm. In the present study all the reinforced model walls are reinforced with four layers of reinforcement that are run through the bolts which are the part of the facing system.

To achieve uniform density, sand is placed in the laminar box using pluviation (raining) technique. The height of fall to achieve the desired relative density was determined by performing a series of trials with different heights of fall and maintained same height of fall corresponding to that density. However, the actual relative densities achieved in each test are monitored by collecting samples in small cups of known volume placed at different locations and levels during the model retaining wall preparation. All the walls discussed in this paper are built to the same density. The average unit weight and relative density achieved were within the range of 16.35 – 16.50 kN/m3 and 62 – 65% respectively for the same height of fall. The total quantity of sand consumed in each test is about 370 kg.

The retaining walls are constructed using wooden plank – formwork for each lift. After completion of all lifts up to full height of the wall (600 mm), a nominal surcharge of 0.5 kPa in the form of concrete slabs (two nos. each of 8.9 kg weight and size 480×370 mm) is applied at the top. The supported formwork is carefully withdrawn lift wise sequentially from bottom to top after the backfill layers and surcharge are completed. Figure 3 shows the finished wall picture of rigid faced model wall. Length of reinforcement (L) at the interface of sand layers is kept same in all tests as 420 mm for the reinforced soil walls. This length corresponds to the L/H ratio of 0.7 that is minimum required for reinforced earth structures (FHWA 2001; Sankey and Segrestin 2001).

Schematic of typical model configuration along with layout of the instrumentation for the test wall constructed with four layers of reinforcement is shown in Figure 4. Accelerometers (A) and pressure transducers (P) were embedded in the soil while filling sand at different levels as shown in the figure. One accelerometer, A0, is fixed to the shaking table to record the base acceleration and the other three accelerometers A1, A2 and A3 are placed at elevations 150, 300 and 600 mm respectively from the base at a constant distance of 100 mm from the facing. Four pressure sensors; P1, P2, P3 and P4 are placed inside the wall, in contact with facing at elevations 100, 230, 380 and 500mm respectively from the base to observe horizontal soil pressures on facing. To measure horizontal displacement, three non-contact USDTs U1, U2 and U3 are positioned at elevations 150, 350 and 550 mm respectively along the facing.

Testing program is devised to observe the influence of different reinforcement materials on wall behaviour. Table 2 shows the test parameters for different model walls. After completing the construction (after removal of external wooden plank formwork), each model wall is subjected to 20 cycles of sinusoidal motion of base shaking corresponding to 0.2 g acceleration, where ‘g’ is the acceleration due to gravitational force, at 3 Hz frequency. Dynamic response of each model wall in terms of accelerations, horizontal soil pressure distribution at different elevations and displacement along the facing is monitored through data acquisition system.

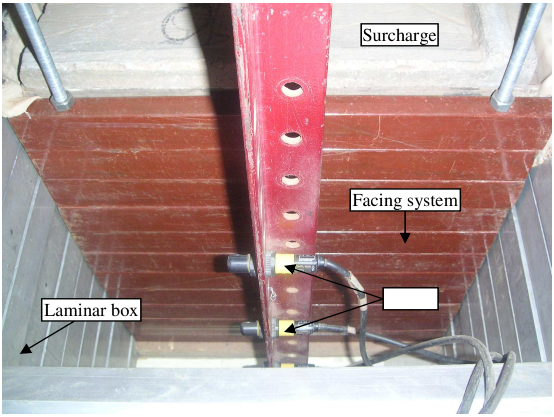

FIG. 3 Constructed model wall face

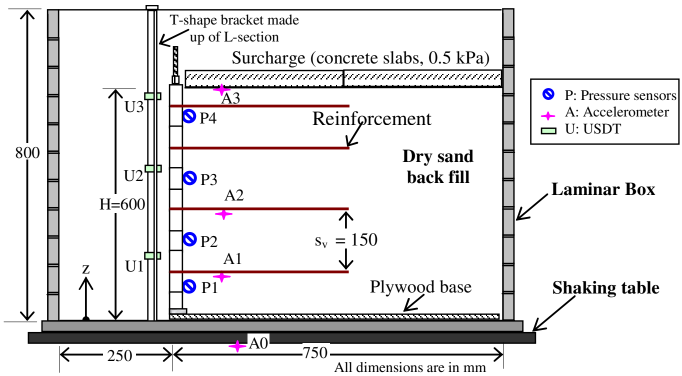

FIG. 4 Schematic diagram of typical rigid faced reinforced soil wall configuration and instrumentation

Table 2. Test parameters for different model walls

Sl. No.	Test	Reinforcement	Acceleration, g	Frequency, Hz
1	UR	--	0.2	3
2	R1	Geonet		
3	R2	BX		
4	R3	UA		

RESULTS AND DISCUSSIONS

Variation of displacements at different elevations of the wall with increasing number of dynamic loading cycles is shown in Figure 5, for the test UR. Figure shows the hyperbolically increasing trend of displacement with increase in number of cycles. Further, higher displacements at higher elevations are noticed. Figure 6 shows the displacement profiles, at the end of 20 cycles of dynamic motion, revealing the influence of reinforcement materials on the horizontal displacement response. It is observed, from the figure, that the displacements are reduced to a very great extent with the incorporation of the reinforcement in retaining wall. The top maximum displacement of about 11 mm in the case of unreinforced model wall is reduced to about 1 mm or less in the case of reinforced walls. Moreover, the effect of reinforcement tensile strength is insignificant for the range of tests conducted, giving more or less similar displacements in all the cases. This behavior can be justified with the similar reinforcement stiffness values for all reinforcement materials, corresponding to the strain levels of 1 to 2%, which is the typical range of strains that could be observed in similar tests.

Figure 7 shows typical variation of accelerations with number of cycles of dynamic loading, at different elevations for the test R1. It is observed from the figure that accelerations are amplified at higher elevations. Peak to peak acceleration amplification at A1 location is 1.07 times to that of base acceleration at A0 location while the amplifications at A2 and A3 locations are 1.18 and1.24 times respectively.

Figure 8 shows the maximum acceleration amplifications along the height of the model walls after the 20 cycles of dynamic motion. Acceleration amplification factors were calculated using the root mean square (RMS) method (Kramer 1996) applied to the acceleration-time history for each accelerometer device. From the figure, it is observed that the accelerations are amplified more on top of the wall in all the tests. This observation is in concurrence with the studies reported by Latha and Krishna (2006) and El-Emam and Bathurst (2007). However, there is no significant change in amplification values in the case of reinforced soil walls compared to the unreinforced soil wall. Maximum acceleration amplification values at top are in the close range of 1.24 to 1.31 for unreinforced, UA and geonet reinforced walls while it was found to be 1.55 for BX reinforced wall. The higher amplification measured in wall with BX reinforcement could infer relatively more rigid behavior of this model wall, possibly due to increased interlocking effect due to aperture size of the BX geogrid compared to other reinforcing materials.

Incremental residual pressures observed, at the end of dynamic excitation along the height of the wall in different tests, are presented in Figure 9. As the pressure levels are very small with respect to the measuring range of pressure sensors, the trend in the pressures distribution along the height of the wall is not consistent among various model walls. However, they may provide the range of incremental pressures that can be expected for the tests conducted.

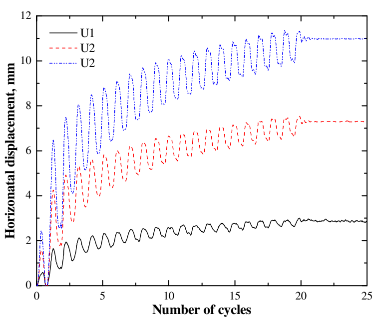

FIG. 5 Typical displacements variation with number of cycles for the test UR

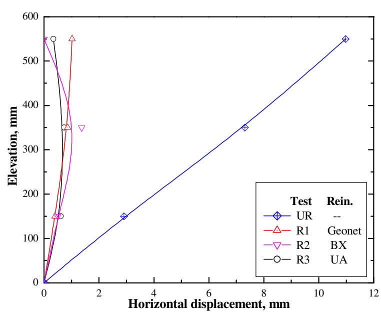

FIG. 6 Displacement profiles at the end of 20 cycles of dynamic motion

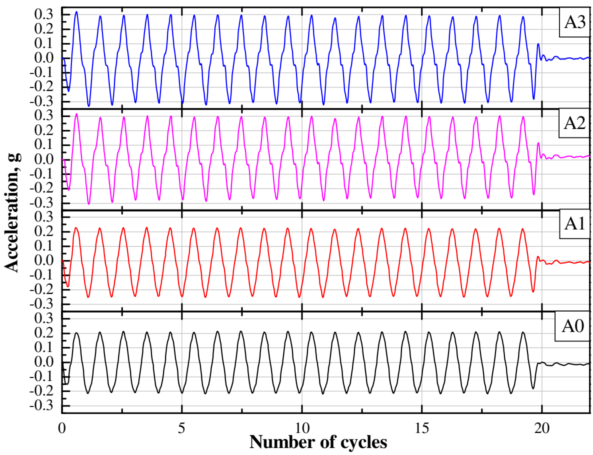

FIG. 7 Typical accelerations variation with number of cycles for the test R1

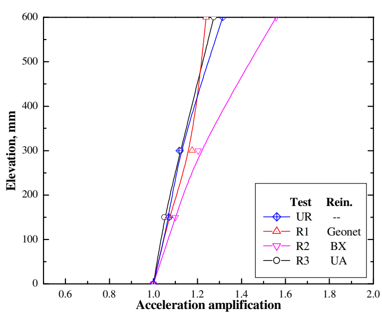

FIG. 8 Acceleration amplifications at the end of 20 cycles of dynamic motion

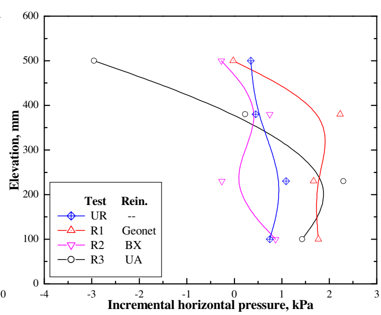

FIG. 9 Incremental pressures at the end of 20 cycles of dynamic motion

Though it is not possible to directly extrapolate the results from these model tests to obtain the response of field walls because of gravity and scaling effects, the results obtained from this study will help in understanding the relative performance of reinforced soil retaining walls subjected to base shaking with varying reinforcement type.

CONCLUSIONS

Seismic response of rigid faced soil retaining walls reinforced with different type of reinforcement materials is studied through shaking table tests on model walls. Introduction of reinforcing layers in the retaining wall resulted in drastic reduction of the face displacements. In all reinforced walls, the maximum horizontal displacement is reduced by about 10 times compared to the unreinforced wall, irrespective of reinforcement tensile strength. It is observed that the ultimate tensile strength of reinforcing material has no bearing on the wall behaviour, as the strain levels in the reinforcement layers are very low. In general, accelerations are amplified at higher elevations but least affected by reinforcement. Test with biaxial geogrid reinforcement showed slightly increased acceleration amplifications at all levels, possibly due to the increased interlocking effect, leading to relatively rigid behaviour.

REFERENCES

ASTM D 6637(2001). *Standard Test Method for Determining Tensile Properties of Geogrids by the Single or Multi-Rib Tensile Method*, ASTM standards, West Conshohocken, Pennsylvania, USA.

El-Emam, M. and Bathurst, R.J. (2007). "Influence of reinforcement parameters on the seismic response of reduced-scale reinforced soil retaining walls." *Geotextiles and Geomembranes*, Vol. 25 (1): 33-49.

FHWA (2001). "*Mechanically Stabilised Earth Walls and Reinforced Soil Slopes. Design and Construction Guidelines*," Federal Highway Administration Publication No. FHWA-NHI-00-043, US Department of Transportation, Washington, D.C., USA, 418p.

Kramer, S.L. (1996). "*Geotechnical Earthquake Engineering*," Prentice Hall, Upper Saddle River, NJ.

Latha, G. M. and Krishna, A. M. (2006). "Dynamic response of reinforced soil retaining walls." *Advances in Earth Structures – Research to Practice* (GSP 151) ASCE, Shanghai: 348-355.

Ling, H.I., Leshchinsky, D. and Perry, E.B. (1997). "Seismic design and performance of geosynthetic-reinforced soil structures." *Geotechnique*, Vol. 47 (5): 933–952.

Madhavi Latha, G. and Murali Krishna A. (2006). "Shaking table studies on reinforced soil retaining walls." *Indian Geotechnical Journal*, Vol. 36 (4): 321-333.

Richardson, G.N. and Lee, K.L. (1975). "Seismic design of reinforced earth walls." *Journal of the Geotechnical Engineering Division*, ASCE, Vol. 101 (2): 167–188.

Sankey, J.E. and Segrestin, P. (2001). "Evaluation of seismic performance in mechanically stabilized earth structures." *Proceedings of the International Symposium on Earth Reinforcement*, Kyushu, Japan, Vol.1: 449-452.

Using EPS-Block Geofoam for Levee Rehabilitation and Construction

John S. Horvath[1], Ph.D., P.E., M.ASCE

[1]Professor, Manhattan College, Civil and Environmental Engineering Department, Bronx, NY 10471, U.S.A.; john.horvath@manhattan.edu

ABSTRACT: *Block-molded expanded polystyrene (EPS-block)* is the material of choice worldwide for most of the functional applications of the *cellular-geosynthetic* product family called *geofoam*. In particular, the use of EPS-block for the very common geofoam functional application of *lightweight-fill* is now considered a generic, commodity design alternative in routine geotechnical engineering practice. Despite the relatively widespread use of EPS-block geofoam for certain lightweight-fill applications such as road embankments, there are many other applications that have received relatively little attention and use to date in practice. One such underutilized lightweight-fill application that has significant potential worldwide is for levees. There are technical and economic benefits for both new and existing levees. The primary benefits derive from the fact that EPS-block geofoam has a density approximately 1% that of soil so can have a significant impact on both reducing stress-dependent settlements and improving stability, issues that are often critically important for levees. This paper outlines the technical bases for using EPS-block geofoam for levees as well as describes case histories where this concept has been used in practice.

INTRODUCTION

EPS-block geofoam is now widely accepted and increasingly used throughout the world as the geofoam material of choice because of its inherent material properties, multifunctional capabilities, and lower cost relative to other geofoam materials (Horvath 1995). In particular, applications utilizing its lightweight-fill geosynthetic function under both gravity and seismic loads is now considered a generic, commodity design alternative in routine geotechnical engineering practice. However, the vast majority of projects where the lightweight-fill function of EPS-block geofoam has been utilized to date have involved transportation earthworks and earth-retaining structures for roads and railways. Thus there are other potential applications still to be identified, researched, and developed to their full potential. One of the more intriguing of these is the use of EPS-block geofoam with water-resources structures in general and levees in particular.

OVERVIEW

This paper focuses on the use of EPS-block geofoam for its lightweight-fill functional application with levees. The presentation and discussion of this subject is divided into three sections. The first addresses the technical issues associated with this particular application. Sufficient information is presented for an experienced geotechnical engineer to be guided as how to logically analyze and design a levee incorporating EPS-block geofoam within the levee cross-section. The second section describes some case histories where this geotechnology has actually been used in practice. While the number of known case histories is relatively small available information indicates that they have been successful which should lend confidence to pursue this geotechnology further in the future. The third and final section makes some suggestions for both refining this geotechnology in future applications as well as possible areas of novel technological development to make this geotechnology more attractive economically.

TECHNICAL ISSUES

Application Concept

The primary benefits of the geosynthetic function of lightweight-fill derive from the fact that EPS-block geofoam has a density approximately 1% that of soil yet if properly designed and specified can have surprising load-carrying capacity (e.g. spread footings for buildings and even road bridges have been founded directly on EPS blocks). Because both the vertical stresses that act on a subgrade beneath a levee under gravity loading as well as the additional inertia forces that develop within a levee under seismic loading are linearly proportional to material density, there are obvious benefits to using EPS-block geofoam as a lightweight-fill material for levees under a wide range of loading conditions and geotechnical behavior modes. These include both initial (undrained) and primary-consolidation settlements as well as bearing capacity and slope stability, all of which are often critically important issues for levees by virtue of the soft-ground conditions on which many levees are constructed.

With this basic understanding of how EPS-block geofoam can be used conceptually to enhance the performance of levees, Figure 1 illustrates the generic execution of this concept. A core portion of a levee that would otherwise consist of soil is constructed (if new) or reconstructed (if existing) to include an assemblage of EPS blocks. Research and experience indicates that if proper design and construction protocols are

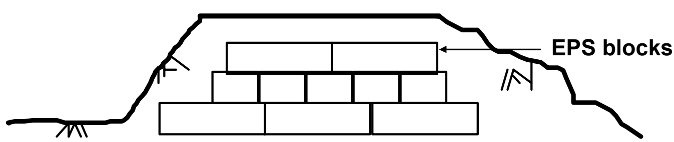

FIG.1. Generic example of levee incorporating EPS-block geofoam.

followed this assemblage of individual blocks will perform as a homogeneous, isotropic mass, even under dynamic loading such as seismic shaking.

Note that the volume of EPS to be used as a relative proportion of the cross-sectional volume-per-unit-length of the levee is not fixed but is a project-specific design variable. The cross-sectional geometry of the assemblage of EPS blocks is not fixed either although a stair-stepped geometry as shown in Figure 1 is generally considered desirable when practicable so that differential settlements of the levee in a plane transverse to its longitudinal axis (i.e. in the same plane depicted in this figure) do not occur abruptly between the portions of the levee without and with the EPS-block geofoam and cause cracking within the levee soils.

Analysis and Design Methodology

The use of EPS-block geofoam for levees as illustrated in Figure 1 is actually a relatively generic lightweight-fill application where load bearing in vertical compression on the EPS blocks is the primary behavioral mode to consider for both analysis of existing fills and design of new ones. Thus the decades of extensive worldwide experience with analyzing and designing lightweight fills for roads using EPS-block geofoam is directly applicable to the levee application.

The current state of practice for analyzing and designing lightweight fills for roads that incorporate EPS-block geofoam in their subgrade is stiffness- and displacement-based as opposed to the strength-based approach used in the early years (1970s-1980s) of this geotechnology (Stark et al. 2004a, ASTM 2005). The reasons for this evolution of analysis and design methodologies are discussed in detail in Horvath (1995) with a concise summary in Horvath (1999).

This stiffness-and-displacement-based methodology has as its technical basis the fact that in uniaxial compression block-molded EPS has nominally linear-elastic behavior up to what is called the *elastic-limit stress*. This is assumed to be the uniaxial compressive stress corresponding to 1% compressive strain as measured in the standard rapid loading tests normally specified by the reference standards cited in current standards developed for EPS-block geofoam (Stark et al. 2004b, ASTM 2004). The elastic-limit stress also turns out to be a convenient threshold for defining the stress level beyond which long-term compressive creep strains are likely to be significant. Thus the elastic-limit stress can be used to define a limiting stress for both linear-elastic behavior under transient loads and acceptable long-term creep magnitudes under permanent loads. Note that the slope of the stress-strain curve between 0% and 1% compressive strain has historically been defined as the *initial tangent Young's modulus* although based on currently available knowledge it is perhaps more accurately defined as the *initial secant Young's modulus*.

As noted above, a levee incorporating EPS-block geofoam can be modeled reasonably as a road embankment. A key design variable for such earthworks is the vertical distance between the pavement surface and top of the EPS blocks. For roads, this is based on the need to have a pavement system within this depth as well as to place the EPS deep enough so that reasonable vertical-normal-stress attenuation of live loads from vehicles occurs. Prevention of differential icing is also a consideration in climates where freezing or near-freezing temperatures can occur. Experience indicates that the vertical distance between the pavement surface and the top of the EPS blocks is typically of the order of 1 metre (3 ft).

Note, however, that this rule-of-thumb is not applicable for levees. Not only are pavement, vehicle, and differential-icing considerations typically not relevant but far more important is the fact that buoyant uplift of the assemblage of EPS blocks is typically the critical design consideration for levee applications. Because of its closed-cell structure and extremely low density, EPS floats readily and permanently in water. Therefore, the uplift water pressure that might act at the base of the assemblage of EPS blocks during the design life of the levee must be estimated and a sufficient downward stress provided on the top of the assemblage of EPS blocks to counteract this. Historically this has been done by placing sufficient soil on top of the assemblage of EPS blocks so that the vertical overburden stress from the soil counteracts the expected uplift water pressure. In round numbers this is typically a one-to-two ratio, i.e. 1 metre of soil counteracts 2 metres of head at the base of the assemblage of EPS blocks. Note that side friction along the sides of the assemblage of EPS blocks is typically neglected in this simplistic analytical model although it certainly is present and could be included a more-refined analysis.

As an alternative to resisting uplift water pressures by dead-weight alone, there have been proposals, at least in concept, to use some type of vertically-oriented tiedown system using ground anchors as the primary component to restrain the assemblage of EPS blocks against uplift. These tiedown elements, which would terminate at their top within a reinforced-portland-cement-concrete slab cast over the top of the assemblage of EPS blocks, are typically proposed to be installed in what is referred to as the *passive* mode which means they would be left unstressed after installation. While such a tie-down system appears effective from a simplistic equilibrium-of-forces perspective the issue of displacements needs to be considered carefully. This is because typical passively-installed bar-type tiedown elements require significant displacement at the top of the element to mobilize the design force, typically of the order of tens of millimetres (one inch or more). Such displacements of the anchorage system might prove detrimental to the long-term stability of the assemblage of EPS blocks in particular and levee in general. In addition, there is the likelihood that during times of no uplift water pressures that these anchorage elements would actually act as de facto minipiles in compression due to inevitable secondary (creep) settlements of the levee. Such undesirable-but-unavoidable compression loading could structurally compromise the anchorage elements (due to buckling) and/or overlying slab (due to punching-shear failure of the anchor heads through the slab).

The final major design detail to note is the need for mechanical connectors between the EPS blocks. Although the friction angle between the molded surfaces of EPS blocks is relatively high (of the order of 30º), research and experience have clearly indicated the need to provide supplemental shear resistance between horizontal block surfaces, at least when seismic or other dynamic loads are expected. Given the potential for uplift water pressures that could tend to cause distortion between the assemblage of EPS blocks, it would seem advisable to use mechanical connectors with levees even if seismic or other dynamic loading is not a design consideration unless and until future research indicates that such connectors are unnecessary.

Material Requirements

The mechanical (stress-strain-time-temperature) properties of block-molded EPS are discussed in detail in Horvath (1995) with an updated summary in Stark et al. (2004a). The most relevant mechanical characteristic of block-molded EPS is that it can be molded within a range of densities/unit weights (roughly 12 to 40 kg/m^3 (0.75 to 2.5 lb/ft^3) on a routine basis although both lower and higher values have been obtained in practice). If all aspects of the molding process are equal except for density, research indicates that there is a proportional relationship (which may or may not be linear based on the particular database used) between EPS density and the key stiffness parameters of elastic-limit stress and initial Young's modulus (Horvath 1995, Stark et al. 2004a).

That having been said, experience indicates that it is very important to emphasize that density/unit weight alone should <u>never</u> be used as the sole criterion for assessing these critical stiffness parameters for block-molded EPS, whether for design or manufacturing quality control and assurance purposes. The reason is that it is possible for block-molded EPS of a given density to have a range in stiffness properties depending on numerous variations that can occur during the actual molding process. Therefore design using EPS-block geofoam should always be done by first analytically determining the minimum elastic-limit stress and initial Young's modulus that is required to satisfy the anticipated compressive stresses on the EPS blocks. Then a project-specific, performance-based specification should be developed using appropriate standards as a guideline. At the present time there are two standards that have been promoted for use in U.S. practice although they could be used worldwide. One was developed specifically for use with roads where load demands, especially under seismic loading, are relatively severe (Stark et al. 2004b). The other is simply a slightly-modified version of the long-used standard for non-load-bearing thermal insulation used in buildings (ASTM 2004). Either standard is likely to be satisfactory for the relatively modest load demands of most levee applications. The important thing is that both standards have material requirements that include required minimums for the stiffness parameters and not just material density. It cannot be emphasized too strongly that material density alone is not sufficient as a material-design parameter any more than soil density alone defines the strength and stiffness of soil.

CASE HISTORIES

River Torne - United Kingdom

The first known use of EPS-block geofoam as lightweight fill incorporated within a levee was in the U.K. to raise an existing levee along the River Torne in Humberside. This work is believed to have been executed circa 1995 on behalf of the National Rivers Authority (now part of the Environment Agency) as it was reported in a trade publication in early 1996 (*Ground Engineering* 1996) and then discussed in greater detail by Sanders (1996). This project involved a 100-metre (330-foot) long section of an existing levee where EPS-block geofoam was used in an attempt to break the never-ending cycle of levee settlement on soft ground that is caused by using soil to restore a levee to its design grade to compensate for settlement. The levee in question had apparently settled as much as 800 millimetres (32 inches) in the approximately five years prior to its rebuilding using EPS-block geofoam. The design cross-section used was very similar to that shown conceptually in Figure 1. Other design details employed were:

- placing a geotextile on the existing soil subgrade exposed after excavating into the core of the existing levee,

- encapsulating the assemblage of EPS blocks on all four sides with a geomembrane, and

- installing a drain pipe that led from within the assemblage of EPS blocks to an external drainage ditch on the landside of the levee.

The design logic for use of the planar geosynthetics (geotextile and geomembrane) and drainage system were not discussed in Sanders (1996).

No further published information is known about this project and its performance to date. However personal communication in January 2000 with the EPS molder (manufacturer) that supplied this project indicated it was apparently sufficiently successful that one or more additional levee projects had been executed in the U.K. by that date. However no details were available about these follow-on projects nor has additional information concerning possible subsequent projects since 2000 been found.

Roaring River Slough - Solano County - State of California, U.S.A.

Subsequent to the initial public reporting in 1996 of the first River Torne project there was an effort made to educate design professionals and owning agencies worldwide about the potential use of EPS-block geofoam with levees. What is believed to have been the first project in the U.S.A. to embrace this geotechnology was the reconstruction and raising of a levee located along the Roaring River Slough in the Suisun Marsh in Solano County, California. This work was performed circa 1999 under the auspices of the State of California Department of Water Resources. The construction plans and under-construction photos for this project suggest that the design concept used for the first River Torne project was used for guidance to a significant extent, including the use of both geotextile underlayment and geomembrane encapsulation of the assemblage of EPS blocks. However the use of the drainage system from within the EPS blocks to the landside of the levee was apparently not replicated on the Roaring River Slough project.

Figure 2 shows the Roaring River Slough project under construction. Figure 2a shows EPS blocks temporarily stockpiled on site and being placed using a backhoe. It appears that a backhoe was the primary, if not exclusive, piece of mechanical equipment used for most if not all of the work including not only moving soil and EPS blocks but placing the rolled planar geosynthetics as well.

(a) (b)

FIG. 2. Roaring River Slough project under construction.

This photo does highlight a very significant benefit and superiority of EPS-block geofoam as a lightweight-fill material and that is its extraordinary ease of handling in very remote and difficult-to-access project sites. Although apparently not utilized on this project would be the ability to bring the EPS blocks to levee project sites via barge if necessary or desired. Figure 2b shows the geomembrane being installed over a section of the levee where the EPS blocks have already been placed. Although this project is known to have been completed successfully no further information is available concerning the performance of this project or any other similar projects performed in the U.S.A. to date.

SUGGESTIONS FOR IMPROVEMENTS

Although the basic geotechnology of using EPS-block geofoam as lightweight fill in various types of earthworks is reasonably well known and mature, there are various specific applications that are more or less developed than others in terms of specific design details, documented case-history performance, education of design professionals and owners, and other considerations that are necessary to advance a technology to meet its full potential. At this point in time, this is certainly true with regard to using EPS-block geofoam as a lightweight-fill material for use with levees. Despite at least a decade of such use there is relatively little documented information about projects that have been executed and how they have performed. It is hoped that this will change in the future with greater acquisition and sharing of knowledge.

Coincident with this it is hoped that design professionals will carefully reconsider design details used with such earthworks rather than simply replicate what has been used before. Specifically, the use of planar geotextiles (geotextiles and geomembranes) to underlay and encapsulate the assemblage of EPS blocks should be critically evaluated. Such details are not used with EPS-block geofoam fills in general so there should be well-defined reasons for using them with the levee application. Use of planar geosynthetics obviously adds cost, not only for materials but also for placement in what can be a very remote working environment. This is exemplified in Figure 2(b) where the need to transport and handle planar geosynthetics was not a trivial aspect of the construction. In summary, there should be a rational, zero-based assessment of all design details associated with using EPS-block geofoam for levees in order to develop a cost-effective yet technically-adequate design. The need for an overall efficient design detail is particularly important for levees given the enormous potential for applying this geotechnology.

SUGGESTIONS FOR FUTURE DEVELOPMENTS

Consistent with the suggestion to focus on developing efficient, cost-effective designs there should be research into developing cost-effective block-molded EPS to be used with levee applications. EPS cost-per-unit-volume is a significant design consideration and more than one-half the cost of EPS is due to raw-material cost which is highly dependent on the always-volatile price of petroleum (crude oil). One intriguing aspect of using EPS-block geofoam for levees is that although it is a load-bearing application the compressive stresses are likely to be less than those typically encountered in more-severe earthwork applications such as road embankments. Consequently it might be possible to develop an EPS block specifically for levee applications that contains a significant relative quantity of 'regrind' which is the EPS-industry term for in-plant recycled material such as production scrap. Use of regrind reduces raw material costs when making EPS. However it also produces material that has a reduced stiffness and elastic-limit stress. Nevertheless because the material-stiffness requirements for many levee applications are likely to be modest it may be possible to develop a formulation for EPS blocks incorporating regrind that meets the technical requirements but is very cost effective. Such an EPS block would also be attractive as a 'green' product that makes productive use of waste material (regrind).

REFERENCES

ASTM (2004). "Standard specification for rigid cellular polystyrene geofoam." *Standard D6817-04*, ASTM Intl.

ASTM (2005). "Standard guide for use of expanded polystyrene (EPS) geofoam in geotechnical projects." *Standard D7180-05*, ASTM Intl.

Ground Engineering (1996). "NRA banks on lightweight fill." Jan.-Feb.: 12.

Horvath, J. S. (1995). *Geofoam geosynthetic*. Horvath Engineering, P.C., Scarsdale, NY, U.S.A., 229 p.

Horvath, J. S. (1999). Discussion of "Status of ASCE standard on design and construction of frost protected shallow foundations" by L. S. Danyluk and J. H. Crandell. *J. of Geotechnical and Geoenvironmental Engrg.*, 125 (2): 166-167.

Sanders, R. L. (1996). "United Kingdom design and construction experience with EPS." *Proc. Intl. Sym. on EPS Construction Method (EPS Tokyo '96)*, Tokyo, Japan: 236-246.

Stark, T. D., Arellano, D., Horvath, J. S. and Leshchinsky, D. (2004a). "Geofoam applications in the design and construction of highway embankments." *NCHRP Web Document 65*, Transportation Research Board.

Stark, T. D., Arellano, D., Horvath, J. S. and Leshchinsky, D. (2004b). "Guideline and recommended standard for geofoam applications in highway embankments." *NCHRP Report 529*, Transportation Research Board.

Geo-Challenge as a Curricular Activity in Geotechnical Engineering Education

Jeffrey C. Evans[1], M. ASCE and Michael A. Malusis[2], A.M. ASCE

[1]Professor and Chair, Department of Civil and Environmental Engineering, Bucknell University, Lewisburg, PA 17837; evans@bucknell.edu
[2]Assistant Professor, Department of Civil and Environmental Engineering, Bucknell University, Lewisburg, PA 17837; mam028@bucknell.edu

ABSTRACT: Geo-Challenge is a student competition that has been held at the two most recent ASCE GeoInstitute national meetings (i.e., GeoFrontiers 2006 and GeoDenver 2007). In this event, students design and build a mechanically stabilized earth (MSE) wall in a plywood box using posterboard for the facing, paper for the reinforcing strips, and sand for the backfill. Geo-Challenge has been a successful co-curricular activity but also presents a tremendous opportunity for active learning if incorporated in the geotechnical engineering curriculum. For example, Geo-Challenge is now a standard assignment in the Ground Improvement Engineering course at Bucknell University. In this course, students first study the principles of MSE as part of the lecture series and then compete in Geo-Challenge as part of the laboratory series. The competition has been held twice at Bucknell University and has proven to be an excellent tool for active learning that also is useful for addressing ABET outcomes associated with students' ability to (1) design and conduct experiments, (2) design a system, (3) work effectively in a collaborative environment, and (4) provide effective written communication. This paper presents the details of the Bucknell Geo-Challenge assignment and describes the benefits of Geo-Challenge as a regular curricular activity.

INTRODUCTION

The ASCE-sponsored Geo-Challenge is a co-curricular competition where student teams design and build a laboratory-scale mechanically stabilized earth (MSE) wall using sand backfill, paper reinforcement, and poster board wall facing. The Geo-Challenge resulted from the work of an ad hoc committee created by ASCE's Board of Governors of the Geo-Institute in 2001 charged to develop a national geotechnical competition for students analogous to the concrete canoe competion (Elton, et al., 2007). The first two Geo-Challenge national competions were held as part of ASCE's national meetings of the Geo-Institute in Austin, TX (GeoFrontiers, 2006) and Denver, CO (GeoDenver, 2007). Selected teams of graduate and undergraduate students from selected universities competed at these venues. The Geo-Challenge was originally developed by a team of faculty members (Elton et al., 2005) noting that "The intent of this competition is to foster teamwork and sportsmanship in geotechnical engineering design. The competition rewards innovative engineering in minimizing the amount of construction materials used, while maintaining practicality in assembly and construction times." This paper hopes to demonstrate that the Geo-Challenge, when used as a curricular activity, offers a substantial learning opportunity for students. Further, it allows the students to demonstrate they have attained the required abilities identified in at least four of the ABET outcomes. As a curricular activity, the Geo-Challenge does all this in an active learning environment (Goff, 2002) in a way that motivates students to accomplish the task at hand with enthusiasm and professionalism.

Geo-Challenge offers numerous opportunities for active student learning in both the design and construction phases of the activity. During the design phase, students must draw upon principles of MSE and consider the many design variables such as length of reinforcing strip, width of reinforcing strip, location of reinforcing strips on wall facing, and extent and nature of compaction. In this phase, the students also design and conduct experiments to determine properties for use in their wall design calculations. The students work in teams during the construction phase of the competition, which serves to develop both teamwork and leadership skills. Lastly, a design report is required that provides the students an opportunity for development of their communications skills. Thus, the Geo-Challenge co-curricular intercollegiate competitions held to date have offered a wonderful opportunity for those participating schools and students. Moreover, the benefits of Geo-Challenge can be extended to a wider range and greater number of students by incorporating the activity into the geotechnical engineering education curriculum. This paper describes the incorporation of the Geo-Challenge into a geotechnical engineering course at Bucknell University and the links to ABET outcomes.

CONTEXT FOR GEO-CHALLENGE AT BUCKNELL UNIVERSITY

The undergraduate program in Civil Engineering at Bucknell University is designed to provide technical breadth in civil engineering, capitalize on the liberal arts environment of the University, and to allow students to develop additional expertise in selected areas of civil engineering including geotechnical engineering. In the area of geotechnical engineering, all students are required to take two courses, i.e., (1) Engineering Geology and (2) Introduction to Geotechnical Engineering. Both of these required courses include laboratories. Beyond these two required courses, geotechnical engineering elective courses include a course in Ground Improvement Engineering that also has regularly-scheduled lecture and laboratory periods.

Ground Improvement Engineering is normally taken by seniors or first-year graduate students. The laboratory period is utilized for traditional laboratories, field laboratories, field trips and seminars by guest speakers. A portion of the Ground Improvement Engineering course is allocated to MSE walls including regularly-scheduled class time for lectures regarding the fundamental concepts and principles associated with MSE walls. Conventional homework problems are also assigned. The Geo-Challenge competition has been included the last two times the Ground

Improvement course has been offered and represents an allocation of two laboratory periods over the course of two weeks. After the students first study the principles of MSE as part of the lecture series, they are then are assigned the "design" of a MSE wall, meeting the constraints of the Geo-Challenge, as part of the laboratory series. More details regarding the assignment and the student activities during laboratory are provided below.

IMPLEMENTATION OF THE GEO-CHALLENGE

After students have completed the lecture component of the Ground Improvement Engineering course relating to the principles of MSE, they turn their attention to the Geo-Challenge. During the first of two laboratory periods, students are divided into groups of four to balance the teams with respect to student level (graduate or undergraduate), gender, and overall academic prowess. Each group then is provided the competition rules and assignment requirements as well as the materials and plywood box that are to be used in the competition. The rules used for the Geo-Challenge as a curricular activity are attached as an appendix to this paper and vary slightly from the original sources (Elton et al, 2005; Elton et al., 2007).

Materials provided include the sand, posterboard for the wall facing, and paper for the reinforcing strips. The assignment is open-ended in that the students simply are assigned the task of designing and building a MSE wall. The students also understand that the scoring rubric requires optimization of the reinforcement and the need to balance cost versus safety. That is, a safe design (i.e., one that has adequate reinforcement such that the wall does not fail or deflect excessively under its own weight and under the weight of a design surcharge) containing less reinforcement is better than a safe design with more reinforcement. Thus, the points earned on the assignment decreases as the total area of reinforcing increases.

With this open-ended, end-product driven assignment in hand, the students first establish the properties needed for design of the MSE wall. The students are told neither what properties are needed nor how to measure them. The competitive nature of this laboratory inspires creativity, and students quickly set about to measure the soil shear strength, strip/soil friction, and strip tensile strength. During the following week, each group of students completes the design and collaboratively prepares a design report. The students also are given the option to test their designs in advance during this period. Again, the competitive nature of this activity inspires students to do their best and, without being required to do so, each group tested their design and construction methods in advance.

During the second laboratory period, the students construct and test their designs in a competition following the rules of the Geo-Challenge (see appendix). Students should have organized their team in advance such that

FIG. 1. Layout of reinforcing strips.

each has specific and clear responsibilities. Shown in Figure 1 is the first lift of sand and the first layer of reinforcing strips for one particular group. Note that the front of the box includes a plywood board that remains in place until wall construction is completed.

FIG. 2. Construction technique.

Each group determines the construction methods including the method of sand placement and method of compaction. Most commonly, compaction is by hand tamping as shown in Figure 2. Once the wall is constructed, the front is removed and the wall is expected to be stable for a minimum of one minute. Depending upon the design (spacing, length, and width of the reinforcing strips) the wall may be stable, deform excessively, or fail completely.

A photograph of a successful MSE wall being subjected to the deformation check (using a straight edge) is shown is Figure 3. If the design is stable under its own weight, the MSE wall is surcharged using 0.22 kN (50 pounds) of sand added to a bucket as shown in Figure 4. This photograph depicts a successful design-build MSE wall following the rules of the Geo-Challenge. Of course, the wall could be over-designed compared with others and the scoring rubric would account for the inefficiency.

FIG. 3. Measuring deflection of constructed MSE wall.

ABET OUTCOMES

For the 2007-2008 Accreditation cycle, engineering programs are required by ABET, Inc. (formerly the American Board for Engineering and Technology) to demonstrate under Criterion 3 (ABET, 2007) that students attain:

3.a. an ability to apply knowledge of mathematics, science and engineering;
3.b. an ability to design and conduct experiments as well as to analyze and interpret data;

3.c. an ability to design a system, component or process to meet desired needs within realistic constraints;
3.d. an ability to function on multi-disciplinary teams; and
3.g. an ability to communicate effectively.

The above ABET outcomes associated with the Geo-Challenge as a curricular activity are mapped as follows. The students apply mathematics and engineering (3.a.) in their design calculations for wall stability. The students design and conduct experiments and analyze and interpret data (3.b.) as they must to figure out what properties are needed, determine appropriate methods to measure these properties, and collect and interpret the resulting measurements to determine the relevant design parameters. The students design a system and component (3.c.) as they design the MSE wall and the tensile strips used in the wall system. The students work effectively in a collaborative environment (3.d.) and while not in a multidisciplinary team in the broadest sense, the same teamwork skill and principles apply. The students also must provide effective written communication (3.g.) via their design report. As implemented at Bucknell University, students are neither given the parameters needed for design nor are given any methods to determine these parameters. The students, therefore, examine the design theory and methods to determine what to measure (e.g., the friction angle of the sand), then decide how to perform the measurements (e.g., usually direct shear test or angle of repose to determine friction angle), and then proceed to make the measurements. Thus the Geo-Challenge provides an outstanding student exercise in "designing and conducting experiments" as expected by ABET. Similarly, the independent and competitive nature of the Geo-Challenge directly challenges the students to apply mathematics, design a system, work collaboratively, and provide effective communications.

FIG. 4. A safe MSE wall.

SUMMARY AND CONCLUSIONS

ASCE's Geo-Challenge has been successfully used as an active learning exercise in the Ground Improvement Engineering course at Bucknell University. The Geo-Challenge provides the students with a wonderful opportunity to employ class fundamentals of MSE walls and create a design that they can actually build and test. Along the way, the students decide what properties they need to measure, decide how to measure the selected properties, make the measurements, and use the data in design. The students work in a collaborative environment on the design and construction of the wall and communicate their work via a design report. The Geo-Challenge incorporates five of the ABET outcomes including application of mathematics, designing and conducting experiments, designing a system, teamwork, and effective communications. The students do all this willingly driven, in part, by the desire to be the best group in the competition. It is hard to imagine a better assignment.

REFERENCES

ABET, Inc. (2007). "Criteria for accrediting engineering programs, effective for evaluations during the 2007-2008 accreditation cycle." March 2007, www.ABET.org.

Elton, D., Loehr, E., Luke, B., Sutterer, K., Townsend, F. and Zornberg, J. (2005) "ASCE student conference geotechnical competition." http://www.ce.unlv.edu/egl/asce/ASCE%20geo-event%20rules.pdf.

Elton, D., Shannon, D., Luke, B., Townsend, F. and Roth, M. (2007). "Adding excitement to soils: a geotechnical student design competition." *International Journal of Engineering Education*, Vol. 22, No. 6: page #s?.

Goff, R. (2002). "The art of creating an active learning environment." *Proceedings of the 2002 American Society for Engineering Education Annual Conference and Exhibition*, Montreal, Canada, June, 2002.

APPENDIX: Bucknell University Geo-Challenge Competition and Laboratory[1]

Objective – The objective of the geotechnical competition and laboratory is to design and build a miniature reinforced earth (MSE) retaining wall using paper reinforcement taped to a poster-paper wall facing. Design competition is to use the least area of paper strips and sustain a "footing" load of 0.22 kN (50 lbs.) in a 189. L (5 gallon) plastic bucket placed 75 mm (3 in) behind the wall top.

Teams and Design Report – There are three to four-person teams as designated by the faculty member in charge of the class and each time is required to submit a design report. The report is a maximum of 1600 words long (not including references or title page). One inch margins, single spacing and 12 point font are required. The report provides information regarding the engineered design and plan for construction of the mechanically stabilized earth wall. The report describes methods (lab tests, correlations, assumptions) used to obtain the sand and material engineering properties. The report includes design equations, material properties assumed, and factors of safety applied. The report must also state dimensions (X = ___ by Y = ___) of reinforcement paper coupon from which reinforcement strips is cut. Evaluation of the submittal considers reasonableness of design equations, material properties, factors of safety, and assumptions. "Trial and error" designs are not acceptable.

Sandbox – An apparatus, referred to as the sandbox, is used. In this curricular activity, each team is provided a plywood sandbox for the competition. The sandbox is made up of a bottom and three fixed vertical sides. The fourth side, also vertical, is a removable panel that serves as the temporary form against which the reinforced wall is constructed. The inside surfaces are planar. The removable panel is flush with the front of the box. The removable panel is held in place with threaded inserts and wing bolts as shown on Figure 1. When the front panel is removed, the two fixed parallel sides of the box are held in place by a threaded tie rod located one inch below

[1] Procedure modified for curricular use from the version of the GeoChallenge provided to competitors for ASCE's GeoDenver 2007.

the top of the box and one inch back from the inside face of the removable panel. The sandbox shall be made of ¾ inch “A-C” type plywood, with the “A” side to the inside. The inside dimensions of the sandbox are 26 inches long by 18 inches wide by 18 inches high.

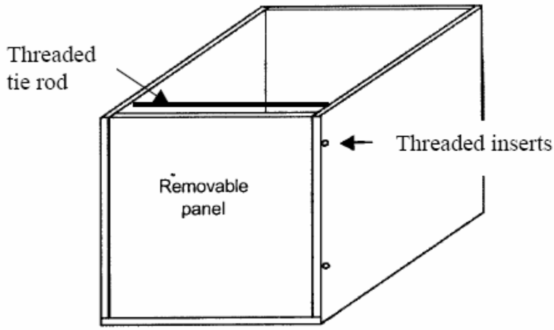

Figure 1. Schematic of plywood sandbox: front view.

Material and Methods – Prior to competition, a sample of sand backfill and reinforcement paper is provided to the students for their use and evaluation. The backfill material is a clean, dry play sand**.** The backfill material is used as provided, i.e., no water, additives, or chemical stabilizers may be placed in the backfill material. Kraft Standard Grade paper is used for reinforcement. Reinforcing materials are provided to the teams at the competition. Facing is made from one sheet of poster board, standard grade, 0.43 m x 0.56 m (17 X 22 in). To attach the reinforcement to the wall face, packaging tape or carton sealing tape, standard grade, 48 mm (1.89 in) wide is provided. Construction tools are provided by each team (quantities of these items are not be restricted) including pencils, pens, markers, rulers, straightedge, cardboard or poster board templates, cutting instruments such as scissors and razor blades, cutting boards to protect table surfaces from damage, design notes, calculations and drawings. In addition, construction tools provided at the competition include scoops, buckets, and shovels so each team has the same equipment..

Teams will be given poster-board facing which has been pre-folded for the wing-walls and bottom. A precut coupon of reinforcement is provided and includes overages for taping the reinforcement to the poster-board.

Wall construction – The assembly stage is limited to 30 minutes. During this time, reinforcement and facing are marked, cut, configured, taped, and placed in the box as appropriate, preparatory to placement of sand. No sand is placed or otherwise handled during this stage. The facing panel provided is larger than the height and width of the MSE wall so that small “wings” are folded back to protect against spillage (leakage) of sand around the edges. All tape used must be laid flat against the poster board wall facing, with the sticky side facing the poster board. (i.e. tape can only be placed vertically on the wall facing; tape cannot be used to increase the strength of the paper reinforcement in a horizontal direction.)

During the construction stage, execution stage is limited to 30 minutes. During this time, the box must be filled with sand to within 25 mm (1 in) of the top; i.e., wall height = 0.43 m (17 in), and the sand surface shall be horizontal. The loading bucket (a standard five-gallon plastic bucket) is placed on top of the sand, 75 mm (3 in) back from the wall facing and centered between the side walls. Construction shall not be considered complete until the loading bucket is in place.

The Competition – Wall loading includes the backfill and, as needed, a surcharge loading. When directed by judge, the team removes the front panel of the sandbox. After a stabilizing period of one minute, team members applies a 0.22 kN (50 lb) surcharge load by pouring sand into the loading bucket. The 0.22 kN (50 lb) of sand is measured and verified by the judges prior to this stage. Loading is completed within 5 minutes of the stabilization period. The wall must sustain the surcharge for at least 1 minute prior to measuring for “failure”.

Failure of the wall will be declared if any part of the wall system, included paper, tape and retained sand, reaches the front plane of the sandbox. If failure occurs before loading is complete, the judge will record the weight of sand in the loading bucket at time of failure.

The team that scores the most points shall be declared the winner. Points shall be awarded as follows:

1. (200-1550*X) points for total area of paper requested by the team where X is the area measured in square meters.
2. (– Y) points for the time taken during the assembly stage where Y is the time measured in minutes exceeding 30 minutes.
3. (– Z) points for the time taken during the execution stage where Z is the time measured in minutes exceeding 30 minutes.
4. Up to 25 points shall be awarded based on the quality of the summary report developed by the team to document the design process used.
5. Surcharge weight will only be used if all walls fail prior to carrying the 0.22 kN (50 lb) surcharge or if a tie occurs for the square inches of paper used.

For example: Team A used 0.090 m^2 (140 $in^{2)}$ for the paper strips, supported 0.22 kN (50 lb) surcharge, took 35 minutes in assembly, 20 minutes in execution, and report grade = 20; their score would be: 60 (paper area) + (-5 assembly) + 0 (execution) + (20 report) = 75 points.

Judging – The judge reserves the right to disqualify teams for the following reasons including: 1. Failure to adhere to the prescribed construction standards for the retaining wall, 2. Judges agree that a team has deliberately tried to violate the spirit of the competition, and 3. Design calculations, safety factors, material properties, and execution techniques provide an <u>unfair</u> advantage.

Information Literacy: Moving Beyond Wikipedia

Andrea L. Welker[1], PE, AM ASCE and Barbara Quintiliano[2]

[1]Associate Professor, Department of Civil and Environmental Engineering, Villanova University, 800 Lancaster Avenue, Villanova, PA 19085; andrea.welker@villanova.edu
[2]Instructional Design Librarian, Falvey Memorial Library, Villanova University, 800 Lancaster Avenue, Villanova, PA 19085; barbara.quintiliano@villanova.edu

ABSTRACT: In the past, finding information was the challenge. Today, the challenge our students face is to sift through and evaluate the incredible amount of information available. This ability to find and evaluate information is sometimes referred to as information literacy. Information literacy relates to a student's ability to communicate, but, more importantly, information literate persons are well-poised to learn throughout life because they have learned how to learn. A series of modules to address information literacy were created in a collaborative effort between faculty in the Civil and Environmental Engineering Department at Villanova and the librarians at Falvey Memorial Library. These modules were integrated throughout the curriculum, from sophomore to senior year. Assessment is based on modified ACRL (Association of College and Research Libraries) outcomes. This paper will document the lessons learned in the implementation of this program and provide concrete examples of how to incorporate information literacy into geotechnical engineering classes.

INTRODUCTION

When most professors were in college, the challenge was to find enough information to adequately research a topic. Today, students have instant access to a sea of information of varying quality. In addition, much to our dismay, Wikipedia is often the first item retrieved in a World Wide Web (WWW or Web) search. While Wikipedia can provide students some information, its reliability is dubious. Furthermore, we want our students to move beyond the general Internet sources and utilize the paid databases and scholarly journals to which their library subscribes.

The ability to find and evaluate information and use it properly has come to be known as "information literacy." The American Library Association (1989) provides this succinct definition: "ultimately, information literate people are those who have learned how to learn." Because information literacy is of crucial importance to our students while at Villanova and after, a program was developed at Villanova

University to teach students this set of skills. This continuously evolving program is a collaborative effort between Civil and Environmental Engineering faculty and librarians.

RELATION TO THE CIVIL ENGINEERING BODY OF KNOWLEDGE

Information literacy is directly related to two outcomes in the Body of Knowledge (2004) and ABET criteria 3 (2002) (given in parentheses). First, 7 (g). an ability to communicate effectively.The ability to find and use information in a report and cite it properly is a key component of communication. Second, 9 (i). a recognition of the need for, and an ability to engage in life-long learning: Information literacy is really the keystone of life-long learning. One must know how to obtain and evaluate information to continue learning.

PLACEMENT IN THE CURRICULUM

The literature of information literacy (Catts and Appleton 1999; ACRL 2000; Nerz and Weiner 2001; Popescu and Popescu 2003, Welker et al. 2005), as well as the findings of a focus group conducted at Falvey (Hewlett 2002), attest to the fact that students are more receptive to learning research skills when these are incorporated into their coursework, particularly into courses that have greatest relevance for them, especially in their major. Consequently, we have placed one module per semester throughout the students' time in our department (Table 1).

FOCUS ON THE SOPHOMORE YEAR

The modules developed for use in the sophomore year will be described in detail in this paper. Two courses required of all sophomore civil engineering majors, GLY 2805 (Geology for Engineers) and CEE 2311 (Environmental Engineering Science), provided a framework for a variety of activities, each of which gave the students an opportunity first to learn and then to further refine information literacy skills. The assignments used in these classes and our assessment of the program will be described.

Description of Assignments Incorporated into GLY 2805 [Use bold lowercase with capitalization for next level heading,]

The assignments and activities for the GLY 2805 class included

- Completion of the pre-class activity, "Are You Search-Savvy?"
- Participation in a hands-on database session, taught by the librarian and course instructor.
- Evaluation of two WWW sites, according to a set of criteria.

- Development of a plan for researching and completing a term paper, including a time line.
- Completion of a five-page term paper on a topic chosen after consultation with the course instructor.
- Reading and critiquing another student's term paper, following a set of criteria.

Table 1. Courses with Information Literacy Modules (from Welker et al. 2005)

Year	Course	Assignment	Implementation
Sophomore	Geology for Engineers (GLY 2805)	Term paper on issue or issues dealing with geology, environmental geology, or engineering geology	Fall 2004
	Environmental Engineering Science (CEE 2311)	Annotated bibliography on a selected topic	Spring 2005
Junior	Soil Mechanics Laboratory (CEE 3901)	Case study of a civil engineering failure	Spring 2006
	Transportation Engineering (CEE 3211)	Term paper on and analysis of a contemporary issue in transportation engineering	Spring 2008
Senior	Foundation Design (CEE 4801)	Evaluation of the resources available on a geotechnical engineering project	Fall 2005
	CEE Professional Practice (CEE 4601)	Technical report on a selected project	Fall 2007

Assignment instructions and other supporting materials were posted in the WebCT course management software, and students uploaded their assignments to the WebCT module as well. This allowed easy access to the completed assignments both by the librarian and the course instructor. Use of the WebCT module also creates additional opportunities for contact between librarian and students beyond the usual one-shot instruction session. Literature has shown (Hine 2002) that gaining mastery of information literacy skills is an iterative process. Activities and assignments of increasing levels of complexity that allow students repeated opportunities to use the resources, to ask the librarian (or course instructor) questions concerning difficulties encountered, and then to use the resources again, encourage the kind of reflection required for the higher-order learning processes of analysis, evaluation, and synthesis (Bloom 1956; Felder and Brent 2004).

Recognizing that the Millennial Generation is at home on the WWW and tends to go there first when looking for information, librarians have assumed responsibility for preparing students to find, evaluate, select, and correctly cite information found on the 'free" Web. Thus was "library instruction" transformed into "information literacy instruction." We asked our Millennial Generation students in GLY 2805 to find two websites giving background on their term paper topic. We then provided them with a list of criteria for evaluating the quality and reliability of the information and asked them to do a formal evaluation of the two websites they had chosen. We next asked the students to reflect on the types information they had not been able to find on the Web and to list them. Finally, we required them to draw up a plan and timeline for researching their paper. The website evaluation and search plan were submitted via WebCT.

One week prior to attending the hands-on session, students completed "Are You Search Savvy?" This activity consisted of two 15-item matching quizzes introducing students to essential Web and database search concepts that they would need to know when participating in the hands-on session. The students were allowed two attempts at the quiz. It was automatically graded, and the students could access their scores immediately. This provided a more interactive (and verifiable) mode of learning terms and concepts, than simply distributing print copies and asking the students to look them over.

The hands-on session consisted of a visit by the librarian to the students' classroom during which she demonstrated how to search two or three subscription databases pertinent to geology. Having brought their laptops to class, the students formed pairs and then performed searches. The librarian also explained how to access online, full text versions of the articles, how to locate articles in the library's print collection, and how to place interlibrary loan requests for articles not available through a library subscription. Finally, the students were required to keep a journal of their search activities, also to be submitted via WebCT.

Assessment of Student Performance in Information Literacy Module for GLY 2805

We used a rubric to assess level of student performance in the website evaluation and search plan, the search journal, and the term paper. In addition, an information literacy review quiz was administered via WebCT later in the semester, near the term paper due date. The quiz consisted of 10 multiple choice questions with a possible score of 100. We chose to have the students take the quiz after researching their papers and putting into practice the skills taught in the hands-on session. The median score was 70.5.

WebCT's quiz grading mechanism provides statistics not only on performance on the quiz as a whole, but also on how the students performed in each question. This allowed us to determine which items the students found most difficult, with a view to revising the method of teaching those skills in the following academic year. Figure 1 shows that the students had the most difficulty with the proper formulation of a nested Boolean search, a necessary skill for searching library databases.

The following open-ended opinion question was also included in the review quiz:

For your work in this course you have used one or more search engines (such as Google) to search the World Wide Web and library databases (such as Applied Science Index and GeoRef) to search for journal articles.

- Did you find one easier to use than the other?
- What other feedback can you offer about Web searching and library database searching?

  Please type your remarks in the box.

  NOTE: Your response to this question does not count toward your score. Thanks for your comments!

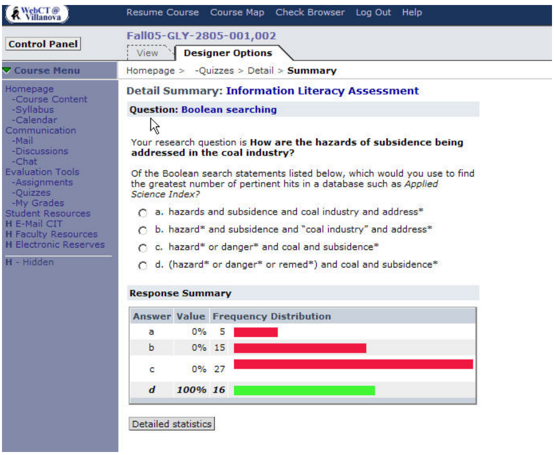

FIG. 1. Example of Boolean search question

Our purpose in including this non-graded question was twofold: 1) to encourage students to reflect on the research process they had recently engaged in and 2) to gather anecdotal information on student attitudes regarding searching on the Web and searching in subject-specific databases. Some of the very revealing student responses are presented below. Note that these are actual responses; they have been edited for spelling only.

- I feel as though they were all pretty much the same and of equal difficulty to use, which was not difficult at all. Web searching and library database searching is very helpful and really contributed to my paper.
- I think that Google was easier to use to find information however this information is questionable. Although it's harder to use the library databases they are a lot more credible.
- Google was certainly the easiest search engine to use because it required no logging in, and gave quick results. Unfortunately about half of the websites on google are product or service related, and are not very credible. Using Applied Science index and Georef are very beneficial if you have a lot of time to spend

> searching, and want to come up with very credible information, so for a project like the one just compleeted, they work great. I was very satisfied with both my google searches and my alternate source and book searches through Villanova's library, but the majority of the information I used for my paper came from books, articles, and publications found through the library's database.

Many students came to understand the importance of evaluating Web information for accuracy and reliability. Quite a few also noted that Google was easier to search than the library databases, a fact unfortunately all too true and one that presents a constant challenge.

Finally, by including three questions on the geology final exam, the incorporation of information literacy concepts and skills into the course work was completed. Two questions from the 2005 final are shown below.

> 1. You watch an investigative report on your local Fox News station about a landfill located close to your neighborhood. According to the reporter, the landfill is on the verge of failing and will release a cocktail of toxic liquids into the groundwater you cook and clean with. In an attempt to get more information on the factors that the reporter claims are causing the failure, you do a Google search on failed landfills and find a lengthy article in the Wikipedia. What features will help you determine whether the Wikipedia's information is reliable? (Check off all that apply.)
>
> a. References to books and journal articles.
> b. Links to other Wikipedia articles.
> c. Evidence that the author(s) of the Wikipedia article has (have) an advanced degree in environmental engineering or a related area of study.
> d. The fact that the information is free.
>
> 2. You search a topic in General Science Index. Two articles listed in your results are very relevant and you wish to read them, but they are not available full text online. You immediately fill out an interlibrary loan form. Did you proceed correctly?
>
> Yes. When an article is not available full text online, your only other option is to try to get it from another library.
> No. You must first check VUCat to see if the article is available in print at the library.

Assignments and Activities in CEE 2311

In the civil engineering curriculum, CEE 2311 follows immediately upon GLY 2805 in sophomore year. This provided opportunities for immediate reinforcement of the information literacy skills and concepts the students had learned in GLY 2805, as well as a framework within which to build upon them. In CEE 2311 the students were given a single information literacy assignment:

> In this module you will learn how to create an annotated bibliography of materials concerning an outbreak of waterborne diseases that occurred in Wisconsin, Milwaukee, in the spring of 1993. Your bibliography will contain 8 items or citations, that is, 1 citation for each of the following 5 types of sources:
>
> - 2 annotated journal article citations (1 citation for each of 2 journal articles)
> - 1 annotated citation to a conference proceeding
> - 1 annotated citation to a federal regulation
> - 1 annotated citation to a state regulation
> - 3 book citations (1 citation for each of 3 books).

We again used the WebCT platform to post materials explaining and illustrating the different types of information sources in the field of engineering, allowing the students to read them outside of class and then take a short multiple-choice quiz to see how well they absorbed the material. As in GLY 2805, this provided a more interactive way of learning introductory material. During the hands-on session, students searched specialized databases, such as *Compendex,* to search for journal articles and conference proceedings. The librarian introduced students to the online versions of the *Code of Federal Regulations* and, as an example of a compilation of state regulations, the *Pennsylvania Code.* She then offered guidance as they used the search engines provided on the respective sites to find regulations governing the purification of drinking water.

Assessment of Student Performance in Information Literacy Module for CEE 2311

The annotated bibliographies were submitted in paper form and were scored according to a rubric. The librarian and course instructor shared the task of grading, with the librarian scoring the category “ASCE Documentation Style” and the course instructor scoring the other three categories. Possible scores for application of ASCE style were 25, 20, 10, and 0.

CONCLUSIONS

Information literacy has been part of our curriculum since 2004 when the assignment for CEE 4801 was developed. This assignment then spurred the development of the modules in the other classes. Information literacy is a critical skill that must be included in our already packed curriculums. We would all like to believe that our students come to college with this skill set, but unfortunately that is not the case. The investment in class time results in far superior work products from the students.

We believe that the success of our program can be attributed to the integration of the modules throughout the curriculum and the collaboration between librarians and faculty. When the faculty fully incorporate these assignments into the classes, the students respond with quality work.

REFERENCES

Accreditation Board for Engineering and Technology (ABET) (2002). *Criteria for Evaluating Engineering Programs*. Available on line at <http://www.abet.org/criteria.html>.

Association of College and Research Libraries (ACRL) (2000). *Information Literacy Standards for Higher Education*. Available on line at http://www.ala.org/Content/NavigationMenu/ACRL/Standards_and_Guidelines/Information_Literacy_Competency_Standards_for_Higher_Education.htm.

American Library Association Presidential Committee on Information Literacy. (1989). *Final Report*, American Library Association, Chicago, IL. Available online a at < http://www.ala.org/ala/acrl/acrlpubs/whitepapers/presidential.cfm>.

American Society of Civil Engineers (ASCE) (2004). *Civil Engineering Body of Knowledge for the 21st Century*. Available online at <http://www.asce.org/files/pdf/bok/bok_complete.pdf>.

Bloom, H. (1956). *Taxonomy of Educational Objectives. 1. Cognitive Domain.* Longmans, Green, New York.

Catts, R.M. and Appleton, M. (1999). "Assessing Models of Information Literacy," *Selected Papers from the 10th International Conference on College Teaching and Learning*, J.A. Chambers, Ed. 23-32.

Felder, R.M. and Brent, R. (2004). "The ABC's of Engineering Education: ABET, Bloom's Taxonomy, Cooperative Learning, and So On." *Proceedings of the American Society for Engineering Education,* session 1375. Available online at <http://www4.ncsu.edu/unity/lockers/users/f/felder/public/Papers/ASEE04(ABCs).pdf>.

Hewlett, D. (2002). *Focus Group Report: Information Literacy Program at Villanova University.* Villanova: Office of Planning, Training and Institutional Research, Villanova University.

Hine, A., Gollin, S., Ozols, A., Hill, F., and Scoufis, M. (2002). "Embedding Information Literacy in a University Subject through Collaborative Partnerships." *Psychology Learning and Teaching*, 2(2), 102-107. Avalable online at <http://www.ala.org/ala/acrlbucket/is/projectsacrl/infolitdisciplines/psychology.htm>.

Nerz, H.F. and Weiner, S.T. (2001). "Information Competencies: A Strategic Approach," *Proceedings of the 2001 American Society for Engineering Education Annual Conference and Exposition*. Available on line at <http://www.asee.org/conferences/search/00510_2001.pdf>.

Popescu, A. and Popescu, R. (2003). "Building Research Skills: Course-Integrated Training Methods," *Journal of Professional Issues in Engineering Education and Practice*, 129(1), 40-43.

Welker, A., Quintiliano, B., and Green, L. (2005). "Information Literacy: Skills for Life," *Proceedings of the 2005 Annual Conference*, June 12-15, Portland, Oregon. Available on line at <http://www.asee.org/acPapers/2005-1019_Final.pdf>.

Invigorating Geotechnical Engineering Education at the University of Illinois

Abouzar Sadrekarimi[1], S. M. ASCE, Nejan Huvaj-Sarihan[2], S. M. ASCE, and Scott M. Olson[3], M. ASCE, P.E.

[1] Ph.D. Candidate, Department of Civil & Environmental Engineering, University of Illinois at Urbana-Champaign, Urbana, IL, 61801 USA. email: asadrek2@uiuc.edu
[2] Ph.D. Candidate, Department of Civil & Environmental Engineering, University of Illinois at Urbana-Champaign, Urbana, IL, 61801 USA. email: huvaj@uiuc.edu
[3] Assistant Professor, Department of Civil & Environmental Engineering, University of Illinois at Urbana-Champaign, Urbana, IL, 61801 USA. email: olsons@uiuc.edu

ABSTRACT: In recent years, U.S. geotechnical academic programs have experienced decreasing numbers of enrolled students; meanwhile, the demand for qualified, professional geotechnical engineers has increased. The Geo-Institute (G-I) of the American Society of Civil Engineers (ASCE) was founded primarily to advance and promote the geo-engineering community. As part of its recent strategic plan (Geo-Institute 2005), the G-I plans to increase its membership and expand its programs for students at all levels, as well as to promote and support G-I student chapters. As part of this effort, graduate students at the University of Illinois at Urbana-Champaign (UIUC) recently established a G-I student chapter. Since its founding, the UIUC G-I student chapter has organized numerous educational, research, and outreach programs and activities. These activities already appear to reaping benefits by raising civil engineering undergraduate student awareness of geotechnical engineering and increasing graduate enrollment in geotechnical engineering. This study demonstrates the activities of this student chapter and their effectiveness in fulfilling the goals of this organization.

INTRODUCTION

Engineering degrees awarded in the United States at the bachelor's, master's and doctoral levels have increased in number since reaching a low point in the late 1990s. Similarly, the number of bachelor's and master's degrees awarded in civil engineering also has increased in recent years (Heckel 2006). Geotechnical engineers constitute a small portion of the civil engineering community, with only 7% of the American Society of Civil Engineers' (ASCE) 130,000 membership classifying themselves as geotechnical engineers (Townsend 2005). Recently in U.S. universities, undergraduates seem to show less interest in selecting geotechnical engineering as a major. But the demand for qualified, professional geotechnical engineers is expected to increase in the near future (Geo-Institute Strategic Plan 2005, Townsend 2005). The Geo-Institute (G-I) of ASCE was founded primarily to advance and promote the geo-engineering community. As part of its recent strategic plan, the G-I plans to increase its membership and expand its programs for students at all levels, as well as to promote and support G-I student chapters (Geo-Institute Strategic Plan 2005). As part of this effort, graduate students at the University of Illinois at Urbana-Champaign (UIUC) recently established a G-I student chapter.

In this paper, we describe some of the educational, research, and outreach activities of the Geo-Institute Student Chapter at UIUC, discuss how we integrate active learning opportunities into chapter events, and highlight the importance of having a dynamic geotechnical group within the Civil and Environmental Engineering (CEE) Department. Furthermore, we discuss early indicators of the Chapter's positive influence on increasing student awareness of geotechnical engineering and increasing enrollment in our graduate geotechnical engineering programs at the University of Illinois. We anticipate that these changes reflect the importance of undergraduate student involvement, as well as the need for and value of providing leadership opportunities in geotechnical engineering programs.

INVIGORATING GEOTECHNICAL EDUCATION AND OUTREACH

Graduate students in the Civil and Environmental Engineering Department at UIUC established a G-I student chapter in August 2006 (www.uiuc.edu/ro/GESO). One of the chief motivations for creating the student chapter was to foster a dynamic and active geotechnical engineering group within the CEE Department. The objectives of the student chapter are to: (1) gain greater understating of geotechnical engineering; (2) improve the members' social interaction skills and appreciation for teamwork; (3) increase interest in geo-engineering; (4) help members to establish professional contacts; and (5) develop and improve leadership skills. Specifically, the chapter's regularly-scheduled open forums, invited lectures, and general meetings promote student social interaction, and provide opportunities for students to enhance their education and improve their geotechnical knowledge and skills. In addition, community outreach activities introduce local and state K-12 students to geotechnical engineering while affording the chapter members leadership and teaching opportunities. Finally, the chapter emphasizes the importance of being an active member in the geotechnical community via significant contributions to conferences and workshops. Thanks to a substantial effort by several graduate students to promote the chapter, 18 undergraduate and 26 graduate students joined the UIUC student chapter, increasing student membership in the Geo-Institute and increasing subscription to Geo-Strata magazine. In its first year, the student chapter organized a number of activities and events to achieve its goals. We mention some of these activities here in order to share our experiences with students at other universities and to encourage them to establish their own Geo-Institute student chapters.

Invited Seminar Series

The student chapter, with the help of geotechnical faculty in the CEE Department, organized an informal geotechnical and geoenvironmental engineering invited seminar series. Six speakers from industry and academia spoke on topics including waste containment facilities, landslides, tsunami sediments, pile foundations, and reinforced earth walls. Faculty, graduate students, and undergraduates attended the seminars and interacted with the speakers.

Discussion Forum

The student chapter organized a bi-weekly "Geotechnical Discussion Group" as an outlet for graduate students to present their research, rehearse for upcoming presentations, or discuss topics/projects from their classes. The informal group forums allow students to get immediate feedback from their fellow graduate students, as well as undergraduate upperclassmen. Several graduate students had mentioned the need for such an open/friendly atmosphere to talk about their own research projects, and also learn about the ongoing research in the department, and commended the student chapter for organizing the discussion group.

Documentary Screenings

The student chapter organized a "Lunch & a Movie" series to watch geoengineering-related documentaries, typically over the lunch hour. Chapter officers observed that the undergraduate student attendance was high for these events.

Field Trips

The student chapter organized two field trips to observe belled drilled shaft (Figure 1) and tieback wall construction with the help of geotechnical faculty. It is well-known that students better absorb lessons when learning them actively rather than in a passive lecture environment, particularly at under-graduate level (Langdon 2003), and the field trips offered excellent opportunities to expose students to geotechnical construction while learning the design procedures that precede construction. The geotechnical students greatly enjoyed the field trips and requested more field trip opportunities from the faculty.

FIG. 1. Geotechnical students observing belled drilled shaft construction with geotechnical faculty Professor Olson.

Outreach and Service-based Events

The importance and benefits of engineering educational outreach also is well known. Elton et al. (2006a; among many others) provide examples of geotechnical outreach activities. To introduce geotechnical engineering to K-12 students and the general public, the G-I student chapter participated in the annual Engineering Open House (EOH) event organized by the College of Engineering at UIUC. During the two-day event, chapter members described to hundreds of visitors the concepts of quicksand, seepage, and liquefaction (Figure 2), and how reinforced earth walls are built. Each demonstration allowed visitors (particularly young children) an opportunity to "play in the sand." Chapter members explained basic soil mechanics concepts such as effective stress, seepage forces, and lateral earth pressure. The chapter presenters noted that explaining these concepts in simple terms to the EOH visitors helped them understand the subjects better. The demonstrations were very well received by the audiences, generating questions and interest in geotechnical engineering, and even earning the presenters a College of Engineering EOH Award.

In addition to EOH, chapter members participated in the Worldwide Youth in Science and Engineering "Exploring Your Options" program. During one day of this week-long event, high school junior and seniors from local schools visited the CEE Department and gained hands-on experience in geotechnical engineering. After a brief discussion of basic geotechnical concepts, students divided into small groups to design and build a reinforced earth wall. After each team finished the constructing their walls, the walls were load tested to failure (Figure 3).

FIG. 2. G-I Student Chapter members describing quicksand during Engineering Open House 2007.

FIG. 3. High school juniors and seniors observing their reinforced earth wall under surcharge load during "Exploring Your Options" 2007.

Geo-Challenge 2007

Two undergraduate and two graduate student chapter members formed a team and participated at the Geo-Institute's Geo-Challenge competition (Figure 4; see Elton et al. 2006b for competition details) held in Denver, Colorado in February 2007. The student team designed a reinforced earth wall consisting of sand as the backfill material, paper strips as the reinforcement and post board as the wall facing. The UIUC team obtained a backfill sand sample and performed direct shear and triaxial tests on the sand. The team also measured the pull-out capacity of the paper strips and constructed several trial walls. The competition incorporated elements of: theoretical soil mechanics, design, optimization, creativity, teamwork, and written communication. The competition provided the chapter team members with an opportunity to apply their knowledge and skills to a design situation. Involving undergraduate students in the competition proved to be very beneficial in promoting geotechnical engineering among undergraduates, motivating the two undergraduate team members to pursue master's degrees in geotechnical engineering and to accept summer internships with geotechnical engineering firms.

Geo-Institute Annual Conference

Four student chapter members traveled to Denver, Colorado for the Geo-Institute's annual conference. As mentioned above, participating in the conference and the Geo-Challenge helped motivate the two undergraduate students to pursue geotechnical engineering as a career. All four of the student chapter members enjoyed the conference presentations, benefited from the professional career fair and exhibits, and got to interact with geotechnical engineering legends such as Professor Peck and Professor Lacasse (Figure 5).

FIG. 4. G-I Student Chapter members competing at Geo-Institute's Geo-Challenge 2007 event held in Denver, Colorado during the annual G-I conference.

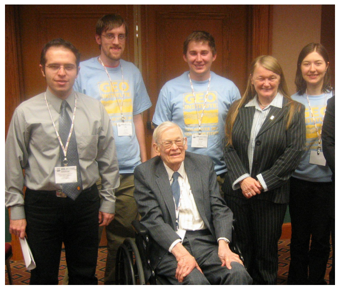

FIG. 5. G-I student chapter members with Professor Peck and Professor Lacasse at the 2007 G-I Annual Conference in Denver, Colorado.

IMPORTANCE OF UNDERGRADUATE STUDENT INVOLVEMENT

Early in the planning stages for the G-I student chapter at UIUC, we felt it was important to engage undergraduate students in the chapter and its activities. Ample research has shown that engineering students learn better through hands-on projects and activities, rather than by only watching and listening to lectures (e.g., Langdon 2003; Aydilek 2007). Engaging students in activities that promote critical thinking (i.e., problem analysis, synthesis, and evaluation) is highly effective in improving engineering education.

As a result, we believe that the student membership in Geo-Institute and our student chapter should be open to undergraduate students, and therefore we allowed and encouraged undergraduates to join the UIUC student chapter. By including undergraduate students, we can engage younger undergraduate students who may be interested in geotechnical engineering but don't get exposed to the geotechnical curriculum until later in their undergraduate career. Additionally, for those who enter geotechnical engineering, this early exposure increases their likelihood of staying as active members of the geo-profession after graduation.

PROVIDING LEADERSHIP OPPORTUNITIES

In the recent years, national educational and engineering organizations (e.g., ABET, National Academy of Engineering, ASCE) have increased their emphasis on the importance of “professional” (or “soft”) skills for engineering graduates (ABET Engineering Criteria 2000; National Academy of Engineering 2004; Kumar and Hsiao 2007). Some of these skills include effective communication, teamwork, understanding ethics and professionalism, and lifelong learning. In addition to strong analytical skills and technical excellence in science and engineering, employers expect engineering graduates to have leadership, teamwork, and management skills in order to succeed in rapidly changing work environments (Kumar and Hsiao 2007).

Similarly, the National Academy of Engineering (2004), in their study of *The Engineer of 2020* emphasized the importance of these skills in future engineering leaders. The opportunities for engineers to exercise their leadership potentials will increase in nonprofit and governmental sectors and they will be the policy decisions makers in technological societies. Therefore, engineers should be prepared for this opportunity by learning the principles of leadership and applying them in their careers (National Academy of Engineering 2004). For these reasons, it is important to provide students with a platform to develop leadership skills. The UIUC student chapter of the Geo-Institute provides opportunities for its members to develop these leadership and professional skills through executive board positions (leading the chapter), organizing visits and student interaction with geoprofessionals, holding geotechnical forums, and organizing “learning” visits to geotechnical project sites.

CHAPTER EVALUATION

In order to preliminarily evaluate how well the student chapter met the chapter’s objectives, as well as to plan for future activities, the chapter officers conducted a brief written survey of the membership, invited speakers, and geotechnical faculty. Of the 44 surveys distributed, we received 25 responses. Table 1 summarizes the survey results. These initial results demonstrate that the student chapter was successful in achieving its goals, despite being in its first year. The students also expressed their satisfaction by stating, for example, “I think GESO is a great way for the geotechnical engineers at the University of Illinois to interact outside of the classroom.” The participants of the survey suggested having more lectures about field case histories, more field trips, as well as more social activities.

The invited speakers also expressed their approval of the student chapter. For example, one speaker stated that, “The folks at UIUC make it a very hospitable place. I've enjoyed both of my visits there. I've also been impressed with the quality of students too, based on my brief meetings in the labs with them to see what they're up too.” Another speaker said, “I had a great experience last time; couldn’t ask for better. Moreover, I’d like to come back and give another talk this fall.”

TABLE 1. Average results of the G-I student chapter survey

Question	Response[a]
I enjoyed being a member of GESO.	4.5
I would like to continue to be a member of GESO.	4.6
The "Lunch & a Movie" program improved my geotechnical engineering knowledge.	4.1
The lecturers improved my geotechnical engineering knowledge.	4.2
The discussion group meetings improved my geotechnical engineering knowledge.	3.8
The field trips improved my geotechnical engineering knowledge.	4.2
GESO improved my social interaction skills.	3.6
GESO improved my interest in geotechnical engineering.	4.1
GESO helped me to establish professional contacts through invited speakers.	3.5
I would like to participate in the next Geo-Challenge and Engineering Open House activities.	3.3
GESO improved my leadership skills (if you were a GESO officer)	3.5
I developed appreciation for teamwork (if you were a GESO officer)	3.5

NOTES
[a] 5 = Strongly agree; 4 = Agree; 3 = Neutral; 2 = Disagree; 1 = Strongly disagree.

Lastly, as the G-I student chapter is only one year old, it is difficult to quantify its effect on the geotechnical program at UIUC. However, preliminary indicators appear to show that the student chapter has contributed to an increased interest in geotechnical engineering among undergraduates. For example, comparing enrollment rates from Fall 2006 (prior to the formation of the G-I student chapter) to Fall 2007 (after its formation), the total number of applications to the geotechnical engineering graduate program increased by more than 100%. In addition, graduate enrollment in geotechnical engineering increased from 5% (in Fall 2006) to 13% (in Fall 2007) of the total new graduate student enrollees in the CEE department. These trends are quite promising, and we believe a continued effort by the G-I student organization will help to sustain these trends.

CONCLUSIONS

Recently, graduate and undergraduate students in the Civil and Environmental Engineering Department at the University of Illinois at Urbana-Champaign formed a Student Chapter of the ASCE Geo-Institute. The educational, research, and outreach activities of the G-I Student Chapter at UIUC already are helping to integrate active learning opportunities in the geotechnical engineering curriculum, and are beginning to result in increased enrollment in the graduate geotechnical engineering program. We believe that one of most important missions of the chapter is to provide opportunities to geotechnical and civil engineering students for developing their leadership and interpersonal skills, as the role of future geo-engineers is increasingly becoming leadership, management, and teamwork oriented. Our experiences with the Geo-Institute student chapter at the University of Illinois was very successful in achieving its goals during its very first year of establishment based on feedback from student members, invited speakers, and CEE faculty, as well as preliminary indicators related to enrollment in the graduate geotechnical engineering program. Based on this successful performance, we are planning future activities for the chapter to sustain these initial successes.

ACKNOWLEDGMENTS

The G-I Student Chapter and its members would like to thank the UIUC Civil and Environmental Engineering Department for financially assisting the student chapter and its activities.

REFERENCES

ABET (2000). "Criteria for accrediting engineering programs." Engineering Accreditation Commission, Nov 2003. http://www.abet.org/criteria_eac.html.

Aydilek, A. H. (2007). "Digital image analysis in geotechnical engineering education." *Journal of Professional Issues in Engineering Education and Practice*, 133(1), 38-42.

Elton, D.J., Hanson, J.L., and Shannon, D.M. (2006a). "Soils magic: bringing civil engineering to the K-12 classroom." *Journal of Professional Issues in Engineering Education and Practice*, 132(2), 125-132.

Elton, D., Shannon, D., Luke, B., Townsend, F., Roth, M. (2006b). "Adding excitement to soils: a geotechnical student design competition." *International Journal of Engineering Education*, 22(6), 1325-1336.

Geo-Institute (2005). Geo-Institute Strategic Plan, www.geoinstitute.org.

Heckel, R.W. (2006). "Historical trends and near-term predictions of statistics on degrees, enrollments, and research expenditures for engineering education in the United States." *Engineering Trends Report 0806A – August 2006*, www.engtrends.com, last viewed on June 10, 2007.

Kumar, S., and Hsiao, J.K. (2007). "Engineers learn 'soft skills the hard way': planting a seed of leadership in engineering classes." *Leadership and Management in Engineering*, January, 18-23.

Langdon, N. (2003). "Geotechnical engineering education and the lost 60,000; who mislaid them? A personal view." *Proc. Institution of Civil Engineers Geotechnical Engineering*, 156(1), 5-6.

National Academy of Engineering, (2004). "The engineer of 2020: visions of engineering in the new century." The National Academies Press, Washington, DC,

Townsend, F.C. (2005). "Challenges for geotechnical engineering graduate education." *Journal of Professional Issues in Engineering Education and Practice*, July, 163-166.

Modeling Instruction in an Environmental Geotechnics Course

Marina Pantazidou[1], A.M. ASCE and Paul S. Steif[2], M. ASME

[1]School of Civil Engineering, National Technical University of Athens, Iroon Polytechniou 9, Zografou 15780, GREECE, mpanta@central.ntua.gr
[2]Department of Mechanical Engineering, Carnegie Mellon University, Pittsburgh PA 15213, USA, steif@andrew.cmu.edu

ABSTRACT: Although modeling of physical systems is a key engineering task, the educational literature provides little guidance on how to systematically include modeling exercises in instruction. To this end, this paper presents work-in-progress involving the introduction of a framework of modeling in an environmental geotechnics course. The framework unpacks the components of the modeling process, placing particular emphasis on the simplifications made when considering relevant phenomena, determining parameters and variables, specifying geometry and boundary conditions, selecting and solving governing equations. Explicit modeling instruction required modification of learning outcomes and corresponding revisions of instructional material, example problems and exam questions. The development of a larger-scale term project is underway, designed so that students gain confidence when selecting different levels of approximations, through comparisons of numerical solutions at different degrees of idealization with simplified analytical solutions.

INTRODUCTION

The key role of modeling in geotechnical engineering has been identified by leading researchers and revered teachers in the field (Burland 1987, 2006; Lundell-Sällfors and Sällfors, 2000). Modeling of environmental geotechnics problems shares the complexities of geotechnical problems, with the additional difficulty of deciding to account for all or ignore some of the phenomena related to the release and the fate of contaminants in the subsurface. However, despite its importance, the process of modeling remains a "black box" for instruction purposes. While on the surface modeling appears to be a mainstay of engineering education, engineering instruction focuses much more heavily on model analysis than on model formulation.

With the aforementioned motivation, this article has the following two objectives. First, to review an existing modeling framework (Pantazidou and Steif, 2003; Steif and Pantazidou, 2004). Second, to propose possible applications of the framework in instruction, using as example its introduction in an environmental geotechnics course taught at the last year of a five-year civil engineering program. The aim is that this paper serve as catalyst for the kind of discussion that could both (i) advance further the proposed framework and its applications and (ii) bring forward alternatives, with the ultimate goal of increasing the instances of explicit instruction on engineering modeling.

ON MODELING IN GEOTECHNICAL ENGINEERING

The central role of modeling in geotechnical engineering was highlighted early on by Burland (1987). In this seminal address, Burland (1987) introduced a graphic where he placed at the apexes of a triangle three main aspects of soil mechanics, namely *ground profile*, *soil behavior*, and *applied mechanics*, with a fourth aspect, *empiricism-experience*, at the center of the triangle, intertwined with the other three. Regarding *applied mechanics*, he noted that it includes "idealization, modeling and analysis". In a later revision of the, now known as, "Burland triangle", *applied mechanics* is replaced by *appropriate model* and is accompanied with the explanatory note "idealization followed by evaluation, conceptual or physical modeling, analytical modeling" (Burland, 2006). In the same vein, Lundell-Sällfors and Sällfors (2000) placed particular emphasis on the use of realistic problems in instruction as means for students to acquire experience with the demanding task of translating a real-life situation into a well-defined engineering problem.

Problems in environmental geotechnics naturally share similar difficulties with geotechnical problems, e.g., same issues with approximations of geometry and properties, reductions of dimensionality and idealizations of boundary conditions. Moreover, geoenvironmental problems offer a larger menu of phenomena (to take into account or ignore) and of corresponding parameters. In addition, they are characterized by a wider variety of initial conditions, e.g., types of contaminant releases at the source. Hence, as in many applied engineering courses, it becomes a challenging task for the instructor to bring rich "solvable" problems in class.

A MODELING FRAMEWORK

The aim of developing a framework for modeling was to articulate its constituent components. The motivation was to come up with guidance, in the form of a framework, to assist instructors with teaching the modeling process and help students practice modeling. Pantazidou and Steif (2003) and Steif and Pantazidou (2004) discuss in detail the background of framework development. This section summarizes the main premises and features salient for instruction.

Seeking the constituent components of a complex mental task, like engineering modeling, rests on the assumption that such components exist and can be found. The literature of cognition and instruction provides evidence that this indeed is the case [e.g., see work by Goel and Pirolli (1992) on design]. What is more, there is evidence that explicit task decomposition improves student performance [e.g., see work by Lovett and Greenhouse (2000) on statistical modeling].

Constituent components of cognitive tasks can be determined by following either a prescriptive or a normative approach. Developers of prescriptive frameworks focus on what a particular task *should look like*, judging from their experience as either seasoned instructors or experts in the respective discipline, or both. In contrast, normative approaches are based on studies of subjects performing the task and hence their results may come closer to what a cognitive task *actually looks like*.

The authors followed the normative approach, using interviews and protocol analysis. For this purpose, three open-ended sample problems were constructed, all involving a real situation or object. The problems were drawn from the areas of mechanics, soil mechanics and contaminant transport. The contaminant transport problem can fit very well in an environmental geotechnics course. It is drawn from an actual project and addresses the common question of confirming or discarding the possibility that a spill at a particular location is the source of contaminant detections in groundwater. The data for this problem consisted of an air photograph and a contour map of the groundwater table elevation, marked with the locations of the potential sources and the contaminant detection. Figure 1 provides a zoomed-in sketchy version (due to space limitations) of the contour map and a summary of the problem statement.

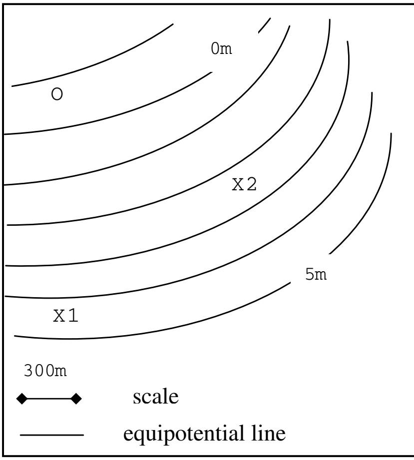

A trichloroethylene (TCE) spill took place in 1970 at one of two possible locations, X1 or X2. In 1995, TCE is detected in a groundwater sample from location O. It is difficult to obtain additional samples between the X's and O because there is an airplane landing strip between them. Could you make a first estimate whether X1 or X2 could be a potential source?

X potential TCE source
O TCE detection

FIG. 1 Sample modeling problem used in student interviews (spill problem).

During interviews, graduate students were asked to “think aloud” about how they would go about formulating and solving the problems. The interviews were tape-recorded and transcribed. These transcripts are often referred to as protocols. Protocol analysis consists of (1) developing a coding scheme (i.e., deciding on suitable labels that describe the categories of subtasks on which subjects focus), (2) segmenting the protocol (i.e., grouping related utterances) and (3) coding (i.e., labeling) the segments. A following short excerpt from a transcript of the spill problem (Figure 1), coded as *qualitative solution*, serves as an example: [Since I know it is going in this direction, I know it would be a spill here (Note: student sketches contour) and then with time it would be growing (Note: student sketches wider contours), it would be traveling, but then it would also get longer and wider … so the question would be in some time could it spread big enough…].

The developed coding scheme includes ten categories of focus corresponding to the hypothesized components of the modeling task, some of which can be grouped together. The ten modeling components are indicated with italics on Figure 2, where they are numbered for reference purposes.

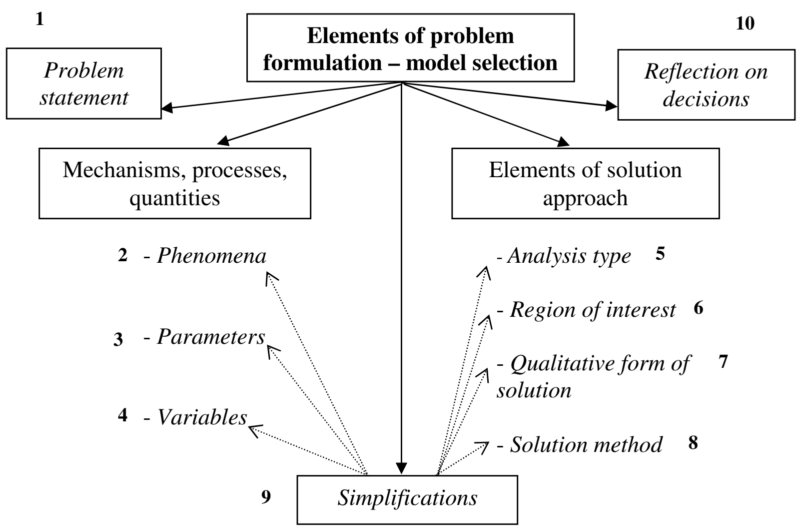

FIG. 2 Constituent components of engineering modeling.

Transcript analysis indeed showed that subjects attended to subtasks suitably described by the chosen focus categories, thus providing confirmation that the selected coding scheme is meaningful and an indication that the coding categories represent the constituent components of modeling. It is worth noting that various attempts at simplifying the problems were explicitly mentioned during the interviews. *Simplifications* were thus acknowledged as a separate component, despite their necessary relation to the other modeling components (e.g., simplifications of parameters, simplifications of analysis type, etc.).

The ten categories were accompanied by detailed annotations, developed both to clarify each category and to reduce ambiguity during coding. Because the annotated version of the coding scheme is two-page long, annotations of only two categories, *phenomena* and *simplifications*, are included as examples next.

2. Phenomena

- statements about what is happening physically
- causal relationships or interactions between effects or events
- related physical effects that would be relevant if present (often not obvious from problem statement)

• statements about what can go wrong (failure modes or critical conditions)
• proper names for physical phenomena.

9. Simplifications

• Idealization, approximation, estimation, or neglect
• Must include recognition that a relative simplification has been made
• Simplifications are always with respect to another element, such as:
    • Phenomena: idealize operative phenomena or neglect phenomena
    • Parameters: approximation (replacing a known complex variation with a simpler one), estimation (rough quantification of the value of an unknown parameter), neglecting the role of a parameter
    • Variables: neglect the variation with an independent variable or idealize the variation with respect to a variable. Can involve anticipating whether or not a quantity has a magnitude to be of further concern.
    • Analysis type: Simplification of mathematical relationships, including idealized relations (e.g., linear) between quantities, bounding behaviors (such as rigid body, potential flow) with specific mathematical consequences, approximate or partial implementation of principles
    • Region (or subsystem) of interest: neglect of a region as not being worth investigating, simplify geometry of subsystem, simplify external interactions
    • Solution method: each method can have a variety of simplifications.

USING THE MODELING FRAMEWORK IN INSTRUCTION

Including modeling instruction in a course starts with stating the corresponding learning outcomes. The instructor is required to describe what modeling is and decide on levels of modeling performance for purposes of assessment. For all these decisions, the modeling framework can serve as a useful guide. The instructor then has to create instructional materials compatible with the aforementioned decisions. This section describes the evolution of course modifications made by the first author while introducing modeling instruction in an environmental geotechnics course, an advanced undergraduate course taught at the fifth year of the civil engineering program at the National Technical University of Athens (NTUA), Greece.

Learning outcomes

The overarching goal of the course is to develop environmental thinking related to risk assessment, recognition of the mechanisms affecting the fate of a contaminant release in the subsurface, and selection of suitable remedial measures and/or technologies. The goal of the course is mapped to the learning outcomes below, i.e., the goal is achieved if at the end of the course the students:

• can locate reliable data on the effects of contaminants on human health,
• are confident in applying principles of mass transfer, groundwater flow and contaminant transport to problems of contamination and restoration of the subsurface,
• are able to address the geoenvironmental aspects of landfill and clay barrier design,
• are familiar with a wide range of remediation technologies,
• are able to take initiatives related to modeling, i.e., related to the formulation of a

simplified problem that admits solution,
• are aware of some social or public policy dimensions of the problems of subsurface contamination and restoration.

The statement of the learning outcome related to modeling may correspond to levels of student performance ranging from attending to a few or most aspects of modeling of an open-ended problem to producing a fully-defined problem statement accompanied with the information necessary for its solution, the solution itself and reflections on decisions. Based on the pervasiveness of explicit references to simplifications in the protocols and given the supporting role of modeling in the course under discussion, a decision was made to focus performance expectations primarily on familiarity with the simplifications aspect of modeling.

Instructional materials

The materials produced for the purposes of modeling instruction consist of a handout with guiding questions for problem formulation and model selection. These questions correspond to shorter versions of the annotations produced for the constituent components of modeling. The guiding questions are accompanied with the schematic of the modeling framework depicted in Figure 2. The questions originating from the annotations for *phenomena* and *simplifications* listed earlier are included as examples next.

2. What is happening here?

- Which phenomena are relevant to the problem?
- The consideration of which mechanisms may contribute to setting up the problem?

9. Can I make any simplifications? Can I approximate something? Ignore something? Specifically, can I…

- simplify or neglect some phenomenon?
- approximate/estimate/neglect some parameter?
- neglect the variation of some variable?
- simplify some mathematical relationship?
- neglect some region, some system?
- simplify the geometry?
- simplify the solution method?

The modeling handout is introduced in class at an opportune time, following discussion of a few groundwater-flow problems solved with alternative ways, producing answers of different accuracy. References are later made to the handout throughout the duration of the course, both in the presentation of the theory and during in-class solution of problems. Apart from the modeling-specific instructional material, the emphasis on modeling prompted modifications of the presentation of the subject matter. Contaminant transport is an ideal topic to introduce aspects of modeling, as there are many closed-form solutions to the advection-dispersion equation for one, two or three dimensions, for specific conditions at the contaminant source and accounting (or not) for various phenomena (e.g., sorption, degradation). To this end, a handout was prepared with different versions of the advection-dispersion differential equation and alternative corresponding solutions, depending on the boundary conditions, phenomena considered, etc. It is important to stress that the inclusion of modeling instruction offered the opportunity to enrich contaminant transport instruction.

Without the prospect of using the material in modeling-related exercises, the compiled equations would make a dry mathematical handout for reference purposes. On the contrary, given the emphasis on model selection, the thinking behind transport equation choice enhances the understanding of contaminant transport phenomena.

The problems solved in class and assigned as homework were also modified accordingly. Fully-defined problems were restated as partly open-ended, paying attention to eliminating as much as possible references to variables and parameters that invariably point to a unique “right” solution. It should be stressed here that in curricula that give students few opportunities to practice the decision making required by open-ended assignments, it is expected for students to feel discomfort with such assignments. The discomfort often prompts questions of the type “what do *you* want me *exactly* to do?”, i.e., implicit requests to fully define the problem. Students, understandably, will not welcome the responsibility of problem definition. Hence the gradual introduction of modeling components could perhaps be sound not only from a cognitive but also from a psychological point of view as well.

The in-class discussion of problems includes first a lengthy stage of problem formulation, where students see how many modeling decisions does it take to transform a real-life question, such as:

- following a contaminant spill in a pond, there is concern whether a downgradient canal may be impacted if no measures are taken

to corresponding fully-defined assignment-type problems:

- what is the contaminant travel time between the pond and the canal?
- when will 1% of the concentration of the contaminant in the pond reach the canal?

In addition, several solutions are presented for most problems, each at a different level of simplification. The use of partially-defined problems enables selective attention to specific aspects of modeling, which is consistent with the learning outcome defined for the particular course. For example, some problems are good for deciding which phenomena can be ignored under certain circumstances. Others offer opportunities for considering reductions of the dimensionality of a problem. In future versions of the course, students will also practice anticipating the effects of simplifications, with the aid of numerical modeling and comparisons of numerical solutions at different degrees of idealization with simplified analytical solutions. For this purpose, a user-friendly web-based educational software (Valocchi and Werth, 2004) will be used for a term project.

Practicing modeling and assessment of modeling performance

As mentioned, modeling performance was more narrowly defined, in the particular course, as familiarity with the simplifications aspects of modeling. As a result, partially-defined problems were used not only during class discussions, but also in assigned homework and in exam questions. When assignments do not include information on parameters that directly point to phenomena, only then can students decide on their own which phenomena to include. Similarly, when maps of a wider study area are given (i.e., unlike the zoomed-in version of Figure 1!), students have to specify themselves the region of interest for the particular problem. These are examples of how to force students to model in the context of assignments. Modeling-type skills can equally well be assessed with "theory-type" questions that require anticipating general trends of phenomena or giving examples of certain simplifications (e.g., an example where steady-state transport conditions may apply).

CONCLUDING REMARKS

A modeling framework can guide both the instructor who seeks to introduce modeling instruction in a course and the student to acquire experience with modeling. While for both it will be a gradual process, the instructor must anticipate that incorporating modeling instruction in an engineering course will not simply add a new component, but will also alter the way the course is taught. Ideally, teaching of modeling should be part of engineering courses throughout the curriculum. One would rightly argue that modeling instruction takes up time from instruction on the subject matter of the course. However, it is time well spent: insight into differences between models has the potential to enhance understanding of the modeled phenomena.

ACKNOWLEDGMENTS

Marina Pantazidou thanks the students at NTUA for their contributions and lively participation in the environmental geotechnics course. Paul Steif acknowledges the support of the Department of Mechanical Engineering, Carnegie Mellon University.

REFERENCES

Burland, J.B. (1987). "The teaching of soil mechanics: a personal view" Proc. of 9th European Conference on Soil Mechanics and Foundation Engineering, Dublin, Vol. 3: 1427-1447.

Burland, J.B. (2006). "Interaction between structural and geotechnical engineers", *The Structural Engineer*, 18 April 2006: 29-37.

Goel, V. and Pirolli, P. (1992). "The structure of design problem spaces", *Cognitive Science*, Vol. 16 (3): 395-429.

Lovett, M.C. and Greenhouse, J.B. (2000). "Applying cognitive theory to statistics instruction", *The American Statistician*, Vol. 54 (3): 196-206.

Lundell-Sällfors, L. and Sällfors, G.B. (2000). "Focus on real life problems facilitating learning and understanding", Proc. of 1st International Conference on Geotechnical Engineering Education and Training, Manoliu, I., Antonescu, I. & Radulescu, N. (Eds.), Sinaia, Romania: 425-431.

Pantazidou, M. and Steif, P. (2003). "Modeling of physical systems: a framework based on protocol analysis", International Meeting on Civil Engineering Education, Ciudad Real, Spain, Sept. 18–20.

Steif, P. and Pantazidou, M. (2004). "Identifying the components of modeling through protocol analysis", American Society of Engineering Education (ASEE) Conference, Salt Lake City, Utah, June 20–23.

Valocchi, A.J. and Werth, C.J. (2004). "Web-based interactive simulation of groundwater pollutant fate and transport", *Computer Applications in Engineering Education,* Vol. 12: 75-83, http://www.cee.uiuc.edu/transport/

Professional Development of Engineering Educators: Stressing on Pedagogical Knowledge and the Practice

Waddah Akili, Ph.D., P.E., M. ASCE

Professor of Civil Engineering (Retired), Principal, Geotechnical Engineering, 3222 Evergreen Rd. Ames, Iowa; w.akili@isunet.net

ABSTRACT: The paper explores ways to effective professional development of junior engineering educators, to enable them to assume the roles they are entrusted with. The purpose here is to offer a new way to think about the development of the professional engineering educator. The paper focuses on:(i) the cognitive processes that faculty would tend to follow as they grow and learn more about teaching, (ii) the discipline-based industrial/practical experience they need to acquire to add to their repertoire as "practitioners", and (iii) the institutional initiatives, including: administrative support, and resources. What is needed is a change in culture within the institution, i.e., the department or college, to generate a comprehensive integrated set of components: articulated expectations, a reward system aligned with expectations, and opportunities for professional development to occur. Ultimately, to identify what educators and their institutions can do to generate more powerful and responsive forms of education that improves the quality of student learning.

INTRODUCTION

This paper focuses on professional development of faculty members (teaching engineering subjects) and argues that good teachers are those who keep up with new developments in their areas; and, learn new approaches to teaching and learning.

Traditionally, research and teaching have been approached in very different ways. To prepare for research we undergo years of training, both in scientific knowledge and in methods of gaining new knowledge through experimentation, analysis and modeling. To prepare for teaching, we acquire the same knowledge, except for a stint as teaching assistants; we receive almost no training in how to impart it. There is now a well developed science of human learning that is explicit in the ways in which students learn, and how teachers should teach (e.g. National Research Council 2000, Stice et al. 2000).They address learning styles (Kolb 1984, Dunn 1990), focus on communication, team, and leadership skills (e.g. "Engineering education for a changing world" 1994), and stress on educating students for life by helping them learn how to learn (e.g. "Restructuring eng. education: a focus on change"1995).

According to Fink et al.(2005), "expert teachers" are those who are committed to the profession, and, at the same time, do possess knowledge in three domains: engineering knowledge (i.e., their main disciplinary expertise and its related areas), pedagogical knowledge (i.e., how students learn, effective pedagogies in achieving learning goals), and pedagogical content knowledge (e.g., how best to demonstrate procedures, relate concepts, and correct students' misconceptions within given constraints). However, expertise in any domain is usually developed over time through determination, personal effort, and years of practice; and teaching is no different! It is a skill that can be acquired and improved with the right information, appropriate practice, and corrective measures through proper feedback. Characteristics such as "enthusiasm", "care", and "knowledge of subject matter" show up almost on everyone's list of the qualities of a good teacher.

The paper argues that the introduction of "well thought out" professional development strategies of engineering educators, would raise their self-confidence and equip them with tools to create and sustain more powerful forms of education.

RELEVANT COGNITIVE PROCESSES FOR FACULTY DEVELOPMENT

The primary focus in this article is on the development of junior engineering faculty and the cognitive processes they presumably follow as "they get immersed" in teaching. In this regard, they most likely progress through several stages of development. Awareness that there is a lot to be learned can be both exciting and daunting. The amount of information available can be overwhelming to any junior instructor; however, the path forward is traversable with the advice and assistance of experienced academics, available to help with the journey (Fink et al. 2005).

I. Emulate a Role Model

At their very start, junior engineering faculty begin to remember their teachers; and sketch out the dominant positive characteristics of those they wish to emulate, and attempt to follow their way of teaching as they recall from their students days. Following the footsteps of their *role model* is often reflected in junior faculty classroom disposition, attitudes, teaching activities, and may, in some instances, overshadow their true personality. Eventually, they come to grip with the fact that imitating their previous teachers is no solution; and begin their "sole-search" by redirecting efforts towards: self realization and fulfillment, attempting to improve their own skills, and redefining their own role in the teaching/learning arena.

II. Enhance Teaching Skills

When junior faculty begin to get some negative feedback on their class performance, coupled with a "gut feeling" that their handling of the teaching material is not up to desirable standards; they begin to ponder the question of how to select appropriate strategies to improve their teaching, i.e., to learn about the "nuts and bolts" of teaching. At this stage, young faculty may ask how they can make their lectures more interesting, how they can engage students, and how best to use in-class delivery techniques to enhance their teaching. At some point, young faculty will realize that they need to be selective in what they chose as a preferred strategy and may need guidance from a senior faculty. Eventually, they will realize that a gap exists between students' performance and their expectations as teachers. To narrow the gap, faculty need to move to the next level: examine what constitutes effective teaching; what defines deep-level learning, and what characterizes appropriate faculty and student roles in the teaching/learning process (e.g. Gross 1993, Mckeachie 1999).

III. Comprehend the Principles of Teaching and Learning

While learning about teaching techniques helps instructors to become more effective in course delivery and related protocols, understanding the *basic principles* of learning and how they impact teaching in general would help them create new and more powerful forms of learning. The principles of learning focus on fundamental issues such as: how people learn, how students process information, and the varied ways different individuals learn. Because students have different learning styles, some teaching (and learning) methods are effective for some students but ineffective for others. Various models of learning styles preferences have been described by Dunn (1990). The following statements, based on the work of Dunn (1990), add meanings to the concept of learning style from different perspectives.

- Each student is unique and has a learning style that should be acknowledged.
- Learning style is a function of heredity and experience, and develops over time.
- Learning style is a mixture of affective, cognitive, environmental, developmental, and physiological responses that characterizes how a person learns.
- Teaching individuals through their learning style strengths, improves their achievement, self-esteem, and attitude toward learning
- Students are entitled to instruction that is compatible with their learning style.

Incorporating some or all of the elements listed above in an "engineering" course, in which one is already faced with the problem of too much material in too short a time, is daunting to experienced teachers, let alone young and inexperienced faculty members. Nevertheless, the challenge is exciting to any instructor who wishes to "humanize" teaching, and reconcile within oneself that: he/she is teaching students rather than "unloading" teaching material in accordance with a time schedule.

IV. Focus on Active Learning Strategies

Here we proceed onward from general issues of learning to more specific questions about learning goals, including: the different kinds of knowledge that would constitute significant learning for students. According to Anderson (1990), researchers have categorized knowledge under different headings: *declarative knowledge* (define and describe), *procedurals knowledge* (how may learners use declarative knowledge), *structural knowledge* (how concepts in a domain are interrelated), and *contextual knowledge* (when to access selected principles and when to use certain procedures). A related and a very important question is: what *active learning* really means and why research supports the notion that the more active the students are the deeper their understanding would be (Prince 2004, Smith et al. 2005). The core elements of *active learning* are student activity and engagement in the learning process. *Active learning* is often contrasted to the traditional lecture where students passively receive information from the instructor. In short, *active learning* requires students to be active in order to learn! And think about what they are doing.

Despite these challenges, junior faculty should be strongly encouraged to examine the literature on *active learning*. Some of the documented material on *active learning* is compelling, and should stimulate junior faculty to think about teaching & learning in nontraditional ways, leading to their adoption of an *active learning* strategy.

V. Align Activities with Assessment

To optimize on course resources, learning activities should be aligned with assessment by developing activities that support declared goals and student learning, often referred to as *educative assessment*. This would include decisions on how to provide information on students' strengths and their mastery of course material, as well as guidance on how to proceed with learning activities to insure compliance with defined goals. Students will eventually need feedback on their performance that allows them to move forward as learners, and deepens their understanding of the subject matter. This feedback could come from the instructor, their classmates, their own self-reflection, or a combination of the three (Wiggins 1998)

VI. Affirm the Human Dimension of Education and Build Trust with Students

At its core, teaching has a profound human dimension. At times of uncertainty, students will draw strength from teacher's passion, understanding, and conviction. Instructors should demonstrate that they are thoughtful people, and possess deeply felt conviction about their specific role in the teaching process. Demonstrating that they know where they are going and why they believe it is important to take students there, imbues the students with a sense of confidence. Knowing where the journey is leading comes into play when students feel lost, afraid, and confused along the way.

Underlying all significant learning is the element of trust. Trust between teachers and their students is the affective glue that binds the educational relationships together. Not trusting teachers has grave consequences for students. They are unwilling to submit themselves to the perilous uncertainties of new learning. The more profound and meaningful the learning experience is to students, the more they need to be able to trust the teacher. What make teachers more trustworthy in students' eyes are two components: teacher *credibility* and teacher *authenticity*. Teacher *credibility* refers to teachers' ability to present themselves as ordinary people with something to offer to students. Teachers who have *credibility* are perceived by students as having depth and breadth of knowledge that far exceeds students' own. It is the competence that students expect of their teachers, to help them overcome uncertainty they experience when exposed to unfamiliar territory (Brookfield 1990).

Authentic teachers are, those that the students feel they could trust. They are real human beings with passion, frailties, and emotions. They are perceived as whole persons, say what they feel and do what their conscience directs them to do. Research has shown that various dimensions of students' personal growth does occur during students' college experience, and that educators impact this growth and development, often without being aware of their actions (Pascarella and Terenzini 1991).

PROFESSIONAL ENGINEERING EXPERIENCE

Concurrent with equipping junior engineering faculty with pedagogical knowledge and related skills in the teaching/learning arena; attention ought to be paid to junior instructors' growth and development in their engineering field, i.e., their declared area of expertise. It is known that "engineering instructors are engineers first and instructors second", which implies that keeping pace with new development in their fields enhances their abilities as engineers and bolster their role in the teaching arena.

No one would dream of building a medical school without an explicit mechanism to encourage teaching staff to keep up with their practice of medicine. If engineering is also a real-world profession, its teachers, particularly the young, should be encouraged to practice engineering. The one-day per week consulting rule does encourage this, but the reality is that these activities are, unfortunately, frowned upon, largely because they tend to distract instructors from their main functions, i.e., their teaching, research and service to the department and the college. On-campus facilities and institutional arrangements such as consulting and enterprise incubators should be investigated by appealing to other professional models, i.e., medicine, law, etc. The author believes that there are feasible action plans that should be adopted to pave the way for potential collaboration between industry and academe. These would include:

i) First, Seeding and propagating the idea, that gaining practical experience enhances junior instructors' teaching competence without adversely affecting his/her research capability. A faculty member should strive to do both! (be a good teacher and a researcher at the same time). Simply stated, the prevailing perception that time and effort should be spent mostly pursuing research and research funds, and that time and effort spent enhancing one's teaching competence does not count toward promotion and tenure, need to be changed! The positive relationship between having practical experience and faculty's performance, commitment, and positive attitude toward the classroom environment, requires administrators to "rethink" their current hiring, promotion and tenure policies. Sufficient weight should be allocated to the "practice", and to begin a change in cultural norms that have favored research.

ii) Second, Initiating and supporting efforts to educate graduate students, early on, about the benefits of acquiring industrial experience; its relevance to their future careers as potential faculty members. Encourage them to get in touch with industry, have a connection with someone on the inside, and plan to get involved with the practice when they do graduate. If we desire to do a better job in equipping our students with the "tools of the trade" then we need to alert the graduates (the future engineering teachers) to the need of developing enduring connections with industry.

iii) Third, Reaching out to the industrial sector, striving to form symbiotic partnerships between local industry and academia through: capstone projects, theses work with practical overtones, and applied research in selected domains, is extremely desirable and beneficial. The surest way to having a working college-industry relation is to come to a mutual understanding that both would gain from such a relationship.

The discussion noted above may remain academic and not feasible unless preceded by steps borrowed largely from the world of business. These steps include:

- "Rethink" students–faculty roles beyond the egocentric model-building with the precept that the ideal educational output and the ideal student is one just like me!
- Identify customers' needs on two fronts: their future manpower needs, and the support services that they are likely to require (e.g. technical consultation, applied research, testing, monitoring, etc.), now and in the future.
- Reorganize internally to streamline, and redirect efforts to integrate with external clients, particularly industry that hires graduates and uses institution's services.
- Privatize portions of the College-if at all feasible- to eliminate red tape, and allow industrial partners to make more effective use of college resources.

In this vein, the major problems of local industries along with their potential solutions should be focused on, properly framed, and clearly identified in open forums. This helps to set the stage by: disseminating relevant information, generating technical debate, and examining solutions from different perspectives. Invariably, it has to be a team approach, and among the major players are the junior instructors.

INSTITUTIONAL ROLE

Colleges of engineering would excel at teaching and learning when the majority of their faculty develop and achieve a reasonable level of pedagogical knowledge, and at the same time, are able to enrich the learning process by bringing in their own practical engineering experience into the classroom. Irrespective of individual faculty member own initiative and commitment to the process, institutional support and faculty leadership is absolutely necessary for achieving success and reaching the desired level of teaching competence. There are several action items that institutions need to adopt to see junior faculty grow as professional educators, over time.

I. Correct Misconceptions

To start, the institution should strive to change the mind set that has gripped academe for years. First of all, the prevailing antiquated model of teaching/learning needs to redefine the "proper" roles of faculty and students in the educational process. Introducing a higher level of professionalism, make both: what the students are doing and what faculty are doing with their students, substantially more effective.

II. Provide the Necessary Environment and Support Service

Faculty and the "beginners" in particular, may feel good about themselves, their class performance, and their handling of the subject matter they are entrusted with, but are not prompted to explore alternative perspectives, i.e., to venture into new skill areas, or to scrutinize critically those habitual assumptions underlying their thoughts and actions. Faculty are sometimes so enclosed within their narrow frames of reference that they are the last to recognize that these may be misleading or even harmful. What could be done to lift the faculty member out of the "rut" is to challenge him/her with alternative perspectives, fresh ideas, new activities and critical reflection. At this juncture, the role of the institution in providing the environment for growth and development of its faculty is "key" to fostering a positive change.

III. Reward Good Teaching

Administrators should strive to make effective teaching and instructional development higher institutional priorities. Many faculty would participate in professional educational development when the institution begins to reward good teaching or learning about good teaching. It is difficult to buck the trend that has continued to reward faculty for writing grant proposals, doing research, and writing for publication. To counter this tendency, administrators should reexamine the institution's infrastructure (i.e., faculty incentive and reward structure) as it affects faculty attitudes and behavior. Using incentives to encourage faculty to increase their commitment to teaching helps; but to hire new faculty whose primary emphasis is in research, inevitably reinforces existing norms that favor research over teaching.

IV. Facilitate and Support Faculty in Acquiring Relevant Practical Experience

Encourage faculty members, the young in particular, to get involved with the practice, and devise equitable system(s) that allows faculty to gain the engineering experience they desperately need, in order to keep up with new developments in their areas of specialization. Administrators should find ways to help new faculty gain industrial experience by spending a semester and/or summer release time on-site at a cooperating industry, or allow for a dual appointment, say fifty-fifty, i.e., fifty percent of faculty time at an industry nearby. Details of plans deserve closer benchmarking.

The above action items do require a change in prevailing culture accompanied by commitment by academic leaders, including senior faculty and department heads. However, any significant change in the *status quo* can only be brought about through: i) leadership of visionary administrators, ii) needed support, iii) adequate resources, and iv) faculty's willingness to learn. All four could come as a result of a new culture that values future role of junior faculty in the educational process.

CONCLUSIONS

The engineering profession is facing challenges that need to be addressed to insure that future engineers have the capabilities and skills to perform well in a world driven by rapid technological advancements and diminishing resources. These challenges require new and better kinds of teaching, which in turn requires engineering faculty and decision makers to think about teaching and learning in more scholarly ways.

At the center of it all, is the engineering educator who is the major player, the facilitator of learning, and the care taker. If engineering colleges want to introduce meaningful change in how engineering education should be practiced, faculty members, and juniors in particular, will need a new perspective that: i) validates why learning about teaching is important; ii) provides opportunities to engage in what and how to learn about teaching, iii) enables them to gain the experience to become better teachers of civil engineering; and, iv) propagates a culture that values good teaching and introduces a positive change in how engineering education is to be practiced.

The paper dwells on the potential development of the engineering educator by focusing on the cognitive processes that faculty most likely follow as they get immersed in teaching. The paper argues that the institution's role is paramount in initiating and sustaining change. What is necessary to bring about a change in culture is for the institution, to have a comprehensive and integrated set of components: clearly articulated expectations, a reward system compatible with those expectations, supportive leadership, and opportunities for the professional development to occur.

When the engineering institutions mount these strategically important initiatives, leading to effective professional development of the engineering educator; then future generations of engineering students would have a better and more relevant education. An education that provides them with the knowledge and skills they need to tackle the complex engineering problems that they are likely to face in the future.

REFERENCES

Anderson, J.R. (1990). "Cognitive Psychology and Its Implications", *W.H. Freeman and Company*, New York, NY.

Brookfield, S.D. (1990). "The Skilful Teacher." *Jossey-Bass*, San Francisco, CA.

Dunn, R. (1990). "Understanding the Dunn and Dunn Learning Styles Model and the Need for Individual Diagnosis and Prescription." *Reading, Writing and Learning Disabilities*, Vol.6: 223-247.

"Engineering Education for a Changing World."(1994). *Engineering Deans Council and ASEE.*

Fink, L.D., Ambrose, S., and Wheeler, D. (2005). "Becoming a Professional Engineering Educator: A New Role for a New Era." *Journal of Engineering Education,* Vol.94 (1):185-1941.

Gross Davis, B. (1993). "Tools for Teaching." *Jossey- Bass*, San Francisco, CA.

Kolb, D.A.(1984)."Experiential Learning: Experience Source of Learning & Development." *Prentice Hall*, Englewood Cliffs, CA.

McKeachie, W.J. (1999). "Teaching Tips: Strategies, Research and Theory for College and University Teachers." *Houghton Mifflin*, Boston MA.

National Research Council, (2000). "How People Learn: Brain, Mind, Experience, and School.", *National Academy Press,* Washington, DC.

Pascarella, E.T., and Terenzini, P.T.(1991). "How College Affects Students", *Jossey-Bass*, San Francisco, CA.

Prince, M.(2004). "Does Active Learning Work? A Review of the Research." *Journal of Engineering Education,* Vol. 93(3):223-231.

"Restructuring Engineering Education: A Focus on Change."(1995). *Division of Undergraduate Education*, *National Science Foundation*, Washington, D.C.

Smith, K.A., S.H. Shepard, D W. Johnson, and Johnson, R.T.(2005)."Pedagogies of Engagement: Classroom – Based Practices." *Journal of Engineering Education*, Vol.94 (1): 87-101.

Stice, J.E., Felder, R.M., Woods, D.R., and Rugarcia, A. (2000). "The Future of Engineering Education. Part IV: Learning How to Teach." *Chemical Engineering Education*, Vol.34 (2):118-127.

Wiggins, G. (1998). "Educational Assessment: Designing Assessments to Inform and Improve Student Performance", *Jossey-Bass*, San Francisco, CA.

Research-Based and Service-Learning Modules for Undergraduate Geotechnical Engineering Courses

Mandar M. Dewoolkar[1], A.M. ASCE, P.E., Lindsay George[2], P.E., and Nancy J. Hayden[3], P.E.

[1]Assistant Professor (mandar@cems.uvm.edu), [2]Graduate Student (lgeorge@cems.uvm.edu), [3]Associate Professor (nhayden@cems.uvm.edu), School of Engineering, University of Vermont, 301 Votey Hall, 33 Colchester Ave., Burlington, VT 05405

ABSTRACT: Hands-on educational modules were designed for two undergraduate geotechnical engineering courses at the University of Vermont. The modules were designed to incorporate *inquiry-based learning* and expose students to a *systems approach* to engineering education, which are the two major thrusts of an NSF funded curricular reform within the civil and environmental engineering programs. All modules were conducted within a group setting and required students to write technical papers in the ASCE conference format or prepare a technical report and a presentation, with an additional underlying objective of the development of students' interpersonal and communication skills. The educational modules included: (1) Atterberg limits using Casagrande and fall cone devices; (2) physical, analytical and numerical modeling of steady-state seepage; (3) validation of undrained slope stability, bearing capacity of shallow foundations and active and passive lateral earth pressure solutions using centrifuge modeling; and (4) service-learning projects related to foundations, retaining structures or slope stability for rehabilitation of historic structures. Integrated reflection and assessment activities were conducted. Student assessment results indicate that many of the curricular reform objectives are being successfully implemented into undergraduate geotechnical engineering courses.

INTRODUCTION

The civil and environmental engineering programs at the University of Vermont (UVM) are undergoing NSF funded curriculum reform. The goal of the reform is to create an inquiry-based, environmentally-conscious undergraduate learning experience that prepares students to be capable of adopting a systems approach to define and solve complex engineering problems. At the core of the reform is the concept of *service-learning*. Service-learning projects generate meaningful work for the community while helping students learn academic material and develop interpersonal skills. They are open-ended in nature and promote a systems approach to engineering. One of the goals of our reform is to include hands-on research-based activities because they develop a variety of investigative, creative, and communicative skills in students.

An ancient Chinese proverb "I hear and I forget, I see and I remember, I do and I understand" sums up the importance of hands-on activities in any curriculum. Established learning theories such as Kolb's theory of experiential learning (Kolb, 1984) have hands-on experiences at their core.

Inquiry-based, hands-on educational experiences were implemented through three research projects and one service learning project in two undergraduate geotechnical engineering courses, Geotechnical Principles and Geotechnical Design. The earlier is a 4-credit introductory soil mechanics course including a 1-credit laboratory component offered in the spring semester. The latter is a 3-credit course on foundations, retaining structures and slope stability, without a laboratory component offered in the fall semester.

The first two modules are conducted in Geotechnical Principles, a requirement for civil as well as environmental engineering students in their junior year. The enrollment is typically around 40 students. The first module is a research project where students conduct and analyze results of Atterberg limits tests on the same soil using both Casagrande and fall cone methods. The second module involves the students constructing physical models of earth structures in tanks to observe seepage and verify their graphical and finite element based (using SEEP/W) solutions. The third research module utilizing an instructional centrifuge and the service-learning module are conducted in Geotechnical Design, which is a senior/graduate course and counts as a design or professional elective. It is not a required course, but is usually taken by about 20 students (a few graduate students with the majority being seniors). The instructional centrifuge module studies stability problems (slope stability, retaining wall and shallow foundation) to observe failure patterns and verify associated classical analytical solutions. In the service-learning module, students work on evaluation and design of remedial schemes for historic structures with foundations, retaining structures or slope stability issues. The students are expected to devise their remedial schemes while maintaining the original elements of the structures as much as possible.

The three research modules require students to write a technical paper, 6 to 8 pages long, in the ASCE conference paper format. The service-learning module concludes with a technical presentation and a report. All four projects are conducted in group settings (3 to 5 students per group). The service-learning project involves community partners. These activities are expected to cultivate technical writing, communication and interpersonal skills in the students.

The four educational modules are described sequentially in the subsequent sections. Associated reflection and assessment activities and preliminary results of assessments are also discussed.

EDUCATIONAL MODULES

Module 1: Atterberg limits using Casagrande and fall cone devices

Student groups conduct Atterberg limits tests, liquid and plastic limits, on the same soil using two types of techniques; (1) Casagrande apparatus (commonly used in the U.S.) and (2) fall cone apparatus (used in Europe and Asia). The students share data from all groups (typically 10) and analyze in ways of their choice. They are graded based on the quality and depth of their analyses (e.g. statistical analysis on repeatability of results, is one method better than the other, operator dependence) and written quality of their technical paper. The project is worth 5 percent of the total course grade.

The purpose of this exercise, other than obtaining a greater knowledge of test methods and the Atterberg limits, is to understand that test results should not be accepted blindly. Traditional laboratory exercises on this subject have students obtain liquid and plastic limits for the purpose of soil classification. The tests are performed once, and the limits are taken by the students as absolute values without regard for the possibility of operator or experimental error. This traditional laboratory exercise is still done in the beginning of the semester with the research project as a follow-up project. This shows students that there are multiple methods for obtaining the limits, and that care should be taken in following experimental standards (e.g. ASTM) to obtain accurate and repeatable results. Most importantly, this exercise brings students through the process of collecting multiple sets of data, analyzing and presenting the data, as well as discussing and concluding meaning from the data. The project is relatively simple to conduct, so additional time can be devoted to writing the research paper in the ASCE conference format, which the students are doing for the first time.

Module 2: Steady state seepage – physical model and analytical solutions

This module allows student groups to construct physical models of hydraulic structures to study steady-state seepage. Five models are constructed and are shown in Figure 1. All seepage tanks are made of clear acrylic, similar to the ones used by Elton (2001). The tanks are 7.5 cm wide, and their sectional dimensions range between 40 cm x 40 cm and 30 cm x 80 cm.

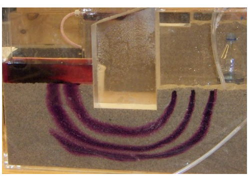
(a) dike

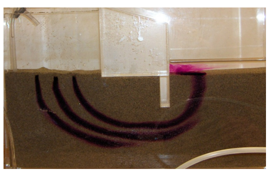
(b) dike with a cutoff at downstream toe


(c) earth dam with a blanket drain


(d) dike with upstream cutoff


(e) sheet pile cutoff wall

Figure 1: Physical models to study steady-state seepage

This project is conducted after the constant head and falling head permeability laboratory exercise is concluded with a written laboratory report. The students are asked to use the same sand and follow generally the same sample preparation procedure in constructing their flow model as the ones used in preparing the permeability test specimens. This allows them to use the hydraulic conductivity determined through these tests in the analysis of the flow models. In the permeability laboratory, students are also asked to conduct mechanical sieve analysis test on the sand to determine its effective size (D_{10}) to estimate hydraulic conductivity based on Hazen's (1930) equation. Before the research project on seepage is conducted, a laboratory session on numerical modeling of steady state seepage is also held where students learn to use the finite element-based software SEEP/W.

A small network of tubes is placed in the bottom of the flow tank before the sand is introduced using light tamping. The model is saturated slowly under a small hydraulic head until the soil is fully saturated. Potassium permanganate crystals are placed near the acrylic front of the tank at three to four locations once the water starts appearing on the upstream soil boundary. Water is then added from the top on the upstream and downstream soil boundaries. Constant water levels are maintained by utilizing overflows and a continuous water supply. The saturation process usually takes over half an hour. This time allows students to record the actual model dimensions and draw a flow net to estimate flow rate, piezometric heads at some locations, and exit gradient, if relevant.

It usually takes about 20 to 30 minutes for the flowlines to develop. The students then compare the observed flow patterns with those predicted by their hand-drawn flownets and later with computer outputs from SEEP/W. An example of such a comparison is shown in Figure 2. The students obtain the flowrate by measuring overflowing water from the downstream side over a specified time period. When divided by the width of the container, the flowrate per unit width is obtained. Students also measure piezometric heads at various locations in their model. These quantities are then compared to those predicted from the graphical solution and computer analysis. Students are asked to consider hydraulic conductivity data from all groups, from the constant and falling head tests and the estimates based on Hazen's equation. The data from about 10 groups are over a reasonably wide range. This also illustrates how much variation can typically exist in the laboratory measurements of hydraulic conductivity.

This research project is also worth 5 percent of the total grade. Students are graded based the quality of their analyses, comparisons between experimental and analytical results, and quality of their technical paper.

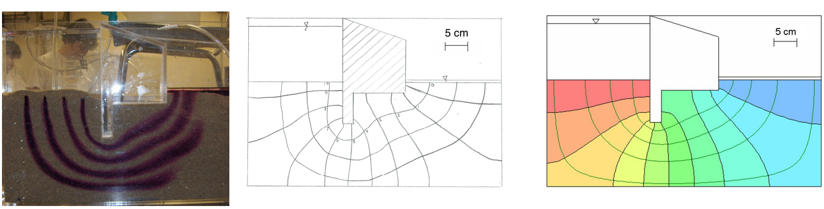

(a) physical model *(b) hand drawn flownet* *(c) numerical solution using SEEP/W*

Figure 2: Physical model, graphical solution and computer output from a research project on steady-state seepage

This exercise stimulates student interest and creates a visual representation of concepts learned in class. It also gives meaning to flow lines and flow nets and the concepts of piezometric head and exit gradient are made tangible by measuring the heads. The students are also made aware of the three modeling techniques and the connections and differences between them, and how various techniques can be used to validate each other. They also get to see five different sets of flowlines since in a given laboratory session, five different models are created. Student response to this research project has been very positive.

Module 3: Stability evaluations using an instructional centrifuge

This module consists of three separate projects and is being introduced at the time this paper was written (Fall 2007). An instructional centrifuge was fabricated (Figure 3a) at UVM. This centrifuge is very similar to the one at the University of Colorado at Boulder (Znidarcic, et al., 2007). The UVM centrifuge is equipped with a loadcell and displacements are obtained through analysis of digital images of the models. A large consolidometer (20 cm in diameter) was also fabricated to prepare large consolidated clay cakes for making centrifuge models. The centrifuge is used to study the following stability problems: (1) undrained slope stability (Figure 3b) (validation of Taylor's stability chart and limit equilibrium-based computer program SLOPE/W); (2) retaining wall (Figure 3c) (Rankine's active and passive earth pressure theories); and (3) undrained bearing capacity (validation of Prandtl's bearing capacity theory), as described by Dewoolkar, et al. (2003). Since this course does not have a separate laboratory component, classroom time is used to conduct these experiments. A research paper on each project is worth 5 percent of the final course grade.

(a) instructional centrifuge at UVM *(b) failed centrifuge slope model* *(c) centrifuge model of a retaining wall*

Figure 3: Instructional geotechnical centrifuge and centrifuge models

The primary purpose of these modules is to validate analytical methods students are learning in the course through physical modeling. Principles behind the centrifuge modeling technique are explained only briefly. These modules have shown to be very useful in the illustration of theoretical concepts taught in the class (Dewoolkar, et al., 2003). For example, students actually observe a circular failure surface in a model slope similar to the one assumed in the analysis.

Module 4: Service-learning - geotechnical evaluation and remedial design

Service-learning is a form of experiential education in which students engage in activities that address human and community needs together with structured opportunities intentionally designed to promote student learning and development (Jacoby, 1996). It is a teaching and learning approach that promotes academic enhancement and personal growth through civic engagement.

Each student group is assigned a historic structure in Vermont for a semester-long service-learning project. The project spans over 12 weeks and is worth 35 percent of the course grade. So far (2005 through 2007), students have worked on shallow foundations, retaining structures and slope stability issues related to heritage facilities such as the one shown in Figure 4a. The projects have been with non-profits, such as the Preservation Trust of Vermont and a National Historic Landmark, Shelburne Farms. Typically, students survey the damage, study archived documents if available, and conduct site investigations using hand augers and sampling equipment (Figure 4b). They typically also conduct in-situ borehole shear tests, and occasionally assist in professional drilling activities, if the community partner has funds available. Soil samples are colleted to determine relevant soil properties. Students perform index testing and consolidation and shear strength testing using fully automated consolidation, triaxial and direct shear devices (Figure 4c). The above data are used in performing relevant analysis, making recommendations for repairs, and preparing cost estimates. The experience is unique because students need to develop remedial schemes while maintaining original elements of the structure as much as possible. The projects conclude with comprehensive project reports and presentations.

(a) Grand Isle Lake House with differential foundation movement

(b) augering and sampling using hand operated devices

(c) student performing a direct shear test

Figure 4: Sample collection and laboratory testing in service–learning projects

Representatives of community partners are present at the initial site visit, attend the mid-semester progress report and final presentations, and provide input at these key stages. Such communication is important to ensure successful projects from the perspectives of the students, the instructor and the community partners alike. It is clearly communicated to the community partners that the analyses, designs and recommendations should be independently reviewed by a professional engineer if they wish to adopt them.

These projects introduce students to the complex nature of real engineering projects. They are introduced to the field of historic preservation, as well as societal and economic aspects of engineering projects promoting the systems approach to engineering. They also use many skills they learned in their Geotechnical Principles course, which reinforces the basic concepts through real applications.

INTEGRATED REFLECTION AND ASSESEMENT

Although many definitions of reflection exist, there is agreement that reflection is essential to the learning process and improving retention of the academic material (e.g. Kolb, 1984). Reflection is a process designed to promote the examination and interpretation of experiences and the promotion of cognitive learning (Clayton and Moses, 2005). Evaluation is also an important component of the education process, both for the instructor and the student, for making improvements and determining success (or lack of success) in meeting objectives of the educational activity. The specific methods for conducting the assessments could be broadly divided into three categories: qualitative (typically suitable for formative evaluations), quantitative (typically desired for summative evaluations) and a mixed or combination method (NSF, 2002).

At the conclusion of the above modules students are asked to answer a relatively comprehensive questionnaire, which acts as an integrated reflection and summative assessment tool. Often, additional reflections are conducted through classroom discussions. Overall student attitudes towards the exercises conducted to date were positive. Overall, they found the research projects to be a better experience than traditional laboratory assignments. As one would expect, students are generally more enthusiastic towards the modules involving physical models (seepage and centrifuge) than they are towards the module involving Atterberg limits.

Students agreed that the service-learning projects introduced them to the diverse nature of engineering problems and solutions, societal and economical aspects of engineering and the personnel involved. A majority of the students felt that they provided meaningful service to the community. They preferred the real-world service-learning projects to "made-up" projects. For example, even out of 19 students in the course in Fall 2006 voluntarily responded to a question on their formal course evaluation "What did you like most about this course?" by answering "the service-learning project".

The assessments indicated that these modules helped the students in developing their technical writing, communication and interpersonal skills further. The modules are also useful in meeting many of the ABET (the Accreditation Board for Engineering and Technology) program outcomes including those of a non-technical nature.

CONCLUSIONS AND DISCUSSION

The above exercises are not about simply teaching new tools. They were introduced as an attempt to help students understand the fundamentals better while also learning about research, the open-ended and complex nature of engineering projects, and the importance of validating concepts and solutions. All four modules were very hands-on in nature. They also used statistical, analytical or numerical methods in addition to laboratory testing, physical modeling experiments and field work. The preliminary analysis of the assessments indicates that the overarching goal of the curricular reform, which was to train the students in the systems approach to engineering through inquiry-based learning, has been largely successful in the undergraduate geotechnical courses.

The first two modules require minimal to modest resources. The exercises can easily be completed in a traditional two-hour laboratory session. The third module requires a more substantial equipment investment, but the centrifuge can be utilized in graduate courses and other research projects. Additional modules such as reinforced earth, trapdoor and contaminant transport can also be developed using the centrifuge.

The service-learning projects benefited significantly from having access to the borehole shear tester and automated direct shear, consolidation and triaxial devices. Key soil properties could be determined relatively quickly given the short durations of the projects. So far, the community partners have adopted some of the low-cost recommendations made by students. At the very least, the student reports are used as a basis for planning purposes or more detailed analysis later.

Students usually perceive these modules to be time-consuming while in progress; however, they find the projects to be valuable learning experiences at the conclusion. Instructors will need to invest greater than normal time to plan, coordinate, provide timely guidance, and grade papers and reports. However, these modules do bring a lot of variety and unpredictability to the classroom making the courses more interesting and rewarding for the students and the instructor alike.

ACKNOWLEDGEMENTS

The authors would like to acknowledge the National Science Foundation for the funding which has made this work possible through NSF-EEC-0530469. Support from the University of Vermont Community-University Partnerships and Service-Learning (CUPS) is also appreciated. The authors are grateful to Lalita Oka, Adel Sadek, Donna Rizzo, Maureen Neumann and Floyd Vilmot for their help in implementing the educational modules described here, and to the students of these courses for their hard work and enthusiasm.

REFERENCES

Clayton, P. H., and Moses, M. G. (2005), "Integrating reflection and assessment to improve and capture student learning", CUPS Workshop, September 26-27, University of Vermont.

Dewoolkar, M. M., Goddery, T., and Znidarcic, D. (2003) "Centrifuge modeling for undergraduate engineering instruction", *Geotechnical Testing Journal*, Vol. 26(2), 201-209.

Elton, D. (2001), *Soils Magic*, Geotechnical Special Publication 114, ASCE.

Hazen, A. (1930), *Water Supply, American Civil Engineers Handbook*, Wiley, New York.

Jacoby, B. (1996), *Service-learning in higher education*, Jossey-Bass Publishers, San Francisco, CA.

Kolb, D. A. (1984), *Experiential Learning: Experience as the Source of Learning and Development*, Prentice Hall, Englewood-Cliffs, NJ.

NSF (2002), *The 2002 User-Friendly Handbook for Project Evaluation*, Available at: http://www.nsf.gov/pubs/2002/nsf02057/start.htm

Znidarcic, D., Ko, H. Y., Goddery, T., and Wallen, R. (2007), *Instructional Geotechical Centrifuge*, Available at: http://bechtel.colorado.edu/web/grad/geotech/faci/centrifuge/iccentrifuge.html

Why is sustainability important in Geotechnical Engineering?

Abreu, D. G.[1]., Jefferson, I[2]., Braithwaite, P. A.[3] and Chapman, D.N.[4]

[1]Ph.D. Student, BSc (Eng), Department of Civil Engineering, University of Birmingham, Birmingham, B15 2TT, UK; email: dgf505@bham.ac.uk
[2]Senior Lecturer, BEng(Hons), DIS, PhD, FGS, Department of Civil Engineering, University of Birmingham, Birmingham, B15 2TT, UK; email: I.Jefferson@bham.ac.uk
[3]Director, Arup, BSc(Hons), MSc, DIC, SiLC, CEng, CEnv, FICE, MCIWM, MIEnvSc Honorary Professor, University of Birmingham, The Arup Campus, Blythe Gate Valley Park, Solihull, B90, UK; email: peter.braithwaite@arup.com
[4]Senior Lecturer, BSc(Hons), DIS, PhD, CEng, MICE, ILTM, Department of Civil Engineering, University of Birmingham, Birmingham, B15 2TT, UK; email: D.N.Chapman@bham.ac.uk

ABSTRACT: One of the key contributing fields to sustainable development, almost no matter what the project, is geotechnical engineering, which faces a challenging dichotomy between delivering project goals and maintaining sustainability. In an era when we are striving for minimal adverse environmental impact and high added value (economically and socially), all engineers are in a position to have a major influence on sustainable development. However, geotechnical engineering has a crucial role in shaping and achieving the sustainability credentials of a project, therefore better geotechnical practices would reduce impacts at the point in a construction project when some of the greatest gains can be made. However, there is still resistance and reluctance for the geotechnical world to change. This paper will examine the role sustainability has to play in geotechnical engineering and what the key barriers and enablers are for its adoption in a constructive way.

INTRODUCTION

Sustainable development aims to improve quality of life now and for future generations. The most frequently quoted definition is in the report Our Common Future, also known as the Brundtland Report, 1987. In a more contemporaneous way Forum for the Future defines sustainable development as a dynamic process which enables all people to realise their potential and improve their quality of life in ways which simultaneously protect and enhance the Earth's life support systems. A popular way of understanding sustainable development is the concept of the triple bottom line of economic, environmental and social accountability. "People, Planet and Profit" are used to succinctly describe the triple bottom lines and the goals of sustainability.

In the last two decades much effort has been spent trying to find solutions to implement sustainable development goals in a practical way. In the United Nations conference on Environment and Development (UNCED), Rio de Janeiro, 1992, 179 governments met and voted to adopt Agenda 21 (United Nations (1992)). Since then sustainable development has been adopted as an overarching policy goal in many different countries around the world.

The challenges facing society today are complex and ignoring the issue of sustainable development has many consequences. To address the challenges of unsustainable development there is need for engagement of all parts of society in taking action at all levels, globally and locally. For example, civil engineers as professionals with a key position in society are responsible for large impacts on the economy through provision of infrastructure, transport services and buildings. They have the opportunity to lead positive action by considering sustainable development in all of their activities. Geotechnical engineers, directly linked with civil engineering, also have an important role to play in sustainable development. Geotechnical engineering has a big potential to embed sustainability at the early stages in projects reducing adverse environmental impact and adding social and economical value to society.

To understand where and how geotechnical engineering can influence and evolve in the direction of sustainable development is a major challenge at the moment. Taking this into consideration, the main objectives of this paper is to discuss why sustainability is important for geotechnical engineering, where the opportunities for geotechnical engineers to embed sustainability in their projects are and what is still holding back the geotechnical engineering field from fully embracing the sustainability agenda.

THE CONSTRUCTION INDUSTRY AND SUSTAINABLE DEVELOPMENT

The room to improve sustainability in construction is huge as construction is not only a key industry for economical and social development but also is responsible for major environmental and social impacts.

Although the industry has been directing more attention to sustainability, developing action plans and new indictors – see BREEAM, CEQUAL, Sigma, SPeAR® and Key Performance Indicators, as examples - there is still a long way to go in order to address this challenge. Assessing projects is the first step in understanding where the weaknesses, problems and opportunities are but solutions and new technologies need to be developed to overcome these problems.

To change the mind set and culture within the industry will require all of the professionals involved in the construction chain to be aware of the dimension of the problem and the opportunities for improvement on a day to day bases. Considering that the timescale is far too long to rely on new entrants into the industry receiving appropriate training, it is clear that we must change the mindset of our current professionals, as well as reviewing actual procedures and methodologies to adjust to a more sustainable outcome.

If the civil engineering industry embraces the challenge then there is enormous opportunity for sustainable development in construction. Construction can lead the way in considering sustainability in all of its activities reducing impacts in the environmental and improving social and economical aspects.

GEOTECHNICAL ENGINEERING AND SUSTAINABILITY

Geotechnical engineering, as an important part of the construction industry, has potential for making major impacts on sustainable development. Geotechnical works can be responsible for huge movement of soil with matching large energy consumption and considerable use of natural material and man-made materials (Jefferis (2005)). Geotechnical engineers have a major impact on the natural environment and water resources by reforming the earth's surface, changing soil properties and addressing contamination and often are involved in site selection for major infrastructure works transport services and buildings which can have a significant impact on the social and economics aspects of the project.

Addressing sustainability in geotechnical engineering is fundamental to addressing sustainability in construction. Geotechnical engineering, being the first link in the chain of construction, has the potential for setting the principles of impact reduction throughout the construction process (see Figure 1) and also has the potential for the reduction of high environmental impacts at a low additional cost (see Figure 2).

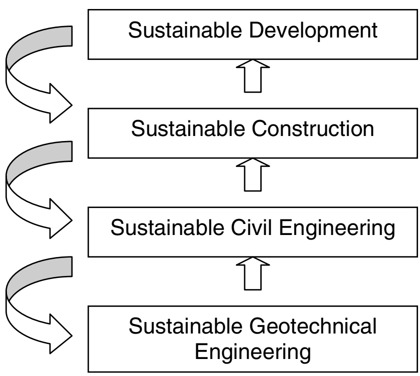

FIG.1: Geotechnical engineering in the construction chain.

Geotechnical engineering is a well established field but there are many barriers to change. In a field where risk and liability are likely to take precedence over sustainability, due to the high level of responsibility attributed to professionals, any attempt to change can be treated with extreme caution. In a recent meeting of the British Geotechnical Association, professionals agreed that although better geotechnical practices would help reduce impact at an important point in the construction chain most claimed to not yet know enough about the impact of their design choices on sustainability (Macdonald, 2006). This reflects the difficulty of promoting change to investigation and design processes in order to improve sustainable development and implement sustainable choices.

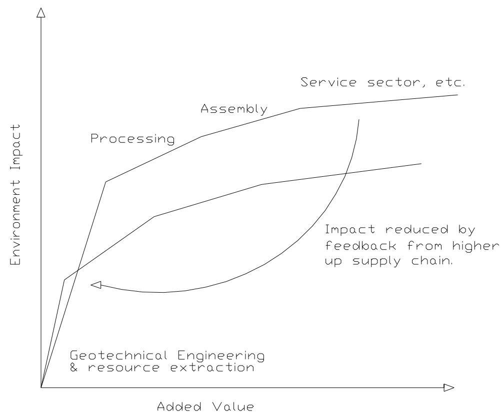

FIG. 2: The environment impacts of geotechnical engineering (Jefferis, 2005).

Another barrier to the adoption of sustainability principles is the fact that at the present there is little published with regards to sustainability in geotechnical engineering. A variety of different strategies - see Building a Better Quality of Life DETR (2000), as example - and sustainability assessment methodologies have been developed and published in respect of construction - see BREEAM, CEQUAL, Key Performance Indicators and SPeAR as examples - but there are no equivalents which can be specifically applied to geotechnical engineering. Excluding the Highways Agency Sustainable Geotechnics Report (Hilier et al., 2005) and Sustainable Indicators for Environmental Geotechnics (Jefferson et al., 2007), two innovative examples of approaching geotechnical projects, very little is available in regards to strategies or indicators for sustainability in geotechnical engineering.

This absence of established strategies and indicators can be considered as the main barrier to embedding sustainability into geotechnical engineering. Although sustainable indicators are not developed enough to say whether a project is sustainable or not, the development of a reference system is vital if we are to present alternative choices for a project and be able to say alternative A is more sustainable than alternative B. Also, such a system should be able to demonstrate that sustainability can be embedded in a geotechnical project by sequencing it into a series of small steps, so helping to remove the mystique that surrounds sustainable geotechnics.

Another significant barrier is time and cost associated with implementation of more sustainable practice, as clients are more often than not primarily focussed on achieving the lowest design cost with maximised acceleration of schedules. Furthermore, a risk adverse, conservative approach often leads to inefficiencies and wasteful use of resources. This can only be overcome by engaging with clients demonstrating the key benefits to sustainability, which a number of companies in other parts of the construction industry are starting to see benefits from its adoption.

Despite the barriers, there are some innovative projects pushing the sustainability boundaries in geotechnical engineering, with some researchers developing new technologies in order to delivery more sustainable solutions. At the moment there are just a few examples of projects that have evolved from the discussion stage of ‘what should be done?’ to actually taking action to do something about improving sustainability. Table 1 outlines some examples of projects that have embedded sustainable thinking into geotechnical procedures.

OPPORTUNITY FOR RESEARCH INTO SUSTAINABILITY IN GEOTECHNICAL ENGINEERING

In many ways the time is ripe for geotechnical engineers to embrace the sustainability agenda. There are numerous indicators that sustainable development is increasingly becoming a mainstream priority in construction projects and therefore geotechnical engineers will have to have answers to address the challenge.

There remains a huge gap in research into sustainability in geotechnical engineering and therefore there are research opportunities in this area. Although researchers are starting to perceive that sustainability is an important new subject, the gap in knowledge, data, evaluation, technologies, strategies and policies in geotechnical engineering are still large. Key areas for research can be identified as:

- Energy: reducing energy consumption, being more energy efficient and using renewable energy and alternative technology both in investigation techniques and designed solutions. Example: Ground Storage of Building Heat Energy (DTI et al., 2005).
- Materials: Choosing, using, re-using and recycling materials during design, manufacture, construction and maintenance to reduce resource use and waste; Example: Achieving sustainability in vibro stone column techniques (Serridge, 2005).
- Pollution: Produce less toxicity, water, noise and spatial pollution. Example: Can we identify sustainable remediation techniques for contaminated land? (Jefferis, 2002)
- Waste: Management of the waste production reducing and recycling waste; Management of waste disposal. Example: Reuse of Foundations for Urban Sites (Butcher et al., 2006).

There is also much need for research to develop indicators to evaluate sustainability in geotechnical engineering projects. There is a strong demand for reliable and applicable indicators in order to help geotechnical engineers to compare different options of projects and understand the impact of each choice and identifying ways towards sustainable development in geotechnical engineering. Indicators are also fundamental in helping to build the business case for sustainability in geotechnical engineering. In order to improve the market for geotechnical sustainable solutions, knowledge is essential to help to enlighten clients to make informed choices about sustainable projects.

Table 1 – Examples of geotechnical projects focused in solutions to improve sustainable development.

Project	Description
Ground Storage of Building Heat Energy. (DTI et al. (2005).	The project investigated Ground Sourced Heat Pump systems (GSHPs) as a means of heating and cooling buildings utilising the constant temperature of the ground or groundwater beneath a building (typically 10 to 14°C in the UK) to provide cooling in the summer and/or heating in the winter. GSHP systems typically use a third of the energy consumed by traditional heating and cooling systems.
Achieving Sustainable Underground Construction in Birmingham Eastside? (Jefferson et al., 2005)	This project investigates the complexity of providing the sustainable underground construction within the Eastside redevelopment project and investigates the barriers that stand in the way of their implementation. The research also highlights the sustainable options for underground development that should be consider when constructing on a city centre Brownfield site, including controlling rising groundwater levels an the sustainable provision of utility service
Reuse of Foundations for Urban Sites (Butcher et al., 2006).	This project discusses in detail the opportunity for the re-use of existing foundations when redeveloping a building. The study also developed a hand book with technical information about cases where re-use of foundation was a good option.
Use of Recycled Materials to Substitute Natural Aggregates. Example: Achieving sustainability in vibro-stone column techniques (Serridge, 2005)	Studies of the possibility to use recycled materials to substitute natural aggregates in geotechnical projects. (e.g.: track ballast, crushed concrete aggregate, demolition material and waste steel slag).
Remediation of Contaminated Land. Example: Can we identify sustainable remediation techniques for contaminated land? (Jefferis, 2002).	Research focused on the issues of sustainability as applied to remediation of contaminated land.

Considering the absence of strategies and indicators the main barrier for embedding sustainability, researchers at the University of Birmingham in partnership with Arup have already started a project to develop a methodology to apply sustainability to geotechnical problems using an approach that provides quantified information for the geotechnical engineer. The aim of this project is to develop a framework to help geotechnical engineers to visualise the key priorities to be addressed in regards to sustainable development during the design process. The main idea is to enable geotechnical engineers to have a better understanding of sustainability implications of alternatives and to assist decisions on specific issues such as materials, recycling, energy, etc. In order to achieve this objective the researchers are working on a design support tool which quantifies data, and benchmarks sustainability performance of a project option. Results of this research are to be published in the first semester of 2009.

The greatest task for researchers it stills being to understand the big picture of sustainability and apply it to research. Keeping the multidisciplinary focus in research in geotechnical engineering is the key point to evolve to sustainable solutions in this area. Maintain a balance between economical, social and environmental aspects during research process is also vital. To keep in mind that sustainability is not synonymous with environmentalism and projects which are 'green' are not necessarily sustainable is very important.

CONCLUSION

For geotechnical engineering, sustainability is a vital subject. Being associated with economic growth, social development and environmental impacts geotechnical engineering is related to all areas of sustainability. Geotechnical engineers as designers and deliverers of main structures and infrastructures have power and opportunity to embed sustainability in their projects and promote the sustainable agenda.

There are still many barriers holding back changes in geotechnical procedures. The complexity of the sustainable agenda is not yet fully understood by the professionals in geotechnical engineering and the lack of knowledge about how to embed sustainability on a day to day decision making still remains a problem to be overcome. There is also a huge gap in research in geotechnical engineering and the existing research is based more with environmental concerns than sustainability. The absence of established indicators can be considered the main barrier to embedding sustainability into geotechnical engineering and address this problem is vital to enable geotechnical engineers to have a better understanding of sustainability choices during design process.

Despite these difficulties there is some innovative research pushing the boundaries and finding different solutions to old problems. Alternative resources for materials, recycling and energy efficiency are being the mainstream for geotechnical engineering research in sustainability.

Arguably, the geotechnical industry has a huge opportunity to improve sustainable development in all its procedures and lead the construction industry to improve and sustain the built and natural environment and subsequently improve quality of life of society.

REFERENCES

Brundtland, G.H. (1987). "Our Common Future: Report of the World Commission on Environment and Development." Oxford University Press, UK. 416p.

Butcher A. P., Powell J. J. M. and Skinner H. D. (editors), (2006). "Reuse of Foundations for Urban Sites: Proceedings of the International Conference." BRE Books, UK.

Department of Environment, Transports and the Regions (DETR) (2000). "Building a Better Quality of Life: Strategy for More Sustainable Construction." Eland house, London, UK.

Department of Trade and Industry (DTI), ARUP Geotechnics (2005). "Ground Storage of Building Heat Energy." Overview Report DTI / ARUP, London, UK.

Hillier R. P., Thompson R.P., Schroder F., Baardvik G. and Harvik L. (2005). "Sustainable Geotechnics." Highway Agency, EDGE Consultants LTD & The Norwegian Geotechnical Institute, UK.

Jefferis, S.A. (2002). "Can we identify sustainable remediation techniques for contaminated land?" Proc. 4th Int. Cong. On Environmental Geotechnics, Rio de Janeiro, Brazil, August , Eds.: de Mello & Almeida, 1039-1058.

Jefferis, S.A. (2005). "Geotechnology in harmony with the global environment: dream or deliverable?" *Proc. of the 16th International Conference on Soil Mechanics and Geotechnical Engineering*, Sept., Osaka, Japan. Paper No UK15.

Jefferson I., Birchall C. A., Hunt D.V.L., and Rogers C. D. F. (2007). "Sustainability indicators for Environmental Geotechnics." *Engineering Sustainability*, 160, 57-78.

Jefferson I., Rogers C. D. F., Hunt D.V.L., (2005). Achieving Sustainable Underground Construction in Birmingham Eastside? *Proc. of IAEG 2006,* CD-rom, Nottingham, UK.

Macdonald A. (2006). "Moving Towards Sustainabilty." Ground Engineering, August 2006, British Geotechnical Association, UK.

Serridge C. J. (2005). "Achieving Sustainability in Vibro Stone Column Techniques." *Engineering Sustainability*, 158, 211-222.

United Nations (1992). "Agenda 21, the Rio Declaration on Environment and Development." United Nations Conference on Environment and Development, Rio de Janeiro, Brazil.

SUSTAINABILITY BASED ON LEAN THINKING AND ETHICS

Christopher A. Sneider[1], P.E., M. ASCE and Kay Carnes[2], PhD, CPA

[1]Senior Engineer, Golder Associates Inc., 1004 North Atlantic Street, Spokane, WA 99201, csneider@golder.com
[2]Associate Dean - Coordinator of Accounting Programs, Gonzaga University 502 East Boone, Spokane, WA 99258, carnes@jepson.gonzaga.edu

ABSTRACT: Toyota used lean thinking to become the world's leading automotive manufacturer. The company successfully manufactures automobiles in Japan as well in the United States -- and beats American car manufactures hands down. Lean thinking has led to Toyota's success. Lean thinking can also be used by the geo-sciences to improve efficiencies, develop sustainable engineering solutions, and lead in protecting the geo-environment.

For lean thinking to succeed, a company must have a culture that can embrace the philosophy and methodology. Such a company should have a culture of trust, heart, and spirit. This kind of culture will provide the energy and support needed to engage lean thinking. One way to develop such a culture is to fully implement the company's code of ethics. Unfortunately, many companies either do not have a code or do not fully implement the one that has been developed.

This paper summarizes the application of lean thinking as it relates to the geo-environment and then describes how to implement lean thinking into the company culture using the code of ethics. Lean thinking can be applied to the geo-environment industry and can help with developing sustainable solutions. However, to implement lean thinking a company must have solid core values.

INTRODUCTION

Lean thinking techniques have made Toyota highly efficient, effective, and prosperous. These same techniques can be used by the geo-science industry to free up resources for developing sustainable solutions. With the ever increasing amount of bureaucracy and litigation in the culture, it has become ever more important for the geo-sciences to improve business operations and processes to free up technical resources and provide time for analyses.

The geo-sciences community has a tremendous responsibility and role in the development and implementation of sustainable solutions. We understand how the geo-environment, often not visible to the public, affects short and long-term health and public safety. Since much of the geo-environment, such as soils that support foundations or aquifers that supply water to public wells, are not visible to the public, the impact of quality sustainable solutions is often unknown or underappreciated by society. Our entire society infrastructure, including buildings, highways, bridges, mines, landfills, water supply systems, required to support life relies in some manner on a sustainable geo-environment. The geo-sciences need to develop sustainable solutions that will maintain and even improve our society's quality of life both now and in the future while respecting the ecological systems on which life depends. Sustainable solutions may often be complex and integrate knowledge from many of the natural sciences, requiring significant time to fully understand and analyze the consequences of a geo-environmental project.

Many professional organizations have incorporated sustainability goals and objectives into their professions. For example, Canon 1 of the ASCE code of ethics calls for civil engineers to incorporate sustainability into their practice. The National Academy of Engineering in Washington D.C. on June 24, 2002 declared, "Creating a sustainable world that provides a safe, secure, healthy life for all peoples is a priority for the engineering community." (ASCE 2002).

These are significant goals for the geo-sciences. In order to achieve them, significant resources will be required to develop innovative solutions using science and engineering. However, in modern society, with increased litigation costs and increased bureaucracy, fewer dollars are available for science and engineering. Also, due to intense competition, budget shortages, and client focus on cost, less funding is available to develop innovative solutions. In addition, society as a whole typically does not understand the complexity or value of how the geo-environment affects life. This makes it even more difficult to free up the dollars needed for subsurface exploration, testing, and analyses.

Technology has helped free up analytical resources. Such technology includes computers, email, internet, conference calls, integrated systems, and other technological advances. (Spitzer 2003) However, legal concerns, bureaucracies, and departmental barriers within organizations and between companies have grown exponentially faster. For example:

- Project managers are required to maintain a clear paper trail to protect their companies from potential lawsuits and litigation.
- Staff employees are bombarded with paper work to keep them accountable.
- Verbal agreements between subcontractors and consultants are turned into multi-page contracts requiring continual oversight due to feared lawsuits and litigation.
- Contracts between clients and consultants continually increase in length and complexity and often require review by in-house councils and/or contract specialists.
- Departments such as geology, engineering, human resources, accounting, graphics, and marketing become isolationists focused on their own disciplines and goals.

All of the above issues are part of operating a business, and considerable resources are required to meet these demands. Lean thinking can be used to make each of these issues more efficient and effective to free up resources and time for developing innovative sustainable solutions. However, as will be shown in this paper, lean thinking will require significant change, commitment, and trust throughout a company to flourish. Lean thinking can only flourish if all staff levels including owners and upper management embrace the concept. Staff at all levels can see areas for improvement, and these insights are needed to continually eliminate waste and improve efficiency and effectiveness throughout the company.

There is considerable literature written about lean thinking in regard to the manufacturing industry and little written for service industries such as the geo-sciences. Lean thinking is a continual improvement process, which can be successfully applied to the geo-sciences. Value is defined by the end customer, waste is eliminated from the value stream, production steps are made to flow, the end product is provided when the customer wants it, and, lastly, perfection is relentlessly pursued. Perpetually following these steps will improve efficiency allowing more time to focus on value added service including ever more sustainable solutions.

LEAN THINKING

The manufacturing industry has used lean thinking for over 20 years and as a result has become more efficient and effective. Automotive and steel companies that use lean principles extract twice the productivity from inventory, space, and equipment as do traditional mass-producing competitors. (Allway 2002)

Lean thinking is a simple concept, but complicated process to implement. Lean thinking is primarily about eliminating non-value activities from work processes by applying a robust set of performance change tools, and emphasizing excellence in operations to deliver superior customer service. (Allway 2002). As described by Abdi (2006), "it is a way of giving people at all levels of an organization the skills and a shared means of thinking systematically to drive out waste by designing better ways of working, improving connections and easing flows within supply chains".

Toyota has been thoroughly analyzed by researchers to uncover Toyota's technique for lean thinking. The most well known steps for implementing lean thinking were described by Womack (1996). These steps include the following:

1. Define value precisely from the perspective of the end customer.
2. Identify the entire value stream.
3. Make the remaining value creating steps flow.
4. Design and provide what the customer wants only when the customer wants it.
5. Pursue perfection (Womack 1996).

Lean thinking is prevalent in the manufacturing industry, but not so prevalent in the service industry, especially in geo-sciences companies. These same principles can be applied to the service industry to make companies more efficient and effective. Studies have shown that where service companies have implemented lean thinking, there have been significant benefits. For example, an insurance company reduced the cost of processing new business by 10 to 40%. A financial institution had 20% productivity improvement and 50% processing time reduction. A bank realized $7 million annual savings. Airlines and hospitals have cut waste in labor, materials, and space by 20 to 40%. (Allway 2002) A specific example of a company that has benefited from lean thinking is Southwest Airlines (Abdi 2006). In addition, Ball

(2003) describes how two environmental firms implemented lean thinking. These firms both support petroleum companies by performing environmental site assessments.

Manufacturing and services companies are similar in that they involve a compilation of operations and processes to provide value to customers in the form of products and/or services. (Allway 2002) For this reason lean thinking can be applied to the service industry and more specifically the geo-sciences. Abdi (2006), and Ball (2003) modified Womack's original 5-steps to fit the service industry. Their approach consists of the following 5 revised steps:

1 Customize according to the needs and expectations of customers.
2 Engage all parts of the organization to get involved in providing service.
3 Facilitate clearer meaning and direction.
4 Adjust approach to meet demand to fluidly meet expectations.
5 Create transparent environment for immediate feedback to pursue perfection.

Implementing lean thinking is not easy. Operations and processes change dramatically, which require trust and commitment throughout the company. Flinchbaugh (2005), describes 10 factors that a company should anticipate before implementing lean thinking:

- People need to focus on a multi-year journey
- Lean is born from what you think
- It is a journey that never ends
- Change will have resistance
- Leaders and not managers are needed
- Requires significant investment
- Improve in all aspects of the business
- No recipes but road maps
- Each company is unique.

Implementing lean thinking will require tremendous organizational energy, significant leadership, and commitment throughout the organization. Commitment can not be driven or coerced and will need to be cultivated through trust. Trust and commitment will be required throughout the company. Employees must trust management and management must trust their employees. Without trust there will be no commitment and lean thinking will never get off the ground floor. A company must have an ethical culture in order to have trust and commitment. If management is dishonest or unethical, employees will not trust management. If employees are dishonest, they will not trust each other or be trusted by management. A company that embraces ethics will develop employees and managers who are honest and fair. Such a company will develop trust and commitment throughout the company culture.

IMPLEMENTATION

Based on our research, we have developed a five step approach to implement lean thinking in a geo-science organization. This approach can be applied to both commercial and governmental organizations and all sizes of organizations ranging from one person to over thousands of employees. One of the authors is currently implementing this approach into one of Golder's smaller offices in Spokane, Washington. Our approach is outlined and briefly described in the five following paragraphs:

1 Customize services to needs and expectations of clients.

The geo-science community has already done an excellent job of making this step a priority. Many firms provide training on understanding needs and expectations. This only needs to be continued to be implemented.

2 Engage all employees.

Each employee in the organization must be engaged in improving quality, reducing cost, and improving delivery time. Each employee will see service flow from a different perspective and will have varying ideas of how to make improvements. Viable improvements should be implemented no matter how small.

3 Map out processes and establish metrics

All processes for providing service should be mapped either in outline form or flow charts. The map should show all connections between functions and departments, and show how the work flows within each function or department. It must be clear so that each employee can understand it and make suggestions. The plan should present a consistent set of processes so that everyone is working as team, but allow individual creativity and thinking to find improvements. Employees should be trained to find ways to improve processes. Also, if there is a problem, it must be clear who they contact to resolve issues immediately.

Metrics should also be established. Quality can be measured by keeping track of defects such as report rework and addendums. Cost and schedule can be measured by tracking cost and schedule ranges for varying project types and sizes.

4 Implement the approach.

With a firm grasp of client needs and expectations, the plan is implemented. Work must follow the plan explicitly. This way, areas for improvement can be clearly identified.

5 Evaluate, revise, and relentlessly pursue perfection.

Each employee will continuously help evaluate, revise and perfect the plan. When metrics are not met, employees must ask themselves what needs to be done to meet the metric so that suggestions for improvement come from those involved in the process. Managers should be responsible for their respective parts of the plan. Managers should also be responsible for deciding which ideas should be implemented and how and when the plan is revised.

We do not yet have hard numbers to demonstrate benefits for implementing such an approach in a geo-science organization. As described previously, several industries have successfully implemented lean thinking. Based on one author's experience in small and large consulting geo-science organizations including the Army Corps of Engineers, implementation of the proposed plan will reduce overhead time for project managers from 20 to 30 percent. This reduction in overhead time will result in increased profits and more time for analyses and engineering. It will also improve quality, increase speed, and have the additional benefit of increased employee moral.

ETHICS

Fully implementing a code of ethics provides focus allowing for quicker decisions, less second-guessing, and improved morale, all of which can create the energetic and opportunity-seeking culture necessary for lean thinking to flourish. Sustainable solutions will then develop for three primary reasons. First, by following good ethics, the choices a company makes will naturally lean toward sustainable solutions. Second, companies will be more efficient in providing increased value added service to these sustainable solutions. Third, individuals will naturally look for opportunities to develop sustainable solutions.

Successful implementation of lean thinking requires acceptance from all employees. Unfortunately, many employees will see lean thinking as just another management tool. Some may feel it is not their job to help design and redesign an approach. And many employees may fear loss of their position due to changes. In order for the approach to work, all involved need to feel engaged and want to contribute. This can only take place in a company with an ethical culture where there is high trust and commitment.

Vast volumes of literature have been written about implementing lean thinking, but there is minimal literature discussing the role of ethics necessary for implementing lean thinking. Because of the abstract nature of the service industry strong ethics are even more critical. Note that most of the recent collapses of companies due to unethical debacles have been professional service companies. Manufacturing companies typically do not collapse because of ethical failures.

Unfortunately, ethics in modern culture is low. Fortunately, there seems to be new concern for ethics as demonstrated by increased ethics training courses and research. However, increased interest does not necessarily equate to an ethical culture. A national survey by Prentice Hall concluded that the standards of ethical practice and moral leadership of business leaders gets a C grade at best. In the same survey, 68% of people believe that unethical behavior of executives is the primary cause of lower business standards, reduced productivity, and decreased success. The survey also indicated that because of the low standards of their leaders, employees felt they were justified in absenteeism, petty theft, indifference and poor job performance. The survey concluded that American workers are as ethical in doing their jobs as their bosses are perceived to be ethical/dutiful in leading and directing their companies. (Ciulla 2004)

The lack of high ethical standards in the organizational culture is partly a misunderstanding of what ethics is. Most people believe they are more ethical than they really are. Ethics is about how we distinguish between right and wrong, or good and evil in relation to the actions, volitions, and character of human beings. (Ciulla 2004) Ethics is doing the right thing even if it costs you. It is not a marketing statement to attract new business. Ethics is not the law. The law is a low common denominator managed by attorneys.

Many different approaches can be used to cultivate an ethical culture. There are many ethical philosophies including utilitarianism, egoism and principles based ethics. Most companies and organizations already have a set of guiding principles in their code of ethics so companies already have a starting point. Unfortunately, too few companies actively embrace or encourage their employees to be aware of their code of ethics. This is a tremendous resource that should be developed. If an organization does not have a code of ethics, it should create one with the help of all employees. Following ethical principles in a code will help provide common cause in the company. This will result in quicker decisions, common goals, keeping the company on track and create esprit de corps. All of which are necessary for implementing lean thinking. Strong understanding of the code allows employees to willingly make correct choices with a guideline without being coerced. "A code of ethics is a creed, a code of conduct to which a person voluntarily adheres because it reflects his or her values and is believed to be beneficial to both society and the individual." (Garret 2006)

Most people want to be ethical and want to work for companies with ethical leaders. When employees feel their work is meaningful and helps the common good, their efforts are aligned with their heart. This will result in increased energy and synergy where people will be excited about their work. Employees will look for ways to improve operations and processes, and won't waste time with politics. Such an environment will result in crisper thinking, higher quality work, and less burnout. Other benefits include:

- Reducing transaction costs
- Creating an opportunity seeking culture
- Attracting highly qualified people
- Avoiding situational ethics
- Making decisions faster
- Retaining employees
- Developing an environment of inspiration instead of one of inspection
- Improving Deming's four quality objectives – design, defects, reduction of waste, improved process.

In addition, thoroughly implementing a company code of ethics will show employees that leadership cares about ethics. Employees take their cues about ethics, character, and integrity from the highest levels of leadership. If leadership ignores ethics, trust will decline, resulting in an overly politicized and protectionist culture. (Spitzer 2003).

CONCLUSION

The geo-sciences have a leading role to play in developing a sustainable world. Additional time and budget for developing innovative creative solutions can be found by implementing lean thinking techniques in organizations. This has been done successfully in the manufacturing industry and can be transferred to the service industry. Implementing lean thinking in a geo-science organization will lead to more sustainable solutions and increased profit and improved morale.

Geo-science organizations that implement lean thinking must have strong leadership, embrace change, and have a culture of trust and commitment. This can only be accomplished by having an ethical culture. A starting point for developing an ethical culture is by developing and embracing and living out a company code of ethics.

REFERENCES

Abdi, F., Shavarini, S. K. and Hoseini, S. M. (2006). "Glean Lean: How to Use Lean Approach in Service Industries?" *Journal of Services Research*, Volume 6, Special Issue, p. 191-206.

Allway, M. and Corbett, S. (2002). "Shifting to lean service: Stealing a page from manufactures" playbooks', *Journal of Organizational Excellence*, p. 45-54

ASCE, (2004). *Sustainable Engineering Practice, an Introduction*, Committee on Sustainability, American Society of Civil Engineering.

Ball, Daniel R., and Maleyeff, John (2003). "Lean Management of Environmental Consulting", *Journal of Management in Engineering*, January 2003, p. 17 – 24.

Ciulla, Joanne, B., (2004). *Ethics, the Heart of Leadership*, 2nd Edition, Praeger Publishers.

Flinchbaugh, Jamie (2005). "Getting Lean Right", *Industrial Engineer*, Jan. Vol. 37 Issue 1, p. 44-44, 1p.

Garret, Michael F. P.E., M. ASCE (2006). "What's the Use?", *Leadership and Management in Engineering*, October 2006.

Spear, S. and Bowen, H. K. (1999). "Decoding the DNA of the Toyota Production System", *Harvard Business Review*, September – October, p. 96-106.

Spitzer, Robert J., S.J., Ph.D. (2003). *Six Steps for Remedying Contemporary Ethical Problems*, Gonzaga Institute of Ethics.

Spitzer, Robert J., S.J., PhD. (2000). *The Spirit of Leadership*, Publishers Press.

Womack, J.P. and Jones, D.T. (1996). 'Beyond Toyota: How to Root Out Waste and Pursue Perfection', *Harvard Business Review*, p. 140-155.

Sustainable Solutions for an Environmentally and Socially Just Society

Sukhmander Singh[1], Ph.D., P.E., G.E., and Mark Aschheim[2], Ph.D. P.E. M.ASCE

[1] Nicholson Family Professor, Civil Engineering, Santa Clara University, Santa Clara, CA 95053, USA; ssingh@scu.edu
[2] Associate Professor, Civil Engineering, Santa Clara University, Santa Clara, CA 95053, USA; maschheim@scu.edu

ABSTRACT: Increasing per capita resource consumption in developed nations on one hand and global poverty, hunger, and poor sanitation in some poor countries on the other hand require efforts directed at both environmental and social sustainability. A model is presented for addressing sustainability in society. In this model, society, environment, and technology are interlocking parameters that dictate the nature and types of efforts for sustainability. Society provides for all its citizens the very basic necessities: potable water, food, education, housing, and sanitation. Environment (or ecosystem) includes the natural resources possessed by society. Technology enables the resources to be exploited economically in service to society, and determines the value of the resource. These factors must be considered simultaneously in developing appropriate and sustainable solutions for an environmentally and socially just society. The model is applicable to any country that seeks sustainability and justice for its citizens. Specific examples related to the use of geo- and bio-materials are presented, including production of adobe-like and fired clay bricks and bamboo beams. Distinctions between technology- and energy-intensive production in developed countries and labor-intensive production in developing countries are made, considering the United States and India as examples.

INTRODUCTION

It is obvious that the state of a society's economic system influences the production systems that are appropriate to that society, and the production systems and standard of living further impact the ecosystem. The ecosystem contains the resources that support our standard of living. While we depend on it, the ecosystem is autonomous and will continue even as it changes under the pressure of human activity. The ecosystem has been viewed as a commons that can be tapped for production; production often is motivated by the profits to be had, with degradation of the commons ignored to the degree possible. Increasing per capita consumption of resources, and the resulting pollution, waste and global warming have led to widespread recognition that we must not deplete and/or pollute the ecosystem to the extent that the ability of future generations to meet their needs is compromised. Such a view accepts human-induced change to the ecosystem, but recognizes that environmental problems are now of such magnitude that they require concerted global efforts. This concern has been expressed and articulated in many ways and through many international conferences (WCED, 1987, Peter et al 1997, Earth Summit, Rio, 1992). Terms such as "sustainability," "renewability," and "sustainable development" are attracting worldwide attention. The key thrust which emerges from these deliberations is the notion of "sustainable development," which is closely tied to "economic development" and thus does not reflect a shift away from the present view that the commons is available to support further development. It is not clear that the standard of living that we have become accustomed to can be supported sustainably.

The calculus of sustainability has not truly entered into decision-making about production and engineering. Therefore, there is a need to change the curricula to explicity teach engineers to consider sustainability in their design decision-making. Sustainability is a cross-cutting theme that should be present throughout an engineer's education rather than being contained within a single dedicated course. Thus, it is useful to have examples that can carry the essential themes and background to support the emergence of a calculus of sustainability in engineering design. At Santa Clara University, sustainability concepts are taught using some of the examples that follow, in the following undergraduate courses: Geotechnical Engineering (CENG 121, for juniors), Civil Engineering Materials (CENG 115, for juniors), Green Construction Design (CENG 119, for seniors), Sustainable Water Resources (a new elective course), and Civil Engineering Design Methods (CENG 192a, for seniors). In addition, Masters degree students at Santa Clara University soon will be required to complete a 5-unit thesis on Sustainable Design, consisting of a design project or directed research report.

SUSTAINABLE DEVELOPMENT

The term "sustainable development" is being interpreted differently by developed nations on one hand and by developing countries on the other. For example, a measure against pollution in a developed country may make sense, but would be a luxury for a developing country. Developing nations may insist on more attention to economic growth than to environmental problems. In developed countries, a check on economic growth to protect the ecosystem is often considered a check on freedom and free enterprise. How then to resolve the conflict between a desire to develop, and the need to maintain the integrity of the ecosystem?

Figure 1 presents a simple schematic model for a country, which can help guide sustainability decision making. The big box represents a country. As the growth accelerates/cranks faster to further the development of a country, (i) the balance between ecosystem and economic prosperity becomes more delicate for developed nations; and (ii) the balance between economic prosperity and social development becomes more delicate for developing countries. For example if development is linked only to gross national product (i.e. GNP should rise every year), the society may be headed to the depletion of its ecological base, and therefore society may be becoming poorer (Warner, 2006). This means that developed countries must recognize limits to their growth and should look for alternate but sustainable resources and alternate ways of obtaining pollution-free energy.

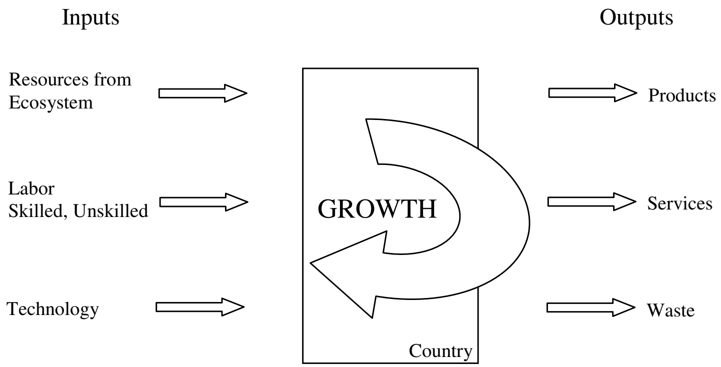

FIG 1. Schematic model for sustainability decision making.

Mario Belotti, an internationally known professor of economics at Santa Clara University argues that "resource is a function of technology" (Belotti, 2006). Accordingly, developed nations should focus on advancing technology to find alternate ways to meet the requirements of society while preserving the balance of ecosystem. For example, resources in developed countries should be used to develop bio-based and fusion energy sources, while also improving the efficiency of current renewable energy sources such as wind, hydro, geothermal, and solar technologies. Improved energy technologies would benefit both developed and developing countries.

In developing countries, where production is not highly advanced, indiscriminate expansion of production systems may not only lead to an undue burden on the ecosystem, but also to the concentration of wealth in relatively few hands. Sustainable development, however, must consider three dimensions: 1) protection of eco-system, 2) social development and 3) economic prosperity (Earth Summit, 1992). In some poor countries where poverty, hunger and poor sanitation exist, both environmentally acceptable, economically accessible, and socially sustainable solutions must be found to bring about a developed and socially just society. These solutions ought to be simple, inexpensive and environmentally safe. Examples of such solutions are presented below.

MASS PRODUCTION VERSUS PRODUCTION BY MASSES

In developing countries, where rice production is the main crop, for example in India and China, large scale burning of rice straw (harvest waste) often creates widespread emissions of CO_2 and other pollutants all over the countryside. This straw, however, when shredded and mixed with clay, can be molded into bricks. Thus a mixture of the shredded straw and clay can be used to produce both lightweight and insulating building materials. Shredding, mixing and molding can be achieved using cheap manual labor; with small scale-kilns or solar ovens employed to bake these bricks. This would provide employment to a large number of persons as well as minimize pollution caused by burning rice straw. Such a labor-intensive process can be termed "production by masses" in contrast to "mass production". Labor-intensive processes also may be more sustainable; in this case, waste rice straw available at harvest time is harnessed each year.

SUSTAINABLE BUILDING MATERIALS

Construction materials represent a large percentage of the raw materials used in developed countries. Figure 2 illustrates relative amounts of materials used in the United States, with construction materials by far being the largest of the categories listed. The environmental consequences are significant. For example, in both the United States and globally, the manufacture of Portland Cement for use in concrete accounts for approximately 7% of anthropogenic emissions of CO_2 (Mehta, 1999). Thus, alternative, more sustainable materials must be found.

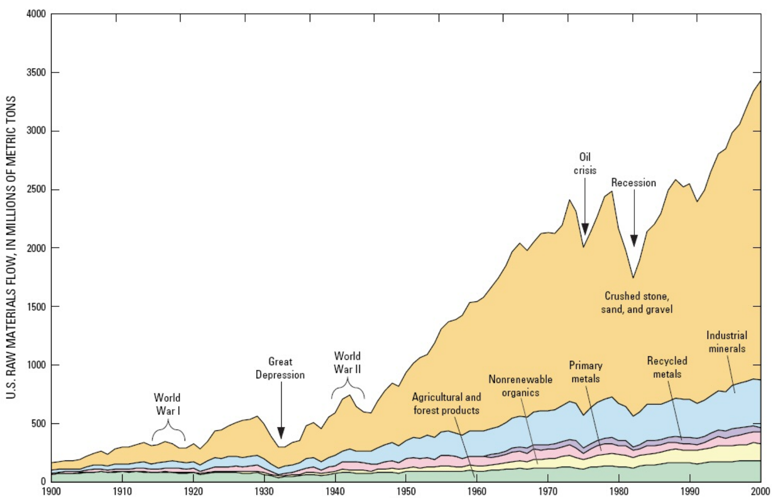

FIG. 2. Raw materials consumed in the United States: 1900-2000. (Wagner, 2002)

In developed countries, high labor costs relative to materials costs tends to result in high performance products that embody significant amounts of energy and technology. Examples include very strong chemical adhesives used for making engineered lumber and plywood. Sustainable alternatives may make use of sophisticated technologies to allow a savings in energy but possibly with some reduction in performance. Thus, it may be feasible to use manufactured biocomposites in place of steel or concrete. An example is the use of engineered lumber or a new alternative in which beams are made from harvested bamboo. The bamboo is attractive because it is stronger than wood and rapidly renewable, since the stalks can be harvested every 3 to 5 years. The bamboo beams may be formed from strips of bamboo assembled together into solid section I-beams or by extruding a beam made from bamboo chips and a bonding agent; the latter being especially appropriate in developed countries where labor is costly, while the former being more applicable in developing countries. Technologies to allow more sustainable adhesives to be used would be especially valuable; lignin resulting from anaerobic digestion is one binder that is currently being explored.

In developing countries, low labor costs and high needs may dictate solutions in which even basic technologies are employed to make production processes more efficient. For example, the firing of clay bricks in developing countries often relies upon relatively simple technologies implemented widely by small businesses. In some cases, the kilns are very crude and inefficient, leading to excessive consumption of wood and emissions of CO_2 and other pollutants At the same time, there may be little or no quality control and the strengths of the bricks may be far in excess of the strengths required for dwelling construction. Businesses operating at this scale are often unaware of better technologies already in existence, and standards of production are often not closely tied to the requirements of use. Consequently, the application of relatively simple technologies could dramatically reduce wood consumption, CO_2 emissions, and the cost of masonry construction. Lower costs would allow this form of construction to be more widely used, displacing cheaper alternatives that have a worse history of performance in natural disasters such as earthquakes (Aschheim et al, 2007).

SOCIAL CONCERNS IN GEOTECHNICAL DESIGN

Application of solutions to certain geotechnical problems such as building high earthen enhancements to raise highways that pass thru potentially waterlogged areas can be handled in a both socially and environmentally safe way. For example, although high-technology earth-moving machinery can accomplish this task in a more time efficient way, geotechnical solutions for such problems require slow construction to allow the dissipation of pore water pressures typical of high water table situations in water logged areas for soil to consolidate and be able to support the load of the highway embankment and the traffic. Use of manual labor (usually a large number) for hauling and placing fill on the embankment is a very common practice in India and in many developing countries. This can not only be economical on fuel consumption thereby minimizing pollution, but can also be a socially and geotechnically acceptable solution.

Geotechnical engineering often require clearing, excavating, or moving large amounts of earth for the construction of highways, dams, tunnels and housing construction. Whereas large highly advanced machinery is used to accomplish these tasks, it may be possible that the geotechnical construction can be achieved in a more environmentally friendly way. Instead of one large dam two small dams requiring lesser environmental damage may be considered. Use of lightweight construction material for housing construction may help in reducing deep side hill cuts often made to build large view homes. Use of bamboo for housing has already been discussed. Since building in, on, and with earth is what geotechnical engineers do, the aforementioned considerations can help preserve the health of the earth (NRC 2006).

CONCLUSIONS

1. Sustainable solutions to protect ecosystems (including geoenvironment) can vary from country to country and are influenced by economies and social constitution of the country.

2. Sustainable development, which includes both environmentally and socially sustainable solutions, for example, can be achieved by incorporating available geomaterials, wealth, and labor.

3. Solutions in developed countries often involve high technology and high energy approaches. Less intensive approaches may be better tailored to actual performance requirements while providing for greater sustainability.

ACKNOWLEDGMENT

We thank Professor Keith Warner of Santa Clara University for his insightful discussions on the subject.

REFERENCES

Aschheim, M., Flanagan, S., Harlander, J., Pitt, C., Alfaro, A., Rivas, C., Rodriguez, M. E., (2008) "Enhancing the Sustainability and Earthquake Resistance of Confined Masonry Dwellings in El Salvador," to appear in *Journal of Earthquake Engineering.*

Beloti, Marie, (2006) "Personal Communication" Santa Clara University.

Daly, H. and Cobb, J. (1989) *For the Common Good: Redirecting the Economy toward Community, the Environment and a Sustainable Future*, Boston: Beacon Press, 1989.

National Research Council (2006). *Geological and Geotechnical Engineering in the New Millennium—Opportunities for Research And Technological Innovation*, Committee on Geological and Geotechnical Engineering, National Academies Press. Also available from http://www.nap.edu/catalog.php?record_id=11558#toc

Peter M. Vitousek, Harold A. Mooney, Jane Lubchenco, and Jerry M. Melillo, (1977). “Human Domination of Earth’s Ecosystems.” *Science* 277(1997):499.

Wagner, L. A. (2002). *Materials in the Economy—Material Flows, Scarcity, and the Environment*, Circular 1221, United States Geological Survey, 34 pp. Also available from http: \\pubs.usgs.gov\circ\2002\c1221\ .

Warner, Keith Douglas, (2006) “Personal Communication” Santa Clara University.

World Council on Economic Development (1987). *Our Common Future*, Oxford University Press.

Moving Towards Sustainability in Geotechnical Engineering

Stephan A Jefferis[1]

[1]Director, Environmental Geotechnics Ltd, Talbot Lodge, Ardley Road, Bicester, Oxford, OX25 4AD, England. Email: egl@environmentalgeotechnics.com

ABSTRACT: The concept of sustainability appears regularly in current engineering publications. It is often considered in terms of economic, social and environmental constraints and these can now be addressed using a wide variety of sustainability indicator tools. Upon examination, however, these tools are found to be mainly applicable at the project conception stage of civil engineering works. There is little specific advice to the practising geotechnical engineer on how to implement the principles of sustainability in the design office or on site. Although some useful indicators for these stages of geotechnical engineering work can be found amongst the indicators applicable to higher levels of the development hierarchy they can be difficult to identify and may be lost amidst the array of other indicators. This paper addresses some of the key issues that will be relevant for the geotechnical engineer in the design office and on site.

INTRODUCTION

There is a substantial and growing literature on sustainability but much of it is focused on high-level decisions concerning the competing constraints of social, economic and environmental issues and how to make decisions when there are diverging stakeholder opinions and conflicting constraints. What appears to be largely lacking is guidance applicable at the stage when the stakeholders have been consulted, the overall project plan has been developed and the various construction professionals are beginning to develop their particular technical parts of the project. For the geotechnical engineer, guidance is needed at both the design office and site practice levels.

This lack of guidance is surprising as geotechnical work can involve major changes of landform that will persist for centuries (e.g. mining), use of large amount of natural materials (e.g. aggregates) and manufactured materials (e.g. cement) all of which may involve the use of large amounts of fuels and oils in mobile plant (generally fossil derived fuel rather than biofuel). The technical opportunities for reduction in the geotechnical 'footprint' are enormous. Furthermore, as the impact of geotechnical works may last for centuries, energy use in service must be considered and not just in construction. Despite the many opportunities for sustainable development in geotechnical engineering, specific guidelines are few.

THE SCALE OF GEOTECHNICAL IMPACTS AND THE INDIVIDUAL

The impacts of geotechnical products and processes need to be quantified before any guidance on sustainability practice can be implemented. The various stages of geotechnical work need to be considered but the following two examples, cement production and soil excavation show the enormous energy demands of geotechnical processes compared with those of our daily lives and the impact that these energy demands might have on land-use if sourced from biofuels.

- The embodied energy in cement is perhaps 5 MJ/kg (Kibert, 1999), while the total energy demand for an individual person may be around 200 GJ/yr including energy for all aspects of life from food to fuel and including travel (Jackson, 2006, citing data derived for Gronigen, Netherlands). The annual personal energy use in Gronigen is thus equivalent to the embodied energy in 80 metric tonnes of cement which could be used to produce about 200 m^3 of concrete.
- As an example of energy use and possible land-use impacts, consider the fuel demand for a backhoe excavating soil for removal with a dump truck. These two items of plant might use a total of 40 litres of fuel per hour – an energy demand of about 1.6 GJ/hr which represents an hourly usage of about 0.8% of the annual personal usage in Gronigen. If the fuel was biodiesel derived from rape seed then, per day, this plant might consume the equivalent of the annual growth of over 2000 m^2 of rapeseed (assuming 1400 litres biodiesel per hectare of rape seed per year).

These are but two examples. Geotechnical engineers should develop their own so as to gain an insight as to how their professional work will impact on everyday life now and in the future.

INDICATORS OF SUSTAINABLE DEVELOPMENT

Individual geotechnical engineers may be keen to contribute to sustainable development but despite the burgeoning literature on sustainability they may be unsure how to proceed.

The International Federation of Consulting Engineers (FIDIC) (2004) provides a classification of sustainable development indicators considering the scale of the problem addressed. Table 1 provides an outline of their classification which starts with indicators at the global/regional scale appropriate for the consideration of the current state of the world. Smaller scale indicators are then considered but only at the foot of the table at the "Project Performance" scale is the construction phase considered. Few geotechnical engineers are regularly involved at the stages above "Project Performance", listed in Table 1, most will be involved at or below this level – the design office or site operations level. Therefore it seems that much of the current guidance is at too high a level to be relevant to the construction phase of geotechnical projects. At the stage, at which the geotechnical engineer becomes involved, for example, in a project for foundations for a new building the headline social indicators for the project (local investment, new jobs, local amenity, recreation areas, etc.) if considered, will have been finalised.

Table 1: Outline sustainable development classifications condensed from FIDIC (2004)

Scale	Description	Example
Global / regional	Overall assessment of the current state of the world mapped to Agenda 21 and response to Local Agenda 21.	Millennium assessment
Industry / NGOs	Sustainability of the operations of an organisation. Indicators of how an organisation is performing in terms of a set of indicators for sustainable development.	Global Reporting Initiative
Project risk assessment	Investor-based indicators. Principles, processes and indicators for assessing project risk.	The Equator Principles
Financial performance	Any published index that tracks the financial performance of companies that have committed to sustainability principles.	Dow Jones sustainability index, FTSE4Good
Project screening	Project-based indicators. Indicators for project as to their likelihood of achieving sustainability outcomes.	World Bank, The Equator Principles
Project performance	Contribution a project makes towards sustainable development. Includes efforts made in the construction phase.	SPEAR, CRISP, BEQUEST

Note: References for the various indicators are given in FIDIC (2004)

What then are the actions the geotechnical engineer should undertake on a day to day basis in the office or on-site to improve sustainability? The thinking required to develop the actions may have parallels with those required to improve the individual's sustainable development performance in the home. Goodall (2007) provides examples of what the individual can do at home to live a low-carbon life and texts such as his usefully can raise awareness of some of the underlying issues. Consideration of how to live more sustainably as an individual also forces us to consider demand side sustainability as well as supply side – recognising that we can do much to reduce our impact by managing demand and not just seeking materials and services with ever lower impacts and promoting research to develop such materials. The geotechnical engineer must consider demand as well as supply. Can impacts be completely avoided rather than just reduced? Much more research is needed on managing the demand side.

ASSESSMENT OF IMPACTS

The first step on the technical side is to be aware that materials, energy and indeed all site processes have impacts at the local site level and at wider scale and that although the use of a particular material may reduce local impacts, this may be at the expense of global impacts. As will be discussed below, there are now a number of tools available to address local and wider impacts. Outputs from the use of these tools can help the engineer gain an awareness of the impacts from the materials, energy, etc. used in geotechnical work. They will be particularly useful in the design office though less so for the geotechnical engineer on-site once materials selection decisions have been made. Examples of four impact assessment tools are set out below. It should be noted that each of the tools requires the collection and analysis of substantial amounts of data but the manner in which the final results are presented differs considerably. For examples of practical applications of some of the tools see Azapagic et al. (2004). For a more general discussion of the impacts of construction materials see Berge (2000).

Life Cycle Assessment (LCA): this is a technique for the assessment of the actual and potential (some impacts may occur in the future, e.g. dismantling of current infrastructure) environmental impacts associated with a product. The principles steps involved are compilation of an inventory of inputs and outputs, evaluation of the impacts of the inputs and outputs and interpretation of the results. Typically the impacts are presented as contributions to global warming potential, acid rain, photochemical smog, etc. (see British Standard, BS EN ISO 14040:1997). LCA does not provide data on where the impacts occur.

Materials and Substance Flow Analysis (MFA and SFA): These tools are used to track the flow of materials and substances in the human economy. MFA is typically used for bulk materials such as iron and steel, while SFA is applied to particular substances and chemicals. MFA tracks the origins and use of materials whereas SFA, with a focus on individual chemicals, is useful when compiling the input data for human health impact assessments (see Brunner and Rechberger, 2004). The procedures for MFA and SFA are similar to those for LCA but the outputs are more specific (e.g. flows of individual chemicals rather than summed outputs such as global warming potential). The procedures can provide information on where materials are used and where impacts occur.

Embodied Energy is the energy used to make a material or product. The results will depend on where in the world the product is made, what processes are employed, plant efficiencies, the scale of manufacture, the sources of materials, etc. When comparing results of embodied energy analyses, it is essential to compare like for like. Thus when comparing steel and concrete piles systems it is necessary to consider systems of equal performance as foundations. In addition to embedded energy, embedded carbon may be considered.

Ecological Rucksack (or material intensity per service or material input): this is the material input of a product (or service) minus the weight of the product itself. The material input is defined as the life cycle wide total quantity of natural material moved (physically displaced) by humans in order to generate the good (EEA, 1999). The results will depend on the production process. For example, the ecological rucksack of primary steel might be about 9 whilst that of secondary steel produced from recycled metal might be about 3 because of the reduced materials movements.

Each of these tools is an example of a different way of analysing and presenting the impacts of goods and services. They are all essentially tools to enable comparisons, such as to compare the impacts of a concrete pile system performing the same function as a steel pile system. For the geotechnical engineer it will be important to ensure that the comparison is not at the raw material level (one kg of steel versus one kg of concrete) but for systems that perform equivalent functions.

When using any of these assessment tools, it is important to specify the boundary conditions, the processes that are included within the study boundaries and those that are excluded. It is also necessary to consider the time frame. Is this to be the whole project life cycle, from cradle to grave, which for geotechnical projects may be decades? With some current and pressing environmental concerns it may be appropriate to look for short-term reductions in impacts as well as life cycle reductions.

There is a considerable amount of academic work on eco-indicators yet to be done. It is to be hoped that reliable, peer reviewed, data on the eco-performance of geotechnical processes will be available in the near future.

SITE LEVEL INDICATORS / ACTIONS

The tools discussed above will, if applied to a sufficient range of geotechnical processes, provide useful information to ensure that the geotechnical engineer is aware of the impacts that follow from the choices of materials and processes although the engineer may not be in a position to influence these choices if issues of cost or practicality dominate. What then can the geotechnical engineer influence?

Bartlett and Guthrie (2005) conducted a "comparative analysis of seventeen of the leading documents addressing sustainable development in relation to the built environment". The documents were selected "on the basis of being widely recognised and commonly used in the UK" and being publicly available. They analysed the frequency of the actions called for in the seventeen documents and produced a list of over sixty of these actions for the assessment of sustainable development.

A review of the sixty actions suggests that the following may be relevant to the geotechnical engineer on site or in the design office (this list is focused on geotechnical engineering and excludes broader issues of stakeholder engagement, health and safety, etc.). The percentage range quoted against each group of actions is the percentages citation in the seventeen documents.

- Materials: re-use; minimise use; prefabricate; use recycled, lower impact, durable, local, water efficient in manufacture with minimum embodied energy (80-100%);
- Energy: minimise use; maximise efficiency; use renewable; minimise CO_2 and NO_x, emissions; audit; encourage on-site generation (80-100%);
- Pollution: minimise the risk of pollution and eliminate ozone depleting substances (60-80%);
- Waste: minimise the creation of waste; recycle; compost; and use local energy recycling 60-80%);
- Water: minimise use; use efficiently; protect quality; reuse greywater; capture rainwater; control run-off; treat on-site; and use passive treatment (60-80%);

- Natural resources: minimise use and maximise efficiency (20-40%);
- Develop and use environmental management systems, comparison frameworks and decision making tools (20-40%);
- Undertake efficient, safe, considerate construction and minimise the impacts of construction (20-40%);
- Provide landscaped outdoor space for public and building users (20-40%);
- Engage the supply chain and use local suppliers (<20%);
- Innovate and use new technology (<20%);
- Take a precautionary approach and take account of climate change and environmental risk (<20%);
- Minimise impacts on neighbouring buildings and spaces (<20%);
- Support local businesses and the local economy (<20%);
- Aim for quality (<20%).

From consideration of the percentages quoted against each of the above actions, it is interesting to note that only two (those involving to materials and energy) had some mention in all the documents. Clearly the documents reviewed in Bartlett and Guthrie (2005) were not specific to geotechnical engineering but they were "leading documents addressing sustainable development in relation to the built environment". It follows that if a sustainability analysis had been carried out on a geotechnical project using the methodology set out in any one of the documents or derived from a composite of them, then only the above indicators could have been used. Thus despite the substantial literature on sustainability, there appear to be rather few indicators specific to geotechnical engineering – or indeed more generally to the construction phase of civil engineering works. Furthermore, there appears to be no specific guidance for the geotechnical engineer at the design office or site level.

AWARENESS OF SUSTAINABLE DEVELOPMENT ACTIONS

If sustainable development indicators are to be effective at site level, then it is important that all involved with site work should be aware of them and respect them. Leiper et al. (2003) considered how to obtain value through sustainability at a company level. In their list of "Ideas for action" they included "add sustainability to the site induction process". Site inductions as practised in the UK are a required introduction to the site for all those who enter the site – workers and visitors. They are necessarily addressed to people of all disciplines and skills level. Introducing sustainability at the induction stage allows the site specific issues to be considered by a much wider audience than otherwise might be achieved and could generate useful feedback. However, it can be agued that to mix sustainability and safety would reduce the impact of the safety induction. In practice separate inductions may be appropriate but the key message is that all those visiting or working on a construction site should be aware of the sustainable development issues relevant to the site.

SIMPLE INDICATORS

From a consideration of the nature of geotechnical processes, the materials used, the analysis of the indicators presented by Bartlett and Guthrie (2005), and the need for sustainable development awareness, headline indicators/actions for sustainable geotechnical delivery therefore must include:

Initial awareness training

Awareness of the impact of materials and processes using information from tools such life cycle assessment. In due course, outputs from assessment tools may be widely available as part of product or process descriptions. There also must be awareness of the amount waste generated by construction works (in the UK it is estimated that 10% of construction waste is unused materials and 26% is packaging, New Civil Engineer, 2007).

Respect for neighbours and local neighbourhoods

Emissions of noise, dust, light
Community cohesion

Respect for the natural resources initially on site and in the environs

Protection of flora and fauna
Avoidance of soil degradation including structural soils and top soils
Management of traffic movements on and off site
Appropriate water management including surface water
Recognition that soil sealing promotes flooding

Inputs to the site

Materials including water
Energy

Outputs from the site

Soil initially on site but no longer required
Materials initially on-site including demolition arisings
Waste materials from site works: demolition and construction waste, packaging waste. It will be important to segregate waste types to enable recycling
Waste water: from site dewatering and contaminated by site activities
Pollutants including chemicals, fuels and oils (also noise, dust, light)

Timeframe

All the above to be considered during the works and assessed for the estimated life cycle of the project.

Dissemination of information on sustainability drivers

Hold sustainability inductions as well as safety inductions so that both workers and visitors know what is required, what may be achieved and the contribution that the geotechnical engineer is making to sustainable development.

CONCLUSIONS

At present there are few if any guidelines to sustainability available to the geotechnical engineer which are appropriate and relevant for use either in the design office or on site. Guidelines at these stages of a project are key to promoting sustainable development. Tools such as life cycle assessment can help with the selection of materials and processes at the design office stage but an agreed set of indicators is needed for work on site. This stage of the sustainability process may be called 'sustainable delivery' and the geotechnical community needs to address this area and build and develop the list of 'simple indicators' presented in this paper. If sustainable delivery is not addressed, the skills, enthusiasm and goodwill of many geotechnical engineers will be lost. The proposed list of simple indicators is very basic and requires development. However, from the work by Guthrie and Bartlett (2005) we delude ourselves, if we believe that the existing indicators buried in the substantial literature will give us a more sophisticated system.

Finally, although this paper calls for further development in the indicators to implement sustainability at design office and site stages of a project, they should not become so elaborate that they cannot be rapidly assimilated rather like a site health and safety plan.

REFERENCES

Azapagic, A. Perdan, S. and Clift, R. (2004). *Sustainable development in practice*, Wiley.

Bartlett, H.V. and Guthrie, P.M. (2005). "Guides to sustainable built environment development." *Journal of Engineering Sustainability*, Vol. 158, Issue ES4, Institution of Civil Engineers, London.

Berge, B (2000). *The ecology of building materials*, Architectural Press.

British Standards Institution (1997). *BS EN ISO 14040:1997 Environmental management – life cycle assessment – principles and framework*, BSI, London.

Brunner, P. and Rechberger, H. (2004). *Practical handbook of material flow analysis*, CRC Press.

European Environment Agency (1999). "Making sustainability accountable: Eco-efficiency, resource productivity and innovation." *Topic report 11/1999.*

Goodall, C. (2007). *How to live a low-carbon life,* Earthscan, London.

International Federation of Consulting Engineers (FIDIC) (2004). *Project Sustainability Management Guidelines.*

Jackson, T. ed. (2006). *Sustainable consumption*, Earthscan, London.

Kibert, C.J. and Wilson, A. (1999). *Reshaping the built environment,* Island Press, Washington D.C.

Leiper, Q., Fagan, N., Engstrom, S and Fenn, G. (2003). "A strategy for sustainability." *Journal of Engineering Sustainability*, Vol. 156, Issue ES1, Institution of Civil engineers, London.

McKenna, J. (2007). "Defra reviews site waste plans", *New Civil Engineer*, 18 October, p9.

Risk Based Design of Levee System

Yuewen Huang[1] and Xiong (Bill) Yu[2], Member, Geo-Institute

[1]Senior Engineer, Guangzhou Investigation Design and Research Institute of Water Conservancy & Hydropower, Guangzhou, Guangdong, China, 510640, huangyuewen1973@163.com
[2]Assistant Professor, Department of Civil Engineering, Case Western Reserve University, Cleveland, OH 44106-7201, xiong.yu@case.edu

ABSTRACT: Conventional designs of levees, including the selection of geometry and superelevation, are generally based on assigning a special design class from perception of its relative importance. The process of assigning the design class is subjective. They do not treat the area under protection as the integral components in selecting levee type and design standard. A risk-based design aims to control risk in the most economic fashion. Implementing a risk-based design requires a system vision, i.e., to treat the levee and flood plain as the integral system components. The investment in levee design, construction and maintenance then becomes a dynamic optimization problem accounting for the economic and societal factors. The analyses can be assisted with tools such as GIS and remote sensing. This paper illustrates the necessity of employing risk based levee design to achieve resiliency and sustainable development.

INTRODUCTION

The catastrophic failure of the New Orleans levee system during Hurricane Katrina presses a comprehensive review of the design, construction and maintenance of critical levee structures. Significant efforts have been spent to identify the factors attributed to this failure (IPET 2006). Reconnaissance constructions are currently underway. To make the reconnaissance worthwhile, a long term plan is necessary to prevent the reoccurrence of similar tragedy. With the increasing number of major hurricane events global-wise, design and maintain of safe levee systems is becoming a topic of common interests. Such systems need to maximize the effectiveness of risk reduction. Risk based levee design is the logic step to improve the current levee design practice. International exchange of experience is important to prompt the implementation of this design philosophy.

THE CONCEPT OF RISK

Risk is a measure of the probability of failures and the extent of the associated damage (Krezner 2000). According to Australia National Council on Large Dams (ANCOLD 2003), risk is the measure of the probability and severity of the negative impacts on life, health, property and environment. In the mathematic term, risk is the production of the probability of failure and the associated amount of damages. Assessing flood risk can be challenging due to the large amount of uncertainties. These include, for example, the uncertainties associated with its frequency, the capability of protection structure, and the administrative strategy prior to, during and post flood events. Absolute safe is unrealistic and also in most cases not necessary from economic considerations. Thus most flood protection system must accommodate certain level of risk.

A useful tool for flood risk assessment is zoning the protection areas. The speed of flood and the depth of inundation are crucial as they determine the stability and mobility of human being during flood event. Different categories can be assigned according to the extent of damage a given flood will induce in the area (Li et al. 2006), Jiang et al. (2005), for example, categorized flood inundation zones into five levels of risk categories according to the maximal inundation depth, maximal flow speed, time of flood arrival, duration of inundation (Table 1). Such classification helps to develop efficient algorithm for flood damage and risk assessment.

Table 1 Levels of risk in flood inundation areas (Jiang et al. 2005)

Risk category	Description
1. Dangerous	High flow speed, high destruction force, unprepared break out of flood, fatalities, complete damage of farm land, collapse of all houses and buildings, interruption of transportation and communication, server damage to hydraulic structures, complete loss of properties
2. Heavy risk	Severe economic loss. Large inundation depth, damage of asylum, threat resident life, severe loss of agriculture production, portions of houses collapse, blockage of transportation and communication, damage of hydraulic structures, failure of drainage system, server property damage
3. Middle risk	Depth of inundation is 0.5 to 1.0m, agriculture production reduce up to 70%, damage of houses, interruption of part of transportation and communication system, damage of hydraulic structures, flood prevention system still in function, no fatalities but property loss are significant
4. Light risk	Depth of inundation less than 0.5m. Reduction of agriculture productivity by 30% to 50%, portion of houses slightly damaged or moderately damaged. Transportation communication works normally. Flood asylum area functions. Slight property damage
5. Safe	No inundation

SELECTION OF FLOOD PROTECTION STANDARD FOR LEVEES

River channels and levees are essential components of flood protection system that have been utilized since ancient time. The safety of levee system determines the safety of protection zone. Increasing the height of levee, while typically provides higher flood protection capability, also posts severer threat to protection zone if the system failures. Thus, the design standard for levees needs to be set based on the status of river channel and the role of levee in the regional flood protection system. The standard also set the level of risk a given levee needs to accommodate.

Selection of the design standard for levee is a deciding factor with both important economical and safety implications. Adoption of flood protection standard that is too low will cause high risk. On the contrary, standard set to be too high will cause huge economic burden for project construction and maintenance. Under the current levee design specifications, the design flood (year of recurrence) is first selected based on the importance of the area under protection. The design parameters of levee, such as the class, the superelevation, and the width are then selected. An example is illustrated in Table 2 and 3.

Table 2 Class of flood protection zone and design flood selection for levee[1]

Class of Protection Area		I	II	III	IV
Urban	Importance	Very important	Important	Middle	Ordinary
	Urban Population (thousand)	≥1500	1500~500	500~200	≤200
	Design flood (year of recurrence)	≥200	200~100	100~50	50~20
Suburb	Population (thousand)	≥1500	1500~500	500~200	≤200
	Size of arable land (thousand ace)	≥3000	3000~1000	1000~300	≤300
	Design flood (year of recurrence)	100~50	50~30	30~20	20~10
Industry zone	Size of industry	Ultra-big	Big	Middle	Small
	Design flood (year of recurrence)	200~100	100~50	50~20	20~10

Table 3 Requirement of levee design according to the design flood[1]

Class of Levee		1	2	3	4	5
Design flood (year of recurrence)		≥100	[50, 100]	[30, 50]	[20,30]	[10, 20]
Super elevation （m）	wave overtopping prohibited	1.0	0.8	0.7	0.6	0.5
	Wave overtopping allowed	0.5	0.4	0.4	0.3	0.3
Width of levee at top（m）		≥8	≥6	≥3	≥3	≥3

[1] Levee design specification of China, GB50286-98

Similarly, the current U.S. levee design specification, while embraced the components of risk analyses, does not explicit analyze the risk associated with a given project. As the consequence, levees designed using the same standard can carry significant different risk levels.

To illustrate this point, assume a flood protection system of class II protects two cities A and B of similar importance (Table 2). Under the current design specifications, both levees will be designed with a design flood of 150 year recurrence. From risk aspects, however, city A has high elevation with inundation depth of smaller than 0.5m, i.e., it belongs to the category of light risk (Table 1) whose failure causes no fatalities and only slight property damage; City B has lower elevation with a depth of inundation typically larger than 1.5 m, i.e., city B is subjected to heavy risk (Table 1). In addition, because of the differences in elevation, city A has lower probability of failure than city B during similar flood event. Consequently, both cities bear different risk although both levees are designed using the same standard. This example illustrates that the current design specification does not achieve optimal risk control among the flood protection system.

TOLERABLE RISK ANALYSES AND SELECTION OF TOLERABLE RISK LEVEL

A better approach of levee design is to achieve optimal risk control. The concept of tolerable risk can serve for this purpose. This requires considering both the economic and societal factors. The design requires limiting the potential risk associated with a certain project, R, to be below the allowable risk acceptable by the public, R^*, i.e.,

$$R \leq R^* \tag{1}$$

The tolerable risk level is the risk level perceived as acceptable by the general public. It depends upon the value the public place upon life and also on the level of safety perceived. The level of tolerable risk changes with the development of society, economy, environment and psychological conditions. Tolerable risk level can generally be described in terms of the probability of failure and the number of fatalities. Figure 1 shows the tolerable risk level for newly constructed dams by Australian National Committee on Large Dams (ANCOLD). A division line (zone) divided areas into risk levels that are tolerable or intolerable. Similar criteria are adopted for dam design in U.S., Canada and Germany. A commonly used value of maximal tolerable risk, R*, is 0.0001 person per year. For new dam or major water supply reservoir, the maximal tolerable risk value is as high as 0.0001 person per year.

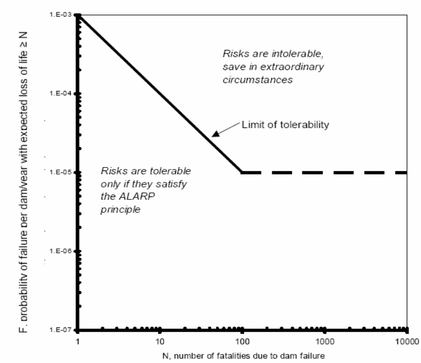

Fig. 1 Tolerable risk level for new dams (ANCOLD 2003)

Similar concepts should apply for levee design as well. The tolerable risk level can be moderately reduced considering the fact that the extent of damage by levee failures is generally smaller than that by dam failure. For example, the design code of levee in Netherland utilizes a maximal tolerable risk level of 0.1~0.001 person per year (Jiang et al. 2005).

For the example discussed in the earlier context, if similar tolerable risk level is accepted by both cities A and B. The design standard of city A can be lower than city B due to its lower level of risk under the same flood event. Such design philosophy optimizes the risk distribution among the flood protection system.

FACTORS AFFECTING FLOOD RISK ASSESSMENT

Both inherent and external factors affect the level of risk associated with flood damage. The inherent factors are those related to flood protection structure. For levees, these include its heights, construction materials and construction quality, slopes angels, seepage and erosion protection measures, and subsurface geological conditions. The external factors are related to characteristics of protection areas. These include its topological conditions, the level of economic development, population and distribution, and flood administrative measures (warning and evacuation). Both internal and external risk factors have high uncertainties, which make the accurate assessment of flood risk a challenging task. New tools such as GIS and remote sensing can be utilized to improve the efficiency of risk assessment.

It needs to be pointed out the level of risk is also dependent upon the human factors, especially the experience of residents for flood responses. A recent example occurred in China helps to illustrate this point. On June 22, 2005, historical level of flood hit Wuzhou City in the Southern province of Guangxi. The flood level is over 1 m higher than the designed flood level by this levee. Thus excessive overtopping occurs (Fig. 2). This, however, caused no fatalities. Post-flood investigation shows that this city is subjected to flood throughout the history. The local residents have extensive experience in adopting proper survival strategies in flood events. This example shows flood preparedness helps to reduce risks associated with levee failure. This can be achieved by providing training to residents.

Fig. 2 Photo of flood overtopping at Wuzhou city

RISK BASED LEVEE DESIGN

Incorporation of risk-based design for levees can further improve the current design practice. This requires determining the tolerable risk, based on which to determine the project reliability, its design standard and construction scale. Due to the highly distributive character, the failures of the components of a flood protection system can result in malfunction of the whole system. The risks associated with different failure modes, however, can be quite different. Risk based aims to optimize the control of risk levels when failure occurs.

For the recent case during Katrina (IPET 2007), the drainage canals (17^{th} st. Canal and London Ave Canal) is surrounded by areas with low ground elevation. This caused high inundation depth and increased the difficulty of post-hazard rescue activities. As a consequent, failure of levees along these canals caused half of the total fatalities and property damages (Fig. 3). A few breaches also occurred along the Industrial Canal. Because of the high ground elevation of the protection zone, the damages are much lower due to lower inundation depth (Fig. 3). Adopting risk-based design strategy during reconstruction should help to prevent similar catastrophic failures in the future.

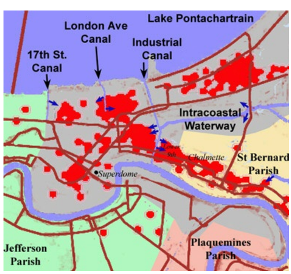

Fig. 3 Distribution of fatalities (red) during hurricane Katrina

CONCLUSIONS

The conventional levee design methods do not achieve an optimal risk control. A risk-based design has advantages to control risks in the most economic fashion. Implementing this design philosophy requires embracing system theory into the levee design practice, i.e., to treat the levee and the protection zone as an integral system. The investment in levee design, construction and maintenance then becomes a dynamic optimization problem. A sustainable development of flood plain requires embracing risk based design to improve the current practice.

REFERENCES

ANCOLD (Australian National Committee on Large Dams) (2003). Guidelines on risk assessment. ANCOLD, Sydney, New South Wales, Australia.

Interagency Performance Evaluation Task Force (IPET) (2007). Performance Evaluation of the New Orleans and Southeast Louisiana Hurricane Protection System, Final Report of the Interagency Performance Evaluation Task Force, Volume II—Geodetic Vertical and Water Level Datums, March 26, 2007, from http://ipet.wes.army.mil /

Fan, Z.W and Jiang S.H. (2005). Application of tolerable risk analyses in flood protection safety decision, Chinese Journal of Hydraulic Engineering, 36(5): 1~7.

Jiang S.H., Fan, Z.W. and Wu, S.Q., (2005). Flood risk assessment and safety decisions, Hydraulic and Hydropower Publisher, Co., Beijing.

Krenzer H. The use of risk analysis to support dam safety decision and management[A]. Q76 General Report. The Proceedings of 21th Int. Congress on Large Dams[C].Beijing China.2000.799-801.

Li, N and Zhou, K.F, (2006). Methods for evaluation of life loss induced by dam failure, Advancement of Science and Technology of Water Resources,26(2)：76~80.

The Development Timeline Framework:
A tool for engendering sustainable use of underground space

Hunt, D.V.L[1]., Lombardi, D. R. [2]. Jefferson, I. [3] and Rogers, C.D.F.[4]

[1]Research Fellow, The University of Birmingham, Edgbaston, Birmingham, d.hunt@bham.ac.uk
[2]Research Fellow, The University of Birmingham, Edgbaston, Birmingham, d.r.lombardi@bham.ac.uk
[3]Senior Lecturer, The University of Birmingham, Edgbaston, Birmingham, i.jefferson@bham.ac.uk
[4]Professor of Geotechnical Engineering, Head of Infrastructure and Research, The University of Birmingham, Edgbaston, Birmingham, c.d.f.rogers@bham.ac.uk

ABSTRACT: This paper explores the variety and timing of choices available to decision-makers during a redevelopment project for underground infrastructure space for utility services. The issues are explored using the Development Timeline Framework (DTF), a simple tool that makes explicit the importance of the timing of decisions and highlights when choices are locked-out or locked-in. It addresses the complex issues of trade-offs in decision making between various sustainable choices above ground and their requirement for underground space. The DTF enables the practitioner to optimize decision-making so as ultimately to mitigate future impacts, e.g. the potential effects of climate change and provide sustainable utility management practices, whilst enhancing community resiliency.

INTRODUCTION

The various uses for underground space have critical implications for sustainable development (Sellberg, 1996, Choguill, 1999, Durmisevic, 1999, Sterling, 1999, Clough et al., 2004). Unfortunately considerations for the use of underground space are not sufficiently detailed during the redevelopment decision-making process; thus, 'windows of opportunity' to progress toward a more sustainable outcome are often missed. In essence, the decision-making process itself may act as a barrier to or an enabler of sustainable underground construction. This paper explores the choices for sustainable water supplies available to decision-makers during a (re)development project and subsequent implications for sustainability (limited to utility infrastructure, underground space, end users and investors). In so doing it introduces the concept of the Development Timeline Framework (DTF), a simple tool that makes explicit the consequence of the timing of decisions, highlighting when choices are locked-out or locked-in. The next section describes briefly the outcome of research into the DTF carried out at the Universities of Birmingham (UK) and Central England (UK).

THE DEVELOPMENT TIMELINE FRAMEWORK (DTF)

According to the Oxford English dictionary a timeline is defined as '*a representation or exhibit of key events within a particular historical period, often consisting of illustrative visual material accompanied by written commentary, arranged chronologically.'* The development timeline framework (DTF) provides a forward looking view of decision-making processes from the earliest visioning stages of a redevelopment project through to final occupation. It is a tool for conceptualizing and analyzing decision-making with respect to sustainability. The DTF is used to identify elements of 'Lock In' (the stage at which a choice can no longer be changed) and 'Lock Out' (the stage at which it becomes logistically complex or un-economical to include such a choice; this is not to say that consumers willing to pay large additional green premiums could not retrofit such facilities).

Main Stages and Sub-Stages of the DTF

The decision-making processes for re-development projects have been mapped many times within the literature. The authors drew upon three types of decision-making process in order to define the appropriate stages of the DTF; these included:

A. Design (Design Advisor, 2004, Houghton, 2000 and Boyko, 2006)
B. Development (Design Advisor, 2004 and RESCUE, 2005); and
C. Planning (English Partnerships, 2006) including Infrastructure (Parkin and Sharma, 1999).

It was found that common activities (shown in brackets) could be collectively grouped within a five-stage DTF framework, as shown in Figure 1.

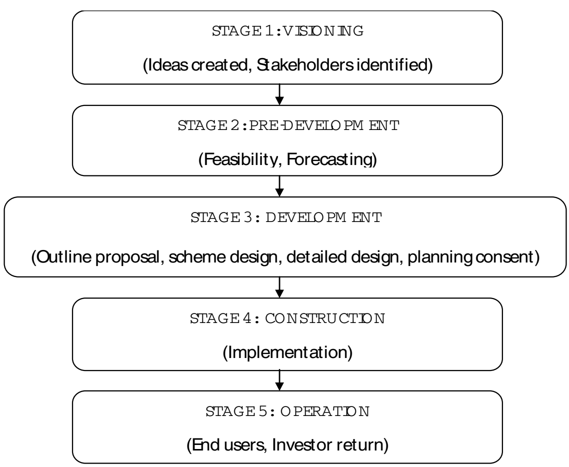

Figure 1 Overarching five-stage process of the DTF (showing key activities)

Each main stage (1-5) of the DTF consists of sub-stages which are used to illustrate the timing and interdependencies for decision making during a (re)development project. Within the following text, and for the purposes of this conference paper, the main stages and sub-stages of the DTF have been limited to selected aspects of sustainable water supplies, i.e. Rainwater (RW) harvesting, greywater (GW) recycling and Bore Hole (BH) abstraction. (The decisions required for implementing each option are considered against their implications for utility infrastructure, underground space and the wider population, i.e. investor and end-user):

Stage 1: The 'Visioning' stage of the DTF is the stage at which ideas are created for the development and stakeholders are identified (Figure 1). One of the first decisions to be made is the type of building that will be built (Table 1, 1.1). At this stage the benchmarks used to measure sustainable performance of water and utility infrastructure must be selected if realistic demand forecasts are to be made. In addition the capacity of existing utility infrastructure will need to be known (Table 1, 1.2). In all cases location of existing assets will need to be known and the geology stipulated so that risks and difficulties with: (1) rehabilitating, (2) renewing, (3) re-using, or (4) re-engineering infrastructure below ground may be highlighted. The density and location of existing infrastructure may ultimately 'lock-out' more sustainable methods of utility placement (e.g. multi-utility conduits, Rogers and Hunt, 2006). An investor will target end-user markets in order to maximise sales potential and will have a specific timeline in mind for securing economic returns, therefore the 'window of opportunity' to consider new infrastructure technologies is short. However the sustainable impacts of infrastructure are far reaching and long lasting (Parker, 1996, 2004), and therefore should be given much consideration.

Table 1 Selected 'Visioning' decisions within Stage 1 of the DTF.

(1.1) Type of development to be constructed	a. Demand benchmarks for water are needed by building type *Investor targets end-user market in order to maximise sales potential and has specific timeline in mind for securing economic returns*
(1.2) Sustainable underground utility infrastructure networks	a. Assessment needed of/for (i) underlying geology (ii) hydrogeology (iii) location of existing infrastructure (iv) existing capacity for water supply/disposal *Investor needs to consider early introduction of new infrastructure, not least for new technologies (e.g. non-potable water supplies)*

Stage 2: The 'Pre-development' stage occurs prior to design. Within this stage Haughton (2000) highlighted the importance of 'feasibility' and Parkin and Sharma (1999) highlighted the importance of forecasting (i.e. predicting future scenarios) in 'Infrastructure Planning'. Selected decisions for Stage 2 are shown in Table 2. In Stage 2 an estimate of the floor plan areas (e.g. 10,000m^2 of retail) and the number of units will become known (Table 2, 2.1), hence it is the earliest stage at which benchmarks sourced in Stage 1, which have requirements for prior knowledge of floor areas, can be applied. Subsequently current and future demands for water can be forecast. It is necessary to check that supply meets demand and to estimate

requirements for new utilities and their respective use of underground space. Stage 2 provides a 'window of opportunity' for seeking other sources of water supply (e.g. GW, RH and BH). The decision for adopting RH will be highly dependent on rainfall patterns; in areas of less than 300mm/yr rainfall, such an option is not economically viable, therefore lock out occurs. The volume collected depends on the roof details and these are not decided upon until Stage 3. In addition whilst GW can be recycled the exact amounts produced will depend on occupancy and behaviour, something which is not fully known until final occupancy has occurred (Stage 5). It is well known that offices and retail sectors produce very little GW and hence the choice of this type of development automatically locks out GW recycling systems. However, it should be noted that a best estimate can be made using floors areas and benchmarks for building type. Adoption of BH will depend on pumping rates and as with RH and BH will require: filtration, cleaning, and storage of water; importantly the last of these has requirements for underground space. These non-potable supplies will 'lock in' the requirement for non-potable infrastructure and need to be backed up by existing supplies to avoid 'lock out' in the case of system failures.

Table 2 Selected 'Pre-development' decisions within Stage 2 of the DTF.

(2.1) Floor plan area	a. Benchmarks based on water demand per floor area/per person/per room can be applied in order to estimate a total water demand profile for a development. N.B. these may remain variable until end of Stage 3 *An investor in residential accommodation may want more rooms of lower size (i.e. studios) thereby increasing localised water demands*
(2.2) Feasibility of using sustainable localised water supplies	a. GW - Need to know (i) recycling is 'locked out' in offices and retail; (ii) production depends on occupancy (Stage 5 decision). b. RW - Need to know (i) volumes of rain water collected depend on rainfall and roof size, roof material and design i.e. whether it is sloping or not. (Stage 3 decisions); (ii) rainfall is very dependent on geographical location, and 'lock out' occurs if rainfall < 300mm/yr . c. BH - Need to know (i) location of existing local abstractors, and (ii) possible abstraction rates. Need to obtain (iii) license to abstract. d. GW, RW and BH require new utility infrastructure, including underground storage tanks for non-potable water, and these requirements for space need to be estimated at the earliest stage (should be highlighted during Stage 1). e. Dual infrastructure is required to allow for mains 'back up'. f. Site-specific feasibility studies are required to assess if supply can meet demand, as are full sustainability costs (e.g. economic costs and 'embodied energy' costs from additional materials manufacture, transport and placement). Studies take time and could potentially delay planning process. g. For consequences to end-users, see Table 5. *An investor needs to know if added costs will be recoverable and if there is a market for developments with 'sustainable' non-mains water supplies.*

The sizing of underground tanks has critical implications for use of underground space and can only be agreed once predictions for the volumes of water collected (mentioned previously) are ascertained. It is important to note the considerable effect that choices made above ground can have on the use of underground space and therefore the need for accurate demand information early on.

Stage 3: The 'Development' stage is when: detailed designs are drawn up; outline proposals are made, and planning consent is given. During this stage decisions will be made that influence sustainable water supplies and ultimately impact on the use of underground space (Table 3). One of these decisions is with respect to sustainable roof design, which affects RH collection volumes and dictates the size of tanks and utility infrastructure (e.g. sewerage, potable and non-potable water supply pipes, tanks, etc.) required underground (Table 3, 3.1). The choice of sustainable roof will depend on whether the aim is to maximise water collection through RH, or as part of a Sustainable Urban Drainage Scheme (SUDS) to reduce flash flooding storm water surges in dry periods. Many aspects of the roof design will affect the volumes of water collected and amounts of infrastructure required; whether it is flat or sloped [N.B. 50% of a sloped roof will collect the same amount of water as 80% of a flat roof - assuming the same roofing material]; and the type of roofing material chosen; the percentage roof space area set-aside for each purpose (e.g. SUDS and RH).

There are also many other considerations to be made when assessing roof type, most being site- and development-specific these necessarily lie beyond the scope of the DTF presented here. However an example is given below to emphasise the trade-offs with other disciplines (e.g. energy and biodiversity), a major feature of the full DTF:

A green/brown roof can be used to enhance biodiversity and it is important to note that certain types of green roofs are locked out if a flat roof is not chosen.

Table 3 Selected 'Development' decisions within Stage 3 of the DTF.

(3.1) Sustainable Roof design	a. Need to know whether roof will be used for (i) RH or (ii) SUDS etc. b. Need to consider: (i) % roof space that will be set aside for RH as plan area will affect volume of rain collected (the larger the roof plan area, the more water that can be collected), (ii) sloped roof versus flat roof (more water can be collected from sloped - 80%, compared to flat - 50%), (iii) roof material (this will affect volume and quality of water collected). c. Decisions taken in (a) and (b) will determine tank sizes required underground (Stage 1 decision), once set aside roof area is decided and tanks are sized, 'lock-in' for storage capacity will occur. *N.B. QS may remove sustainable technologies due to additional costs. Investor may sell on the development when planning consent has been secured. Consents delay may compress construction period (Stage 4) for developer which impacts on Investor returns (Stage 5).This may also result in sustainable features dropping off the project.*
(3.2) Sustainable Water fittings	a. Need to decide what type of: Cisterns (e.g. 6.0 or 4.5 litre); Showers and Taps (e.g. aerating) will be used. These affect requirements for water demand and GW supply (needed for Stage 2 decisions) and have knock-on effects for underground supply and disposal (Stage 1 decision). These are not 'locked in' and can easily be changed.

A green roof may reduce water outflow as part of a SUDS scheme (Lipton and Strecker, 2002), which is good if that is the aim. However, if the aim is for RH this is a poor choice as the water has been reported to be of lower quality, which then requires increased amounts of treatment (which requires energy). The roof space can also be used to maximise energy production by use of Solar thermal and Photo Voltaics (PV), the latter being most efficient on a slope of 40-55^o (i.e. a sloped roof). If energy saving is also a local priority then trade-offs may exist and should be considered during the design stages so as to optimise a decision. High embodied energy (EE) costs for roofing materials should be considered against those with lower EE costs (e.g. single layer roof membrane - 45,500 kW/tonne; aluminium - 27,000 kW/tonne; clay tiles 800 kW/tonne; and local slate - 200 kW/tonne),taking into account the effect this will have on water quality and quantity and architectural finishes (which may also be a priority for the investor). The EE of green roofs is as yet unknown; however, they provide some thermal mass and any of these energy cost savings could also subsequently be offset. Water fittings can be chosen at Stage 3 and, as with roof type, these will affect supply requirements above and below ground, not least potable and non-potable infrastructure. They are, however, not locked in and are easily changed at a later stage (i.e. Stage 4 during construction or Stage 5 during occupation) to provide a more sustainable outcome.

Stage 4: The 'Construction' phase is where the designs are implemented and construction takes place. It consists broadly of three sub-stages: mobilisation, construction and demobilisation. Construction in 'underground space' will involve geotechnical processes, some of which will require water. Environmental geotechnical indicators (EGI) applicable to Stage 4 decisions can be found in Jefferson et al. (2007), those appropriate to water are captured in Table 4. Problems with groundwater should be highlighted at Stage 1; if not opportunities for using continual pumping of BH water as a potential supply source and as an alternative to tanking may be 'locked out' due to delays it would cause.

Table 4 Selected 'Construction' decisions within Stage 4 of the DTF.

(4.1) Mobilisation	1. Need to know if rising groundwater levels are problematic on site (Stage 1 decision). Expensive temporary dewatering schemes and tanking for underground construction will be required unless alternative sustainable options (e.g. permanent BH abstraction) have been explored and found feasible in Stage 2. Initial extracted water needs to be directed away from site to SUDS scheme or other. 2. Non-potable water infrastructure needs to be in place prior to construction above ground. Delays in implementing such infrastructure may cause delays or removal of systems from project. Retrofit infrastructure may be 'locked out' once construction starts.
(4.2) Construction	1. Need to reduce mains water use with construction processes (e.g. plant wash using GW or RH water) and reduce water build up on site, possibly by recycling (e.g. bentonite slurry for tunnelling).

Mains water consumption is likely within the construction phase (e.g. plant washing) and should be reduced through the use of alternative water sources (e.g. GW, BH, RH). Where large amounts of water are consumed, recycling may be more appropriate (e.g. bentonite slurry for tunnelling).

Stage 5: The 'Occupancy' stage is where the development will be occupied, operation will take place and investor returns are secured. In Stage 5 the true water demand, which is dependent on user behaviour, will be known. More frequent/longer use of showers/baths will produce higher amounts of grey water which could potentially be recycled for use elsewhere, and that is good. However, greater use of potable water should be avoided because of the undue burden it places on supply (water is a vital resource) and disposal requirements below ground. Development type can influence occupancy, which is not locked in but can change water demands dramatically (i.e. no occupant = no demand). Lower demands for water can be achieved by advocating (according to the European rating scale) Grade A rather than Grade E water-using technologies. Such technologies are stipulated by the end-user and will reduce underground supply infrastructure requirement; however, they are not locked in. Advice should be given.

Table 5 Selected 'Occupancy' decisions within Stage 5 of the DTF.

(5.1) End-users And sustainable water	a. End-user may want high water usage using power showers and baths, which goes against sustainable water use. b. Non-potable water use, not least GW, may not be acceptable to end-users. In all cases water quality needs to be guaranteed. c. It is important to note that higher density living will logically bring higher water demands and higher GW production. d. End users should be advised on reasons for sustainable water use, e.g. (i) how ratings A to E affect water demands, (ii) maintenance requirements of stand alone GW and RH systems, (iii) reduced water costs at small scale BUT increased energy cost (i.e. cleaning & pumping unless gravity fed system), (iv) washing machines can use RH water. e. *Aspects of a – c are important considerations for Investor returns.*

CONCLUSIONS

This paper described briefly research into the Development Timeline Framework (DTF) carried out at the Universities of Birmingham (UK) and Central England (UK). The DTF shows great potential as a decision making tool because it makes explicit: (i) the choices available to decision-makers during the overall decision-making process; (ii) information required by decision-makers to make a decision final; (iii) considerations for sustainability; and (iv) challenges of 'Lock In' and 'Lock Out'. An example of the application of the DTF has shown how the timing and interdependencies of decisions can impact upon sustainable water use.

ACKNOWLEDGEMENTS

The authors wish to thank the reviewers for their helpful comments and the EPSRC for their financial support during this Sustainable Urban Environments (SUE) research project under grants GR/S 20482, EP/C 513177 and EP/E 021603.

REFERENCES

Boyko, C. (2006). VivaCity Project 2020. www.vivacity2020.eu

Choguill, C.L. (1999). "Ten steps to sustainable infrastructure." *Habitat International,* September, Vol. 20 (3): 389-404.

Clough, P., Duncan, I., Steel, D., Smith, J. and Yeabsley, J. (2004) "Sustainable infrastructure" *A policy framework report to the Ministry of Economic Development.*: 85pp.

Design Advisor (2004). www.designadvisor.org/

Durmisevic, S. (1999). "The future of the underground space." *Cities*, Vol. 16 (4): 233-245.

English Partnerships (2006). "Advisory Team for Large Applications Planning Delivery Agreements." *(ATLAS) Report,* January 2006: 48pp.

Houghton, T. (2000). "A guide for developers and building professionals." *Enfield City Council Report*. CAG consultants in the London Borough of Enfield, UK: 47pp.

Jefferson, I,. Hunt, D.V.L., Birchal, C. and Rogers, C.D.F. (2007). "Sustainable Indicators for Environmental Geotechnics." *Engineering Sustainability*. Vol. 160 (2): 57-78.

Lipton, T. and Strecker, E. (2002) "EcoRoofs (Greenroofs) – A More Sustainable infrastructure." *ASCE Proceedings of the 9th International Conference on Urban Drainage*: 198-214.

Parker, H.W. (1996). "Tunneling, urbanization and sustainable development: The infrastructure connection." *Tunnelling and Underground Space Technology*. Vol. 11 (2): 133-134.

Parker, H.W. (2004). "Underground Space: Good for Sustainable Development, and Vice Versa." *International Tunnelling Association (ITA) Open Session, World Tunnel Congress,* Singapore, May: 17pp.

Parkin, J. and Sharma, D. (1999). Infrastructure planning. Thomas Telford. 248 p.

RESCUE (2005). "Best practice guidance for sustainable brownfield regeneration." *Regeneration of European Sites in Cities and Urban Environments*, May 2005, available at www.rescue-europe.com/html/project/html.

Rogers, C.D.F. and Hunt, D.V.L. (2006). "Sustainable Utility Infrastructure via Multi-Utility Tunnels." *Proceedings of the Canadian Society of Civil Engineering 2006 conference*, Towards a Sustainable Future, Paper CT-001.

Sellberg, B. (1996). "Environmental benefits: a key to increased underground space use in urban planning." *Tunnelling and Underground Space Technology*. 11 (4): 369-371.

Sterling, R. L. (1999). "Underground technologies for liveable cities." *Tunnelling and Underground Space Technology*. 12 (4): 479-490.

Embodied Energy as an Environmental Impact Indicator for Basement Wall Construction

Chris Chau[1], Kenichi Soga[2], Duncan Nicholson[3], Nick O'Riordan[4] and Toru Inui[5]

1. Researcher, Department of Engineering, University of Cambridge, UK. cykc2@cam.ac.uk
2. Professor, Department of Engineering, University of Cambridge, UK. ks207@cam.ac.uk
3. Director, Geotechnics, Arup and Partners, UK. Duncan.Nicholson@arup.com
4. Director, Geotechnics, Arup and Partners, UK. Nick.ORiordan@arup.com
5. Lecturer, Graduate School of Global Environmental Studies, Kyoto University, Japan. inui@mbox.kudpc.kyoto-u.ac.jp

ABSTRACT: Attempts were made to quantify the environmental impacts of the basement walls of two commercial buildings in London. Four different retaining wall options were designed based on steel and concrete systems for each of the sites. It was considered that excavation would take place with the aid of a one or two anchors system. Evaluation of embodied energy (EE) and CO_2 emissions for each of the wall designs and anchoring systems were compared. Results show that there are notable differences in EE between different wall designs. Using the averaged set of Embodied Energy Intensity (EEI) values, the use of recycled steel over virgin steel would reduce the EE of the wall significantly. The difference in anchor designs is relatively insignificant, and therefore the practicality of the design for the specific site should be the deciding factor for anchor types. Generally, the scale of environmental impacts due to constructions is large compared to other aspects in life as demonstrated with the comparisons to car emissions and household energy consumption.

INTRODUCTION

At present there are growing concerns regarding the rate at which the human population is extracting resources from the earth and emitting pollution and wastes to the environment. This has raised issues of sustainability and efficiency in many industries, including construction, which presently consumes about 50% of all resources in the world (Edwards, B., 2002). To address this issue, one of the fields of research is the study of Embodied Energy [EE] consumed by the residential buildings, as done by the Hong Kong Polytechnics University (2000) and Australia RMIT etc.

Chau et al. (2006) conducted a study on the EE of several commonly seen retaining walls options for a highway widening project based on a hypothetical London geotechnical profile. This study extends the former work by calculating the embodied energy of various basement perimeter wall designs and anchoring systems alternatives;

based on two real sites in London. Upon completion, this study will allow comparisons to be made as to the relative environmental performance of some commonly available retaining wall options.

EMBODIED ENERGY BACKGROUND

Embodied energy is defined as the total energy that can be attributed to bringing an item to its existing state and its units are in joules. For the construction practice, embodied energy will include the energy used in extraction of the raw materials from the earth, the processing of the raw materials into finished products, the transportation to the suppliers and then to the site, the construction processes, the demolition and recycling and the construction and maintenance of any associated temporary works.

Research into embodied energy is important because embedded into the measurements are associated environmental implications such as resource depletion and greenhouse gases. In fact, research into the relationship between embodied energy and carbon dioxide, the main contributor of the greenhouse gases, shows a high correlation: every GJ of embodied energy produces 0.098 tonnes of carbon dioxide (CSIRO, 2007). Therefore, although there are no physical environmental impacts associated with embodied energy, with the link to carbon dioxide, it now has a tangible meaning and so sheds light on how embodied energy should be interpreted.

EMBODIED ENERGY INTESITY

For this study, the calculation of embodied energy involves the use of the published Embodied Energy Intensity (EEI) values. This indicates the amount of embodied energy required in producing 1kg of construction material from the point of resource extraction to the end product; its units are MJ/kg or MJ/L for liquids. There has been research into EEI values since 1979 from both the public and private domains. However, there are sometimes a wide range of values found for certain materials. One important example is steel. The varying in value can be due to the different types of steel in question, assumptions and study boundaries drawn for the EEI evaluations.

Kiani (2006) summarised all published EEI values from around the world including the UK. Values used in this study are derived from his summarisation by discarding values which are more than two standard deviations from the mean. From the values remained, the mean values of each material were used for the EE calculation; the maximum and minimum values were used for a sensitivity analysis. Table 1 lists the mean and the range of the materials and fuel EEI values adopted for this paper.

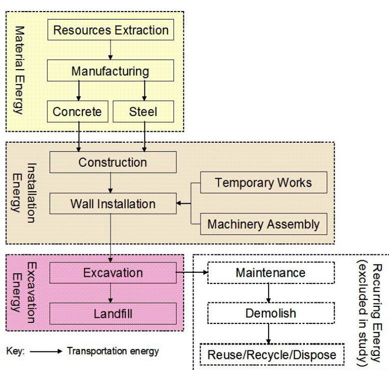

Fig 1: Processes flowchart of EE

Table 1: Summary EEI table

Materials		Virgin Steel	Recycled Steel	Concrete	Cement	Fuel
EEI [MJ/kg] or [MJ/L]	**Max**	60	18	2	4	41.2
	Mean	38.1	11.1	1.8	3	36
	Min	20	9	1.5	2.5	35.4

CALCULATION METHODOLOGY

To evaluate the EE of a construction, the first step is to identify all the processes in question for each stage of the calculation. Figure 1 shows an example flowchart for this purpose. In this calculation, types of processes are broken into three types: materials, installation and transportation energies. After that, each stage is calculated separately as follows. First is the material energy calculation, which is done by finding the total volume of each material used, hence its weight and multiplying this by its EEI value. Next is the transportation energy which includes the moving of the machineries and the materials used. This is calculated using the litres of fuel consumed by the vehicles multiplied by the respective EEI value for the fuel. The installation energy is calculated by multiplying the amount of fuel and electricity used by the machinery with its EEI value; this stage includes any temporary work required. All three values of the material, transportation and installation energy are then summed to give the total embodied energy. Note that excavation energy is not required in this project but would otherwise be included.

SITES

Two sites situated in central London near Thames river were used for this study. Projects at both sites are still ongoing at the time of this paper, therefore only brief details of the sites and their geotechnical profiles are disclosed here.

At Site 1, the proposed building is 40 storeys, about 150m in height, with a three level basement at about -6m, where ground level is at +5m, resulting in an expected 11m dig, and the toe of the retaining wall at close to -13m. The soil profile and geotechnical properties are shown in Table 2. This site has a layer of made ground and terrace gravel overlaying the Lambeth clay and sand, and underlying Thanet sand.

At Site 2, the proposed development involves six commercial buildings varying between 6-50 storeys high and seven residential buildings varying between 30-50 storeys high. The study takes an average of the buildings so that a 40 storey building was evaluated for easier comparison with Site1. There will be three levels basement at +0.0m, where ground level is at +5.4m. Table 2 shows the materials properties and ground strata layout used for the wall designs. This site has a layer of made ground, a thin layer of alluvium, then terrace gravel and an underlying Lambeth clay layer.

DESIGN SPECIFICATIONS

The retaining walls for basement construction are designed according to BS 8002 (1994). They are assumed to be left in place at their end of their design life of 120 years and corrosion is taken into account. No maintenance work is assumed to be required during the service life. In UK, serviceability requirement is based on lateral wall deflection of less than 50mm during any point of the construction. For the exposed section of retaining wall, the retaining specification includes water tightness according to the ICE wall specification (1996): allowing damp conditions but no running water. The walls were designed using OASYS's software FREW. This study has considered the wall deflections under serviceability limit state (SLS) conditions. Partial factors were applied to soil parameters to assess the walls for ultimate limit state (ULS) conditions. Different systems were chosen for either their ULS or SLS constrains. Corrosion allowances were made to increase the steel wall thickness.

Table 2: Materials properties and site ground profiles

	Bulk Unit Weight [kN/m^3]	Phi [^{o}]	Key
Made Ground	19	25	
Soft Alluvium	16	24	
Terrace Gravel	20	36	
Lambeth Clay	20	30	
Lambeth Sand	20	36	
Thanet Sand	21	36	

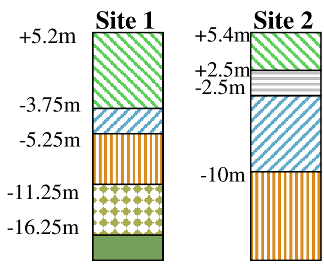

TYPES OF RETAINING WALLS CONSIDERED IN THIS STUDY

A basement perimeter wall was designed for the car park within a commercial building. In reality, extra layers of internal walls are sometimes inserted to give a more presentable finish. For the purpose of this study, it has been excluded.

As with all large basement projects, different design options are required around the perimeter of the wall. This is due to the varying profiles, surrounding structures and water conditions. In this case,

Site1 investigated a generic section which (a) is far away from the river and other underground structures and (b) has enough room behind the wall for anchorages. Therefore, four standard retaining wall options were considered for this site: sheet pile, secant pile, steel tubular piles and contiguous walls. For each design, a two levels anchorage design was considered. Additionally, the sheet pile option was used as an example to further investigate the EE of six anchor design options most commonly used in industry: three standard sizing of anchors: 0.12m, 0.15m or 0.20m in diameters arranged in either one or two level of anchors. The respective lengths and the number of steel bars for each anchoring system were designed and EE were calculated.

Site2 has a location which is close to the river with an aging canal wall that has to be either strengthened or replaced. Three propped options and a cantilever option were considered. Excavations for the propped options were completed by tying the props across to the existing canal wall using either a sheet pile or two different diaphragm walls, all with their toe levels at around -12m. The cantilevered option was found to have its toe level at -18m, resulting in a 23m wall: hence a diaphragm wall was chosen.

Table 3: Site 1 pile design configurations, materials used and required anchor forces.

	Sheetpile AZ48	**Secant pile**	**Steel tubular piles**	**Combi wall**
	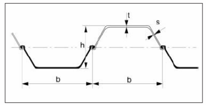	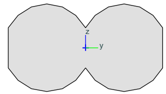	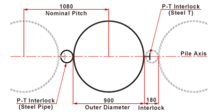	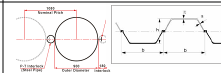
Toe level	-12m	-12m	-12m	-12m
Volume of materials/m [m3]	Steel: 0.57m3	Steel: 0.16m3 Concrete: 17.9m3	Steel: 0.42m3	Steel: 0.62m3
1 level anchors	971.4kN @+1m	-	-	-
2 levels anchors	384kN@+3m 320kN@-3m	470kN@+1m 320kN@-2.5m	420kN@2.25m 605kN@-3m	348kN@2.25m 640kN@-3m

Table 4: Site 2 pile design configurations, materials used and required anchor forces.

	Sheetpile AZ34	**Propped Diaphragm 1**	**Propped Diaphragm 2**	**Cantilever Diaphragm**
	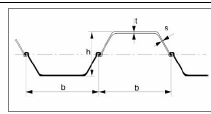	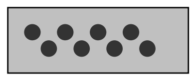	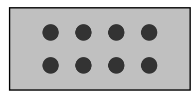	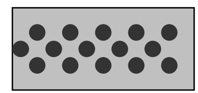
Toe level (length)	-12m (17.4m)	-12m (17.4m)	-12m (17.4m)	-18m (23.4m)
Sizing (width)	AZ34	800mm	1000mm	1500mm
Volume of materials/m [m3]	Steel: 0.42m3	Steel: 0.13m3 Concrete: 13.8m3	Steel: 0.13m3 Concrete: 17.3m3	Steel: 0.30m3 Concrete: 34.8m3
Strut load	239kN @+1m	239kN @+1m	260kN @+1m	-

RESULTS

Table 3 and 4 show the configurations and sizes of the wall designs, the volume of materials used and design forces for anchors for Site1 and 2 respectively. Figure 2 and 3 show the overall EE of the wall designs described in Table 3 and 4 respectively. EE values are shown in per meter run values for ease of comparison.

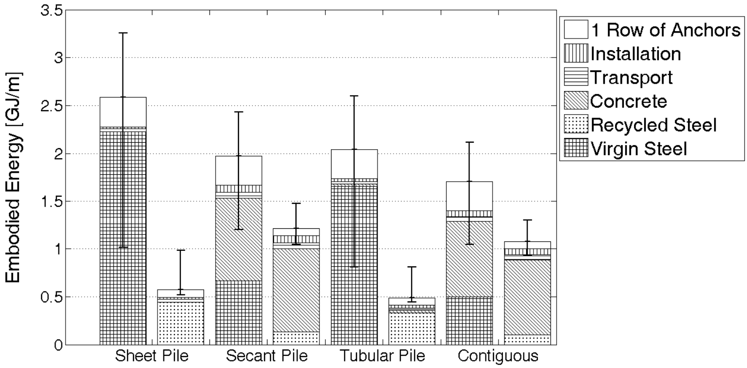

Fig 2:EE of Site1 Basement Wall Designs/m-run

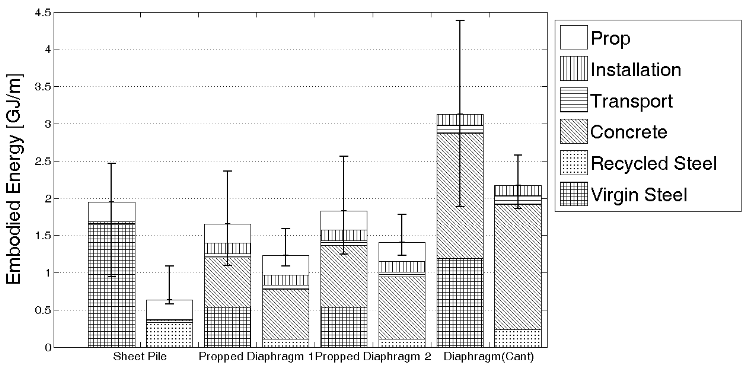

Fig 3:EE of Site2 Basement Wall Designs/m-run

The total energy consumed in a meter run of wall on average is approximately 100GJ/m. This is approximately 1.6 times the UK average annual household energy consumption from 2005 (National Statistics & Defra 2006). Comparing within the same site, the maximum difference in EE between the most energy consuming and efficient walls is in the order of 250GJ/m. For an average 200m perimeter wall for a commercial building with an approximately 250m^2 area, this difference in EE would result in an extra EE of 50TJ or 785 annual household equivalent in joules. This shows that careful choice of retaining wall designs and materials can contribute significantly in reducing the environmental impacts.

Secondly, the material energy is the greatest contributor to the overall embodied energy value in all cases; the proportion of energy is much greater than the transportation and installation energy combined. This result is consistent with that from Chau et al (2006) who designed retaining walls on a hypothetical ground condition. This shows that the choice of material is important, and that where possible, recycled steel should always be used due to the large reduction in embodied energy in comparison to virgin steel. However, note that nowadays when purchasing steel, clients do not have a choice between virgin or recycled steel. It is uncertain which type of steel is generally being consumed by the construction industry. Therefore the overall EE values for both virgin and recycled steels are presented in the results for completeness.

Thirdly, comparing across designs built from the same steel, results from Site 1 suggests that the EE of steel based designs such as sheet pile, steel tubular piles and combi-walls built purely from recycled steel consumes significantly less energy than other retaining wall options. The reverse is true when only virgin steel is available. This again stresses the importance in the general understanding for the steel being used in the construction industry. Meanwhile, results from the two sites collectively show that the cantilever diaphragm wall system consumes much more EE than any of the propped systems. This is because a cantilever system will always have to be found to a lower toe level, resulting in the use of much more materials and hence a larger EE.

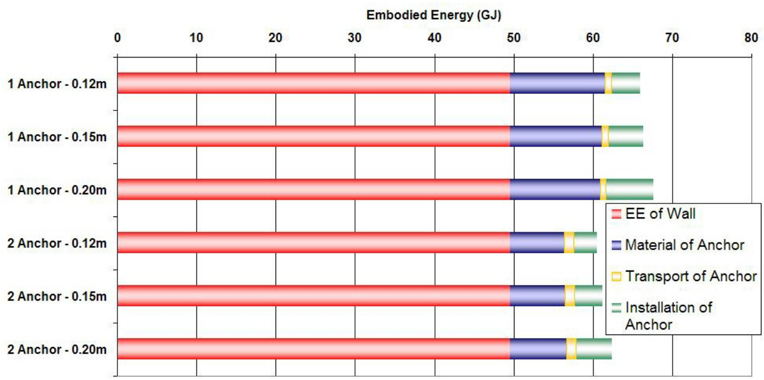

Figure 4: Site1 Sheet pile EE with various Anchoring Systems

Figure 4 shows the EE comparison of the different anchoring systems using the same sheet pile wall from Site1. Comparatively, designs with two rows of anchors rather than a single row consume less energy. This is because the required anchoring force for a one row design is larger than the sum of the required forces from the two rows of anchors. Therefore, the length of the anchor on the one row is much longer resulting in more use of materials.

However, the results show that on average, the anchoring systems consume approximately 25% of the total energy. The difference between the one or two rows systems is very small. Therefore, the decision between one or two rows of anchors should be based on the practicality of the solution rather than the environmental impacts.

CARBON EMISSIONS

On a separate study, the CO_2 emissions of all the walls presented in this paper were evaluated. The calculation methodology was similar to the one adopted in this study; the main difference is that instead of EEI, CO_2 emission factors published by Architectural Institute of Japan (2003 & 2005) and Japan Society for Civil Engineering (1997) were used. The CO_2 emissions in general are strongly correlated to the EE values, the average for all the walls is approximately 10-15t-CO_2/m-run. According to the official UK Car Fuel Data Organisation website, an average 2.0L engine family car emits approximately 200 g-CO_2/km. Therefore, the emission of this wall would be equivalent to running a family car for 50 – 75 thousand km. This is a significant result considering the amount of basement walls being constructed globally.

CONCLUSION

This study designed various retaining walls for large basement construction at two riverside sites in London under a chosen set of design criteria. Their embodied energies were computed to assess their relative environmental impacts.

Results show that recycled steel wall system generally consumes less EE and emits less CO_2 than the equivalent concrete wall systems. Comparing across materials, there is significant difference between designs built with virgin steel and with recycled steel. Therefore, it is important to ensure recycled steel is used for foundation construction. The difference in anchor designs is generally insignificant in terms of difference in EE. The scale of constructions was very large compared to other aspects in life as demonstrated with the comparisons with car emissions and household energy consumption. Therefore, it may be possible to optimise foundation system by minimising embodied energy and reducing environmental impacts.

REFERENCES

Architectural Institute of Japan (2003). *Guideline on the lifecycle assessment of buildings*, *2nd edition*, Architectural Institute of Japan.

Chau, C., Nicholson, D. and Soga, K. (2006). "Comparison of embodied Energy of Four Different Retaining Wall Systems", *Proceedings of International Conference, Reuse of Foundation for Urban Sites,* A.D. Butcher, J.J.M. Powell, H.D. Skinner (eds.), HIS Press, EP73, pp. 277-285

Edwards, B. & Hyett, P. (2002). *Rough Guide to Sustainability*, RIBA Publications.

Japan Society of Civil Engineers (1997). *Report on lifecycle assessment of environmental impact, JSCE Committee on LCA of Environmental Impact*, (in Japanese).

Kiani, M. (2006). *The Whole Life Environmental Impact of Glass within Glazed Commercial Building Envelopes*, Ph.D Thesis, University of Brighton.

BS 8002 (1994). *Code of practice for earth retaining structures*, British Standards Institution.

Institution of Civil Engineers (1996). *Specification for Pile and Embedded Retaining Walls*, Thomas Telford.

National Statistics and Defra (2006). *The Environment in Your Pocket 2006.*

CSIRO (2007). www.cmmt.csiro.au

UK Car fuel Data Organisation (2007). http://www.vcacarfueldata.org.uk/

Life Cycle Impacts for Concrete Retaining Walls vs. Bioengineered Slopes

Rune Storesund[1], P.E., M. ASCE, Jake Massey[2], A.M. ASCE, and Youngmin Kim[3], A.M. ASCE

[1]Consulting Engineer, Storesund Consulting, Albany, CA 94706; rstoresund@earthlink.net
[2]Graduate Student, University of California, Berkeley, CA 94720; jmassey@uclink.berkeley.edu
[3]Graduate Student, University of California, Berkeley, CA 94720; youngmin@berkeley.edu

ABSTRACT: A case study at the site of a creek restoration project within the Presidio in San Francisco, California is presented that analyzes the life-cycle environmental impact between a conventional reinforced concrete retaining wall compared with a bioengineered slope. Evaluation criteria were based on overall life-cycle costs (planning, design, construction, operations/maintenance, however decommissioning was not evaluated) and the magnitude of environmental impact. For our study, environmental impact was characterized based on total energy consumption (TJ) and associated Global Warming Potential (GWP, $CO_{2Equivalent}$). The magnitude of environmental impact was calculated using the online Economic Input Output Life Cycle Analysis (EIO-LCA) tool. We found that biostabilization methods had about one-half the environmental impact as compared with utilization of conventional reinforced concrete retaining walls. However, the total (design) lifetime cost for biostabilization was found to be higher than that of the reinforced concrete wall (due mainly to maintenance costs where we assumed that the bioengineered slope would be actively maintained).

INTRODUCTION

This case study was completed in order to evaluate, from a life-cycle approach, the differences in financial and environmental impacts for a typical slope stabilization project using biostabilization approaches compared with conventional reinforced concrete retaining walls.

The project site selected was from a creek restoration site within the Presidio in San Francisco, California. The restoration project involved the excavation and daylighting of a creek that was culverted and filled between 1900 and 1915 as part of military development at the Presidio (Frey, 2004). The creek daylighting excavation extended as much as 8 meters below surrounding grade and physical constraints such as existing structures and a parking lot required the excavation slopes to be stabilized.

The evaluated slope stabilization methods were configured so that an acceptable factor of safety (F.S.=1.5) was provided against possible slope failure during the construction and operation life cycle phases of the project. The configuration was also required to ensure no detrimental performance of the retaining wall or biostabilization as a result of possible meandering of Tennessee Hollow Creek. A minimum 20-foot setback to the toe of the biostabilized slope and edge of footing for the reinforced concrete retaining wall was selected to account for possible future creek migration. This creek offset and existing site constraints (such as buildings, walkways, parking lots, etc) were used to develop the required geometry for the biostabilized slope and reinforced concrete retaining wall.

Design analyses for the reinforced concrete retaining wall included stability (short-term, long-term, seismic), sliding, overturning, structural, and concrete mix design. Design analyses for the biostabilization included stability (short-term, long-term, seismic), vegetation and planting, temporary cut slope, and stormwater runoff.

Stabilization components were selected to accommodate site constraints and stabilize the slope in areas where it was not possible to grade the hillside slopes to 2:1 (horizontal:vertical) or less. The biostabilized slope extended from the setback to existing site grades at a slope of 2:1. The reinforced concrete retaining wall was situated outside the creek setback zone and offset from existing structures so that underpinning and/or temporary support would not be needed during construction. Figure 1 shows an overview of the site excavation and two slope stabilization alternatives.

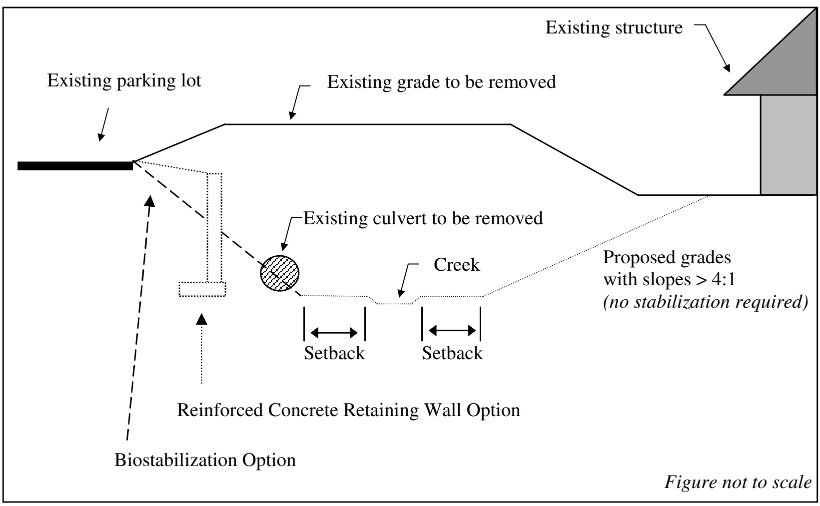

FIG. 1. Conceptual overview of slope stability techniques.

APPROACH AND METHODOLOGY

In order to evaluate and compare the environmental impacts of bioengineered stabilization with traditional reinforced concrete retaining walls for slope stabilization, we evaluated the resources required to accomplish the project from the planning, design, construction, operations, and maintenance life cycle phases. The purpose of this approach was to not only evaluate life cycle environmental impacts, but life cycle costs as well. Resources at each life cycle stage were converted to U.S. dollars based on RS Means and State of California Department of Transportation cost guides. Global warming potential and energy consumption were calculated using the Economic Input Output Life Cycle Assessment (EIO-LCA) program available from www.eiolca.net.

EIO-LCA Model

The EIO-LCA model uses the U.S. Department of Commerce's 491-sector industry input-output model of the U.S. economy (EIO-LCA, 2007). The software uses a matrix with 491 rows and 491 columns, each row and column representing one economic sector. The tables can represent total sales from one sector to others, purchases from one sector, or the amount of purchases from one sector to produce a dollar of output from the sector (EIO-LCA, 2007). Resources required to implement the biostabilization and reinforced concrete retaining wall were converted to dollar amounts, the appropriate economic sectors were selected in EIO-LCA and the associated energy consumption and global warming potential was calculated.

Life Cycle Costing

Our evaluation of project planning included professional services and fees required to complete an initial site characterization, restoration configuration, permits, and preliminary cost estimate and schedule. The resulting labor effort (measured in dollars) was then input into EIO-LCA to estimate environmental impacts.

The design phase was evaluated based on professional services (labor) required to complete the required detailed design necessary for the construction of the stabilization method. Design elements included scour analyses, structural analyses (slope stability, static and dynamic stability, etc.), site grading, material quantities, preparation of construction plans and specifications, and finalized construction schedule and budget. Design guidelines from Caltrans (2005) were used to design the reinforced concrete retaining wall. The bioengineered slope was designed based on brush layering guidelines from Gray and Sotir (1996). The resulting labor effort (measured in dollars) was then input into EIO-LCA.

The construction, operations, and maintenance phases were evaluated in a similar fashion, but our analyses considered only construction activities and material consumption. We assumed construction labor was represented in the material costs. For the operations and maintenance life cycle phases, we assumed the majority of the cost was labor and 25% of the cost was materials. Energy consumption and GWP gasses for O & M were based on the materials, not labor.

In order to obtain an accurate breakdown of material requirements for the construction of the reinforced concrete retaining wall we subdivided the construction phase into segments: earthwork, formwork, reinforcement, concrete placement, curing and removal of formwork, and backfill once the wall was completed. For the biostabilization, our construction segments consisted of earthwork, vegetation planting, and temporary erosion control installation.

The design operation life of the slope stabilization methods was assumed to be 50 years. For the reinforced concrete retaining wall, our analyses assumed that graffiti removal was the only required maintenance and no operational resources were required. Unlike the reinforced concrete wall, the biostabilized slope requires active maintenance as a result of its location within a highly urbanized landscape where aesthetics impact public perception. The major maintenance tasks identified were pruning and removal of non-natives, replacement planting, vector control, and weed control.

RESULTS

The breakdown of tasks and resources required to generate the dollar value for each of the reinforced concrete retaining wall life cycle stages are summarized in Table 1. These dollar values were then input into the EIO-LCA program (selecting the appropriate economic sector) to generate the corresponding energy consumption (measured in GJ) and contribution of global warming potential (measured in kg, $CO_{2\ \text{Equivalent}}$). The results of our study are presented in Table 1.

Table 1. Reinforced Concrete Retaining Wall Life Cycle Phase Analysis

Life Cycle Phase	Life Cycle Component	Quantity	Unit	Unit Cost	Value ($)	Energy (GJ)	GWP (Kg)
Planning	Permits	2	per	500	1,000	2	190
	Permit preparation	100	hrs	100	10,000	20	1,890
	Configuration & layout	120	hrs	100	12,000	30	2,270
	Cost & schedule	48	hrs	100	4,800	10	900
	Environmental impact	7,500	per	1	7,500	20	1,420
	Site-characterization	15,000	per	1	15,000	30	2,840
Design	Scour evaluation	36	hrs	100	3,600	15	1,365
	Design analyses	248	hrs	100	24,800	103	6,819
	Plans, specs, schedule	230	hrs	100	23,000	96	8,721
	Material quantities	60	hrs	100	6,000	25	1,135
	Stormwater runoff	60	hrs	100	6,000	25	1,135
Construction	Earthwork	11,100	per	1	11,100	27	2,010
	Formwork	20,800	per	1	20,800	71	6,140
	Steel & concrete	18,846	per	1	18,846	154	15,257
	Backfill	30,133	per	1	30,133	128	9,595
O & M	Grafitti Removal	50,000	Per	1	50,000	203	14,800

Table 2 presents a summary of the total costs, energy consumption, and global warming potential contribution for the planning, design, construction, and O & M.

Table 2. Summary of Reinforced Concrete Retaining Wall Analyses

Life Cycle Phase	Value ($)	Energy (GJ)	GWP (Kg)
Planning	50,300	112	9,510
Design	63,400	249	19,175
Construction	80,879	380	33,002
O&M	50,000	203	14,800
Total	244,579	959	76,487

The breakdown of tasks and resources required to generate the dollar value for each of the biostabilization life cycle stages are summarized in Table 3. These dollar values were then input into the EIO-LCA program (selecting the appropriate economic sector) to generate the corresponding energy consumption (measured in GJ) and contribution of global warming potential (measured in kg). The results of our study are presented in Table 3 and a summary of the total costs, energy consumption, and global warming potential contribution for the planning, design, construction, and O & M life cycle phases are presented in Table 4.

Table 3. Biostabilization Life Cycle Phase Analysis

Life Cycle Phase	Life Cycle Component	Quantity	Unit	Unit Cost	Value ($)	Energy (GJ)	GWP (Kg)
Planning	Permits	2	per	500	1,000	2	190
	Permit preparation	100	hrs	100	10,000	20	1,900
	Configuration & layout	120	hrs	100	12,000	30	2,280
	Cost & schedule	48	hrs	100	4,800	10	912
	Environmental impact	7,500	per	1	7,500	20	1,420
	Site-characterization	15,000	per	1	15,000	30	2,840
Design	Scour/ erosion evaluation	46	hrs	100	4,600	9	874
	Design analyses	213	hrs	100	21,300	43	4,047
	Plans, specs, and schedule	230	hrs	100	23,000	46	4,370
	Material quantities	60	hrs	100	6,000	12	1,140
	Stormwater runoff	60	hrs	100	6,000	12	1,140
Construc tion	Earthwork	9,500	per	1	9,500	20	1,520
	Vegetation Implementation	29,600	per	1	29,600	8	700
	Erosion Control	8,000	per	1	8,000	16	1,240
O & M	Pruning and weeding	150,000	per	1	150,000	0	0
	Vegetation replacement	25,000	per	1	25,000	7	591
	Insect and disease control	25,000	per	1	25,000	90	7,150

Table 4. Summary of Biostabilization Analyses

Life Cycle Phase	Value ($)	Energy (GJ)	GWP (Kg)
Planning	50,300	112	9,542
Design	60,900	122	11,571
Construction	47,100	44	3,460
O&M	200,000	97	7,741
Total	358,300	375	32,314

A direct comparison between the costs, energy consumption and global warming potential between the reinforced concrete retaining wall and biostabilization methods are presented in Figures 2 through 4.

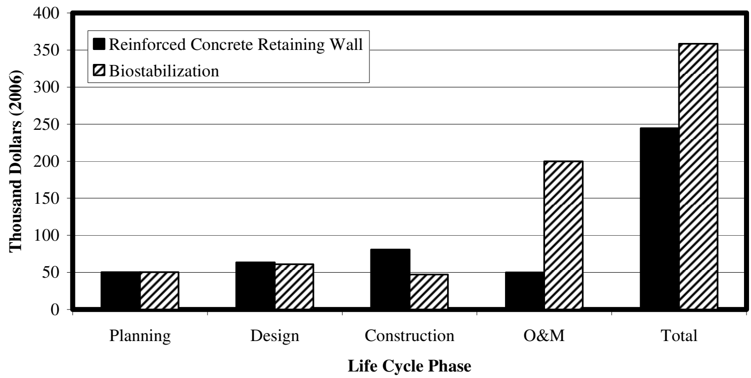

FIG. 2. Comparison of life cycle cost in thousands of dollars.

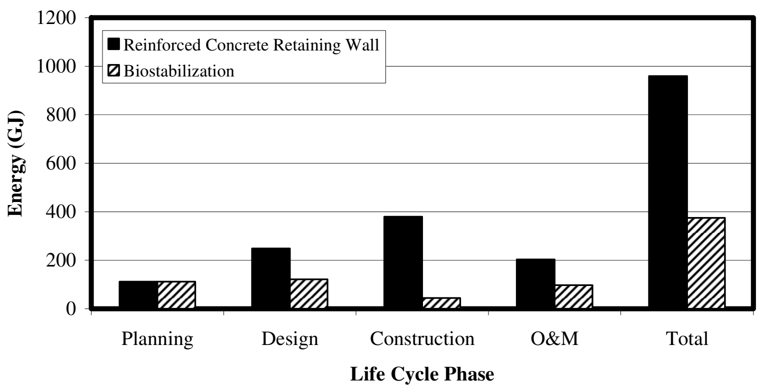

FIG. 3. Comparison of life cycle energy consumption in GJ.

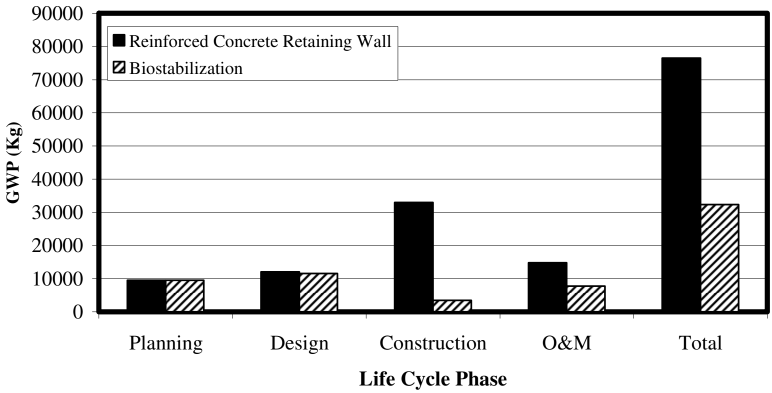

FIG. 4. Comparison of life cycle global warming potential in kg.

As seen in Figure 2, the actual construction cost for the biostabilization method is lower than that of the reinforced concrete retaining wall. Depending on the maintenance strategy employed (active maintenance was assumed for this study), the lifetime costs associated with the biostabilization method can be large. Actual environmental impacts as measured by energy consumption (Figure 3) and global warming potential (Figure 4) are approximately half as much as that required to construct the reinforced concrete retaining wall.

DISCUSSION

From our analyses, we found that the reinforced concrete retaining wall was a cheaper stabilization alternative in comparison with the biostabilization method, due to the high degree of maintenance required over the 50-year life of the biostabilized slope.

We found the planning and design phases to have similar costs, while biostabilization had a significantly lower construction cost, yet a higher maintenance cost. The biostabilization maintenance costs can, however, be deferred through the use of community groups, volunteer organizations, and Friends of Creek groups, thereby further reducing the cost of the biostabilization method. The other benefit of mobilizing community resources for the maintenance of biostabilized slopes, besides reducing incurred maintenance costs, is to promote community-based environmental stewardship. By being involved in the process, these community groups encourage citizens to be part of the environmental movement. We found that the reinforced concrete retaining wall had a greater energy utilization requirement and contributes more global warming potential gasses.

On an annual basis, biostabilization has a higher cost due to the active maintenance required, but significantly lower energy requirements and emits about half of the global warming potential gasses as the reinforced concrete retaining wall stabilization method. Our analyses did not include the effects of CO_2 emission credit as a result of photosynthesis from the vegetation used to implement the slope biostabilization.

CONCLUSION

We found that the bioengineering solutions for stabilizing slopes had less impact on the environment than the traditional reinforced concrete retaining wall. EIO-LCA proved to be an effective tool to analyze the environmental impacts associated with these two stabilization methods. In addition, viewing the two stabilization approaches from a life cycle standpoint allowed for a total cost overview of the two systems and allowed for more comprehensive long-term planning and decision making considerations.

ACKNOWLEDGMENTS

The authors originally developed this case study for a graduate course at the University of California at Berkeley under the guidance of Professor Arpad Horvath. The authors would also like to recognize the support of Mr. Mark Frey of the Presidio Trust, who provided access to project information associated with the Tennessee Hollow restoration project.

REFERENCES

California Department of Transportation (Caltrans). 2005. "Bridge Standard Detail Sheets, Retaining Walls with Soundwalls." Available from: http://www.dot.ca.gov/hq/esc/techpubs/manual/bridgemanuals/bridge-standard-detail-sheets/sec14.html. Date accessed: May 1, 2006.

EIO-LCA. (2007). "Economic Input Output Life Cycle Assessment." Available from: www.eiolca.net. Date accessed: May 5, 2006.

Frey, M. 2004. Ecological Restoration Design for Fill Site 6A (9/27/04 Draft). Presidio Trust. Presidio of San Francisco, CA.

Gray, Donald H. and Robbin B. Sotir. (1996). *Biotechnical and Soil Bioengineering Slope: A Practical Guide for Erosion Control*. New York: John Wiley & Sons, Inc.

R.S. Means. 2004. *Means Building Construction Cost Data Western Edition*. R.S. Means Company. Kingston, Massachusetts.

Soil-Bioengineering for Slope Stabilization in Ohio

Tien H. Wu[1], Brian R. Trenner[2], Patrick J. Fox[3], Christopher M. Kokesh[4], Kirk Beach[5], and David H. Barker[6]

[1]Prof. Emeritus, Dept. of Civil & Env. Eng. & Geodetic Sci., Ohio State Univ., Columbus, OH 43210, wu.26@osu.edu;
[2]Grad. Res. Asst., Dept. of Civil & Env. Eng. & Geodetic Sci., Ohio State Univ., trenner.2@osu.edu;
[3]Prof., Dept. of Civil & Env. Eng. & Geodetic Sci., Ohio State Univ., fox.407@osu.edu;
[4]Geotechnical Engr., GeoEngineers, Inc., Everett, WA 98201, ckokesh@geoengineers.com;
[5]Geology Program Supervisor, Ohio Dept. of Transportation, Columbus, OH 43223; kirk.beach@dot.state.oh.us;
[6] Managing Dir., Prima Subur Sdn Bhd, Kuala Lumper, Malaysia; Visiting Scholar, Ohio State Univ., ecological_ir@yahoo.co.uk.

ABSTRACT: This paper describes the use of live poles for the stabilization of shallow slope failures in clay-silt soils. Design and construction techniques are summarized. Long-term monitoring of the slope performance is currently in progress. Measured performance data includes displacement, pore pressure and suction, moisture content, survival of willow poles, and lateral resistance provided by the poles. Preliminary results and potential benefits and problems are presented.

INTRODUCTION

Soil-bioengineering has been used mostly for erosion control but has been shown to be successful in the stabilization of shallow slope failures. A recent development is the use of live poles, with diameters up to 50 mm and lengths up to 2 m, to stabilize shallow slips on road embankments in the UK (Barker 1997). This paper describes the use of live (i.e., willow and poplar) poles for the stabilization of shallow slips on three slopes constructed by the Ohio Department of Transportation (ODOT) as a research project. The purpose of the project is to investigate soil-bioengineering as a cost-effective alternative to conventional stabilization methods.

The lateral resistance of the poles contributes to shearing resistance along the sliding surface and increases the safety factor. In addition, the root systems of established poles can contribute an additional component to the shearing resistance. On the other hand, if the poles die and decay over time, their contribution to stability will also disappear. Thus, the long-term vitality of the poles is critical. Long-term monitoring of slope performance is currently being conducted and results obtained to date are presented. Construction time and costs are compared with those of conventional repair methods used by ODOT.

SITE CONDITIONS

Principle features of the three test slopes are given in Table 1. Profiles of the slopes are shown in Figs. 1-3. Indications of instability include bulges and cracks and soil blocks that have moved down slope. These blocks are 0.5 -1.0 m wide and less than 0.6 m in depth and the soil is generally wet.. Movements of about 50 mm took place during winter-spring 2004-2005. The soils at the sites are CL to ML. Strength properties from laboratory and in-situ tests are also given in Table 1.

Case histories of slope failures in Ohio (Wu et al. 1993) have shown that slopes on stiff clays or compacted clays generally deteriorate with age. The layer near the surface is subject to wet-dry and freeze-thaw cycles and its strength gradually approaches the state of $c' = 0$, $\phi' > 0$. During the wet season, the ground becomes saturated. Under vertical seepage, a 2H:lV slope would have a safety factor close to l.0. Local slips develop because of non-uniform soil and seepage conditions. Such slips are not usually noticed by maintenance crews. Over a period of several years, however, these slips grow, coalesce, and extend to greater depths. The condition becomes critical when the upper limit of a failure reaches the shoulder. To protect the roadway, the conventional repair measure is to excavate the soft material and replace with compacted fill, which is fairly costly. Then the cycle is repeated. The service life of such slopes ranges between 10 to 20 years, depending on the site conditions.

DESIGN AND CONSTRUCTION

To stabilize the slopes at New Concord and East Liberty, live poles were installed in the zones with shallow slips. At Marysville, the slips are located close to the bridge abutment and ODOT decided to repair this section with their conventional method. Willow poles were installed in the adjacent section, which had no slips, as a preventive measure. In the present study, live poles approximately 2 m long and 25-50 mm in diameter were installed vertically in a grid pattern approximately 1 m on center. The poles consisted of stems cut from willow and poplar trees located within 20 km from the sites, during early spring (March-April) and prior to sprouting of leaves. The poles were trimmed to the required dimensions. The installation at New Concord was delayed until late May 2005 and it became necessary to store the

Table 1. Principal Features of the Test Slopes.

Highway Routes	I-70/SR83	US33/SR347	US33/US36
Location	New Concord, Ohio	E. Liberty, Ohio	Marysville, Ohio
Type	embankment fill	cut slope	embankment fill
Pre-existing condition	shallow slides	shallow and deep rotational slides	shallow slides
Soil Type	compacted residual clay	till	compacted till
Cohesion, c’	0-30 kPa	0-20 kPa	
Friction angle, ϕ'	27-30°	30-34°	
Undr. strength, s_u	20-40 kPa	<50 kPa	
Pole species	willow, poplar	willow	willow

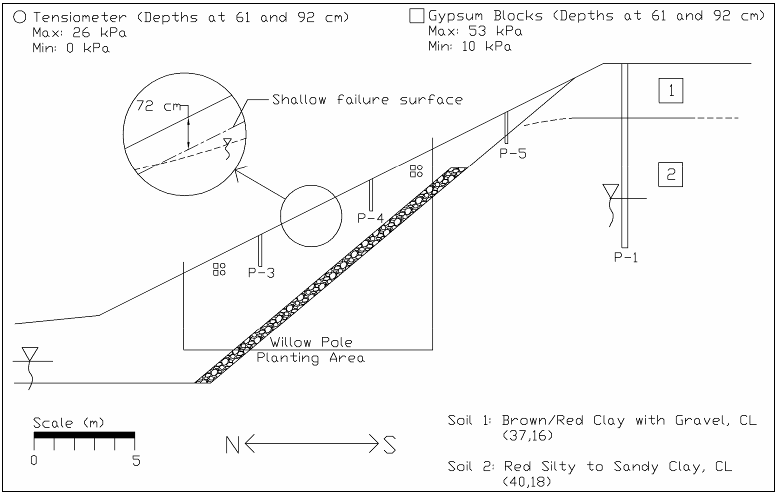

Fig. 1. New Concord Site.

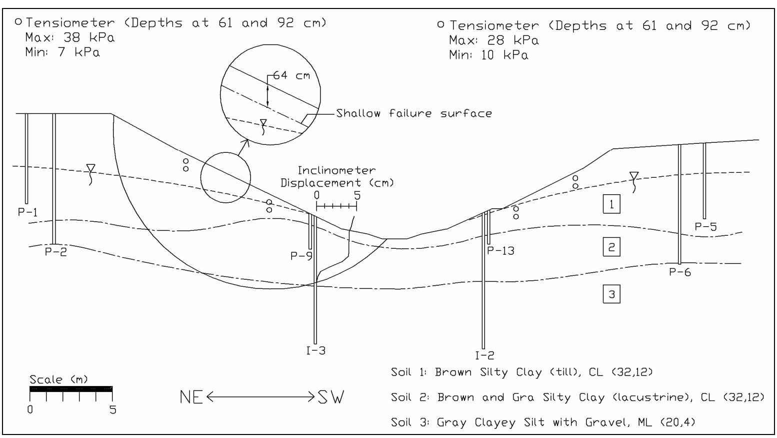

Fig. 2. East Liberty Site.

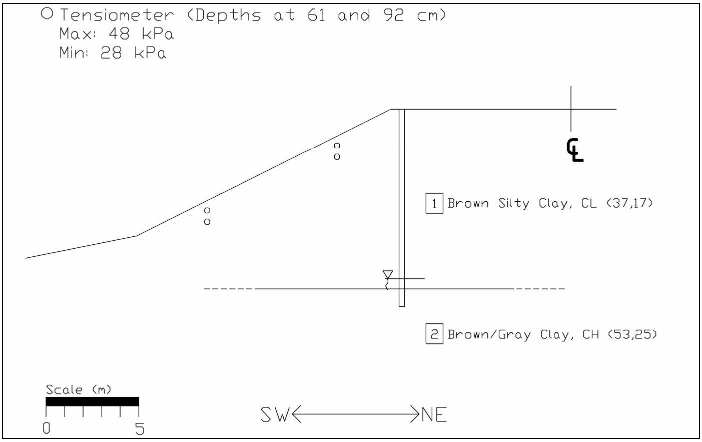

Fig. 3. Marysville Site.

harvested stems in refrigeration (2°C) as has been done in the UK (Barker 1997, Steele et al. 2004) until installation. At the other two sites the poles were transported to the site and installed within two days after harvest according to the procedures of Gray and Sotir (1996) and Barker (1997).

All poles were placed in pre-made 75 mm diameter holes. Two installation methods were used. Method A is considered to be the best method and is also the most labor-intensive. In this method, each pole is cut to a bevel at the bottom, the top is wrapped with wire to prevent splitting, the pole is driven 150 mm into the bottom of the hole with a mallet, and then the top is cut off, rewired and painted with a protective sealant. For Method B, which is simpler and less labor-intensive, the poles are simply dropped into pre-made holes, backfilled and painted with a protective sealant. Other details are shown in Fig. 4. Both installation methods were used at East Liberty to provide a side-by-side comparison. Only Method A was used at New Concord and only Method B was used at Marysville. The sand-gravel backfill and vent pipe provides aeration and should encourage root growth. To test the importance of aeration, about half of the holes at New Concord were backfilled with the embankment material and had no vent. A 0.6 m diameter biodegradable cover was placed around each pole to reduce competition from other vegetation (e.g., grass).

The infinite slope model was used to estimate the stability of the shallow slides before and after stabilization. Measured displacements (next section) indicated that the depth of the slip surface was at most 0.6 m and the measured suction was near 0 during the wet season, which indicated that the slopes were saturated with vertical seepage at East Liberty. At New Concord, piezometer levels suggested a perched water table near the surface and seepage parallel to the slope. The shear strengths in Table 2 represent the estimated "softened" strength (Skempton 1970). Calculated safety factors for the initial condition (i.e., before stabilization) are given in Table 2.

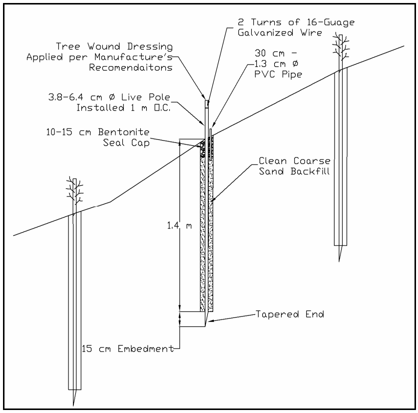

Fig. 4. Method A for live pole installation.

Table 2. Strength Parameters and Safety Factors at New Concord and East Liberty Sites.

Site	Seepage	c'	ϕ'	F_s (initial)	F_s (final)
New Concord	parallel to slope	2.4 kPa	27°	1.00	1.08
East Liberty	vertical	0	30°	1.15	1.40

Live poles installed vertically or perpendicular to the slope and extending to sufficient depth below the slip surface serve as soil reinforcements. The mechanism is analogous to that of piles. Immediately after installation, but with no root growth, the stability was calculated for the failure modes described by Vigiliante (1981) and Poulos (1995), which include the “flow mode” and “pile capacity mode”. In the flow mode, the soil layer above the slip surface moves between the poles and resistance is the passive pressure against the poles. In the pile capacity mode, lateral resistance provided by the portion of the pole below the slip surface is overcome. For the flow mode, the passive pressure was calculated with the range in s_u given in Table 1. The s_u of the undisturbed embankment was used to calculate lateral resistance for the pile capacity mode. It was found that the flow mode controls. The increase in shear strength was taken as the pole resistance divided by the square of the pole spacing. Calculated final safety factors are approximately 1.1 and 1.4 (Table 2). This represents the most unfavorable condition. The strength of the soil is expected to increase with root growth and the safety factor should increase with time. The safety factor with respect to deep movement at East Liberty was approximately 1.0. The construction of a toe berm at the same time of pole installation should increase the safety factor to about 1.25. These safety factors are small compared to those used in practice. However, for research purposes these factors of safety are acceptable.

MEASUREMENT OF PERFORMANCE

Slope performance before and after stabilization has been monitored using inclinometers, piezometers, tensiometers, and moisture blocks. Load tests on the poles were conducted to measure vertical and lateral resistances. Survival rates have obtained been obtained periodically. Results obtained to date are summarized below.

Pore Pressure and Moisture

Shallow and deep piezometers were used to measure pore pressures at the locations shown in Figs. 1-3. Tensiometers were used to measure total soil suction at shallow depths (< 2 m). Measurements from 2005 to present show that suctions developed in the top 0.5 m during the summer and autumn. From November to March, the ground was often near saturation. This agrees with the ranges in water levels observed in piezometers as shown in Figs. 1 and 2.

Displacements

Slope indicator tubes were installed at locations shown in Figs. 1-3 to measure deep movements. No such movements have occurred at New Concord and Marysville. At East Liberty, significant horizontal displacements occurred prior to stabilization at about 3 m below the bottom of the slope. This suggests that rotational failure occurred along the deep slip surface shown in Fig. 2.

To monitor the shallow slips, copper tubes and plastic tubes 10 mm in diameter were placed in predrilled holes. The positions of their tops were monitored. Excavations were then made on one side to expose the tubes. This showed that the movements were limited to the top 0.6 m. In addition, a row of stakes were placed along the slope and their movements were monitored relative to fixed benchmarks. The measurements showed that shallow movements of 5 cm occurred during the winter of 2005-6 at New Concord and East Liberty. After the repairs at New Concord, the movements were minimal during the last wet season, although soil moisture remained high and near saturation.

Survival Rates

Observed survival rates of live poles are given in Table 3. The low survival rates for the first installation (May 05) at New Concord (50%) are attributed to the late date of installation, which was followed by a period of hot weather. In addition, the poplar poles had a very low survival rate as compared to the willow poles, which reduced the overall rate. Most of the dead poles at New Concord were replaced with willow poles during the following spring (Feb 06). These poles were installed shortly after harvest and had a good survival rate (90%). Survival rates at East Liberty are also low, with differences for the SW and NE slopes attributed to differences in soil moisture. The method of installation did not influence the survival rate. Survival rates at Marysville are high 4 months after installation. Comparison of the survival rates at East Liberty and Marysville also indicates that installation method did not influence survival rate.

Table 3. Survival Rates of Live Poles.

	New Concord		East Liberty		Marysville
			NE	SW	
Installation	May 05	Feb 06	Mar 07	Mar 07	Mar 07
1st Spring	**74%**	**90%**	**49 %**	**72 %**	**91 %**
1st Autumn	**50 %**	**90 %**			
2nd Spring	**34 %**	**90 %**			
2nd Autumn	**32 %**				

Load Tests

Vertical pull-out and lateral load tests were performed on dead poles at New Concord to verify the pile equations used for predictions. Dead poles represent the worst case scenario, which is the state with no roots. The vertical load at pullout is compared with that using the undrained soil shear strength. The lateral resistance is compared with that calculated using Broms (1964) solution. The results are shown in Table 4, where the range in calculated resistance represents the range in undrained shear strength. The measured lateral resistance is within the range of the calculated values. The low measured vertical resistance, relative to the predicted resistance, is attributed to poor contact between the pole and the backfill material.

Table 4. Measured and Calculated Resistances for Load Tests of Live Poles.

	Measured	Calculated
Lateral Resistance	1.09-2.43 kN	0.89-3.11 kN
Vertical Resistance	0.29-3.11	1.47-8.90

CONSTRUCTION COST AND TIME

At New Concord, ODOT operators graded the slope and students installed the live poles. Construction at East Liberty and Marysville was done by a private contractor. Cost and construction times for the three sites are given in Table 5. The cost and time

Table 5. Comparison of Construction Cost and Time.

Site	Method	Cost ($/m^2)*	Time (days)
New Concord	Soil-bioengineering	52	15
East Liberty	Soil-bioengineering	115	7
Marysville	Soil-bioengineering	93.5	3
Marysville	Conventional	155	60

*areas measured from plan view.

for the conventional repair at Marysville are also provided. The cost of soil-bioengineering repair is 30% lower. This cost is expected to decrease significantly as local contractors become familiar with the techniques, as indicated by the cost at New Concord.

SUMMARY AND CONCLUSIONS

Results obtained to date indicate that live poles, if they can be established, can be effective for stabilization of shallow slides at depths of approximately 1.5 m or less. The low survival rate at the East Liberty site is of concern and will be studied further. The potential benefits of soil-bioengineering are reduced time and cost of repair and minimum or zero interruption of traffic. In a larger sense, this approach represents a proactive slope maintenance strategy. It is not only economical but is a step towards sustainable development that minimizes environmental impact and uses renewable materials. The principal limitations are constraints on construction time and the procedures for installing plant materials, which are critical but unfamiliar to many civil engineers and contractors. Also, the survival of poles requires additional and maintenance beyond what is typically necessary for conventional stabilization repairs.

ACKNOWLEDGMENTS

The work reported here is supported by ODOT and the Federal Highway Administration. Donald H. Gray and Daniel K. Struve were consultants on the design and construction. The poles were harvested from sites owned by Honda and the Ohio Department of Natural Resources. The writers thank these individuals and organizations for their support and assistance.

REFERENCES

Barker, D. H. (1997). "Live willow pole for slope stabilization on the A249 at Iwade." Report PR/CE/133/97, TRL Ltd., Crowthorne, UK.

Broms, B. B. (1964). "Lateral resistance of piles in cohesive soils." *J. Soil Mechanics and Foundations Division*, Vol. 90:27-64.

Gray, D. H., and Sotir, R. B. (1996). *Biotechnical and Soil Bioengineering Slope Stabilization*. John Wiley and Sons, New York.

Poulos, H. G. (1995). "Design of reinforcing piles in increase slope stability." *Canadian Geotechnical J.*, Vol. 32(5):808-818.

Skempton, A. W. (1970). "First-time slides in over-consolidated clays." *Geotechnique*, Vol. 20:320-324.

Steele, D. P., MacNeil, D. J., Barker, D., and McMahon, W. (2004). "The use of live willow poles for stabilizing highway slopes." Report TRL619, TRL Ltd., Berkshire, UK.

Viggiani, C. (1981). "Ultimate lateral load on piles used to stabilize landslides." *Proc., 10th Int. Conf. Soil Mechanics and Foundation Engrg.*, Stockholm, Vol. 3:555-560.

Wu, T. H., Randolph, B. W., and Huang, C-S. (1993). "Stability of shale embankments." *J. Geotechnical Engrg.,* Vol. 119(1):127-146.

Ground Improvement Technologies for a Sustainable World

Charles Spaulding[1], P.E., M. ASCE, Frederic Masse[2], M. ASCE
and Justin LaBrozzi[3], E.I.T., M. ASCE

[1]Regional Manager, Austress-Menard, 13-15 Lyonpark Road – Macquarie Park, NSW 2113, Australia – cspaulding@menard.com.au
[2]Vice-President of Engineering, DGI-Menard, Inc. 275 Millers Run Road, Bridgeville, PA 15241, USA – fmasse@dgi-menard.com
[3]Project Engineer, DGI-Menard, Inc. 275 Millers Run Road, Bridgeville, PA 15241, USA – jlabrozzi@dgi-menard.com

ABSTRACT: In an effort to assess the carbon footprint for a range of geotechnical construction methods, several case studies were selected where a conventional deep foundation technique was compared to a ground improvement alternative. The case studies are: improvement of an uncontrolled fill using Dynamic Compaction versus excavation, replacement and compaction in-place; installation of a driven pile foundation under a structural slab compared to the use of Controlled Modulus Columns under a slab-on-grade for a residential townhouse development; and the installation of a cement bentonite cut-off wall compared to a Soil-Bentonite wall.

Each technology's carbon footprint was analyzed using recognized carbon emissions calculation tools and values both for direct and indirect emissions. The authors have found that, in all cases, ground improvement technologies were not only more cost effective but also did significantly reduce the carbon footprint during the project construction phase; in two applications the reduction of carbon footprint was the result of the use of more 'carbon-efficient' construction materials, such as slag/flyash mixes or even recycled materials from site; in the remaining case, engineering the exisiting fill by Dynamic Compaction simply proved to be a much better use of resources.

INTRODUCTION

Evaluation of the carbon footprint of a given work activity is one of the first steps towards the reduction of greenhouse gas (GHG) emissions. Within the construction industry, one of the primary GHG contributors is the cement manufacturing sector, which alone accounts for about 3-4% of global man-made CO2 emissions through calcining of limestone. The transportation of material to and from borrow pits, fabrication plants and storage facilities, as well as the fuel consumption of the on-site equipment, are other causes of large GHG emissions by the construction sector.

General strategies are starting to be developed at government levels through tax breaks and rewards for energy-efficient processes. Other private / public initiatives, such as the development of Life Cycle Assessment tools designed to measure the environmental performance of buildings, contribute to promote the use of construction technologies with reduced carbon footprint including through the utilization of more ‘carbon’ efficient materials (slag/flyash mixes instead of concrete for example).

This paper will compare the carbon footprints of three ground improvement technologies with traditional foundation methods in the light of recent case histories.

CASE HISTORY #1: Industrial / Office Building in Pittsburgh, PA

This project was developed on a fill site located in the northern part of Pittsburgh, PA along Interstate 279. A two-story building and satellite dish farm totaling about 4,000 m^2 were proposed to be built. The building is constructed with a brick and masonry façade supported by interior and exterior columns. The southern half of the building is constructed with a mezzanine. Maximum column loads range from about 200 to 900 kN. The building is constructed using a slab-on-grade and spread footings approach.

The proposed building site is covered with a man-made fill material that varies in thickness from zero at the western side to a maximum of about 15 m at the eastern side. The fill material is very heterogeneous both in composition and in-situ densities. It ranges from fine-grained silts with boulders and rock fragments to coarse-grained sands and gravels in a matrix of silty sands. Based on the standard penetration resistance values (SPT-N), the fill exhibits medium dense to dense characteristics. However, it has been recognized that some of the higher blow counts may be attributed to the sampler hitting boulder size obstructions and not being representative of the soil matrix compactness. Accordingly, the fill has the potential for experiencing large differential settlements with time and was deemed not suitable as a foundation material for a slab-on-grade and footings structure. The initial design proposed to excavate 3 m of existing fill material across the building footprint and replace it with engineered fill placed and compacted in lifts with a roller. An alternate was proposed using Dynamic Compaction (DC) across the building footprint using a 15 t weight dropped from 25 m height. This solution, more economical than the initial design, was selected by the general contractor and approved by the Engineer.

The basic principle behind DC is that high-energy shockwaves are transmitted to the soil in order to improve its characteristics. Essentially, the soil is densified by the repetition of impacts of a pounder (10 to 40 t) dropped from heavy lifting cranes (10 to 40 m) in a pre-designed grid pattern. The impact of a falling weight results in immediate densification of granular soils through the generation of high energy waves. This energy is transmitted to the soil by applying several blows for each impact location and with several phases of a variable impact grid. DC can be applied on granular soils (sand, rock, mountain fill, etc…) but is also efficient for the rehabilitation of landfills, for road construction, industrial complexes or recreational landscaping.

For the calculation of the carbon footprint of the initial solution, it was assumed that a total of 12,000 m^3, corresponding to 4,000 m^2 of 3 m high fill material, would need to be excavated and replaced by granular material and compacted in place using a roller. A swell factor of 1.2 was calculated to evaluate the volume of material that will be hauled away and brought on site. Based on discussions with the general contractor, it was assumed that 100% of the fill material would have to be transported to a disposal location situated 35 km from the jobsite. The borrow pit location was assumed to be 22 km from the jobsite. All emissions related to the following activities were calculated using values published in ADEME (2007), as well as fuel consumption data from a leading equipment manufacturer found in Caterpillar (2007):

- excavation and loading of the 10 t dump trucks using 2 - 35 tons excavators
- disposal by dump trucks of all the fill material
- spreading of fill material at disposal facility
- processing and loading of granular material at borrow pit
- transport of granular material by dump trucks to the jobsite
- unloading and placement of granular fill by D6 type bulldozers
- re-compaction of granular fill using several passes of vibratory roller.

In summary, for the initial design, the above calculations showed that a total of 218,000 l of diesel fuel would have been necessary to perform the work, with a total duration of roughly 30 days.

The carbon footprint of the alternative ground improvement solution using DC was calculated based on actual production data, as the jobsite is now completed. A 15 t weight dropped from 25 m was used for the production passes and a 15 t ironing weight dropped from 17 m for the ironing pass; the compactive effort resulted in 0.85 drops/m^2 for a total 3,468 drops. The job was performed in 8 days with an average of 425 drops per day. The on-site equipment included a crawler crane type Bucyrus Erie BE71 and a D6-type bulldozer to backfill the craters after each pass of Dynamic Compaction.

As a result of the fill densification process by DC, an overall volumetric reduction of the fill material occurs (0.3 m on this site). The fuel usage corresponding to the quarrying, transport and compaction of the quantity of import fill needed to restore the working platform to its initial level was also included.

In total 15,000 l of diesel fuel were used for the DC alternative, translating into a total savings of approximately 200,000 l of diesel fuel compared to the initial design. Overall, the foundation works helped reduce the overall carbon footprint of the building by 160 t eq. C, representing the offset for emission of carbon of 28 persons for a year based on a per capita carbon emission of 5.6 t eq. C as given in Blasing et al. (2004) and World Bank (2004)

CASE HISTORY #2: Luxury Townhouse / Condominiums in Weehawken, NJ

The second case study to be presented considers a luxury townhouse and condominium subdivision along the banks of the Hudson River in Weehawken, New Jersey. The project called for the construction of 68 individual 3-story units located on a reclaimed railroad yard overlooking the financial district of Manhattan. The as-built foundation system featured Controlled Modulus Columns (CMC) as the sole foundation and slab support means.

This technology is a proprietary ground improvement system in which CMCs are used as an alternative to traditional deep foundations. CMCs are semi-rigid inclusions that are made of a specially designed cementitious grout mix, installed using a displacement tool that generates only a minimal amount of spoil. The CMCs reinforce the soil rather than function as distinct structural elements or piles, resulting in an improved soil matrix having increased stiffness with improved settlement and bearing characteristics. As a result, the entire foundation design plan can be optimized for a substantial reduction of concrete and steel since large pile caps, grade beams, and heavy steel reinforcement are no longer needed to support the building loads. Consequently, the emissions reductions associated with CMC technology (from both direct material costs and production-related operational costs) have an immediate impact on the total carbon output of the foundation system and, in turn, of the project.

For the current investigation, site soil conditions included a stiff upper layer of urban fill underlain by up to 23 m of highly compressible organic silts and clays. A suitable bearing stratum of dense sand and glacial till was found at an average depth of 23 m, with sandstone bedrock appearing between 13 and 39 m below grade.

Due to the thickness of the compressible organics, deep driven piles were recommended as the most feasible foundation support method, with an average target depth of 33 m. The alternate proposal relied on CMCs installed to an average depth of 23 m, which would bridge the compressible soils and terminate in the sand and till strata. The sustainability analysis was based on the comparative carbon emissions of the recommended deep foundation scheme of driven H-piles with a structural slab versus the as-built ground improvement system consisting of CMCs supporting a slab-on-grade.

A detailed quantity takeoff was done using the bid package, where it was determined that a total of 164 t of rebar, 6725 t of HP14x73 piles and 4358 m^3 of concrete would have been required for the original foundation plan. These values included concrete from slabs, pile caps and grade beams; steel quantities were derived from the piling and any required concrete reinforcement. Then, the direct carbon emissions associated with the deep foundation method were calculated using accepted constants and conversion factors for these building materials. This resulted in a total output of 3697 t eq. C for the driven H-pile support system.

Using the same procedure, the CMC-supported slab was analyzed, considering the grout from the CMCs and the concrete for the slab as the CO2 sources (steel was not required with this design). It was found that 7908 m^3 of grout and 4925 m^3 of concrete were required. With CMCs, it was found that the ground improvement system had a total emission of 1857 t eq. C, half of that of the deep foundations.

In order to put this number into perspective, it was assumed that the completed townhouses would have a total operating capacity of 136 residents. Adopting the same per capita carbon emission as previously, the total annual carbon footprint of the community was calculated to be 731 t eq. C. Using these results it was found that the carbon savings directly attributable to CMC technology was able to offset the environmental impact of all 136 residents for two and a half years.

Table 1. Comparative Emissions in t eq. C

	STEEL[1]	CONCRETE[2]	GROUT[2]	TOTAL
H-Pile System	3256.0	440.6	0.0	3696.6
CMC System	0.0	498.0	1358.9	1856.9
CMC Savings				**1839.7**

1 – Rawlins et al. (2007).
2 – Wilson (1993).

CASE HISTORY #3: Soil-Bentonite Slurry Cut Off Wall in Australia

The strategy selected by the Regional Land Management Corporation (representing the New South Wales government) for the remediation of a former steelworks facility, located at Mayfield in NSW, was to confine the contaminated area using an up-gradient groundwater barrier associated with a low permeability clay cap on a 37 hectare site; the cut-off wall, 800 mm wide, represented 50,000 m^2 and impacted the riverfront over a length of 900 m.

One advantage of that scheme was that no collection system was needed; instead, the hydrogeological model showed that the rapid exhaustion of the aquifer gradient between the contaminated area reservoir and the Hunter River would significantly reduce the migration of contaminants and bring them to acceptable levels within a short period. A more detailed description of the project is given in Jones et al. (2007).

The two alternative methods selected at tender time were Cement Bentonite (CB) and Soil Bentonite (SB) barriers. The SB option was finally selected on the basis of a range of parameters, which did not include carbon emission. An analysis of the equivalent carbon emissions for each scheme however, as summarized in Tables 1 and 2, shows that the difference in carbon footprint for each method is quite significant.

For the SB wall, the level of emissions of greenhouse gases related to the consumption of energy by the machinery was taken directly from the actual site fuel consumptions. The incorporated raw materials consisted of natural dry bentonite imported from India as well as a quantity of local 'Virgin Excavated Natural Material' clay used to increase the fines content in the SB mix; native materials dug from the trench were predominantly re-used in the wall backfill (approximately to a rate of 75%) ; the remainder of the excavated material, including material with some level of contamination, was permanently stockpiled on site in a series of buried containment areas.

For the CB option, the use of cement was the main carbon contributing factor, resulting in a significantly higher level of carbon emissions compared to SB.

Table 2. Carbon Emissions for a SB Wall (in t eq. C)

Soil Bentonite		Carbon print		Quantity	Unit	teqC
Energy	diesel during construction	4.2	kg eq C/m^2	50,000	m^2	209
Material	bentonite extraction & transport	8.0	kg eq C/t	2,500	tons	20
	clay extraction & transport	1.5	kg eq C/t	29,000	tons	45
Labour	staff and labour (21)	6	t eq C/year	12.25	pers.yr	74
Total Carbon Emissions in t eq. C						**348**

Table 3. Carbon Emissions for a CB Wall (in t eq. C)

Cement Bentonite		Carbon print		Quantity	Unit	teqC
Energy	diesel during construction	2.9	kg eq C/m^2	50,000	m^2	147
Material	Cement	235	kg eq C/t	8,350	tons	1,962
	Bentonite extraction & transport	8.0	kg eq C/t	2,500	tons	20
Labour	staff and labour (21)	6	t eq C/yr	12.25	pers.yr	74
Total Carbon Emissions in t eq. C						**2,203**

CONCLUSIONS

Through the comparative study of three case studies, this paper has shown that various acceptable geotechnical solutions for improving subsoil conditions can directly mitigate unfavorable environmental impacts. As shown in Table 4, estimates of carbon emissions resulting from selected site construction activities could vary in a ratio of over 10 to 1 depending on which option was selected. An example was given by comparing the fuel consumed during the construction of engineered foundation soils, in one case using the excavation and backfill approach (45 kg eq. C / m^2) and in the other relying on a ground improvement alternative using dynamic compaction (5 kg eq. C / m^2).

Table 4. Comparison of Carbon Emissions for Three Case Histories (in t eq. C)

Case History	Reduction Using Ground Improvement Alternative	Ratio of Carbon Emissions Traditional Technology / Ground Improvement
Industrial / Office Building – PA	160 t eq. C	1,450 %
Townhouses / Condominium – NJ	1840 t eq. C	200%
Soil Bentonite Slurry Cut-off Wall - NSW	1,855 t eq. C	630%

In addition, the materials used for the foundations can be one of the most important factors in determining the carbon footprint of a foundation system. In the last example, it was estimated that replacing the soil bentonite wall with a cement bentonite wall would have multiplied the carbon emissions by a factor of 7. The second case history, which compared a suspended slab supported on piles to a slab-on-grade built on Controlled Modulus Columns (using a flyash based mix), showed that the use of steel piles and a thicker concrete slab would have resulted in twice the carbon emissions as the selected method.

Overall, as demand for new construction continues to increase worldwide, so does the need for developing sustainable means and methods through which projects can be delivered while keeping adverse environmental impacts to a minimum. This creates a somewhat paradoxical situation when one considers that many of the current material production and construction implementation practices are inherently very energy intensive, releasing significant quantities of greenhouse gases into the atmosphere each year. As discussions on rising emissions levels have recently come to the forefront in political, social, and economic arenas, so too has the push towards a more environmentally conscious construction industry. To this end, it follows that any advance in technology or technique that promotes the reduction of GHG emissions would be at once both interesting and beneficial to the construction community at large, as more engineers, designers, and contractors re-evaluate their approach to sustainable building practices. The preceding analyses presented three such cases whereby the selection of an alternate ground improvement system resulted in significant emissions reductions for the project; this should serve as an indication that with the proper consideration and construction technique selection, progress towards a long-term sustainability goal can be achieved without compromising schedule, budget, or quality.

REFERENCES

ADEME (2007) "Bilan Carbone – Guide des facteurs d'emissions" www.ademe.fr

Blasing, T.J., Broniak, C.T., and Marland, G. (2004) "Estimates of Annual Fossil-Fuel CO2 Emitted for Each State in the U.S.A. and the District of Columbia for Each Year from 1960 through 2001". *In Trends: A Compendium of Data on Global Change, Carbon Dioxide Information Analysis Center, Oak Ridge National Laboratory, U.S. Department of Energy, Oak Ridge, TN, U.S.A.*

Caterpillar Inc. (2003) "CATERPILLAR Performance Handbook" Edition 30

Leone, M. (2005) – "The Quest for an Environmental Metric." *CFO Publishing Corporation 2007* http://www.cfo.com/printable/article.cfm/5300667

Coal Utilization Byproduct Research, U.S. Department of Energy, 17-Nov 2006

EIA – Fuel and Energy Source Codes and Emissions Coefficients http://www.eia.doe.gov

EPA - For diesel CO2 emissions equivalent, EPA website http://epa.gov/oms/climate/420f05001.htm

Fleming, Paul R., et al (2006). "Sustainable Earthworks Specifications for Transport Infrastructure." – *Transportation Research Record: Journal of the Transportation*

Research Board, No 1975, Transportation Research Board of the National Academies, Washington, DC, 2006, pp73-80

Jones, S., Spaulding, C. and Smyth, P. (2007). " Design and construction of a deep soil-bentonite groundwater barrier wall at Newcastle, Australia " *10th Australian New Zealand Conference on Geomechanics Common Ground* Brisbane, Oct. 2007

Pilson, M.E.Q. (1998) "An Introduction to the Chemistry of the Sea." Prentice Hall, NJ.

Prusinski, J.R., et al. (YEAR?) " Life Cycle Inventory of Slag Cement Concrete." *Eighth International Conference on Fly Ash, Silica Fume, Slag and Natural Pozzolans in Concrete – CANMET/ACI*

Putt Del Pino, Samantha, et al. (2006) "Working 9 to 5 on Climate Change: An Office Guide" – *World Resource Institute.*

Rawlins, C. Hank, Richards, Von L., Peaslee, Kent D., Lekakh, Simon N. (2007). "Experimental Study of CO2 Sequestration by Steelmaking Slag." *Materials Processing Fundamentals.*

University of New Hampshire – Durham Campus (2004) «1990-2003 Greenhouse Gas Emission Inventory».

Wackenagel, Mathis, et al (2004). « Establishing National Natural Capital Accounts Based on Detailled Ecological Footprint and Biological Capacity Accounts. » *Land Use Policy, 21(2004)231-246.*

Wilson, Alex (1993). "Cement and Concrete: Environmental Considerations."
*Environmental Building News, Vol. 2, No. 2.*World Bank (2007) – The Little Green Data Book

Deep Borehole Heat Exchanger with a CO_2 Gravitational Heat Pipe

Roman Zorn[1], Dr., Hagen Steger[2], Dr., Thomas Kölbel[3] and Horst Kruse[4], Prof. Dr.

[1] 'Senior' Manager, European Institute of Energy Research, Karlsruhe University, 76131Karlsruhe, Emmy-Noether-Straße 11, Germany, zorn@eifer.uka.de
[2]Scientific assistant, Department of Applied Geology, Karlsruhe University, 76131 Karlsruhe, Kaiserstraße 12, Germany, steger@agk.uka.de
[3] 'Senior' Manager, EnBW Baden Württemberg AG, Karlsruhe, Durlacher Allee 93, 76131 Karlsruhe t.koelbel@enbw.com
[4]Director, Forschungszentrum für Kältetechnik und Wärmepumpen GmbH, Weidendamm 14, 30167 Hannover, email@fkw-hannover.de

ABSTRACT: Vertically installed borehole heat exchangers based on the gravitational heat pipe principle seem to be an attractive alternative to conventional brine borehole heat exchangers. The heat pipe has to be filled with a suitable working medium and has to be pressurized. The coupling of cooling, for example by the use of a heat pump at the head of the pipe and heating of the heat pipe in the underground zone leads to a closed self-circulation system with no additional energy input. In this study the thermodynamic design for a deep gravitational heat pipe filled with liquid and gaseous carbon dioxide is presented. The thermodynamic analyses have led to an installation of a 250 meter deep steel heat pipe with an inner diameter of 65 mm. The heat pipe was placed in a relatively homogenous part of the Triberg-Granite formation at the black forest, Germany.

INTRODUCTION

The use of geothermal energy from shallow depths (up to ~400 meter) is gaining importance world-wide with respect to energy efficiency in both heating and cooling operations. The ground acting as a heat storage zone offers the possibility of damping the effects of the outside air temperature fluctuations, in colder climates it enables monovalent operation of a heat pump (there is no need of an additional operation system like, for example, a gas boiler). The geothermal energy can be used in different ways, direct use with no changing of the source temperature and an indirect use with a Ground-Coupled Heat Pumps (GCHP). With a heat pump the source temperature can be adjusted as desired to higher or lower values. The extraction of heat from underground and its transfer to a heat pump or for a direct use is usually done with borehole heat exchangers (BHE). BHE are normally filled with a calorific medium that extracts energy from the underground to the surface. An innovative alternative to brine BHE is the use of gravitational heat pipes. In this case, there is no need for a circulating pump (the phase change of an internal medium makes it circulate). This leads to higher efficiencies and lower costs. Heat pipes are currently used to heat roadways and bridges to remove snow and ice, to cool soil in permafrost locations to improve its mechanical strength (Nydahl et. al. 1987, Vasilew 1988, Fukada et al. 1990, Kovalev et al. 1992, Tanaka et al. 1992). Results from an 18 meter deep CO_2 ground coupled heat pipe are given in Kruse (2004). Feldmann (2004) suggests applications of heat pipes for heating of rail switches and platforms. Theoretical calculations for heat pipes are described e.g. in Hegab and Colwell (1994). Commercially applied heat pipe solutions for house heating purposes are described, for example, in Mittermayer (2007). However, there is no information available about deep CO_2 heat pipe solutions.

HEAT PIPE AT TRIBERG-NUSSBACH, BLACK FOREST, GERMANY

The heat pipe at Triberg-Nußbach consists of a pressure resistant, flexible high-grade steel pipe, filled with liquid and gaseous carbon dioxide. The probe was installed vertically into the ground to a depth of 275 meter and was backfilled with a thermally enhanced grout (fig. 1).

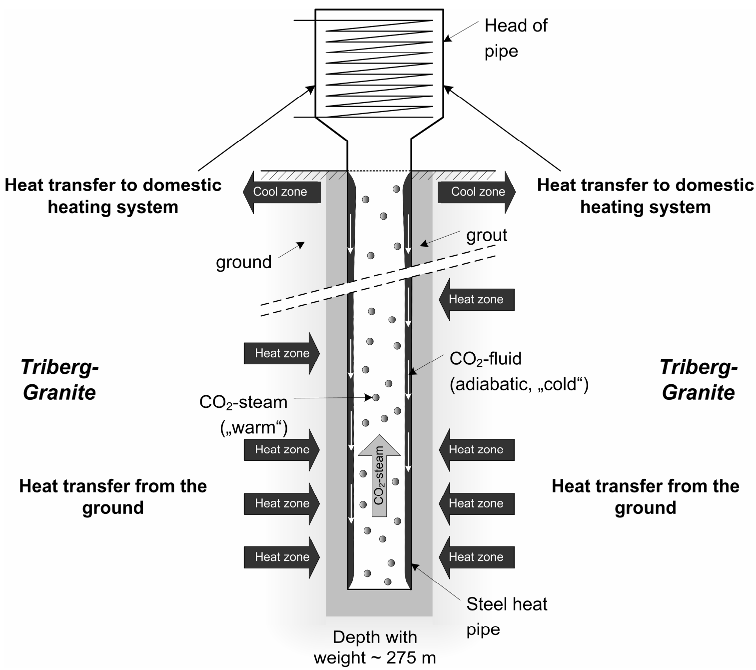

FIG. 1: principle sketch of the installed CO_2 borehole heat exchanger.

The ground at the test site in Triberg-Nußbach (black forest, Germany) consists of a relatively homogeneous granite formation. Because of the high thermal conductivity of the granite the heat transfer from the soil to the liquid CO_2 is assumed to be predominantly due to thermal conduction. The existing and renewable underground heat (ground heat and solar heat flow) causes the evaporation of the liquid CO_2 in the heat pipe.

The evaporated "warm" CO_2 rises to the top of the pipe due to his lower density (thermosyphon effect). At the pipe head, the evaporator of the heat pump, the CO_2 condenses by heat release and flows down as a "cool" liquid at the inner wall so returning to the vaporization zone of the heat pipe. This results in an independent self circulating cycle.

The heating zone in the ground should be relatively long to use the heat pipe as a BHE, where as the cooling zone near the surface has to be short. The cooling zone is realized by a heat exchanger developed particularly for the heat pipe. The heat pipe functions as the evaporator of the heat pump and as the condenser for the gaseous CO_2. CO_2 is an ideal medium, because the phase conversion of CO_2 is within the range of the underground and surface temperatures of approximately 0-20°C (fig. 2).

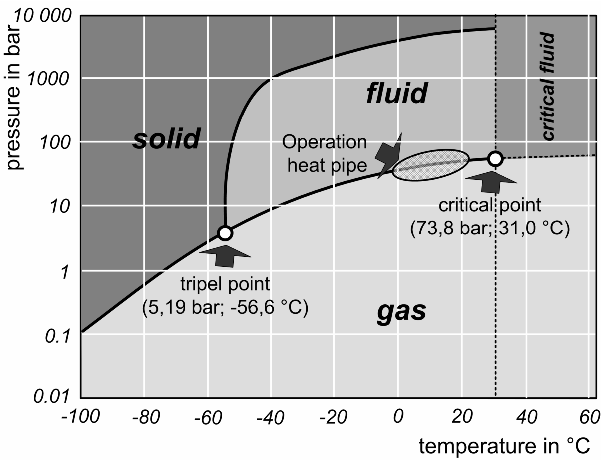

FIG. 2: CO_2 phase diagram, the shaded area marks the range for the phase change (the pipe is kept under constant pressure of ~55 bar).

A self-acting CO_2 BHE promises to be particularly favourable, because in comparison to a based brine BHE no additional energy is necessary for the operation of a brine circulating pump. The seasonal (annual) performance factor (SPF) of a heat pump system is increased by the removal of the need for additional electrical energy expenditure. Additional increases in efficiencies are achieved because the steel heat pipe has a much higher thermal conductivity than conventional systems. The heat extraction of such a CO_2-heat pipe is about 15–35 % higher than conventional brine

BHE (according to the present level of knowledge, following Mittermayr 2007 and the authors' own theoretical calculations).

In classical U-tube BHE's antifreeze additives are used in the underground brine pipe cycle. These antifreeze additives are often regarded as potentially problematic for groundwater. In contrast the working medium CO_2 is completely harmless for groundwater and thus ideally suitable for groundwater protection areas and/or other hydrogeologically problematic areas. A heat pipe length of 250 meter should supply enough heat for many buildings (up to ~20 kW). Also, single heat pipe solutions are potentially useful for many sites with limited space. Thus, with the help of deep heat pipes many old buildings could be supplied by means of a GCHP. This will important as less energy efficient heating systems are replaced in the future.

The main disadvantage of the heat pipes is the fact that an efficient and economically meaningful operation for cooling purposes is not yet possible.

The theoretical calculations which have led to the design of the deep heat pipe are presented below.

THERMODYNAMIC DESIGN

The heat transfer phenomena in the ground for a coupled heat pipe in the vaporization zone are very similar to "normal" thermosyphons which are substantially shorter. A thermosyphon consists of a closed box, in which a certain quantity of a suitable fluid is enclosed for a phase change. Under equilibrium conditions the medium in the lower part is in liquid phase and the upper part in gaseous phase (the equivalent of steam). Now if the lower part of the pipe is heated (the evaporation area and/or heating zone), the liquid evaporates and flows to the cold end of the pipe (the condensation area and/or cooling zone, see in fig. 1).

Definition and assumption for thermodynamic calculations of the ground coupled thermosyphons (GCTS)

In a GCTS the heat is transported from the bottom up. At the top the vapour condenses at the cold wall and flows back to the evaporator area. Usually the evaporator and condenser areas are separated by an adiabatic transport zone in which there is no exchange of heat (see e.g. in Dunn and Reay 1994 and Ochterbeck 2003).

<u>Heating zone:</u> Heat extraction from ground (assuming 10°C constant ground temperature at the beginning, also a temperature gradient of for example 2-4°C per 100 meter depth).

<u>Neutral or transport zone:</u> Zone without heat extraction and dissipation, usually in the upper 10-15 meter of the ground (temperatures in winter less than 10 °C). The neutral zone represents the link between heating and cooling zone.

<u>Cooling zone:</u> Zone of heat dissipation to another medium, e.g. the ambient air or in the case of heat pump the evaporator of the pump (medium=refrigerant).

The evaporator pipe has following dimension,

$$D_a = D_i + 2 \cdot s \qquad (1)$$

where s is wall thickness in m, D_a is the outer and D_i is the inner diameter of the pipe.

The evaporator pipe separates the fluid with a saturation temperature T_S (K) from the ground temperature T_E (K), with $T_E > T_S$. Under steady state conditions a heat $\dot{Q}$ (W) flows from the ground to the fluid film of the heat pipe due to the temperature difference of $T_E - T_S$,

$$\dot{Q} = k\ A\left(T_E - T_S\right) \tag{2}$$

and after Baehr and Stephan (1991) is,

$$\frac{1}{k\ A} = \frac{\delta_E}{\lambda_E\ A_E} + \frac{\delta_m}{\lambda_m\ A_m} + \frac{1}{\alpha_S\ A_S} \tag{3}$$

λ_E (W/(mK) is the thermal conductivity of ground, k (W/(m²K) is the heat transfer coefficient, δ_E (m) is the ground thickness and A_E (m^2) the logarithmic average area. For the simulation the ground is normally subdivided into several concentric circles, thus resulting in a corresponding number of terms. α_S (W/(m²K) is the heat transfer coefficient of the film evaporation at the inner pipe wall. The heat transfer coefficients of the evaporation of liquids are usually between 1000 and 6000 W/(m²K). λ_m (W/(mK) is the average thermal conductivity of the pipe (e.g. $\delta_m = 15$ W/(mK) for X12CrNi 18,8), δ_m (m) is thickness and A_m (m^2) is the logarithmic average area of the pipe.

Considering the surface, the diameter, the length L (m) and the Area $A = \pi dL$ (m^2) of the pipe, the heat transfer through the heat pipe can be calculated with following relationship (Baehr and Stephan 1991),

$$\frac{1}{k\ A} = \frac{1}{\pi\ L}\left(\frac{ln\,D_E / D_a}{2\ \lambda_E} + \frac{ln\,D_a / D_i}{2\ \lambda_m} + \frac{1}{\alpha_S\ D_i}\right) \tag{4}$$

where the heat transfer coefficient α_S (W/(m²K) can be determined after a method of Groß (1991). The value for a specific heat flow in relation to the length L (m) is,

$$\frac{\dot{Q}}{L} = \frac{k\ A}{L}\left(T_E - T_S\right), \tag{5}$$

and the heat flow density $\dot{q}$ (W/m^2) is,

$$\dot{q} = \frac{\dot{Q}}{A_m} \text{ with } A_m = L\,\pi\frac{D_a - D_i}{ln\left(D_a / D_i\right)} \tag{6}$$

A_m (m^2) is the calculation of the geometric average of the heat pipe area.

The film is formed at top of the heat pipe due to condensation of the ascending steam. If the heat pump is operated with a certain evaporation temperature T_0 (K), the carbon dioxide has a liquefaction temperature T_c (K) and a liquefaction enthalpy h_v (J/kg), which are dependent on the adjusted evaporation temperature T_0 of the heat pump,

$$\Delta h_v, T_s = f(T_0) \text{ with } T_0 = T_s + \delta_0 \tag{7}$$

where δ_0 (K) is the temperature difference in the heat exchanger.

CALCULATION OF THE HEAT PIPE

Commercially "readily" available heat pipes have tubing inside diameters of 65 mm or 80 mm. Thus the heat pipe length has to be chosen in relation to these two diameters. The location at which to install the heat pipe was chosen in the region of the Triberg-Granite, black forest (Germany). The Triberg-Granite formation is characterised by its homogeneity. Thus only small lithological variations were found with increasing drilling depth regarding the decomposition degree of the granite or in the number of small dykes and fractures as well as in the local different water flow conditions. In spite of these differences the ground thermal conductivity variations with increasing depth could be in first approximation neglected. Specific heat extractions of 55-85 W/m could be expected for granite (according to the VDI 4640, 2001, assumption double U-tube BHE with variable operation times). For the design of the heat pipe a conservative specific heat extraction range of 40-70 W/m were assumed to obtain a certain security factor (fig. 3).

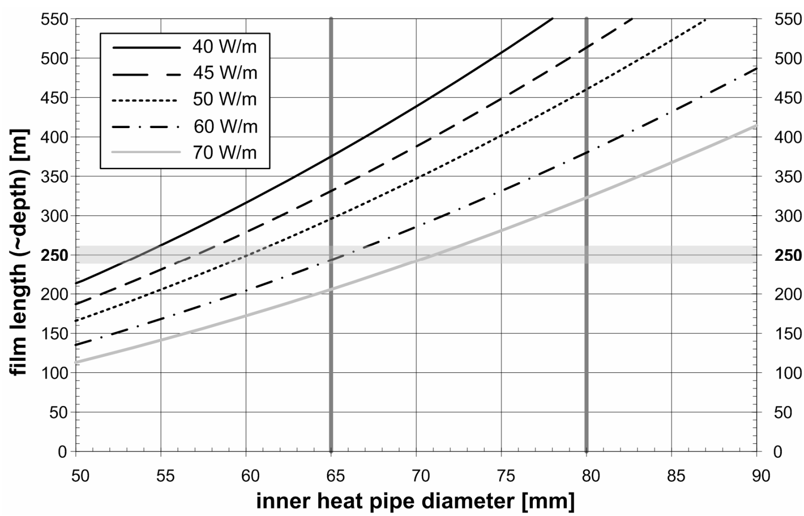

FIG. 3: CO_2-evaporation temperature of ~ 0°C with variation of the specific heat transfer.

The numerical calculations were done with the assumptions of an evaporation temperature of 0°C using Eq. 1-7 and the method given by Groß (1991). The figure shows that a heat extraction of something less than 60 W/m at an inner heat pipe diameter of 65 mm requires a film length or drilling depth of ~250 meter. Due to the higher degree of efficiency of a heat pipe in comparison to brine BHE the heat extraction has to be increased by at least 15 W/m. Also not considered in the calculations were the increasing saturation temperature at higher pressure, the temperature and thermal conductivity increase with depth. All of these factors indicate a higher real heat extraction. Thus a drilling depth of 250 meter and inner heat diameter of 65 mm seem to be a secure option for the Triberg test site. Fig. 4 shows that the heating capacity can be adjusted with the CO_2 evaporation temperature. This means that there is the possibility to react under real operation conditions, if the theoretical design is differing from the real operation.

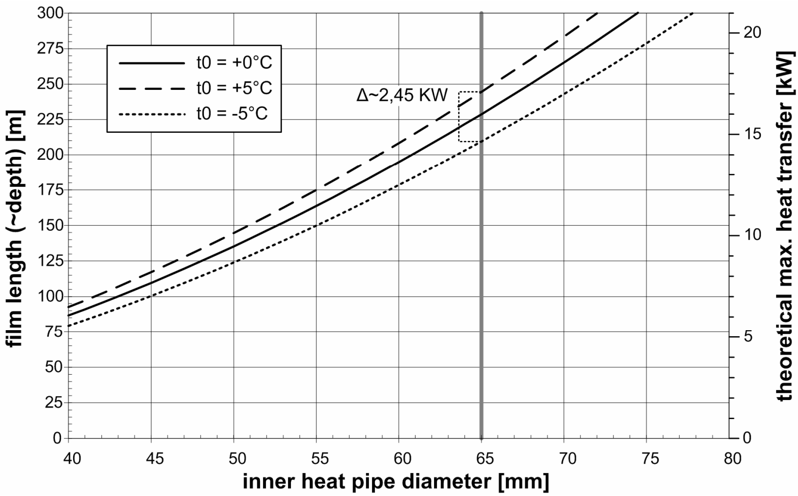

FIG. 4: Theoretical maximal heat transfer and film length for 70 W/m with variations of the CO_2 evaporation temperature.

CONCLUSIONS

The theoretical design of a ground coupled heat pipe with the working medium CO_2 shows that for the special case at the test site Triberg, Germany, an inner diameter of 65 mm and a length of 250 meter should guarantee a meaningful operation of the heat pipe. A monitoring system consisting of fiber optic cable, Pt100 temperature, electric conductivity, pressure and flow sensors was installed at the site. The combination of these measurement methods guarantees reproducible data collection and processing of the deep CO_2 heat pipe. The ongoing monitoring should also help to validate the given theoretical calculations. The electrical consumption and the heat flow meter data should enable a comparison with a virtual conventional brine BHE possible.

ACKNOWLEDGMENTS

The research project is funded by EnBW Baden Württemberg AG, Research, Development and Demonstration.

REFERENCES

Baehr, H.D., and Stephan, K. (1996): *Wärme- und Stoffübertragung*, 2. Auflage, Springer-Verlag, Berlin

Dunn, P.D., and Reay, D.A (1994): *Heat Pipes*, fourth ed., Pergamon Press, Oxford.

Feldmann, W. (2004): "Heizung von Verkehrsanlagen, Nutzung von Erdwärme und Wärmerohr.", *EI-Eisenbahningenieur*, Vol. 55(9): 84-94

Fukada, M., Tsuchiya, F., Ryokai, K., Mochizuki, M. and Mashiko, K. (1990): "Development of an Artificial Permafrost Storage Using Heat Pipes.", *7th International Heat Pipe Conference*, Minsk, Belarus, Paper D18

Hegab, H.E, and Colwell, G.T. (1994): "Thermal Perfomance of Heat Pipe Arrays in Soil.", *Numerical Heat Transfer*, A26:619-630

Kovalev, S., Buchalov, M. Sidorov, A., and Bayaisan, R. (1992): "The Soil Thermal Stabilization by Means of Two-Phase Thermosyphon.", *8th International Heat Pipe Conference*, Beijing, China, Paper E-P41

Kruse, H. (2004): "WÄRMEROHR - Entwicklung einer CO_2-Erdwärmesonde nach dem Prinzip des Wärmerohres.", *Ki Luft und Kältetechnik*, Vol. 40(2): 54-61

Mittermayr, K. (2007): "Idee – Entwicklung – Feldversuche – Marktreife von selbstzirkulierenden CO_2 Sonden.", *7th Internationales Anwenderforum Oberflächennahe Geothermie*, 26.-27 Avril 2007, Freising, Germany

Nydahl, J., Pell, K., and Lee, R. (1987): "Bridge Deck Heating with Ground-Coupled Heat Pipes.", *ASHRAE Trans.*, Vol. 93 (1): 939-958

Groß, U. (1991): "Kondensation und Verdampfung im geschlossenen Thermosyphon.", *VDI-Fortschrittsberichte*, Reihe 19: Wärmetechnik /Kältetechnik, Nr. 59, VDI-Verlag, Düsseldorf

Ochterbeck, J.M. (2003): "Heat pipes", in: Bejan, A., and Kraus, A.D. (Eds.), *Heat Transfer Handbook*, John Wiley & Sons, New Jersey, USA, 2003, 1181–1230.

Tanaka, O., Koshino, H., Xiao, C., Egawa, H., Kashizawa, H., and Hamada, H. (1992): "Development of a Snow Melting Using Pipes with Electric Cartridge Heaters.", *8th International Heat Pipe Conference*, Beijing, China, Paper E-P39

Vasilew, L. (1988): "Heat Pipes for Ground Heating and Cooling.", *Heat Recovery Systems CHP*, Vol. 8(2): 125-138

VDI 4640 Part 2 (2001): *Thermal use of the underground*, VDI-Verlag, Düsseldorf.

Aspects of Sustainability in Ground Energy Systems

David Whitaker[1] and Ryan Law[2], Arup Geotechnics.

[1] 13 Fitzroy Street, London, W1T 4BQ; david.whitaker@arup.com
[2] 13 Fitzroy Street, London, W1T 4BQ; ryan.law@arup.com

ABSTRACT: In the temperate regions of the world the energy demand of buildings is split between energy used for heating and energy used for cooling. The thermal mass of the ground may be utilised to store energy from one season to the next and so reduce the net annual energy demand in cities. Open and closed loop borehole systems and energy foundations are all methods of exploiting the thermal capacity of the ground. The long term stability of all ground energy systems depends upon adoption of an operating regime which maintains a balance between heat rejection and abstraction. This is not as widely appreciated as it should be. A case history from the UK is presented which illustrates sustainable aspects of implementing ground energy storage schemes for commercial buildings.

INTRODUCTION

The long term stability of all ground energy systems, open and closed, depends upon adopting a scheme design and an operating regime which maintain an approximate balance between heat rejection and abstraction. It is often said that the basis for ground sourced energy schemes is the relatively constant temperature of the ground below about 15m. It may be, however, that the reason for this equilibrium is that energy flows in this zone are rather low relative to the thermal mass. When assessing the long term sustainability of a ground energy scheme involving much more than a handful of closed boreholes or energy piles, or more than one or two open boreholes, the question: "Where is the energy coming from (or going to)?" must be answered. The natural geothermal gradient in most parts of the world is insignificant in the context of ground sourced energy, and solar radiation is remote from deep strata. Groundwater flow rates are seldom large enough to carry a significant part of the temperature deficit or surplus beyond the site boundaries. A simple calculation of the energy fluxes within the top 100m of the ground surface suggests that large ground energy schemes depend substantially on thermal capacity and not upon replenishable sources.

REPLENISHMENT OF GROUND ENERGY – CLOSED LOOPS

Design calculations for ground energy systems, and for closed systems in particular, usually omit reference to the ultimate source of the net energy abstraction. This is in contrast to groundwater supply engineering, in which a hydrogeological evaluation of sustainable resources is as important as the design of the abstraction system.

Bandyopadhyay et al (2006) have reviewed the design of many systems and concluded that "….models developed for loop design take into account the long term drift of ground temperature….However…the boundary heat flow either from the atmosphere or from…depth below the (ground heat exchanger) is ignored." Rybach & Eugster (2002) observe that "the oldest…(ground energy)…installations are not older than about 15 – 20 years, thus experience and…detailed studies on long-term performance…are lacking."

Where the question of long term performance and sustainability has been recognized and attempts have been made to understand the issues, efforts have been focused on modelling and measurement of conditions in the close vicinity of the ground heat exchangers. The ground surface, if it is included in the model at all, is represented as a fixed head (temperature) boundary. The meteorological, geophysical, and hydrogeological processes which control thermal recharge to a ground energy scheme are not explicitly modelled.

Let us carry out some basic calculations of energy flux and thermal capacity, considering notional ground heat exchanger loops. The continental geothermal flux is between 0.025 and 0.160W/m^2 approximately (Badino, 2005); an average figure might be about 0.05W/m^2. If the geothermal heat flow rising through one hectare of granite terrain could be efficiently captured, it would light eight 60 watt light bulbs. On the other hand, the average net solar flux, that part of the total solar influx which reaches the ground surface, is about 50W/m^2 in the UK. Clearly, in the undisturbed condition that influx is exported from the surface (or else the ground would be warming up), but a proportion could potentially be induced to flow towards an energy abstraction. It could be likened to the infiltrating portion of rainfall which has the potential to replenish groundwater storage and thereby support an abstraction.

For a horizontal near-surface ground heat exchanger it is perhaps easy to see how the winter depletion is replenished by summer recharge. Even for vertical ground heat exchangers the balance seems to be quite achievable, on first inspection. Thus, assume the average input of solar radiation at the ground surface is 18kWh/m^2 per month, equivalent to a constant 25W/m^2 (50% of the net solar flux at the surface). Assume a single energy borehole of 70m depth is operated so as to yield 3.5kW. If all the incident solar energy could be captured and extracted, a catchment area of only 140m^2 would be required, which would be equivalent to a circular area of radius only 6.7m.

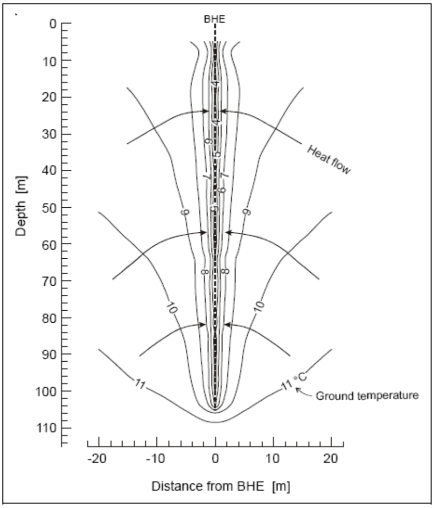

Figure 1. Calculated temperature isolines around a BHE (from Rybach and Eugster, 2002)

To achieve this, however, there would have to be a predominantly vertical thermal gradient within the ground around the energy borehole, which is not possible with the conductor tubing aligned with the length of the borehole. Figure 1, from Rybach and Eugster (2002), shows the temperature isolines around a single borehole heat exchanger (BHE): heat flow is radial and near horizontal, indeed upwards rather than downwards. The simple notion of solar energy incident upon the ground surface immediately above an energy borehole supporting the energy extraction of that borehole clearly cannot hold. The radius of influence of the borehole is going to be much greater than 6.7m. The point, however, is that, assuming all the heat energy abstracted from a borehole heat exchanger is derived from solar recharge at the ground surface, each borehole requires an average catchment area of 140m^2. Energy piles and closed energy boreholes within an array, however, are generally sited at closer centres than this; for example, less than 5m apart.

Interference between adjacent vertical ground heat exchangers at close spacings will become significant unless they are operated so as to exploit thermal capacity, or thermal mass, as opposed to intercepting thermal flux originating from solar recharge. The peripheral units may generate a temperature gradient over a sufficiently large area that abstraction from those peripheral heat exchangers is balanced by solar input, but “internal” boreholes are bounded by other units and these are unable to access any significant source of recharge. The larger the field of energy boreholes the more of these are “internal” and dependent upon energy storage due to the thermal capacity of the ground.

Considering the case of an array of closed energy boreholes, the thermal capacity available for energy storage and abstraction may be calculated quite easily. Assume the boreholes are positioned at 5m centres and are 70m long and the ground is a damp quartz sand with specific heat capacity 840J/(kg·K). The thermal capacity of a cylinder of ground of radius 2.5m and length 70m is then approximately 2.3 x 10^{6}kJ/K, equivalent to about 640kWh/K. Let the average temperature of this cylinder of ground be changed by 10^{o}C: the total amount of energy which is available in storage is 6.4MWh. Over a six-month extraction period (4320 hours) this would support a yield of 1.5kW approximately. Operation at any higher average rates, or for longer, would require energy transport from some source of recharge, or remote storage, into the envelope of ground occupied by the pile, otherwise the temperature change will be greater then $10^{o}C$. Note that with reference to Figure 1, an average temperature change of ten degrees would mean that the temperature change immediately adjacent to each borehole would be significantly more than ten degrees. There is no other source of energy: each borehole in the array is in an identical situation to the one for which this calculation is performed (except for the peripheral ones, which are relatively few in number if the array is a large one).

A review of the literature on case histories suggests that, indeed, most ground energy systems based on closed vertical ground heat exchangers do operate on the storage principle and are therefore not sustainable unless either the abstraction is reversed seasonally (it does not have to be a year but in practice this is most practical) so that the total of heating and cooling is approximately balanced within the year, or the system is "rested" periodically (Rybach, 2007).

It is quite possible that there have been many ground energy schemes based on closed loop ground heat exchangers which are in effect over-abstracting heat or coolth. While the consequences to the operator of over-abstraction of groundwater are water level lowering, falling well yields and increased pumping costs, in the case of ground energy schemes the effects are seen as increasing (or decreasing) temperature of entering flow and reduced efficiency of heat pumps. The wider environmental costs are, of course, also significant in both cases. The Environment Agency in the UK is adopting a precautionary approach to the licensing of open borehole schemes, although it has no jurisdiction over closed systems.

REPLENISHMENT OF GROUND ENERGY – OPEN SYSTEMS

An open system comprising pairs of abstraction and recharge wells (doublets) is designed to operate either on the hot well – cold well principle, or on the basis of using the flow of groundwater between the two wells to allow energy transfer between the groundwater and the aquifer matrix.

In the latter case it can be advantageous to make use of the background hydraulic gradient to carry recharged groundwater offsite: in this way a proportion of the energy deficit (heat or coolth) is exported beyond the boundaries of the site. In practice, however, the natural hydraulic gradient is seldom large enough and flow beneath the site is dominated by the artificial gradient between the injection and abstraction wells (Arup, 2006). In the Chalk beneath London for example, typical drawdowns associated with an open system in which wells are operated at 5 - 10l/s are within the range of 3 - 5 m (McDonald, 2001). These are matched by equivalent injection heads, so that the head difference between pairs of wells in a doublet may be 6 - 10m. A building footprint in central London will seldom exceed 100m at its maximum dimension which means that the local gradient will be between 0.06 and 0.1. Typical background hydraulic gradients for central London, however, are of the order of 0.001. The hydraulic gradient generated by the abstraction and injection wells is therefore up to 100 times greater than the background gradient. Only a small proportion of the re-injected water, carrying the temperature anomaly, will be carried off in the regional groundwater flow system and the majority of the heat rejected from the building will remain beneath the site as shown in Figure 2.

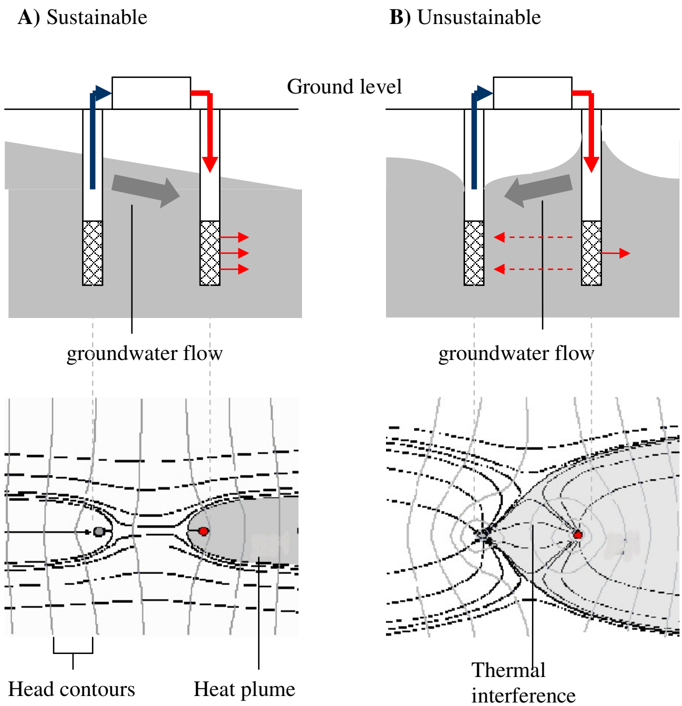

Figure 2. Effect of artificial hydraulic gradient

Hydrogeological conditions can be complex, particularly in fractured aquifers such as the Chalk. Assumptions of flow rate and residence time between injection and abstraction wells based on constants applicable to an intergranular flow regime can be seriously in error. There have been a number of cases reported in the literature (Packsoy, 2003; Allen, 1996) where a lack of knowledge about the hydrogeology caused problems to occur.

In an open system once the number of pairs of abstraction and injection wells has been chosen, the individual pumping rates are fixed. The volume flux or Darcian rate of groundwater flow through the aquifer between injection well and abstraction well is therefore also fixed; however, the true seepage velocity depends upon the nature of the permeability. Flow might actually be rapid within a small number of fractures or it may occur as slow seepage along a very large number of (tortuous) pore tubes in an intergranular aquifer: the permeability could be identical in either case. The implications of very different flow regimes for thermal behaviour between the boreholes, however, are major. The residence time – the length of time during which the groundwater is in contact with the aquifer matrix – would be very different in the two extreme cases. Also, the surface area of the interface would be quite different: much greater in the case of the intergranular aquifer, which would improve thermal transfer across the boundary. On the other hand turbulent conditions, which are more likely to occur in the fissure flow case, assist the process of thermal transfer.

The short and medium term sustainability of a ground energy scheme based on abstraction and recharge doublets is consequently very dependent upon the hydrogeology at the site. The long term sustainability, however, depends upon a balance between the heat rejection and heat abstraction loads.

CASE STUDY – HYBRID ENERGY PILE AND OPEN BOREHOLE SYSTEM

The geology of the London area comprises largely clay strata of low permeability overlying the Chalk aquifer. Above about 100m depth the geology is only suited to closed systems while the Chalk is more suitable for open systems. A ground energy system was to be used to both heat and cool the new development, which is a large office, residential and retail complex. The energy demands of the building are large, and a hybrid scheme was devised comprising an array of energy piles and an open borehole system (Figure 2). In this way the maximum utilization of energy storage potential of the ground beneath the site could be made.

The overall objective was to meet 10% of the total energy demand from renewable sources, and the ground sourced scheme was required to contribute a large part of that figure. Restrictions on new abstractions from the confined aquifer meant that groundwater abstracted from the borehole system should be returned to the aquifer through recharge boreholes at the same site.

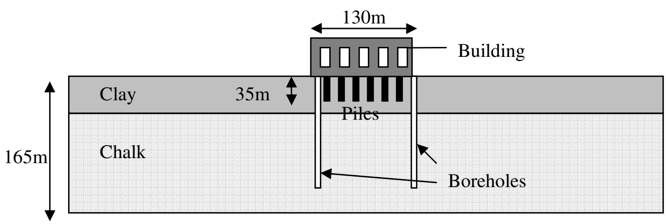

Figure 2. Schematic representation of the proposed system (not to scale)

An iterative approach was followed to design the scheme. Once the thermal ground model had been developed, an energy abstraction/rejection system was chosen which would provide the maximum energy transfer capacity. This involved using some 180 of the structural piles for energy transfer, and siting 4 pairs of abstraction and injection boreholes within the site. Numerical models were developed of the upper part of the system, to simulate pile operation, and of the aquifer incorporating the borehole array. The numerical models were constructed using the United States Geological Survey (USGS) SUTRA code.

The design load profiles were revised and refined in successive model iterations to maximize the short term and annual yield without causing long term temperature changes beneath the site. Early iterations demonstrated poor long term performance, and these findings resulted in some quite major revisions being made to the building HVAC design. The major changes were towards achieving an annual balance in the heating and cooling loads applied to the piles and a near-balance in the case of the borehole system, and adjusting the distribution and timing of the loads on the two parts of the scheme.

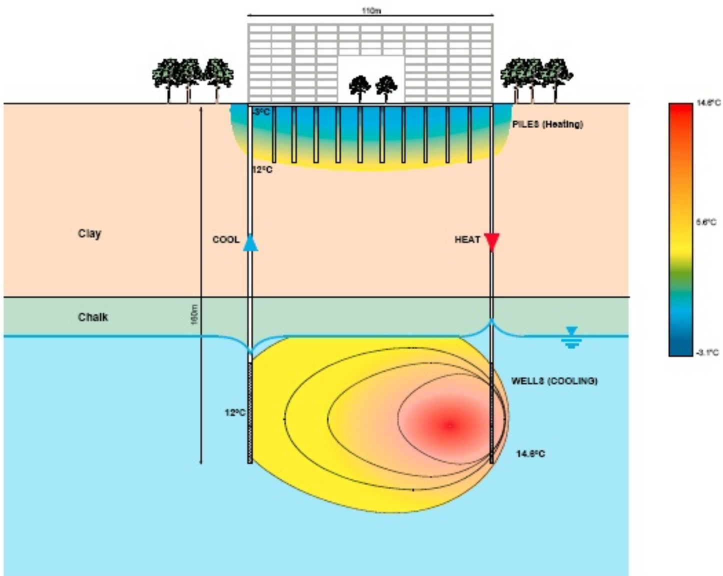

Figure 3. Simplification of model predictions after 2 years operation

Figure 3, which is a simplification of the output from an early run of the model using the demand figures given in Table 1, shows that the spread of energy outward from the ground surrounding the energy piles is minimal. The temperature of the ground surrounding the energy piles (used for heat abstraction only) had dropped to approximately 10°C after only two years of operation, indicating that the system is significantly out of balance and consequently unsustainable in the long term. It is clear from the figures in Table 1 that there is a substantial imbalance between the total heating and cooling demands.

In Figure 3 it can be seen that the open borehole system has caused a temperature deficit in a larger volume of ground (aquifer) than the energy piles. The temperature of the aquifer surrounding the open system (used for heat rejection only) has been

Table 1. Initial energy loads

	Energy Piles (kW)	Boreholes (kW)	Number of Hours	Total Demand (MWh)
Cooling Demand	0 kW	1650 kW	2500	4125
Heating Demand	450 kW	0 kW	500	225
Net				**3900 (Cooling)**

raised by almost two degrees after two years. The model predicted that after a period of 10 years the system would no longer function as the entering fluid temperatures would have exceeded the economical limits of the heat exchanger.

CONCLUSIONS

In order for ground energy systems to function in a sustainable manner in the long term the system configuration and energy demands must be matched to the ground conditions. Numerical models can assist with predicting the performance of ground energy systems at the design stage to avoid potential problems that may only be discovered after many years of operation.

REFERENCES

Allen, D.M. (1996). “Steady-state and Transient Hydrologic, Thermal and Chemical Modelling of a Faulted Carbonate Aquifer used for Aquifer Thermal Energy Storage”. Carleton University, Ottawa, Ontario, Canada. *Unpublished Ph.D. thesis*, Ottawa-Carleton Geoscience Centre and the Department of Earth Sciences, Carleton University, Ottawa, Ontario, Canada, 642 pp.

Badino, G., (2005). “Underground drainage systems and geothermal flux”. *Acta Carsologica*, 34 (2), 277-316

Bandyopadhyay, W.D. Gosnold, M. Mann, (2006). “Thermal study of a large ground heat exchanger in clay soil the cold weather environment of northern USA: some initial findings”. *Research report*, Stockton University.

Kavanaugh, S.P., and K. Rafferty, (1997). “Ground-source heat pumps: Design of geothermal systems for commercial and institutional buildings.” Atlanta: American Society of Heating, Refrigerating and Heating Engineers, Inc.

MacDonald, A. M. and Allen, D. J., (2001). “Aquifer properties of the Chalk of England”. *Quarterly Journal of Engineering Geology and Hydrogeology*. 34, 371 – 384.

Packsoy, H., Turgot, B., Gurbuz, Z., (2003). “First Aquifer Thermal Energy Storage (ATES) plant in Turkey”. *Proc., 9th International Conference on Thermal Energy Storage*, Warsaw, 77-81.

Rybach, L. (2007) “Geothermal Sustainability.” *Proc., European Geothermal Congress 2007*, Unterhaching, Germany, 30 May-1 June 2007.

Rybach, L., and W.J. Eugster, (2002). “Sustainability Aspects of Geothermal Heat Pumps.” *Proc., 27th Workshop on Geothermal Reservoir Engineering*, Stanford University, Stanford, California, p. 50-64.

COMPRESSIVE CREEP BEHAVIOR OF HDPE USING TIME TEMPERATURE SUPERPOSITION

Amir Bozorg-Haddad[1], Magued Iskander, PhD, PE[2],

ABSTRACT: This paper is concerned with the compressive creep behavior of viscoelastic materials, such as high density polyethylene (HDPE) commonly used to manufacture Fiber Reinforced Polymeric (FRP) piling. Accelerated methods to predict the tensile creep of polymers are already available. The Time-Temperature Superposition (TTS) phenomenon is the basis of several available methods, and an ASTM standard for tensile creep is based on one of its derivatives. In this paper, TTS has been adapted to study the compressive creep of HDPE. Experimental test results on virgin HDPE indicated that TTS is applicable for compressive loading with, some limitations.

INTRODUCTION

Coastal communities recovering from disasters in Louisiana, Mississippi, and elsewhere are now required to build above the *Advisory Base Flood Elevations,* which may result in structures being elevated by as much as 25 feet above ground level, requiring large amount of exposed piling. Use of piling made of recycled plastics in these situations is advantageous because (1) it is unlikely to be attacked by termites, which feed on exposed timber piling, and (2) it utilizes plastics, which would have been otherwise landfilled. The primary reason preventing designers from specifying polymeric piling is lack of information regarding their long-term performance. Polymers are viscoelastic and designers are concerned that polymeric piling may exhibit unacceptable creep under service loads (Karbhari et al, 2002).

To be able to predict the creep behavior of the polymeric piles, studying the creep behavior of High Density Polyethylene (HDPE) is inevitable. Most polymeric piling available today consists of an extruded recycled HDPE, with steel or E-glass reinforcement (Iskander and Hassan, 1998). Additives are used to improve mechanical properties, durability, and ultraviolet protection. Foaming is used to make the piling lighter. The matrix may also contain a small percentage of fiberglass to enhance its physical properties. Virgin HDPE is used in this study in order to

[1] Graduate Research Assistant, Polytechnic University, Amirpoly@gmail.com
[2] Associate Professor, Polytechnic Univ., 6 Metrotech Ctr., Brooklyn, NY 11201, Iskander@poly.edu

eliminate the variability introduced by recycled materials, and concentrate on the applicability of accelerated methods for compressive creep of virgin HDPE.

CREEP of POLYMERS

Creep is an important design consideration for civil engineering structures, especially when a viscoelastic element like FRP is involved. Creep refers to a time-dependent deformation at stress less than the strength of the material. The creep property varies with the type of polymer and in-service temperature with respect to the glass transition temperature and melting temperature (Nielsen, 1974). The manufacturing processing varies with polymer type, causing a large difference in the creep behavior among different polymeric products. Therefore, the creep property of each product should be evaluated so that the appropriate reduction factors can be applied in the design calculation. Creep of FRP is made complex by a combination of factors as follows:

- The materials are often loaded in the plastic non-linear range, and the stress-strain behavior of the material is highly time (rate) dependant.
- Unlike conventional construction materials which have well documented creep behavior in service, there is virtually no reliable data on the in-service creep behavior of FRP that can be used to calibrate the predictive models.
- Most HDPE used in construction is recycled. The physical and engineering properties of recycled HDPE typically exhibit a high coefficient of variation.

Ideally, the creep behavior of polymers should be evaluated according to the ASTM D 5262, which requires a long testing time to obtain data at ambient temperature. Although ASTM D 5262 allows for extending creep data by to one log cycle (e.g. from 10,000 hrs to 100,000 hrs), this is not practical for predicting creep for the 50 to 100 years design life. The alternative is to use an accelerated test method. The available accelerated methods can be grouped under two main categories

- **Thermal Methods**, such as *Time Temperature Superposition* (TTS), and its derivative *Stepped Isothermal Method* (SIM). These methods take advantage of the similarity between the effect of time and temperature on the creep behavior of polymers. Thus time is accelerated by elevating temperature (Nielsen, 1974).
- **Energy Methods**, such as the Strain Energy Density Method (Lynch, 2002). These methods take advantage of the equivalence of energy points in specimens tested using different strain rates. Thus creep is predicted by extrapolating the stress-strain behavior of specimens tested under different strain rates (Merry et al., 2005).

THERMAL CREEP ACCELERATION METHODS

The tensile creep behavior of HDPE geogrids has been evaluated using TTS and SIM (Farrag 1998). TTS is already a well-accepted acceleration method to evaluate viscoelastic behavior of polymeric materials in tension (Zornberg et al 2004).

Meanwhile SIM has been developed mostly in the last decade to shorten testing time and utilize a single test specimen to minimize material property's variability effects (Hsuan & Yoe 2005a, b and Thornton et al. 1998a, b). In TTS and SIM, a sequence of creep responses is generated using a series of temperature steps under a constant load. TTS uses different specimens for each temperature step, while SIM uses the same specimen for all temperature steps. Four 2-hour isothermal exposures are typically used in either method.

Both methods depend on the time–temperature superposition concept, i.e. that time can be scaled by a known shift factor that depends on the creep test temperature. The fundamental premise of thermal acceleration testing is that viscoelastic processes are accelerated at elevated temperatures in a predictable manner. The Arrhenius equation provides the basis for the relation between the rate of reaction and temperature. In addition, The Williams–Landel–Ferry (WLF) equation and Boltzmann superposition principle provide justification for scaling and shifting strain data obtained at each isothermal exposure in order to define a master creep curve corresponding to the reference (room) temperature.

Arrhenius Equation

The Arrhenius (1912) equation describes the relation between the rate of reaction and temperature for many reactions. This methodology was first used in civil engineering by Koerner *et al* (1992) to predict the degradation of geosynthetic materials. The equation can be used to predict the creep strain rate at a reference (room) temperature from the creep strain rate measured at an elevated temperature. The Arrhenius equation assumes that the viscoelastic creep mechanism remains unchanged at elevated temperatures.

Williams–Landel–Ferry Equation

A procedure for shifting data obtained at elevated temperatures to a reference temperature was developed by Williams, Landel, and Ferry (Ferry 1980). Specifically, the WLF equation introduces a time shift factor, a_T, to relate strains at different temperatures. The shift factor, a_T, is the ratio between the time for a viscoelastic process to proceed at an arbitrary temperature and the time for the same process to proceed at a reference temperature:

$$\varepsilon(T_0, t) = \varepsilon(T, a_T t) \qquad (1)$$

WhereT_0 is an arbitrary reference temperature, T is the elevated test temperature, t is time, and a_T is the shift factor. The shift factor, a_T, is described by the empirical WLF equation as (Ferry 1980):

$$Log \quad a_T = \frac{c_1(T - T_0)}{(c_2 + T - T_0)} \qquad (2)$$

where c_1 and c_2 are empirical constants given by Ferry (1980) as 5.77 and 155.6, for HDPE respectively for temperatures in Fahrenheit.

Thus, creep strain measured at various isothermal steps during an accelerated test can be shifted to form a master creep curve. The empirical constants c_1 and c_2 are a function of the polymer type and the reference temperature, T_0. Use of the WLF equation to quantify strain shifts is discussed in detail by Farrag (1998).

EXPERIMENTAL PROGRAM

This study was initiated in order to verify that accelerated thermal procedures are valid for compressive loading. Virgin HDPE rods were used to eliminate scatter and uncertainties that may be introduced due to the use of recycled HDPE commonly used to manufacture FRP piling. The diameter of all specimens reported tested is 1.5" (38 mm) and the ratio of the height to the diameter is 2.

Prior to beginning the creep testing protocol, stress strain tests were performed at different strain rates in order to define the strength characteristics of virgin HDPE (Fig. 1). The stress strain curves exhibited a bi-linear behavior, with noticeable strain softening occurring at a stress of 2000-3000 psi (14-21 MPa) depending on the strain rate. The creep stresses used in this study were 400, 800, 1600, and 3200 psi (2.8, 5.5, 11, and 22 Mpa). These stresses were selected such that they fall in the first linear part of the curve.

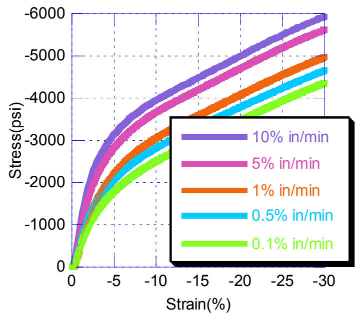

Fig. 1 – Stress-Strain on HDPE

In this study TTS was employed with the following temperatures 24, 38, 49, and 60°C for each stress level. These temperatures were selected to match the ones prescribed in ASTM D6992-03 standard test method for accelerated tensile creep and creep rupture of geosynthetic materials based on time temperature superposition using SIM. Higher temperatures were also not possible due to softening in the material stress-strain response at elevated temperatures. When these temperatures are substituted in Eq. 2, the shift factors shown in Table 1 are obtained.

Table 1 — Shift factors for Different Temperatures According to Eq. 2

Temperature	24° C (72°F)	38°C (100°F)	49°C (120°F)	60°C (140°F)
a_T	1	5.26	14.45	33.12

Creep tests were performed using an *Instron* 8800 controller and an *MTS* load frame. Stress was ramped at a rate of 80 psi (550kPa)/min until the desired creep stress, was reached and maintained constant for the duration of the test. Specimens were immersed in a water basin during loading. The water was heated using thermal tape and temperature was controlled using an *Omega* CNI3233 temperature controller.

TTS Test RESULTS

Creep test results at 24, 38, 49, and 60°C are presented for the four selected creep stresses in Fig. 2-5. In each figure the actual strain versus time is plotted on the left, and time is scaled on the right according to Table 1. For 400 psi specimens were tested for 2.5 hours according to ASTM D6992. A 4 hour test time was used in later experiments to increase the predicted time.

Time temperature superposition works well in compression up to 1600 psi. This is established by comparing the shifted curves for tests conducted at 38-60°C to each other and to the creep data obtained at room temperature. Time temperature superposition was not possible for the creep tests conducted at 3200 psi (Fig. 5). At 3200 psi, HDPE experiences significant plastic deformation, which is not represented by the Arrhenius model. As the stresses approach the linear limit the results are worse.

Comparison with a conventional creep test (Fig. 6) shows good correlation between conventional creep and accelerated creep for 3 months. This good correlation is expected to continue over a much longer period because unlike tensile loading where creep ends in rupture (Fig. 7) compressive loading densifies the polymer chains, thus the constant linear creep stage is expected to sustain until creep ends.

A logarithmic equation can be fit in the accelerated master creep curve for 400 psi (2.8 MPa). Substituting in the logarithmic equation for a duration of 100 years, yields a creep strain of 1.7% (Fig. 8). A stress of 400psi (2.8 MPa) represents 5% of working stress for the tested HDPE (taken at 2% strain). Therefore, it is reasonable to assume that HDPE piles loaded in compression may sustain a creep on the order of 2% in 100 years.

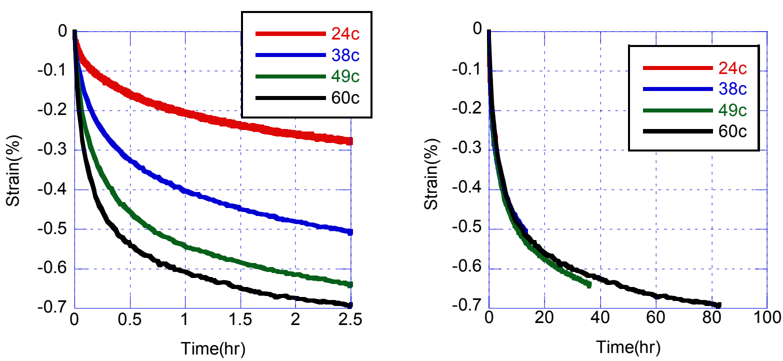

Fig. 2 — Creep at 400 psi, LHS before scaling, RHS after scaling with a_T

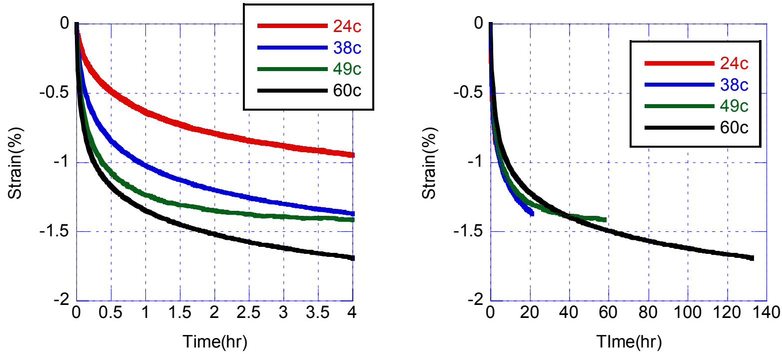

Fig. 3 — Creep at 800 psi, LHS before scaling, RHS after scaling with a_T

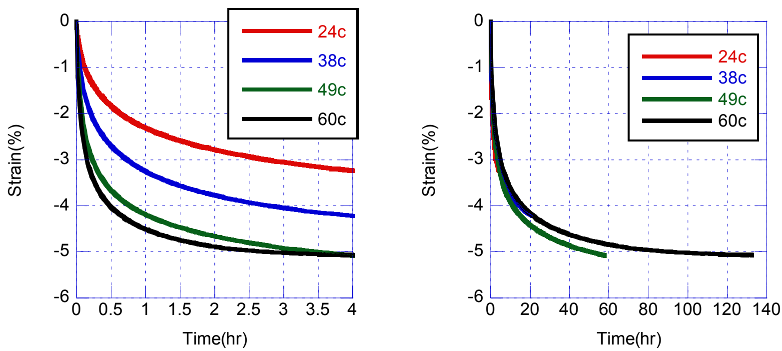

Fig. 4 — Creep at 1600 psi, LHS before scaling, RHS after scaling with a_T

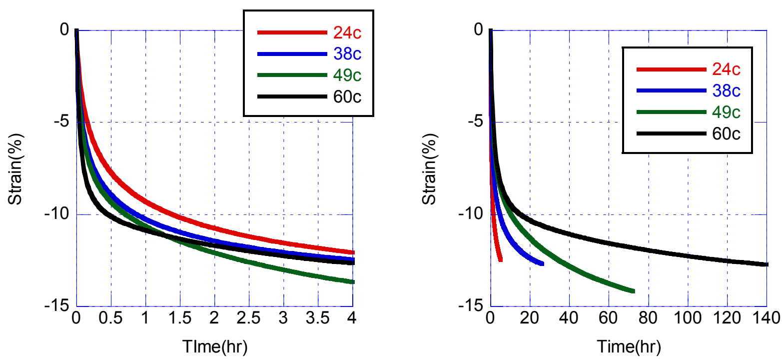

Fig. 5 — Creep at 3200 psi, LHS before scaling, RHS after scaling with a_T

Fig. 6 — Real & Accelerated Creep

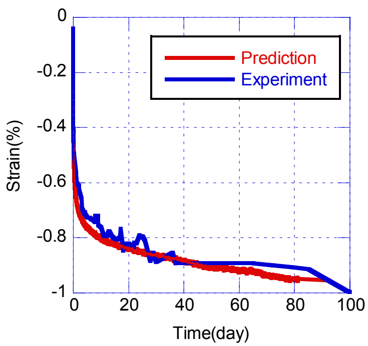

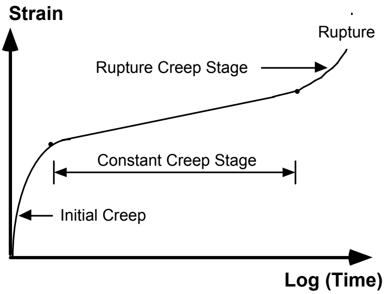

Fig. 7 — Tensile Creep in Polymers

CONCLUSIONS

The results of the accelerated creep tests conducted on virgin HDPE indicate that (1) time temperature superposition is an appropriate method for accelerating creep in compression at stresses below 1600 psi; (2) the constants, C_1, C_2, and the shift factor a_T appear to be the same in tension and compression, at least at low stress levels; and (3) preliminary results indicate that the tested HDPE loaded in compression will creep by approximately 2% in 100 years when loaded at 400 psi (2.8 MPa)

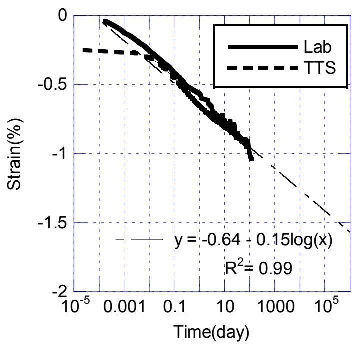

Fig. 8 — Projected creep of HDPE

ACKNOWLEDGEMENTS

The authors thank Mahsa Rejei and Carlos Cabrerra, who carried out the laboratory tests described herein under the authors supervision.

REFERENCES

Arrhenius, S. (1912). *Theories of Solutions*, Oxford University Press

Farrag, K. (1998). “Development of an accelerated creep testing procedure for Geosynthatics. II: Analysis.” *ASTM Geotech. Test*. J., Vol. 21, No. 1, pp. 38-44

Ferry, J. D. (1980). *Viscoelastic properties of polymers*, 3rd Ed., Wiley, New York.

Hsuan, Y. G., Yeo, S. S. (2005a) “Comparing the Creep Behavior of High Density Polyethylene Geogrid Using Two Acceleration Method.” *Slopes and Retaining Structures Under Seismic and Static Conditions (GSP 140)*, ASCE 166, 23

Hsuan, Y. G., Yeo, S. S. (2005b) “Compression Creep Behavior of Geofoam Using the Stepped Isothermal Method.” *Geosynthetics Research and Development in Progress* (GRI-18), ASCE 161, 12

Iskander, M, Hassan, M. (1998) “State of The Practice Review in FRP Composite Piling,” *ASCE Journal of Composites for Construction,* Vol. 2., No. 3, pp. 116-120.

Karbhari, V. M., Chin, J. W., Hunston, D. (2002) “Durability Gap Analysis for Fiber-Reinforced Polymer Composites in Civil Infrastructure.” *ASCE Journal of Composites for Construction*, Vol. 7, No.3, pp. 238-247

Koerner, R. M., Lord, A. E., Jr., and Hsuan, Y. H. (1992). “Arrhenius modeling to predict geosynthetic degradation.” *Geotext. Geomembr*., Vol.11, No.2, pp. 151–183.

Lynch, J. K (2002) “Time Dependence of the Mechanical Properties of an Immiscible Polymer Blend” *PhD. Dissertation*, Rutgers University, NJ

Merry, S.M., Bray J.D., Yoshitomi S. (2005), "Axisymmetric Temperature- and Stress-Dependent Creep Response of ‘New’ and ‘Old’ HDPE," *Geomembranes Geosynthetics Internationa*l, Vol. 12, No. 3, pp. 156-161.

Nielsen, L E. (1974) *Mechanical properties of polymers and composites*.

Thornton, J. S., Allen, S. R., Thomas, R. W., and Sandri, D. (1998a). “The stepped isothermal method for time-temperature superposition and its application to creep data on polyester yarn.” *Proc., 6th Int. Conf. on Geosynthetic*, Atlanta, 699-706.

Thornton, J. S., Paulson, J. N., and Sandri, D. (1998b). “Conventional and stepped isothermal methods for characterizing long term creep strength of polyester geogrids.” *Proc., 6th Int. Conf. on Geosyntheti*c, Atlanta, 691-698.

Zonberg, J. G., Byler, B. R., Knudsen, J. W. (2004) “ Creep of Geotextiles Using Time-Temperature Super position Methods” *ASCE Journal of Geotechnical and Geoenvironmental Engineering*, Vol. 130, No.11, pp. 1158-1168

Flexural Behavior of Composite IsoTruss Reinforced Concrete Piles

David W Jensen[1], F. ASCE, P.E., Kyle Rollins[2], M. ASCE, Monica Ferrell[3], P.E., and David McCune[4], M. ASCE

[1]Professor and Director, Center for Advanced Structural Composites, Department of Civil and Environmental Engineering, Brigham Young University, 368-E CB, Provo, UT 84602-4066; david@byu.edu
[2]Professor, Department of Civil and Environmental Engineering, Brigham Young University, 368-K CB, Provo, UT 84602; rollinsk@byu.edu
[3]Structural Engineer, Patrell Engineering Group, Inc., 751 Sunny Grove Lane, Glendora, CA 91741; monica@patrell.com
[4]Structural Engineer, Horrocks Engineers, One West Main, American Fork, UT 84003; davidm@horrocks.com

ABSTRACT: Four-point bending tests were performed in the laboratory to investigate the strength, stiffness and failure of carbon composite reinforced concrete columns for use in deep foundation applications. Two carbon/epoxy composite three-dimensional lattice structure (IsoTruss®) reinforced concrete (IRC) and two steel reinforced (SRC) concrete piles, each approximately 4.3 m (14 ft) in length and 36 cm (14 in.) in diameter, were loaded to failure while monitoring load, deflection, and strain. The steel and composite cages were designed to have equal flexural stiffness to permit a relative strength comparison. At failure, the IRC beams held nearly twice the bending moment as the SRC beams [194 kN-m vs. 101 kN-m (1,720 kip-in vs. 895 kip-in)], although the failure modes were noticeably different. As expected, SRC piles exhibit more ductile failure behavior than IRC piles, which exhibit linear load-deflection behavior to failure. At 165 kN (35 kips) – the maximum load on the SRC piles – the ductility of the SRC piles was double that of the IRC piles (0.0084 vs. 0.0042, respectively). Likewise, at failure, the SRC piles absorbed approximately twice as much total energy in flexure due to the highly ductile failure. Further investigation is required to explain the low ductility observed in the IRC piles, since higher ductility had been previously observed in similar structures in flexure. In summary, the carbon composite reinforcement in IRC piles is substantially lighter, more rigid and more corrosion-resistant than steel reinforcement, resulting in a pile that is substantially stronger, although less ductile at ultimate load, than SRC piles.

INTRODUCTION

Pile foundations are used throughout the world to support structures founded on soft soils. Pile foundations are most often used to support high rise buildings and bridge structures where the loads would cause excessive settlement or even shear failure if supported by a mat foundation or spread footings. Piles are also used to resist lateral loads produced by wind, wave action, and earthquakes. Although piles can be made of many different materials, most of these materials are susceptible to degradation with time which can significantly reduce axial and lateral capacity. For example, reinforced concrete and steel piles are susceptible to corrosion, timber piles may be attacked by marine borers and other pests, while the high alkalinity of concrete can degrade fiberglass in fiberglass-concrete composite piles. It is estimated that the deterioration of timber, concrete, and steel piling costs the United States nearly $1 billion per year for repair and replacement (Lampo et al. 1998). Corrosion damage of piles has led the Florida Dept. of Transportation to place jackets on over 8000 piles for 279 bridges (FDOT 1999). As the Federal Highway Administration and other agencies work to increase the design life of bridge structures to over 100 years, improvements in long-term pile foundation performance become even more important.

One alternative for increasing pile design life involves the use of a unique carbon fiber reinforcing system known as the IsoTruss® for concrete pile foundations. The IsoTruss is a combination of carbon fiber and resin that is wound in interlocking patterns and cured to form a three-dimensional lattice structure. Although some similarities to cylindrical composite isogrid structures exist, composite IsoTruss structures have a unique three-dimensional form that can not be easily described by conventional nomenclature. The interlocking pattern is composed of helical members that follow a diagonal path wrapping around the structure, and longitudinal members that run along the length of the structure as shown in Figure 1, cured into a single unit. The IsoTruss design incorporates primarily axial force members oriented at angular intervals (30 and 60 degrees) to form stable triangular cells – much like a simple truss system (Jensen et al. 1996). This is the key to its high strength-to-weight ratio. The longitudinal members resist axial and flexural loads while the helical members stabilize the longitudinal members while carrying torsion and shear loads. By varying the number of members and the winding pattern, the strength of composite lattice structures can be tailored to match the requirements of many different structural applications.

In contrast to steel, carbon reinforcement does not corrode. In addition, the IsoTruss configuration is extremely lightweight, yet rigid. While a forklift might be required to handle a steel reinforcing cage, a composite lattice reinforcing cage could be easily positioned by hand. Although the initial cost of carbon fiber reinforcing is high compared to conventional reinforcing steel, carbon fiber resistance to degradation with time gives it a decided advantage in life-cycle cost comparisons. In addition, carbon fiber prices have decreased over the past several years making the use of composite materials increasingly more attractive.

To evaluate the feasibility of composite lattice reinforced concrete piles, prior to driving similar 9.1 m (30') piles in the field, flexure tests were performed in the laboratory on two carbon/epoxy composite three-dimensional lattice structure (IsoTruss®) reinforced concrete (IRC) piles and two conventional steel reinforced concrete (SRC) piles (McCune 2005, Ferrell 2005 and Richardson 2005). The piles were approximately 4.3 m (14') long with a 36 cm (14") diameter. Four-point bending test results enable comparison of strength, stiffness, ductility and toughness of composite lattice versus steel reinforced concrete piles.

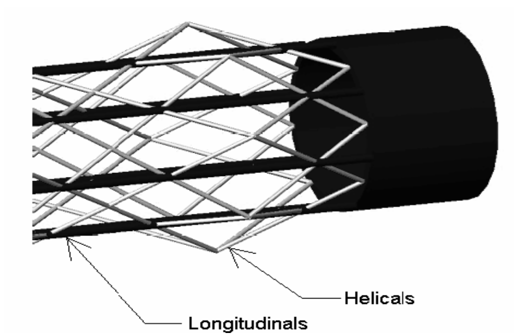

FIG 1. Arrangement of helical and longitudinal carbon fiber composite elements in the IsoTruss reinforcing system.

TEST PILES

The SRC piles incorporated a steel reinforcing cage the full length of the piles, constructed from eight #4 longitudinal bars with a yield strength of 410 MPa (60 ksi). The longitudinal bars were enclosed within 229 mm (9.0 in.) diameter hoops fabricated from #2 bars and spaced 94 mm (3.7 in.) apart. A 70 mm (2.75 in.) OD inclinometer pipe with a wall thickness of 5.5 mm (0.22 in.) was installed at the center of each pile to simulate piles used in subsequent field tests.

The longitudinal members of the IRC piles were designed to match the flexural stiffness, EI, of their steel counterparts [1.18 MN-m^2 (412x10^6 lb-in^2)], where E is the modulus of elasticity and I is the cross-sectional moment of inertia. The modulus of the composite reinforcement was determined based on the fiber volume fraction and the rule of mixtures, allowing determination of the required moment of inertia for the composite lattice structure to compensate for the difference between the moduli of elasticity of the composite [150 GPa (22x10^6 psi)] and steel [200 GPa (29x10^6 psi)].

The composite lattice structure geometry was modified to increase the moment of inertia while decreasing composite weight and consisted of an outer diameter of 330 mm (13 in.), an inner diameter of 289 mm (11.4 in.) and a bay length of 189 mm (7.4 in.). Based on the required stiffness, 133 tows of carbon fibers were used in each longitudinal member, resulting in a member diameter of 11 mm (0.43 in.). For each helical member, 89 tows was arbitrarily selected, representing 2/3 of the tows in each longitudinal member, leading to a member diameter of 9 mm (0.35 in.). The transverse steel reinforcement was designed to have a stiffness equivalent to the composite reinforcement, although the effect of the steel overlap was neglected. The contributions of the helical members of the IsoTruss were compared to circular steel ties. Vector calculations accounted for the non-transverse orientation of the helical members. A summary of the geometrical properties of the composite and steel reinforcing cages is provided in Table 1.

Table 1. Reinforcement Cage and Individual Member Diameters and Weights for Steel and IsoTruss Reinforcement Materials

Measurement	Steel	IsoTruss
Outer Cage Diameter [mm (in.)]	230 (9.0)	330 (13.0)
Longitudinal Member Diameter [mm (in.)]	13 (0.50)	11 (0.44)
Transverse/Helical Member Diameter [mm (in.)]	6.4 (0.25)	9.1 (0.36)
Weight of Reinforcement [kg (lb)]	44 (97)	17 (37)
Reinforcement Weight per Length [kg/m (lb/ft)]	11 (7.3)	4.2 (2.8)

The IsoTruss reinforcement was manufactured from T300C 200NT 12K tow carbon fiber pre-impregnated with TCR UF3325-95 epoxy resin. The tows were hand wound on an aluminum mandrel with wooden dowels and vinyl ester heads. Individual members were consolidated with shrink tape and the composite reinforcement was cured in a simple oven. Based on the epoxy resin requirements, the structures were cured by raising the temperature to 140˚C (290˚F) at a rate of 9˚C (5˚F) per minute. This temperature was held for two hours, and then cooled at the same rate until the temperature reached 66˚C (150˚F). This construction procedure resulted in a strength reduction of approximately 20% relative to design predictions (McCune 2005).

Self-consolidating concrete was placed within circular tube forms around the respective reinforcing cages of all piles and cured simultaneously. The concrete had an average compressive strength (from three tests) of 55 MPa (8.0 ksi) with a standard deviation of 3.4 MPa (0.5 ksi).

TEST LAYOUT AND PROCEDURE

Each pile was loaded laterally in the four-point test fixture shown in Figure 2. The load was applied at two interior points spaced 1.22 m (4.0 ft) apart with pinned reactions preventing lateral movement at each end of the test pile, producing a constant moment between the two interior load points. Load was applied by a 450 kN (100 kip) hydraulic actuator positioned at the center of a very stiff I-beam so that the applied load was equally distributed to the two points. The reaction for the actuator and test pile was provided by large beams bolted to the structural floor. Each pile was loaded monotonically to failure with a loading rate of 2.2 kN/sec (0.5 kips/sec), slow enough to be considered quasi-static loading. Failure was defined as the point where the piles experienced a significant decrease in load and maintained that lower load for at least one minute. Applied load was measured with two load cells while lateral deflections along the pile length were measured by nine string potentiometers attached to an independent reference frame as shown in Figure 2(a). Strain gauges were applied to opposite edges of the reinforcing cage at 9 locations as detailed in Figure 2(b). In addition to the strain gauges mounted on the reinforcing bars, two strain gauges were attached to the outside edge of the concrete pile at location 6. All data was recorded by a high speed data acquisition system.

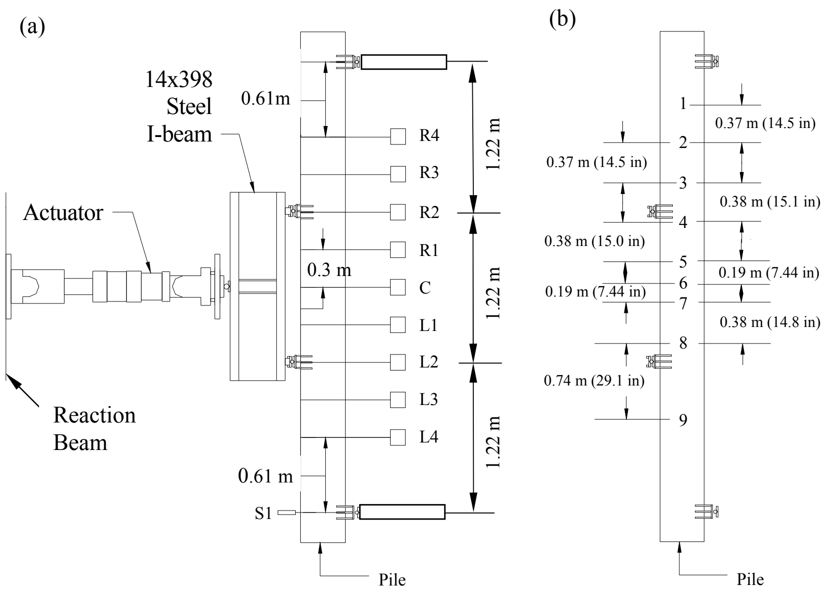

FIG 2. (a) Layout of four point bending test fixture and (b) location of strain gauges in test pile.

TEST RESULTS

The behavior of the IRC piles was quite different from the SRC piles (Figure 3). The IRC piles sustained approximately twice as much load as the SRC piles and sustained a very linear path prior to failure. The higher strength of the IRC piles is partially due to the difference in ultimate strength of the reinforcement materials [134 kN/cm^2 (195 ksi) for IRC vs. 47 kN/cm^2 (67.8 ksi) for SRC], the different geometries of the reinforcement cages, and different individual member areas.

The SRC piles also behaved as expected. In the initial stages of testing, the loading followed a fairly linear path until yielding in the steel occurred due to cracking in the concrete. After this, the load-deflection curves flattened out until the sample was unloaded. The IRC piles, on the other hand, did not exhibit a flattened region where the deflection continued to increase with very small change in load. The load continued to grow in a linear manner until ultimate failure occurred, at which point the pile could no longer support the load. Both the SRC and IRC piles exhibited similar cracking patterns, although the cracks were fewer and larger in the SRC piles.

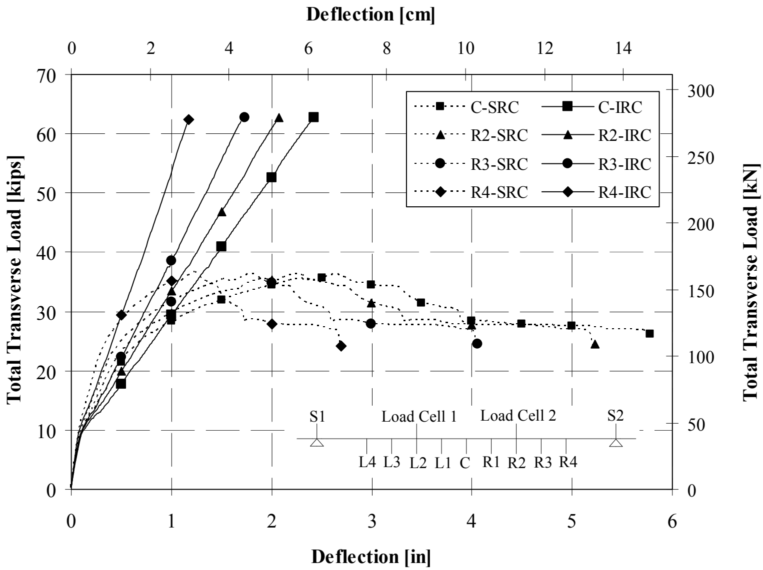

FIG 3. Average Load vs. Deflection Curves for SRC and IRC Piles

Others have researched the use of the IsoTruss® as a method of reinforcement in concrete beams. Similar conclusions were obtained from tests using a rectangular composite lattice structure as reinforcement in rectangular concrete beams (Jarvis, 2001). The flexural performance of IsoTruss structures alone (not embedded in concrete), however, exhibited brittle characteristics locally, with ductile global behavior, due to the redundancy of members in the lattice structure (Jensen 2000).

The test results, including strains derived from deflections, are summarized in Tables 2 and 3. The failure strength of both the SRC and IRC piles [165 & 267 kN (35 & 60 kips), respectively] was limited by a compressive strain of 8400 $\mu\varepsilon$ at the concrete surface. Deflections in the SRC pile at 165 kN (35 kips), the maximum load in the SRC pile, were nearly twice the deflections in the IRC pile at the same load. Deflections in the IRC pile at 245 kN (55 kips) nearly matched the deflections in the SRC pile at the maximum load of 165 kN (35 kips) as shown in Figure 4.

For design purposes, ductility has traditionally been defined as a measure of deformation after yielding. Since the IRC piles are essentially linear elastic to failure, while the steel yields, the concept of ductility effectively only applies to the SRC piles. Nevertheless, the deformation at the maximum loads of each is approximately equal in both the composite and steel reinforced piles. Ductility is essentially a factor of safety based on deformation for materials that yield. The IRC piles, comprised of linear elastic materials, have a significantly higher factor of safety based on load. This is significant because load control situations (realistic) generally lead to catastrophic failure, implying better practical margins of safety for IRC piles.

Table 2. Summary of Results for Lab Tests

Property	SRC	IRC
Flexural Stiffness [kN-cm^2 (kip-in^2)]	109 (3.8)	98 (3.4)
Maximum Moment [kN-m (kip-in)]	101 (895)	194 (1719)
Maximum Curvature from Strain Gage [με/cm (με/in)]	413 (1049)	199 (505)
Maximum Curvature from Deflections [με/cm (με/in)]	472 (1200)	472 (1200)
Maximum Strain in Reinforcement [με]	5400	7200
Toughness at Maximum Displacement [kN-m (kip-in)]	1900 (168)	940 (83)
Toughness at Maximum Loads [kN-m (kip-in)]	836 (74)	940 (83)

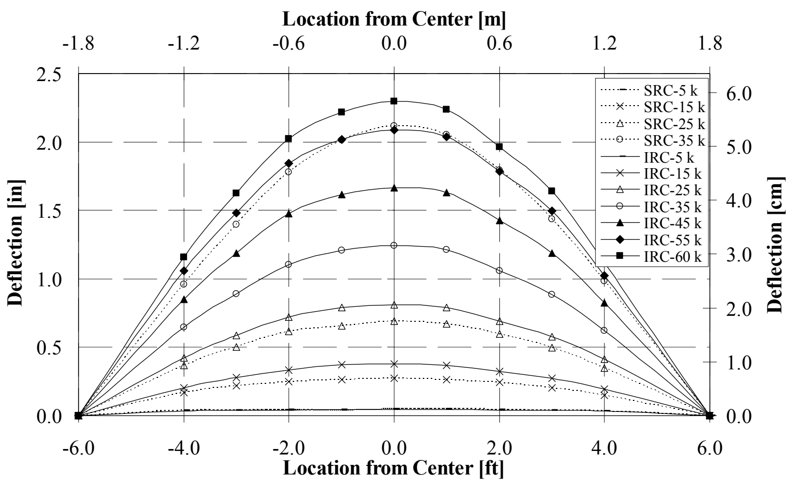

FIG 4. Average Deflections of SRC and IRC Piles at Selected Loads

Table 3. Deflection-Based Strain Comparison in Piles

	Pile Type	Load	Surface		Reinforcement	
			Distance, z	Strain	Distance, z	Strain
		[kN (kips)]	[cm (in.)]	[microstrain]	[cm (in.)]	[microstrain]
Equal Loads	SRC	165 (35)	18 (7)	8,400	11 (4.5)	5,400
	IRC	165 (35)	18 (7)	4,200	15 (6)	3,600
Maximum Loads	SRC	165 (35)	18 (7)	8,400	11 (4.5)	5,400
	IRC	267 (60)	18 (7)	8,400	15 (6)	7,200

CONCLUSIONS

Carbon/epoxy composite three-dimensional lattice structure (IsoTruss) reinforced concrete piles exhibit linear elastic behavior to failure with twice the flexural capacity of their steel counterparts, based on similar stiffness designs. Smaller cracks exist in composite lattice structure reinforced concrete piles compared to steel reinforced concrete piles, implying a more uniform crack distribution, most likely due to the lattice structure geometry. In spite of the redundancy in composite lattice structures, the failure of composite lattice reinforced concrete piles in flexure is sudden, typical of brittle materials, with steel reinforced concrete piles being substantially more ductile than their carbon composite lattice reinforced counterparts. For reinforced concrete pile applications, three-dimensional carbon composite lattice structures are lighter and more rigid, simplifying installation; twice as strong; and more corrosion resistant than equivalent steel reinforcement, albeit without ductility.

REFERENCES

Ferrell, M.J. (2005). "Flexural Behavior of Carbon/Epoxy IsoTruss®-Reinforced Concrete Beam-Columns," M.S. Thesis, Brigham Young University, Provo/UT.

Florida Dept. of Transportation (1999) "Ultimate Capacity of Corrosion Damaged Piles" Summary of Final Report, WPI #00510795, Tallahassee, Florida, 2 p.

Jarvis, D. (2001). "Development of a Rectangular IsoTruss® for Reinforced Concrete Beams," M.S. Thesis, Brigham Young University, Provo/UT.

Jensen, C. (2000). "Flexural Behavior of a Graphite/Epoxy IsoTruss®," Technical Report, CASC, Brigham Young University, Provo/UT.

Jensen, D.W., Redford, M., and Francom, L.R. (1996). "On the Structural Efficiency of Three-Dimensional IsoGrid Designs," *Proc. 37th AIAA/ASME/ASCE/AHS/ASC Struct., Struct. Dynamics, and Mat'l Conf.*, AIAA-96-1508-CP, 1996, pp. 1704-12.

Lampo, R., Nosker, T., Barno, D., Busel, J., Maher, A., Dutta, P., and Odello, R. (1998). "Development and Demonstration of FRP Composite Fender, Load-bearing, and Sheet Piling Systems," Report, US Army Corps of Engineers, Construction Engineering Research Laboratories, Champaign/IL.

McCune, D. (2005). "Manufacturing Quality of Carbon/Epoxy IsoTruss® Reinforced Concrete Structures," M.S. Thesis, Brigham Young University, Provo/UT.

Richardson, S. (2005). "In-Situ Testing of a Carbon/Epoxy IsoTruss®-Reinforced Concrete Foundation Pile," M.S. Thesis, Brigham Young University, Provo/UT.

Lateral Load Behavior of a Concrete-Filled GFRP Pipe Pile

Thomas J. Weaver[1], Scott A. Ashford[2], Kyle M. Rollins[3]

[1]Assistant Professor, Dept. of Civil Engrg., University of Idaho, Moscow, ID 83844-1022, tweaver@uidaho.edu
[2]Professor and Head of School of Civil and Construction Engrg., Oregon State University, Corvallis, OR 97331-3212, scott.ashford@oregonstate.edu
[3]Professor, Dept. of Civil and Environ. Engrg., Brigham Young University, Provo, UT 84602, rollinsk@byu.edu

ABSTRACT: This paper presents results of full-scale lateral load tests to failure of a concrete-filled glass-fiber reinforced polymer (GFRP) pipe pile in comparison to a typical pre-stressed concrete pile. Soil conditions at the test site consisted of fine grained, poorly graded, medium dense sand underlain by soft clay with the groundwater table near the ground surface. A diesel hammer was used to drive the piles. Both the pre-stressed concrete and concrete-filled GFRP piles displayed good drivability. The concrete-filled GFRP pile was more flexible than the standard pre-stressed concrete pile, which resulted in larger displacements at equivalent lateral loads and reduced service load capacity of the GFRP pile. The ultimate lateral load capacity of the concrete-filled GFRP pile was greater than the pre-stressed concrete pile, though the GFRP pile exhibited brittle behavior at failure. A comparison of the predicted and measured behavior shows that concrete-filled GFRP piles can be adequately modeled using traditional p-y curves and classical beam theory.

INTRODUCTION

Piles made from fiber reinforced polymers (FRP) have seen increased use in environments where typical pile materials such as concrete, steel, and wood would be susceptible to corrosion or attack from marine organisms. Geotechnical engineers often have little experience in the design of FRP piles for axial and lateral loads. As a result, a number of research projects have focused on providing engineers with data on drivability (Ashford and Jakrapiyanun 2001, Juran and Komornik 2006), durability (Iskander and Hassan 1998, Shao and Koudio 2002, Pando et al. 2002), axial response (Han et al. 2003, Juran and Komornik 2006), and lateral behavior (Han et al. 2003, Pando et al. 2003, Pando et al. 2004, and Thomann et al. 2004). However, as mentioned by Juran and Komornik (2006) more full-scale experiments are needed to develop reliable testing procedures and design methods prior to their widespread use.

The purpose of this paper is to report results of a full-scale lateral load test on a concrete-filled GFRP pile, compare the lateral response of the GFRP pile with the performance of a similar diameter pre-stressed concrete pile, and provide additional validation on the use of traditional analytical methods in the design of concrete-filled GFRP piles for lateral loading. A unique facet of the tests reported on in this paper is that the piles were loaded to structural failure.

SITE CONDITIONS

The location of the lateral load tests was on Treasure Island in the San Francisco Bay. Based on borehole logging carried out at the site, the soil profile consists of three main layers: a fine poorly graded sand from the ground surface to an elevation of approximately +0.9 m, a saturated silty fine sand from an elevation of 0.9 m to -5.8 m, and a gray low plasticity clay (locally known as San Francisco Bay mud) extending from -5.8 m to the bottom of the borehole at an elevation of -15 m. In order to characterize the soils at the test site, both Standard Penetration Tests (SPT) and Cone Penetration Tests (CPT) were conducted. The results of these tests are shown in Fig. 1 as $N_{1(60)}$ values for the SPT and q_c values for the CPT, where $N_{1(60)}$ is the SPT N-value corrected for field procedures and overburden pressure and q_c is the CPT tip resistance. The relative density of the soils, also shown in Fig. 1, was estimated from the SPT and CPT results using relationships presented by Kulhawy and Mayne (1990) and show that the sand is loose to medium dense.

The soil properties required to perform lateral pile analyses with p-y curves in sand are the modulus parameter (k), friction angle (ϕ), and effective unit weight (γ'). The modulus parameter was obtained using a relationship with relative density proposed by the American Petroleum Institute (1987). Friction angles were obtained from $N_{1(60)}$ values using a correlation by Peck et al. (1974), and from q_c values using a correlation proposed by Kulhawy and Mayne (1990). The resulting k and ϕ based on SPT and CPT results are shown in Fig. 1.

Parameters required for the lateral load analysis in clay are the undrained shear strength (S_u), axial strain at 50% of the undrained strength (ε_{50}), and effective unit weight (γ'). Undrained shear strength for the clay was estimated to be 12 kPa, based on the site-specific SPT tests and strength testing at nearby sites. An ε_{50} value of 0.02 was used based on recommendations by Reese and Wang (1997) for lateral load analyses of piles in soft clay. Reasonable values of total unit weight were assumed for each of the layers: 19.5 kN/m^3 for sand above the water table, 20.1 kN/m^3 for sand below the water table, and 17.0 kN/m^3 for the clay.

The GFRP pile and pre-stressed concrete pile were driven into the ground using an open ended diesel hammer. The GFRP pile and pre-stressed concrete pile required similar number of blows per foot of driving, typically 1 to 2 blows per foot until the final toe elevation was reached.

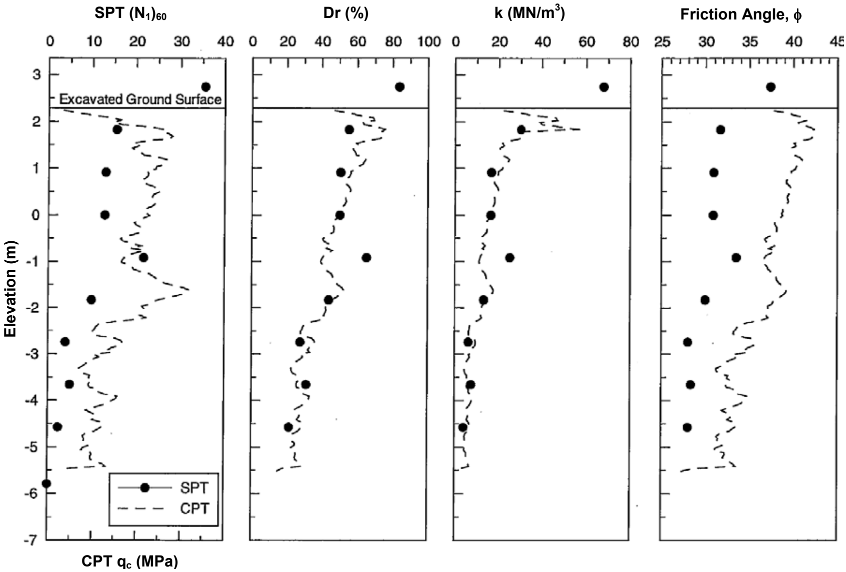

Figure 1 In-situ test results and interpreted soil properties.

TEST SET-UP AND PILE PROPERTIES

Lateral load tests were carried out on two piles, a concrete-filled GFRP pile and a pre-stressed concrete pile. The concrete-filled GFRP pipe pile had a 324-mm outside diameter and a 5.5-mm wall thickness. The GFRP pipe was constructed using the filament winding technique. This pipe was then filled with an expansive concrete and cured prior to installation. The pre-stressed concrete pile was 305 mm square. Both piles were driven with the same diesel hammer through the upper sand layer and far enough into the soft clay that both piles essentially behaved as infinitely long piles. The piles were tested approximately two months after installation.

Properties of the materials used in both piles are shown in Table 1. Moment-curvature analyses were performed for the GFRP and pre-stressed concrete piles to estimate a secant bending stiffness, EI, that should be used for the lateral load analyses. The bending stiffness for the GFRP and pre-stressed concrete piles were estimated as 8.65 MN-m^2 and 2.82 MN-m^2, respectively. Material properties for the GFRP pile were provided by the manufacturer, Lancaster Composites. The moment-curvature relationship for the pre-stressed concrete pile and concrete-filled GFRP pile were calculated based on cross-section properties.

Each pile was instrumented with two string activated linear potentiometers to measure displacement and rotation. The potentiometers were placed at 0.67 m and 0.98 m above the ground surface for both piles. Lateral load was applied 0.61 m above the ground surface for the GFRP pile and 0.55 m above the ground surface for the pre-stressed concrete pile. Lateral load was applied by a CAT 325 BL track mounted excavator connected to the piles with a 25.4 mm high strength alloy steel chain (Grade 8). Load was measured with an instrumented high strength pre-stress rod with an ultimate load capacity of 667 kN placed in line with the chain. Each pile was loaded at 40 kN to 50 kN increments to failure. Load increments were increased every five minutes.

Table 1 Material Properties for Piles.

Material	Moment of Inertia (I) (mm^4)	Young's Modulus (E) (MPa)	Compressive Strength (MPa)	Tensile Strength (MPa)
Concrete-fill	4.74×10^8	30440	41.4	n.a.[a]
Glass FRP	6.62×10^7	27,580[b]/19,305[c]		
Pre-stressed Concrete	7.07×10^8.	30,440	42	n.a.
Pre-stress Steel[d]	1.28×10^3	200,000	n.a.	1723

[a] n.a. = not applicable, [b] Tension, [c] Compression, [d] Pre-stressed to 600 MPa

TEST RESULTS

Load-displacement results from the lateral load tests are shown in Fig. 3. Review of Fig. 3 shows that the ultimate lateral load capacity of the concrete-filled GFRP pile was approximately 160 kN. At the ultimate load, brittle failure occurred, resulting in a total loss of lateral load carrying capacity. The ultimate load was reached at a displacement of 440 mm. Removal of the upper section of the GFRP pile revealed a horizontal failure surface occurring 0.9 m below the ground surface. The ultimate capacity of the pre-stressed concrete pile was 116 kN. After reaching the peak load, the pile deformed excessively displaying a ductile failure mode. Small cracking occurred in the pre-stressed concrete pile 0.62 m below the ground surface. Large cracks were located 0.78 m below grade. Drops in the load with increasing displacement prior to failure are most likely a result of applying the load with an excavator that stopped momentarily during the loading process.

LATERAL LOAD ANALYSES

Lateral load analyses were performed using a Winkler spring procedure with standard p-y curves to represent the non-linear soil resistance. The sand was modeled using a sand p-y curve proposed by Reese et al. (1974), and the clay was modeled using a soft clay p-y curve developed by Matlock (1970). Each pile was analyzed using friction angles obtained from the SPT correlation and again with friction angles obtained from the CPT correlation. The piles were modeled as linear elastic and therefore do not predict pile response after the piles yield or fracture excessively. The bending stiffness values for the piles were obtained from moment curvature analyses. Although the moment curvature relationships for the piles are not linear, a bending stiffness value for the analyses was chosen to account for a limited amount of non-linear behavior that may occur due to some concrete cracking. Results from the analyses along with the experimental results are shown in Fig. 4. Although the pre-stressed concrete pile is square, the influence of pile shape is negligible (Reese and Van Impe 2001).

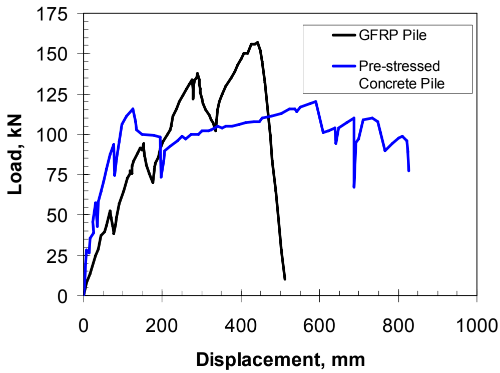

Figure 2 Pile head load-displacement test results.

DISCUSSION

A comparison of the lateral response of the GFRP pile and the pre-stressed concrete pile is important in understanding GFRP pile behavior in relation to typical structural foundations. Because the GFRP pile has a lower bending stiffness than the pre-stressed concrete pile, the GFRP pile response was more flexible at load levels less than the pre-stressed concrete pile ultimate load. In the design of highway bridges, pile flexibility may impact the number of piles required to meet lateral serviceability requirements. According to AASHTO LRFD Bridge Design Specifications (2004), the maximum allowable lateral pile head displacement is 38 mm. The lateral load at a displacement of 38 mm for the GFRP and pre-stressed concrete piles is 28.9 kN and 44 kN, respectively. As a result of the lower bending stiffness, the GFRP pile would have an allowable load approximately 15% lower than the pre-stressed concrete pile at the Treasure Island test site. In addition to the difference in stiffness, the failure mode of the two piles was quite different. Failure of the GFRP pile was brittle, while the pre-stressed concrete pile displayed a much more ductile behavior at failure. When designing piles for seismic lateral loads, ductility of the foundation elements may be considered desirable in order to limit ductility demand on the superstructure (Martin 2004). More testing and analysis of GFRP piles is desirable to assess foundation and superstructure performance under seismic loads. If ductility is needed for GFRP piles in seismic areas, a study by Shao and Mirmiran (2005) has shown that concrete-filled FRP tubes can be designed with ductility behavior similar to reinforced concrete.

Load-displacement estimates are somewhat conservative compared with test results from the GFRP pile test, but the agreement between the predicted and measured displacements is good for the two analyses performed. These results indicate that the use of classical beam theory with standard p-y curves is adequate for the lateral analysis of concrete-filled GFRP piles. From the moment-curvature analysis, we would expect the GFRP pile to fail at a depth where the moment reaches 227 MN-mm. Post test observations indicate this occurred at a load of 155 kN and at a depth of 0.9 m below grade. The analyses predicted a moment of 227 MN-mm at a lateral load of 125 kN at a depth of 1.4 m when friction angles were obtained from CPT tests and 107 kN at a depth of 2.1 m when friction angles were obtained from SPT results.

Agreement between the measured and predicted load and displacement was very good for the pre-stressed concrete pile using friction angles from both the CPT and SPT until the pile began to yield excessively.

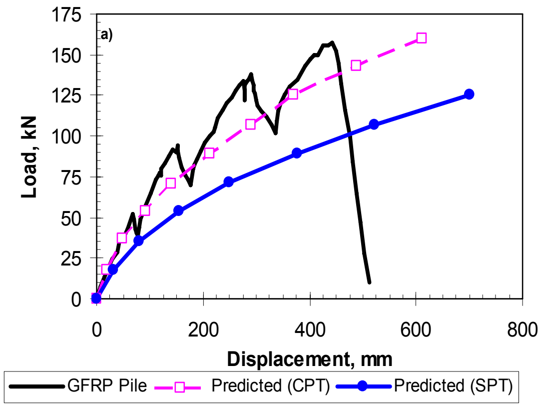

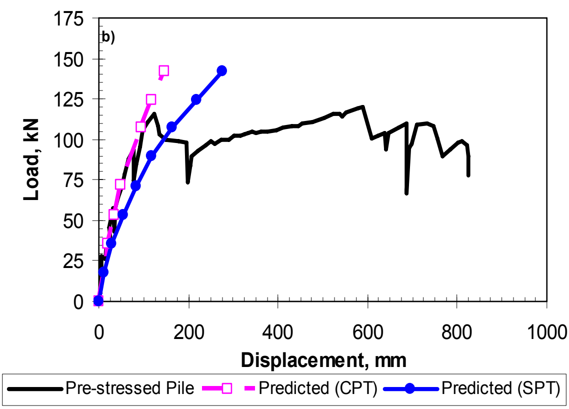

Figure 3 Comparison of load-displacement test results and predicted response a) GFRP pile b) Pre-stressed concrete pile.

CONCLUSIONS

A set of full-scale lateral load tests and analyses were carried out on a concrete-filled GFRP pipe pile and a typical pre-stressed concrete pile in order to better understand the lateral load behavior of GFRP piles. Based on the test and analytical results, the following conclusions can be made:

- Standard p-y curves with classical beam theory can be used to model the lateral load-displacement behavior of concrete-filled GFRP piles.
- Concrete-filled GFRP piles are more flexible than a similar-sized pre-stressed concrete pile. More or larger diameter GFRP piles may be needed to meet lateral serviceability limits compared to standard sized pre-stressed concrete piles.
- The concrete-filled GFRP pile tested displayed greater ultimate lateral capacity than a similar sized pre-stressed concrete pile. However, the GFRP pile failure mode was brittle. Ductile behavior may be incorporated into FRP piles if needed.

The use of GFRP in foundations may be most economical and beneficial in corrosive environments or where attack from marine organisms are of concern with typical foundation materials. The foundation engineer should be familiar with the behavior of GFRP piles in order to provide reasonable foundation design recommendations and to prevent undesirable performance under service load and extreme loading events. We hope this study provides some of the needed field data which will assist with the appropriate use of this type of pile.

ACKNOWLEDGEMENTS

The authors wish to thank the sponsors of this project: Caltrans, Alaska DOTPF, Missouri DOT, Oregon DOT, Utah DOT, and Washington State DOT, as well as other project participants including the United States Navy, the City of San Francisco, Lancaster Composites, and Foundation Constructors.

REFERENCES

API (1987). *Recommended practice for planning, designing and constructing fixed offshore platforms*, API RP 2A, 17th ed., American Petroleum Institute, Houston, Texas, 133p.

Ashford, S.A., and Jakrapiyanun, W. (2001). "Drivability of glass FRP composite piling," *J. Compos. for Constr.*, ASCE, 5(1), 1-3.

AASHTO (2004). *AASHTO bridge design specifications*, American Association of Highway and Transportation Officials, 1450p.

Iskander, M.G., and Hassan, M. (1998). "State of the practice review of FRP composite piling," *J. Compos. for Constr.*, ASCE, 2(3), 116-120.

Juran, I., and Komornik, U. (2006). "Behavior of fiber-reinforced polymer (FRP) composite piles under vertical loads," FHWA Report No. FHWA-HRT-04-107, 97p.

Kulhawy, F.H., and Mayne, P.W. (1990). *Manual on estimating soil properties for foundations design*, EL-6800, Research Project 1493-6, Electric Power Research Institute, Palo Alto, California.

Martin, G.R. (2004). "The seismic design of bridges – geotechnical and foundation design issues," *Geotechnical Engineering for Transportation Projects*, Geotechnical Special Publication No. 126, Vol. 1, Mishac Yegian and Edward Kavizanjian, Eds., ASCE, 137-166.

Pando, M.A., Lesko, J., Fam, A., and Rizkalla, S. (2002) "Durability of Concrete-Filled Tubular FRP Piles", Third International Conference on Composites in Infrastructure, San Francisco, California, June 10-12, 2002., Paper No. 80 (CD-ROM), 12p.

Pando, M., Filz, G., Ealy, C., and Hoppe, E. (2003). "Axial and lateral load performance of two composite piles and one prestressed concrete pile," Transportation Research Record No. 1849, Paper No. 03-2912, 61–70.

Pando, M.A., Brown, D., and Filz, G.M. (2004). "Performance of a laterally loaded composite pile at the Nottoway river bridge," *Geotechnical Engineering for Transportation Projects*, Geotechnical Special Publication No. 126, Vol. 2, Mishac Yegian and Edward Kavizanjian, Eds., ASCE, 1317–1326.

Peck, R.B, Hanson, W.E., and Thornburn, T.H. (1974). *Foundation Engineering*, 2nd Ed., John Wiley and Sons, NY, 514p.

Reese, L.C., Cox, W.R., and Koop, F.D. (1974). "Analysis of laterally loaded piles in sand," *Proc., Sixth Ann. Offshore Tech. Conf.*, API, Houston, Texas, Vol. 2, 473-483.

Reese, L.C., and Van Impe, W.F. (2001). *Single piles and pile groups under lateral loading*, Taylor and Francis, Balkema, 480p.

Shao, Y., and Kouadio, S. (2002). "Durability of fiberglass composite sheet piles in water," *J. Compos. for Constr.*, ASCE, 6(4), 280-287.

Shao, Y., and Mirmiran, A. (2005). "Experimental investigation of cyclic behavior of concrete-filled fiber reinforced polymer tubes," *J. Compos. for Constr.*, ASCE, 9(3), 263-273.

Thomann, T.G., Zoli, T., and Volk, J. (2004). "Lateral load test on large diameter composite piles," *Geotechnical Engineering for Transportation Projects*, Geotechnical Special Publication No. 126, Vol. 2, Mishac Yegian and Edward Kavizanjian, Eds., ASCE, 1239–1247.

Static and Dynamic Load Tests on Driven Polymeric Piles

Brent Robinson[1], PE, M. ASCE and Magued Iskander[2], Ph.D., PE, M. ASCE

1. Graduate Research Assistant, Department of Civil, Construction, and Environmental Engineering, North Carolina State University, Campus Box 7908, Raleigh, NC, 27695, phone: 919-544-0361 e-mail: brrobins@ncsu.edu
2. Associate Professor, Department of Civil Engineering, Polytechnic University, Six Metrotech Center, Brooklyn, NY, 11201 phone: 718-260-3016 e-mail: iskander@poly.edu

ABSTRACT: Repair and replacement of deteriorating piling systems cost the United States up to $1 billion per year. In the case of marine piling, actions required by the Clean Water Act rejuvenated many of the nation's waterways, but also allowed the return of marine borers, which attack timber piles. At the same time, less than 10% of the 13.7 million tons (122 GN) of plastic containers and packaging produced annually in the U.S. are recovered by recycling. Using recycled plastics to manufacture piles utilizes material which (1) would have been otherwise landfilled and (2) can be more economical in aggressive environments when life-cycle costs are considered.

A series of polymer piles were driven in Elizabeth, New Jersey. Three concrete filled fiberglass shell piles, three polyethylene piles reinforced with steel bars, three polyethylene piles reinforced with fiberglass bars, and two solid polyethylene piles were installed. One closed end steel pipe pile was also driven for reference purposes. Three static load tests were performed on one of the concrete filled fiberglass shell piles, and one of each of the reinforced polyethylene piles. High strain dynamic pile tests were performed on all piles during initial driving and restrike after load testing. This study describes the adjustments to assumed material properties required during installation testing and the correlation between static and dynamic load tests.

INTRODUCTION

A decade ago, Lampo et al. (1998) noted that repair and replacement of deteriorating piling systems cost the United States up to $1 billion per year. In the case of marine piling, actions required by the Clean Water Act rejuvenated many of the nation's waterways, but also allowed the return of marine borers, which attack timber piles. In Boston, New Orleans and other areas of the country prone to fluctuations in ground water levels timber piles and other foundation systems are subject to attack by rot and termites. Infrastructure and private facility owners must consider these end-of-life costs when approving a design or repair.

According to EPA (2006), less than 10% of the 13.7 million tons (122 GN) of plastic containers and packaging produced annually in the U.S. are recovered by recycling. As demand for petroleum products skyrocket with increasing global economic growth, recycled plastic resins will become more cost competitive over time. Using recycled plastics to manufacture piles utilizes material which (1) may have been otherwise landfilled and (2) can be more economical in aggressive environments when life-cycle costs are considered.

The past decade has shown some advancement in our understanding of recycled plastic piles. A range of products have come on the market: Fiber Reinforced Polymer (FRP) wraps for existing piles, concrete filled polymer shells, recycled polymers reinforced with stiffer bar elements, or piles manufactured purely from recycled plastics. Han et al. (2003) summarize these various categories and propose a design framework for computing the buckling, lateral and axial load capacities for a subset of these pile types.

Iskander et al. (2001), through a parametric wave equation study using polymeric material properties, investigated the impacts of pile and hammer type on pile driveability. That study concluded that the hydraulic hammers may be more effective at installing plastic piles and that the plastic piles' lower density and elastic modulus compared to conventional steel, concrete and timber piles appeared to have a more significant impact on the pile's driveability. Iskander and Stachula (2002) further investigated driveability of FRP piles using measured data from three field sites.

Since 2002, full scale installation projects have occurred in practice as well as research efforts. Pando et al. (2006) provided a well documented study that included laboratory and field components. This paper describes the installation and testing efforts of another full-scale field test performed between November 2001 and May 2002.

Table 1. Approximate soil profile at Elizabeth, NJ site.

Depth (m)	Soil Description	Average SPT N-Value (blows/0.3 m)
0 – 4.5	Fill—Sand with gravel	56, reducing to 15 with depth
4.5 – 7.3	Organic Clay with Peat	6
7.3 – 10.7	Fine Sand, some silt	29
10.7 – 23.2	Silt and Clay	14
23.2 – 27.4	Sand with some silt, clay	47
27.4 – 28.2	Weathered Shale	141
28.2 – 29.7	Red Shale	Fractured

SITE DESCRIPTION

At the Port Authority of New York and New Jersey's facility in Elizabeth, New Jersey, construction efforts for an express railway bridge over McLester Ave were underway in November of 2001. A site below the western approach ramp of the bridge near the corner of West Bay Avenue and Polaris Street was available for a full scale installation of a series of plastic piles. Table 1 summarizes the soil profile encountered at one soil boring near the site of the load test program. Prior to pile installation the upper five feet of fill was excavated to remove existing construction debris that may have impeded pile driving.

PILES

Pile driving on the site consisted of one steel pipe pile, three fiberglass cased concrete piles manufactured by Lancaster Composites, Inc., three fiberglass bar reinforced plastic piles manufactured by Seaward, three steel bar reinforced plastic piles manufactured by Plastic Pilings, Inc., one recycled plastic pile manufactured by American Ecoboard and one recycled plastic pile manufactured by Trimax. A static load test was performed on a representative pile from the concrete filled fiberglass shell piles, from the steel reinforced plastic pile and from the fiberglass bar reinforced plastic pile. The static load test piles and the steel indicator pile will be the focus of this study.

All piles had outer diameters of 406 mm. The steel pipe pile was driven closed-ended with a 0.5 inch thick wall and a 45 degree rock point on one end. The pipe was manufactured from A252, Grade 2 steel. The concrete filled fiberglass shells were constructed with concrete that had a design 28 day compression strength of 6 ksi. The steel reinforced plastic piles were reinforced with a full length cage of 16 one-inch diameter steel bars, similar to those reported in Pando et al. (2006). The fiberglass reinforced plastic pile included sixteen 1.75-inch diameter fiberglass bars.

Fig. 1. Photographs of Installation and Load Testing at

HAMMER

Pile handling was easy with two pickup points, and the pile installation was uneventful (Fig. 1). The test piles were driven with an ICE 70 single acting hydraulic hammer, which had a 31.1 kN ram with a rated maximum stroke of 0.9 m. This hammer has a pump controlled stroke that was varied from 1 to 3 feet during initial driving and restrike. Plywood cushions were used to protect the pile top. In most cases, the cushion was nominally 243 mm thick. The concrete filled fiberglass shell pile, however, used a reduced 150 mm thick cushion during initial driving given the experience with two other piles of this type.

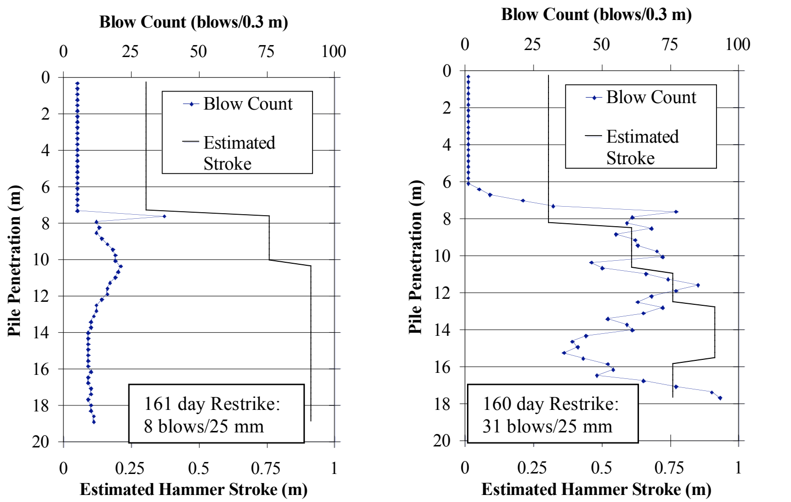

Fig. 2. Steel pipe (left) and concrete filled fiberglass (right) pile driving records

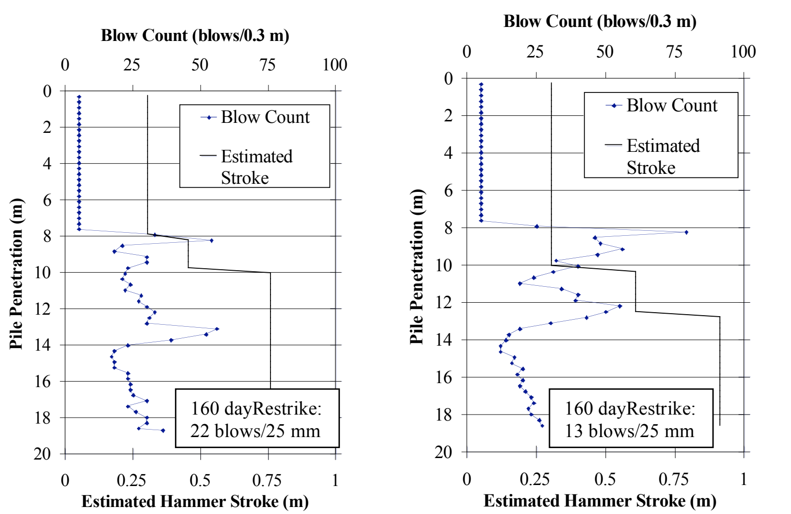

Figure 3. – Fiberglass reinforced (left) and steel reinforced (right) plastic pile driving records.

The driving record for each static load test pile is shown in Fig. 2 and 3. Note that the upper six to eight meters of driving were generally intermittent blows, and thus represent an average blow count over the upper portions of the pile. Similarly, the estimated strokes were those requested to the contractor during driving. Restrike blow counts over the first 25 mm of driving and the time after installation is also included on these figures.

STATIC AND DYNAMIC LOAD TESTS

High strain dynamic testing was performed per ASTM D4945-00 using a Pile Driving Analyzer (PDA) (GRL, 2002). Four strain transducers and four accelerometers were placed three to five feet from the pile top. The reinforced polymer piles were drilled and tapped for gage attachment in a manner similar to the steel pipe pile, while the concrete filled shell had one pair of strain and acceleration sensors attached directly to the surface of the shell (although bolted with concrete anchors) and one pair placed directly on the interior concrete exposed by cutting windows in the fiberglass. For this latter pile type, the collected data were quite similar whether windows were cut or not.

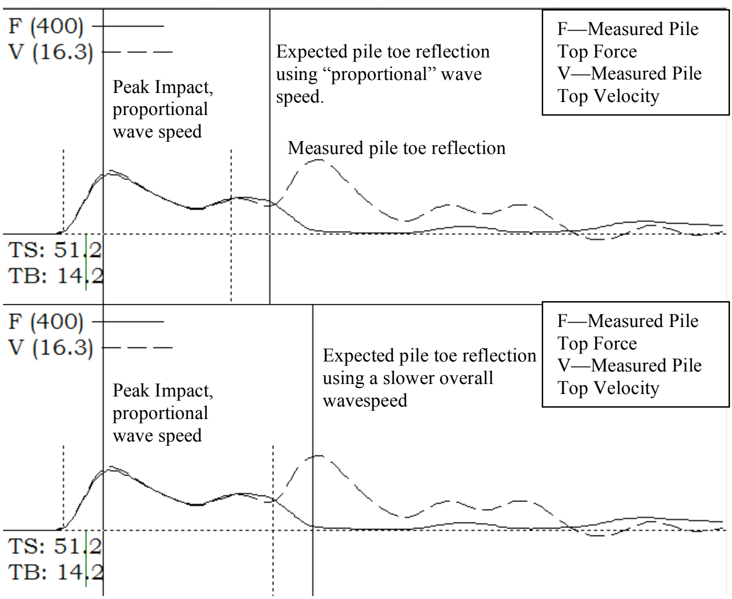

Fig. 4. Comparison of proportional and overall compressive wave speed on fiberglass bar reinforced plastic pile.

The polymeric piles in particular showed some unusual behavior in the dynamic testing records. Typically, data quality is assessed by comparing the velocity data at the impact peak to the strain data at the peak impact. The two quantities are proportional by the pile material's 1-D compression wave speed. Because the composite material's properties were largely unknown, the compression wave speed was determined by forcing proportionality. When proportionality was forced on the reinforced plastic piles, a second measure of the overall compression wave speed in the pile based on the time required for the wave to travel to the pile toe and back did not match (Fig. 4). To maintain the underlying theoretical assumptions of the PDA's calculations, two different wave speeds were used so that both measured compressive stresses and forces at the gage location and estimated tensile stresses and ultimate resistance values would be correctly calculated.

Table 2 summarizes the differences in proportional and overall compressive wave speeds observed in each pile type. Note the concrete filled fiberglass shell pile (and, of course, the steel pipe pile) showed very little difference between the two values. However, as the stiffness of the pile's reinforcing material decreased, the overall percent decline of the observed overall wave speed compared to the proportional wavespeed increased. These differences are believed to be a by-product of the manufacturing process of the recycled plastic piles, which are foamed from the outside to the inside. Often, the interior plastics are considerably less dense than the exterior plastics, which could lead to slower wave propagation through the composite section than at the surface.

Table 2. Compression wave velocity measurements from dynamic tests.

Pile Type	**Reported Specific Weight (kN/m^3)**	**High Strain Dynamic Testing**			
		Proportional Wave speed c_p (m/s)	**Estimated Elastic Mod. E_p (GPa)**	**Overall Wave speed $c_{2L/t}$ (m/s)**	**Estimated Elastic Mod. E_h (GPa)**
Polymer only	7.9	1829	2.68	1372	1.51
Concrete filled	22.0	4176	39.07	4023	36.27
Steel bar reinf.	8.0	3810	11.85	3322	9.01
Fiberglass bar	8.5	3048	8.03	2530	5.53

Selected blows were analyzed using the CAPWAP computer program during end of drive and restrike. This program more rigorously evaluates the distribution of the ultimate shaft and toe static resistance under a blow.

Figure 5 and 6 present the static and dynamic load test results. Despite the overall uncertainty in the material properties, the static load test and CAPWAP results are similar. The concrete filled pipe pile was underpredicted slightly, although the very high blow counts observed during the restrike implies the available static resistance was not fully activated. The fiberglass reinforced pile was slightly overpredicted, for reasons that will be investigated in future studies. In general, these piles were designed such that they could be driven, and as such the static capacity of the concrete filled shell and the steel pipe pile were likely much lower than their structural capacity.

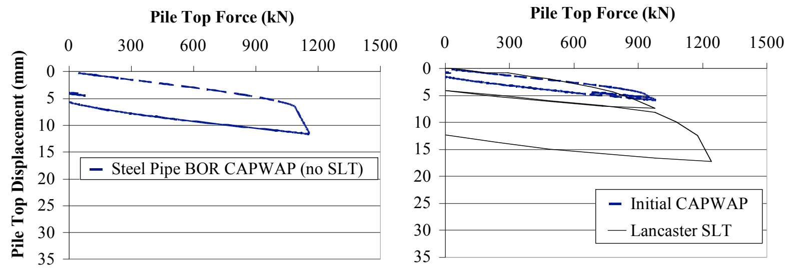

Fig. 5. CAPWAP simulated load test curve for steel pipe (left) and Static and CAPWAP load curves for concrete filled fiberglass shell pile (right).

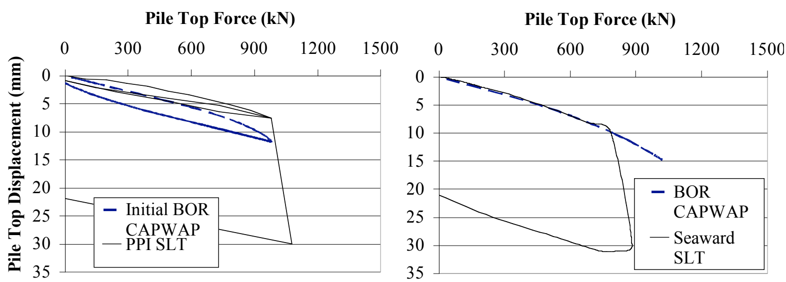

Fig. 6. Static and dynamic load test results for FRP pile reinforced with steel bars (left) and fiberglass bars (right).

CONCLUSIONS

This study summarized the installation and load testing behavior of four piles driven on the grounds of Port Elizabeth, New Jersey. Installation and dynamic testing of 12 piles and static testing of three piles were performed. Representative piles were summarized as a starting point for future work. While further work is needed on the long term creep performance and durability of these pile materials under typical load conditions, this project has shown the possible applicability of plastic piles to traditional axial loading applications. Dynamic testing of the polymeric piles showed an unusual reduction in the compression wave speed from the value measured at the gage location and as measured from 1-D wave travel. This variation merits further exploration. Static testing showed similar geotechnical capacities across all four piles tested, and reasonable comparisons to the CAPWAP simulated static load test curves.

ACKNOWLEDGEMENTS

The authors gratefully acknowledge support of the Federal Highway Administration, New York State Empire Development Corporation, the Port Authority of New York and New Jersey and the New York State Department of Transportation. The authors wish to acknowledge the professional contributions of the following individuals: Ilan Juran, Arnold Aronowitz, Uri Komornik, Sherif Hanna, Ray Sandiford, John Lizzo, Steve Borg, Keith Lashway, Frank Heartly, George Goble, and Carl Ealy. The project would also not have been possible without their contributions. Finally, the authors thank GRL Engineers, Inc., H.R. Reid General Contracting, Lancaster Composites, Plastic Pilings, Inc., Seaward International, American Ecoboard, and Trimax Building Products for donating time and materials to this project.

REFERENCES

Environmental Protection Agency, EPA. (2005). "Municipal Solid Waste Generation, Recycling, and Disposal in the United States: Facts and Figures for 2005." http://www.epa.gov/epaoswer/osw/conserve/resources/msw-2005.pdf

GRL Engineers, Inc. (2002). *Polymer Pile Driving Research Project.* Report No. 011121 to Polytechnic University. Cleveland, Ohio.

Han, J., Frost, J.D., and Brown, V.L. (2003). "Design of Fiber-Reinforced Polymer Composite Piles Under Vertical and Lateral Loads." *Transportation Research Record*, no. 1849, 71-80.

Iskander, M.G. and Stachula, A. (2002). "Wave equation analyses of fiber-reinforced polymer composite piling." *Journal of Composites for Construction*, v 6, n 2, 88-96.

Iskander, M.G. and Stachula, A. (2001). "Driveability for FRP composite piling" *Journal of Geotechnical and Geoenvironmental Engineering*, v 127, n 2, 169-176.

Lampo, R., et al. (1998). "Development and demonstration of FRP composite fender, load-bearing and sheet piling systems." Report. Construction Engineering Research Lab., U.S. Army Corps of Engineers.

Pando, M., Ealy, C., Filz, G., Lesko, J. and Hoppe, E. (2006). "A Laboratory and Field Study of Composite Piles for Bridge Substructures." Report FHWA-HRT-04-043. FHWA, http://www.tfhrc.gov/structur/pubs/04043/index.htm

Foundation Design Against Progressive Collapse of Buildings

N. O. Nawari, Ph.D., P.E., M.ASCE[1]

[1] Bock and Clark Corporation, 537 N Cleveland-Massillon Rd., Akron, OH 44333

Abstract

While statistical data indicate that risk of progressive collapse in buildings is very low, loss of human life and severe injuries would be significant when a fully occupied multi-story building encounters partial or total failure. As a result of recent terrorist attacks on buildings throughout the world, particularly U.S. owned and occupied buildings, and recent natural hazards like Katrina Hurricane; several U.S. government agencies with large construction programs have developed their own design requirements (GSA 2003; DOD 2005) to provide resistance against progressive collapse. Each agency, however, with its own mission, has adopted different performance objectives for buildings subjected to abnormal loads. Foundation and geotechnical design considerations to provide resistance against progressive collapse are important components of the overall building performance under abnormal loadings. This work discusses the role of geotechnical and foundation system design considerations to reduce the likelihood of progressive collapse of buildings in the event of anomalous loadings. This includes outlining of acceptable risk approach to progressive collapse along with definitions of threats, events control, risk mitigation and practical recommendations for enhancing foundations resistance to progressive collapse.

Introduction

The 1995 attack on the Oklahoma City Murrah Building was a major thrust to raise government interest in explosion protection for its facilities in the United States and oversees. In response, the federal Interagency Security Committee (ISC) addressed the issue promptly by developing a blast-resistance standard outlining new criteria for design. Subsequently, the horrific structural collapses of Sept. 11, 2001 and the catastrophic damages caused by hurricane Katrina 2005, refocused attention and emphasis on design for extraordinary loads.

In light of these events, two major building owners, the General Service Administration (GSA) and the Department of Defense (DoD) are requiring engineers to consider building security as additional criterion. Even private sector owners and developers of high profile buildings are taking a serious look at security risks as their buildings may be considered as target of both domestic and international terrorists.

The primary design objective is to save the lives of those who visit or work in these government buildings in the unlikely event that an explosive terrorist attack occurs. In terms of building design, the first goal is to prevent progressive collapse which historically has caused the most fatalities in terrorist incident targeting buildings. Beyond this, the goal is to provide design solutions which will limit injuries to those inside the building due to impact of flying debris and air-blast during an incident..

Progressive collapse is defined as a situation where local failure of a primary structural element(s) progresses to adjoining members, which in turn leads to additional collapse. Hence, the extent of total damage is disproportionate to the original cause. Different standards describe the term in slightly various ways. ASCE 7-05 defines the term as:" the spread of an initial local failure from element to element, eventually resulting in the collapse of an entire structure or disproportionately large part of it." On the other hand DOD gives the following definition: "A progressive collapse is a chain reaction of failure of building members to an extent disproportionate to the original localized damage. Such damage may result in upper floors of a building collapsing onto lower floors.

Regardless of the definition, blast loading or other abnormal events can cause progressive collapse due to damage of some key element(s) which can either make the structure unstable or trigger the failure of the main portions of the structural system. Explosion generally results in a high-amplitude impulse loading which lasts for a very short period of time and produces high pressure loading. The loading in many situations is local in the sense that only those elements closest to the blast may be directly impacted. Elements far from the blast site may experience little or no direct impact due to sharp dissipation of blast energy with distance. The forces experienced by structural components depend on the size, geometry and proximity of the explosion. Because all of these parameters can vary, it is not easy to accurately predict the force level that a particular structure could experience as a result of an unexpected blast.

Risks of these events cannot be totally eliminated; rather it must be controlled. Building codes are key tools for engineers to manage risk in the interest of public safety. The provisions for foundation and structural design in codes and standard for load combination and safety and partial safety factors addresses risks in building performance. However, risks of blast events have not been part of limit states in previous codes and quite often managed judgmentally. However, the aftermath of recent natural and terrorists disasters has made it clear that judgmental approaches to risk management are not sufficient. Rational approaches to progressive collapse mitigation require engineering knowledge-base along with risk analysis techniques..

Threat Definition

Federal guidelines define three threat levels that delineate blast protection of building structures:

• A high threat level entails a verified high threat of attack. These projects typically are buildings of high importance, buildings whose loss will have high consequences, or those that are cultural icons.

• A medium threat level consists of a verified threat of attack. These buildings may be regional symbols, or their loss will highly impact governing powers.

• A low threat level constitutes a suspected threat. These buildings may be regional symbols, or their loss will have moderate consequences.

To gain a systematic approach of investigating terrorist's threats, FEMA 427 classifies terrorist threats into the following groups:

Explosive Threats: (i)Vehicle weapon; (ii) Hand-delivered weapon.

Airborne Chemical, Biological, and Radiological Threats: (i)Large-scale, external, air-borne release; (ii) External release targeting building; (iii) Internal release.

Although the dominant threat mode may change in the future, bombings have historically been a favorite tactic of terrorists. Ingredients for homemade bombs are easily obtained on the open market, as are the techniques for making bombs. Bombings are easy and quick to execute. Finally, the dramatic component of explosions in terms of the sheer destruction they cause creates a media sensation that is highly effective in transmitting the terrorist's message to the public, as was shown in the recent UK's car bombs in London and Glasgow June 2007..

The primary threat is mostly a vehicle weapon located along a secured perimeter line surrounding the building (see Figure 1). Depending on the accessibility of the site to vehicles there may be more than one line of defense to consider. The outermost perimeter line is often a public street secured against vehicular intrusion using barriers and with limited secured access points. The size of the vehicle weapon considered outside the perimeter line may vary from hundreds to thousands of pounds of TNT equivalent depending on the criteria used.

This threat is to be considered on all sides of the building with a public street or adjacent property lines along the secured perimeter line.

This work focuses primarily on bomb (explosion) threats, likely targets, and likelihood of occurrence.

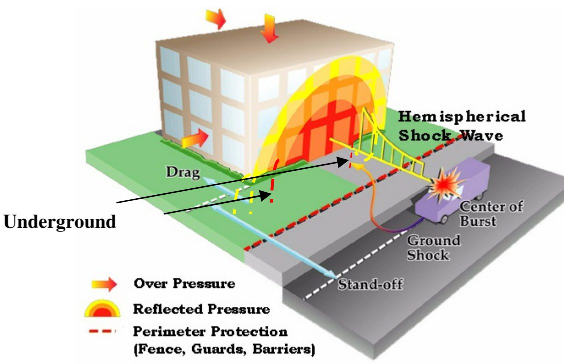

Figure. 1. Vehicle Weapon Threats (FEMA 427)

Damage Mechanisms

Building damages due to a blast event can be categorized into the following groups:

- Non structural damages; generally taking place on the building envelope.
- Superstructures damages: beams, columns, slabs, … etc
- Substructures damages: footings, raft, pile, and soil failures.

It is notwithstanding that these hazards are interrelated during an explosion event and the occurrence of one may lead to the other with the likelihood of a progressive collapse. Figure 2 below illustrates the relationships among these groups.

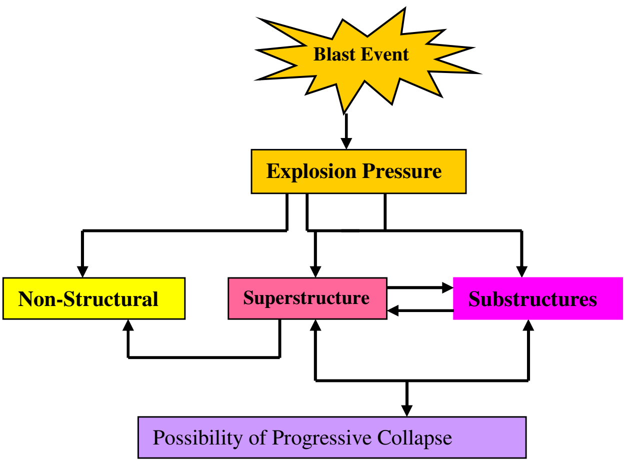

Figure. 2. Building's hazards due to Blast Event.

Superstructures

The response of a structure to blast loading is different from its response to typical static and dynamic loads because of the very short duration and extreme pressure loading caused by explosion. According to FEMA 427, the structural damages caused by large exterior explosion can be summarized as follows:
- The pressure wave acts on the exterior of the building and may cause window breakage and wall or column failures;
- As the pressure wave continues to expand into the building, upward pressures are applied to the ceilings and downward pressures are applied to the floors;
- Floor failure is common due to the large surface area upon which the pressure acts;
- Failure of floor slabs eliminates lateral support to vertical load-bearing elements, making the structure prone to progressive collapse

All of the damages mechanisms described by FEMA(2003), DOD(2005) or GSA(2003) are primarily focused on superstructure effects. Foundations and geotechnical aspects were not considered in these reports. The next section examines different foundation and geotechnical damage scenarios caused by blast effects.

Substructures

Because there are many potential means by which a local collapse in a specific structure may propagate from its initial extent to its final state, there is no universal approach for evaluating the potential for progressive collapse in buildings. This case specific behavior differentiates progressive collapse from other well defined structural engineering concerns, such as design to resist gravity, wind, seismic or vibration loads. The following general statement can be made, however, of all progressive collapse scenarios: When an initiating event causes a local failure, the resulting failure front will propagate through the building structure until specific structural conditions in its path arrest the progression of failure, or until the remaining structure becomes statically unstable and the entire building collapses. Because progressive collapse is a dynamic event, the failure boundary divides the structure into a zone that has not yet experienced the effects of the progression of failure and the failed portion of the structure.

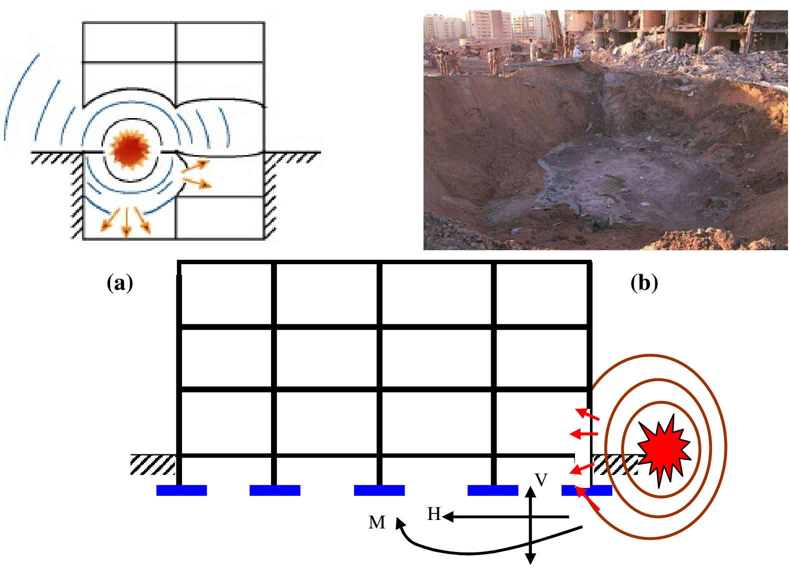

Figure 3. Explosion affecting directly both Super- and sub-structures.

A failure front may propagate laterally, vertically, or both. Blast affects foundations either directly or indirectly or both. In the first case explosion reaches part of the foundations and causes damages on the footings or piles foundations (FEMA 427). In addition to these damages, excessive dynamic forces impose additional stresses in other existing foundation structures.

In figure 4 above, detonation of explosion inside (figure 3a and 3b) or outside (Figure 3c) the building caused damages to the framed superstructure and at the same time foundation was directly affected by the explosion. Furthermore, additional vertical, lateral and vibration forces in the foundation domain due to the blast are generated. As a result, these forces may cause additional drift of the structural frame. The magnitude of the drift and the associated stability issues depends upon the type of the frame (rigid or flexible), type of foundation (single, combined footings, or piles) and the geotechnical properties of the foundation soils (Figure 4) along with the strength of blast.

The second scenario is when explosion damages only parts of the superstructure. Figure 3 illustrates some possible collapses of the superstructure. The failure of columns, beams and slabs will generally be associated with load redistribution and collapse may progress if the remaining elements are at the stage of reaching their ultimate limit states. As a consequence, foundation structures (single footing, combined footings, raft, or pile foundations) will be subjected to additional loading conditions. For instance, figure 6 shows the redistribution of forces after the loss of an exterior column. In the next sections, damage mechanisms are discussed for single and combined footings. Future research will focus on damage scenarios for raft and pile foundations.

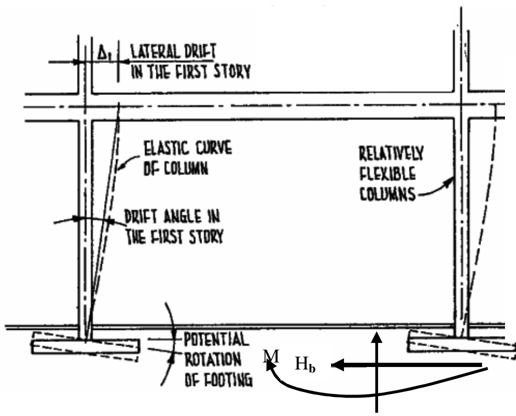

Figure. 4. Drift due to blast

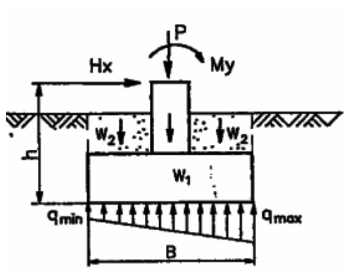

Figure 5. Foundation hazards due to Blast.

Single Footing Foundations

In the case of loss of any external or internal column due to blast, loads on the other adjacent remaining footings will increase due to the load redistribution and changes in tributary areas. Thus, changes in the applied compression (P), shear force (H) and bending moment (M) may exceed the design values causing structural failure of the footing.

Other risk of this abnormal loading is excessive settlement or bearing capacity failure. For example, in figure 5 if the value of the soil pressure q_{max} after the load redistribution surpasses the safe contact bearing pressure, soil bearing failure takes place and the support provided by the spread footing could be critically endangered. Soil liquefaction and collapses may also be experienced by the supporting subsurface soils.

Combined Footing

Removal of a column supported by a combined footing due to blast event would cause redistribution of forces on the remaining adjacent columns in the combined footing which in turn affect the contact pressure distribution. Figure 6a illustrates a combined footing designed such that a uniform soil pressure would result in the contact area.

Under an abnormal load case of a blast, the soil pressure distribution after the removal of one or more columns is entirely different than the uniform pressure assumed during the design phase. Figure 6b depicts the redistribution of the soil pressure as a result of an exterior column failure. This change in the pressure diagram at one edge may lead to excessive rotation and/or differential settlement of the footing particularly in case of low and medium soil strengths. The redistribution in the contact pressure will also lead to changes in the bending moments and shear forces acting on the footing, that are not accounted for during the design. This creates additional risks of bending and shear failure of the combined footing

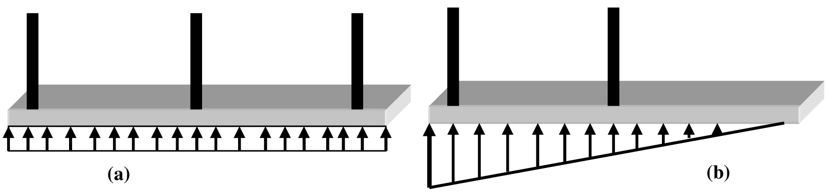

(a) (b)

Figure. 6. Redistribution of soil pressure before and after the loss of a column.

.

Another abnormal loading case for the combined footing is under applied pressure reversal during explosion events near the foundation. Figure 7a and 7b illustrate the bending surface of the footing before and after such case respectively.

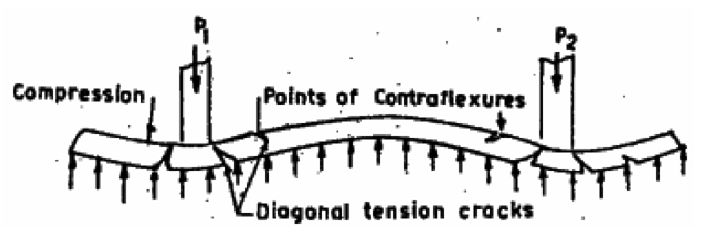

(a)

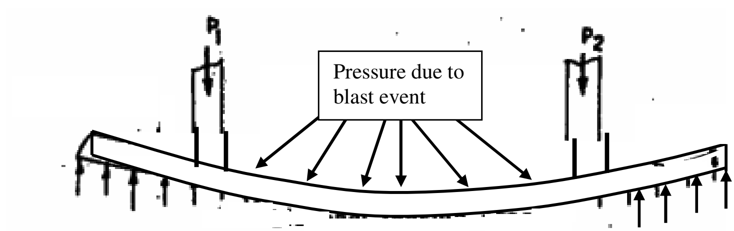

(b)

Figure.7. Load reversal effects on combined footing

Basic progressive collapse risk mitigation strategies must be aimed at three basic levels: (i) to prevent the occurrence of intentional abnormal loads through social or political means; (ii) to prevent the occurrence of local significant structural damage that is likely to initiate a progressive collapse; and (iii) to prevent structural system collapse and loss of life through structural design, compartmentalization, development of alternate load paths, alternate exit-ways, and other active and passive measures (Ellingwood et. al., 2007). According to the ASCE Standard 7-05, the basis of treating abnormal load combination is given by:

$$P[C] = P[C|LD]\, P[LD|H]\, P[H] \tag{1}$$

Where P[C] = probability of structural collapse event, P[H] = probability of hazard H, P[LD|H] = probability of local damage, given that H occurs, and P[C|LD] = probability of collapse, given that hazard and local damage both occur. The term P[C] must be limited to some acceptable value

Reductions in P[C] can be achieved by reducing any one, or all three, of the terms in equation (1). The most cost-effective strategy for most buildings is likely to involve some combination of the three. Controlling P[H] require action such as changes in the building site or access to it (e.g., imposing a minimum stand-off distance through placement of physical barriers and similar devices (Conrath, et al. 1999), or preventing access to certain building zones), by controlling hazardous substances within the building and by educating the building occupants on the need for caution with dangerous substances or unauthorized access. Often controlling the probability or mean rate of occurrence of the hazard is the most cost-effective route to risk reduction. The main goal of foundation design against the effect of abnormal loads is to mitigate progressive collapse and to obtain an acceptably low probability of a catastrophe involving loss of life and significant structural losses. In meeting these performance objectives, a certain amount of damage to the building structure may be incurred and tolerated. Foundation design is focused on the terms P(C|LD) and P(LD|H) in equation (1). The design options include designing the structure to withstand specific abnormal loads or designing and detailing the building to withstand local damage without collapse (alternate load path design). In a "specific local resistance" design strategy, the focus is on controlling P[C] by limiting P(LD|H), that is, to minimize the likelihood of initiation of damage that may lead to progressive collapse. Normally, this requires that a specific threat be identified in order to determine the stress placed on the structural member, component or subsystem. In an "alternate load path" design strategy, the focus is on controlling P[C] by limiting P(C|LD). In any event, it is in minimizing these two probabilities that the science and art of the engineer becomes dominant.

As shown previously, foundation and geotechnical considerations can play an important role in minimizing P[C|LD] and P[LD|H]. For instance, establishing criteria to ensure that both the soil and the foundations of load-bearing elements adjoining the removed columns were not overloaded. This is achieved by performing strength check on the remaining foundation structure, especially the adjacent columns using a realistic extreme event loads. Another approach to reduce these two probabilities is by the addition of an alternate load path.

Recommendations

Foundation Engineers must determine which hazardous events and damage scenarios to consider and what are the acceptable probabilities and consequences. Collapse prevention begins with awareness by architects, planners and engineers that design of foundations against collapse is important enough to be carefully considered in design. Features to improve general structural safety against progressive collapse can be incorporated into common buildings at affordable cost. At a higher level, design for progressive collapse can be accomplished by the alternate path method (i.e. design for removal of specific elements) or by direct design of components for air-blast loading or by the indirect method of prescribing design features, which promote redundancy and ductility. The following practical considerations related to geotechnical and foundation design are suggested to enhance resistance against progressive collapse of buildings:

- Loss of a column and/or footing will increase distress to other adjacent columns as load redistributes, verify that ultimate bearing capacity is not exceeded.

- Excessive settlement and foundation rotation might be critical near blast location and need to be minimized by providing redundancy in terms of footing thickness and width.
- Provide thicker footings to improve resistance to rotation and punching failure at column interface.
- Provide extra capacity for load reversal by adding adequate bottom and top reinforcement in footings to resist any load reversal during detonation of explosives (Figure 7).
- Tie footings together with strip footings or grade beams to improve load redistribution.
- Column connections to the foundation should be checked for additional flexure that might result from load redistribution as a consequence of the loss of a structural element.
- Avoid ground liquefaction during blast event by checking soil liquefaction properties to prevent settlement, tilting, instability and rupture of the structure.

Designers must also note that measures taken to mitigate explosive loads may reduce the structure's performance under other types of loads, and therefore an iterative approach may be needed to achieve an optimum solution. As an example, increased mass generally increases the design forces for seismic loads, whereas increased mass generally improves performance under explosive loads (FEMA 427).

Conclusions

Local failure of one structural element may result in the failure of another element of the same structure. Failure might thus progress throughout a major part or all of the building. The role of geotechnical and foundation systems design considerations to reduce the likelihood of progressive collapse of buildings in the event of anomalous loadings in form of explosion is shown to be significant. Thus, prevention of progressive collapse in case of impulse-type high-amplitude loading can be introduced as an important design criteria in foundation engineering practice. Design and analysis of substructures against progressive collapse is recommended to include risk assessment along with definitions of threats, events control, and risk mitigations. Furthermore, practical recommendations for enhancing redundancy and foundations resistance against progressive collapse of buildings are provided.

References

ASCE (2005). "Minimum Design Loads for Buildings and Other Structures (SEI/ASCE 7-05)", *American Society of Civil Engineers, Washington, DC.*

Conrath, E.J., et al., (1999), "Structural Design for Physical Security—State of the Practice," *Task Committee Report, American Society of Civil Engineers/SEI*, Reston, VA.

Department of Defense, (DOD), (2005), "Design of Buildings to Resist Progressive Collapse," *Unified Facilities Criteria* (UFC) 4-023-03.

Ellingwood, B. , Smilowitz, R., Dusenberry, D., Duthinh, D., and Lew, H. (2007), "Best Practices for Reducing the Potential for Progressive Collapse in Buildings". NISTIR 7396, *National Institute of Standards and Technology, Technology Administration, U.S Department of commerce, Washington, D.C.*

Federal Emergency Management Agency, FEMA 427 (2003). "Primer for Design of Commercial Buildings to Mitigate Terrorist Attacks". *Federal Emergency Management Agency*, *Washington, D.C.*

General Services Administration (GSA), (2003), "Progressive Collapse Analysis and Design Guidelines for New Federal Office Buildings and Major Modernization Projects". *General Services Administration, Washington, D.C.*

Interagency Security Committee (ISC), (2001), "Design Criteria for New Federal Office Buildings and Major Reorganization Projects".

Jet Grouting for Support of Excavations Near Historic Structures

Nasser Massoudi [1], M. ASCE, P.E.

[1] Principal Engineer, Bechtel Power Corporation, 5275 Westview Dr., Frederick, Maryland, 21703; nmassoud@bechtel.com

ABSTRACT: Results of a recent jet grouting application for a historic structure are presented. The project required deep excavations immediately adjacent to foundations of the historic structure. Jet grouting was used for soil improvement and underpinning, to enhance the performance of a 12.2-m (40-ft) deep excavation ultimately supported by a concrete diaphragm wall. The effectiveness of jet grouting with respect to maintaining ground support for the adjacent structure was documented during both the grouting operations and as excavation progressed, resulting in final excavation movements of less than 6.4 mm (0.25 in.). Results confirmed that jet grouting was a successful alternative to the more conventional methods, helping meet the very restrictive project movement requirements.

INTRODUCTION

Jet grouting has been in use since the 1970's. Its application has grown rapidly in the last decade, primarily for work in urban environments, for improving foundation soils and support of excavations. Jet grouting can provide a component or the entire excavation support system. The project that will be discussed herein falls into the former category. For a project at the Virginia State Capitol in Richmond, Virginia, jet grouting was used to enhance the performance of an excavation supported by a concrete diaphragm wall by improving the ground between the diaphragm wall and the Capitol building foundations. Summary of design, construction, and performance of the jet grouting operation are presented.

BACKGROUND

The Virginia State Capitol building in Richmond was designed by Thomas Jefferson and is over 200 years old. It is designated a National Historic Landmark and is listed on the National Register of Historic Places. The building rests on shallow footings made of deteriorated bricks, with contact pressures in the range of 240 to 480 KPa (5 to 10 ksf) and are considered very sensitive to disturbance caused by any construction. Capitol renovation required construction of an underground extension immediately adjacent to the Capitol building, requiring deep excavations, about 12.2

m (40 ft) below the ground surface. Historic preservation and protection of the Capitol building against damage during construction required establishing extraordinarily limiting movement criteria for the building, consisting of a maximum settlement of 6.4 mm (0.25 in.) and maximum distortion between adjacent columns of L/2000, or 2.5 mm (0.1 in.).

The deep excavation was designed to be supported by a permanent concrete diaphragm wall. However, the soils between the diaphragm wall and the Capitol building required improvement. Jet grouting was considered a feasible approach for it allowed excavations to be made in improved soils immediately adjacent to the sensitive Capitol foundations, an undertaking that would not have been permissible in soils in their natural state. The design and construction requirements for the jet grouting operation are listed in Table 1.

Table 1. Jet Grouting Requirements

Parameter	Requirement
1. Contractor	Experienced, Specialty Contractor
2. Grouting Method	Triple Fluid Jet
3. Column Diameter	0.9-1.2 m (3-4 ft)
4. Column Overlap	Minimum 152 mm (6 in.)
5. Unconfined Compressive Strength	Minimum 5.5 MPa (800 psi)
6. Grouting Parameters Verification	Test Column Installation
7. QA/QC During Construction	Grout/Column Sampling and Testing
8. Foundation Movement	Maximum 6.4 mm (0.25 in.)

The site soils consist of Coastal Plain deposits. A typical stratigraphy is about 6.1 m (20 ft) of primarily loose to very dense clayey and silty sand with gravel underlain by more than 18.3 m (60 ft) of firm to very stiff low to high plasticity clay containing sand lenses. Jet grouting, however, was limited to soils in the upper 7 m (23 ft). The Capitol building and the jet grout columns layout are shown in Figure 1.

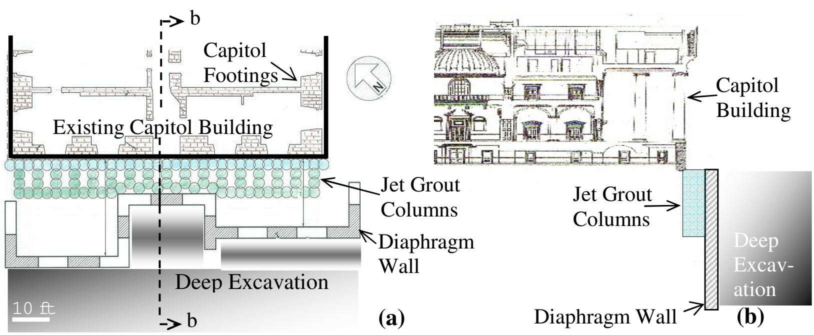

FIG. 1. Jet grouting locations in (a) plan view and (b) cross-section.

CONSTRUCTION

Jet grouting operations started by installing several test columns to different depths, using varying grouting parameters. Samples of neat cement grout and "wet grab" mix were obtained during test column installation for laboratory testing. Samples of the jet grout columns were also obtained using coring techniques, once the test columns had sufficiently cured, which was typically about one week after installation.

The coring also provided an opportunity to visually observe the uniformity of the mixing within the grout columns. Subsequent to coring, the columns were partially or fully exhumed for further observations and measurements of the column geometry. The mixing appeared reasonably homogeneous, except in the high plasticity clay zones where relatively large chunks of clay were present in the mix. The laboratory unconfined compressive strength results on test column samples indicated mixed results, with strengths varying quite considerably, in the range of about 1.4 to 6.2 MPa (200 to 900 psi). The difference was mainly attributed to testing of various materials containing primarily clay or primarily sand and gravel, as wells as materials with varying degrees of mixing homogeneity.

Based on field observations and laboratory test results, final grouting parameters were established for the production phase, as shown in Table 2.

Table 2. Jet Grouting Parameters for Production Phase

Grouting Parameters	
Lift Rate	1.3 ft/min
Flow Rate	40 gpm
Rotation	17 rpm

Pressure Demands	
Water	6,000 psi
Air	100 psi
Grout	150 psi

A total of 110 columns were installed in a period of about 3 weeks. Typical column length and diameter was 7 m (23 ft) and 0.9 m (3 ft), respectively. The clay zones were double-cut to improve the homogeneity of the mix. Some columns were also reamed several times. Over 10% of production columns were cored for final testing and observations. Wet grab samples of the mix were taken as well. Results of the laboratory unconfined compressive strength (UCS) tests are shown in Figure 2.

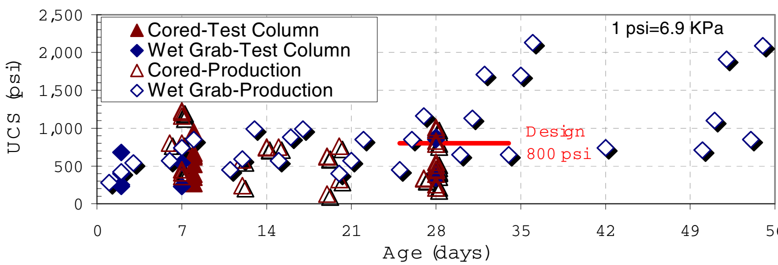

FIG. 2. Laboratory compressive strength results of jet grout samples.

As evident in Figure 2, large scatters were common in the test results, likely due to variations in method of sampling, soil type, and homogeneity of the mix. Variations are evident in condition and quality of the mix, shown in Figure 3, both in cored samples and in an exhumed test column, with clay, sand and gravel, or small voids dominating various portions of the mix. Despite the variation, observations of drilling, sampling, and the overall condition of the cores indicated sufficient mixing and strength. This was later corroborated by difficult excavation of a few jet grouted columns encountered during the diaphragm wall excavation and at other occasions when excavated using pneumatic drills.

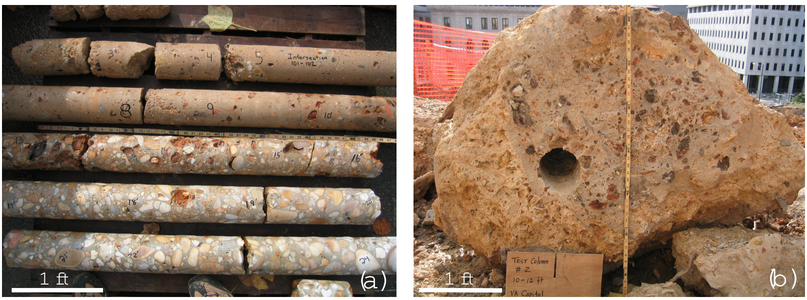

FIG. 3. Jet grouted soils (a) cored samples and (b) exhumed column.

MOVEMENT MONITORING

The extraordinary and limiting movement tolerances for the project required monitoring all phases of construction on a continual basis, including monitoring of the jet grouting. A real-time, automated instrumentation system was used for monitoring. It consisted of total station theodolites, optical prisms, in-place inclinometers, temperature sensors, and a data acquisition system. An example of settlement monitoring at one of the building columns is shown in Figure 4.

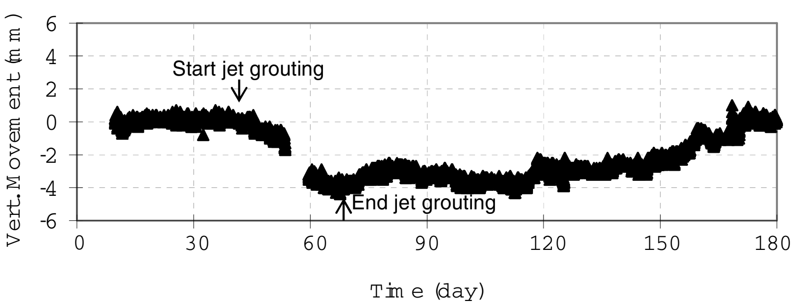

FIG. 4. Foundation movement monitoring.

The instruments proved extremely useful in monitoring of the construction. During an episode of jet grouting, the instruments issued an alarm rather unexpectedly. A movement of 4.3 mm (0.17 in.), or about 70% of the maximum allowable, was measured for some foundations, although, it was unclear whether this was entirely due to the jet grouting operation. The movements for one of the affected foundations are shown in Figure 4.

The monitoring results prompted taking additional measures to prevent such occurrences from repeating, and as evident in Figure 4, further foundation movements ceased and the unexpected movements were all but recovered. The additional measures included increasing the distance between columns installed in one day, limiting the number of columns that could be installed in one day per area, and more rigorous monitoring.

CONCLUSIONS

Jet grouting provided a successful ground improvement alternative and excavation retention for the renovation of the historic Virginia State Capitol building. The success is owed to detailed knowledge of the soils and the project, early involvement of an experienced, specialty contractor; calibration of grouting measures with site specific soils, and detailed verification and monitoring. Jet grouting was found to be most effective in improving granular soils, although clayey soils were similarly improved, however, requiring greater effort. Jet grouting operations are highly site-specific and their performance must be calibrated with the site soils and verified. QA/QC during initial testing and construction is paramount, particularly monitoring of grouting near sensitive structures for movement. Caution should be exercised when grouting near sensitive foundations for movements can develop unexpectedly. The latter confirms the important role of geotechnical instrumentation, especially real-time monitoring, when warranted by the degree of project complexity and movement tolerance that is specified. It goes without saying that the more restrictive the movement tolerances, the greater the required redundancy in design, the more comprehensive the testing and QA control, and the more extensive the monitoring.

ACKNOWLEDGEMENT

The author greatly acknowledges the support and cooperation from the Virginia Department of General Services.

Performance Expectations of Early 20th Century Urban American Building Foundations

Debra Laefer[1], M. ASCE

[1] Director of Conservation Research, School of Architecture, Landscape and Civil Engineering, University College Dublin, Newstead, Room G25, Belfield, Dublin 4, Ireland debra.laefer@ucd.ie

ABSTRACT: Foundation reuse is a tricky business at the best of times. For structures predating the mid-20th century, the challenge is exacerbated by the presence of a variety of foundation types, techniques and materials no longer in current usage, such as lime-based mortar. Accordingly, the modern engineer is presented with the difficulty of making decisions about assessment and intervention strategies for construction systems, geometries, and methods for which there is no applicable current building code or easily accessible textbook. As foundation reuse, particularly of early 20th century urban buildings, gains in popularity, accessing such information will only gain in criticality. This paper was designed to help amalgamate such information and provide upper limits regarding performance expectations of such foundations based on the building codes, practices and testing data of the early 1900s, with a typical upper compressive strength of 10MPa for hard brick in lime.

INTRODUCTION

Prior to the 20th century, foundations, unlike many architectural elements, remained largely undocumented. They are not the subject of coffee table books or extensive scholarly treatises that delve into their origin, development, or geographic distribution. Existing written documentation, sparse at the time of construction, is largely now out of print and generally inaccessible. Furthermore, existing foundations are for all intents and purposes invisible, until critical information about them is needed. This paper is an attempt to begin to rectify this deficit in the literature. For geotechnical engineers, the importance of such knowledge relates mostly to issues of tunneling, adjacent excavation, underpinning, and most recently foundation reuse.

BACKGROUND

Foundation reuse is slowly gaining popularity in the United States (Strauss et al. 2007, Laefer and Manke 2008). Already a major topic in Europe, drivers related to cost, sustainability risk, and historic preservation are creating additional incentives for foundation reuse within the American market (Figure 1). Demarcations closer to the center of the targets represent stronger drivers than those either unmarked or located towards the outsides of the various target centers.

FIG. 1. Drivers for foundation reuse (adapted from Strauss et al. 2007)

Foundation reuse may take a variety of forms from simply adding additional load to an existing structure due to a usage change (e.g. from residential to commercial) to the entire removal of the above ground structure and construction of a larger, heavier structure (Laefer and Manke 2008). Before an assessment can be made as to the viability of foundation reuse or even the development of a testing plan, the engineer must know the foundations' composition, probable layout, and initial load capacities.

Each of these aspects presents major challenges, especially in light of the fact that original drawings (to say nothing of as-built records) rarely exist. To gauge the magnitude of the problem (composition, layout and/or capacity), even in the more regulated area of bridges, the vast majority of the structure's foundations are unknown. According to North Carolina's Department of Transportation (NCDOT), knowledge is lacking as to the type, geometry, and material of the foundations for over half of NCDOT's more than 13,000 bridges (Kim 2003).

CONTRIBUTING FACTORS

By using historical records, if it can be shown that the existing foundations are inadequate or of highly limited potential, an expensive, field testing program may be avoided with respect to determine their modern performance potential. Assuming no age-based, water-related, or chemically induced degradation, the maximum load bearing capacity of existing foundations is dependent mainly upon three things: (1) the original assumptions about capacity, (2) the foundations' in situ geometry, and (3) the original composite strength of the foundation material.

Original Capacity Assumptions

By the time of Kidder's watershed publication in 1916, American states as far east as New York and as far west as Oregon had in place guidelines, if not regulations, on allowable loads based on apparent soil type. Although, the categories are not congruent with currently used soil classification systems, strong trends about allowable loads readily emerge (Table 1).

Table 1. Allowable loads (kPa) on foundation beds (data from Kidder 1916)

Character of Foundation-bed	VA	MN	PA	GA	OR	KY	NY	MN	OH	MO	CA
Alluvial soil					48						
Firm dry loam		287		192-287		239	287				287
Soft clay	96	96		96			96	96			96
Ordinary clay								192			
Good solid natural clay										287	
Clay in thick beds, always dry									383		
Clay in thick beds, moderately dry									192		
Firm dry clay	287	287		192-287		239	287				287
Hard clay	383	383		287-383		383	383	383			383
Dry hard clay		335		383							
Ordinary clay & sand together in layers; wet & spring	192	192		192			192				
Moderately dry clay & sand					287						
Stratified clay & stone									383		
Quicksand					48						
Wet sand								96			
Fine sand, firm & dry	287	287		192-287	383	239	287				287
Clean dry fine sand									192		
Dry sand								287			
Coarse compact sand									383		
Firm coarse sand								383			
Very firm coarse sand	383	383		287-383		383	383				383
Stiff gravel	383			287-383		383	383				
Firm gravel		383									
Cemented gravel			575								
Sand loose gravel			335								
Compact sand & gravel									479		
Compact sand & gravel, well cemented									766		
Firm coarse sand & gravel								575			
Gravel & coarse sand, well cemented					766						
Hard-pan							0-1436				
Hard shale, unexposed											1915
Rock					766						1915

The values listed in Table 1 were used in conjunction with allowable loads for certain building types. Although knowledge of the anticipated load does not specifically preclude significant over-designing, there would need to be additional evidence to justify a capacity greater than the anticipated load multiplied by some safety factor.

Typical anticipated live loads were 0.24-0.48 kPa for household and office furniture, 0.48-4.80 kPa for safes, bookcases or filing cases, and 1.20 kPa for dry good stock (applied to 50% of the floor area) [Kidder 1916]. Dead load was largely based on the wall width with 55 kg/m attributed to a 0.10m thick wall, 118 kg/m for a 0.20m thick wall and 179 kg/m for a 0.31m thick wall. Kidder further generalized this for 11 cities as a percentage of building loads (Table 2).

Table 2. Generalized footing design loads for 11 cities (after Kidder 1916)

Load	Percentage of Building Load (%)
Live	50
Wind	40
Dead	100

The allowable compressive loads are dependent upon the specifics of the brick and mortar being used, and the city in which the structure was constructed (Table 3). According to other data collected by Kidder (1916), within a certain class or type of brick, the allowable loads were generally a quarter to a third higher for eastern states than western states). Rationale is not given but may be reflective of more modern and, thus, hotter kilns in the East (for more information on kiln development in the U.S., see Laefer et al. 2004). An alternative set of allowable capacities was presented a decade earlier by Mitchell and Mitchell (1904), where stocks is another term for brick. Similar to present-day design, the allowable loads differed from the ultimate loads, as discussed in the following section.

Table 3. Comparison of building laws for allowable compressive loads (kPa)

Materials	Boston 1909	Buffalo 1909	Chicago 1914	Denver 1898	New York 1906	Philadelphia 1914	St. Louis 1907
Hard-burned brick in Portland cement mortar	1,915	1,149	2,059	-	1,436	-	2,059
Hard-burned brick in natural cement mortar	1,724	862	958	862	-	1,436	-
Hard-burned brick in cement and lime mortar	1,149	-	-	-	1,101	1,149	1,101
Hard-burned brick in lime mortar	766	575	622	766	766	766	1,053
Pressed brick in Portland cement	-	1,149	-	-	-	-	-
Pressed brick in natural cement	-	862	-	1,149	-	-	-

Table 4. Allowable compressive loads for masonry (Mitchell and Mitchell 1904)

Mortar composition	Proportions	Age (mo.)	Safe load (kPa)
Grey chalk lime : sand	1:2	6	239
Lias lime : sand	1:2	6	478
Lias lime : river ballast	1:6	12	1,436-1,915
Rubble masonry in Lias lime	1:6	12	383
Portland cement : sand (with well burnt stocks)	1:1	3	766
Portland cement : sand (with hard stocks)	1:1	3	958

Original Composite Strength

Lead, natural cements, seashells, and grog (in the form of broken or crushed terra cotta or brick) are just a few of the materials that may be found in historic foundations. By the early 20^{th} century, at least in urban areas, most of the foundations were of brick, either dry-laid or set in a lime-based or cement-based mortar. Alternatively, natural stone or some type of concrete existed, but the most common by was brick in a lime or lime/cement mortar. As early as the 1880's, a variety of large and small scale tests were conducted to understand how various brick and mortar component strengths contribute to the ultimate strength. Additionally, similar to modern concrete, bricks were manufactured with a wide range of resulting capacities. The compressive strength of the mortar is usually substantially less than that of the brick. The final masonry strength, however, is considered to be an intermediate value between that of the mortar and brick. To calculate this intermediate strength, a brick assemblage is tested and equation (1) is used to predict its strength:

$$f_p' = \frac{\left[f_{cb}' \cdot \left(f_{tb}' + \alpha \cdot f_j'\right)\right]}{\left[U_u \cdot \left(f_{tb}' + \alpha \cdot f_{cb}'\right)\right]} \qquad (1)$$

where f'_p=the composite strength, f'_{cb}=the compressive strength of a masonry unit, f'_{tb}=the tensile strength of a masonry unit, f'_j=the mortar strength, U_u=a non-uniformity factor, and a=j/(4.1*h), where j=mortar thickness and h=masonry unit thickness. The compressive strength-strain relationships for the brick, mortar and combined assemblage are depicted in Figure 2. The resulting composite strength is between the masonry unit's compressive strength and the mortar's (Figure 2).

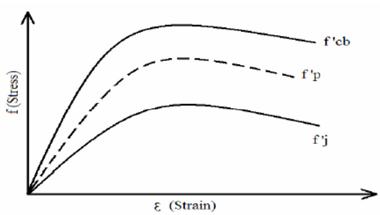

FIG. 2. Comparison of brickwork, brick, and mortar strengths (after Hilsdorf 1969)

A sampling of masonry testing that was contemporary with the structures of interest is provided in Tables 5 through 7. As described above, the mortar and bricks both contribute to the final capacity. As indicated by its greater hardness, higher density, and lower absorption, bricks that were more fired were inherently stronger. Bricks marked as salmons were the least-fired bricks available on the market and were of a class usually reserved for non-structural work. Additional component data can readily be found in Richardson (1897), Cummings (1897), and Stang et al. (1929).

Molitor (1899) published the results of some pier tests that used extremely high strength brick for the period (f'_c ranging from 95-134 MPa, where brick up to an order of magnitude lower in compressive strength was not unusual). Depending upon pier height and contributing material, most piers tested at 6.9-13.8 MPa, when using a variety of mortars with compressive strengths of 0.7-1.4 MPa.

Table 5. Pier capacity (MPa) as a function of mortar composition (Anon 1907)

	Water struck Rochester, NH Hard	Water struck Rochester, NH Salmon	West Cambridge Hard	West Cambridge Salmon	East Brookfield Hard	East Brookfield Salmon
Neat cement	31.4	12.8	32.4	10.4	13.6	7.3
Cement 1:3	23.6	10.8	12.4	10.5	12.4	8.4
Lime 1:3	6.6	4.5	6.9	5.0-5.6	5.0-6.2	3.2

Table 6. Strength of piers based on brick class and mortar types (Keele 1908)

Brick Manufacturer	Class	Absorption % by weight	Brick crushing (MPa)*	Pier in lime mortar (MPa)^	Pier in cement Mortar (MPa)^
Kingston	Best	-	-	-	17.6
	First class	11.9	26.1	3.8	10.5
	Second class	14.9	11.9	-	5.8
	Third class	17.1	12.8	2.0	-
Carlton Clinker	Best	12.7	39.2	4.2	16.6
	First class	16.4	22.0	3.7	15.7
	Second class	-	-	-	7.2
Yorkville	First class	22.7	32.0	3.5	7.3
	Second class	26.7	22.0	2.7	8.1
Humber	First class	12.6	10.0	2.4	-
	Second class	16.7	12.0	2.0	5.6
Don Valley	First class (buff)	9.3	37.0	4.7	7.0
Pressed	Second class (buff)	9.7	24.6	8.4	-

*Two whole bricks tested flat with a thin Portland cement bedding material; lime mortar 1:2 lime:sand mortar f'c=0.5MPa at 2.5 months ^Piers of various heights 8"x8" or 9"x9" in area

Table 7. ASCE 1887-88 Pier Test Data (as reported by Street and Clark 1896)

Brick type	Brick f'c (MPa)	Pier f'c (MPa)	Mortar type	Height (m)	Age (mo.)
Common	8.1	11.6	1:2 PC:S	3.1	24.0
Common	8.1	12.3	1:2 PC:S	3.0	24.0
Face	6.1	13.8	1:2 PC:S	3.0	23.5
Face	6.1	13.8	1:2 PC:S	2.0	20.0
Face	6.1	22.4	1:2 PC:S	0.6	18.5
Bay State	5.0	10.0	1:2:6 PC:LM:S	1.9	20.5
Bay State	5.0	12.1	1:2 PC:S	1.8	20.0
Bay State	5.0	11.0	1:2 PC:S	1.8	20.0
Bay State	5.0	8.7	1:2 PC:S	1.9	20.5
Bay State	5.0	14.5	1:2 PC:S	1.8	19.5

PC = Portland cement, S=sand, LM=lime

Foundation Geometry

Similar to present-day delineations, traditional foundations can be classified as either shallow or deep. A primary distinguishing feature between historic foundations and their more modern counterparts is that there is a greater likelihood of the older foundations to be discontinuous. This is true with respect to both a higher reliance on individual pillars and to a lack of continuity along a strip footing, in which a present-day engineer would expect to see a continuous element (Figure 3). The dimensions of such foundation elements were heavily influenced by local practice and soils. As per

Mitchell and Mitchell (1904), however, typical footing widths were 2.4-2.8 times of the brick wall or pier, whereas, Braley (1947) later lists the minimum width as 2:1, as does Garrett (1948) but only as a minimum. By the second decade of the 20th century, wall thicknesses were well regulated for commercial structures (Table 8).

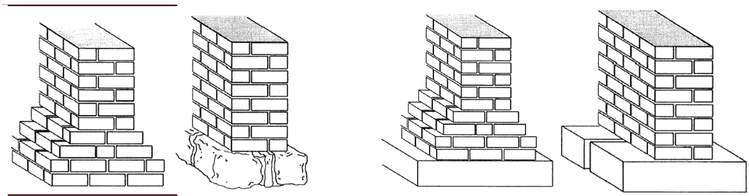

(a) Corbelled brick (b) Ashlars (c) Corbelled brick with continuous concrete slab (d) Uncemented paving stones

FIG. 3. Typical early 20th century foundations (Laefer 2001)

Table 8. Required wall width per 1916 building codes for commercial structures (data from Kidder 1916)

City	First Floor	Second Floor
New York, Minneapolis, Chicago	304mm	304mm
New Orleans, Denver	330mm	330mm
Boston	406mm	304mm
San Francisco	432mm	330mm
St. Louis	457mm	330mm

For 2-story structures, Kidder (1916) further reported that the Chicago Building Ordinance for residences, tenements, hotels and office buildings required a thickness of 304mm for the basement and first floor walls, with 203mm for the 2nd floor walls. For one-story buildings, wall thicknesses of only 304mm and 203mm, respectively, were required for the basement and first floor walls, with or without basement (Kidder 1916). For all buildings, the cellar and basement wall thickness increased with building height (Table 9).

Table 9. Required basement/cellar wall thickness in Chicago (after Kidder 1916)

Building Stories	Dwellings, hotels, etc (mm)	Warehouses (mm)
Two	304 or 406	406
Three	406	508
Four	508	610
Five	610	711
Six	711	813

CONCLUSIONS

For early 20th century American building, conservative assumptions about foundation capacities would be that foundation widths are twice the thickness of ground floor walls. This assumes walls of medium hard brick in lime mortar, with an upper bound compressive strength of 10MPa. More typical values are half this, with strengths on the west coast being lower than those in the east. For design purposes considerations of degradation caused by water, chemical, aging, and repetitive loading may also have to be considered.

REFERENCES

Anon. (1907). "Strength of Brick and Brick Piers." *Brickbuilder*, 16 (4) 62-65.

Braley, E.L. (1947). *Brickwork: A Comprehensive Treatise on the Theory and Practice of the Handicraft of the Bricklayer*, Pitman & Sons Ltd., London.

Cummings, U. (1897). "Mortar and Concrete: American Cement." *Brickbuilder*, 6 (1) 11-13.

Garrett, A.J.W. (1948). *Brickwork Including Its Bond, Manufacture and Material Used in Connection Therewith,* Crosby Lockwood and Son Ltd., London.

Hilsdorf, H.K. (1969). "Investigation into the Failure Mechanism of Brick Masonry Products Designing". Johnson F B (Ed.), *Engineering and construction with masonry products.* Gulf Publishing, Houston, TX.

Keele, J. (1908). "Brickwork Masonry." *Applied Science (Incorporated with the Transactions of the University of Toronto Engineering Society)*, 2 (2), 69-78.

Kidder, F.E. (1916). *The Architects' and Builders' Pocket-Book*, John Wiley and Sons, Inc., New York.

Kim, K.J. (2003). Personal communication with Senior Geotechnical Engineer of the North Carolina Department of Transportation. March 13.

Laefer, D.F. (2001). *Prediction and Assessment of Ground Movement and Building Damage Induced by Adjacent Excavation*. PhD Thesis Univ. of Illinois. pp. 803.

Laefer, D.F., Boggs, J., and Cooper, N. (2004). "Engineering Properties of Historic Brick – Variability Considerations as a Function of Kiln Type." *J. American Inst. Conservation of Historic and Artistic Works*, AIC Fall/Winter 43 (3) 255-72.

Laefer, D.F. and Manke, J. (2008). "Building Reuse Assessment for Sustainable Urban Reconstruction." *J. Construction Eng. and Mgmt*, ASCE 22 (2) 10 pp.

Mitchell, C.F. and Mitchell, G.A. (1904). *Brickwork and Masonry. A Practical Text Book for Students, and Those Engaged in the Design and Execution of Structures in Brick and Stone,* B.T. Batsford Ltd., London.

Molitor, D. (1899). "The Present status of engineering knowledge respecting masonry construction." *Trans. Assoc. Civil Engineers of Cornell Univ.,* 7, 102-34.

Richardson, C. (1897). "Lime, Hydraulic Cement, Mortar, and Concrete." *Brickbuilder*, 6 (4), 78-79.

Stang, A.H., Parsons, D.E. and McBurney, J.W. (1929). "Compressive Strength of Clay Brick Walls." *Bureau of Standards J. Research*, 3 (108), 507-71.

Strauss, J., Nicholls, R., Chapman, T. and S. Anderson. (2007). "Drivers affecting the frequency of foundation reuse and the relevance to U.S. Cities". *Geo-Denver 2007: New Peaks in Geotechnics*. Ed. H. W. Olsen, ASCE. Reston, VA: ASCE, 0-7844-0897-1.

Street, W.C. and Clark, M. (1896). "Brickwork tests. Report on the first series of experiments." J. Royal Inst. British Architects, 3 (2) April 2, 333-44.

Sustainable Design Concepts and Galvanized MSE Reinforcements

Robert A. Gladstone[1], M. ASCE, P.E., Kenneth L. Fishman[2], M. ASCE, Ph.D., P.E. and Thomas J. Langill[3], Ph.D.

[1]Executive Director, Association for Metallically Stabilized Earth, P.O. Box 9142, McLean, VA 22102-0142; bobgladstone@amsewalls.org
[2]Principal, McMahon & Mann Consulting Engineers, P.C., 2495 Main Street, Suite 432, Buffalo, NY 14214-2154; kfishman@mmce.net
[3]Technical Director, American Galvanizers Association, 6881 S. Holly Circle, Suite 108, Centennial, CO 80112-1145; tlangill@galvanizeit.org

ABSTRACT: Mechanically Stabilized Earth (MSE) structures have been constructed in the United States since 1971 using galvanized steel soil reinforcements. Their excellent structural performance, reliability, and economy fit well with the concept of sustainable design and development. Performance data, and inferences based on results from reliability analyses, indicate that reliability of the design is significantly improved when using galvanized reinforcements compared to plain steel reinforcements.

INTRODUCTION

This paper discusses Mechanically Stabilized Earth structures in the context of sustainable design. MSE facing, reinforcements and backfill are reviewed, with emphasis on the sustainability benefits gained not only by using zinc to protect the soil reinforcements, but also by incorporating those galvanized reinforcements in MSE structures. Corrosion monitoring and condition assessment results from over 150 US and European projects are analyzed to explore the advantages and limitations of galvanized vs. plain steel reinforcements. Consistent with modern methods of reliability-based design, inferences from reliability analysis are employed in this comparison. The Association for Metallically Stabilized Earth provides an extensive list of references in its White Paper (AMSE, 2006); they are not repeated here due to space limitations, but are available by downloading the White Paper from www.amsewalls.org.

SUSTAINABLE BENEFITS OF GALVANIZED STEEL

Materials – Steel and Zinc

Steel is the most commonly used construction metal and over 50% of the steel produced in the last 50 years has been recycled into new steel products (Steel Recycling Institute, 2007). Today, more than 66% of the steel produced in North America is from recycled steel. This percentage will rise as new steel processes consume more recycled steel as their feed stock. This valuable construction material is protected by hot-dip galvanizing, a process that metallurgically bonds a layer of zinc to the surface of the steel, dramatically increasing the steel's service life. Zinc is fully recyclable and can be reclaimed from both scrap and end-product recycling (International Zinc Association, 2007), with over 30% of the zinc produced in the world coming from recycled material. Steel reinforcements for MSE structures are hot-rolled primarily from recycled steel, and are corrosion-protected by hot-dip galvanizing.

Environmental, Economic and Social Impacts of Zinc

Zinc is the 27th most common element in the earth's crust and all living organisms require zinc to function correctly. In humans, zinc supports proper functioning of respiratory, cognitive, reproductive, and digestive processes. Since too much zinc can be toxic, zinc toxicity must be balanced against zinc deficiency when assessing its environmental impact. Efforts are underway in Europe to perform an environmental risk assessment on zinc metal (http://ec.europa.eu/food/fs/sc/sct/out197_en.pdf). The environmental impact of zinc specifically from fabrication of MSE reinforcements is minimal, however, since only a small amount of zinc is required to produce long-term corrosion protection of steel and zinc emissions from the galvanizing process are low.

Galvanization reduces construction costs by extending the service life of a steel member and by reducing the need for sacrificial steel (steel in excess of that required for structural function, provided solely to allow corrosion to occur without loss of the structurally-required section). The cost savings derives from both the reduced steel consumption and the energy savings associated with that reduced steel quantity. In contrast to other corrosion protection systems that are weather-dependent and have specific handling requirements, hot-dip galvanized steel can be handled like plain steel and has no weather restrictions. Therefore, construction deadlines and budgets can be better met with galvanized steel. Another significant economic benefit is reduced disruption from repair and/or replacement. Major maintenance of walls, bridges, and related highway structures interferes with traffic flow and can significantly impact local economies; galvanization dramatically reduces the need for such repair and replacement by extending the life spans of structures.

MSE WALL APPLICATIONS, COMPONENTS, PERFORMANCE/BENEFITS

Applications

MSE structures with galvanized steel reinforcements (Fig. 1) are used throughout the United States. The first was constructed in 1971 on California Highway 39 in the Angeles National Forest (Walkinshaw, 1975); many have been in continuous service over 30 years. The reasons are the structural performance, economy, sustainability and reliability of MSE technology. Within the civil works infrastructure, MSE retaining walls and bridge abutments are a standard construction methodology for highway, mass transit and railroad, airport, port, waterfront, industrial, commercial and residential projects. Specifications for highway and most other MSE structures are derived from the AASHTO Bridge Specifications (AASHTO, 2004).

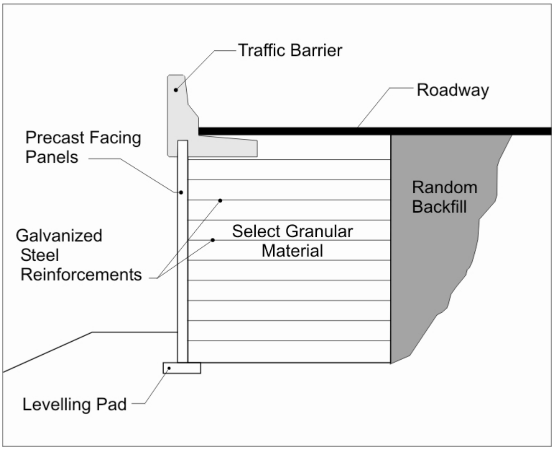

FIG. 1. Typical Section of an MSE Highway Retaining Wall

While many structures are typical "ordinary" retaining walls and bridge abutments 4-10 m high, some are extraordinary load-carrying and load-distributing structures such as the 43 m high runway- and aircraft-supporting MSE wall at the extremely environmentally-sensitive Seattle-Tacoma International Airport (Sankey et al, 2007). Yet all MSE structures are built from the same three basic components – prefabricated concrete face panels, galvanized steel reinforcements and granular backfill – each of which offers its own sustainability benefits (discussed below) while also contributing to the sustainability of the whole system. MSE wall manufacturing and construction processes are largely independent of seasonal and weather fluctuations, allowing projects to run faster, smoother and more energy-efficiently. For highway structures, and for larger and/or structurally-significant non-highway structures, galvanized steel-reinforced MSE offers both speed and economy (compared to cast-in-place concrete construction), characteristics that contribute to environmental sustainability.

MSE Structure Components

Precast Concrete Facing Panels

The thin (14 cm) MSE facing panels are manufactured in controlled, factory-like facilities and require less energy for fabrication and installation than is required for the three-to-nine-times thicker face of a cast-in-place concrete wall. Installation of panels and other components can be carried out from the backfill side of the wall, minimizing the impact on the surrounding environment. Facing panels are made in a variety of shapes and architectural treatments, allowing MSE walls to visually blend with their surroundings. In addition, if an MSE wall is ever deconstructed, the thin panels are easily rubblized and recycled.

Galvanized Steel Soil Reinforcements

Steel reinforcements for MSE structures (strips, grids, wire mesh) are inextensible, have high strength and are hot-dip galvanized according to ASTM A123 (86 µm of zinc per side) (ASTM, 2004). When embedded in the specified granular backfill, discussed below, they undergo very low strains under load and do not pull out, assuring predictable structure behavior and long-term internal stability. When the backfill has the required electrochemical properties, as discussed below and listed in Table 1, galvanized steel reinforcements offer a service life of 75-100 years or more. Fabricated from 100% recycled steel before being hot-dip galvanized, MSE reinforcements are themselves recyclable, including full recovery of any zinc remaining on the deconstructed steel.

Backfill

Backfill for MSE walls is natural or quarried granular material, typically specified to have a top size of 4 in, 0-60% passing the No. 40 sieve, 0-15% passing No. 200, PI $\leq$ 6, and an angle of internal friction $\geq$ 34º. This material also must conform to soundness (durability) and electrochemical requirements, assuring the long-term stability of MSE structures. Placement and compaction of most MSE backfills is fast and energy-efficient, typically requiring little or no application of water and as few as 3-4 passes of a vibratory roller. In addition, compared to finer-grained material used behind other wall types, granular backfill requires less energy to place and compact and is easily reused if a wall must be deconstructed.

Performance/Benefits

The Federal Highway Administration's construction challenge to "Get in, Get out and Stay out," is met by MSE construction. An MSE structure can be built correctly and economically the first time, with little need for rework, and it can be relied upon to perform structurally throughout its design life. Compared to cast-in-place techniques, MSE technology uses smaller construction material quantities and fewer, smaller pieces of construction equipment, creating less noise and exhaust pollution during the relatively shorter time of construction. These beneficial characteristics of MSE structures derive from the simple, repetitive construction process, low initial cost, prefabricated components and low maintenance requirements.

Nearly four decades of in-service performance have proven that MSE structures distribute loads over varying foundation conditions, accommodate differential settlement, withstand seismic loading without loss of structural function and can be constructed quickly and economically. The greatest single benefit, however, is the longevity and the extraordinary durability of MSE structures and the confidence that these structures will continue to perform as designed throughout their design life. This confidence derives from the well-developed design philosophy for MSE structures, supported by the extensive performance documentation now available (AMSE, 2006).

DOCUMENTED PERFORMANCE OF GALVANIZED MSE REINFORCEMENTS

Overview

The approach to metal loss has been to calculate the expected loss of both zinc and steel during the design life, then to add sufficient sacrificial steel to the reinforcement cross section to ensure the end-of-design-life allowable stress condition. Table 1 describes the metal loss model recommended for design of MSE structures by AASHTO and the corresponding backfill requirements. Significant efforts have been devoted to documenting the performance of in-service reinforcements and to verifying the reliability of this and other models used in design.

Table 1. AASHTO Metal Loss Model and Backfill Requirements

Metal Loss Model		**Backfill Requirements**	
Component Type (age)	Loss (µm/yr)	pH	5 to 10
		Resistivity	≥ 3000 Ω-cm
Zinc (< 2 yrs)	15	Chlorides	< 200 ppm
Zinc (> 2 yrs)	4	Sulfates	< 100 ppm
Steel (after zinc)	12	Organic Content	< 1%

Sources of Performance Data

AMSE (2006) and Gladstone et al (2006) describe worldwide sources of performance data depicting metal loss from both laboratory and field studies. Data has been collected by the industry in both the United States and Europe, including from many U.S. state transportation agencies. Existing performance data have been archived into a database as part of an ongoing research effort sponsored by the National Cooperative Highway Research Program under the auspices of NCHRP Project 24-28, *"LRFD Metal Loss and Service-Life Strength Reduction Factors for Metal Reinforced Systems in Geotechnical Applications"* (NCHRP, 2006). The database includes information from 160 MSE projects and incorporates more than

2000 electrochemical measurements and more than 400 direct observations of reinforcement condition.

Sustainability of Zinc & Steel

Existing performance data indicate that, for select backfill conditions meeting current AASHTO criteria, the mean corrosion rate for galvanized elements that have been in-service for more than two years is approximately 0.75 μm/yr, with a corresponding coefficient of variation (COV) of 45%. Sample statistics for plain steel reinforcements depict a mean corrosion rate of approximately 9 μm/yr and a rather high COV of approximately 120%. This indicates that corrosion is less variable for galvanized reinforcements than for plain steel, which has an important impact on the reliability analysis. Also, because these observations are from linear polarization resistance measurements, which reflect the average rate of metal loss over the total surface area of the reinforcement (Lawson et al, 1993), a factor of two is applied to the mean corrosion rates for steel to account for localized corrosion.

Modern methods of design, including Load and Resistance Factor Design, incorporate reliability concepts and utilize information on the probability of exceeding estimated metal loss. Thus, it is important to recognize the relationship between sacrificial thickness and the probability of exceeding estimated metal loss. Sagues et al (1998) formulated a probabilistic deterioration model for service-life forecasting of galvanized soil reinforcements. This formulation is based on the following assumptions:

1. The distribution of corrosion loss over all elements in the structure mirrors the overall distribution of corrosion measured in the field,
2. During the early life of the structure, the corrosion rate distribution reflects that of the galvanized elements,
3. Subsequent to depletion of the zinc layer, corrosion will continue at a rate that reflects the metal loss rate of plain steel (i.e., protection of the steel from residual galvanization is not considered),
4. The highest rate of metal loss takes place in the region of maximum reinforcement stress and the service life of a given element is over when the sacrificial steel in the highest stressed region is consumed, and
5. Corrosion rates are constant with time.

Figure 2 depicts the probability of exceeding estimated metal loss for galvanized and plain steel elements computed using the Sagues model applied to sample statistics from performance data described in the preceding paragraphs. This analysis considers a design life of $t = 75$ years and the standard initial zinc thickness, z_i, of 86μm per side, and the measurements of corrosion rate for plain steel samples are multiplied by a factor of two as discussed above. Based on analysis of the data, the distribution of corrosion rates for galvanized and plain steel reinforcements are considered as normal and lognormal, respectively.

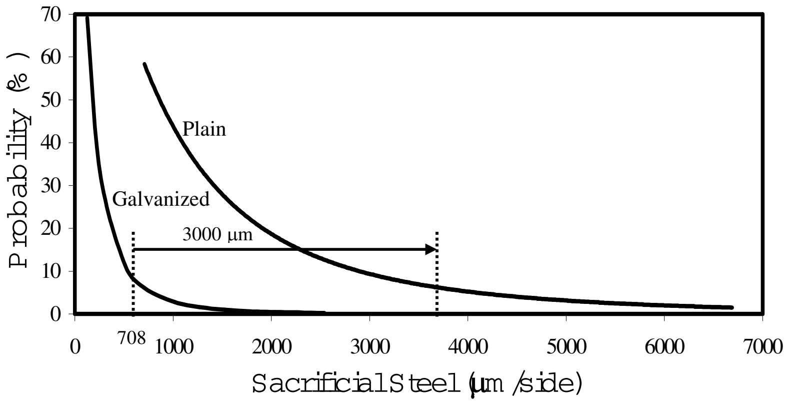

FIG. 2. Probability of exceeding estimated metal loss for plain and galvanized reinforcements; t = 75 years, z_i = 86 μm/side.

The distance between the two curves in Figure 2 represents the additional sacrificial steel that must be added to plain steel reinforcements to provide the same probability of exceeding the estimated metal loss as is provided by the galvanized reinforcements. For example, according to the ASSHTO model, for a 75-year design life, 86 μm of zinc per side will last at least 16 years and, considering the remaining 59 years, 708 μm of sacrificial steel must be added to each side to achieve the 75-year life. Given the sample statistics, this renders approximately a 6% probability that the estimated metal loss will be exceeded. According to the data in Figure 2, approximately 3000 μm of steel (in addition to the 708 μm already considered) must be added to a plain steel element to achieve the same probability. Thus, a typical 4 mm thick galvanized reinforcement needs to be approximately 2.5 times as thick if designed as a plain steel reinforcement.

The information presented in Figure 2 is sensitive to the data variances and these data are considered preliminary. Field data from plain steel reinforcements are mainly from coupons that were less then two years old (as older walls were wired for monitoring, coupons were installed as a basis for comparison with galvanized reinforcements). As more data are collected from older steel coupons, lower mean rates and less variation will be observed.

CONCLUSION

Zinc is a broadly useful material and produces little impact on the environment during the manufacturing of MSE reinforcements. Although galvanized reinforcements contribute to sustainable design of MSE structures, construction efficiency and the use of other natural materials are also important contributing factors. As more data on the in-service performance of MSE structures are collected, the benefits of using galvanized compared to plain steel reinforcements are better quantified. Inferences from reliability analyses provide better information on the expected performance of galvanized versus plain steel reinforcements compared to the previous practice of comparing mean corrosion rates.

ACKNOWEDGEMENTS

A portion of the work described herein was conducted in the National Cooperative Highway Research Program. The opinions and conclusions expressed are those of the authors and not necessarily those of NCHRP or its affiliates. The authors also thank the Association for Metallically Stabilized Earth and the American Galvanizers Association for their contributions of both intellectual property and time.

REFERENCES

American Association of State Highway and Transportation Officials (AASHTO). (2004). *LRFD Bridge Design Specifications*. Washington, D.C., Third Edition.

American Society for Testing and Materials (ASTM). (2004). *Annual Book of ASTM Standards*. Coated Steel Products, Volume 1.06, West Conshohocken, PA.

Association for Metallically Stabilized Earth (AMSE). (2006). *Reduced Zinc Loss Rate for Design of MSE Structures*. White Paper, McLean, VA. www.amsewalls.org.

Gladstone, R.A., Anderson, P.L., Fishman, K.L., and Withiam, J.L. (2006). "Durability of Galvanized Soil reinforcement: 30+ Years of Experience with MSE," *Journal of the Transportation Research Board*, No. 1975, Transportation Research Board, Washington, D.C., pp. 49-59.

International Zinc Association (IZA). (2007). www.iza.com/recycling.html.

Lawson, K.M., Thompson, N.G., Islam, M., and Schofield, M.J. (1993). "Monitoring Corrosion of Reinforced Soil Structures," *British Journal of NDT,* British Institute of Nondestructive Testing, Liverpool, England, 35(6), pp. 319-324.

National Cooperative Highway Research Program (NCHRP). (2006). Project 24-28, *"LRFD Metal Loss and Service-Life Strength Reduction Factors for Metal Reinforced Systems in Geotechnical Applications.* Transportation Research Board, Washington, D.C. www.trb.org/TRBNet/ProjectDisplay.asp?ProjectID=727.

Sagues, A.A., Rossi, J., Scott, R.J., Pena, J.A. and Simmons, T. (1998). "Influence of Corrosive Inundation on the Corrosion Rates of Galvanized Tie Straps in Mechanically Stabilized Earth Walls", *Final Report WPI0510686*, Florida Department of Transportation Research Center, Tallahassee, FL.

Sankey, J.E., Bailey, M.J. and Chen, B. (2007). "SeaTac Third Runway: Design and Performance of MSE Tall Wall," *5th International Symposium on Earth Reinforcement*, Fukuoka, Japan.

Steel Recycling Institute (SRI). (2007). www.recycle-steel.org/rates.html.

Walkinshaw, J.L. (1975). "Region 15 Demonstration Project No. 18, Reinforced Earth Construction." FHWA Final Report, Federal Highway Administration, Washington, DC.

Widening of the George P. Coleman Memorial Bridge

Jan J. Hartman [1], P.E., Frank Pepe, Jr.[2], P.E. , and Raymond J. Castelli [3], P.E.

[1] Supervising Geotechnical Engineer; PB, One Penn Plaza, New York, NY 10119, e-mail: hartmanj@pbworld.com.
[2] Assistant Vice President, Geotechnical Manager, PB, One Penn Plaza, New York, NY 10119, e-mail: pepe@pbworld.com.
[3] Senior Vice President, Principal Geotechnical Engineer, PB, One Penn Plaza, New York, NY 10119, e-mail: castelli@pbworld.com.

ABSTRACT: The George P. Coleman Memorial Bridge carries U.S. Route 17 across the York River, between Gloucester Point and Yorktown, Virginia. Construction of the original 1,143.3 m (3,750 ft) long bridge structure was completed in 1952, with 1 travel lane in each direction and with twin 150.6 m (494 ft) long swing spans at the 137.2 m (450 ft) wide navigation channel. In 1993, the Virginia Department of Transportation and its consultants completed design of a superstructure replacement project for the bridge to provide a pair of 3.7 m (12 ft) wide lanes each way with inside and outside shoulders and a center median barrier. The width of the new superstructure design was almost three times that of the original. Extensive design-phase geotechnical investigations and analyses indicated that the original open well caisson foundations supporting the two original swing spans and four adjoining piers could be reused without modification to support the significantly heavier widened superstructure. Reuse of the existing caissons eliminated much of the time, cost, and disruption of constructing new foundations or modifying the existing foundations. Construction for the $72.7M bridge widening was successfully completed by Tidewater Construction Corporation of Norfolk, Virginia in 1996. The project was honored with many awards including the 1997 ASCE Roebling Award and the 1997 ACEC Grand Conceptor Award.

INTRODUCTION

Construction of the original George P. Coleman Bridge over the York River at historic Yorktown, Virginia was completed 1952. As early as 1985 the Virginia Department of Transportation (VDOT) began studies for widening the 2-lane U.S. Route 17 bridge, which by then was already carrying nearly twice the 15,000 vehicles per day for which it was originally designed. For the widening studies and design, VDOT retained the designer of the original bridge. In 1993, Parsons Brinckerhoff Quade & Douglas, Inc. (PB) completed designs for widening the original 7.9 m (26 ft) wide 2-lane roadway to a 4 lane facility, retaining the original double swing span bridge configuration. The widened bridge provides four 3.7 m (12 ft) wide travel lanes, 0.6 m (2 ft) wide inside shoulders, 3.0 m (10 ft) outside shoulders, and a median barrier. The new superstructure is significantly heavier and almost three times as wide as the original superstructure. The approaches were also extensively redesigned to match the new four lane bridge. Figure 1 shows a general elevation diagram of the bridge. Table 1 provides a summary of the original bridge foundations from abutment to abutment.

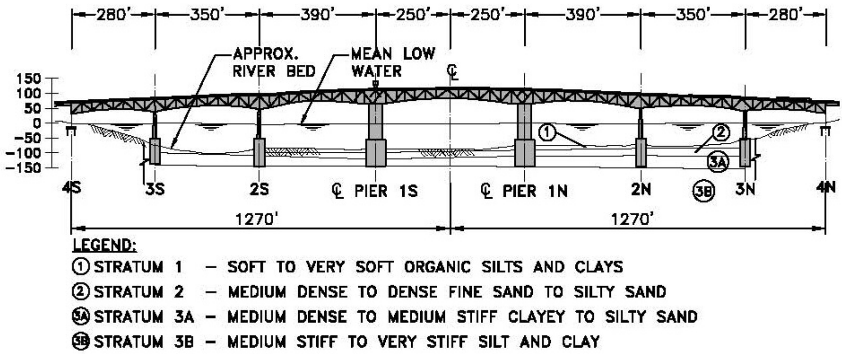

Figure 1. Elevation of George P. Coleman Memorial Bridge

Table 1. Original Bridge Foundations

Location	Foundation Type	Foundation Size	Approximate Caisson Base Elevation*
South Abutment	Cast-in-Place Concrete Piles	356 mm diam. (14 in)	N.A.
Piers 9S to 4S	Timber piles	(Varies)	N.A.
Pier 3S	Open Well Caisson	20.1 m x 12.8 m (66 ft x 42 ft)	El. -40.5 m (El. -133 ft)
Pier 2S	Open Well Caisson	20.1 m x 12.8 m (66 ft x 42 ft)	El. -43.0 m (El. -141 ft)
Pier 1S	Open Well Caisson (South Swing Span)	20.1 m x 15.9 m (66 ft x 52 ft)	El. –46.0 m (El. -151 ft)
Pier 1N	Open Well Caisson (North Swing Span)	20.1 m x 15.9 m (66 ft x 52 ft)	El. –43.0 m (El. -141 ft)
Pier 2N	Open Well Caisson	20.1 m x 12.8 m (66 ft x 42 ft)	El. –42.7 m (El. -140 ft)
Pier 3N	Open Well Caisson	20.1 m x 12.8 m (66 ft x 42 ft)	El. -40.5 m (El. -133 ft)
Piers 4N to 11N	Timber Piles	(Varies)	N.A.
North Abutment	Cast-in-Place Concrete Piles	356-mm diam. (14 in)	N.A

* Vertical datum used is National Geodetic Vertical Datum (NGVD) inferred 1972.

The project's geotechnical design included reuse of the six river caissons and widening of the on-land approach pier and abutment foundations, and design of extensive retaining walls for the bridge approach embankments. The most significant and unusual geotechnical engineering challenge of the project, however, was the evaluation of the existing caisson foundations for the six river piers to support the increased superstructure loads of the widened bridge structure without pier modifications. The challenge was even greater for the 2 main span piers of the bridge, which support the bridge's twin 150.6 m (494 ft) long swing spans, where dynamic inertial operating forces and operating tolerances of the swing span machinery and span closing mechanisms demanded even more restrictive tolerances for foundation settlement. The foundations at the approach piers and abutments were modified by adding additional piles. However, it was recognized at early stages of the widening studies that modification of the six open well caisson foundations at the river piers to increase their capacity would be difficult, costly, time consuming, and possibly unnecessary. Figure 2 provides a view of Pier 1S during a test bridge opening after installation of the new swing span.

Figure 2. Test Opening of Swing Span at Pier 1S

This paper describes the results of the geotechnical subsurface investigations and geotechnical analyses for the evaluation of the original river pier caisson foundations, and compares predicted to actual measured displacements of the caissons during original construction in 1952 and during the widening construction in 1996.

GEOLOGY OF AREA

The George P. Coleman Memorial Bridge is located approximately in the middle of the Atlantic Coastal Plain Physiographic Province. Bedrock is at a depth of more than 460 m (1,500 ft) and is overlain by thick deposits of Cretaceous and more recent ages. The materials of interest, however, are limited to the upper 200 ft of the geological profile. As shown on Figure 1, all river pier caissons bear on or near the top of medium stiff to very stiff Miocene silt and clay of Stratum 3B, locally identified as the Yorktown Formation. Water depth at the river piers varies from 16.8 m to 25.3 m (55 to 83 ft).

SUBSURFACE INVESTIGATION PROGRAM

The subsurface investigation program for the Coleman Bridge widening project included geotechnical test borings drilled from floating equipment at the six caisson foundations, along with other test borings for the land piers, approach retaining walls, and roadways. In addition to the test borings, in situ pre-bored pressuremeter (PMT) and flat-plate dilatometer (DMT) testing was performed at four of the caisson foundations to obtain additional information for improved definition of the subsurface profile. Most importantly, the in situ pressuremeter and dilatometer testing provided additional data concerning the stiffness and compressibility properties of soils at the caissons that would be especially important in forming more reliable predictions of settlement and lateral displacement of the existing foundations under the increased load of the widened superstructure. Design soil parameters determined from the in situ testing, conventional test boring data, and laboratory testing of recovered soil samples are summarized in Table 2.

Table 2. Design Soil Parameters for Foundation Analysis

Soil Properties and Parameters	Units	Soil Stratum				
		Stratum 1	Stratum 2	Stratum 3A	Stratum 3A/3B Transition	Stratum 3B
Saturated Unit Weight	kN/m^3 (pcf)	14.9 (95)	17.3 (110)	18.8 (120)	18.8 (120)	18.8 (120)
Total Strength						
Cohesion, C	kPa (psf)	0.22 Po*	---	0	---	86.2(1800)
Friction, Phi	degrees	0°	---	28°		12°
Effective Strength						
Cohesion, C’	kPa (psf)	---	0	0	---	57.4(1200)
Friction, Phi’	degrees	---	33°	34°		23°
Undrained Modulus						
Eu	MPa (tsf)	---	---	230 (2400)	---	55 (570)
Er**	MPa (tsf)	---	---	17.2 (180)	---	17.2 (180)
Consolidation						
CR	Cc/(1+eo)			0.0067	0.0098	0.0027
CC	Cr/(1+eo)	---	---	0.087	0.15	0.25
OCR	---	---	---	3.0	3.0	3.0

* Po = effective pre-construction overburden pressure

** Er = pressuremeter reload modulus

RIVER PIER CAISSON FOUNDATIONS

The foundations at the river piers consist of classic, deep, large rectangular open-well caissons. This type of largely hollow foundation was selected for the original design to minimize the load on the underlying soils. This was necessary to address settlement and bearing capacity concerns. According to Quade (1954), the net load under the caissons was limited to between 191 kPa (2.0 tsf) for vertical loads and 364 kPa (3.8 tsf) under combined vertical and horizontal wind loads. These net bearing pressures correspond to a gross pressure under the caissons of approximately 383 kPa

(4.0 tsf) for vertical loads, and 555 kPa (5.8 tsf) for combined horizontal and vertical loads. Also, the original design assumed an average unit friction resistance of 9.6 kPa (200 psf) along the embedded sides of the caissons.

Each caisson was sunk into place as a prefabricated unit by self-weight. This was accomplished by incrementally alternating between operations of excavating materials at the base of the caissons through their inside dredge wells, and the addition of tremie-placed concrete inside separate concrete ballast wells. The final base elevations were determined based on the type and condition of materials removed in the excavation process. During construction, it became apparent that the foundation soils were considerably stiffer than had been anticipated. Blasting actually became necessary in at least one of the caissons to sink the caisson into a partially cemented zone within Strata 3A and 3B (Stevenson 1991).

BEARING CAPACITY

Extensive bearing capacity analyses were performed for each river pier caisson foundation to determine if the caissons would be sufficiently stable under the increased loads of the new, widened superstructure. Safety factors were computed on the basis of both final net loading and final gross loading versus corresponding ultimate soil bearing capacities. Appropriate combinations of dead, live, and wind load effects were considered. The governing safety factors were found to be the gross safety factors for the wind load cases, which were computed to range from 2.0 to 2.8 for the lightweight concrete deck alternative that was ultimately constructed. All of these values equal or exceed the critical minimum acceptable safety factor of 2.0 for wind loading, and were therefore judged to be acceptable.

PREDICTED RIVER PIER SETTLEMENTS

Predicted settlements for the river pier caisson foundations were computed by conventional methods, where the total settlement, S, of a foundation is given as the combined sum of immediate settlement, primary consolidation settlement, and secondary compression settlement.

Since the soils beneath the caisson foundations consist of dense silty sand and very stiff clay with little or no organic soils, no significant secondary compression settlement was expected. This meant that for practical purposes, the total settlement for the widening design would be composed of the immediate and primary consolidation settlement components alone.

Immediate settlements for the caisson foundations were evaluated both by conventional elastic theories and by pressuremeter theories. For the river pier evaluations, immediate settlements computed by these two methods were found to be in reasonably close agreement, with the pressuremeter method predictions generally of slightly lower magnitude than those predicted by conventional methods.

Field and laboratory testing showed the soils supporting the caisson foundations in 1991 to have been compressed by past geologic processes to a preconsolidation pressure approximately three times greater than the combined existing overburden pressures and then-existing foundation pressures within the soil mass. Analysis of the predicted final distribution of load around the piers indicated that even with the increased weight of the widened superstructure, final pressures on the soils supporting the river piers would not exceed the preconsolidation pressures, suggesting that new additional loads on the foundation soils would remain in the stiffer recompression range of their past loading history.

Based on extensive settlement analyses performed during the superstructure widening design phase, it was predicted that the primary consolidation settlement would account for approximately 30 to 50 percent of the total settlement of the caisson foundations, with the remainder of the total settlement accounted for by immediate settlement effects.

RIVER PIER SETTLEMENTS PRIOR TO WIDENING

The original Coleman Bridge was constructed between 1949 and 1952. Repeated elevation measurements were made between January 1951 and January 1952 at the top of the river pier stems. Total settlement values for that period were computed from respective pier stem top elevation measurements made during the later stages of the original construction. Similar pier stem top elevation measurements were then made again in 1991. Measured and computed total settlements are compared in Table 3.

Table 3. Predicted Versus Measured Total Settlement of River Piers

Pier Number	Original Superstructure Construction (1951 to 1952)		Original Service (1952 - 1991)	Widened Superstructure Construction (1992-1996)	
	Measured Settlement	Calculated Settlement	Measured Settlement	Predicted Settlement	Measured Settlement
	mm (inches)	mm (inches)	mm (inches)	mm (inches)	mm (inches)
3S	30 (1.2)	28 (1.1)	Comparison of surveyed pier stem top elevations in 1991 versus similar readings taken in 1952 showed no discernable settlement.	67 (2.7)	44 (1.7)
2S	25 (1.0)	28 (1.1)		61 (2.4)	35 (1.4)
1S	*18 (0.7)	25 (1.0)		76 (3.0)	51 (2.0)
1N	43 (1.7)	25 (1.0)		71 (2.8)	53 (2.1)
2N	*10 (0.4)	23 (0.9)		51 (2.0)	34 (1.3)
3N	48 (1.9)	20 (0.8)		53 (2.1)	38 (1.5)

* Field data varied erratically

Data presented in Table 3 confirms that the river piers did not experience significant settlement either during or soon after original construction. In fact, there was no discernable settlement at all during service between 1952 and 1991. Table 3 also presents the results of calculations performed in 1991 to estimate the settlements that would have been expected during that earlier period, ranging from 20 to 28 mm (0.8 to 1.1 in) for the six river piers. Calculated settlements for the original construction were judged to be in reasonable agreement with measured settlements that ranged from 10 to 48 mm (0.4 to 1.9 in). The predicted and measured settlements from the 1952 construction compared reasonably well considering the many simplifying assumptions that were necessary to perform the settlement calculations, and uncertainties regarding the actual sequence of superstructure erection and its actual rate of progress at the various piers during the original construction.

RIVER PIER SETTLEMENT DURING WIDENING CONSTRUCTION

To reduce the time that the bridge was to be closed to traffic, the contractor prefabricated the entire superstructure and deck, including all appurtenances, off-site in six sections, and within a six day period floated out the existing superstructure in sections on barges and replaced them by floating in the new widened superstructure sections. Figure 3 provides a photograph of the bridge during this superstructure replacement phase of the project.

Figure 3. Float-In for New Pier 1N Swing Span Superstructure

Settlement of the six river caisson foundations was monitored during bridge widening operations, including both monitoring for upward rebound movements during removal of the existing steel truss spans, and settlement during placement of the new float-in superstructure. Initially, settlement monitoring was performed using total station survey equipment with prisms attached to the sides of the pier stems. However, at the beginning of truss removal operations, erratic readings from the total station equipment forced change to conventional optical settlement monitoring procedures. Optical monitoring was performed with conventional theodolite instruments sighting to project control benchmarks and gages attached to the bridge piers. Theodolites were set up both on-shore and on adjacent piers.

Table 3 illustrates that calculations of predicted settlement for the pier foundations under the new widened superstructure ranged from 51 to 76 mm (2.0 to 3.0 in), or approximately two times the settlements measured and calculated for the original construction. Measured settlements during construction of the widened superstructure were approximately one-third less than the predicted settlement values.

Differential settlement was also a major consideration in evaluation of the caisson foundations, particularly for the twin swing span foundations. Two separate types of differential settlement were considered in evaluating the superstructure widening, namely differential settlement of an individual caisson (i.e. tilting), and differential settlement between adjacent caissons.

Borings drilled at each river pier on opposite sides of the foundations indicated only small differences in strata elevations and soil conditions, and none that would produce significant differential settlements across the individual foundations. In addition, the rigidity of the caisson structures themselves would allow the foundation base to "arch" over any local soft zones. Since the new widened superstructure was designed to be symmetric about the existing roadway centerline, no new eccentric vertical loading of the piers was expected. The most significant overturning moments for the Coleman Bridge piers were determined to be those generated by wind loads that were not considered to present the potential for permanent rotation of the base and pier tilting.

From the data presented in Table 3, it can be seen that both measured and predicted pier-to-pier differential settlements are less than 25 mm (1 in) between all piers which, for the span distances involved, is well within tolerable limits.

All these conclusions are consistent with the successful performance of the existing bridge since original service began in 1952, particularly considering the long record of successful performance of the swing span opening and closing mechanisms, which were the components of the bridge least tolerant to differential settlement or tilting.

CONCLUSIONS

Based on the results of extensive site investigations and the analyses for bearing capacity and settlement, it was concluded that the original river pier caisson foundations would safely support the increased loads from the proposed bridge widening. As described above, the analyses included considerations of bearing capacity failure, short and long-term total settlement, as well as differential pier-to-pier settlement and pier tilting.

Based on the findings of these analyses, the caisson foundations for the original 2-lane U.S. Route 17 superstructure will continue to provide excellent service in supporting the new 4-lane superstructure. The bridge widening was accomplished with disruption to traffic occurring only during a brief 6-day superstructure replacement period in May 1996. The conversion of the bridge from 2 to 4 lanes was accomplished with much less cost, time and disruption than would have been necessary with a full bridge replacement if new foundations had been required. The bridge has performed successfully since the completion of bridge widening construction in 1996.

ACKNOWLEDGMENTS

Geotechnical subsurface investigation work for the project was performed by TLB Associates of Crofton, Maryland and Warren George, Inc. of Jersey City, New Jersey under PB's direction. The authors wish to acknowledge the Virginia Department of Transportation for its successful management of the project throughout its planning, design, and construction phases, and Tidewater Construction for its performance during the project's construction phase.

REFERENCES

Quade, M.N. (1954). "Special Design Features of the Yorktown Bridge," American Society of Civil Engineers, Paper No. 2661, *Transactions*.

Stevenson, R. (1991), *Personal Communication*, Project Engineer (Retired), Parsons Brinckerhoff, Hall & MacDonald.

Underground Expansion of a 27-year old Cultural Centre
Excavation and Foundation Reuse Concerns

Vishnu Diyaljee, F.ASCE, P.Eng.

Managing Director, GAEA Engineering Ltd, 2408-113A Street, Edmonton, Alberta, Canada, T6J 4Y2; diy001@gaeaeng.com

ABSTRACT: This paper addresses the geotechnical, structural and construction issues, with emphasis on the geotechnical issues, which had to be taken into consideration in the 2005 basement construction below a 930m^2 one-storey Cultural Centre supported primarily by cast-in-place (bored) concrete piles. The Cultural Centre was constructed in 1978 with a partial basement and extensions undertaken beneath its footprint in 1984 and 1993. Due to the unavailability of the original geotechnical report a new geotechnical investigation was undertaken from which capacities were evaluated for the original piles, as well as for the piles influenced by the proposed basement construction. After much discussion, which included the use of helical piles to enhance the capacity of the existing piles, spread footings were constructed around a few critical piles. Basement construction has since been completed without any problems. This case study demonstrates some of the concerns in reusing existing foundations, when design and construction records are unavailable.

INTRODUCTION

In March 2005, Management of the Cultural Centre, St Albert, Alberta, proposed further basement development below the existing Centre at locations not previously developed in 1978 and subsequent constructions in 1984, and 1993. Figures 1 - 3 show some views and features of the existing building while the existing and 2005 basements, amongst other features are visible in Figure 4.

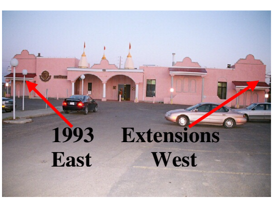

FIG.1 North Side **FIG.2. West and South Sides** **FIG.3. Northwest Side**

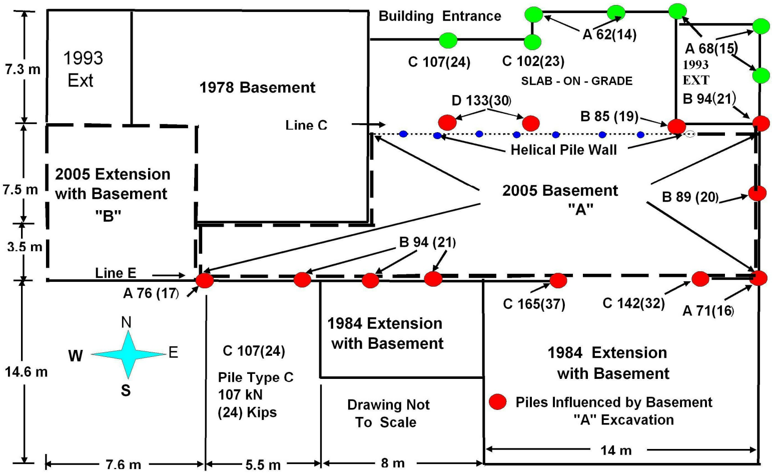

Fig 4. Schematic of Building Plan Showing Existing and Proposed Basement, Pile Types and Capacities

Availability of Past Design and Construction Documentation

Original building design drawings from 1978 and 1984 were the only documentation available for the project. There were no as-builts for either of those years, and the architect of the original building could not be located, however, the original structural engineer was reachable and indicated a belief that all foundations were constructed as designed. Neither the structural engineer nor any directors of the cultural centre could remember the geotechnical firm responsible for undertaking the site investigation or the whereabouts of the geotechnical report. As noted in the general notes on the “Index of Drawings” of the 1978 drawings “A Soils Report is available for the building site and may be obtained from the Architect”. Reference was also made to this report in the 1984 drawings regarding the 3 m deep water table.

Committee on Feasibility of Proposed Work

An adhoc volunteer committee was organized to discuss the feasibility of the proposed work and what approach should be taken to undertake the work in a safe manner. This committee was comprised of a project manager, a structural engineer, a geotechnical engineer, the contractor, the president, and a director of the Cultural Centre. The project manager, also a director of the Cultural Centre, was responsible for laying out of the proposed expansion. The structural engineer was also member of the Cultural Centre, while the geotechnical engineer was an independent volunteer. The Contractor had undertaken extensions on the East and West sides of the building in 1993 (Figure 4). After 2.5 months strategies were finalized and plans were assembled for obtaining a Development Permit from the City of Edmonton in Alberta.

GEOTECHNICAL AND STRUCTURAL CONSIDERATIONS

Following a meeting on March 15, 2007 a geotechnical investigation of the site and an assessment of the existing ground and foundation conditions were scheduled. These are outlined below.

Geotechnical Investigation

On March 19, four testholes were drilled with a solid stem auger within the property boundary. TH#1 and TH #2, were located on the southwest side of the property. Testhole, TH #3 on the southeast corner while TH #4 was located at the northeast corner. Testholes TH #1 and TH #3 were drilled to a depth of 9.1 m, which varied from about 1 to 3 m below the depth of installation of the cast-in-place piles. The remaining two holes, TH #2 and TH #4, were drilled to depths of 4 and 6 m, respectively. Grab samples were taken in all holes for moisture content determination while pocket penetrometer tests were done on auger cuttings for shear strength determination.

The generalized soil profile obtained from these borings consisted of frozen silty sandy gravelly clay (clay till) in the top 1.5 m followed to a depth of 4 m, by a medium to high plasticity clay till, which was above its standard Proctor optimum moisture. A very soft zone was encountered between 4 and 4.5 m with shear strength of about 12 kN/m^2. This layer was very wet and in excess of its standard Proctor optimum moisture. Below this weak zone, the clay till was generally stiff in consistency at a depth of 7 m but consisted of some weaker zones and pockets of water bearing sand, with a layer of gravelly sand below 8 m to the end of drilling at 9.1 m.

Shear strengths determined from Pocket Penetrometer tests averaged 48 kN/m^2 over the depth of pile installation. Two standpipe piezometers were installed in TH #2 and TH #3, to a depth of 3 m, one in each hole. The standpipe in TH #2 was dry a week following drilling, while the standpipe in TH #3 showed water at a depth of about 3 m. This groundwater level was consistent with that provided on the 1984 drawings, as indicated previously.

Concerns about Existing Pile Foundations

One of the foremost concerns was the determination of whether the piles would be able to carry the existing superstructure loads when the basement excavation was being undertaken since this would result in removing material from around the piles. There were also a few piles, which were considered critical by the structural engineer from a loading perspective. These were piles C-165 kN (37 Kips), C-142 kN (32 kips) and B-94 kN (21 kips) piles along Line E, Figure 4.

Other concerns were the determination of the structural integrity of the piles, since it was felt that the piles would be under-reinforced for lateral loads, and whether piles were constructed to the specified design diameter and lengths, despite the indication of belief expressed by the original structural engineer. Since the building could be subject to wind loading resulting in substructure movement, such defects could result in a significant safety concerns since the building was to be in use during construction. In the majority of cases, piling construction to the design depths and diameters would be undertaken, but uncertainty existed, because of the absence of piling records and personnel involved with the original design and construction.

One approach regarding pile capacities was to leave a 1.3 m wide block of soil adjacent to the piles. This approach, it was felt, would assist in preserving the original pile capacity since the strength characteristics and cohesive nature of the soil would allow a stable vertical cut in excess of the 3 m, the depth of proposed basement excavation. Since the excavation would be a short-term event to facilitate basement construction, total stress conditions would be applicable. The downside of leaving the block of soil, however, would be a reduction of useable basement area.

Assessment of Existing Pile Capacities

To check the design pile capacities, use was made of (a) the pile schedule on the 1978 drawings, which provided the sizes of piles, depth of installation and design pile capacities, and (b) the soil and ground characteristics determined from the March 2005 geotechnical investigation. All pile heads were terminated in 0.6 m deep grade beams. The pile information was used to back-calculate the shaft resistance and hence the pile capacities based on the assumption that the piles were designed as friction piles, a concept normally used for the design of straight shaft bored piles in Alberta. The ultimate shaft resistance used in the original design was determined to be 31 kN/m^2.

Based on the March 2005 investigation, the average shear strength of the soil to the depths of pile embedment was determined to be about 48 kN/m^2, which provided an ultimate shaft resistance of 26 kN/m^2 using the alpha-method (Reese and O'Neill, 1988). However, it was decided to use 31 kN/m^2 as the ultimate shaft resistance determined from back calculation. While the top 2 m of soil is often neglected in pile capacity determination, the calculations were based on determination of capacities for (a) the entire length of pile, (b) length minus 2 m, and (c) length minus 3 m. The 3 m depth represented the depth of the proposed basement excavation. Table 1 below shows the capacities determined for the various pile embedment lengths using the total stress approach.

Using a factor of safety (FOS) of 2, the pile capacities determined from shaft resistance compared well with pile capacities determined for the embedment length minus 2 m as shown on the design drawings and in red in Column 6. The similarity of these results is indicative that shaft resistance of the top 2 m of pile was neglected in the computation of the pile capacities. This was and still is often the practice in the design of straight shaft bored piles in Alberta.

Of note is that if the entire embedment lengths were used in determining the pile capacities, then the capacities shown in Column 4 would have been 1.5 to 1.7 times larger than the capacities reported on the 1978 drawings and shown in red in Column 6. As can be expected, the pile capacities were much lower with the 3 m depth of soil removed (Column 8), with reference to the original capacity of the fully embedded condition (Column 4) but slightly less than the capacity of the pile with the top 2 m neglected as shown in Column 6.

TABLE 1: SUMMARY OF PILE CAPACITIES – TOTAL STRESS

Pile Type (1)	Size mm (in) (2)	Design Length m (ft) (3)	Original Capacity kN (kips)(4)	Length below Exc m (ft) (5)	Capacity kN (kips) (6)	Length below Exc m (ft) (7)	Capacity kN (kips) (8)
A	406(16)	6.7 (22)	129(29)	4.9 (16)	93(21) 17	3.7(12)	71(16)
B	406 16)	7.6(25)	147(33)	5.8(19)	111(18)21	4.6(15)	89(20)
C	610 24)	6.4 (21)	187(42)	4.6 (15)	134(30)24	3.4(11)	98(22)
D	610(24)	7.3(24)	214(48)	5.8(19)	169(38)30	4.3(14)	125(28)
E	610(24)	8.2(27)	240(42)	6.4(21)	187(42)37	5.2(17)	156(35)

TABLE 2: SUMMARY OF PILE CAPACITIES – EFFECTIVE STRESS

Pile Type (1)	Size mm (in) (2)	Design Length m (ft) (3)	Original Capacity kN (kips) (4)	Length below Exc m (ft) (5)	Capacity kN (kips) (6)	Length below Exc m (ft) (7)	Capacity kN (kips) (8)
A	406(16)	6.7 (22)	129(29)	4.9 (16)	58(13) 17	3.7(12)	38(8.5)
B	406 16)	7.6(25)	147(33)	5.8(19)	80(18) 21	4.6(15)	40(9)
C	610 24)	6.4 (21)	187(42)	4.6 (15)	71(16) 24	3.4(11)	33(7.5)
D	610(24)	7.3(24)	214(48)	5.8(19)	107(24)30	4.3(14)	53(12)
E	610(24)	8.2(27)	240(42)	6.4(21)	142(30)37	5.2(17)	80(18)

Solicited Geotechnical Input

Because of varying opinions and concerns by committee members, and for safety in particular, the Geotechnical Engineer solicited the opinion of Dr. Bengt Fellenius (Private Communication, 2005) on March 26, by providing some project background information and Table 1 for his review and comments. Fellenius commented that the total stress analysis was not useful in calculating the effect of an excavation as the total stress method cannot model the effect of stress change in the soil below the bottom of the excavation. He also noted that pile toe resistance was not used in determining pile capacity. Table 2 above shows the calculations based on effective stress analysis provided by Fellenius.

The effective stress calculations were undertaken to determine what beta-coefficient the shaft capacities corresponded to using a unit shaft resistance of 31kN/m^2, the same used in the total stress analysis, soil unit weight of 20 kN/m^3 and water table at a depth of 3 m. Beta coefficients ranging from 0.44 to 0.56 with an average close to 0.5 were obtained. This average value was considered reasonable for the soils encountered. Using the beta coefficient of 0.5 and the proposed excavation depth of 3 m the effective stress analyses returned capacities that were about one quarter to one third of the shaft capacities in comparison with the capacity of a fully embedded pile (Columns 4 and 8). The pile capacities determined were about half those determined using the total stress method (Compare Column 8, Tables 1 and 2). In neglecting the top 2 m of soil, the capacities determined were smaller than the design capacities (Column 6, Table 2) and those determined using the total stress analysis (Column 6, Table 1).

Based on these results, Fellenius (2005) suggested that without relying on toe resistance compensating capacity loss, the proposed excavation should not be chanced without determining the actual pile response. He recommended that one or two piles be freed by digging under a grade beam, cutting off a length of pile and undertaking low strain testing to assess the pile lengths. This would then be followed by placing a hydraulic jack on the pile head and conducting a static load test.

SUBSEQUENT COMMITTEE MEETINGS AND DECISIONS

Following receipt of Fellenius's assessment, his comments and recommendations were discussed at a Committee meeting. However, because of logistical problems perceived in undertaking these tests and the associated costs, these recommendations were not pursued. A second volunteer structural engineer who was to be the "Coordinating Responsible Professional" for the project suggested the use of 2m x 2m spread footings around the piles to provide additional load support. This would mean that the excavation would have to be undertaken before the footing was constructed, negating the original concerns.

As an alternative, the geotechnical engineer proposed the concept of using helical piles to provide additional support to the existing piles that were to be exposed by the excavation. This would entail the use of two helical piles at each existing interior pile location and one or two helical piles at each existing exterior pile. These helical piles would be installed from the inside of the building for the interior piles. In addition, helical piles would be required to retain soil on the north side of the excavation along line C (Figure 1), to avoid loss of soil under slab-on-grade at the main entrance of the Cultural Centre. However, except for the use of the helical piles to retain the soil, the "Coordinating Responsible Professional" finally decided on the use of the spread footings around the piles for additional load support. These footings were to be used around the critical piles only. The concern about possible movements of the piles laterally or vertically following excavation and before the spread footings could be cast was to be addressed by vigilance of the contractor who would have on site necessary shoring including teleposts to undertake temporary support should problems become obvious.

CONSTRUCTION CONSIDERATIONS

Excavation of the basement started sometime in September 2005 from the west side of the building where there was more space for placement of excavated material. Prior to the basement excavation helical piles (140 mm shaft diameter with twin 355 mm diameter helixes) with were installed along Line C, Figures 5 and 6, and the tops connected by chains to dowels embedded in the floor slab (Figure 5). This was done to prevent the piles from moving laterally. Small equipment was used for the excavation below the building (Figure 6). During the period of excavation, the contractor took survey measurements on certain piles on a daily basis to determine whether they were moving vertically or laterally, Figures 7-10. No movements of any of the piles were reported either by survey or visual observation.

FIG.5. Helical Piles

FIG. 6. Basement Excavation

FIG.7. Pile C-142(Line E)

FIG.8. Pile C-165(Line E)

FIG.9. Pile B -94 (Line E)

FIG.10. Pile B-94 (Line E)

Figures 11-14 show elements of the completed 2005 Basement "A", in Fig 4.

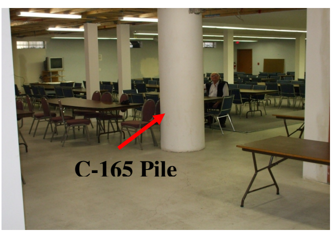

FIG.11. In Vicinity of C-165 Pile

FIG.12. In Vicinity of C-142 Pile

FIG.13. North and East Walls

FIG.14. South and West Walls

SUMMARY AND CONCLUSIONS

A lack of geotechnical, structural and construction documentation resulted in a cautious approach taken in the construction of a basement below a 27-year old Cultural Centre founded predominantly on bored concrete piles. This resulted in a committee being established to discuss and resolve the issues regarding uncertainty of the integrity of the existing foundations and strategy for construction. A geotechnical study was undertaken to assess the pile capacities before and after basement excavation, through total stress and effective stress approaches. The effective stress analyses produced pile capacities that were a quarter to a third of the original capacities and much smaller than the total stress capacities. Despite that this signaled a concern that the excavation could be unsafe, the decision made was to excavate and construct spread footings around piles considered critical.

No problems were encountered during construction suggesting that there was sufficient conservatism with the FOS of 2.0 that was used to determine the pile capacities. Since the excavation was temporary, a much smaller FOS closer to 1, say 1.2 could have sufficed. In addition, no toe resistance was utilized. This toe resistance would have provided additional support, despite in the design phase this is discredited because of uncertainty of the soil condition at the pile toe.

Had the recommended low strain and static load testing being undertaken, some useful information could have been obtained from this case study. While there was success with this venture, this should not be taken to be valid for all similar situations. The time spent in addressing the problem allowed confidence to be developed, although there was still concern about possible pile movement vertically and laterally.

This case study illustrates in a small way some of the issues that need to be addressed in the reuse of foundations where documentation is lacking. In dealing with such uncertainty, the geotechnical and structural engineer, and contractor must work together. This case study highlights the importance for developing methods to preserve project documentation and to evaluate the integrity of foundations throughout the life of a structure.

REFERENCES

Fellenius, B. (2005): “Private Communication”
Reese, L.C., and O’Neill, M.W. (1988): “Drilled Shafts: “Construction Procedures and Design Methods” FHWA-HI-88-042, 564 p.

Three-Dimensional Performance of an Over-Size Complex Excavation in Shanghai

Y. M. HOU[1], W. D. WANG[2], J. H. WANG[*]

[1]Civil Engineering Department, Shanghai Jiaotong University, 1954 Hua Shan Road, Shanghai, CHINA; email: ymhou@sjtu.edu.cn
[2]East China Architectural Design & Research Institute Co., LTD., 151 Han Kou Road, Shanghai, CHINA; email: weidong_wang@ecadi.com
[*]Corresponding author. Civil Engineering Department, Shanghai Jiaotong University, 1954 Hua Shan Road, Shanghai, CHINA; email: wjh417@sjtu.edu.cn

ABSTRACT: This paper presents an over-size complex excavation project. In order to control retaining wall lateral displacement and associated ground movement within specified limits, this project was constructed using the method of "central part by bottom-up method and peripheral part by top-down method". A comprehensive monitoring system was installed on this project to reduce risk and study the deformation behavior of such excavation. Wall displacement, ground surface movement and bottom heave were separately measured and analyzed during the excavation. Field observations indicate that the wall lateral displacement is correlated with the zoned excavation and floor slabs installation sequence. The ground surface settlement near the corner of the excavation is less than that near the center, which corresponds to those reported in the literature. The behaviors of the diaphragm wall and ground surface settlement are affected by the "creep effect".

INTRODUCTION

To meet the increasing demand for economic growth, extensive underground structures have been rapidly constructed in Shanghai. For those large excavations in sensitive areas, complex construction sequences are generally adopted to limit the excavations deformation and protect the adjacent structures and utilities. The Zhongsheng Shopping Mall excavation project is the biggest soft clay excavation in Shanghai district up to now. This pit occupies an area of about 50000 m^2 and the depth of excavation is about 13.5 m. In order to control retaining wall lateral displacement and associated ground movement within specified limits, this project was constructed using the method of "central part by bottom-up method and peripheral part by top-down method". A comprehensive monitoring system was installed on this project to reduce risk and study the deformation behavior of such excavation. This paper presents the field performance data and discusses the behaviors of the diaphragm wall lateral displacement, ground surface settlement, and bottom heave.

SITE DESCRIPTION AND INSTRUMENTATION

The Zhongsheng Shopping Mall is located in the southwest of Shanghai and occupies an area of about 50000 m^2. The building has 5 above-ground stories devoted to shopping mall uses and three underground levels for parking. The excavation of this project is about 13.5m. A 0.8-m-thick and 23.25-m-deep diaphragm wall was used as the earth-retaining structure. Figure 1 shows the layout of the excavation. As indicated in this figure, the central part where is excavated using the bottom-up method occupies an area of about 21000 m^2, while the peripheral part where are excavated using the top-down method occupies an area of about 29000 m^2.

To monitor the performance of the excavation, various instruments were installed on site. As shown in Fig. 1, 29 inclinometer tubes whose length was equal to the depth of the diaphragm wall were affixed to the steel reinforcement cages and concreted at various critical locations of the wall. The rotation of the diaphragm wall was measured at 1 m intervals along its depth to observe the deflection of the diaphragm wall. In order to study the settlements of the roads around the excavation, road surface settlements were monitored throughout the construction period. Figure 1 shows the locations of the 35 settlement measurement points. Fig. 1 also indicates that nine magnetic extensometer systems consisted of five arrowhead magnets at 19.8 m, 18.3 m, 16.8 m, 15.8 m and 14.8 m below the ground surface were installed inside nine boreholes in central part to measure subsurface soil movements, respectively.

SUBSURFACE CONDITIONS AND CONSTRUCTION SEQUENCE

According to the site investigation report, the site is underlain by thick, relatively soft Quaternary alluvial and marine deposits. The groundwater table is at about 1 m below ground level. Fig. 2 shows the profile of soil layers and the variations of some geotechnical properties. As indicated in this figure, the soils in this excavation site are generally clays with high water content and low shear strength.

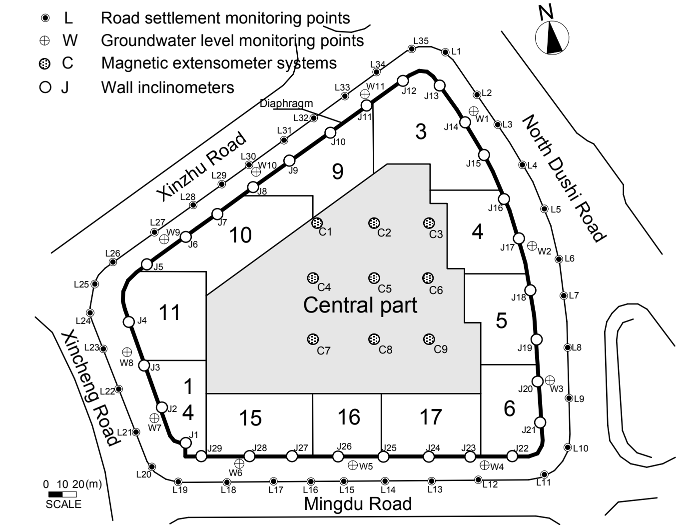

FIG. 1. The location and instrumentation of the excavation site.

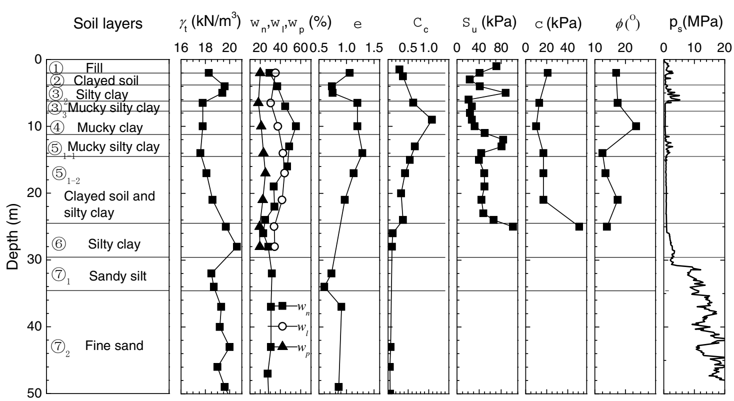

FIG. 2. Soil profiles and variation of geotechnical parameters with depth.

Table 1 presents the time sequence of construction activities for this project. Three levels of concrete floor slabs were employed to support the diaphragm walls at depths of 0.00 m, -5.65 m and -9.35 m. As revealed in Table 1, stages 2 and 3 represent excavation of the central part while stages 6, 7 and 8 represent excavation of the peripheral part. To reduce the wall deflections during the construction, the peripheral part of the excavation were excavated with zoning and the concrete floor slabs were also cast by zones, as shown in Fig. 1. It should be noted that after excavating the central part to the bottom, the excavation had been halted for 64 days. It is a good opportunity to investigate "creep" effects on wall deflections. Table 1 also indicated that floor slabs of some zones were not cast in time.

Table 1. Construction Sequence of the Excavation

Stage	Interval (d)	Construction operation
1	235	Excavate to elevation of -3.80 m and construct diaphragm wall and pile foundation
2	118	Excavate the central part to -9.35 m and excavate the peripheral part to -6.60 m, cast the floor slab (B1F) of the peripheral part at elevation of -5.65 m (except zone 5 and zone 16), zone 9 and zone 10 were braced by concrete struts
3	136	Excavate the central part to -14.8 m, complete the floor slab (B1F) of the peripheral part and cast floor slab (B0F) of the peripheral part at elevation of 0.00 m (except zone 6 and zone 10)
4	64	Halt excavation
5	42	Complete the floor slab (B1F) of the peripheral part, cast the foundation slab and the floor slab (B2F) at elevation of -9.35 m of the central part
6	111	Cast the floor slab (B1F) at elevation of -5.65 m of the central part, excavate the peripheral part to -10.35 m
7	37	Cast the floor slab (B2F) at elevation of -9.35 m of the peripheral part and the floor slab (B0F) at elevation of 0.00 m of the central part
8	109	Excavate the peripheral part to -14.80 m and cast the foundation slab of the peripheral part

OBSERVED PERFORMANCE

Displacement of Diaphragm Wall

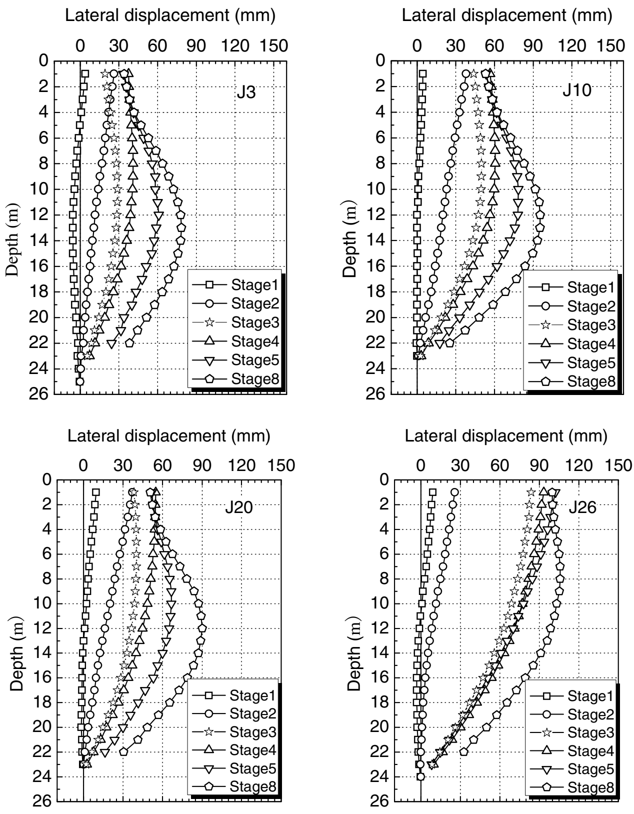

FIG. 3. Variation of wall displacement at inclinometers J3, J10, J20 and J26.

Fig. 3 shows the lateral displacement of the diaphragm wall at inclinometers J3, J10, J20 and J26 at various stages. As shown in Table 1, the central part of the site was first excavated down to -9.35 m while the peripheral part was excavated to -6.60 m at stage 2. The floor slabs were not cast at that time. Hence, the wall deformation at stage 2 behaved as a cantilever. As the excavation proceeded to stage 3, the floor slab (B1F) of the peripheral part at elevation of -5.65 m was constructed. The diaphragm wall at J3, J10 and J20 rotated with respect to the position of the floor slab because the high axial stiffness of the slab prevented the wall from moving at that position. However, the diaphragm wall at J26 still behaved as a cantilever because the floor slabs (B1F) at zone 5 and zone 16 had not been cast at that time.

As the excavation proceeded, deep inward displacement gradually developed on the diaphragm wall at J3, J10 and J20, with the maximum wall displacement occurring near the excavation surface. The diaphragm wall at J26 continues to behave like a cantilever. The ratios between the maximum lateral displacement and the excavated depth were 0.58%, 0.71%, 0.68% and 0.78% at J3, J10, J20 and J26, respectively, which are higher than the general trends found by Ou et al. (1993).

After the central part of the site was excavated to the elevation of -14.8 m, the excavation was halted which lasted about 60 days. It is a good opportunity to investigate the "creep" effect. Fig. 5 indicates that the maximum lateral displacement increases of diaphragm wall at J3, J10, J20 and J26 were 18.2 mm, 12.8 mm, 14.1 mm and 9.3 mm during the period that excavation was halted, respectively. It can be seen that the "creep" effect induced a significant increase of the diaphragm wall lateral displacement.

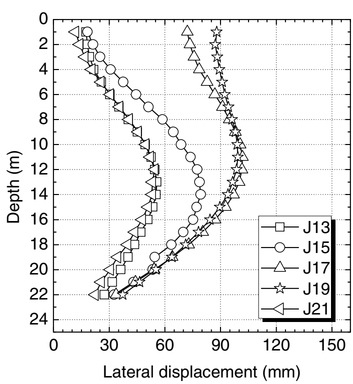

FIG. 4. Wall lateral displacement at final stage at inclinometers J13, J15, J17, J19 and J21.

Fig. 4 summarizes the measured lateral displacement of the wall along the North Dushi Road at final stage. The three-dimensional deformation behavior of the diaphragm wall is illustrated clearly in this figure. The maximum wall deflections at

J13 and J21 near the corners are 55.7 mm and 54.6 mm, respectively. The maximum wall deflection at J17 near the midspan of the edge is 101.8 mm. There is a significant reduction in lateral displacement as one moves from the midspan towards the corner of the excavation. The maximum wall deflection at J19 is 99.3 mm, which is similar to the deflection at J17. It could be attributed to the fact that the floor slab (B1F) at zone 5 was not cast in time.

Ground Surface Settlement

Fig. 5 shows the ground surface settlement along the roads around the site at various stages. As revealed in this figure, the three-dimensional behavior of the ground surface settlement is exceedingly clear. The settlements near the corners are much smaller than those near the center; this observation is consistent with that noted by Lee et al. (1998). The settlement increased gradually with excavation depth. The maximum settlement of the ground surface was about 200 mm at final stage.

Excavation Bottom Heave

Fig. 6 shows the variation of bottom heave with excavation depth at C8. This figure indicates that the bottom heave increased with the excavation depth. It should be noted that no significant bottom heave was observed while there was no excavation carried out at stage 4. As excavation proceeded to the final stage, the magnitude of the heave at excavation bottom was about 6 cm.

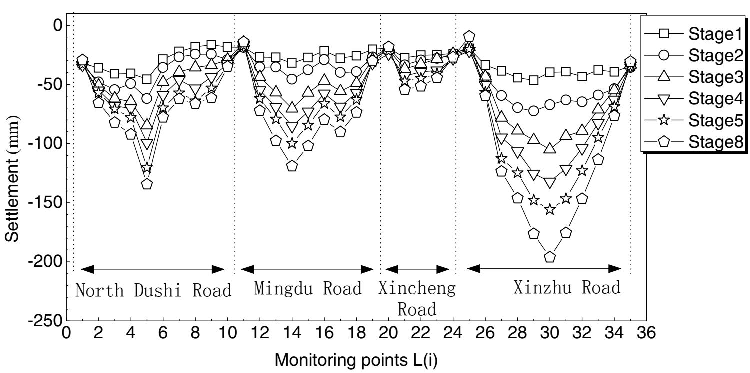

FIG. 5. Ground surface settlement along the roads around excavation.

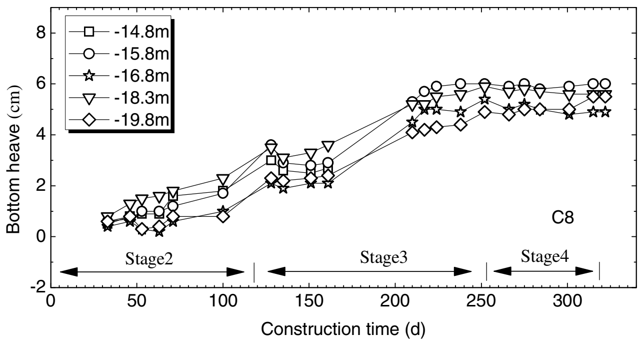

FIG. 6. Variation of bottom heaves with time at C8.

CONCLUSIONS

This paper presents a case history of field behavior of an over-size complex excavation. Based on the in-situ measured results, the following conclusions can be deduced:

1. The ratio between the maximum lateral displacement and the excavated depth ranges from 0.58% to 0.78%, which is higher than the general trends found by Ou.

2. The observed maximum wall deflection continued to creep inward during the period when the excavation was halted.

3. Both the wall deflection and the ground surface settlement are affected by the "corner effect". There is a significant reduction in wall deflection and the ground surface settlement as one moves from the midspan towards the corner of the excavation.

4. The bottom heave generally increased with the excavation depth. However, bottom heave remains unchanged with time while the excavation was not carried out.

REFERENCES

Ou, C.Y., Hsieh, P.G. and Chiou, D.C. (1993). "Characteristics of ground surface settlement during excavation." *Can. Geotech. J.,* Ottawa, Canada, 30, 758-706.

Lee, F.H., Yong, K.Y., Quan C.N. and Chee, K.T. (1998). "Effect of corners in strutted excavations: Field monitoring and case histories." *J. Geotechnical & Geoenv. Engrg.*, Vol. 124 (4): 339-349.

Resilient Modulus and Dynamic Modulus of Warm Mix Asphalt

Shu Wei Goh[1] and Zhanping You[2], P.E.

[1] Ph.D. Student and Research Assistant, Department of Civil and Environmental Engineering, Michigan Technological University, Houghton, Michigan 49931, USA. Tel: (906)487-2528, Fax: (906)487-1620, Email: sgoh@mtu.edu

[2] Tomasini Assistant Professor of Transportation Engineering and Associate Director of the Transportation Materials Research Center, Department of Civil and Environmental Engineering, Michigan Technological University, Houghton, Michigan 49931, USA. Tel: (906)487-1059, Fax: (906)487-1620, Email: zyou@mtu.edu

ABSTRACT: Warm Mix Asphalt (WMA) is produced at temperatures in the range of 30˚F to 100˚F (17˚C to 56˚C) lower than the traditional hot mix asphalt (HMA). It has a number of benefits including reducing energy consumption, emissions from burning fuels, and volatiles generated from the heated asphalt binder at the production plant at the paving site. Several technologies used in WMA are available today, such as synthetic zeolite (Aspha-min®), Sasobit®, Evotherm®, and WAM-Foam®. In this paper, the results of a laboratory evaluation of WMA made with synthetic zeolite were discussed. A control HMA mixture, WMA with 0.3% synthetic zeolite, and WMA with 0.5% synthetic zeolite were used in the test. Based on the tests conducted, it was found that the WMA mixture made with synthetic zeolite had a higher resilient modulus. For dynamic modulus test, WMA with 0.5% synthetic zeolite have a higher dynamic modulus. In addition, dynamic modulus for WMA compacted at 120˚C was significantly higher than the WMA compacted at 100˚C.

Keywords: Warm Mix Asphalt, Dynamic Modulus, Superpave, Simple Performance Test, Synthetic Zeolite, Master Curve

INTRODUCTION

The goals for Warm Mix Asphalt (WMA) are to use the existing HMA plants and the existing standards of the HMA specifications, and to focus on dense graded mixes for wearing courses (FHWA 2007). Europeans were using WMA technologies, which allowed significant reduction in the temperatures when asphalt mixes are produced and placed. A typical compaction temperature range is 250°F (121°C) to 275°F (135°C). Based on research done in Europe and North America, there are usually several technologies that have been used to produce WMA: 1) the addition of a synthetic zeolite called Aspha-Min® during mixing at the plant to create a foaming effect in the binder; 2) a two-component binder system called WAM-Foam® (Warm Asphalt Mix Foam) that introduces a soft and hard foamed binder at different stages during plant production; 3) the use of organic additives such as Sasobit®, a Fischer-Tropsch paraffin wax; 4) the application of Asphaltan B®, a low molecular weight esterified wax; 5)and, the use of Evotherm®, a technology based on a chemistry package that includes additives to improve coating and workability, adhesion promoters, and emulsification agents (FHWA 2007).

All those technologies reduce the viscosity of the asphalt binder at a given temperature and allow the aggregate to be fully coated at a lower temperature. They have a significant impact on pavement projects in and around non-attainment areas. It was reported that the manufacturers and materials suppliers indicated energy savings on the order of 30%, with a reduction in CO_2 emissions of 30%. The mixture production and placement temperature could bring several cost, environmental, and performance benefits (Jones 2004, Goh et al. 2007, You and Goh 2008, Goh and You 2008). The advantages of the WMA are briefly summarized as: lower energy consumption (reduce fuel costs); reduce mixing and compaction temperature; early site opening; lower plant wear; slowed binder aging potential by reducing the temperatures; lower fumes and emissions; cool weather paving; improve workability; and an extend paving window.

LITERAFTURE REVIEW

Synthetic zeolite, often referred as Aspha-min®, is a product of Eurovia Services GmBH Bottrop, Germany (Barthel et al. 2004), simplified as Eurovia. It is a manufactured synthetic zeolite (Sodium Aluminum Silicate), which has been hydro-thermally crystallized. Eurovia recommended adding synthetic zeolite at the rate of 0.3% of the mass of the mixture, which can result in a potential 54°F (30°C) reduction in temperature and decrease 30% in fuel energy consumption for typical HMA production. Eurovia stated that all commonly known asphalt and polymer-modified binders can be used with synthetic zeolite (Harrison and Christodulaki 2000; McKeon 2006).

A laboratory study was conducted by the National Center for Asphalt Technology (NCAT) to determine the applicability of synthetic zeolite to typical paving operations and environmental conditions (Hurley et al. 2006). The main results obtained from NCAT indicated that the additional synthetic zeolite has lowered the air void levels in the gyratory compactor, increased the potential of moisture damage, has lowered the TSR (Tensile Strength Ratio) as compared to the control mixture, and did not affect the resilient modulus and rutting potential.

However, the resilient modulus decreased as the compaction temperature decreased and air void level increased, and the rut depth increased as the temperature decreased for all the factors in combination.

A study on field performance of WMA was conducted at the NCAT test track (Prowell et al. 2007). The results indicated that both HMA and WMA sections showed excellent field performance in terms of rutting after the application of 515,333 ESALs in a 43 day period.

Researchers (Wasiuddin et al. 2007) studied the rut depth and the rheological properties of binders WMA made with synthetic zeolite and Sasobit®. The results show that synthetic zeolite did not give any beneficial effect in temperature reduction based on rotational viscometer. The rutting potential decreases with a decrease in mixing and compaction temperature for both Sasobit® and synthetic zeolite mixture and no significant direct decrease in production temperature with synthetic zeolite.

There are several synthetic zeolite comparison tests done by Eurovia. Results of the field test indicated that the synthetic zeolite section was comparable to the traditional HMA comparison section (BARTHEL et al. 2004). A field demonstration test was conducted by Hubbard Group at Orlando, Florida in February 2004 (McKeon 2006). The conclusions and recommendations drawn from Hubbard Group on adding the synthetic zeolite into the mixture are: 1) comparison of all laboratory tests is favorable with almost no change in volumetric properties and Marshall Stability; 2) the amperage meter dropped from 34amps to 32amps on the mix elevator, possibly indicating better workability in the warm mix asphalt; 3) the nuclear density was 2.8pcf (44.85Kg/m^3) higher after initial compaction in the warm mix; 4) and, the lower temperature did not change the workability and the material texture was the same.

Synthetic zeolite is a relatively new technology. Although it shows a significant promise in energy saving and emission reduction, currently there have been only a few laboratory experiments conducted. Further detailed studies and tests are needed to evaluate the performance of synthetic zeolite in terms of mixture volumetric design and asphalt binder properties. This paper will evaluate the volumetric Properties of WMA made with synthetic zeolite through indirect tension test and dynamic modulus test.

SCOPE

In this study, asphalt mixtures and WMA made with synthetic zeolite were discussed. The control mixture (HMA) and WMA mixture were prepared in the lab. The synthetic zeolite was added to the WMA mixture at the rate of 0.3% and 0.5% based on the total weight of the mixture.

As discussed above, the objective in this study was to evaluate the asphalt mixture made with synthetic zeolite through the resilient modulus and the dynamic modulus test. The general test flow chart is illustrated as Figure 1.

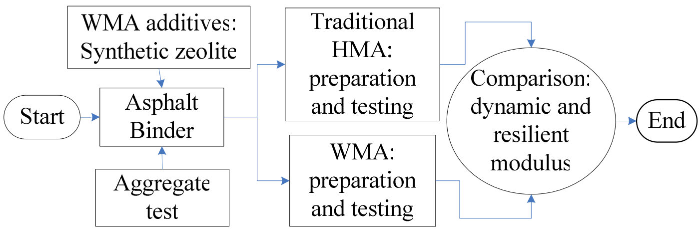

FIG. 1. The General Test Flow Chart for the Asphalt Mixtures

The control mixture's mixing and compacting temperatures (150°C for mixing and 140°C for compacting in this experiment) were evaluated through the viscosity-temperature chart. In this study, two temperatures, 100°C (212°F) and 120°C (216°F) were chosen during the WMA compaction using a gyratory compactor.

IDT Resilient Modulus Test

The Indirect tension test was performed to find out the resilient modulus for both the control mixture and WMA mixture based on AASHTO T322-03. Tests were performed at 4 temperatures (i.e., 4°C, 21.1°C, 37.8°C, and 54.4°C). In this study, only the results of the resilient modulus tested at 4°C were presented to show the effect of the synthetic zeolite on the asphalt mixture's resilient modulus.

Figure 2 shows the resilient modulus tested at 4°C for the control mixture and WMA mixture. Figure 2 indicated that the WMA has a slightly higher resilient modulus with 0.3% and 0.5% synthetic zeolite (Aspha-min®) compacted at 100°C and 120°C than the control mixture compacted at 140°C. The reason may be due to the different aggregate skeletons in the control mixture compacted at a high temperature (140°C) and WMA compacted at lower temperatures (100°C and 120°C). The WMA was easy to compact to the desired air void levels at lower temperatures with the assistance of the additives. A stronger aggregate skeleton or aggregate-aggregate contacts in the asphalt mixture may increase the asphalt mixture modulus because of the better capability of the loads to transfer from one aggregate to another aggregate (You and Dai 2007).

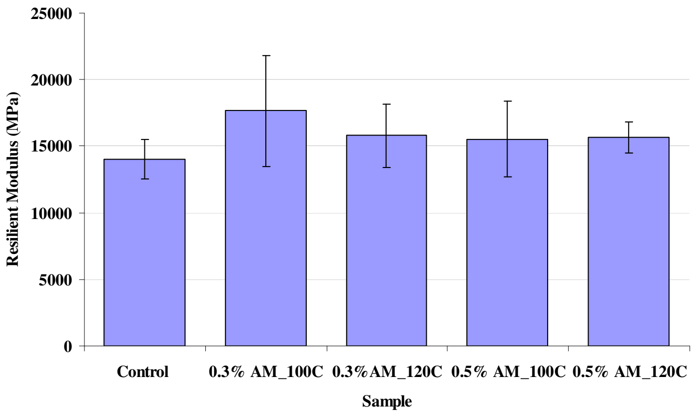

FIG. 2. Resilient Modulus tested at 4°C for Control Mixture Compacted at 140°C and WMA Mixture Compacted at 100°C and 120 °C

NCAT indicated that two parameters (i.e., air void content and temperature) affect the resilient modulus (Hurley et al. 2006). In the tests shown here, the temperature affected the modulus: the resilient modulus increases when the compacting temperature increases and the air void level decreases. However, Figure 2 shows there were no significant effect on the resilient modulus for WMA mixtures under two different compacting temperatures. When a paired t-test is applied for the dataset of both 0.3% and 0.5% additives tested at a given temperature, there is no significant difference in the resilient modulus between the two compaction temperatures under a 95% confidence level.

DYNAMIC MODULUS TEST

The purpose of the Dynamic Modulus test is to find out the dynamic modulus, |E*| of asphalt mixture. E* is the ratio of stress to strain under sinusoidal loading conditions. The greatest advantage of the dynamic modulus (E*) is that it can be used in developing a series of prediction models through Mechanistic-Empirical Pavement Design Guide (M-EPDG). In this paper, the dynamic modulus test was performed and was conducted according to AASHTO TP62-03. The temperatures used to measure E* are -5°C, 4°C, 21.1°C, and 39.2°C (37.8°C for control mixture). The frequencies used in this test were 0.1Hz, 0.5Hz, 1Hz, 5Hz, 10Hz, and 25Hz. Five types of mixture were use: a control mixture, 0.3% synthetic zeolite mixture compacted at 100°C and 120°C, and 0.5% synthetic zeolite mixture compacted at 100°C and 120°C. The recoverable axial micro-strain in this test was adjusted to the value in between 50 and 100 so that the material is in viscoelastic range.

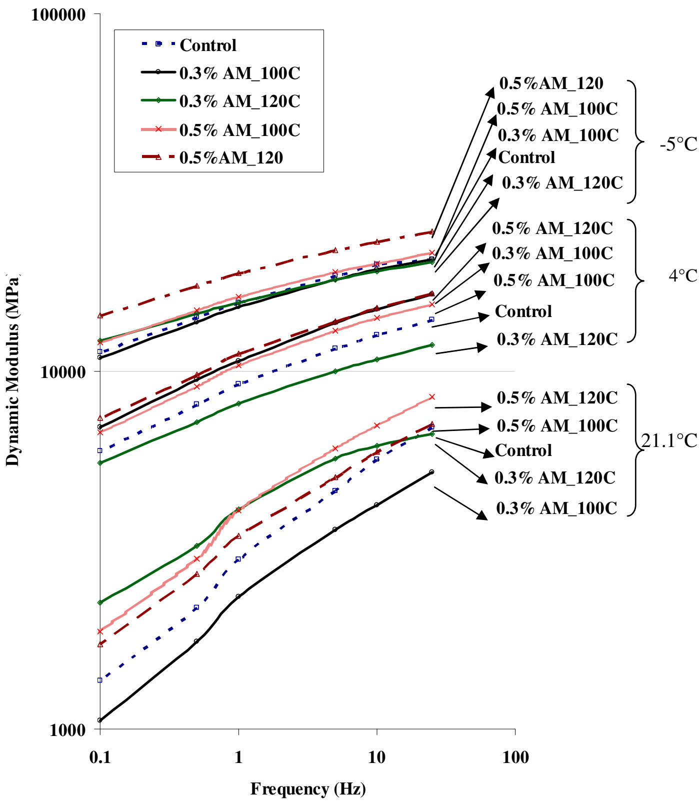

FIG. 3. Dynamic Modulus Results for Control Mixture and WMA Mixture

The results of the dynamic modulus test are presented in Figures 3. A note for the graph is: "Control" is the control mixture, "0.3% AM_100C" and "0.3%AM_120C" are the WMA with 0.3% synthetic zeolite compacted at 100°C and 120°C respectively, and "0.5% AM_100C" and "0.5% AM_120C" are the WMA with 0.5% synthetic zeolite compacted at 100°C and 120°C respectively.

Through Figure 3, it was observed that the mixtures with the additional 0.5% synthetic zeolite have a higher E* value. Figure 3 also indicated that WMA compacted at 120°C has a higher E* when a paired t-test is used. This indicated that WMA made with synthetic zeolite has a better performance in terms of rutting distress compared to control mixture.

CONCLUSIONS AND RECOMMENDATIONS

Due to the benefits of the use of WMA in reducing energy consumption and lowering emissions and volatiles, the market for this new technology will likely be very promising. This paper presented the results of a laboratory evaluation of WMA made with synthetic zeolite. For the resilient modulus under the indirect tension test setup, the resilient modulus of asphalt mixture increased slightly when the synthetic zeolite was added. Probably, this is due to the different aggregate skeletons in the control mixture compacted at a high temperature (140°C) and WMA compacted at lower temperatures (100°C and 120°C). In addition, there were no significant differences for the resilient modulus of WMA mixtures under two different compacting temperatures. Through the dynamic modulus test, E* was found to have a higher value when 0.5% of synthetic zeolite was added into the mixture compared with the rest of the mixtures. In addition, WMA compacted at 120°C has a higher E* compared to WMA compacted at 100°C.

Several recommendations are given based upon the preliminary laboratory evaluation: 1) a life cycle cost analysis should be performed to evaluate whether synthetic zeolite will give any economic saving for pavements; 2) the long term field performance should be monitored; 3) a guideline of the design, construction, and maintenance of WMA is needed for successful field applications.

REFERENCES

Barthel, W., Marchand, J.-P., and Devivere, M. V. "Warm Asphalt mixes By Adding A Synthetic Zeolite." *Eurasphalt & Eurobitume Congress 2004 Proceedings*.

Goh, S.W. and You, Z. (2008). Mechanical Properties of Warm Mix Asphalt Using Aspha-min®, *Proceedings of 2008 Annual Transportation Research Board Meeting*, Washington, D. C., USA, January 13-17 [CD-ROM], 21 p.

Goh, S.W., Z. You, and T.J. Van Dam (2007). Laboratory Evaluation and Pavement Design for Warm Mix Asphalt. in 2007 *Mid-Continent Transportation Research Symposium*. 2007. Iowa State University, Ames, Iowa [CD-ROM], 11p.

FHWA (2007). "Highway Statistics 2000." Office of Highway Policy Information, Federal Highway Administration, Washington, D.C.

Harrison, T., and Christodulaki, L. (2000). "Innovative processes in asphalt production and application - strengthening asphalt's position in helping build a better world." *First International Conference of Asphalt Pavement,* *Sydney*.

Hurley, G.C., B.D. Prowell, G. Reinke, P. Joskowicz, R. Davis, J. Scherocman, S. Brown, X. Hongbin, and D. Bonte. Evaluation of Potential Processes for Use in Warm Mix Asphalt. *Journal of the Association of Asphalt Paving Technologists*, Vol. 75, P. 41-90, published by the Association of Asphalt Paving Technologist, White Bear Lake, MN 55110, United States.

Jones, W. (2004). "Warm Mix Asphalt Pavement." Asphalt Institute.

McKeon, B., Aspha-min in warm asphalt mixes. 2006: Presentation at 51st Annual Convention of the National Asphalt Pavement Association. Lanham, Maryland.

Prowell, B. D., Hurley, G. C., and Crews, E. (2007). "Field Performance of Warm-Mix Asphalt at the NCAT Test Track." *Transportation Research Board 86th Annual Meeting*, CD-ROM, Washington DC, United States.

Wasiuddin, N. M., Selvamohan, S., Zaman, M. M., and Guegan, M. L. T. A. (2007). "A Comparative Laboratory Study of Sasobit® and Aspha-min® in Warm-Mix Asphalt." *Transportation Research Board 86th Annual Meeting*, Washington DC, United States.

You, Z., and Dai, Q. (2007). "A Review of Advances in Micromechanical Modeling of Aggregate-Aggregate Interaction in Asphalt Mixture." *Canadian Journal of Civil Engineering /Rev. can. génie civ.*, 34(2), 239-252.

You, Z. and Goh, S.W. (2008), Laboratory Evaluation of Warm Mix Asphalt: A Preliminary Study, *International Journal of Pavement Research and Technology*, 1(1): 2008, ISSN 1996-6814.

The Dynamic Modulus of Asphalt Mixture with Bottom Ash Aggregates

Shu Wei Goh[1] and Zhanping You[2], P.E.

[1] Ph.D. Student and Research Assistant, Department of Civil and Environmental Engineering, Michigan Technological University, Houghton, Michigan 49931, USA. Tel: (906)487-2528, Fax: (906)487-1620, Email: sgoh@mtu.edu

[2] Tomasini Assistant Professor of Transportation Engineering and Associate Director of the Transportation Materials Research Center, Department of Civil and Environmental Engineering, Michigan Technological University, Houghton, Michigan 49931, USA. Tel: (906)487-1059, Fax: (906)487-1620, Email: zyou@mtu.edu

ABSTRACT: The objective of this paper is to study the mechanical properties of asphalt mixture using an aggregate of bottom ash. When bottom ash is used as asphalt pavement material, it will decrease the aggregate cost and also reduces the dumping of bottom ash in landfills. Most states reported that the performance of fly ash as a filler material was fair to good, while Michigan and Nebraska reported fly ash had a poor performance. However, bottom ash (with the sieve size up to #4) in asphalt mixtures has not been evaluated to replace other aggregates. In this study, bottom ash was introduced to replace a portion of the aggregates. The asphalt mixture using bottom ash used more asphalt content. In the asphalt mixture tests, the Superpave gyratory compacted samples were prepared and the specific gravity (bulk and rice) and air void were measured. In addition, the dynamic modulus was conducted to evaluate the mixture performance. Through the dynamic modulus test, the replacement of bottom ash in the asphalt mixture has shown a lower dynamic modulus compared to the control mixture.

Keywords: Bottom Ash, Dynamic Modulus, Master Curve, Asphalt Pavements, Asphalt Mixtures

INTRODUCTION

Large amounts of waste materials were produced everyday and the number of landfill sites was decreased over the past few years. This problem has become a serious environmental issue and thus forces the nation to look for a better way to recycle and utilize the waste materials. Using the coal ash (a by-product of coal-fired generation) as the mineral filler and construction material in numerous areas was one of the approaches to solve this issue.

According to the American Coal Ash Association (ACAA), coal combustion in the United States alone generated about 123.1 million tons of coal combustion products in the year 2005 (71.1 million tons of fly ash, 17.6 million tons of bottom ash, 31.1 million tons of flue gas desulfurization (FGD) materials, and 1.4 million tons of boiler slag) and there was also an increase of about 2.31% in coal production each year. This trend is expected to continue and will result in the increase of coal ash production (American Coal Ash Association 2006). Bottom ash is one of several coal combustion products (CCPs). It is dark or brown granular, porous, predominantly sand sized material and consists of inorganic, incombustible matter present in the coal that has been fused during combustion into a glassy, amorphous structure.

Bottom ash is mainly used as an alternative for aggregates in applications such as sub-base and base course under rigid and flexible pavement and was used as coarse aggregate for hot mix asphalt (HMA). It is noted that the performance of bottom ash as a mineral filler in the asphalt pavement is very important because it will utilize the waste material and also may improve the asphalt pavement life cycle cost. Therefore, the objectives of this study are to perform research on literature reviews on bottom ash and evaluate the performance of bottom ash through the dynamic modulus test. The general test flow is shown in Figure 1

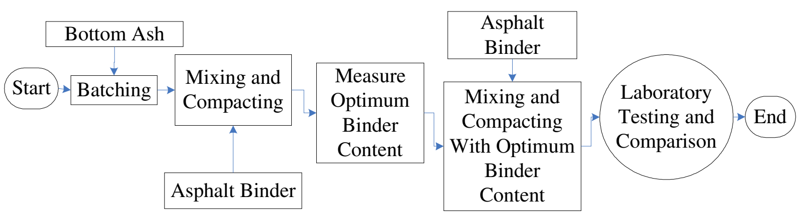

FIG. 1. General Flow Chart for Laboratory test on Ash Mix

LITERATURE REVIEW

A decreasing source of traditional aggregates, increasing haulage distance, and diminishing landfill space are the main reasons that favor the recycling of construction-quality waste materials in asphalt pavements. Much research has been done on evaluating the characteristics of bottom ash in the application of asphalt pavement. Researchers (Ramme and Tharaniyil 2004) have studied the physical, chemical and mechanical properties of bottom ash using the AASHTO standards. The study indicated that bottom ash is non-plastical, non-liquid material using the Atterberg Limit test, bottom ash is not as sound or durable as natural aggregate, bottom ash meets the requirement for Wisconsin Department of Transportation (WisDOT) Standard specification for the Atterberg Limit test and the Los Angeles Abrasion test, bottom ash meets Michigan Department of Transportation (MDOT) specifications for dense grade aggregate, and bottom ash needs to be blended with other aggregates to meet the WisDOT gradation requirement.

Bottom ash has a different text in terms of slope and curvature than traditional aggregate, so it may give a significant change in design asphalt content for the mixture and voids in mineral aggregate. A study of gradation control for bottom ash aggregate in Superpave binder bituminous mixture was performed by researchers (Ogunro et al. 2004) based on this issue. The study indicated that the design binder content in mixtures was increased, the effective asphalt decreased from 5.1% to 4.4%, and absorbed asphalt increased from 1.3% to 3.2% after bottom ash was added as mineral filler.

Studies regarding the environmental issues on the bottom ash were conducted. Researchers (D'Andrea et al. 2004) performed the leaching test for the bottom ash from the Hospital and Municipal Solid Waste Incinerator (HSWI and MSWI bottom ash). The studies indicated that asphalt mixture containing waste material has the same teachability of the traditional mixtures. However, the concentration of pollutant elements is within the limits set by Italian national rule. Researchers also confirmed that the use of bottom ash coming from HSWI and MSWI as aggregate in asphalt concrete is suitable and environmentally safe (D'Andrea et al. 2004). Researchers (Huang et al. 2006) also investigated both physical and environmental properties of asphalt mixture containing incinerator bottom ash (IBA) using the Marshall mix design method. The results indicated that the IBA-asphalt mixtures were shown to have excessively high Marshall Flow and excessively low VMA (void in mineral aggregate) with adequate Marshall Stability. In addition, IBA-asphalt mixtures were found to have higher tensile strength ratio (TSR) through the water sensitivity test when compared with the conventional asphalt mixtures. Also, the outdoor leaching test showed that IBA had a high level of daphnia toxicity and it could be identified as hazardous waste from the ecological perspective. On the other hand, researchers (Huang et al. 2006) indicated that the concentration of the metal level and levels of daphnia toxicity were significantly reduced when mixed with asphalt binder.

Laboratory and field tests were performed in the past to examine the effect of bottom ash as the mineral filler in the asphalt pavement. A Researcher (J.H. Lee 2001) had performed consolidated drained triaxial compression tests to investigate the stress-strain behavior of bottom ash. Researchers performed a two year demonstrated project on US Route 3, New Hampshire by using bottom ash to substitute 50% of the aggregate (Musselman et al. 1994). Ksaibat and Conner 2004 used Georgia loaded wheel, thermal strength restrained specimen and tensile strength tests to evaluate the effect of the additional coal combustion remnant, bottom ash, into asphalt mixtures. The results indicated that the quality of ash mixes maintained a desirable tensile strength property without any additional lime when compared to control mixtures. The ash mixes displayed slightly improved properties over control mixtures in the presence of lime. Researchers had investigated Sulfur-Modified Bottom Ash (SMBA) as aggregate in HMA through laboratory and field tests (Estakhri and Saylak 2000).

The laboratory results showed the asphaltic mixture design in which bottom ash represents 50% to 100% of the aggregate fraction can be achieved. The SMBA HMA overlay was under traffic by heavy haul trucks entering the plant facility and early indications of field performance were good. Hjelmar et al. (2007) had performed a study of utilization of MSWI bottom ash as sub-base in road construction. The first results from the test site constructed in October 2002 indicated that the comparison between laboratory leaching tests on bottom ashes and observation of the leachate show fairly good agreement for salts but less agreement for some trace elements. Hjelmar et al. (2007) indicated that this is partly due to the fact that the pH observed in the leachate from the field site is lower than that observed in the eluates from the laboratory leaching tests. Currently, the project is still ongoing and further study will be provided.

Ksaibati and Stephen (1999) studied the utilization of bottom ash in asphalt mixtures. The laboratory evaluations indicated that the ash mixtures have higher optimum asphalt contents compared to standard HMA using the Marshall Mix design. The ash mixes required lesser compactive effort to achieve their desire densities in the field construction and no difference in field performance between control and ash mixes after one season of being in service. The laboratory asphalt mixtures processed significantly different high-temperature rutting characteristics when compared to each other through the statistical analysis of the Georgia Load Wheel Tester (GLWT). Only the control and Wyodak mixtures had statistically equal rut measurements. The laboratory mixtures processed significantly different low-temperature cracking characteristics through the analysis of the Thermal Restrained Specimen Tester (TSRST) and the asphalt mixtures containing bottom ash from different power plants had significantly different low temperature cracking and high temperature rutting characteristics.

Ksaibati and Plancher (2006) studied the moisture resistance of bottom ash and the study investigated the feasibility of incorporating bottom ash in asphalt mixtures. The study indicated that the moisture resistance of all bottom ash mixtures was comparable to or exceeded the control mixture performance after running the indirect tensile strength test and nitrogen analyses.

Zeng and Ksaibati (2003) had examined the moisture susceptibility of asphalt mixtures containing bottom ash. The results indicated that the addition of bottom ash did not substantially change the tensile strength values. However, all mixtures tested met the Superpave volumetric mix design requirement of TSR after one freeze-thaw cycle. It was also indicated that on the basis of TSR rate (TSRR), the additional lime significantly improved the moisture resistance of the asphalt mixtures subjected to multiple freeze-thaws. The bottom ash played a role similar to lime in improving the TSRR for the material tested if the lime was not added into the mixture.

Although there has been a lot of a research conducted to evaluate performance and ability of bottom ash in replacing the mineral filler of asphalt mixture, laboratory data is significantly lacking in terms of mechanical properties. This paper is being conducted using the simple performance test in term of dynamic modulus to fill this gap, at least partly.

MATERIAL DESCRIPTION

The materials used in this study were bottom ash, which is produced after a coal burning process from Michigan, aggregate, from a plant in Lansing (Michigan), and asphalt binder with the performance grade of PG 64-28. The bottom ash from Michigan consists of SiO_2, $Al2O_3$, Fe_2O_3, CaO, MgO, SO_3, Na_2O and K_2O. The particle size distributions for control and ash mixes are shown in Table 1. The control mixture and the new mixture (with the bottom ash) have the same gradation.

Table 1. Gradation of Control Mixture and Bottom Ash

Sieve Size (mm)	Control Mixture	Bottom Ash as Aggregate	Blended Aggregate in Asphalt Mixture with Bottom Ash
	% Passing	% Passing	% Passing
19	100	100	All similar as the Control Mixture
12.5	98.7	100	
9.5	86.5	100	
4.75	71.8	99.5	
2.36	51.4	97.6	
1.18	36.1	94.4	
0.6	25.5	89.3	
0.3	14.7	77.7	
0.15	7.7	52.6	
0.075	5.4	28.8	

In order to match the gradation of the control mixture, a total 9% of bottom ash was used. Therefore, as a summary, two kinds of mixtures were used in the entire laboratory tests:

1. Control mix: 0% replacement of mineral filler (bottom ash)
2. Ash mix: 9% replacement of mineral filler with bottom ash

DYNAMIC MODULUS

The dynamic modulus (E*) test measures the response of the material to cyclic loading at different frequencies in the undamaged state. It is the ratio of stress to strain under a sinusoidal loading condition. In this study, the E* test was conducted using the Universal Testing Machine (UTM) 100 based on AASHTO TP62-03 specification. The temperatures used in this test were -5°C, 4°C, 13°C, and 21.3°C (23°F, 39.2°F, 55.4°F, and 70.34°F, respectively) for the control mixture and -5°C, 9°C, and 21.3°C and 39.2°C (23°F, 48.2°F, 70.34°F, and 102.56°F, respectively) for the ash mix. The frequencies were 0.1Hz, 0.5Hz, 1 Hz, 5Hz, 10Hz, and 25Hz. At each temperature and frequency, tests were conducted at two different air void levels, which were 4% and 7%.

The comparison of E* for ash mix and control mixture are presented in Figure 2. It is notable that "BA_4%AV" means an ash mix with 4% air void level, "BA_7%AV" means an ash mix with 7% air void level, "Control_4% AV" means a control mixture with 4% air void level, and "Control_7%" means a control mixture with 7% air void level.

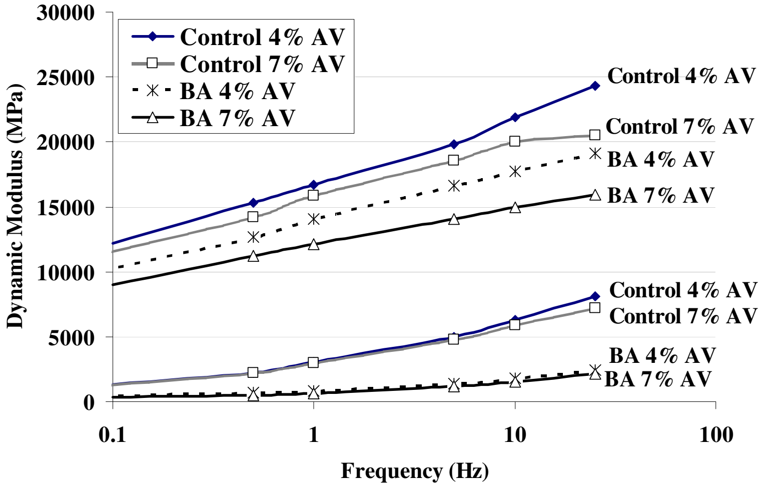

FIG. 2. Comparison of Dynamic Modulus for Control mixtures and Ash Mixes at -5°C and 21.3°C

Figure 2 shows the comparison of the E* test result conducted at -5°C and 21.3°C. Both results indicated that ash mixes had a lower E* compared to the control mix, statistically. This also means that the replacement of the bottom ash in the asphalt mixture lowered the modulus of the mixture.

In order to observe the entire results in a single graph, a Sigmoidal master curve was constructed. A Sigmoidal master curve is constructed using the principal of time-temperature superposition or time-temperature equivalence, which means the same modulus value of a material can be obtained either at low test temperatures and a long period time or at high test temperatures. It is the same as that under long loading times or slow loading rates and the material behavior at low temperatures is the same as that under short loading time or fast loading rates. Figure 3 shows the Sigmoidal master curve for control mixture and ash mix. As expected, the ash mix had shown a lower E*. The E* master curves will be used in the M-EPDG to predict different kinds of distresses over time including rutting and fatigue cracking. An Ongoing research study at Michigan Tech is focusing on the mechanistic empirical design and life cycle cost analysis of using the bottom ash to replace a portion of aggregates.

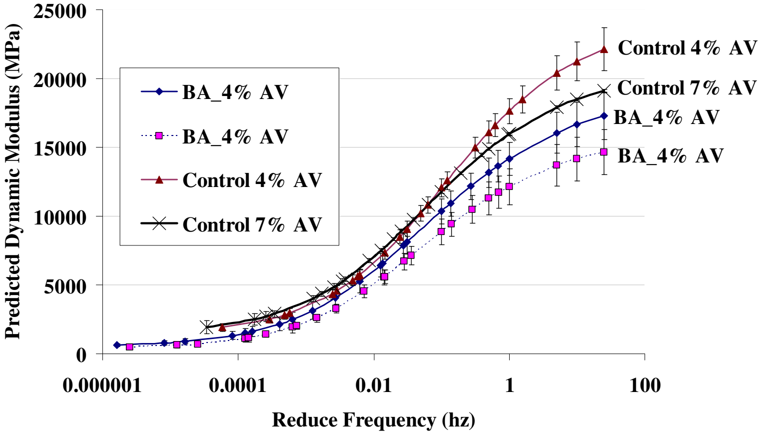

FIG. 3. Comparison of dynamic modulus for control mixture and ash mix using Sigmoidal Master Curve

CONCLUSIONS

The use of bottom ash to replace a portion of aggregate in the asphalt mixture has shown a significant promise in reducing the aggregate cost and utilizing the waste material from dumping to the landfills. Research in literature has shown the bottom ash was an environmentally safe material and replacement of bottom ash in the asphalt mixture would increase the optimum binder content. In addition, moisture resistance of all bottom ash mixes was comparable to or exceeded the control mixture performance after running the indirect tensile strength test and nitrogen analyses. In this study, dynamic modulus test was conducted and the replacement of bottom ash had lowered the value of E* in the asphalt mixture. Further evaluation is needed to assess the rutting, fatigue and thermal cracking behaviors.

ACKNOWLEDGMENTS

The authors wish to express their gratitude to former visiting scholar Dechao Li at Michigan Technological University for helping running some preliminary tests. The authors also wish to acknowledge the discussions with Dr. Thomas Van Dam at Michigan Technological University in the bottom ash application.

REFERENCES

American Coal Ash Association (2006). "2005 Coal Combustion Product (CCP) Production and Use Survey."

Ksaibati, K. and Conner, G. L. (2004). "Laboratory Evaluation Of Bottom Ash Asphalt Mixes." MPC Report No. 04-159, Mountain-Plains Consortium, published by the University of Wyoming, Laramie, WY.

D'Andrea, A., Bonora, V., and Drago, D. "Asphalt concrete with bottom ash: Environmental aspects." Cesena, Italy, 56-63.

Estakhri, C. K., and Saylak, D. (2000). "Sulfur-modified bottom ash as aggregate in hot-mix asphalt concrete: Field demonstration project." *Transportation Research Record*(1723), 57-65.

Hjelmar, O., Holm, J., and Crillesen, K. (2007). "Utilisation of MSWI bottom ash as sub-base in road construction: First results from a large-scale test site." *Journal of Hazardous Materials*, 139(3), 471-480.

Huang, C.-M., Chiu, C.-T., Li, K.-C., and Yang, W.-F. (2006). "Physical and environmental properties of asphalt mixtures containing incinerator bottom ash." *Journal of Hazardous Materials*, 137(3), 1742-1749.

J.H. Lee. (2001). "Compaction and Shear Strength of Fly and Bottom Ash Mixtures." The Journal of Solid Waste Technology and Management.

Ksaibati, K., and Plancher, H. (2006). "Moisture Resistance of Bottom Ash." TRB 85th Annual Meeting Compendium of Papers CD-ROM, Washington DC, United States.

Ksaibati, K., and Stephen, J. (1999). "Utilization of Bottom Ash in Asphalt Mixes." University of Wyoming, Laramie, WY.

Musselman, C. N., Eighmy, T. T., Gress, D. L., Killeen, M. P., Presher, J. R., and Sills, M. H. "New Hampshire bottom ash paving demonstration US route 3, Laconia, New Hampshire." Boston, MA, USA, 83-90.

Ogunro, V. O., Inyang, H. I., Hooper, F., Young, D., and Oturkar, A. (2004). "Gradation control of bottom ash aggregate in superpave bituminous mixes." *Journal of Materials in Civil Engineering*, 16(6), 604-613.

Bruce W. Ramme, and Mathew P. Tharaniyil. (2004). "Coal Combustion Products Utilization Handbook." WE Energies.

Zeng, M., and Ksaibati, K. (2003). "Evaluation of Moisture Susceptibility of Asphalt Mixtures Containing Bottom Ash." *Transportation Research Record* (1832), 25-33.

Evaluation of Asphalt Mixtures Containing Sasobit® Warm Mix Additive

Louay Mohammad[1], M. ASCE and Shadi Saadeh[2], A.M. ASCE, Samuel Cooper[3], P.E.

[1] Professor, Louisiana State Univ. and Louisiana Transp. Res. Cent., 4101 Gourrier Avenue, Baton Rouge, LA 70808. E-mail: louaym@lsu.edu , Tel.: 225-767-9126.
[2] Assistant Professor, Department of Civil Engineering & Construction Engineering Management, California State University, Long Beach, 1250 Bellflower Blvd. Long Beach, California, 90815.
[3] Senior Asphalt Research Engineer, Louisiana Transportation Research Center, 4101 Gourrier Ave, Baton Rouge, LA 70808.

ABSTRACT: This paper presents field and laboratory performance of conventional hot mix asphalt mixture and mixture containing warm mix additive named Sasobit®. The laboratory evaluation included indirect tensile strength test (ITS), Hamburg-type loaded wheel tracking test (LWT), Dynamic modulus (E*) test, and Semi-Circular Bend (SCB) Test. Test results indicated that the ITS of Sasobit® modified mixture was significantly lower than the conventional mixture. However, the fracture resistance, as determined from the critical value of J-integral of the SCB test, of the conventional mixture was slightly lower that the Sasobit® modified mixture. Sasobit® modified mixture exhibited lower modulus values, E*, than the conventional mixture. This difference between the conventional and the Sasobit® modified moduli decreased as the temperature increased, indicating that the modulus was minimally affected at higher temperature due to the Sasobit® modification. In this limited evaluation, the moisture susceptibility of both mixtures was similar. The rut depth, as measured from the LWT test, of Sasobit® modified mixture was slightly lower that the rut depth of the conventional mixture.
Key Words: HMA Mixtures, Sasobit®, ITS, SCB, LWT, E*

INTRODUCTION

Conventional HMA production takes place between 250°F and 325°F, not to exceed 350°F, and placement and compaction between 260°F and 300°F [1]. Before mixing with hot liquid asphalt, fine and coarse aggregates are heated to high temperatures to drive off moisture, to ease coating of the mineral aggregates with the liquid asphalt, and to keep the complete mix fluid enough to be workable during placement. A number of new processes and products have become available that can reduce the temperature at which hot mix asphalt (HMA) is mixed and compacted.

Since the introduction of warm asphalt mixes into North America, the asphalt industry has gotten closer to producing low-emissions HMA mixtures. Warm asphalt mixes are of particular interest because of their potential for reduced plant emissions, benefits in construction in the field, and reduced energy consumption in the plant. The use of warm mixes may also extend the construction season in colder weather because contractors may no longer fear the critical loss of temperature in the cold [2].

The use of warm asphalt technologies was developed in Europe with the aim of reducing greenhouse gases produced by manufacturing industries [3]. Specifically, the European Union has agreed to reduce CO2 emissions by 15 percent by 2010. With this goal, the European hot mix industry has begun the use of warm mix asphalt technology to construct asphalt pavements at much lower temperature.

OBJECTIVE

The objective of this study was to perform a laboratory evaluation of conventional HMA mixtures and mixtures containing the additive "Sasobit®". In particular, the objectives included the following:

- Fundamental material characterization.
- Evaluate the influence of Sasobit® on moisture sensitivity.

SCOPE

Evaluation of the Sasobit® test section was done on an active Louisiana construction project. Two HMA binder courses, conventional and Sasobit® modified HMA mixture types, were selected for evaluation in this study. The job mix formulas for each mix type considered were identical except for the asphalt cement binder type used. The conventional mixture contained asphalt cement, PG 76-22m, meeting Louisiana specifications [4]; whereas the other mixture had a Sasobit® modified PG 76-22m asphalt cement binder. Siliceous limestone was the predominate aggregate used in the HMA mixture types considered. Indirect tensile strength test (ITS), Loaded Wheel Tracking (LWT) test, Simple Performance Test (SPT, Dynamic Modulus), and Semi-Circular Bend (SCB) test were conducted to define the permanent deformation and endurance life of HMA for the mixtures considered.

MIXTURE DESIGN

The design criteria were set by the "Louisiana Standard Specifications for Roads and Bridges" for this project [4]. Table 1 shows the composition of the HMA binder course mixtures evaluated in this study.

SAMPLE PREPARATION

According to the test factorials described, cylindrical and rectangular beam samples were fabricated. The Superpave gyratory compactor (SGC) was used to compact all cylindrical specimens. A kneading compactor was used to compact LWT (Hamburg type) beam specimens. Specimens fabricated through various methods at the target air voids (7 ± 1%) were used to conduct laboratory mixture performance tests as outlined in table 2. A brief description of each test is provided below.

DESCRIPTION OF LABORATORY AND FIELD TESTS

INDIRECT TENSILE STRENGTH TEST (ITS)

This test was conducted at 25°C according the AASHTO T245. A cylindrical specimen is loaded to failure at a deformation rate of 50.8 mm/min (2 in/min) using a MTS machine. The indirect tensile strength (ITS) was used in the analysis.

Table 1 Mixture Design for mixtures considered

Material	**Conventional**	**Sasobit®**
Binder Content	3.8	3.8
Sasobit®, %	0	1
Permatac 99 anti-strip	0.6 by Wt. of AC	0.6 by Wt. of AC
G_{mm}	2.515	2.509
$\%G_{mm}$, N_i	87.2	87.7
$\%G_{mm}$, N_d	96	96.3
% VMA	12.8	12.6
% VFA	68	71
% V_a	4	3.7
% AC	3.7	4.1
Sieve	Gradation Analysis	
1 ½”	100	100
1”	95	97
¾”	87	91
½”	74	79
3/8”	66	70
No. 4	46	50
No. 8	29	32
No. 16	22	23
No. 30	17	18
No. 50	11	11
No. 100	8	8
No. 200	6.4	6.2

Table 2 Mixture performance tests

Performance Characteristics	**Test**	**Dimension - mm**	**Test Temp.**	**Protocol**
Durability	HWT	320x260x40	50 ºC	AASHTO T 324
Permanent Deformation	Complex Modulus	ϕ150x100	54 ºC	AASHTO TP7
	HWT*	320x260x80	50 ºC	AASHTO T 324
Fatigue Cracking	ITS	ϕ100x63.5	25 ºC	AASHTO TP9-96
	Semi Circular Bend	ϕ150x57	25 ºC	Mohammad *[5]*

SEMI-CIRCULAR FRACTURE ENERGY TEST

In this study, the fracture resistance of the designed mixtures was characterized using this test based on notched semi-circular specimens [6]. During the test, a pre-notched specimen was loaded monotonically to failure at a constant cross-head deformation rate of 0.5 mm/min in a three-point bend load configuration. The load and deformation were continuously recorded determined and as follows:

$$J_c = -\left(\frac{1}{b}\right)\frac{dU}{da} \quad (1)$$

where, b is the specimen thickness, a is the notch depth, and U is the total strain energy to failure , i.e. the area up to fracture under the load-deflection plot.
To determine the critical value of J- integral, semi-circular specimens with at least two different notch depths need to be tested for one mixture. In this study, three notch depths of 25.4 mm, 31.8 mm, and 38 mm were selected based on an a/rd ratio (the notch depth to the radius of the specimen) of between 0.5 and 0.75 ,[6]. For each notch depth three specimens were tested. The test temperature was 25° C.

DYNAMIC MODULUS TEST (E)*

This test consists of applying a uniaxial sinusoidal (i.e., haversine) compressive stress to an unconfined or confined HMA cylindrical test specimen. The stress-to-strain relationship under a continuous sinusoidal loading for linear viscoelastic materials is defined by a complex number called the "complex modulus" (E*). The absolute value of the complex modulus, |E*|, is defined as the dynamic modulus. The dynamic modulus is mathematically defined as the maximum (i.e., peak) dynamic stress (σ_0) divided by the peak recoverable axial strain (ε_0):

$$|E^*| = \frac{\sigma_0}{\varepsilon_0} \quad (2)$$

The dynamic modulus test consists of testing samples at –10, 4.4, 20, 37.8, and 54.4ºC (14, 40, 70, 100 and 130ºF) at loading frequencies of 0.1, 0.5, 1.0, 5, 10, and 25 Hz at each temperature for the development of master curves for use in pavement response and performance analysis. The haversine compressive stress was applied on each SPT sample to achieve a target vertical strain level of 100 microns in an unconfined test mode.

WHEEL TRACKING TEST (HWT)

A Hamburg type of Loaded Wheel Tracking (LWT) tester manufactured by PMW, Inc. of Salina, Kansas was used in this study. This test is considered a torture test that produces damage by rolling a 703N (158 lb) steel wheel across the surface of a slab that is submerged in 50°C (122°F) water for 20,000 passes at 56 passes a minute. A maximum allowable rut depth of 6 mm at 20,000 passes is used in LADOTD Specifications.

RESULTS

INDIRECT TENSILE STRENGTH TEST

Table 3 presents the indirect tensile strength (ITS), strain, and toughness index (TI) results from the ITS test for aged and un-aged replicates of conventional and Sasobit mixtures and their corresponding P-value from the statistical paired t-test. The results of the indirect tensile strength shows that the Sasobit® modified mixes had a lower indirect tensile strength, strain, and TI than the conventional mixes in the aged and un-aged cases. The statistical parameter, P-value, indicated that there is a significant difference between the ITS of the aged samples. The indirect tensile strain showed significant difference for the unaged samples, whereas there was no significant difference for the aged case. The TI showed no significant difference between the aged and unaged samples.

Table 3 Results from ITS on aged and un-aged samples

Parameter	Strength (psi)		Strain (%)		TI	
	Conv	Sasobit®	Conv	Sasobit®	Conv	Sasobit®
Unaged Samples						
Average	220	188	0.506	0.33	0.76	0.72
%CV	5	10	10.80	18.28	2.91	5.16
P-value	0.175		0.016		0.314	
Aged Samples						
Average	223	177	0.48	0.40	0.75	0.70
%CV	5	2	8.33	17.23	1.93	8.48
P-value	0.01		0.24		0.44	

SEMI-CIRCULAR BEND (SCB) TEST

Table 4 represents the SCB test results for the PG 76-22m and 1 percent Sasobit® modified PG 76-22m HMA mixtures evaluated in this study. It shows that the critical value of J-integral (Jc) for the 1 percent Sasobit® modified PG 76-22m HMA mixture is slightly higher than the PG 76-22m conventional HMA mixture, 0.78 and 0.76 respectively. The results reveals that modifying the original PG 76-22m asphalt cement binder with 1 percent Sasobit® did not significantly affect the fracture resistance of the HMA mixture when compared to the conventional PG 76-22m HMA mixture. Since this was a limited study, only generalized conclusions can be made at this time.

Table 4 Semi-circular bend test results

	Conventional	Sasobit®
Jc	0.76	0.78

*DYNAMIC MODULUS, E**

Table 5 presents the difference in E* between the Sasobit and conventional mixtures and the corresponding statistical P-value of the paired t-test. In general, the results indicate that for the same temperature the difference increases as the frequency increases. For the same frequency the difference decreases as the temperature increases. The statistical parameter, P-value, indicated that there is no significant difference between the E* of the Conventional and Sasobit mixes. However, the P-value was close to 0.05 (the value under which the difference is considered significant) at low temperature and high frequency. For the phase angle, the statistical parameter, P-value, indicated that there is no significant difference between the phase angle δ of the Conventional and Sasobit mixes in most cases. However, there was a significant difference between the Sasobit and conventional mixes phase angle at high temperature and high frequency, the P-value was less than 0.05. For the crack resistance parameter (E*Sinδ) at 4 and 25°C; the results indicate a lower E*Sinδ for the Sasobit mixture at all frequencies. However, the P-value indicated no significant difference in the E*Sinδ of the conventional and Sasobit at all frequencies except case of 10Hz and 4°C. For the rutting parameter E/Sinδ at all temperatures and frequencies; the analysis indicates no significant effect of the mix type, conventional versus Sasobit, on the measured parameter.

Table 5 Avg Sasobit® E*-Avg conventional E*

Temperature	Frequency (Hz)	25	10	5	1	0.5	0.1
4°C	E_s-E_c (ksi)	-574	-557	-521	-443	-406	-313
	P-value	0.064	0.057	0.058	0.07	0.075	0.096
25°C	E_s-E_c (ksi)	-208	-145	-110	-58	-43	-13
	P-value	0.097	0.216	0.252	0.423	0.506	0.774
38°C	E_s-E_c (ksi)	3	-58	-40	-11	-4	1
	P-value	0.299	0.395	0.469	0.714	0.851	0.958
54°C	E_s-E_c (ksi)	-28	-15	-7	-1	1	2
	P-value	0.327	0.431	0.574	0.821	0.878	0.562

MOISTURE SUSCEPTIBILITY

Table 6 presents the average ITS, strain, and TI for the moisture-conditioned and unconditioned specimens for conventional and Sasobit mixtures along with their %CV and the corresponding P-value of the paired t-test. Also shown is the tensile strength ratio percentage (% TSR), which is the ratio of the moisture-conditioned to the unconditioned specimens in percentage notation. The Sasobit samples showed lower ITS, Strain, TI in unconditioned and moisture conditioned cases. The P-value from the paired t-test indicated that there is significant difference between conventional and Sasobit mixtures in terms of strain for the unconditioned case and strength in the moisture conditioned case. In all other cases there was no significant difference between the two mixes.

HAMBURG WHEEL TRACKING TEST

The statistical analysis of the variance ANOVA for the effect of mix type (conventional versus Sasobit®) on the measured rut depth was performed. The statistical analysis suggests that there is no significant effect of the mix type on the measured deformation of HWT (Pr=0.166> 0.05). The ANOVA calculation assumed no variation in the void content among all the samples.

Table 6 Results for indirect tensile strength test

Unconditioned						
Parameter	**Strength (psi)**		**Strain (%)**		**TI**	
Mixture	**Conv**	**Sasobit®**	**Conv**	**Sasobit®**	**Conv**	**Sasobit®**
Average	220	188	0.51	0.33	0.76	0.72
%CV	5	10	11	18	3	5
P-value	0.175		0.016		0.314	
Moisture-Conditioned						
Average	234	189	0.51	0.60	0.72	0.70
%CV	6	12	18	55	7	18
P-value	0.032		0.708		0.841	
TSR	106.0	100.5				

CONCLUSIONS

This study in hand provides an experimental investigation on the effect of using the organic additive Sasobit® on the performance of asphalt mixes. The study included indirect tensile strength test (ITS), Loaded Wheel Tracking- Hamburg type (HWT) test, Simple Performance Tests (SPT) E*, and Semi-Circular Bend (SCB) Test. The tests were performed on a conventional and Sasobit® mixes.

- In general, the ITS results showed that there is a significant difference between the conventional and the Sasobit® mixes in terms of ITS parameters. The conventional mix had a higher ITS than the Sasobit® mix. The effect of aging is investigated using the ITS test. The results showed no significant difference between conventional and Sasobit® mixes due to aging.
- The SCB test results showed no significant difference between the conventional and the Sasobit® mixes.
- The dynamic modulus (E*) results show that the Sasobit® Modified mix experienced lower modulus values than the conventional mix. However, the difference between the conventional and the Sasobit® Modified moduli decreased as the temperature increased. The statistical parameter, P-value, indicated that there is no significant difference between the E* of the Conventional and Sasobit mixes.
- The performance parameter E*Sinδ showed no significant difference between conventional and Sasobit mixtures form the paired t-test. The cracking performance parameter (E*Sinδ) showed P-values close to 0.05. The cracking parameter showed significant difference between the mixes from the analysis of variance on the results of all temperatures and frequencies. However, this parameter showed poor correlation to field cracking measurement, Pellinen and Witczak [7]. Consequently, E*Sin δ is a less reliable parameter for evaluating the cracking resistance.
- The ITS test is used to examine the moisture susceptibility of the two mixes (conventional and Sasobit®). The ANOVA analysis indicated no significant effect of the moisture conditioning on the tensile strength (Pr> 0.05). However

it indicated that there is a significant effect of the mix type (conventional versus Sasobit®) on the measured tensile strength (Pr< 0.05).

- The HWT showed that both mixtures are good performers. The HWT test showed slight differences between the conventional and the Sasobit® mixes in terms of the developed deformation. The statistical analysis showed that there is no significant difference in the deformation due to the mix type. The statistical analysis did not include the effect of void content variation.

ACKNOWLEDGMENTS

This research was supported by the Louisiana Transportation Research Center (LTRC) and the Louisiana Department of Transportation and Development (LADOTD). The authors would like to express thanks to all the people involved in the Engineering Materials Characterization Research Facility for all their help in conducting this research.

REFERENCES

1. Freddy L. Roberts, Prithvi S. Kandhal, E. Ray Brown, Dah-Yinn Lee; and Thomas W. Kennedy. "*Hot Mix Asphalt Materials, Mixture Design, and Construction*". Second Edition, NAPA Research and Education Foundation, Lanham, Maryland, 1996.
2. Kuennen, T., "*Warm Mixes are a Hot Topi*c". Better Roads, June 2004.
3. Australian Asphalt Pavement Association. "*Warm Mix Asphalt- A state of the Art Review*". Advisory Note 17, June 2001.
4. "Louisiana Standard Specification for Roads and Bridges," State of Louisiana, *Department of Transportation and Development*, Baton Rouge, 2000 Edition.
5. Wu, Z., L. Mohammad, and M.A. Mull. "*Characterization of Fracture Resistance of Superpave Mixture using the Semi-Circular Bending Test.*" Journal of ASTM International (JAI), Vol. 2, No.3, March 2005 (in print).
6. Mohammad L. N., Wu, Z., Mull, M.A. (2004). "Characterization of Fracture and Fatigue Resistance on Recycled Polymer-Modified Asphalt Pavements". Proceeding of the 5th RILEM International Conference on Pavement Cracks, France, 2004.
7. Pellinen, T. K., and Witczak, M. W. (2002). "*Use of stiffness of hot-mix asphalt as a simple performance test.*" TRB CD, Transportation Research Board, Washington, D.C.

Ground Penetration Radar as a Tool for Pavement Condition Diagnostics

Desh R. Sonyok[1], S.M. ASCE and Jie Zhang[2], M. ASCE, P.E.

[1] Graduate Student, Civil Engineering Department, New Mexico State University, P.O. Box 30001, MSC-3CE, Las Cruces, NM 88003-8001; drsonyok@nmsu.edu
[2] Assist. Professor, Civil Engineering Department, New Mexico State University, P.O. Box 30001, MSC-3CE, Las Cruces, NM 88003-8001; jzhang@nmsu.edu

ABSTRACT: Ground Penetration Radar (GPR) is a reliable and high performance nondestructive testing tool for pavement management in a network level, which requires pavement condition assessment and deterioration modeling. GPR can determine the layer thickness, detect voids, and estimate moisture content of the in-situ soil underlying the pavement. Therefore, it is considered to be a promising tool for the assessment of pavement conditions. Pavement condition information obtained by GPR is very useful to predict the pavement structural capacity and performance. This will further help improve pavement maintenance and rehabilitation strategies and also provide rationalities in allocating available funds. However, the application of GPR in pavement is limited due to incomplete understanding of dielectric properties of pavement materials. This review paper presents the state-of-the-art GPR applications in pavement condition assessment and its future development. Finally, issues related to further investigation of the GPR improvement is also discussed.

INTRODUCTION

GPR is a very powerful, reliable, and high performance nondestructive testing tool for solving different kinds of engineering problems such as geotechnical site investigation, construction, and maintenance of highways and bridges. Management of road pavement on a network level requires condition assessment and deterioration modeling. GPR can provide reliable input data for this purpose. This will further help to design feasible improvement strategies and intelligent allocation of resources for a long term (Sobanjo and Tawfiq, 1999).

GPR has been used to determine the pavement layer thickness, detect subsurface distresses, and estimate moisture content of the in-situ soil underlying flexible pavement. In rigid pavement, GPR has been used to measure concrete slab thickness, detect voids or loss of support under slabs, detect rebar location, and estimate reinforcement cover depth (Al-Qadi et al, 2006). Furthermore, it can also be used to investigate other highway-related problems. For example, it can be helpful in solving geologic issues such as faults, landslide slip-planes, stratigraphy and soil structure, geologic structure, groundwater table location, bedrock depth and bedrock topography, etc (Lewis et al., 2002). It is also useful to evaluate underlying structures of roadways and foundations of highway system to determine construction quality, locations and types of buried foundations, pipes and other underground utilities.

This paper reviews basic principles of GPR and its application in pavement-related fields. Also, issues related to the possible integration of GPR with other non-destructive evaluation methods and their developments for a network-level pavement management system are discussed.

OVERVIEW OF GROUND PENETRATION RADAR TECHNOLOGY

Ground Penetration Radar, also known as subsurface radar, impulse radar or ultra-wide radar, is the most commonly used non-destructive field testing equipment at present (Martinot and Zhang, 2002). A modern GPR system comprises a signal generator, transmitting and receiving antennae, recording facilities, and a graphical output unit. As shown in Figure 1, the system can generate a continuous electromagnetic (EM) pulse which is transmitted through the ground. When the transmitted signal enters the ground, part of the EM waves reflects back from the interface due to changes in dielectric properties; while the rest of the waves pass through to the next interface. The reflected signals return to the receiving antenna and are recorded. The arrival time of the reflection at the layer interface is used to calculate relative dielectric constant and then convert to individual layer thickness. The amount of EM waves transmitted and reflected through the interface is a function of the electromagnetic impedance contrast between the two contact layers. Stronger reflected signal is obtained if the difference in the electromagnetic properties of the two layers is larger.

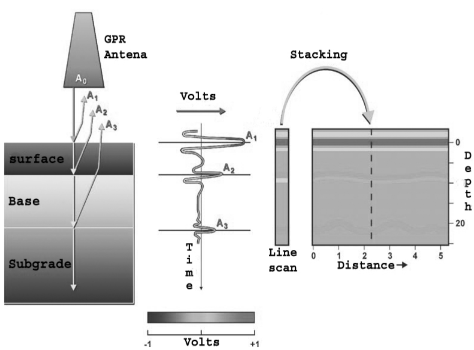

FIG. 1. Typical air-coupled GPR measurement system (after Krugler and Fults, 2002)

The radar frequency of GPR system influences both the spatial resolution and the penetrating depth. Generally, the depth of penetration is a function of EM wave frequency and pavement and soil types. Higher frequencies provide higher spatial resolutions but lower penetrating depths, whereas lower frequencies can reach larger penetrating depths but lower spatial resolutions. For pavement applications, GPR systems give best results over the frequency range of 500 MHz to 2.5 GHz. However, the frequency range of GPR in highway applications should comply with the Federal Communications Commission (FCC) regulation, which restricts the frequency range of operating GPR below 960 MHz or between 3.1 and 10.6 GHz (Liu et al., 2006).

Depending on the arrangement, antennae of GPR systems are classified as air-coupled (or launched) and ground-coupled. The air-coupled antennae (also called horned antennae) are typically 150 to 500 mm (6 to 20 in.) above the surface (Al-Qadi et al, 2006). The air-coupled GPR antenna allows to survey in a highway speed without road closure. However, the penetrating depth of this system is limited due to the reflection of EM energy by pavement surface. On the other hand, ground-coupled antennae are in full contact with the ground, which give higher depths of penetration at the same frequency. The limitation of ground-coupled antenna is that it greatly reduces the survey speed, which is not desirable for a network-level survey.

Estimation of Pavement Layer Thickness

Pavement management system requires an accurate prediction of pavement layer thickness for the design of overlay, quality control and assurance, and structural capacity estimation of existing pavement to predict their remaining life. For these purposes, GPR technology could be a good non-destructive evaluation choice, which is rapid, cost-effective, and can be operated more efficiently without disturbing the traffic. Depending on the surveyed pavement structure, age, GPR calibration, and data analysis technique, the accuracy of pavement thickness measurement varied from ±2.9% to ±12% (Maser, 1996; Lahouar et al., 2002; Al-Qadi et al., 2003). Reported data indicates that the accuracy of layer thickness in newly built hot-mix asphalt (HMA) pavement is higher than that in old pavement. Similarly, the accuracy of layer thickness in HMA layer is higher than that in granular base layer of the pavement.

The thicknesses of pavement layers from a pulse GPR can be determined by the time difference between the reflected pluses from different layers and the dielectric properties of surveyed layers. The thickness can be calculated through

$$d_i = \frac{c\ t_i}{2\sqrt{\varepsilon_{r,i}}} \tag{1}$$

where d_i is the thickness of layer i; c is the speed of light in free space ($\approx 3\times10^8$ m/s); t_i is the EM wave two-way travel time between the interfaces of layer i and i+1; and $\varepsilon_{r,i}$ is the relative permittivity or dielectric constant of layer i (Wimsatt et al., 1998). For the implementation of Equation (1), priori knowledge of dielectric properties of layer material is necessary, which makes it impractical to apply directly. Recently, an efficient way of estimating dielectric constant at highway speed is based on the amplitudes of the reflected pulses collected by GPR antennae. Detailed algorithm of this method can be found in Al-Qadi et al. (2006). In this approach, two assumptions are made: (1) pavement layers are considered to be homogenous throughout the entire thickness and (2) they are non-conductive. However, if the HMA layer is not uniform, the first assumption will be violated. Therefore, this method is generally more reliable for relatively newly constructed pavement. For older pavement, the accuracy can be improved by utilizing dielectric correction factor based on limited field cores (Al-Qadi and Lahouar, 2005 and Al-Qadi et al., 2006).

Evaluation of In-Situ Pavement Material Properties

The application of GPR to evaluate in-situ pavement material properties has been dramatically increased in the past three decades. The information obtained from GPR, such as time delays, frequency modulations, and the amplitude of reflected signals, are useful indicators to evaluate the in-situ pavement material properties (Benedetto et al., 2005). GPR can produce images of subsurface and delineate underlying structures with different electric and dielectric properties. The dielectric constants of subsurface materials are calculated and converted into equivalent densities and water contents.

Construction materials can be characterized by their unique dielectric properties and EM wave propagation capability. The velocity of EM wave in a material is a function of the material's dielectric constant and water content. Typical dielectric constants of dry asphalt and concrete pavement material lie in the range of 5 to 6 (Shang and Umana, 1999 and Janoo et al., 1999). This value increases as the water content increases because of the high dielectric constant of water (around 80). Increase in subgrade dielectric constant may indicate the increase in volumetric water content of the subgrade, which can degrade the structural integrity of pavement. Therefore, variation in dielectric properties of concrete can be used to determine its deterioration (Maser, 2001). Significant departure of dielectric constant from the mean value could indicate that the area has either high or low moisture content, indicating either excessive moisture infiltration or high void content. In summary, the precursor to pavement failure, i.e., moisture content is directly related to the dielectric constants of pavement materials and can be estimated by GPR.

Based on the volumetric mixing model, Roth et al. (1990) gave a relationship to estimate volumetric water content. Recently, several researchers carried out their studies to investigate the influence of water content and soil density on dielectric constant (Roth et al.,1990; Saarenketo, 1998; Shang et al., 1999; Janoo et al., 1999; Olhoeft, 2000; Benedetto and Benedetto, 2002 & 2003; Benedetto et al., 2005 etc). Results showed that the dielectric properties are highly correlated with the water content in soil. This is the basis for GPR to be used as a diagnostic tool to identify pavement damages, if the damages are related to the anomalous water content or bad compaction. However, this finding is not conclusive and needs further investigation. Therefore, a clear understanding of the material dielectric behavior as a function of moisture content, pavement type, frequency, and the structure of material is necessary to develop GPR as a pavement conditions diagnostic tool.

APPLICATIONS IN NETWORK LEVEL PAVEMENT MANAGEMENT

Pavement functional performance is evaluated through the visual inspection of pavement surface conditions such as pavement roughness and surfaces distresses (Zaghloul et el., 2004). This is the most commonly used method to monitor pavement performance and determine maintenance activities. However, this method only deals with pavement surface conditions and not its structural integrity. Therefore, maintenance works based on the surface data may only lead to premature failure if applied to structurally weak pavement section. On the other hand, pavement with high surface distresses may be structurally sound and a pavement preservation treatment may work quite well to extend its life.

The structural capacity of pavements can be evaluated using destructive or non-destructive testing (NDT). The destructive testing includes laboratory testing of core samples and field testing. The nondestructive testing (NDT) includes Benkelman Beams, Dynaflects, Ground Penetrating Radar (GPR), Seismic Pavement Analyzer (SPA), and Falling Weight Deflectometer (FWD), etc. Among the available NDT methods, GPR is the most versatile and popular one. The GPR technique is used by many agencies for the management of roadway pavement to evaluate the layer thickness, anomaly location such as the presence of voids or separation, and in-situ soil water content and density (Benedetto el al., 2005). GPR is very productive in measuring the structural integrity of pavements on a network basis due to its mobility.

Asphalt Pavement

GPR is useful to determine layer thickness and water content of asphalt concrete pavement. The accuracy of thickness determination of asphalt pavement depends on not only the dielectric constant of asphalt materials, but also the thickness of pavement layer itself. The reflected pulses in GPR would have minor to non-existent overlap when surveying relatively thick pavement layer, which results detecting the layer interface reflection easier than in the case of thin layer (Al-Qadi and Lahouar, 2005). Flexible pavements are usually composed of at least one thin layer, such as wearing surface or any newly placed overlay. Therefore, thick layer conditions are not applicable for flexible pavement. However, newly built and non-aged flexible pavements can be considered as relatively thick layers if they are composed of the same type of aggregate (Al-Qadi and Lahouar, 2005). Thin layers are typically found in in-service flexible or rigid pavements. Details of signal processing techniques for thin layers can be found in Lahouar et al. (2002) and Al-Qadi and Lahouar (2005).

Reinforced Concrete Pavement

GPR can be used to estimate thickness of reinforced concrete pavement accurately. Reinforced concrete structures are subject to deterioration caused by internal and external factors. Deterioration or damage is expressed in the form of cracking, spalling, delamination, excessive deflection, and corrosion. By recording the arrival time of reflected GPR pulse, deterioration of reinforced concrete can be inferred from the corresponding dielectric constant. However, reliable evaluation technique for mechanical deterioration is still unsolved due to the lack of consistent physical approach that links the GPR measurement to mechanical deterioration (Maser, 2001). Therefore, relationships between the deterioration of reinforced concrete pavement and its dielectric properties are required for further investigation for the successful application of GPR in reinforced concrete pavement evaluation.

Composite Pavement

In composite pavement, the thickness of asphalt layer and the condition of the underlying concrete base are necessary for planning a rehabilitation and reconstruction program. Therefore, GPR can be used to estimate the asphalt thickness which is necessary to determine the original concrete surface after asphalt removal and to find total asphalt removal quantities (Maser, 2001). Furthermore, GPR can assess the condition of underlying concrete in order to estimate the location and extent of any repair necessary for rehabilitation program. Any deterioration in concrete base can be inferred from the changes in dielectric properties as mentioned earlier. For example, concrete with high water and chloride content, is usually associated with corrosion damage. These conditions can be quantified using the calculated dielectric constant of the concrete.

APPLICATION IN MECHANISTIC-EMPIRICAL PAVEMENT DESIGN

Recently, AASHTO member states are moving towards mechanistic-empirical pavement design procedures. Mechanistic-Empirical Pavement Design Guide (MEPDG) requires input data being related to local climate, material, traffic, and the structure of pavement layer (NCHRP, 2004). For this propose, GPR can provide useful information related to pavement thickness, water content, and density. This information together with the deflection data from FWD can be used to back-calculate the resilient modulus of the pavement layers (Uzarowski et al. 2005). GPR can also be used to provide a continuous profile of pavement layers and identify areas of poor pavement condition. This will reduce the extensive requirement of coring, thus reduce the rehabilitation cost. Thickness information from GPR can also be used to increase the accuracy of FWD result.

GPR is especially useful when the subgrade is composed of clay and clay-till whose performance are susceptible to water content. In order to increase the accuracy of water content determination, the use of a broader range of frequency is desirable (Olhoeft and Stanley, 2000). For such cases, two antennae are required, one at a higher frequency above 1 GHz and the other at a lower frequency below 500 MHz. The information related to water content and density can also be employed in “Enhanced Integrated Climate Model” of MEPDG. However, GPR data interpretation is still subjective and may give inconsistent result with ground truth (Morey, 1998). GPR data interpretation requires experienced interpreters and it is time-consuming. Therefore, a rapid and objective data analysis technique is necessary in successful implementation of GPR in MEPDG framework.

SUMMARY AND CONCLUSIONS

Ground Penetration Radar is one of the most commonly used non-destructive testing equipments in highway industry. It can accurately determine pavement layer thickness with the error of ±2.9% to ±12% and estimate water content of the in-situ soil underlying the pavement surface. GPR can be an effective alternative to coring for various pavement engineering applications. In the mean time, GPR accuracy and data processing techniques are being improved rapidly. The GPR information is reliable and provides significant information to pavement condition evaluation, which is very useful to predict the pavement structural capacity and performance. Since the FWD is not productive for network-level survey, coupling of GPR data with Rolling Wheel Deflectometer (RWD) deserve further research. Integration of RWD with GPR data can be a reliable basis for mechanistic pavement performance prediction model.

Despite the advantages mentioned above, the current GPR technology has some technological as well as physical limitations. Interpreted GPR thickness may be influenced by field conditions and the calibration of velocities. There is always a compromise between penetration depth and target resolution. Moreover, exploration depth is governed by material to be tested not an instrument itself. For example, clayey soils attenuate GPR signals and limit penetration depth significantly. Determination of soil water content requires fairly uniform soil. If the soil is not homogeneous, other factors may influence the velocity of EM waves and give false water content values. Finally, it is necessary to clearly understand the relationships among the electromagnetic wave, dielectric constant, water content, and pavement behavior in order to develop an objective and meaningful GPR data analysis technique. GPR equipment with high accuracy and resolution coupled with reliable software for interpretation and display of results on real-time is urgently needed.

REFERENCES

Al-Qadi, I.L., Jiang, K., and Lahouar, S. (2006). "Analysis tool for determining flexible pavement layer thickness at highway speed". *85th Annual Meeting of Transportation Research Board*, (CD ROM)

Al-Qadi, I.L. and Lahouar, S. (2005). "Measuring layer thickness with GPR - Theory to practice". *Construction and Building Materials*, 19(10), 763-772.

Al-Qadi, I.L., Lahouar, S. and Loulizi A. (2003). "Successful application of GPR for quality assurance/quality control of new pavements." *Trans. Res. Rec.1861*, 86-97.

Berthelot, C., Gehlen, T., Scullion, T., and Drever, D. (2005). "Use of non-destructive testing in the structural rehabilitation decisions of a primary urban corridor". *84th Annual Meeting of Transportation Research Board* (CD ROM)

Benedetto, A. and Benedetto, F. (2002). "GPR experimental evaluation of subgrade soil characteristics for rehabilitation of roads". *Proc. of SPIE*, 4758, 708-713.

Benedetto, A. and Benedetto, F. (2003). "Sub-surface remote sensing by ground penetrating radar for subgrade soil characterization and possible road damage detection." *Proc. 2003 Tyrrhenian Intl. Workshop on Remote Sensing*, 467-476.

Benedetto, A., Benedetto, F., Blasiis, M.R., and Giunta, G. (2005). "Reliability of signal processing technique for pavement damages detection and classification using ground penetration radar". *IEEE Sensor Journal*, 5(3), 471-480.

Janoo, V., Korhonen, C., and Hovan, M. (1999). " Measurement of ware content in Portland cement concrete." *J. Trans. Engrg.,* 125, 245-249.

Krugler, P. and Fults, K. (2002). "Implementation of Ground Penetrating Radar Technology for Pavement Evaluation." [Online] Available: http://tig.transportation.org/sites/aashtotig/docs/GPR%20Presentation.pdf

Lahouar, S., Al-Qadi, I.L., Loulizi, A. Clark, M.T., and Lee, D.T. (2002). "Development of an approach to determine in-situ dielectric constant of pavements and its successful implementation at Interstate 81". *81st Annual Meeting of Transp. Research Board*, Paper No. 02-2596, Washington, D.C.

Lewis, J.S., Owen, W.P., and Narwold, C. (2002). "GPR as tool for detecting problems in highway related construction and maintenance". *2nd Annual Conf. on the Application of Geophysical and NDT Methodologies to Transportation Facilities and Infrastructure*. [Online] Available: http://www.dot.ca.gov

Liu, R., Li, J., Chen, X., Xing, H., Ekbote, A., and Wang, Y. (2006). "Investigation of new generation of FCC compliant NDT devices for pavement layer information collection". *Texas DOT Project*, FHWA/TX-05/0-4820.

Martinot, A.R. and Zhang, Z. (2002). "Evaluation of data collection methods for pavement layer data". *81st Annual Meeting of the Trans. Research Board*.

Maser, K.R. (1996). "Measurement of as-built conditions using ground penetrating radar." *In: Structural materials technology: an NTD conference*, 61-67.

Maser, K.R. (2001). "Use of ground penetration radar for rehabilitation of composite pavement on high volume roads". *Transp. Res. Rec.,* No. 1808.

Morey, R.M. (1998). "Ground penetrating radar for evaluating subsurface conditions for transportation facilities." *Transp.Res.Board*, Washington, D.C.

NCHRP (2004). "Guide for mechanistic-empirical design of new and rehabilitated pavement structures." *Final Report*, NCHRP Project, 1-37A.

Olhoeft, G.R. (2000). "Maximizing the information return from ground penetrating radar." *J. Appl. Geophysics*, 43, 175-187.

Olhoeft, G.R. and Stanley, S.M. III (2000). "Automatic processing and modeling of GPR data for pavement thickness and properties". *GEORADAR* [Online] Available: http://www.g-p-r.com/GPR2000A.PDF.

Roth, K., Schulin, R., Fluhler, H. and Attinger, W. (1990). "Calibration of time domain reflectometry for water content measurements using composite dielectric approach." *Water Resour. Res.* , 26 (10), 2267-2273.

Saarenketo, T. (1998). "Electrical properties of water in clay and silty soils." *J. Applied Geophysics,* 40, 73-88.

Shang, J.Q., Umana, J.A., Barlett, F.M., and Rossiter, J.R. (1999). "Measurement of complex permittivity of asphalt pavement materials." *J Trans. Engr*, 125 (4), 347-356.

Sobanjo, J.O. and Tawfiq, K.S. (1999). "Framework for incorporating nondestructive evaluation (NDE) into pavement and bridge management systems". *Proc.of SPIE*, 3587, 138-145.

Uzarowski, L., Maher, M., and Balasundaram, A. (2005). "Practical application of GPR to supplement data from FWD for quick pavement performance prediction." *2005 Annual Conf. of the Transp. Assoc. of Canada* (CD-ROM).

Wimsatt, A.J., Scullion, T., Ragsdale, J., and Servos, S. (1998). "The use of ground penetrating radar data in pavement rehabilitation strategy selection and pavement condition assessment." *Transp.Res.Board*, 98-0729, Washington, DC.

Zaghloul, S., Marukic, I., Ahmed, Z., Vitillo, N., Sauber, R., and Jumikis, A. (2004). "Development of a network level structural adequacy index model for NJDOT PMS". *83rd Annual Meeting of the Tranps. Research Board* (CD ROM).

The Urban Heat Island Effect and Impact of Asphalt Rubber Friction Course Overlays on Portland Cement Concrete Pavements in the Phoenix Area

Mark Belshe[1], P.E., Kamil E. Kaloush[2], Ph.D., P.E., Jay S. Golden[3], Ph.D., SCPM, REA and Michael S. Mamlouk[4], Ph.D., P.E.

[1]FNF Construction, Inc., 115 S. 48th Street, Tempe, Arizona 85281; mbelshe@fnfinc.com

[2]Associate Professor, Arizona State University, Department of Civil and Environmental Engineering, PO Box 875306, Tempe, AZ 85287-5306,; kaloush@asu.edu

[3]Assistant Professor, Arizona State University, School of Sustainability, P.O. Box 873211, Tempe, Arizona 85287-3211; jsgolden@asu.edu

[4]Professor, Arizona State University, Department of Civil and Environmental Engineering, PO Box 875306, Tempe, AZ 85287-5306; mamlouk@asu.edu

ABSTRACT: Larger volume of paving and building materials gives urban areas a much higher thermal storage capacity than natural surfaces. Satellite thermal imagery of the Phoenix region showed that paved surfaces, including parking lots, local roads, and highways play a significant role in regards to the Urban Heat Island (UHI). In the past few years, the Arizona Department of Transportation's (ADOT) "Quiet Pavements" program have been highly successful with the traveling pubic in addressing roadway noise; the urban freeway in the Phoenix metropolitan has been resurfaced with an Asphalt Rubber Friction Course (ARFC) layer to reduce the noise impact to the surrounding neighborhoods by as much as 4 to 6 decibels.

This paper looks into the hypothesis that one consequence of the overlay program is to extend the life of the Portland Cement Concrete Pavement (PCCP) due to mitigation of daily thermal variances. Counterbalancing this benefit, the use of a dark material to overlay hundreds of lane miles in an urban setting plagued by a growing UHI may need consideration. It is hypothesized that by adding a "blanket" over the PCCP, the underlying material will experience higher low temperatures and lower high temperatures. Thermally induced stresses to PCCP can be very damaging, and anything that would lessen the temperature swings would be very beneficial.

This study includes a field instrumentation effort with pavement temperature sensors to quantify the thermal behavior of the PCCP with and without the ARFC

overlays. Thermally induced curling stresses are calculated, the benefit to the overall pavement service life is modeled, and the overlay strategy viewed as a pavement preservation tool is summarized.

INTRODUCTION

Phoenix, Arizona is one of the fastest growing areas in the nation with an increase of over three times it 1975 population. Urban land use has more than doubled during this same period (U.S. EPA, 2007). This rapid urbanization is resulting in the transition of native vegetation to engineered paved surfaces and high density building structures. The urban environment, with its impervious paved surfaces, varied building geometries, and reduced vegetation, causes less of the incoming sun radiation to be reflected, to be re-released or to be converted to latent energy associated with evaporation or transpiration of moisture (Golden, 2004). In addition, this larger volume of paving and building materials gives urban areas a much higher thermal storage capacity than natural surfaces. UHI is primarily a nighttime phenomenon, though many areas report higher temperatures both day and night. However, UHI manifests most obviously at night with elevated low temperatures. In Phoenix the summer nighttime temperatures have been recorded to be 5°C to 16°C higher today than 30 to 50 years ago (Ingley, 2003). Evidence of this can be observed by satellite images which present the impact of engineered materials to surface and ambient temperatures.

Since the late 1980's the Arizona Department of Transportation (ADOT) has been placing Asphalt Rubber Friction Course (ARFC) mixes over existing Portland Cement Concrete Pavements (PCCP). The initial intent of the overlay was to restore smoothness and assist in the redevelopment of skid resistance of the riding surface. Prior to the overlay, the PCCP was typically rehabilitated by spall repairs, slab replacements and resealing of joints. Bridge decks and bridge approach areas were sealed. The ARFC mix proved to be excellent in retarding reflective cracking of the PCCP jointing with many mixes serving ten years or more without significant maintenance costs (Rodezno et al, 2005).

As more of the surfacing was placed, public interest with considerable general approval motivated ADOT in 2003 to begin placing the ARFC as a noise mitigation strategy. Addressing a quality-of-life issue through a paving strategy was innovative and taxpayers have been very supportive of the program. A reduction from roadway noise of 4 to 6 decibels has typically been documented in adjacent neighborhoods. As of January 2007, approximately 175 kilometers of a total of 195 urban freeway kilometers have been overlaid in the greater Phoenix urban area and about an additional 80 kilometers of urban freeway have been surfaced similarly in other separate projects.

Many benefits have been identified by this strategy. The restoration of a smoother ride and the increase in skid resistance were the initial goals. The highly popular noise mitigation program evolved from the early programs, but little has been discussed about the effects of these overlays on the PCCPs upon which they are placed.

As a consequence of studying the impact of the overlays on the Phoenix area UHI, it was hypothesized that the insulating effects of the additional ARFC mix were mitigating the daily thermal stresses within the PCCP. This could lead to a longer service life and preservation of a significant public works investment. The protection of the PCCP structure with its high initial costs and long, disruptive construction schedules could be added as another excellent reason to pursue this paving strategy.

OBJECTIVE AND SCOPE

The objective of this study was to assess and quantify the impact of ARFC overlays on PCCP with particular focus on the influence to curling stresses. The scope of work included a field instrumentation effort with pavement temperature sensors to quantify the thermal gradient of the PCCP with and without the ARFC overlay and calculations of the thermally induced curling stresses using established equations to model the pavement behavior.

TEMPERATURE GRADIENT EFFECTS ON PCCP

It is well known that the stresses affecting rigid pavements are mostly the result of combined effects of repeated wheel loading, varying temperature and moisture gradients (Mohamed and Hanson, 1997, Bouzid and Mang, 1995). Temperature variations affect the PCCP in two ways. Temperature changes between summer and winter causes stresses due to restrained expansion and contraction in the whole slab. Additionally, temperature changes between day and night cause temperature differentials between the top and bottom of the slab resulting in stresses due to curling. This paper addresses the effect of ARFC overlays on curling stresses.

When the temperature at the top of the slab is greater than the bottom, the top tends to become longer with respect to the neutral axis due to thermal expansion (Huang, 2004). This is a positive temperature differential. The weight of the slab restrains the expansion and contraction which induces compressive stresses at the top and tensile stresses at the bottom. Similarly, at night, the top of the slab tends to become cooler while the retained thermal energy at the bottom of the slab results in higher bottom temperatures. This would be considered a negative temperature differential. Since the top tends to contract with respect to the bottom, tensile stresses are induced in the top and compressive stresses at the bottom.

According to several studies, temperature-induced pavement responses could be significant (Mahboub et al, 2004). Temperature differentials in a rigid pavement slab have been shown by some researchers to directly relate to fatigue damage (Masad et al, 1996, Gillespie et al, 1993). They reported that a gradient of 0.6 °C/inch in the slab increases fatigue damage due to truck traffic by a factor of 10 as opposed to a zero-temperature-gradient condition.

FIELD INVESTIGATION OF PCCP THERMAL BEHAVIOR

Temperature Sensors

As part of a larger study investigating pavements' contribution to Urban Heat Island Effect, the thermal behavior of PCCPs began to be intensely investigated by Arizona State University in early 2003 (Belshe, 2006). Seeking a convenient and reliable method to collect temperature data, the use of sensors called iButtons® was found to fit the study's parameters. These sensors were primarily designed for use as maturity meters in the production of portland cement concrete structures. The sensors are approximately one-half inch in diameter and include the battery and micro circuitry to record and store over 2000 readings at a pre-programmed rate. They are encased in a protective rubber-like material. A 20-minute reading interval will continuously store data for 28 days before data begins to be replaced by new readings. The battery is advertised to last approximately ten years. Data is recovered from the exposed leads using a laptop computer and proprietary software provided by the vendor. The probes are manufactured to have an accuracy of ±1°C. The cost of each sensor is about $35 and the software to read the sensors is listed at $550. A laptop or handheld computer must also be available.

Test Sites and Sensor Installation

Initially, nearly one hundred sensors were placed throughout the Phoenix metropolitan area. Sites for sensor placement were selected based on available construction opportunities that were ongoing at the time, and as data was collected, it was clear a well-planned installation encompassing several controlled conditions was needed if a study focus on curling stresses was to be pursued. Two major test sites had been developed as part of the earlier larger study, the Shea site and the Durango site. A third site was developed on Interstate 10 at Ray Road in Phoenix to facilitate an investigation into the impact of the overlays on PCCP curling stresses. Data analyzed in this paper were obtained from the Ray Road site.

Interstate 10 at Ray Road offered an opportunity to create excellent modeling conditions for quantifying the effects of ARFC overlays of PCCP. The I-10 pavement north of Ray Road had been overlaid with ARFC and the area south of Ray Road remained with only the PCCP surface. Areas either side of Ray Road on I-10 were instrumented in May 2006. With two locations within the vicinity of the start of the overlay, one within the ARFC overlay area and one with only PCCP, data were generated for both conditions of PCCP with and without ARFC. Also, each location included sensor placement located in the shoulder areas of each condition allowing a matrix that included data from areas with and without traffic.

The existing PCCP was cored and sensors were placed using dowels to insure top to bottom spacing. Sawcut lines were then made from the cores to the shoulder so that future data collection could be made without impacting traffic. The cores were filled and the sawcut lines were sealed with joint sealant including the use of backer rod.

Analysis of Temperature Differentials

Data was recovered from the months of June through December 2006, and two days were examined in depth. June 2006 was the warmest June ever with a mean temperature of 34.7°C, almost 2.8°C above the normal mean of 32.1°C. June 25th recorded a monthly high of 45°C. The lowest ambient temperature of 2006, 1.7°C, was recorded on December 23, 2006. Therefore, data from June 25th and December 23rd were selected for analysis. Figure 1 illustrates a typical thermal signature showing that as the depth in the PCCP increases, the difference between the daily high and low mediates. The depth of the sensor embedment in the PCCP is recorded in the respective legend data.

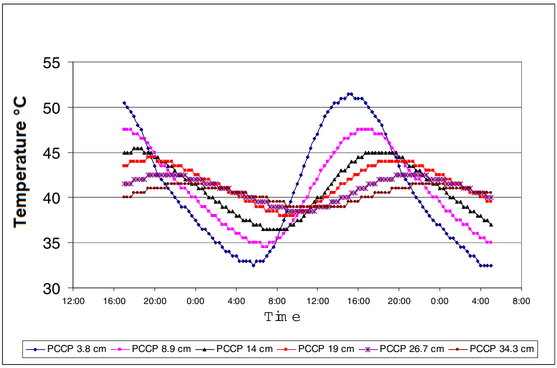

FIG. 1. Temperature vs. Time at Different Depths for PCCP with ARFC Overlay Subjected to Traffic.

Figures 2 and 3 compare the ΔTs (temperature difference between top and bottom of the PCCP) for June 25, 2006 and December 23, 2006. These figures compare the effect of an ARFC overlay on a PCCP with traffic. Note that the section with ARFC generally records less extremes in ΔTs than the section without the overlay for June 25th. Similarly, a thermal blanket effect helps the heat retention of the mass in the lower reaches of the PCCP in the December 23rd graph.

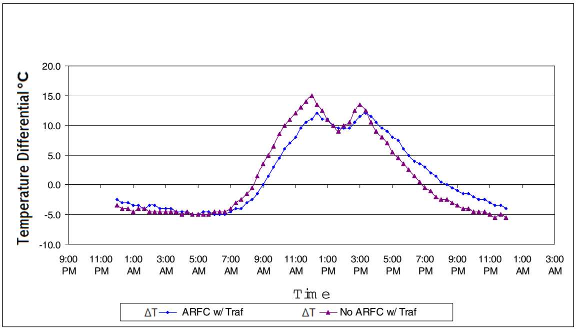

FIG. 2. Comparison of ΔT for June 25, 2006.

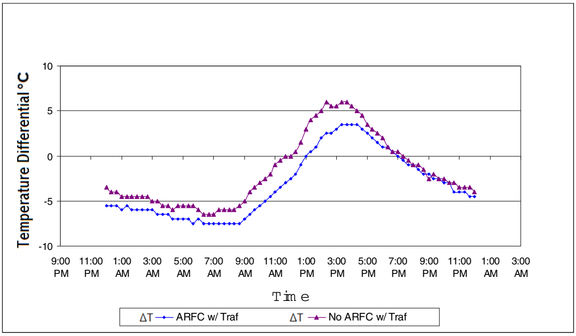

FIG. 3. Comparison of ΔT for December 23, 2006.

STRESS ANALYSIS

In order to quantify the mitigating impact of ARFC overlays on PCCP temperature gradients, the induced stresses in the x and y direction, as well as the edge stress at the midspan of slab were calculated using well-known equations (Huang, 2004). The equations that were used assume a linear distribution of the temperature gradient, which has been shown not to be the case, so the calculations should be regarded as approximations. Table 1 presents this data. The Location 1 referred to is in the section north of Ray Road which has been overlaid, and Location 4 is in the section south of Ray Road which has not been overlaid. Both locations are in the same traffic lane and would have identical traffic conditions.

TABLE 1. Stress Calculations for June 25th and December 23rd.

Stress Calculations (kPa)		σ_x	σ_y	$\sigma_{midspan}$
Location 1 - June 25, 2006	Daily ΔT			
PCCP w/ ARFC w/ Traffic	High	827	538	745
PCCP w/ ARFC w/ Traffic	Low	-448	-290	-407
Location 4 - June 25, 2006				
PCCP w/o ARFC w/ Traffic	High	1035	627	934
PCCP w/o ARFC w/ Traffic	Low	-483	-314	-529
Location 1 - December 23, 2006				
PCCP w/ ARFC w/ Traffic	High	518	336	467
PCCP w/ ARFC w/ Traffic	Low	-242	-157	-218
Location 4 - December 23, 2006				
PCCP w/o ARFC w/ Traffic	High	449	291	405
PCCP w/o ARFC w/ Traffic	Low	-414	-269	-374

Note that the aeration effect of traffic aids in the reduction of daily high stress for the section with the overlay for the summer data, but the thermal blanket effect results in slightly higher stress levels at the daily high for the section with the overlay in the winter data. In all cases the range of daily stress level is reduced in the sections with the overlay. This range of reduction appears to be 13% to 27%. Figure 4 shows the stress profile for the December data for the σ_x parameter.

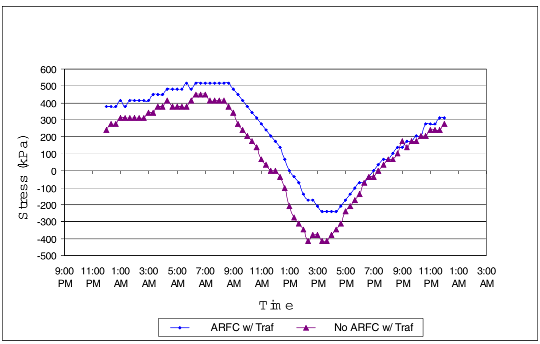

FIG 4. Calculated σ_x Stress for 24 Hour Cycle – December 23, 2006.

Effect of ARFC on Curling Stresses

On average in the summer data, the existence of ARFC decreased the curling stresses due to the decrease in the temperature differentials between the top and bottom of the slab. For example, the interior stress in the longitudinal direction in the slab with ARFC overlay was 25% less than that without an overlay for June 25th at the highest positive temperature differentials recorded. At the lowest differentials recorded the interior stress was about 8% less. The interior stress with the ARFC overlay for December 23rd was about 15% higher than the interior stress without the ARFC overlay at the highest positive temperature differentials recorded. Clearly the thermal blanket effect is assisting in the retention of heat. Significantly, the range of daily stress cycles appears to be lessened by the presence of the overlay. It should be pointed out that this data includes the effects of aeration from traffic. Although data was collected for non-traffic areas, it is beyond the scope of this paper to present this information.

CONCLUSIONS

ARFC overlays have a significant impact on the induced stresses in PCCP due to thermal gradients. When coupled with the aeration effect of traffic, an ARFC overlay can reduce the daily stresses from thermal gradients by about 25% during the heat of the day and by about 8% in the night time lows during the summer extreme temperatures. The effect of a thermal blanket in the winter months appears to result in higher stress levels in the overlaid sections at the daily high gradient, but the overall range of the daily stress cycle is mitigated. The aeration effects of traffic have a great impact on the magnitude of the thermal gradients. When considering that damage to a PCCP structure from thermal gradient induced stresses can be significant, the service life of the PCCP may be extended with the use of ARFC overlays as a pavement preservation strategy.

ACKNOWLEDGEMENT

The authors would like to acknowledge the following personnel for their valuable help in this study: Paul Burch and Ali Zareh of ADOT Materials Group, Kevin Woudenberg and Ray Galaviz of United Rentals Highway Technologies, Tom Drysdale of DBA Construction, Inc., Dan Foley of Sunstate Equipment, the staff of FNF Construction, Inc. and the staff and graduate students of the National Center of Excellence on SMART Innovations at Arizona State Univeristy (www.asuSMART.com): Joby Carlson, Joo Gui, Ajatshatru Patni, Ryan Evjen, Arvind Pappu, and Kiran Mohanraj.

REFERENCES

Belshe, M., “Impact of Asphalt Rubber – Asphaltic Concrete Friction Course Overlays on Portland Cement Concrete Pavements and Urban Heat Island Effect”, Masters Thesis, Arizona State University, 2006.

Bouzid, C., Mang C.,, “Analysis and Verification of Thermal-Gradient Effects on Concrete Pavements”, Journal of Transportation Engineering.(ASCE), Vol.121, Issue 1, pp 75-81, 1995.

Golden, J.S. and Kaloush, K.E., “Mesoscale and Microscale Evaluation of Surface Pavement Impacts on the Urban Heat Island Effects”. International

Journal of Pavement Engineering, Volume 7, No. 1, pp 37-52, Taylor & Francis, March 2006.

Huang, Y. H., 2004: Pavement Analysis and Design, Second Edition, Pearson Eduation, Inc.

Ingley, K., "The Asphalt Furnace", An article from the Arizona Republic, September 19, 2003.

Mahboub, K. C., Liu, Y., Allen, D., 2004: Evaluation of Temperature Responses in Concrete Pavement, *Journal of Transportation Engineering*.

Masad, E., Taha, R., Muhunthan, B., 1996: Finite element analysis of temperature effects on plain-jointed concrete pavements, *Journal of Transportation Engineering.*

Mohamed A.R., Hansen W., "Effect of Non-Linear Temperature Gradient on Curling Stress in Concrete Pavements" Transportation Research Record (TRB), Vol. 1568 pp 65-71, 1997.

Rodezno, M.C., Kaloush, K., and Way, G., "Assessment of Distress in Conventional Hot-Mix Asphalt and Asphalt-Rubber Overlays on Portland Cement Concrete Pavements - Using the Mechanistic-Empirical Design of Pavement Structures", Journal of the Transportation Research Board, No. 1929, pp 20-27, Washington, D.C., 2005.

United States Environmental Protection Agency (U.S. EPA), "The Urban Environment", www.epa.gov/urban/phx/index.htm., 2007.

.

Visco-Elastic Portrayal of Bituminous Materials: Artificial Neural Network Approach

Morched Zeghal[1]

[1]Research Associate, Institute for Research in Construction, National Research Council Canada, Building M-20, Ottawa, Ontario K1A 0R6, Canada; morched.zeghal@nrc.ca

ABSTRACT: This paper presents a scheme to circumvent the need for extensive laboratory testing to determine the dynamic modulus of asphalt concrete materials. It calls for using existing complex modulus test results and applying an analytical tool to expand this data. This study presents the artificial neural network (ANN) technique as a promising method that can help designers have a good estimation of the dynamic modulus based on data accumulated over the years. The study highlights the use of ANN method, which utilizes simple physical parameters as input, to predict the dynamic modulus of asphalt concrete. Results of ANN simulations showed the ability of the ANN technique to predict the dynamic modulus of mixes prepared to different air voids and with different gradations and binders. Such a tool represents an attractive alternative to testing for small jurisdictions with limited budget and personnel.

INTRODUCTION

The new mechanistic–empirical pavement design guide (MEPDG), developed under the NCHRP project 1-37A, adopted the dynamic modulus to characterize the visco-elastic behavior of bituminous materials (NCHRP 2004). In level 1 of input, the dynamic modulus is determined in the laboratory, which requires special equipment and training of technical staff, a capability that the majority of road jurisdictions in Canada lack today. The complex and time consuming nature of the laboratory test motivated the developers of the MEPDG to introduce two more levels of inputs (level 2 and 3) which do not require testing to characterize asphalt concrete materials. In level 2 and 3, the dynamic modulus is estimated using a predictive model based on results of tests performed on binders, aggregate gradation and mix properties. Attempts to estimate the dynamic modulus using empirical predictive models fall short of providing accurate estimates of this parameter. Consequently, there is a need for an alternative to determine the dynamic modulus of asphalt concrete materials. This paper presents an approach that circumvents the need for extensive laboratory testing and overcomes the shortcoming of the empirical predictive models. The proposed scheme is based on combining the use of existing laboratory-generated data with analytical modeling based on artificial neural network (ANN) to produce adequate estimate of dynamic moduli of asphalt concrete materials.

DYNAMIC MODULUS DETERMINATION

The complex modulus concept is used to evaluate the fundamental stress-strain response of asphalt concrete mixes. The modulus is a complex number, which defines the relationship between the stress and strain for a linear visco-elastic material subjected to a sinusoidal loading.

Laboratory Testing

Within the visco-elastic domain, the response of an asphalt concrete material subjected to a sinusoidal loading is also sinusoidal but with a phase lag (Sayegh 1967). Equations 1 to 4 describe the visco-elastic approach mathematically (Heck et al. 1998, Richard et al. 2003 and Sayegh 1967).

The applied stress function is given by:

$$\sigma = \sigma_0 . e^{iwt} \tag{1}$$

and the corresponding strain is given by:

$$\varepsilon = \varepsilon_0 . e^{i(wt-\phi)} \tag{2}$$

where σ_0 is the stress amplitude, ε_0 is the strain amplitude, ω is the angular velocity and ϕ is the phase angle describing the time that the strain lags the stress. The phase angle is an indicator of the degree of the visco-elastic behavior of asphalt concrete mix.

The complex modulus is defined (by analogy to the Young modulus of elasticity) as shown in Equation 3 (Witczak and Root 1974):

$$E^*(iw) = \frac{\sigma}{\varepsilon} = \frac{\sigma_0}{\varepsilon_0} e^{i\phi} = E_1 + iE_2 \tag{3}$$

where the real part of the complex modulus (E_1) is a measure of the material elasticity and the imaginary part (E_2) is a measure of its viscosity.

The ratio of the stress to strain amplitudes defines the absolute value of the complex modulus which is known as the dynamic modulus and is expressed by:

$$\left|E^*\right| = \frac{\sigma_0}{\varepsilon_0} \tag{4}$$

Predictive Modeling

While the determination of the dynamic modulus in the laboratory remains the most reliable means, many predictive models have been used to estimate this parameter based on the physical properties of the mix, aggregates and binder. The use of predictive models has been popular mainly due to the lack of laboratory equipment in addition to the highly demanding nature of the test. In the MEPDG, the predictive model used has this form (NCHRP 2004):

$$\log\left|E^*\right| = -1.249937 + 0.029232P_{200} - 0.001767(P_{200})^2 + 0.002841P_4 - 0.058097V_a$$
$$-0.802208\frac{V_{beff}}{(V_{beff}+V_a)} + \frac{[3.871977 - 0.0021P_4 + 0.00395P_{38} - 0.000017(P_{38})^2 + 0.00547P_{34}]}{1+e^{(-0.603313-0.313351\log f-0.393532\log\eta)}} \quad (5)$$

where
$\left|E^*\right|$ = Asphalt mix dynamic modulus, in 10^5 psi,
η = Bitumen viscosity, in 10^6 poise,
f = Loading frequency, in Hz,
V_a= Percent air voids in the mix, by volume,
V_{beff} = Percent effective bitumen content, by volume,
P_{34} = Percent retained on ¾-inch sieve, by total aggregate weight (cumulative),
P_{38} = Percent retained on 3/8-inch sieve, by total aggregate weight (cumulative),
P_4 = Percent retained on No. 4 sieve, by total aggregate weight (cumulative), and
P_{200} = Percent passing No. 200 sieve, by total aggregate weight.

Zeghal et al. (2005) assessed the capabilities of this predictive equation in estimating the dynamic modulus. They concluded that the predictive equation came short of accurately predicting the dynamic modulus measured in the laboratory. An average absolute relative error of 77% was reported. The shortcomings of the predictive model motivated the search for other alternative methods to determine the dynamic modulus of asphalt concrete materials.

ARTIFICIAL NEURAL NETWORK MODELING

The ANN technique is a relatively new method of modeling that was originally presented by Ghaboussi et al. (1990 and 1991). Unlike other modeling techniques that rely on mathematical expressions to describe experimental observations, ANN modeling relies on the learning capabilities of its elements.

An ANN model is a collection of interconnected elements (neurons) that are linked together in a way similar to the architecture of the human brain and have the performance characteristics of biological neurons (Fausett 1994). It is capable of recognizing, capturing and mapping features (known as patterns) contained in a set of data mainly due to the high interconnections of neurons that process information in parallel. The learning capabilities allow neural networks to be directly trained with the results of experiments. Once an ANN model has learned the patterns defining the relationship between the input and output of a certain test or process, it can generalize from its training set data to novel cases. Presenting a network with facts for which the input and output are known to delineate the embedded patterns is an integral part of the ANN modeling process.

An ANN model is made up of at least three layers. The first layer contains the input parameters while the last layer contains the output (solution). One or more layers known as hidden layers are usually placed between the input and output layers. The hidden layers constitute the network's means of delineating and learning the patterns governing the data that the network is presented with.

There are many ways a neural network can be trained. The back propagation technique is the most popular process and has been used in many fields of science and engineering such as construction simulation (Flood 1990 and Moselhi et al. 1991), constitutive modeling (Rogers 1994) and structural analysis (Garrett et al. 1992). In a back propagation learning process, training is accomplished by assigning random connection weights to the connections and calculating the output using the present connection weights. At a second stage, the process involves back propagating the error defined as the difference between the actual and computed output through the hidden layer(s). This procedure is repeated for all training facts until the error is within a certain tolerance. The final network with final connection weights is then saved to serve as a prediction model.

Architecture and Optimization

The development of an ANN model involves defining the number of nodes in the input, output and one or more hidden layers. The input layer size is generally predetermined based on the parameters known or assumed to affect the targeted output. However, the number of hidden layers as well their nodes is usually determined by a-trial-and-error procedure. Determination of the number of hidden layers and their nodes involves training and testing the built network against test sets made of examples with known input and output.

Using a subset of laboratory-determined dynamic modulus values used in the calibration of the MEPDG (NCHRP 2001), an ANN investigation was initiated to examine the effectiveness of the analytical technique in expanding the database without the need for further testing. The laboratory data used in this study included experimental results of complex modulus test performed on 42 mixes. The laboratory database included dynamic modulus values of mixes covering a wide range of air voids (4.0% to 11.0%). These mixes also enveloped different binders, with a wide range of high temperature (75 to 52) and low temperature (–10 to -34) performance grades, and binder content (3.6% to 6.4%). The data also reflected mixes with different aggregate characteristics as shown in Table 1.

Table 1. Characteristics of Aggregates

	Percent passing No. 200 sieve	**Percent retained on No. 4 sieve**	**Percent retained on 3/8-inch**	**Percent retained on ¾-inch sieve**
Maximum value	7	60	97	100
Minimum value	3	27	60	78

In this study, the dynamic modulus is the single targeted output. The inputs included the major parameters known to affect the visco-elastic behavior of asphalt concrete, namely, the binder performance grade, the binder content by weight, the mix's air voids, the four aggregate characteristics shown in Table 1, temperature and frequency. The number of nodes in the hidden layer(s) was investigated in order to arrive at a robust network. The investigation consisted of training ANN models with varying number of hidden layers and nodes. Ten percent of the data was randomly set aside for testing the trained network and another ten percent of the data was reserved for comparing the predictions of the built network with laboratory obtained data. The effect of the number of hidden nodes on the accuracy of the network was measured by the percentage "Absolute value of the Relative Error" (|ARE|) defined as:

$$|ARE| = abs. \{(X_{prediction}-X_{actual})/X_{actual}\} \times 100\% \qquad (6)$$

Through trial-and-error, it was found that using more than one hidden layer did not improve the accuracy of the predictions as depicted by the typical results obtained for a network consisting of two hidden layers and for which the first hidden layer (H1) had 14 nodes (see Figure 1). Consequently, the number of nodes in the single hidden layer was the only parameter left to be determined. The effect of the number of hidden nodes in the single hidden layer on |ARE| is also displayed in Figure 1. It shows that the number of nodes in the hidden layer plays a major role in the accuracy of the network. Further, the network consisting of 20 nodes in the single hidden layer was found to provide the best accuracy with an |ARE| of about 17%, which was considered acceptable since it was observed that replicate samples tested in the laboratory might exhibit a difference in the order of 10 to 20%.

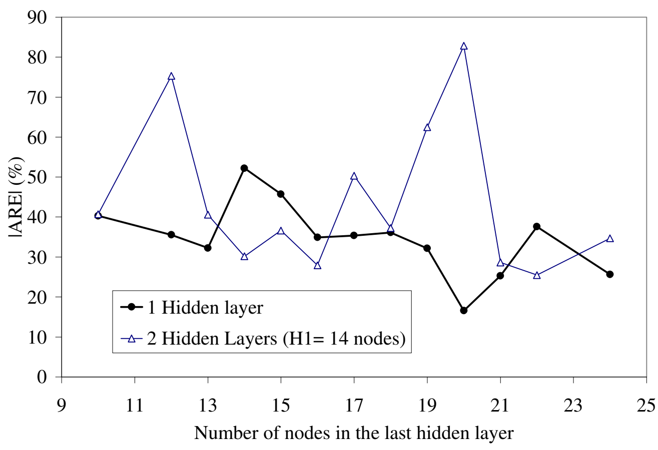

FIG. 1. Optimizatin of the ANN model.

Adequacy

Once the ANN structure was optimized, the ability of this technique to learn the features known to affect the visco-elastic behavior of asphalt concrete materials and embedded in the training data was checked. The optimized network was used to check trends related to variations in temperature and frequency. Predictions generated by the

ANN model were checked against trends established in the literature for these two variables. Figure 2 shows the results of ANN predictions obtained for an asphalt concrete mix prepared to an air void of 5.2% using a neat binder (PG 58-22) and a binder content of 5.0%. It is clear that the ANN model is capable of reproducing the known effect of temperature and frequency. At all frequencies, a decrease in the temperature results in an increase in the dynamic modulus. Further, at any temperature, an increase in frequency yields an increase in the dynamic modulus.

PREDICTION OF DYNAMIC MODULI

The ability of the ANN technique to predict the dynamic modulus in a satisfactory manner was determined by comparing ANN predictions and laboratory results of several asphalt concrete mixes that the model did not see before. A typical comparison done for a mix (for which the binder performance grade was PG 52-34, the binder content by weight was 5.2% and the air voids were 6.0%) is presented in Table 2. The gradation characteristics of this mix are shown in Table 3. Table 2 indicates that the ANN technique is capable of predicting the dynamic modulus with satisfactory accuracy. The |ARE| of the 2/3 of predictions were lower than 15%. Further, with the exception of few data points, the predictions of the optimized ANN had an |ARE| consistently lower than 25%, which is much lower than the error encountered when the predictive model was used (77%).

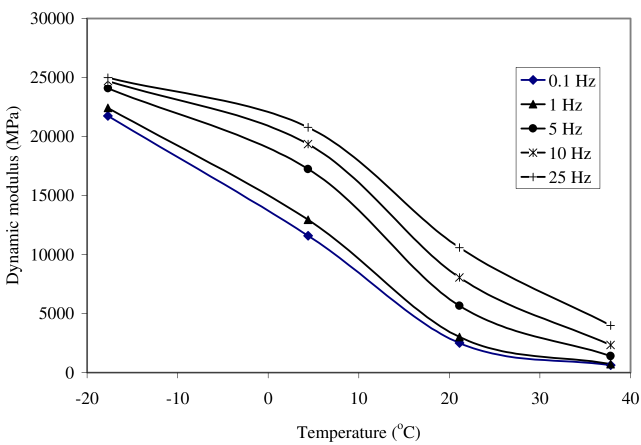

FIG. 2. Effect of temperature and frequency on the dynamic modulus.

Table 2. Typical |ARE| Obtained with ANN Predictions

Frequency (Hz)	Temperature (°C)	|ARE| (%)
0.1	-17.7	11
1	-17.7	14
10	-17.7	10
25	-17.7	14
0.1	4.4	13
1	4.4	28
10	4.4	15
25	4.4	12
0.1	21.2	23
1	21.1	24
10	21.1	20
25	21.1	6
0.1	37.8	33
1	37.8	3
10	37.8	10
25	37.89	25

Table 3. Typical Gradation Characteristics Used in ANN Predictions of Dynamic Moduli

Percent passing No. 200 sieve	Percent retained on No. 4 sieve	Percent retained on 3/8-inch sieve	Percent retained on ¾-inch sieve
7.0	44	81	97

CONCLUSIONS

The mechanistic-empirical pavement design guide requires the use of the dynamic modulus to characterize bituminous materials. However, the dynamic modulus test is complex and time consuming. In addition, only few Canadian jurisdictions have the required testing capabilities and human resources to perform such a test. The adoption of the design guide will be hampered by such limitations unless other options are made available to generate such material input. This paper presented the artificial neural network as an alternative to performing the test to cover the wide spectrum of factors that are known to influence the dynamic modulus. Results obtained from the current study showed that the ANN technique is a valuable tool that has the capability of learning trends observed in laboratory testing of asphalt concrete and satisfactorily predicting the dynamic modulus of bituminous materials. Further, artificial neural network models were found to yield better accuracy than the empirical predictive equation adopted in MEPDG, which was developed using statistical analysis. Overall, an absolute average relative error lower than 25% was observed when the ANN model was used, which is about the third of the 77% error obtained when the predictive equation was employed.

REFERENCES

Fausett, L. (1994). “Fundamentals of Neural Networks: Architectures and Applications.” Prentice Hall, Upper Saddle River, NJ, USA.

Flood, I. (1990). “Simulating the Construction Process Using Neural Networks.” Proceedings of the Seventh International Symposium on Automation and Robotics in Construction, ISARC, Bristol Polytechnic, England.

Garrett, J.H., Ranjitham, S., and Eheartt, J.W. (1992). “Application of Neural Network to Groundwater Remediation.” In Expert Systems for Civil Engineers: Knowledge Representation, Edited by Allen, R.

Ghaboussi, J., Garret, J.H.Jr, and Wu, X. (1990). “Material Modeling with Nerural Networks.” Proceedings of the International Conference on Numerical Methods in Engineering: Theory and Applications, Swansea, UK, pp. 701-717.

Ghaboussi, J., Garret, J.H.Jr, and Wu, X. (1991). “Knowledge Base Modeling of Material Behaviour with Neural Networks.” *Journal of Engineering Mechanics Division,* ASCE, 117(1), 132-153.

Heck, J.V., Piau, J.M., Gramsammer, J.C., Kerzreho, J.P. and Odeon, H. (1998). “Thermo- Visco-Elastic Modelling of Pavements Behaviour and comparison with Experimental Data from LCPC Test Track.” 5th International Conference on the Bearing capacity of Roads and Airfields.

Moselhi, O., Hegazi, T. and Fazio, P. (1991). “A Hybrid Neural Network Methodology for Cost estimation.” Proceedings of the Eighth International Symposium on Automation and Robotics in Construction, ISARC, Stuttgart, Germany.

NCHRP project 1-37A. (2001). “Guide for Mechanistic–Empirical Design of New and Rehabilitated Pavement Structures – Final Report, Appendices CC.” TRB, National Research Council, Washington, D.C.

NCHRP project 1-37A. (2004). “Guide for Mechanistic–Empirical Design of New and Rehabilitated Pavement Structures – Final Report.” TRB, National Research Council, Washington, D.C.

Richard, Y., Youngguk, K., King, M. and Momen, M. (2003). “Dynamic Modulus Testing of Asphalt concrete in Indirect tension Mode.” *TRB Annual Meeting*, Washington D. C., USA.

Rogers, J.L. (1994). “Simulating Structural Analysis with Neural Network.” *J. Comp. Civ. Engng,* ASCE 8, 80-100.

Sayegh, G. (1967). “Viscoelastic properties of bituminous mixtures.” Proceedings of the 2nd International conference on structural design of asphalt pavement, 743-755.

Witczak M.W., and Root. R.E. (1974). “Summary of Complex Modulus Laboratory Test Procedures and Results.” *American Society for Testing Materials,* ASTM Special Technical Publication, Vol. 561, 67- 94.

Zeghal, M., Adam, Y.E., Ali, O. and ElHussein, H. Mohamed. (2005). “Review of the New Mechanistic-Empirical Pavement Design Guide - A Material Characterization Perspective.” Transportation Association of Canada Annual Conference, Calgary, Alberta.

Accelerated Testing of Geogrid-Reinforced Subgrade in Flexible Pavements

Xiaochao Tang[1], S.M.ASCE, Ghassan R. Chehab[2], M.ASCE, and Angelica M. Palomino[3], A.M.ASCE

[1]Ph.D. Candidate, Department of Civil and Environmental Engineering, Pennsylvania State University, University Park, PA 16802, Email: xxt103@psu.edu
[2]Assistant Professor, Department of Civil and Environmental Engineering, Pennsylvania State University, University Park, PA 16802, Email: gchehab@engr.psu.edu
[3]Assistant Professor, Department of Civil and Environmental Engineering, Pennsylvania State University, University Park, PA 16802, Email: angel.palomino@engr.psu.edu

ABSTRACT: This paper describes a pit-scale experimental study aimed at quantifying and evaluating geogrid reinforcement in flexible pavements. Two sets of pavement sections are constructed on two different subgrades and trafficked using a Model Mobile Load Simulator (MMLS3). Each set of test sections consists of the same pavement materials and structure except for the geogrid type used for stabilizing the subgrade. Rutting of all sections are measured using a profilometer at various trafficking stages. Geogrid reinforcement effectiveness is found to be related to the difference in geogrids properties. Test results show that the geogrid reinforcement enhances the pavement performance with respect to rutting resistance compared to a non-reinforced system.

INTRODUCTION

Strengthening a weak soil subgrade improves pavement structure performance. One method of subgrade reinforcement is placing a geogrid at the interface between soil subgrade and aggregate base course. Several laboratory tests using a monotonic or cyclic plate loading show the benefits of geogrid reinforcement for flexible pavements (Hass et al 1988; Al-Qadi et al 1994; Perkins 1999). Furthermore, field-scale experiments demonstrate that the performance of pavement on a weak subgrade can be improved by including a geogrid at the subgrade-aggregate base layer interface (Barksdale et al 1984; Hufenus et al. 2006; Al-Qadi et al. 2007).

Accelerated pavement testing (APT) offers excellent means to conduct pavement performance tests and has been used to evaluate pavement performance and products since 1909 in USA (Metcalf, 1996). The advantages of APT over full-scale testing are the ability to conduct performance tests at much lower costs over a shorter time period, and the ability to control the loading environmental conditions.

In this study, accelerated testing is conducted on four types of geogrid products, here named Grid A, Grid B, Grid C, and Grid D, using a Mobile Model Load Simulator 1/3 scale (MMLS3). The MMLS3 is an accelerated pavement testing device that applies unidirectional trafficking to the pavement in a controlled laboratory environment or on full-scale pavements in the field. Materials used for the pavement construction follow the relevant specifications of the Pennsylvania Department of Transportation (PennDOT).

ACCELERATED PAVEMENT TESTING FACILITIES

Test Pit

The pavement slabs are constructed in a test pit with reinforced concrete walls and foundations. The pit is backfilled with aggregate base and compacted to serve as pavement bedrock. Figure 1 shows the layout of the constructed pavement sections for the two sets of accelerated pavement testing (APT), APT I and APT II. For APT I, four constructed sections labeled as R1, R2, R3, and R4 are reinforced with Grids A, B, C, and D, respectively. An additional four pavement sections – P1, P2, P3, and P4 – are constructed for APT II. Section P1 is a control section, i.e. no geogrid, while sections P2, P3, and P4 are reinforced with Grid B, C, and D, respectively.

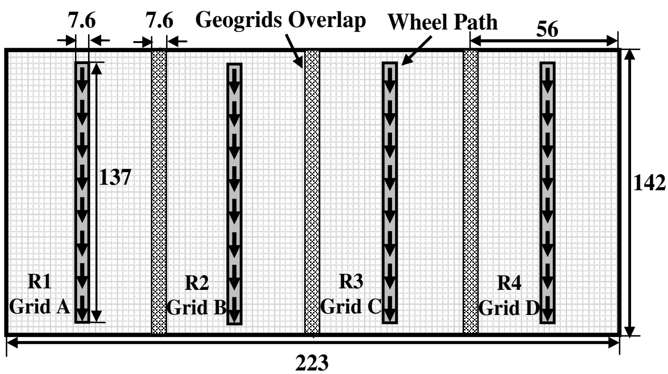

FIG.1. Pavement sections layout (plan view) and dimensions, units in cm.

MMLS3 Trafficking

The MMLS3 has four tires, each with diameter of 30.5 cm and width of 7.6 cm. The actual wheel path generated by the MMLS3 is 137 cm long. The load exerted by each wheel of the MMLS3 is 2.7 kN with a corresponding tire pressure of 621 kPa. The MMLS3 suspension system is designed so that the wheel load is independent of the wheel vertical displacement; thus, the applied load remains constant even if rutting occurs. The traffic speed is set to 7,200 axles (wheels) per hour, or two axles (wheels) per second. Testing is conducted at room temperature under dry conditions with no wandering, i.e. a linear trafficking path.

CONSTRUCTION OF PAVEMENT SECTIONS

Materials

The soil used as subgrade material is commonly found in central Pennsylvania and classified as silty sand (SW-SM). Sieve analysis shows that 6.2% of the soil passes #200 sieve (0.074 mm), and 50% passes the #20 sieve (0.841 mm). The optimum moisture content is 10%, and maximum dry density is 2066 kg/m^3. The direct shear friction angle is 31.8°.

A set of laboratory unsoaked CBR tests (ASTM D 1188) are performed for the soil at different water contents, as shown in Figure 2. The trend shows that CBR decreases significantly with increase in water content beyond the optimum water content, indicating the soil is water sensitive. Hence, the soil is compacted at a water content greater than optimum to induce weak soil conditions.

Dense-graded crushed stone is as the pavement aggregate base layer. The base course aggregate meets PennDOT 2A grading requirement according to grain size analysis. A standard Proctor test yields an optimum moisture content of 3.9% and maximum dry density of 2329 kg/m^3. Hot mix asphalt (HMA) is provided by a local mixture plant (State College, PA). The asphalt mixture has a theoretical maximum specific gravity of 2.505.

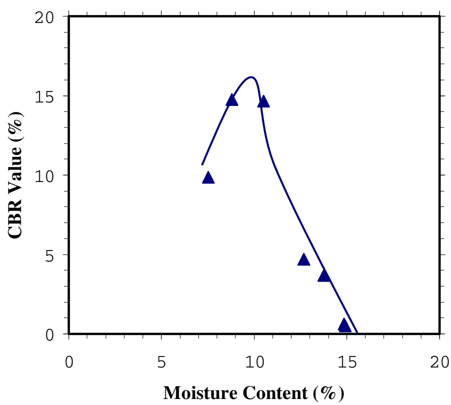

FIG.2. CBR variation with water content for the subgrade soil.

Four biaxial geogrid products are selected for this study. Grids A and D are composed of high tenacity polyester (PET) multifilament yarns and coated with polymer and polyvinyl chloride (PVC) coating, respectively. Grid B is made of woven polypropylene (PP) yarns, while Grid C is made of extruded PP sheets. Grids A, B, and D are classified as flexible geogrids and Grid C as a stiff geogrids based on measured flexural rigidity per ASTM D 1388.

Construction Procedure

The pavement slabs are constructed in the pit using the same materials for the individual layers. Type SW-SM subgrade soil and PennDOT 2A aggregate base are prepared at the desired moisture content. The subgrade is placed on top of a waterproof membrane to avoid moisture loss to the aggregate bedrock layer below. The only difference among the sections is the geogrid type at the subgrade-aggregate base course (ABC) interface.

Pavement subgrade is compacted in three lifts with a vibratory plate compactor. The compactor travel direction ensures consistency of the soil density throughout the pit (refer to Figure 3-a). In-situ soil density and moisture content are measured by means of the sand cone method and presented in Table 1.

Table 1. As-constructed pavement layer properties

APT	Subgrade Thickness (cm)	Base Course Thickness (cm)	Asphalt Concrete Thickness (cm)	Subgrade Moisture Content (%)	CBR Value (%)
I	23.6	6.6	3.8	14	3
II	15.2	6.6	3.8	14.8	1.5

The geogrids are placed directly on the subgrade layer. The grids are carefully unrolled to avoid folds and wrinkles; grids from adjacent sections have a 7.6 cm overlap. The ends of the geogrid sectionse are folded against the pit walls to obtain necessary anchorage and slight pre-tensioning, as well as to prevent shifting of the geogrids out of position. The geogrid is overlaid with a compacted aggregate base course layer using a vibratory plate compactor.

A relatively low air void (AV) content is targeted for the asphalt concrete (AC) layer construction to minimize the contribution of densification of the asphalt layer to overall pavement rutting. Based on the desired density and volume for the constructed AC layer, the mass of the asphalt mixture is calculated and weighed to ensure proper compaction. HMA compaction is achieved using the same technique as that adopted for the subgrade and ABC compaction.

The AC layer density is measured along the wheel path for each section using a Pavement Quality Indicator™ (PQI) Model 301A prior to MMLS3 trafficking. Figure 3 presents a contour plot of the measured AV distribution for each section measured after construction and before trafficking. The asphalt layer in sections R3 and P3 reinforced by Grid C has significantly higher air voids than the other sections in both test sets. It is likely that the high AC air voids in these two sections results from the attributes of the geogrid itself, given the uniform compaction technique and consistent pavement structure and materials. Geogrid C has a significantly higher stiffness than the other grids tested. While the stiffness is not the only differing characteristic among the geogrids, it has the greatest potential for interfering with initial compactability, and subsequently, achievable densification. Further investigation incorporating different types of geogrids highlighting stiffness and other characteristics and subgrade soils are needed to confirm and further understand the mechanisms causing this phenomenon.

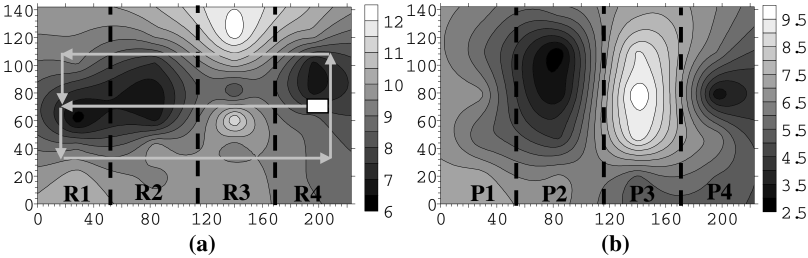

FIG. 3. Air void content distribution: (a) APT I; (b) APT II; shading represents range of air void content; arrows indicate the compaction path.

RESULTS AND DISSCUSSION

Accelerated Testing APT I

A total of 140,000 MMLS3 load cycles are applied to each section. Rutting accumulation at specific locations throughout each section are measured and averaged. Figure 4-a shows that the greatest rutting occurs for section R3. However, because that section had the highest AV, one cannot evaluate the effectiveness of Geogrid C in subgrade strengthening solely based on rutting measured at the surface. Comparing the other three sections R1, R2, and R4, Grids A and B show similar performance for this type of subgrade soil, with less rutting than that of Grid D in section R4.

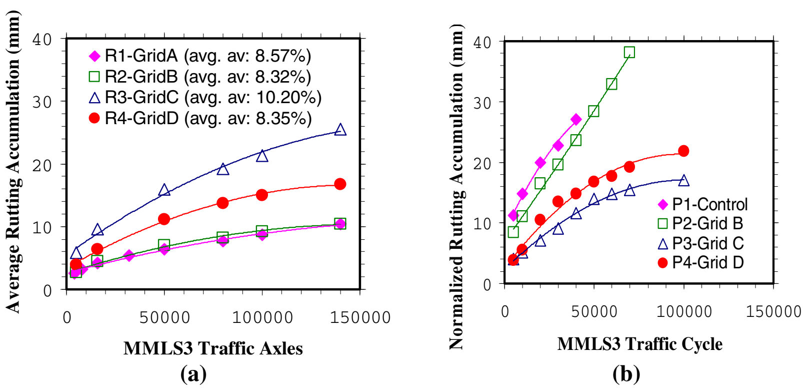

FIG.4. Rutting accumulation based on average from all locations for each section: (a) APT I; (b) APT II.

After trafficking, the slab is trenched across the travel direction to expose the pavement cross-section. Figure 5 shows that the rutting measured at the surface is partially due to deformation in the subgrade, especially, the weaker subgrade contributes more to the surface rutting. A significant amount of soil slurry is observed underneath the wheel path, indicating soil pumping occurs during loading.

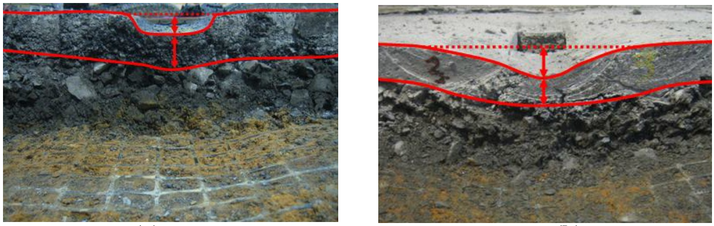

(a) **(b)**

FIG. 5. Trench cross-section of the pavement: (a) APT I-R3; (b) APT II-P3.

Accelerated Testing APT II

Four additional slabs are constructed to investigate the effectiveness of geogrid reinforcement under lower subgrade CBR conditions. MMLS3 trafficking is applied to each section. The control section P1 exhibited extensive deformation after 40,000 wheel applications; similar deformation is observed at 70,000 applications for section P2. Trafficking is stopped at 100,000 wheel applications for section P3 and P4.

An attempt is made to account for the variation in AV content among the four test sections by measuring asphalt air voids content before and after trafficking. The percentage densification in the AC layer is 25.4%, 18.3%, 33.0%, and 22.0% for sections P1, P2, P3, and P4, respectively. The percent asphalt densification is greater for sections with higher initial air void content. To consider the effect of initial air voids and densification, rutting for each test section is normalized using percent densification as the normalization factor and average rutting in control section P1 as the reference. The normalized average rutting accumulation for each section as a function of wheel applications is plotted in Figure 4-b.

Control section P1 exhibits significantly higher rutting that accumulated relatively quickly compared to the other reinforced sections. This illustrates the ability of geogrids to stabilize weak subgrade and potential to minimize pavement deformation under traffic load. Section P2 (Grid B) has the second highest cumulative rutting among the four test sections. The rate of rutting accumulation for sections P1 and P2 is slightly higher than for sections P3 and P4 (Figure 4-b). More rutting is observed for section P4 (Grid D) when compared to that of P3 (Grid C). Overall, the relatively stiffer geogrid, Grid C shows the best performance with respect to the rutting resistance for the tested pavement on this specific weak subgrade.

The relative performance of the geogrids from APT I is not repeated in APT II. The ranking of rutting performance between Grid B and Grid D was opposite in the two APT tests. The only significant difference between APT I and APT II is the subgrade CBR, with subgrade CBR of 3 for APT I and 1.5 for APT II. While more replicates are necessary, particularly for different subgrade soil types, the measured rutting and observation from trenching provide evidence that the effectiveness of geogrid reinforcement and strengthening of weak subgrade is dependent on the interaction between the reinforcement and surrounding materials. Thus, proper selection of the geogrid type for a given subgrade is essential. While a specific geogrid provides adequate support for a particular subgrade, it might not perform as well when used for a different type of soil and/or aggregate base. In the case of this study, the section with Grid B experiences significantly higher rate of rutting accumulation in APT II than in APT I, indicating Grid B might not be suitable for reinforcing a subgrade as weak as that in APT II.

Figure 6 shows the comparison between the rutting of each geogrid type from the first and second APT tests. The rutting is measured at locations with similar AC air voids. The rutting resulting from APT II is greater than that of APT I for all geogrid types, given the weaker subgrade in APT II. Note, however, that the Grid C sections exhibit very similar rutting in both APT tests, despite the difference in subgrade CBR. This indicates the contribution of subgrade weakness to pavement surface deformation.

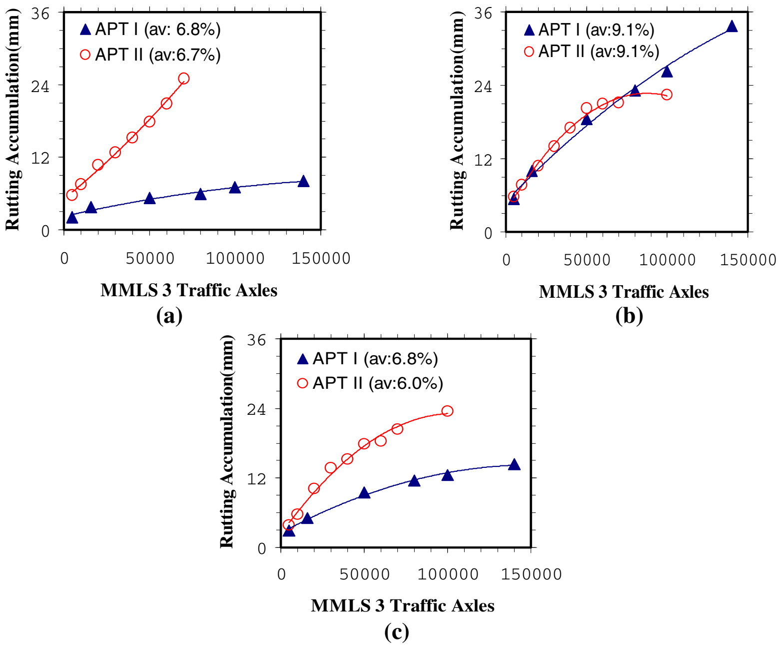

FIG.6. Rutting for geogrid reinforcement in APT I and II: (a) Grid B; (b) Grid C; (c) Grid D.

SUMMARY AND CONCLUSIONS

For two rounds of accelerated tests, APT I and APT II, with four geogrid products, A, B, C, and D, a total of eight pavement sections are constructed over two subgrade soils with different CBR values. Pavement materials and structure are kept constant within each APT test. From APT I, the section reinforced by Grid C has the most severe rutting, which is attributed to its higher AC air voids. Grids A and B show greater rutting resistance than Grid D with similar AC air voids. Subgrade soil pumping underneath the wheel path is observed from the trenched pavement sections.

A control section is included in APT II, and the pavement slabs are built on a weaker subgrade (CBR 1.5). The control section exhibits significantly higher rutting accumulation, demonstrating the benefits of geogrid reinforcement for weak subgrade. The stiff geogrid, Grid C, exhibits the best performance when rutting is normalized for AC air voids. The variation in geogrid performance for different subgrade soils indicates that proper selection of the geogrid type for a given subgrade is important.

It should be noted that during construction of the pavement sections for both APT test sets, the sections reinforced with a stiff geogrid exhibit difficulty in achieving proper compaction of the asphalt layer. It is speculated that the property of the geogrid itself leads to the insufficient compaction. Geogrid stiffness is one possible cause, considering the stiffness as the major difference between Grid C and other geogrid products used in this study; nevertheless, care should be taken to ensure the proper construction of thin geogrid-reinforced pavements.

ACKNOWLEDGMENTS

The authors would like to thank and acknowledge the Pennsylvania Department of Transportation for their financial support. Technical supports from Dan Fura are gratefully acknowledged.

REFERENCES

Al-Qadi, I.L, Brandon, T.L., Valentine, R.J., Lacina, B.A., and Smith, T.E. (1994). "Laboratory Evaluation of Geosynthetic-reinforced Pavement Sections." *Transportation Research Record 1439*, Washington D.C.: 25-31.

Al-Qadi, Tutumluer, E., Kwon, J., and Dessouky, S.H. (2007). "Accelerated Full-scale Testing of Geogrid-reinforced Flexible Pavements." *TRB 2007 Annual Meeting* (CD-ROM), Transportation Research Board, National Research Council, Washington D.C.

Barksdale, R.D., Brown, S.F., and Chan, F. (1989). "Potential Benefits of Geosynthetics in Flexible Pavement Systems." *National Cooperative Highway Research Program (NCHRP) Report No.315*, Transportation Research Board, National Research Council, Washington D.C.

Hass R., Wall, J., and Carroll, R.G. (1988). "Geogrid reinforcement of granular bases in flexible pavements." *Transportation Research Record 1188*, Washington D.C.:19-27.

Hufenus, R., Rueegger R., Banjac, R., Mayor, P., Springman, S.M., and Bronimann, R. (2006). "Full-scale Field Tests on Geosynthetic Reinforced Unpaved Roads on Soft Subgrade." *Geotextiles and Geomembranes*, Vol. 24(1):21-37.

Metcalf, J.B. (1996). "Application of Full-scale Accelerated Pavement Testing." *NCHRP Synthesis of Highway Practice No. 235*, TRB, National Research Council, Washington D.C.

Perkins, S.S. (1999). "Geosynthetic Reinforcement of Flexible Pavements: Laboratory Based Pavement Test Sections." *Report No. FHWA/MT-99-001/8138*, U.S. Department of Transportation, Federal Highway Administration, Washington, D.C.

Effectiveness of Geogrid Base-Reinforcement in Low-Volume Flexible Pavements

Jayhyun Kwon[1], Erol Tutumluer[2], Imad Al-Qadi[3] and Samer Dessouky[4]

[1]Senior Pavement Engineer, Tensar International Corporation, 5883 Glenridge Dr. Suite 200, Atlanta, GA 30328; jayhyunkwon@tensarcorp.com
[2] Associate Professor, Newmark Civil Engineering Laboratory, Department of Civil and Environmental Engineering, University of Illinois, 205 N. Mathews, Urbana, Illinois 61801; tutumlue@uiuc.edu
[3] Founder Professor of Engineering, Newmark Civil Engineering Laboratory, Department of Civil and Environmental Engineering, University of Illinois, 205 N. Mathews, Urbana, Illinois 61801; alqadi@uiuc.edu
[4] Assistant Professor, Department of Civil and Environmental Engineering, University of Texas at San Antonio, BSE Building, 1-322, One UTSA Circle, San Antonio, TX 78249; samer.dessouky@utsa.edu

ABSTRACT: Geogrids have been widely used to reinforce paved and unpaved roads constructed on soft subgrade. To quantify the effectiveness of geogrids in low-volume flexible pavements when constructed on weak subgrade, full scale pavement test sections were constructed at University of Illinois. The pavement sections were tested using the full-scale Accelerated Testing Loading ASsembly (ATLAS). The pavement sections were instrumented, during construction, to monitor in-situ pavement response to various vehicular and environmental loading conditions. The testing was conducted using a dual-tire assembly at 44-kN load, 8 km/h speed, and 690-kPa tire inflation pressure. Post-failure forensic evaluation of the pavement sections was conducted. The evaluation included transverse profile measurements. The study found that reinforced pavement sections experienced less rutting than the unreinforced sections. Observations of the pavement cross section profile, through trenches dug after the testing was complete, confirmed that pavement failure was mainly due to subgrade shear.

INTRODUCTION

Geogrids are high-strength extruded sheets produced by biaxial stretching of polyethylene or polypropylene and then punched to produce holes in a regular pattern, a grid-like pattern. Compared to other geosynthetic products, geogrids are very stiff with high tensile strength and elastic modulus. The main purpose of utilizing geogrids in flexible pavements is to improve pavement performance, either by extending its service life or by reducing its overall thickness. Geogrids have been found to be effective for improving pavement construction working platform as well as for unsurfaced roads, where relatively large rut depth is usually expected. In addition, incorporation of geogrid layers in low volume flexible pavement systems can improve the performance of the pavement system (Al-Qadi et al., 1994; 1999).

Field investigations suggested that use of geogrids could improve pavement performance; however, its benefit-cost ratio had to be quantified (Berg et al., 2000). Although significant testing was conducted in the laboratory and used to develop theoretical models to quantify the geogrid effectiveness, these models have never been validated. In addition, only limited instrumented field testing have been conducted (Brandon et al., 1996) Because of the complexity of layered pavement systems as well as the applied vehicular and environmental loadings, the mechanisms of geogrid as a reinforcing system of flexible pavements are difficult to simulate. Therefore, a carefully instrumented full-scale pavement sections need to be constructed and tested as recommended by Barksdale et al. (1989).

In this study, nine full-scale pavement test sections were built at the University of Illinois Advanced Transportation and Research and Engineering Laboratory (ATREL) to evaluate the effectiveness of low-volume flexible pavements. The granular base layer was reinforced with geogrids (Al-Qadi et al., 2006). The test sections were heavily instrumented with pressure cells, linear variable pressure transducers (LVDTs), and strain gauges to measure pavement response to vehicular loading. The instrumentation also included thermocouples and time domain reflectometry (TDR) probes to capture environmental changes and piezometers to measure pore-water pressure. Pavement response testing and performance evaluation were conducted. The loading was applied using the mobile Accelerated Testing Loading ASsembly (ATLAS).

The nine test sections were divided into three categories based on the granular base layer thickness: Cells A, B/C, and D, which had 203-, 305-, and 457-mm-thick aggregate base layer, respectively. A 76-mm hot-mix asphalt (HMA) layer was used as surface layer; except for section C1, which had 127-mm HMA layer. All cells had control sections constructed with no reinforcement. Two test sections in cell A had different strength biaxial geogrids placed at the base-subgrade interface. Geogrid reinforcement was placed at the base-subgrade interface in section B2. In cell D, geogrid was placed at 152 mm from top of the base layer; while in section D2 and additional layer of geogrid was added at the base-subgrade interface. Locations of geogrid in the pavement sections are shown in Table 1. The subgrade conditions were maintained similar for all pavement sections; the California Bearing Ratio (CBR) values were at less than 4%. No variations in the moisture content were measured throughout the response and trafficking tests.

PERMANENT SURFACE DEFORMATION

Permanent deformation was measured periodically during testing at the surface of each section; the longitudinal measurements were taken at 1200 mm intervals; while the transverse measurements were taken at 152 mm. Table 1 provides a summary of the average accumulated surface ruts with respect to number of loading cycles applied to the pavement test sections. Transverse profiles obtained at the end of load testing indicated that reinforced pavement sections showed less rutting than unreinforced pavement sections. In addition, for cell A, visual surveys clearly showed severe longitudinal cracking at 150-200 mm from the edge of the loading wheel. This suggests a subgrade shear failure. This failure type was pronounced in control sections and to a lesser degree in the other two geogrid-reinforced pavement sections.

Table 1. Summary of Number of Passes for Each Pavement Test Section

Test Cell	Thickness (mm)		Section	Geogrid Type and Location	Number of Passes for a 25-mm Rut
	Base	HMA			
A	203	76	A1	GG1 @ Subgrade-base Interface	Final rut of 20.3 mm after 4500 passes
			A2	GG2 @ Subgrade-base Interface	Section close to A3 (Unreinforced) failed after 3700 passes Section close to A1 had final rut of 20.3 mm after 4500 passes
			A3	Control	3,300 passes
B/C	305	76	B1	Control	28,000 passes
			B2	GG2 @ Subgrade-base interface	44,000 passes
		127	C1	127 mm HMA	Final rut of 7.6 mm after 62300 passes
D	457	76	D1	GG2 @ 152mm from top base	Final rut of 22.9 mm after 89000 passes
			D2	GG2 @ Subgrade-base interface & GG2 @ 152mm from top base	Final rut of 22.9 mm after 89000 passes
			D3	Control	70,000 passes

No significant differences existed between the observed rutting at sections D1 and D2. The excessive rutting in section A3 resulted in more rutting in part of section A2. Figure 1 shows the rut development during the traffic testing at the middle stations of pavement test section B1 (unreinforced) and B2 (reinforced). The rutting data show that the difference in performance between unreinforced and reinforced sections increased with loading.

PAVEMENT CRACKS

The sections were visually inspected regularly to monitor surface crack development. After high numbers of load repetitions applied to cells A and B/C, transverse cracks were initiated at 150-200 mm from the edge of the wheel path. Although the load repetitions applied on cell A were only one tenth of the loading repetitions applied on cell B/C to achieve rutting failure, high severity of surface cracking was observed in cell A. The relatively weak pavement structure and subgrade shear failure resulted in surface cracking. More frequent transverse cracks were also observed in the unreinforced B1 section compared to the reinforced B2 section (Figure 2). This behavior was not observed in sections C3 and D1 through D3, however, because of their relatively high structural capacity. In the weak sections, the reinforcement helped in reducing the shear failure; while in a stronger section, the reinforcement appeared to reduce the shear in the granular base layer.

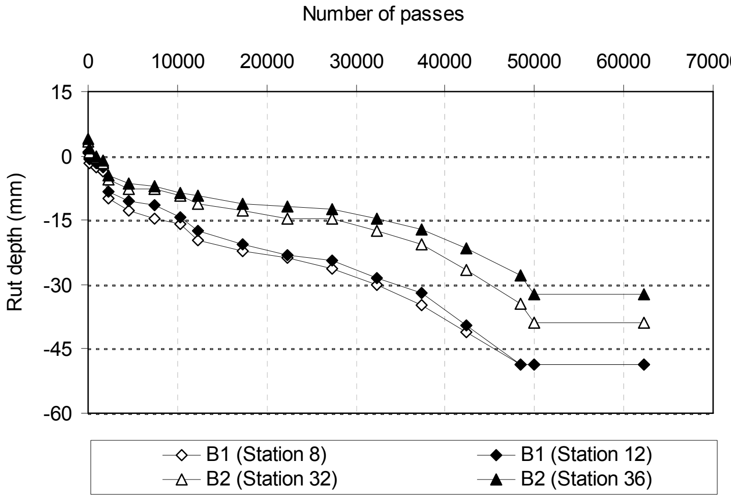

FIG. 1. Summary of the accumulative rutting in section B1 and B2

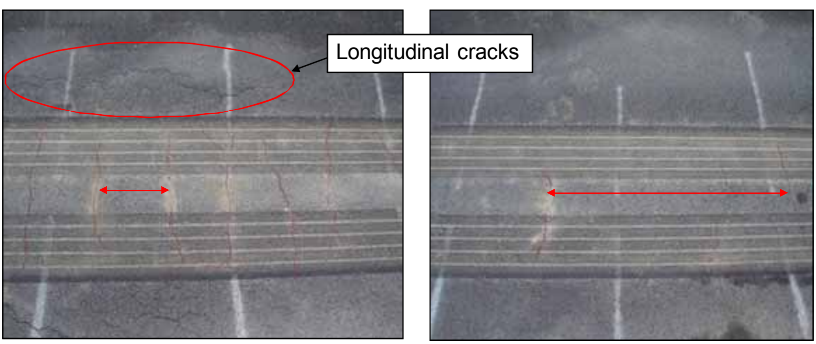

(a) B1 (Unreinforced Section) (b) B2 (Geogrid-Reinforced Section)

FIG. 2. Transverse and longitudinal cracks on the test section surface

PAVEMENT TRENCH

After the loading testing was completed, trenches were excavated in the middle of each section for further examinations of the pavement section profiles. The pavement layer profiles measured showed generally that geogrid provided partial separation between subgrade and aggregate layer. Although section B1 appeared to have thicker base layer than the geogrid-reinforced section B2, the latter experienced 15mm less rutting at almost the same number of loading repetitions (Figure 3).

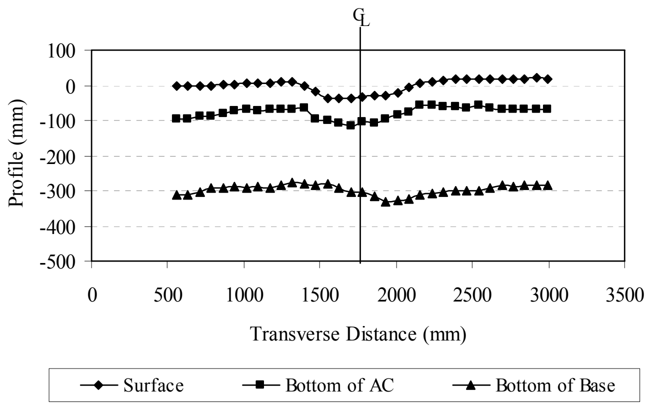

(a) Cross-Section Profile for Section A2 (Geogrid Reinforced Section)

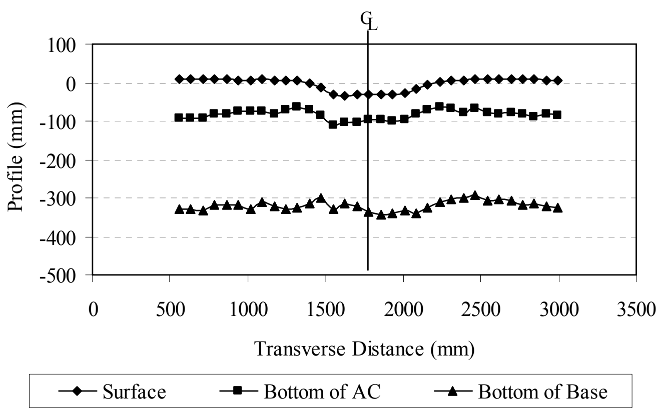

(b) Cross-Section Profile for Section A3 (Unreinforced Section)

FIG. 3. Post-failure trench rut profiles of the pavement sections

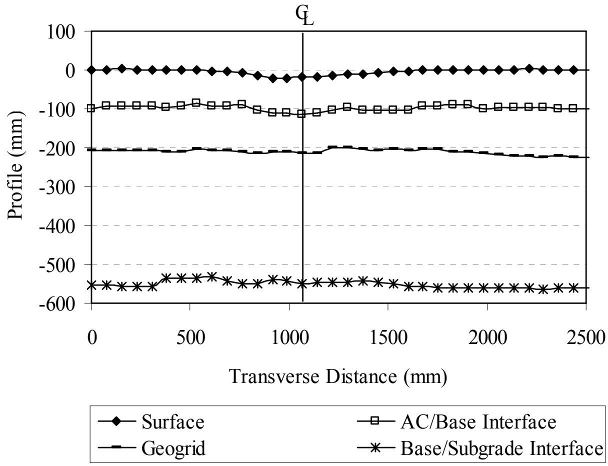

(c) Cross-Section Profile for Section D1

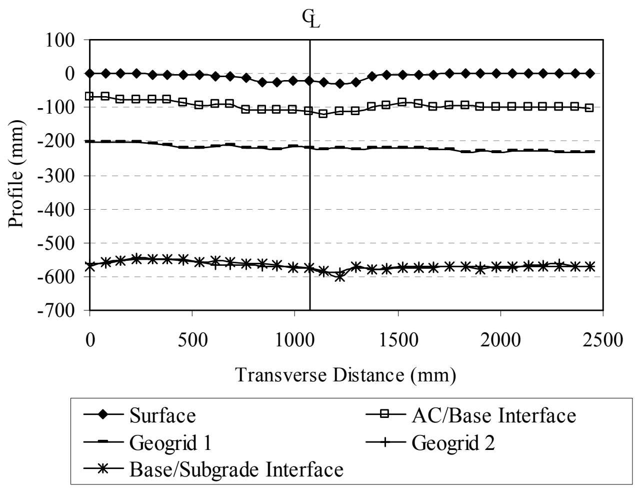

(d) Cross-Section Profile for Section D2

FIG. 3. Post-failure trench rut profiles of the pavement sections (continued)

Rut profile data obtained from open trench measurements clearly indicated that all test sections experienced shear failure. Subgrade shear failure was more pronounced in the control pavement sections compared to other reinforced pavement sections. The reinforced sections appeared to have constrained movement in the granular base layer and as a result, higher lateral confinement resulted in increased stiffness above geogrid reinforcement. This would reduce the potential for appearance of surface cracking as well as vertical deflection. In-situ Dynamic Cone Penetrometer (DCP) testing supported these findings.

For cell D, geogrids were installed at different depths in the base course. Sections D2 and D1 showed very good performances as no significant permanent deformation occurred in the base layer profile. Pavement section D2 is doubled reinforced; while pavement section D1 has a single geogrid layer installed at the top one third of the base layer thickness.

Placing geogrid at the top one third of the base layer thickness could reduce the horizontal deformation in the base layer. This would reduce the pavement rutting and potential of surface cracking. This study results suggest that the effectiveness of geogrid reinforcement depends on the pavement cross section and structural capacity. In general, if a relatively thick aggregate base course is used, the pavement performance benefits of using geogrids could be maximized when the geogrid reinforcement is positioned in the upper middle of the base course. In the case of thinner base courses, 200 to 305 mm used in this study, the geogrids placed at the base-subgrade interface successfully decreased vertical subgrade stress and resilient deformation.

SUMMARY

Full-scale testing of low-volume flexible pavements was conducted at the University of Illinois Advanced Transportation and Research and Engineering Laboratory (ATREL) using an Accelerated Testing Loading ASsembly (ATLAS). The main purpose of the testing was to quantify the effectiveness of geogrid reinforcement on pavement response to loading as well as on pavement performance after high number of load repetitions. The tested pavement sections included nine sections. All reinforced pavement sections performed better than the control sections: the number of load repetition to failure was greater; while the surface-measured rutting was lower for the same number of load applications. The study found that geogrid tends to reduce the localized lateral movement of aggregate. This would reduce the vertical deformation as well as the horizontal movement of aggregate. In addition to pavement instrument response and rutting surface-rutting measurements, this was verified by post-failure dynamic cone penetrometer testing and excavated trenches of the pavement sections. The cross-section profile of failed pavement sections confirmed the aforementioned findings.

ACKNOWLEDGMENTS

This study was sponsored by Tensar Earth Technologies, Inc. The assistance of J. Baek, P-J Yoo, E. Fini, J. Meister, M. Elseifi, B. Harkanwal, J. Anochie-Boateng, C. Montgomery, K. Jiang, and Z. Leng during pavement construction and instrumentation is greatly appreciated. The content of this paper reflects the views of the authors, who are responsible for the facts and the accuracy of the data presented herein. This paper does not constitute a standard, specification, or regulation.

REFERENCES

Al-Qadi, I.L., Tutumluer, E., and Dessouky, S. (2006). "Construction and Instrumentation of Full-Scale Geogrid-Reinforced Flexible Pavement Test Sections," In Proceedings of the ASCE Transportation and Development Institute (T&DI) Airfield and Highway Pavement Specialty Conference, Airfield and Highway Pavements, Edited by I.L. Al-Qadi, Atlanta, Georgia, April 30-May 3, pp. 131-142.

Al-Qadi, I.L., T. L. Brandon, R.J. Valentine, Lacina, B.A. and Smith, T.A. (1994). "Laboratory Evaluation of Geotextile and Geogrid Reinforced Pavement Sections," Transportation Research Record, No. 1439, Transportation Research Board of the National Academies, pp. 25-31.

Al-Qadi, I.L. and Bhutta, S.A. (1999). "Designing Low Volume Roads with Geosynthetics," Transportation Research Record, No. 1652, Vol. 2, Transportation Research Board of the National Academies, pp. 206-216.

Barksdale, R.D., Brown, S.F., and Chan, F. (1989). "Potential Benefits of Geosynthetics in Flexible Pavement Systems," NCHRP Report 315, Transportation Research Board, National Research Council, Washington, DC, 56p.

Berg, R.R, Christopher, B.R. and Perkins, S.W. (2000). "Geosynthetic Reinforcement of the Aggregate Base/Subbase Courses of Pavement Structures-GMA White Paper II," Geosynthetics Materials Association, Roseville, MN, 176p.

Brandon, T.L., Al-Qadi, I.L., Lacina, B. A., and Bhutta, S.A. (1996). "Construction and Instrumentation of Geosynthetically Stabilized Secondary Road Test Sections," Transportation Research Record, No. 1534, Transportation Research Board of the National Academies. pp. 50-57.

Improving the Tensile Strength and Toughness of a Soil-Cement-Fly Ash Pavement Subgrade with Recycled HDPE Strips

Khaled Sobhan[1], A. M. ASCE

[1]Associate Professor, Department of Civil Engineering, Florida Atlantic University, 777 Glades Road, Boca Raton, Florida 33431; ksobhan@fau.edu

ABSTRACT: Cementitious stabilization of soil and base is a common practice for improving the strength and stability of pavement foundations. However, the resultant stabilized material has a brittle matrix with strong potential for developing tensile cracks under repeated traffic loadings. This phenomenon often leads to reflection cracking in asphalt overlays which are underlain by cemented base or subgrade layers. An experimental investigation was conducted to evaluate the split tensile load-deformation-strength and toughness properties of a granular soil chemically stabilized with cement and fly ash, and mechanically reinforced with recycled plastic strips (High Density Poly Ethylene or HDPE) obtained from post consumer products. As an extension to the ASTM C 496 procedures for split tension tests, two lateral linear variable differential transformers were attached to measure the tensile deformation of the horizontal diameter due to loading in the orthogonal direction; this method permitted an evaluation of the fiber toughening action under split tension. It was found that the inclusion of HDPE strips does not meaningfully improve the tensile strength, but significantly enhances the toughness properties, which may be beneficial in delaying the propagation of traffic-induced tensile cracks in pavement applications.

INTRODUCTION

Sustainable and green construction is a relatively new concept aligned with the ideas of resource conservation, waste minimization, and the use of alternative and recycled materials, while pursuing the ultimate goal of building more durable structures and long-term preservation of the infrastructure systems. The current study was undertaken to evaluate the mechanical properties of an alternative pavement foundation material composed of soil-cement-fly ash mixtures reinforced with reclaimed HDPE (High-density Polyethylene) plastic strips. The inherent objective of this endeavor was to produce a synthetically-reinforced composite material which is lean in cement content but has enhanced mechanical properties compared to traditional stabilized base/subbase materials. According to the data published by the EPA, the solid waste stream in the United States in 1988 included 14.4 million metric tons of plastics occupying 20% by volume of the available landfill spaces. Approximately 2.2 million metric tons of HDPE are produced annually and only 7 percent are currently being recycled. Therefore, the incorporation of reclaimed plastics into pavement foundation layers holds promise in terms of environmental benefits, superior performance, and potential economic savings.

TECHNICAL BACKGROUND

A cement stabilized pavement foundation is subjected to repeated tensile stresses due to traffic loads, and failure is generally initiated by the formation and propagation of tensile cracks. These underlying discontinuities and defects eventually propagate into and through the overlying asphalt layer in the form of reflection cracking, which is considered to be one of the most recurring problems for asphalt overlays. Therefore, understanding and improving the properties of such stabilized materials in tension are crucial for predicting the ultimate durability and performance of the pavement system. Accordingly, the main focus of the present study was to characterize the proposed stabilized base material by conducting a series of split tension tests. Moreover, since it is well established that the inclusion of discrete fibers increases the toughness characteristics of Portland cement concrete (Balaguru & Shah, 1992), the current study also incorporated reclaimed HDPE strips as “fiber” reinforcements in the soil-cement-fly ash matrix for improving the mechanical performance.

RELATED STUDIES

A number of investigations have been conducted in the past 25 years on the mechanics of unbound and stabilized soils reinforced with discrete fibers for geotechnical and pavement applications (Santoni et al. 2001; Benson & Khire, 1994; Maher & Ho, 1993; Crockford, et al. 1993). In related studies, the static and dynamic behavior of fiber reinforced stabilized recycled aggregate were evaluated for possible base course applications (Sobhan and Mashnad, 2003; Sobhan et al. 2003). Additionally, several investigators used split tensile tests for evaluating the tensile properties of stabilized materials, roller compacted concrete, and fiber-reinforced cementitious composites (Kennedy & Hudson, 1968; Nanni, 1989).

SCOPE AND OBJECTIVES

The specific objectives of this study were as follows: (1) to evaluate if the inclusion of recycled HDPE strips can enhance the strength and post-peak toughness characteristics of the composite, and (2) to suggest procedures for quantifying this improvement in mechanical performance for geotechnical and pavement applications.

MATERIALS

The soil used in this study was a poorly graded sand with a grain size distribution such that 100%, 94%, 56%, 22%, 9%, 5%, and 2% of the material passes the No. 10, No. 20, No. 40, No. 60, No. 140, and No. 200 sieves, respectively. Ordinary Type I Portland cement, and Class C Fly Ash were used as stabilizing agents. Recycled strips from milk jugs are reported to have tensile strength of 16.4 MPa and Young’s

Modulus of 900 MPa (Benson & Khire, 1994). The strips used in this study had widths of 6.35 mm, lengths of 19 mm and 38 mm, and typical thickness of 0.50 mm.

EXPERIMENTAL PROGRAM AND SPECIMEN PREPARATION

The experimental program consisted of (i) preliminary laboratory tests, which included grain size analysis, and a series of standard Proctor compaction tests; and (ii) a series of unconfined compression and specially instrumented split tensile tests on unreinforced and strip reinforced specimens. Standard Proctor moisture density tests conducted on soil-cement mixtures containing 4% to 12% by weight of cement indicated that the optimum moisture content varied between 12.5% and 14%, and the maximum dry density varied between 1698 kg/m^3 and 1794 kg/m^3. All specimens in this study were 101.6 mm in diameter, and 190.5 mm in height, and prepared at a target dry density of 1794 kg/m^3 with a molding water content of 12%. Usually five specimens were prepared from each mix; three were tested in split tension and two in unconfined compression. Specimens were sealed-cured in their molds in a controlled temperature room for 28 days. A total of 21 different mix designs (discussed later) were investigated in which the amount of cement and/or fly ash varied from 2% to 12%. The reinforced specimens contained an additional 0.25% to 0.5% (by weight) recycled HDPE plastic strips. The mixes were divided into two major groups: (i) *Lightly Stabilized Soils* containing 2% to 5% cement; and (ii) *Moderately Stabilized Soils* containing 10% to 12% cement.

EXPERIMENTAL PROCEDURES

All tests were performed with a 90-kN universal testing machine. The split tensile tests on unreinforced specimens were conducted according to ASTM C 496 procedure, which deals primarily with the determination of split tensile strength. In order to measure the tensile deformation of the horizontal diameter due to compressive loading in an orthogonal direction, two diametrically opposite linear variable differential transducers (LVDTs) were attached to each specimen at its longitudinal and vertical mid-point. The schematic of this instrumented split tensile test setup is shown Figure 1. Two PVC arcs are attached as shown to provide a suitable surface with a groove for anchoring the tip of the LVDT.

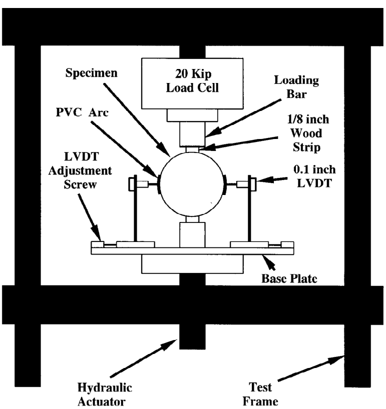

Figure 1. Split Tensile Test Setup

This technique permitted an evaluation of the load deformation response in tension, and the toughness characteristics of the strip reinforced specimens.

EXPERIMENTAL RESULTS AND ANALYSIS

Compressive and Split Tensile Strengths

Figure 2 provides the details of the mix-design and the strength properties. Split tensile strength is calculated according to ASTM C 496 as follows: $s_t = 2P/(\pi ld)$, where σ_t is the split tensile strength, P is the applied maximum load, and l and d are respectively the length and diameter of the specimen. Comparing Mix 2 with Mix 10 it is found that the compressive strength increased by almost 5 times (from 652 kPa to 3284 kPa) when the cement content was increased from 4% to 12%. Similarly, a comparison between Mixes 4 and 5, Mixes 6 and 7, and Mixes 8 and 9 (in all of which the cementitious material was doubled by adding fly ash) showed significant improvement in strength due to fly ash stabilization. Therefore, these initial mix-design tests indicated that a mix containing 8%-10% cement and the same amount of fly ash may produce a compressive strength ranging between 4500 kPa to 5600 kPa (650 psi - 800 psi), which is considered very suitable for base/subbase applications.

Mix No	Mix Design
Mix 1	2%C+2%F
Mix 2	4%C
Mix 3	4%C+4%F
Mix 4	5%C
Mix 5	5%C+5%F
Mix 6	8%C
Mix 7	8%C+8%F
Mix 8	10%C
Mix 9	10%C+10%F
Mix 10	12%C
Mix 11	2%C+2%F+0.50%S(L=38)
Mix 12	2%C+2%F+0.50%S(L=19)
Mix 13	5%C+5%F+0.25%S(L=38)
Mix 14	5%C+5%F+0.50%S(L=38)
Mix 15	5%C+5%F+0.50%F(L=19)
Mix 16	10%C+0.25%S(L=19)
Mix 17	10%C+0.25%S(L=38)
Mix 18	10%C+0.50%S(L=19)
Mix 19	10%C+10%F+0.25%S(L=38)
Mix 20	10%C+10%F+0.50%S(L=38)
Mix 21	10%C+10%F+0.50%S(L=19)

Variations in Strength with Mix Design

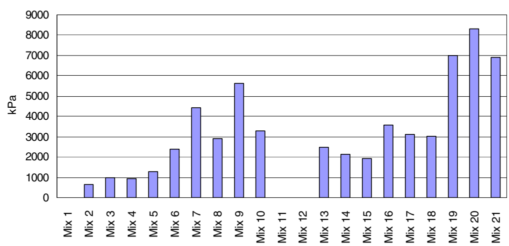

Compressive Strength

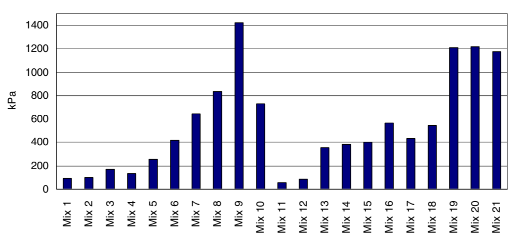

Split Tensile Strength

Figure 2: Mix Design Matrix and Variations in Strength (C: Cement; F: Fly Ash; S: Strips; L: Length of Strips in mm)

In case of *Lightly Stabilized* strip reinforced soils (5%C + 5% F), significant improvement in compressive strength (as much as 50%) and slight improvement in split tensile strength are observed due to strip reinforcement (Mixes 13, 14, and 15), when compared with corresponding unreinforced mix (Mix 5). In case of *Moderately Stabilized* strip reinforced soils (Mixes 16 through 21), it is found that the addition of strips in mixes containing 10% cement does not meaningfully improve the strength. However, a similar comparison considering Mixes 19, 20, and 21 (all strip reinforced, and contain 10% fly ash in addition to 10% cement) with Mix 9 (unreinforced) shows that there is a notable increase in compressive strength (as much as 30%). Important findings from the strength behavior are as follows: (i) Doubling the cementitious materials with fly ash has beneficial effects on the strength of soil-cement mixes; and (ii) any noticeable improvement in strength due to strip reinforcement was only realized in mixes containing fly ash as a supplementary cementitious material.

Split Tensile Load-Deformation Behavior

Figure 3 shows typical variations of the diametral tensile deformation with vertical load for strip reinforced *Lightly* and *Moderately stabilized* specimens (plots A, B, D, and E) containing 0.5% HDPE strips with lengths of 19 mm and 38 mm. Behavior of corresponding control unreinforced specimens is also presented in these plots. It is found that immediately following the peak, there is a sharp drop in the load carrying capacity indicating that the matrix tensile strength has been exceeded. In case of unreinforced specimens, the load deformation curves abruptly dropped to failure showing a brittle behavior. In case of *Moderately stabilized* soil, the load-deformation curves for the reinforced specimens become undulating and attain a second peak before failure. The attenuation of a second peak was also reported by other researchers (Rocco, et. al., 1999). This behavior indicates that recycled plastic strips were able to stabilize the propagation of the tensile cracks by transferring stresses across the cracks (called the "fiber-bridging" action).

Toughness Characteristics

In order to quantify the toughness characteristics in the post-peak region, the load axis of the load-deformation diagram was normalized with respect to the peak load P_p, and the deformation axis was normalized with respect to the deformation occurring at the peak load (d_p) as shown in Figure 3 (Plots C and F). To focus only on the post-peak behavior, a dimensionless split-tensile *Toughness Index*, *TI* is defined as follows:

$$TI = \frac{A_d - A_p}{d/d_p - 1} \tag{1}$$

where, d_p = deformation at peak load P_p; d = any deformation which is greater than the d_p value; A_p= area under the normalized curve up to the peak; and A_d = area under the normalized curve up to deformation ratio d/d_p . The *TI* value calculated in this way compares the performance of a specimen with that of an elastic-perfectly-plastic reference material, for which the *TI* is unity for any value of deformation ratio. On the other hand, *TI* is zero for an ideal brittle material with no post-peak load carrying capacity.

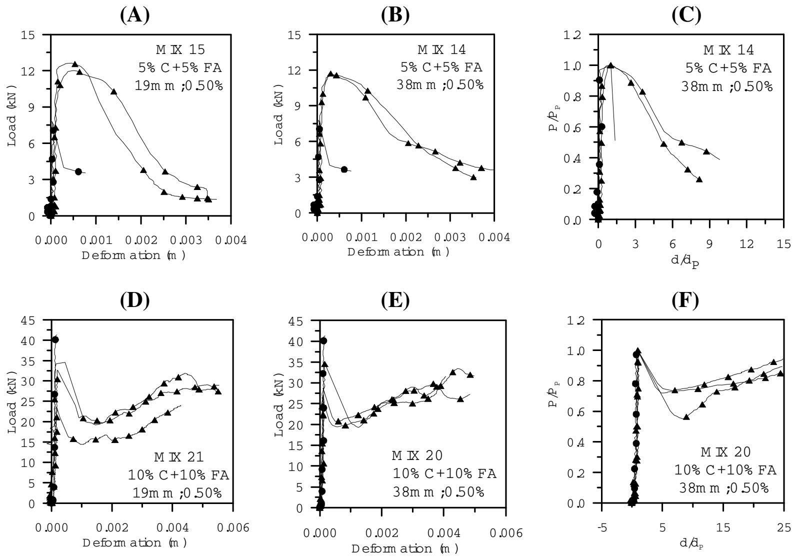

Figure 3: Load Deformation Behavior for Lightly Stabilized (A, B, and C), and Moderately Stabilized (D, E, and F) Soils; Solid Circles Represent Corresponding Unreinforced Control Specimens

The average values of *TI* are plotted in Figure 4 for all mixes, which also shows the *TI* value for a corresponding unreinforced specimen of the same mix. For the purpose of *TI* calculation, the d/d_p value was chosen to be 10 for *Lightly stabilized* mixes and 15 for *Moderately stabilized* mixes. For most mixes, the strip reinforced specimens showed a noticeable increase (ranging from 4% to 40%) in *Toughness Index* compared to unreinforced Mixes.

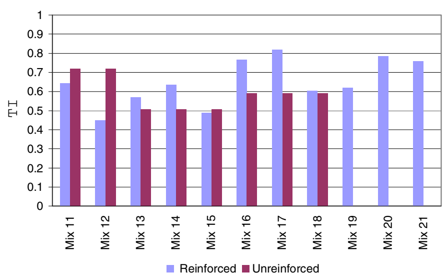

Figure 4: Toughness Index for all Mixes

For Mixes 20 and 21, the *TI* was zero for unreinforced mixes because they had no post-peak load carrying capacity (as shown in Figure 3). Therefore, particularly for these mixes, the strip reinforcement was able to convert a completely brittle behavior into a pseudo-ductile behavior, which is considered to be very desirable in a cementitious composite.

Influence of HDPE Strips

In an attempt to better visualize the effect of the HDPE strips, the split tensile strength and the *TI* were plotted against a unitless parameter, *wL/t*, where 'w' is the weight percent of strips, 'L' is the length and 't' the width of the strips; this is shown in Figure 5. It is found that for all mixes, the *TI* shows a gradual increase with increasing *wL/t* factor. However, the split tensile strength either remains unchanged or shows trends of slow decline for all mixes except the one with 10% cement and 10% fly ash, which shows a gradual improvement with the *wL/t* factor. Accordingly, the primary motivation for adding HDPE strips in a lean cementitious mix should be the improvement in toughness behavior without significantly compromising tensile strength. Figure 5 demonstrates that this objective is in general satisfied with the addition of recycled plastic strips used as fibers. It also shows that both the *TI* and the *wL/t* factor may be considered as useful parameters to evaluate and quantify the performance of recycled plastic strips or other fibers in such lean composites.

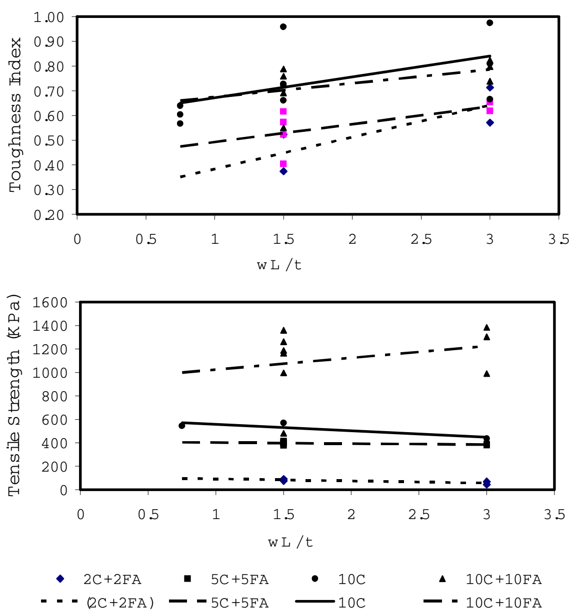

Figure 5: Influence of *wL / t* Factor on Tensile Strength and Toughness

SUMMARY AND CONCLUSIONS

The study evaluated the performance of recycled HDPE strips as a micro reinforcement in a lean cementitious pavement base/subbase material. Specific conclusions are as follows: (1) The recycled plastic strips used at an appropriate length and amount can enhance the toughness characteristics of the mix; (2) The Toughness Index, *TI* and the *wL/t* factors used in this study can provide a suitable means to evaluate the performance of randomly distributed discrete synthetic inclusions in a soil-cement mix; and (3) Addition of fly ash has a beneficial effect on both strength and toughness of the alternative base course composite developed in this research.

REFERENCES

Benson, C. H., and Khire, M. V. (1994). “Reinforcing Sand with Strips of Reclaimed High-Density Polyethylene,” *Journal of Geotechnical Engineering*, American Society of Civil Engineers, Vol. 120, No. 5, pp. 838-855.

Crockford, W. W., Grogan, W. P., and Chill, D. S. (1993). “Strength and Life of Stabilized Layers Containing Fibrillated Polypropylene,” 72nd Annual Meeting, *Transportation Research Board*, Washington, D. C.

Kennedy, T. W., and Hudson, W. R. (1968). “Application of Indirect Tensile Test to Stabilized Materials,” *Highway Research Record 235*, pp. 36-48.

Maher, M. H., and Ho, Y. C. (1993). Behavior of Fiber-Reinforced Cemented Sand Under Static and Cyclic Loads,” *ASTM Geotechnical Testing Journal*, Vol. 16.

Nanni, A. (1989). “Properties and Design of Fiber Reinforced Roller Compacted Concrete,” *Transportation Research Record 1226*, Transportation Research Board, Washington, D. C., pp. 61-68.

Rocco, C., Guinea, G. V., Planas, J., and Elices, M. (1999). “Mechanisms of Rupture in Splitting Tests,” *ACI Materials Journal*, Vol. 96, No. 1, pp. 52-60.

Santoni, R. L., Tingle, J. S., and Webster, S. L. (2001). “Engineering Properties of Sand-fiber Mixtures for Road Construction,” *Journal of Geotechnical and Geoenvironmental Engineering*, Vol. 127, No. 3.

Sobhan, K., Ahmad, T., and Mashnad, M. (2003). “Use of Discrete Fibers for Tensile Reinforcement of an Alternative Pavement Foundation with Recycled Aggregate,” *Cement, Concrete, and Aggregates*, Vol. 25 No. 1, ASTM International, American Society for Testing and Materials.

Sobhan, K. and Mashnad, M. (2003). “Fatigue Behavior of a Pavement Foundation with Recycled Aggregate and Waste HDPE Strips,” *Journal of Geotechnical and Geoenvironmental Engineering*, Vol. 129 No. 7, American Society of Civil Engineers.

Performance Evaluation of Stabilized Base and Subbase Material

Louay Mohammad[1], A.M. ASCE and Shadi Saadeh[2], A.M. ASCE

[1] Professor, Louisiana Sta. Univ. and Louisiana Transp. Res. Cent., 4101 Gourrier Avenue, Baton Rouge, LA 70808. E-mail: louaym@lsu.edu , Tel.: 225-767-9126.
[2] Assistant Professor, Dept. of Civil Eng. & Const. Eng. Mgmt., California Sta. Univ., Long Beach, 1250 Bellflower Blvd. Long Beach, California, 90840.

ABSTRACT: The resilient modulus and permanent deformation are important material properties in the characterization of unbound base materials and subgrade soils and in the design of pavement structures. This study evaluates the effect of stabilizing the base and subbase layers on the performance of a pavement structure. Three test lanes with six sections were constructed at the pavement research facility (PRF) of the Louisiana Transportation Research Center (LTRC). The six sections incorporated six different base course and two sub-base materials. The base materials were crushed limestone, Blended Calcium Sulfate (BCS), BCS stabilized with slag (BCS-Slag), BCS stabilized with flyash (BCS-Flyash), foamed asphalt treated 100% recycled asphalt (RAP) (FA-100RAP), and foamed asphalt treated blend of 50% RAP and 50% soil cement (FA-50RAP-50SC). The subbase materials were lime-treated and cement-treated soils, whereas subgrade was a clay (A-4) soil. The laboratory repeated load triaxial resilient modulus, permanent deformation, and material property tests were performed on these pavement materials. The BCS treated with slag showed the lowest permanent deformation base material followed by BCS treated with flyash, BCS, crushed limestone, and recycled asphalt pavement. Cement-treated soil, among subbase material, showed the lowest permanent deformation followed by lime-treated soil.

INTRODUCTION

The resilient modulus (Mr) of an unbound pavement material is a stress-dependent measure of the elastic modulus. It is the ratio of the maximum deviator stress (σ_d) to the recoverable resilient (elastic) strain (ε_r) in a repeated dynamic loading. The Guide for Mechanistic-Empirical Design of New and Rehabilitated Pavement Structures 2004 (M-E Design Guide) and the guide for design of pavement structures of the American Association of State Highway and Transportation Officials (AASHTO) (1993) recommend the use of resilient modulus of base or subbase as a material property in characterizing pavements for their structural analysis and design.
The resilient modulus of base materials can be estimated from laboratory repeated load triaxial tests. It can also be estimated from empirical correlations with soil properties or non-destructive test results. A model was recommended to describe the variation of resilient modulus with the bulk stress of materials in the 1993 AASHTO Guide for Design of Pavement Structures. Among the various treated pavement base or subbase materials, cement-treated and lime-treated soils are popular. Mohammad et al. (2004) studied the resilient properties of cement-treated subgrade soils. They also developed a model to predict the resilient modulus of cement-treated cohesive soils from the cement content and basic soil properties.

This paper presents the findings of laboratory evaluation of resilient modulus and permanent deformation properties of six treated and untreated pavement materials from recently constructed field sites at the accelerated loading facility of the Louisiana Pavement Research Facility (LPRF).

OBJECTIVE

The objective of this study was to evaluate the effect that providing a stronger and more durable base or subbase layer will have on the performance of a pavement.

SCOPE

Three experimental pavement lanes with six test sections total at the LPRF of the Louisiana Transportation Research Center (LTRC) were constructed. Each test section was 107.5 feet in length and 13 feet in width. The lane configurations and materials are presented in Table 1. Material samples were obtained from these lane sections. Ten different treated and untreated unbound pavement materials were tested for laboratory repeated load triaxial permanent deformation, resilient modulus, and material property tests.

Table 1. Configurations of the Test Section

Lane 4-1 A	**Lane 4-2 A**		**Lane 4-3 A**
2.0” HMA-19 mm	2.0” HMA-19 mm		2.0” HMA-19 mm
8.5” BCS-Slag	Sta. 0 to 0+20 ft.; 8.5” BCS	Sta. 0+20 to Sta. 1+7.5 ft.; 8.5” BCS-Flyash	8.5” Foamed-asphalt 50% RAP, 50% SC
12” Lime-treated Subbase (10%)	12” Lime-treated Subbase (10%)		12” Cement-treated Subbase (8%)

Lane 4-1 B	**Lane 4-2 B**	**Lane 4-3 B**
2.0” HMA-19 mm	2.0” HMA-19 mm	2.0” HMA-19 mm
8.5” Stone	8.5” Stone	8.5” Foamed-asphalt 100% RAP
12” Lime-treated Subbase (10%)	12” Cement-treated Subbase (8%)	12” Cement-treated Subbase (8%)

BCS- Blended Calcium Sulfate, RAP-Recycled Asphalt Pavements, HMA- Hot-mix asphalt, SC- Soil cement

SAMPLE PREPARATION

For base materials, cylindrical specimens of 152.4 mm (in diameter) x 304.8 mm (in height) were compacted for laboratory permanent deformation and resilient modulus tests. The samples were compacted in six (50 mm) layers. An electric vibratory hammer was used for the compaction. The compacted BCS-Slag and BCS-Flyash samples were sealed with polythene bags and kept in a moisture-controlled room for 28-day curing.

For subbase and subgrade materials, cylindrical specimens of 71.1 mm (in diameter) x 142.2 mm (in height) were compacted for laboratory permanent deformation and resilient modulus tests. The samples were compacted in five layers. An impact compactor was used for the compaction of subbase and subgrade materials. The compacted lime-treated and cement-treated samples were sealed with polythene bags and kept in a moisture-controlled room for 7-day, 14-day, and 28-day curing. The untreated subbbase and subgrade samples were tested immediately after the compaction. For all materials two replicates were tested for each test.

DESCRIPTION OF LABORATORY AND FIELD TESTS

REPEATED LOAD TRIAXIAL TEST (RESILIENT MODULUS TEST)

The resilient modulus is experimentally determined by applying a repeated axial load on a soil sample that is mounted inside a triaxial cell. The resilient modulus in a repeated load test is defined as the ratio of the maximum deviator stress (σ_d) and the recoverable elastic strain (ε_r) as follows:

$$M_r = \frac{\sigma_d}{\varepsilon_r} \tag{1}$$

The Standard Method of Test for Determining the Resilient Modulus of Soils and Aggregate Materials, AASHTO T 307 (2003), was used in this study to determine the resilient modulus of pavement unbound materials. The resilient modulus was also estimated from the permanent deformation test that is described below.

PERMANENT DEFORMATION TEST

In this test a haversine load pulse of 0.1-second loading period and 0.9-second rest period was used with 10,000 cycles. This test for base materials was conducted at a vertical stress level of 103.4 kPa (15 lbf/in.^{2}) that included a cyclic stress level of 93.0 kPa (13.5 lbf/in.^{2}) and a contact stress level of 10.3 kPa (1.5 lbf/in.^{2}). A confining stress level of 34.5 kPa (5 lbf/in.^{2}) was also maintained during the test. These stress levels were selected based on a stress analysis conducted to compute a field-representative stress condition in the base layer NCHRP 1-28 A (2003). The samples were conditioned before the test by applying 1,000 cyclic stress levels of 93.0 kPa (13.5 lbf/in.^{2}) together with a confining stress level of 103.4 kPa (15 lbf/in.^{2}). This test for subgrade soils was conducted at a vertical stress level of 41.3 kPa (6 lbf/in.^{2}) that included a cyclic stress level of 37.2 kPa (5.4 lbf/in.^{2}) and a contact stress level of 4.1 kPa (0.6 lbf/in.^{2}). A confining stress level of 14.0 kPa (2 lbf/in.^{2}) was also maintained during the test. These stress levels were selected based on a stress analysis conducted to compute a field-representative stress condition in the subgrade layer, Asphalt Institute (1989) and NCHRP 1-28 A (2003). These stress levels also account for the "resilient modulus at the break point" proposed by Thompson et al. (1979). The samples were conditioned before the test by applying 1,000 cyclic stress levels of 25 kPa (3.6 lbf/in.^{2}) together with a confining stress level of 41.3 kPa (6 lbf/in.^{2}). Permanent (plastic) strain (ε_{pn}), resilient strain (ε_r), total strain (ε_{tn}), and resilient modulus were determined from the test results for each load cycle number N (where N=1 to 10,000). The total strain is expressed as follows:

$$\varepsilon_{tn} = \varepsilon_{pn} + \varepsilon_r \tag{2}$$

where,
ε_{pn} - Permanent (plastic) strain,
ε_{r} - resilient strain, and
ε_{tn} - total strain at cycle number N (N=1 to 10,000).

RESULTS

COMPARISON OF M_R OF TREATED AND UNTREATED SOILS

Figure 1 compares the resilient modulus values of the cement-treated, lime-treated, and untreated soils. The resilient modulus values of cement-treated soils and lime-treated soils were higher than those of untreated soils. This implies that lime and cement treatments improve the subgrade soils. The percent increase in the resilient modulus of cement-treated soil with respect to the resilient modulus of untreated subgrade soil ranged from 1000 percent to 1500 percent, whereas that of the lime-treated soil ranged from 225 percent to 325 percent (Figure 2). Therefore, the rate of increase in the resilient modulus of the cement-treated soil is far greater than that of the lime-treated soil (Figure 2). The lowest resilient modulus was observed in the untreated subgrade soil. The cement-treated soil achieved the highest resilient modulus followed by the lime-treated soil did (see Figure 1). The higher the resilient modulus the better the pavement material is. Therefore, the performance of the cement-treated soils is better than that of both lime-treated and untreated soils. However, shrinkage cracks in the cement-treated soils is a major drawback of using it as a pavement material.

COMPARISON OF M_R OF TREATED AND UNTREATED BASE MATERIALS

As shown in Figure 3, among the base materials, BCS-slag material showed the highest resilient modulus followed by BCS-Fly ash, BCS, and crushed limestone.
As shown in Figure 3, among the base materials, the resilient modulus of the foamed-asphalt treated 100 percent RAP base material was the lowest, followed by that of foamed-asphalt treated 50 percent RAP with 50 percent soil cement, and that of the crushed limestone material. Among the base materials, BCS-Slag material achieved the highest resilient modulus base material followed by the BCS-Flyash. The results implied that the BCS-Slag provides higher resilient modulus of pavement bases than BCS-Flyash does.

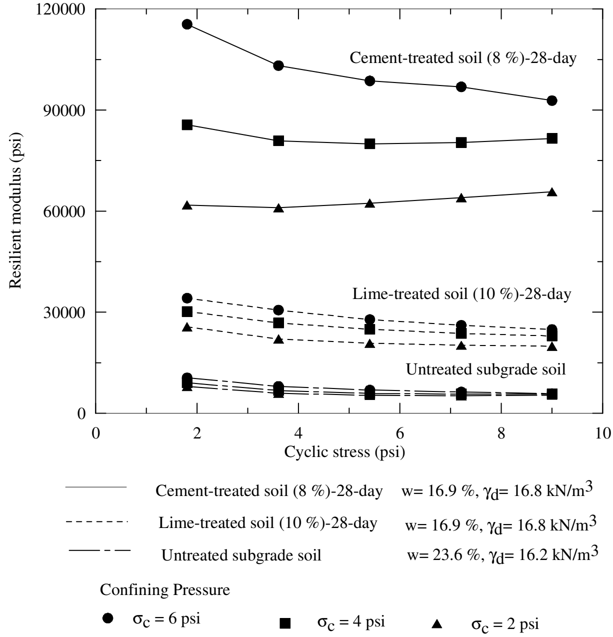

Figure 1 Resilient modulus of treated and untreated soils.

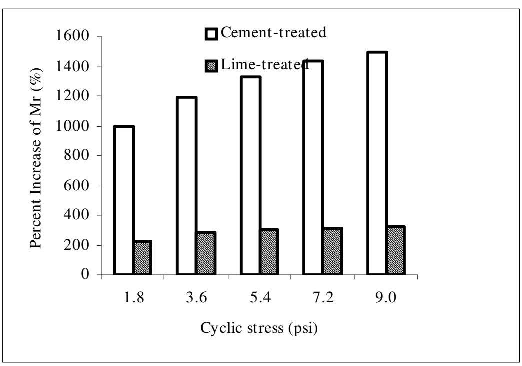

Figure 2 Increase in resilient modulus at confining pressure 6 psi

COMPARISON OF PERMANENT DEFORMATION OF UNTREATED AND TREATED BASE MATERIALS

Figure 4 presents the variation of permanent strain with the number N for all base materials considered. It is noted that FA-100RAP had the highest permanent strain, followed by FA-50RAP-50SC, RAP, crushed limestone, BCS, BCS-Flyash, and BCS-Slag. The majority of the base materials showed low permanent strains due to the low cyclic stress applied during the permanent deformation test. Table 2 indicates that there is still permanent deformation at the 10000 cycles and also it indicates that more cycles will be required to virtually eliminate the permanent deformation.

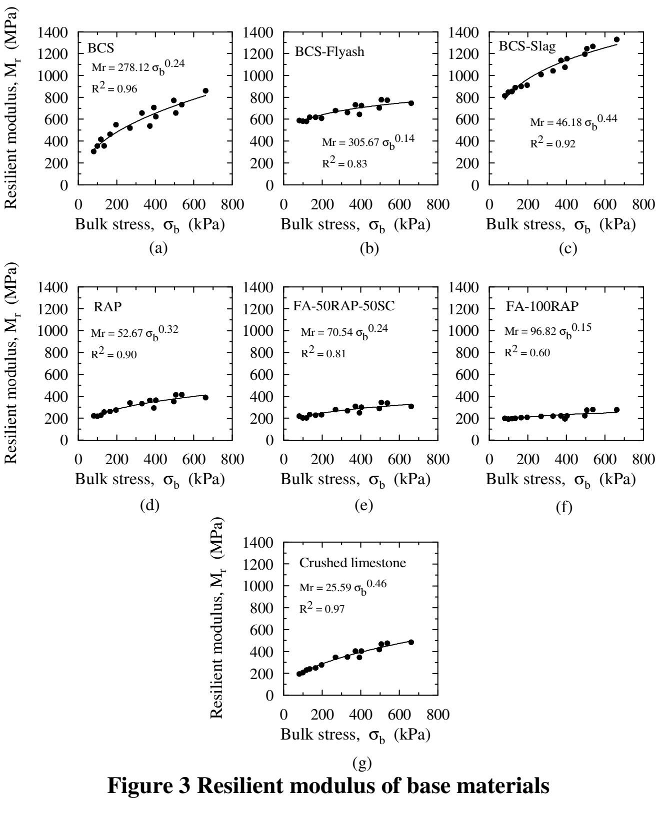

Figure 3 Resilient modulus of base materials

Table 2. Strain Ratio at 10000 Cycles for Soils

	Cement-treated soil	**Lime-treated soil**
$\varepsilon_p/\varepsilon_t$	0.32	0.21
$\varepsilon_r/\varepsilon_t$	0.68	0.79

ε_p- Permanent strain, ε_t- Total strain, ε_r - Resilient strain

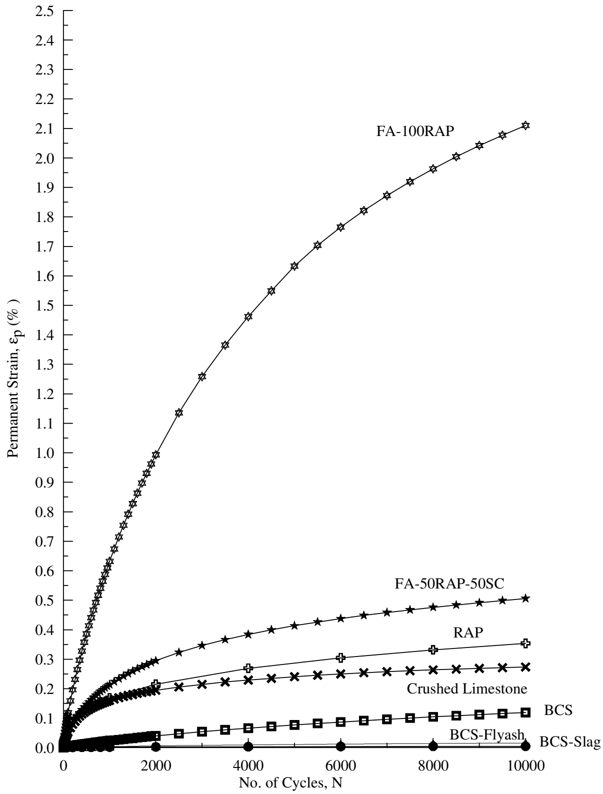

FIGURE 4 Permanent strains of treated and untreated base materials

CONCLUSIONS

The findings of this study are summarized below.

- Adding the slag as a stabilizer to the BCS was effective in increasing resilient modulus and controlling permanent deformation in base materials. Fly ash was also effective in controlling the permanent deformation of the BCS.
- Among subbase materials, cement-treated subbase achieved the highest resilient modulus followed by lime-treated subbase. Also cement-treated subbase showed low deformation in the permanent deformation test.
- BCS-slag material showed the highest resilient modulus among the investigated materials, followed by BCS-Fly ash, BCS, crushed limestone, RAP, foamed-asphalt treated blend of 50 percent RAP and 50 percent soil cement, and foamed-asphalt treated 100 percent RAP.

- BCS-slag showed the lowest permanent deformations among the investigated materials, followed by BCS-Fly ash, BCS, crushed limestone, RAP, foamed-asphalt treated blend of 50 percent RAP and 50 percent soil cement, and foamed-asphalt treated 100 percent RAP.
- The proposed permanent deformation test in this study is recommended for the unbound aggregate characterization.

ACKNOWLEDGMENTS

This work supported by the Louisiana Transportation Research Center in Cooperation with Louisiana Department of Transportation and Development and the Federal Highway Administration. The contribution of the staff of the asphalt and geotechnical laboratories to this project is greatly appreciated.

REFERENCES

AASHTO Guide for Design of Pavement Structures (1993), American Association of State Highway and Transportation Officials.

AASHTO T 307 (2003). "Determining the Resilient Modulus of Soils and Aggregate Materials, *American Association of State Highway and Transportation Officials*, T 399-07.

Asphalt Institute (1989). The Asphalt handbook. Manual Series No. 4 (MS-4), Lexington, KY, 435-437.

Guide for Mechanistic-Empirical Design of New and Rehabilitated Pavement Structures, Part2, Design Inputs (2004), *National Cooperative Highway Research Program (NCHRP)*, *NCHRP 1-37A*, Final Report, March 2004.

Mohammad, L.N, Herath Ananda, Gudishala, R., and Abu-Farsakh, M.Y., (2004), "Development of a Prediction Model for Resilient Modulus of Cement-Treated Cohesive Soils," *International Journal of Pavements*, (Vol. 3, No. 3), 2004 Sept, 59-70.

National Cooperative Highway Research Program (NCHRP) (2003), Project 1-28 A "Harmonized Test Methods for Laboratory Determination of Resilient Modulus For Flexible Pavement Design"

Thompson, M.R., and Robnett, Q.L. (1979) "Resilient Properties of Subgrade Soil." *Transportation Engineering Journal*, American Society of Civil Engineers, 1-89.

A Process to Identify and Verify the Binder Grades of HMA Mixtures Containing Asphalt RAP Materials

Raghubar Shrestha[1], M.ASCE and Peter E. Sebaaly[2] P.E., M. ASCE

[1]Senior Staff Engineer, (Ph.D. Candidate), Terracon Consultants, Inc., 7401 Galilee, Suite 450 Roseville, California 95678, rshrestha@terracon.com

[2] Professor and Director of WRSC, Department of Civil & Environmental Engineering, University of Nevada/MS 258, Reno, NV 89557, psebaaly@unr.edu

ABSTRACT

This paper presents a laboratory study conducted to identify the virgin binder grade required to blend with extracted RAP binder based on rheological properties of the binders. A total of twelve different combinations were studied to produce two target binder grades of PG64-22 and PG64-28 from three different RAP sources at two RAP contents. It was determined that five virgin binder grades are needed to be blended with RAP binders to achieve the properties of the target binder grades. The final grades of the blended binders were verified by actual blending the extracted RAP and virgin binders at different proportions to ensure that they met the target binder properties. Furthermore, validation of the blending process was conducted by extracting the final blended binder from asphalt mixtures that includes RAP and testing for the rheological properties. The results of this study were encouraging and found even better than target binder in some cases.

INTRODUCTION

Reclaimed asphalt pavement (RAP) is produced either by cold planning or by heating/softening of the existing old asphalt pavement. Recycling of asphalt pavements has become more popular since the late 1970s, although it had been practiced as early as 1915 (TRB 1978). Based on a report issued by the Federal Highway Administration and the United States Environmental Protection Agency, 80 percent of the asphalt pavements removed each year during widening and resurfacing projects is reused as part of new roads, roadbeds, shoulders and embankments. Besides the cost savings, up to 40 percent material and construction (http://www.dot.state.tx.us/services/general_services/recycling/recycleable.htm), the need to conserve energy and preserve natural resources has increased the interest in the use of RAP. Furthermore, several studies (e.g. Huang 2005, 2004, McDaniel 2001, and Paul 1996) showed that asphalt mixtures containing RAP perform similarly to virgin mixtures; but often at reduced material and construction costs. Hence, different agencies and contractors have made extensive use of RAP in constructing new asphalt pavements. The central plant process (hot mix recycling) of asphalt pavement is becoming more and more popular as one of the major rehabilitation methods by highway agencies throughout the United States.

Introduction of RAP to an asphalt mixture alters the properties of the hot mix asphalt (HMA) and ultimately affects the pavement performance (i.e. fatigue, rutting and thermal cracking). The change in the mixture properties is primarily caused by introducing the aged binder to the mixture as a part of the RAP. The binder in the RAP has different chemical composition and properties than the virgin binder that is added during the mixing process (Huang 2005). These two binders mix to some extent, changing the properties of the RAP containing mixture from the one that contains only virgin materials. The studies performed by McDaniel et al (2001, NCHRP Report 9-12), and Huang et al (1994) have shown that the addition of RAP increased the binder stiffness and decreased its shear strain. In order to compensate for these effects in a mix design, some adjustments in the virgin binder are imperative.

Inclusion of RAP materials in the HMA mix can improve resistance to rutting while it may decrease resistance to fatigue and thermal cracking. The key to successfully including RAP in the HMA mix is the ability to assess its impact on pavement performance while recognizing the uniqueness of each project. Identification of the virgin binder, which blends with the RAP binder, is the most critical part in the use of RAP in the asphalt mixtures. The rheological properties of the extracted binders are used to determine the performance grade (PG) of the virgin binders to be blended with the RAP materials from different sources.

Khandhal et al in 1997 performed research for the National Center for Asphalt Technology (NCAT) and concluded that the original high critical temperature was very reliable for determining the required high temperature grade of the virgin binder, whereas the intermediate temperature was not. Research conducted for NCHRP Project 9-12 showed that the difference between the measured and estimated critical temperatures with the rolling thin film oven (RTFO) aging and pressure aging vessel (PAV) are non-significant. Performance tests conducted in Louisiana (Paul 1996) and Georgia (Khandhal 1995) showed no difference between the performances of RAP added mixtures and conventional (without RAP) mixtures.

OBJECTIVES

The objectives of this research were to measure the rheological properties of the binders extracted from RAP materials, identify the required rheological properties of the virgin binders, and verify the entire process through measurements on the actual blended mixtures.

EXPERIMENTAL DESIGN AND ANALYSIS

This paper is part of the research conducted to assess the feasibility of using RAP on the Regional Transportation Commission (RTC) of Washoe County, Nevada, projects using prevailing RTC practices and techniques. Three different RAP sources at three proportions were used: (1) plant waste material, less than one year old (RAP I); (2) 15 year old HMA pavement (RAP II); and (3) 20 year old HMA pavement (RAP III). Three RAP contents were evaluated: none (control mix), 15 percent RAP, and 30 percent RAP. Two binder grades, which are typically used in Northern Nevada for bottom and top lifts of the asphalt layer were targeted: PG64-22 and PG64-28NV (Polymer modified), respectively. The extraction of the binder from all the three RAP sources was accomplished by the AASHTO T164-01[1](Method A) procedure using trichloroethylene (TCE) as a solvent. The asphalt binders from the solution were recovered using the Rotovapor in accordance with the AASHTO T319-03[1,2] recovery procedure. Subsequently, rheological properties were tested for asphalt binder grading.

PG Grading System

In this research, the PG asphalt binder system was adopted in accordance with AASHTO M 320-05 for the binder grading. This grading system is designed to improve the performance of HMA pavements by selecting asphalt binder with physical properties that resist permanent deformation, fatigue cracking, and low temperature cracking at different environmental conditions. The dynamic shear rheometer (DSR), bending beam rheometer (BBR), and direct tension (DT) are used to evaluate the rheological properties of a binder. The criteria set forth for these performance characters are briefly discussed below.

Permanent deformation is controlled by requiring the $G^*/\sin\delta$ (rutting factor) to be equal or greater than 1.0 kPa for unconditioned binder (original binder without short term aging) and a 2.2 kPa $G^*/\sin\delta$ for short term aged in the RTFO. Fatigue cracking is controlled by requiring $G^*.\sin\delta$ (fatigue factor) to be less than or equal to 5,000 kPa for RTFO and PAV aged binders. Low temperature cracking is controlled by requiring the creep stiffness value (S) to be less than or equal to 300 MPa and stress relaxation (slope) value (m) to be equal to or greater than 0.3. If the creep stiffness value is between 300 and 600 MPa, and a slope value higher than 0.3, the DT test result is used instead of the creep stiffness. The requirement for the direct tension is equal to or greater than 1.0 percent failure strain.

Besides these physical tests for a binder, there are a few additional tests required in order to facilitate handling, mixing and compaction, and safety. The minimum flash point temperature should be 230^{o}C, maximum viscosity of 3.0 Pa.s @ 135^{o}C, and maximum mass loss of 1.0 percent. These tests are not required in the case of RAP binder grading.

Extracted binders from all three sources were conditioned and prepared for the PG process. The binder tests were performed in accordance with AASHTO T315-04, T313-04, and T314-02, using the DSR, BBR, and DT where applicable. Critical high, intermediate, and low temperatures were determined meeting the above stated criteria. The summary of binder grades is shown in Table 1.

Table 1. RAP Binder Grades According to Superpave

Grade	RAP I	RAP II	RAP III
Actual Grade	PG82-19	PG82-16	PG82-18
PG Grade (MP1)	PG82-16	PG82-16	PG82-16

Blending and Identification of Virgin Binder Grade

Two methods of binder blending are used depending upon whether a known RAP (Method A) or known virgin binder (Method B) is used. In this research, known percentages of the RAP (i.e. 0%, 15% and 30%) materials were used, and only method A will be discussed with an example. This method uses the properties of the RAP binder along with the percent of RAP to be used and the PG of the target binder to determine the required PG of the virgin binder. The following blending equation (McDaniel et al 2001, NCHRP Report 9-12) was used to calculate the critical temperatures of the virgin binders.

$$T_{virgin} = \frac{T_{Blend} - (\%RAPbinder \times T_{RAP})}{(1 - \%RAPbinder)} \qquad (1)$$

Where:
T_{Blend} = the critical high, intermediate, or low temperature of the blended binder
T_{virgin} = the critical high, intermediate, or low temperature of the virgin binder
T_{RAP} = the critical high, intermediate, or low temperature of the RAP binder
$\%RAP_{binder}$ = percent RAP binder in the RAP in decimal format

Using Eq.1, the temperature grades of the virgin asphalt binder required to achieve the target binder grade were determined. The summary of the standard virgin asphalt binder grades required to blend with the different RAP sources at different percentages are shown in the Table 2.

Table 2. Summary of Virgin Binder Required to Blend with RAP Binders to Obtain Target PG Binder Grades

Descriptions	Target Binder Grade			
	PG64-22		PG64-28NV	
	15% RAP	30% RAP	15% RAP	30% RAP
RAP I (Plant Waste)	PG64-22[a]	PG58-28	PG64-34	PG58-34
RAP II (20 yrs old)	PG64-28NV	PG58-28	PG64-34	PG58-34
RAP III (15 yrs old)	PG64-28NV	PG58-28	PG64-34	PG58-34

[a] Actual required grade was PG60.9-22.4, but the standard PG grade PG64-22 was considered.

Verification of Binder Grade of the Blended Asphalt

Binders from all three different RAP sources were extracted and recovered in accordance with AASHTO T164-01[1](Method A) and AASHTO T319-03[1,2] respectively. The recovered binders were treated as if they were original binders, e.g. they were subjected to both short term (RTFO) and long term aging (PAV). Based on the percent binder content in each RAP source, the actual proportion of RAP binder that will blend with the proportion of virgin binder at 15 percent and 30 percent RAP aggregate were calculated. Table 3 shows the summary results of the proportion of RAP and virgin binders indicating the virgin binder grade required to blend with the RAP.

Table 3. Proportion of RAP and Virgin Binder for Actual Blending

RAP Sources	% Effect of RAP Binder on Total Mix (@ Actual AC% in Mix)	% Virgin Binder Required for Target Grade (@ Actual AC% in Mix)	Virgin Binder Grade Blended with RAP Binder	Target Binder Grade	Blend
RAP I (Plant waste)	15.7	84.3	PG64-22	PG64-22	AI15
	30.7	69.3	PG58-28		AI30
RAP II (20 yrs old)	18.7	81.3	PG64-28		AII15
	36.6	63.4	PG58-28		AII30
RAP III (15 yrs old)	21.0	79.0	PG64-28		AIII15
	39.9	60.1	PG58-28		AIII30
RAP I (Plant waste)	16.1	83.9	PG64-34	PG64-28	BI15
	30.7	69.3	PG58-34		BI30
RAP II (20 yrs old)	19.6	80.4	PG64-34		BII15
	38.3	61.7	PG58-34		BII30
RAP III (15 yrs old)	21.0	79.0	PG64-34		BIII15
	39.9	60.1	PG58-34		BIII30

Note: I, II, III - RAP binder sources
A & B - Denote the final target binder grades PG64-22 and PG64-28NV respectively
15 & 30 – Denote 15 percent and 30 percent RAP aggregates added in the mixture

After blending the appropriate proportions of RAP binder with the virgin binder as shown in above Table 3, the PG system was used to identify the grade of the blended binders. The blended binders were treated as if they were original as usual for normal grading. These binders were conditioned as original, RTFO and RTFO+PAV. Original and RTFO binder samples were tested to find the high temperature and RTFO+PAV samples were tested for intermediate and low temperature properties. The summary test results of blends for verifications are presented in Table 4.

Analysis:

The data in Table 4 show that the final grades of the blended binders, satisfy the required target binder grade in all the mixtures In addition the blended binders had a wider range of working temperature than the target binders of PG64-22 and PG64-28, indicating that the working temperatures of the blends were better than the control (target binder). In the case of the target binder of PG64-22, all the final grades of the blends were PG64-22 except the blend AIII15 which was PG70-22. Whereas for the target binder PG64-28, two out of six had the final grade of PG64-28, both of which contained 30 percent RAP, and four had final grade of PG64-34, which obviously were softer and better than control binder. Therefore, it is evident from the test results observed in this research that the target blend obtained from blending of estimated virgin binder required to blend with the RAP binder is at least comparable, or at times even better, than the required target binder.

Validation of Binder Grade of Extracted Binders from Mixtures

Testing on extracted binders was performed to validate the blending approach that was used. Binders were extracted from the samples which were already mixed, compacted, and had gone through performance tests. No further aging in the RTFO was done for these extracted binders. They were treated as if they had already short term or RTFO aged. Extracted binder samples were aged in the PAV for simulation of long term aging. The extracted aged binders were tested according to the Superpave system. The test results are summarized in the Table 4.

Analysis:

As indicated in Table 4, the data generated from the lab test results for extracted binders showed that the final grade of the extracted binders met the requirements of the target binders of PG64-22 and PG64-28. All extracted binders were better than the required target binder grades. For the target binder grade of PG64-22, the upper temperatures were higher than the target upper temperature of 64, indicating that the extracted binder can perform even at a higher temperature than the target high temperature. This observation indicates that the binders aged somewhat more, but the low temperature did not change. They still remained at the same required lower temperature. This means that the extracted binder can perform well at a higher temperature without significantly losing its stiffness or its rheological properties at the lower temperatures.

Looking at the results of the extracted binders for the target binder grade of PG64-28, it can be seen that all of the extracted binders had grades that better than the target grade. All the extracted binders are graded as PG70-34 except the BI15 blend where the extracted graded as PG64-34.

Table 4. Summary Test Results of Actual and Extracted Binder Grade

Blend	Summary PG Grading of Actual Bended Binders		Summary PG Grading of Extracted Binders	
	Actual Grade	PG grade	Actual Grade	PG grade
Control Grade A	**PG64-22**	**PG64-22**	**PG64-22**	**PG64-22**
AI15L1	PG69.7-23.4	**PG64-22**	PG74.0-21.8	**PG70-22***
AI30L1	PG67.6-26	**PG64-22**	PG75.5-22.5	**PG70-22**
AII15L1	PG69.7-25.2	**PG64-22**	PG75.6-22.3	**PG70-22**
AII30L1	PG67.3-26.6	**PG64-22**	PG71.7-25.2	**PG70-22**
AIII15L1	PG70.2-25.7	**PG70-22**	PG76 -24	**PG76-22**
AIII30L1	PG68.3-25.5	**PG64-22**	PG76.6-22	**PG76-22**
Control Grade B	**PG64-28**	**PG64-28**	**PG64-28**	**PG64-28**
BI15L1	PG66-39	**PG64-34**	PG67-39	**PG64-34**
BI30L1	PG68.5-35	**PG64-34**	PG72-35.6	**PG70-34**
BII15L1	PG64.9-37.3	**PG64-34**	PG72-38	**PG70-34**
BII30L1	PG66.8-32	**PG64-28**	PG72-34	**PG70-34**
BIII15L1	PG65.3-37.9	**PG64-34**	PG75-36	**PG70-34**
BIII30L1	PG67.4-32	**PG64-28**	PG75-36	**PG70-34**

* This symbol indicates that the binder grade does not meet the superpave grading criteria. This might work if actual temperature of the site condition is low than -21.8^{o}C.

CONCLUSIONS AND RECOMMENDATIONS

The following conclusions can be drawn from this study:

1. Consideration of high and low temperatures for the determination of the extracted RAP binder grade, as recommended by NCHRP, strongly correlated with the lab test results presented in this paper.
2. The NCHRP recommended RAP binder grading process does not always give the correct binder grade. Based on data generated from this research, it is true for old RAP materials, but not for RAP materials produced from plant waste. Therefore it is more appropriate to adopt the standard Superpave binder grading system where new sources of RAP materials, that are less or about a year old, are being considered.
3. Binder grade results obtained from the actual blending of extracted RAP binder and estimated virgin binder have been similar to or better than the required binder grade. The reason for the better grade could be due to the use of a softer

binder than required. The use of softer binders was necessary in order to use standard PG grades within the six degrees increments.

4. Binder grade results obtained from testing of rheological properties of extracted binders from asphalt mixtures have also yielded equal or better binder grades than the required.
5. Based on conclusions 4 and 5, it can be concluded that the AI equation is somewhat conservative in estimating the virgin binder grade based on the RAP binder properties and proportions.
6. Based on this research, a target binder grade can be reasonably produced by mixing a virgin and an extracted RAP binder at any desired proportion without significantly losing any rheological properties.

ACKNOWLEDGEMENTS

This study was supported by the Washoe Regional Transportation Commission (RTC), Reno. The authors would like to thank everybody who helped accomplishing this project successfully.

REFERENCES

Transportation Research Board (TRB 1978). “Recycling Materials from Highways”, *National Cooperative Highway Research Program Synthesis of Highway Practice No. 54*, Washington, DC, 1978.

Huang, B., Li. G., Vukosavljevic, D., Shu, X., and Egan, B.K. (2005). “Laboratory Investigation of Mixing HMA with RAP”, *Transportation Research Board Annual Meeting*.

McDaniel, R. S., Soleymani, H. R., Anderson, R. M., Turner, P., and Peterson, R. L. (2001). “Recommended Use of Reclaimed Asphalt Pavement in the Superpave Mix Design Method”, *NCHRP Project 9-12, Transportation Research Board*, *National Research Council*, Washington, D.C.

Huang, B., Egan, B.K., Kingery, W.R., Zhang, Z., and Zuo, G. (2004). “Laboratory Study of Fatigue Characteristics of HMA Surface Mixtrues Containing RAP”, *Transportation Research Board* prep reprint.

Kandhal, P. and Foo, K.Y. (1997). “Designing Recycled Hot Mixture Asphalt Mixtures Using Superpave Technology,” *NCAT Report No. 96-5*, 1997, 7 – 22.

Paul, H. R. (1996). “Evaluation of Recycled Projects for Performance”, *Journal of the Association of Asphalt Paving Technologists*, From the proceedings of the Technical Sessions, Baltimore, Maryland March 18-20.

Khandal, P.S., Rao, S.S., Watson, D.E., and Young, B. (1995). “Performance of Recycled Hot-Mix Asphalt Mixtures in Georgia,” *Transportation Research Record 1507*, TRB, 67-77.

Laboratory Study on Effects of Geogrid Properties on Subgrade Stabilization of Flexible Pavements

Xiaochao Tang[1], S.M.ASCE, Ghassan R. Chehab[2], M. ASCE, Angelica M. Palomino[3], A.M. ASCE, Sam R. Allen[4] and C. Joel Sprague[5], P.E.

[1]Ph.D. Candidate, Department of Civil and Environmental Engineering, Pennsylvania State University, University Park, PA 16802; xxt103@psu.edu
[2]Assistant Professor, Department of Civil and Environmental Engineering, Pennsylvania State University, University Park, PA 16802; gchehab@engr.psu.edu
[3]Assistant Professor, Department of Civil and Environmental Engineering , Pennsylvania State University, University Park, PA 16802; angel.palomino@engr.psu.edu
[4]Vice President, TRI/Environmental, Inc., 9063 Bee Caves Road, Austin, TX 78733; sallen@tri-env.com
[5]Senior Engineer, TRI/Environmental, Inc., PO Box 9192, Greenville, SC 29604; jsprague@tri-env.com

ABSTRACT: The objective of this study is to identify mechanical and physical geogrid properties critical to performance in geogrid-reinforced pavements. Properties such as aperture size, wide-width tensile strength, and junction strength of several geogrid types are determined from laboratory index testing. Performance tests, including direct shear and pullout, are performed to investigate the interaction characteristics of the soil-geogrid interface. Correlations are made between the geogrid index properties and performance test results to identify the critical properties that have the most impact on performance. Analysis reveals a strong relationship between performance and junction and tensile strength of geogrids at moderate strain levels, and aperture size has a positive correlation with pullout results. Such findings aid in selection of appropriate geogrid types for subgrade reinforcement purposes and prediction of performance in the field based on index properties.

INTRODUCTION

Geogrids have been widely used as reinforcement in structures with unbound materials, such as pavements, slopes, retaining walls, and embankments. In a pavement system, the presence of a geogrid at the interface between the aggregate base course and subgrade layer strengthens that zone by providing additional shear strength and transferring vertical compressive stresses on the subgrade to horizontal tensile stresses in the geogrid (Hass et al. 1988; Perkins, 1999). Additional types and mechanisms of reinforcement are mobilized by the presence of geogrids depending on the application and environmental and loading conditions. Such mechanisms include surface friction along the geogrid, passive thrust against the geogrid's bearing ribs, aggregate interlock in the apertures, and/or soil-soil friction (Shukla 2002).

The effectiveness of geogrid reinforcement is highly dependent on properties of the interface between geogrids and surrounding materials. Results from direct shear and pullout tests are the most commonly used parameters depicting the soil-geogrid interaction characteristics. Characteristics identified through those tests are function of various factors including applied normal stress, geogrid material properties, soil and aggregate properties such as gradation, plasticity, density, moisture content, geogrid shape and texture, in addition to the loading displacement rate (Ingold 1983; Farrag et al. 1993; Jewell et al. 1984).

Direct shear and pullout tests are conducted in this study to characterize the interaction properties of various types of geogrids installed between a specific subgrade-aggregate base medium. The subgrade used is a typical soil common in central Pennsylvania, and the aggregate base is that normally specified by the Pennsylvania Department of Transportation (PennDOT) for flexible pavement construction.

EXPERIMENTAL INVESTIGATION

Material Properties

Four commonly used biaxial geogrid products are selected for this study and are herein designated as Grid A, Grid B, Grid C, and Grid D. Grids A and D are composed of high tenacity polyester (PET) multifilament yarns and coated with a proprietary polymer and polyvinyl chloride (PVC) coating, respectively. Grid B is made of woven polypropylene (PP) yarns, while Grid C is made of extruded PP sheets. Based on the measured flexural rigidity per ASTM D 1388, grids A, B, and D are classified as flexible geogrids, while Grid C is classified as a stiff geogrid (Koerner 1998). Table 1 presents the tested index properties of the four geogrid products.

The soil subgrade material used in the study is classified as silty sand (SW-SM). According to the sieve analysis, 6.2% of the soil passed the #200 sieve (0.074 mm) and D_{50} = 0.841 mm. The optimum moisture content is 10% at a maximum dry density of 2066 kg/m^3. The friction angle is 31.8° based on direct shear test results conducted at the optimum water content and 95% of maximum dry density.

Dense-graded crushed stone is used as the pavement aggregate base layer. Sieve analysis indicates that the aggregate meets the PennDOT 2A grading requirements, and D_{50} = 7.2 mm. A standard Proctor test of the aggregate yields an optimum moisture content of 3.9% and maximum dry density of 2329 kg/m^3.

Test Procedures

Direct shear tests are conducted for the four listed geogrids according to ASTM D 5321. Specimens are prepared to be consistent with the pavement structure; that is, geogrids are placed between the upper aggregates box and the lower soil box. Dimensions of both boxes are 30.5 cm × 30.5 cm × 10.2 cm. Base aggregates are remolded and compacted to 100% of maximum dry density at optimum moisture content. Subgrade soils for these tests are compacted to 92.5% of maximum dry density and at optimum moisture content (10%). Tests are performed under three different normal pressures: 12 kN/m^2, 27 kN/m^2, and 36 kN/m^2. Shear force is applied at a low constant rate of displacement, 1.02 mm/min, to allow for soil pore pressure dissipation. The shear and normal stresses are calculated based on corrected specimen contact area.

Table 1. Tested Index Properties of the Geogrids

Index Property	Test Method	Geogrid							
		Grid A		Grid B		Grid C		Grid D	
		MD*	TD**	MD	TD	MD	TD	MD	TD
Aperture size (mm)	Calipers	27.18	28.96	35.05	41.15	25.65	36.58	25.65	26.42
Rib thickness(mm)	Calipers	0.76	1.12	1.98	1.09	0.76	1.07	1.42	2.03
Junction thickness(mm)	ASTM D 5199	1.17		2.29		3.94		1.55	
Mass per unit area (g/m^2)	ASTM D 5261	298.37		252.26		319.06		350.93	
Tensile strength at 2% strain (kN/m)	ASTM D 6637	7.5	10.1	14.8	15.0	9.8	15.6	10.3	11.2
Tensile strength at 5% strain (kN/m)		13.1	14.1	30.1	30.0	16.8	29.2	18.1	17.4
Ultimate tensile strength (kN/m)		33.3	57.8	36.5	35.7	23.9	32.9	39.5	52.8
Elongation at break (%)		10.5	14.0	7.1	6.7	20.6	10.9	10.5	12.0
Junction Strength (kN/m)	GRI GG2	6.1	7.6	10.2	4.3	17.7	28.1	7.4	7.1
Flexural rigidity (mg-cm)	ASTM D 1388, mod.	146119		271509		1429355		452671	
Torsional stiffness (cm-kg/degree)	COE / GRI GG9	3.47		3.97		7.50		3.43	

* MD: machine direction; **TD: transverse/cross-machine direction

Pullout tests are performed in the machine direction for the fours geogrids according to ASTM D 6706. The geogrid samples are cut into 1.2-m by 0.6-m sections and inserted into a 0.4-m-thick compacted aggregate layer with the machine direction parallel to the pullout direction. All pullout tests are carried out under normal pressure of 7 kN/m^2 and at a displacement-rate of 1.02 mm/min. Pullout forces and geogrid displacements are measured at the front and at 31 cm, 61 cm, 89 cm, and 116 cm away from the front face of the pullout box.

RESULTS AND ANALYSIS

Direct Shear Tests

Figure 1 (a) shows the direct shear tests results for the control interface, i.e. subgrade soil-base aggregates. As expected, the applied shear stress increases with increasing normal pressure. The shear strength parameters of the interface, adhesion and friction angle can be obtained from the Mohr-Coulomb failure envelope derived from the peak values of direct shear test results (Figure 1 -b).

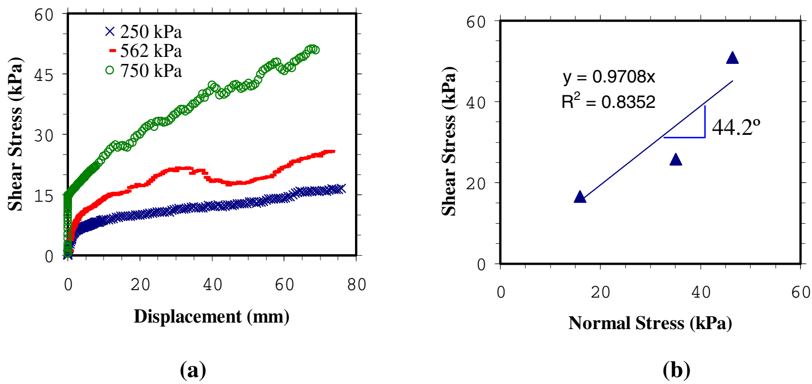

FIG.1. Direct shear tests: (a) shear stress – displacement under various normal pressures; (b) friction angle of the control interface.

Given the shear strength parameters of the control interface, the interface efficiency factor, E_ϕ can be calculated as (Koerner 1998):

$$E_\phi = \left(\frac{\tan\delta}{\tan\phi}\right)\times 100 \tag{1}$$

where δ is friction angle of geogrids reinforcement interface, and ϕ is friction angle of control interface. The efficiency factor for geotextiles varies from 0.6 to 1.0, but can be greater than one for geogrids (Juran et al. 1988). Table 2 provides a summary of the tested properties from direct shear tests for the tested geogrids. All the geogrids reinforcement had interface efficiency factors greater than 50%, especially, Grid B and C that exhibited higher shear strengths.

Table 2. Results of the direct shear and pullout tests

Property	Grid A	Grid B	Grid C	Grid D
Friction angle, δ_{peak} (deg)	28.6	44.0	48.0	32.7
Efficiency factor, E_ϕ (%)	56.1	99.4	114.3	66.0
Adhesion, c (kN/m^2)	1.72	0.00	0.00	3.69
Interaction coefficient, C_i	0.86	1.00	0.82	0.62

The shear strength of the soil-geogrid-aggregate interface against direct sliding movement consists of geogrid's skin friction, soil-aggregate friction, and passive resistance against the geogrid's transverse ribs. However, the contribution from the geogrid skin friction is likely to be minimal due to its relatively small surface area with respect to the total area of the interface. The area of the geogrid's aperture determines the contact surface between the subgrade soil and sub-base aggregates, and thus affecting the overall soil-aggregate interface friction. Figure 2 (a) illustrates the relationship between the interface efficiency factor and aperture area.

The passive resistance exerted on the bearing members of the geogrid to some extent depends on the junction strength when considering the sliding movements against ribs between junctions, and possibly tensile strength at moderate strain levels. The combination of junction strength and tensile strength at 2% strain in machine direction has a strong correlation with interface efficiency factor as seen in Figure 2 (b).

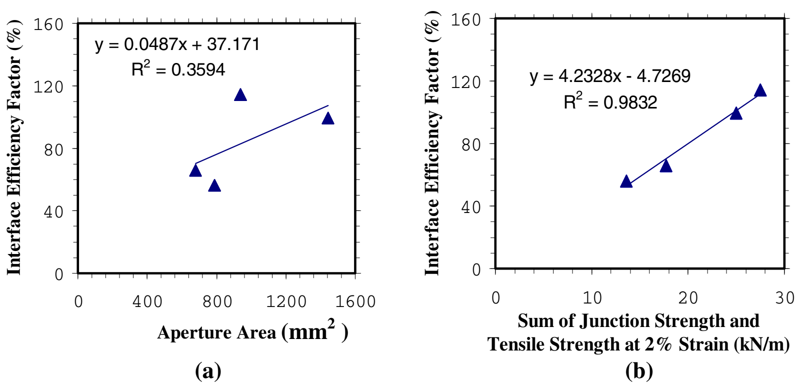

FIG.2. Correlation between E_ϕ and geogrid index properties: (a) aperture area; (b) combination of junction strength and tensile strength at 2% strain in machine direction.

Pullout Tests

The interaction coefficient, C_i, represents the ratio of the average interface strength to the internal shear strength of the backfill and is used herein to quantify the reinforcement effectiveness for pullout tests. C_i can be calculated as (Bergado and Chai 1994; Tatlisoz et al. 1998):

$$C_i = \frac{P}{2WL(c + \sigma_n \tan \phi)} \tag{2}$$

where:
C_i is the coefficient of interaction,
P is maximum pullout load,

σ_n is the applied normal pressure,
c is the cohesion of soil medium tested,
Φ is the friction angle of soil medium tested,
W is the width of the geogrid specimen, and
L is embedded length of geogrid in the soil.

C_i is a function of various parameters including frictional characteristics between the geogrids and surrounding unbound materials, strength of the geogrid junctions, flexural stiffness of the transverse ribs, and geogrid percent open area. The calculated interaction coefficients for the four geogrid cases are presented in Table 2. A strong bond between the soil and the geosynthetic corresponds to an interaction coefficient value greater than one. An interaction coefficient less than 0.5 implies a weak bond between the geogrid and surrounding materials and/or possible breakage of geogrid cells.

Figure 3 shows the pullout force-displacement relationships for Grids A, B, C, and D at locations 31 cm from the front face of the pullout box. Grid B exhibited the highest peak pullout force, while Grid C had the best pullout resistance at small displacements. Similar trends are observed at the other locations: 61 cm, 89 cm, and 116 cm from the front face. Note that the attributes of geogrids at moderate strain levels are important when geogrids are used as pavement reinforcements, considering the traffic- induced minimal deformation of geogrids in pavements.

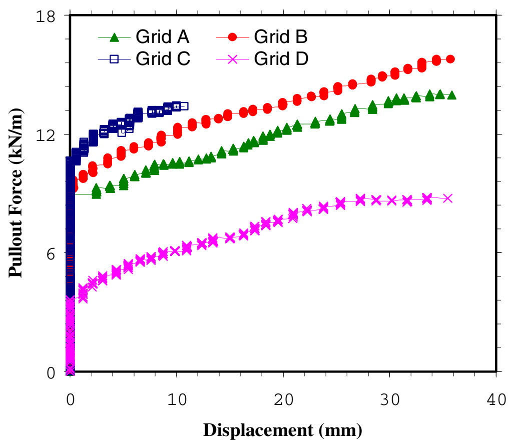

FIG.3. Pullout Load-Displacement for Grid A, B, C, and D at locations 31 cm from the Front

The pullout test result is a function of various parameters including physical and mechanical properties of geogrids. However, not all geogrid properties necessarily affect the interface interaction. Figure 4 shows that the interaction coefficient correlates well with the geogrid aperture area but not junction strength and ultimate tensile strength. Grid B has larger apertures compared to the other geogrid specimens (refer to

Table 1), which partially contributes to the highest interaction coefficient since the opening in the geogrid allows aggregates to interlock among ribs, increasing its shear resistance.

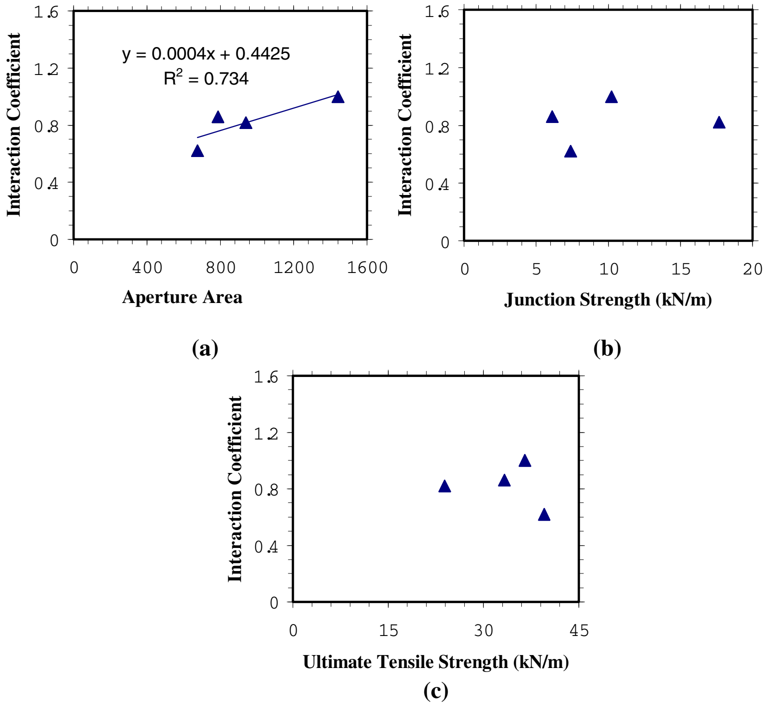

FIG.4. Correlation between the interaction coefficient and geogrid index properties: (a) aperture area; (b) junction strength; (c) ultimate tensile strength in machine direction.

CONCLUSIONS

Both direct shear and pullout tests are conducted on four types of geogrid products integrated with pavement materials to investigate performance of the geogrid at the interface, particularly the interface between the subgrade soil and subbase aggregate. Tests results show that all four geogrid reinforcements provide higher interface strength than when no geogrid is present. Grids B and C have relatively higher efficiency factor indicating better shear resistance. From pullout test results, Grid B exhibits the highest peak pullout force while Grid C has better pullout resistance at small displacements.

The difference in response of geogrid specimens in direct shear and pullout tests can be attributed to the characteristics of the geogrids. All other system variables are kept constant to reduce their influence on test results. An attempt is made to relate the differences between geogrid index properties and subsequent performance through correlation analysis. A good correlation is found between combined geogrid tensile strength and junction strength and results of direct shear tests, showing junction strength and tensile strength at moderate strain levels influences the interface efficiency factor in a complex manner. Aperture size correlates with interaction coefficient, which indicates that aperture size of the geogrid plays an important role in its interaction with the subgrade-base course interface. It is noted that ultimate strength of geogrids does not correlate well with pullout tests results while junction strength exhibits some relationship with pullout test results.

ACKNOWLEDGMENTS

This study is part of the research work conducted at Pennsylvania Transportation Institute of Pennsylvania State University. The authors acknowledge and appreciate the support provided by the Pennsylvania Department of Transportation.

REFERENCES

Bergado, D.T. and Jin-Chun Chai. (1994). “Pullout force/displacement relationship of extensible grid reinforcements.” *Geotextiles and Geomembranes*, Vol.13: 295-316.

Farrag, K., Acar, Y.B., and Juran, I. (1993). “Pull-out resistance of geogrid reinforcements.” *Geotextiles and Geomembranes*, Vol. 12 (2): 133-159.

Hass R., Wall, J., and Carroll, R.G. (1988). “Geogrid reinforcement of granular bases in flexible pavements.” *Transportation Research Record 1188*, Transportation Research Board, National Research Council, Washington D.C.:19-27.

Ingold, T.S. (1983). “Laboratory pullout testing of grid reinforcements in sand.” *Geotechnical Testing Journal*, Vol.6 (3):101-111.

Jewell, R.A., Milligan, G.W.E., Sarsby, R.W., and Dubois, D. (1984). “Interaction between soil and geogrids.” *Proceedings of the Conference on Polymer Grid Reinforcement*, Thomas Telford, London: 18-30.

Juran, I., Knochenmus, G., Acar, Y.B., and Arman, A. (1988). “Pull-out response of geotextiles and geogrids (Synthesis of available Experimental Data).” *Proceedings of Symposium on Geotextiles for Soil Improvemen*t, ASCE, GSP No.18, ASCE, Reston, VA: 92-111.

Koerner, R.M. (1998). *Designing with Geosynthetics*, 4th Edition, Prentice Hall, New Jersey.

Perkins, S.W. (1999). “Geosynthetic reinforcement of flexible pavements: laboratory based pavement test sections.” *Report No. FHWA/MT-99-001/8138*, U.S. Department of Transportation, Federal Highway Administration, Washington, D.C.

Shukla, S.K. (2002). Geosynthetics and their Applications, Thomas Telford, London.

Tatlisoz, N., Edil, T.B., and Benson, C.H. (1998). “Interaction between Reinforcing Geosynthetics and Soil-tire Chip Mixtures.” *Journal of Geotechnical and Geoenvironmental Engineering*, Vol. 124(11): 1109-1119.

An Integrated Monitoring Plan for BioInfiltration BMPs

Krista Hankins[1], Student Member ASCE, Andrea L. Welker[2], Associate Member Geo-Institute and ASCE, P.E., and Lynn Mandarano[3], P.E.

[1]Graduate Student, Villanova University, 800 Lancaster Avenue, Villanova, PA, 19085, krista.hankins@villanova.edu
[2]Associate Professor, Villanova University, 800 Lancaster Avenue, Villanova, PA, 19085, andrea.welker@villanova.edu
[3]Assistant Professor, Temple University – Ambler, Center for Sustainable Communities, 580 Meetinhouse Road, Ambler, PA 19002, lynn.mandarano@temple.edu

ABSTRACT: With the change in regulations governing NPDES permitting, stormwater best management practices (BMPs) are increasing in popularity. Structural and vegetative BMPs help to restore the natural hydrologic cycle by infiltrating stormwater into the ground and encouraging evapotranspiration. One device, known as a bioinfiltration BMP or rain garden, improves the quality of local river systems by decreasing the volume of water reaching nearby streams during storm events and maintaining baseflow during dry seasons; in addition, the soil in these devices acts as a filter for the contaminants often found in stormwater. Engineers, planners, and community groups often wish to verify the effectiveness of these BMPs. For research efforts, intensive monitoring is needed at all levels: ecological, water quality, and hydrologic. This level of intensive monitoring is not practical for all purposes. This paper presents a plan to monitor the effectiveness of bioinfiltration BMPs using a low, medium, and high effort.

INTRODUCTION

Stormwater management has become increasingly important over the last couple of decades. As new residential and commercial complexes are being built on rural farmland, the amount of pervious land cover has begun to diminish. The stormwater runoff produced can not infiltrate into the ground and is forced to travel to the nearest stream producing an increase in volume and peak flow rate. This affects not only the area of new development, but extends to the remainder of the watershed (e.g. Traver and Chadderton 1983; Schueler 1997; Wang, et al. 2001, US EPA 2005; Heasom, et al. 2006). Best Management Practices (BMPs) are therefore being incorporated into these residential and commercial complexes to carry the burden of the excess stormwater.

BMPs are designed to serve three main purposes: (1) to control the volume of runoff, (2) to control the peak flow rates, and (3) to control the pollutants while restoring the natural hydrologic cycle (PADEP 2007).

Bioinfiltration basins (Figure 1), also known as rain gardens, are most often applied in suburban and urban settings. Bioinfiltration BMPs are typically designed to capture the runoff of smaller storms (2-year or less). Excess water produced from larger storms will exit through a series of overflow pipes. The structural components of the BMP act to contain the water for a short period of time and control the flow. Vegetation serves to slow down the initial flow rate, transpire water and treat pollutants. Water not taken up by evapotranspiration recharges the groundwater table.

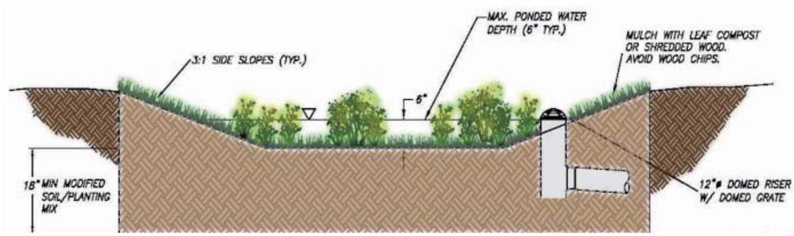

Figure 1: Bioinfiltration Basin (PADEP 2007)

How can one tell if a bioinfiltration basin is working efficiently? This paper presents an Integrated Monitoring Plan (IMP) that can be used to determine the effectiveness of a bioinfiltration BMP dependent on practicality and budget issues.

Our IMP breaks down monitoring into three levels: high, medium, and low. Depending on the desired level of monitoring, recommendations are provided on the equipment and monitoring effort. The proposed plan includes hydrologic, water quality and ecological monitoring. By breaking down an intensely monitored site, which could be found at a university, a medium (commercial), and low (residential) monitoring methodology can be recommended.

POSSIBLE MONITORING OPTIONS FOR BIOINFILTRATION BASINS

Hydrologic Monitoring

Precipitation

Precipitation and peak intensity are measured through the use of a rain gage. There are several variations of rain gages. The cheapest and most simplistic rain gage is an analog rain gage. An analog rain gage is a graduated cylinder with measurement markings that can be read at any point during the storm or an overall reading at the end. Larger rain gauges of this type have the capacity to be read from afar, making readings during a storm more feasible. A disadvantage of this device is that is must be manually emptied in between storm events.

The most practical rain gage used is the tipping bucket rain gage which requires little maintenance and is self draining. The tipping bucket rain gage records precipitation data continuously at a user-defined time interval. The data collected may be directly connected to a computer or downloaded to a data logger.

Antecedent dry time is the amount of time that has passed since the last rain event. It can be observed through the rain gage data. A tipping bucket rain gage monitors continuously and the dry time can be found by determining the period when the rain gage first reads 0 to the next known value greater than 0. A manual method would be recording the time a storm ends and the start of the next, if using a non-electronic rain gage.

Ponded Depth

Traditional methods for depth include placement of a rod placed at a designated location to provide a visual indicator of water level (i.e. a staff gage). Although easy to maintain, it requires several visitations to the field during a rain event. An ultrasonic transducer records data digitally and can be attached to a data logger for continuous readings.

Water surface elevation or ponded depth is important because it helps to determine the infiltration rate. The infiltration rate is the key determinant of the effectiveness of a BMP. A simple method of determining this parameter is by drawing a regression curve of ponded depth against time and finding the slope (Ermilio and Traver 2005).

The total volume of water can also be determined via the ponded depth. A contour map of the site should be drawn up during development of the basin. The contour map, in conjunction with the maximum ponded depth of a storm helps to determine the volume. If the maximum volume of the basin is reached, there will be overflow.

Overflow

A pressure transducer in conjunction with a weir can be used to determine the volume of water exiting the site. A pressure transducer records changes in pressure as a voltage which is transmitted back to a source that converts it to pressure head values. When a weir is present and the water depth is known, a calculation can be done using the ponded water on the other side of the weir. The pressure transducer can also be used alone to determine the depth of ponded water.

Volumetric Water Content

Moisture meters are used to determine volumetric water content. Located at various depths in the soil, moisture meters can help determine the capacity of soil pores to collect water and provide information on the infiltration rate as the moisture front moves through the soil. The volumetric water content at the start of a rain event has a large impact on the infiltration rate. The infiltration rate will be higher when the antecedent water content is lower; conversely, a high antecedent water content indicates that the soil pores are already filled with water and the infiltration rate will be lower.

Monitoring Quality

Runoff Samples

Runoff samples are collected through first-flush samplers or grab samples. First flush samplers are typically placed on the outskirts of the bioinfiltration basin where runoff from a paved area first comes in contact with the basin (Figure 2). A first flush sample and grab sample can be compared to see the effects of sheet flow over land.

First flush samplers are designed to collect the runoff created from the early part of a storm. Depending on the antecedent conditions, this portion of the runoff can have significantly higher contaminants than runoff generated during later parts of the storm (e.g. Deletic 1997; Soller 2005).

Grab samples from the ponded water in the middle of the basin are composed of rain that falls directly into the basin and runoff that has entered the basin. Grab samples are harder to obtain because they must be obtained by someone at the time of the rain event or shortly there after.

Subsurface Samples

Subsurface soil moisture samples are sometimes referred to as lysimeters. The cup is placed under suction before a storm to create negative air pressure inside, thus drawing the water in. Pressure is applied after a storm using a pressure-vacuum pump to draw the water out of the cup into a sampling bottle. Lysimeters can be placed at several locations beneath the basin to obtain information or water quality as it varies with depth.

Quality Tests

The pollutants found in stormwater are extremely site dependent. Great care needs to be used when designing a BMP to ensure that contaminants are not introduced to the groundwater system (Kwiatkowski, et al. 2007). If significant contaminants are present, pretreatment may be required. Contaminants often stick to sediment or fines suspended in runoff, therefore determination of Total Suspended Solids (TSS) and Total Dissolved Solids (TDS) is recommended (Kwiatkowski, et al 2007). In addition, pH, nutrients, and hydrocarbons may be of concern depending on the sources of runoff.

Ecological Monitoring

Plant Diversity

At the time of planting, a plant chart should be developed with permanent transects. Each transect should be reviewed periodically to see if the original species still remain, if any one species has become dominant, the relative frequency of each planting, and the interactions of the different species. Any additional plant migrations should be noted and invasive species should be monitored and removed.

Nutrient Uptake

After evaluating the species positions, sample roots and shoots should be collected for plant nutrient uptake analysis. Plant nutrient uptake evaluates the effectiveness of the plantings to absorb nutrients.

Faunal and Vertebrate Utilization

A site like a bioinfiltration basin can be a habitat to a several different species of plants, vertebrates and invertebrates. Because of their relatively small size, it is highly unlikely that there will be an overabundance of mammals. The focus is instead shifted to insects and birds. A sweep net sampling procedure can be used for identification of insects. Sweeps should be completed for each transects with identification and counts conducted for each species. A sweep should be completed twice a year with one during pollination season and one just before seasonal death. A correlation can possibly be drawn up between the insects and pollination of various plant species per transect. At this time, bird counts through inspection can also be completed.

MONITORING LEVEL

Depending on budget and staffing restrictions, monitoring effort for a bioinfiltration BMP can either be low, medium, or high. A monitoring plan for each level is presented as Table 1.

Table 1. Monitoring Level and Required Equipment

	Low	Medium	High
Hydrologic			
Staff gage	✓	✓ or	
Ultrasonic level		✓	✓
V-notch weir with a pressure transducer		✓	✓
Rain gage			✓
Moisture meters			✓
Water Quality			
Surface water samples (first flush or grab)		✓[a]	✓[b]
Subsurface water samples			✓[b]
Ecologic			
Plant identification and monitoring			✓
Plant uptake monitoring			✓
Animal and insect monitoring			✓

[a]testing performed off site, [b]testing performed on site

EXAMPLE OF BIOINFILTRATION TRAFFIC ISLAND

The Bioinfiltration Traffic Island was constructed in August 2001 as part of the BMP Demonstration Park on Villanova University's campus. The BMP was a retrofit of an existing traffic island and was designed to capture the first inch of runoff from 1.21 acres of land with 50 % impervious cover (Figure 3). The island is part of an ongoing research project being conducted by the Villanova Urban Stormwater Partnership (VUSP). Our current monitoring effort would be considered highly monitored, however, it does lack an ecological component.

Hydrologic Monitoring

The equipment used to monitor the site hydrologically is a tipping bucket rain gage, an ultrasonic level sensor, a v-notch weir in conjunction with a pressure transducer, and moisture meters. The v-notch weir is used to better control the volume entering through the south inlet and measures the maximum water depth inside the pond which can be compared to the ponded depth read on the staff gage. The ultrasonic level is located inside the basin and is used to measure the height of the ponded water. Moisture meters were placed at various depths below the surface which measured passing moisture fronts through the use of volumetric water content.

The data from this instrumentation is collected in five minute increments and stored on a data logger housed in an equipment box located on the north side of the traffic island. The data collected includes precipitation, peak intensity and antecedent dry time. These measurements are then downloaded weekly to an excel spreadsheet that helps to calculate overflow, volume, infiltration rate, and performance.

Monitoring Quality

Water quality samples are collected when rainfall exceeds 0.25 inches. Samples of surface runoff and sub-surface pore water are obtained. Surface runoff samples are obtained from two first flush samplers and grab samples (Figure 3). The first flush samples are located at the north and east side near curb cuts. The samplers collect the first 2 liters of water before flowing though a rip rap channel into the detention basin. Typically, two grab samples are taken from the detained water in the basin: one is collected during the storm and one is collected after. Subsurface samples are collected at 0, 4, and 8 feet beneath the basin (Figure 4).

The water quality samples are then transferred to Villanova University's Water Resources Lab where the VUSP team tests for physical properties, nutrients, metals, and chlorides. All tests are completed with in 24-hours of the rainfall event with the exception of the metals. Metals are preserved and tested at a later date because of the limited number of samples. 2 or 3 storms are typically collected before running standards to create calibration curves and determine sample results.

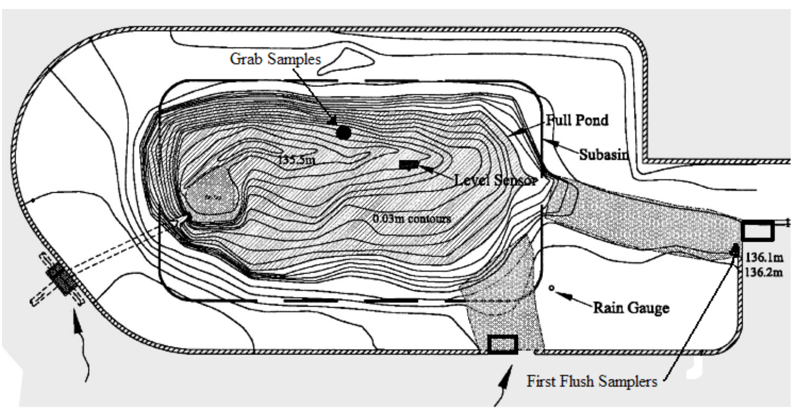

Figure 3: Surface Sample Location (from Heasom, et al. 2006)

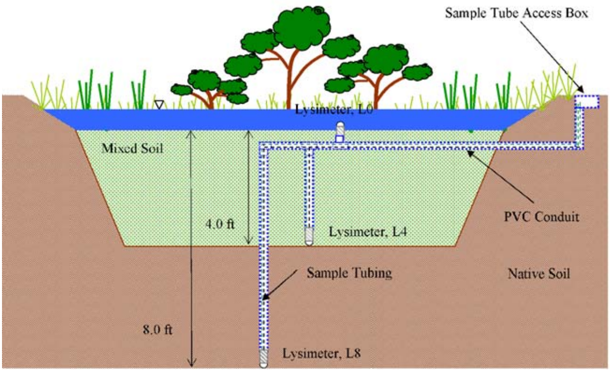

Figure 4: Sub-surface Sample Location (from Ermilio and Traver 2005)

Ecological Monitoring

Although the bioinfiltration traffic island is heavily monitored, the one field of research lacking is ecological monitoring. The original plantings at the site include grasses, herbs and woody plants native to the New Jersey coast. These plants were selected because of their ability to tolerate high chlorides and cycles of inundation and dry periods. No further research has been completed on the plant life at this time, but future investigations are being considered.

CONCLUSION

This paper presented an Integrated Monitoring Plan to monitor the effectiveness of an infiltration BMP. Three levels of monitoring effort were presented depending on personnel and budget constraints.

Each level of monitoring may contain hydrologic, quality, or ecological monitoring. Hydrologic monitoring uses rain gages, ultrasonic transducers, pressure transducers with weirs, and moisture meters to determine properties. Water quality monitoring uses surface samples such as first flush and grab samples and sub-surface samples collected from lysimeters. Quality samples are then tested in a laboratory for TSS, TDS, pH, nutrients, hydrocarbons, metals or any other chemicals of concern. Ecological monitoring focuses on vegetation and wildlife.

A high level of monitoring would include all three aspects (hydrologic, water quality, and ecological) and would most likely be found on a university's campus or at a research facility. At this level, all equipment mentioned should be incorporated in studies and all parameters should be monitored. A bioinfiltration basin found on Villanova University's campus was provided as an example of a heavily monitored site with the absence of ecological studying. A moderate level of monitoring would be expected at industrial and commercial sites. These sites would monitor the site hydrologically; in addition, some water quality tests would be performed. The lowest level of monitoring would be completed in rural, urban and suburban communities or highways. At this level of effort, the infiltration would be the sole parameter monitored.

REFERENCES

Deletic, A. (1998). “The first flush load of urban surface runoff.” *Water Resource Technology*, Vol. 32 (8): 2462-2470.

Ermilio, J. and Traver, R. (2005) “Bioinfiltration traffic island BMP.” *Proceedings of the 2005 Watershed Management Conference*, ASCE/EWRI, July 19-22, Williamsburg, VA.

Heasom, W., Traver, R. and Welker, A. (2006). “Hydrologic monitoring of a bioinfiltration traffic island.” *Journal of American Water Resources Association,* Vol. 42(5): 1329-1347.

Kwiatowski, M., Welker, A., Traver, R., Vanacore, M., and Ladd, T. (2007). “Evaluation of an infiltration BMP utilizing pervious concrete.” *Journal of American Water Resources Association*, in press.

Pennsylvania Department of Environmental Protection (PADEP) (2007). *Pennsylvania Stormwater Best Management Practices Manual*. Available online at <http://www.dep.state.pa.us/dep/deputate/watermgt/wc/Subjects/StormwaterManagement/announcements/default.htm>

Schueler, T. (1997). “Impact of suspended and deposited sediment: risks to the aquatic environment rank high.” *Watershed Protection Techniques*, Vol. 2(3), 443-444.

Soller, J., Stephenson, J., Olivieri, K., Downing, J., and Olivieri, A.W. (2005). “Evaluation of seasonal scale first flush pollutant loading and implications for urban runoff management”, *Journal of Environmental Management*; Vol. 76 (4): 309-318.

Traver, R.G. and Chadderton, R.A. (1983). “The downstream effects of stormwater detention basins”, *Proceedings of the 1983 International Symposium on Urban Hydrology, Hydraulics, and Sediment Control*, Lexington, KY, 455-460.

United States Environmental Protection Agency (US EPA) (2005) EPA Stormwater Program, http://cfpub.epa.gov/npdes/home.cfm?program_id=6, last accessed 27 July 2007.

Wang, L., Lyons, J., Kanehl, P. and Bannerman, R. (2001). “Impacts of urbanization on stream habitat and fish across multiple spatial scales”, *Journal of Environmental Management*, Vol. 28(2), 255-266.

Design of an Instrumented Model Green Roof Experiment

Gregory O'Keeffe[1], Kathryn Schulte[2], Patricia Culligan[3], Franco Montalto[4] & Wade McGillis[5]

[1]Graduate Student, Earth & Environmental Engineering, Columbia University, New York, NY
[2]Graduate Student & Student Member ASCE, Civil Engineering, Columbia University, New York, NY
[3]Professor, & Member ASCE, Civil Engineering, Columbia University, New York, NY
[4]Post-Doctoral Fellow, Earth Institute, Columbia University, New York, NY
[5] Doherty Research Scientist, Lamont Doherty Earth Observatory & Professor, Earth & Environmental Engineering, Columbia University, New York, NY

ABSTRACT: This paper describes the design, instrumentation, and data collection techniques developed for a research program to study model green roof performance as a pre-cursor to the design of a full-scale instrumented green roof. A model rubber roof and an instrumented non-vegetated model green roof were constructed and placed on the roof of the Pupin Building at Columbia University, New York City. Meteorological data and data pertaining to the storm water detention performance of the roofs were collected. Examples of these data, along with data describing the temperature and volumetric water content profile through the model green roof, are reported.

INTRODUCTION

Green roofs are roofs that have been modified to support plant growth. They typically consist of a waterproof membrane placed over the standard roof, on top of which are a drainage layer and several centimeters of lightweight (800-900 kg/m^3 [1600-1825 lb/yd^3]) growing medium in which diverse types of vegetation can be planted [Lazzarin et al. 2005). There are two main types of green roofs: extensive and intensive. Extensive green roofs are generally 10-16 cm (4″-6″) thick and planted with drought-resistant plants such as sedums. They are more common than intensive green roofs, which are deeper than 16 cm (6″) and can support more diverse plant life, including trees (which can be up to 10 m high if properly anchored), shrubs, and even some crops [Rosenzweig et al. 2005]. Extensive green roofs are more common than intensive green roofs due to their weight advantage; notably extensive roofs only have a maximum density of about 122 kg/m^2 (25 lbs/ft^2) when saturated with water [Rosenzweig et al. 2005]. Because intensive green roofs can only be used when the weight capacity of the roof structure is not exceeded, buildings must usually be designed to support an intensive green roof. Conversely, an extensive green roof can be applied to many existing buildings with few structural modifications. Extensive green roofs also require little maintenance, while intensive roofs require tending-to, and irrigation during periods of low rainfall [Lazzarin et al. 2005].

Green roofs are believed to provide numerous benefits, including mitigation of the urban heat island effect, improved building insulation and energy efficiency, increased biodiversity and aesthetic appeal, and storm water detention capacity. For cities with combined sewer systems, storm water detention by green roofs can lead to fewer combined sewer overflow events [VanWoert et al. 2005].

Although an estimated 15% of new flat roofs in Germany are green, the use of green roofs in the U.S. is quite recent. Hence, an understanding of green roof performance in cities like New York has yet to be developed. Even though several green roofs have been installed In New York City, the authors are not aware of any such roof that has been fully instrumented. This might be due to the fact that instrumentation for a full-scale green roof is expensive (upwards of $20,000.00 per instrument station), labor intensive, and time-consuming. For this reason, the construction and instrumentation of scaled-down model roofs are an appealing way to (a) identify suitable instruments and calibration protocol for green roof monitoring and (b) obtain initial data to indicate how a full-scale green roof might perform.

The work here involved the design and instrumentation of a model green roof and a model rubber roof, toward a goal of generating results that could be used to design an instrumentation system and data collection protocol for a full-scale, green roof.

MODEL ROOF AND INSTRUMENTATION

Two model roofs, with the same length to width ratio of a typical New York City brownstone roof, were constructed and instrumented. One roof is a model of a standard black rubber roof (Figure 1a); the other is a model extensive green roof without vegetation (Figure 1b). The decision to obtain data on the performance of a non-vegetated green roof, before gathering information on a vegetated system, was made because prior research had indicated that the performance of vegetated and non-vegetated green roofs were nearly identically with respect to storm water detention [VanWoert et al. 2005]. Hence, there was a desire to investigate whether this observation held true for New York City conditions.

(a) (b)

FIG. 1. (a) Model rubber roof ; (b) Non-vegetated model green roof .

A HOBO® Weather Station was mounted between the two roof boxes. Several sensors, all manufactured by Onset Computer Corporation and described below, were mounted on the meteorological mast of the HOBO® Weather Station and placed in and around the green roof box. A more detailed description of the experimental setup follows.

Location of Equipment Instrumentation

The experimental setup is located on an approximately 2 m × 4 m (6′ × 12′) section of roof on the northwest corner of the Pupin building at West 120th street on Columbia University's Morningside Campus in New York City. Data was collected beginning on October 24, 2006.

The black rubber roof box, referred to as the "control" box because it models the behavior of a non-green roof, is lined with standard black roofing rubber and located to the west of the green roof box. A meteorological mast located between the boxes records ambient weather conditions. The sensors mounted on the mast are: (a) An anemometer recording wind speed, gust speed, and wind direction; (b) a Photosynthetically Active Radiation (PAR) sensor measuring solar radiation; (c) a tipping bucket rain gauge, and (d) a temperature/ Relative Humidity sensor

Under the control box there is a second tipping bucket rain gauge recording runoff (i.e. outflow from the box) during rain events. A third tipping bucket rain gauge is mounted under the green roof box to record runoff from the model green roof. The decision to use of tipping buckets for measuring roof run-off was based on cost and compatibility with the HOBO® Weather Station data logging system. Other investigated alternatives, such as flow meters, were not only more expensive, their output signals were incompatible with the HOBO® setup.

Two "temperature smart sensors" and two Echo volumetric water content sensors (termed "soil moisture smart sensors") were placed within the green roof's substrate. Data collected from these provide profiles of temperature and water content gradients through the growing medium. Figure 2 is a schematic cross-section through the non-vegetated model green roof box. The measurement interval for all instruments, including the tipping buckets, was set at one-minute.

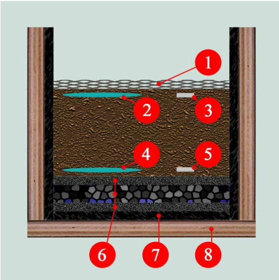

FIG. 2. Schematic cross-section through non-vegetated model green roof: (1) Mesh to prevent wind-blown loss of substrate, (2) volumetric water content sensor (surface), (3) soil temperature sensor (surface), (4) volumetric water content sensor (base), (5) soil temperature sensor (base), (6) geotextile drainage liner, (7) rubber roof membrane, (8) plywood box.

Model Roof Boxes

Each box was constructed from 1.9 cm (¾″) thick pressure-treated plywood with rubber roofing material glued directly to the wood. The interior dimensions of the boxes are 122 cm × 61 cm (48″ × 24″). The control box has sides that are 10.2 cm (4″) in height, while the green roof box has sides that are 19 cm (7½″) tall, so that it extends 10.2 cm (4″) above the surface of the green roof growing medium, which has a depth of 8.9 cm (3½″).

There is a 5.1 cm (2″) interior diameter PVC drain, flush with the rubber roof surface, located in the corner of each box. The drains drop to 5.1 cm (2″) below the underside of the boxes. Each box slopes approximately 1% in the direction of the drain, which is the lowest point in each box.

The performance of the model roofs is believed to be a good analogue for the performance of a full-scale roof provided that, for both model and full-scale roofs, flow through the green roof growing medium is predominately vertical, while flow through the underlying drainage layer is predominately horizontal and unrestricted. For a full-scale roof the latter criterion will depend on the roof design. Hence, it is difficult to generalize how well model roof data will indicate full system behavior.

Flow Divider

Due to the tipping bucket rain gauge capacity limitations (the gauge capacity is exceeded by flows greater than about 2.3 L/hr [78 oz/hr]), it was necessary to incorporate custom-built flow dividers in the roof drains to reduce the flow to the tipping buckets used to measure outflow from the control and green roof boxes. The flow divider was designed to divert a constant fraction of the outflow from a box away from the tipping bucket, and the remainder into it. The flow divider attaches directly to the outlet of the drain (Figure 3a). The runoff then passes through a runoff distribution medium to split the outflow evenly among the ten outlets, one of which flows into to the tipping bucket (Figure 3b). The flow dividers each divert about 10% of the flow into the rain gauge and 90% away from it. In the first version of the flow divider a sponge was used as the runoff distribution medium. However, it was found that the sponge clogged on a weekly basis. Hence, it was replaced by coarse aquarium gravel in February 2007.

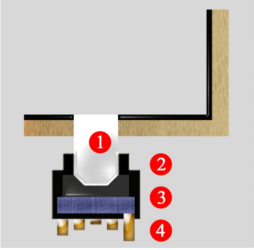

(a) (b)

FIG. 3. (a) Flow divider cross-section: (1) PVC drain, (2) PVC flow divider, (3) runoff distribution medium, (4) brass outflow drains (receding from view); (b) Runoff flow divider on the Pupin building: (5) PVC drain, (6) PVC flow divider, (7) one outflow tube is directed into roof runoff gauge (gauge not pictured).

Calibrations of Experimental Measurement Devices

Calibrations for the surface and base *temperature sensors* in the green roof substrate were conducted in the following manner: A hot water bath was brought to the experiment site and set to cool for several minutes. The model green roof temperature sensors were then placed in the water bath alongside a factory-calibrated temperature sensor ("standard"). The sensors were left overnight while the water bath equilibrated with the ambient air temperature. The data for the surface and base temperature sensors were then plotted against the standard to obtain the necessary calibration curves.

Calibration to verify the accuracy of the *tipping bucket rain gauges* used in the research was as follows: A known volume of tap water was introduced into each tipping bucket over a two-minute interval, and compared to the volume recorded by the system. The procedure was repeated three times for each bucket, and the values were averaged. The results are presented in Table 1. Note: the slight discrepancy between the introduced and recorded volumes is due to losses inherent to the tipping bucket rain gauge design (i.e. water sticking to surfaces). Such losses (<10 ml [0.34 oz]) are negligible when considering the much larger flows generated during rain events.

Table 1. Tipping Bucket Calibration Data

Tipping Bucket Measurement:	Injected (ml)	Average Reading (ml)	Accuracy
Atmospheric Precipitation	100	94.85	94.85%
Model Rubber Roof Runoff	100	93.03	93.03%
Model Green Roof Runoff	100	96.68	96.68%

The calibrations for the substrate surface and base *volumetric water content sensors*, were conducted as follows: Three samples of the green roof growing medium were prepared with known volumetric water contents (6%, 16%, and 30%, respectively). The samples, each of which had the same mass, were packed into containers of identical volume, and the sensors were then individually placed into the containerized sample for a 10-minute interval. Readings for each sample were obtained in triplicate and then averaged to obtain one reading for each volumetric water content. This reading was plotted against the calibrations provided by the manufacturer to obtain a calibration curve. In this case, it was determined that the manufacturer's calibration curves were only accurate to within +/- 25%.

The calibrations for the runoff *flow dividers* mounted under the model green roof and model rubber roof were conducted as follows: Both flow dividers were left attached to the model roof drains. Tap water was then injected into the roof drain using a syringe at a constant rate for a period of three minutes. The rates of water injection were 60, 120, 240, and 360 mL/min (2, 4, 8.1, 12.2 oz/min), respectively. Three runs for each input flow rate were performed for each flow divider. The outflow rates recorded by the tipping bucket for each input flow rate were averaged, and the fraction of the total inflow going into the tipping bucket was calculated. Calibration results are presented in Table 2. Discrepancies in the percent of total inflow are likely due to the angle and rate of injection, which might have favored some drain outlets over others. Note: The calibrations presented in Table 2 are for the flow dividers that were redesigned in February 2007; the fraction of outflow from events occurring before this time is approximated at 10%.

Discussion of Calibrations The calibrations described above were modified during the analysis of the several rain events for which data were recorded. First, after the recorded temperature data was adjusted according to the calibration equations, it was determined that the raw data better represented the model green roof reaction to atmospheric temperature change and solar radiation than did the modified data. This was attributed to the placement of the sensors in the hot water bath, which was believed, in hindsight, to have generated erroneous readings. Hence, the raw sensor data were used.

The tipping bucket accuracy was determined to be within an acceptable range, and thus no adjustments were made to the data logged by the tipping buckets. The original volumetric water content sensor placed at the base of the model green roof substrate failed prior to the calibration tests described above, which involved a replacement sensor. As a result, the calibration curve for the original sensor had to be approximated based on the curve generated for the replacement sensor, an estimated maximum data point from the un-calibrated sensor (obtained when the green roof medium was saturated) and a minimum data point (obtained when the green roof medium was at field capacity). The data points were selected from the raw data logged by the sensor while it was still functioning. Finally, as noted, the calibrations presented in Table 2 are for modified versions of the flow dividers that were in operation after February 2007. For results obtained prior to this date it was assumed that the fraction of runoff diverted to the tipping-buckets was 10%.

Table 2. Flow Divider Calibration Data

Model Green Roof Flow Divider			
Trial #	Total Inflow (mL)	Average Outflow (mL)	Percent of Total Inflow
1	180	26.75	14.86%
2	360	46.21	12.84%
3	720	97.29	13.51%
4	1180	144.71	12.26%
Model Rubber Roof Flow Divider			
Trial #	Total Inflow (mL)	Average Outflow (mL)	Percent of Total Inflow
1	180	27.97	15.54%
2	360	53.51	14.86%
3	720	107.01	14.86%
4	1180	160.52	13.60%

EXAMPLE MEASUREMENTS

The data presented in this section are from a seventeen-hour rain event from December 22nd to 23rd, 2006. During the event, the tipping bucket rain gauge mounted between the two model roofs recorded a total precipitation of 29.8mm (1.17″), while the tipping bucket mounted under the model rubber roof recorded 29.2mm (1.15″) of outflow and that under the green roof only 19.94mm (0.78″) of outflow, Figure 4a. Hence, there was a 31.6% runoff reduction from the green roof compared to the rubber roof. Furthermore, the model green roof delayed the onset of runoff by approximately 4½ hours. There were three instances of particularly heavy rainfall during the event and the recorded runoff from the model roofs fluctuated accordingly. The model green roof peak runoff rates were approximately 3 to 4mL/ minute (0.1 to 0.14 fl.oz./ minute), or 6% to 16% lower than the model rubber roof peak runoff rates.

Temperature and volumetric water content data within the model green roof substrate were also recorded. At night, when conduction is the primary mode of energy transfer, the substrate's surface temperature lags behind the air temperature, Figure 4b. However, when the sun rises the dark substrate absorbs radiation and warms more rapidly than the air. During daylight hours, the base temperature sensor, which is insulated by the substrate, records lower temperatures that the surface sensor.

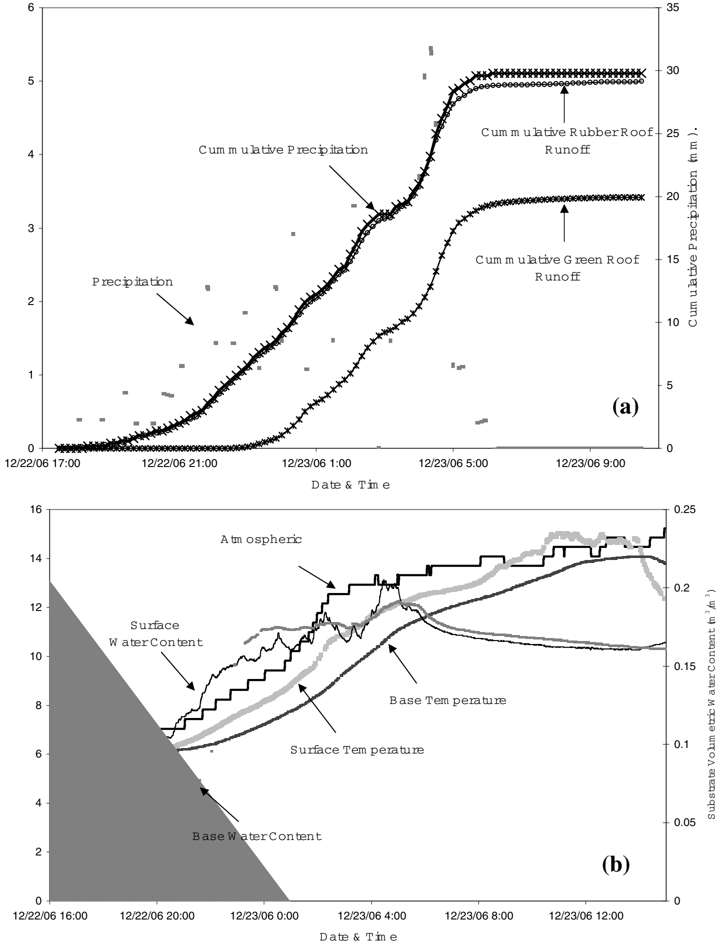

FIG- 4. Data from a seventeen-hour rain event, December 22nd to 23rd, 2006: (a) Precipitation and cumulative runoff/ precipitation; (b) Temperatures and volumetric water contents within the green roof substrate.

Volumetric water content data for the rain event (Figure 4b) indicated that the surface sensor reacts more acutely to changes in rainfall intensity. Also, the sensor located at the substrate base initially lagged the surface sensor because of the time it took for precipitation to percolate through the substrate. However, as water accumulates at the base of the substrate, the volumetric water content at the base surpasses that at the surface. This remains the case well after the event ends.

4. CONCLUSIONS & FUTURE WORK

A model green roof and a model rubber roof, termed the control roof, were constructed and placed on the roof of the Pupin Building at Columbia University in New York City. Meteorological data and data pertaining to the performance of the roofs were collected at 1-minute intervals. Since many green roof experiments are not designed to monitor performance at such short intervals (e.g., VanWoert et al. 2005 logged at 5-minute intervals, while Lazzarin et al. 2005 logged at 15-minute intervals) the design presented here is considered an advance that has potential to lead to a better understanding of green roof performance under a range of meteorological conditions.

As a result of experience gathered to date, the following recommendations can be provided to assist in the design of similar studies. First, factory provided calibrations for temperature smart sensors and the tipping buckets appear adequate. However, calibration of the Echo soil moisture smart sensors is strongly recommended. Although the use of the tipping buckets for monitoring outflow from the model roofs is considered justifiable based on economic considerations and compatibility with the HOBO® data logging system, some redesign of this part of the set-up is needed. Currently, the authors are investigating a system that subdivides each model roof into two watersheds, one 90% of the model roof area and the other 10%. Water from the 10% catchment area is directed to the tipping bucket while the rest drains to atmosphere. To date, this system has proven to be reliable.

Data collected from the non-vegetated green roof (e.g., Figure 4b) have demonstrated that a non-vegetated green roof can reduce storm water runoff, and hence contribute to storm water management practice. Model green roof experiments starting in Spring 2008 will collect data on a vegetated model green roof for comparison. The instrument system described in the paper is currently being proposed as an instrument system for a full-scale green roof that will be constructed, in the near future, on a Columbia University building. Future comparison of data gathered from the full-scale roof and that from the model green roof, will provide information on whether the performance of model roofs are useful indicators for the performance of full scale systems.

REFERENCES

Lazzarin, R.M.; Castellotti, F.; Busato, F. (2005). "Experimental measurements and numerical modeling of a green roof." *Energy and Buildings*, 37 (12): 1260-1267

Rosenzweig, C., Gaffin, S., Stanton, C. (2005). "Green Roofs: Recreating Natural Processes in Cities." *The Tidal Exchange*, Summer 2005: 1-5

VanWoert, N.D., Rowe, D.B., Andresen, J.A., Rugh, C.L., Fernandez, R.T., Xiao, L. (2005). "Green roof stormwater retention: Effects of roof surface, slope, and media depth." *Journal of Environmental Quality*, 34 (3): 1036-1044

Gravity Drainage of Large Stormwater Volumes into Epikarstic Bedrock

Jim L. Lolcama[1], P.G. and Philip E. Gauffreau[2], M.ASCE, P.E.

[1]Principal and Hydrogeologist, KCF Groundwater Inc., 4916 Woodbox Lane, Mechanicsburg, PA 17055; PH (717) 691-8025 FAX (717) 691-8028; jll@kcfgroundwater.com
[2]Principal Engineer, NTH Consultants, Ltd., 2770 Emrick Boulevard, Bethlehem, PA 18020; PH (484) 893-1450 FAX (484) 893-1449; pgauffreau@nthconsultants.com

ABSTRACT: For projects located in karst terrain, compliance with recent NPDES regulations by utilizing conventional infiltration BMPs to manage the volume of runoff from large storms can bring considerable risk of ground failure from sinkhole collapse and subsidence. Through a collaboration of hydrogeologists and geotechnical engineers, an approach to disposing of stormwater in karstified bedrock has been developed with the potential to accept a volume of water greater than that of a 2-year storm event. After pre-treatment to remove contaminants, the stormwater will enter the deeper epikarstic flow conduits through a series of vertical gravity drains. The drains isolate the stormwater from the soil mantle, which reduces the risk of sinkhole formation.

Upon entering the epikarst, the stormwater will flow laterally through open channels until the driving head dissipates. Long-term monitoring of the hydrogeologic response of the epikarstic zone must be performed to verify that the karstic permeability is not being reduced; to confirm that the water table elevation is appropriate for risk management; and to calibrate the hydrogeologic response to storm magnitude. Regulatory requirements consist of a detailed description of the approach and site evaluation in the NPDES permit application, and registration with USEPA for gravity drains as Class V injection wells.

INTRODUCTION

The management of stormwater runoff volumes from large commercial developments to comply with the most recent National Pollutant Discharge Elimination System (NPDES) regulations has become a critical element of the design and permitting of such projects in many parts of the United States. Waivers to permit off-site discharge of the stormwater are becoming less commonplace under any circumstances. Of particular concern are projects with high impervious ground cover on sites located in karst terrain (where the soil overlies limestone and dolomite bedrock, which is prone to sinkhole formation and subsidence). Approximately 25 percent of the United States is underlain by bedrock with the potential for developing sinkholes. Sinkholes form by a process of surface water flowing through a permeable fissure in the soil layer or along the soil-bedrock interface and into an epikarstic opening. The draining water can scour out a soil cavity, and the cavity enlarges, weakening the support to the overlying ground, which can collapse into the soil cavity.

Attempts to dispose of the runoff volume generated by the design 2-year and greater storm events using soil infiltration techniques in karst terrain have an inherent risk of ground subsidence and collapse. These risks are particularly large where heavy structures, roads, traffic, and other infrastructure are concerned. This is not to say that Best Management Practices (BMPs) for infiltrating some stormwater into soil in karst areas at slow rates and under controlled conditions are inappropriate. These techniques are well-described in a number of publications, two of which are: Pennsylvania Stormwater Best Management Practices Manual, (PADEP, 2006); and McCann and Smoot (1999). Even though infiltration BMPs attempt to reduce the probability of sinkhole formation, they do not eliminate it entirely.

This paper describes the concept, site evaluation techniques, and permitting issues for a large-scale stormwater management system for properties underlain by karst with substantial post-construction runoff volumes that must be managed on-site. This technique employs both hydrogeologic and geotechnical engineering evaluations of the subsurface conditions, including the extreme permeability characteristics of epikarstic bedrock, to safely dispose of large volumes of stormwater without significantly increasing the risk for sinkhole formation. Regulatory criteria for groundwater quality will be met through a comprehensive pre-treatment program, combined with a long-term monitoring program during the post-construction period.

BACKGROUND

Epikarst formations are created in the top of carbonate bedrock over geologic time of 100,000 years or more, by downward percolation of slightly acidic (corrosive) groundwater (see Figure 1). The groundwater finds vertical pathways, including inter-connected fractures and joints, and slowly dissolves the bedrock to form “cutters,” which are usually filled with residual or transported sediment. The rate of dissolution of the carbonate rock declines with depth as the groundwater reaches carbonate mineral saturation (Palmer, 2004). Rock pinnacles are found between the cutters. Any number of cutters can initially form on a carbonate surface, but over time only a few of them will develop into very deeply penetrating solution conduits. Palmer explains this phenomenon by preferential enlargement of the more permeable channels in the bedrock by the concentration of recharge into these channels.

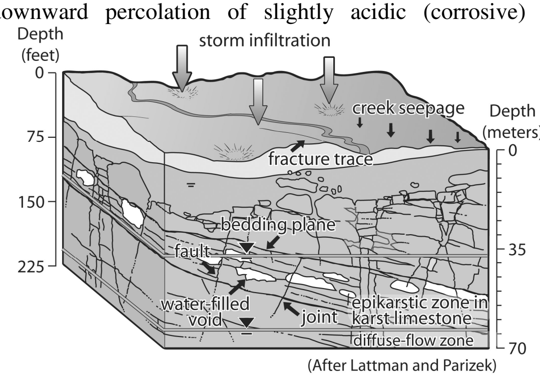

Fig. 1. Cross-section showing typical epikarst layer.

The permeability of karst limestone and dolomite is very large; Freeze and Cherry (1979) assign a hydraulic conductivity of up to 10 centimeters per second, or in excess of 28,000 feet per day. Groundwater can flow rapidly through the conduits due to secondary porosity. Our experience at 20 sites in the Mid-Atlantic area has located flow in excess of 10 meters per minute in epikarst layers that have penetrated to depths of up to 20 meters into the carbonate bedrock.

NPDES permit regulations now require that the difference between the post-construction stormwater runoff volume and pre-development runoff volume for the 2-year frequency storm event be managed on-site, emphasizing the use of BMPs to the extent possible. However, in karst terrain, the conventional pre-development runoff volume must typically be reduced for the "karst loss" such as runoff draining into sinkholes and other solutioned openings in the bedrock. Guidance for estimating these reduction factors (which are often 50 percent or more), including PSU-IV (Aron and Kibler, 1981), is available. On large sites, this additional differential often results in significant volumes of stormwater runoff to be managed on-site. Furthermore, the fine-grained residual soils that typically weather from limestone or dolomite bedrock often have relatively low infiltration rates. As a result, normal infiltration BMPs would have to be impractically large to store the runoff volume while it percolates. Added to these problems is the concern for sinkhole formation where water is permitted to infiltrate in concentrated areas. Geotechnical engineers and municipal officials discourage this practice near proposed buildings or other critical site features without some form of protection. The combination of these factors creates a dilemma that is difficult to resolve by conventional means.

However, by employing vertical drains that transmit the stormwater directly into epikarstic bedrock, potentially large volumes of stormwater can be managed successfully on-site, and the amount of potential off-site discharge can be greatly reduced. In addition, by sealing the water from the soil overburden, and by ensuring that the groundwater levels within the epikarst do not rise to the extent that they begin to erode the overlying soil mantle, the risk for sinkhole formation is greatly reduced. Water quality treatment of the stormwater, using a host of available engineering and/or BMP surface technologies (bio-filtration swales, forebays, hydrodynamic separators, etc.) also greatly reduces the risk of impairment of groundwater quality.

GENERAL DISCUSSION OF THE GRAVITY DRAIN APPROACH

The gravity drain stormwater management system consists of a distributed array of vertical, steel-cased shafts completed at locations where regional-scale karstic permeability has been located and tested in the bedrock beneath the site. The regionally permeable features are a laterally expansive network of natural, interconnected solution channels or flow conduits that can rapidly accept and dissipate large storm volumes with little impact on the water table. Flowing groundwater moving through fractures, joints, and bedding planes have formed these conduits over geologic time periods. Stormwater is conveyed through the soil overburden to the epikarst in water-tight steel casing grouted in place, effectively isolating the flow from soil thus eliminating soil scouring and piping into the bedrock. The wells are driven into the epikarst up to 30 meters below ground, depending on local site conditions. Pre-treatment systems remove sediment and other pollutants and improve the overall water quality before the stormwater enters the drains. The system is designed so that the entire 2-year storm volume can be drained away to the epikarst regardless of the off-site flow during the pre-development period. Such systems should be able to exceed the regulations of most state or local agencies responsible for stormwater regulation.

This technique assumes that stormwater infiltration into the overburden in karst terrain is all but eliminated by the impervious ground cover of the site development. The stormwater recharge directly to the epikarst will temporarily increase flow velocity through the conduit network. Where present, soft sediment-fill material can be scoured from the flow pathways, enhancing the permeability of the epikarst. However, the isolation of the soil mantle from the stormwater recharge by the impervious ground cover means that vertical piping of stormwater through the mantle will be managed, thus reducing the risk of sinkholes on site.

PRELIMINARY ASSESSMENT OF SITE SUITABILITY

The objective of the preliminary assessment of a site is to determine if regional-scale epikarst of large permeability exists within the bedrock, and therefore if a site warrants further investigation. A review should be completed of the geology, hydrogeology, and geotechnical literature on the site, and mapping and hydrogeologic testing should be completed, as described below. Consideration should be given to the intended use of the site. Where industrial uses are intended, with risk of chemical spills, appropriate pre-treatment measures for the stormwater runoff will be required.

The sinkholes and bedrock exposures should be mapped. Sinkholes that are widely distributed across a property can be indicative of a widely distributed fabric of flow conduits within the shallow bedrock, thus regional permeability. Evidence of well-developed solution conduits, such as along bedding planes, fractures, and joints, indicates the presence of epikarstic permeability beneath a site. The bedrock openings to the epikarst beneath some of the larger sinkholes should be uncovered and plumbed. A water-injection test of the bedrock openings should be completed, and the sustained rate of recharge determined.

Care should be taken when mapping a site and vicinity to locate all evidences of artesian spring flow and to determine the water source both prior to and during recharge testing. Chemical fingerprinting techniques (Lolcama, 2003) can identify the source of the discharge. Artesian discharge from the epikarst during and after stormwater injection can lead to problematic flooding and soil erosion problems, if the rate of discharge is large. Artesian discharge that has its source in some other aquifer may not be affected by the local stormwater recharge.

EVALUATION OF REGIONAL KARSTIC PERMEABILITY

Once the preliminary assessment has demonstrated that a site may have sufficient potential for large permeability without problematic artesian discharge, an evaluation of the regional-scale permeability is warranted. This will include a targeted investigation of those areas where gravity drain discharge is to be directed. Large-scale karst flow conduit features can be detected using geophysical equipment for measuring self-potential anomalies, as described by Corwin (1990). The Self- or Spontaneous Potential (SP) technique detects at the ground surface the differences in natural potentials between two points. Several sources of potential exist in the ground, and the dominant source is that resulting from flowing groundwater, under most geologic settings. The SP anomalies should be added to the conceptual model to confirm the locations of conduits.

Next, drilling of the SP anomalies, geologic faults, and deeply penetrating joints should be performed to obtain evidence of rapid, karstic flow. During such a study, watertight casing is installed through the overburden and into the upper meter of epikarst, and a bentonite clay seal is installed at the base of the casing. The open borehole is then advanced through the epikarst layer, and evidence of large-scale karstic permeability is logged during drilling (air, soil, and water-filled voids). High-pressure air connection between boreholes is also a useful indicator of the presence of an epikarstic flow conduit.

After each successful borehole is allowed to equilibrate with the groundwater table, it is then tested for karstic permeability by injection of a large slug of potable water (typically several thousand liters) over several minutes. If large karstic permeability is present, the water level in the borehole will decline to the ambient level almost instantaneously. Successful tests will define the locations of the site exhibiting the necessary permeability.

Several questions remain, specifically, could the stormwater recharge method potentially flood the epikarst and therefore contribute to sinkhole formation, and where does all of the stormwater flow? To answer these questions, the system must be tested on a large scale. A temperature tracing technique (Davis et al., 1985) is used where we prepare a reservoir of hot or cold potable water, and release the water to the epikarst at a rate that simulates the intended stormwater recharge rate, such as several thousand liters per minute. Water quality sensors with dataloggers, placed in wells in a radial array nearby and about 100 meters from the injection location, detect the movement of the thermal slug of tracer, and measure the rise in the water table from the large slug of tracer. A small rise in the water table lasting only a short time demonstrates that flooding of the epikarst into the soil overburden is unlikely. The wells exhibiting the largest temperature response to the tracer slug are located within the primary epikarstic flow paths. The orientation of those pathways will be the directions of flow of the injected stormwater. The stormwater, if perched, will infiltrate downwards to mix with the permanent groundwater table, or will mix into the epikarstic groundwater flow. The proportional volume of the stormwater is typically very small compared to that of the groundwater naturally flowing through this system in any given day.

REGULATORY REQUIREMENTS

An NPDES Permit Application for stormwater discharges will be required to contain a detailed narrative describing the proposed gravity drainage to epikarst system. This narrative should typically include the results of both the preliminary suitability assessment and the evaluation of regional karstic permeability; the concepts for incorporating pre-treatment of the runoff using BMPs and other methods to control the quality of the water to be discharged into the drains; the proposed monitoring programs to evaluate the performance of the gravity drains and their impact on the groundwater (quality, fluctuations in elevations, etc.); and the intended evaluation, documentation, and sequence of installation during construction.

Gravity drainage to the epikarst using stormwater wells is regulated through the Underground Injection Control (UIC) program as Class V injection wells. In those States that are not primacy States, the drains are "authorized by rule" by the USEPA. Federal UIC requirements include: 1) submitting basic inventory information about gravity drainage to epikarst to the State or EPA; 2) constructing and operating the drains in a manner that does not endanger underground sources of drinking water; and 3) meeting any additional prohibitions or requirements specified by a primacy State or EPA region.

GEOTECHNICAL CONSIDERATIONS OF GROUND SUBSIDENCE

Figure 2 is an extreme example showing a schematic of building construction where the geostructural supports have been installed through a thick epikarstic zone, using a standard bond-zone technique (i.e. micro-piles). Groundwater scouring of the terra-rossa and other sediments from the interior of the karst created larger bulk permeability within the karst, lowering the water table. The karstified zone above the final resting elevation of the water table experienced a loss of buoyant support, placing additional stress on the rock structure. In addition, a large portion of the critical supporting mass – the terra rossa and other sediment – had been removed through the scouring action of turbulent flowing groundwater. The residual limestone rock fragments and thin layers or ledges of highly weathered/soft limestone was then compressed under the added stress, resulting in subsidence of the ground surface, as well as additional stress and loss of support for the building foundations by the densification and downdrag processes.

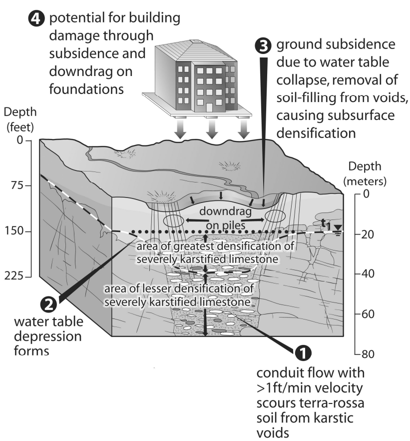

Fig. 2. Densification of severely karstified limestone, leading to ground subsidence.

Since such extreme cases of poor rock quality subject to such aggressive processes are not the norm, we believe that gravity drain discharge can be performed safely on most sites where sufficient karstic permeability is found. However, as part of the gravity drain installation procedure, pilot holes will be drilled through the overburden and the epikarst to evaluate these conditions.

THE HYDROGEOLOGIC METHOD FOR GRAVITY DRAIN DISCHARGE

Figure 3 shows the nature of epikarstic bedrock underlain by competent carbonate bedrock. Flow conduits are pervasive throughout the epikarst; some open and some partially plugged with terra rossa and rock debris. The epikarst layer has a very large water storage capacity and karstic permeability, and is underlain by predominantly diffuse-type permeability in the more competent bedrock. The permanent water table resides within the carbonate bedrock. A temporary, perched water table is found within the epikarst layer immediately following stormwater recharge. The temporary water table dissipates laterally and by infiltration to the permanent water table, as shown with vertical dashed lines.

The hydrogeologic method to epikarstic stormwater disposal requires vertical pipes, termed gravity drains, that penetrate through the epikarst layer but terminate above the competent bedrock. The drain piping is pressure-grouted into the soil overburden so as to seal off the annular space to prevent piping of water down the annulus. Figure 3 shows the drains opening to the upper epikarst, or the drains can be fitted with well screens that penetrate the epikarst. The drain diameter is determined by the runoff rate requirements, and the permeable nature of the flow conduit network in the epikarst. By enlarging the diameter of the drain, a greater number of conduits can be intersected, which provides more drainage capacity.

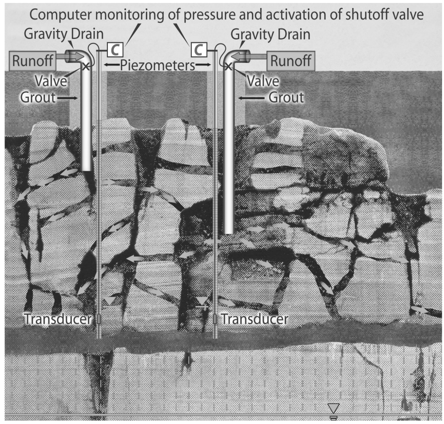

Fig. 3. Schematic of gravity drains and flow pathways in epikarst layer.

The water table in the epikarst at each of the drains is monitored continuously, because of the risk of sinkhole formation if the stormwater were to repeatedly flood the epikarst and erode the overlying soil overburden. Sensor technology enables automated monitoring with automatic notification if the level of the water table were to rise up to a threshold elevation which is below the soil-bedrock interface. Along with the notification, a signal would be sent to the automated valve, shutting it off to stop any further recharge.

SUMMARY AND PERSPECTIVE

A stormwater management approach is described that is beneficial for handling large water volumes and flow rates in karst terrain in compliance with NPDEP permit requirements. It employs hydrogeology and geotechnical engineering analyses of the regional permeability characteristics of epikarstic bedrock to dispose of treated stormwater in karst. Besides the obvious benefit of eliminating the majority of off-site discharge, the risk of sinkholes is reduced by maintaining and in some cases restoring the pre-development water table, by eliminating much of the overland drainage across a site, and by continuous monitoring and managing of the water table to prevent a flooding condition. The stormwater management system consists of a distributed array of stormwater gravity drains, grouted in place, and completed at locations where regional-scale karstic bedrock permeability has been located beneath the site. The system employs automated, continuous monitoring of the water table with the ability to control the recharge to individual drains to prevent flooding of the epikarst.

In most cases, a site-wide assessment of the carbonate bedrock will be needed to locate and characterize the karstic permeability. This will require input from the disciplines of geology, hydrogeology, water chemistry, geophysics, and geotechnical engineering. A contingency plan will be required for post-construction geotechnical needs, such as sinkhole occurrences and repairs. Groundwater quality monitoring may be required for a period of time to demonstrate that no degradation is occurring as the result of the treated stormwater recharge. Regulatory requirements generally consist of a detailed description of the approach and methods in the NPDES Permit Application, and following a registration process with the USEPA for the gravity drains as Class V injection wells.

Subsequent technical papers will address the installation and performance of a gravity drain system. Topics to be covered will include the development of construction specifications and details, the use of pilot holes to evaluate the suitability of selected locations for gravity drains, the equipment and materials used to construct the gravity drains, and performance data after the gravity drains have been placed in service.

REFERENCES

Aron, G. and Kibler, D.F. (1981). "Field Manual of Procedure PSU-IV for Estimating Design Flood Peaks on Ungaged Pennsylvania Watersheds." Department of Civil Engineering, Pennsylvania State University, University Park, PA.

Corwin, R.F. (1990). "The Self-Potential Method for Environmental and Engineering Application." *Geotechnical and Environmental Geophysics*, Vol. 1.

Davis, S.N., Campbell, D.J., Bentley, H.W., and Flynn, T.J. (1985). *Ground Water Tracers*, National Ground Water Association.

Freeze, R.A. and Cherry, J.A. (1979). *Groundwater,* Prentice-Hall, Inc., Englewood Cliffs, N.J., 604 pp.

Galloway, D., Jones, D.R., and Ingebritsen, S.E., eds, (1999). "Land Subsidence in the United States." Washington, D.C., *U.S.G.S. Circular 1182*, 177 pp.

Lattman, L.H. and Parizek, R.R. (1964). "Relationship between fracture traces and the occurrence of ground water in carbonate rocks." *J. Hydrology*, No. 2, 73-91.

Lolcama, J.L. (2003). "Cement kiln dust landfills in karst limestone: Delineation of groundwater flow conduits, and sinkhole risk." *Sinkholes and the Engineering and Environmental Impacts of Karst,* A.S.C.E. Geotechnical Special Publication 122.

McCann, M.S. and Smoot, J.L. (1999). "A review of stormwater best management practices for karst areas." *Hydrogeology and Engineering Geology of Sinkholes and Karst,* Beck, Pettit, and Herring (eds), 1999 Balkema, Rotterdam, ISBN 90 5809 046 9.

Newton, J.G. (1987). "Development of sinkholes resulting from man's activities in the Eastern United States." *U.S.G.S. Circular 968.*

Palmer, A.N. (2004). "Growth and Modification of Epikarst." Karst Waters Institute, Special Publication 9.

Pennsylvania Department of Environmental Protection (1999). *Pennsylvania Stormwater Best Management Practices Manual.* PADEP Bureau of Watershed Management, Document 363-0300-002.

Permeable Concretes for Railway Abutment and U-Wall Drainage Remediation

C. D. Wright, P.E., RLS-B GIS

Civil Engineer VI, M. AREMA, M. ASDSO, M. ASPRS, MARTA Office of Engineering, 2424 Piedmont Rd., Atlanta, GA 30324; PH (404) 848-5625; FAX (404) 848-4329; email: wrightD@itsMARTA.com or bullet_man@mindspring.com

ABSTRACT: Pervious concrete has been used in recent years to improve the safety and environmental effects caused by precipitation runoff from pavements. However, significant use of permeable concretes for other applications has apparently not been made and documented. This article chronicles the development of several subsurface drainage applications that utilized cementitious permeable concrete as a fundamental construction material.

The applications presented are remedial solutions to drainage problems that developed under bridge abutments, under ballasted track approaches and transitions to bridges, and outside of cast-in-place U-walls. After considering traditional solutions and some new technologies, it was decided that permeable, soil filtering drainage elements should be installed to fill voids and prevent future erosion damage without disrupting the existing unintended drainage pathways. In some cases, the projected capacity of the drainage systems required pervious concrete with flow rates approaching that of fabrics installed for soil filtering.

Standard permeability testing methods had not been developed for permeable concrete. Commercial high flow permeability test apparatus were not found to be available. High flow test apparatus development and methods are described.

INTRODUCTION

As the oldest sections of the MARTA heavy rail facility in Atlanta, Georgia began to exceed 25 years of age, significant efforts were made by the Authority to institute regular budgetary planning, inspections, and remedial construction projects. An inventory of railroad bridge structures was assembled and scheduled inspections revealed a group of similarly configured bridge abutments with ballasted track approaches exhibiting significant soil erosion. The bridges identified with problems all had stub abutments with short back walls founded on piles or caissons. At another location, significant loss of ground was discovered on the outsides of a U-wall carrying two tracks below a roadway. A U-wall is a pair of cast-in-place retaining walls on either side of a depressed trackway.

A detailed investigation program began with field visits by engineers to determine the nature and extent of the erosion damage. It became apparent that characteristic erosion was occurring at the bridges. Soil was washing out from under the abutment back walls and causing eroded gullies down the embankment slopes. It was noted that processes happening at various bridges had progressed in a similar pattern depending on the age of the individual bridge. Sixteen bridge abutments and a section of U-wall were subjected to detailed investigations and geotechnical services were employed to verify specific problems that had been detected.

Several of the bridges are in a section of track running in the median and five feet above a divided toll road with cast-in-place retaining walls on either side. The sub-ballast course under a pair of ballasted tracks drains to a continuous underdrain system in the center of the trackway. Other bridges are built on combinations of earth embankments and precast reinforced earth walls with track sub-ballast course draining to the outside of the track pairs. In addition, encased electrical conduit ductbanks are buried under the edge of the tracks along their length at all of the bridges with variously configured transitions to the abutments. The bridges that are road overpasses are not difficult to access except for one that is extraordinarily high. The bridges over watercourses, however, present challenges ranging from problems with residential neighbors not wanting construction activities nearby to traffic control on adjacent high-speed highways or the challenge of operating equipment on steep embankment grades around existing bridge columns and structures.

Some of the affected bridges that are over road underpasses have slope pavement concealing the embankment slopes. Ground penetrating radar and probing through drilled holes were utilized to determine that significant eroded gullies exist under the slope pavement at some of the bridges. Measurements revealed the volume of these voids were similar in size to the ones at other bridges.

This article is about the most damaging erosion identified directly under the abutments but it is worth noting that other erosion was regularly evident along cantilevered wing walls retaining backfill behind some of the stub abutments. The most likely cause of this erosion seems to have been drainage system filter material that has begun to become fouled with clay soil from the backfill. Once the hydraulic conductivity of the filter material fell into the same range as the embankment soils, the water did not have a sufficiently high conductive path to the underdrains and began washing out under the cantilever wing walls where there are no footings.

While the extent of ground loss and voids detected at the bridges were not considered severe, concerns about how they might be communicating with the area behind the abutments and beneath the approach slabs or how voids might quickly enlarge in an intense rain event justified further investigation.

Additional investigations were conducted to determine the magnitude of voids that had formed under the abutment approach slabs if any. A crew was mobilized to dig track ballast, core the approach slabs, test the competency of the embankment, and return the ballasted track to serviceable condition. Hand augers were used in conjunction with dynamic penetrometers to determine conditions of abutment backfill and probes were driven to confirm that the sloped alignment of the concrete approach slabs were as designed. Most of the approach slabs exhibited some degree of soft soils or voids directly underneath.

Approach slab soil loss investigations proved to be a difficult task. The bridges studied carry rail transit vehicles 20 hours every day and delaying service is limited for non-emergency inspections or routine maintenance. As a result, most of the work had to be conducted during short non-revenue service hours in short, late-night windows.

At the conclusion of the wayside investigations, one of the sources of the water was determined to be surface drainage flowing under the ballast and over the sub-ballast course especially where there are downgrades to the abutments. The other was water collecting in the electrical conduits and leaking from the low points and through the embankment soils where the ductbanks transition vertically to pass through the top of the abutments.

TERMINOLOGY

Considerable work was needed to determine the appropriate mix criteria and design for permeable cementitious materials. Relevant material properties were material mobility at time of concrete placement, strength, and the hydraulic conductivity of the set material. Standard ASTM tests were selected to determine concrete strength and grout mobility but a survey of the industry for hydraulic conductivity standards and tests in the ranges required revealed an underdeveloped area of knowledge that required study and innovation by the design team.

It became apparent that some confusion about terminology existed. The general terminology adopted for this project was as follows.

pervious – free flowing, highly conductive material
permeable – seeping, moderately conductive material

These definitions, however, do not adequately define material properties for contract specification purposes. Traditional literature researched concerning material permeability is almost exclusively related to soils. From a survey of tradition soil mechanics texts, some terms are proposed for all materials to standardize terminology:

pervious - materials with permeability more than 10^{-2} cm/sec
permeable - material with permeability between 10^{-2} cm/sec and 10^{-4} cm/sec
slow-permeable - material with permeability between 10^{-4} cm/sec and 10^{-6} cm/sec
semi-permeable - material with permeability between 10^{-6} cm/sec and 10^{-9} cm/sec
impermeable - material with permeability less than 10^{-9} cm/sec

Some material vendors also state permeability in terms of ***flow rate***. This is especially common in the pervious concrete pavement industry. These values may seem intuitive to non-technical personnel but depend on hydraulic gradient. Therefore, flow rates should always be stated under a specific head. The proposed standardized nomenclature for this value: Required flow rates under 1, 3, and 10 feet of hydraulic head.

DESIGN CONSIDERATIONS

Early in the design process it was decided that the general philosophy should be to fill voids and regions with ground loss, filter and pipe the water seeping through the embankments without changing the existing watercourses. The design team felt that any diversions of the seepage inside the embankments would be unpredictable and could cause additional damage to the earthwork. Conventional drainage solutions did not appear to be suitable under the circumstances for a variety of reasons. Chief among these reasons was the requirement that the abutment embankments, backfill, or drainage filter zones could not be excavated or rebuilt because the rail lines had to remain in constant service. Also, the solution had to be installed at the top of constructed embankments with new backfill to return the grade to original condition. The new drainage system had to reliably collect all of the water even if some settlement of the new fill material occurred.

Access obstacles presented extra issues for delivery of materials and installation procedures. Consultations with specialty contractors yielded some interesting perspectives on this matter. Manual labor could have been utilized but costs and worker safety concerns would have been considerable especially at the highest bridges. Tasks such as achieving adequate soil compaction would have been impractical without machinery.

When interviewed, a geotechnical contractor proposed cutting soil out from under the front face of the abutment deeply enough to build a road parallel to the abutment high on the slope to accommodate construction equipment under the bridge girders. Supporting the remaining vertical soil face with soil nailing and shotcrete was the focus of the proposal. Although this solution has been used under highway overpasses to make space for additional traffic lanes, it was deemed unsuitable for this project because of the risks of undercutting the stub abutment backfill while rail transit vehicles were in service on the structure above. This alternative also had the disadvantage that vertical wick type drains typically installed with soil nailing and shotcrete lined walls do not provide the continuous drainage feature needed to remedy the actual erosion occurring.

Field visits were conducted to Alabama and Georgia highway department construction sites to observe repairs with urethane foam injections into voids and loose soils under road bridges with erosion similar to this project. This technique has been considered to stabilize slab track exhibiting settlement elsewhere on the MARTA rail system. For the highway repairs, it was used to consolidate saturated deep embankment soils, raise the surface mounted road approach slabs to match adjacent structure profiles, fill voids and seal the eroded areas under the stub abutment walls. Although effective in some applications, this technology was unsuitable for this project because the urethane foam is not permeable and if used, would have caused undesirable drainage diversions through the embankments.

These matters expose some fundamental differences between highway embankments and rail transit embankments. Highway pavements provide ideal surface drainage elements that protect the soils below from water and the overall shape of roadway embankment surfaces are built to conduct surface flows away from bridge abutments. Ballasted track on the top of the embankments do not afford the same ability to conduct surface runoff even where the sub-ballast is in optimal condition. Often, aging track bed materials break down and rock flour (granite dust and sands) foul the ballast and interfere with intended drainage pathways. Walls, foundations, and other facilities in the trackway can complicate drainage under the ballast particularly when installations are not a part of the original design. Also, internal electrical supply and communications ducts required for rail transit facilities can transmit water into the embankment.

A number of providers of permeable, mobile cementitious materials were located. One company was identified that produced cellular grouts used for self-levelling road base installation in areas of permafrost. This material insulates and prevents road surfaces from freezing before surrounding ground because of accelerated heat loss from unprotected road pavements. The vendor guaranteed the cellular product could be made with open cells and with varying permeability.

This material was not selected because the patented process required use of a one-of-a-kind van located in Canada which would be difficult to schedule and because the authority follows a strict 'Buy American' policy.

Flowable fill providers also stated that their products were permeable but experience with this material indicated that the mix proportions are not usually precisely controlled.

Two companies were located offering preformed foam that could be used to transport aggregates and would dissipate after a few hours. The vendors use foam and other patented concrete additives to make a variety of permeable concrete and grout.

The design produced consists of filtered pervious concrete placed into the voids below the stub abutment walls with a drainage ditch along the front of the wall. This concrete filled ditch was called a drain beam. It will be graded to drain and filled with pervious concrete. Piping will be installed with cleanouts connected to slope drains to carry water away. It will be lined with an impervious liner. Stiff impermeable grout will be pumped between the filtered pervious concrete elements to encase the steel piles. Field observations uncovered the least compacted soils and some of the largest voids around the piles, perhaps due to inadequate compaction after the earth was vibrated and disturbed when they were driven.

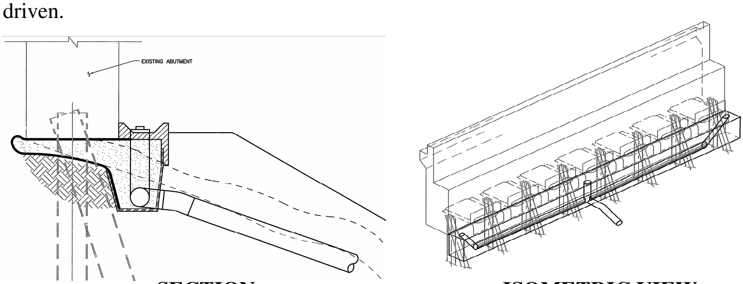

SECTION **ISOMETRIC VIEW**

Diagram 1 – Drain Beam Detail

An embankment drain was designed to penetrate the drain beams where the heaviest erosion was detected. This feature consists of perforated steel casing pipe driven approximately six feet behind the back face of the abutment wall with a filtered, slotted drain pipe connected to the drain beam piping system.

Several permeable concrete test batch sessions were conducted by the design team with various contractors and testing agency professionals. The primary ingredients of the samples were cement, silica fume, various gap graded coarse aggregates including regularly shaped river stone, water, preformed foam, and various additives. The additives tested were plasticizers, polymers, and water reducers. Some unsuccessful tests were conducted by a concrete supplier with a patented water reduced, super placticized mix.

In addition to the sheer volume of combinations possible, some special difficulties were encountered during this process. A prime concern was finding a suitable method for measuring preformed foam. The foam was so lightweight that accurate mass measurements were impossible. Volumetric measurements proved to be problematic as well. Small laboratory generators are obtainable but were not available when this work was performed.

Some acceptably strong and pervious concrete was tested and produced in the field similar to what is commonly made for pervious concrete pavement. It was installed into a pilot 'drain column' application. Twenty foot deep holes were excavated outside of a U-wall, the drain inlets at the bottom fitted with filter elements, and the holes backfilled with pervious concrete. In this location the local water table occasionally rises high enough to apply hydrostatic pressures on the wall so filtered drainage blankets were originally installed outside the wall to protect the drains (1986). Recently, large sinkholes had formed over the drainage system inlet pipes where the drainage blankets had failed and this application was developed to remediate the problem.

While freezing increases the void volume in coarse aggregates by as much as 9%, the internal particle structure remains unchanged (Terzaghi 1948).

The bulk of the test batching efforts by the design team were devoted to trying to formulate a mobile permeable grout. The intent was to pump this material under the approach slabs behind the abutments. The desire was to produce a material that would not block drainage and had large enough particles that it would not flow into buried conduit cracks. Small graded aggregate made mobile with foam was considered and rejected because of concerns that the loose material could migrate as the filter material and soils had already been shown to have done. It was judged that using Portland cement would make adequately large blocks in the set material to form in spite of expected vibration cracks caused by trains returning to service a few hours after material placement.

The test batching showed that there is an inverse relationship between strength and hydraulic conductivity when using preformed foam to achieve material mobility during installation.

TESTING

In order to quantify permeability, a method for measuring high flow conductivity that did not exist in literature researched was required. ASTM tests prescribed constant head methods for high hydraulic conductivity material. This was also recommended in some geotechnical texts. This kind of test directly yields permeant flow and velocity values and generally yields accurate average values if allowed to run for a period of time. However, commercially available apparatus for testing the permeability of soils were sized for small permeant quantities and small material samples.

If the requirements for sample sizes in aggregate permeability tests were valid (ASTM D2434 - Permeability of Coarse Aggregates with Constant Head Test), corresponding samples sizes of non-homogeneous pervious concrete (6-inch to 10-inch diameter cored samples depending on aggregate gradation) had to be taken to avoid getting imprecise average void ratios The permeant flows through these sized samples were very large and sustaining them for constant head tests would require a very large reservoir. Figure 2 is an example of a falling head test device for coarse aggregates.

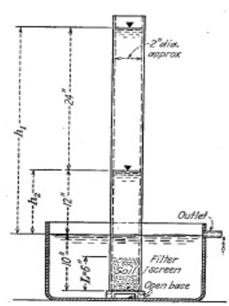

Diagram 2 Granular Material Falling Head Permeameter
(Tschebotarioff 1951)

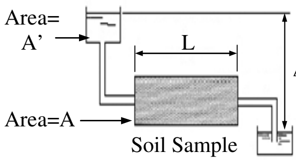

Diagram 3 Henri Darcy's Basic Permeameter
(Sowers 1970)

The project apparatus devised took the form of a basic textbook permeameter. It was a simple 'J' shape made from 6 inch PVC pipe with a manometer fixed to the reservoir (upper end) of the device. This configuration eliminates the effects of the sample material holding capacity under the influence of gravity and insures a continually saturated sample. The permeable concrete sample cores were coated with sealant and attached to the lower end of the device. A five gallon bucket with a water closet valve was affixed to the top of the device to test very pervious materials that conducted large flow quantities.

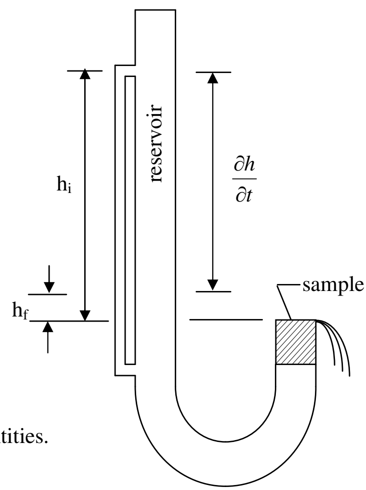

Diagram 4 – High Flow Permeameter

The calculations required to determine the permeability coefficient from data collected with the falling head permeameter are as follows (Wu 1966):
Beginning with Darcy's Law:

$$q = vA = kiA$$

$$\frac{Q}{t} = kA\,\frac{h}{L}$$

$$k = \frac{QL}{Aht}$$

$$\frac{\partial Q}{\partial t} = -\frac{A'\partial h}{\partial t} = k\frac{h}{L}A$$

$$-\frac{\partial h}{h} = \frac{kA}{A'L}\partial t$$

<u>Variables</u>

A = cross sectional area of sample
A' = cross sectional areas of reservoir
h = height of water column; head
i = hydraulic gradient
k = permeability coefficient
L = length of sample
Q = permeant flow quantity
v = permeant velocity

integrating from h_i to h_f:

$$\log_e \frac{h_i}{h_f} = \frac{kA}{A'L} t \qquad \text{and} \qquad k = \frac{L}{t} \log_e \frac{h_i}{h_f} = \frac{L}{t} \ln \frac{h_i}{h_f}$$

For relatively slow flowing samples, this method has the advantage of allowing multiple measurements to be evaluated and compared.

SUMMARY

Design mixes were formulated and tested by the design team that met the project specifications. High mobility cementitious cellular grout was produced with 41 day compressive strength greater than 70 psi and permeability greater than k=2x10^{-2} cm/sec. Pervious concrete was produced with 7-day compressive strength greater than 120 psi and permeability greater than k=6x10^{-2} cm/sec. Construction is scheduled to begin in the spring of 2008.

Another possibility for future study is the unpublished work of Mr. Hough, late Chief of the U.S. Soils Laboratory in Eastport, Maine, reported by Plummer (1942). He determined the permeability of a range of coarse soils with particles not passing a no. 14 sieve, all exhibiting non-laminar flow. He related the flow to an empirically determined coefficient, n, that depended on the soil particle sizes. The following calculation is derived from Darcy's Law: Q=kiA

$$k = \frac{AL^n}{A(t_f - t_i)(1-n)}[h_f^{(1-n)} - h_i^{(1-n)}]$$

It may be possible to select aggregate sizes and shapes and relate to the Kozeny-Carmen equation that calculates permeability coefficients based on facts about the geometry of voids and void ratios in coarse aggregates if suitable cement mixes that generate adequate strength without blocking hydraulic communication between voids are discovered. Continued improvements to permeable concrete technology will provide engineers with valuable and effective solutions in the future that could be applied to a variety of drainage conditions.

ACKNOWLEDGMENT

The author wishes to recognize Mr. Jerry Bland, P.E. for his experience, humour, and friendship that made this work successful.

REFERENCES

Plummer, Fred L. and Dore M., *Soil Mechanics and Foundations*, Second Edition Jan. 1942, (London, Sir Isaac Pitman & Sons, Ltd., 1940), Ch 5.

Sowers, George F., *Introductory Soil Mechanics and Foundations: Geotechnical Engineering*, Third Edition, 1970 (New York, MacMillan Publishing Co., Inc., 1951), Ch.3.

Terzaghi, Karl and Peck, Ralph B., *Soil Mechanics in Engineering Practice*, Corrected Second Edition, March 1968, (New York, London, Sydney: John Wiley & Sons, 1948), Ch 3 and 4.

Tschebotarioff, Gregory P., *Soil Mechanics, Foundations, and Earth Structures*, 1952 (New York, McGraw Hill Book Co., 1951), Ch. 5.

Wu, T. H., *Soil Mechanics*, Seventh Printing, 1974, (Boston: Allyn & Bacon, Inc., Dec. 1966), Ch 2 and 3.

Stormwater Management that Combines Paved Surfaces and Urban Trees

Susan D. Day[1], Joseph E. Dove[2], M. ASCE, P.E., Julia Bartens[3], J. Roger Harris[4]

[1]Research Assistant Professor, Department of Forestry, Virginia Tech, Blacksburg, VA, 24061; sdd@vt.edu.
[2]Research Assistant Professor, Via Department of Civil and Environmental Engineering, Virginia Tech, Blacksburg, VA, 24061; jodove@vt.edu.
[3]Graduate Research Assistant, Department of Horticulture, Virginia Tech, Blacksburg, VA, 24061; jbartens@vt.edu (currently Graduate Research Assistant, Department of Forestry).
[4]Associate Professor, Department of Horticulture, Virginia Tech, Blacksburg, VA, 24061; rharris@vt.edu.

ABSTRACT: Urbanization disrupts natural soil profiles, increases impervious surfaces and decreases vegetative cover. The resulting increase in runoff can impair aquatic habitats, prevent groundwater recharge, and adversely affect water quality. Because urban land can also be scarce and valuable, there may be little space for conventional stormwater management systems that retain water on site and space for bioswales and other best management practices (BMPs) is often restricted. We describe a new type of infiltration BMP in the context of two installations in Blacksburg, Virginia. The system detains stormwater under pavement in a reservoir of load-bearing tree soils (structural soils) currently used to permit root growth under pavement in urban areas. Limited root space is a primary cause of restricted growth of urban trees. This system uses structural soils that both allow expanded tree rooting volume and have high porosity. Thus they increase tree canopy cover (and therefore rainfall interception) and detain stormwater. Supporting experiments show that root development is species dependent and root penetration of compacted subsoils can increase infiltration rates by as much as a factor of 27. The system may enhance landscape hydrologic function by increasing rain interception, channeling rainfall via trunkflow, and increasing soil permeability through root activity.

INTRODUCTION

New approaches to stormwater management in highly built settings include detaining stormwater under pavement in reservoirs created by gravel beds. This double use of land surface area increases land-use efficiency and allows water infiltration over a large area to more closely mimic natural hydrology than systems that concentrate storm flow. We are evaluating a novel practice that combines the features of these systems with engineered, load-bearing tree soils (*structural soils*) and large canopy trees. We will describe two site installations and present results of supporting experiments concerning tree root distribution and water uptake from the system and the potential for tree roots to enhance infiltration rates. Results have implications not only for this novel system, but for a wide range of stormwater best management practices (BMPs) that rely on infiltration for groundwater recharge.

Trees and Stormwater Management

Urban forests are widely recognized as an effective means of handling stormwater by rainfall interception and storage on the canopy surface (Xiao and McPherson 2003). They also direct precipitation into the ground through trunk flow (Johnson and Lehmann 2006) and take up stormwater through their roots. The possibility of roots penetrating through impermeable layers into more permeable zones could greatly aid overall stormwater infiltration, while larger tree canopies can reduce rain throughfall. However, canopy cover (and thus rain interception) is greatly limited by urban soil conditions (e.g., compaction, reduced rooting volume, elevated pH) (Day and Bassuk 1994; Grabosky and Gilman 2004), and even open soil in urbanized areas can prevent or restrict direct infiltration (Gregory et al. 2006). Therefore innovation is needed to optimally harness the ability of trees to mitigate stormwater in urbanized settings.

Structural Soils

The installations described below detain stormwater in under-pavement reservoirs of structural soil. The first of these soils, CUSoil®, was developed at Cornell University, Ithaca, NY, in the mid 1990s (Grabosky and Bassuk 1998) to address insufficient soil volumes for tree root development. The primary objective of the structural soil research was to create a substrate that would both allow adequate tree root growth *and* support pavement for sidewalks, streets, and parking lots (Grabosky and Bassuk 1995). Since then, other structural soils have been developed that use other components (e.g. Carolina Stalite, a heat expanded shale (Carolina Stalite Company, Salisbury, NC)). When compacted, structural soils form a rigid matrix filled with a mineral soil component. They have a high load-bearing capacity and greatly increase rooting depth and width when compared to standard sidewalk treatments in the United States (Grabosky and Bassuk 1995; 1996).

Distributed stormwater management techniques, such as bioswales, retain stormwater at many sites throughout the landscape. But many urban sites do not have sufficient open ground to handle water collected from surrounding impervious surfaces in a non-concentrated fashion. These sites also do not support large trees and are thus typically unable to benefit from tree canopy interception and the influence of roots on soil hydrology. For these confined settings especially, the system described here can facilitate using distributed stormwater management that takes advantage of the stormwater mitigation services provided by trees.

PARKING LOT STRUCTURAL SOIL TEST SECTION

A two-car experimental parking lot test section was constructed on the Virginia Tech campus (Figure 1). The section consisted of a woven geotextile placed at the bottom of a 60-cm-deep excavation followed by 60 cm of structural soil (Carolina Stalite). An overflow pipe to direct water out of the test section was installed at a height of 35 cm above the excavation base. Monitoring equipment (water depth, temperature, roots) was distributed throughout. A geomembrane was temporarily installed to mimic an "asphalt" surface leaving infiltration zones of 30 cm on three sides (Figure 2). Outflow through the overflow pipe was directed into a closed container to quantify runoff. Water elevation in the structural soil was monitored weekly during spring of 2006 then periodically.

FIG. 1. Excavated site for parking lot test section. Minirhizotron tubes and perforated observation wells shown.

No overflow was collected during the study, and the water depth was always less than or equal to 1 cm. Initial infiltration tests indicated slow infiltration in several locations (≤ 1 cm h^{-1}). Lateral water movement was assessed via rapid test filling at one corner and monitoring water levels in observation wells over time. Water depth throughout the lot during active filling and draining, always remained within 5 cm of the depth at the water introduction point (maximum distance 6.5 m). In 2.5 hours, the water level dropped 24 cm (indicating complete drainage). It was concluded that lateral water movement is very rapid through the structural soil media.

FIG. 2. Parking lot test section with geomembrane installed and twelve 'Red Sunset' red maples planted on perimeter and in interior cutout.

ROADWAY TEST SECTION

A structural soil test section was installed in May 2007 as part of the construction of a new access road by a private landowner in Blacksburg, Virginia. The entire paved section is 6.7 m wide with 2 m drainage swales on each side. The structural soil test section is located within one lane and is 29 m long, 3.9 m wide and 0.67 m deep. This allows direct comparison of runoff water between the two swales on the test and conventional sides. The site grade is 14 percent, which is common in several physiographic provinces of the Eastern US and typical of the Blacksburg area. The steep grades and rainfall intensities in the Eastern US pose challenges for stormwater infiltration practices.

The test section excavation included a series of diversion mounds that intersect the drainage swale and direct water under the pavement surface (Figures 3 & 4). A woven separation geotextile was placed over the prepared subgrade. Then CUSoil® was installed and compacted with a 7-ton vibrating compactor in three lifts to a dry unit weight of about 113 pounds per cubic foot. To prevent buildup of pore pressures

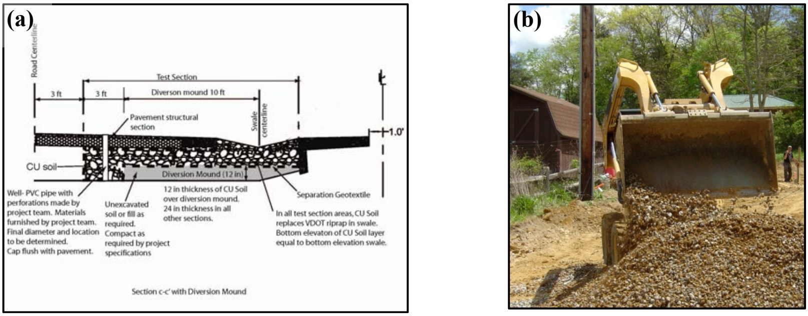

FIG. 3 (a) Detail of diversion mound section; (b) Mixing CUSoil®

under the pavement in the lower test section elevations, three perforated steel pipes were installed at the top of the CUSoil®, just under the Virginia Department of Transportation No. 21B aggregate base course. These pipes route water filling the CUSoil® section to the swale. Infiltration in the compacted CUSoil® was estimated at 0.143 cm s^{-1} via three field infiltration tests. Observation wells have been installed and monitoring continues. Some moisture has been observed after rainfalls, suggesting the diversion is effective. However, there has not yet been an opportunity to evaluate water depth from a heavy rainfall.

FIG. 4. (a) Excavation with diversion mounds; (b) Placement of CUSoil®

TREE ROOTS & SUBSOIL INFILTRATION RATES

Two supporting experiments addressed whether roots would penetrate subsoils in this system and thereby increase infiltration rates. Three tree species were used: *Acer rubrum* (red maple), *Quercus velutina* (black oak), and *Fraxinus pennsylvanica* (green ash). A third supporting experiment documented the extent of root development in the fluctuating water tables inherent to this system (experiment not described, see Bartens, 2006).

In February, 2006, two-year-old maples and oaks were planted in cylindrical reservoirs of pine bark nursery substrate (2.2 L) in the center of 26.5-L containers, with compacted subsoil on all sides and below the pine bark at the Virginia Tech greenhouses, Blacksburg, Virginia, USA (Figure 5). The subsoil particle size distribution was 15.4% sand, 35.3% silt, and 49.4% clay and was compacted to two different degrees, severe (1.59 g cm^{-3} (15.5 kN m^{-3} dry unit weight)) and moderate (1.31 g cm^{-3} (12.8 kN m^{-3} dry unit weight)). Thirty containers were placed in a completely randomized design with five replications of three treatments (two species + no-tree) at two compaction levels (severe and moderate) [30 = 5 × 3 × 2].

Containers were saturated and infiltration rate measured on 15 May, 15 June, 9 and 20 July, 3 August, and 6 September 2006 by pouring a fixed volume of water into the PVC collar and timing infiltration. Because the system was saturated, this measurement provided a relative measurement of saturated hydraulic conductivity (K_{sat}) of the most restrictive part of the system (the subsoil in this case). At the end of the experiment, root distribution throughout the subsoil was evaluated via root counts.

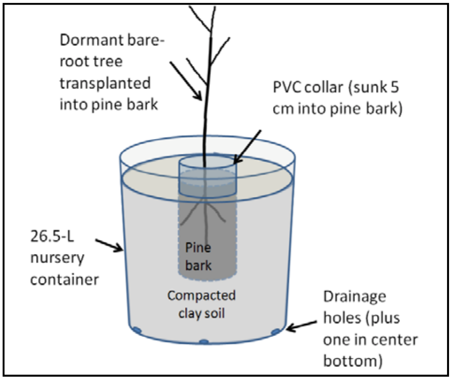

FIG. 5. Schematic maple/oak experiment

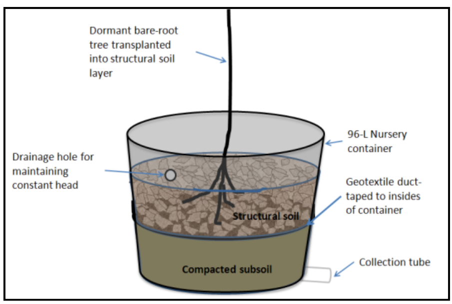

FIG. 6. Schematic ash experiment

Ash trees were grown for two years outdoors in soil profiles simulating a stormwater reservoir of CUSoil® soil separated from compacted subsoil by a woven geotextile (Figure 6). Containers were treated with copper paint to prevent roots growing along container walls. The subsoil was compacted (1.51 g cm^{-3} (14.8 kN m^{-3} dry unit weight)) clay loam. In May 2005, ten pots were prepared and ash trees were planted into 5 randomly selected pots. K_{sat} was measured using a constant head technique in May 2007. Earlier drain holes were sealed and pots and subsoils were saturated via repeated irrigation and rainfall for one week in advance of measurements. In addition to saturating the system, this was intended to reduce or eliminate boundary flow down the sides of the container by settling soil completely against the container sides. We assumed no loss of hydraulic head in the highly permeable structural soil layer. K_{sat} was calculated as $K_{sat} = Lq\,/\,\Delta H$ where ΔH = the height of upper drain hole from the bottom of the pot, L = the height of the subsoil profile, and q = flux density (volume per mean cross-sectional area of subsoil per second) out the drain tubes. In May 2007, trees were harvested and root penetration through the geotextile and subsoil layers evaluated.

Tree Root Growth Increased Infiltration Rate

In both experiments roots penetrated compacted soils and increased K_{sat} compared to controls. In the maple/oak experiment, the presence of trees increased K_{sat} by 153% in the severely compacted treatment when compared to unplanted controls. Trees have been shown to increase infiltration when long-established trees are present (Bramley et al. 2003) and when woody roots decayed after plants were removed (Yunusa et al. 2002). However, in our greenhouse study, the increase in drainage rate occurred before the first test date (within 12 weeks) indicating that woody roots can increase infiltration relatively quickly, before there is opportunity for very large diameter roots to form and when root turnover is likely minimal. Ash root penetration also dramatically increased K_{sat} (Table 1). Roots grew through woven geotextiles although it was observed that roots proliferated more where the geotextile had been punctured by compaction of the structural soil (Figure 7).

FIG. 7. Ash roots penetrating geotextile after compacted subsoil has been washed away. Roots increased K_{sat} by a factor of 27.

Table 1. Saturated hydraulic conductivity (K_{sat}) and root penetration in a structural soil-geotextile-compacted subsoil profile designed for stormwater infiltration with and without green ash trees.

	K_{sat} cm/s^{Z}	Mean roots penetrating	Mean diameter of roots ≥ 2mm
With trees	$1.31 \cdot 10^{-3}$	6.33	5.28 mm
Without trees	$4.83 \cdot 10^{-5}$	n/a	n/a
p-value^{y}	0.008	n/a	n/a

^{z}N=5.

^{y}P-value calculated in SAS with the Wilcoxon Rank Sum Test.

ROOT DEVELOPMENT & WATER UPTAKE

In May 2005, three-yr-old bare-root *Fraxinus pennsylvanica* 'Georgia Gem' and *Quercus bicolor* were planted into either CUSoil® or Carolina Stalite structural soils in 94.6 L nursery containers constructed with a series of valves to allow filling and draining that would simulate rainfall storage in stormwater reservoirs of structural soil and subsequent infiltration into the subsoil below. After an initial plant establishment period, three drain-and-fill regimes were instituted to mimic three typical subsoil infiltration rates: rapid infiltration (2 cm h^{-1}), moderate infiltration (1 cm h^{-1}), and slow infiltration (0.1 cm h^{-1}). Treatments were assigned in a completely random experimental design with five replications: [1 species × two structural soils + 1 species × one structural soil] × 3 drainage regimes × 5 replications = 45 total trees.

Regimes were imposed for two growing seasons. Water uptake was assessed via calculating whole day transpiration rates via stomatal conductance (LiCor 1600 Steady State Porometer; LI-COR Biosciences, Lincoln, NE, USA) and leaf area measurements; and, for comparison, whole-tree sapflow measurements ((Flow 32-AO Sap Flow Measurement System, Dynamax, Houston, TX, USA) (Steinberg et al. 1989). At the conclusion of the experiments, leaf area, stem and root dimensions, and dry mass were measured.

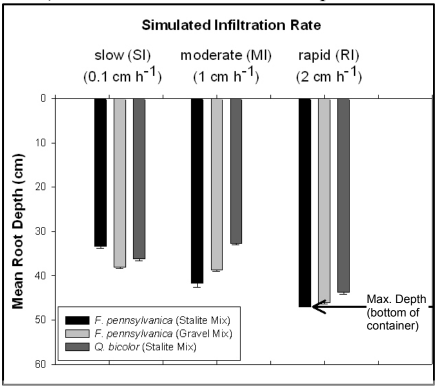

FIG. 8. Rooting depth was restricted by slower drainage, but is species dependent.

Drainage regime affected rooting depth, with species that are both flooding and drought tolerant (ash) being the least affected (Figure 8). All trees grew well, but those in the moderate infiltration regime grew best and transpired the most water (e.g. for green ash 2.14 L day^{-1} for moderate infiltration vs. 1.24 and 1.55 L day-^{1} for rapid and slow infiltration respectively). There was some indication that this increased water uptake was a treatment effect ($p=0.08$). Transpiration volume is dependent upon leaf area which is exponentially larger in full-grown trees. Therefore these data should not be interpreted as static predictions of uptake. In addition, transpiration halts in the dormant season for deciduous trees. Therefore, rainfall season should be considered if transpiration expectations are included in the design.

CONCLUSIONS

We make the following recommendations for implementing these systems:

- Design should allow a layer of structural soil 60 cm deep for adequate rooting volume. This depth will be able to hold 15 to 20 cm of water. Lateral water movement is rapid, but dependent upon slope and supply.
- Select species tolerant of flooding and high pH (if limestone is used).These include many common street trees, such as elms, honey locust, and London plane. Design should allow water to drain within two days to avoid restricting tree root development, although some species will tolerate more flooding.
- Although high water tables may limit tree rooting depth, when species selection and site design allow trees to root into lower soil regions and penetrate through impervious zones, they may be an effective tool to increase infiltration. This increase can be expected to be most dramatic in highly restrictive soils.

- Trees should ideally be established in mineral topsoil, with the structural soil components being reserved for under the pavement.
- Tree root systems are wide spreading. For maximum tree growth, provide rooting area about twice the diameter of the ultimate canopy you are designing for.
- Assessing infiltration by sampling may not accurately reflect integrated drainage of the entire excavated area.

ACKNOWLEDGEMENTS

This project was supported in part by the USDA-Forest Service Urban & Community Forestry Program on the recommendation of the National Urban & Community Forestry Advisory Council. We thank the Blacksburg Society of Friends, J. Williams, J. James, V. Groover, J. Wallen, and S. Worthington.

REFERENCES

Bartens, J. (2006). "Trees and Structural Soil as a Stormwater Management System in Urban Setting." Master's Thesis. Department of Horticulture. Virginia Tech.

Bramley, H., Hutson, J., and Tyerman, S. D. (2003). "Floodwater infiltration through root channels on a sodic clay floodplain and the influence on a local tree species *Eucalyptus largiflorens*." *Plant and Soil*, 253(1), 275-286.

Day, S., and Bassuk, N. (1994). "A review of the effects of soil compaction and amelioration treatments on landscape trees." *Journal of Arboriculture*, 20(1), 9-17.

Grabosky, J., and Bassuk, N. (1995). "A new urban tree soil to safely increase rooting volumes under sidewalks." *Journal of Arboriculture*, 21(4), 187-200.

Grabosky, J., and Bassuk, N. (1996). "Testing of structural urban tree soil materials for use under pavement to increase street tree rooting volumes." *Journal of Arboriculture*, 22(6), 255-263.

Grabosky, J, and Bassuk, N. (1998). "Urban tree soil to safely increase rooting volume." Patent Number 5,849,069. U.S. Patent and Trademark Office, Cornell Research Foundation, Inc..

Grabosky, J., and Gilman, E. F. (2004). "Measurement and prediction of tree growth reduction from tree planting space design in established parking lots." *Journal of Arboriculture*, 30(3), 154-159.

Gregory, J. H., Dukes, M. D., Jones, P. H., and Miller, G. L. (2006). "Effect of urban soil compaction on infiltration rate." *Journal of Soil and Water Conservation*, 61(3), 117-124.

Johnson, M. S., and Lehmann, J. (2006). "Double-funneling of trees: Stemflow and root-induced preferential flow." *Ecoscience*, 13(3), 324-333.

Steinberg, S., Vanbavel, C. H. M., and McFarland, M. J. (1989). "A gauge to measure mass-flow rate of sap in stems and trunks of woody plants." *Journal of the American Society for Horticultural Science*, 114(3), 466-472.

Xiao, Q., and McPherson, E. (2003). "Rainfall interception by Santa Monica's municipal urban forest." *Urban Ecosystems*, 6, 291-302.

Yunusa, I. A. M., Mele, P. M., Rab, M. A., Schefe, C. R., and Beverly, C. R. (2002). "Priming of soil structural and hydrological properties by native woody species, annual crops, and a permanent pasture." *Australian Journal of Soil Research*, 40(2), 207-219.

Temperature Response in a Pervious Concrete System Designed for Stormwater Treatment

John T. Kevern[1], M. ASCE and Vernon R. Schaefer[2], M. ASCE, P.E.

[1]Ph.D. candidate, Department of Civil, Construction, and Environmental Engineering, Iowa State University, Ames, IA, Phone: 515-294-8496, Fax: 515-294-8216, Email: kevernj@iastate.edu
[2]Professor, Department of Civil, Construction, and Environmental Engineering, Iowa State University, Email: vern@iastate.edu

ABSTRACT: For pervious concrete to function optimally as both a pavement and stormwater treatment solution, both aspects must be considered together as a system. The pavement must possess the required strength and freeze-thaw resistance for surface durability and also an appropriate permeability to convey stormwater to the lower aggregate base retention area. This paper presents data obtained from a fully instrumented pervious concrete parking lot at Iowa State University (ISU). The site contained two 15 cm (6 in.) thick pervious concrete sections overlying 30 cm (12 in.) or 46 cm (18 in.) base configurations, while the control concrete section was placed directly on compacted soil. Temperature sensors monitored the freeze-thaw behavior of the system for both pervious sections and a standard concrete control. Ultimately, water samples will be collected from both the standard concrete control section and from tiling installed in the pervious concrete aggregate base for comparison of stormwater constituents and flow. The freeze-thaw results show a substantial lag in frost penetration of the pervious system and immediate thaw once melt water becomes present. Maximum temperature observed in the pervious concrete layer was always greater than the surrounding air temperature.

INTRODUCTION

Recently the EPA, under the Clean Water Act, has implemented the National Pollutant Discharge Elimination System (NPDES) permitting of the stormwater for point sources as well as non-point source pollutant runoff. Developed sites are required to provide treatment to the stormwater discharge as well as reducing the overall volume to predevelopment rates (Federal Register 2004). Best Management Practices (BMPs) are structural or non-structural ways to meet the required standards (WERF 2005). One common method is detention/retention ponds, which hold the stormwater and allow controlled discharge into the system. Some of the disadvantages include limited pollutant reduction and large areas of land must be purchased for the BMP, reducing optimal land usage. Porous pavement systems combine the parking surface with the detention/retention area for better site utilization, pollutant removal, and groundwater recharge (Tennis *et al.* 2004).

Portland cement Pervious concrete (PCPC) is comprised of relatively uniform graded coarse aggregate, a small amount of fine aggregate, cement, and water to form a series of interconnected voids which allows water infiltration for the maximum design rainfall intensity. The goal is to allow the water to pass through the pavement into the aggregate base where the water is stored while it infiltrates into the natural soil. The large surface area of the concrete and aggregate base adsorbs hydrocarbons, allowing removal through evaporation and, in the lower moist portions, microbic degradation. Studies have shown substantial removal rates of hydrocarbons, nitrates, phosphates, and heavy metals by pervious concrete systems through physical and chemical processes (Pratt *et al.* 1996, Park and Tia 2004).

Benefits of pervious pavement also include the elimination of stormwater collection systems, improved pavement skid resistance, decreased glare, and increased visibility and traction. PCPC is currently used for parking lots, pathways, and in some places, low-volume roads for stormwater purposes in the United States (U.S.) (Tennis *et al.* 2004).While used in Florida for stormwater treatment since the 1970's, a high percentage of failures due to limited construction experience, low strength, and lack of freeze-thaw durability have restricted application, especially in regions that experience hard-wet freeze conditions (i.e. Midwestern, Northern, and Northeastern states) (NRMCA 2004). Like other pavement systems, pervious pavements must posses the strength and freeze-thaw durability to support applied loads and to resist environmental conditions. However, PCPC must also have adequate permeability for the design storm as well as the ability to provide pollutant treatment.

Laboratory tests performed at the National Concrete Pavement Technology Center (CP Tech Center) at Iowa State University (ISU) show that adding a small amount of fine aggregate (sand) back into the traditionally single-sized coarse aggregate mixture design improved the load transfer between particles, increasing strength and ultimately creating freeze-thaw durable concrete under saturated conditions (Schaefer *et al.* 2006). While continued research into the mixture design has improved strength and durability, the following issues dealing with the entire pervious concrete pavement system still require investigation.

- How is the permeability of the system affected by freezing conditions?
- How does the predicted system permeability compare with the actual values?
- What level of pollutant removal can be expected from the system?
- What, if any, is the impact on the local groundwater table?
- How does temperature vary with depth?
- How will the system results impact the design methodology?

In order to better understand the pervious pavement system, a fully-monitored parking lot was constructed at ISU comprised of pervious concrete and traditional Portland Cement Concrete (PCC) pavement. Stormwater was collected and compared from both sections and temperature and soil moisture sensors along with monitoring wells and water level sensors in the base.

BACKGROUND and OBJECTIVES

Pervious Concrete Experience at Iowa State

In 2004, the Iowa Concrete Paving Association (ICPA) partnered with ISU on a research project to determine the freeze-thaw durability of typical pervious concrete mixtures and to design a concrete mixture that was appropriate for use in Iowa. Background investigation showed that pervious concrete had been used in Florida since the 1970's for stormwater purposes. The concrete mixture designs incorporated single-sized coarse aggregate and no fine aggregate (Maynard 1970). Permeability was adequate, but strength was (low 3.4 MPa to 17.2 MPa (500 to 2,500 psi)) and failures were common. However, Europe and Japan had been using pervious concrete as an overlay material, in limited applications, for noise reduction and skid resistance for high speed applications (Tamai and Yoshida 2003). European mixtures contained smaller-sized coarse aggregate and included some fine aggregate, along with chemical admixtures to produce higher strengths. Combining both the high permeability of U.S. mixtures with the higher strength from the European mixtures, ISU developed mixtures that withstood 300 saturated freeze-thaw cycles according to the ASTM C 666A procedure.

A poorly graded, non-uniform, coarse aggregate was combined with fine aggregate in proportions to obtain enough permeability, > 36 cm/hr. (14.7 in./hr.), and compressive strength, > 20.7 MPa (3,000 psi) (Kevern 2006). Since the initial study, pervious concrete freeze-thaw research performed at the CP Tech Center has included aggregate from 11 states, effect of air entrainment on PCPC, characterization of entrained air, the effect of supplementary cementitious materials, and compaction level. Freeze-thaw durability was the main concern, but the emerging research suggests that construction practices and curing methods have the greatest potential to produce pervious concrete failures.

Objectives of the Lot 122 Project

The objectives of the Lot 122 project were to evaluate the permeability and pollutant removal rates of pervious concrete pavement systems with different surface permeabilities and aggregate base depths under freeze-thaw conditions, and to determine if current design methodology is adequate.

SITE INVESTIGATION

An initial site investigation was required to determine what soils were present, the location of high/low permeability strata, seasonal high water table level, and soil subgrade support values. The soil survey described the soil as Webster Clay Loam, a A-6/A-7 type soil under the American Association of State Highway Transportation Officials (AASHTO) classification scheme. Borings revealed as about 30 cm (12 in.) of gravel overlying about 30 cm (12 in.) black clay fill. Underneath the black clay was about 3 cm (1 in.) layer of gravel overlying 30 cm (12 in.) of gleyed sandy clay above sandy clayey silt. The apparent water table was located between 102 cm (40 in.) and 165 cm (65 in.) below surface elevation. Permeability testing on 8 cm (three inch) diameter samples in a triaxial permeability apparatus resulted in permeability values ranging from $1x10^{-5}$ cm/s to $4x10^{-7}$ cm/s. Because the site was an old parking lot, the upper gravel layer and clay fill along with the lower gravel layer were removed to expose the natural soil and restore permeability under the pervious pavement.

SITE LAYOUT and SECTION DESIGN

The site layout for Lot 122 is comprised of the south half pervious concrete and the north half is traditional PCC. The total area is 1,115 m^2 (12,000 sq. ft.) to produce 35 parking stalls.

Current pervious concrete section designs are based more from empirical knowledge than from actual loading and support conditions. The NRMCA, along with many state agencies, suggest using a 15 cm (6 inch) pervious pavement for parking areas and 20 cm (8 inch) if the pavement supports light but routine truck traffic. The suggested minimum base thickness is 15 cm (6 inch) if the soil has medium permeability, 1.3 cm/hr (1/2 in. /hr) (Tennis *et al.* 2004). Many areas in the Southern U.S., especially Florida, do not use an aggregate base since the *in-situ* soil permeability is equal to or greater than that of the pavement (NRMCA 2005). The thickness design of the aggregate base has been a function of the required stormwater detention volume, rather than adding to the structural capacity of the pavement system.

The pervious sections were selected and designed to evaluate different surface infiltration rates and aggregate base storage capacities. The southwest quarter of Lot 122 contained a pervious concrete mixture with primarily a smaller 4.75 mm (No. 4) sized rounded-river gravel for a finer surface texture and slightly lower permeability. A 30 cm (12 in.) aggregate base was placed under the smaller aggregate mixture. The southeast quarter of Lot 122 contained a pervious concrete mixture with a larger rounded-river gravel aggregate sized from 9.5 mm (3/8 in.) to 12.7 mm (1/2 in.). Generally, the larger aggregate produces larger pore diameter and greater permeability. A 46 cm (18 in.) aggregate base was placed under the larger aggregate pervious section. The drainable base was a limestone aggregate with about 40% compacted void space, producing 12 cm (4.8 in.) total storage capacity in the 30 cm (12 in.) section and 18 cm (7.2 in.) total storage capacity in the 46 cm (18 in.) section. Total storage in the 30 cm (12 in.) section represents the 10-year, 24 hour rain event, while total storage in the 46 cm (18 in.) section is greater than the 100-year event. Drain tiles were placed at 23 cm (9 in.) above the aggregate base to allow monitoring and collection of stormwater volumes greater than 9 cm (3.6 in.). In Iowa, 9 cm (3.6 in.) represents the 5-year, 24-hour rain event.

RESULTS and DISCUSSION

Concrete Results

The results from the pervious concrete cylinder samples taken during the parking lot placement are shown in Table 1. Values represent an average of three samples. The smaller-sized coarse aggregate mixture had slightly lower voids, 23.0% versus 27.8%, and consequently, lower permeability and higher compressive strength. Since the concrete mixture contained fly ash as a supplementary cementitious material, the ultimate strength was reported at 56-days. The compressive strength of both mixtures was above the required 20.7 MPa (3,000 psi) at 28-days and the permeability will increase the time between required maintenance activities due to clogging.

Pervious concrete core samples were taken from the parking lot for verification purposes at random locations. The core samples had a large degree of variability in unit weight and consequently voids and permeability. The smaller aggregate mixture had voids ranging from 18.6% to 29.0%, a difference of 10.4% and the larger mixture from 24.8% to 36.9%, a difference of 12.1%. The Coefficient Of Variation (COV) from the smaller mixture voids was 23% and 21% from the larger mixture. The unit weight ranged from 1,855 kg/m^3 (115.8 pcf) to 2,083 kg/m^3 (130.1 pcf) for the smaller mixture and from 1,695 kg/m^3 (105.8 pcf) to 1,973 kg/m^3 (123.2 pcf) for the larger mixture. COV of the unit weight was 6% from the smaller mixture and 8% from the larger one.

The concrete was discharged from the ready mixed concrete truck in piles and then raked into position before finishing with the roller-screed. The inconsistencies inherent in hand placement caused the variability in compaction level and the poor uniformity in the final product. Visual inspection of the surface does not detect any uniformity issues, suggesting that the roller-screed creates a more consistent surface layer.

TABLE 1. Pervious concrete cylinder sample properties

Mix	Voids (%)	Hardened Unit Weight kg/m^3(pcf)	Compressive Strength MPa(psi) 7 day	28 day	56 day	Permeability cm/hr. (in/hr) dia. 10 cm (4 in.)
Small Agg.	23.0	1,999 (124.8)	17.8 (2,578)	22.8 (3,305)	24.3 (3,521)	1,763 (694)
Larger Agg.	27.8	1,922 (120.0)	16.0 (2,322)	22.8 (3,304)	23.4 (3,399)	2,268 (893)

Temperature Results

The temperature profile of the pervious concrete section from December 15, 2006 to March 15, 2007 is shown in Figure 1. From mid-December to mid-January, Lot 122 experienced typical winter weather with some daily highs above freezing and the daily lows below freezing. From mid-January to mid-February, there were 35 consecutive days were the daily maximum temperature was below 0ºC (32ºF), with the exception of January 26 when the high temperature was 4ºC (40ºF). The infiltration rate of the pervious concrete system is controlled by that of the soil, so the critical location is the temperature at the aggregate base/subgrade interface. The insulating properties of the aggregate base delayed the frost line formation until 21 days into the cold period. Once the air temperature rose above freezing, the base thawed within 24 hours. Only in the extended period of extreme cold did the aggregate base/subgrade interface freeze. During the remaining cold periods permeability was maintained.

As Figure 1 shows, while the daily low air temperature was always cooler than that of the pervious pavement, absorption of sunlight caused the maximum PCPC temperature to be significantly higher than the air during most days. The transfer of heat and insulating ability of the aggregate base produced a buffered temperature response with increased depth.

The temperature profile of the PCC pavement is shown in Figure 2 for the same time period. The low end temperature response of the PCC pavement was similar to that of the PCPC pavement, although the high temperature experienced by the PCC pavement is always less than the maximum air temperature. As expected, the PCC/soil interface temperature closely followed that of the PCC slab. At 46 cm (18 in.) into the soil profile the effect of temperature was delayed, the formation of the frost line underneath the pavement was not effected by air temperature as much as under the pervious pavement. The base/soil interface under the pervious pavement (Figure 1), is close to the same mean elevation as the 46 cm (18 in.) deep sensor beneath the traditional pavement (Figure 2). Before the thaw at the end of February, the response shape of both curves is similar, with the pervious values six degrees warmer. After the thaw, due to the infiltration of melt water and transfer of absorbed energy, the base/soil interface under the PCPC continued to warm while the frost remained under the PCC side.

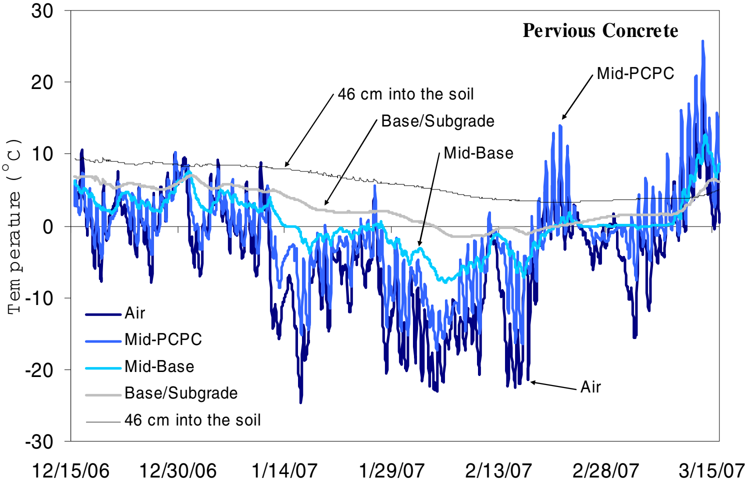

FIGURE 1. Pervious concrete winter temperature profile

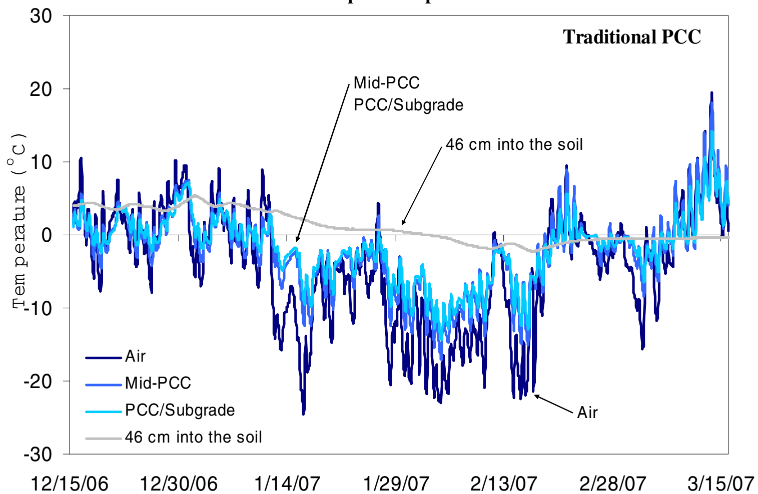

FIGURE 2. Traditional concrete winter temperature profile

The initial results for the soil moisture sensors indicate the soil was driest directly beneath the PCC pavement and moisture increases with depth. Conversely, beneath the PCPC pavement, when stormwater was infiltrating, the highest moisture level was nearest the aggregate base and decreases with depth. Unfortunately, after a few months of monitoring, the circuit board from the sensor array underneath the PCPC corroded and data collection ended. The sensor is being reworked and will be installed in a moisture-free enclosure later in 2007.

At the time of publication, Lot 122 had not experienced a storm event or combination of events large enough to produce effluent from the drain tile underneath the pervious pavement. A number of storm event combinations in the spring of 2007 were larger than the design storage capacity of the system and should have produced effluent, but did not, suggesting the permeability of the system from unforeseen soil discontinuities have produced a higher than expected infiltration rate.

CONCLUSIONS and DESIGN RECOMMENDATIONS

The following conclusions can be made from this study:

- The hand-placement of the pervious concrete slab caused a greater amount of variability than the concrete cylinder samples placed at the site.
- Sunlight absorption caused the surface of the pervious concrete slab to have higher temperatures than that of the air.
- The formation of a frost layer was significantly delayed underneath the pervious pavement aggregate base.
- The system appears to be much more permeable than lab testing predicted.

Initially, the current design recommendations for pervious pavement thickness appear adequate. No pavement distresses have been observed related to load capacity. The aggregate base provides pavement support under poor soil conditions, such as Lot 122, acts as an insulator to frost formation, and provides time for water infiltration. An aggregate base should be utilized under all pervious pavements, especially in freeze-thaw climates. This research suggests PCPC BMP systems reduce stormwater flow leaving a project site through initial abstraction by the pavement and base, increase in evaporation from the aggregate base caused by the elevated temperature profile, and through fractured soil flow. Furthermore, results indicate the efficiency of the system (i.e. estimated soil permeability) is greater than anticipated through field and lab testing. A reduction in total stormwater discharge volume must be considered for all situations when pervious concrete systems are utilized.

ACKNOWLEDGEMENTS

This study was funded by the Iowa Department of Natural Resources, the Iowa Ready Mixed and Concrete Paving Associations, and the National Concrete Pavement Technology Center at Iowa State University. The assistance provided by Steve Jones installing the sensors and soil testing performed by Heath Gieselman, Mark Thompson, and Muhannad Suleiman is greatly appreciated. The opinions, findings and conclusions presented here are those of the authors and do not necessarily reflect those of the research sponsors.

REFERENCES

Federal Register. (2004) Effluent Limitations Guidelines and New Source Performance Standards for the Construction and Development Category. Federal Register 69.80.

Kevern, J. T., (2006) "Mix Design Development for Portland Cement Pervious Concrete in Cold Weather Climates." M.S. Thesis. Ames, IA: Iowa State University.

Maynard, D.P. (1970) "A Fine No-Fines Road." *Concrete Construction*, p. 116. C700116.

National Ready Mixed Concrete Association (NRMCA). (2004*) Freeze-Thaw Resistance of Pervious Concrete*. Silver Spring, MD: NRMCA.

National Ready Mixed Concrete Association (NRMCA). (2005) "Text Reference for Pervious Concrete Contractor Certification." *NRMCA Publication #2PPCRT*, Silver Spring, MD.

Park, S., and Tia, M. (2004) An Experimental Study on the Water-Purification Properties of Porous Concrete. *Cement and Concrete Research*, V. 34, p. 177-184.

Pratt, C.J., Newman, A.P., and Brownstein, J.B. (1996) Bio-remediation Processes Within a Permeable Pavement: Initial Observations. Paper presented at the seventh International Conference on Urban Storm Drainage, Hannover, Germany.

Schaefer, V.R., Wang, K., Suleiman, M.T., and Kevern, J. (2006) Mix Design Development for Pervious Concrete in Cold Weather Climates. A Report from the National Concrete Pavement Technology Center, Ames, IA: Iowa State University. http://www.ctre.iastate.edu/reports/mix_design_pervious.pdf

Tamai, M., and Yoshida, M. (2003) Durability of Porous Concrete. Paper presented at the Sixth International Conference on Durability of Concrete, Thessaloniki, Greece.

Tennis, P.D., Leming, M.L., and Akers, D.J. (2004) Pervious Concrete Pavements, EB302, Portland Cement Association, Skokie, Illinois, and National Ready Mixed Concrete Association, Silver Spring, Maryland.

Water Environment Research Foundation (WERF). (2005) International Stormwater Best Management Practices Database. http://www.bmpdatabase.org, accessed May 2, 2005.

Fuzzy Classification System to Assess Hydrocarbon Contamination

Silva[1] , M. A. B., Almeida[2], M. C. F., Almeida[3], M. S.S.

[1] Engineer Petrobras, Rio de Janeiro, Brazil, mabs@petrobras.com.br
[2] Associate Professor, Polytechnic School of Engineering, Federal University of Rio de Janeiro, Brazil, mariacascao@globo.com
[3] Professor, Graduate School of Engineering, COPPE, Federal University of Rio de Janeiro, Brazil

ABSTRACT: This paper proposes a methodology for the fuzzy classification of contaminated sites. The methodology calculates a numerical value representing the contamination potential of a site. This numerical value takes into account the characteristics of the contaminant and its propagation, the goods to be protected and other socio-cultural, geopolitical, technical and economic aspects. This tool is able to assist environmental decision makers in site remediation decisions, thus helping to optimize the financial resources. The methodology is applied to a case of soil contamination due to the improper disposal of oily sludge and allowed estimating which variables, quantitative or qualitative, most affect the degree of the contamination of the site.

INTRODUCTION

The oil industry presents a potential risk of spillages of oil and its derivatives. From the oil fields up to the consumer, about a dozen of transfer operations can occur, involving tanks, pipelines, petrol tankers and railway cars. Accidents can occur during any of these stages involving the transfer, handling or storage of oil and its derivatives (Fingas, 2000). The majority of these spills results in soil contamination, causing human and environmental impacts. The contaminated sites need to be characterized in order to implement intervention or remediation strategies.

In order to evaluate the contamination potential, information is required on:

- the contaminant (type, physical state, volume leaked or improperly disposed);
- the propagation of contaminant in the environment (soil, water and air, with an emphasis on the soil);
- the possible resources that can be impacted (goods to be protected – human being, animals and the environment) and;

- other socio-cultural, geopolitical and technical and economic aspects (Lee et al., 2001).

After site characterization, a risk evaluation is carried out to choose the best strategy (technically and economically) for site remediation (Sharma and Reddy, 2004).

The definition of the contamination potential of a site depends on numerous variables with complex interrelationships, which makes the remediation decision a difficult task (Lee et al., 2001). The use of fuzzy logic (Zadeh, 1998) is especially suitable to such a decision making problem where the variables involved have quite distinct natures. Therefore, a fuzzy logic system was developed (Silva, 2005) in order to calculate the Priority Index for the Level of Contamination (PILC) of a site.

MAIN FACTORS AND VARIABLES

A general view of the main factors involved in the fuzzy classification system is presented in Fig. 1. Three factors must be present (USEPA, 1998) so that a site may be in risk to be potentially contaminated:

- Source, associated with the contaminant characteristics;
- Transport mechanisms, associated with the propagation forms of the contaminant: through soil, water (underground or surface), air and direct skin contact;
- Receptors or goods to be protected, associated to human beings, animals and the environment;

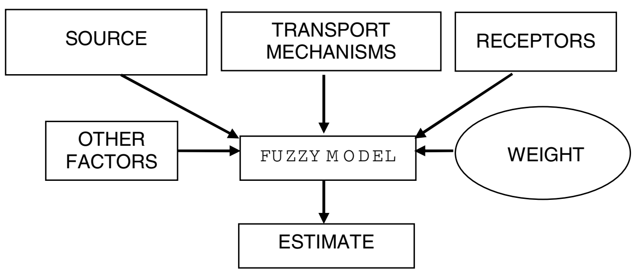

FIG. 1. General scheme of the proposed fuzzy classification system.

Other factors also contribute, but are not usually considered rationally to the remediation decision of a contaminated site (Veiga and Meech, 1994 and Silva, 2005). These factors, which are considered here, are related to socio-cultural, geopolitical and technical and economic aspects.

Each of these factors involves a number of related variables. Each variable has a weight associated to the potential contamination of the site. These weights, defined on the basis of knowledge and experience of specialists, are taken into account in the proposed fuzzy model in order to determine the potential contamination of the site.

All variables taken into account in the fuzzy classification system are summarized in Fig. 2 for each of the factors (Silva, 2005).

The contaminant characteristics factor can be described by the following variables: type of contaminant, spilled volume, impacted area and physical state of the contaminant.

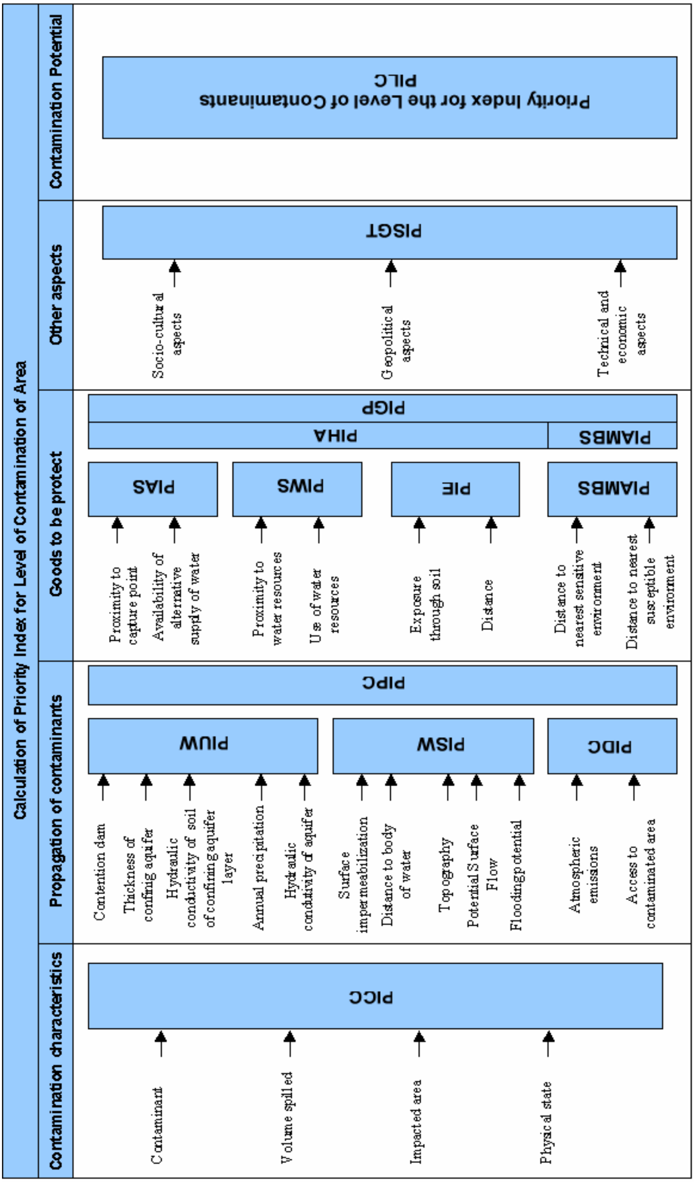

FIG. 2. Variables of the fuzzy classification system of the contaminated sites.

The contaminant propagation factor consists of the variables describing the contamination potential of the: soil and underground water, surface water and direct contact.

The goods to be protected factor is related to the health and welfare of the population, the fauna and flora, the quality of the soil, water and air, nature protection interests and landscape, urban territorial planning and structure, as well as public order and security.

Other factors cover socio-cultural, geopolitical and technical and economic aspects. Socio-cultural aspects include information on: educational level of the neighbouring community, its access to the means of communication and the existence of associations of residents or Non-Governmental Organizations (NGOs). Geopolitical aspects contain information related to the local environmental agency, political pressure and actions of the local District Attorney's office. Technical and economic aspects cover information on local availability of financial and technological resources.

The classification system described in this work is concerned with obtaining the Priority Index for the Level of Contamination (PILC) of the site. This number varies from 22.5 to 100 and determines the potential or level of contamination of the site by hydrocarbons. A PILC value close to 100 indicates a large contamination potential or level of contamination in the site, showing urgency for making decisions on the remediation of the contaminated site.

FUZZY CLASSIFICATION SYSTEM

The general structure of a typical fuzzy inference system (Hammel II, 1990) includes: the variable entry stage, the 'fuzzying' of these variables, the application of inference procedures on the basis of fuzzy rules, the process of the fuzziness and the output of the variables (Fig. 3).

The fuzzy sets have been determined based on the weight of each parameter, for each of the variables of each factor (contaminant characteristics, transport mechanism of contaminants, receptors and other factors). In other words, the fuzzy sets were determined based on the knowledge of specialists through the weights associated with each variable. To make the variables fuzzy, Eq. (1) was used:

$$A = \{x, \mu_A(x)\}, \forall x \in E \quad (1)$$

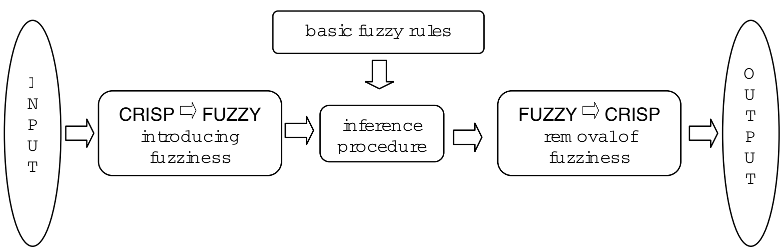

FIG. 3. General structure of a fuzzy inference system (Hammel II, 1990).

where $\mu_A(x)$ is denominated the "degree of relevance of x in A". For simplicity, $\mu_A(x)$ is assumed within the interval [0, 1], with 0 representing non-relevance and 1 total relevance, in a fuzzy set (Zadeh, 1998).

For each factor, the rules were determined based on the relationship, or possible combinations, between the variables involved. Based on these combinations, the value of the priority index is calculated for each factor. This is named fuzzy inference, which corresponds to the computation of its relevancies: aggregation (computation of the IF part of the rules) and composition (computation of the THEN part of the rules). For the aggregation, Eq. (2) and (3) were used and Eq. (4) was used for composition:

$$\textbf{AND}: \mu_{A\cap B}(x) = \textbf{MIN}\{\mu_A(x); \mu_B(x)\} \quad (2)$$

$$\textbf{OR}: \mu_{A\cup B}(x) = \textbf{MAX}\{\mu_A(x); \mu_B(x)\} \quad (3)$$

$$\mu_1(x)=\textbf{MAX}[FC_1.\textbf{MIN}(\mu_{A11}(x), \mu_{A21}(x),.., \mu_{Am1}(x)),.., FC_n.\textbf{MIN}(\mu_{A12}(x),..,\mu_{Amn}(x))] \quad (4)$$

Each rule possesses an individual weighting factor, denominated the Certainty Factor (CF), between 0 and 1, which represents the importance of the rule in relation to the others. In the system developed CF is taken to be equal to 1, in other words, all rules have the same importance in the calculation of the potential of each factor or variable.

The adopted process for removing fuzziness is the Method of Maximum Centre (Von Altrock and Krause, 1994) the value following the removal of fuzziness, or output, x^*, is obtained through Eq. (5), where $\mu_{o,k}(x_i)$ indicates the points in which the maximums of the functions relevant to the output occur:

$$x^* = \frac{\sum_{i=1}^{N} x_i \cdot \sum_{k=1}^{n} \mu_{o,k}(x_i)}{\sum_{i=1}^{N}\sum_{k=1}^{n} \mu_{o,k}(x_i)} \quad (5)$$

In this process, for each factor or set of variables in Fig. 2 the following priority indexes have been obtained:

(a) PICC, Priority Index of Contaminant Characteristics;

(b) PIPC, Priority Index of Progation of Contaminant, which is obtained through the sum of PIUW, PISW and PIDC;
- PIUW, Priority Index of Underground Water;
- PISW, Priority Index of Surface Water;
- PIDC, Priority Index of Directed Contact;

(c) PIGP, Priority Index of Goods to be Protected, which is obtained through the sum of PIHA and PIAMBS;
- PIHA, Priority Index of Human Being and Animals, in its turn is obtained through the sum of PIAS, PIWS and PIE;
  - PIAS, Priority Index of of Impact in Water Supply;
  - PIWS, Priority Index of Impact in other Water Resources;
  - PIE, Priority Index of Human Exposure;
- PIAMBS, Priority Index of Impact in the Environment;

(d) PISGT, Priority Index of Socio-cultural, Geopolitical and Technical and Economics Aspects.

The CubiCalc (1998) application possesses implemented routines for fuzzy inference and the removal of fuzzy variables. These routines are always used whenever there is a need to calculate the Priority Index.

The Priority Index for the Level of Contamination is finally calculated as:

PILC = PICC + PIPC + PIGP + PISGT (6)

In this equation, the three first indexes (PICC, PIPC and PIGP) have maximum scores equal to 30 and the maximum score for PISGT is 10, and therefore the maximum value of PILC is 100. The application of this system to sites suspected of contamination, or already contaminated, will determine a rank of prioritization which will assist in the decision making process on the intervention or remediation strategy for these sites.

ANALYSIS OF SYSTEM SENSITIVITY

To evaluate the sensitivity of the fuzzy classification system Silva (2005) analyzed different scenarios, through the simulation of four cases of contamination by oil and its derivatives, in an increasing order of potential contamination. Through the application of the fuzzy classification system to the scenarios, the values of the priority indexes, for each factor, have been calculated.

Fig. 4 presents, for the four scenarios analized, the evolution of each of the indexes PICC, PIPC, PIGP and PISGT. In addition, the evolution of the Priority Index of Level of Contamination is also presented in this figure. The increasing PILC values obtained for the scenarios are: 33.16 (case 1), 54.75 (case 2), 73.61 (case 3) and 93.16 (case 4). As far as the evolution of PILC is concerned, it can be observed that, as the contamination condition gets worse, the PILC value increases.

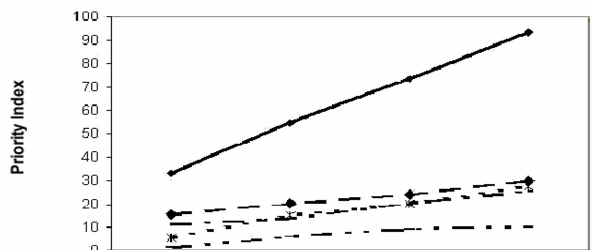

	Case 1	Case 2	Case 3	Case 4
PICC	15.4	20.27	24.16	30
PIPC	5.47	14.93	20	27.72
PIGP	10.96	13.55	20.35	25.44
PISGT	1.33	6	9.1	10
PILC	33.16	54.75	73.61	93.16

Scenarios

FIG. 4. Contribution of each priority index to PILC (Silva, 2005).

APPLICATION TO A REAL CASE

The fuzzy classification system has been applied to a real case, which involves the contamination of an industrial site in a refinery through the disposal of oily sludge directly on the soil (Silva, 2005). This oily sludge resulted from the cleaning of storage tanks for oil and its derivatives. The site analysed can be seen in Fig. 5. To the north of the evaluated site is Canal A, with a cement bottom, which runs through pipes to the natural drainage coming from Lake B to form Stream A. The processing area is to the north and to the northwest is the polishing pond of the unit which empties into Canal A.

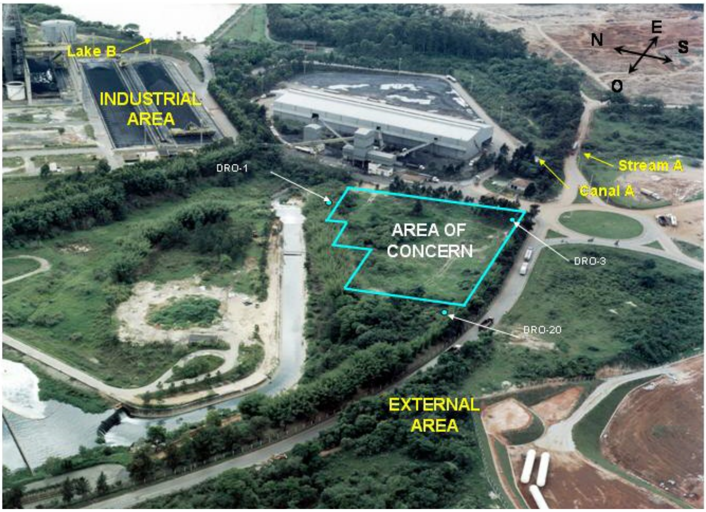

FIG. 5. Aerial view of the contaminated area and its surrounds (Silva, 2005).

Environmental evaluation studies carried out in this site concluded that it was contaminated by hydrocarbons and metals. These studies involved three phases: preliminary studies, exploratory studies and risk assessment. The preliminary studies were carried out based on historical data and information about the site usage. In the exploratory studies direct and indirect techniques were used for the proper formulation of the problem, with the identification of the contaminants, their propagation and the goods to be protected. The risk assessment consisted of an evaluation of the environmental risk.

The values of the variables adopted in the system were processed in the fuzzy classification system, and the results can be observed in Table 1. The overall score for the level of contamination (PILC) equal to 69.04 indicates that there is a need for an investigative process to confirm the contamination, especially due to the propagation of the contaminant by direct contact (PIDC= 10) and through underground water (PIUW= 6.36).

CONCLUSIONS

A procedure for the computation of a priority index for the level of contamination of sites contaminated with hydrocarbons has been developed. The proposed classification system uses fuzzy logic and considers four important variables, the contaminant characteristics, the contaminant propagation, the goods to be protected and other aspects. The latter are related to socio-cultural, geopolitical and economic questions and have not been considered in previous proposals due to difficulties in quantifying subjective aspects.

Table 1. Result of level of contamination of the contaminated site by oily sludge.

Priority Index (PI)	Possible score (minimum to maximum)	Score obtained
Contaminant characteristics (PICC)	8 - 30	**20.58**
Underground water (PIUW)	1.8 - 10	6.36
Surface water (PISW)	1.2 - 10	3.60
Direct contact (PIDC)	1 - 10	10
Contaminant propagation (PIPC)	4 - 30	**19.96**
Men and animals (PIHA)	3.7 - 16	9.27
Environment (IPMAS)	6.5 - 14	13.23
Goods to be protected (PIGP)	10.2 - 30	**22.50**
Other aspects (PISGT)	0 - 10	**6.0**
Level of contamination of the site (PILC)	22.1 - 100	**69.04**

The application of the fuzzy logic allowed estimating which variables, quantitative or qualitative, most affect the degree of the contamination of a site contaminated with hydrocarbons. Also, when a number of sites are contaminated, the procedure is able to rank the sites in terms of the priority for remediation.

A sensitive analysis was carried out so that the variables, parameters and their weights were assessed. Therefore, it is believed that proposed fuzzy classification system may be a useful tool for the decision making process in the strategy regarding the intervention or remediation of sites contaminated with hydrocarbons.

REFERENCES

Cubicalc (1994), “Manual of CubiCalc v. 2.0”, HyperLogic Corporation, California.

Fingas, M. (2000). “The Basics of Oil Spill Cleanup” (2nd Ed.), CRC Press LLC, Boca Raton.

Hammel II, R. J. (1990). “Fuzzy Logic*”, www.arl.mil, accessed on 08/08/2003*.

Lee, J., Cheon, J., Lee, K., Lee, S., Lee, M. (2001). “Factors Affecting the Distribution of Hydrocarbon Contaminants and Hydro Geochemical Parameters in a Shallow Sand Aquifer”, *Journal Contam. Hydr.*, vol. 50: 139-158.

Sharma, H. D., Reddy, K. R. (2004). “Geoenvironmental Engineering: Site Remediation, Waste Containment, and Emerging Waste Technologies”, Hoboken, New Jersey.

Silva, M. A. B.. (2005). “Fuzzy Classification System for Sites Contaminated by hydrocarbons (in Portuguese)”, DSc Thesis, COPPE/UFRJ, Rio de Janeiro.

USEPA (1998), “Guidelines for Ecological Risk Assessment”, *EPA/630/R-95/002F, 04/98.*

Veiga, M. M., Meech, J. A. (1994). “Heuristic Approach to Mercury Pollution in the Amazon” 123rd Congress of TMS, The Mineral, Metals and Materials Society, San Francisco, pp. 23-38.

Von Altrock, C., Krause, B. (1994). “Multi-criteria Decision Making in German Automotive Industry Using Fuzzy Logic”, *Fuzzy Sets and Systems*, vol. 63: 375-380.

Zadeh, L. A. (1998). “Fuzzy Sets, Information and Control”, vol. 8: 338-353.

A Framework for Decision Support System for Sustainable Management of Contaminated Land

A.A. Javadi[1], A. Bello-Dambatta[1], J.C Martin[2] and B. Evans[3]

[1] Computational Geomechanics Group, School of Engineering, Computer Science and Mathematics, University of Exeter, Exeter, EX4 4NA, Devon, UK
[2] School of Earth, Ocean and Environmental Sciences, University of Plymouth, Drake Circus, Plymouth, Devon PL4 8AA, UK
[3] Exeter Environmental Consulting Services, Harrison Building, New North Road, Exeter, EX4 4QF, UK

ABSTRACT: Due to increased environmental awareness and pressures from governmental policies, sustainable techniques are increasingly being employed for the reclamation and re-development of contaminated land. Addressing the complex issues involved in such a process requires knowledge from a number of multi-disciplinary fields. There are currently some Decision Support Systems (DSS) and tools available for this, but most have limitations – especially with the incorporation of sustainability appraisal. This paper proposes a framework for a multi-disciplinary DSS as a computer-based IT system for contaminated land management, based on current UK legislation. The proposed framework is theoretically explained with a real-life landfill case study and looks into the application of this framework within the UK regime.

Keywords: Decision support systems; contaminated land; management; sustainability

INTRODUCTION

The UK has a legacy of contaminated land as a result of its historic industrial past, which poses risk to humans, properties and protected resources such as surface and ground waters, flora and fauna, and the ecosystem as a whole. There is a need therefore to clean-up and redevelop these lands in an effort to protect human health and preserve the natural ecosystem and protected resources.

There is a surge of interest amongst industry, local authorities and practitioners in remediating derelict and contaminated land, given the UK government's target of at least 60 per cent of all new developments to be on previously developed land to ease the pressure of building on green-belts, as part of its sustainable development plans. A lot of these 'previously developed' lands are by definition, derelict or contaminated.

This project explores an integrated multi-disciplinary process for decision-making and proposes a framework for the sustainable management of contaminated land. Using this framework, a computer-based Decision Support System is being developed that should provide an integrated framework for easy access to modelling and data analysis tools.

UK CONTAMINATED LAND REGIME

Various national estimates have been made on the amount of contaminated land in the UK, which has varied considerably over the years as definitions and contexts evolved. The Environment Agency (EA) in its 'State of the Environment' Report in 2000 estimated that there may be as many as 100,000 sites affected by contamination in England and Wales (EA 2000) alone. Between 5 and 20 per cent of these were thought to require action to ensure that unacceptable risks to human health and the environment are minimized (EA 2002) or eliminated.

Due to the diversity of awareness, interests, concerns and priorities, there has always been a controversy surrounding the definition of contaminated land (Martin 2001). This is mainly because of geographical, financial, social and political interests through a wide range of disciplines, especially within the environmental and engineering fields.

The European Union is moving towards European wide standards derived mainly from the legislations of European nations (Germany, Denmark and Holland) with leading environmental legislations (Kiely 1997). The UK, like most of the North-West EU member states already has its own environmental management policy in place, which is far ahead of any current EU policy. For example, the new EU Directive, *2004/35/EC*, on Environmental Liability with regard to the prevention and remediation of environmental damage required that all member states introduce the directive into their legislation by April 2007. The UK had already introduced statutory regulations covering this in its current Contaminated Land Regime which came into force in April 2000. Under the EC treaty, the UK is free to go beyond the minimum requirements laid down by the Directive.

The UK contaminated land regime is covered in Part IIA Environmental Protection Act (EPA) (DEFRA 2006). This sets out a joint regulatory role between the EA and Local Authorities (LA) to deal with historically contaminated land by assessing, identifying and remediating contaminated land where there is an identifiable and significant risk.

The main underlying principle of the regime is a risk-based assessment and remediation approach with emphasis on human and ecological risks. This legislation incorporates both the '*polluter pays principle*' where liability for clean-up falls on person(s) that caused or knowingly permitted the presence of the contaminants, and the '*suitable for use'* approach which takes into account cost-benefit considerations, in line with the government's sustainable development policy that encourages ways of responsibly dealing with increasing land use pressures (DETR 2000).

Also key to this legislation is the *pollutant-linkage* concept between a contamination source and a receptor, where one must exist to render land contaminated. In order for land to be considered contaminated, there must be a 'contaminant (source)-pathway-receptor (target)' linkage present, which poses a 'significant harm'. In retrospect therefore, not all contaminated lands are considered to be contaminated or need to be cleaned up – by legal definition at least!

In August 2006, Part IIA was modified and extended to cover radioactively contaminated land. As with other forms of land contamination, the Environment Agency (EA) and local authorities are jointly responsible for this new extension. The EA provides an overview of their responsibilities; with guidance and a framework for local authorities on how to effectively deal with it. Also, as with other contaminated land legislations, this extension supplements, not replace the existing UK Radioactive Substances Act 1993.

All these multiple objectives to be satisfied against multiple criteria and the wide range of professionals and practitioners involved make management of contaminated land a complex and uncertain multi-disciplinary task that draws expertise from a broad range of fields.

DECISION SUPPORT SYSTEMS AS SOLUTION

Decision Support Systems (DSS) and tools have been used for a long time to assist with effective, affordable and feasible management options. DSS are tools that aid decision-makers arrive at effective decisions with alternatives, without replacing any underlying heuristic human reasoning and expertise. A decision is a choice between alternatives, where each alternative represents a different course of action, based on certain criteria (Feoli c2003). These decisions are based on a set of rules that determine the best course of action.

DSS make use of powerful Decision Analysis (DA) techniques and processes, by incorporating quantitative, qualitative and progressive analytical methods (sometimes a hybrid of these). DA is a multi-disciplinary field that deals with matching the most suitable tools, methodologies, techniques and theories to relevant decisions. In terms of contaminated land management DA, a broad range of DA techniques are used. The most widely used technique are Multi-Criteria Decision Analysis (MCDA) (Hämäläinen, Kettunen et al. 2001; Semenzin, Critto et al. 2005; Critto, Agostini et al. c2002) and Bayesian Decision Analysis – and their derivatives – as they take into account all the complexities involved with contaminated land DA and decision-making, including all multiple and often very conflicting criteria and objectives involved (Kiker, Bridges et al. 2005), that are very typical in the currently important environmental issues (Hämäläinen, Kettunen et al. 2001).

In the past decade, the use of computer-based systems in support of decision-making in environmental management has increased dramatically (Xuan, Richard et al. 1998). The role of DSS in geotechnical and geo-environmental engineering, in terms of contaminated land management is to assist decision maker(s) and managers arrive at relevant, effective and feasible scientifically sound solutions to contaminated land problems, within a reasonable time frame. DSS developed for contaminated land management have simulation and optimization modeling components to help decision makers make informed decisions and also provide alternatives solutions.

CURRENT SYSTEMS

Environmental Decision-Making (EDM) is a complex, non-linear, time intensive process usually with high cost overruns that depends on a diverse range of inputs from industry, civic communities, researchers and government officials in the form of policy makers and regulators, with multiple objectives against multiple criteria; and resource constraints. This diversity calls for a need in understanding and incorporating the various multi-disciplinary processes and techniques across all interests.

Collating, aggregating and processing complex information for decision-making in several formats and using it to aid in decision support is impossible for any one expert or group of stakeholders and requires not only expertise but analytical and simulation models, techniques and collaboration within a group structure.

Also, with the increasing trend towards grassroots environmentalism and governmental legislations on transparency to all stakeholders involved, more and more people from all walks of life are getting involved in environmental decisions that they may not necessarily understand, but hugely impact. As a result, DSS for the dissemination of information and management of environmental problems are being developed.

A lot has been done computationally for contaminated land management. Projects within the European 4th and 5th frameworks especially have contributed a lot recently, with tools and systems developed for help in dealing with important components of contaminated land management, especially with cost-benefit analysis, feasibility studies, and remediation technology selection. A lot of these tools come with powerful simulation models.

The move of DSS development and deployment from model and knowledge-driven systems to service-driven (with a hybrid of other types in most cases) has some obvious advantages. There is no catch – organizations no longer have to buy dedicated hardware to run bespoke software that they have to commit to, for financial and practical reasons. With service-delivery alternatives, software is available as a service, so organizations have the flexibility of subscribing and using on a pay as you go basis. Also, no installation is necessary, so all organizations need is a thin-client to be used for accessing, as all processes execute on a centralized remote server managed by the service owners.

However, despite all these advances, the full potential of the technologies have yet to be fully realized as most systems are hard to use (MacEachren, Cai et al. 2005). In most cases, the system user interface is inaccessible as human-computer interaction considerations have not been taken into account during development. Also, a lot of these systems tend to be expert, windows-based, discipline specific and non-intuitive, and therefore unusable to the other (possibly lay) decision makers, who may play a key role in any EDM. Even the expensive commercial and proprietary alternatives tend to be bespoke, and run on dedicated hardware. It is not surprising then that a lot of decision makers have not really adopted these systems. Decision-makers are more interested in results and not the problem solving processes, and expert and assisting systems to be automated, and ubiquitous (Yan, Xiao et al. 1999).

Recent techniques, especially those of Web-based DSS (WebDSS), take into account all of these short comings, and as a result a new breed of DSS aimed at contaminated land DM are emerging. Technologies of Group DSS (GDSS), Collaborative DSS (CDSS) and Spatial DSS (SDSS) are hybridized and deployed over the Web, using accessible thin-clients (e.g. mobile tablet PCs, PDA, Internet Browsers et cetera) as a front-end where data and information are more distributed and accessible to all parties involved.

SUSTAINABLE MANAGEMENT

The sustainability ideology is not new, and has had widespread applications and implications over the years. It is not an academic discipline as of yet however, and as a result its definitions and applications are quiet subjective and used differently in different fields and contexts.

Due to increased societal environmental awareness and pressures from governmental policies, sustainable technologies and methodologies are increasingly being employed for management of contaminated land. To address the complex issues involved in such techniques requires knowledge from a number disciplines.

With the current mainstream surge of interest in the effects of 'our' activities on earth, research interest into sustainable alternatives is increasing. The implications of these effects, their causes and impacts call for a sustainable framework that not only immediately minimizes these impacts, but also progressively provide long term sustainable alternatives.

In terms of environmental sciences and thus contaminated land management, sustainability is geared towards '*dealing with current problems in such a way future generations are not compromised*' as defined by the Brundtland Commission, convened by the United Nations in Norway (UN 1987). Decision Support Systems (DSS) offer a platform for the incorporation of sustainability appraisal in contaminated land management decisions.

FRAMEWORK FOR DECISION SUPPORT SYSTEM

A '*Collaborative Group Web-based Spatial DSS'* is currently being developed using an integrated multi-disciplinary approach incorporating UK statutory and non-statutory regulations and guidelines with industry best practice approaches. This DSS is intended to address the insufficiencies and problems we've found with current available systems (addressed above) by developing a functional DSS as a platform that fully integrates and synergizes all components necessary for effective management of contaminated land.

The DSS will aid planning and decision making processes by providing useful and scientifically sound information to a wide range of stakeholders as a support tool to aid with effective management by providing guidance and support, alternatives, options and comparisons of technologies within a reasonable time frame. The DSS will be able to deal with all multiple objectives, criteria, uncertainties, and non-linearities associated with contaminated land management; and act as a portal for the dissemination of information across all interested parties and for knowledge transfer between all professionals involved.

The DSS will provide an integrated framework for easy access to advanced tools of data analysis, simulation and optimization modeling, risk assessment and multi criteria, objective decision support for a broad range of contaminated land management problems. Strong emphasis will be on data analysis and decision-making techniques, and not modeling per se. There is a common misconception amongst practitioners that models are decision support tools, while they are merely input tools that help visualize data. Previously developed standardized and Open Source models are being reviewed during the development phase of the system and integrated into new models currently being developed.

The DSS is based on current UK legislation as set out by Part IIA EPA 1990. Although there are provisions in EU directives, it is felt that present UK legislation is more comprehensive. In addition, there have not been any integrated DSS developed so far specifically based on UK legislation, at least in academia and the public domain. The system will have a strong emphasis on sustainability the sustainability component of the system is based on the Elkington triple-bottom line model that takes into account three factors for accountability social, economical and environmental (Elkington 1997). Sustainability has so far been under explored in contaminated land research and has not really been incorporated into computer-based systems. This DSS offers a platform for complete sustainability appraisal in contaminated land management decisions.

The system will have 6 main components (FIG.1): ***1***) site characterization for site assessment, reconnaissance and investigation; ***2***) a GIS component for visualization and representation of spatial data; ***3***) risk assessment component in line with Part IIA; ***4***) remediation technology component for the selection and comparison of clean-up methods; ***5***) cost-benefit analysis component; and finally ***6***) a sustainability appraisal component to consolidate all findings of the other components and recommend a decision based on a defined sustainable criteria.

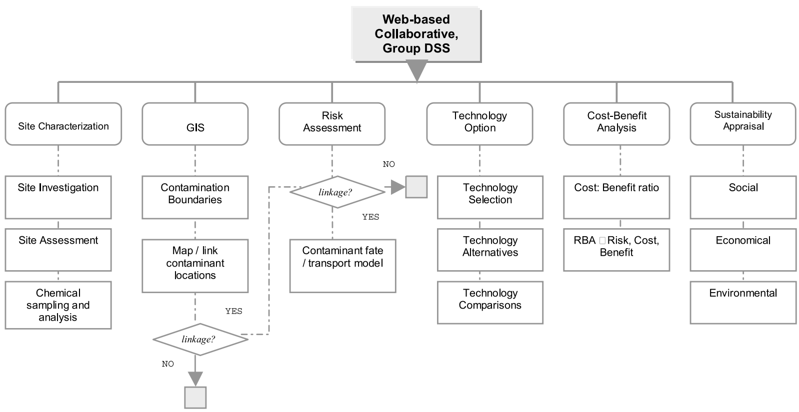

FIG. 1 - Components for the Decision Support System

The system architecture (FIG. 2) will be based on a 3-tier client server architecture with GIS, DSS and Knowledge base servers and a Graphical User Interface client communicating with TCP/IP over HTTP. The system end-users will communicate with the system with a standard Internet browser.

This framework could be better explained using a real life case study to explain one of components of the system to put the applications of the project in context. The sustainability appraisal component (see FIG. 1) which is the core of both the project and the system helping a DM arrive at the most sustainable decision, taking into account the three criteria of economic, environmental and societal coming up with and recommending the most balanced decision.

This framework could be better explained using a real life case study to explain one of components of the system to put the applications of the project in context. The sustainability appraisal component (see FIG. 1) which is the core of both the project and the system helping a DM arrive at the most sustainable decision, taking into account the

three criteria of economic, environmental and societal – coming up with and recommending the most balanced decision.

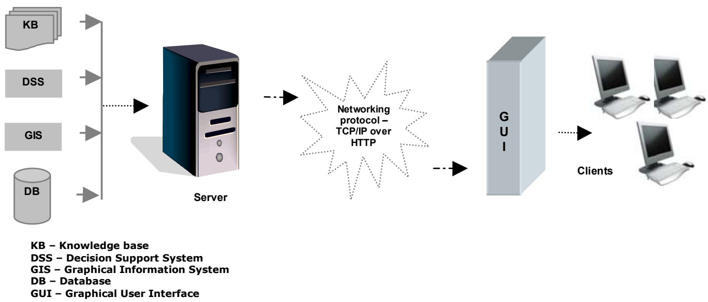

FIG. 2 - DSS architecture

The case study is of an old petrol filling station and garage repair (FIG. 3) that is in the process of being decommissioned and remediated. A site investigation, reconnaissance and assessment were first carried using the EA risk-based approach, which identified the contaminants present, their sources, pathways and receptors. Using this information, a conceptual model of the site was developed. Remedial target concentrations for soil, surface and groundwater were set based on the then current Dutch Intervention Values (*DIV* – 1994) as there where no UK equivalents at the time. All relevant information and data were then analyzed and based on that it was decided that site should be able to naturally remediate with time without posing any undue risks, and therefore Monitored Natural Attenuation (MNA) will be sufficient as a remedial technology.

Boreholes were installed at the station and within its boundaries for monitoring water and gas samples, soil was collected by drilling (at the surface) and dipping (below the tanks), and samples were collected from nearby streams for surface water monitoring and testing. The sampling and testing will continue for sometime therefore, until all tests return satisfactory (at least to original background levels).

Our framework proposes a more ubiquitous and transparent approach at decision making that is user-friendly and accessible to all parties involved at all times – taking into account all risks, uncertainties, complexities and all defined sustainability criteria. After the initial site investigation and assessment phase, all monitored and observed data could be fed into the system using the site investigation component. The system will then map this information into the GIS component which should help a DM with not only defining site boundaries but also mapping out key contaminant locations, concentrations and depth information, visualized all at once onscreen, making identifying pollutant-linkages not only easier, but helping with a more precise and effective risk assessment process.

As a requirement of Part IIA, if a linkage has been identified, as with this case study, the site will be considered contaminated and therefore further action will be required to effectively either clean-up or contain (sealing / barrier) the contaminants. Our framework proposes a sustainable way of tackling this by finding a balance between the economical, environmental and social criteria defined – taking into account Part IIA suitable for use approach.

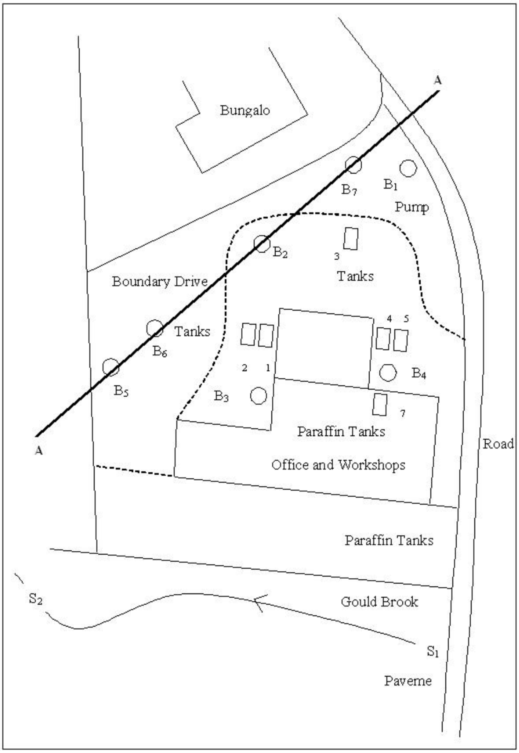

FIG 3 - Site plan

The data and information collected could then be added to the system to model contaminant fate and transport – and depending on how comprehensive the data and information is, be able to possibly project future contaminant behavior. Using all these information entered into the system so far, the technology selection component could be used to determine the most sustainable option the particular site. This is site specific and takes into account the topography; the historical, present and intended future use; and type(s) of contamination of the site et cetera.

Also in line with Part IIA suitable for use approach, a cost: benefit analysis will then be done, which determines whether the long term benefit of the remediation outweighs the cost, taking into account overall management and remediation time, overall costs and benefits, technical effectiveness, emissions and other waste generated et cetera. Finally, all these results will be consolidated into the sustainability appraisal component (the core) which should use a DA (MCDA) be able to help recommend the most sustainable viable decision alternatives.

CONCLUSIONS

Approaches to decisions for contaminated land management have changed rapidly over the past three decades, evolving from simple hazard assessments, to cost-centered approaches of the 1970s, technology feasibilities of the 1980s, risk-based approaches of the 1990s through to sustainability appraisals in the new millennium (Pollard, Brookes et al. 2004).

The ubiquitous nature of the web and the its simple and intuitive user interface has made possible the deployment of complex applications such as SDSS over the web (Sugumaran and Sugumaran 2005). So many companies, organizations and developers offer interactive web-based mapping services for decision-making purposes, indicating a new paradigm shift in decision support technologies incorporating GIS, GPS and other technologies over the Internet using the Web as a front-end.

Using our Web-based DSS, the whole process should be automated and the system should be able to help simulate and project future results based on already collected data. This depends on how complete and correct the data used is. The DSS should be able to use the GIS component to map and link all contaminant locations and boundaries, quickly determining if there are any risks posed. If there are, then the system should be able to use contaminant information already entered to model contaminant fate and transport and recommend the most sustainable alternative that should effectively deal with the contamination.

The system should also, based on the type of contamination present, be able to offer other suitable alternatives that a decision maker might consider due to cost and / or time constraints. All this will be deployed online – so decision maker(s) can access it from anywhere, anytime.

REFERENCES

Critto, A., P. Agostini, et al. (c2002). "The role of Multi-Criteria Decision Analysis in a DEcision Support sYstem for REhabilitation of contaminated sites (the DESYRE software)." Retrieved 2006, December, from http://www.iemss.org/iemss2004/pdf/dss2/carlther.pdf.

DEFRA. (2006). "Environmental Protection Act 1990: Part 2A." Defra Circular Retrieved Oct. , 2006, from http://www.defra.gov.uk/environment/land/contaminated/pdf/circular01-2006.pdf.

DETR. (2000). "National land use database-final estimates of previously developed land in England: 1998." Retrieved March, 2007.

EA (2000). The state of the environment of England and Wales: the land. London, The Stationery Office Ltd.

EA. (2002). "Dealing with contaminated land in England." Retrieved Jan., 2007, from http://www.environment-agency.gov.uk/commondata/acrobat/dealing_with_contaminated_land_i.

Elkington, J. (1997). Cannibals with Forks: Triple Bottom Line of 21st Century Business, Capstone Publishing Ltd.

Feoli, E. (c2003). "Decision-support systems (DSS) and Spatial DSS." Retrieved June, 2007, from http://www.ics.trieste.it/Documents/Downloads/df2278.pdf.

Hämäläinen, R., E. Kettunen, et al. (2001). "Evaluating a Framework for Multi-Stakeholder Decision Support in Water Resources Management." Group Decision and Negotiation **10**(4): 331-353.

Kiely, G. (1997). Environmental engineering. London, McGraw-Hill.

Kiker, G. A., T. S. Bridges, et al. (2005). "Application of Multicriteria Decision Analysis in Environmental Decision Making." Integrated Environmental Assessment and Management **1**(2): 95–108.
MacEachren, A. M., G. Cai, et al. (2005). "Enabling collaborative geoinformation access and decision-making through a natural, multimodal interface." International Journal of Geographical Information Science **19**(3): 293-317.
Martin, J. C. (2001). A knowledge-based system for assessing contaminated land. School of Engineering. Durham, Durham. **PhD**.
Pollard, S. J. T., A. Brookes, et al. (2004). "Integrating decision tools for the sustainable management of land contamination." Science of The Total Environment **325**(1-3): 15-28.
Semenzin, E., A. Critto, et al. (2005). "ERA-MANIA DSS: a decision support system for site-specific Ecological Risk Assessment (ERA) for contaminated sites." Retrieved January 2007, from http://venus.unive.it/eraunit/complement/ERA-MANIA%20project.pdf.
Sugumaran, V. and R. Sugumaran (2005). Web-based Spatial Decision Support Systems (WebSDSS): Evolution, Architecture, and Challenges. Third Annual SIGDSS Pre-ICIS Workshop. Designing Complex Decision Support: Discovery and Presentation of Information and Knowledge Las Vegas, Nevada.
UN. (1987, 11th Dec. 1987). "Report of the World Commission on Environment and Development." Retrieved April, 2007, from http://www.un.org/documents/ga/res/42/ares42-187.htm.
Xuan, Z., G. H. Richard, et al. (1998). "A Knowledge-Based Systems Approach to Design of Spatial Decision Support Systems for Environmental Management." Environmental Management **22**(1): 35-48.
Yan, S., C. Xiao, et al. (1999). Spatial Decision Support System and its General Platform. Towards digital Earth — Proceedings of the International Symposium on Digital Earth.

Non-Compliant Setback of Existing Buildings From Sloping Ground Geotechnical and Legal Ramifications

Vishnu Diyaljee, F.ASCE, P.Eng

Managing Director, GAEA Engineering Ltd, 2408 113 A Street, Edmonton, Alberta, Canada, T6J 4Y2; diy001@gaeaeng.com

ABSTRACT. A single-family residence built in 1983 near the crest of a 105 m deep valley with a creek at its base was deemed non-compliant in 2006 based on the County's setback By-Law. As a result, "an acceptable geotechnical study" was required to demonstrate that the County's setback requirement could be relaxed. The geotechnical study was undertaken using visual inspection, aerial photo interpretation, past setback studies in Alberta and judgment since drilling, installation and monitoring of instrumentation would have been time consuming and costly. Although the geotechnical study showed that the site was stable and the setback could be relaxed, an annual inspection (changed to bi-annual by the County) was recommended to guard against possible future changes in site conditions. The landowner rejected this inspection requirement and initiated legal action against the County in February 2007. This case study demonstrates some of the geotechnical and legal ramifications associated with a building deemed non-compliant (23) years after its construction.

INTRODUCTION

The single-family residence is situated in the County of Northern Sunrise near the Town of Peace River, Alberta. The property on which the residence is located, Fig.1A, is bounded on its north and north-west by the Kauffman Hill Road and on its south and southeast by the south valley slope of Pat's Creek. Fig.1B is a blowup of the property showing the residence and associated buildings.

FIG.1. Location of Property

FIG.1B. Blowup of Property

Fig. 2 shows a part-plan of the Real Property Report done on July 19 and 20, 2006 by an Alberta Legal Survey Company on behalf of a prospective homebuyer and property owner. Pertinent features were – depth of watercourse 105 m from top-of-bank and setback of residence 16-32 m from top-of-bank.

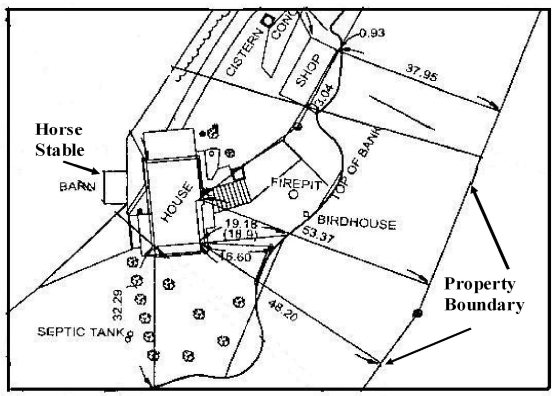

FIG. 2. Part Plan of Surveyor's Real Property Report

On August 3, 2006, the County advised the prospective homebuyer "Based on the Alberta Land Surveyor's Real Property Report with the "***Top of Bank"*** 105 m, the minimum building or structure setback is to be 60.1 m (200 ft)". The existing structures including, house, shop and barn do not meet this requirement thus they are non-conforming use of the land." Subsequently, the homeowner made a presentation to the County Officials to persuade them to enact the "Notwithstanding Clause" of the County's By-Law B008/02 whereby the Development Authority may alter the building or structure setbacks where deemed necessary. This By-law also stated, "A setback from a coulee, ravine, or valley may only be relaxed when it can be shown through an acceptable geotechnical analysis that the proposed development site is suitable for the proposed development".

GEOTECHNICAL ENGINEERING INPUT

General

With the likelihood of the County's decision not to grant a relaxation of its setback requirement, and the inability to sell the property otherwise, the homeowner engaged the services of an Alberta based Geotechnical Consultant, on August 20, 2006. The Geotechnical Consultant sought clarification from the County on the nature of the acceptable geotechnical analysis. This led to the understanding that the type and extent of geotechnical analysis was the prerogative of the Geotechnical Consultant and that the County would, on receipt of the geotechnical report, determine whether it was satisfactory for their needs.

Historic Geotechnical Information

In October 1979, a soils investigation was undertaken within the landowner's property situated in S.E. 1/4-5-84-W.5 by an Alberta based Consulting Engineering Company for the purpose of determining the near surface soil profile to provide recommendations for the suitability of constructing a single family residence. Three (3) testpits were dug with a backhoe, each to a depth of 4 m. In general, the soil stratigraphy consisted of predominantly sandy silts and/or silty sands, which were free draining. These pits were dry conditions during and on completion of excavating. The sandy and silty nature of the soils in the testpits was considered in the geotechnical report, "a good aspect to keep the upper soil strata drained thus eliminating the potential of a water table causing slipping problems".

The Testpit #3 location presented the most acceptable conditions for housing construction in comparison to the locations at Testpit #1 and Testpit #2, which were less desirable because of a clay layer and steep slopes to the south and east, respectively. While the slopes were steep to the east of Testpit #3, they were not as steep or as long, and old slide blocks below the property appeared to be stable. The Lot 2 site, Fig. 2, was eventually chosen for the construction of the residence.

Site Inspection - September 2, 2006

A site reconnaissance was undertaken on September 2, 2006. The site constituted the uppermost level of the valley slope with the ground sloping to the south from the house gently at an approximate slope of 50:1 to the crest, Fig. 3. Immediately below the crest, the slope was around 1:1 for about a 7 m drop, Fig. 4. Because of the steepness and treed nature of the slope beyond the 7 m drop, Fig. 5, only a partial reconnaissance was undertaken. The Shop located to the northeast of the residence is very close to crest of the valley slope, which drops steeply to the east, Fig. 3. An old isolated small erosion slump was visible, along the northeast slope near the Shop.

FIG. 3. Residence

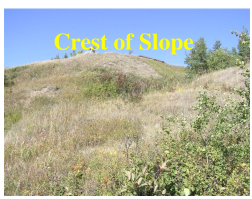

FIG.4. View of 1:1 Slope

FIG.5. Trees to Creek

FIG.6. S.W From Crest

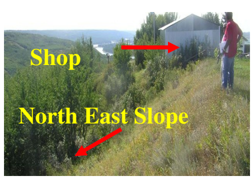

FIG. 7. Shop near Slope

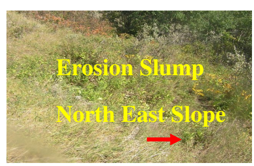

FIG.8. Old Slump

On the residence itself, rainwater leaders were attached to eavestroughs to discharge rainfall and snow melt runoff to troughs for watering a garden and for consumption by the horses, Fig. 9. The leader on the east side of the residence was linked underground to a corrugated steel pipe cistern that was used for domestic water supply consumption prior to the residence being serviced with piped water. Water from this cistern is used to water a garden on the east side of the house. A septic system located to the south west of the residence showed the outlet pipe to be broken, Fig. 10.

Review of the interior of the residence, which consisted of a walkout basement, showed no visible signs of any cracks along window joints, wall corners, interior and exterior walls. However, there was a noticeable horizontal crack in the concrete driveway pad leading to the garage door. This crack was not associated with any slope instability problem but rather with normal concrete shrinkage. Based on these observations and the fact that the house was built about 23 years ago indicated that the ground on which the house is built was in a visually stable condition.

FIG.9. Rain Water Leaders at Front, Rear and East Sides of Residence

FIG.10.Underground CSP Cistern, Sewer Tanks, Broken Discharge Pipe

Further Correspondence From County

On September 5, the County provided comments to the homeowner in relation to the acceptable geotechnical analysis as follows (sic). "From our review of this issue that ordinarily a geotechnical analysis would include on-site testing (i.e. Test Holes) in order to analyze the slope stability and analysis of the test results; if your Geotechnical Engineer is of the view that on-site testing is not warranted, then your Geotechnical Engineer should be willing to take responsibility for that decision. Further, we would also suggest that the geotechnical analysis would contain representations:

a) "That the development proposed in the development permit application is feasible from a geotechnical perspective;

b) That no negative impacts on the slope (or the lands in the vicinity of the proposed development) are envisaged as a result of the development; and
c) Outlining appropriate conditions/recommendations in relation to the proposed development (such as restrictions or prohibitions relating to vegetation, surface water discharge, underground sprinkler systems, septic systems, fill placement

However, we stress that these are general comments only, and the County reserves the right to review the scope and nature of the geotechnical report on receipt of the same."

GEOTECHNICAL EVALUATION AND ASSESSMENT

Based on the site review and in view of the County's letter, it was decided that the geotechnical evaluation and assessment would be based on the observational approach, and involve aerial photo interpretation and setback analysis.

Aerial Photo Interpretation

Stereo pairs were examined from aerial photos of the site taken during 1949, 1951, 1979, 1983 and 2004. It was evident from the review that the homeowner's land was bounded by old landside topography, which dominates the north and south valley slopes of Pat's Creek up to the crest of slope on which the homeowner's house is situated. To the north of the house, the Kauffman Hill roadway is situated along a hogs back with old slide scars along its downhill slope. This slope forms the east valley slope of the Peace River. This observation of old slide activity near the site confirms the description provided in the 1979 geotechnical report.

It is of interest to note that the aerial photo review showed that over a 54 year period from 1949 to 2004 the disposition of the north slope determined from super positioning 1949 and 2004 aerials to the same scale was essential the same at the crest and along the valley slope to Pat's Creek.

Setback Analysis

As a further geotechnical evaluation of the stability of the valley slope, the suggested approach in determining setbacks of buildings from rivers, which utilizes the ultimate angle of a stable slope (De Lugt et al 1993). It was determined from this study that the ultimate slope angles ranges from 8 - 26 degrees for overburden slopes, 6-17 degrees for bedrock based slopes and 7.5 to 14 degrees for bedrock slopes. The bedrock based and bedrock slopes have similar ranges of ultimate slopes, reflecting the performance of Upper Cretaceous bentonitic shales and sandstones in Alberta. Since the Peace River bedrock geology is quite similar in nature to that encompassing the case studies, the bedrock ultimate angles of the De Lugt et al paper was used as a basis for evaluating the ultimate angle of the north valley slope of Pat's Creek.

In the absence of any topographical survey of the north valley slope, Google Earth was used to determine the distances and elevations along the slope. The slopes at the residence, Shop and sewer tank locations, respectively, along three cross sections, Fig 2. The cross section at the residence location is shown in Fig.12 near the homeowner's residence. Overall, these overall slopes ranged around 9 to 10 degrees, which fit in the range for bedrock and bedrock based ultimate slope angles suggested by de Lugt et al (1993). The slope angles downhill to the roadway were also in the same order of magnitude. This finding along with the site reconnaissance observations of no cracks further reinforces the overall stability of the site over the years.

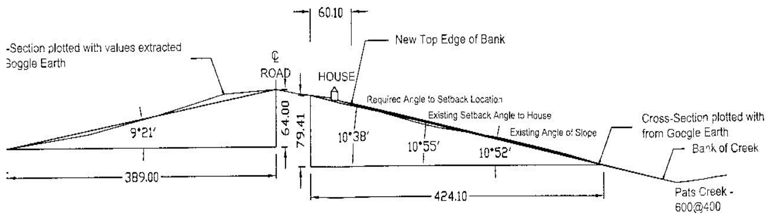

FIG.11. Cross-Section at Residence location

RECOMMENDATIONS FOR THE EXISTING DEVELOPMENT

Sewer Effluent Disposal

The sewer system showed a broken end section and some bank erosion caused by effluent discharging onto the break of slope. Based on discussion with the homeowner, the bulk of effluent is removed from the sewer tanks on a 6-month cycle. While the erosion did not appear to be significant, it was important to prevent any further erosion from continuing. A preferred method was the creation of a filter field by allowing the effluent to discharge from a perforated pipe at the outlet end into gravel bedding. This would allow the effluent to disperse within the gravel and avoid effluent discharging as a pipe flow at the outlet end as is presently occurring.

Rainfall and Snow Melt Precipitation Runoff Disposal

The present system of collecting rainfall and snow melt precipitation from the buildings- houses and barn has been working well over the last 23 years and should be maintained. However, if new homeowners would have no requirement for horses, then the rainfall and snowmelt runoff can continue to be collected in the trough systems or can be removed via a pipe system buried at a shallow depth in the ground with its outlet terminated in a soakaway system similar to that as suggested for the sewer effluent discharge. The pipe system would be constructed with materials and methods that would prevent any leakage at the joints before reaching the soakaway.

Integrity of the Cisterns and Underground Piping

The cisterns being of Corrugated Steel Pipe (CSP) are to be checked for corrosion and possible leakage. Leakage underground is not desirable and leads to instability with time. An alternative would be to plug the cisterns since this storage is only used for watering the gardens around the house. Any underground piping would need to be checked, as well, for possible leakage.

Changes to Topography and Present Use of Land

Since the existing land within the boundaries of the homeowner's property has been stable for the last 54 years, no changes are recommended that would incur earthwork cutting and filling beyond the break of the crest or on the crest itself. No additional buildings or additions are envisaged except, perhaps, in the horse corral location. Permission for any such constructions would have to satisfy the requirements of the County. Any such building development that would require soil being removed for example by excavation for a walkout basement of similar construction to the homeowner's residence would have to be taken away from the site as was recommended in the 1979 Geotechnical report.

As before, all run off water and sewage disposal systems have to be properly constructed to avoid concentrated water discharging in or onto the land. Such new or additional constructions would require site specific geotechnical investigations. At no time, whatsoever, is fill material imported from other sources to be brought in and placed on the existing land on the crest level or downslope of the crest. Further, vegetation growth down slope of the crest should not be removed by cutting or deliberate burning. The grassed lawn of the grounds around the residence and buildings should not be changed to a concrete or paved surface, as this would allow runoff to be more concentrated down slope if allowed to follow the grade of the land. If a change to the ground surface is contemplated then runoff needs to be carefully directed away from the slope.

Future Inspection of Property

An annual inspection of the property is recommended since with climate changes that appear prevalent today are no way to determine whether stability that exists at the time of the geotechnical evaluation can be assured indefinitely in the future. While this may seem restrictive given the good behaviour of the site over the last 54 years, litigation aspects require a 10-year period of responsibility by the Geotechnical Consultant in this case.

GENERAL DISCUSSION AND LEGAL ISSUES

The recommended annual inspection of the site was modified to a bi-annual one by the County. This requirement, however, was considered restrictive by the homeowner as this presented an additional cost, which would detract potential homebuyers from purchasing the residence by giving the impression that there was an impending problem. As a result, the homeowner refused to sign the second Development Permit, since this permit contained the stipulations outlined in the geotechnical report. However, while the County Officials were sympathetic to the homeowner's problem, they were not willing to relax the inspection requirement.

The question of whether there is a moral obligation on the part of the County to be responsible for some of the past events that allowed the residence to be constructed despite its non-compliance has been and continues to be a debatable one. Prior to its becoming the County of Northern Sunrise, the County was known as the Municipal

District (M.D) of East Peace #131 and Improvement District (I.D) #17. The Development Permit was granted on April 26, 1983 when the County was an I.D. As well, on May 18, 1983, the I.D issued a letter to the homeowner with contents as follows “Upon reviewing your application for development permit which we have granted, it would appear that the location of the home is too close to the embankment. We would ask you to adhere to the following setbacks regarding your proposed residence. The side facing on to the coulee should be 200 ft back from the edge of the Coulee. As you can see this setback is necessary to protect your residence from the unstable condition of the embankment”.

It should also be noted that setback requirements of other jurisdictions were also stipulated in the Development Permit, which along with the proposed 60.1 m setback would have resulted in the inability to construct a residence that was fully compliant with the regulations. It was somewhat surprising that with this understanding nothing was done by the I.D to prevent the construction of the residence.

SUMMARY AND CONCLUSION

After its construction approximately 23 years ago, a single-family residence situated near the crest of a valley slope was deemed non-compliant with the County’s By-Law for buildings near to watercourses and water bodies because of insufficient setback distance. In order to waive the By-Law requirements, the County requested an acceptable geotechnical study to be undertaken. This geotechnical study involved visual observation, aerial photo review and evaluation of setbacks from rivers based on research in Alberta.

The lack of any distress to the residence, absence of visible cracks within the top of slope and downhill of the slope, absence of changes in slope shape over the last 54 years confirmed that the slope has achieved an ultimate slope angle. In this condition, the existing setback of the residence was considered satisfactory and acceptable. Nonetheless, geotechnical recommendations were made to ensure that land use remained status quo to preserve the existing stability of the property in relation to the existing homeowner and any future buyers. The County stipulated a bi-annual inspection of the property, which was a modification of an annual inspection stipulated in the geotechnical report.

Following unsuccessful representations by the landowner to the County to waive the inspection requirement, the homeowner started legal proceedings against the County in February 2007. The outcome of the proceedings was not known at the time of writing this paper.

In conclusion, apart from demonstrating that the setback By-Law could be waived, this study has highlighted some of the geotechnical and legal ramifications associated with such an undertaking.

REFERENCES

de Lugt, J.S., Thomson.,and Cruden, D.M (1987). “A suggested method for estimating setbacks from the crests of slopes on the interior Plains of Alberta.” Canadian Geotech.J,30 (5): 863-875.

Radiological Risk Assessment and Ecological Rehabilitation for a Romanian Uranium Tailing Pond

P.D. Georgescu[1] and M. Popescu[2]

[1]R&D National Institute for Rare and Radioactive Resources, 70 Carol I Blvd., 020917, Bucharest, Romania, e-mail: petre-dan.georgescu@icpmrr.ro
[2]R&D National Institute for Rare and Radioactive Resources, 70 Carol I Blvd., 020917, Bucharest, Romania, e-mail: popescu_geor@yahoo.com

ABSTRACT: In the uranium mining industry the most significant “hazard” is constituted by the tailing ponds, especially due to radon emissions and gamma debit dose, but also to possible expansion of some radionuclides and heavy metals. With a view to recommending the most efficient measures and prevention and remediation technologies for reducing effective doses to acceptable values for member of community and critical groups, it is necessary to perform a detailed risk assessment. This paper uses a case study of a tailing pond of a uranium ore plant in Romania, from a radiological point of view - looking into the pollution sources and the environmental impact of the radionuclides on the affected area. As a result of this assessment, more scenarios have been conceived and on the basic of a radiological risk assessment, we have recommended some corresponding technological solutions for the ecological rehabilitation of the tailing pond. We concluded the safest way to rehabilitate was by covering and encapsulating the area, thereby isolating it from the environment, preventing the migration of the polluting elements, limiting infiltrations in material mass and stopping radon emissions. The conclusions of the radiological risk assessment constituted the basis for elaborating the technical documentation.

INTRODUCTION

The tailing pond Cetatuia 2 was commissioned in 1997 and its purpose was to store the tailings from the uranium ore processing plant which is located in Brasov County in the central part of Romania. The nearby settlement considered as the critical group is Rotbav, located at 2.5km distance from the tailings pond. The tailing pond (Figure 1) - which is formed by three compartments – was made by embankment of The Cetatuia Valley by a heavy bulk dam of clay materials with a concrete screen upstream. The 1st compartment has 35ha and 2.25mil.mc. storage capacity. It was filled and decommissioned in 2002 because of reaching its maximum capacity. For these reasons the second tailings pond compartment had to be commissioned.

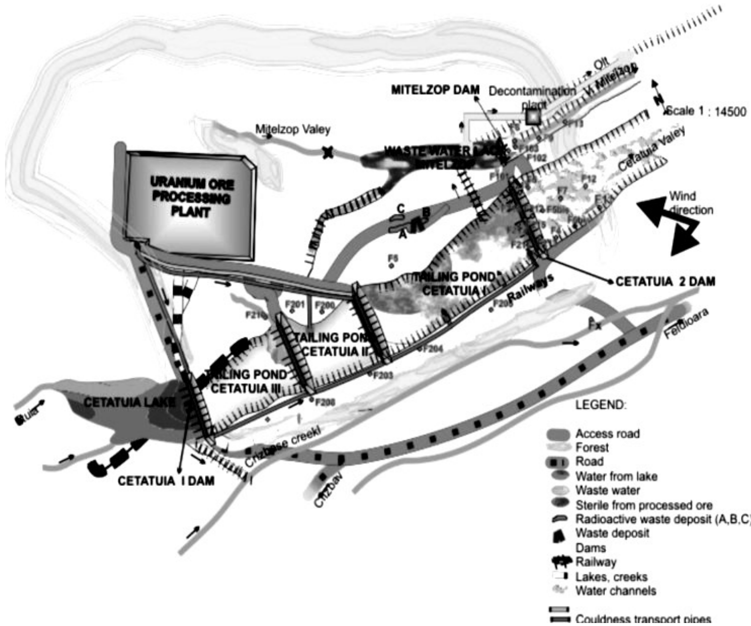

FIG. 1. The uranium ores processing plant tailing pond

POLLUTION SOURCES CHARACTERIZATION AND RADIONUCLIDES DETERMINATION IN ENVIRONMENTAL FACTORS

For stored material characterization, samples were collected from the central dam area and closed to the right bank. The U/Ra ratio content is an important parameter for the irradiation potential evaluation and for accurate radiometric measurements interpretation.

Because of the radioactive elements content, of its fine structure and of its disequilibrium unto Ra, the tailings pond from uranium ore processing represent the most important hazard in uranium mining industry. The total material activity from the tailings pond is about 1100GBq.

The Radiometric Pond Characterization and the Surrounding Areas Impact Assessment

On the wet material areas and in function of the material variations the value of gamma debit dose varied between 1.9 – 3.8μSv/h at 1m height and in the areas covered by water depending on deepth, the gamma debit dose is up to 1.20μSv/h as shown in Figure 2.

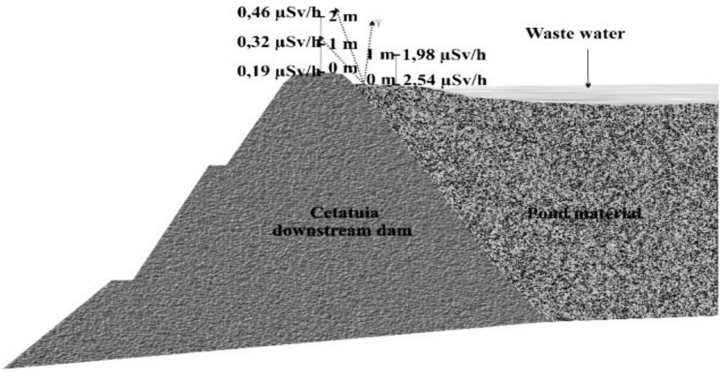

FIG. 2. Gamma debit dose distribution on dam – pond material area

In aim to approach the fine material impact and other possible events like damages of the sterile pipe, there were performed 50x12m grid measurements, on the right bank dyke. The results show a contamination of the right bank on 430m length and on an area of 19000m^2 and the gamma debit dose between 0.3-1.8μSv/h. The U/Ra ratio from soil samples is between 22-28, corresponding to the average value of U/Ra ratio of the tailings pond material which is 26, meaning 250ppm U and 95Bq/g Ra.

According to national standards for unrestricted land use, the soil activity value $\Sigma Ra^{226} + Th^{232}$ must be up to 0.2Bq/g. The measurements show that the value of Ra^{226} contamination is up to 5Bq/g. This fact imposes that the contaminated material has to be relocated at 0.35m depth on a surface of 13000m^2.

The Pollution Sources Represented by Gaseous Effluents - Radon

The tailings pond material includes 85% from initial radioactivity by presence of products with long disintegration time, such as Th^{230} - 80x10^3 years, Ra^{226} – 1.6x10^3 years. Radon, the gaseous emission from tailings pond, has a half-life value of 3.8 days and decays into Bi^{212} and Pb^{214}, with high gamma activity and into Po^{218}, Po^{214} and Po^{210} with high alpha activity.

The tailings pond major hazard is given by Rn emission which produces a long time contamination.

The Pollution Sources Represented by Liquids Effluents – Industrial Waste Waters

The sterile obtained from uranium ore processing was transported in the sterile pipe as a hydro mass in the first settling pond compartment. After settling, the clear waste waters were permanently discharged and stored into the second adjacent settling pond. Presently, the tailings pond surface is about 75% covered by rainwater from recent precipitation, leading to elements concentration and pH decrease.

CHARACTERIZATION OF THE POLLUTION PROCESS OF ENVIRONMENTAL FACTORS

The Impact on the Underground and Surface Waters

The increase of radioactive elements concentration in underground and surface water is a complex process depending on a lot of factors (Georgescu 2004). The uranium migration depends on its own presence in solution and its migration takes place under hexavalent state like a carbonate compound. Under lower pH conditions, (pH = 2 – 3), U and Ra migration in solution is a very strong process. In case of waste water with pH between 4.6 - 6.5 it was observed a relative migration of Ra in water and for pH higher than 7.0, uranium was found in a high percentage. For assessing the impact of liquid and solid sources due to the radioelements migration process, samples were collected and analyzed from drillings, wells, springs, rivers, lakes and surface water channels.

In the tailings pond influence area there were not present in aquifers values higher than the natural background level. In the waste water collected from the piezometer drillings located on dam lower levels, the contamination was about 25 times more than the background value. In the surface waters, the radioactive and non-radioactive elements values are between the background limits.

The Impact on Soil and Sediments from Downstream Dam Area

For tailings pond impact assessment there were collected soil samples from the dam base and sediments samples from downstream of the dam.

According to national standards for unrestricted land use the Ra^{226} specific activity value in soil must be up to 0,2Bq/g, while in the bottom dam soil the Ra^{226} specific activity is about 4Bq/g that impose the soil relocation on a strip with 2m width, 200m length and 30cm depth.

Concerning the sediments samples the Ra^{226} value are lower than 0.2Bq/g, with a single exception of a sample collected from the dam downstream area.

RISK ASSESSMENT METHODOLOGY

The risk assessment involves two stages. In the first stage the existence of the potential risk for receivers is analyzed by studding the following aspects: identification and characterization of the contamination sources, potential contaminants, the exposure pathways, the presence of human receivers and site specific factors such as soils, whether, topography, hydrology etc.. The contamination sources from the uranium processing plant areas – the tailings pond – are “punctual sources” and the potential exposure pathways of human receivers are: terrestrial, aquatic and aerial. The potential receivers are represented by humans (workers, and critical group population). The second stage is a qualitative assessment by estimation of the additional effective doses for potential receivers and is performed in three steps, respectively concentration determination in the exposed place, dose estimation and the risk assessment as a result of exposure hazard.

For biological risk assessment of the population affected by uranium mining industry, it was set up a classification system based on the occurrence probability and the process magnitude influence on receivers.

The probability could be rated: high – 4th degree (certainly or almost certainly), medium – 3rd degree (likely to produce) – low - 2nd degree (seldom) and extremely low – 1st degree (possible but never happened).

The magnitude could be rated: strong – 4th degree (human disasters, long term illness, ecosystems changing, irreversible damage by species elimination), moderate – 3rd degree (short term illness, ecosystem changing without species elimination), low – 2nd degree (some human illness, some negative changes on ecosystems, reversible damage), insignificant – 1st degree (some negative aspects on the human psychic, there are no ecosystem changes). The risk assessment matrix is represented in table 1.

Table 1. The Biologic Risk Matrix

Probability Rate	**Annual Effective Dose Magnitude (mSv/year)**			
	Strong (4)	Moderate (3)	Low (2)	Insignificant(1)
High (4)	16	12	8	4
Medium (3)	12	9	6	3
Low (2)	8	6	4	2
Extremely low (1)	4	3	2	1

EFFECTIVE DOSE ESTIMATION

International and national radioprotection standards allow 1mSv/year total additional effective dose E_{SUP} to be received by a person from population. This dose has to be added to the background total effective dose $E_{FOND.}$ The total annual effective dose E_T, represents the sum of all external doses received by a person via aquatic, terrestrial and air pathways, plus internal doses received via ingestion, soils, sediments, water, sand, aliments and inhalation of radon or its short life decays.

The Background Effective Dose Determination

Since people live in a geographical environment characterized by geological sub-layers and different altitudes, the annual effective dose is a specific characteristic of the local background.

The total effective dose has two components (Georgescu, 1997): external effective dose due to gamma external radiation, internal effective dose due to ingestion and inhalation of radionuclides from water, air, aliments, dust etc.

Total and Additional Effective Dose Determination

Based on the same methodology used for the annual effective dose produced by the local background, it has been calculated the total effective dose for the critical group of the population living in the tailings pond influence area. By subtraction, it was calculated the total effective additional dose.

Based on this approach there were established some potential scenarios located both outside the controlled area and inside the critical groups living downstream the uranium activity area or on the main wind direction. The doses estimation has been done for all the three pathways: terrestrial, aquatic and aerial.

Exposure Scenarios

For dose assessment, there were figured five scenarios, one for the uranium plant critical group (scenario X) and four for the critical group population from neighboring settlements (scenarios 1, 2, 3, 4), represented in figure 3.

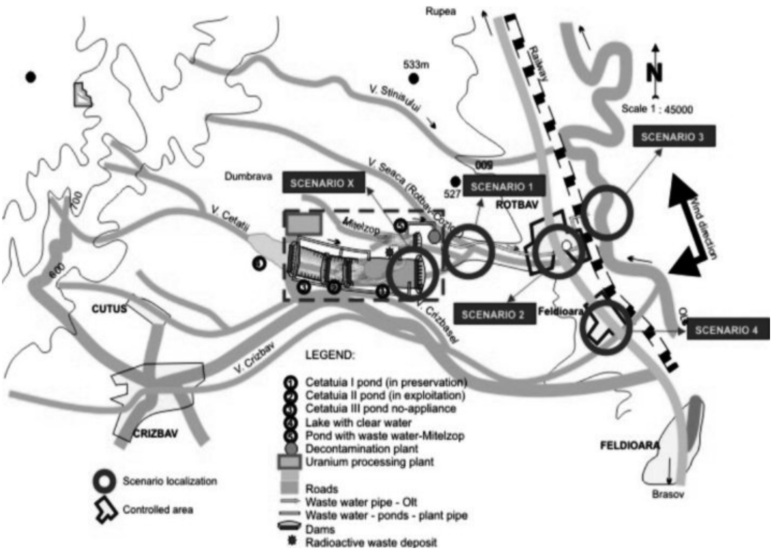

FIG. 3. Scenarios localization

Scenario 1 – on 700m downstream of the tailing pond dams on the confluence of the Cozlop and Mitelzop creeks, near Rotbav village, composed by three potential alternatives: (a_1) – one person from the critical group who uses for a year the water from Mitelzop creek for cattle and irrigation water; (a_2) – one person uses the water from Cozlop creek after merging the pollution source Mitelzop, having a minimum debit value; (a_3) - one person uses the water from Cozlop after merging Mitelzop creek having a maximum debit value.

Scenario 2 – exposure area located at 3km downstream of the uranium processing plant, and includes the critical group from Rotbav village. This scenario has two potential alternatives: (a_1) - one person uses the water from Cozlop creek after the confluence with the pollution source, having a minimum debit value; (a_2) – one person uses the water from Cozlop creek after the confluence with the pollution source, having a maximum debit value.

Scenario 3 – located on Olt river valley, at the waste water discharge point, at 3.5 km downstream of the tailings pond. There are three potential alternatives of this scenario: (a_1) – one person who uses water directly from waste water discharge chanel; (a_2) – one person uses the water from Olt river after the confluence with the waste water, having a minimum debit value; (a_3) – similar with a_2 but for a medium debit value of Olt river.

Scenario 4 – located in Feldioara village at 3.5km east of the radioactive sources – tailings ponds.

Scenario X – exposure is located on the dam area of the tailing pond Cetatuia 2 - 1st compartment. The scenario is based on the situation when the uranium processing activity would be stopped and after site rehabilitation and access restrictions releasing of the controlled area it could be possible that some people live there.

Based on measurements and results interpretation, the additional effective doses received by population and critical groups analyzed in the previous scenarios, are represented in Table 2.

Table 2. Additional Effective Doses

Scenario	Alternative	Background Effective Dose, mSv/year	Total Effective Dose, mSv/year	Additional Effective Dose, mSv/year
X	-	0.972	5.102	4.13
1	a_1	0.972	1.301	0.329
	a_2		1.265	0.293
	a_3		1.017	0.045
2	a_1	0.972	1.153	0.181
	a_2		0.9817	0.0097
3	a_1	0.972	1.038	0.066
	a_2		0.972	0
	a_3		0.972	0
4	-	0.972	0.972	0

According to the additional effective dose values calculated for the elaborated scenarios and on the basis of matrix biologic risk and, for scenarios 1 – 4, the risk level is negligible. In the case of scenario X, located on the tailing pond dam area, the additional effective dose is more than 1mSv/year, so the risk contamination level is low to medium. The risk coefficient is 8, corresponding to a low probability (2nd degree) and to a high magnitude (4th degree).

CONCLUSIONS

In the case of the X scenario the additional effective doses have high values especially for terrestrial pathway due to gamma radiation and for aerial pathway due to inhalation of radioactive dust and Rn with its short-life decay products.

Generally, the ecological remediation and the tailings ponds rehabilitation consist in their covering – encapsulation, considering that the used methods and the technical solutions have to be accepted by the government and community in order to offer short, medium and long term effects and have to accomplish the environmental and health protection in an acceptable costs/benefit ratio.

The radioactive tailings pond cover-system has to be designed in order to obtain separation between pond and environment, to prevent the elements leaching and migration, to restrict the rainfall infiltrations on the tailings body and to control the radon emission. The main factors to be considered are wind and water erosion, dry and wet period alternation, plant roots and animals burrows penetration and the extreme temperatures.

According to these reasons it has been established the cover system main components: radon barrier, infiltration barrier, the drainage layer, bio intrusion and erosion barrier. For gamma radiation attenuation, the thickness of the covering layers of the radioactive sterile is calculated as a function of gamma debit dose on the tailings pond surface and its linear attenuation coefficient depending on the used materials. For example, natural materials like clay and sand have an attenuation coefficients between $0.08cm^{-1}$ - $0.16cm^{-1}$.

Beside natural materials, in recent years there were also been used synthetic geo-materials like geo-membranes and geo-textiles etc.

In the study case of close-up and ecological rehabilitation of the Romanian tailings pond resulted from uranium ores processing. Based on the radiological risk assessment conclusions and results it has been elaborated the technical project study for the tailings pond cover system, as a sequence of natural and synthetic materials: land with fertilizer, biodegradable sowed geo-textile, 30cm local soil, geo-material based on sand, bentonite and 7cm TRISOPLAST polymer, local material 15cm clay; drainage geo-textile for waste water discharge.

By this cover system of the studied tailings pond, the value of calculated additional effective dose received by one person from critical group who has lived for 7000 hours on the rehabilitated pond area is up to 0.220mSv/year, corresponding of national and international standard limits (e.g., ICPR, 1993).

REFERENCES

Georgescu, D., Popescu, M. and al. (2004). "Assessment of environmental impacts due to radioactive contamination from uranium mining activities in Romania.", *Proc., 1st International Conference AMIREG 2004*, Hania, Greece, Conferences publisher: 449 – 454.

Popescu, M., Georgescu, D. and Filip, G.(1997)."A study of interface between radioactive ore dumps vegetation aiming at limitation of the contamination process in uranium mining areas, *Ingineering Geology and Environment*Balkema, Rotterdam,ISBN 9054108770.

ICPR, Publication 65 (1993), "Protection against Radon-222 at Home and at Work."*Annals of ICPR,* Vol. 23, no.2.

Stochastic Modeling of Redundancy in Mechanically Stabilized Earth (MSE) Walls

Ioannis E. Zevgolis[1], S.M. ASCE and Philippe L. Bourdeau[2], M. ASCE

[1] Geotechnical Engineer, PhD; 7-9 Gavriilidou Str., Athens, 11141, Greece (formerly: PhD Student, Purdue University, School of Civil Engineering); i.zevgolis@alumni.purdue.edu
[2] Assoc. Professor; Purdue University, School of Civil Engineering, 550 Stadium Mall Dr., West Lafayette, IN, 47907-2051, USA; bourdeau@ecn.purdue.edu

ABSTRACT: A probabilistic model is developed in order to assess the reliability of the internal stability of MSE walls. Geotechnical uncertainty is explicitly considered by modeling shear strength properties of reinforced, retained, and foundation soil as random variables following beta distributions. The model is developed in two steps. First, an in-series configuration addresses the reliability per reinforcement layer and provides a profile of reliability with depth. Second, an r-out-of-m configuration is used to model the inherent redundancy of MSE structures. Reliability analyses are performed using Monte Carlo simulations and propagation of failure is modeled using transition probabilities and Markov stochastic processes. As an illustration, a case example of an MSE wall used as direct bridge abutment is analyzed in the context of the developed model.

INTRODUCTION

Reliability analysis of mechanically stabilized earth (MSE) walls requires consideration of several failure mechanisms and how these are affected by various sources of uncertainty. In conventional design methods, the reinforced soil mass is assumed to behave as a rigid body in terms of external stability and safety assessment is performed with respect to sliding, bearing capacity, and excessive eccentricity. In terms of internal stability, MSE walls are analyzed with respect to tensile and pull out resistance of the reinforcement elements (Elias et al. 2001; AASHTO 2002). Particularly with respect to internal stability, MSE walls are inherently redundant systems. This means that if a reinforcement element fails, the remaining elements are expected to assume additional responsibility so that the system is still in a position to continue its operation, even if not as initially intended. So, the reliability of the internal stability of an MSE wall is a function of its redundancy, although commonly accepted simplifications ignore this aspect. Provided some modeling simplifications are accepted, stochastic models offer the framework to determine not only the original reliability per layer of reinforcement of an MSE wall, but also the updated reliability given that one or more layers have already failed. In this paper, the development of such a model is described. Internal stability is approached in two steps using Monte Carlo simulations. The framework for consideration of redundancy and propagation of failure is formulated based on transition probabilities and Markov stochastic processes. As an illustration, an example case of an MSE wall used as direct bridge abutment is analyzed in the context of the developed model.

FORMULATION OF THE PROBABILISTIC MODEL

Performance functions

In contrast to deterministic approaches, in probabilistic analysis of MSE walls, sources of uncertainty are characterized and explicitly accounted for in the computation of reliability. In order to represent limit states of equilibrium, it is convenient to define performance functions by analogy with safety factors, as Safety Ratios (SR). So, safety ratios with respect to tensile and pull out failure of each reinforcement layer i, $[SR_{T_i}]$ and $[SR_{PO_i}]$ respectively, are expressed by:

$$\left[SR_{T_i}\right] = \frac{F_Y}{T_{\max,i}} \qquad \text{for } i = 1, 2, \ldots, m \tag{1}$$

$$\left[SR_{PO_i}\right] = \frac{P_{R,i}}{T_{\max,i}} \qquad \text{for } i = 1, 2, \ldots, m \tag{2}$$

where m is the number of reinforcement layers, F_Y is the tensile strength of the reinforcement elements, $T_{max,i}$ is the maximum tensile force applied on each reinforcement layer i, and $P_{R,i}$ is the pull out resistance of each reinforcement layer i. Definitions of F_Y, $T_{max,i}$ and $P_{R,i}$ are provided in specifications and guidelines (Elias et al. 2001; AASHTO 2002). Failure is defined as the case where the corresponding SR is less than one. Then, the probability of failure (P_F) for any mechanism is given:

$$P_F = P\left[SR < 1\right] \qquad \text{for any mechanism} \tag{3}$$

Assessment of reliability

Each reinforcement layer is modeled as an in-series system. This means that if the layer fails either in tension or in pull out, then that specific layer does not contribute anymore to the internal stability of the structure. So, failure of an individual layer i is the event in which $\left[SR_{T_i} < 1\right]$ and/or $\left[SR_{PO_i} < 1\right]$ occurs. The probability of occurrence of the failure (P_{F,INT_i}) is given by the union of these two events:

$$P_{F,INT_i} = P\left[\left(SR_{T_i} < 1\right) \cup \left(SR_{PO_i} < 1\right)\right] \tag{4}$$

where $P[-]$ denotes the probability of the event indicated within the brackets. Since the events $\left[SR_{T_i} < 1\right]$ and $\left[SR_{PO_i} < 1\right]$ are not mutually exclusive (nor independent), the above can be written as following:

$$P_{F,INT_i} = P\left[SR_{T_i} < 1\right] + P\left[SR_{PO_i} < 1\right] - P\left[\left(SR_{T_i} < 1\right) \cap \left(SR_{PO_i} < 1\right)\right] \quad (5)$$

The components of the above equation are given by:

$$P\left[SR_{T_i} < 1\right] = \frac{n_{F,T_i}}{N} \quad (6)$$

$$P\left[SR_{PO_i} < 1\right] = \frac{n_{F,PO_i}}{N} \quad (7)$$

$$P\left[\left(SR_{T_i} < 1\right) \cap \left(SR_{PO_i} < 1\right)\right] = \frac{n_{F,T_i\text{-}PO_i}}{N} \quad (8)$$

where n_{F,T_i} and n_{F,PO_i} are the number of Monte Carlo realizations in which the safety ratio of the respective mode is less than one, n_{F,T_i-PO_i} is the number of times in which the two safety ratios are simultaneously less than one, and N is the total number of Monte Carlo realizations. Once the probabilities of failure per layer (P_{F,INT_i}) have been found for all layers, then a profile of probability of failure with depth can be obtained. Such a profile would indicate which reinforcement layers are subjected to higher risk of failure.

CONSIDERATION OF REDUNDANCY

As already explained in the introduction, MSE walls are characterized by redundancy. Therefore, it is of interest to determine not only the original reliability per layer of reinforcement, but also the reliability of a layer given that another layer has already failed. An appropriate model for doing so would be an *r-out-of-m* system. This model refers to a system of *m* components, *r* of which must be operable for the system to survive (Ang and Tang 1984; Harr 1987). In the case of an MSE wall, *m* is the total number of reinforcement layers and *r* is the number of reinforcement layers that shall not fail in order for the structure to remain in operation. The updated profile of reliability with depth will be assessed using transition probabilities and Markov stochastic models.

Markov processes are stochastic processes that can be used in probabilistic modeling of systems that satisfy the following criterion: the transition of the system from one state to another depends only on the current state of the system and not on the previous states. In Markovian models, the probability of transition from one state *i* to another state *j* is called transition probability, and will be denoted herein as $p_{i \to j}$.

For a system that has *(m+1)* possible states, the array of all transition probabilities can be written in the form of an $(m+1)\times(m+1)$ matrix, called transition probability matrix Π. Details about the theory of Markov models can be found in classical textbooks (Benjamin and Cornell 1970; Ang and Tang 1984; Harr 1987).

So, a fundamental step in Markovian models is to clearly define all possible states that the system can move from, and towards to, during its lifetime. Considering an MSE structure with *m* reinforcement layers, the following states (herein called "*states of failure*") are defined:

State of failure 0 → All layers are intact
State of failure 1 → One layer has already failed
State of failure 2 → Two layers have already failed
... ...
State of failure i → *i* layers have already failed
... ...
State of failure m-1 → *m-1* layers have already failed
State of failure m → All layers have failed

where states of failure *0* and *m* are the original and final states, respectively. Taking into consideration the nature of an MSE structure, the following statements can be made for the model:

- The model does not allow for reverse of failure. In other words, having reached a certain state *i*, the system cannot return to *i-1, i-2,* ... states.
- When failure occurs at a certain state *i*, it may or may not propagate to a following state *j*. If the system remains in its present state, then this is called an *absorbing state*.
- The model is free from restrictions of continuous propagation of failure. This means that when failure propagates, it may do so to any of the remaining states.

The transition probability matrix takes the following form (Zevgolis 2007):

$$\Pi = \begin{bmatrix} p_{0\to0} & p_{0\to1} & \cdots & p_{0\to i} & \cdots & p_{0\to j} & \cdots & p_{0\to m} \\ 0 & p_{1\to1} & \cdots & p_{1\to i} & \cdots & p_{1\to j} & \cdots & p_{1\to m} \\ \vdots & \vdots & & \vdots & & \vdots & & \vdots \\ 0 & 0 & \cdots & p_{i\to i} & \cdots & p_{i\to j} & \cdots & p_{i\to m} \\ \vdots & \vdots & & \vdots & & \vdots & & \vdots \\ 0 & 0 & \cdots & 0 & \cdots & p_{j\to j} & \cdots & p_{j\to m} \\ \vdots & \vdots & & \vdots & & \vdots & & \vdots \\ 0 & 0 & \cdots & 0 & \cdots & 0 & \cdots & 1 \end{bmatrix} \tag{9}$$

The above is an upper triangular matrix, with $(m+2)(m+1)/2$ non-zero elements. The following equations hold true for this matrix:

$$0 \le p_{i\to j} \le 1 \qquad \textit{for any i and j} \tag{10}$$

$$\sum_{j=1}^{m} p_{i \to j} = 1 \qquad \textit{for any } i \tag{11}$$

$$p_{i \to j} = 0 \qquad \textit{if } i > j \tag{12}$$

$$p_{m \to m} = 1 \tag{13}$$

In order to determine the transition probabilities that compose the matrix Π, an iterative process is followed (Zevgolis 2007). In the first iteration, Monte Carlo simulation is performed considering that all reinforcement layers are in place. This is the *state of failure 0*. P_{F,INT_i} is calculated based on equations 5 to 8, and the corresponding profile of probability of failure is obtained. In addition, the number of realizations where simultaneous failures of different layers occur, is counted. The number of realizations of simultaneous failure of *0 out of m* layers, corresponds to *state of failure 0*, the number of realizations of simultaneous failure of *1 out of m* layers, corresponds to *state of failure 1*, and so on. Finally, the number of realizations of simultaneous failure of *m out of m* layers, corresponds to *state of failure m*. Then the probability of transition from *state of failure 0* to *state of failure i* ($p_{0 \to i}$) is given by:

$$p_{0 \to i} = \frac{n_{F,0 \to i}}{N} \qquad \textit{for } i = 0, 1, 2, \ldots, m \tag{14}$$

where $n_{F,0 \to i}$ is the number of realizations of simultaneous failures of i out of m layers, and N is the total number of realizations in the Monte Carlo simulation. The array of transition probabilities of equation 14 can now be written in the form of a $1 \times (m+1)$ row matrix Π_0 as following:

$$\Pi_0 = \begin{bmatrix} p_{0 \to 0} & p_{0 \to 1} & \cdots & p_{0 \to i} & \cdots & p_{0 \to m} \end{bmatrix} \tag{15}$$

The subscript 0 means that Π_0 refers to the *state of failure 0* as the initial state for this simulation. In the second iteration, Monte Carlo simulation is performed again, this time considering that one reinforcement layer has already failed (so, Π_1 is obtained) . The iterative process is repeated $m+1$ times in total. Every time the failing layer is assumed to be the most critical one. Assembling the row matrices Π_0, Π_1, …, Π_m into one matrix, gives us the transition probability matrix of equation 9.

CASE EXAMPLE

A case example of an MSE wall used as direct bridge abutment is analyzed as an illustration of the developed model (Figure 1).

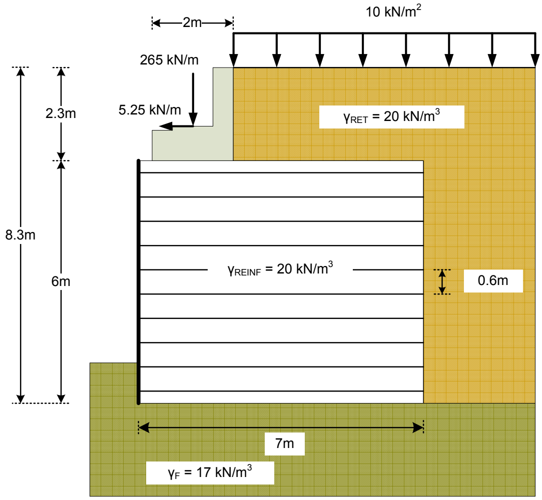

Figure 1. Schematic representation of the analyzed case example

The present model includes four random variables (Table 1). Each one is represented by the first two order moments (mean value μ and coefficient of variation C.O.V.) and the minimum and maximum value. Therefore, based on the principle of maximum entropy, the random variables are modeled using beta distributions (Oboni and Bourdeau 1985; Harr 1987). All other properties (such as unit weights, reinforcement characteristics, and loading conditions) are considered deterministic variables with values shown in Figure 1. Note that perfect autocorrelation is assumed over the volume of interest for all four random variables. This simplifying assumption should slightly affect the analysis numerical results but without loss of general validity.

Table 1. Probabilistic parameters of random variables

Soil property	Notation	μ	C.O.V.	Min	Max
Friction angle of reinforced backfill	φ_{REINF} (^{o})	34	0.10	20.4	47.6
Friction angle of retained backfill	φ_{RET} (^{o})	30	0.15	12	48
Friction angle of foundation soil	φ_{F} (^{o})	20	0.20	4	36
Cohesion of foundation soil	c_F (kN/m^2)	40	0.30	0	88

Figure 2 illustrates the variation of the computed standard deviations, $\sigma[SR_T]$ and $\sigma[SR_{PO}]$, with depth. As shown in the Figure, while the variation of $\sigma[SR_T]$ is relatively constant, this is not the case for $\sigma[SR_{PO}]$, which demonstrates a continuous increase with depth. This implies that SR_{PO} is subjected to higher degree of uncertainty compared to SR_T. In addition, it is shown that the uncertainty of SR_{PO} increases with depth.

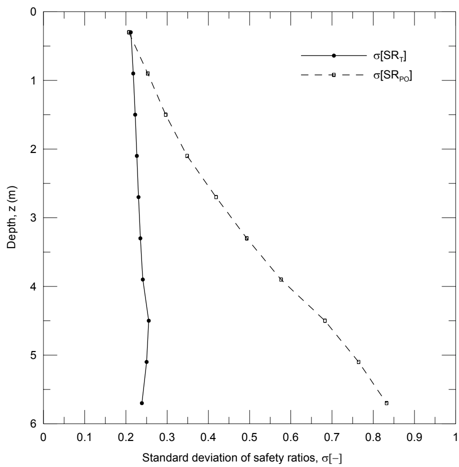

Figure 2. Variation of σ[SR$_T$] and σ[SR$_{PO}$] with depth

Based on the computations, and for the analyzed case example, the top layer of reinforcement was the most critical. This was reasonable, considering that this layer is located below the bridge seat. So, failure was assumed to initiate from that one. This may not always be the case, particularly in conventional (non-abutments) MSE walls. Following the iterative procedure that was described earlier, different profiles of probabilities of failure corresponding to different states of failure, were obtained. These are shown below, in terms of the transition probability matrix, for the top two layers:

$$\begin{bmatrix} 0.92935 & 0.06423 & 0.00560 & 0.00028 & 0.00033 & 0.00007 & 0.00008 & 0.00002 & 0.00003 & 0 & 0 \\ 0 & 0.83458 & 0.12525 & 0.03195 & 0.00625 & 0.00030 & 0.00013 & 0.00145 & 0.00008 & 0 & 0 \\ 0 & 0 & 0.54998 & 0.29860 & 0.11537 & 0.01928 & 0.00815 & 0.00827 & 0.00035 & 0 & 0 \\ 0 & 0 & 0 & ... & ... & ... & ... & ... & ... & ... & ... \\ 0 & 0 & 0 & 0 & ... & ... & ... & ... & ... & ... & ... \\ 0 & 0 & 0 & 0 & 0 & ... & ... & ... & ... & ... & ... \\ 0 & 0 & 0 & 0 & 0 & 0 & ... & ... & ... & ... & ... \\ 0 & 0 & 0 & 0 & 0 & 0 & 0 & ... & ... & ... & ... \\ 0 & 0 & 0 & 0 & 0 & 0 & 0 & 0 & ... & ... & ... \\ 0 & 0 & 0 & 0 & 0 & 0 & 0 & 0 & 0 & ... & ... \\ 0 & 0 & 0 & 0 & 0 & 0 & 0 & 0 & 0 & 0 & 1 \end{bmatrix}$$

In this example, the number of reinforcement layers is m = 10, so the transition matrix is an *(m+1)×(m+1)* = *11×11* matrix. So for instance, the element $p_{3\to 3} = 0.54998$ corresponds to the following transition probability: given that the top 2 layers have already failed (state of failure 2), the probability that there will not be any further propagation of failure is 54.998 %. The probability that there will be propagation to the third from the top layer is 29.860 % ($p_{3\to4} = 0.29860$), to the fourth from the top is 11.537 % ($p_{3\to5} = 0.11537$), and so on.

CONCLUSIONS

MSE walls are often characterized by redundancy. This means that in the event of failure of one or more layers of reinforcement, the wall does not necessarily collapse, because the remaining layers assume additional responsibility in terms of loads. This is typically an aspect that is ignored by previous models.

In this paper, a stochastic model was developed in order to assess the reliability of MSE walls with respect to their internal stability, taking into account the redundant nature of this type of structures. So, using an r-out-of-m configuration the proposed model is able to determine not only the original reliability per layer of reinforcement, but also the updated reliability given that one or more layers have already failed. Propagation from one state of failure to another were modeled using transition probabilities and Markov stochastic models.

To illustrate the developed methodology, a case example of an MSE wall used as direct bridge abutment was analyzed. For this example, the results indicate that the mechanism subjected to higher risk of failure is the one in pull out. In addition, the transition probability matrix provides the probabilities of failure propagation for three different states of failure.

ACKNOWLEDGEMENTS

Financial support provided by the *Empirikion Foundation* to the first author during his doctoral studies is greatly appreciated.

REFERENCES

AASHTO. (2002). "Standard Specifications for Highway Bridges." American Association of State Highway and Transportation Officials, 17th edition, Washington D.C., USA.

Ang, A. H.-S., and Tang, W. H. (1984). *Probability Concepts in Engineering Planning and Design. Volume II: Decision, Risk and Reliability*. John Wiley & Sons.

Benjamin, J. R., and Cornell, C. A. (1970). *Probability, Statistics, and Decision for Civil Engineers*. McGraw-Hill.

Elias, V., Christopher, B. R., and Berg, R. R. (2001). "Mechanically stabilized earth walls and reinforced soil slopes – Design & construction guidelines." FHWA-NHI-00-043, US Department of Transportation, Federal Highway Administration, Washington D.C., USA.

Harr, M. E. (1987). *Reliability-Based Design in Civil Engineering*. McGraw-Hill.

Oboni, F., and Bourdeau, P. L. (1985). "Simplified use of the beta distribution and sensitivity to the bound locations." *Structural Safety*, 3(1), 63-66.

Zevgolis, I. E. (2007). "Numerical and Probabilistic Analysis of Reinforced Soil Structures." PhD Dissertation, Purdue University, West Lafayette, IN, USA.

An Earthquake Warning System Using Fuzzy Logic and Geospatial Analysis

Pritwiraj Moulik[1], Student Member, ASCE

[1]Undergraduate Student, Birla Institute of Technology & Science (BITS-Pilani), Room-182, Krishna Bhawan, Vidya Vihar Campus, Pilani, Rajasthan, India 333031; theprithwi@gmail.com

ABSTRACT: The various methodologies of earthquake prediction have been based on approaches, which either did not take the physics and geology involved into consideration or were based on small datasets. The present work is based on a combination of geological understanding and modeling of previous seismic data to provide a reliable warning system. This process is illustrated by categorizing different types of stations using geospatial analysis and showing similarities in waveform from two earthquakes by finding average standard deviation of 0.00693728 cm/s^2 and through visual inspection over the P-S time interval. Fuzzy membership functions and Data Clustering methods are then used to statistically model the seismic data identified through geospatial analysis. The study involved using earthquake and geological data of the Parkfield region and it has shown positive results up to a threshold cumulative membership grade of 0.73. The primary limitation of the proposed warning system is the need for a large amount of data.

INTRODUCTION

Earthquake prediction has long been considered the ultimate goal of seismology. The present work proposes an imminent earthquake warning system based on the presence of similar amplitudes and waveforms that imply the same seismic moment, focal mechanism, and tele-seismic wave path (Bakun et al., 2005). The algorithm in the proposed warning system is based on the concepts of Fuzzy Logic, Data Clustering and Real Time Analysis of data using an evolutionary algorithm to optimize the result.

The dataset used in the present work is from the 40-km-long Parkfield section of the San Andreas Fault, recognized two decades ago as a promising earthquake physics laboratory. For a more detailed description of the tectonics of the Parkfield area, the reader is referred to Eberhart-Phillips & Michael (1993). Earthquakes of comparable size to the recent 2004 earthquake (Magnitude 6) occurred in the year 1857, 1881, 1901, 1922, 1934, and 1966. There is substantial overlap of the aftershock zone of the recent earthquake with that of the aftershock zone of the 1966 earthquake, which makes it perfect to satisfy the constraints proposed in this work.

Geospatial analysis of the epicenter and station SMC-format data from the COSMOS (Consortium of Organizations for Strong-Motion Observation Systems)

Virtual Data Center was performed using ArcGIS 9.1 software to find the effect of the tele-seismic path and other factors on the resultant accelerogram. The soil GIS (Geographical Information System) data was retrieved from Consortium for Spatial Information (CGIAR-CSI) which provides Shuttle Radar Topography Mission (SRTM) data and the Soil Data Mart service of the Natural Resources Conservation Service (NRCS).

WARNING SYSTEM

In the effort to predict earthquakes, people have tried to associate an impending earthquake with such varied phenomenon as seismicity patterns, electromagnetic fields, weather conditions, unusual clouds, radon or hydrogen gas content of soil or ground water, water level in wells and animal behavior. Most assessments rely on chance models for earthquake occurrence that are difficult to test or validate, because large earthquakes are so rare and earthquake activity is naturally clustered in space and time. So far, controversy on forecasting has arisen because most conclusions have been made from a small data set, sometimes without well-understood physical phenomenon in mind to explain the claims (Wyss, 2001).

Statistics and Probability has been an important tool in seismology and earthquake prediction with catalogue studies of past seismicity (Kagan & Jackson, 2004). Recently, efforts have been made to investigate the potential of Artificial Neural Networks (ANN’s) as a black-box approach so that the user need not know much about the physics of the process simulated (Bodri, 2001). In contrast to other models, a comprehensive warning system has been proposed in this work, which models the observed similar seismicity using fuzzy membership functions combined with an understanding of the physics and geology behind the earthquake using geospatial analysis.

The time scale of forecasting of earthquakes is generally classified as short, intermediate, and long-term, according to the expected time interval to an impending earthquake (Wallace et. al., 1984). This warning system is aimed to be an imminent system with a time scale in the order of minutes. Countries like Japan, Mexico, and Taiwan are investing in early warning systems that can offer precious seconds of warning before a major tremor (Normile, 2004). Though critics debate the effectiveness of such systems, it is indeed true that these methods will be beneficial on a larger scale by helping authorities take prompt actions such as shutting off gas pipelines, stopping trains and saving computer databases in major cities (Table 1.).

Table 1. Approximate Time Lag in the Arrival of P & S waves during the 2004 Parkfield Earthquake.

City	Latitude	Longitude	Epicentral Dist.(km)	Time Lag(s)
San Francisco	37.48N	122.33W	254.6832	49.522
Berkeley	37.86359N	122.3115W	285.9886	55.609
Los Angeles	33 56' 0"N	118 24' 0"W	276.3433	53.733
Sacramento	38 31' 0"N	121 30' 0"W	316.8871	61.617
San Diego	32 44' 0"N	117 10' 0"W	452.3993	87.966

Fuzzy Logic and Membership Functions

Fuzzy logic can be defined as a logical system that generalizes classical two-valued logic for reasoning under uncertainty. Therefore, fuzzy logic theory eliminates the problem of two-valued logic reasoning in classical set theory (Zadeh 1965). This logic system is a mathematical control system, which analyzes analog input values in terms of logical variables. It takes on continuous values between 0 and 1 in contrast to classical or digital logic that operates on discrete values of 0 and 1. The very basic notion of fuzzy systems is a fuzzy set, which is a pair (A, m), where A is a set and m: $A \rightarrow [0, 1]$. For each $x \varepsilon A$, m(x) is the grade of membership of x such that $x \varepsilon (A, m) \Leftrightarrow x \varepsilon A$ and $m(x) \neq 0$.

Arriving at the Algorithm: Geospatial Analysis

Geospatial Analysis, used to filter the voluminous seismic data based on specific system constraints that affect a waveform, provides the input data for the algorithm. The system constraints can be broadly classified into-

(1) *Earthquake Parameters:* The system is based on the recurrent behavior of the classes of characteristic earthquakes, which have the similar faulting mechanism, magnitude, rupture direction and have occurred on the same fault segment or the same epicenter. Lower variability may be achieved if events are further constrained to have the same rupture time history and distribution of slip.

(2) *Source and Station Characteristics:* The geological setting of the station, the source and the path of propagation is also a major consideration.

The 1934, 1966 and 2004 Parkfield earthquakes used to arrive at this model are remarkably similar in size and location of rupture, albeit not in epicenter or rupture propagation direction (Bakun & McEvilly (1979), Bakun et al. (2005)). The 2004 and 1966 Parkfield Earthquake data from COSMOS were converted to the Microsoft Excel format and used for geospatial analysis using ArcMap 9.1. Due to the lack of data, the system constraints used in this study were the hypocenter parameters (latitude, longitude, depth etc.), the station/event parameters and the sensor description (type, natural frequency etc.). The raster data from the CGIAR-CSI were then taken and 3-Dimensional models constructed using ArcScene 9.1 (Fig. 1). The station location and the soil data from NRCS were taken as layers for analysis.

A list of stations satisfying the constraints under consideration was grouped into six types (Table 2). One station of special interest was the City Recreation Bldg - 864 Santa Rosa at San Luis Obispo, California that had the records of both the earthquakes. Thus, a study was done of the waveforms of the station for the 2004 earthquake and the aftershock of magnitude 5. A statistical analysis of the P-S interval of the two waveforms gave an average standard deviation (S.D.) of 0.00693728 cm/s^2 with a minimum S.D. of 4.24264E-6 cm/s^2 and maximum S.D. of 0.046028692 cm/s^2. These results coupled with visual inspection of the waveforms further proved that there was a remarkable similarity between the waveforms (Fig. 2). This study paves the way for the proposed algorithm, which is dependent on such analysis of data on a much larger scale. The lack of publicly accessible data is one of the primary limitations that restricted the further study of the algorithm using a larger dataset.

Table 2. Types of stations based on similar soil profile and epicenter distances for the two earthquakes (2004 & 1966 Parkfield, CA)

Type	Year	Station	MUID	Area (sq. km)	Bedrock Depth(m)	Soil Profile (L1-L11)
I	1966	Chalome Array 2	CA501	53642	152	9;9;9;9;6;6;6;6;6;15;15
	1966	Chalome Shandom Array 5 & 8	CA502	187777	150	9;9;9;16;16;16;16;16;16;15;15
II	2004	Vineyard Canyon	CA561	59483.1	140	6;6;6;6;6;12;12;12;7;15;15
	2004	Jack Canyon	CA344	623444	73	6;6;3;3;3;15;15;15;15;15
	1966	Temblor	CA344	623444	73	6;6;3;3;3;15;15;15;15;15
III	1966	San Luis Obispo	CA515	831475	89	12;12;9;11;11;11;11;11;15;15;15
	2004	San Luis Obispo	CA515	831475	89	12;12;9;11;11;11;11;11;15;15;15
	2004	Hollister; Airport Building	CA568	129241	152	12;12;12;12;12;12;12;12;12;15;15
IV	1966	Taft, Lincoln School Tunnel	CA347	2809850	152	3;3;3;3;3;3;3;3;3;15;15
	1966	Chalome Array 12	CA503	23115.4	141	3;3;3;3;3;3;6;6;16;15;15
	2004	Fresno;VA Medical Center	CA309	41103.9	147	3;3;3;3;3;7;16;16;16;15;15
	2004	Fresno; NAMP USGS Office	CA307	2262820	152	3;3;3;3;3;3;3;3;3;15;15
	2004	Parkfield;Eades	CA503	29183.2	141	3;3;3;3;3;3;6;6;16;15;15
	2004	Coalinga; Fire Station	CA346	394110	152	3;3;3;6;6;6;6;6;6;15;15
V	2004	Hollister; City Hall	CA548	172888	152	9;9;9;9;9;9;16;16;16;15;15
	2004	Joaquin Canyon	CA558	531502	63	9;9;9;9;9;11;15;15;15;15;15
	2004	Donna Lee	CA558	531502	63	9;9;9;9;9;11;15;15;15;15;15
	2004	Parkfield;Froelich	CA502	52690.8	150	9;9;9;16;16;16;16;16;16;15;15
VI	2004	Middle Mountain	CA555	49159.6	82	8;8;8;8;8;8;8;15;15;15;15
	2004	Parkfield;Gold Hill	CA505	529707	82	8;8;8;8;8;9;16;15;15;15;15
	2004	Hog Canyon	CA555	286145	82	8;8;8;8;8;8;8;15;15;15;15
	2004	Work Ranch	CA505	686713	82	8;8;8;8;8;9;16;15;15;15;15
	2004	Parkfield;Red Hills	CA505	529707	82	8;8;8;8;8;9;16;15;15;15;15
	2004	Parkfield; UPSAR (1-3,5-13)	CA555	286145	82	8;8;8;8;8;8;8;15;15;15;15

MUID - Map Unit Identification; L1 to L11 are the various layers as prescribed by NRCS [1-Sand, 2-Loamy sand, 3-Sandy loam, 4-Silt loam, 5-Silt, 6-Loam, 7-Sandy clay loam, 8-Silty clay loam, 9-Clay loam, 10-Sandy clay, 11-Silty clay, 12-Clay, 13-Organic materials, 14-Water, 15-Bedrock, 16-Other]

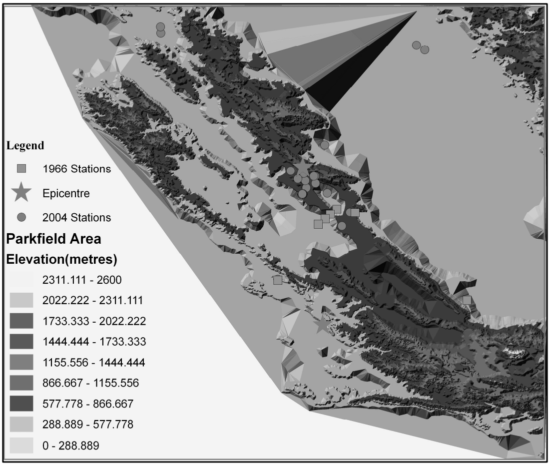

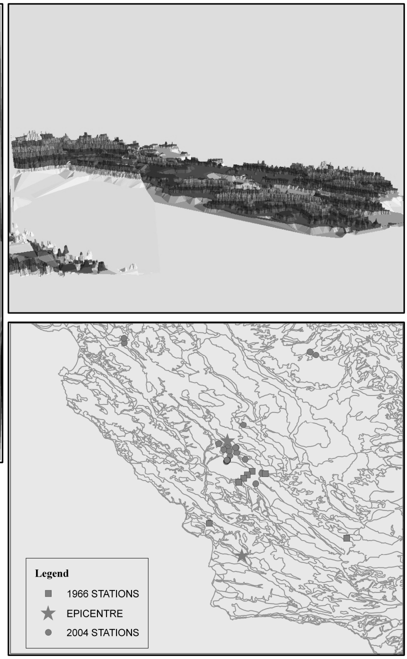

FIG.1. Geospatial Analysis results in the Parkfield Area (9.853698 sq.km. area centered at 120.683251 W, 35.582818 N): Digital Elevation Model showing the station elevations (Left); 3-D Model of the Area (Right Top); Location of stations with soil segmentation map (Right Bottom).

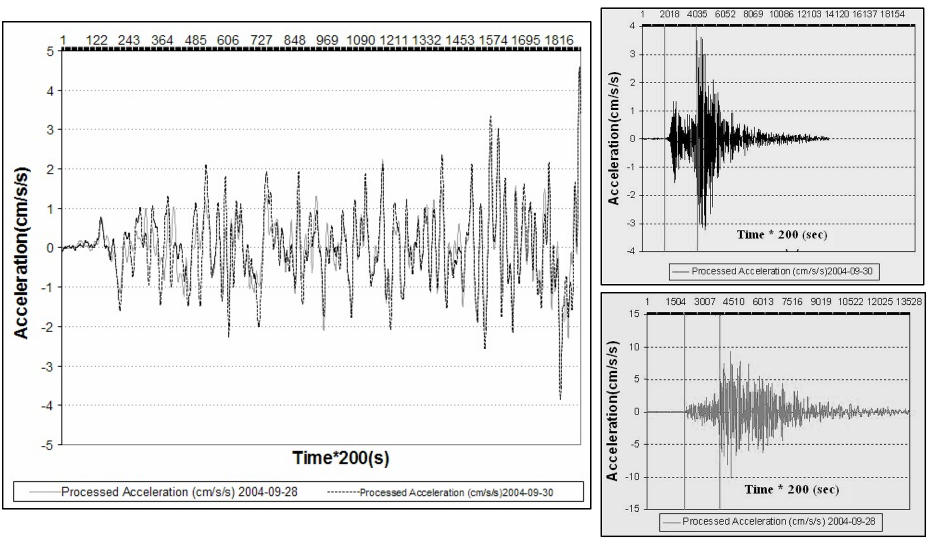

FIG.2.P-S interval similarity for Parkfield 2004 and aftershock (left); P-S wave region of Parkfield aftershock (30/9/04) & Parkfield (28/9/04) between vertical lines (right)

Algorithm

The seismic data identified from Geospatial analysis provides a reliable input for finding the general pattern of the waveform expected at that station from an active seismic zone. This is done using three processes: (1) Clustering (2) Membership Function Development (3) Evolutionary Algorithm. Processes (1) and (2) are performed offline using the data from previous earthquakes and different stations as found out by the geospatial analysis. Process (3) incorporates any undetected earthquake acceleration value in real-time.

(1) Clustering

A graph, specific to an instant from the onset of P waves, is plotted between acceleration and magnitude of the corresponding earthquake. Due to the large number of points, clustering of data is done to make a smooth curve joining them (Fig. 3). The complete process of generalized hierarchical clustering includes: (i) Calculating the distance between all initial clusters. (In this case, the initial clusters will be made up of the individual points). (ii) Fusing the two most similar clusters and recalculating the distances. (iii) Repeating step 2 until all cases are in one cluster.

The clustering algorithm used in the process is Ward's Method wherein cluster membership is assessed by calculating the total sum of squared deviations from the mean of a cluster. The criterion for fusion is that it should produce the smallest possible increase in the error sum of squares with the distances measured using Euclidean method or Pythagoras Theorem. The process is repeated to find curves for every instant in the P-S interval.

(2) Membership Function Development

The graph formed using Clustering Analysis as explained above is fuzzified using Gaussian membership functions (Fig. 3). At a value of acceleration every 0.005 cm/s^2, a Gaussian curve (Eq. 1) pertaining to that acceleration and corresponding magnitude membership grade is drawn. The Gaussian curve is defined as-

$$f(x) = ae^{-(x-b)^2/(2c^2)} \tag{1}$$

Where,

f(x)=Membership function of the incoming signal being a precursor to an Earthquake whose Magnitude equals the Amplitude of Gaussian Curve on the Magnitude Scale.

a=Amplitude of the Gaussian Curve on Membership function scale=1/σ√2Π

b=Incoming acceleration corresponding to amplitude point=μ

c=Standard deviation as calculated from Chebyshev's Theorem=σ

The Gaussian curve is constructed using Chebyshev's theorem (Eq. 2) and an accuracy of 90%**.** The Chebyshev's theorem is applied for each point of time in the region between the onset of p-wave and s-wave-

$$\Pr(|X - \mu| \geq k\sigma) \leq \frac{1}{k^2}. \tag{2}$$

Where,

X = Incoming acceleration corresponds to Earthquake of Magnitude "Y" (Fig. 3)

k = A constant

Thus, the assumption to be used is- "There is *less than or equal to* 10% probability X will fall above or equal to $(\mu+k\sigma)$ or below or equal to $(\mu-k\sigma)$ if it corresponds to the earthquake of the specified magnitude." Thus, $1/k^2=0.1$. The unknown σ is found out by applying Chebyshev's Theorem using the following values-

$X = Max\ (a_i)$; where a_i= acceleration corresponding to the specific earthquake magnitude for the station i (i ε "set of stations of a given type as specified in Table 1")

μ = every incoming acceleration for which membership function is to be found

The membership function for the other points at an interval of 0.005 sec is found out in the same manner. Gaussian membership function is used to provide the scope of including anomalies that may appear in the actual waveform.

(3) Real-Time Processing using an Evolutionary Algorithm

The incoming value of acceleration at that station in real-time is fed as input into these graphs at an instant and earthquake magnitudes and corresponding membership grades are found out. Only those values of magnitude are stored for which the corresponding membership grade is greater than 0.8. This is done again at every instant of time and the cumulative grade of the occurrence of an earthquake of a given magnitude is thus known. $C.G._m=\prod_{t=t1}^{t2} M.G._m$, where m denotes a particular magnitude, $M.G._m$ and $C.G._m$ denote Membership Grade and Cumulative Grade respectively and the product is from t1= onset of P waves to t2=onset of S waves. Depending upon the tolerance and alert level, the threshold value may be set, for which an alarm is sounded if the corresponding membership grade is exceeded. For an undetected earthquake, the various values of acceleration at different time intervals are included in making the smooth curve to provide an evolutionary algorithm. Initial testing of the algorithm in MATLAB 7 on a small dataset of accelerograms from Type II stations (Table 2) gave successful warnings up to a threshold level of 0.73. The algorithm proposed here is largely data dependent and thus the accuracy could not be improved and verified due to the lack of public domain data in the Parkfield. In addition to the need for a large amount of data, fast real-time processing is required.

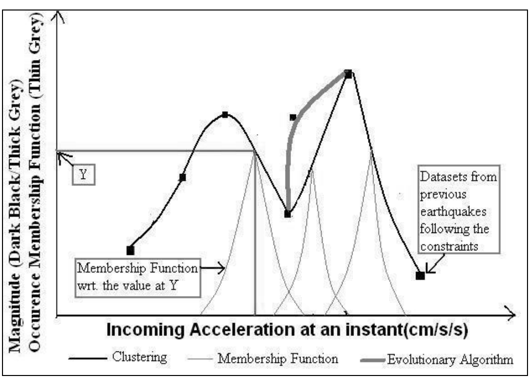

FIG.3. Overview of the Algorithm for a station and at a particular instant.

CONCLUSIONS

The present work aimed to provide a comprehensive warning system based on Fuzzy membership functions to model the data identified through Geospatial Analysis, thus taking the effect of the physics and geology of the earthquake into consideration. The data from Parkfield was analyzed to find station types that would give rise to similar waveforms provided the earthquake parameters were also satisfied. The waveforms for a station that had the records of both the 1966 & 2004 earthquakes showed visual similarity and an average standard deviation of 0.00693728 cm/s^2. The analyzed data was then modeled using a combination of fuzzy logic, clustering algorithms and statistical methods. The algorithm tested on a set of earthquakes in the Parkfield region, gave positive results for a cumulative grade of 0.73. The system is mostly dependent on data and with minor changes, will be applicable in different scenarios.

ACKNOWLEDGMENTS

The author would like to appreciate the various organizations such as COSMOS, USGS, NCSN, CSMIP, NRCS, CGIAR-CSI who provided the data used extensively in this work. The author sincerely acknowledges the encouragement given by the faculty of Civil Engineering at BITS-Pilani, India while carrying out this work. The author is also grateful to the two anonymous reviewers for their helpful remarks that significantly improved the manuscript.

REFERENCES

Bakun, W.H., Aagaard, B., and Dost, B. et al. (2005), "Implications for prediction and hazard assessment from the 2004 Parkfield earthquake". *Nature* 473, 969-974.

Bakun, W.H. & McEvilly, T.V. (1979), "Earthquakes near Parkfield, California; comparing the 1934 and 1966 sequences." *Science* 205, 1375–-1377

Bodiri, B. (2001) "A neural-network model for earthquake occurrence". *Journal of Geodynamics*, (32):289 -310.

Eberhart-Phillips, D. & Michael, A. J. (1993), "Three-dimensional velocity structure, seismicity, and fault structure in the Parkfield region, Central California". *J. Geophys*. Res. 98, 15737–-15758.

Kagan, Y. Y., and D. D. Jackson (2000), "Probabilistic forecasting of earthquakes", *Geophys. J. Int.*, *143*, 438–453.

Normile, D. (2004). "Earthquake Preparedness: Some Countries Are Betting That A Few Seconds Can Save Lives", *Science*, Vol. 306. no. 5705, p. 2178 - 2179

Shaw, B.E., Carlson, J.M., Langer, J.S., (1992). "Patterns of seismic activity preceding large earthquakes". *J. Geophys.* Res. 97, 479–488.

Wallace, R.E., Davis, J.F., McNally, K.C. (1984). "Terms for expressing earthquake potential, prediction, and probability." *Bull. Seism. Soc.* Am. 74, 1819–1825.

Wyss, M., Burford, R.O., (1987). "Occurrence of a predicted earthquake on the San Andreas fault". *Nature* 329, 323–325.

Wyss, M. (2001), "Why is earthquake prediction research not progressing faster?", *Tectonophysics*, 338, p. 217–223.

Zedeh, L.A. (1965). "Fuzzy sets", *Information and control* 8, 338-353.

Subject Index

Page number refers to first page of paper

Author Index

Page number refers to first page of paper